UVIC - McPHERSON
3 2775 90382609 6

TREATISE ON SOLID STATE CHEMISTRY

Volume 3
Crystalline and Noncrystalline Solids

Digitized by the Internet Archive
in 2022 with funding from
Kahle/Austin Foundation

https://archive.org/details/treatiseonsolids0003hann

TREATISE ON SOLID STATE CHEMISTRY

Volume 3
Crystalline and Noncrystalline Solids

TREATISE ON SOLID STATE CHEMISTRY

- Volume 1 • The Chemical Structure of Solids
- Volume 2 • Defects in Solids
- Volume 3 • Crystalline and Noncrystalline Solids
- Volume 4 • Reactivity of Solids
- Volume 5 • Changes of State
- Volume 6A • Surfaces I
- Volume 6B • Surfaces II

TREATISE ON SOLID STATE CHEMISTRY

Volume 3

Crystalline and Noncrystalline Solids

Edited by

N. B. Hannay

Vice President
Research and Patents
Bell Laboratories
Murray Hill, New Jersey

PLENUM PRESS • NEW YORK-LONDON

H35
V.3

Library of Congress Cataloging in Publication Data

Hannay, Norman Bruce, 1921-
Crystalline and noncrystalline solids.

(His Treatise on solid state chemistry; v. 3)
Includes bibliographical references and index. 1. Crystallography. 2. Solids. I. Title.
QD478.H35 vol. 3 [QD905.2] 541.'042'1s [548'.8]
ISBN 0-306-35053-X 76-18863

Seven-volume set: ISBN 0-306-35050-5

© 1976 Bell Telephone Laboratories, Incorporated

Published by Plenum Press, New York
A Division of Plenum Publishing Corporation
227 West 17th Street, New York, N.Y. 10011

All rights reserved

No part of this book may be reproduced, stored in a retrieval system, or transmitted, in any form or by any means, electronic, mechanical, photocopying, microfilming, recording, or otherwise, without written permission from the Publisher

Printed in the United States of America

Foreword

The last quarter-century has been marked by the extremely rapid growth of the solid-state sciences. They include what is now the largest subfield of physics, and the materials engineering sciences have likewise flourished. And, playing an active role throughout this vast area of science and engineering have been very large numbers of chemists. Yet, even though the role of chemistry in the solid-state sciences has been a vital one and the solid-state sciences have, in turn, made enormous contributions to chemical thought, solid-state chemistry has not been recognized by the general body of chemists as a major subfield of chemistry. Solid-state chemistry is not even well defined as to content. Some, for example, would have it include only the quantum chemistry of solids and would reject thermodynamics and phase equilibria; this is nonsense. Solid-state chemistry has many facets, and one of the purposes of this *Treatise* is to help define the field.

Perhaps the most general characteristic of solid-state chemistry, and one which helps differentiate it from solid-state physics, is its focus on the chemical composition and atomic configuration of real solids and on the relationship of composition and structure to the chemical and physical properties of the solid. Real solids are usually extremely complex and exhibit almost infinite variety in their compositional and structural features.

Chemistry has never hesitated about the role of applied science, and solid-state chemistry is no exception. Hence, we have chosen to include in the field not only basic science but also the more fundamental aspects of the materials engineering sciences.

The central theme of the *Treatise* is the exposition of unifying principles in the chemistry, physical chemistry, and chemical physics of solids. Examples are provided only to illustrate these principles. It has, throughout, a chemical viewpoint; there is, perforce, substantial overlap with some areas of solid-

Contents of Volume 3

Chapter 1
Metastable Phases Produced by Rapid Quenching from the Vapor and the Liquid **1**
A. K. Sinha, B. C. Giessen, and D. E. Polk

1. Introduction 1
   1.1. Definition 1
   1.2. Kinetic Considerations 2
   1.3. Free Energy and Phase Diagram Considerations 3
   1.4. Energetic Considerations 8
   1.5. Structural Considerations 9
   1.6. Classification of Metastable Phases and Outline of Chapter 10
2. Experimental Techniques 11
   2.1. Evaporation 11
   2.2. Sputtering 13
   2.3. Electrodeposition 16
   2.4. Rapid Liquid Quenching 17
3. Amorphous Phases 19
   3.1. Elemental Amorphous Phases 20
   3.2. Alloy Amorphous Phases 24
   3.3. Structural Analysis 26
   3.4. Electrical Properties 30
   3.5. Magnetic Properties 32
   3.6. Transformation Kinetics 35

4. Metastable Elemental and Near-Elemental Crystalline Phases . . 36
4.1. Topologically Close-Packed Structures 36
4.2. Spherically Close-Packed Structures 44
5. Metastable Crystalline Intermediate Alloy Phases 48
5.1. Occurrence and Study of Intermediate Alloy Phases 48
5.2. Structures and Crystal Chemistry of Metastable Intermediate Phases 51
5.3. Further Structural Relationships 57
6. Supersaturated Terminal or Intermediate Solid Solutions 61
6.1. Occurrence and Study of Extended Solid Solutions 61
6.2. Crystal Chemistry and Properties of Metastable Solid Solutions 64
7. Concluding Remarks 75
7.1. Significance of Research on Metastable Phases 75
7.2. Review of Metastable Phase Formation 76
7.3. Alternate Methods and Products of Metastable Phase Preparation 77
7.4. Present and Suggested Applications of Metastable Phases 78
7.5. Areas for Further Research 79
Acknowledgment 80
References 81

Chapter 2
Inclusion Compounds **89**
F. R. Gamble and T. H. Geballe

1. Introduction 89
2. Metallic Clathrates 90
2.1. Electrical Properties 94
2.2. Low-Temperature Heat Capacity 94
3. Boron Compounds 95
3.1. Icosahedral Grouping 95
3.2. Octahedral Grouping 96
4. Graphite Intercalation Compounds 106
4.1. Introduction 106
4.2. Compounds with Electron Donors 107
4.3. Compounds with Electron Acceptors 111
4.4. Order–Disorder Transitions 111
4.5. Reaction Mechanisms 112
4.6. Fermi Surface and Transport Measurements 115
4.7. Superconductivity 120
4.8. Spin Resonance 120
4.9. Magnetic Properties 121

5. Chalcogenide Intercalation Compounds 124
5.1. The Layered Chalcogenides 124
5.2. The Intercalation Compounds of Layered Dichalcogenides and Elemental Metals 127
5.3. Molecular Intercalates 134
6. Layered Halide and Similar Intercalation Compounds 144
7. Tungsten Bronzes and Similar Compounds 148
Epilogue 155
References 155

Chapter 3
The Structural Chemistry of Some Complex Oxides: Ordered and Disordered Extended Defects **167**
LeRoy Eyring and Leung-Tak Tai

1. Introduction 167
1.1. Types of Defects in Crystals 167
1.2. Methods of Observing Extended Defects 170
2. Complex Structures Based on Crystallographic Shear 173
2.1. Introduction 173
2.2. Compounds Containing One-Dimensional Crystallographic Shear 183
2.3. Compounds Containing Two-Dimensional Crystallographic Shear 201
2.4. Disorder in Block Structures 210
2.5. Disorder in Systems Related to the Tetragonal Tungsten Bronze 216
3. The Fluorite-Related Structures 223
3.1. Introduction 223
3.2. The Relationship between the Fluorite and Other Structures 227
3.3. Fluorite-Related Phases with Excess Oxygen 229
3.4. The Fluorite-Related Homologous Series 231
4. Extended Defects in the NaCl Structure Type 238
4.1. Nonstoichiometry and Defect Structure of Titanium and Vanadium Monoxides 238
4.2. The Defect Structure of $Fe_{1-x}O$ 240
5. Stoichiometry and Structure of Highly Conducting Solid Electrolytes 242
5.1. The Structure of Calcia-Stabilized Zirconia 242
5.2. The Structure of Some Beta-Aluminas 244
5.3. The Structure of Halide and Chalcogenide Solid Electrolytes 246
Acknowledgment 248
References 249

Chapter 4
Interstitial Phases **253**
A. L. Bowman and N. H. Krikorian

1. Introduction 253
2. Crystallography of Interstitial Phases 255
   2.1. Geometrical Basis of Close Packing 256
   2.2. The Radius Ratio 258
   2.3. Crystal Structures of Interstitial Phases 259
   2.4. Polymorphism in Interstitial Compounds 266
   2.5. Ternary Interstitial Phases 267
3. Properties of Interstitial Phases 268
   3.1. Phase Diagrams 268
   3.2. Melting Points 272
   3.3. Thermodynamic Properties 273
   3.4. Hardness 276
   3.5. Thermal Expansion 279
   3.6. Electrical Resistivity 280
   3.7. Superconductivity 281
   3.8. Diffusion 283
   3.9. Bonding 283
4. Summary 284
   References 285

Chapter 5
Inorganic Amorphous Solids and Glass-Ceramic Materials **293**
D. R. Uhlmann

1. Introduction 293
2. Atomic Structure of Glasses 295
   2.1. Models of Glass Structure 296
   2.2. Structure of Oxide Glasses 298
   2.3. Structure of Nonoxide Glasses 303
   2.4. Effects of Pressure, Thermal History, and Irradiation 305
3. Submicrostructure of Glasses 306
   3.1. Introduction 306
   3.2. Spinodal Decomposition vs. Nucleation Growth Coalescence 311
4. Electronic Structure of Glasses 316
   4.1. Introduction 316
   4.2. Density of States 316
5. Glass Formation 318
6. Macrostructure of Glasses 322

7. Glass-Ceramic Materials 325
7.1. Commercial Glass-Ceramic Systems 326
7.2. Microstructural Features and Properties 328
8. Concluding Discussion 329
References 330

Chapter 6
The Morphology of Crystalline Synthetic Polymers **335**
F. Khoury and E. Passaglia

1. Introduction 335
1.1. General and Historical 335
1.2. Scope of the Chapter 337
2. Crystallinity in Polymers 338
2.1. Requisites for Crystallization 338
2.2. Polymer Crystal Structures 347
2.3. Degree of Crystallinity 355
3. The Morphology of Polymers Crystallized from Solution 357
3.1. Preliminary Remarks 357
3.2. Crystallization Procedures, with Comments on Polydispersity in the Molecular Weight of Polymers and the Incidence of Fractionation during Crystallization 358
3.3. Optical and Electron Microscopy, with Comments on the Susceptibility of Polymers to Electron Irradiation 359
3.4. Polymer Crystals 362
4. The Morphology of Polymers Crystallized from the Melt 441
4.1. Preliminary Remarks 441
4.2. General Comments on Spherulites and Their Structures 442
4.3. The Fine Structure of Polymer Spherulites 445
4.4. Crystallization under Pressure 476
5. Concluding Remarks 480
Acknowledgments 481
References 481

Chapter 7
The Rate of Crystallization of Linear Polymers with Chain Folding **497**
John D. Hoffman, G. Thomas Davis, and John I. Lauritzen, Jr.

1. Introduction 497
1.1. Aims and Objectives 497
1.2. Nature of Crystallizable Linear Macromolecules 500
1.3. Chain-Folded Crystals from Bulk and Dilute Solutions 503

2. Thermodynamic Preliminaries and Work of Chain Folding 528
2.1. Fold Surface Free Energies from Melting Point and Crystal Thickness Data. 528
2.2. Melting Behavior 531
2.3. Interpretation of σ_e in Terms of Fold Structure 537
2.4. The Driving Force for Crystallization in Strongly Subcooled Systems 540
3. Theory of Growth and Lamellar Thickness 541
3.1. Approach and Model 541
3.2. Calculation of the Total Flux 545
3.3. Initial Lamellar Thickness 548
3.4. Growth Rate 553
3.5. Interpretation of ψ 561
3.6. Effect of Chain Ends 564
4. Comparison of Theory and Experiment 565
4.1. Objectives 565
4.2. Growth Rate versus Crystallization Temperature Curves . 566
4.3. Polymers Where Data Allow Test of Expressions for Both Growth Rate and Lamellar Thickness 574
4.4. The Fold Period as a Function of the Undercooling in Dilute Solutions: Verification of $l_g^* = (C_1/\Delta T) + C_2$ 584
4.5. Generalized Treatment to Obtain Work of Chain Folding from K_g 587
5. Theories with Fluctuations of Fold Period 592
6. Homogeneous Nucleation in Polymers 597
Acknowledgments 604
Note Added in Proof 605
References 605

Chapter 8
Organic Molecular Crystals: Anthracene **615**
R. G. Kepler

1. Introduction 615
2. The Molecule 618
3. The Crystal 620
4. Optical Absorption 623
4.1. Singlet Excitons 624
4.2. Triplet Excitons 627
5. Fluorescence 629
6. Energy Transport 631
6.1. Singlet Excitons 632
6.2. Triplet Excitons 638

7. Electrons and Holes 645
7.1. Electron and Hole Transport 645
7.2. Electron and Hole Generation 651
8. Theory 661
8.1. Excitons 661
8.2. Electrons and Holes 665
References 667

Chapter 9
Organic Molecular Crystals: Charge-Transfer Complexes **679**
Zoltán G. Soos and Douglas J. Klein

1. Introduction 679
1.1. Contrast of Solution and Solid-State Complexes 679
1.2. Molecular-Exciton Approach 681
1.3. π-Molecular Ion-Radical Solids 683
1.4. Hubbard Models and CT Crystals 685
1.5. Relation to Other Work: Scope of the Review 687
2. Development of Phenomenological Theory 690
2.1. The Ion-Radical Dimer 690
2.2. Intermolecular Forces 693
2.3. Orthonormal Basis for Dimers 696
2.4. Site Representation for Molecular Crystals 697
2.5. Minimum Basis for CT Crystals 699
2.6. Fermion Representation of $\mathscr{H}$ 702
2.7. Matrix Elements 703
2.8. Charge-Transfer Hamiltonian 707
3. Classification of π-Molecular CT Crystals 708
3.1. Structural Variations of Molecular Stacks 708
3.2. Collective Physical Properties 711
3.3. Mixed, Simple Stacks: Neutral or Ionic 713
3.4. Crystals of Dimers and Complex CT Crystals 717
3.5. FR Crystals with Simple, Regular Stacks 720
3.6. Segregated Simple Alternating Stacks 723
3.7. Complex, Regular FR Stacks: Fractional Charges 725
3.8. Complex, Segregated, Alternating FR Stacks 727
4. Electronic Properties of Ion-Radical Crystals 729
4.1. Excitations of the CT Hamiltonian 729
4.2. Optical Properties: CT Bands 732
4.3. Electric Conduction 734
4.4. Magnetic Properties: Antiferromagnetic Exchange 736
4.5. One-Dimensionality and Spin Dynamics 740

5. Quantum Computations 743
5.1. Approximate Molecular Computations 743
5.2. Crystal-Perturbed States 745
5.3. Improved Matrix Elements 749
5.4. Hubbard and Heisenberg Models 753
5.5. Hubbard Model Computations 755
6. Conclusions 757
Acknowledgments 758
References 759

Index **769**

1

Metastable Phases Produced by Rapid Quenching from the Vapor and the Liquid

A. K. Sinha
Bell Laboratories
Murray Hill, New Jersey

and

B. C. Giessen and D. E. Polk
Department of Chemistry and
*Institute of Chemical Analysis, Applications and Forensic Science**
Northeastern University
Boston, Massachusetts

1. Introduction

1.1. Definition

Though some metastable phases are obtained readily, e.g., common inorganic oxide glasses or some phases present in many varieties of steels, the phases of interest here are those which can be obtained only through the use of high effective quenching rates from the vapor or liquid phase. This includes many thin-film phases obtained by evaporation or sputtering and not-so-thin film phases obtained by rapid cooling from the melt and by electrodeposition from a liquid electrolyte. In the case of evaporation or sputtering of a metal, the substrate is exposed to a gaseous ambient containing metal as well as nonmetal atoms, whereas in the case of rapid quenching from the melt and electrodeposition, the ambient of the substrate is made up of a crystallographically uncorrelated assembly of atoms in the liquid phase or in solution.

* Communication No. 9.

1.2. Kinetic Considerations

The above-mentioned thin-film preparation techniques employ an atom-by-atom deposition process; this, as well as rapid liquid quenching, can impose severe kinetic limitations on attaining thermodynamic equilibrium in as-prepared materials. Using vapor quenching methods as an example, one may state that, if there were no sources of thermal, kinetic, electrostatic, lattice, or other energies available at the substrate and a high sticking coefficient were assumed, the condensed phase at the substrate would, from statistical considerations, have an amorphous structure. Such an amorphous film would lack any long-range crystallographic order but would possess a pair correlation function qualitatively similar to that[1] for random packing of hard spheres.

Moreover, this amorphous film would be in a state of high free energy, containing relatively large lattice and surface energy terms. The transition from the amorphous phase to the low-energy crystalline state is an irreversible and usually thermally activated process. On the basis of available experimental data on irreversible phase transformations, it can be concluded that if the formation of a metastable crystalline phase involves a smaller activation energy (often because of relatively short-range atomic movements) than the transition to the equilibrium phase, this second metastable phase would represent an intermediate stage prior to transformation to the ultimate equilibrium phase or phases having the lowest free energy.

This situation is schematically illustrated[2] in the form of a diagram of free energy vs. configurational coordinates (Figure 1); Figure 1 shows the thermal activation energies ε_1 and ε_2 ($\varepsilon_1 < \varepsilon_2$) for the transformations from state A $\rightarrow$ B and A $\rightarrow$ C. If we assume state C to represent the equilibrium state and A and B to represent metastable forms, it may be seen how the approach toward equilibrium may proceed along A $\rightarrow$ B $\rightarrow$ C. This example can be made specific, if, e.g., C represents bcc (A2 type) W and A represents amorphous W, where B (or B_1, B_2, B_3, ...) can represent metastable fcc (A1 type) W or A15-Cr_3Si type W ("β-W"). A supersaturated solution of Ar, O_2, N_2, etc., in bcc W may also occur.

Figure 1 also helps to clarify the important distinction between a metastable and an unstable state. Whereas the former lies in the region of a local free energy minimum, the latter lies in positions of Figure 1 where the free energy decreases on going in at least one direction (the direction of transformation); constrained equilibria

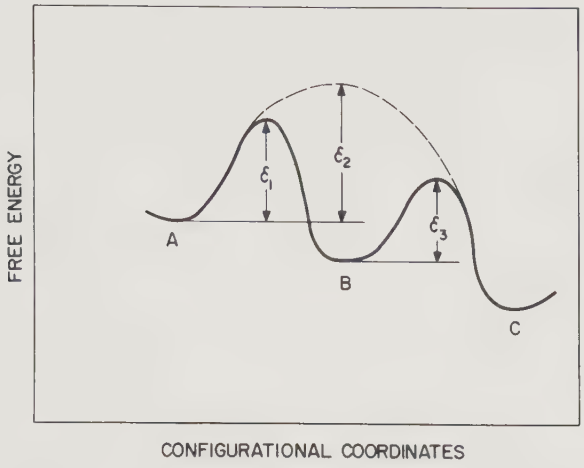

Fig. 1. Schematic variation of free energy vs. configurational coordinates of a hypothetical single-component material system involving states A, B, and C.

involving metastable phases and their transformation are discussed in Ref. 3.

1.3. Free Energy and Phase Diagram Considerations

For one-component systems at constant pressures the metastable phases are simply represented by free energy diagrams of the type

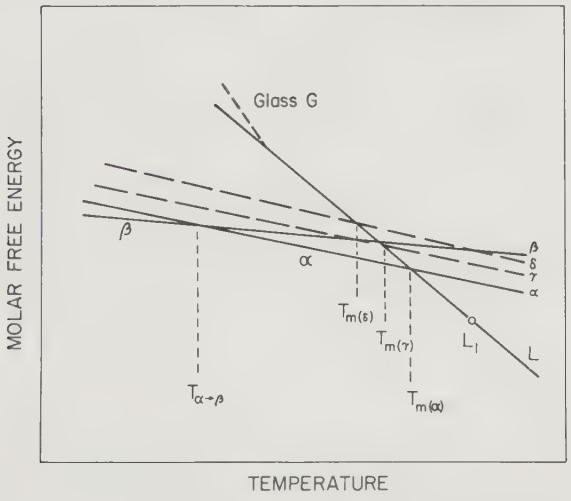

Fig. 2. Schematic representation of the free energies of phases present in a hypothetical one-component system as a function of temperature at constant pressure.

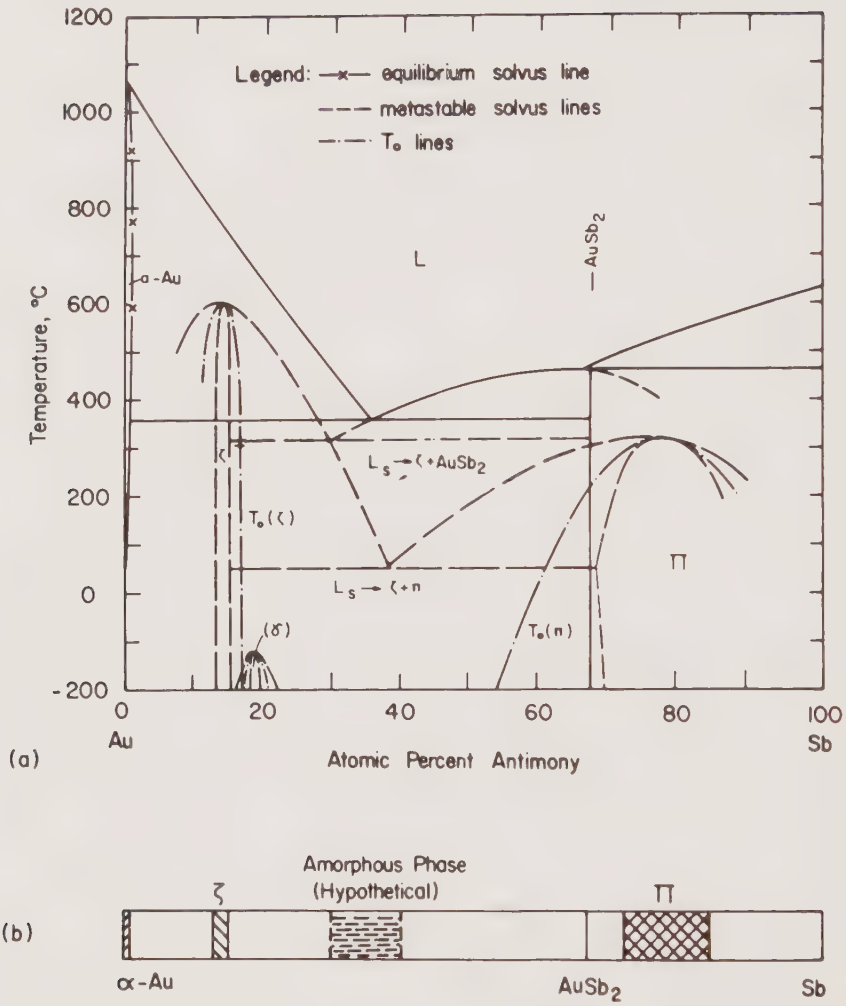

Fig. 3. The system Au–Sb: (a) stable and metastable phase diagram; —×—, equilibrium solvus lines; — — —, metastable solvus lines; —·—, T_0 lines (see page 7); (b) quenched-phase plot; (c) hypothetical free energy diagram at $T \sim 250°C$; (d) ΔT_s–x diagram showing the role of supercooling in metastable phase formation.[4]

shown in Figure 2.[3] Here, stable modifications α (solid), β (solid), and L (liquid) are indicated, as well as metastable phases γ and δ and a glass G. Upon quenching, the state point of the system moves from its original position, such as L_1 at temperature $T(L_1)$, along $G(L)$. The γ phase will form from the liquid only if the latter can be super-

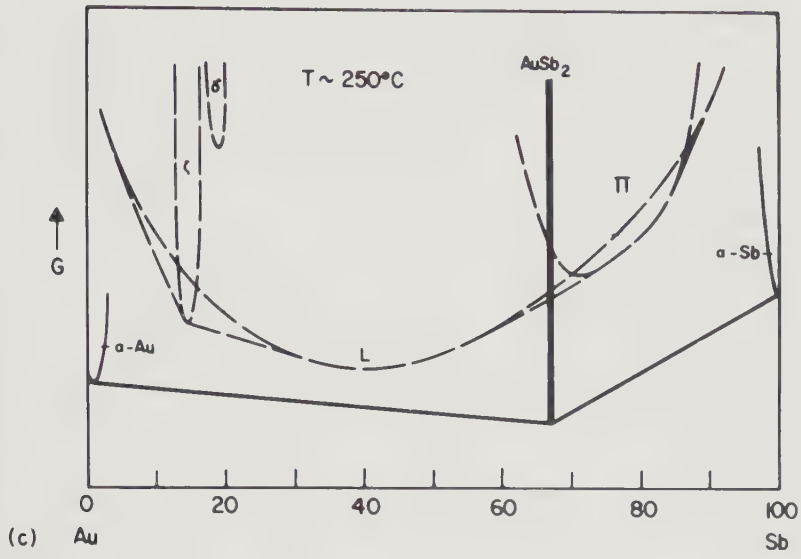

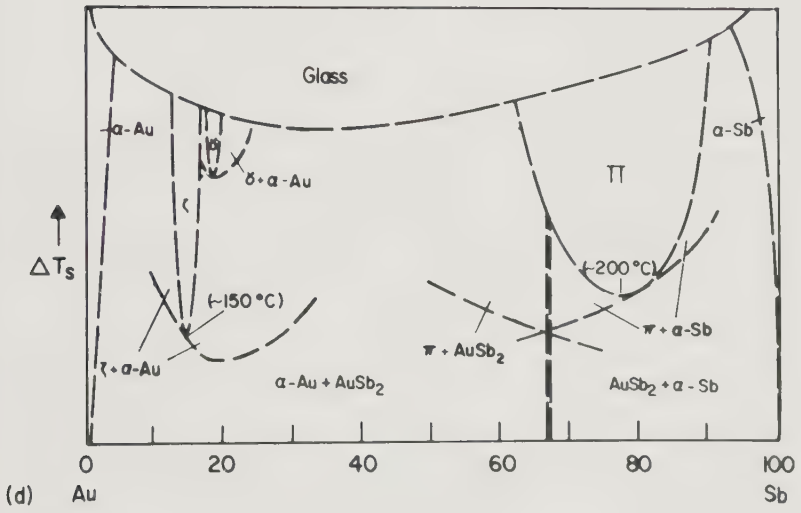

cooled below $T_m(\alpha)$, the melting temperature of α, down to the metastable melting temperature of γ, $T_m(\gamma)$; δ forms only upon supercooling of the liquid below $T_m(\delta)$. (It may be mentioned that the activation energy diagram, Figure 1, is based on a vertical constant-temperature section through the free energy diagram, Figure 2.) Upon vapor

deposition, the state curve of the system begins the condensation process at a point corresponding to the vapor free energy. Cooling and condensation of the vapor may then lead to crystallization in a sequence similar to that for nonequilibrium solidification from the melt; in either case, lack of mobility (high viscosity) of the condensed phase may cause equilibration to be arrested at intermediate steps, such as G, δ, γ, or β.

For a binary system, some thermal parameters pertaining to rapid quenching from the melt can be represented by the diagrams given in Figure 3.[4] Figure 3(a) shows the constitution diagram of the Au–Sb system, which has been chosen as an example because thermal data on the nonequilibrium phases ζ and π are available from calorimetric measurements.[5] Metastable congruent melting points for ζ and π are indicated; the corresponding phase transitions would be observed if the L–ζ or L–π equilibria were constrained to exclude the intervention[3] of the stable phases Au, $AuSb_2$, and Sb. A schematic representation of the stable and metastable phases present after splat-cooling is shown in the quenched-phase plot, Figure 3(b). Figure 3(c) shows the hypothetical free energy diagram for Au–Sb at $T \sim 250°C$, which indicates the possibility for the formation of ζ and π from the supercooled melt. The free-energy curve for another crystal-chemically possible alloy phase (here, γ with a cubic γ-brass type structure) at higher G values is indicated. In Figure 3(d), the observed and unobserved Au–Sb phases are represented in terms of the minimum supercooling temperature ΔT_s thermodynamically required for their retention. In systems where higher degrees of supercooling are experimentally possible, the glass region may be reached as shown.

A diagram qualitatively relating the observed metastable phases to the measured or estimated cooling rate $\dot{T}$ has also been used.[6] Since supercooling temperature ΔT_s and $\dot{T}$ are related,[7] the $\dot{T}$ plot incorporates the results of the ΔT_s plot, while also indicating the presence of the conditions required for retention of the metastable phases during the subsequent cooling in the solid state.

The extent of metastable solid solution formation in eutectic systems is treated next. Thermodynamically, this effect also depends on features of the constitution diagram, Figure 4(a), and the corresponding free energy diagram, Figure 4(b). Details of the interpretation of these diagrams are given in Refs. 4 and 7; here only some pertinent points will be discussed. It is a necessary condition for the formation of a complete solid solution that the free energy curve of the liquid which has been supercooled to the actual crystallization

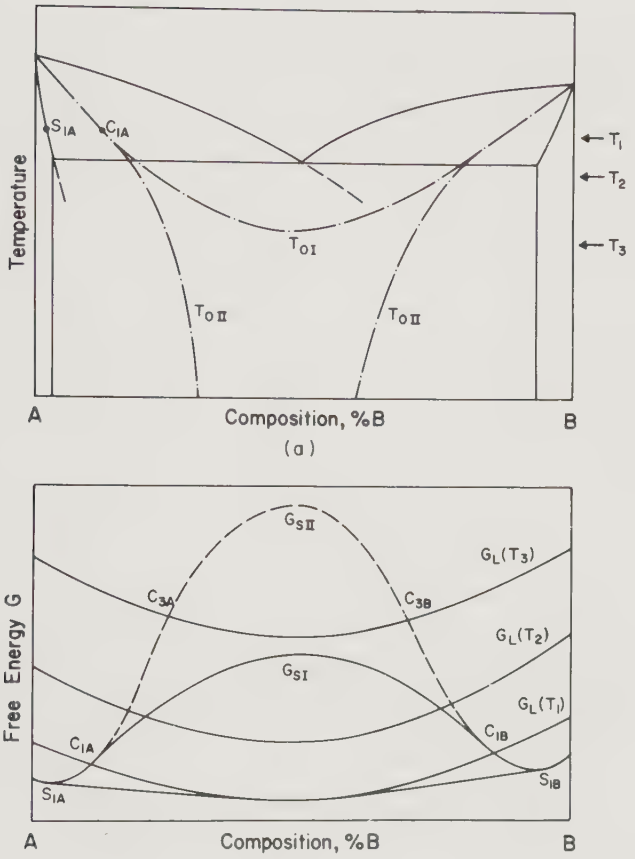

Fig. 4. Hypothetical eutectic binary system: (a) phase diagram indicating role of the parameter T_0; (b) free energy diagram for three temperatures $T_{1,2,3}$ and two solid solutions with different positive deviation from Raoult's law.[4]

temperature lies above the free energy curve of the metastable solid solutions over the total concentration range, as indicated in Figure 4(b) for curves $G_L(T_3)$ and G_{SI}. Of the cases shown in Figure 4, this is the only one in which the complete solid solution can form; greater instability (higher free energy) of the intermediate solid solution (e.g., G_{SII}) will lead to the formation of two terminal crystalline solid solutions even upon quenching to 0°K. (Alternate phases that may form instead of S include the amorphous solid or other metastable intermediate phases of different structure, see Figure 3.) It will be seen from Figure 4(b) that complete metastable solid solutions cannot be expected to form if the curve T_0 connecting the free energy crossover points, indicated in Figure 4(a), is discontinuous and intersects the

composition axis at sufficiently low temperatures. The constitutional requirement of a continuous T_0 curve is apparently not met in the Cd–Zn system, in which only limited terminal solid solubility can be obtained by rapid liquid quenching.[3] The interesting question whether complete metastable solid solutions could be formed and retained in systems of this type by vapor deposition has not yet been decided experimentally. While it may be possible to produce metastable solid solutions of relatively high energy if the impinging vapor atoms have higher energies than G_{SII}, it is not certain that their subsequent decomposition can be prevented; conversely, the high cooling rates and low substrate temperatures required to retain a metastable crystalline phase once it has formed may prevent its initial crystallization, leading to glass formation instead.

1.4. Energetic Considerations

A straightforward calculation[3] based on a Carnot cycle using observed supercooling temperatures shows that it is generally impossible to produce a metastable crystalline phase from the melt having an excess free energy relative to the equilibrium form larger than $\Delta F^m_{\text{exc}} \sim 0.3\,\Delta H_m$, while for the vapor quenching process the corresponding maximal value is $\Delta F^v_{\text{exc}} \sim \Delta H_v$, if the substrate is kept at very low temperatures. Here, ΔH_m and ΔH_v are the melting and vaporization enthalpies, respectively; hence, $\Delta F^v_{\text{exc}} \sim 30\,\Delta F^m_{\text{exc}}$, making vapor condensation a potentially much more powerful method for crystalline phase retention than melt solidification.

The data are put in perspective by considering that the energy differences, where known, between various metastable and stable phases are relatively small (typically 10–100 meV) compared to the bonding energies of solid metals (a few eV). (It is, of course, the relatively small magnitude of the energy differences of competing structures which forms the principal obstacle to theoretical stability calculations from first principles, e.g., by the pseudopotential method,[8] since many small corrections to large energy terms must be considered.) Kaufman[9] has derived thermodynamically a series of lattice stability parameters for fcc (A1), bcc (A2), and hcp (A3) modifications of several metals. Table 1 shows his results in the form of excess free energies in meV at 300°K of various hypothetical modifications over those of the stable allotropes for many metals. Furthermore, it has been found in a limited number of cases that the energy difference between an amorphous and the corresponding

TABLE 1
Relative Free Energies of Various Polymorphs of Some Common Metals*

Metal	Free energy relative to that of stable allotrope, meV (at 300°K)		
	bcc	fcc	hcp
Ti/Zr	33.0	34.7	0.0
Hf	67.7	34.7	0.0
V/Nb/Ta	0.0	104.3	75.5
Cr/Mo/W	0.0	110.4	86.8
Tc/Re	22.6	14.8	0.0
Ru/Os	59.0	15.6	0.0
Rh/Ir	68.3	0.0	8.5
Ni/Pd/Pt	39.5	0.0	14.7
Cu/Ag/Au	34.3	0.0	10.4
Zn/Cd	22.6	14.3	0.0

* Based on thermodynamic calculations by Kaufman.[9]

crystalline phase is also rather small at ~ 1 kcal/mole (~ 43 meV).[10] These small energy differences should be borne in mind when considering the influence of various processing variables in stabilizing metastable structures.

1.5. Structural Considerations

Of the metastable phases discussed here (amorphous and crystalline), the amorphous phases represent the greatest departure from the equilibrium structure. Interestingly, some of the structural characteristics of dense random packing, namely, a high atomic coordination (with the coordination number CN $\geq$ 12) and a preponderance of local atomic arrangements having fivefold symmetry,[1,11–13] are shared by topologically close-packed structures.[14] The fivefold symmetry of an icosahedron precludes a crystal lattice based on this polyhedron alone. However, the importance of icosahedral grouping of atoms in early stages of film formation is clearly borne out by calculations[15] of relative values of surface energy and bond energy for various types of atomic clusters.

Experimental observations have made clear the importance of alloy composition in determining whether or not a metastable phase is obtained. Small amounts of trapped impurities may lead to the appearance of a different phase; this effect is especially important for

nominally pure metals prepared by vapor deposition. Small departures from the stoichiometry of an intermetallic phase may lead to different structures. Metastable phases are formed most readily at compositions for which the equilibrium phase has a complex crystal structure or for compositions which have two or more phases in equilibrium. While the latter observation may be explained kinetically, the former appears to relate to the deeper relationship between topologically close packed or other complex phases and amorphous phases suggested above.

Whereas dense, randomly packed, amorphous structures possess some relatively large interstitial sites[16] which can accommodate alloy components of small size, the topologically close-packed structures contain exclusively tetrahedral interstices which are relatively small. The spherically close-packed structures generally possess a greater degree of crystallographic symmetry and a smaller number of nonequivalent atomic sites than the topologically close-packed structures; however, they also contain a large number of relatively large octahedral interstices which are able to accommodate appreciable amounts of suitable impurities;[17] this geometric argument is one of the reasons why carbon has a much greater solubility in fcc γ-Fe than it does in bcc α-Fe. This is equivalent to saying that C-like interstitial impurity atoms may tend to stabilize the fcc A1-type structure over the bcc A2-type structure. Such impurity stabilization is a possible reason for stabilization of abnormal spherically close-packed structures in normally bcc A2-type metals discussed in detail below. Another well-documented reason for abnormal structure formation valid for some very thin films involves stabilization by interaction with the substrate lattice (pseudomorphism). It is true, however, that a majority of the thin films prepared possess the normal crystal structure. Vapor-condensed films frequently contain an abnormally large concentration of gaseous or metallic impurities, well beyond the equilibrium solubility limits. Therefore, strictly speaking, these films are also metastable.

1.6. Classification of Metastable Phases and Outline of Chapter

For the purposes of this chapter, the metastable phases will be classified on the basis of the atomic arrangement, if it is not that of the equilibrium phase, or on the basis of the constitution if the crystal structure corresponds to that of an equilibrium phase. The various metastable phases will be discussed in the following order: amorphous structures, elemental and near-elemental crystalline phases, including

topologically close-packed and spherically close-packed structures, metastable crystalline intermediate phases, and supersaturated terminal solid solutions with the equilibrium crystal structure.

Since the formation and subsequent stability of metastable phases critically depends upon the exact preparation technique employed, a description of these will precede that of the actual metastable phases. In reviewing the thin-film deposition techniques, it should be emphasized that contaminants are generally present in the usual bell-jar environment due to, e.g., desorption and/or backstreaming effects (of hydrocarbons); the resulting impurities in the thin film can alter the chemical constitution from the presumed one. In reading the literature, it is often difficult to assess the influence of this effect on the observation of anomalous phases. Similar limitations should be borne in mind when reviewing anomalous phases produced by electrodeposition.

The field of metastable phases is still in a stage of active growth, as it is being realized that a number of materials displaying unusual properties of condensed matter can be prepared only in a non-equilibrium state. The total literature is far too large to be presented here; however, helpful review articles on certain topics of this chapter can be given. These include, for metastable phases produced from the liquid, Refs. 4, 7, and 18–23, and for vapor-deposited phases, Refs. 24–26.

2. Experimental Techniques

2.1. Evaporation

Vacuum evaporation[24,25] offers a simple and direct means of metal-film deposition. The source material is vaporized by heating under vacuum; the metal atoms in the vapor stream travel to the substrates where they condense along with other impurity atoms present in the vapor stream.

The thermal energy needed for evaporation is commonly obtained by means of resistive heating of a W filament or of a strip metal crucible; alternatively an electron-beam or a laser source might be employed. In addition to the heating source, most evaporators are equipped with a shutter and a substrate holder with provision for external heating or cooling of the substrates during deposition (Figure 5). A quartz crystal oscillator is generally used to monitor the thickness of the film during deposition. High purity of the source material and proper out-gassing with shutter in position prior to deposition are

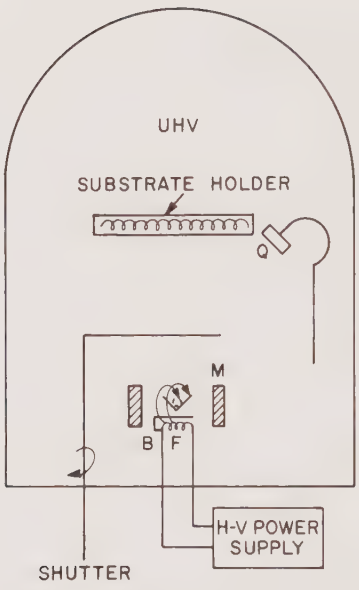

Fig. 5. Conventional electron-beam evaporation station.[27] UHV, ultra high vacuum; Q, quartz crystal thickness monitor; M, permanent magnets in the electron gun; B, beam former; F, filament.

necessary in order to ensure purity in the deposited film. Alloy films are best deposited by simultaneous evaporation from independently controlled and monitored multiple sources. Flash evaporation, or electron beam evaporation from a single alloy source, also has been used in a limited number of cases; however, the latter method suffers from the limitation that fractionation of the alloy components can lead to films which have different composition from the source.

There are three chief process variables which control the degree of impurity incorporation and the extent of microstructural perfection in the metal film.[27,28] They are: the ambient pressure (usually kept better than 10^{-5} Torr), the deposition rate (power, and substrate-to-source separation), and the substrate temperature.

The background pressure P results from a balance between the ultimate pumping speed, and effects of desorption (from walls and fixtures of the evaporation chamber) and backstreaming (of hydrocarbons in poorly trapped oil-pumped systems). It determines the impingement rate (and the mean free path) of impurity molecules

such as O_2, N_2, H_2O, and C_xH_y at the substrate. According to the kinetic theory, the arrival rate v_i (in atoms cm^{-2} sec^{-1}) at the substrate of gaseous atoms is

$$v_i = 3.513 \times 10^{22} P_i/(TM_i)^{1/2}$$

where P_i is the partial pressure in Torr of the gas molecules, M_i is the molecular weight, and T is the ambient temperature. The amount of gaseous impurities actually incorporated in the film is, however, less than v_i by a factor of α_i, which is called the sticking coefficient. For common impurity gases, the amount of gas incorporation μ_i in the film can then be roughly described as

$$\mu_i \approx 6 \times 10^5 P_i \alpha_i \quad \text{monolayers/sec}$$

where the sticking coefficient α_i is generally less than unity and it decreases with increasing substrate temperature.

The deposition rate R (in Å/min) can be controlled by adjusting the power to the heating source and the distance between the source and the substrate. It determines the arrival rate v_M at the substrate of the metals atoms being evaporated:

$$v_M = 1.67 \times 10^{-10} R\delta N/A \quad \text{atoms cm}^{-2} \text{ sec}^{-1}$$

$$\approx 6 \times 10^{-3} R \quad \text{monolayers/sec}$$

where δ is the density in g cm^{-3}, N is Avogadro's number, and A is the gram atomic weight of the metal.

The substrate temperature T_S affects both the constitution and the structure of the film during growth. High T_S and low deposition rates would favor a large amount of surface diffusion of the adatoms, and therefore a low concentration of microstructural defects in the film. On the other hand, increasing the rate lowers the impurity concentration v_i/v_M, but would tend to limit the atomic mobility, i.e., increase the microstructural defect concentration. Among other, more complex factors which may be operative at the substrate during thin-film deposition is the presence of electrostatic fields, especially during the nucleation stage. External fields have been shown to affect the nucleation density and promote early coalescence of the growing islands.

2.2. Sputtering

Cathodic sputtering[24,25] involves ionic bombardment by Ar^+, Ne^+, etc., ions of a negatively biased target (cathode); momentum

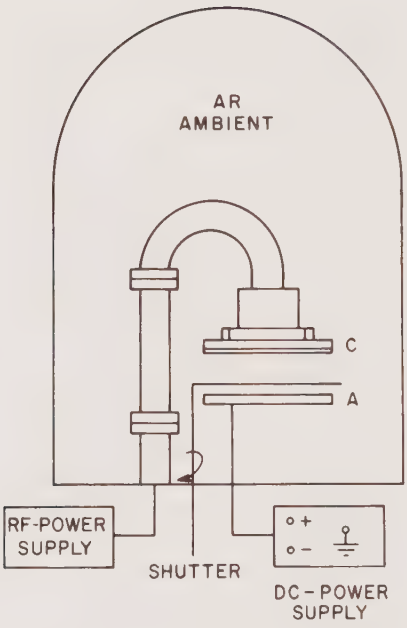

Fig. 6. Conventional rf diode sputtering station.[27] C, cathode; A, substrate table (anode).

transfer processes cause metal atoms from the cathode to be dislodged, which are then deposited on the substrate table (anode) (Figure 6). A sputtering threshold energy exists which is primarily a function of the binding energy of the target atoms. The source of positive ions is a plasma which can be created by a dc- or an rf-induced (capacitively coupled) glow discharge between the cathode and the anode. In order to sustain the plasma, it is necessary that the ambient pressure be in the range of several microns. The mean free path of the sputtered atoms and those in the gaseous ambient is accordingly low and they tend to get diffusely scattered before reaching the substrate. This feature promotes reaction with other active gases which may be present as impurities in the noble gas sputtering environment, or may be purposely introduced, as in the case of reactive sputtering.

The sputtering yields at a given power for various common metals differ by less than one order of magnitude, as opposed to the case of evaporation. the rates for which may differ by several orders of magnitude (nine at 2000°C for W and Al) at a given temperature. This factor, as well as the fact that sputtering involves a layer-by-layer removal of atoms from the surface of the target, makes this process

attractive for alloy deposition using targets of suitable composition. Such targets can, however, be expensive, and for exploratory studies, cosputtering has been successfully used with independently controlled multiple targets in the form of half-disks or alternating rods.

Besides the pressure and the composition of the sputtering environment, other common process variables[27,29] are the sputtering power, nature (dc or rf) and amount of bias on the substrates, and geometry of the system, all of which determine the exact mode of sputtering. Thus, rf-induced discharge is more efficiently produced than a dc discharge, permits use of smaller ambient pressures, and enables one to sputter insulators in addition to metals. Another sputtering mode which has proved very fruitful in producing metastable structures is ion-beam sputtering[30] (Figure 7). Here, the actual sputtering chamber containing the cathode substrate holder assembly is differentially pumped (i.e., it is separated by an aperture) with respect to the ionizing chamber where the plasma is generated. A narrow, magnetically collimated noble ion beam such as Ar^+ is used

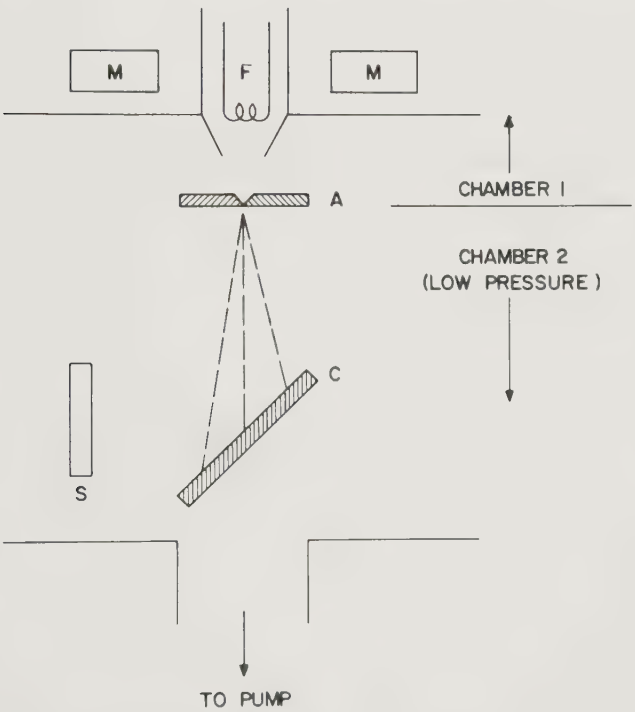

Fig. 7. Ion-beam sputtering apparatus.[30] F, Filament; M, magnet; A, aperture; C, cathode (target); S, substrate holder.

to sputter away the target at oblique incidence, and the metal films are deposited on substrates held at 45° with respect to the target.

The substrates can, if desired, be biased positive or negative (dc or rf) in order to control the ionic bombardment as well as the extent of incorporation (sticking coefficient) of the various ionized gases present in the sputtering ambient.[31] Generally, a negative substrate bias serves to decrease the oxygen content of the film, since much of the oxygen in the plasma is negatively ionized and then there are backsputtering effects at the substrate due to Ar^+ ions. An opposite effect may be expected for Ar^+ and other noble gas ions; however, it has been shown that there is a threshold energy for Ar^+-ion incorporation in metal films;[32] below this threshold, negative substrate bias causes removal of material (backsputtering) at the substrate.

In addition to the substrate bias, the substrate temperature is another powerful parameter which helps control the microstructural perfection and the extent of gaseous impurity incorporation within the film. The same considerations as those stated under evaporation apply.

2.3. Electrodeposition

In the case of conventional electrolytic deposition (cathodic reduction) a dc electric field applied across an electrolyte is used to drive metal-like ions (free or complex) toward the cathode, which also acts as the substrate. Both the electrolytic bath and the anode can provide cations for deposition. The electrolytic bath composition can be easily adjusted to control the composition of the thin-film deposit. Amorphous Ni–P alloys having different P contents have been obtained in this manner using a Ni rod anode, a Ni sheet cathode, and baths containing $NiSO_4$ and H_3PO_4.[33] In order to prevent gas bubbles (e.g., H^+) from adhering to the cathode, it is necessary to vibrate the cathode as well as to stir the bath during plating.

Electroless deposition makes use of a catalyzed chemical reduction process at the surface of the substrate. It is generally necessary to initiate the nucleation of the deposit by dipping the substrate in a sensitizing/activating solution. For Ni–P depositions,[34] this treatment consists of a dip in $SnCl_2$ and then in $PdCl_2$ solution; nucleation of the film occurs at the catalyzed spots and this is followed by growth until the islands merge into each other. A typical solution for Ni(P) consists of an aqueous solution of $NiSO_4$, Na hypophosphite (reducing agents), Na succinate, and succinic acid (complexing agents).

As is the case with electrolytic deposition, presence of P in the bath leads to incorporation of relatively large amounts of P (up to $\sim 16\%$) in the metal film and the resulting film structure is metastable.

2.4. Rapid Liquid Quenching

The techniques and results of rapid liquid quenching, often generically called "splat-cooling," have recently been extensively reviewed[7] and catalogued.[22] Many different metastable phases have been produced with cooling rates greater than 10^5 °C/sec.[7,20,22] Since the heat transfer coefficients between a gas or liquid and the liquid to be quenched are generally too low to produce such cooling rates, the desired quenching has been achieved by forming a thin layer

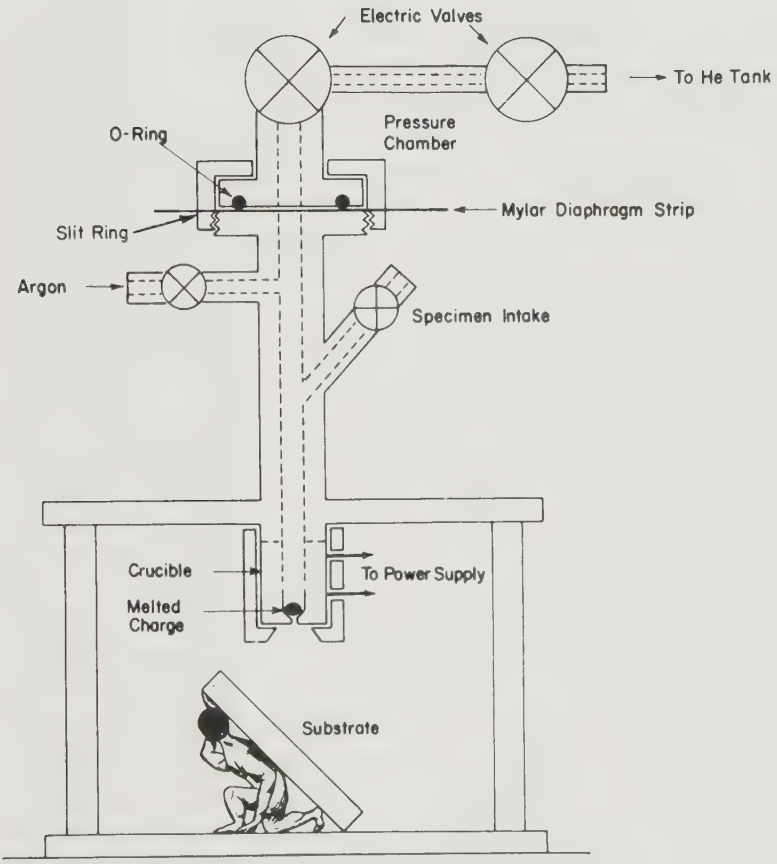

Fig. 8. Splat-cooling apparatus using a shock wave (gun technique[36]).[23]

of liquid in contact with a colder metal substrate which absorbs the heat, predominantly by conduction.

The systematic study of metastable phases produced in this way began with the development of the gun technique.[35,36] In this process, which is illustrated by Figure 8, a diaphragm is ruptured by high-pressure gas. The ensuing shock wave travels down a tube to a crucible with a small hole in its bottom. The sample, a molten drop resting above the hole and kept there by its surface tension, is driven from the crucible by the shock wave in the form of small droplets. These droplets impinge on a metal substrate held below the crucible so as to produce irregular foils typically averaging 5–25 μm thick. Improvements of this design are listed in Ref. 22.

Subsequently, many other techniques[7] have been developed which produce rapid quenching by contacting a thin layer of molten metal to a metal substrate. Examples are: the piston-and-anvil method,[37] which spreads the molten sample between two flat plates which rapidly approach each other; the twin-roll technique,[38] in which the molten sample is fed to the nip of two rapidly rotating cylinders pressed toward each other; the melt spinning technique,[39] in which a liquid stream is quenched to a ribbon-shaped filament on a moving substrate; and the plasma-spraying process,[40] in which a fine powder is melted in a plasma torch which propels the droplets against a substrate.

A technique for rapid liquid quenching distinct from the above has been the melting of a small region of a sample with an intense pulse of heat, such as with a laser.[7] The portion of the sample that remains solid replaces the substrate used in the other methods.

The cooling rates $\dot{T}$ achieved by splat methods will depend on the interface contact between the splat and substrate, the thicknesses and thermal properties of the splat and substrate, and the initial temperature difference. The interface contact will determine the heat transfer coefficient h at the interface. For perfect contact $h = \infty$ and ideal cooling occurs with $\dot{T} \propto 1/t^2$, where t is the splat thickness. At much lower h, interface-controlled or Newtonian cooling occurs with $\dot{T} \propto 1/t$. The two regimes are separated by an intermediate region. In practice, ideal cooling is not achieved, because of effects such as oxide films or less than total surface contact.

Ruhl[42] has calculated the average cooling rates as a function of h and t for iron cooled on a copper substrate. As an example, $\dot{T} = 10^8$ °K/sec for ideal cooling of a 10-μm-thick splat. In a more extensive treatment the solidification rate was also calculated.[43]

Several direct experimental measurements of actual cooling rates have been made.[7] Such studies suggest that rates about one order of magnitude less than that expected for ideal cooling are achieved and that typical experiments produce cooling intermediate between ideal and Newtonian cooling.

3. Amorphous Phases

Amorphous, i.e., noncrystalline, solids are also referred to as glasses when they are obtained directly by cooling the melt. The diffraction pattern from an amorphous material does not contain sharp Bragg-type maxima; it is made up of 3–6 broad, diffuse bands of rapidly decreasing intensity. The transmission electron micrographs of amorphous films lack the orientation and defect features typical of most crystalline materials. However, dark-field electron micrographs of amorphous Ge have shown bright patches of from 5 to 15 Å[44–48] and interference electron microscopy has produced "lattice fringes."[44,47] However, these contrast effects may be due to instrumental artifacts rather than coherently diffracting regions.[49]

Upon heating, the relatively more stable metallic amorphous phases recrystallize at temperatures about one-half of their absolute melting point. If the heating rate is sufficiently fast, the recrystallization is accompanied by a "burst" phenomenon, i.e., a sudden release of energy (~ 1 kcal/mole) at a well-defined temperature. An extreme case appears to be that of amorphous Ge films ($> 10\ \mu$m thick), in which explosive crystallization has been initiated even at room temperature by pricking the film surface with a sharp point.[50]

Some of these amorphous phases obtained using high effective cooling rates also exhibit a sudden rise in the specific heat prior to crystallization. This behavior is schematically shown in Figure 9. The specific heat of the amorphous phase is only slightly higher than that of the corresponding crystalline phases below the glass transition temperature T_g, while above T_g it levels off to a value which is a reasonable extrapolation of the specific heat of the liquid. The dashed region between the crystallization temperature of the amorphous phase and the temperature to which the liquid can readily be undercooled is inaccessible to measurement for those amorphous phases that can be obtained only by using high effective cooling rates. Many common glasses also exhibit such behavior,[51] which is the thermal manifestation of the glass transition; a liquid becomes a glass upon cooling without undergoing a first-order phase transition. The observation

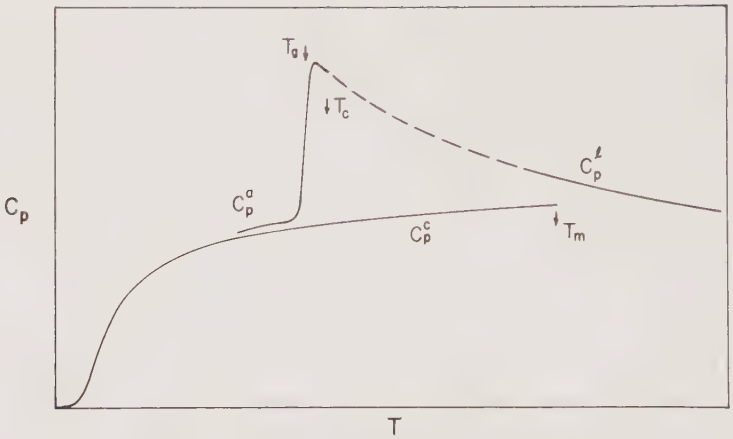

Fig. 9. Schematic representation of the relation between the specific heat of the crystal C_p^c, that of the solid amorphous phase C_p^a, and that of the liquid, C_p^l. Here T_M is the crystalline melting point; T_g is the glass transition temperature, i.e., the temperature at which the specific heat of the glass increases to a value characteristic of the extrapolated liquid phase; and T_c is the temperature at which rapid crystallization occurs upon heating.

of such specific heat behavior is strong evidence that these amorphous metastable phases are distinct from the crystalline state.

3.1. Elemental Amorphous Phases

Because of their inherent simplicity, elemental amorphous phases have been the subject of many recent studies. In most cases, these phases can not be obtained by liquid quenching and have been produced by a thin-film deposition process. These elemental amorphous phases are often categorized as metals or semiconductors, though some elements are intermediate in nature. The semiconductors have structures with a low coordination number and bonding which is covalent and directional. Metallic bonding is associated with structures having a large packing density, i.e., high coordination number.

For metallic elements, the impurities present initially or introduced during deposition can have a significant effect upon whether or not an amorphous phase is obtained and upon the thermal stability of that phase. This is illustrated by the behavior of metal films formed by condensation in ultra high vacuum (10^{-9} Torr) onto liquid-helium-cooled substrates.[52] The purest nickel film produced was crystalline, while the inclusion of only $\sim 0.7\%$ gaseous impurities resulted in an

amorphous film (as judged by the variation of resistance with temperature) which crystallized at 77°K. Iron films were always crystalline, while cobalt films appeared to be amorphous. The crystallization temperature of the cobalt films increased from 39°K for ~0.04% gaseous impurity to 58°K for an impurity content of ~0.27%.

Table 2 lists the various "elemental" amorphous phases that have been reported in the thin-film form. The metals in this table span a wide range of equilibrium-state crystal electronic structures. In most

TABLE 2
Amorphous Phases in Thin Metal Films

Element*	Deposition technique†	Substrate‡	Deposition temperature, °K	Thickness limit, Å	Ref.
Li, Na, K(?)	e	—	—	—	53
Be	e	1, 2, 3	4	750	54–57
Y	e	3	77–300	—	58
Ti	e	3	77–300	—	58
Zr	ib-s	1, 4	300	500	30
Hf	ib-s	1, 4	300	—	30
V	e	—	4	200	58
Nb	e	—	—	—	59
Ta	ib-s, rf-s	1, 4, 5	—	500	30, 60
Cr	e	1, 3, 8	4	650	52, 58, 61, 62
Mo	ib-s, t-s	1, 4, 5	300	2000	30, 63
W	ib-s	1, 4, 5	300	500	30, 58
Mn	e	1, 3, 8	77–300	1000	52, 58
Re	ib-s	4	300	500	30
Fe	e	6	—	80	62, 64
Co	e, s	1, 3, 8	4–300	1200	52, 58
Ni	e, s	1, 8	4	280	52, 58
Pd	e	3	77–250	—	58
Zn	e	1, 7	77	—	65
Cd	e	1, 7	77	—	65
Al	e	6	300	15	64
Ga	e	3	<90	250	57, 66
Si	e	1, 3	300	—	67
Ge	e	6	<650	—	68, 69
Sn	e	1, 7	77	—	65
As	e	1	—	—	70
Bi	e	3	—	250	59, 66

* In approximate order of their appearance on the periodic table.
† e: evaporation; ib-s: ion-beam sputtering; rf-s: rf-diode sputtering; s: dc-diode sputtering; t-s: triode sputtering.
‡ 1, glass; 2, quartz; 3, collodion; 4, NaCl; 5, mica; 6, amorphous carbon; 7, copper; 8, sapphire.

cases, it may be expected that the formation of an amorphous phase will be accompanied by changes in the physical properties and in the electronic structure of the element. Thus, whereas normal Be (hcp, group IIA) is a weak superconductor with $T_C \sim 0.026$ K,[71] the thin-film amorphous phase is a high-temperature superconductor with T_C of 8–9°K.[54,55] Increase in the T_C of a simple metal such as Be might imply an enhancement in the electronic density of states at the Fermi level in the case of amorphous Be. This amorphous phase has been obtained by evaporation on glass substrates held at 4.2°K; on heating above 40–60°K, the high-T_C phase transforms irreversibly into a lower-T_C amorphous phase ($T_C \sim 6$°K), which remains stable up to 130°K. The amorphous structure of cold-deposited Be films was confirmed by Fujime[56] using electron diffraction measurements on Be deposited on collodion (or amorphous carbon) substrates.

Many transition metals of group IIIB through group VIIIB tend to assume an amorphous structure upon evaporation or sputtering on unheated substrates. These are refractory and chemically fairly reactive metals with large core size; therefore, the atomic mobility at the surface of the substrate is expected to be low and the sticking coefficient high. It is apparent that these factors favor a (dense) randomly packed arrangement, i.e., an amorphous structure in the films. The structure of such phases will be discussed below. On going across the periodic table, we find that the noble transition metals Cu, Ag, and Au have not been reported to form an amorphous phase. Among the non-transition metals of groups IIB (Zn, Cd, Hg) and

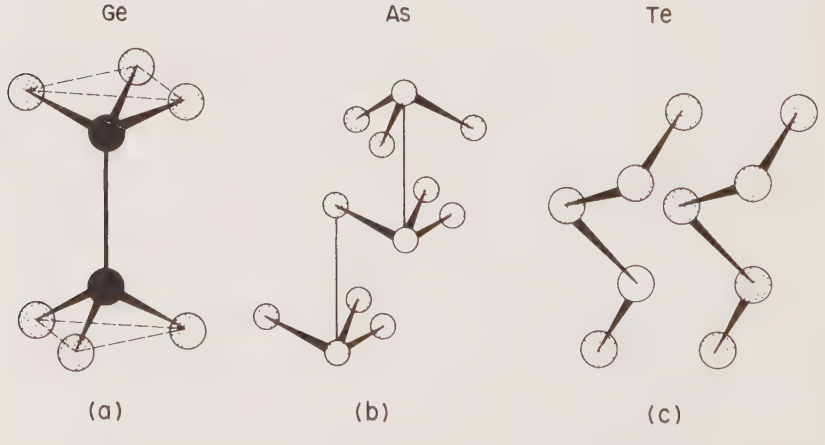

Fig. 10. Crystal structures of Ge, As, and Te showing the $(8 - N)$ type atomic coordinations.

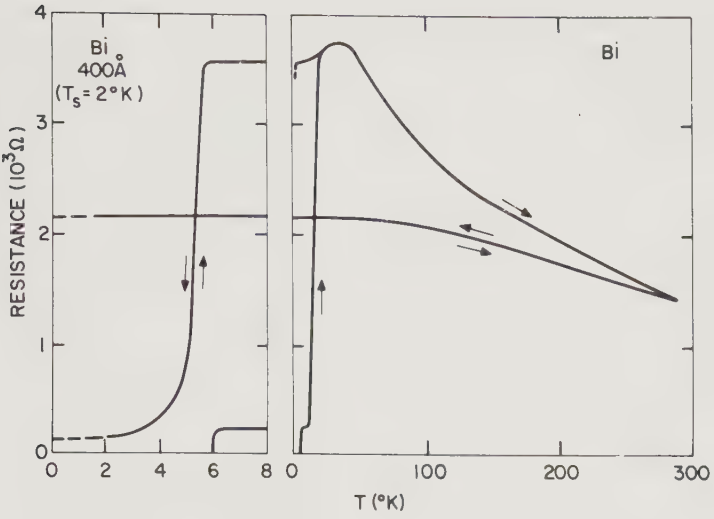

Fig. 11. Temperature dependence of electrical resistance of a Bi film deposited at 2°K.[73]

IIIA (Al, Ga, In, and Tl), only Zn, Cd, and Ga have been reported as forming amorphous phases upon low-temperature condensation.

The subsequent metalloids of groups IVA (C, Si, Ge), VA (P, As, Sb, Bi), and VIA (S, Se, Te) are rather prolific amorphous phase formers. These metalloids generally form amorphous phases rather more readily and the amorphous phases have much greater thermal stability than those formed by the metals. The normal crystal structures of these elements are dominated by largely covalent and directional bonding forces.[17] The tendency to complete the octet of electrons results in atomic coordinations of $8 - N$, where N is the number of outermost electrons outside the corresponding rare gas shell. Thus, Ge assumes a diamond cubic structure containing a tetrahedrally directed fourfold coordination, As has a double layer type of rhombohedral structure with threefold coordination, and Te crystallizes in a chainlike structure having twofold coordination (Figure 10). When all the bonding orbitals are full, as in the case of Si and Ge, the elements are semiconductors. On the other hand, elements like As, Sb, and Bi are poor metals because of weak interlayer bonds associated with the rhombohedral symmetry of their lattice.[72]

Buckel[73] found that amorphous Bi films deposited at 2°K are good superconductors, with a T_C of 6°K (Figure 11). At 20°K, these films transform from an amorphous to a high-resistivity

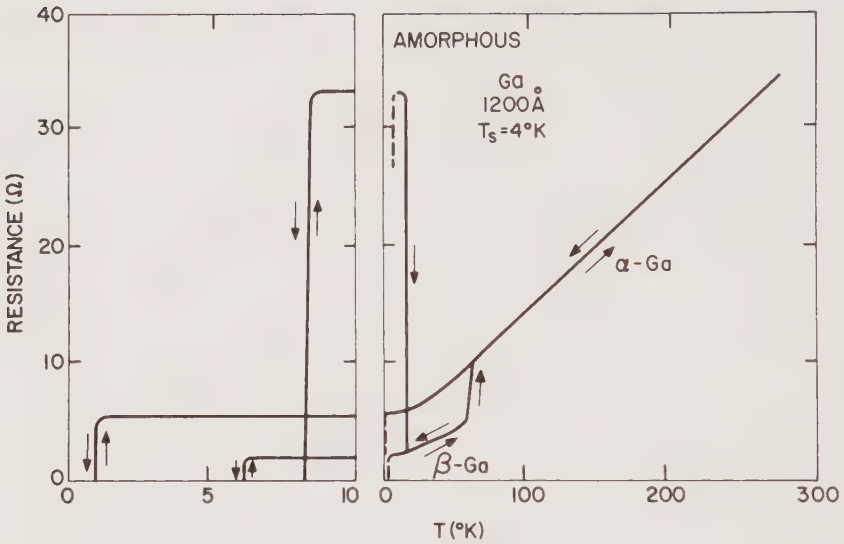

Fig. 12. Temperature dependence of electrical resistance of a Ga film deposited at 4°K.[73]

microcrystalline phase with the normal crystal structure. This transformation is associated with a gradual loss of superconductivity and the films that have been warmed to room temperature are nonsuperconducting.

In the case of Ga, which is a weak superconductor in the bulk crystalline state (T_C = 1.07°K), low-temperature (4°K) condensation leads to an amorphous film with a greatly enhanced T_C of 8.4°K.[73] The resistivity behavior of such Ga films is shown in Figure 12. Based on these and transmission electron diffraction data, there appears to be evidence for three different phases of Ga as the Ga films deposited at 4°K are warmed to room temperature. The lowest temperature phase is amorphous, with T_C = 8.4°K. At 15°K, the amorphous phase transforms irreversibly into a metastable crystalline phase now recognized as having the β-Ga structure (see Section 5.2.2), with T_C = 6°K. Finally, at 60°K the normal structure of Ga is observed, with T_C = 1.07°K, which is close to that for bulk Ga.

3.2. Alloy Amorphous Phases

Alloy amorphous phases have been obtained by various thin-film deposition techniques and by rapid liquid quenching. As expected, vapor quenching is a more powerful technique for obtaining amor-

phous alloys than rapid liquid quenching. While rapid liquid quenching "works" for those alloys having relatively high stability in the amorphous state, vapor quenching must be used to obtain the amorphous state for a greater variety of alloys and for a wider range of compositions for any one type of alloy.

Rapid liquid quenching of metallic alloys has generally been effective in producing an amorphous phase only for metal–metalloid

TABLE 3
Amorphous Phases in (Binary) Alloys

A_xB_y*	at % B	Preparation technique†	Ref.
(a) Metal–metal combinations			
Gd–Fe	15–94	2	79
Gd–Co	60–90	1	80
Tb–Fe	67	1	81
Cr–Ni	—	—	82
Nb–Ni	—	6	75
Ta–Al	63	1	83
Ta–Ni	—	6	75
Fe–Ni	30–75	2	58
Fe–Au	3–55	2	84
Co–Ag	10–50	2	77
Co–Au	35–75	2	85–88
Cu–Ag	35–65	2	86, 89, 90
Cu–Mg	20–90	2	77, 89
Cu–Sn	90	2	91
Cu–Zr	—	6	74
Au–Mg	75	2	77
(b) Metal–metalloid combinations			
Cr–Si	25–83	1	92, 93
Cr–Ge	87	—	94
Fe–P	24	5	95
Co–Si	1–6	2	96
Co–P	18	3	97
Ni–P	16–30	3, 4	33, 34, 98–100
Pd–Si	16–22	6	18
Ag–Te	40–60	3	101
Pb–Bi	12, 30	2	102, 103
(c) Metalloid–metalloid combinations			
As–S	—	2	104
As–Se	—	2	104

* In approximate order of appearance of component A in the periodic table.
† 1, sputtering; 2, coevaporation; 3, flash evaporation; 4, electrolytic deposition; 5, electroless deposition; 6, rapid liquid quenching.

type alloys having compositions near a deep eutectic,[12,18] for inter-transition metal alloys, and for rare earth–transition metal alloys. While initial examination[74,75] of the liquid-quenched inter-transition metal alloys (e.g., Zr–Cu, Nb–Ni, Ta–Ni) characterized them as microcrystalline, it now appears on the basis of studies of their structural and thermal properties that they are amorphous.[76]

It is interesting to note that among thin-film amorphous alloy phases, many of the alloy components are noble metals and some non-transition metals which do not by themselves form elemental amorphous phases (Table 3). The factors which, according to Mader,[77] favor the appearance of an amorphous phase in coevaporated alloy films are (a) a relatively large difference ($>10\%$) in the atomic radii of the components and (b) the absence of an extended equilibrium solid solubility.

3.3. Structural Analysis

A Fourier transformation of the properly normalized (in electron units) and corrected (to remove inelastic components) intensities of the broad, diffuse bands observed in the diffraction patterns (in k space) leads to a radial distribution function (RDF) in real space of the atomic arrangement in the amorphous material.[12,78] From such RDF analysis can be deduced the average number and distance of atoms in spherical shells around an atom (origin) within the structure. This information is statistical, however, and cannot be used to define a unique structure, i.e., the three-dimensional arrangement of atoms, as does diffraction from crystals.

Many of the evaporated or sputtered amorphous phases are too thin to be analyzed by X-ray diffraction since the diffracted intensities are too low. A particularly attractive method of studying very thin films (<1000 Å) is the scanning electron diffraction (SED) technique, which is schematically illustrated in Figure 13.[64] A magnetic field is used to scan the electron diffraction pattern in times of the order of 50 msec, and filters are provided to eliminate the inelastically scattered electrons having energies less (0.5–5 eV) than that of the incident electron beam (30 keV). The fast scanning speeds permit *in situ* structural studies during the earliest stages of film growth. The alternative to SED is, of course, to photographically record the transmission electron diffraction pattern and quantize the data with a photometer. The precision of electron diffraction measurements can be poorer than that of X-ray diffraction (transmission or reflection),

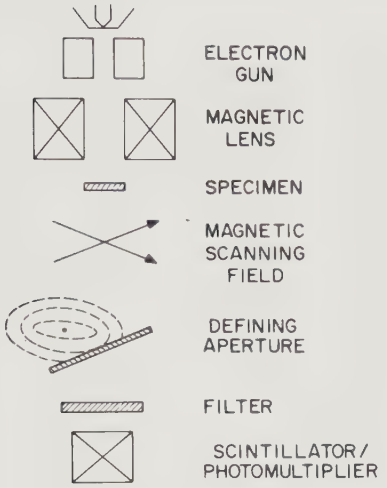

Fig. 13. Schematic of scanning electron diffraction technique.[64]

which, however, require the use of thicker films (several thousand angstroms or more).

Amorphous alloys easiest to analyze are the electrodeposited or liquid-quenched specimens, which can be produced with sufficiently large thicknesses (10–100 μm) and dimensional regularity. These films can be considered to be infinitely thick for the purposes of X-ray diffraction; they can be examined in the reflection mode whereby uncertainties due to absorption corrections are eliminated.[98]

Experimental RDF's have been produced for a wide variety of amorphous phases. Of these, those of Ni–P and Si can serve as an example of the RDF's of the metals and semiconductors, respectively.

Figure 14 shows the pair distribution function obtained together with the corresponding RDF from the experimental interference function $a(K)$ for electrolytically deposited $Ni_{76}P_{24}$.[33] The oscillations in both functions are found to decrease with increasing r, i.e., the RDF approaches the average atomic density $4\pi r^2/\rho_0$. These functions are qualitatively similar to those of other amorphous metal alloys, including those of nominally pure metals such as Be[56]; the coordination number, as measured by the area under the first peak, is generally approximately 12. They differ from the $a(K)$ and RDF's of liquid metals primarily in that the peaks for the solid amorphous structures are sharper; this can be due in large part to the differences in thermal motion, since the data for the solid and liquid forms of the same alloy are of necessity taken at different temperatures.

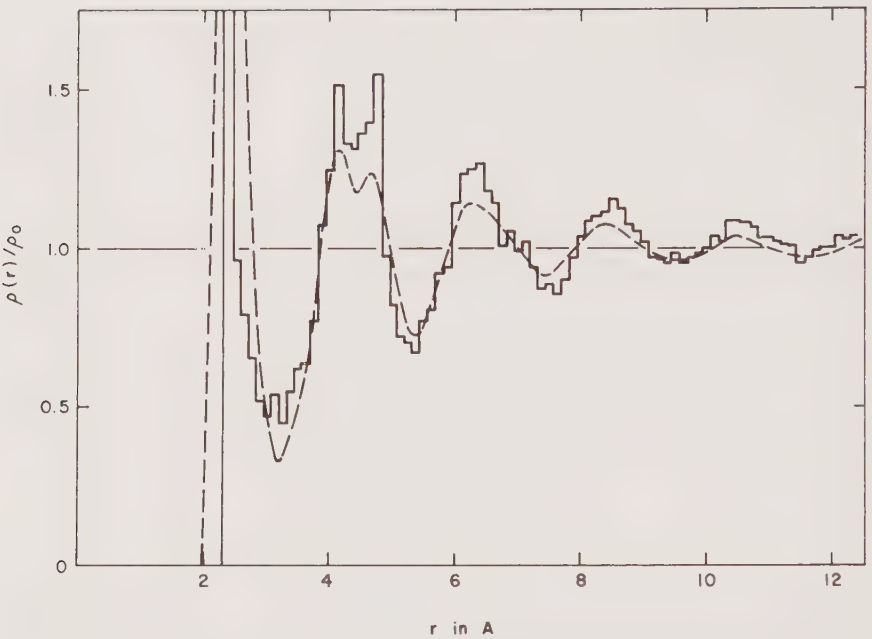

Fig. 14. Structural data for $Ni_{76}P_{24}$ [33] superimposed on a histogram for dense, random packing of hard spheres[1] scaled to a sphere diameter of 2.49 Å.

Additionally, the shoulder on the second peak of the $a(K)$ and the splitting of the second peak in the RDF, seen for Ni–P and many other amorphous metals, are not observed for corresponding liquids.

Cohen and Turnbull[105] first suggested the use of dense, random packing of hard spheres to model the structure of monatomic glasses. It was subsequently pointed out[106] that the experimental RDF's of the amorphous metals were similar to that of dense, random packing of hard spheres. Figure 14 shows the superposition of the pair distribution function of hard spheres[1] for a hard-sphere diameter of 2.49 Å and that of $Ni_{76}P_{24}$.[33] The peaks of the hard-sphere RDF are sharper since it does not include broadening effects, e.g., thermal vibration. However, the comparison is encouraging in that the oscillations decrease with increasing r at a similar rate and the splitting of the second peak occurs for both.

It was later suggested that amorphous phases such as Pd–Si and Ni–P had short-range order similar to that of the intermetallic phases Pd_3Si and Ni_3P such that compositional ordering was present with the metal and metalloid having different effective sphere sizes.[107–109] Such a structure has since been considered in more detail.[110]

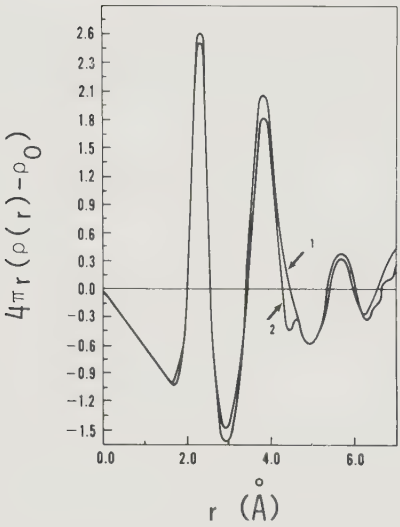

Fig. 15. Superposition of $4\pi r[\rho(r) - \rho_0]$ for a thermally broadened random network model (curve 1[117,118]) and for amorphous Si (curve 2[116]).

While dense, random packing can be used to model the structure of other amorphous alloys, the effective sphere size of each alloy component, the degree of compositional ordering, and the packing density (i.e., coordination number) must be specified for each alloy.

A competing structural model is the microcrystallite model, in which the atoms are arranged in very small crystals; each microcrystal would have a random orientation so that no long-range periodicity was present. However, studies suggest[33,111] that such a model does not produce as good agreement with diffraction data as does dense, random packing.

Of the amorphous semiconductors, the structures of Si and Ge have received the most attention.[112] The RDF of amorphous Ge[113,114] and that of amorphous Si[115,116] are similar; the positions and areas of the first two peaks of the RDF's show that the tetrahedral coordination is preserved in the amorphous structure, though apparently in a distorted form. However, on the basis of examinations of their RDF for various microcrystallite models, Moss and Graczyk[115,116] concluded that the amorphous silicon was not microcrystalline.

Figure 15 shows the $4\pi r[\rho(r) - \rho_0]$ of amorphous Si[116] with the corresponding, thermally broadened function of a tetrahedrally

coordinated random network model[117,118] superimposed on it. The random network structure was constructed using the concepts[119] which have previously been applied to fused silica.[120,122] For the random network concept, each atom is bonded to the number of nearest neighbors required to satisfy its chemical valence; the noncrystalline nature of the structure is due primarily to variations in the bond angle, the angle formed by the bonds to any two neighbors of an atom.

Though there is uncertainty as to details, such as the relative number of five- and six-member rings and the average distortion of the bond angle within the structure,[123] the random network is presently the most widely accepted structural model for amorphous Ge and Si. The agreement in Figure 15 is reasonably good, especially in regard to the relative widths of the first and second peaks, the absence in both curves of the crystalline third neighbor peak, and the oscillations at higher r.

It is expected that other amorphous semiconductors could have structures based on the same network concepts. However, structures which are predominantly three- or two-coordinated are inherently more complex than the tetrahedrally coordinated structures since a greater number of alternative arrangements satisfying the same bonding criteria can be postulated; in addition to nearby atoms connected by covalent bonds, other, nonbonded or weakly bonded nearby atoms can be present for these low-coordination structures. As an example, amorphous tellurium has been reported[124] to have two near neighbors, as in its crystalline forms; it is concluded[124] that the atoms are arranged in chains.

3.4. Electrical Properties

Electronic properties of amorphous alloys, including conductivity, superconductivity, and magnetism, have become a very rich field of activity, having an extensive body of literature, last comprehensively reviewed by Giessen and Wagner in 1972.[23] It is not possible to give more than a few examples here. It should be pointed out, however, that until recently variations in alloy preparation parameters have prevented the duplication and confirmation of the structure-sensitive electronic properties and led to a number of differing interpretations of the observations.

One major consequence of the absence of long-range crystalline order in amorphous films is that the electronic conduction processes

in these films are probably dominated by the structural disorder in a manner somewhat analogous to the case of liquid metals[125–127] and certain amorphous alloys produced by quenching from the melt.[128] The relative contributions due to usual phonon scattering or by surface scattering effects, which are commonly encountered in crystalline films, get progressively smaller as the structural disorder increases.

The structure parameter in terms of which electron scattering in simple (e.g., nonmagnetic, not too thin) amorphous metals and alloys can be treated, following Ziman,[125] is the interference function $a(K)$. This function is equivalent to a structure factor.[129] Ziman's theory will predict a positive temperature coefficient of resistivity (TCR) if $a(K)$ at Fermi level E_F for the alloy increases with temperature, i.e., if the Fermi level E_F of the metal is located at off-peak positions of $a(K)$ curves. A negative temperature coefficient of resistivity is predicted if E_F is located at or very near a peak of the $a(K)$ curve. At these locations $a(K)$ most likely decreases with increasing temperature because of temperature-induced broadening effects on the interference function.[128]

Mader *et al.*[86] have carried out resistivity measurements on amorphous CuAg films (500–1000 Å thick), among others. Their results, typical for amorphous metals, are shown in Figure 16. It may

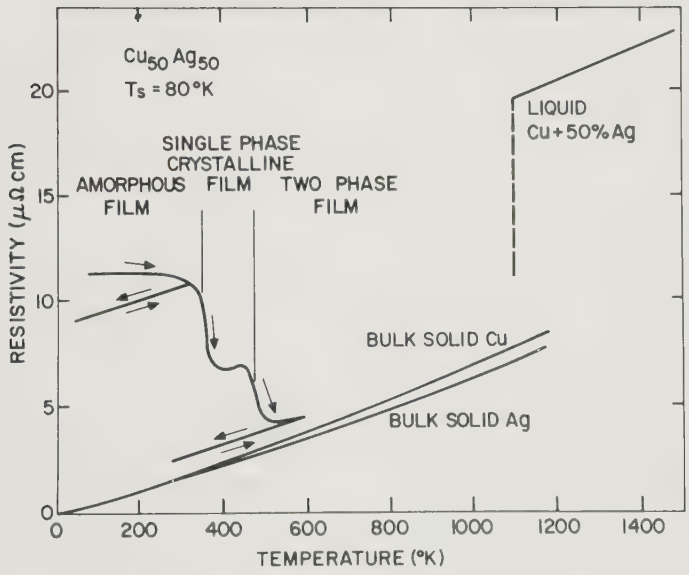

Fig. 16. Electrical resistivity behavior of thin films of CuAg initially deposited in amorphous state at 80°K.[86]

be seen that the electrical resistivity of the amorphous phase is several times higher than that of the crystalline modification. The temperature coefficient of resistivity is very low and may even be slightly negative. In this particular case, however, the amorphous film transforms at very low temperatures and the initial decrease in resistivity with increasing temperature appears to be an irreversible effect.

3.5. Magnetic Properties

For several years now, it has been realized both theoretically and experimentally that long-range structural disorder does not preclude various types of magnetic ordering, which depend primarily on near-neighbor atomic interactions. All of the presently known magnetically ordered amorphous alloy films (Table 4) contain at least one component derived from the group Fe, Co, Ni, Gd. These films have been prepared using coevaporation, flash evaporation, or sputtering and the amorphous phase has been retained for thicknesses as large as 6000 Å.

The magnetic data for these films have been analyzed assuming that the moment is localized on the normally ferromagnetic atoms, i.e., Fe, Co, or Gd. An interesting consequence of the amorphous structure in ferromagnetic Fe–Au (3–55 at % Au) is that the Fe atoms are associated with a relatively large moment of 2.9 μ_B/atom, as compared to 2 μ_B/atom generally found for bcc Fe. The moment per Fe atom remains high even after recrystallization for Fe-Au films (40–55 at % Au) that crystallize into an fcc structure, whereas it decreases to $\sim 2\,\mu_B$ for films (3–35 at % Au) crystallizing in the bcc structure. Assuming that the magnetic moment in such alloy films is mainly determined by the local atomic environment effects,[130] the above results may be taken as further evidence for a (random) close-packed atomic arrangement in the amorphous Fe–Au films.

In the case of amorphous films of Gd–Fe and Gd-Co, where both components are magnetic, their moments appear to be coupled opposite to each other and these alloy films are ferrimagnetic. Such a behavior is illustrated in Figure 17, which shows the magnetization at 77 and 4.2°K of amorphous Fe–Gd alloy films[79] as a function of composition. A ferrimagnetic alloy of composition $Fe_{77}Gd_{23}$ has a net saturation moment of nearly zero since at this composition, the weighted moments of Fe (2.2 μ_B) and Gd (7.3 μ_B) cancel out. On the other hand, if the moments were ferromagnetically coupled, this alloy would have an average moment of 3.4 μ_B. In Figure 17, the apparent

TABLE 4
Amorphous Magnetic Alloy Films

Composition	Method of preparation	Substrate	Film thickness, Å	Magnetic structure	Ref.
$Fe_{97-45}Au_{3-55}$	Coevaporation	Quartz (20°K)	500–1000	Ferro ~	84
$Fe_{94-15}Gd_{6-85}$	Coevaporation	Quartz (77°K) sapphire, collodion	1370–6000	Ferri ~	79
$Fe_{67}Tb_{33}$	Sputtering		—	Ferro ~	81
$Co_{75-40}Au_{25-60}$	Coevaporation	Sapphire (77°K), collodion	200–600	Ferro ~	88
$Co_{82}P_{18}$	Flash evaporation	Glass (300°K)	—	Ferro ~	97
$Co_{99-94}Si_{1-6}$	Coevaporation	Quartz (20°K)	500–800	Ferro ~	96
$Co_{90-60}Gd_{10-40}$	Sputtering	Glass (300°K)	> 2000	Ferri ~	80

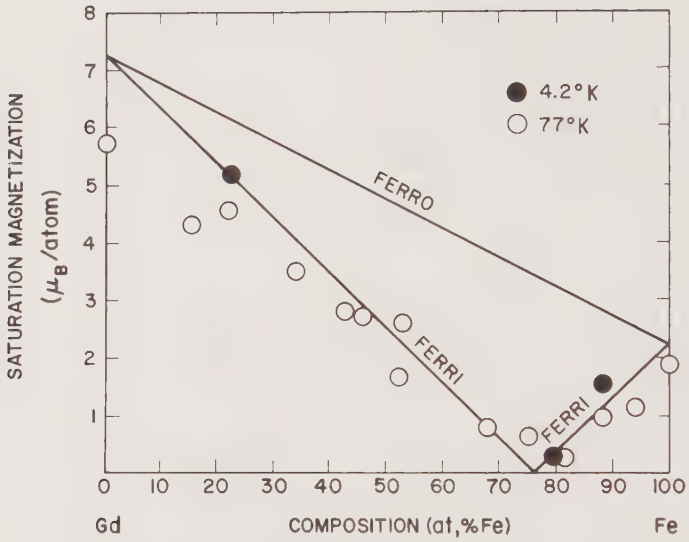

Fig. 17. Saturation magnetization vs. composition of amorphous Gd–Fe alloy films.[79] ●, 4.2°K; ○, 77°K.

deviation of data points for Gd-rich compositions (at 77°K) is caused by a pronounced temperature dependence of magnetization in these alloys.[79]

Two other interesting characteristics have been observed in most amorphous magnetic alloy films: (a) the coercivity of these films is relatively low[80,54,96] compared with that for crystalline material having the same composition, and (b) the films (for thicknesses $\gtrsim 2000$ Å) possess a relatively strong uniaxial anisotropy perpendicular to the plane of the film, which is independent of constraints (stresses) imposed by the substrate.[79,80] It has been suggested[80] that such anisotropy might be an intrinsic property of the amorphous film and that it may be ascribed to pair ordering and shape anisotropy contributions.

The combination of relatively small saturation magnetization, low coercivity, and strong perpendicular anisotropy in certain sputtered Co–Gd amorphous films leads to a striped domain configuration.[80] Under the influence of suitable orthogonal fields, bubble domains can be nucleated; these films can be utilized[131] for several interesting magnetooptical device applications.

3.6. Transformation Kinetics

Some of the important features of the transformation behavior of many amorphous alloy films can be illustrated with reference to the kinetics observed[86] for amorphous CuAg. As shown in Figure 16, at temperatures above ~300°K, the amorphous phase in the CuAg alloy film undergoes a transformation into a single-phase fcc A1-type structure which is also metastable. This phase is fine-grained and the large grain boundary contributions may be responsible for its resistivity, which is intermediate between that of the amorphous phase and of the equilibrium two-phase mixture. This crystalline CuAg phase is really analogous to the corresponding single-phase fcc Cu–Ag alloy described in a subsequent section, which has been obtained by rapid liquid quenching methods.[18] Finally, on heating above ~425°K, the metastable fcc phase decomposes into a stable equilibrium mixture of Cu-rich and Ag-rich fcc terminal solid solutions.

The first stage of transformation of an amorphous $Cu_{46}Ag_{54}$ alloy film was shown, using transmission electron microscopy, to involve the formation and then growth of very small (< 50 Å diameter) nuclei of the metastable fcc phase. The difference in free energy between the amorphous and the fcc phases in CuAg was estimated to be ~70 meV at 370°K. The phase transformation is a diffusion-controlled process with a relatively high activation energy of about 1.2 eV. Such a large energy barrier of transformation has been ascribed[86] to the requirement of extensive diffusion, which is required to break up the atomic "log-jam" in the amorphous phase. The second stage of transformation from single-phase fcc to the two-phase fcc structure appears to be an example of the spinoidal decomposition wherein statistical fluctuations in the composition create a thermodynamic instability which leads to "uphill diffusion" and decomposition into the two terminal solid solutions. There is an apparent activation energy of ~1.4 eV involved for this diffusion process, even though no nucleation is necessary because of the spontaneous nature of the decomposition.

Another class of amorphous alloys whose transformation kinetics has been studied are Ni–P alloys obtained by electrodeposition and by flash evaporation. Differential scanning calorimetry experiments on amorphous $Ni_{75}P_{25}$ obtained by electrolytic deposition were carried out.[98] Two exothermic transformations were observed: one at 280°C with an energy release of 42 meV/atom, which corresponds

to the transformation from an amorphous to a complex crystalline Ni–P phase; the second at ~410°C with energy release of 13 meV/atom. Following this transformation, the alloy was single-phase Ni_3P. Microstructural work was done on flash-evaporated amorphous Ni–P alloy films from W filaments which were electrolytically coated with amorphous Ni–P.[79] Amorphous films containing 25 at % P were found to transform on heating above 175°C through a nucleation and growth type mechanism, supporting the view that these films were not microcrystalline. Only grain growth could be observed upon heating films containing 21.2 at % P; such transformation behavior can occur for either an amorphous structure or for a metastable microcrystalline structure.

The crystallization behavior of amorphous Pd–Si based alloys has been studied[10] in detail as a function of composition. For these alloys, the thermal manifestation of the glass transition (see Figure 9) was observed to occur upon heating before crystallization.

4. Metastable Elemental and Near-Elemental Crystalline Phases

4.1. Topologically Close-Packed Structures

The TCP phases[14] are characterized by large atomic coordination numbers of 12, 14, 15, or 16, the most common coordination polyhedron being the icosahedron with CN = 12, which possesses a fivefold symmetry. Crystallinity is achieved by introduction of polyhedra of CN 14, 15, or 16. The interstitials in the TCP structures are exclusively tetrahedral, so that a good degree of atomic packing is achieved. Another feature of topological close-packing is that it generally leads to a layered arrangement of atoms.[14]

TABLE 5
Topologically Close-Packed Structures in Thin Films

Composition	Structure type	Deposition technique*	Ref.
Nb_3Ge	Cr_3Si (β-W)	rf-s	140
Ta	β-Ta	e, dc-s	141, 147
$Ta_{80-60}Al_{20-40}$	β'-Ta	dc-s	143
Ta_3Ge	Cr_3Si (β-W)	rf-s	140
W	β-W	e, rf-s	29, 132–134
$Mo_{0.7}Re_{0.3}$	Cr_3Si	dc-s	169

* e: evaporation; dc-s: dc-sputtering; rf-s: rf-sputtering.

4.1.1. The β-W Phase

The β-W phase in thin W films has been obtained by electron beam evaporation onto cold substrates[132,133] or by rf sputtering of W under zero or positive substrate bias.[29,134] It is thought to be an oxygen-stabilized phase, although the amounts of oxygen necessary to stabilize it are certainly much smaller than those expected from an A_3B stoichiometry of most Cr_3Si (β-W) compounds. The X-ray diffraction pattern of thin-film β-W phase can be fully explained in terms of a disordered W_3W or a $(W_{1-x}O_x)_3(W_{1-x}O_x)$ structure (Cr_3Si type); an ordered W_3O type structure predicts several extra lines which are not actually observed.[39] On the other hand, recently obtained transmission electron diffraction patterns[134] from β-W films contain additional rings at $d = 4.16$ and 3.52 Å which correspond to forbidden reflections of "W_3W" structure. These are believed to arise from stacking faults and/or microtwins in the β-W lattice. The situation in this respect may be similar to that of "hexagonal" Au, where microtwins in fcc Au films apparently give rise to additional hexagonal reflections in the transmission electron diffraction patterns (see Section 4.2.2).

The microstructure of sputtered β-W films is quite distinct from that of sputtered α-W films (Figure 18).[39] Thus, whereas α-W films are characterized by a ridgelike surface morphology and grain size of 250–1000 Å, the β-W films possess a very fine granular surface with a small grain size of 100–500 Å. In the bright-field transmission electron micrographs of Figure 18, the grain boundaries are not clearly resolved, due to the high lattice defect density; however, the dark-field micrographs allow an unambiguous determination of the grain size.

The metastable nature of the β-W phase in W thin films is clearly illustrated by the results of electrical resistivity measurements during annealing of thin, rf-sputtered W films (Figure 18).[134] The β-W films have a high resistivity of $\sim 130\ \mu\Omega$-cm, which is probably the result of a very small grain size (< 100 Å) as well as electronic effects. The temperature coefficient of resistivity of β-W films is relatively low and negative, at about -270 ppm/°C,[135] as compared to that of many bcc α-W films ($+450$–1500 ppm/°C).[135,136] The resistivity data of Figure 19 show that the transformation β-W $\rightarrow$ α-W is irreversible and occurs at relatively low temperatures of 130–350°C. The density of β-W (19.1 g/cm^3) is nearly the same as that of α-W (19.3 g/cm^3) and no weight change was found to result from the β-W to

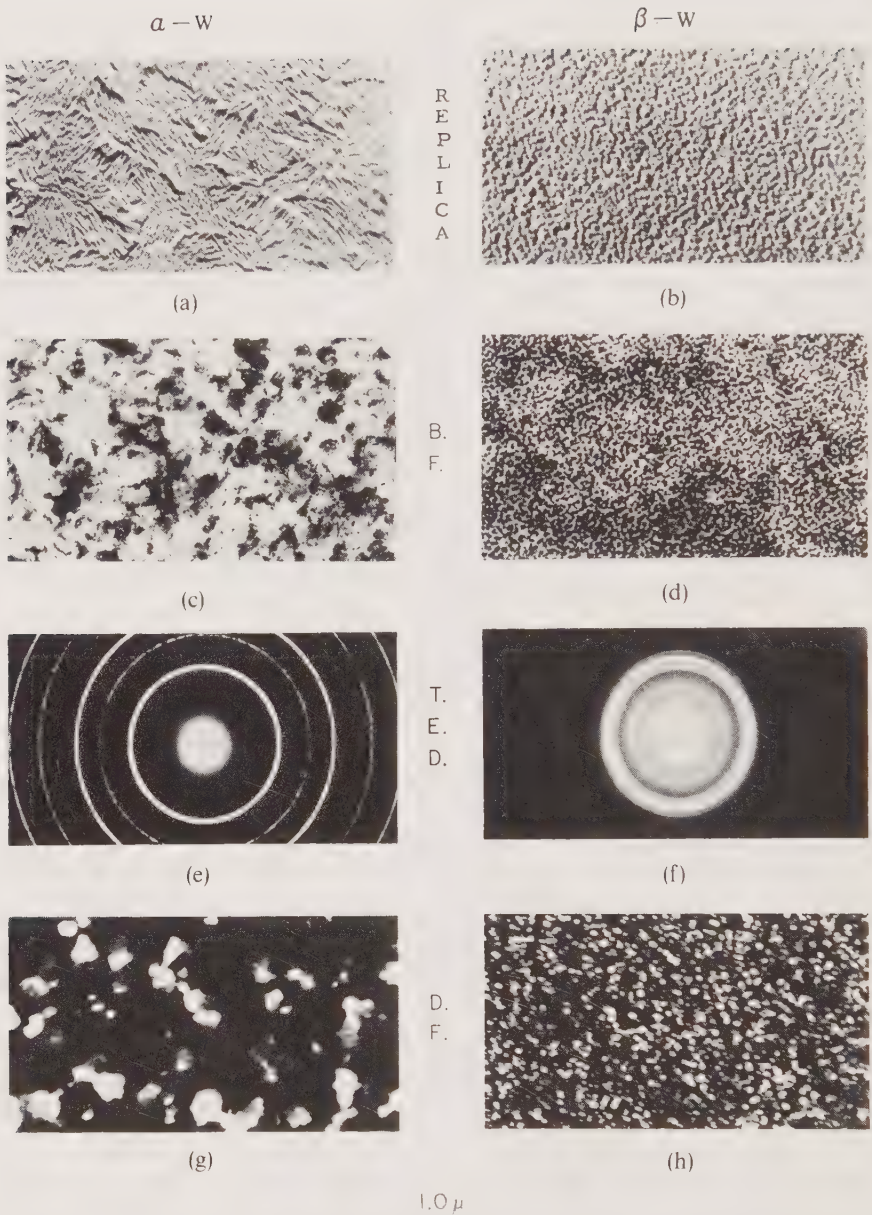

Fig. 18. Microstructure of α-W and β-W thin films prepared by rf diode sputtering.[29] (a, b) Surface replica; (c, d) bright-field transmission electron micrograph; (e, f) transmission electron diffraction pattern; (g, h) dark-field micrograph.

α-W transformation.[137] All these data agree with the conclusion that β-W is an essentially metallic phase of W, and that deposition conditions determine the formation of β-W.

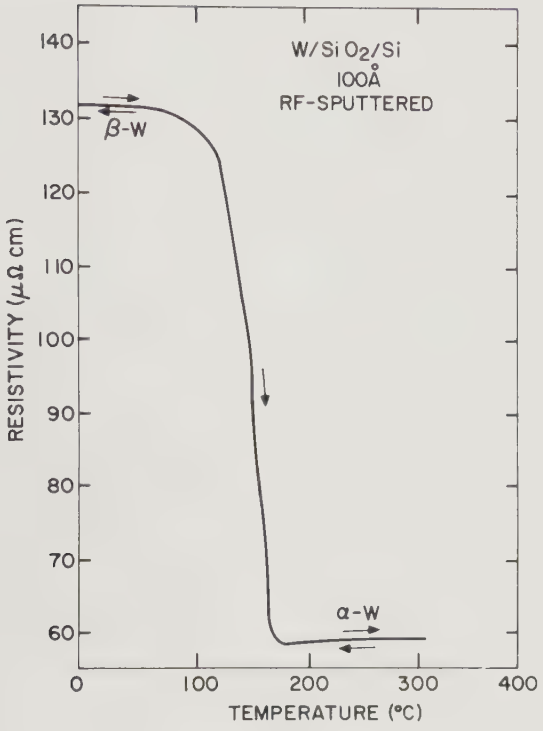

Fig. 19. Temperature dependence of resistivity of very thin β-W films produced by rf diode sputtering.[134]

One very interesting property of β-W thin films is their relatively high superconducting transition temperatures (up to 3.2°K) compared with that of α-W (0.004°K).[132,138] Electron-gun evaporated β-W films have been shown[132] to be well-behaved superconductors; the temperature dependence of the superconducting energy gap follows the Bardeen–Cooper–Schrieffer[139] theory quite well. The enhancement of superconductivity in the β-W phase of W is almost certainly caused by *d*-band structure effects. Indications are that the density of states at the Fermi level increases upon formation of the β-W structure.[14]

The rf cosputtering of several β-W type alloys (A_3B) has been accomplished by using composite targets made up of half-disks of the component metals A and B.[140] The sputtered alloy films were then annealed at 750°C. Using this technique, Hanak *et al.*[14] were able to synthesize the high-temperature superconductor Nb_3Ge

(T_C = 17.0°K, 4000-Å-thick film), which is normally stable only at the off-stoichiometric composition of $Nb_{78}Ge_{22}$ (T_C = 6.9°K). A new β-W compound, Ta_3Ge, which is not stable at all in equilibrium alloys, was also synthesized and found to be a superconductor with T_C of 8°K (400 Å thick, 750°C anneal).

4.1.2. The β-Ta and Related Phases

The β-Ta phase[141] in thin Ta films has attracted great interest because of its technological importance as a thin-film capacitor and resistor material. There are strong reasons to believe that the β-Ta structure (and its variants) may involve topological close-packing of atoms. Recently, a sputtered $Mo_{38}Re_{62}$ alloy film[142] of σ phase composition was found to have an X-ray pattern which bore resemblance to that of β-Ta. Another structure, called β'Ta, similar to β-Ta, has been reported[143] in dc cosputtered Ta–Al alloy films containing 20–40 at % Al. This composition is also similar to that of the equilibrium σ-phase Ta_2Al, and this might again be taken as an indication that the β'Ta structure is possibly σ-related. The β'Ta phase is part of a succession of phases formed in sputtered Ta–Al alloy films with increasing Al:[143]

$$\underset{\text{up to 20\% Al}}{\text{bcc}} \rightarrow \beta\text{-Ta} \rightarrow \underset{\text{20–40\% Al}}{\beta'\text{Ta}} \rightarrow \underset{\text{63\% Al}}{\text{amorphous}}$$

Yet a third and perhaps less closely related variant of β-Ta appears to be that obtained by Das[144] in Ta films sputter-deposited under negative substrate bias and apparently stabilized by a small quantity of nitrogen. Burbank[145] made a detailed X-ray study of thick (7.5 μm), sputtered β-Ta film which possessed a very high degree of preferred orientation, but was still not quite a single crystal. On the basis of his studies, it appears that β-Ta might only have a pseudocrystalline character. He proposed an hexagonal subcell with a = 2.831 Å and c = 5.337 Å, which form the building blocks for domains $\sim$250 Å in diameter and $\gtrsim$1000 Å high; these domains in turn are arranged in layers. Most recently, Moseley and Seabrook[146] prepared β-Ta by electrodeposition from a molten fluoride bath at 800°C. Their material had an X-ray pattern very similar but not identical to that earlier observed by Read and Altman.[141] Moseley and Seabrook[146] have indexed their β-Ta X-ray pattern assuming a tetragonal unit cell with a = 10.194 and c = 5.313 Å, with 30 atoms/cell. These data as well as the relative intensities of their diffraction pattern lines led them

to the conclusion that β-Ta is isomorphous with β-U, whose structure is nearly the same as that of the σ phase. The differences between the X-ray patterns for electrodeposited β-Ta[146] and those for sputtered β-Ta[141,145] are small but real and leave open the question whether the latter films contain relatively large microcrystals (macromolecules) with a topologically close-packed σ-type arrangement inside each microcrystal.

The β-Ta films have been prepared by dc diode sputtering[141,147,148] (with zero or positive substrate bias), rf diode sputtering,[149,150] triode sputtering,[151] electrodeless ring discharge sputtering,[152] and by electron-beam evaporation.[153] The formation of β-Ta, as opposed to bcc α-Ta, requires critically "clean" deposition conditions with respect to both the ambient and the substrate. For details of the exact deposition parameters, the original references or the review by Baker[154] should be consulted. Once nucleated, the β-phase of Ta is stable with respect to thickness up to several thousand angstroms. The metastable nature of β-Ta is indicated by the fact that it transforms irreversibly to bcc Ta on heating above 800°C;[155] there is apparently little volume change accompanying this transformation.[141]

The solubilities of several light elements in β-Ta have been reported; β-Ta can dissolve up to 4 at % oxygen,[156,157] 10 at % hydrogen,[156] 3–4 at % carbon,[157] 3 at % nitrogen,[157] 2 at % argon,[157] and ~15 at % Si.[158] The grain size of dc sputtered β-Ta films was reported as ~250 Å.[158] The β-Ta films undergo a superconducting transition at 0.96–0.67°K (cf. bcc Ta, $T_C = 4.48$°K).[155]

The electrical resistivity of β-Ta films is rather high, ~200 $\mu\Omega$-cm (cf bcc Ta, 13.5 $\mu\Omega$-cm) and its temperature coefficient of resistivity is low and negative, -150 ± 30 ppm/°C.[155] Both of these electrical parameters are sensitive to the constitution of the Ta films. The presence of rather small amounts of bcc Ta in mixed β-Ta, α-Ta films can be ascertained by monitoring the film resistivity and TCR.[152,155] This technique has been used by Schauer *et al.*[152] to examine the constitution of Ta films as a function of partial pressure of N_2 bled into the sputtering ambient. Their results (Figure 20) show that β-Ta is formed in a critical range of N_2 partial pressure, both above and below which bcc Ta results.

Several attempts have been made to correlate the appearance of β-Ta phase with the nature of impurities in the sputtering ambient. These investigations have led to seemingly contradictory conclusions, namely (a) β-Ta is formed only under the cleanest Ar-containing

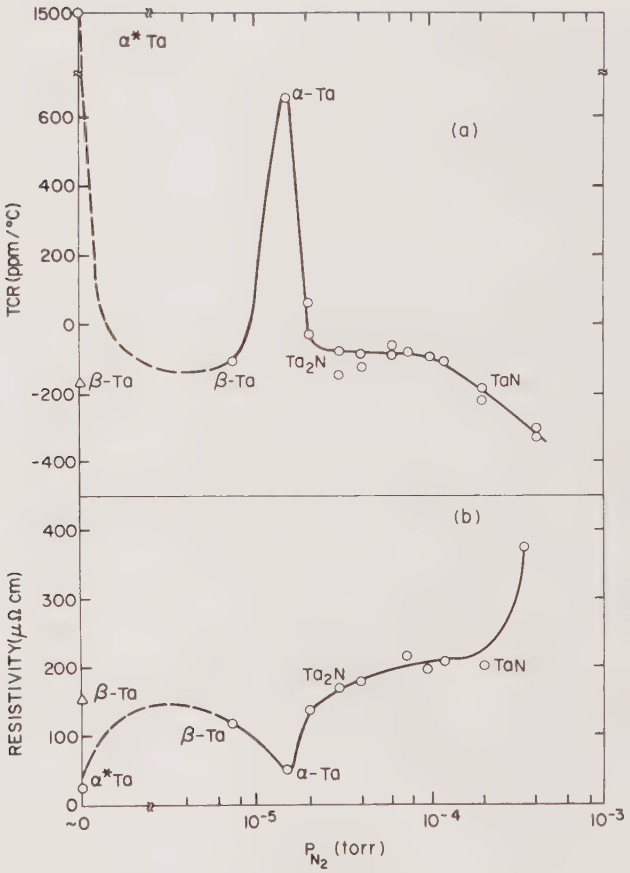

Fig. 20. Temperature coefficient of resistivity and resistivity of sputtered Ta films as a function of partial pressure of N_2 in the sputtering ambient.[152]

sputtering ambients,[64,151,153,160,161] (b) β-Ta is formed only when impurities such as N_2 and O_2 are present in the sputtering ambient,[147,162–164] and (c) β-Ta is formed in a critical range of impurity concentration, both above and below which bcc α-Ta phase is stable.[152] Part of such disagreement is due to the fact that β-Ta generally possesses various degrees of preferred orientation (Figure 21), which are best revealed by the use of wide-film glancing angle X-ray diffraction techniques.[165] Under usual operating conditions, the X-ray diffractometer would only reveal lattice reflections lying in the equatorial portions of the X-ray patterns of Figure 21. The problem is further compounded by abnormal intensities of the lattice

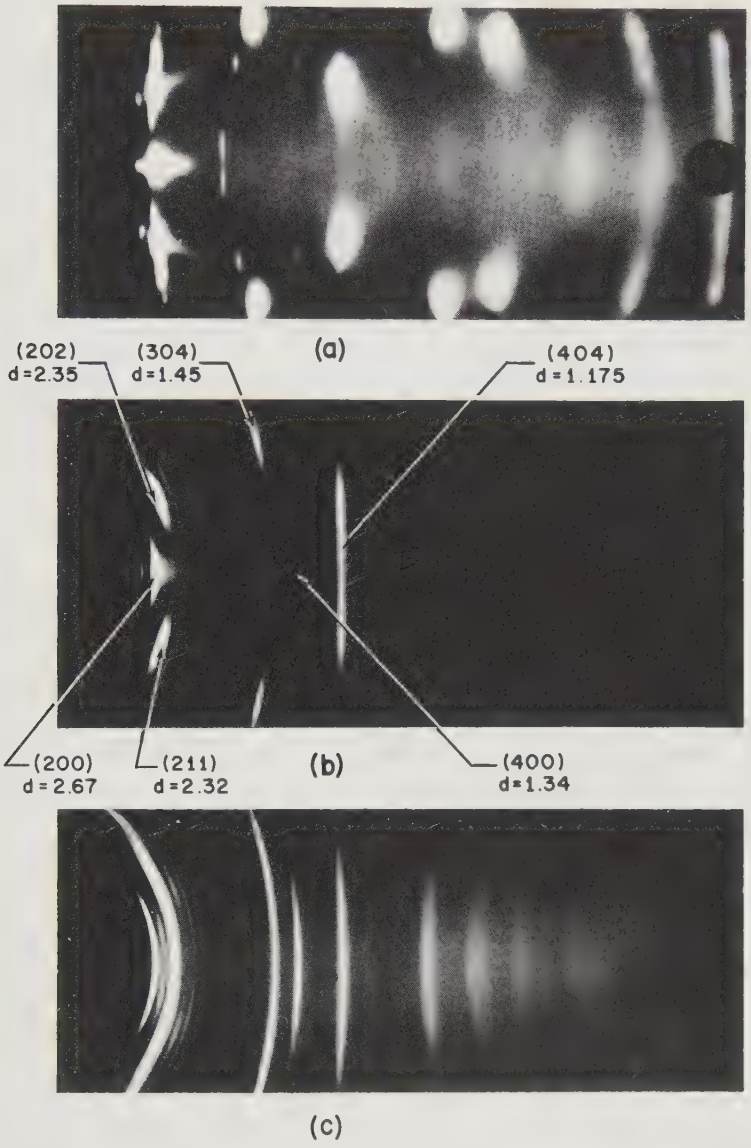

Fig. 21. Wide-film glancing angle X-ray photographs of β-Ta films illustrating the effect of decreasing extent of a (200)-type preferred orientation on going from (a) → (b) → (c).[165]

reflections of both α- and β-Ta due to preferred orientation, and hence, the diffractometer data can be subject to misinterpretation. Even the use of the wide-film X-ray diffraction technique by itself, when employed to prove a "pure" β-Ta phase, has some pitfalls, since X-ray

film techniques often do not reveal very small amounts ($< 5\%$) of the second (e.g., bcc Ta) phase. As pointed out by Schwartz *et al.*[155] detailed TCR measurements (in the range 4.2–300°K) provide a more sensitive indication of mixed β-Ta + α-Ta films since the two have very different TCR's.

The above-mentioned experimental difficulties notwithstanding, it may be concluded on the basis of more reliable data in the literature that the amount of any impurities such as oxygen, nitrogen, or hydrogen in β-Ta films is generally small and is comparable to or even less than that present in most bcc Ta films. The role of impurities or other deposition parameters then primarily consists in affecting the nucleation process. Once nucleated, β-Ta will form readily and is fairly stable. Recent careful work[156,166] indicates that the nucleation of β-Ta requires the presence, at the substrate, of oxygen in the form of O_2 or O^- or OH^-. Using both rf and dc sputtering and under identical ambients, Feinstein and Huttemann[156] could produce either β-Ta or α-Ta, depending upon whether the substrates did or did not contain oxygen (e.g., glass vs. Au). The exact mechanism as to how oxygen favors the nucleation of the β-Ta phase is not clear. It may be speculated that the presence of oxygen inhibits atomic mobility at the substrate, a factor which would promote topological close-packing of atoms present in β-Ta. It is interesting to note that both the high resistivity and the negative temperature coefficient of resistivity of β-Ta are similar to those of a V–Co σ phase[14] or of an amorphous Ni–Pt–P alloy.[128] In the latter case, a structural scattering of electrons was shown to dominate over phonon scattering, and a combination of this effect and Fermi level effects was thought to give rise to the observed negative TCR. Read and Altman[141] have suggested that the complex crystal structure (and electronic effects possibly resulting therefrom) may be responsible for the observed resistivity behavior of β-Ta. Until these and other mechanisms for producing a negative TCR in metallic conductors, such as anomalous phonon scattering[167] and temperature-sensitive changes in the band structure,[168] are considered, it may be premature to accept the suggestion that semiconductivity (i.e., a band gap) is involved in the case of β-Ta.[163]

4.2. Spherically Close-Packed Structures

Under this heading we will consider two groups of phases: (a) pseudomorphic structures. These are abnormal close-packed (epitaxial) structures which have been found in very thin films ($\lesssim 100$ Å

thick) on generally single-crystal metallic substrates. The primary stabilizing mechanism involves epitaxial forces which, beyond a critical thickness, give way to lattice misfit dislocations and growth of the normal structure. (b) Abnormal spherically close-packed (e.g., fcc and hcp) structures in not-so-thin films of elements normally crystallizing in the bcc structure. These phases, like the topologically close-packed ones (Section 4.1), may be considered as representing an intermediate stage between the amorphous and the equilibrium bcc phases.

4.2.1. Pseudomorphic Structures

Very thin films of certain metals are known to assume the crystal structure of the substrate rather than that of any normal modification (polymorph) of the bulk metal. The metastable structure so formed is called a pseudomorph. The pseudomorph may or may not have the same lattice parameter as that of the substrate. Frank and van der Merwe's model[170] of the film/substrate interface also applies to the pseudomorphs; according to this model, if the lattice mismatch is less than 14%, the film will be elastically strained so as to become coherent with the substrate. Above 14% lattice mismatch, misfit dislocations are generated at the interface. It is further assumed that there is a sharp interface between the substrate and the pseudomorph, i.e., alloying effects are not present. Beyond a critical thickness, the "pseudomorphic" films tend to assume the normal "polymorphic" structure. Pseudomorphism has been observed in several transition metal films on (a) metallic single-crystal substrates that are also transition metals with close-packed lattices and (b) sometimes on MgO and NaCl substrates (Table 6). The pseudomorphic metal films are prepared either by evaporation or by electrodeposition, e.g., in the case of Co and Ni. In the latter two cases, the critical thicknesses are 1 μm and 1000 Å, substantially larger than those ($\sim$20 Å) for evaporated films of the same metals.

A quantitative theory of pseudomorphism for the case of evaporated metal films has been developed by Jesser.[181] Pseudomorphism is promoted mainly by: (a) a large lattice misfit (relative difference in interatomic separation in lattice planes of the film and those of the substrate parallel to the interface) for the normal structure and a small misfit for the pseudomorph; (b) a large degree of supersaturation during evaporation, i.e., a high deposition rate and a low substrate temperature; (c) a relatively large difference in atomic volumes of the

TABLE 6
Pseudomorphic Structures in Metal Films

Element	Structure	Substrate	Pseudo-morphic structure	Critical thickness, Å	Ref.
Ti	hcp	NaCl	fcc	—	177
Nb	bcc	MgO	fcc	—	176
Cr	bcc	Ni	fcc	10	175
Fe	bcc	Cu	fcc	20	171, 172
Co	hcp	Cu, Ni	fcc	20	174, 180
Co*	hcp	Cu	fcc	10,000	178
Ni	fcc	Co	hcp	—	173
Ni*	fcc	Co	hcp	1,000	179

* Electrodeposited, all others evaporated.

normal and the pseudomorphic phases. The critical thickness beyond which the pseudomorph becomes unstable depends upon the thickness dependence of above factors, and, of course, the relative thermodynamic stability of the pseudomorphic structure with respect to the normal one (Table 1). Good agreement between theory and experiment was obtained by Jesser for Fe, for which the experimentally determined critical thickness is ~ 20 Å.

4.2.2. Abnormal Spherically Close-Packed Structures

Table 7 summarizes the various abnormal spherically close-packed structures which have been found in thin films of various metals. Many of these phases were obtained by Chopra *et al.*[30] using ion-beam sputtering at substrate temperatures ranging from 150 to 400°C. Below this temperature, amorphous phases formed, whereas above this temperature range, the normal crystalline modification was obtained. An interesting feature of these fcc phases of normally bcc or hcp refractory metals is that their densities are significantly (5–29%) lower than those of the bulk. This combination of low density along with high atomic coordination (CN = 12) found in the abnormal fcc phases is generally also present in the corresponding amorphous metallic structures. Therefore, we might have here a possible relationship between the amorphous and the low-density fcc phases. This view is also supported by a further finding of Chopra *et al.*,[30] who observed an intermediate fcc phase when amorphous films of these metals were undergoing recrystallization into the equilibrium bcc structure.

TABLE 7
Abnormal Spherically Close-Packed Structures

Element*	Normal structure	Abnormal structure	Preparation technique†	Ref.
Zr	hcp	fcc	1	30
Hf	hcp	fcc	1	30
Nb	bcc	fcc	2	176
Ta	bcc	fcc	1, 2, 3	30, 60, 182
Mo	bcc	fcc	1, 2	30, 182
W	bcc	fcc	1	30
Re	hcp	fcc	1	30
Co	hcp	fcc	2, 4	185, 186
Ni	fcc	hcp	1, 4	183, 184
Ni Fe	fcc	hcp(?)	2	171
Cu	fcc	hcp(?)	2	187
Ag	fcc	hcp(?)	2	188, 190
Au	fcc	hcp(?)	2	188, 189

* In approximate order of their appearance in the periodic table.
† 1, ion-beam sputtering; 2, evaporation; 3, rf-sputtering; 4, electrodeposition.

Denbigh and Marcus[182] have observed microcrystalline (grain size ~ 16 Å) fcc modifications in very thin (< 250 Å) films of Ta and Mo films obtained by vacuum evaporation on MgO or C substrates at temperatures below 400°C. Fcc Ta has been also obtained by Schrey *et al.*[60] by rf-sputtering Ta on glass substrates held at 325°C. All of these phases, like those of Chopra *et al.*[30] exhibit densities which are smaller than those of bulk bcc structures. A fcc phase in very thin films of Nb evaporated[176] on MgO crystals or sputtered on NaCl has been also reported; but this fcc structure was attributed by Hutchinson and Olsen[176] to an oxide phase (similar to NbO) resulting from an interaction between the film and the substrate. However, the amount of oxygen available in such experiments is usually too small to account for any stoichiometric oxide, so that this "oxide" may be also considered to be a metallic phase of Nb, though stabilized by oxygen in a somewhat analogous manner as that found for β-W.

In the preceding discussion, we had examples of bcc and hcp transition metals forming abnormal fcc phases. There has been considerable controversy as to whether a normally fcc metal can form a metastable hcp modification. It is well known that evaporated Au films give rise to extra reflections when examined by transmission or

reflection electron diffraction and these may be indexed on the basis of an hexagonal structure.[188,189] A similar situation exists with evaporated films of Ag and of Ni–Fe alloys.[191] It has not been possible to confirm these anomalous reflections using X-ray diffraction. This raises the possibility that the extra reflections are an artifact of the sample preparation technique for transmission electron diffraction studies or are caused by deformation-induced twins. Pashley *et al.*[192] have attributed the extra reflections from Au films to double-diffraction effects across (111) twins and this seems to be the accepted explanation for the anomalous reflections from normally fcc films.

5. Metastable Crystalline Intermediate Alloy Phases

In this section, crystalline nonequilibrium alloy phases not based on terminal components are treated. Where comparisons are possible, the crystal structures of such phases are found to be similar to those of crystal-chemically-related equilibrium phases, as will be shown. It is therefore reasonable to assume that many of the physical properties of metastable phases will not differ much from those of the corresponding equilibrium phases. With the exception of Nb_3Ge, whose superconducting properties have been studied,[4,193] metastable phases have not been considered for applications suggested by any interesting physical properties. Their structures and alloy chemistry are presently the best-known aspects of intermediate metastable alloy phases, and they will therefore be treated in the following.

5.1. Occurrence and Study of Intermediate Alloy Phases

5.1.1. Phase Diagram Aspects and Classification

One of the most interesting aspects of the study of metastable phases is the possibility of "seeing behind" the equilibrium phase diagram and observing directly some of the binary or other multicomponent phases that may form in the absence of the equilibrium phases (including the terminal constituent phases). This is especially valuable in the case of systems which have no significant crystal chemical features in equilibrium, such as the simple eutectic systems common in inter-B-metal combinations.

It is useful to consider that every possible known or unknown binary alloy phase type (including, in addition, variations over a broad range of mean atomic volumes, axial ratios, interaxial angles,

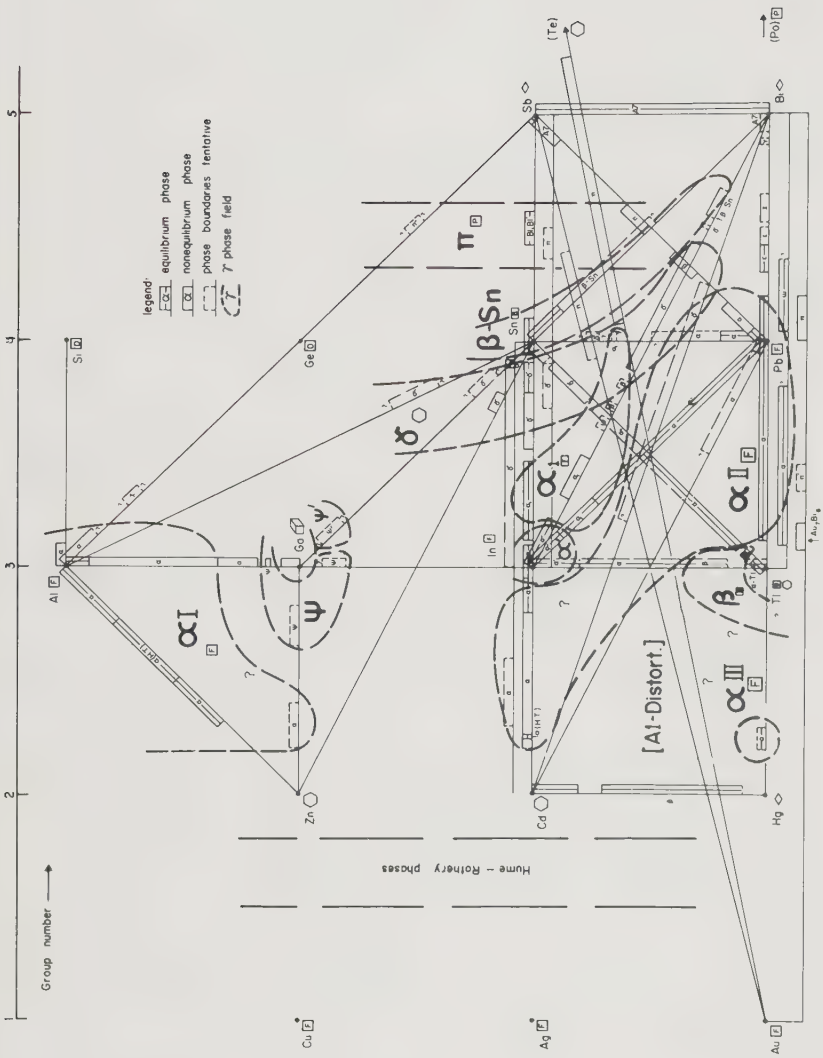

Fig. 22. Phase fields formed by stable and metastable B-metal phases and solid solutions.[20]

atomic positions, and site occupancies) can be considered as a candidate structure for each composition in a given binary system. Of these candidate structure types, even the one resulting in the lowest free energy for the given composition will occur in the equilibrium diagram only if the corresponding phase competes successfully with mixtures of adjacent equilibrium phases; often, the latter are the terminal solid solutions. As a result, for the vast majority of alloy compositions, there is no crystal-chemically useful information available from equilibrium constitution studies.

Metastable intermediate phases produced by splat-cooling include two principal types: Extended disordered solid solutions (items 1–3 below) and ordered metastable phases (items 4,5). Beyond this, there is a smaller but growing number of vapor-deposited or sputtered phases, of which only one example will be treated (item 6).

1. Metastable Hume-Rothery phases based on noble metals, e.g., ζ-(Au-Sb) and γ-(Au-Sn).
2. Inter-B-metal phases, such as the phases forming the phase fields indicated in Figure 22, which are composed of stable and metastable phases. This figure includes elements up to the group B6 (Te). Examples are listed below.
3. Inter-transition metal phases, such as ζ-(Nb–Ni), which simulate the structure of other transition metals at whose position in the periodic table they occur.
4. Stoichiometric metastable phases, such as $Au_{6-7}Bi_8$, GeSb, *m*-$TiCu_3$, *m*-ThCo, ThCu, and a recently prepared Al–Ge phase, Al_3Ge_2.
5. Ordered nonstoichiometric solid solutions of extended composition range which are based on a metastable intermediate phase, such as $Pu(Ga_{1-x}Pu_x)$ and $GeFe_{1-x}$.
6. Metastable intermediate phases produced by vapor deposition in systems with liquid immiscibility.

5.1.2. Crystal Structure Studies of Metastable Intermediate Phases Produced by Rapid Quenching

A brief comment concerns the difficulty of obtaining definitive crystal structure data from metastable crystalline thin films, either liquid- or vapor-quenched. This problem has delayed progress in the alloy chemistry of metastable phases substantially, since phase identification often has been either impossible or, what is worse, wrong.

The principal tool for definitive crystal structure studies to date is single-crystal X-ray diffraction; this technique, however, is inapplicable for most metastable phases, since crystals of sufficient size for present methods ($>50\ \mu$m edge) do not grow during rapid cooling. There are, however, occasional cases where the supercooling required for metastable phase formation can be produced by somewhat slower cooling of metals, as was the case for Al_3Ge_2 discussed below, or by droplet cooling, as was the case for the Ga modifications β, γ, and δ;[194] definitive crystal structures can then be obtained.

Where slow cooling is not sufficient to reach the required supercooling, positive identification based on single crystals may be possible by using selected-area electron diffraction to obtain the correct unit cell in combination with intensity measurements from X-ray powder patterns. Electron diffraction intensities can also be used directly if allowance for dynamic scattering effects can be made.

The remaining avenue is unit cell determination from powder patterns. This method is fraught with danger, which has led to its almost complete disuse for equilibrium alloys except for very simple structures or for the direct identification of a compound by comparison of the pattern to that of an isotypic phase of known structure. Experience shows that direct powder pattern indexing, e.g., by Ito's method, cannot be assumed to have led to a correct unit cell identification unless the unit cell content can be determined subsequently and a complete structure determination results from this indexing. Where this is not possible, the indexing of a powder pattern must be judged by applying analytic criteria such as that by DeWolff,[195] which can aid in eliminating spurious indexings, especially those made by assuming very large unit cells of intermediate symmetry. The Al–Ge system offers an example of these problems: In a total of eight papers (see Refs. 196 and 197), unit cells for two splat-cooled metastable phases were discussed. However, these unit cells were not confirmed when the complete structure of Al_3Ge_2 was derived from single-crystal data,[198] although comparison of the reported powder patterns with that of Al_3Ge_2 showed that the same phase had been treated. None of the reported unit cells was even remotely related to the final structure.

5.2. Structures and Crystal Chemistry of Metastable Intermediate Phases

The metastable intermediate phases tend to fall into characteristic, discrete structure families as listed above. These families generally

also contain equilibrium phases representing crystal-chemically-related systems and are discussed in the following.

5.2.1. Metastable Hume-Rothery Phases

The phases of this family known to date occur at the predicted compositions in alloy systems that contain a noble metal and an addition element located in the periodic table in a position immediately following the last addition element capable of forming the Hume-Rothery phase in question as an equilibrium phase. This is demonstrated in Figure 23.[199] Thus, a metastable hcp Mg–A3 type Hume-Rothery phase can be formed in the Au–Sb system that corresponds to the equilibrium phase ζ in the Au–Sn system;[200] similarly, a metastable phase γ-(Au–Sn) of the cubic $D8_{1-3}$ γ-brass type corresponds to the stable phase γ-(Au–In) of the same type. This empirical rule simply reflects the fact that the valence electron concentration (VEC) required for Hume-Rothery phase formation

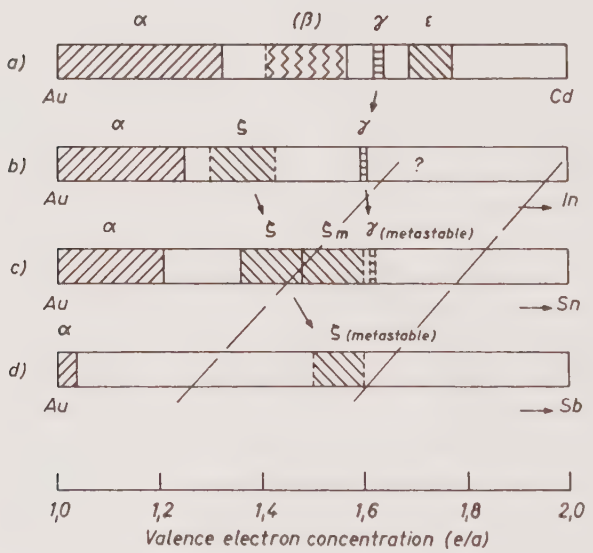

Fig. 23. Maximum concentration ranges of the Hume-Rothery phases in the systems (a) Au–Cd, (b) Au–In, (c) Au–Sn, and (d) Au–Sb. Range of metastable Hume-Rothery phases produced by splat-cooling indicated by dashed lines.[199]

can be attained with addition elements other than those forming the phases in equilibrium, but that the size factor will become too unfavorable for the formation of disordered intermediate solid solutions if the solute elements have too high periodic table group numbers. Increasing electronegativity differences with increasing group numbers of the solutes will act in the same way to limit stable or, further on, metastable phase formation.

5.2.2. Nonstoichiometric Metastable Inter-B-Metal Phases

Isostructural or closely related inter-B-metal phases, both equilibrium and nonequilibrium, have been found in composition ranges that can be characterized in terms of their periodic table positions.[7,20] As for Hume-Rothery phases, the principal factors determining the formation of these phases are their average VEC's as indicated by their horizontal periodic table positions (group number) and, in second order, their average atomic potentials, as indicated by their vertical periodic table positions (period). These relations are demonstrated in Fig. 22, modified from Ref. 20; heavy broken lines outline the principal B-metal phase fields found by considering both disordered equilibrium and metastable phases from over 40 binary alloy systems. This plot is discussed in greater detail in Refs. 20 and 201. While the structure type characteristic of a given phase field will predominate in it, phases with other, competing crystal structure types are occasionally found in element combinations falling into this phase field; this indicates some second-order differences in the structural energies of both structure types for different alloy combinations. Figure 22 shows two extended phase fields of the fcc Al type, αI and αII, at VEC > 2.2 and a third, small field of this type, αIII. The αI and αII fields are separated by a miscibility gap extending between the first and second long period. The αI phase field includes Zn–Al, Zn–Ga, and Al–Ga alloys. The αII phase field involves metals from the second and third long period. It extends toward higher VEC's than the αII field and includes Pb and some of its alloys. Between αII and αIII, especially in Hg–In alloys extending to pure Hg, the fcc Al type is not stable; instead, the Hg–In system contains two orthorhombic phases and a rhombohedral phase closely related to each other. All of these Hg–In phases are based on the Hg–A11 type of elemental Hg, which represents a rhombohedral distortion of the A1 type structure.[202]

Other phase fields shown in Fig. 22 are as follows.

The ψ phase is now recognized to be a metastable binary extension of metastable β-Ga;[76] the latter phase can be retained by slow supercooling of a suspension of pure gallium particles. (There are two further, metastable Ga modifications, γ and δ, that have been prepared in this way and have been identified structurally.[194])

The α_1 phase, a tetragonal distortion variant of α, is of the In–A6 type but with $c/a < 1$; it occurs to the right of α'. The α_1 phase does not merge continuously with α' or α; instead, there is a discontinuous transition between α_1 and α, as well as between α_1 and α'. The latter phase is centered around In and has the In–A6 type with $c/a > 1$. The decrease of c/a for α_1 with increasing VEC is characteristic and has also been considered in terms of interactions between the Fermi surface and Brillouin zone boundaries.[203]

The γ phase (simple hexagonal, $c/a \sim 0.94$) is located at VEC 3.5–3.9, to the left of Sn; it is of special interest because it demonstrates well the structure-determining principles involved in these phases. Found in three equilibrium alloy systems based on Sn, it has been retained as a metastable phase in at least 11 other systems.[204] Of the metastable γ phases, most contain Sn as a majority component; all of these phases contain addition elements which lower the VEC. Lead acts in the same way, probably due to the substantial s–p electron splitting resulting from increased spin–orbit coupling in third long period elements. [Formally, this effect is equivalent to the "reduced valence electron contribution" used in the metallurgical literature;[205] it is also responsible for the general sloping of the phase fields (e.g., α_1, γ) to the lower right, as discussed in Ref. 20.] In addition to Sn-based systems, γ occurs as a metastable phase in systems without Sn, such as In–Sb,[206] In Bi,[207] and Cd–Bi.[208] A fundamental discussion of the stability and axial ratio of γ in terms of the pseudopotential formalism has been given.[209] The crystal structure of γ is closely related to that of β-Sn;[207] as seen in Fig. 22, the phase field of the latter structure type is strongly extended in nonequilibrium toward Bi and includes a tin-free metastable In–Bi phase having the β-Sn–A5 type.[207]

We further mention the π phases typically located at valence electron concentrations between 4 and 5, with the specific value depending on their constituents. The π phase has the primitive cubic α-Po structure type with one atom/cell; thus, it is structurally identical with a disordered NaCl–B1 type. Gold additions promote formation of metastable π phases in Sb, Bi, and Te alloys.[210] Ordered and

tetragonally distorted variants are also found; metastable GeSb[211] is an example discussed below.

The last group of phases to be listed here is composed of some β phases of the bcc W–A2 type and variants of this type, such as the trigonal ω type; ω phases have an atomic arrangement closely related to that of the β phase and are found in metastable Tl–Sn and stable Tl–Bi alloys.[20] These phases occur typically in competition with α_1 and γ at VEC 3.5–4.5.

We summarize these observations. Consideration of the metastable phases as well as the stable ones is necessary to characterize B-metal alloy phase formation. There is a tendency to form stable or metastable phases with simple disordered crystal structures; the structures of these phases are strongly correlated with their positions in the periodic table. A discussion of these structures in terms of pseudopotential theory[8] provides some theoretical foundations for the simple periodic table representation[20] used here.

The occurrence of metastable phases has also been discussed in terms of the first derivative of the excess partial entropy of the corresponding liquid.[212] The generally observed close relation between stable and metastable phases would seem to require the same criterion also to apply to stable alloy phases; this, however, has not been demonstrated.

5.2.3. Inter-Transition Metal Phases

It had been observed earlier[213] that the crystal structures of intermediate phases found in inter-transition metal systems, especially those combining early and late transition metals, tend to show a characteristic sequence typical of the structures of phases found in the elements bridged, especially W–A2 type (bcc) → σ-phase-related (complex) → Mg–A3 type (hcp) → Cu–A1 type (fcc).

An example is Mo–Rh, where the phases of this sequence occur at the appropriate average group number (AGN; for transition metal alloys, there is a preference for the use of the looser concept of the AGN over the VEC as used for non-transition metal alloys).

In splat-cooled transition metal alloys, the type of phase formed appears to depend on the size and valence difference of the constituents, the nature of the phase diagram, and the composition. Large size and valence differences as well as low reduced melting points[214] at intermediate compositions favor formation of amorphous phases, as discussed above. If the size and valence differences are small or

intermediate and the reduced melting points are high, which is the case especially at low solute contents, metastable crystalline phases form, such as the bcc W–A2-type β phase in the V–Ni system and the hcp Mg–A3-type ζ phase at $Nb_{0.19}Ni_{0.81}$. The latter phase simulates in composition and structure the hcp ε modification of Co.[215]

5.2.4. Stoichiometric Metastable Phases

Phases of this type occur throughout the periodic table, generally at compositions where an equilibrium phase might be expected by crystal-chemical analogy but is found to be absent. Examples are: (a) $Au_{6-7}Bi_8$, with a NiAs–B8-type related structure,[76,210] which is the metastable analog of stable AuSn (B8 type) (the differing stoichiometry of the two compounds is due to the valence difference of Bi and Sn). (2) GeSb, with a tetragonally distorted NaCl–B1 type structure,[211] related to the NaCl or π phases at VEC $\sim$ 4.5 discussed above.[210] (3) m-$TiCu_3$, with the orthorhombic Cu_3Sb type structure; its characteristic axial ratios show that m-$TiCu_3$ forms a transition type between a more Cu-rich ordered phase $TiCu_4$ based on the hcp Mg–A3 type and the CsCl–B2 type expected at intermediate compositions in this system.[216] ThFe and ThCu (orthorhombic, CrB–B_f type) are metastable stoichiometric phases whose possible presence in nonequilibrium is suggested by the existence of ThCo as a stable phase with the same structure type.[217]

An ordered metastable Al–Ge phase of the composition Al_3Ge_2 was recently prepared as a single crystal of size sufficient for a structure study.[198] The structure is monoclinic and related to the La_2O_3–$D5_2$ type of Mg_3Bi_2, from which it differs, however, by the presence of a substantial distortion in Al_3Ge_2 which has been attributed to the departure from valence stoichiometry present in Mg_3Bi_2. Prior structure determinations of metastable Al–Ge phases based on powder patterns[196] were not confirmed by the single-crystal work, as discussed above.

5.2.5. Extended Ordered Metastable Phases

Structurally intermediate between the solid solutions with broad disordered regions typical of the B metals (Section 5.2.2) and the stoichiometric phases with narrow composition ranges (Section 5.2.4) are nonstoichiometric, ordered metastable phases such as

$Pu(Ga_{1-x}Pu_x)$ (CsCl–B2 type), which has been retained by splat-cooling at compositions of ~20–35 at% Ga,[218] and $GeFe_{1-x}$ (CsCl–B2 type), with ~55–90 at% Ge.[217] Both phases are based on stoichiometric AB phases that cannot be retained at the stoichiometric composition by rapid quenching with the crystal structure of the metastable phase based on them. The Pu–Ga phase is of the simple, substitutional type (the degree of ordering, however, has not yet been established); recent results indicate that $Pu(Ga_{1-x}Pu_x)$ may be identical with an extended high-temperature intermediate phase. The Fe–Ge phase is particularly interesting because it represents an extreme example of the cation vacancy type found, e.g., in Al-rich NiAl. With increasing Ge content, vacancies form in the Fe sublattice; the appropriate formula is therefore $Ge(Fe_{1-x}\square_x)$. In contrast to any other similar phase, it extends to very high anion contents. At 90 at% Ge, only 20% of the Fe sites are occupied and the structure approaches that of a solid solution of Fe in a nonexistent modification of Ge with a six-coordinated, simple cubic (α-Po type) structure. Iron atoms then occupy eight-coordinated, hexahedral interstitial sites in this Ge structure. The stabilization of this type over the normal four-coordinated form of Ge by Fe has also been followed by Mössbauer spectroscopy to assess the direction of *s*-electron transfer. Several other first-long-period transition metal elements near Fe show isotypic phases with Ge, while Si does not form comparable phases.

5.2.6. Vapor-Deposited Metastable Intermediate Phases

The formation of elemental and near-elemental phases via atom-by-atom deposition methods was discussed earlier (Section 4). We mention here only one group of results on intermediate alloy compositions: Ricci-Bitti *et al.*[219] have vapor-deposited metastable intermetallic phases of AB stoichiometry with NiAs–B8 type structures in T–B metal systems with extensive liquid immiscibility, where metastable phase formation from the liquid would be impossible. NiPb is an example; these results allow a better outline of the region of occurrence of the crystal-chemically important NiAs type.

5.3. Further Structural Relationships

5.3.1. Absence of Crystalline Single Phases

The miscibility gap between the first and second long periods described above for the metastable phase fields αI and αII at

VEC ~ 2.2–2.5 (fcc Cu–Al type)[20] also exists between Zn and Cd at VEC = 2 (hcp Mg–A3 type) and extends toward higher VEC values into the Ga–In system. In this system, metastable phases with intermediate or high In content could not be retained by rapid quenching; there is only a Ga-related ψ phase at low In contents. It is theoretically possible that there are some compositions in the region outlined by the elements Zn, Ga, Cd, and In for which no single crystal structure has a smaller free energy than an amorphous solid down to 0°K, i.e., it is possible that the metallic glass is the lowest energy condensed single phase at these compositions. If this is indeed the case, a hypothetical element with a (nonintegral) VEC and atomic potential corresponding to a composition in this range would not form a thermodynamically stable crystalline solid at any temperature; an element of this type would only have a glass transition and a boiling point. Any crystalline modification would be metastable with respect to the amorphous solid, which would be the ground state of this element. For alloys, this possibility has been discussed theoretically;[23,220] it is not yet known whether there are alloy compositions for which the amorphous solid has a higher enthalpy of formation than any crystalline phase, but the behavior of the alloys discussed here suggests this possibility.

5.3.2. Relations to High-Pressure and Possible Negative-Pressure Phases

A number of elements and intermetallics have high-pressure phases with the same structure as the standard low-pressure form of other elements or compounds. Typical examples are found in rare earth metals,[201] where some high-pressure modifications have the crystal structures of the adjacent elements with lower charge, and Tl, which has an fcc Cu–Al type high-pressure form that is isostructural with the equilibrium intermetallic phase α-(Tl–In).[221] The latter relation is especially interesting because α-(Tl–In) has the same valence as Tl, but a small atomic volume; the structural effect of alloying A with a smaller element B thus is seen to simulate hydrostatic compression of A. Conversely, the structural effect of alloying B with the larger element could then be expected to simulate hydrostatic expansion of B. In contrast to the case of compression, substantial hydrostatic expansion cannot be produced in a direct experiment since large hydrostatic tensile stresses ("negative pressure") cannot be sustained due to material failure. Therefore,

it would be especially valuable to be able to simulate the condition of volume increase by alloying with a somewhat larger isovalent element. Although a direct demonstration is not possible as it was in the positive-pressure case, there is no reason why the structural effects of pressure and alloying should not be similar over a limited range of volume changes for negative pressures as well.

The number of alloy systems showing a pressure–composition relation can be significantly increased if metastable phases are also considered. The Al–Ga system is a good example and will be discussed here; it also illustrates a number of the phases forming the phase fields discussed in Section 5.2.2. The Al–Ga equilibrium diagram and a plot of the metastable phases retained after quenching to −190°C are given in Figure 24.[20,222] The supercooling and subsequent cooling rates of splat-quenching were sufficient to retain metastable phases in good yield over almost the total composition range; one may assume that the observed extended terminal solid solutions and disordered intermediate phases are the disordered alloy phases with the lowest free energies at their respective compositions. (In some other systems, e.g. Au–Bi,[210] ordered metastable phases of lower free energy can be formed by heat-treating of disordered phases, but this effect is unlikely to take place in Al–Ga

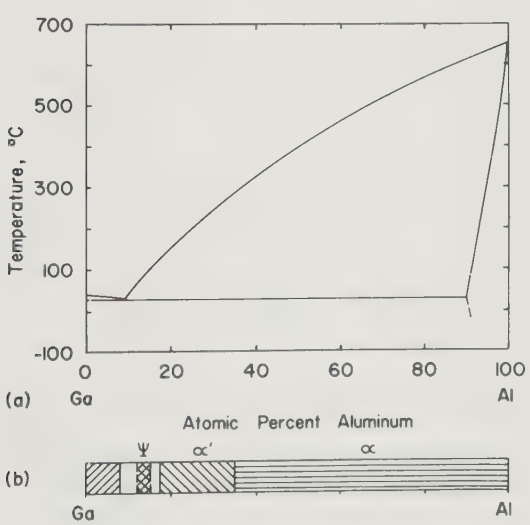

Fig. 24. The Ga–Al alloy system: (a) equilibrium phase diagram and (b) quenched-phase plot of metastable phases retained at 77°K.[222]

alloys; in any case, it is immaterial to the present discussion, which involves element-like disordered phases.)

On adding Ga to Al, the metastable α solid solution continually distorts into the α' phase (In–A6 type, see Fig. 22) at higher Ga contents; the axial ratio c/a of α' (in face-centered tetragonal setting) increases from 1.00 at 65 at% Ga to 1.086 at 82.5 at% Ga. The α' phase is isostructural with a reported high-pressure form of gallium, GaII. Apparently, an even stronger distortion of α' upon alloying would be energetically unfavorable and a new phase, ψ (orthorhombic), appears which is structurally closely related to β-Ga (monoclinic) and another high-pressure form of gallium, GaIII.[76,222] A parabolic atomic volume plot for α and α' allows the determination of the atomic volume for Ga in 12-fold coordination by extrapolation.

Both ψ and α' are identical or closely related to reported high-pressure forms of Ga; although no experimental data seem to exist, one would predict that the α'-type high-pressure modification GaII will have decreasing axial ratios with increasing pressure until at a sufficiently high pressure an fcc Cu–Al type modification corresponding to α appears. Conversely, the large range of extended metastable solid solution in Al-Ga suggests that under conditions of hydrostatic expansion, Al would retain its fcc Cu–Al type crystal structure to high negative pressures.

Further study of the pressure–composition effect in stable and metastable phases would be desirable. Thus, it would be important to establish whether the structure changes scale with the volume change in the same way if several isovalent solute elements with different atomic size are dissolved in a given element to form metastable phases. Unfortunately, it has not yet been possible to prepare the appropriate metastable solid solutions by liquid quenching, since the respective phase diagrams are unfavorable; vapor quenching would probably be required for this. Also, calorimetric measurements would be useful to obtain structural energy differences directly.

If a limited equivalence of alloying and high-pressure effects is confirmed for simple metals, it would be likely that the effects of hydrostatic expansion are correctly represented by alloying as suggested here. A check on the validity of fundamental calculations of the structural energy, e.g., by the pseudopotential method,[8] would then be possible for increasing as well as decreasing volumes. Information on the relation between enthalpy and volume may also assist in partitioning the effect of increasing volume from other

thermal effects which may lead to phase changes as the temperature is increased.

6. Supersaturated Terminal or Intermediate Solid Solutions

One of the first effects involving metastable alloy formation observed on studying the structures of rapidly quenched alloys was the extension of the terminal solid solubility within their equilibrium crystal structure.[35,36,223,224] This effect was found to be very common and is present to some degree in almost every alloy system investigated under appropriate quenching conditions. It includes the formation of several complete metastable solution series;[35] a related, later development was the metastable extension of intermediate equilibrium phases. Subsequently, analogous effects were observed in vapor-deposited and sputtered alloys. Reviews are found, e.g., in Refs. 4, 7, 19, and 21.

6.1. Occurrence and Study of Extended Solid Solutions

6.1.1. Extent of Solid Solubility

The extensions of the compositions of metastable solid solutions in splat-cooled alloys range from a fraction of the equilibrium value in the case of alloys having considerable equilibrium solid solubility to a factor of about 100 of the equilibrium value for systems with very low equilibrium solid solubilities, as found, e.g., in some aluminum-based transition metal alloys.[7]

As in the case of amorphous and crystalline intermediate phases (see Sections 3 and 5), vapor quenching by coevaporation and sputtering are potentially more powerful methods of achieving supersaturated metallic solid solutions than rapid quenching from the liquid. This is due to the reasons discussed above (Section 1), especially the thermodynamic arguments given, the atomistic nature of the deposition process, which allows "burial" of one component in the other, and the faster quenching rate following atom deposition. Beyond this, there are other unique advantages to vapor quenching methods. Thus, terminal solid solutions of metals immiscible both in the liquid and the solid equilibrium modifications, which are therefore not amenable to preparation by rapid liquid quenching, can be synthesized by vapor quenching using coevaporation or sputtering from the appropriate composite sources; an analogous approach was described above for intermetallic phases formed by

elements immiscible in the liquid, e.g., Ni–Pb (Section 5.2.6). Another type of supersaturated solid solution that is unique to the atomistic film deposition techniques (evaporation and sputtering) is that of metals incorporating abnormally large amounts of gases, as discussed below.

The principal types of extended solid solutions to be reviewed here are (1) complete metastable solid solutions; (2) partial substitutional metastable solid solutions; (3) partial nonsubstitutional metastable solid solutions; (4) metastable solid solubility increases of equilibrium intermediate phases; (5) metastable solutions of gases in metal films.

6.1.2. Formation and Characterization of Metastable Solid Solutions

Most metastable solid solutions reported to date have been produced from the liquid by fast cooling methods reviewed in Section 2;[4,7,35–39] however, there is a growing body of work on vapor-deposited solid solutions.[24,25] In some of these, e.g., Cu–Co and Cu–Au, a metastable amorphous phase was found to precede formation of the metastable solid solutions under the appropriate conditions of low substrate temperatures (see below).[86] More extensive comparisons of the properties of vapor-deposited solid solutions with those of the corresponding liquid-quenched phases would be desirable; the same, of course, is true for other types of metastable phases. A step in this direction has been made by work on flash-evaporated Al(Ni) solid solutions, which can be compared to liquid-quenched alloys of the same compositions.[225]

Concerning the quality of data on metastable solid solutions produced from the liquid, including their reproducibility, a word of caution is required. Extensions of the solid solubility are often observed qualitatively in splat-cooled alloys; however, reliable, quantitive data on the properties of these alloys are generally scarce. This is due to several causes whose effects are usually not considered in the primary literature:

1. The actual composition of a metastable phase may differ significantly from the nominal composition of the alloy, even if a second phase is not noticed in the X-ray diffraction pattern. Failure to observe its formation may be due to the small amount of second phase or strong line broadening, which may reduce the maximum intensities of diffraction peaks due to the second phase to the level of the background fluctuations. In the case of extreme broadening,

a fine-crystalline precipitate or a small amount of an amorphous phase may be overlooked. Coring and dendrite formation are other microstructural features which cause departures of the local compositions from the nominal overall value. The discussion of microsegregation given in Ref. 7 is especially appropriate in this context. A clear distinction between homogeneous and inhomogeneous supersaturation is also required in each case.

2. The lattice parameters of splat-cooled alloys and their variations with composition may contain a significant component (generally a fractional reduction by $\sim 10^{-3}$) due to vacancy formation.[226] This effect is generally not considered in data presentation. If allowance is made for it,[227] this is done by using the departure of the lattice parameters of the rapidly quenched terminal phases from their equilibrium values as a calibration for the intermediate alloys. This treatment, however, assumes the effect of vacancies on the lattice parameter to be independent of composition, although this assumption probably is not generally valid; in many systems, attractive solute–vacancy interactions exist which may affect both the effect of excess vacancies on the lattice parameter per vacancy as well as their concentration.

3. Diffraction patterns of splat-cooled phases generally show considerable line broadening. In the case of metastable solid solutions, this effect increases with the increasing supersaturation, probably largely because of crystallite size decreases due to increased supercooling (composition-dependent line broadening in metastable β-Zr alloys is discussed below, Section 6.2.2.4). While size effects generally cause symmetric line broadening, alloy inhomogeneities and structure defects such as strains, stacking faults, and twinning, most of which cause asymmetric broadening, may also be present; this error source is generally not considered quantitatively in lattice parameter determinations. The presence of a substantial amount of stacking faults in noble metal alloys has been shown by transmission electron microscopy;[228] by a careful evaluation of line broadening in a splat-cooled ε-Pu(Ti) solid solution using Fourier methods,[229] the presence of strains and stacking faults resulting in asymmetric line shapes has been determined.

4. Frequently, forward reflections are the only lines in the diffraction pattern of splat-cooled phases that are sharp enough for measurement; they are often evaluated using standard extrapolation procedures which are not applicable without adequate internal calibration.

Other quantities may pose measurement problems comparable to those for lattice parameter data. Thus, the limit of solid solubility extension is often difficult to determine by X-ray diffraction; the problems encountered are the same as in the application of the isoparametric method for the determination of equilibrium solid solubilities. Problems arise, e.g., if solute and solvent have similar apparent atomic volumes, or in nonsubstitutional solid solutions (see below) which have almost constant lattice parameters. Even if the limit of solid solubility extension is measurable, it is a property that depends very strongly on processing variables such as the cooling rate; it is therefore useful only in a very general way unless the thermal history of the sample is also reported, e.g., in the form of a cooling rate parameter or, better, set of parameters. Plots of the maximum homogeneous extension of the solid solubility versus the cooling rate would be particularly desirable from a practical viewpoint; however, the necessary data are difficult to obtain experimentally because most rapid liquid quenching techniques, such as the gun technique (Section 2.4), are not well suited for operation with a controlled, variable range of cooling rates.

6.2. Crystal Chemistry and Properties of Metastable Solid Solutions

Some systems typical of the categories listed in Section 6.1.1 are presented in the following (for details of quenched phase plots and other data, see Refs. 4 and 7; for a listing of specific systems see Refs. 19 and 21).

6.2.1. Complete Metastable Solid Solutions

Phases of this type have been retained by splat-cooling in the systems Ag–Cu,[35] Ge–GaSb,[230] Ag–Pt,[231] Rh–Cu,[232] Rh–Ni,[232] Zr–RE (RE = rare earth metals),[233,234] and Pu–Ce.[227] The binary or pseudobinary combinations listed here generally fall into the category of systems having appreciable equilibrium terminal solid solubility (>5 at %); the substantial metastable extension of the solid solutions is therefore not unexpected.

The constituents of binary systems forming complete metastable solid solutions tend to belong to one of three categories; metals in the same group but different periods (Ag–Cu); more frequently, metals from adjacent groups and different periods (Rh–Ni, Ag–Pt, Zr–RE); or other crystal-chemically related elements (Pu–Ce).

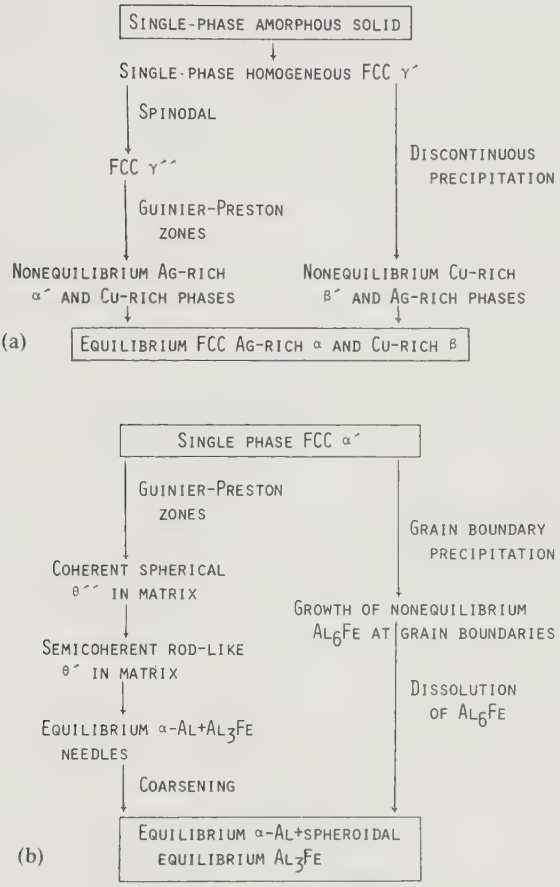

Fig. 25. (a) Transformation sequence for splat-cooled and vapor-quenched Cu–50 at % Ag alloys; (b) transformation sequence for metastable fcc Al–Fe solid solutions containing 2–4 at % Fe.[7]

The Ag–Cu system was the first system in which a metastable complete series of solid solutions was produced by splat-cooling;[35] its free energy diagram has been discussed in Section 1.3. Subsequently, a complete series of crystalline Ag–Cu solid solutions was also produced by vapor quenching;[86] an amorphous phase has also been prepared in a limited composition range by this technique. The modes of decomposition of Ag–Cu solid solutions prepared by both methods have been studied; they are presented in Figure 25(a).[7] Both a continuous and a discontinuous pathway

exist from the homogeneous solid solution to the equilibrium two-phase mixture.

Strictly speaking, the Ge–GaSb[230] does not belong in the present category of complete metastable solid solutions, since the terminal phases are not isostructural. Although the atomic sites are identical in Ge (Si–A4 type) and GaSb (ZnS–B4 type), the two structures differ by the presence of order in the latter; on going from Ge to GaSb, at least partial ordering must appear in metastable alloys at an intermediate composition and increase toward higher GaSb contents. This aspect has not yet been studied. As in the similar situation in the Ti–TiFe partial system (Section 6.2.4), the question still remains whether the order parameter observed in the quenched alloy at a given composition indeed corresponds to the lowest free energy.

In the Pu–Ce system, both constituent elements have isostructural fcc Cu–A1 type modifications; however, in the metastable Pu–Ce alloys an electronic phase transition occurs which is analogous to that between α- and γ-Ce, where two isostructural phases of different valence and, hence, different size exist. The system is listed here since there are metastable continuous solid solutions based on the structure of one or the other fcc modifications over almost the complete composition range.[227]

The Zr–RE solid solutions[233] are treated in Section 6.2.2.3. The remaining systems listed under the present heading will not be discussed here in detail; the occurrence of extended metastable solid solutions in them can generally be understood from simple crystal-chemical considerations.

6.2.2. Partial Substitutional Metastable Solid Solutions

In most alloy systems tested by rapid quenching from the melt, there is at least some increase of the partial solid solubility over the maximum equilibrium value C_{max}. The main constitutional requirements for a substantial solid solubility increase are: Decrease, or at least a slow rather than a steep increase, of the free energy curve of the solid solution with composition; a liquidus curve that does not rise rapidly with composition; absence of competing crystalline intermediate phases. By comparison, other features of the equilibrium diagram, such as the position of the eutectic or incipient liquid immiscibility, are less effective.

The main groups of systems studied and discussed in detail in the following are based on Al; Fe, Co, and Ni; and actinides and rare earths. Other groups of systems are discussed here more summarily; they are based on the noble metals Cu, Ag, and Au, early transition metals such as Zr, and B metals as discussed above in the context of their intermediate phases.

6.2.2.1. Aluminum-Based Solid Solutions

Because of their importance and readily accessible melting temperatures, metastable Al-based alloy systems have been studied more than any other family of metastable crystalline alloys; to some degree, this pattern repeats the historic development in the physical metallurgy of nonferrous equilibrium alloys, where Al played a similar role. As mentioned, the equilibrium solid solubilities of the transition metals Fe, Co, and Ni in Al are very small ($< \sim 0.02$ at%).[235] The ability to prepare supersaturated solid solutions with appreciable maximum solid solubilities of the order of several atomic percent of Fe, Co, and Ni in Al by nonequilibrium methods was therefore valuable since it allowed the study of many properties of these alloys which have potential technical importance. It was of special interest to determine whether age hardening phenomena similar to those in Al(Cu) occur in Al-based solid solutions of the transition metals adjacent to Cu.

Alloys of Al with the transition metals of the first long period, especially Fe and Ni, and with Mo, W, Cu, Zn, Mg, Si, and Ge have been studied most. These investigations have yielded many experimental data which are not always in agreement (see Section 6.1.2). It is not surprising that the maximum metastable terminal solid solubilities vary in different studies, since they depend strongly on the cooling rates obtained; one finds, however, that other properties reported for these solid solutions, such as the lattice parameters, also vary substantially, indicating a need for better material characterization, as discussed above.

By flash evaporation, supersaturated Al(Ni) solid solutions with up to 13 at% Ni were prepared.[225] Aluminum-based alloys have been used in calibration methods for rapid liquid quenching processes, both in the dendrite arm spacing method[236] and the method based on the eutectic lamellar spacing,[237] which utilizes the Al Al_2Cu eutectic. Lattice parameters have been measured in many Al based

systems, including all those listed above, as well as those with other transition metals of groups 4–6 and 10, noble metals, and others. Reviews are given in Refs. 19 and 21. There have been attempts to correlate the slopes of the composition plots of the lattice parameter or atomic volume with various solute characteristics, following the state of the art of the theory of dilute metallic solid solutions. Slopes were correlated with solute atomic number,[238] size,[239] and predictions derived from quantum mechanical calculations.[240]

Resistivity changes have been measured and interpreted in a number of Al alloys.[241,242] In view of potential applications of metastable Al alloys, transformation studies on supersaturated Al solid solutions have been important. Activation energies of precipitation have been derived from lattice parameter measurements on metastable Al(Si) solid solutions with up to 11 at% Si.[243] In recent work, the activation energies of incipient precipitation in metastable Al(Si) alloys have been determined by transmission electron microscopy[244] and have been found to be substantially lower than the overall values,[243] probably due to a large excess vacancy concentration in liquid-quenched alloys. For Al(Fe), the transformation sequence given in Figure 25(b)[7] was established by work discussed in Ref. 7; there are different transformation paths for material inside the grains and at their boundaries. The former sequence is similar to that for Al(Cu); the latter involves a metastable intermediate phase Al_6Fe of undetermined structure. Mechanical properties have been determined, primarily by microhardness measurements;[245] increased strength and high-temperature plasticity were demonstrated.[7] Microhardness variations have been correlated with lattice parameter changes for different transition metal solutes.[245]

6.2.2.2. Metastable Solid Solutions Based on Iron, Cobalt, and Nickel

A large body of work exists on alloys of these technologically important transition metals; substantial solid solubility increases have been reported. Extended Fe(W)[246] and Fe(Ga)[247] solid solutions have been prepared; the latter order at and near the composition Fe_3Ga.[248] Coevaporated Fe–Cu films with up to 78 at% Cu were also studied.[249] Cobalt-based metastable solid solutions are characterized by stabilization of the fcc Cu–Al type α-Co modification by alloying additions, with typical metastable increases of 15–100% of the equilibrium solid solubility for Al, Cu (the solid solubility was increased from 12 to 25 at% Cu in liquid-quenched

films),[250] Ga, Ge, and Sn.[19,21] In Co(Au) alloys, there was an especially large solubility increase from 2.5 to 31 at% Au (in incompletely quenched, multiphase alloys);[250] however, in the same system, a complete series of solid solutions has been produced in vapor-quenched films by annealing of the initially formed, amorphous Co–Au phase, as mentioned above.[86] Nickel-base solid solutions with V,[251] Nb,[215] and other transition metals[21] show only small solid solubility increases; this is assumed to be largely due to the occurrence of competing intermetallic phases.[215]

6.2.2.3. Solid Solutions Based on Actinides and Rare Earths

A number of interesting alloying effects were observed in splat-cooled actinide alloys based on Pu and Np. These alloys also illustrate the possibility of producing metastable solid solutions based on solvent element modifications with acceptable cold-working properties in cases where the room-temperature equilibrium structure of the element in question has an undesirably low ductility.

The α-Pu modification is monoclinic, i.e., it has low crystallographic symmetry, and it is characterized by poor workability. For some purposes, the fcc Cu–Al-type δ modification is therefore used, as stabilized by small alloying additions of elements such as Ga.[252] While it would be of interest to be able to retain Pu also in the bcc W–A2-type ε modification, no room-temperature ε-stabilizer is known, although a number of elements such as Ti extend the high-temperature ε range substantially. Splat-cooling of Pu(Ti) alloys with 18 to >45 at% Ti resulted in the retention of ε solid solutions, while splat-cooled alloys with <5 to 25 at% Ti showed the δ structure.[253] Thus, both forms occur in the narrow composition range between 18 and 25 at% Ti; which Pu(Ti) modification is present in any portion of the alloy is probably a function of the local cooling rate. These results indicate the potential of splat-cooling for the manufacture of Pu alloys.[254]

The behavior of Np(Ga) solid solutions is especially interesting from a crystal-chemical viewpoint. Neptunium has three modifications, α, β, and γ, of which α and β have lower symmetry; like ε-Pu, γ-Np is bcc, W–A2 type. Splat-cooled alloys of Np with 10–40 at% Ga were found to have a γ-Np type structure.[255] Figure 26(a) shows the lattice parameters of these γ solid solutions; they show an unexpected, strong increase, as compared to a Vegard's law straight line. The changing partial atomic radii of Np [Figure 26(b)] were

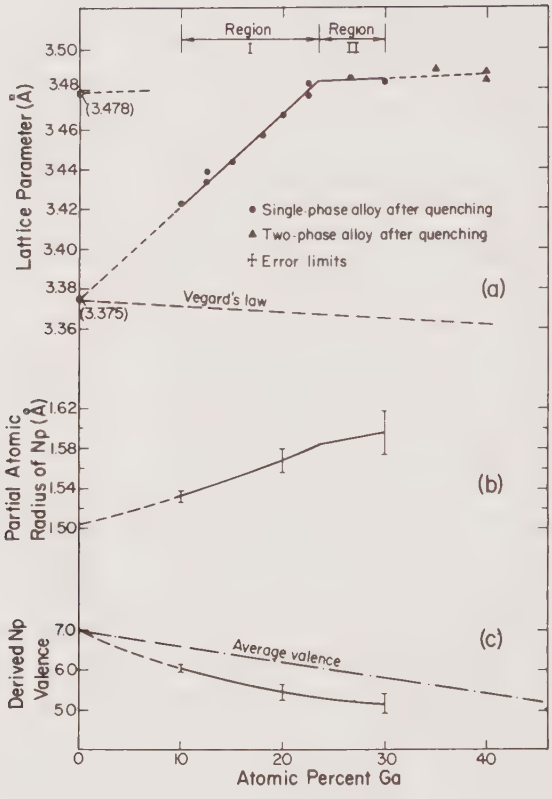

Fig. 26. Parameters of splat-cooled Np–Ga alloys vs. composition. (a) Lattice constants of metastable bcc γ-Np(Ga) solid solution; (b) partial atomic radius of Np, $PR_{Np}(x)$, in γ-Np(Ga); (c) valence of Np in γ-Np(Ga).[225]

calculated from the data in Figure 26(a); from the radii the valence n of γ-Np in solid solution was assessed [Figure 26(c)] and found to decrease between 0 and 40 at% Ga by $\Delta n = 1.8$, probably due to the increasing mutual separation of Np atoms by Ga; the resulting reduced orbital overlap was thought to be the cause of the observed valence decrease by electron localization.[255]

In a systematic study of metastable solid solutions of the heavy trivalent rare earths and Y with Zr,[233] partial solid solubility of the hcp Mg–A3 type modifications of the rare earths and Zr was found in splat-cooled alloys of Gd, Tb, and Y and complete or "nearly" complete solid solubility in alloys of Lu and Dy, Ho and Er, respectively. These solid solutions were formed at least in part by martensitic

transformations of metastable high-temperature solid solutions of the W–A2 type; higher cooling rates probably would have led to complete metastable solid solubility in all investigated systems of rare earths with Zr despite the marginally unfavorable atomic size factors of these systems. The metastable solid solubilities in RE–Zr and RE–Ti systems have been discussed as a function of electronegativity and atomic size differences.[234]

6.2.2.4. Other Systems with Partial Substitutional Solid Solutions

We review here briefly results on alloys from a number of systems not covered under other, specific headings of Section 6.2.2.

Solid solutions based on the noble metals Cu, Ag, and Au, especially those with B metal solutes of group IV, have been studied extensively, partly in the context of metastable intermediate Hume-Rothery phases in systems such as Ag–Ge (see Section 5.2.1) and the transition between the terminal solid solution and the intermediate phase. Both of these phases represent polytypes (i.e., stacking variants) of 12-coordinated close-packing.[201] The generally observed decrease of the stacking fault energy of the terminal fcc Cu–Al type with increasing B-metal solute content suggests the possibility of a gradual transition from the c-type atomic coordination of the noble metals to the h-type coordination in the hcp Mg–A3 type intermediate alloy phase if both are connected by a series of metastable alloys. Solid solutions with an increasing percentage of h-type coordinated close-packed layers are expected to form as the solute concentration and, with it, the average valence electron concentration increase.[201,203] Conversely, starting from the hcp crystal structure of the compound, a decrease of the solute concentration will result in a decrease of the corresponding stacking fault energies of the hcp type and increased faulting. The intermediate region, however, has not yet been adequately explored experimentally. Thus, it is likely that metastable close-packed polytypic phases with stacking sequences intermediate between those of the pure c- and h-type phases but with periodic layer arrangements, such as the α-La and α-Sm structure types (with 50 and 66.7% h-type stacking, respectively),[201,256,257] would have lower free energies than the corresponding disordered phases with the same composition and percentage of h-type stacking and should therefore form. This assumption is based on a consideration of the enthalpy term, which is expected to dominate due to the low entropy of a one-dimensionally disordered structure.

Other metastable, noble-metal-based solid solutions have been produced by vapor deposition. A film of Cu + ~8 at% W having a thickness of 1 μ was prepared by electron beam coevaporation; spiral growth features were observed and attributed to screw dislocations.[258] Coevaporated Au–Co alloys have been studied repeatedly[86,259] (see also above, Section 6.2.2.2); in the latter study, Au(Co) alloys with up to 30 at% Co were prepared on Ni substrates cooled to liquid N_2 temperature.

Metastable solid solutions of many transition metals and Cu in Zr were prepared and studied by Ray;[260] all of these solutes stabilize the bcc β-modification of Zr. A determination of the grain size from X-ray linewidths showed a rapid decrease at 10–30 at% solute. In most of the investigated systems, a noncrystalline phase was retained at higher solute concentrations;[74] however, this phase does not seem to be continuously connected to the solid solution range.

Metastable solid solutions have also been prepared in many of the inter-B-metal alloy systems formed by elements of the Zn and Al groups, Sn, Pb, and others discussed earlier in the context of the crystal chemistry of their intermediate phases (Section 5.2).[20] These extended solid solutions form an integral part of the phase fields described there and need not be treated further in this section. As mentioned, only very limited metastable solid solubility could be obtained in the Zn–Cd binary system;[261] terminal solid solutions form in a system of this type under conditions of local nonequilibrium, as discussed in Ref. 3. It is assumed that solidification proceeds by burial of one component whose chemical potential increases in the process while the overall free energy decreases.

6.2.3. Partial Nonsubstitutional Solid Solutions

Two groups of metastable solid solutions representing this category are discussed here; they differ primarily in the chemical nature of the solute element. The first group consists of solid solutions of metal atoms with small atomic radii in rare earth, actinide, and B-metal hosts having large atomic radii; extended solid solutions of combinations of these elements exist only in the metastable state. The second group is based on the well-known interstitial solid solutions of metalloids such as carbon in late transition metals; in alloys of this kind, rapid quenching leads only to a moderate extension of the equilibrium solubility, but, in addition, an interesting hexagonal, metastable Fe–C solid solution has been produced.

6.2.3.1. Nonsubstitutional Solid Solutions of Metals in Metals

The equilibrium solid solubility of metals in metals is extremely limited if the atomic sizes of solvent (radius R) and solute (radius r) differ by more than $\pm 15\%$. Substantial electronegativity differences will likewise reduce the solubility. Thus, the equilibrium solubility of Ag and Au in Pb is of the order of 0.1 % ($r/R = 0.80$); solutions of Fe and Cu in rare earths ($r/R \sim 0.71$) are other examples of undetermined, very low solid solubilities.[235]

In lead and rare earth alloys such as those listed, rapid liquid quenching leads to large solid solubility increases. By splat-cooling to $-190°C$, metastable solid solutions with up to about 12 at% Ag or Au in Pb were produced;[262] splat-cooling to 20°C resulted in the dissolution of up to ~ 15 at% Fe or Cu in Y or Gd.[263,264] X-ray and density studies have suggested that Y(Cu) solid solutions are interstitial[263] and Gd(Fe) and Gd(Cu) solid solutions are di-substitutional,[264] i.e., in the latter type, two solute atoms occupy one solvent atom site (this configuration is also called a split interstitial). Neither Pb(Ag) nor Pb(Au) solid solutions could be studied densitometrically, due to the low decomposition temperature; however, the type of solid solution present was derived from a measurement of the change of their superconducting transition temperatures with composition. Evaluation of the slope of this plot in terms of simple BCS theory, using a comparison with other Pb-based solid solutions to assess the effect of valence change, suggested that the Pb-based alloys also form disubstitutional solid solutions.[262] Substantial microhardness increases were found in the Gd- and Y-based solid solutions, indicating considerably higher solid solution strengthening by nonsubstitutional than by substitutional solutes.[265] The solution mechanism, however, may be more complex than assumed in the model presented.[263,264] This is suggested by internal friction studies of Gd(Fe) and Gd(Cu) alloys,[266] which have failed to yield the internal friction peak expected from stress-induced rearrangement of stress-active disubstitutional solute atom dumbbells in the hcp matrix; it was concluded that there is probably further defect association in these solid solutions, making the defect non-stress-active.

It may be mentioned that diffusion studies of equilibrium solid solutions[267] based on rare earths and lead had indicated the presence of nonsubstitutional solutions prior to the work on metastable alloys reported here; the presence of disubstitutional and, more recently, higher order solute clusters has been suggested from such data.[268,269]

6.2.3.2. Interstitial Solid Solutions of Metalloids in Transition Metals

The most important system in this category is Fe–C. Splat-cooling of Fe(C) alloys has resulted in the retention of metastable solid solution in alloys with about 13.7–16.9 at % C, in which Fe atoms form an hcp Mg–A3 type arrangement.[270] This phase may be considered as a solid solution of C in the high-pressure modification ε-Fe; because of probable ordering of the C atoms, it is also related to hexagonal ε-carbide. The effect of ternary additions of Si, Co, Mn, etc. on the formation of this phase and its decomposition mechanism were also studied.[270] Enhanced metastable solid solubilities of C in Ni (7.4 at % C) and Co (3.5 at % C) were observed in a related study.[271] Last, the lattice parameters of splat-cooled [Fe, Ni](B) alloys were studied; their values could be understood by assuming that B forms both interstitial and substitutional solid solutions with the solvent.[273]

6.2.4. Metastable Solid Solubility Increases of Equilibrium Intermediate Phases

Intermetallic phases of some structure types, especially the CsCl–B2 type, are capable of substantial nonstoichiometric extensions (see Section 5.2.5 for a discussion of a metastable Ge–Fe phase of this type). In equilibrium, the Fe–Al system offers an example of a continuous transition from the CsCl–B2-type phase FeAl to α- and δ-Fe.[235] A similar transition is found in metastable Ti–Fe alloys, which form a continuous series of solid solutions between TiFe and β-Ti.[273] Upon departing from stoichiometry, TiFe(Ti) begins to disorder at 55 at % Ti; it is completely disordered and has a transition to a metastable β-Ti(Fe) solid solution at 65 at % Ti. The metastable TiFe(Ti) phase falls into an average group number (AGN) range of 5.4–6, comparable with many observed equilibrium phases of this type.[273] TiCo and TiNi form partial metastable solid solutions with Ti, possibly by Ni or Co vacancy formation.[260]

6.2.5. Metastable Solutions of Gases in Metal Films

Solid solutions of gases in metal films are undesirable for technological applications, and various measures are taken to keep the gas incorporation low. Even though the equilibrium solid solubility of most common ambient gases (e.g., O_2, N_2, H_2O, H_2, Ar, He, etc.) present during evaporation or sputtering is well below

1 at%,[235,274,275] abnormally large amounts tend to get incorporated during the deposition (see Section 2 for the various mechanisms). A rather extreme example is that of dc diode sputtered Au films in a He discharge (80–150 μm pressure) on cold substrates and at -80 V substrate bias; such films have been reported to contain 40 at% He.[276] These "Au" films had a matte texture and brown color and were brittle because of high internal stresses. In general, sputtered films are more prone to contain large quantities of gases because of the high background pressures employed and because of the high energies that can be acquired by gaseous atoms or ions under the influence of the electrical fields present in the system. Under usual sputtering conditions, a few at% of Ar, O_2, and N_2 is quite common in thin films of metals like Mo[277] and W.[29,278] A potentially important physical effect of the incorporation of controlled amounts of noble gas in metal thin films was recently reported by Schmidt *et al.*[279] They were able to prepare superconducting Cr by incorporating ~ 0.1 at% Xe or Kr in their ion-beam sputtered films, which had a T_C of 1.52 and 0.96°K, respectively.

7. Concluding Remarks

In this section, the significance of metastable phase research will be treated, followed by a review of metastable phase formation, a brief discussion of alternate methods and products of metastable phase formation, a review of applications of metastable phases, and an outline of areas for further research.

7.1. Significance of Research on Metastable Phases

Major progress in research on solids has often depended on the development of new preparation techniques, which have made new classes of materials available for study, such as, e.g., metals and semiconductors in the form of very high-purity materials and single crystals. Similarly, the possibility for the routine synthesis of metastable materials with high free energy has opened up a new era of materials research, now yielding the first benefits in terms of fundamental understanding and usable materials. This era is characterized by the partial ability to "make what one wants," i.e., the ability to produce inorganic single-phase solids of many compositions as well as some composite materials according to the interest and needs of the concerned scientists and technologists regardless of thermodynamic

stability, subject only to the basic limitation of maintaining structure and shape. These limitations are both energetic and kinetic. The excess enthalpy must not exceed the enthalpy of fusion and the atomic mobility must be sufficiently low. One can envision the preparation of any desired crystalline or noncrystalline material of the types discussed as a metastable phase in constrained equilibrium if it satisfies these necessary conditions. In general, the most suitable preparation methods for these materials will be atom-by-atom techniques such as sputtering or ion implantation.

The current extensive inclusion of metastable materials into the scope of materials science establishes a further relation of this science with chemistry, where nonequilibrium states are commonly encountered in many areas. Thus, much of inorganic and organic chemistry deals with metastable compounds; in fact, it is part of the art of the preparative chemist to find reaction pathways which yield these products. Often thermal treatments are minimized to reduce the risk of undesired equilibration taking place. By contrast, metals, semiconductors, and other inorganic solids are generally prepared at high temperatures, e.g., by vapor-phase reactions or from the melt. (The temperature as used here is a dimensionless, reduced quantity; it is expressed as a fraction of the temperature associated with bond-breaking. Thus, high temperatures correspond to thermal energies high with respect to the bond energy.) Because of this processing parameter, few metastable alloy phases had been observed until recently; most retained nonequilibrium phases were quenched terminal or intermediate high-temperature phases having low excess free energy and atomic mobility at room temperature.

7.2. Review of Metastable Phase Formation

Although thermodynamic data are not yet generally available for the metastable thin-film phases treated in the present chapter, these phases can be classified qualitatively on the basis of the degree of their departure from the equilibrium structure as (1) amorphous (generally dense, randomly packed), (2) topologically close-packed elemental (i.e., σ-phase-related), (3) spherically close-packed elemental (with element-like fcc Cu–Al type or hcp Mg–A3 type phases occurring in nominally elemental materials not normally possessing these structures), (4) intermediate crystalline alloy phases, and (5) supersaturated terminal solutions possessing the equilibrium crystal structure. Of these, phases of the second and third types have so far

been prepared only from the vapor phase, while those of the fourth and fifth types have been generally prepared from the liquid phase, although this is not a requirement for formation.

The factors leading to the formation of metastable phases in thin films deposited from the vapor phase may be materials- and/or process-related. Strong substrate–film interaction in the form of epitaxial forces is responsible for the formation of abnormal pseudomorphic phases such as the spherically close-packed ones. The topologically close-packed, metastable thin-film structures represent an intermediate case between the amorphous, dense, randomly packed and the spherically close-packed structures; they are "nucleation-stabilized" in the sense that once nucleated (usually at low substrate temperatures and in the presence of certain impurities at the substrate), they may continue to grow to films of several thousand angstroms thickness, irrespective of the ambient during further deposition.

Metastable phase formation in thin films is also favored by conditions of low surface mobility, such as a large sticking coefficient and a low substrate temperature, as well as by factors which inhibit the kinetics of equilibration during film deposition, such as fast deposition rates, gaseous impurities in the deposition ambient, and particular modes of film deposition. Thus, ion-beam sputtering has proven particularly fruitful in producing metastable phases in thin films of several transition metals.

In alloys rapidly quenched from the liquid, the effectiveness of alloy chemical factors in determining metastable phase formation relative to that of the processing parameters appears to be generally larger than in vapor-quenched phases. The cooling rate, however, is critical due to its relation to the supercooling, which must exceed a threshold value for metastable phases to be retained, as shown in Section 1.3. At a given cooling rate, though, the type of phase retained (type 1, 4, or 5 of the classification given above) depends largely on the character of the stable and metastable phase diagram, as discussed in detail in Sections 3, 5, and 6.

7.3. Alternate Methods and Products of Metastable Phase Preparation

In the present discussion, several interesting and promising areas of metastable material preparation had to be omitted or were treated only briefly. Among them is ion beam implantation, which has advanced from the status of a specialized technique for the controlled

doping of semiconductors with low concentrations of atoms in the ppm range to a powerful method for the preparation of alloy layers with solute concentrations lying in the percent range. Predominantly substitutional solid solutions have been formed by high-dose implantation of W (up to 15 at %) in single-crystal Cu at room temperature.[280] For hydrogen implanted in Pd alloys, hydrogen/metal atomic ratios of 1–1.2 were obtained;[281] hydride superconductors with $T_C = 16°K$ have been formed in this study. Many other physically and metallurgically interesting materials, such as metals with surface layers having enhanced oxidation and wear resistance,[282] as well as magnetic and optical materials[283] have been prepared by ion implantation.

High-deposition-rate sputtering as a means of manufacturing amorphous metals and metastable crystalline materials in bulk has not been treated here in proper relation to its significance as a preparation method for bulk materials with high free energy.[284] Electrodeposited or electroless solution-deposited films are the product of a well-known technology expressed in many published and proprietory procedures, which has only been dealt with briefly here.

With respect to the materials treated here, it is apparent that the emphasis has been on metals, with complete or partial neglect of such topics as (1) fundamental aspects and applications (e.g., as switching elements) of amorphous semiconductors; (2) ceramic and other nonmetallic amorphous solids related to traditional oxide glasses; (3) crystalline ceramics with nonequilibrium crystal structures, such as the fcc metastable $MgO–Al_2O_3$ phase;[285] and (4) metal–organic compounds prepared by evaporation methods.[286]

7.4. Present and Suggested Applications of Metastable Phases

Sputtered films of β-Ta are extensively used as counterelectrodes for thin-film capacitors and as precision resistors in hybrid integrated circuits. Sputtered films of amorphous Co–Gd have been used to fabricate magnetic bubble devices for memory applications.

Amorphous metals produced by rapid liquid quenching are also being actively investigated for many applications. Present work is concentrated on three topics: mechanical, magnetic, and electronic properties. In the first topic, studies are directed toward developing high-strength materials for applications where the available ribbon or wire shapes resulting from melt spinning or extraction are suitable.

In the second area, there are studies of hard, high-remanence magnets, e.g., those based on rare earth–transition metal alloys,[287] soft magnets, based on iron alloys,[287,288] and memory elements.[289] In the third area, work is directed toward electronic components such as resistors.

For metastable intermediate phases, no applications have as yet been developed; this may largely be due to the choice of the constituent alloy systems, which have been selected following crystal-chemical rather than property considerations.

Materials based on terminal solid solutions presently show promise in two areas: first, as solid solutions proper, either with suitable strengthening or grain-refining additions or as solution-stabilized, technically desirable modifications, as in Pu or Be alloys; second, as fine-grained or precipitation-strengthened alloys after transformation. Solid solutions may also find applications as starting materials for dispersion strengthening by internal oxidation, e.g., in a Ni(Be) alloy.

7.5. Areas for Further Research

For the materials discussed in Section 7.4 with respect to their application potential, extensive research and development work is in process.

Areas for further theoretical work on metastable phases include those discussed in the following: The structural energies of stable as well as metastable crystalline alloy phases are not yet well understood theoretically; presently, pseudopotential calculations do not yield quantitatively correct values which have predictive character.

Amorphous metals pose many questions. The theory of magnetic and other electronic properties, such as the resistivity, is still speculative, although the pertinent literature is increasing fast; magnetic moments of amorphous paramagnets and the magnetization of amorphous ferromagnets are mostly rationalized on an *ad hoc* basis. Theoretical understanding of the mechanical properties of amorphous metals, e.g., their strength and fracture mechanism, and the conditions of their formation are also important areas for further research.

The metastable phases observed in vapor-deposited thin films are of considerable importance. They are most commonly found in very thin films ($< \sim 100$ Å) deposited at low temperatures; this makes them of interest to theoreticians studying relative magnitudes of the energy components associated with surfaces and interfaces, such as

the chemical bonds and packing forces in atomic aggregates only several monolayers thick.

Areas of desirable experimental studies include: Comparison of the properties of metastable phases, especially amorphous metals, with nominally identical compositions which have been prepared by different techniques; measurements of the thermodynamic properties of metastable phases, especially the free energies of formation of amorphous metals; kinetic studies of metastable phase formation continuing and generalizing the investigations of the conditions for amorphous phase formation as a function of cooling rate parameters;[290,291] studies of nucleation and isothermal growth of crystalline phases from metallic glasses.

Other areas for experimental study are the preparation and testing of novel materials, such as amorphous alloys with one or more magnetic components, for magnetic property measurements; amorphous metals with a Kondo-type resistivity minimum for applications as resistors with near-constant temperature characteristic; and topologically close-packed transition metal phases or gas-supersaturated solid solutions for superconductivity measurements.

The technologists will continue work on metallic glasses to develop new materials utilizing their high inherent strength, their potential low magnetic energy product for soft magnets, domain formation for magnetic storage applications, and their potential high coercivity for permanent magnets. In the area of crystalline metastable materials, they will attempt to develop solution- or dispersion-strengthened alloys. The success of β-Ta and amorphous Co–Gd films for device applications highlights the importance of continuing research and development aimed at both exposing and understanding new metastable thin-film phases.

It appears that the research field of metastable alloy phases is now in the steep-slope region of the sigmoid curve described by Swalin for the growth of scientific disciplines and their subareas;[292] this region corresponds to a phase of explosive growth. Quite likely, the maximum growth rate has not yet even been reached at present; much progress both in scholarly understanding and engineering applications can therefore be expected in the years ahead.

Acknowledgment

One of us (B.C.G.) acknowledges financial support by the Office of Naval Research, Contract N14-68-A207-3.

References

1. J. L. Finney, *Proc. Roy. Soc.* (Lond.) *A* **319**, 479 (1970).
2. J. W. Christian, *The Theory of Transformations in Metals and Alloys*, Pergamon Press (1965).
3. J. C. Baker and J. W. Cahn, in *Solidification*, American Society of Metals, Metals Park, Ohio (1971), p. 23.
4. B. C. Giessen and R. H. Willens, in *Phase Diagrams: Materials Science and Technology*, Vol. 3 (A. M. Alper, ed.), Academic Press, New York (1970), p. 103.
5. A. K. Jena, B. C. Giessen, M. B. Bever, and N. J. Grant, *Acta Met.* **16**, 1047 (1968).
6. T. R. Anantharaman, H. L. Luo, and W. Klement, *Trans. Met. Soc. AIME* **233**, 2014 (1965).
7. H. Jones, *Rep. Prog. Phys.* **36**, 1425 (1973).
8. V. Heine and D. Weaire, in *Solid State Physics*, Vol. 24 (H. Ehrenreich, F. Seitz, and D. Turnbull, eds.), Academic Press, New York (1970), p. 249.
9. L. Kaufman, in *Phase Stability in Metals and Alloys* (P. S. Rudman, J. Stringer, and R. I. Jaffee, eds.), McGraw-Hill, New York (1967), p. 125.
10. H. S. Chen and D. Turnbull, *Acta Met.* **17**, 1021 (1969).
11. J. D. Bernal and J. Mason, *Nature* **188**, 910 (1960).
12. A. K. Sinha and P. Duwez, *J. Phys. Chem. Solids* **32**, 267 (1971).
13. D. Watanabe and R. Miida, *Jap. J. Appl. Phys.* **11**, 296 (1972).
14. A. K. Sinha, in *Progress in Materials Science* (B. Chalmers, J. W. Christian, and T. B. Massalski, eds.), Pergamon Press, Oxford (1972), Vol. 15, No. 2.
15. J. G. Allpres and J. V. Sanders, *Aust. J. Phys.* **23**, 23 (1970).
16. J. D. Bernal, in *Liquids: Structure, Properties, Solid Interactions* (T. J. Hugel, ed.), Elsevier, Amsterdam (1965), p. 25.
17. W. Hume-Rothery, R. E. Smallman, and C. W. Haworth, *The Structure of Metals and Alloys* (The Institute of Metals, London (1969).
18. P. Duwez, *Trans. Am. Soc. Metals* **60**, 607 (1967).
19. B. C. Giessen, in *Developments in the Structural Chemistry of Alloy Phases* (B. C. Giessen, ed.), Plenum Press, New York (1969), p. 227.
20. B. C. Giessen, in *Advances in X-Ray Analysis*, Vol. 12 (C. S. Barrett, J. B. Newkirk, and G. R. Mallett, eds.), Plenum Press, New York (1969), p. 23.
21. H. Jones and C. Suryanarayana, *J. Mater. Sci.* **8**, 705 (1973).
22. P. Duwez, in *Intermetallic Compounds* (J. H. Westbrook, ed.), Wiley, New York (1970).
23. B. C. Giessen and C. N. J. Wagner, in *Liquid Metals, Chemistry and Physics* (S. Z. Beer, ed.), Marcel Dekker, New York (1972), p. 633.
24. L. I. Maissel and R. Glang, Eds., *Handbook of Thin-Film Technology*, McGraw-Hill, New York (1970).
25. K. L. Chopra, *Thin Film Phenomena* McGraw-Hill, New York (1969).
26. S. Mader, *J. Vac. Sci. Technol.* **2**, 35 (1965).
27. A. K. Sinha, in *Proc. 6th International Vacuum Congress* [*Japan J. Appl. Phys.* Suppl. 2, Part 1 (1974)], p. 487.
28. A. K. Sinha, T. E. Smith, T. T. Sheng, and N. N. Axelrod, *J. Vac. Sci. Technol.* **10**, 436 (1973).
29. R. S. Wagner, A. K. Sinha, T. T. Sheng, H. J. Levinstein, and F. B. Alexander, *J. Vac. Sci. Technol.* **11**, 582 (1974).

30. K. L. Chopra, M. R. Randlett, and R. H. Duff, *Phil. Mag.* **6**, 261 (1967).
31. L. I. Maissel in Ref. 24, p. 4-1.
32. H. F. Winters and E. Kay, *J. Appl. Phys.* **38**, 3928 (1967).
33. G. S. Cargill, III, *J. Appl. Phys.* **41**, 12 (1970).
34. J. P. Marton and M. Schlesinger, *J. Electrochem. Soc.* **115**, 16 (1968).
35. P. Duwez, R. H. Willens, and W. Klement, *J. Appl. Phys.* **31**, 1136 (1960).
36. P. Duwez and R. H. Willens, *Trans. Met. Soc. AIME* **227**, 362 (1963).
37. P. Pietrokowsky, *Rev. Sci. Instr.* **34**, 445 (1963).
38. H. S. Chen and C. E. Miller, *Rev. Sci. Instr.* **41**, 1237 (1970).
39. R. Pond and R. Maddin, *Trans. Met. Soc. AIME* **245**, 2475 (1969).
40. B. C. Giessen, N. M. Madhava, R. J. Murphy, R. Ray, and J. Surrette, *Met. Trans.*, in print (1976).
41. W. A. Elliot, F. P. Gagliano, and G. Kraus, *Metall. Trans.* **4**, 2031 (1973).
42. R. C. Ruhl, *Mater. Sci. Eng.* **1**, 313 (1967).
43. P. H. Shingu and R. Ozaki, *Met. Trans.* **6A**, 33 (1975).
44. M. L. Rudee, *Phys. Stat. Sol.* (*B*) **46**, K1 (1972).
45. P. Chaudhari, J. F. Graczyk, and S. R. Herd, *Phys. Stat. Sol.* (*B*) **51**, 801 (1972).
46. M. L. Rudee and A. Howie, *Phil. Mag.* **25**, 1001 (1971).
47. A. Howie, O. L. Krivanek, and M. L. Rudee, *Phil. Mag.* **27**, 235 (1973).
48. P. Chaudhari, J. F. Graczyk, and S. R. Herd, IBM Research Report RC 4491 (1973).
49. W. Cochran, in *Tetrahedrally Coordinated Amorphous Semiconductors* (M. H. Brodsky, S. Kirkpartrick, D. Weaire, eds.), AIP Conference Proc. # 20, AIP, New York (1974).
50. T. Takamori, R. Messier, and R. Roy, *J. Mater. Sci.* **8**, 1809 (1973).
51. G. O. Jones, *Glass*, Methuen, London (1956).
52. M. R. Bennett and J. G. Wright, *Phys. Stat. Solids* **A13**, 135 (1972).
53. B. G. Lazarev, E. E. Semeneko, and A. I. Sudovtsov, *Soviet Phys.—JETP* **12**, 811 (1961).
54. B. G. Lazarev, A. I. Sudovtsov, and A. P. Smirnov, *Soviet Phys.—JETP* **6**, 816 (1958).
55. R. E. Glover, III, S. Moser, and F. Baumann, *J. Low Temp. Phys.* **5**, 519 (1971).
56. S. Fujime, *Jap. J. Appl. Phys.* **5**, 778 (1966).
57. S. Fujime, *Jap. J. Appl. Phys.* **5**, 764 (1966).
58. J. C. Suits, *Phys. Rev.* **131**, 588 (1963).
59. T. E. Hutchinson, *Appl. Phys. Lett.* **3**, 51 (1963).
60. F. Schrey, R. D. Mathis, R. T. Payne, and L. E. Murr, *Thin Solid Films* **5**, 29 (1970).
61. H. Richter, *J. Vac. Sci. Tech.* **6**, 855 (1969).
62. S. Fujime, *Jap. J. Appl. Phys.* **5**, 1029 (1966).
63. J. R. Bosnell and U. C. Voisey, *Thin Solid Films* **6**, 107 (1970).
64. C. W. B. Grigson and D. B. Dove, *J. Vac. Sci. Tech.* **3**, 120 (1967).
65. J. L. Robertson and B. A. Unvala, *Phil. Mag.* **24**, 1253 (1971).
66. W. Buckel and R. Hilsch, *Z. Phys.* **138**, 109 (1952).
67. M. V. Coleman and D. J. D. Thomas, *Phys. Stat. Sol.* **24**, K111 (1967).
68. R. Grigorovici and R. Manaila, *Thin Solid Films* **1**, 343 (1967).
69. E. I. Alessandrini, R. J. Gambino, and J. D. Kuptsis, *Thin Solid Films* **11**, 415 (1972).

70. H. Richter, *Phys. Z.* **44**, 406 (1943).
71. R. L. Falge, *Phys. Lett.* **24A**, 579 (1967).
72. W. B. Pearson, *The Crystal Chemistry and Physics of Metals and Alloys*, Wiley–Interscience, New York (1972), p. 236.
73. W. Buckel, *Z. Physik* **138**, S136 (1954).
74. R. Ray, B. C. Giessen, and N. J. Grant, *Scripta Met.* **2**, 357 (1968).
75. R. C. Ruhl, B. C. Giessen, M. Cohen, and N. J. Grant, *Acta Met.* **15**, 1693 (1967).
76. B. C. Giessen, M. Madhava, T. X. Mahy, and D. Szymanski, unpublished results.
77. S. Mader, *J. Vac. Sci. Technol.* **7**, 175 (1970).
78. B. E. Warren, *X-Ray Diffraction*, Addison-Wesley, Reading, Massachusetts (1969), p. 116.
79. J. Orehotsky and K. Schroder, *J. Appl. Phys.* **43**, 2413 (1972).
80. P. Chaudhari, J. J. Cuomo, and R. J. Gambino, *IBM J. Res. Dev.* **17**, 66 (1973).
81. J. J. Rhyne, S. J. Pickaert, and H. A. Alperin, Int. Symp. on Amorphous Magnetics. Wayne St. Univ., Detroit, August 1972.
82. R. W. Bicknell, *Brit. J. Appl. Phys.* **17**, 38 (1966).
83. C. A. Steidel, *J. Vac. Sci. Technol.* **6**, 694 (1969).
84. W. Felsch, *Z. Angew. Phys.* **29**, 217 (1970).
85. S. Fujime, *Jap. J. Appl. Phys.* **5**, 739 (1966).
86. S. Mader, A. S. Nowick, and H. Widmer, *Acta Met.* **15**, 203 (1967).
87. E. Klokholm, *J. Vac. Sci. Technol.* **7**, 175 (1970).
88. S. Mader and A. S. Nowick, *Appl. Phys. Lett.* **7**, 57 (1965).
89. C. N. J. Wagner, *J. Vac. Sci. Tech.* **6**, 650 (1970).
90. S. Fujime, *Jap. J. Appl. Phys.* **5**, 643, (1966).
91. A. Fortmann and W. Buckel, *Z. Physik* **162**, 93 (1961).
92. S. M. Kirov, *Izv. Akad. Nauk SSSR, Neorg. Mater.* **7**, 1864 (1971).
93. R. K. Waits, *J. Vac. Sci. Technol.* **6**, 308 (1969).
94. H. Daver, O. Massenet, and B. K. Chakravarty, *Solid Stat. Commun.* **11**, 131 (1972).
95. V. V. Bondar, V. A. Povitsky, and E. F. Nakarov, *Fiz. Met. Metalloved.* **30**, 1061 (1970).
96. W. Felsch, *Z, Angew. Phys.* **30**, 275 (1970).
97. B. G. Bagley and D. Turnbull, *Bull. Am. Phys. Soc.* **10**, 1101 (1965).
98. B. G. Bagley and D. Turnbull, *J. Appl. Phys.* **39**, 5681 (1968).
99. B. G. Bagley and D. Turnbull, *Acta Met.* **18**, 857 (1970).
100. S. T. Pai, J. P. Marton, and J. D. Brown, *J. Appl. Phys.* **43**, 282 (1972).
101. I. E. Bolotov and A. V. Kozhin, *Fiz. Met. Metalloved.* **35**, 383 (1973).
102. S. Fujime, *Jap. J. Appl. Phys.* **5**, 778 (1966).
103. S. Ewert and W. Sander, *Z. Physik* **247**, 21 (1971).
104. J. P. de Neufville, S. C. Moss, and S. R. Ovshinsky, *J. Non-Cryst. Solids* **13**, 191 (1974).
105. M. H. Cohen and D. Turnbull, *Nature* **203**, 964 (1964).
106. G. S. Cargill, III, *J. Appl. Phys.* **41**, 2249 (1970).
107. D. E. Polk, *Scripta Met.* **4**, 117 (1970).
108. D. E. Polk, *Acta Met.* **20**, 485 (1972).
109. C. H. Bennett, D. E. Polk, and D. Turnbull, *Acta Met.* **19**, 1295 (1971).
110. F. Sadoc, J. Dixmier, and A. Guinier, *J. Non-Cryst. Solids* **12**, 46 (1973).
111. L. B. Davies and P. J. Grundy, *Phys. Stat. Sol.* (*A*) **8**, 189 (1971).

112. D. Turnbull and D. E. Polk, *J. Non-Cryst. Solids* **8–10**, 19 (1972).
113. T. B. Light and C. N. J. Wagner, *J. Appl. Cryst.* **1**, 199 (1968).
114. N. J. Shevchik and W. Paul, *J. Non-Cryst. Solids* **8–10**, 381 (1972).
115. S. C. Moss and J. F. Graczyk, *Phys. Rev. Lett.* **23**, 1167 (1969).
116. J. F. Graczyk and S. C. Moss, in *Proc. Intern. Conf. on the Physics of Semiconductors*, Cambridge, Massachusetts, 1970, U.S. AWC (1970), p. 658.
117. D. E. Polk, *J. Non-Cryst. Solids* **5**, 365 (1971).
118. M. G. Duffy, D. S. Boudreaux, and D. E. Polk, *J. Non-Cryst. Solids* **15**, 435 (1974).
119. W. H. Zachariasen, *J. Am. Chem. Soc.* **54**, 3841 (1932).
120. F. Ordway, *Science* **143**, 800 (1964).
121. D. L. Evans and S. R. King, *Nature* **212**, 1353 (1966).
122. R. J. Bell and P. Dean, *Nature* **212**, 1354 (1966).
123. G. A. N. Connell and R. J. Temkin, in *Tetrahedrally Coordinated Amorphous Semiconductors* (M. H. Brodsky, S. Kirkpatrick, and D. Weaire, eds.), AIP Conf. Proc. #20, AIP, New York (1974).
124. T. Ichikawa, *Phys. Stat. Sol.* (*B*) **56**, 707 (1973).
125. J. M. Ziman, *Phil. Mag.* **6**, 1013 (1961).
126. C. C. Bradley, T. E. Faber, E. G. Wilson, and J. M. Ziman, *Phil. Mag.* **7**, 865 (1962).
127. N. C. Halder, D. M. North, and C. N. J. Wagner, *Phys. Rev.* **177**, 47 (1969).
128. A. K. Sinha, *Phys. Rev.* B **1**, 4541 (1970).
129. N. F. Mott, in *Liquids: Structure, Properties, and Solid Interactions* (T. J. Hughel, ed.), Elsevier, Amsterdam (1965), p. 182.
130. H. J. Claus, A. K. Sinha, and P. A. Beck, *Phys. Lett.* **26A**, 38 (1967); **26A**, 611 (1968).
131. P. Chaudhari, J. Cuomo, and R. J. Gambino, *Appl. Phys. Lett.* **22**, 337 (1973).
132. S. Basavaiah and S. R. Pollack, *Appl. Phys. Lett.* **12**, 259 (1968).
133. S. Basavaiah and S. R. Pollack, *J. Appl. Phys.* **39**, 5548 (1968).
134. P. Petroff, T. T. Sheng, A. K. Sinha, G. Rozgonyi, and F. B. Alexander, *J. Appl. Phys.* **44**, 2545 (1973).
135. P. M. Petroff and W. A. Reed, *Thin Solid Films* **21**, 73 (1974).
136. T. T. Sheng, F. B. Alexander, and W. A. Reed, *Thin Solid Films* **14**, 289 (1972).
137. T. Millner, A. J. Hegediis, K. Sasvari, and J. Neugebauer, *Z. Anorg. Allgem. Chem.* **289**, 288 (1957).
138. W. L. Bond, A. S. Cooper, K. Andres, G. W. Hull, T. H. Geballe, and B. T. Matthias, *Phys. Rev. Lett.* **15**, 260 (1965).
139. J. Bardeen, L. N. Cooper, and J. R. Schrieffer, *Phys. Rev.* **108**, 1175 (1957).
140. J. J. Hanak, J. I. Gittleman, J. P. Pellicane, and S. Bozowski, *J. Appl. Phys.* **41**, 4958 (1970).
141. M. H. Read and C. Altman, *Appl. Phys. Lett.* **7**, 51 (1965).
142. L. R. Testardi, J. J. Hemser, and M. H. Read, *Solid State Commun.* **9**, 1829 (1971).
143. C. A. Steidel, *J. Vac. Sci. Technol.* **6**, 694 (1969).
144. G. Das, *Thin Solid Films* **12**, 305 (1972).
145. R. D. Burbank, *J. Appl. Cryst.* **6**, 217 (1973).
146. P. T. Moseley and C. J. Seabrook, *Acta Cryst.* **B29**, 1170 (1973).
147. W. D. Westwood and F. C. Livermore, *Thin Solid Films* **5**, 407 (1970).

148. F. Vratny, B. Vromen, and A. J. Harendza-Harinxma, *Electrochem. Tech.* **5**, 283 (1967).
149. P. N. Baker, *Thin Solid Films* **6**, R57 (1970).
150. A. Schauer and M. Roschy, *Thin Solid Films* **12**, 313 (1972).
151. N. Nakamura, M. Fujimora, and Y. Nishimura, *J. Appl. Phys.* **9**, 557 (1970).
152. A. Schauer, W. Peters, and W. Juergens, *Thin Solid Films* **8**, R9 (1971).
153. R. B. Marcus and S. R. Quigley, *Thin Solid Films* **2**, 467 (1968).
154. P. N. Baker, *Thin Solid Films* **14**, 3 (1972).
155. N. Schwartz, W. A. Reed, P. Polash, and M. H. Read, *Thin Solid Films* **14**, 333 (1972).
156. L. G. Feinstein and R. D. Huttemann, *Thin Solid Films* **16**, 129 (1973).
157. R. D. Huttemann, J. M. Morabito, C. A. Steidel, and D. Gerstenberg, *Jap. J. Appl. Phys.* (to be published).
158. N. Schwartz and F. G. Peters, in *Proc. Elec. Comp. Conf.* (1973), p. 251.
159. M. Croset and G. Velasco, *J. Appl. Phys.* **43**, 1444 (1972).
160. L. G. Feinstein, *Appl. Phys. Lett.* **19**, 137 (1971).
161. L. G. Feinstein and D. Gerstenberg, *Thin Solid Films* **10**, 79 (1972).
162. W. D. Westwood, *Appl. Phys. Lett.* **17**, 264 (1970).
163. W. D. Westwood and N. Waterhouse, *J. Appl. Phys.* **42**, 2946 (1971).
164. N. Waterhouse, P. S. Wilcox, and D. J. Wilmott, *J. Appl. Phys.* **42**, 5649 (1971).
165. M. H. Read and D. H. Hensler, *Thin Solid Films* **10**, 123 (1972).
166. D. Mills, *J. Can. Ceram. Soc.* **35**, 48 (1966).
167. D. K. C. McDonald, *J. Chem. Phys.* **21**, 177 (1953).
168. J. M. Ziman, *Proc. Roy. Soc.* **A252**, 63 (1959).
169. J. R. Gavaler, M. A. Janocko, and C. K. Jones, *Appl. Phys. Lett.* **21**, 179 (1972).
170. F. C. Frank and J. H. van der Merwe, *Proc. Roy. Soc.* (*Lond.*) **A198**, 295, 216 (1949).
171. O. Haase, *Z. Naturforsch.* **A14**, 920 (1959).
172. W. A. Jesser and J. W. Matthews, *Phil. Mag.* **15**, 1817 (1967); **17**, 595 (1968).
173. J. G. Wright and J. Goddard, *Phil. Mag.* **11**, 485 (1965).
174. W. A. Jesser and J. W. Matthews, *Phil. Mag.* **17**, 461 (1968).
175. W. A. Jesser and J. W. Matthews, *Phil. Mag.* **17**, 475 (1968).
176. T. E. Hutchinson and K. H. Olsen, *J. Appl. Phys.* **38**, 4933 (1967).
177. F. E. Warner, Jr. and K. R. Lawless, *Int. Thin Film Conf., Boston, 1969.*
178. J. G. Wright and J. Goddard, *Phil. Mag.* **11**, 485 (1965).
179. J. Goddard, *Brit. J. Appl. Phys.* **15**, 807 (1964).
180. W. A. Jesser and J. W. Matthews, *Acta Met.* **16**, 1307 (1968).
181. W. A. Jesser, *J. Mater. Sci. Eng.* **4**, 279 (1969).
182. P. N. Denbigh and R. B. Marcus, *J. Appl. Phys.* **37**, 4325 (1966).
183. A. I. Bulbick and B. I. A. Pines, *Dokl. Akad. Nauk SSSR* **87**, 215 (1952).
184. J. Goddard and J. G. Wright, *Brit. J. Appl. Phys.* **15**, 807 (1964).
185. T. Honma and C. M. Wayman, *J. Appl. Phys.* **36**, 2791 (1965).
186. J. G. Wright and J. Goddard, *Phil. Mag.* **11**, 485 (1965).
187. N. Takahashi, *Compt. Rend.* **234**, 1619 (1952).
188. K. Bahadur and P. V. Sastry, *Proc. Phys. Soc.* (*Lond.*) **78**, 594 (1961).
189. J. E. Davey and R. H. Deiter, *J. Appl. Phys.* **36**, 284 (1965).
190. O. Goche and H. Wilman, *Proc. Phys. Soc.* (*Lond.*) **51**, 525 (1939).
191. R. D. Burbank and R. D. Heidenreich, *Phil. Mag.* **5**, 373 (1960).

192. D. W. Pashley, M. J. Stowell, and T. J. Law, *Phys. Stat. Sol.* **10**, 153 (1965).
193. B. T. Matthias, T. H. Geballe, R. H. Willens, E. Corenzwit, and G. W. Hull, *Phys. Rev.* **139**, A1501 (1965).
194. L. Bosio, H. Curien, M. Dupont, and A. Rimsky, *Acta Cryst.* **B29**, 367 (1973).
195. P. M. DeWolff, *J. Appl. Cryst.* **1**, 108 (1968).
196. C. Suryanarayana and T. R. Anantharaman, *Z. Metallk.* **64**, 800 (1973).
197. M. G. Scott, *Z. Metallk.* **65**, 563 (1974).
198. B. C. Giessen, A. Melas, D. Morse, P. Kelleher, and R. Raman, to be published.
199. B. C. Giessen, *Z. Metallk.* **59**, 805 (1968).
200. P. Predecki, B. C. Giessen, and N. J. Grant, *Trans Met. Soc. AIME* **233**, 1438 (1965).
201. W. B. Pearson, *The Crystal Chemistry and Physics of Metals and Alloys*, Wiley, New York (1972).
202. T. X. Mahy and B. C. Giessen, to be published.
203. C. Barrett and T. B. Massalski, *Structure of Metals*, 3rd ed., McGraw-Hill, New York (1966).
204. R. H. Kane, B. C. Giessen, and N. J. Grant, *Acta Met.* **14**, 605 (1966).
205. W. Hume-Rothery and G. V. Raynor, *The Structure of Metals and Alloys*, The Institute of Metals, London (1962), p. 55.
206. B. C. Giessen, R. H. Kane, and N. J. Grant, *Nature* (*Lond.*) **207**, 854 (1965).
207. B. C. Giessen, M. Morris, and N. J. Grant, *Trans. Met. Soc. AIME* **239**, 883 (1967).
208. P. K. Srivastava, B. C. Giessen, and N. J. Grant, *Acta Met.*, **16**, 1199 (1968).
209. D. Weaire and A. R. Williams, *Phil. Mag.* **19**, 1105 (1969).
210. B. C. Giessen, U. Wolff, and N. J. Grant, *Trans. Met. Soc. AIME* **242**, 597 (1968).
211. B. C. Giessen and C. Borromee-Gautier, *J. Sol. State Chem.* **4**, 447 (1972).
212. P. Ramachandrarao, C. Suryanarayana, and T. R. Anantharaman, *Met. Trans.* **2**, 617 (1971).
213. W. Hume-Rothery and G. V. Raynor, *The Structure of Metals and Alloys*, The Institute of Metals, London (1962), p. 210.
214. M. H. Cohen and D. Turnbull *Nature* (*Lond.*) **189**, 131 (1961).
215. R. C. Ruhl, B. C. Giessen, M. Cohen, and N. J. Grant, *J. Less Comm. Met.* **13**, 611 (1967).
216. B. C. Giessen and D. Szymanski, *J. Appl. Cryst.* **4**, 257 (1971).
217. M. Segnini, Ph.D. Thesis, Department of Chemistry, Northeastern University, Boston, Massachusetts (1972).
218. R. O. Elliott, F. Schonfeld, and B. C. Giessen, to be published.
219. R. Ricci-Bitti, J. Dixmier, and A. Guinier, *Compt. Rend.* **266(B)**, 565 (1968).
220. D. Turnbull, in *Solidification*, American Society of Metals, Metals Park, Ohio (1971), p. 1.
221. P. N. Adler and H. Margolin, *Acta Met.* **14**, 1645 (1966).
222. B. C. Giessen, U. Wolff, and N. J. Grant, *J. Appl. Cryst.* **1**, 30 (1968).
223. G. Falkenhagen and W. Hofmann, *Z. Metallk.* **43**, 69 (1952).
224. W. Klement, *J. Inst. Met.* **90**, 27 (1961).
225. D. Duzevic, Z. Bonefacic, and D. Kunstelj, *Scripta Met.* **7**, 883 (1973).
226. E. Babic, E. Girt, R. Krsnik, B. Leontic, and I. Zoric, *Phys. Lett.* **33A**, 368 (1970).
227. B. C. Giessen, V. O. Struebing, and R. O. Elliott, *J. Mater. Sci. Eng.* **18**, 239 (1975).

228. P. Furrer, T. R. Anatharaman, and H. Warlimont, *Phil. Mag.* **21**, 873 (1970).
229. R. B. Roof and R. O. Elliott, *J. Mater. Sci.* **10**, 101 (1975).
230. P. Duwez, R. H. Willens, and W. Klement, Jr., *J. Appl. Phys.* **31**, 1500 (1960).
231. W. Klement, Jr. and H.-L. Luo, *Trans. TMS—AIME* **233**, 1438 (1965).
232. H.-L. Luo and P. Duwez, *J. Less Common Met.* **6**, 248 (1964).
233. R. Wang, *Met. Trans.* **3**, 1213 (1972).
234. R. Wang and Y. B. Kim, *Met. Trans.* **5**, 1973 (1974).
235. M. Hansen, *Constitution of Binary Alloys*, McGraw-Hill, New York (1958).
236. H. Matyja, B. C. Giessen, and N. J. Grant, *Trans. Quart. ASM* **61**, 330 (1968).
237. M. H. Burden and H. Jones, *J. Inst. Metals* **98**, 249 (1970).
238. A. Tonejc and A. Bonefacic, *Fizika* **2**, 81 (1970).
239. C. Jansen, Ph.D. Thesis, Department of Metallurgy and Materials Science, Massachusetts Institute of Technology, Cambridge, Massachusetts (1971).
240. J. Bletry, *J. Phys. Chem. Solids* **31**, 1263 (1970).
241. E. Babic, P. J. Ford, C. Rizzuto, and E. Salamoni, *J. Low Temp. Phys.* **8**, 219 (1972).
242. E. Babic, R. Krsnik, B. Leontic, M. Ocko, Z. Vucic, I. Zoric, and E. Girt, *Solid State Comm.* **10**, 691 (1972).
243. M. Itagaki, B. C. Giessen, and N. J. Grant, *Trans. Quart. ASM* **61**, 330 (1968).
244. H. Matyja, K. C. Russell, B. C. Giessen, and N. J. Grant, *Met. Trans.* (in print).
245. E. Babic, E. Girt, R. Krsnik, B. Leontic, M. Ocko, Z. Vucic, and I. Zoric, *Phys. Stat. Sol.* (*a*) **16**, K21 (1973).
246. A. F. Polesya, L. P. Slipchenko, L. M. Burov, V. N. Gudzenko, and V. I. Demeshkin, *Izv. VUZ Chernaya Met.* **1971(9)**, 114.
247. H.-L. Luo, *Trans. Met. Soc. AIME* **239**, 119 (1967).
248. L. R. Newkirk and C. C. Tsuei, *J. Appl. Phys.* **42**, 5250 (1971).
249. E. F. Kneller, *J. Appl. Phys.* **35**, 2210 (1964).
250. W. Klement, Jr., *Trans. TMS—AIME* **227**, 965 (1963).
251. R. C. Ruhl, B. C. Giessen, M. Cohen, and N. J. Grant, *J. Mater. Sci. Eng.* **2**, 314 (1968).
252. F. H. Ellinger, W. N. Miner, D. R. O'Boyle, and F. W. Schonfeld, Los Alamos Scientific Laboratory Report, LA-3870 (1968).
253. R. O. Elliott, A. M. Russell, and B. C. Giessen, *J. Mater. Sci.* **8**, 1325 (1973).
254. R. O. Elliott and B. C. Giessen, in *Proc. 5th International Conference on Plutonium and Other Actinides, Baden-Baden* (1975).
255. R. O. Elliott, P. Russell, and B. C. Giessen, *Scripta Met.* **8**, 1335 (1974).
256. E. E. Havinga, J. H. N. van Vucht, and K. H. J. Buschow, in *Ordered Alloys* (B. H. Kear *et al.*, eds.), Claitor's Publ. Div., Baton Rouge, Louisiana (1970), p. 111.
257. C. H. Hodges, *Acta Met.* **15**, 1787 (1967).
258. M. Oron and C. M. Adams, Jr., *J. Appl. Phys.* **40**, 4218 (1969).
259. E. Klokholm, *J. Vac. Sci. Tech.* **7**, 175 (1970).
260. R. Ray, Sc.D. Thesis, Department of Metallurgy and Materials Science, Massachusetts Institute of Technology, Cambridge, Massachusetts (1969).
261. J. C. Baker and J. W. Cahn, *Acta Met.* **17**, 575 (1969).
262. R. Ray, S. Hahn, and B. C. Giessen, *Acta Met.* **20**, 1335 (1972).
263. B. C. Giessen, R. Ray, and S. H. Hahn, *Phys. Rev. Lett.* **26**, 509 (1971).
264. R. Ray, M. Segnini, and B. C. Giessen, *Solid State Comm.* **10**, 163 (1972).

265. R. Ray, M. Madhava, and B. C. Giessen, to be published.
266. B. S. Berry, W. S. Pritchett, R. Ray, and B. C. Giessen, to be published.
267. T. R. Anthony, in *Vacancies and Interstitials in Metals* (A. Seeger *et al.*, eds.), North-Holland, Amsterdam (1970).
268. W. K. Warburton and D. Turnbull, in *Diffusion in Solids; Recent Developments* (A. S. Nowick and J. J. Burton, eds.), Academic Press, New York (1975), p. 172.
269. W. K. Warburton, *Scripta Met.* **7**, 105 (1973).
270. R. C. Ruhl and M. Cohen, *Trans. Met. Soc. AIME* **245**, 241 (1969).
271. R. C. Ruhl and M. Cohen, *Scripta Met.* **1**, 73 (1967).
272. R. C. Ruhl and M. Cohen, *Trans. Met. Soc. AIME* **245**, 253 (1969).
273. R. Ray, B. C. Giessen, and N. J. Grant, *Met. Trans.* **3**, 627 (1972).
274. R. P. Elliott, *Constitution of Binary Alloys, First Supplement*, McGraw-Hill, New York (1965).
275. F. A. Shunk, *Constitution of Binary Alloys, Second Supplement*, McGraw-Hill, New York (1969).
276. D. M. Mattox and G. I. Koniniak, *J. Vac. Sci. Technol.* **8**, 194 (1971).
277. A. G. Blachman, *Met. Trans.* **2**, 699 (1971).
278. W. W. Lee and D. Oblas, *J. Vac. Sci. Technol.* **7**, 129 (1970).
279. P. H. Schmidt, R. N. Castellano, H. Barz, B. T. Matthias, J. G. Huber, and W. A. Fertig, *Phys. Lett.* **A41**, 367 (1972).
280. J. M. Poate, W. J. DeBonte, W. M. Augustyniak, and J. A. Borders, *Appl. Phys. Lett.* **25**, 698 (1974).
281. W. Buckel and B. Stritzker, in *Applications of Ion Beams to Metals* (S. T. Picraux *et al.*, eds.), Plenum Press, New York (1974), p. 3.
282. G. Dearnaley, in *Applications of Ion Beams to Metals* (S. T. Picraux *et al.*, eds.), Plenum Press, New York (1974), p. 63.
283. G. Dearnaley, in *Annual Review of Materials Science* (R. A. Huggins *et al.*, eds.) (1974), Vol. 4, p. 93.
284. J. P. Heinrich, H. J. Garrett, and R. P. Allen, *J. Appl. Phys.* **45**, 1873 (1974).
285. P. T. Sarjeant and R. Roy, *J. Appl. Phys.* **38**, 4540 (1967).
286. P. S. Skell, D. L. Williams-Smith, and M. J. McGlinchey, *J. Am. Chem. Soc.* **95**, 3337 (1973).
287. G. S. Cargill, III, in *Magnetism and Magnetic Materials 1974*, American Institute of Physics Conf. Proc. No. 24, AIP, New York (1975), p. 138.
288. T. Egami, P. J. Flanders, and C. D. Graham, Jr., in *Magnetism and Magnetic Materials 1974*, American Institute of Physics Conf. Proc. No. 24, AIP, New York (1975), p. 697.
289. P. Chaudhuri, J. J. Cuomo, R. J. Gambino, S. Kirkpatrick, and L. J. Tao, in *Magnetism and Magnetic Materials 1974*, American Institute of Physics Conf. Proc. No. 24, AIP, New York (1975), p. 562.
290. P. Chou, personal communication.
291. H. A. Davies, *Scripta Met.* **8**, 1179 (1974).
292. R. A. Swalin, *J. Met.* **24(1)**, 35 (1972).

2

Inclusion Compounds

F. R. Gamble
Corporate Research Laboratory
Esso Research and Engineering Co.
Linden, New Jersey

and

T. H. Geballe
Department of Applied Physics, Stanford University
Stanford, California and
Bell Laboratories
Murray Hill, New Jersey

1. Introduction

The inclusion concept in crystal chemistry arises because there exist a large number of crystal classes in which one can clearly identify a host structure that contains guest atoms, ions, or molecules. In these, geometric and topological effects are of very great importance, and the concept of inclusion is useful not only in determining whether a compound will form but also in predicting properties. The host is a crystal that can provide a tunnel, planar, or cagelike accommodation for a guest species, depending on whether these are found in one-, two-, or three-dimensional arrays. The restricted dimensionality of some of these systems often substantially affects their properties. The presence of the guest, typically over a variable concentration range, has little effect on the structure and lattice constants of the host in at least two dimensions. In layered compounds the third dimension increases to accommodate the guest, which is termed the "intercalate." In all cases important aspects of the identity of both host and guest are preserved. The strength of the interaction between host and guest varies greatly. In the noble gas clathrates it is weak. At the other

extreme it will be so great that the whole concept of guest and host loses intuitive value. Thus, there is no profit in considering TiS in the NiAs structure to be TiS_2 in the CdI_2 structure with Ti intercalated. There is obviously a high degree of arbitrariness as to what to include in this chapter. We have limited the discussion to systems in which there is appreciable interaction between host and guest resulting in electrical, optical, or magnetic behavior of a rather striking nature which can be manipulated by changes in the concentration or nature of the guest. The reader is referred to already existing reviews which treat such topics as molecular clathrates[1] and insulating ionic complexes,[2] such as the extremely large and technologically important class comprised by the zeolites.[2] Finally, it must be admitted that the authors have stayed fairly close to materials of their own acquaintance.

In the next two sections we treat the silver oxide clathrates and certain borides, systems in which the host provides a three-dimensional framework in which one finds well-defined sites for the guest. In Sections 4–6 we discuss in more detail intercalation compounds, crystals in which the host is a layered structure and in which it is possible to insert planar arrays of guest atoms, ions, or molecules. Finally, we treat certain bronzes in which the guest is found in linear array in tunnels provided by the host.

2. Metallic Clathrates

A small, apparently unique class of inclusion compounds is made up of the silver oxide clathrate salts $[Ag_7O_8]^+X^-$ with $X = NO_3^-$, HF_2^-, ClO_4^-, and BF_4^-. The compounds are prepared by electrolytic oxidation of an acid solution containing silver and the anion X^- desired.[3] The resulting product is a shiny, metallic black powder containing octahedral crystals or long needles, depending on the current density. The salts are composed of Ag_6O_8 polyhedra, each one constituting a cage containing an X^- anion; in between, the polyhedra are cubically coordinated Ag^+ counter ions. The crystal structure, which is rather difficult to visualize (see Figure 1), has been refined by Chou Kung-Du[4] and Náray-Szabó and Argay,[5] the latter study including neutron diffraction of powders as well as single-crystal X-ray diffraction. The face-centered cubic unit cell contains four 26-sided cubooctadodecahedral cages each formed from 12 square planar AgO_4 units. The cages share planar AgO_4 faces in the [111] directions, the Ag atoms being in a square planar array of oxygen.

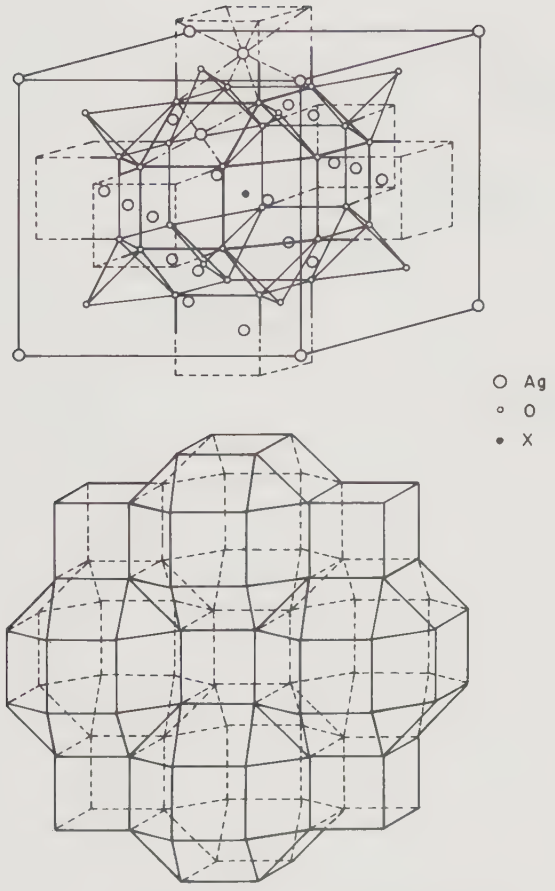

Fig. 1. The unit cell of Ag_7O_8X showing (a) the polyhedral cage with the anion X^- at its center, and (b) the fusion of four Ag_6O_8 polyhedra through sharing of the AgO_4 faces (reproduced with permission from Robin and Day[215]).

In the [100] directions there are small cubic spaces among adjacent cages that are filled with Ag^+ ions. Each of these has eight oxygens around it at the corners of a cube with Ag–O distances all equal to 2.52 Å as expected for monovalent silver. There is one silver of this type per formula unit. The remaining six are found in the cage walls and are all crystallographically equivalent. In the planar AgO_4 polyhedra faces the Ag–O distance is 2.05Å. Formally, the six equivalent Ag ions must balance the charge of the eight oxygen ions in the cage walls. The average formal oxidation state of these six ions is

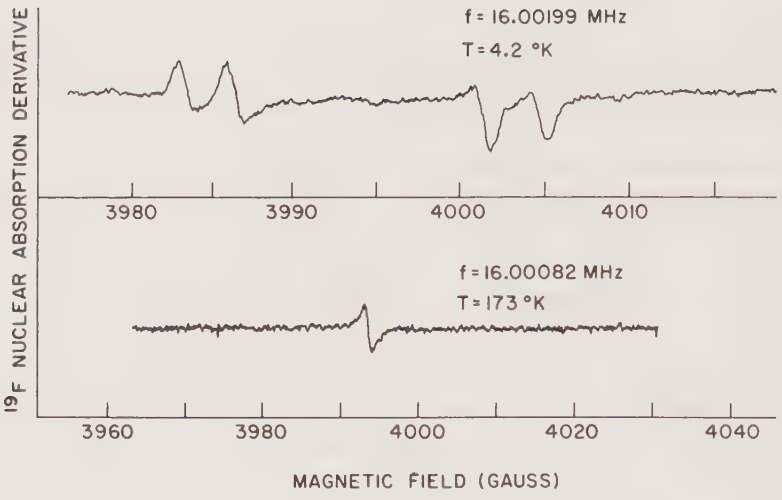

Fig. 2. The ^{19}F NMR spectrum of $Ag_7O_8HF_2$ at 4.2°K (upper) and at 173°K (lower) (reproduced with permission from Gossard *et al.*[7]).

therefore fractional, $+2\frac{2}{3}$, which suggests that one can expect the electronic state of the system to involve resonance. For example, a valence bond picture of the system would comprise a combination of five Ag^{3+} ($4d^8$) ions and one Ag^+ ($4d^{10}$) ion with the two electrons distinguishing the sixth silver resonating among all six silvers. A conduction band (presumably composed of the 4*d* orbitals of silver mixed with the 2*p* orbitals of oxygen) would result. From this, Pauli paramagnetism and metallic conductivity would follow. Nonetheless, early reports were that the clathrates were semiconducting. However, in 1966 Robin and co-workers[6] discovered that these compounds

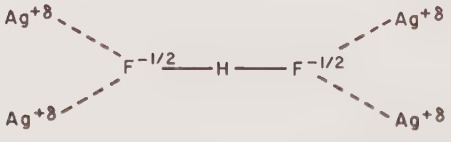

Fig. 3. The HF_2^- ion in one of six positions of minimum electrostatic energy (reproduced with permission from Hindermann *et al.*[8]).

are metallic and superconducting at 1.04, 0.15, and between 1.0 and 1.4°K for the NO_3^-, BF_4^-, and HF_2^-, respectively.

The range of critical temperatures found for $Ag_7O_8HF_2$ is perhaps the result of the variable composition first reported by Náray-Szabó and later rationalized by Gossard *et al.*[7] The compound discussed by early workers was nominally $[Ag_7O_8]^+F^-$. In such a compound with large F–F separation and a lack of abundant silver or oxygen species of sizable nuclear magnetic moment one would anticipate a narrow fluorine nuclear magnetic resonance line on the order of a few tenths of a gauss wide. However, Gossard and co-workers found at 4·2°K the 22-G wide spectrum shown in Figure 2, a spectrum characteristic of the linear, symmetric HF_2^- ions 2.6 Å long. A single line of approximately 2 G width observed above 100°K is evidently the spectrum of the thermally excited, rotating HF_2^- ion. The linear, symmetric HF_2^- ion should have six equivalent low-energy orientations with its end pointing toward pairs of the six equivalent $Ag^{8/3+}$ ions in the cage walls (see Figure 3). Hindermann *et al.*[8] have studied the reorientation of the HF_2^- ions within the cages using both pulsed and CW NMR. They concluded that the frequency of reorientation changes drastically in the neighborhood of 80°K.

Crystals with almost identical unit cell dimensions result regardless of the size of the anion within the polyhedral cages (Table 1). It is for this reason that the compounds are termed clathrates; the anionic species appear to be guests within a rigid silver oxide host. In those cases where the anion is either nitrate or bisulfate, careful chemical analysis shows that each cage must contain one anion. (It appears,

TABLE 1

Lattice Constants and Critical Temperatures of $Ag_7O_8^+X^-$

Anion, X^-	a	T_c
$F^-(HF_2^-)$	9.833 ± 0.002	0.8–1.5
NO_3^-	9.893 ± 0.002	1.04
BF_4^-	9.942 ± 0.004	0.15
$F^-(HF)$	—	0.3*
$(NO_3^-)_{0.75}(F^-)_{0.25}$	—	0.90

* Sample contained paramagnetic impurities.

however, that some variation in composition may exist for the perchlorate.)

The silver oxide clathrates appear to be the only examples of their kind. Although it is possible to prepare crystals with mixed anions, mixed-cation compounds of this class have not been reported. Brief attempts at their synthesis by Robin[9] have yielded only the pure silver compounds.

2.1. Electrical Properties

The electrical resistivity of needles of $Ag_7O_8NO_3$ between the superconducting critical temperature, 1.04°K, and room temperature has been measured. Small, abrupt changes in resistivity were observed at 220, 180, and 110°K; the second corresponds to a transition from a cubic to a tetragonal lattice with $c/a = 0.9603$ at 10°K. The ratios of lattice constants for this compound at 10 and 300°K are $a_{10}/a_{300} = 1.0109 \pm 0.0004$ and $c_{10}/a_{300} = 0.9704 \pm 0.0004$. Because salts containing more spherical ions than NO_3^- (e.g., BF_4^-) remain cubic to 10°K, it is possible that the transition to the tetragonal phase at 180°K involves the alignment of the planes of the NO_3^- groups perpendicular to the c axis. The abrupt change in resistivity at 180°K was sometimes positive and sometimes negative. This was rationalized in terms of the relative amounts of material with a or c axes oriented along the needle axis after the transition. Even though the room-temperature resistance is quite high, $\sim 2 \times 10^{-3}$ Ω-cm, for the nitrate salt it has a very large, metallic temperature dependence and decreases by a factor of 200 before it becomes superconducting. The increase goes roughly as $T^{3.5}$ up to 12°K and less rapidly above that temperature.

2.2. Low-Temperature Heat Capacity

Conway *et al.*[10] investigated the low-temperature heat capacities of the NO_3^- salt and the HF_2^- salt. The latter has a smeared-out superconducting transition between 0.8 and 1.5°K, the smearing possibly due to the presence of a small concentration of paramagnetic impurities. The superconducting transition as measured by the thermal anomaly in the NO_3^- salt, on the other hand, was 90% completed in an interval of 0.04° around 1.03°K. Although a possible importance of the anion vibrational modes upon the superconducting transition is suggested by the strong variation of superconducting transition temperature with anion replacement, no convincing evi-

dence for the direct effect was found. However, a surprisingly strong dependence of the linear heat capacity coefficient and the Debye temperature upon anion identity was found. The substitution of HF_2^- and NO_3^- causes a substantial increase in Debye θ but only a small change in volume. An unusual drop in the effective Debye θ which occurs about 15°K is possibly connected with a rocking motion of the NO_3^- ion. The observed linear heat capacity coefficients γ for the NO_3^- and HF_2^- salts are 44.6 and 72.5 mJ/mole °K^2, respectively, corresponding to a density of states at the Fermi surface an order of magnitude or more greater than the free-electron value. The 60% increase in γ obtained by replacing the NO_3^- with HF_2^- is surprisingly large. Either the very narrow conduction bands are grossly affected by the anion, or the linear term in the heat capacity contains a contribution from the low-temperature modes of the anions. The latter possibly seems quite reasonable in view of recent models of Phillips[11a] and Anderson *et al.*[11b] and of Rollefson[12] put forth to explain the linear dependence of specific heat observed in amorphous solids and impurity-substituted alkali halides. A linear heat capacity coefficient is shown to arise from an ion tunneling between potential minima which have an asymmetric distribution due, for example, to random strain. Further investigation is required to make a quantitative test, but the height of the potential well for the linear HF_2^- ion estimated by Hindermann *et al.* is of the right order at least to explain the increase in γ in going from the NO_3^- to the HF_2^-. Náray-Szabó and Argay[5] remark that the fluoride-containing samples are less well oriented than those containing NO_3^-, which might well generate the distribution of minima required by the model.

3. Boron Compounds

3.1. Icosahedral Grouping

In elemental boron and in many boron-rich compounds, groups of 12 boron atoms are tightly bonded together as icosahedra that behave as large, almost spherical pseudoatoms with a diameter of ~5.1 Å. These pseudoatoms then can stack together in various packings (ccp, hcp, and bcc) and accept guest atoms in the spaces in between.[13] In addition, larger, again nearly spherical groupings of B_{12} icosahedra can occur resulting in B_{84} [14] and B_{156} [15] packing units. Matkovich *et al.*[14] suggest that AlB_{12} and BeB_6 consist of a close-packed

arrangement of B_{84} groupings with some occupation of the interstitial sites. The tetragonal form of B itself is also possibly of this structure, the interstitial sites being occupied by B.

In the YB_{66} structure Richards and Kasper[15] show there are 402 atoms per primitive cell. The B_{156} groups in two orientations are packed in an NaCl arrangement accounting for 1248 B atoms. Some 336 more B atoms and 24 Y atoms are located in large interstitial channels parallel to the cube directions. All icosahedrally grouped boron compounds are insulators. Slack *et al.*[16] have shown that thermal transport in these crystals is by acoustic phonons and, in the case of YB_{66}, not by the large number of optical phonons, which, of course, are the dominant excitations in large unit cells. At the Debye temperature, 1300°C, the thermal transport analysis for YB_{66} shows the mean free path to be about 2×10^{-5} cm. Roughly the same mean free path is found for other compounds with icosahedral groupings at their Debye temperatures. At low temperatures the mean free path falls far below the sample dimension (boundary scattering) limit in YB_{66}, in contrast to β-boron. This is taken as evidence that the Y and B positions in the YB_{66} channels are randomly occupied, and to some extent it behaves like a glass. The random structure easily may have been frozen in at the high temperature, 2100°C, at which the crystals were grown from the melt. More ordered crystals might be obtainable by use of flux methods at low temperatures.

3.2. Octahedral Grouping

Boron-rich phases are also known where the boron forms octahedral groups. These crystallize in either the UB_{12} structure, where the arrangement of cubooctahedral B_{12} pseudoatoms and the U atoms are in the NaCl structure, or in the CaB_6 structure, where the CsCl arrangement is taken. The CaB_6-type hexaborides are ionic semiconductors or metals. The range of structural, electrical, and magnetic properties which they possess can be understood by considering the interaction of the metal cation in a well-defined cage inside the negatively charged boron lattice. In what follows we summarize some of their properties, leaning heavily upon the reviews of Post[17] and Hoard and Hughes.[18]

The boron atoms form an open, yet rigid framework in which varying concentrations of metal ions can be accommodated. The metal ion at the body center of the unit cube with six borons in the form of an

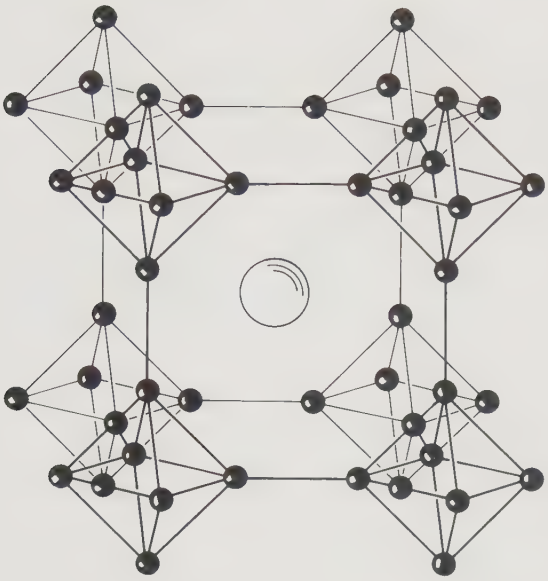

Fig. 4. CaB_6 crystal structure (after Pauling[42]).

octahedron at each corner is shown in Figure 4. The boron–boron bond distances can be determined when single crystals are available. La Placa[19] has found that the boron–boron bonds between octahedra are only a few percent shorter than the intraoctahedral boron–boron bonds, so that for most purposes the structure can be regarded as made up of truncated cubes with regular octagonal faces. The small differences in the unit cell dimension that are observed with different cations are mainly due to changes in the interoctahedral bond length, indicating that they are more elastic than the bonds within the octahedra.

The rigidity of the boron framework dominates the mechanical properties of the hexaborides. They are hard, have small coefficients of expansion, and have high melting points, as can be seen in Table 2. They have lattice constants within 2% of 4.17 Å. As can be seen in Figure 5, the lattice constants of rare earth hexaborides track the corresponding rare earth radii but with substantially smaller fractional changes. Indeed, the heavier rare earths with smaller radii do not crystallize in the hexaboride structure, but rather in the UB_{12} cubic dodecaboride structure, where the boron framework has

TABLE 2
Structural Properties of Representative Hexaborides*

Compounds	M–M Distance = lattice constant		M–B Distance		B–B Distances to compare with $2R_B = 1.76$		Melting point	Coefficient of expansion[206] $\times 10^6$
	Measured	$2 \times R_M(6)$	Observed	$R_M(24) + R_B$	Interoctahedral	Intraoctahedral		
BaB_6	4.269†	4.28	3.14	3.20	1.75†	1.78†	2270[29]	6.8
EuB_6	4.178[207]	3.89	3.07	3.01	—	—	—	6.7
LaB_6	4.154†	3.57	3.05	2.85	1.66†	1.76†	~2550[22]	6.4
CeB_6	4.141[208]	—	—	—	—	—	2190[29]	7.3
SmB_6	4.113[209]	—	—	—	—	—	2540[210]	6.8
YB_6	4.113[208]	3.70	3.04	2.91	—	—	~2600[211]	6.2

* These data are abstracted from Hoard and Hughes.[18] $R_M(6)$ and $R_M(24)$ are the metallic radii estimated for coordination numbers of 6 and 24, respectively, after Hoard and Hughes.[18]
† Data of S. La Placa, quoted by Hoard and Hughes.[18]

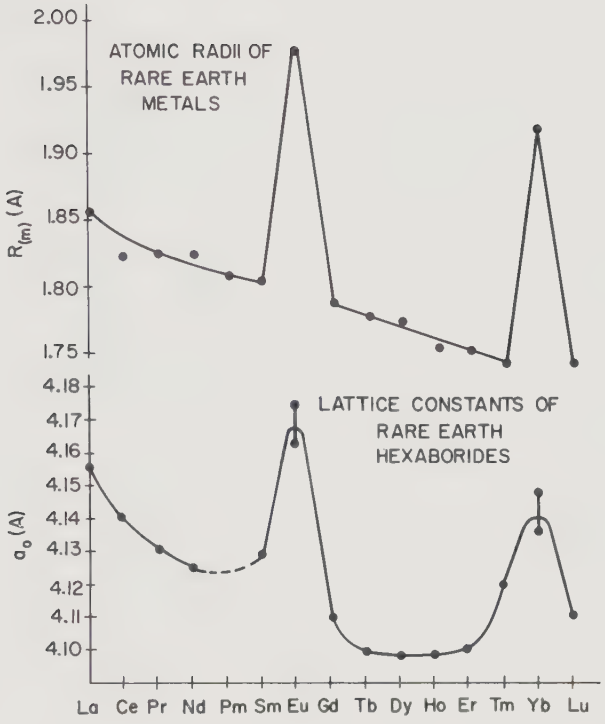

Fig. 5. Lattice constants of the rare earth hexaborides compared with the corresponding rare earrh metal radii (after Post[1]) with lattice constants from Pearson.[13]

smaller holes.* Cations with valences greater than two form metallic compounds in both the hexaboride and dodecaboride structures. Those that are nonmagnetic are frequently superconducting, as can be seen in Table 3.

The electrical properties of the hexaborides can be understood roughly from tight-binding calculations first made by Longuet-Higgins and Roberts.[20] The boron valence band formed from the six borons per unit cell requires a total of 20 electrons (six electrons to form shorter covalent bonds with adjacent octahedra and 14 electrons to fill the seven bonding molecular orbitals of the octahedral

* The cubic dodecaborides based upon equilateral B_{12} cubooctahedral arranged in an fcc lattice represent an even more extreme case of a rigid boron framework which can accommodate cations which are somewhat smaller than the hexaboride cations. The lattice constants for the cubic MB_{12} structure such as ScB_{12} vary less than 1% for a 10% variation of the included cation (see Ref. 18, p. 112).

TABLE 3
Magnetic and Superconducting Properties of Selected Hexaborides and Dodecaborides

Compound/ metal	T_{super},[212] °K	Magnetic ordering temperature, °K	Effective moment (Bohr magnetons)		Curie–Weiss temperature, °K	Range of Curie–Weiss behavior, °K
			Calc.	Obs.		
YB_6	6.5–7.1	—	—	—	—	—
YB_{12}	4.7	—	—	—	—	—
ThB_6	0.7	—	—	—	—	—
ScB_{12}	0.4	—	—	—	—	—
ZrB_{12}	6.0	—	—	—	—	—
LuB_{12}	0.5	—	—	—	—	—
Ce	—	$T_N = 2.3$[36]	2.54	2.36–2.51[26,27,212]	−76 to −82	>150
Pr	—	6.9[36]	3.58	3.59–3.64[26,27,212]	−41 to −68	>70
Nd	—	7.5[213]		3.54–3.84[23,214]	−42 to −74	>125
Sm	—	No ordering		No range of Curie–Weiss behavior		
Eu	—	$T_c = 8$–8.8[26,27,36,212]	7.94	7.9–8.0[26,27,212]	−0.5 to +9	>30–80
Gd	—	$T_N = 14$[23,35,212]	7.94	8.0[26,27,35,212]	−50 to −66	>70
Tb	—	23	9.72	9.43	−35	>50

TABLE 4
Electrical* and Thermal Properties of Selected Hexaborides

Metal	Resistivity, $\mu\Omega$-cm	Hall coefficient R, $\times 10^4$ cm^3	Thermal emf, μV/deg	Mobility of carriers, cm^2/V-sec	Number of conduction electrons per metal atom	Thermal coefficient of electrical resistivity α, $\times 10^3$/deg (0–100°C)
Ca	222	−91.0	−32.8	41.0	0.05	+1.16
Sr	111	−76.3	−30.3	68.7	0.06	+0.83
Ba	77	−57.5	−26.2	74.7	0.08	+1.08
Y	40	−4.6	−0.5	11.4	0.96	+1.24
La	15†	−5.0	+0.1	33.1	0.90	+2.68
Ce	29	−4.2	+0.3	14.2	1.06	+1.00
Pr	20	−4.3	−0.6	22.2	1.02	+1.92
Nd	20	−4.3	+0.4	22.0	1.00	+1.93
Sm	207	+1.5	+7.6	0.74	2.86	−0.42
Eu	85	−50.2	−17.7	59.3	0.09	+0.90
Gd	45	−4.4	±0.1	9.8	0.94	+1.40
Tb	37	−4.6	−1.1	12.2	0.94	+1.31
Yb	47	−83.6	−25.5	179.4	0.05	+2.34
Th	15	−2.2	−0.6	14.7	1.99	+2.31

* The electrical data are all taken from the work of Paderno and Samsonov.[21] Subsequent work by Johnson and Daane[22] show that single-crystal SrB6 has a much higher resistance than tabulated here, as might be expected for a semiconductor. The number of conduction electrons is estimated from the Hall coefficient assuming a single band.

† Obtained by extrapolation to zero porosity.

group). Two additional electrons per cation thus must be donated to fill the bonding orbitals and to stabilize the structure. The overall bonding then also must include some ionic bonding between the M^{2+} guest and the negatively charged boron framework. Although more complete band structure calculations are not available, there is no doubt that the antibonding boron conduction band lies well above the valence band. Thus, the model predicts that the divalent alkaline earth hexaborides are semiconductors, while the trivalent cation hexaborides have an occupied nonbonding metal band with one conduction electron per formula unit. Conductivity and Hall effect measurements have been compiled for a large number of hexaborides by Samsonov and co-workers,[21] as tabulated in Table 4, and offer convincing proof for the validity of the model. Even more reassuring is the subsequent single-crystal work of Johnson and Daane.[22] Measurements of the electrical conductivity give an activation energy for the alkaline earth hexaborides of ~ 0.4 eV. Fisk[23] finds the same for EuB_6.

The rare earth hexaborides are dark purple when prepared as polycrystalline material. Single-crystal LaB_6 is reddish-purple in transmission. Its reflection spectrum has been measured[24] with free-carrier absorption and a well-defined plasma edge about 2 eV. Above the plasma edge the spectrum shows structure similar to CaB_6 with a fairly high reflectivity in the blue.

Except for diamagnetic LaB_6 and anomalous SmB_6, all the rare earth hexaborides show Curie–Weiss paramagnetic behavior above 150°K.[25] The slopes correspond to the free-ion moments, as shown in Table 3. Europium is divalent, $4f^7$ configuration, and the effect of its large radius is evident in Figure 5. The magnetic rare earth hexaborides order at low temperature, EuB_6 being ferromagnetic, and the rest antiferromagnetic,[26] excepting SmB_6, which does not order magnetically, even below 1°K.[27] The observed ordering temperatures are substantially lower than extrapolated from the paramagnetic Curie–Weiss behavior, a not unusual occurrence in situations where crystal-field effects are appreciable with respect to the exchange interaction. However, below 150°K the magnetic susceptibility is larger than the extrapolated Curie–Weiss law, indicating the behavior is not just a simple crystal-field effect. Further, the ordering temperatures scale with the effective magnetic moments.

Useful magnetic data are tabulated in Table 3. The involvement of the conduction electrons in the ordering process of the metals is strongly suggested by the fact that only the semiconductor EuB_6

orders ferromagnetically, while the metals order antiferromagnetically.[27] Gossard and Jaccarino[28] have found the boron nuclear magnetic resonance shifts expected due to the polarization of the conduction electrons by their interaction with the rare earth ion spins. In the less than half-filled *f* shells the resultant spin and orbital momentum vectors are oriented antiparallel to each other, whereas beyond the half-filled shell they are parallel, as expected.

Having covered some general features of the hexaborides, we now discuss specific examples.

3.2.1. LaB_6

Lafferty[29] showed many years ago that LaB_6 cathodes are particularly useful high-current-density thermionic emitters. He explained this by showing that at the 1500°C surface the La atoms slowly evaporate while the boron framework remains intact. Lanthanum atoms diffuse from the bulk, replenishing those atoms that evporate, thus maintaining an active, clean cathode surface. After prolonged operation at high temperatures the framework becomes so depleted of La that it collapses, leaving a boron coating on the cathode. A limiting composition for this collapse is that when there are no longer enough electrons to fill the boron valence band, i.e., when one-third of the La atoms have evaporated, which corresponds to a stoichiometry of $La_{0.67}B_6$. A wide range of stoichiometry extending to $La_{0.68}B_6$ indeed has been found by Johnson and Daane.[22]

LaB_6 is unique among the nonmagnetic hexaboride and dodecaboride metals in not being superconducting.[30] This contrasts with elemental La and other compounds which are good superconductors, and we conjecture that it results from the fact that the boron framework puts the La under negative pressure. Positive pressure is known to push *f* levels to higher energy. For example, Ce metal, with one 4*f* electron, is changed from an antiferromagnet to a superconductor with pressure.[31] The very rapid rise of the superconducting transition of elemental La[32] caused by the initial application of pressure which then saturates seems to be related to the presence of the (almost?) unoccupied *f* band above the Fermi level. It seems reasonable that the rigid boron framework in LaB_6 can put the La ion under negative pressure. La Placa's single-crystal data in Table 2 show that the interoctahedral B–B bonds are about 0.1 Å shorter than would be the case for the ideal boron framework. The negative pressure must

then lower the f levels of the La. If it were of sufficient magnitude, localized magnetic behavior other than the observed Pauli-like susceptibility would eventually result. However, even before that extreme is reached, Cooper-pair breaking scattering from spin fluctuations which prevent the occurrence of superconductivity can take place. Such effects are known in other systems even though the magnetism is insufficiently developed to exhibit localized moments or even substantially exchange-enhanced Pauli susceptibility.*

3.2.2. CeB_6

Nickerson and White[34] have shown the importance of crystal-field effects in the magnetic hexaborides by considering the simplest case: CeB_6. The Ce^{3+} ion with a single $4f$ electron has a $2F_{5/2}$ ground state. The cubic crystal field splits the $J = \frac{5}{2}$ manifold into a higher-lying quartet and a ground doublet. The charge density of the electrons rather than a simple point-charge model is the most reasonable course to take for the crystal-field splitting. It then follows that the quartet, which lies higher by virtue of stronger interaction with the conduction electron charge density, also will have a greater indirect (RKKY) exchange† interaction via the conduction electrons than the lower-lying doublet. As a result the net effective exchange is temperature dependent, decreasing as the quartet is thermally depopulated. The observed saturation moment of the ground state is observed to be 0.74,[36] in good agreement with the 0.71 predicted for the doublet ground state. It would be of interest to study the effect of doping the CeB_6 with an ion such as Gd to see if it can be made to trigger the ordering of the higher-lying states at temperatures above those where the crystal-field splitting causes thermal depopulation.

3.2.3. SmB_6

Again, as in LaB_6, a negative pressure exerted by the boron framework has been invoked to explain the remarkable fact that the

* Pd is perhaps the best studied system which exhibits exchange-enhanced susceptibility, and, of course, no superconductivity. An even more convincing case is α-Ce (fcc form), in which the exchange-enhanced susceptibility can be turned off by application of pressure. (See, e.g., Ref. 33.) Even though increasing pressure reduces the susceptibility in α-Ce, no superconductivity is exhibited until an α′ phase forms for $P > 50$ kbar.

† The $4f$ spins are coupled together by magnetization induced in the conduction electron gas in the model of Ruderman, Kittel, Kasuya, and Yosida (RKKY) (see, for example, Ref. 35).

Sm ion is partly in the $4f^5$ configuration and partly in the $4f^6$ one in spite of there being only one lattice site for the Sm ion. The mixed configuration was established by X-ray absorption measurements.[37] Further reinforcement has come from both Mössbauer[38] and lattice constant[39] studies, which show that ions with $4f^6$ shells and $4f^5$ shells exist in a ratio of about 3:7 in the ground state and over a wide range of temperature. The anomalous electrical data are evident in Samsonov's data (Table 4). Any model seeking to describe SmB_6 would have to show why the narrow f level is locked to the Fermi level, thus producing the nonintegral number of f electrons. A model used by Nickerson *et al.*[39] does so by considering both the elastic free energy of the boron framework and the configurational energy of the Sm ions and asking for the sum to be a minimum. If one could start with a (hypothetically) pure $4f^5$ configuration of Sm having a lattice constant of about 4.11 Å (corresponding to the extrapolated value for $Sm^{3+}B_6$, see Figure 5), then the lattice would spontaneously lower its energy by expanding, while simultaneously the larger $4f^6$ Sm would form from the lower-energy $4f^5$ configuration. The opposite effect is well known; for example, the formation of

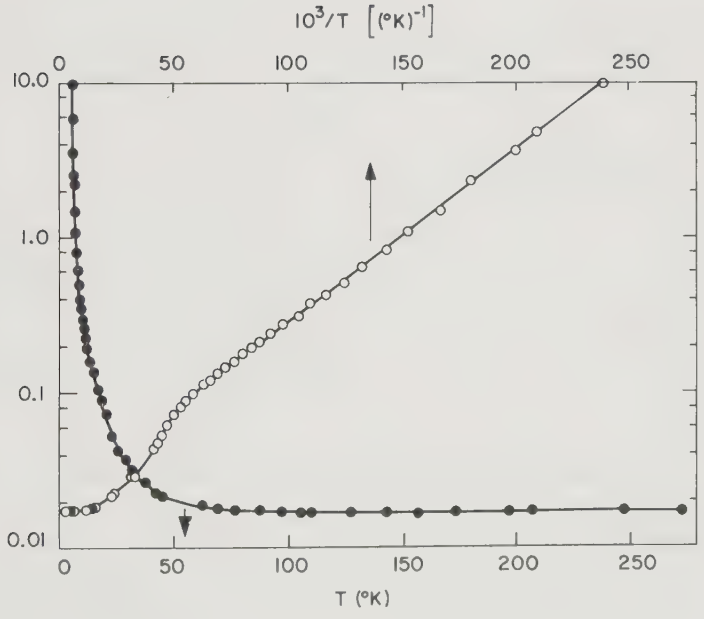

Fig. 6. Resistance of SmB_6 as a function of temperature. Closed circles: resistance versus T; open circles: resistance versus $10^3/T$.[41]

trivalent $4f^5$ Sm from divalent $4f^6$ is found in Sm chalcogenides upon the external application of positive pressure.[40]

The magnetic, electrical, and thermal behaviors of SmB_6 have unexpected characteristics.[39] Unlike the other rare earths, there is no divergence of the magnetic susceptibility at low temperature, and a semiconducting resistivity is found. The latter data are shown in Figure 6. That fraction of the Sm ions in the $4f^6$ configuration, of course, would not be expected to order since it has a $^7F_0$ ground state and no magnetic moment. The fact that the divalent ions contribute no conduction electrons led to the simple, but later proved incorrect, prediction[41] that the $4f^5$ to $4f^6$ ratio would be temperature dependent and all the ions would be in the divalent $4f^6$ configuration at low temperatures. However, both lattice constant and Mössbauer measurements at low temperatures disprove this. Subsequent analysis showed that if a conduction electron were to condense into a hybridized $5d$–$6s$ localized state, it could interact with the $4f^5$ electrons in such a way as to give a ground state with no magnetic moment and thus no divergence in the susceptibility. Such an unusual ground-state ionic configuration would be the consequence of the large metal–metal distance. The resulting narrow bands also can be constructed, in an ad hoc way, to explain the transport data. Perhaps a more natural way of explaining the combined magnetic and transport data will eventually be found via a temperature-dependent hybridization of the $4f^5$ level with the conduction band.[41]

3.2.4. Other Hexaborides

There are a number of other studies of hexaborides in the literature. The details of the magnetic ordering in most cases are not at all well understood. However, we feel that the existence of a negatively charged, spatially almost invariant boron framework throughout the whole family of hexaborides provides a unifying theme that will guide further progress.

4. Graphite Intercalation Compounds

4.1. Introduction

Graphite is the simplest and best known example of a layered lattice. The carbon–carbon bonds within each sheet are 1.418 Å, slightly larger than in benzene (1.39 Å). Three of the four carbon valence electrons are hybridized to occupy sp^2 orbitals which form σ

bonds with 120° angles. The remaining *p* electrons per carbon form a resonating π-bonding system. The layers are separated by 3.35 Å, about twice the van der Waals radius of the carbon atoms, so that in the words of Pauling,[42] "Each of the layers is a giant molecule held together by only weak van der Waals forces." However, energy band structure studies show that it is the weak interlayer interactions that are responsible for the overlap of the valence and conduction bands and the consequent creation of electron and hole pockets containing $\sim 2 \times 10^{18}$ carriers per cm^3 that make graphite a semimetal rather than a semiconductor.[43]

We shall be concerned here with the introduction or intercalation of layers of atoms or molecules between the graphite layers. Graphite can act as either an electron donor or acceptor, and charge transfer can take place. Indeed, both Lewis acid and base intercalates are known. In some cases geometric restrictions also can be important. There exist a number of informative reviews in the literature. The reader is referred, in particular, to those by Hooley,[44] Rüdorff,[45] Hennig,[46] Barrer,[2] and Ubbelohde and Lewis.[47]

4.2. Compounds with Electron Donors

Alkali metals have been known to intercalate since the pioneering work of Fredenhagen and Cadenbach.[48] When the larger alkali metal atoms, M = K, Rb, or Cs, are brought into liquid or vapor contact with graphite (single crystal or pyrolytic) the reaction proceeds in discontinuous steps. Each step corresponds to a different stage compound (where the state of the compound is defined as the ratio of the number of carbon layers to alkali metal layers). Finally, at saturation the first stage, where each carbon layer is separated by a layer of alkali, is formed with the stoichiometric composition of C_8K (Rb or Cs). It is impressive to realize that when going from a third stage to a second stage (by a reduction of temperature, for example) some layers must deintercalate completely. In graphite the planes stack *ABAB* as in hexagonal close packing. In the first-stage compound the graphite layers are directly over each other, *AAAA*; however, it takes the metal atoms four layers to repeat, as is shown in Figure 7. It can be seen from Table 5 that the expansion (C_8K = 2.05 Å) in the *c* axis is less than the ionic diameter ($K^+ = 2.76$), indicating that electrostrictive forces cause a certain amount of nesting of the K^+ within the carbon hexagons. The use of all possible metal positions in the successive layers minimizes the Madelung

TABLE 5
Interlayer Spacings of Intercalation Complex of Graphite

Approximate formula		Layer spacing, Å	Expansion, Å	Ref.
First stage	Higher stages			
C (graphite)	—	3.35	—	—
C_6Li	$C_{6n}Li$, $n = 2, 3$	3.73	—	53
—	$C_{64}Na$	4.6	1.25	45
C_8K, $C_{10}K$	$C_{12n}K$, $n = 2$–5	5.4	2.05	198, 199
C_8Rb	$C_{12n}Rb$, $n = 2$–5	5.65	2.30	198, 199
C_8Cs	$C_{12n}Cs$, $n = 2$–5)	5.94	2.69	198, 199
$C_{12}M(NH_3)_2$, M = Li, Na, K, Rb, or Cs		6.6	3.25	200
$C_{12}Li(CH_3NH_2)_2$		6.9	3.55	200
C_8Br, $C_{16}Br$ (two and four stages)		7.05	3.70	199
C_5ICl		7.24	3.89	201
$C_{24}^{+}HSO_4^{-}2H_2SO_4$		7.98	4.63	202
C_nFeCl_3		9.37–9.45	6.02–6.10	203
$C_m^{+}[HCl_4^{-} + nGaCl_3]$		9.5	6.15	204
$C_m^{+}[AlCl_4^{-} + nAlCl_3]$		9.52	6.17	205
$C_{12}SbCl_5$, $n = 1$–4		9.42	6.07	58
$C_{8n}N_2O_5$, $n = 2$–4		—		59

electrostatic energy. The heats and entropies of formation of the various alkali metal compounds have been measured using effusion techniques,[49,50] (Rb + Cs), and a reversible emf cell (K). The results are shown in Table 6, where small but definite trends are apparent. The heat of reaction becomes less negative in proceeding from the dilute to the more concentrated stages until the first stage reverses the trend. Similarly, the entropies are almost constant until the first stage is reached. The $C_{10}M$ first-stage compounds are only stable above $\sim 300°C$, where their extra entropy with respect to the C_8M first-stage compound becomes important in stabilizing them; at lower temperatures they disproportionate to C_8M and $C_{24}M$. The reversal in trend of the heat and entropy of formation in going from the second stage to the first stage signifies the onset of some three-dimensional bonding. This three-dimensional bonding is also evident in the discontinuous decrease in *c*-axis resistivity (see later). It is only in the first-stage compounds that superconductivity is found.[51] Balesdent and co-workers[52] have also obtained thermogravimetric data which give heats and entropies of formation. The metal packing

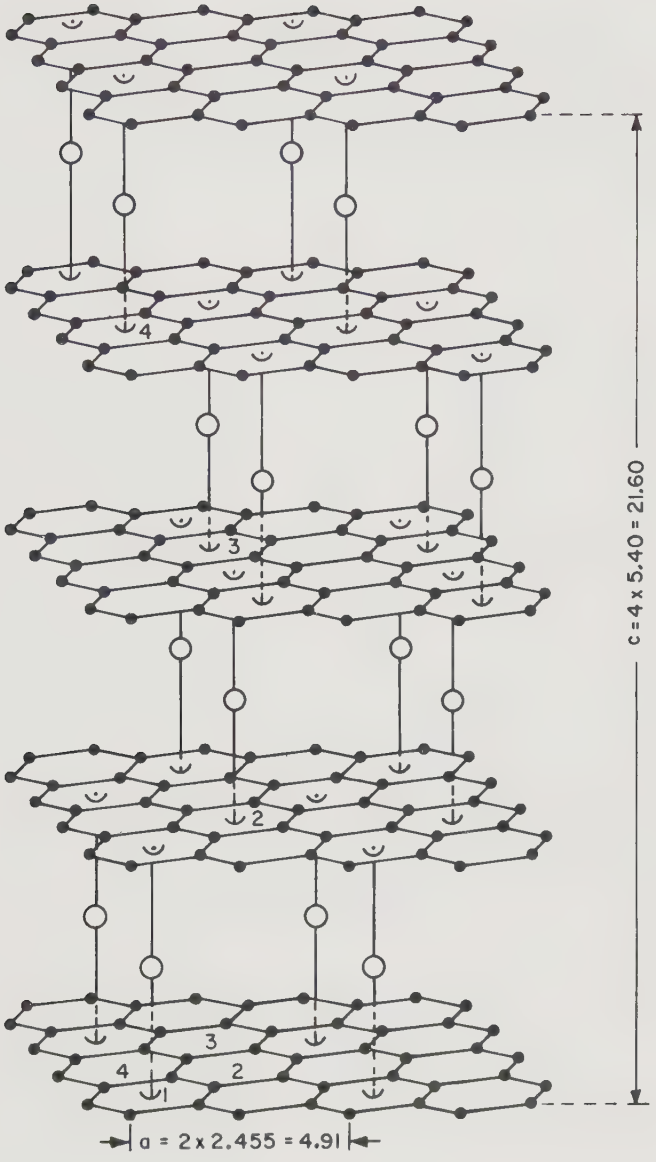

Fig. 7. Structure of C_8K (after Krebs[197]).

in the second- and higher-stage compounds is more open within the metal layer than the first stage; they correspond to formulas $C_{12n}K$, where $n = 2, 3, \cdots$, up to at least 5. The packing of the metal layers in both the first- and second-stage K compounds is illustrated in Figure 8(a).

TABLE 6
Thermodynamic Data in the Region C_8K to $C_{24}K$ Obtained from the Electrochemical Measurements

C/K atom ratio	Phases present	$-\Delta F_{cell}$ at 277°C, kcal/mole K	$-\Delta H_{cell}$ kcal/mole K	$-\Delta S_{cell}$, cal/°K-mole K
8.0	C_8K, K	0.01	—	—
8.3	C_8K	3.4	—	—
8.3	C_8K	3.0–3.3	—	—
8.8	C_8K, $C_{24}K$	3.90	7.5	6.5
	C_8K, $C_{10}K$	3.33	18.7	25.6
9.0	C_8K, $C_{24}K$	3.92	7.4	6.3
9.1	C_8K, $C_{14}K$	3.92	7.2	3.3
	C_8K, $C_{10}K$	3.42	17.8	23.9
10.0	C_8K, $C_{10}K$	3.92	7.1	5.7
13.3	C_8K, $C_{24}K$	3.93	7.1	5.7
	$C_{10}K$, $C_{24}K$	3.68	3.2	−0.5
16.2	C_8K, $C_{24}K$	3.96	6.9	5.4
17.8	C_8K, $C_{24}K$	3.95	7.3	6.0
	$C_{10}K$, $C_{24}K$	3.71	3.7	0

Sodium does not intercalate easily by itself, although Rüdorff[45] has reported a sixth-stage compound $C_{64}Na$. Juza and Wehle[53] have been able to intercalate Li in graphite with a closer packing than found for the larger alkali metals. The distance between the Li atoms in the plane is only 4.29 Å, rather than the 4.91 Å for potassium, and probably corresponds to the packing shown in Figure 8(b).

Rüdorff has found that in the presence of NH_3 and other amines all the alkali metals, alkaline earths, europium, and even aluminum

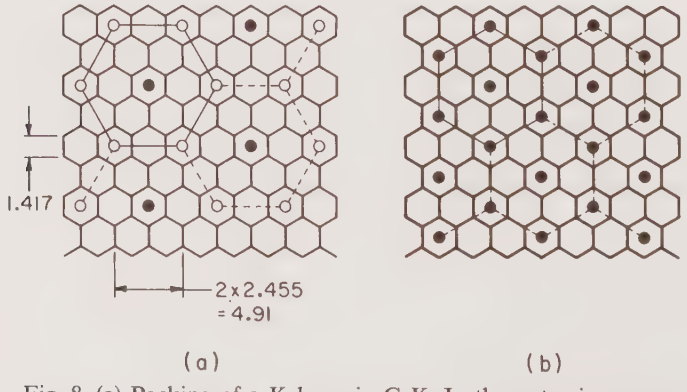

Fig. 8. (a) Packing of a K layer in C_8K. In the potassium-poorer compounds the center of the hexagons are vacant. (b) Packing of lithium atoms in C_6Li (after Krebs[197]).

will intercalate, giving compositions and expansions listed in Table 5. More recently[54,55] it has been found that other organic solvents, such as tetrahydrofurane and dimethoxyethane (DME), cointercalate with the alkali metal complexed with naphthalene to form compounds such as $C_{34}LiDMe_{3.2}$. The expansion in the latter case is 3.85 Å, approximately the thickness of DME.

4.3. Compounds with Electron Acceptors

Graphite forms a number of compounds with electron acceptors which oxidize the graphite layers to the extent that they become metallic. The graphite valence band is depleted, the hole portions of the Fermi surface grow, and the conductivity is *p* type, as we shall see.

The limiting composition of the bromine intercalate is C_8Br. It has been shown by Eeles and Turnbull[56] to be a second-stage compound with the Br atoms arranged in chains. The same chain arrangement is found in the fourth-stage compound, $\sim C_{14}Br$. The bond lengths of Br_2 molecules (2.27 Å) and ICl molecules (2.30 Å) are reasonably close to the spacing of the carbon hexagon center (2.56 Å) and both intercalate, whereas Cl_2 and I_2 (bond lengths of molecules 1.98 and 2.67 Å, respectively) do not. It is empirical evidence of the above kind that leads to the conclusion that in some instances epitaxy or registry is one criterion for intercalation of graphite. In the presence of Cl_2, metal chlorides such as $BeCl_2$, $AlCl_3$, $FeCl_3$, $HgCl_2$, $PtCl_4$, and WCl_6 also have been found to form ionic intercalates such as $C_m{}^+(AlCl_4{}^- + nAlCl_3)$. It is also reported that BCl_3 intercalates.[57] Mélin and Hérold[58] have found that $SbCl_5$ intercalates in at least four stages. N_2O_5 forms compounds of composition $C_{8n}N_2O_5$, $n = 2, 3, 4$.[59] Complexes are formed with oxyacids in the presence of oxidizing agents are electrolysis. Some of them, with representative data, are given in Table 5.

4.4. Order–Disorder Transitions

The ease with which an alkali metal intercalate can transform from stage n to $n + 1$ presupposes a large degree of mobility of the metal ions. Indeed, for $n > 1$ room-temperature X-ray studies by Nixon and Parry[60] indicate that only short-range order exists in each intercalate layer, so that in some sense it can be regarded as a liquid monolayer. By following those Bragg peaks where only the metal ions are involved, they are able to find the temperature where

ordering sets in. For potassium this is lower ($-175°C$) than for Rb and Cs (-114 and $-110°C$), and also the superstructure is different; the potassium involves a doubling of the c axis whereas the others do not. The differences are undoubtedly tied up with differences in electrostatic energy and, hence, with the ionic radius. In the high-temperature form qualitative agreement is obtained between observed and calculated intensities when the K ions are placed over the centers of the carbon hexagons. In the rubidium and cesium compounds, however, major discrepancies between observed and calculated intensities indicate that only a fraction, $\sim 1/2$ or 3/4, of the ions are located over the centers of the carbon hexagons, and that a more complex radial distribution function must actually obtain.

Bottomley and co-workers[61] also found order–disorder transformations in the first four stages of graphite intercalated with NHO_3. The coefficient of expansion goes through a λ-type anomaly near $-20°$ C for each of the different stages. Subsequent X-ray diffraction studies[62,63] show liquidlike behavior above the transition and long-range order below. They further found that the stages form sequentially, i.e., formation of the second stage proceeds through the intermediate formation of the fourth and third stages in which ordered stacking is fully developed. The carbon layers are always found to stack directly over each other if an intercalated layer is in between them (A/A) and staggered, as in graphite, if there is no intercalated layer in between (AB). While the authors postulate that a "Brillouin zone effect," that is, a critical electron-to-carbon atom ratio, is the governing factor in determining the regular sequences found for the higher stages rather than random stacking, Hooley[44] has given an alternate explanation based simply upon strain energy. If the carbon layers on either side of an intercalated layer are more rigid than the original layers, then the intercalation process will stop, until, "at a higher pressure of intercalate, another wave of peripheral openings will sweep through from each basal plane end of the crystal."

4.5. Reaction Mechanisms

The kinetics of graphite intercalation reactions can be followed by observing the changes of the parameters involved, in a number of interesting ways. These include changes in magnetic susceptibility,[64] weight,[65] length of the c axis,[66–68] and electrical resistivity.[69] They are discussed in some detail in Hooley's review.[44] It is necessary to keep the partial pressure close to the equilibrium value in

order to observe reversible changes. The perfection of the graphite can be monitored by the "threshold" pressure necessary to initiate the reaction. For natural single-crystal graphite the threshold pressure relative to saturation can be as low as 3×10^{-4} for potassium at high temperatures. At 20°C it is 0.10 for Br and 0.03 for ICl. Hooley has suggested that the lower value for ICl is due to the polar character, which allows it to transfer charge more readily than Br_2. He postulates that there is adsorption on the end basal planes of the crystal which results in some charge transfer. This modifies the band structure of the whole flake so that every *n*th layer can be intercalated, thus forming an *n*-stage compound. The so-called "threshold" pressure is reached when *n* becomes small enough so a change in the external parameter being monitored can be detected. The results of an experiment demonstrating the attack from the end basal planes are shown in Figure 9. A cylinder of pyrolytic graphite was marked into five sections along its length, as indicated on the inset. Br_2 was admitted at 145 Torr and 20°C, and the five sections were found to change in length with time as indicated. The expansion evidently started at the two ends and proceeded inward, until after 1200 min the overall composition of C_8Br was reached with a net expansion of 55%. Further, if the ends

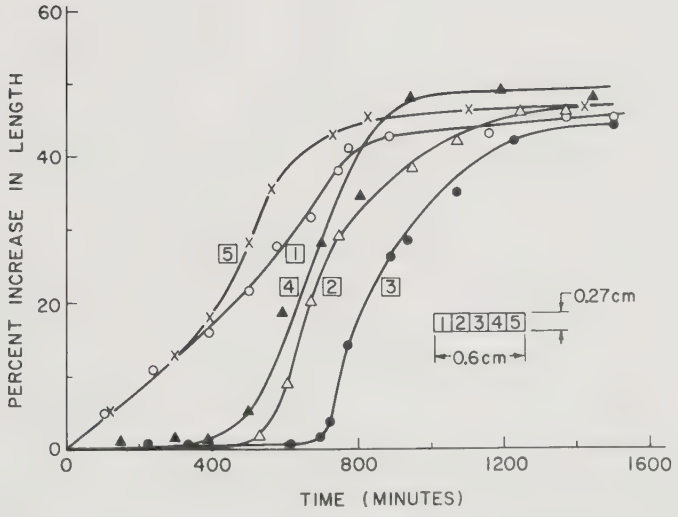

Fig. 9. Elongation of a pyrolytic graphite sample in bromine at 145 Torr, 20°C. The positions of the markers are shown on the inset (after Hooley *et al.*[68]).

were sealed, no intercalation occurred,[70] offering support for the suggestion that the reaction is initiated by adsorption on the end basal planes.

Bach *et al.*[71] have found drastic changes in the valence band of graphite upon intercalation with bromine using X-ray photoelectron emission (ESCA) techniques. Even the most dilute compound examined, of the composition about $C_{50}Br$, has a markedly different valence band than graphite, as can be seen in Figure 10. For pure graphite the solid line shows one major valence band with no evidence for splitting into π and σ bands separated in energy. The half-width of the graphite band is visibly reduced in the intercalation as a result of the electron transfer for some as yet unclear reasons. A new peak appears at higher energy (lower binding energy), the intensity of which is proportional to the bromine content, which is undoubtedly the Br 4*p*-derived band. The protruding shoulder on the low-energy side of the graphite band seems to be the Br 4*s*-derived band. The sensitivity to changes, even in the 12th-stage compound, indicates

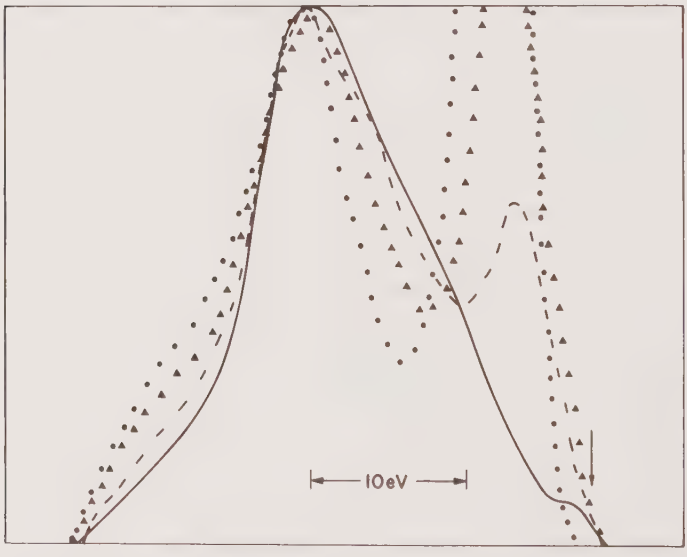

Fig. 10. Normalized valence band plots for graphite and its bromine intercalates. Full line refers to pure graphite; dashed line to a dilute intercalate (around 12th stage, i.e., $C_{50}Br$); triangles to the fourth-stage compound, $C_{16}Br$; and dots to the third stage compound, $C_{12}Br$. The Fermi level is located close to the vertical arrow (after Bach *et al.*[71]).

that the ESCA technique would be useful in studying changes in band structure upon the chemisorption of monolayers, the presence of which, according to Hooley's hypothesis, are necessary to initiate the intercalation reaction.

4.6. Fermi Surface and Transport Measurements

Ever since the cyclotron resonance experiments of Galt *et al.*,[72] it has been known that there are both electron and hole Fermi surfaces in graphite. The electrons have the lower mass. In the past few years some very dilute (high-stage) intercalation compounds have been prepared using Br_2 [73] and HSO_4^-,[74] which show that *p*-type carriers can be added in a very controlled way. Even though it is probably too early to draw definite conclusions at the time of this writing, we feel the results are unusual enough to deserve some discussion here.

Bender and Young[73] have intercalated Br_2 and produced a series of compounds having compositions in the range $C_{4600}Br$ to $C_{140}Br$. Shubnikov–de Haas oscillations of the transverse magnetoresistance were found to be dependent upon intercalation. As the π-electron system of the graphite is depleted, four dominant hole periods are observed. The conditions under which the intercalation was carried out are such that each intercalated layer contains 1.59×10^{14} Br^- per cm^2. The authors assume that the charge transfer comes equally from intervening graphite layers, reducing the Fermi energy by as much as 0.49 eV. The reductions cause the Fermi surface to evolve from the hole and electron surfaces of pristine graphite to a hole void with a single extremum orbit. Enough intermediate Fermi surface shapes are postulated to account for the four observed hole periods in the oscillations. It would seem that other models might also account for the data. Remarkably, not much collision broadening of the Landau levels is observed.

Resistivities and Hall effect measurements have been made by Ubbelohde[74] using carefully prepared bisulfate and, to a lesser extent, perchlorate intercalation compounds down to 1.8°K. By preparing the electrical leads first and making measurements on the pure graphite sample prior to intercalation, he is able to cope with extrinsic effects such as interplanar defects which plague the transport investigations of such anisotropic materials. The intercalation is carried out by electrolysis, which means that one can keep track of the amount of intercalation by measuring charge providing certain

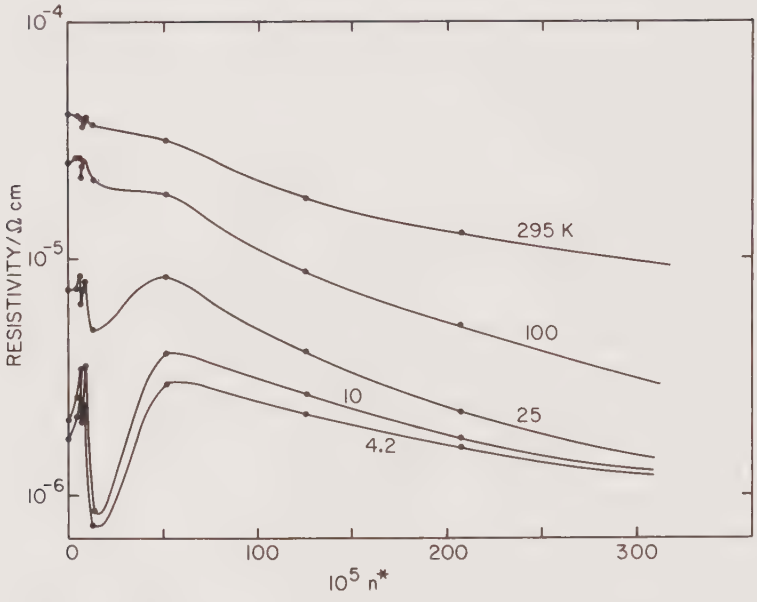

Fig. 11. Resistivity as a function of n^*, where n^* is the nominal number of positive carriers per carbon atom, i.e., $10^5 n^* = 52$ corresponds to the 80th-stage compound $C^+_{10^5/52}HSO_4^-$ (after Ubbelohde[74]).

conditions are met. For bisulfate intercalations there are neither side reactions nor spontaneous intercalation, so, as is evident in the data presented below, even the dilute intercalates can be characterized and studied. Each intercalated layer is assumed to reach its stoichiometric limit of $C^+_{24}HSO_4^-H_2SO_4$, and the layer spacing is assumed to be uniform even in the most dilute case studied, where there are 866 carbon layers for each $HSO_4^-H_2SO_4$ layer, i.e., the 866th stage. It seems, however, that the assumption of uniform periodicity is not necessary. The results are also consistent with a distribution of stages around an average. In Figure 11 resistivity in Ω-cm is plotted as a function of the number of holes per carbon atom n^* assuming each HSO_4^- has a full negative charge. The higher dopings are *p* type, as can be seen in the Hall data plotted in Figure 12, whereas pure graphite is compensated, and *n* type. The Hall effect inversion takes place when the electron and hole concentrations weighted by the squares of respective mobilities become equal. The reversal in the Hall effect near the 500th-stage compound, therefore, is where approximately 8×10^{-5} hole per atom has been added. However, the curious maximum and minimum of the resistivity in the very dilute

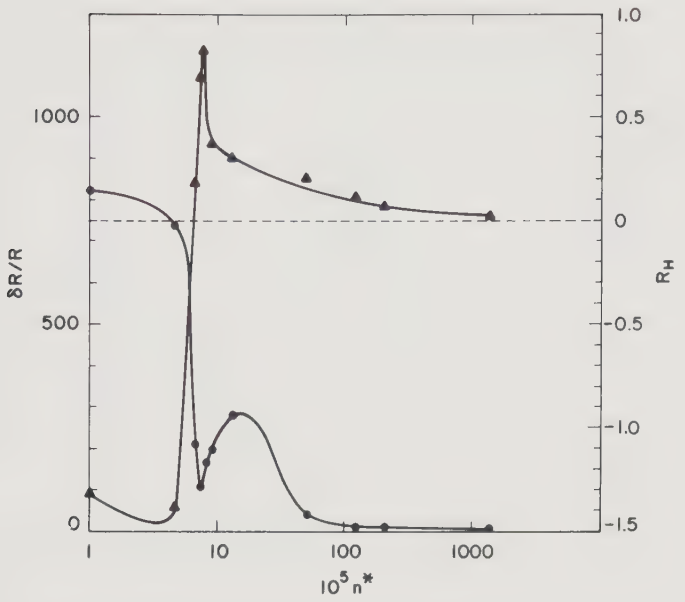

Fig. 12. Magnetoresistance ($\delta R/R$), represented by circles, and Hall effect (R_H), represented by triangles, as a function of n^*, where n^* is the nominal number of positive carrier per carbon.

regime are unexpected, although a number of ad hoc models can be conjured to explain them.

Even before the fifth stage is reached (Figure 13) the effect of intercalating a new layer is nonadditive and means that there are effective c-axis interactions that extend across more than five carbon layers. Such interactions reaching across several graphite layers already have been discussed in connection with the slow decrease in the heat of formation of the alkali metal graphites as the stage decreases. Ubbelohde has also studied the c-axis as well as the a-axis conductivity. Hence, the electrical anisotropy for a variety of intercalates, including potassium, as well as halogens and oxyacids,[75] is known. In all cases except for K and ICl at low temperatures the c-axis resistivity increases upon intercalation. We already have seen that the a-axis resistivity decreases, so that the anisotropy increases from the value $\rho_a/\rho_c \sim 4 \times 10^{-4}$ for the pure graphite. The data for a number of first-stage intercalates are given in Table 7. The increases in c-axis resistance (in which R_0, the c-axis resistance of the unintercalated graphite itself, is used as the scaling parameter to normalize the large dimensional changes) seems quite moderate for the first-stage

TABLE 7
Electrical Parameters of First-Stage Intercalates

Intercalate		295°K		77°K	
Parent graphite	$(\sigma_0)_a, \Omega^{-1}\ cm^{-1}$	2.69×10^4		5.1×10^4	
	$(\rho_0)_c, \Omega$-cm	8.87×10^{-2}		1.78×10^{-1}	
		295°K		77°K	
		$(\sigma/\sigma_0)_a$	$(R/R_0)_c$	$(\sigma/\sigma_0)_a$	$(R/R_0)_c$
ICl		13.07	1.57	46.1	0.12
Br_2		8.31	10.8	21.6	1.61
K		4.07	3.47×10^{-3}	23.5	5.0×10^{-5}
$NO_3^- \cdot CHNO_3$		11.75	14.3	34.11	2.73
$HSO_4^- \cdot 2H_2SO_4$		5.9	29.8	13.9	2.20
$ClSO_3^- \cdot nHClSO_3$		5.35	3.37×10^2	11.3	—
$AlCl_4^- \cdot AlCl_3$		6.0	5.25	—	—

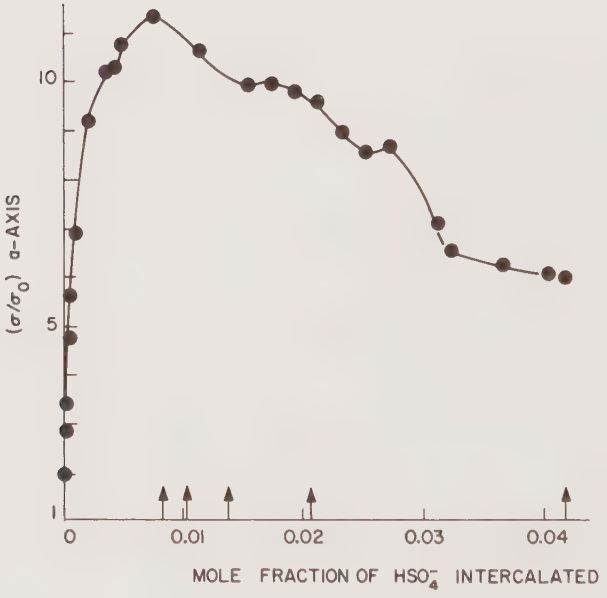

Fig. 13. Effects of the more concentrated HSO_4^- intercalations at 295°K on the *a*-axis conductivity (after Ubbelohde[75]).

Fig. 14. Effects of the more concentrated HSO_4^- intercalations at 295°K on the *c*-axis conductivity of three different samples (after Ubbelohde[75]).

intercalates shown in Table 7. As might be expected, they do not vary monotonically with the stage. The excursions for three different samples of HSO_4^- intercalates are shown in Figure 14. The sample-dependent behavior for the lower stages is probably related to either imperfections which give rise to inhomogeneous field distributions, or ionic diffusion and "voltaic effects," which were noted by Ubbelohde.

It is interesting to note that while $(\rho_0)_c$, the *c*-axis resistance of pure graphite, increases slightly with temperature, that for the intercalates is strongly metallic, as, of course, is the *a*-axis resistance in both intercalated and unintercalated sample. That the above holds for the HSO_4^- intercalation compound, where the expansion of the *c*-axis result is 4.6 Å, indicates that the electronic wave function does not decay appreciably in such short distances. In the related

intercalated layered transition metal dichalcogenides, to be discussed later, the c-axis resistivity above $\sim 30°$K also is found to have a metallic slope; however, the c-axis resistivity is frequently proportional to the a-axis resistivity and in such cases there may be a-axis shorts.

4.7. Superconductivity

The first-stage alkali metal intercalates have been found to be superconducting with rather low transition temperatures[51] ranging up to 0.13 for Cs to 0.15 for Rb and 0.55°K for K. No superconductivity has been found in second- or higher-stage alkali metal intercalates or in any stage of electron acceptor intercalates. The c-axis electrical conductivity of the potassium intercalate is many orders of magnitude greater than for corresponding first-stage electron acceptor intercalates, as shown in Table 7. This suggests that in the graphite intercalates, in contrast to the transition metal dichalcogenides, individual layers do not exhibit independent superconducting behavior. There are proofs[76] that there cannot be infinite-range order (and hence superconductivity) in two dimensions, but, in actual practice a crystal is not prohibited from displaying long-range (as distinct from infinite-range) order, and thus all the manifestations of the superconducting state.

In the superconducting first-stage compounds not only is there good three-dimensional contact between the layers as judged from the c-axis conductivity, but also there must be a greater filling of the graphite π band than in the higher stages, because the alkali metals are partially ionized at all compositions, probably to the extent of one-third to one-fourth.[77] It is not clear which of the above two effects is more important in causing the superconducting interaction to decrease or disappear in the higher stages.[78]

4.8. Spin Resonance

Conduction carrier spin resonance has been observed in alkali metal intercalated pyrolytic graphite.[54,77,79] The ESR line shapes are typically metallic,[80] being a mixture of absorption and dispersion modes, as expected, when (1) the skin depth δ is less than the sample thickness d, and (2) diffusion of the magnetization via the conduction electrons produces additional asymmetries.

In the limit of thick samples ($\delta \ll d$) the ratio of low-field maximum to high-field minimum of the derivative of the power absorption spectrum, known as the Dyson asymmetry parameter[80] A/B, is a function of $(T_d/T_2)^{1/2}$, where T_d is the time required for the electrons to diffuse across the skin depth and is the transverse relaxation time. The ratio A/B varies between the theoretical limits of 2.7 ($T_d/T_2 \to \infty$, no diffusion, as is the case in the NMR measurements of metals) and 19 (as $T_d/T_2 \to 0$). In $C_{24}K$, C_8K, and $C_{24}Rb$ the Dyson[80] asymmetry parameter A/B varies with temperature from 2.7 at 300°K to 4.5 at 77°K.[79] Thus, the above results are in agreement with the increased metallic conduction as the temperature is lowered.

The ESR line shapes are narrower at 77 than at 300°K. But there are no appreciable changes below 77 down to 1.2°K.[77] The narrowing may be explained on the basis of the order–disorder transitions[60] previously mentioned. The difference between the high- and the low-temperature structures then reflects the difference in the mobility of the intercalate layer above and below the transition. An equilibrium distribution of species M, M^+, M_2^+ (M = alkali metal), etc., must be present in the (liquid) disordered monolayer, and exchange and hyperfine interactions can contribute to the ESR linewidth. Below the transition, exchange interactions in the ordered state can lead to the observed narrowing of the ESR lines.

When intercalation is carried out from a solution of M in tetrahydrofurane (or dimethoxyethane) and naphthalene[60] the solvent is also inserted. The ESR linewidths are then an order of magnitude less than for M-intercalated graphite at room temperature,[77,79] undoubtedly the result of motional narrowing in the solvated-M monolayer.

4.9. Magnetic Properties

A number of the electron acceptors which can be intercalated, such as $FeCl_3$, are magnetic, and, as might be expected, the intercalated compounds are magnetic with strongly anisotropic properties. $FeCl_3$ forms an intercalated layer which is approximately the same density as one would calculate for $FeCl_3$ which itself is a layered compound.[44,81] Even though there is some charge transfer at room temperature, there is no indication of epitaxy or registry with the graphite. Mössbauer spectra[82–84] indicate that most of the Fe remains in the 3^+ state ($Fe^{II}/Fe^{III} < 0.05$). There is some discrepancy with earlier room-temperature Hall data which would indicate that

TABLE 8
Parameters of the NGR Spectra for Pure $FeCl_3$ and the Graphite–$FeCl_3$ Compound

Compound	T, °K	δ, mm/sec	Δ, mm/sec
$FeCl_3$	80	0.81 ± 0.02	0
	300	0.68 ± 0.02	0
Graphite–$FeCl_3$	80	0.81 ± 0.02	0
	300	0.77 ± 0.02	0

about one-third of the Fe is present as Fe^{II}.[85] The charge transfer deduced from the Mössbauer experiments is temperature dependent, as can be seen in Table 8. This increase in the chemical shift δ of the trivalent high-spin iron nucleus in the graphite relative to pure $FeCl_3$ indicates a decrease in the *s*-electron contact, presumably due to the shielding effect of electrons transferred from the graphite π system to unoccupied Fe *d* orbitals. The 80°K results indicate there is no longer any measurable charge transfer.

If C_7FeCl_3 or $C_{12}FeCl_3$ is reduced by hydrogen, the loss in weight is compatible with the formation of, respectively, first- and second-stage $FeCl_2$ compounds.[44] The Mössbauer chemical shift indicates no charge transfer even at room temperature; however, two electric quadrupole shifts are observed, indicating there must be two kinds of surroundings for the Fe nuclei, for reasons which are not obvious.

Karimov *et al.* have investigated the magnetic properties of both the $FeCl_3$-intercalated compounds[86] and the corresponding $NiCl_2$ and $CoCl_2$ compounds.[87] $FeCl_2$ and $FeCl_3$ themselves are hexagonal layered structures which undergo antiferromagnetic transitions at 24 and 16°K, respectively. In $FeCl_2$ the spins lie perpendicular to the layers, while in $FeCl_3$ they lie in the plane, and in both compounds the magnetic ions within each plane are aligned ferromagnetically.[88,89] The marked anisotropy along the *c* axis in $FeCl_2$ leads to a relatively strong interlayer coupling. The neutron diffraction studies of Yelon and Birgeneau[90] show the ordering to be that of a three-dimensional Ising antiferromagnet. Upon intercalation the effective moments remain the same as in the pure compounds for both $FeCl_2$ and $FeCl_3$; however, the ordering changes. The first-stage $FeCl_3$ intercalate still orders antiferromagnetically at 3.6°K; however, the second stage orders ferromagnetically at 8.5°K. The increase in the

magnetic ordering temperature for the higher stage with the greater separation between magnetic planes is undoubtedly due to the competition between the ferromagnetic and antiferromagnetic exchange interactions. The ferromagnetic exchange is due to anisotropy within the planes which, however weak, will give rise to a two-dimensional Ising ordering[91] independently of the distance between magnetic planes. The antiferromagnetic interaction between the ferromagnetic planes, on the other hand, will depend upon separation, and in the first-stage compound it is evidently just strong enough to dominate the ordering.

In the $FeCl_2$ intercalates even in the first stage the interplanar interaction now evidently becomes too weak to be effective and the ordering is ferromagnetic at 15°K in both the first- and second-stage compounds.

The structure of the intercalated $NiCl_2$ and $CoCl_2$ layers has not been studied, but the arrangement probably does not differ much from the layers of parent compounds. They both order antiferro-

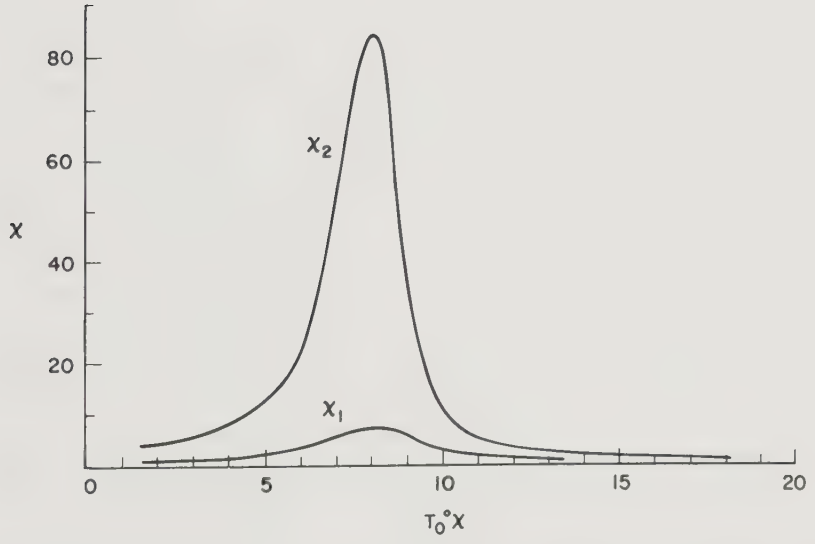

Fig. 15. Temperature dependence of the molar magnetic susceptibility of the compound of $CoCl_2$ with graphite (per g mole of $CoCl_2$) in zero external field. χ_2 is the susceptibility parallel to the c axis, χ_1 is that perpendicular to the c axis (after Ref. 86).

magnetically at 50 and 25°K.[92] In the second-stage intercalates that were studied the interaction between the magnetic layers was too small to be observable. A rather broad ordering peak was observed around 8°K for the $CoCl_2$ in the initial susceptibility curve, as can be seen in Figure 15, and at 18°K for $NiCl_2$. At the peak the susceptibility parallel to the layers is an order of magnitude greater than that perpendicular to the layers. Below the apparent phase transitions no hysteresis or remnant magnetism was observed. Although the curves resemble antiferromagnetic ordering (Figure 15), the authors state that above 1°K, insofar as can be measured, the compounds are still two-dimensional Heisenberg paramagnets. There is obviously more research to be done before the chemical and physical properties we have touched upon here are really well understood.

5. Chalcogenide Intercalation Compounds

5.1. The Layered Chalcogenides

The chalcogens sulfur, selenium, and tellurium are highly polarizable atoms. Unlike oxygen, they frequently form compounds that crystallize in layered structures. The layers in these structures comprise metal atoms sandwiched between chalcogen sheets. Bonding within the layers is strong, while that between adjacent layers is weak. Consequently, it is often possible to form intercalation compounds under rather mild conditions by insertion of atoms, molecules, or ions between the weakly bound layers. Before discussing the resulting compounds we shall describe the layered chalcogenides from which they are formed. Comprehensive reviews of these materials have been written by Hulliger[93] and Wilson and Yoffe.[94]

Chalcogens form layered compounds of general formulas MX, MX_2, and M_2X_3, where M is metal and X the chalcogen. Of these only the dichalcogenides are known to form intercalation compounds. The others may well do so, but we are unaware of such studies. The dichalcogenides form layers of two kinds. The most common is that found in the CdI_2 structure. In this the chalcogens pack in a hexagonal close-packed array *ACACAC*, etc. The metal atoms reside in the octahedral holes between every other pair of chalcogen layers. The structure can then be denoted *AbCAbCAbC*, etc., in which the upper case letters refer to the chalcogen atoms and the lower case to the metal atoms. The metal is located in sites of octahedral symmetry. In Figure 16 those elements whose disulfides or diselenides crystallize with this

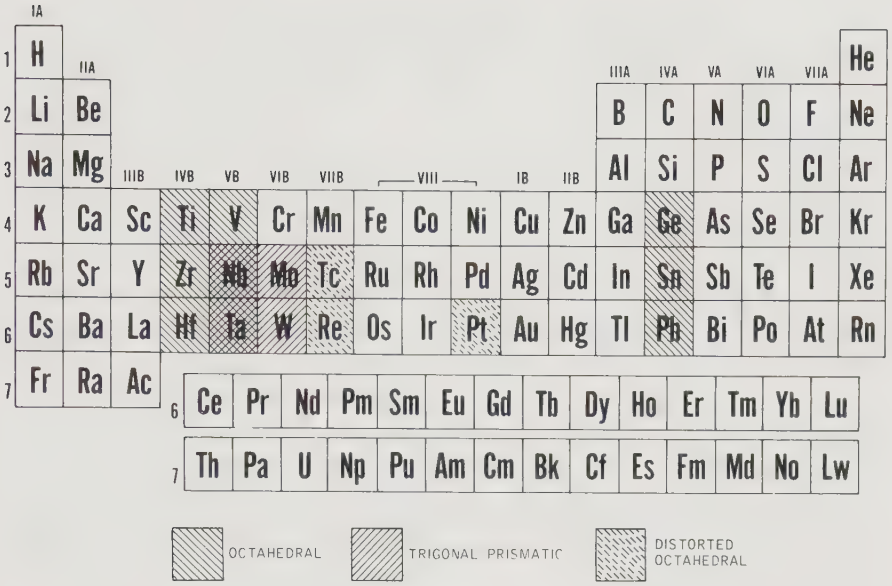

Fig. 16. Periodic table of the elements showing which form layered disulfides and/or diselenides.

structure are shown in the periodic table. They are found only in groups IVa, IVb, and Vb. Among these the *c*/*a* ratio is near the ideal value 1.633. The $CdCl_2$ structure is similar to the CdI_2 structure. The layers are identical, but the stacking of anion layers is *ABCABC*, etc. In group VIIb one finds highly distorted versions of the $CdCl_2$ structure. In the sulfides and selenides of Tc and Re, strong intralayer metal–metal bonds distort the lattice. $PtSe_2$ crystallizes in a highly distorted version of the CdI_2 structure with a very low value for *c*/*a*. The ditellurides of many elements have the CdI_2 structure or a distorted version of it, but we shall not be dealing with them since their intercalation chemistry is very meager. Another structure, found for group Vb and VIb in the cases of Nb, Ta, Mo, and W, involves trigonal prismatic coordination of the metal atoms in the sandwich. These structures are built of *AbA*-type layer units. In group Vb octahedral and trigonal prismatic layers sometimes alternate in the same compound.

Most of the compounds are fairly stable in dry atmospheres, but in moist air many will tarnish. The group IVb materials, especially the Zr and Hf compounds, react readily with moist air. The group Vb compounds are somewhat more stable, but they, too, will tarnish,

especially in the presence of light. The group VIb compounds, the sulfides of which are even found in nature, are very stable.

Of all the sulfides and selenides we are considering, only those of group Vb metals are good metallic conductors. The disulfide and diselenide of Ti are semimetals and the rest are semiconductors. The electrical properties of most of the group IVb, Vb, and VIb materials can be understood qualitatively in terms of semiempirical band schemes put forward by Wilson and Yoffe[94] and Huisman *et al.*[95] These are shown qualitatively in Figure 17. Simply put, there exists a broad valence band composed mostly of chalcogen *s*- and *p*-bonding orbitals, above this a broad antibonding band, and in between a nonbonding band, mostly of metal *d* character. If the metal atom is in a trigonal prismatic environment, a narrow, two-electron *d* band is lowest in energy. Wilson and Yoffe place this band in the gap. Huisman *et al.* place it below the top of the valence band. The photoelectron studies of McMenamin and Spicer[96] and of Williams and Shepherd[97] indicate that the band is somewhere in between these two positions, the top of the band falling above the top of the valence

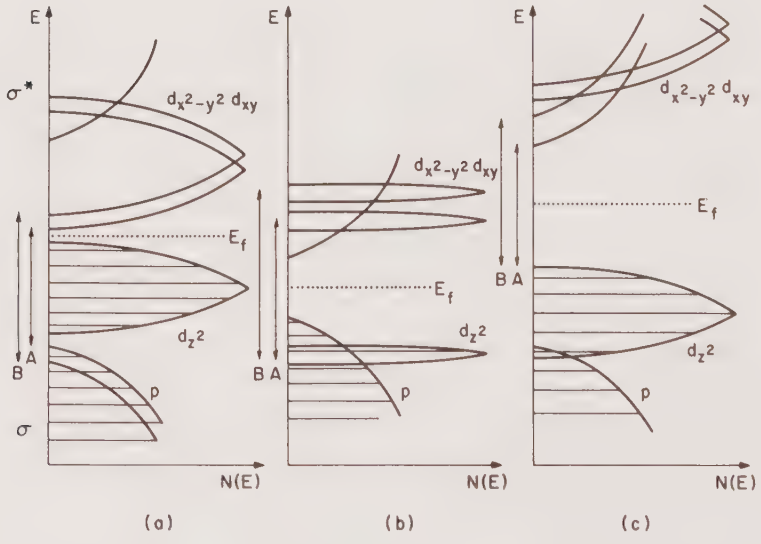

Fig. 17. Band structure of the trigonal prismatic dichalcogenides: (a) suggested by Wilson and Yoffe[94] on the basis of optical data; (b) proposed by Huisman *et al.*[95] on the basis of molecular orbital calculations; and (c) proposed by Williams and Shepherd[97] and McMenamin and Spicer[96] from photoemission spectra (reproduced with permission from Ref. 97).

band, with the bottom at, or slightly below, the top of the valence band. If the transition metal is Nb or Ta, this band is half filled and the material is metallic. If it is Mo or W, the band is full and the material is semiconducting. Recent calculations by Mattheiss[98] indicate that the splitting off of a narrow, nonbonding, two-electron *d* band from the *d* manifold is due to hybridization much more than to crystal field. In this scheme the band labels in Figure 17 apply only at the Γ point of the Brillouin zone.

The octahedrally coordinated transition metal disulfides and diselenides of group IVb and Vb still present something of a puzzle. While those of Zr and Hf are semiconducting and those of V are metallic as one might expect, TiS_2 and $TiSe_2$ appear semimetallic[98a] and the octahedral $1T$-TaS_2 and $1T$-$TaSe_2$ are semiconducting.[98b] In $1T$-TaS_2, however, a semiconducting-to-metal transition appears around 80°C,[98b] below which temperature electron diffraction studies reveal *a*-axis superstructure.[98c] The disulfides and diselenides of Tc and Re contain metal–metal bonds, and these presumably tie up would-be conduction electrons. The group IVa disulfides and diselenides are semiconducting, as expected.

5.2. The Intercalation Compounds of Layered Dichalcogenides and Elemental Metals

Almost all electropositive elements can be inserted between the layers of at least one layered chalcogenide. It is convenient for historical and other reasons to subdivide these intercalates into three groups: (1) alkali metals, alkaline earths, and rare earths; (2) post-transition metals; and (3) transition metals. We shall discuss them in that order.

5.2.1. Alkali Metals, Alkaline Earths, and Rare Earths

In 1959 Rüdorff and Sick[99] discovered that layered transition metal disulfides and diselenides when reacted with electropositive metals dissolved in liquid ammonia would form intercalation compounds similar to those of graphite. These were the first intercalation compounds of the layered chalcogenides. Using liquid ammonia as the solvent for the intercalate, Rüdorff and his co-workers prepared a large variety of such compounds.[45,100–102] The intercalates included the alkali metals, alkaline earths, and europium. The layered

compounds were restricted to sulfides and selenides because tellurides were reduced by the electropositive metals. One exception reported is europium in molybdenum ditelluride.[101]

The general formula for the intercalation compounds can be written $A_n(NH_3)_mMX_2$, where A is the electropositive metal, MX_2 is the dichalcogenide, n is equal to or less than one, and m is highly variable and may be zero. Ammonia intercalates along with the small metals, especially lithium. The intercalation compounds are typically black or blue-black. Those of the more electropositive metals (K, Rb, Cs) are usually pyrophoric. All the compounds are air sensitive and react vigorously with excess water, yielding hydrogen, the original layered dichalcogenide, and the hydroxide of the intercalate. Chemically, they very much resemble the metal they contain between their layers, and it seems appropriate to consider them "intermetallic" with substantial contribution from the configuration $A^+(MX_2)^-$ as opposed to purely ionic compounds. As one would expect, the *interlayer* spacing increases on intercalation by an amount characteristic of the intercalate. The *intralayer* spacings, as characterized by the *a* axis, increase only slightly, usually by 0.1 Å or less. Table 9 is a compilation of some compounds of this class.

Extensive studies of SnS_2, TiS_2, and ZrS_2 intercalation compounds with alkali metals have been reported by Rouxel and coworkers.[103–107] All three sulfides crystallize in the CdI_2 structure. Tin disulfide is a pale yellow material that reacts extremely rapidly

TABLE 9
Some Alkali Metal Intercalation Compounds

Compound	*a*	*c*	Δd	Ref.
$KZrS_2$	3.72	22.23	1.60	106
$NaTiS_2$	3.47	20.58	1.17	105
$KTiS_2$	3.48	22.83	1.92	104
$RbSnS_2$	3.76	24.33	2.24	103
$LiSnS_2$*	3.74	23.89	2.09	103
$NaSnS_2$*	3.69	25.54	2.64	103
$KSnS_2$	3.67	25.61	2.67	103
$Na_{0.6}MoS_2$ (2*H*)	—	15.00	1.35	111
$K_{0.4}MoS_2$ (2*H*)	3.20	16.58	2.14	111
$Rb_{0.3}MoS_2$ (2*H*)	3.20	17.19	2.45	111
$Cs_{0.3}MoS_2$ (2*H*)	—	19.61	3.66	111

* May contain ammonia.

with alkali metals in liquid ammonia to form complexes of the general formula $ASnS_2$.[103,107] Compounds containing less alkali metal could not be prepared. Reaction with excess water yields SnS_2, alkali metal hydroxide, and hydrogen. However, if water is admitted at low pressure, it is possible to isolate $A(OH)SnS_2$. If the $ASnS_2$ compounds are heated to 200°C, they decompose, yielding elemental tin, tin monosulfide, and alkali metal sulfides. The coordination of the alkali metal apparently depends on its size. Lithium and sodium are octahedrally coordinated by sulfur; potassium and rubidium are in trigonal prismatic environments. The cesium compound was not crystalline enough for X-ray analysis.

In contrast to SnS_2, TiS_2 was found[104,105] to form compounds A_nTiS_2, where $0.06 \leq n \leq 1$. Depending on the concentration and size of the intercalate, either octahedral or trigonal prismatic coordination of the intercalate was observed. Three phases were reported for K_nTiS_2: a first-stage compound for $0.28 \leq n \leq 1$, a second-stage compound for $0.14 \leq n \leq 0.16$, and a fourth-stage compound for $0.06 < n < 0.08$. Outside these limits the two adjoining phases were obtained. For n less than 0.06 some unreacted TiS_2 was always observed. In the first stage, the interlayer spacing was equal to the c axis and decreased with increasing alkali metal content. The second- and fourth-stage compounds both contained three layers of alkali metal per unit cell. In other words, in the fourth-stage compound the unit cell contains three layers of alkali metal and 12 layers of TiS_2. Reaction between $KTiS_2$ and water at 10 mm pressure produced $(KOH)_xTiS_2$. Additional water then yields $(KOH)_x(H_2O)_yTiS_2$. This compound is probably not very stable and may eventually decompose, yielding H_2S and hydrous oxides of titanium. ZrS_2 behaves like TiS_2 in that variable stoichiometry and higher stage compounds were observed.[106]

The collection of physical data on the intercalation compounds described above has been impeded by their high reactivity. The data are compatible with a significant transfer of charge from the intercalate to a conduction band belonging primarily to the layered host. Except in the case of magnetic intercalates such as europium,[102,108] the compounds are either slightly paramagnetic or significantly less diamagnetic than the unintercalated host.[100,104] The susceptibility is temperature independent. The intercalation of europium in MoS_2 in the limit yields $Eu(NH_3)MoS_2$, whose magnetic susceptibility[108] between 77 and 298°K yields a θ of approximately 8°K and a molar Curie constant of 7.90, in excellent agreement with 7.88, the value

TABLE 10

Some Superconductors among the Metal Intercalated Layered Dichalcogenides

Compound	Critical temperature, °K	Ref.
$LiMoS_2$ (2*H*)	3.7	111
$Na_{0.6}MoS_2$ (2*H*)	4.15	111
$K_{0.4}MoS_2$ (2*H*)	6.1	111
$K_{0.4}MoS_2$ (3*R*)	5.5	111
$Rb_{0.3}MoS_2$ (2*H*)	6.25	111
$Cs_{0.3}MoS_2$ (2*H*)	6.30	111
Na_xHfS_2	2.1	—

expected for spin 7/2. The compound orders ferromagnetically near 4°K.

Intercalation of the semiconducting dichalcogenides of groups IVb[109] and VIb[110,111] and the semimetal TiS_2 converts them into metals with superconducting transition temperatures up to about 6°K. Some of these are listed in Table 10. On the other hand, intercalation of the superconducting metals such as $NbSe_2$ yields a nonsuperconducting compound[112] presumably well on its way to a semiconducter as the two-electron nonbonding *d* band is filled. In an elegant experiment at Cambridge, Acrivos and co-workers[113] monitored the transmission spectra of thin crystals of MoS_2 and $NbSe_2$ as these were successively intercalated with sodium and then deintercalated. Intercalation of MoS_2 gave rise to characteristic free-carrier absorption similar to that of $NbSe_2$. Intercalation of $NbSe_2$, on the other hand, causes the transmission spectrum to resemble that of MoS_2, particularly *p*-type MoS_2. On deintercalation, the spectra revert to that of the original layered compounds.

The compounds discussed thus far in this section were prepared at room temperature or at the temperature of boiling ammonia (−33.5°C). By heating the elements or by heating the alkali metal with the dichalcogenides, Omloo and Jellinek[114] prepared compounds of general formula A_nMS_2, where A = Li, Na, or K; M = Nb or Ta; and X = S or Se. The sulfides had a homogeneity range from $n = 0.4$ to 0.7. The selenides were homogeneous only for $n = 2/3$. The alkali metals are found between undistorted trigonal prismatic MX_2 layers. The coordination of the alkali metal was usually trigonal prismatic but was sometimes octahedral. In remarkable contrast to similar materials

formed by intercalation at low temperature from liquid ammonia, these compounds react only slowly with water, yielding H_2X rather than H_2. Chemically, they behave more like alkali metal chalcogenides than the alkali metal itself. They have paramagnetic temperature-independent susceptibilities.

The existence of two kinds of "intercalation" compounds of alkali metals was first discussed by Rüdorff,[45] who compared the compounds AMS_2, where M = Ti, V, or Cr. All three have the same structure but they have remarkably different properties. As one proceeds from $ATiS_2$ to $ACrS_2$ the compounds go from a black, highly reactive substance to an orange, inert material with magnetic properties consistent with localized electrons on Cr^{3+}. It should be pointed out that of this series only the Ti compounds can be prepared by lower-temperature reactions.

Sergent and Prigent[115] have prepared a series of air- and moisture-stable, black compounds with metallic luster that have the general formula AMS_2, where A = Li, Na, K, Rb, Cs and M = Mo or W. The crystal structure of these materials is not known. They were prepared not by direct combination of the elements but by reduction with hydrogen of materials with the general formula A_2MoS_6 or $A_2W_2S_8$. The authors refer to the compounds as thio-tungstates and thiomolybdates, in distinction to the intercalation compounds of similar composition. Whether the compounds are indeed as they appear has not been established.

That two kinds of alkali metal intercalation compounds exist with remarkably different chemical properties is clear. There have been enough conflicting reports on certain of the intercalation compounds to suggest that some of them may exist in both modifications. Thus, Rüdorff[45] describes SnS_2 intercalation compounds as thiometallates which hydrolyze in water, whereas Le Blanc *et al.*[103] have found them to behave more like the alkali metals themselves. Our own experience with $NbSe_2$ intercalates[112] prepared from liquid ammonia is at variance with Omloo and Jellinek's reports[114] on compounds of similar composition prepared at high temperature.

5.2.2. Post-Transition Metals

We have described in the previous section the intercalation of electropositive elements in the layered chalcogenides, limiting ourselves to those elements soluble in liquid ammonia. If we examine other potential elemental intercalates, we find that the reaction is in

TABLE 11

The Intercalation Compounds of TaS_2 and Post-Transition Metals

A	X	a, Å	C, Å	Δd,* Å	χ_p†	T_c
Cu	$\frac{2}{3}$‡	3.34	2 × 6.58	0.56	—	§
Zn	$\frac{1}{2}$‡	3.32	2 × 6.30	0.28	—	—
	$\frac{1}{3}$	3.32	2 × 6.20	0.18	—	§
Cd	1‡	3.20	2 × 8.65	2.03	—	§
	$\frac{1}{3}$	3.32	2 × 6.70	0.68	—	§
Hg	1‡	3.30	2 × 8.90	2.88	—	2.1
Al	$\frac{1}{3}$‡	3.29	2 × 6.20	0.18	—	§
Ga	1‡	3.30	2 × 8.53	2.51	+38	§
In	1‡	3.29	2 × 8.70	2.68	+48	1.0
	$\frac{2}{3}$	3.32	7.97	1.95	+38	§
Ge	$\frac{1}{3}$‡	$\sqrt{3}$ × 3.30	2 × 6.80	0.78	+72	§
Sn	1‡	3.38	2 × 8.70	2.68	+47	2.95
	$\frac{1}{3}$	$\sqrt{3}$ × 3.29	2 × 7.18	1.16	−56	§
Pb	1‡	3.30	2 × 8.75	2.73	—	1.7
	$\frac{1}{3}$	$\sqrt{3}$ × 3.32	2 × 7.40	1.38	+55	§
Bi	$\frac{2}{3}$	$\sqrt{3}$ × 3.28	2 × 8.60	2.58	+54	0.78
	$\frac{1}{3}$	$\sqrt{3}$ × 3.29	2 × 7.40	1.38	+130	2.0
TaS_2	—	3.315	2 × 6.02	—	+194	0.8

* Δd = increase in interplanar Ta–Ta distance.
† Corrected for core diamagnetism, molar susceptibility $\times 10^6$.
‡ Indicates $X = X(\max)$.
§ $T_c < 0.5°K$.

fact quite general but limited to the more electropositive elements; that is, the metals. At present let us limit ourselves to the post- transition metals, including groups Ib and IIb.

Van Arkel and Crevecoeur[116] and Koerts[117] described the intercalation compounds of copper and silver in TaS_2 and NbS_2 in 1963. Subsequent work by Voorhoeve-van den Berg[118,119] in this area treated among other things the new compounds Al_xNbSe_2 and Cu_xNbSe_2. A complete study of post-transition elemental intercalates in TaS_2 has now been completed by Di Salvo and coworkers.[120] A similar study including NbS_2, $NbSe_2$, and "alloy" intercalates has been completed by Gentile and Tracey.[121] The compounds of TaS_2 and some of their properties are given in Table 11. Neither the metalloids (B, C, Si, As, Sb) nor the nonmetals react with TaS_2 to form intercalation compounds, an observation in line with the notion that charge transfer drives the reaction.

The maximum concentration of intercalate $X(\max)$ corresponds to a stoichiometric compound. For X less than $X(\max)$ but equal to

1/3, superstructure associated with ordering of the intercalate is sometimes observed. The dilatation of the *c* axis for low concentrations corresponds to that expected for the lowest oxidation state of the intercalate. Note, however, that the dilatation increases with concentration as one might expect if less charge transfer occurred per intercalated atom as the concentration increased. In fact, for $X = 1$ the intercalate has approximately its metallic radius. All the compounds are dark-colored and metallic. The susceptibility corrected for core diamagnetism is paramagnetic and typically temperature independent. The value of susceptibility is typical of *s*-, *p*-band metals except for $Bi_{1/3}TaS_2$, where it is higher, presumably because the *d* band of the TaS_2 has not been as nearly filled. It should be noted that this is the only compound in this group with X less than 1 that superconducts. Attempts to prepare similar compounds with MoS_2 failed. This is probably because the conduction band in MoS_2 is at significantly higher energy than that in TaS_2.

5.2.3. Transition Metals

A number of ternary compounds $M_x'MX_2$ exist, where M′ is a first row transition element, M is from group IVb or Vb, and X is a chalcogen (more likely sulfur or selenium). The structure of these compounds is that of the layered dichalcogenide MX_2 with M′ inserted between the layers. The occurrence of such compounds is indicated in Table 12. Compounds in which M′ = M will be discussed later in the section on metal-rich dichalcogenides.

Of the IVb dichalcogenides, the compounds of TiS_2 and $TiSe_2$ have received the most attention.[122–126] In these compounds M′ is

TABLE 12

Transition Metal Intercalation Compounds of Layered Dichalcogenides

	Ti	V	Cr	Mn	Fe	Co	Ni
TiX_2	—	—	—	—	×	×	×
ZrX_2	—	—	—	—	×	×	×
HfX_2	—	—	—	—	×	×	×
VX_2	—	—	—	—	×	—	—
NbX_2	×	×	×	×	×	×	×
TaX_2	×	×	×	×	×	×	×

apparently limited to Fe, Co, or Ni. The compounds can be prepared by reaction of the powdered elements in evacuated quartz tubes. Research to date has been confined to determination of the extent of intercalation, the phases present, and the crystal structures. In a systematic study of the system Ni_xTiS_2 for $0 \leq x \leq 1$ Danot *et al.*[126] found for X less than 0.20 a solid solution of Ni in the TiS_2 lattice, presumably in the octahedral sites. At $X = 0.25$, 0.40, 0.50, and 0.75 ordered structures were obtained with nickel in the octahedral sites of a slightly distorted TiS_2 lattice. To the extent that they have been examined, the Fe and Co compounds appear similar. Both ZrS_2[127,128] and HfS_2[129] form such compounds.

Insertion of all the first row transition elements in the sulfides and selenides of niobium[130–135] and tantalum[132–135] is apparently possible. In each case the structure is one in which Nb or Ta is in a trigonal prismatic environment in layers of the $2H$-NbS_2 type, and the guest is in octahedral holes between these layers. Ordering of the guest atoms at stoichiometric ratios such as $X = 1/3$ or $2/3$ is typical.

5.2.4. Metal-Rich Compounds

Both group IVb and group Vb dichalcogenides can be prepared metal rich by the insertion of extra metal atoms in the octahedral holes between the layers. The general formula for such compounds is $M_{1+x}X_2$. The excess metal serves to pin the layers together. They become elastic, brittle, and cannot be intercalated by molecules. The value of X can be as great as 1 in TiS_2[136] and $TiSe_2$. In Nb and Ta chalcogenides it is usually less than 1/3.[137] The c axis of the Ti compounds increases. That of the Nb and Ta may increase or decrease, depending on the nature of the octahedral site. In the Nb compounds the superconducting critical temperature drops rapidly with increasing X.[138] Corresponding compounds of Mo and W do not exist, presumably because of the special stability of the d^2 configuration in the trigonal prismatic configuration in covalent compounds.[95]

5.3. Molecular Intercalates

Group IVb and Vb disulfides and diselenides react with a large number of organic and inorganic molecules yielding intercalation compounds of a qualitatively different kind than those we have thus far considered.[139–149] In these the dichalcogenide layers are

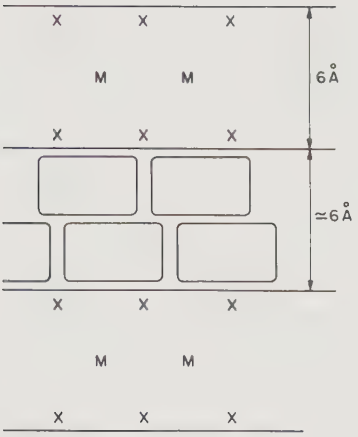

Fig. 18. Schematic representation of the probable structure of $TaS_2(pyridine)_{1/2}$.

separated by molecular monolayers or bilayers. Whereas the anisotropy of the dichalcogenides is decreased by the intercalation of metals, it is enhanced manyfold by intercalation of molecules, and in these compounds one is able to examine the properties of electrons constrained to motion almost entirely within a single layer about 6 Å thick.

The molecular intercalates are electron donors in the Lewis-base sense. Examples are ammonia, phosphine, and pyridine, each of which possesses a lone pair of electrons that can be shared in the formation of a dative covalent bond. The intercalation complexes are stoichiometric and usually highly crystalline. The typical example $TaS_2(pyridine)_{1/2}$ is prepared by immersing $2H$-TaS_2 crystalline powder in hot pyridine for a few minutes.[142,143] At 200°C the reaction is complete in 1 or 2 min at most, and can be followed by the observation of the remarkable swelling that results. The volume of the powder doubles. Large crystals of $2H$-TaS_2 prepared by iodine vapor transport can also be intercalated, but the reaction takes longer. The *a* axis increases a few tenths of a percent, while the interlayer spacing of the sulfide increases from 6.02 to either 11.85 or 12.02 Å.[143] Apparently two phases with somewhat different molecular arrangements are possible. As will be seen below, it appears likely that although other structures are possible, the preferred structure is

one containing a bilayer of pyridine with the plane of the molecules parallel to the disulfide layers (see Figure 18). The molecular packing must be quite snug since the molar volume of the compound is 8% less than that of the reactants. In considering this point, it should be noted that pyridine is liquid at room temperature. The c axis of $TaS_2(pyridine)_{1/2}$ is twice the interplanar spacing, as is the case for the $2H$-TaS_2 from which it is formed. The compound is black to blue-black, not strikingly different from $2H$-TaS_2. It is stable at room temperature in air. On slow heating, the pyridine is released between 100 and 200°C to give back $2H$-TaS_2 almost indistinguishable from the starting material. If TaS_2 is treated with only $\frac{1}{4}$ equiv. of pyridine, a second-stage compound, $TaS_2(pyridine)_{1/4}$, results apparently containing molecular bilayers in every second interlayer space (see Figure 19). NbS_2, TiS_2, and TaS_2 form similar pyridine compounds.[144] Somewhat less stable compounds can also be formed using the corresponding selenides. However, Mo and W dichalcogenides appear totally inert in this respect.

The $2H$-TaS_2 itself is metallic with a resistivity parallel to the layers $\rho_{\parallel}$ of approximately 10^{-4} Ω-cm and a resistivity perpendicular

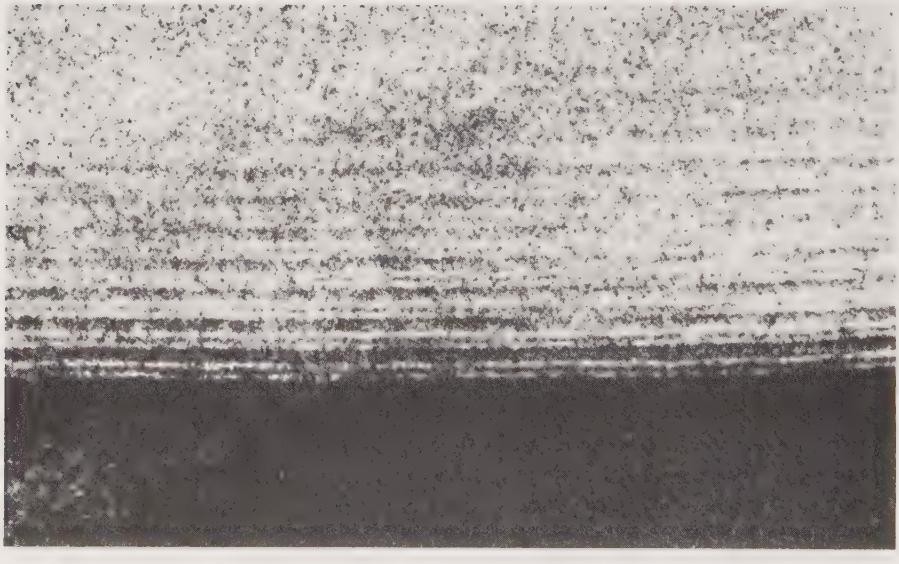

Fig. 19 Transmission electron micrograph of $TaS_2(pyridine)_{1/4}$, a second-stage compound. (Kindly provided by H. Fernandez-Moran, and reproduced with permission from Fernandez-Moran *et al.*[216])

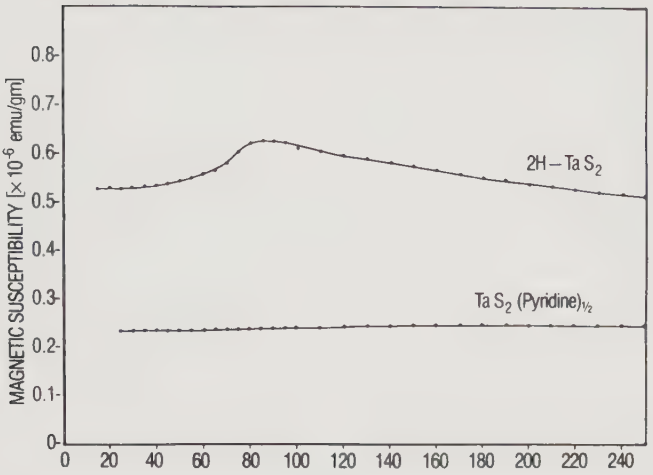

Fig. 20. The uncorrected magnetic susceptibility of $2H$-TaS_2 and $TaS_2(pyridine)_{1/2}$ versus temperature (reproduced with permission from Thompson *et al.*[150]).

to the layers $\rho_\perp$ about ten times greater.[150] It has a superconducting critical temperature of 0.8°K. On intercalation $\rho_\parallel$ increases by a factor of about two, which indicates that the conductivity per layer is nearly unchanged. The resistivity perpendicular to the layers, of course, increases dramatically. The ratio $\rho_\perp/\rho_\parallel$ is sample dependent, but a typical value at room temperature would be 10^5. For most samples $\rho_\perp(T)$ is proportional to $\rho_\parallel(T)$,[150] as one might expect if the layers were in some way shorted together. Typical results are shown in Figure 20. A typical crystal growth mechanism for the layered chalcogenides that might account for this is the screw dislocation. Crystals grown in this manner will be comprised of one or, more likely, several sheets in a helix. In such a crystal the *c*-axis conductivity would be proportional to the *a*-axis conductivity, as observed.[150]

In $2H$-TaS_2, as in $2H$-$TaSe_2$ and $2H$-$NbSe_2$, there exists some manner of phase transition at low temperatures. In $2H$-TaS_2 this is manifested by a cusp in the magnetic susceptibility, a discontinuity of the slope of ρ vs. T, and a reversal of the sign of the Hall effect[150] (see Figures 20–22). This behavior is interpreted in various ways.[150,151] The signs of the Hall constant and the Seebeck coefficient are opposite at room temperature, the Seebeck coefficient being negative. How this arises is still a question under discussion. At the lowest temperatures, below the transition region, a single-

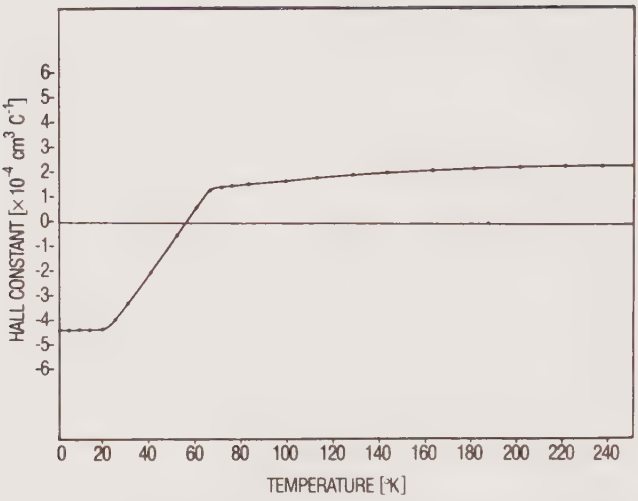

Fig. 21. The Hall constant versus temperature for $2H$-TaS_2 (reproduced with permission from Thompson *et al.*[150]).

band model appears to account for the data. NMR[152] and X-ray diffraction[153] studies show that the analogous transition in $2H$-$NbSe_2$ is associated with a slight distortion of the crystal that produces two nonequivalent Nb sites. Presumably something similar is happening in $2H$-TaS_2. The rising magnetic susceptibility with decreasing temperature probably reflects a rising density of states at the Fermi level which in turn may be promoting a distortion that causes the density of states to fall. Clear resolution of this puzzle awaits further developments. Whatever causes this transition appears to be ineffective or absent after intercalation. No singular behavior is observed on cooling $TaS_2(\text{pyridine})_{1/2}$. At room temperature the Hall constant is $4 \times 10^{-3}\ \text{cm}^3\ \text{C}^{-1}$, substantially greater than that of $2H$-TaS_2, and though it decreases on cooling, it remains positive. The Seebeck coefficient is negative and of the same magnitude as before intercalation. Intercalation, the separation of the layers and the interaction between the molecules and the layer, has produced a qualitatively different material.

The superconducting critical temperature of $TaS_2(\text{pyridine})_{1/2}$ is approximately 3.5°K.[142,143] As would be expected from the structure, its superconducting properties are extremely anisotropic. The critical current parallel to the planes is about $10^4\ \text{A/cm}^2$, and that perpendicular to the planes is about $1\ \text{A/cm}^2$ and is presumably

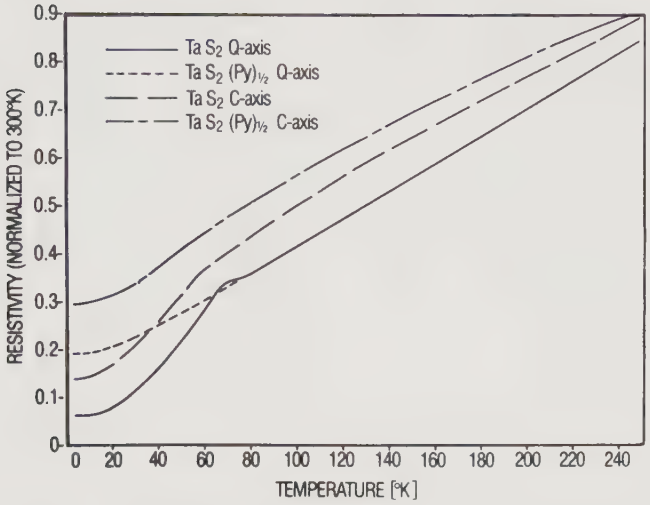

Fig. 22. The electrical resistivity versus temperature for $2H$-TaS_2 and $TaS_2(\text{pyridine})_{1/2}$ (reproduced with permission from Thomson *et al.*[150]).

greater than that of ideal material because of the shorts mentioned earlier.[154] The critical field with flux parallel to the layers $H_{c2}(\|)$, is substantially greater than that found when the flux is perpendicular to the layers $H_{c2}(\perp)$.[155] Both critical fields increase linearly with decreasing temperature (see Figure 23). $H_{c2}(\|) \div H_{c2}(\perp) \approx 30$. The derivative $dH_{c2}(\|)/dT \approx -75\,\text{kG/deg}$. The parallel upper critical field of $TaS_2(\text{pyridine})_{1/2}$ at 0°K, $H_{c2}(\|, 0°\text{K})$, should be around 250 kg, remarkably high for a material with a critical temperature of 3.5°K.

In a superconductor of this structure one is naturally concerned with the coupling between the superconducting layers and the shape of the transition in the context of the general question of the dimensionality of the superconductivity. These are questions that are presently under active study and will probably only be resolved as techniques to prepare reproducibly more nearly ideal crystals are developed. Adjacent superconducting planes will almost surely be coupled by Josephson tunneling, but this has not yet been demonstrated experimentally. The shape of the superconducting transition as revealed by low-temperature heat capacity measurements on $TaS_2(\text{pyridine})_{1/2}$ and similar compounds is broad.[156] This may well be an intrinsic property, but that has not been firmly established. The existence of superconducting fluctuations above T_c has been

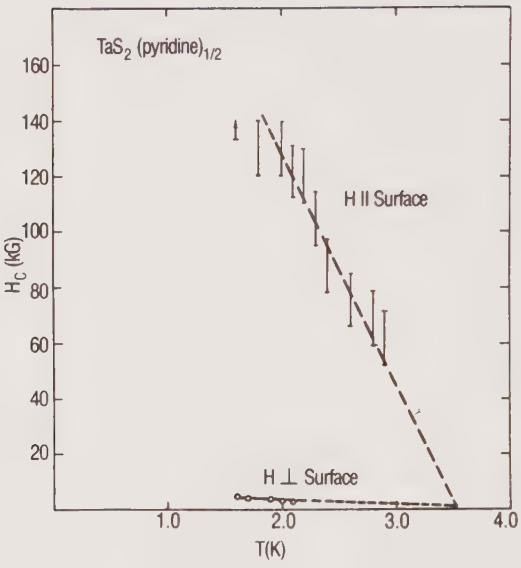

Fig. 23. The upper critical magnetic field of $TaS_2(pyridine)_{1/2}$ as a function of temperature with direction as a parameter (reproduced with permission from Foner *et al.*[155]).

established by measurements in several laboratories,[157–159] but these measurements conflict both in the magnitude of the fluctuations and in the temperature range over which they are observed.

The superconducting critical temperature of molecular intercalation compounds of TaS_2 depends on the molecule intercalated and on the number of molecules per TaS_2, but not on the spacing between the TaS_2 planes. By replacing one or more of the protons on pyridine with various substituents, its properties can be altered and its size increased. Changes in the molecular properties are reflected in the molecule's ability to intercalate and in the superconducting critical temperature of the intercalation compound.[143] Increasing the size of the molecule can prevent intercalation, but more frequently steric factors are reflected in the number of molecules that can be inserted between the layers. Typically, the formula of the resulting compounds can be written $TaS_2(molecule)_{1/n}$, where n is an integer equal to or greater than two. The interlayer Ta–Ta spacings of the compounds fall into clusters about 9.4- and 11.9-Å spacings that are consistent with one and two molecular layers, respectively. For the smaller spacing, the interlayer spacing has increased 3.4 Å, a distance approxi-

mately equal to the thickness of an aromatic carbon system. The 5.9-Å expansion is presumably obtained by nesting of the first and second molecular layers with respect to each other. Although the pyridine reaction proceeds with a net decrease in overall volume, this is by no means the rule. Comparable *increases* in volume are observed for many of the reactions. This and the stoichiometric nature of the compounds suggest that the positioning of molecules is in large measure governed by their interaction with the layer. An increase in net overall volume then results when one molecule renders

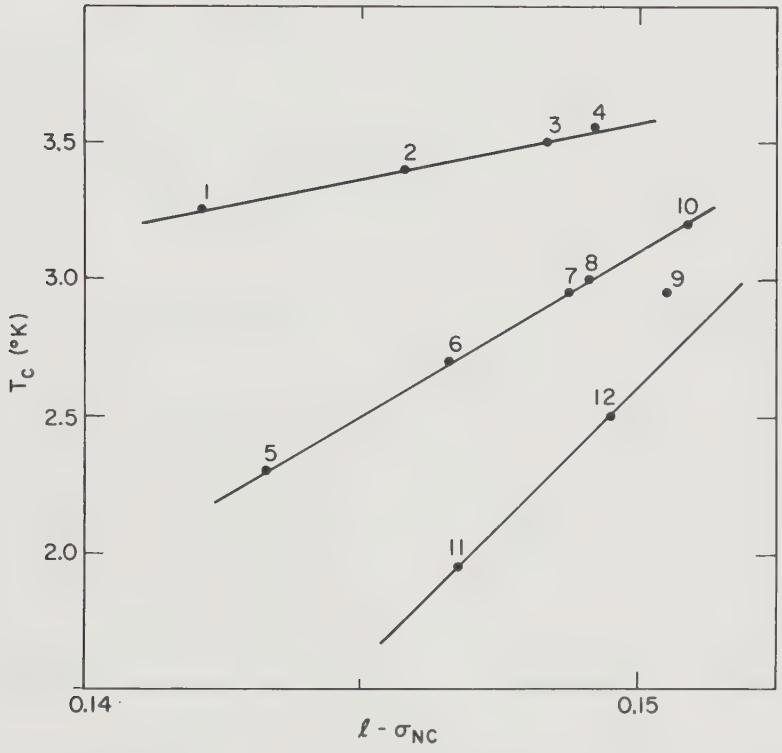

Fig. 24. The critical temperature of intercalation compounds of TaS_2 with substituted pyridines versus $l - \sigma_{NC}$, where l is the lone-pair electron density and σ_{NC} is the density of electrons in the N–C σ bond. The three sets of data correspond to different values of n in the formula TaS_2 (molecule)$_{1/n}$, namely, 2, 3, and 4 (top to bottom). The substituents are: (1) 2-amino, (2) 4-amino, (3) 2,6-diamino, (4) none, (5) 4-dimethyl amino, (6) 4-methyl, (7) 2-methyl, (8) 2-ethyl, (9) 3-methyl, (10) 3-ethyl, (11) 2,4,6-trimethyl, and (12) 4,4-dipyridyl (from Ref. 160).

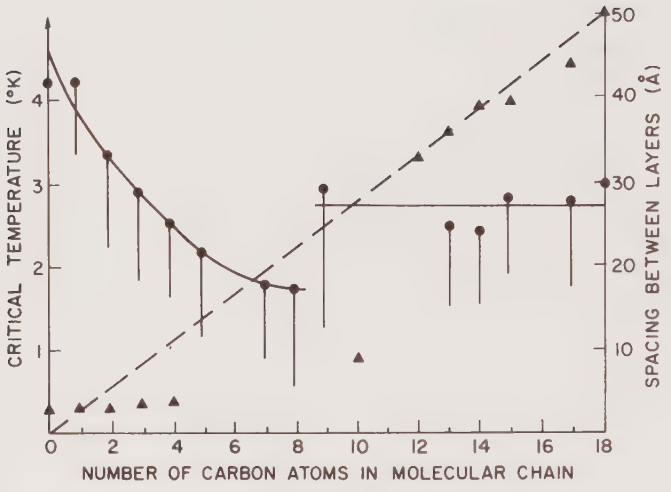

Fig. 25. The superconducting critical temperature (circles) and the dilation (triangles) in interlayer spacing of TaS_2 intercalation compounds with normal aliphatic primary means up to octadecylamine (reproduced with permission from Gamble *et al.*[144]).

an adjacent bonding site unavailable without at the same time totally occupying the space about that site.

The substitution of electronegative elements or groups for the pyridine hydrogens invariably renders the molecule incapable of intercalating. Electron-donating groups, on the other hand, do not have this effect and presumably enhance the stability of the resulting compounds. That this should be so is not surprising. Exactly why it is so is not clear. Electronegative substituents decrease the basicity of the molecule and quite naturally the stability of complexes involving donation of the lone-pair electrons. On the other hand, the lone-pair electrons would presumably interact with the layer much more effectively if the plane of the molecule were perpendicular rather than parallel to the layers. Additional light was shed on this subject by the correlation recently pointed out between the superconducting critical temperature of the TaS_2 intercalation compounds of substituted pyridines and certain ^{14}N nuclear quadrupole data collected on the pure intercalates.[160] For each stoichiometry, i.e., for each value of n in the formula $TaS_2(\text{molecule})_{1/n}$, there is a linear relationship between T_c and a molecular parameter $l - \sigma_{NC}$ (see Figure 24), where l is the charge density in the nitrogen lone-pair orbital and

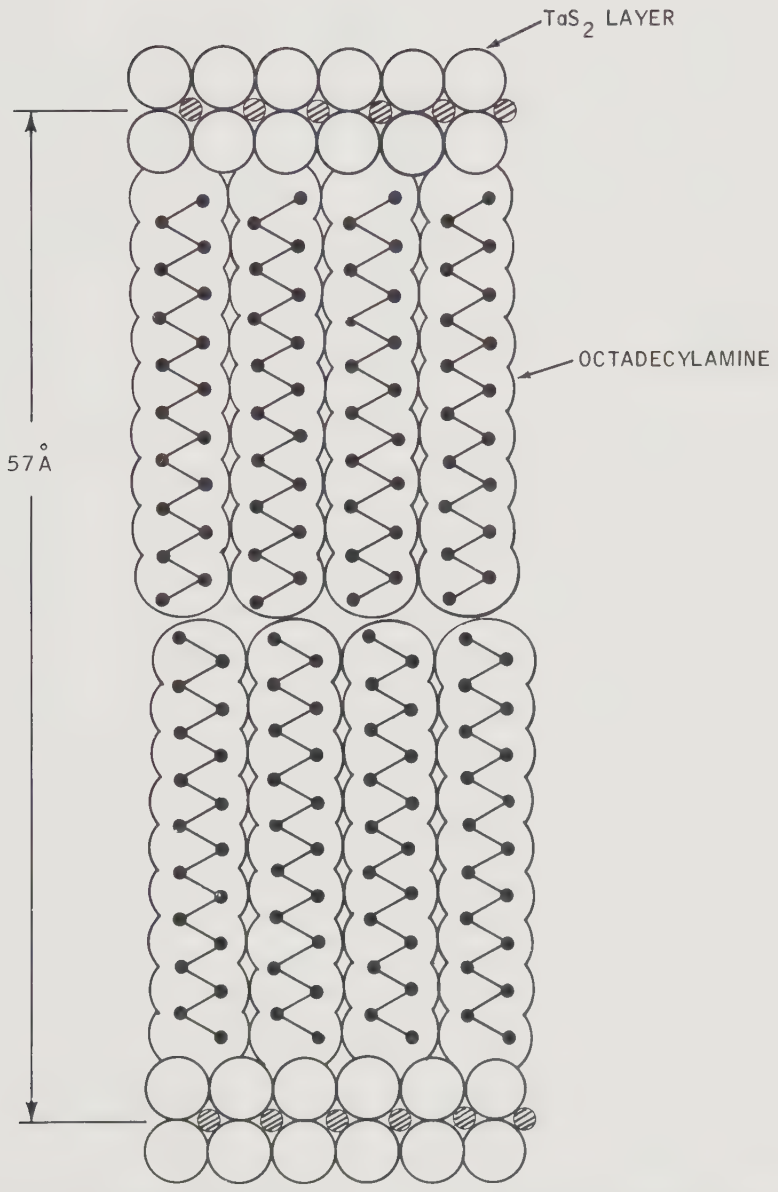

Fig. 26. Schematic representation of the structure of TaS_2–octadecylamine (reproduced with permission from Gamble *et al.*[144]).

σ_{NC} is the sigma charge density in a nitrogen–carbon band. The value of l itself is not available from the NQR data. No correlation was observed with $|\pi - \sigma_{NC}|$, where π is the π-electron charge density on

the nitrogen. As pointed out by Bray and Sauer,[160] the observed correlation of T_c with $l - \sigma_{NC}$ and not with $|\pi - \sigma_{NC}|$ strongly suggests that charge transfer to the layers involves the nitrogen lone-pair orbitals, possibly through overlap with certain sulfur orbitals.

The dependence of T_c on stoichiometry and chemistry is fairly well demonstrated by the pyridine intercalation compounds. Its independence of interlayer spacing is shown in a series of TaS_2 compounds containing normal primary alkylamines.[144] These react with TaS_2 between room temperature and 50°C, the higher temperatures being required for the longer molecules. In Figure 25 the critical temperature and interlayer spacing are both shown as functions of n, the number of carbon atoms in the chain. In this scheme $n = 0$ would correspond to ammonia, $n = 1$ to methylamine, and $n = 18$ to octadecylamine. For small n the increase in the interlayer spacing corresponds to the thickness of the hydrocarbon chain, signifying a parallel configuration of the molecules. At larger values of n a different molecular configuration obtains. The interlayer spacing now corresponds to that which would be produced by a molecular bilayer containing molecules whose chains are now perpendicular to the layers (see Figure 26). In this configuration the stoichiometry is independent of chain length, whereas in the regime of shorter molecules the number of molecules per TaS_2 must decrease with increasing chain length. All of this is reflected in the critical temperatures. As the chain length increases, T_c drops monotonically until the second regime with perpendicular molecules, where it jumps to a higher value and remains.

In this discussion we have limited our scope to a few relatively well studied systems. The scope of this field is much larger than this approach suggests and new compounds are being reported at a high rate.

6. Layered Halide and Similar Intercalation Compounds

The cadmium iodide and cadmium chloride layer structures are commonly found among metal dihalides. They are especially favored in iodides and never seen in fluorides. These compounds have been reviewed by Tubbs.[161] Table 13 summarizes the occurrence of layer structures among metallic dihalides.

In all these compounds the metal ions reside in octahedral holes within the layer. The bonding within layers is strong and primarily ionic; that between layers is weak, primarily van der Waals. Conse-

TABLE 13
Dihalides with Layer Structures

Group II	Transition	Rare earth	Group IV
$Mg(Cl_2, Br, I_2)$	$Ti(Cl_2, Br_2, I_2)$	TmI_2	GeI_2
CaI_2	$V(Cl_2, Br_2, I_2)$	YbI_2	PbI_2
$Cd(Cl_2, Br_2, I_2)$	$Mn(Cl_2, Br_2, I_2)$		
$Zn(Cl_2, Br_2, I_2)$	$Ge(Cl_2, Br_2, I_2)$		
	$Co(Cl_2, Br_2, I_2)$		
	$Ni(Cl_2, Br_2, I_2)$		

quently, the crystals exhibit marked basal cleavage. One might expect in this situation to find intercalation reactions whereby guests can be inserted between layers. In fact, it is possible to prepare layered halides containing alkylammonium ions between the layers. These, however, are not formed by simple intercalation reactions. Instead, the dihalide is dissolved in solution with the alkylammonium species and the layered halides containing these ions crystallize from solutions. In the resulting compounds the metal ions are still in layered arrays surrounded by halide octahedra. The octahedra are no longer face-sharing but corner-sharing, and the structure contains four rather than two halogens per metal atom. The reaction whereby these compounds are formed can be written

$$MX_2 + 2RNH_3^+X^- \rightarrow (RNH_3^+)_2MX_4^{2-}$$

where R may be $(CH_3CH_2)_n^-$, $C_6H_5CH_2^-$, or presumably many other similar moieties. Such reactions are known where M = Cu, Mn, or Fe and these have been used to prepare compounds containing nearly perfectly isolated magnetic layers. The structure of the compound $(CH_3CH_2NH_3)_2CuCl_4$ is typical and is shown in Figure 27. The Cu is located in an octahedron of Cl^- ions four of which are in the Cu^{2+} plane and are shared with, and reside between, nearest Cu^{2+} neighbors. The other two are almost directly above and below. The positive ammonium group resides near the out-of-plane Cl^- ions to give electrical neutrality while the alkyl chain extends perpendicular to the layers. A bilayer of these chains separates the layers. Increasing the length of the chain serves to increase the interlayer spacing and to increase the distance between Cu^{2+} ions in neighboring layers from 9.97 (methyl) to 25.8 Å (decyl).

De Jongh and co-workers[162] have studied $(CH_3CH_2NH_3)_2$-$CuCl_4$ in detail. They find that it behaves very much like a planar

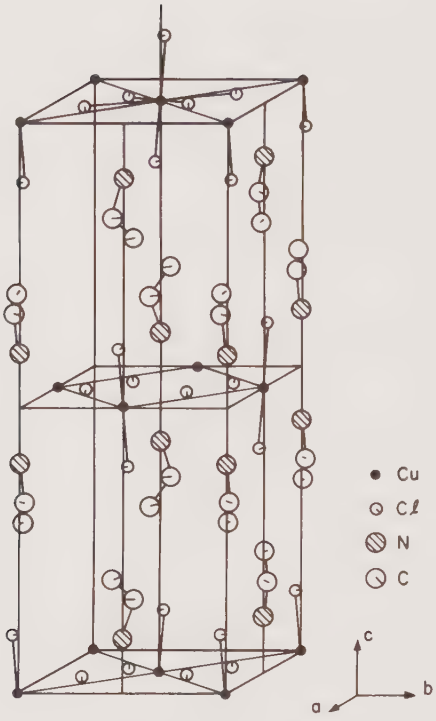

Fig. 27. Crystal structure of $(CH_3CH_2 \cdot NH_3)_2CuCl_4$. For the sake of clarity only part of the ethylammonium groups are shown. The Cl environment is shown completely for the Cu atom in the center of the upper face (after De Jongh *et al.*[162]).

Heisenberg ferromagnet with very weak antiferromagnet coupling between Cu^{2+} layers. Whereas the effective interlayer antiferromagnetic coupling field H_{af} was found to be ~ 800 Oe, the ferromagnetic intralayer exchange field H_f is 5.1×10^5 Oe. Above T_c the system behaves as a two-dimensional ferromagnet. The properties of this region are not affected by interlayer interactions. Near T_c the latter become increasingly important until below T_c, where they completely dominate the magnetic response of the system and the susceptibility is essentially that of a three-dimensional antiferromagnet. De Jongh *et al.* denote the transition temperature by T_c rather than T_N because it is the intralayer ferromagnetic interactions that dominate the transition. T_c is 10.20°K. For example, in the ethyl com-

pound the anisotropy field within the plane, only ~ 75 Oe, is much less than the interlayer exchange field of $\sim 5 \times 10^5$ Oe. Therefore, the three-dimensional ordering takes place via coupling between essentially isotropically fluctuating, almost ferromagnetic layers.

In the methyl analog of the ethyl compound also studied by De Jongh *et al.*[162] the interlayer coupling is ferromagnetic. The manner in which the sign of the interlayer interaction is determined is unknown. In the decyl analog,[162] where $T_c = 7.9°K$, the interlayer coupling is so weak that it is all but impossible to decide experimentally whether the coupling is ferromagnetic or antiferromagnetic. The divergent susceptibility in the transition region for the methyl and decyl compounds contrasts with the antiferromagnetic transition of the ethyl compound, as can be seen in Figure 28.

FeOCl is an orthorhombic structure which consists of layers of FeOCl sheets. Each sheet has planes of Cl^- exposed, and the interlayer Cl^-–Cl^- distance is 3.68 Å, which closely approximates twice the van der Waals radius of chlorine. FeOCl is antiferromagnetic with an ordering temperature of 90°K[163] with sublattice magnetizations coming from high-spin Fe^{3+} ions aligned parallel to the *b* and *c* axes. By reacting it with an excess of pyridine at 80°C, Kanamaru *et al.*[164] have been able to intercalate single-crystal FeOCl. A limiting composition corresponding to $FeOCl(pyridine)_{1/3}$ is reached. The orthorhombic unit cell dimensions change only along the *b* axis, which increases from 7.917 to 13.45 Å after intercalation, indicating that the pyridine molecules cause an expansion of 5.53 Å.

Kamamaru *et al.* have made Mössbauer and resistivity measurements. The intercalated complex orders at 65° with the Fe^{3+} spins probably aligned along the *a* axis. The internal magnetic field at the Fe nucleus arising from the core polarization hyperfine interaction with the Fe^{3+} spin is a sharp function of temperature. The rather square shape of the curve indicates again, as in the case of the alkylammonium-metal chlorides, that the three-dimensional ordering is driven by strong intralayer exchange.

The authors also report a factor of 10^7 increase in the electrical conductivity of FeOCl upon intercalation. This striking increase is undoubtedly due to the charge transfer effect associated with the intercalation process. Systematic studies with other intercalates would be useful in trying to obtain a more quantitative understanding of the charge transfer effect and the role played by such

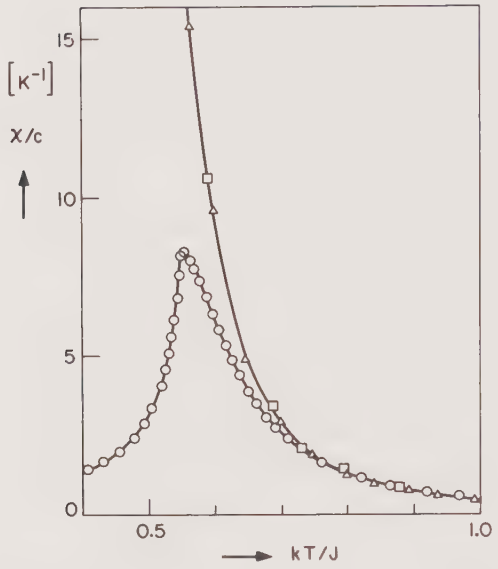

Fig. 28. Comparison of the in-plane susceptibilities of three Cu compounds. (○) $(C_2H_5NH_3)_2 \cdot CuCl_4$; (△) $(Ch_3NH_3)_2CuCl_4$; (□) $(C_{10}H_{21} \cdot NH_3)_2CuCl_4$. In the temperature region shown the curve common to the methyl and decyl compound represents the (divergin) susceptibility of a system of isolated ferromagnetic layers, with an intralayer exchange energy J. Eventually, a very weak in-plane anisotropy would cause two-dimensional Ising ordering to take place. The curve of $(C_2H_5NH_3)_2CuCl_4$ illustrates what happens to the ferromagnetic ordering where a weak ($\sim 10^{-3}$) of the intraplane coupling) antiferromagnetic coupling between adjacent planes is included (after De Jongh *et al.*[162]).

intercalate parameters as Lewis basicity, ionization potential, and geometry.

7. Tungsten Bronzes and Similar Compounds

Bronzes have been reviewed by Wadsley,[165] Dickens and Whittingham,[166] and Whittingham and Huggins.[167] Work in this area is continuing, but a further review of the subject is unnecessary at present. We include a discussion of these materials in the present

context in order to highlight aspects of the bronzes shared by some of the other materials we have taken up here.

In their review article on tungsten bronzes and related compounds Dickens and Whittingham[166] define a "bronze" as a ternary metal oxide of the general formula $A_xM_yO_z$, where M_yO_z is the highest oxide of the transition metal M, and A is either hydrogen, ammonium, or a metallic element currently selected from those outlined in Figure 29. In 1824 Wöhler[168] discovered the first of the tungsten bronzes: Na_xWO_3, golden crystals with metallic appearance. Much more recently bronzes of Ti,[169,170] V,[171] Nb,[172] and Mo[173] have been reported.

These materials are chemically rather inert, highly colored, and, as single crystals, possess metallic luster. The compounds are best considered as transition metal oxide hosts that can accommodate a guest in tunnels or in between layers of the host. The host provides not only the space, but also the low-lying electronic levels necessary to receive charge donated by the guest. As the concentration of the guest changes, substantial variation in color and electrical conductivity are observed. For high concentrations the materials are metallic and at low temperatures, in some cases, superconducting. As x is varied from zero to one one typically finds wide homogeneity ranges, but not always. For example, only $K_{0.28}MoO_3$ and $K_{0.33}MoO_3$ are known. The relation between composition and crystal structure for

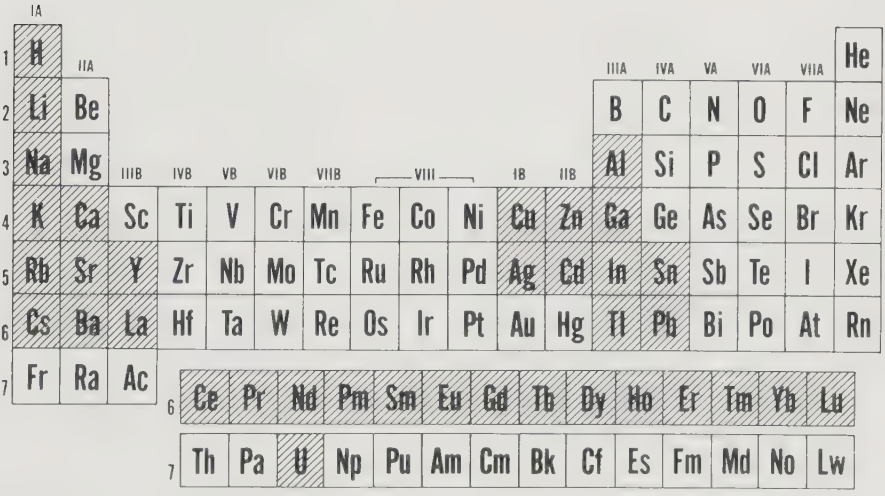
IA
IIA
IIIB
IVB
VB
VIB
VIIB
VIII
IB
IIB
IIIA
IVA
VA
VIA
VIIA
1 H He
2 Li Be B C N O F Ne
3 Na Mg Al Si P S Cl Ar
4 K Ca Sc Ti V Cr Mn Fe Co Ni Cu Zn Ga Ge As Se Br Kr
5 Rb Sr Y Zr Nb Mo Tc Ru Rh Pd Ag Cd In Sn Sb Te I Xe
6 Cs Ba La Hf Ta W Re Os Ir Pt Au Hg Tl Pb Bi Po At Rn
7 Fr Ra Ac
6 Ce Pr Nd Pm Sm Eu Gd Tb Dy Ho Er Tm Yb Lu
7 Th Pa U Np Pu Am Cm Bk Cf Es Fm Md No Lw

Fig. 29. Elements that form tungsten bronzes.

the alkali metal tungsten bronzes of formula A_xWO_3 is given in Figure 30.

Three general features emerge from the crystal structures, which were first determined by Haag and Magneli[174]: (1) As x increases so does the symmetry of the structure; (2) the structure adopted is controlled to a considerable degree by the ionic radius of the guest; (3) all of the structures are based upon corner-sharing of WO_6 octahedra. In the tungsten bronzes tunnels are formed by staking sheets of WO_6 octahedra that contain holes. These openings, depending on their size, are bordered by either four, five or six WO_6 octahedra. The guest then resides in cavities connected by these openings. The radii of these cavities are 0.96, 1.29, and 1.63 Å for four-, five-, and six-sided tunnels, respectively. In WO_3, itself a distorted cubic structure, one finds four-sided tunnels. It is possible to diffuse hydrogen atoms (generated either electrolytically or catalytically) into this structure. However, this is the only example of its kind. Tungsten trioxide structures containing five- and six-sided tunnels are not known in the absence of at least some guest, and although the cavities provided by four-sided tunnels are large enough to accommodate Li and Na, these materials cannot be inserted directly into WO_3 because of the restrictions between adjoining cavities. Formation of tungsten bronzes is therefore accomplished by the generation of the host

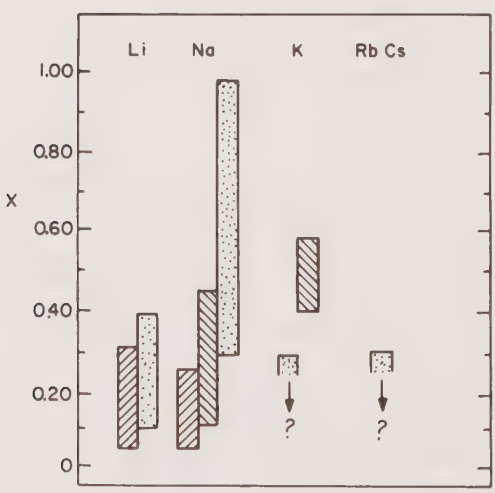

Fig. 30. Occurrence of alkali metal tungsten bronze phases as a function of stoichiometry.

around the guest. As might be expected, the smaller cations stabilize the small cavities and vice versa. Thus, Li ($r = 0.60$ Å) and Na ($r = 0.95$ Å) stabilize the cubic structures with four-sided tunnels, and Rb ($r + 1.48$ Å) and Cs ($r = 1.69$ Å) stabilize the hexagonal phase, which contains six-sided tunnels. After the host has been formed about the guest it is possible to adjust the stoichiometry in certain instances, but as a rule ionic motion is severely limited by intercavity restrictions. This immobility is probably in large measure responsible for the stability of these materials in the presence of oxygen and water. Other bronzes have not been studied as extensively as those of tungsten. To date it appears they may be substantially more complex. Potassium molybdenum bronzes $K_{0.28}MoO_3$ and $K_{0.33}MoO_3$ are constructed of sheets of MoO_6 octahedra with potassium in between. A sodium molybdenum bronze exists, $Na_{0.9}MoO_3$, which has a distorted perovskite structure with four-sided tunnels.

For decades chemists have used the rapid formation of blue hydrogen tungsten bronze from yellow WO_3 and hydrogen atoms as a means of detecting hydrogen atoms. An early extensive study was reported by Melville and Robb[175] in 1949. It was not understood, however, that the blue product was H_xWO_3, not W_4O_{11}, which is also blue.[176] In the presence of platinum at 50°C WO_3 turns blue instantaneously if a hydrogen atom transport agent is present.[177]

In the bronzes there are typically a number of sites of identical energy that can accommodate the guest. This turns out to be among the more important requisites for ionic transport. To the extent that these sites are interconnected, ions may hop from one site to the next. One would, at first, naturally assume that given the spatial restrictions between sites, smaller ions would diffuse more rapidly. This turns out to be incorrect. There is an optimum ionic radius for each structure. As pointed out by Whittingham and Huggins,[167] it appears to be that which just fills the channel. The transport of hydrogen is an interesting case. Dickens[178] has shown by neutron diffraction that the proton does not reside at the center of the cage, but is statistically placed near the oxygen atoms forming the cage, so that H_xWO_3 might better be called $WO_{3-x}(OH)_x$. An NMR study[179] of single-crystal hydrogen bronze show significant motion only above 250°K. The low value of the diffusion constant extracted from these studies is consistent with this model. A similar structure is likely for Li_xWO_3, and at room temperature NMR[180] reveals insubstantial diffusion, although Whittingham and Huggins have shown that Li_xWO_3 can be used as a nonpolarizing electrode on β-alumina.[181] Both

hydrogen and lithium are small enough to move along the tunnels but are prevented from doing so by their attachment to particular oxygens in the cavity walls.

In cubic Na_xWO_3 the sodium is located very near the center of the cavity but cannot move because the restrictions between adjacent cavities prevent it from doing so. Cubic sodium bronzes cannot be used as nonpolarizing electrodes.[182] NMR measurements show no motional narrowing.[183]

High ionic conductivity in the bronzes is restricted to the hexagonal bronzes with six-sided tunnels. Here the mobility of the ion is reflected in a somewhat higher chemical reactivity of the material. A rather thorough study of molecular transport in hexagonal ammonium tungsten bronze has been reported by Clark *et al.*[184] They observed that motional narrowing of the proton resonance in their most concentrated samples $(NH_4)_xWO_3$, $x = 0.33$, began at the same temperature but was not complete until room temperature.

A bonding scheme for the tungsten bronzes which seems to be durable in the light of more experiments was first suggested by Sienko[185] and extended by Goodenough.[186] It is possible with this model to understand the electrical properties as arising from nonbonding t_{2g} orbitals extending from the central cation in the MO_6 octahedron. In the case of tungsten the t_{2g} overlap with the oxygen is sufficient to develop a wide band which is filled to the extent of one electron per alkali metal atom. (Pure WO_3 is distorted from the cubic structure due to W–W pairing, and this distortion persists up to $x \sim 0.3$.) The significant decrease in the radial extension of the t_{2g} orbitals in going from $5d$ to $3d$ is postulated by Perlstein and Sienko[187] to reduce the overlap $(t_{2g}–p_\pi)$, and thus the bandwidth, of $M_xV_2O_5$ sufficiently so that the electrical transport takes place by a hopping process from one localized V site to the next. Fogle and Perlstein[188] have recently shown that the width of the band derived from the $4d$ states of $K_{0.30}MoO_3$ is intermediate and that there is a metal–insulator transition at 180°K.

The metallic conductivity of the tungsten bronzes together with NMR investigations of Knight shifts and relaxation rate by Fromhold and Narath[183] support the model in which the M atoms donate their electrons to the empty conduction band of the host WO_3 lattice. Hall effect measurements on cubic Na_xWO_3 show that the Hall constant is essentially inversely proportional to x.

Sweedler *et al.*[189] discovered superconductivity in noncubic tungsten bronzes and in a systematic study found somewhat sur-

prisingly that it does not occur in the cubic structures that have the higher carrier concentrations. Further, Remeika *et al.*[190] found that the T_c of Rb_xWO_3 ($x \sim 1/3$) could be raised from 2 to 5 or 6°K by acid etching, which roughly reduced x by a factor of two. King *et al.*[191] have recently found by heat capacity measurements that the increased T_c is a bulk effect, and therefore the Rb ions must have been leached uniformly from the hexagonal channels (see Figure 11). They further found an excess heat capacity which fits an Einstein mode from 4 to above 20°K with an oscillator energy corresponding to 57°K. Presumably the mode is associated with the vibration of Rb ions in the hexagonal channels; the magnitude was found to agree with three degrees of freedom for each Rb ion in both the etched and unetched samples. The correlation of such low-lying modes, which of course can only occur in the more open, noncubic bronzes, with the occurrence of superconductivity is tempting. However, the etching was found to stiffen the Einstein oscillator energy to 67° (as well as raising T_c to >4°K), whereas the present state of the theory of superconductivity would lead one to expect that it would be a softening of the mode which should raise T_c. The relationship between T_c and the

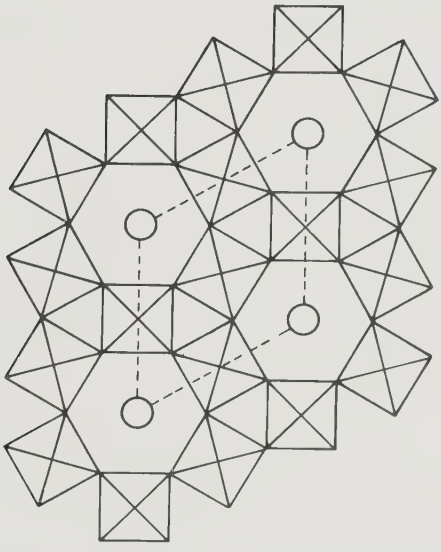

Fig. 31. Projection of hexagonal tungsten bronze showing the oepn channels (reproduced with permission from Ref. 166).

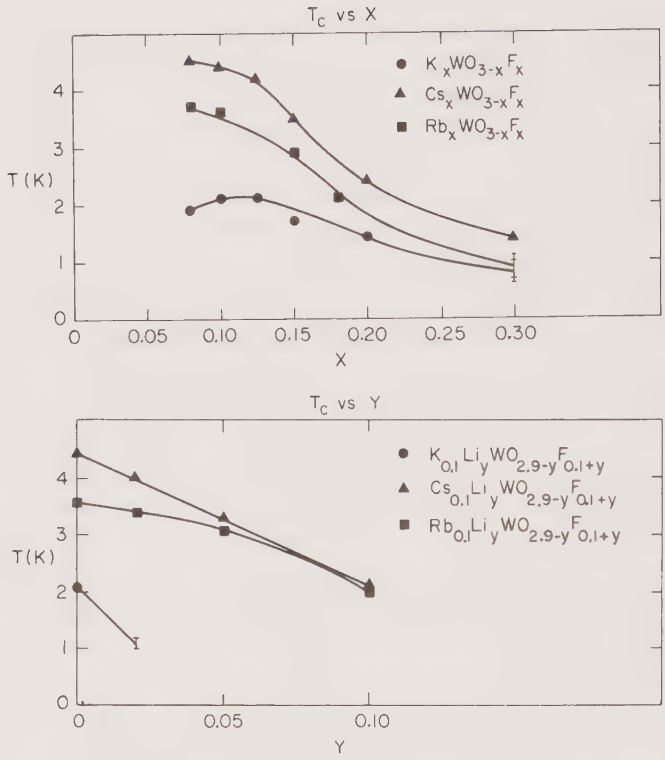

Fig. 32. The superconducting critical temperature versus composition for several tungsten bronzes (reproduced with permission from Ref. 196).

electron–phonon coupling constant is given by McMillan to be

$$T_c = \frac{\theta_D}{1.45} \exp \frac{-1.04(1 + \lambda)}{\lambda - \mu^*(1 + 0.62\lambda)}$$

where λ is inversely proportional to an average of the square of the phonon frequency, θ_D is the Debye temperature, and μ^* is a measure of the repulsive Coulomb interaction between the electrons and is relatively small.

It is likely that anisotropy plays an important role in causing the superconductivity, although it remains for the future to clarify. The 300° resistivity of samples of Rb_xWO_3, $x \approx 1/3$, is $\rho_c = 63\ \mu\Omega$-cm.[192] Both directions have resistivity ratios $\rho_{300}/\rho_{4.2}$ of the order of 60, which is surprisingly high compared to the 4.5 reported by Ellerbeck *et al.*[193] for cubic Na_xWO_3, $x \approx 0.87$. When normalized for carrier

concentration the temperature-dependent part of the resistivity is, however, similar in the *c* direction of the Rb bronze and the cubic $NaWO_3$.

Hubble *et al.*[194] have studied a series of tungsten fluoroxide bronzes. These compounds make it possible to study the effect of varying x in hexagonal $K_xWO_{3-x}F_x$ between 0.09 and 0.30.[195] Banks and Goldstein[196] have found that Li can be introduced independently into bronzes formed from heavier alkali metals and can occupy sites at the centers of the triangles formed by three corner-sharing WO_3 octahedra. Each alkali metal atom, including Li, then contributes one electron to the otherwise empty conduction band of WO_3. Figure 32 shows, in agreement with the results on etched Rb_xWO_3 samples, that T_c increases inversely with carrier concentration over the range below $x = 0.3$. The maximum in T_c for $x \leq 0.15$ may be due to the combined effects of carrier density and screening of the electron–phonon interaction.

Epilogue

We have tried to discuss in some depth how the interplay between the host and guest components of inclusion compounds can be used to understand a variety of unusual physical properties they display. By manipulation of the components, a wide range of magnetic, electrical, and optical features has already been achieved. The beauty of the inclusion concept is that the constraints exerted by the host and guest upon each other are easily visualized. They are frequently both geometric and chemical in nature and they can be relaxed or modified in interesting ways. It is reasonable to predict that in the age of "molecular engineering," which seems to be rapidly approaching, inclusion compounds will offer a rich field for creative synthesis.

References

1. H. M. Powell, in *Non-Stoichiometric Compounds* (L. Mandelcorn, ed.), Chapter 7, Academic Press, New York (1964).
2. R. M. Barrer, in *Non-Stoichiometric Compounds* (L. Mandelcorn, ed.., Chapter 6, Academic Press, New York (1964).
3. I. Náray-Szabó and K. Popp, Die Darstellung und die Eigenscahften der Silber(II)-oxidphase, *Z. Anorg. Allgem. Chem.* **322**, 286–296 (1963).
4. Chou Kung-Du, The crystal structure of $Ag^+[Ag_2^{II}Ag_4^{III}O_8]NO_3^-$, *Sci. Sinica* (*Peking*) **12**, 139–140 (1963).

5. I. Náray-Szabó and G. Argay, The structure of the Ag(I, III) oxide phases, *Acta Cryst.* **19**, 180–184 (1965).
6. M. B. Robin, K. Andres, T. H. Geballe, N. A. Kuebler, and D. B. McWhan, Metallic conductivity and superconductivity in some silver clathrate salts, *Phys. Rev. Letters* **17**, 917–919 (1966).
7. A. C. Gossard, D. K. Hindermann, M. B. Robin, N. A. Kuebler, and T. H. Geballe, Nuclear magnetic resonance and superconductivity in the clathrate salt $[Ag_7O_8]^+HF_2^-$, *J. Am. Chem. Soc.* **89**, 7121–7123 (1967).
8. D. K. Hindermann, M. B. Robin, and N. A. Kuebler, An NMR study of bifluoride ion reorientation in the metallic salt $[Ag_7O_8]^+HF_2^-$, *J. Mag. Res.* **1**, 479–487 (1969).
9. M. B. Robin, private communication.
10. Mary M. Conway, Norman E. Phillips, T. H. Geballe, and N. A. Kuebler, Low-temperature heat capacities of the clathrate salts $Ag_7O_8NO_3$ and $Ag_7O_8HF_2$, *J. Phys. Chem. Solids* **31**, 2673–2678 (1970).

11a. W. A. Phillips, Tunneling states in amorphous solids, *J. Low Temp. Phys.* **7**, 351–360 (1972).

11b. P. W. Anderson, B. I. Halperin, and C. M. Varma, Anomalous low-temperature properties of glasses and spin glasses, *Phil. Mag.* **25**, 1–9 (1972).

12. R. J. Rollefson, Tunneling in $NaBr:F^-$ thermal and dielectric properties, *Phys. Rev.* **B5**, 3235 (1972).
13. W. B. Pearson, *The Crystal Chemistry and Physics of Metals and Alloys*, Wiley – Interscience, New York (1972).
14. V. I. Matkovitch, R. F. Giese, and J. Economy, *Z. Kristallogr.* **122**, 116 (1965).
15. Stepehanie M. Richards and John S. Kasper, The crystal structure of YB_{66}, *Acta Cryst.* **B25**, 237–251 (1969).
16. Glen A. Slack, D. W. Oliver, and F. H. Horn, Thermal conductivity of boron and some boron compounds, *Phys. Rev. B* **4**, 1714–1720 (1971).
17. B. Post, in *Boron, Metallo-Boron Compounds, Boranes*, pp. 301–369, Wiley—Interscience, New York (1964).
18. J. L. Hoard and R. E. Hughes, in *The Chemistry of Boron and Its Compounds* (E. L. Muetterties, ed.), Wiley, New York (1967).
19. S. La Placa, quoted in Ref. 18, and private communication.
20. H. C. Longuet-Higgins and M. de V. Roberts, The electronic structure of the borides MB_6, *Proc. Roy. Soc.* (*London*) **A224**, 336–347 (1968).
21. Yu. B. Paderno and G. V. Samsonov, *Dokl. Akad. Naůk SSSR* **137**, 646 (1960).
22. Robert W. Johnson and A. H. Daane, Electron requirements of bonds in metal borides; *J. Chem. Phys.* **38**, 425–432 (1963).
23. Z. Fisk, Ph.D. Dissertation, University of California, San Diego, 1969 (unpublished).
24. T. Niemyski and E. Kierzek-Pecold, Crystallization of lanthanum hexaboride, *J. Cryst. Growth* **3**, 162–165 (1968).
25. Yu. B. Paderno, S. Pokrzywnicki, and B. Staliński, Magnetic properties of some rare earth hexaborides, *Phys. Stat. Sol.* **24**, K73–K76 (1967).
26. B. T. Matthias, T. H. Geballe, K. Andres, E. Corenzwit, G. W. Hull, and J. P. Maita, Superconductivity and antiferromagnetism in boron-rich lattices, *Science* **159**, 530 (1968).

27. T. H. Geballe, B. T. Matthias, K. Andres, J. P. Maita, A. S. Cooper, and E. Corenzwit, Magnetic ordering in the rare-earth hexaborides, *Science* **160**, 1443–1444 (1968).
28. A. C. Gossard and V. Jaccarino, Boron nuclear magnetic resonance in rare earth intermetallic compounds, *Proc. Phys. Soc.* **80**, 877–881 (1962).
29. J. M. Lafferty, Boride cathodes, *J. Appl. Phys.* **22**, 299–309 (1951).
30. B. W. Roberts, Properties of Selected Superconductive Materials, NBS Technical Note 724, June 1972.
31. Jörg Wittig, Superconductivity of cerium under pressure, *Phys. Rev. Letters* **21**, 1250–1252 (1968).
32. T. F. Smith and W. E. Gardner, Pressure dependence of the superconducting transition temperature of dhcp and fcc lanthanum, *Phys. Rev.* **146**, 291–294 (1966).
33. M. R. MacPherson, G. E. Everett, D. Wohlleben, and M. B. Maple, Magnetic susceptibility of cerium metal under pressure, *Phys. Rev. Letters* **26**, 20–23 (1971); Howard Katzman and J. A. Mydosh, Electrical resistivity of exchange-enhanced α-cerium under pressure, *Phys. Rev. Letters* **29**, 998–1001 (1972).
34. J. Charles Nickerson and Robert M. White, Theory of the susceptibility of CeB_6, *J. Appl. Phys.* **40**, 1011–1012 (1969).
35. C. Kittel, in *Solid State Physics* (F. Seitz, D. Turnbull, and H. Ehrenreich, eds.), Vol. 22, pp. 1–25, Academic Press, New York (1968).
36. K. N. Lee, Ph.D. Dissertation, Princeton University, 1971 (unpublished).
37. É. E. Vainshtein, S. M. Blokhin, and Yu. B. Paderno, X-ray spectral investigation of samarium hexaboride, *Soviet Phys.—Solid State* **6**, 2318–2320 (1965).
38. R. L. Cohen, M. Eibschütz, and K. M. West, Electronic and magnetic structure of SmB_6, *Phys. Rev. Letters* **24**, 383–386 (1970); J. J. Rhyne, Mostly rare-earth compounds, *J. Appl. Phys.* **41**, 898–899 (1970).
39. J. C. Nickerson, R. M. White, K. N. Lee, R. Bachmann, T. H. Geballe, and G. W. Hull, Jr., Physical properties of SmB_6, *Phys. Rev. B* **3**, 2030–2042 (1971).
40. A. Jayaraman, V. Narayanamurti, E. Bucher, and R. G. Maines, Continuous and discontinuous semiconductor–metal transition in samarium monochalcogenides under pressure, *Phys. Rev. Letters* **25**, 1430–1433 (1970); J. M. Rooymans, *Ber. Bunsenges. Phys. Chem.* **70**, 1036 (1966).
41. A. Menth, E. Buehler, and T. H. Geballe, Magnetic and semiconducting properties of SmB_6, *Phys. Rev. Letters* **22**, 295–297 (1969).
41a. S. Doniach, private communication.
42. L. Pauling, *The Nature of the Chemical Bond*, Cornell University Press, Ithiaca, New York (1960), 3rd Ed.
43. D. E. Soule, J. W. McClure, and L. B. Smith, Study of the Shubnikov–de Haas effect. Determination of the Fermi surfaces in graphite, *Phys. Rev.* **134**, A453–A470 (1964).
44. J. G. Hooley, in *Chemistry and Physics of Carbon* (P. Walker, ed.), Vol. 5, pp. 321–372, Pergamon Press, New York (1969).
45. Walter Rüdorff, Über die Einlagerung von unedlen Metallen in Graphit sowie in Metallchalkogenide vom Typ MeX_2, *Chimie* **19**, 489–499 (1965).
46. G. R. Hennig, *Progress in Inorganic Chemistry*, Vol. 1, Interscience, New York (1959).

47. A. R. Ubbelohde and F. A. Lewis, *Graphite and its Crystal Compounds*, Oxford University Press, London (1960).
48. Karl Fredenhagen and Gustav Cadenbach, Die Binding von Kalium durch Kohlenstoff, *Z. Anorg. Allgem. Chem.* **158**, 249–263 (1926).
49. F. J. Salzano and S. Aronson, Thermodynamic properties of rubidium–graphite lamellar compounds, *J. Chem. Phys.* **45**, 4551–4555 (1966).
50. F. J. Salzano and S. Aronson, Stability of phases in the cesium–graphite system, *J. Chem. Phys.* **45**, 2221–2227 (1966).
51. N. B. Hannay, T. H. Geballe, B. T. Matthias, K. Andres, P. Schmidt, and D. MacNair, Superconductivity in graphitic compounds, *Phys. Rev. Letters* **14**, 225–226 (1965).
52. Daniel Balesdent, Bernard Carton, and Albert Hérold, Détermination des grandeurs thermodynamiques partielles et totales dans le systèm graphite–potassium, *Revue de Chimie minérale* **9**, 495–500 (1972).
53. Robert Juze and Volker Wehle, Lithium-Graphit-Einlagerungsverbindungen, *Naturwiss.* **20**, 560 (1965).
54. Michel Rose, Claude Naccache, and Jean Golé, Étude par résonance paramagnétique électronique des composés d'insertion des métaux alcalins dans le graphite, *Compt. Rend.* **266** (Série C), 421–424 (1968).
55. Co-Minh-Duc, Michel Rose, and Jean-Pierre Pascault, Produits d'insertion ternaires graphite-métal alcalin-diméthoxyéthane. Étude radiocristallographique, *Compt. Rend.* **270** (Série C), 657–658 (1970).
56. W. T. Eeles and J. A. Turnbull, The crystal structure of graphite–bromine compounds, *Proc. Roy. Soc.* (*London*) **A283**, 179–193 (1965).
57. A. G. Freeman and J. H. Johnston, The intercalation of graphite by boron trichloride, *Carbon* **9**, 667–671 (1971).
58. Jean Mélin and Albert Hérold, Étude des composés graphite-pentachlorure d'antimoine, *Compt. Rend.* **269** (Série C), 887–879 (1969).
59. Hervé Fuzellier and Albert Hérold, Insertion de hémipentoxyde d'azote dans le graphite, *Compt. Rend.* **267** (Série C), 607–609 (1968).
60. D. E. Nixon and G. S. Parry, The expansion of the carbon–carbon bond length in potassium graphite, *J. Phys. C* **2**, 1732–1741 (1969).
61. M. J. Bottomley, G. S. Parry, and A. R. Ubbelohde, Thermal expansion of some salts of graphite, *Proc. Roy. Soc.* (*London*) **A279**, 291–301 (1964).
62. A. R. Ubbelohde, G. S. Parry, and D. Dixon, Order–Disorder transformations in graphite nitrates, *Nature* **206**, 1352–1354 (1965).
63. D. E. Nixon, G. S. Parry, and A. R. Ubbelohde, Order–Disorder transformations in graphite nitrates, *Proc. Roy. Soc.* (*London*) **A291**, 324–339 (1966).
64. F. R. M. McDonnell, R. C. Pink, and A. R. Ubbelohde, Some physical properties associated with "aromatic" electrons. Part III. The pseudo-metallic properties of potassium–graphite and graphite–bromine, *J. Chem. Soc.* (*London*) **1951**, 191–199.
65. J. G. Hooley, A recording vacuum thermobalance, *Can. J. Phys.* **35**, 374–380 (1957).
66. G. A. Saunders, A. R. Ubbelohde, and D. A. Young. The formation of graphite/bromine I. Hysteresis of bromine insertion between the carbon hexagon layers, *Proc. Roy. Soc.* (*London*) **A271**, 499–511 (1963).
67. J. G. Hooley and J. L. Smee, The mechanism of the bromination of graphite, *Carbon* **2**, 135–138 (1964).

68. J. G. Hooley, W. P. Garby, and J. Valentin, The effect of sample shape on the bromination of graphite, *Carbon* **3**, 7–16 (1965).
69. Tadashi Sasa, Yoichi Takahashi, and Takashi Mukaibo, Electrical conductivity of graphite bromine lamellar compound, *Bull. Chem. Soc. Japan* **43**, 34–38 (1970).
70. J. G. Hooley, private communication.
71. B. Bach, E. L. Evans, J. M. Thomas, and M. Barber, Monitoring changes in the band structure of graphite following chemical reaction: An X-ray-induced photoelectron study of intercalation, *Chem. Phys. Letters* **10**, 547–548 (1971).
72. J. K. Galt, W. A. Yager, and H. W. Dail, Jr., Cyclotron resonance effects in graphite, *Phys. Rev.* **103**, 1586–1587 (1956).
73. A. S. Bender and D. A. Young, Fermi surfaces in graphite–bromine, studied by Shubnikov–de Haas oscillations, *J. Phys. C* **5**, 2163–2178 (1972).
74. A. R. Ubbelohde, Electronic anomalies in dilute synthetic metals, *Proc. Roy. Soc.* (*London*) **A321**, 445–460 (1971).
75. A. R. Ubbelohde, Electrical anisotropy of synthetic metals based on graphite, *Proc. Roy. Soc.* (*London*) **A327**, 289–303 (1972).
76. Alexander L. Fetter and Pierre C. Hohenberg, in *Superconductivity* (R. D. Parks, ed.), Vol. 2, pp. 817–923, Marcel Dekker, New York (1969).
77. J. Poitrenaud, Étude de la susceptibilité du composé C_8K à basse temperature par résonance paramagnétique électronique, *Revue de Physique Appliquée* **5**, 275–281 (1970).
78. F. J. Salzano and Myron Strongin, Dimensionality of superconductivity in graphite lamellar compounds, *Phys. Rev.* **153**, 533–434 (1967).
79. K. A. Müller and R. Kleiner, Conduction carrier spin resonance in the alkali-metal-graphites C_8Me and $C_{24}Me$, *Phys. Letters* **1**, 98–100 (1962).
80. George Feher and A. F. Kip, Electron spin resonance absorption in metals. I. Experimental, *Phys. Rev.* **98**, 337–348 (1955); Freeman J. Dyson, Electron spin resonance absorption in metals. II. Theory of electron diffusion and the skin effect, *Phys. Rev.* **98**, 349–359 (1955).
81. J. M. Cowley and James A. Ibers, The structures of some ferric chloride–graphite compounds, *Acta Cryst.* **9**, 421–431 (1956).
82. B. V. Liengme, M. W. Bartlett, J. G. Hooley, and J. R. Sams, Mössbauer spectra of interlaminar $FeCl_3$–graphite compounds, *Phys. Letters* **25A**, 127–128 (1967).
83. J. G. Hooley, M. W. Bartlett, B. V. Liengme, and J. R. Sams, A. Mössbauer study of graphite iron chloride compounds, *Carbon* **6**, 681–685 (1968).
84. Yu. N. Novikov, M. E. Vol'pin, V. E. Prusakov, R. A. Strukan, V. I. Gol'danskii, V. A. Semion, and Yu. T. Struchkov, Preparation, structure, and nuclear gamma resonance spectra of laminated compounds of graphite with iron chlorides, *J. Struct. Chem.* **11**, 970–976 (1970).
85. Marceline L. Dzurus and Gerhart R. Hennig, Graphite compounds, *J. Am. Chem. Soc.* **79**, 1051–1054 (1957).
86. Yu. S. Karimov, A. V. Zvarykina, and Yu. N. Novikov, Two-dimensional ferromagnetism in layered compounds of graphite with iron chlorides, *Soviet Phys.—Solid State* **13**, 2388–2391 (1972).
87. Yu. S. Karimov, M. E. Vol'pin, and Yu. N. Novikov, Layered compounds of $NiCl_2$ and $CoCl_2$ with graphite as two dimensional heisenberg ferromagnets, *JETP Letters* **14**, 142–144 (1971).
88. M. K. Wilkinson, J. W. Cable, E. O. Wollan, and W. C. Koehler, Neutron diffraction investigations of the magnetic ordering in $FeBr_2$, $CoBr_2$, $FeCl_2$, and $CoCl_2$, *Phys. Rev.* **113**, 497–507 (1959).

89. J. W. Cable, M. K. Wilkinson, and E. O. Wollan, Neutron diffraction studies of the magnetic ordering in $CrCl_3$ and $FeCl_3$, *Bull. Am. Phys. Soc.* **4**, 189 (1959).
90. W. B. Yelon and R. J. Birgeneau, Magnetic properties of $FeCl_2$ in zero field. II. Long-range order, *Phys. Rev. B* **5**, 2615–2621 (1972).
91. M. E. Lines, New approach to Green's-function decoupling in magnetism with specific application to two-dimensional systems, *Phys. Rev. B* **3**, 1749–1763 (1971).
92. R. C. Chisholm and J. W. Stout, Heat capacity and entropy of $CoCl_2$ and $MnCl_2$ from 11° to 300°K. Thermal anomaly associated with antiferromagnetic ordering in $CoCl_2$, *J. Chem. Phys.* **36**, 972–979 (1962).
93. F. Hulliger, in *Structure and Bonding* (C. Jorgensen, ed.), Vol. 4, pp. 83–229, Springer-Verlag, Berlin (1968).
94. J. A. Wilson and A. D. Yoffe, The transition metal dichalcogenides: Discussion and interpretation of the observed optical, electrical, and structural properties, *Adv. Phys.* **18**, 193–335 (1969).
95. R. Huisman, R. De Jonge, C. Haas, and F. Jellinek, Trigonal-prismatic coordination in solid compounds of transition metals, *J. Solid State Chem.* **3**, 56–66 (1971).
96. J. C. McMenamin and W. E. Spicer, Photoemission studies of the layered dichalcogenides $NbSe_2$ and MoS_2 and a modification of the current band models, *Phys. Rev. Letters* **29**, 1501–1504 (1972).
97. P. M. Williams and F. R. Shepherd, He II photoemission studies of transition metal dichalcogenides, *J. Phys. C* **6**, L36–L40 (1973).
98. L. F. Mattheiss, Band structures of transition-metal dichalcogenide layer compounds, *Bull. Am. Phys. Soc.* **18**, 386 (1973).
98a. A. H. Thompson, K. R. Pisharody, and R. F. Koehler, Jr., Experimental study of the solid solutions $Ti_xTa_{1-x}S_2$, *Phys. Rev. Letters* **29**, 163–166 (1972).
98b. A. H. Thompson, F. R. Gamble, and J. R. Revelli, Transitions between semiconducting and metallic phases in 1T-TaS_2, *Solid State Commun.* **9**, 981–985 (1971).
98c. J. A. Wilson, private communication.
99. W. Rüdorff and H. H. Sick, Einlagerungsverbindungen von Alkali- und Erdalkalimetallen in Molybdän- und Wolframdisulfid, *Angew. Chem.* **71**, 128 (1959).
100. Walter Rüdorff, Einlagerungsverbindungen mit Alkali- und Erdalkalimetallen, *Angew. Chem.* **71**, 487–491 (1959).
101. W. Rüdorff and W. Ostertag, in *Proc. 4th Conf. on Rare Earth Research* (L. Eyring, ed.), p. 117, Gordon and Breach, New York (1965).
102. M. Rüdorff, Reaktionen stark elektropositiver Metalle mit Graphit und mit Metalldichalkogeniden, *Angew Chem.* **78**, 948 (1966).
103. Annie Le Blanc, Michel Danot, and Jean Rouxel, Sur l'insertion de métaux alcalins, dans la structure CdI_2 du disulfure d'étain, *Bull. Soc. Chim. Fr.* **1969**, 87–90.
104. Michel Danot, Annie Le Blanc, and Jean Rouxel, Les composés intercalaires K_xTiS_2, *Bull. Soc. Chim. Fr.* **1969**, 2670–2675.
105. Jean Rouxel, Michel Danot, and Jean Bichon, Les composés intercalaires Na_xTiS_2. Étude structurale générale des phases Na_xTiS_2 et K_xTiS_2, *Bull. Soc. Chim. Fr.* **1971**, 3930–3935.
106. Jean Rouxel, J. Cousseau, and Luc Trichet, Les Composés intercalaires—K_xZrS_2, *Compt. Rend.* **273**, 243–246 (1971).

107. Annie Le Blanc and Jean Rouxel, Sur les types structuraux des composés intercalaires $MSnS_2$ (M = Li, Na, K, Rb), *Compt. Rend.* **274** (Série C), 786–788 (1972).
108. G. V. Subba Rao, M. W. Shafer, and L. Tao, in *Proc. Magnetism Conf., Boulder, Colorado, 1972.*
109. J. R. Revelli, Jr., *Bull. Am. Phys. Soc.* **17**, 22 (1972); Ph.D. Dissertation, Stanford Univ., 1973 (unpublished).
110. R. B. Somoano and A. Rembaum, Superconductivity in intercalated molybdenum disulfide, *Phys. Rev. Letters* **27**, 402–404 (1971).
111. R. B. Somoano, V. Hadek, and A. Rembaum, *J. Chem. Phys.*, in press.
112. F. R. Gamble and T. H. Geballe, unpublished.
113. J. V. Acrivos, W. Y. Liang, J. A. Wilson, and A. D. Yoffe, Optical studies of metal–semiconductor transmutations produced by intercalation, *J. Phys. C* **4**, L18–L20 (1970).
114. W. Omloo and F. Jellinek, Intercalation compounds of alkali metals with niobium and tantalum dichalcogenides, *J. Less-Common Metals* **20**, 121–129 (1970).
115. Marcel Sergent and Jacques Prigent, Préparation de thiomolybdites, thiotungstites et thiochromites alcalins, *Compt. Rend.* **261** (Groupe 8), 5135–5137 (1965).
116. A. E. Van Arkel and C. Crevecoeur, Quelques sulfures et séléniures complexes, *J. Less-Common Metals* **5**, 177–180 (1963).
117. K. Koerts, The crystal structure of $Cu_{0.65}NbS_2$ and some related compounds, *Acta Cryst.* **16**, 432 (1963).
118. J. M. van den Berg and C. W. F. Kort, La structure de $Cu_{0.65}TaS_2$, *J. Less-Common Metals* **13**, 363–364 (1957).
119. J. M. Voorhoeve-van den Berg, On the ternary phases of Al_xNbSe_2 and Cu_xNbSe_2, *J. Less-Common Metals* **26**, 399–402 (1972).
120. F. J. Di Salvo, G. W. Hull, L. H. Schwartz, J. M. Vooerhoeve, and J. V. Waszczak, to be published.
121. P. Gentile and T. Tracey, to be published.
122. Harry Hahn, Bernhard Harder, and Wolfgang Brockmüller, Versuche zur Umsetzung von Titansulfiden mit Sulfiden zweiwertiger Übergangsmetalle, *Z. Anorg. Allgem. Chem.* **288**, 260–268 (1956).
123. Gilbert Bérodias and Maurice Chevreton, Étude structurale de nouveaux séléniures ternaires, *Compt. Rend.* **261** (Groupe 6), 2202–2204 (1965).
124. R. H. Plovnick, M. Vlasse, and A. Wold, Preparation and structural properties of some ternary chalcogenides of titanium, *Inorg. Chem.* **7**, 127–129 (1968).
125. Michel Danot and Jean Rouxel, Études de systèmes M_x–TiS_2 (M métal alcalin ou élément de transition de la première période, $0 < x < 1$): les surstructures MTi_4S_8 et $M_3Ti_4S_8$ (M = Fe, Co, Ni), *Compt. Rend.* **271** (Série C), 998–1001 (1970).
126. Michel Danot, Jean Bichon, and Jean Rouxel, Le système nickel–disulfure de titane, *Mem. Soc. Chim. Fr.* **1972**, 3063–3066.
127. Luc Trichet and Jean Rouxel, Étude du système nickel–ZrS_2. Structure et surstructure $Ni_{0.50}ZrS_2$, *Compt. Rend.* **269** (Série C), 1040–1043 (1969).
128. Luc Trichet, Joseph Cousseau, and Jean Rouxel, Les systèmes Fe–ZrS_2 et Co–ZrS_2. Structure M_xZrS_2, *Compt. Rend.* **274** (Série C), 394–397 (1972).
129. J. Rouxel, private communication.

130. J. M. van den Berg and P. Cossee, Structural aspects and magnetic behavior of NbS_2 and TaS_2 containing extra metal atoms of the first transition series, *Inorg. Chim. Acta* **2**, 143–148 (1968).
131. Annie Le Blanc and Jean Rouxel, Étude de systèmes M_xNbS_2 (M élément de transition de la première période): système Ti_xNbS_2 et surstructure $Cr_{0.33}NbS_2$, *Compt. Rend.* **270** (Série C), 1976–1979 (1970).
132. F. Hulliger and E. Pobitschka, On the magnetic behavior of new 2H–NbS_2-type derivatives, *J. Solid State Chem.* **1**, 117–119 (1970).
133. J. M. Voorhoeve and M. Robbins, Intercalation of the niobium diselenide layer structure by first row transition metals, *J. Solid State Chem.* **1**, 134–137 (1970).
134. K. Anzenhofer, J. M. van den Berg, P. Cossee, and J. N. Helle, The crystal structure and magnetic susceptibilities of $MnNb_3S_6$, $CoNb_3S_6$, and $NiNb_3S_6$, *J. Phys. Chem. Solids* **31**, 1057–1067 (1970).
135. B. van Laar, R. M. Turveld, and D. J. W. Ijdo, Magnetic and crystallographic structures of Me_xNbS_2 and Me_xTaS_2, *J. Solid State Chem.* **3**, 154–160 (1971).
136. J. Bernard and Y. Jeannin, in *Symposium of Nonstoichiometric Compounds* (Roland Ward, ed.), Adv. in Chem. Ser. No. 39, pp. 191–303, American Chemical Society, New York (1963).
137. R. Huisman, K. Kadijk, and F. Jellinek, The non-stoichiometric phases $Nb_{1+x}Se_2$ and $Ta_{1+x}Se_2$, *J. Less-Common Metals* **21**, 187–193 (1970).
138. Ye. A. Antonova, K. V. Kiseleva, and S. A. Medvedev, Superconductivity in lamellar structures of the $NbSe_2$ type, *Phys. Met. Metallog.* **27**, 58–62 (1969).
139. Armin Weiss and R. Ruthardt, Über eine Schichteinlagerungs-Verbindung des Titandisulfids mit Hydrazin, *Z. Naturforsch.* **24b**, 256 (1969).
140. Armin Weiss and R. Ruthardt, Schichteinlagerungs-Verbindungen des Titandisulfids mit Säureamiden, *Z. Naturforsch.* **24b**, 355 (1969).
141. Armin Weiss and R. Ruthardt, Schichteinlagerungs-Verbindungen des Titandisulfids mit N-substituierten Carbonsäureamiden, *Z. Naturforsch.* **24b**, 1066 (1969).
142. F. R. Gamble, F. J. Di Salvo, R. A. Klemm, and T. H. Geballe, Superconductivity in layered structure organometallic crystals, *Science* **168**, 568–570 (1970).
143. F. R. Gamble, J. H. Osiecki, and F. J. Di Salvo, Some superconducting intercalation complexes of TaS_2 and substituted pyridines, *J. Chem. Phys.* **55**, 3525–3530 (1971).
144. F. R. Gamble, J. H. Osiecki, M. Cais, R. Pisharody, J. F. Di Salvo, and T. H. Geballe, Intercalation complexes of Lewis bases and layered sulfides: A large class of new superconductors, *Science* **174**, 493–500 (1971).
145. R. Schöllhorn and Armin Weiss, Layer intercalation compounds of dichalcogenides of transition metals of group IVb and Vb with ammonia, *Z. Naturforsch.* **27b**, 1273–1274 (1972).
146. R. Ruthardt, R. Schöllhorn, and Armin Weiss, Layer intercalation compounds of titanium disulfide with nitrogen heterocycles, *Z. Naturforsch.* **27b**, 1275–1276 (1972).
147. R. Schöllhorn and Armin Weiss, Layer intercalation compounds of transition metal dichalcogenides with hydrazine and alkylsubstituted hydrazines, *Z. Naturforsch.* **27b**, 1277–1278 (1972).
148. R. Schöllhorn and Armin Weiss, Layer intercalation compounds of niobium and tantalum disulfide with nitrogen heterocycles, *Z. Naturforsch.* **27b**, 1278–1279 (1972).

149. R. Schöllhorn and Armin Weiss, Layer intercalation compounds of titanium disulfide, niobium disulfide and tantalum disulfide with N-oxides of heterocycles, *Z. Naturforsch.* **27b**, 1428–1429 (1972).
150. A. H. Thompson, F. R. Gamble, and R. F. Koehler, Jr., Effects of intercalation on electron transport in tantalum disulfide, *Phys. Rev. B* **5**, 2811–2816 (1972).
151. R. A. Bromley, A Fermi surface for 2H-$NbSe_2$, *Phys. Rev. Letters* **29**, 357–359 (1972).
152. E. Ehrenfreund, A. C. Gossard, F. R. Gamble, and T. H. Geballe, Absence of antiferromagnetism in $NbSe_2$ and $TaSe_2$, *J. Appl. Phys.* **42**, 1491–1493 (1971).
153. M. Marezio, P. D. Dernier, A. Menth, and G. W. Hull, Jr., The crystal structure of $NbSe_2$ at 15°K, *J. Solid State Chem.* **4**, 425–429 (1972).
154. A. H. Thompson, private communication.
155. S. Foner, E. J. McNiff, Jr., A. H. Thompson, F. R. Gamble, T. H. Geballe, and F. J. Di Salvo, Anisotropic high field superconductors, in *Low Temperature Physics LT-13* (Proc. 13th Int. Conf. Low Temp. Phys.), Plenum, New York (1973).
156. F. J. Di Salvo, R. Schwall, T. H. Geballe, F. R. Gamble, and J. H. Osiecki, Superconductivity in layered compounds with variable interlayer spacings, *Phys. Rev. Letters* **27**, 310–313 (1971).
157. T. H. Geballe, A. Menth, F. J. Di Salvo, and F. R. Gamble, Precursor effects of superconductivity up to 35°K in layered compounds, *Phys. Rev. Letters* **27**, 314–316 (1971).
158. D. E. Prober, M. Beasley, and R. E. Schwall, Fluctuation effects in the magnetic transition of superconducting layered compounds, in *Low Temperature Physics LT-13* (Proc. 13th. Int. Conf. Low Temp. Phys.), Plenum, New York (1973).
159. F. J. Di Salvo, Magnetic susceptibility measurements of intercalated tantalum disulfide, in *Low Temperature Physics LT-13*, (Proc. 13th Int. Conf. Low Temp. Phys.), Plenum, New York (1973).
160. P. J. Bray and Enrique G. Sauer, N^{14} nuclear quadrupole resonance in compounds used as intercalates in superconducting complexes of TaS_2, *Solid State Commun.* **11**, 1239–1242 (1972).
161. M. R. Tubbs, The optical absorption spectra of metal iodides with layer structure, *J. Phys. Chem. Solids* **29**, 1191–1203 (1968).
162. L. J. De Jongh, W. D. van Amstel, and A. R. Miedema, Magnetic measurements on $(C_2H_5NH_3)_2CuCl_4$, *Physica* **58**, 277–304 (1972).
163. M. Eibschütz, H. J. Guggenheim, and L. Holmes, Magnetic behavior of a layer-type antiferromagnet $RbFeF_4$, *J. Appl. Phys.* **42**, 1485–1486 (1971); R. W. Grant, Magnetic structure of FeOCl, *J. Appl. Phys.* **42**, 1619–1620 (1971).
164. F. Kanamaru, M. Shimada, M. Koizumi, M. Takano, and T. Takada, Mössbauer effect of FeOCl–pyridine complex, *J. Solid State Chem.* **7**, 297–299 (1973).
165. A. D. Wadsley, in *Non-Stoichiometric Compounds* (L. Mandelcorn, ed.), Chapter 3, Academic Press, New York (1964).
166. P. G. Dickens and M. S. Whittingham, The tungsten bronzes and related compounds, *Quart. Rev. Chem. Soc.* **22**, 30–44 (1968).
167. M. S. Whittingham and R. A. Huggins, Electrochemical Preparation and Characterization of Alkali Metal Tungsten Bronzes, M_xWO_3, National Bureau of Standards Special Publication 364 (July 1972), pp. 51–61.
168. F. Wöhler, Ueber das Wolfram, *Ann. Physik* **2**, 345–358 (1824).

169. Michael Kestigian and Roland Ward, The lanthanum–titanium–oxygen system, *J. Am. Chem. Soc.* **77**, 6199–6200 (1955).
170. Sten Andersson and A. D. Wadsley, $Na_xTi_4O_8$, an alkali metal titanium dioxide bronze, *Acta Cryst.* **15**, 201–206 (1962).
171. R. P. Ozerov, Vanadium bronzes of elements in the first group of the periodic system, *Russ. J. Inorg. Chem.* **4**, 476–479 (1959).
172. Dana Ridgley and Roland Ward, The preparation of a strontium–niobium bronze with the perovskite structure, *J. Am. Chem. Soc.* **77**, 6132–6136 (1955).
173. A. Wold, W. Kunnmann, R. J. Arnott, and A. Ferretti, Preparation and properties of sodium and potassium molybdenum bronze crystals, *Inorg. Chem.* **3**, 545–550 (1964).
174. Gunnar Haag and Arne Magneli, Recent structure investigations of oxygen compounds of molybdenum and tungsten, *Rev. Pure Appl. Chem.* (*Australia*) **4**, 235–250 (1954).
175. H. W. Melville and J. C. Robb, The kinetics of the interaction of atomic hydrogen with olefines, *Proc. Roy. Soc.* (*London*) **A196**, 445–509 (1949).
176. S. Khoobiar, Particle to particle migration of hydrogen atoms on platinum–alumina catalysts from particle to neighboring particles, *J. Phys. Chem.* **68**, 411 (1964).
177. R. Levy, Ph.D. Dissertation, Stanford Univ., 1973 (unpublished).
178. P. G. Dickens, private communication.
179. P. G. Dickens, D. J. Murphy, and T. K. Halstead, Pulsed NMR study of proton mobility in a hydrogen tungsten bronze, *J. Solid State Chem.* **6**, 370–373 (1973).
180. D. J. Murphy, Ph.D. Dissertation, Oxford Univ., 1971.
181. M. S. Whittingham and R. A. Huggins, Electrochemical preparation and characterization of alkali metal tungsten bronzes, Mo_xWO_3, in *Solid State Chemistry* (R. S. Roth and S. J. Schneider, eds.), p. 51, NBS Special Publication 364 (1972).
182. M. Stanley Whittingham and Robert A. Huggins, Measurement of sodium ion transport in beta alumina using reversible solid electrodes, *J. Chem. Phys.* **54**, 414–416 (1971).
183. A. T. Fromhold, Jr. and Albert Narath, Transient nuclear magnetic resonance study of the conduction band of metallic Na_xWO_3: ^{23}Na relaxation, *Phys. Rev.* **136**, A487–A493 (1964).
184. L. D. Clark, M. S. Whittingham, and R. A. Huggins, An NMR study of ionic motion in ammonium tungsten bronze, *J. Solid State Chem.* **5**, 487–493 (1972).
185. M. J. Sienko, in *Nonstoichiometric Compounds* (R. F. Gould, ed.), Adv. in Chem. Ser. No. 39, p. 224, American Chemical Society, Washington, D.C. (1963).
186. John B. Goodenough, Narrow-band electrons in transition-metal oxides, *Czech. J. Phys. B* **17**, 304–336 (1967).
187. Jerome H. Perlstein and M. J. Sienko, Single-crystal studies of electrical conductivity, Seebeck effect, and Hall voltage in sodium vanadium bronze and a crystal-field model of electron transport, *J. Chem. Phys.* **48**, 174–181 (1968).
188. William Fogle and Jerome H. Perlstein, Semiconductor-to-metal transition in the blue potassium molybdenum bronze, $K_{0.30}MoO_3$: example of a possible excitonic insulator, *Phys. Rev. B* **6**, 1402–1412 (1972).
189. A. R. Sweedler, Ch. J. Raub, and B. T. Matthias, Superconductivity of the alkali tungsten bronzes, *Phys. Letters* **15**, 108–109 (1965).

190. J. P. Remeika, T. H. Geballe, B. T. Matthias, A. S. Cooper, G. W. Hull, and E. M. Kelly, Superconductivity in hexagonal tungsten bronzes, *Phys. Letters* **24A**, 565–566 (1967).
191. C. N. King, J. A. Benda, W. A. Phillips, and T. H. Geballe, Specific heat, optical, and transport properties of hexagonal tungsten bronzes, in *Low Temperature Physics LT-13* (Proc. 13th Int. Conf. Low Temp. Phys., Boulder), Plenum, New York (1973).
192. M. J. Sienko and Sheila MacEnness Morehouse, Electrical and magnetic properties of potassium tungsten bronze and rubidium tungsten bronze, *Inorg. Chem.* **2**, 485–489 (1963).
193. L. D. Ellerbeck, H. R. Shanks, P. H. Sidles, and G. C. Danielson, Electrical resistivity of cubic sodium tungsten bronze, *J. Chem. Phys:* **35**, 298–302 (1961).
194. F. F. Hubble, Joan M. Gulick, and W. G. Moulton, Superconductivity in the K, Rb, and Cs tungsten fluoroxide bronzes, *J. Phys. Chem. Solids* **32**, 2345–2350 (1971).
195. J. C. Gulick and M. J. Sienko, Fluorine-19 NMR relaxation studies in the tungsten fluoroxide bronzes, *J. Solid State Chem.* **1**, 195–204 (1970).
196. E. Banks and A. Goldstein, The solution of lithium in hexagonal potassium tungsten bronze, *Inorg. Chem.* **7**, 966–969 (1968).
197. H. Krebs, *Fundamentals of Inorganic Crystal Chemistry*, McGraw-Hill, Berks., England (1968).
198. S. Aronson, F. J. Salzano, and D. Bellafiore, Thermodynamic properties of the potassium-graphite lamellar compounds from solid-state emf measurements, *J. Chem. Phys.* **49**, 434–439 (1968).
199. W. Rüdorff, Graphite intercalation compounds, *Adv. Inorg. Radiochem.* **1**, 223–266 (1959).
200. W. Rüdorff, E. Schulze, and O. Rubisch, Alakaliammingraphitverbindungen, *Z. Anorg. Allgem. Chem.* **282**, 232–240 (1955).
201. W. Rüdorff, V. Sils, and R. Zeller, Über das Verhalten von Graphit gegenüber Jodmonochlorid and Chromylchlorid, *Z. Anorg. Allgem. Chem.* **283**, 299–303 (1956).
202. W. Rüdorff, Kristallstrucktur der Säureverbindungen des Graphits, *Z. Physik. Chem.* (*Leipzig*) **B45**, 42–68, 174 (1939).
203. W. Rüdorff and Herbert Schulz, Über die Einlagerung von Ferrichlorid in das Gitter von Graphit, *Z. Anorg. Allgem. Chem.* **245**, 121–156 (1940).
204. W. Rüdorff and A. Landel, Über die Einlagerung von Galliumchlorid und Indiumchlorid in Graphit, *Z. Anorg. Allgem. Chem.* **293**, 327–342 (1958).
205. W. Rüdorff and R. Zeller, Über Aluminumchlorid-Graphit-Einlagerungsverbindungen, *Z. Anorg. Allgem. Chem.* **279**, 182–193 (1955).
206. N. N. Zhuravlev, A. A. Stepanova, Y. B. Paderno, and G. V. Samsonov, *Krystallografiya* **6**, 636 (1962).
207. E. J. Felton, I. Binder, and B. Post, *J. Am. Chem. Soc.* **80**, 3479 (1958).
208. P. Blum and F. Bertaut, *Acta Cryst.* **7**, 81 (1954).
209. H. A. Eick and P. W. Gilles, *J. Am. Chem. Soc.* **81**, 5030 (1959).
210. G. V. Samsonov and Yu. B. Paderno, Borides of the Rare Earth Metals, AEC-tr-5264, U.S. Atomic Energy Commission, Division of Technical Information [Translation].

211. K. A. Gschneider, Jr. *Rare Earth Alloys*, pp. 127–128, van Nostrand, New York (1961).
212. H. Hacker, Y. Shimada, and K. S. Chung, *Phys. Stat. Sol.* **4**, 459 (1971).
213. E. F. Westrum, Jr., H. L. Clever, J. T. S. Andrews, and G. Peick, in *Rare Earth Research III* (L. Eyring, ed.), p. 597, Gordon and Breach, New York (1966).
214. H. Hacker and M. S. Lind, *Solid State Commun.* **6**, 379 (1968).
215. M. B. Robin and P. Day, in *Advances in Inorganic Chemistry and Radiochemistry*, Vol. 10, pp. 247–442 (H. J. Emeléus and A. G. Sharpe, eds.), Academic Press, New York (1967).
216. H. Fernandez-Moran, M. Ohstuki, A. Hibino, and C. Hough, *Science* **174**, 498–500 (1971).

3

The Structural Chemistry of Some Complex Oxides: Ordered and Disordered Extended Defects

LeRoy Eyring and Leung-Tak Tai
Department of Chemistry
Arizona State University
Tempe, Arizona

1. Introduction

The examples chosen to illustrate the role of extended defects in structural chemistry are dictated not so much by their practical importance as by the uneven state of existing knowledge and the predilection of the authors. While the systems discussed in this limited space are quite arbitrarily chosen, they do suggest the measure and diversity of structural variety existing in compounds possessing extended defects which occur disordered within a host structure or as an ordered feature of a new structure based on the host.

Many of the interesting and useful properties of solids result from the presence within their structures of imperfections or defects. These defects are so intimately involved in diffusion, reactivity, electronic, and optical properties that an understanding of them is incumbent upon those who would seek to clarify the variety of problems in materials science.

1.1. Types of Defects in Crystals

1.1.1. Point Defects

The simplest structural imperfections are the so-called point defects which involve displaced single atoms at random in the crystal.

These classical defects are very often associated with the names of Schottky, Wagner, and Frenkel and have been discussed in Chapter 5 of Volume 1. In a crystal a vacancy is said to be created when an atom is missing from a normally occupied site. For ionic crystals, cation and anion vacancies must appear in certain ratios such that the crystal as a whole remains electrically neutral. An atom is interstitial when it occupies a position in the crystal normally unoccupied. The imposition of two or more close-packed layers of identical spheres creates two types of interstitial positions, namely octahedral and tetrahedral interstices.

In real crystals, even the most perfect ones, some defects must exist at ordinary temperatures as a direct consequence of the thermodynamic requirement that at temperatures above absolute zero the free energy of a solid system tends toward a minimum by increasing its entropy through disorder.

Defects of the kinds discussed, if introduced into the host crystal in small concentrations, will be distributed rather randomly and will not normally be detected by X-ray diffraction. Of course, there may be radical changes in such properties as optical absorption. When the concentration of defects increases association into clusters is to be expected.

1.1.2. Extended Defects

When at least one of the elements in a crystalline compound is capable of variable valence the composition can be changed without loss of electrical neutrality. In the homogeneity range of a phase a substance is no longer stoichiometric and the traditional Dalton's laws of constant and multiple proportions conspicuously fail. These compounds, reported to have wide composition limits, include hydrides, borides, carbides, nitrides, silicides, phosphides, and oxides and other chalcogenides, as well as intermetallic compounds and certain halides of the transition metals. As better techniques for detection and greater preparative skill are applied, one or more discrete phases may appear within a nonstoichiometric composition range. These would be termed ordered intermediate phases despite their seeming irrational chemical formulas in which the anion-to-cation ratio is not that of small whole numbers. An ordered phase is considered to be a crystallographic phase if it gives rise to a well-defined diffraction pattern.

The formulas of the newly recognized compounds (oxides in the present discussion) are no longer simple, but their structures, mostly

established by single-crystal X-ray diffraction work, are closely related to other members of a family. These structure-related phases derived from the same parent phase form a homologous series[1] which can be expressed in terms of generic formulas of the type M_nO_{2n-1}, M_nO_{3n-1}, M_nO_{3n-2}, etc. Homologues belonging to the same series or family contain the same structural entity or recurring abnormality which may be ordered planar defects as in the case of many transition metal oxides and oxyfluorides or may be ordered vacancies as in the case of rare earth oxide systems. A discussion of these two types of compounds shall occupy our attention through most of this chapter. These anomolous structural entities may grow, decline, diffuse, dissociate, or otherwise be intimately involved with solid-state reactions and transport behavior.

In studies of the higher oxides of Ti, V, Nb, Mo, and W classical point defects are not as apparent as might be expected. In oxide systems in which oxygen atoms define a three-dimensional close-packing arrangement, either cubic or hexagonal, and metal atoms systematically occupy the octahedral positions following a virtual removal of a plane of oxygen atoms, one slab of the parent structure may be displaced or sheared relative to an adjacent slab. The net result is a virtual collapse along a certain crystallographic direction to bring the metal–oxygen octahedra into closer contact across the boundary between the two structure fragments while preserving the integrity of the oxygen framework. The joints or boundaries between the parent slabs are called crystallographic shear (CS) planes.[2] If they are isolated and randomly distributed they are generally called Wadsley defects.* The average composition of the crystal is altered by the presence of these defects. Although these isolated defects are clearly revealed by electron optical methods, unless their concentration is considerable and they are ordered, their presence cannot be detected by conventional X-ray techniques.

As the concentration of Wadsley defects increases, their interaction leads first to ordered regions and then to a periodic sequence eventually producing shear structures or shear phases. Examples of CS compounds[3–5] include the homologous series of oxides V_nO_{2n-1}[6] and Ti_nO_{2n-1},[7] which are derived by CS from a parent of the rutile structure, molybdenum oxides[8] related to the MoO_3 structure, and the complex binary and ternary niobium oxides[3,9] related to the ReO_3 structure. Whereas nonstoichiometry has been

* See the tribute to David Wadsley by Sten Andersson in Ref. 67.

reported in the past in such phases, it is now frequently observed to be a result of closely spaced shear structures. It is clear that classical point defect theory is inadequate to account for either the formation or the composition range of these compounds.

The story is very similar in compounds such as the rare earth oxides in which homologous series are observed but where the structural principle of their formation is not CS. Furthermore, the ordered phases may be observed to disorder at higher temperatures to give what appears to be the best remaining examples of gross non-stoichiometry.

In this chapter there cannot be an exposition of those extended defects which do not involve compositional changes such as antiphase (out of phase) boundaries, dislocations, twin boundaries, and stacking faults.

1.2. Methods of Observing Extended Defects*

1.2.1. X-Ray and Electron Optical Methods

Of all techniques available to the solid-state chemist, X-ray diffraction is perhaps the most important. Structure investigations of complex phases are made possible by the availability of automated diffractometers, high-speed computers, and sophisticated computer programs to carry through the structure determination.

Before high-resolution electron microscopes were successfully developed single-crystal X-ray diffraction was the only method by which structures could be solved; and before the fully automated X-ray diffractometer was commercially available data collection was limited to the film technique or a manual diffractometer. Even when suitable single crystals were obtained, the procedures of structure determination were generally tedious. Nevertheless, many important key structural results were revealed by painstaking X-ray crytallography. These results firmly established the basic principles of structural relationships among many families of complex oxides.

It frequently happens that when the complexity of the structure and the size of the unit cell increase the results may be incomplete or inconclusive. Interpretation of the X-ray profiles obtained from either Guinier photographs or slow-scan diffractometry may not be totally conclusive and assignment of some crystallographic constants such as unit cell parameters and space group symmetry may turn out to be a

* See Chapter 8, Volume 1.

difficult and frustrating problem even when an authentic single crystal is in hand. If the material is disordered in some way, its nature cannot be revealed with certainty by means of X-ray methods. In this event other experimental approaches must be sought.

Transmission electron microscopy combined with selected-area electron diffraction has become the technique of choice for solving structural problems of crystals having extended defects.[9,10] It has been used to advantage in conjunction with X-ray diffraction in studies of these complex structures.

1.2.2. A Comparison between X-Ray and Electron Optical Methods

A comparison of these two methods points up the advantages and disadvantages of each.[11]

1.2.2.1. Wavelength

The wavelength of 100-kV electrons is 0.037 Å, approximately 1/40 that of X rays ($\lambda = 1.54$ Å for Cu $K\alpha$). From Bragg's law the scattering angles are much smaller than those for X rays. Above all, the radius of the Ewald sphere or sphere of reflections, $1/\lambda$, is larger for electron diffraction. When Bragg's law is satisfied for electrons the surface of the sphere where reciprocal lattice points fall is nearly planar. For this reason it is possible to record extensive sections of the reciprocal lattice directly with the crystal fragment remaining stationary. Equivalent patterns are obtainable by a more elaborate precession method in X-ray diffraction (the technique mechanically involves a coupled precession motion of the film and crystal specimen) which is capable of recording higher levels of the reciprocal lattice planes.

1.2.2.2. Scattering Factors

The interaction of electrons with atoms is about 1000 times greater than that of X rays. Because of this thin samples a few hundred angstrom thick are suitable for transmission electron diffraction. This is in contrast to X-ray single-crystal methods where samples several tenths of a millimeter thick are ordinarily used. Furthermore, the electron microscope has the ability to select very small areas of the crystal for the field of view of the microscope. Individual crystals or portions of crystals as small as 10^{-10} cm^2 in cross section are

sufficiently large to yield diffraction patterns of desirable quality. Furthermore, the diffraction pattern can be observed visually on a fluorescent screen and recorded on a photographic plate in just a few seconds compared with the many hours required for an X-ray pattern. This makes it possible to perform immediate adjustments to the orientations of a crystal while watching the change of the electron diffraction pattern.

The large scattering power of electrons has, however, other less favorable consequences. The maximum thickness of the specimen is about 2000 Å for most materials. This immediately raises the problem of sample preparation. The diffracted beams are further complicated by dynamic effects such as multiple reflections and inelastic scattering. As a result, the diffracted intensity bears no relationship to values expected for single or kinematic scattering. Because the variation with thickness is nonlinear, the observed intensities normally cannot be used directly as data for structure analysis.

Another unfortunate consequence of multiple scattering and the strong interaction of the incident electrons is that reflections formally forbidden by the systematic space group extinctions are observed[12] with appreciable intensity. Considerable care, therefore, must be taken in deriving symmetry from electron diffraction patterns.

The scattering of electrons is rather inelastic and a substantial amount of energy is transferred to the crystal causing radiation damage and phase changes due to heating or reaction. If the specimens are heat sensitive and unstable to electron beams, sample stages with special cooling systems are required. On the other hand, the microscope itself becomes an instrument for direct observation of transformations.

1.2.2.3. Charge

In contrast to X rays, electron beams are charged and image patterns can be highly magnified using magnetic focussing. By recording their images at a number of different but known orientations and comparing these to corresponding diffraction patterns, a great deal of structure information including that of various types of extended defects can be obtained.

With skilled application of modern high-resolution electron microscopic techniques some spectacular results have been achieved at 3 Å resolution.[13–15] In favorable cases point-to-point lattice

imaging at high magnifications provides direct structural information at the level of atomic resolution.

The successes in applying electron microscopy to CS systems are attributable to the stability of these compounds under the intense beams. It should be emphasized that this technique should be utilized in conjunction with X-ray diffraction. Without prior accumulation of firmly established structure data by the latter, the interpretation of the lattice images may be rather speculative and inconclusive. The conventional electron microscope does not possess the ability to record higher levels of the reciprocal lattice. However, if the crystal is tilted to obtain diffraction patterns from all accessible zones and the correction of intensity data due to the dynamic effects can be made, a structure determination can, in principle, be accomplished by electron optical methods alone.

2. Complex Structures Based on Crystallographic Shear

2.1. Introduction

2.1.1. Coordination Polyhedra, Crystallographic Shear, and Classification

Crystallographic shear structures thus far studied are principally oxides of the transition elements, Ti, V, Nb, Mo, and W. Their structures are best described in terms of cation coordination octahedra $[MO_6]$, the basic geometric entity common to all CS compounds. The simplest structure utilizing these octahedra is ReO_3, which can be derived by linking these identical units through corner sharing at all corners. Variations must be considered in which partial or complete linkages of higher constraint occur (i.e., edge sharing) in certain specific and systematic patterns depending upon the structures. Figure 1 shows some perspective views of these fundamental octahedral linkages: corner sharing, edge sharing, and face sharing.

Structurally, CS is introduced whenever the linkages between two fragments of a structure are altered from one type to another along some specific crystallographic direction. Alteration in linkages results in a change in the overall O/M ratio in these compounds. For example, an oxygen atom is effectively lost with respect to the bulk wherever there is a conversion of a corner-shared $[MO_6]$ to edge-shared octahedra or edge-shared to face-shared octahedra.

If the crystallographic shear planes are completely ordered, a new phase has formed. The new structure containing periodic recurrence

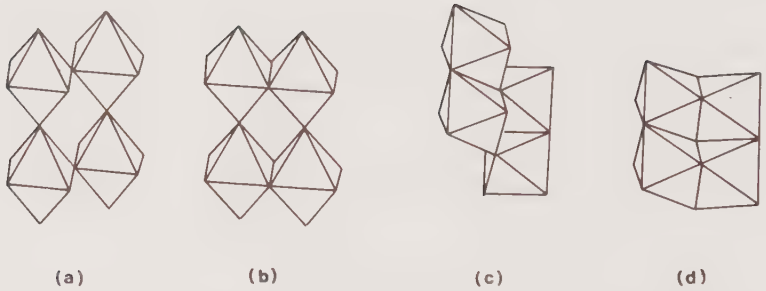

Fig. 1. Progressive conversion of corner-shared to face-shared octahedra. (a) Corner sharing as in ReO_3. (b) and (c) Edge sharing as rutile. (d) Face sharing as in corundum.

of CS planes will give diffraction patterns similar to those obtained from the original compound accompanied by a set of superstructure reflections appearing in directions parallel to the propagation of the CS planes. The fundamental reflections are contributed by the subperiodicity of the predominant arrangement of the cation octahedra characteristic of the parent crystal and the superstructure reflections are caused by the crystallographic translations of the CS planes.

On the other hand, if the CS planes are disordered, streaking and diffuse scattering will be observed depending on the dimension of disordering and the direction in recording. The term dimension can be interpreted as the number of noncollinear sets of CS planes, denoted by the superscript N of $(CS)^N$. For our discussion, compounds are classified according to the number of noncollinear sets of CS planes. Indices of $\{hkl\}$ and $\{\overline{hkl}\}$ or $\{2h2k2l\}$ are collinear. The N superscript represents a maximum dimension of space in which the CS planes reside and must be an integer between the value zero and three.

The absence of CS planes, $(CS)^0$, designates the parent structure upon which the CS structures are based. A value of one in the superscript implies a set of CS planes uniquely defined by (hkl). Common examples of this class are ReO_3-related oxides of molybdenum and tungsten and rutile-related dioxides of titanium and vanadium. Introducing an additional and noncollinear set of CS planes is characteristic of $(CS)^2$. Binary and ternary niobium oxides are typical examples in this class. These structures derived from the parent ReO_3 type are generally referred to as block structures. Compounds containing three sets of CS planes have not yet been discovered. The appearance of superstructure reflections is geometrically related to $(CS)^N$.

Compounds containing one set of CS planes, $(CS)^1$, have one structural feature in common. Ignoring the necessary distortions present in the structures, the oxygen atoms form a three-dimensional close-packed framework either in a hexagonal or cubic manner. The metal atoms regularly but not completely fill the octahedral holes created by these close-packed oxygen atoms. It is this partial filling which provides the flexibility to generate CS. Between boundaries in the structure the metal atoms occupy specific positions which change at the boundary. If this operation is repeated periodically, an ordered phase will be produced.

2.1.2. Space-Filling Polyhedra

The above description centers our attention on the cation octahedra and the linkages they possess. A contrasting approach, though less commonly used, provides a new insight in describing structures of this type. When anions are in a close-packed arrangement such as those considered here it is logical to focus on each individual anion. This is facilitated by considering the so-called anion space-filling polyhedra.[16]

A space-filling polyhedron, SFP, can be obtained by a set of planes bisecting the distances between the atom to be emphasized and all the nearest atoms of the same type; the convex figure formed by these planes is a polyhedron. The entire structure is generated when these identical SFP are stacked to fill space without voids. The word "stacked" is used loosely here. Actually the SFP are placed utilizing the symmetry operations permitted by the space group of the structure. The SFP for the cubic close-packed (ccp) lattice is the well-known rhombic dodecahedron (Figure 2a). For the hexagonal close-packed (hcp) lattice it can be formed by cutting the rhombic dodecahedron into two identical halves by a horizontal section and turning one-half through 180° about a vertical axis (Figure 2b).

The vertices where four edges (or faces) intersect represent the octahedral sites and those where three edges (or faces) meet represent the tetrahedral positions. These sites in our present discussion are occupied by cations. There are in total six octahedral sites and eight tetrahedral sites. However, each octahedral site is shared by six SFP. As a result there is only one octahedral site for each anion. By the same token there are two tetrahedral sites for each coordinated anion. For example, when all octahedral sites are filled the NaCl structure is obtained for ccp $[ClNa_{6/6}]$ and the NiAs structure for hcp $[AsNi_{6/6}]$.

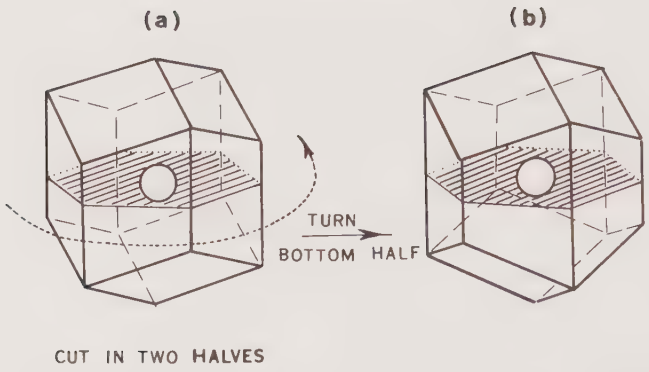

Fig. 2. Space-filling polyhedra (SFP) for : (a) A ccp lattice. (b) A hcp lattice. The hatched planes and the arrow in (a) indicate how the hcp SFP is obtained from the ccp SFP.

When tetrahedral sites are all filled in the ccp lattice the resulting structure is of $Li_2O = OLi_{8/4}$ type or, exchanging anions with cations, the antistructure $CaF_2 = CaF_{8/4}$ is obtained.

Some valuable extensions of this idea may be made. A layer of a structure can be constructed by placing the equatorial faces of identical SFP with filled octahedral positions in contact in an unlimited sheet (denoted by *C* for ccp and *H* for hcp, depending on the kind of SFP). Polytypism can then be considered as a variation in sequential stacking of layer *C* and layer *H*. A great variety of polytypic modifications such as SiC, ZnS, and CdI_2 (with obvious modifications) is thereby produced.

On the other hand, the CS structures are based on a single type of anion SFP throughout with partial filling of the octahedral sites. In a rutile structure only half the number of octahedral positions are occupied. However, in rutile-related CS structures the octahedral positions located near the CS planes are different from those in the bulk and, furthermore, an additional octahedral position is regularly filled. The latter feature clearly illustrates an increase of the coordination number (CN) of oxygen at the boundary and therefore the M/O ratio. The change in coordination direction only is characteristic of an antiphase boundary, whereas CS requires a change in CN. It should be noted that the coordination of the cation is unchanged throughout the entire structure since it occupies only octahedral sites.

2.1.3. The ReO_3 Structure Type as a Basis of Crystallographic Shear

The $(CS)^2$ compounds presently known are virtually all related to the ReO_3 structure type. ReO_3 has a very simple cubic structure which can be idealized as an infinite three-dimensional array of regular octahedra connected through common corners. Each oxygen is therefore a bridge between two metal atoms. The structure can be conveniently represented in projection along one of the cubic axes as an infinitely large chessboard of squares (Figure 3). Outlined squares correspond to filled octahedra and empty squares to voids between them. The voids represented by the empty squares form empty square tunnels in all three dimensions.

Looking down the body diagonal of this simple cubic ReO_3 structure, one discovers that the oxygen atoms form a framework derived from the ccp arrangement by the removal of one-quarter of the oxygen atoms. Each layer perpendicular to the body diagonal contains oxygen atoms arranged in an infinite Kagomé net. A Kagomé net is a special two-dimensional lattice; when the lattice points are completely connected through their shortest distance by straight lines a geometric pattern emerges composed of regular triangles and hexagons, each type of identical size. Each corner is then shared by two triangles and two hexagons in an alternating manner. Introducing lattice points at the centers of all the hexagons converts a Kagomé net into a hexagonal net. When the lattice points of the Kagomé net are

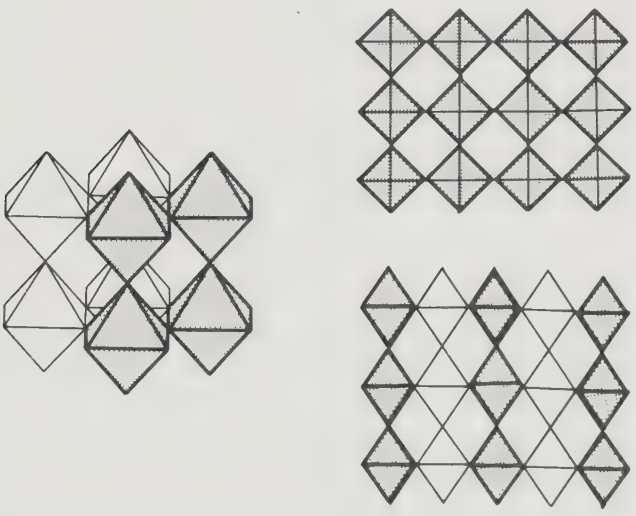

Fig. 3. Some representations of the ReO_3 structures.

occupied by oxygen atoms and these plane nets translate in an *ABCA* sequence, the oxygen framework of the ReO_3 structure is obtained.

There are two kinds of holes generated in this process: one smaller one with octahedral symmetry and one larger one which can be considered as a fusion of eight regular tetrahedra and six half-octahedra of equal sizes. When the smaller hole is completely filled by metal atoms the structure becomes ReO_3-like. When the larger hole is also filled by metal atoms the resulting structure is a perovskite.

It is interesting to note that nearly all the presently known $(CS)^2$ compounds are said to be related to the ReO_3 structure. An exception is Mo_8O_{23} and its family. Perhaps this partially complex oxygen framework facilitates CS in two dimensions.

2.1.4. Composition and Crystallographic Shear

The ideal composition of a CS compound may be obtained from a complete single-crystal structure determination by counting the number of each type of atom in the unit cell. The cumbersome chemical formula thus derived is preferable to the less informative one based on the O/M ratio. There are, however, obvious technical difficulties in confirming such a formula, such as those of distinguishing atoms of similar atomic numbers in an X-ray analysis and of deriving the composition uniquely by chemical analysis even from an authentic single-phase preparation. Some of these difficulties may be overcome by supplementing X-ray studies with electron optical methods. With skillful use of modern high-resolution electron microscopy the idealized structures of many of the complex phases, their compositions, and the nature of defects present have been reliably derived from diffraction patterns and lattice images.

In the $(CS)^1$ families[4,17] the cell composition depends on two factors: the orientation and the translation distance of the shear planes. The former controls the number of anions effectively removed from the parent structure with each shear, while the latter determines the frequency of shear.

The orientation and the translation distance of the shear planes can usually be defined from diffraction patterns alone. The orientation of the shear planes is specified by the Miller indices (hkl) or $\{hkl\}$,* most often expressed with respect to the parent structure. The distance

* The symbols used to designate directions and planes conform to the recommendation given on p. xi of Volume I of the *International Tables for X-Ray Crystallography.*

between two neighboring CS planes is expressed by the parameter D_{hkl}. It becomes clear that the variety of structures is due to the large number of ways of combining these two factors. For $(CS)^2$ compounds both the diffraction pattern and high-resolution lattice images are necessary for the clarification of their composition and defect nature.

To complete the description of a shear plane, it is also desirable to add a displacement vector quantity known as the shear vector in association with the shear plane (*hkl*). This vector quantity represents the crystallographic direction of displacement of two adjacent slabs across the CS boundary. It is denoted by the symbol [*pqr*]. The parameters *pqr* represent the fractional coordinates to which a portion of the structure is displaced relative to the origin and must be a close-contact oxygen-to-oxygen vector. They are often expressed with respect to the unit cell of the host structure. Because of the specific type of idealized oxygen framework mentioned above, the reciprocals of these parameters turn out to be integers, say *uvw*; consequently, a shear plane can be fully described by $[1/u, 1/v, 1/w](hkl)$. The first portion of the symbol denotes the shear vector and the second the orientation of the shear plane.

Thus the production of a CS plane involves the collapse of the parent structure by a shear vector which must be the position vector between adjacent oxygen atoms. Before and after shear the oxygen framework on either side of the shear plane retains its identity. As a result, the stacking sequence of oxygen is not altered by such operations and the framework of oxygen remains unchanged. Ultimately, the CS can be considered as a systematic filling of the available octahedral sites in an unchanging ccp or hcp oxygen lattice.

2.1.5. Derivation of Important Families of Crystallographic Shear

To begin our discussion of CS families three structures unrelated except for their anion framework are introduced: PdF_3, TiO_2, and α-PbO_2.

As mentioned earlier, the anions of the ReO_3 structure are in a ccp arrangement except that the center position, $\frac{1}{2}, \frac{1}{2}, \frac{1}{2}$, is empty. If a unit cell is twisted 60° about the body diagonal without breaking or distorting any intraoctahedral or interoctahedral connections and at the same time eliminating the Kagomé net by completing the hexagonal array of that oxygen layer, an idealized PdF_3 structure is obtained. The $[PdF_6]$ octahedra all retain corner sharing and the anions are in a hexagonal close-packed arrangement. The resulting

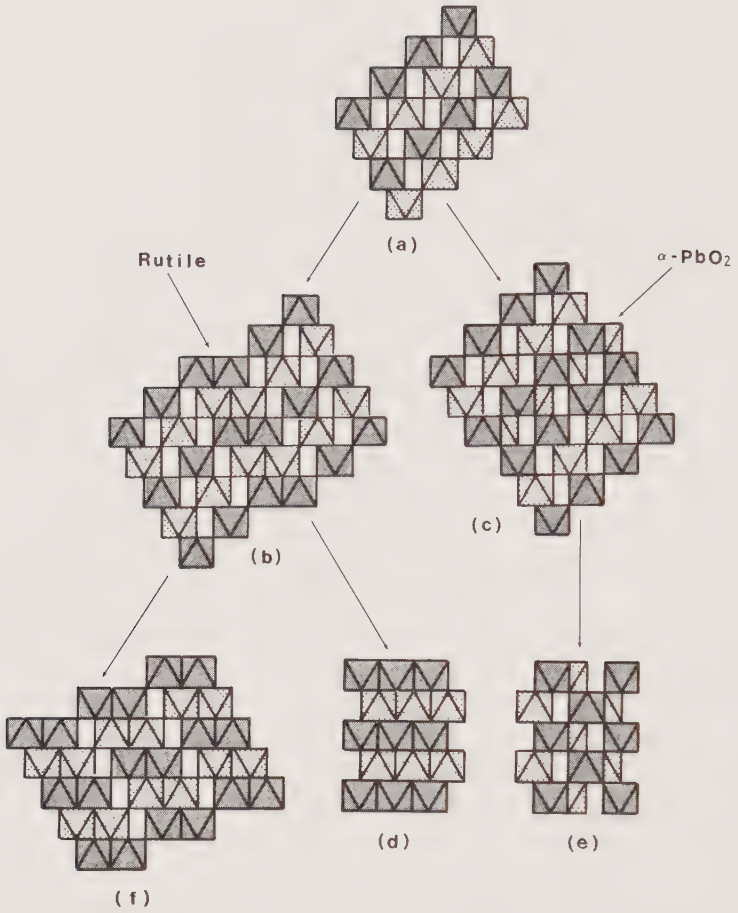

Fig. 4. Shear in PdF_3. (a) The PdF_3 structure type. (b) A single $\frac{1}{3}[12\bar{1}](100)_R$ shear in PdF_3. (c) A single $\frac{1}{3}[1\bar{2}1](001)_R$ in PdF_3. (d) The rutile structure type. (e) The α-PbO_2 structure type. (f) The structure of β-Nb_2O_5.

structure is rhombohedral $R\bar{3}c$ and has a unit cell volume three-quarters that of the equivalent ReO_3. It is therefore believed that the high-pressure form of ReO_3 would be the PdF_3 structure type. Figure 4(a) shows a block of PdF_3 structure type with filled cation octahedra outlined; the viewing direction is normal to the plane $(0\bar{1}1)$ of its rhombohedral cell. A projected presentation of joining octahedra on $(010)_H$ formed by a hexagonally close-packed anion arrangement is given in Figure 5; the subscript H denotes that the indices 010 are based on an hexagonal description. Such a presentation helps visualize the octahedra joined together in various ways in this projection. It also depicts the mutual relationship between structures when CS has taken place.

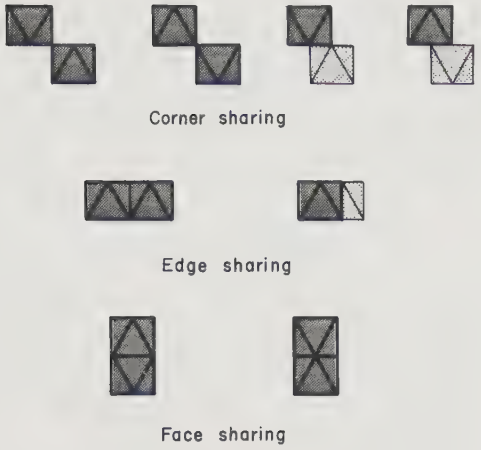

Fig. 5. Characteristic ways of joining octahedra within hexagonally close-packed atoms. (After Andersson and Galy[18].)

Attention is drawn to alternative ways of shearing the PdF_3 structure[18]—one by the shear operation $\frac{1}{3}[11\bar{2}](100)_R$ and the other by $\frac{1}{3}[12\bar{1}](001)_R$, where the subscript R refers to the rhombohedral system. Figure 4 shows these two modes of CS. By a single operation the first one generates a block of rutile with a width of two octahedra in edge sharing, whereas the second produces a block of α-PbO_2 with a width of two octahedra in corner sharing. Octahedra in edge sharing also occur in the latter case but are less easily recognized.

It should be noticed that these two operations are crystallographically nonequivalent despite the similarity in their notations. Their nonequivalence is best illustrated as follows. If the block of rutile (Figure 4b) is viewed in the direction parallel to $[011]_R$, only isolated rows in two levels connected by edge sharing are truly α-PbO_2 (Figure 4c); however, the adjacent rows, instead of being linked horizontally through corner sharing, are joined together in either all-step-up or all-step-down fashion throughout the entire block. Successive shear operations produce a rutile structure on the one hand and an α-PbO_2 structure on the other. They are shown in Figures 4(d) and 4(e).

Crystallographic shear results from a systematic displacement due to the elimination of specific oxygen planes and, of course, this is automatically accompanied by the reduction of the O/M ratio. It is obvious that these Wadsley defects are very likely to exist in those structures yielding intermediate compositions of MO_{3-x} between

PdF_3 and rutile structure types. If the crystallographic shear planes are in periodic repetition, a family of ordered structures with hypothetical composition M_nO_{3n-p} is obtained. The parameter p represents the number of shear planes occurring in the block length n octahedral units parallel to $(100)_R$. If the shear operation $\frac{1}{3}[11\bar{2}](100)_R$ is applied to the PdF_3 structure type alternatively, the structure of B-Nb_2O_5 in which $n = 2$, $p = 1$ is derived (Figure 4f).

In a similar way Wadsley defects and ordered structures can also be introduced between PdF_3 and α-PbO_2 structure types. The latter gives rise to intermediate compositions and generates a homologous series of structural formula identical to the one discussed above except that the layers of octahedra to be considered in determining the block length are now parallel to $(001)_R$.

A single crystallographic shear operation eliminating specific planes of oxygen in the case of the PdF_3 structure type produces a layer of octahedra each of which shares only one edge. Successive operations transform the structure completely either to a rutile or to an α-PbO_2 structure type isomorphous with the high-pressure form of rutile.

If a rutile or an α-PbO_2 structure type is allowed to continue the shear operation, higher constraint is introduced and face sharing between octahedra occurs after each CS operation, yielding blocks of idealized corundum structure (Al_2O_3). The corundum structure can be regarded as the ultimate CS structure descended from that of the PdF_3 structure type by either $\frac{1}{3}[11\bar{2}](100)_R$ or $\frac{1}{3}[12\bar{1}](001)_R$. Octahedral face sharing in a block of corundum is the result of shearing rutile in exactly the same way as led to edge sharing in a block of rutile when PdF_3 was sheared. As would be expected, a nonperiodic shear operation produces planar Wadsley defects while a periodic operation yields a family of ordered phases Ti_nO_{2n-p}, where n and p carry the same physical meaning mentioned before. Figure 6 summarizes the structural relationships of these compounds in terms of CS.

The known members of the homologous series derived from α-PbO_2 by the appropriate CS operation are the mixed oxides $(Cr, Fe)_2Ti_{n-2}O_{2n-1}$ with $n = 3, 4, 5$ and V_3O_5 structure.[19] In the Cr_2O_3–Fe_2O_3–TiO_2 mixed oxide system the formation of the M_nO_{2n-1} phases based on α-PbO_2 is markedly dependent on the Cr/Fe ratio; neither pure $Cr_2Ti_{n-2}O_{2n-1}$ nor pure $Fe_2Ti_{n-2}O_{2n-1}$ is stable by itself.

Examples in the current literature of CS compounds derived from the α-PbO_2 structure type are very limited. Attention is turned, therefore, to rutile and its CS compounds.

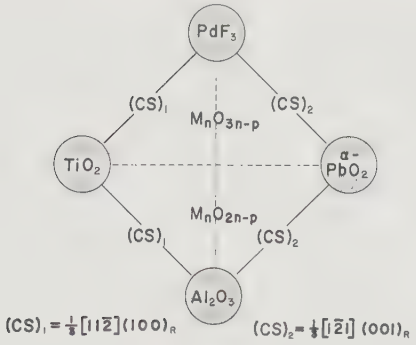

Fig. 6. Conversion pathways in the formation of corundum-type from PdF_3-type structure.

2.2. Compounds Containing One-Dimensional Crystallographic Shear

2.2.1. The Rutile-Related Family

A large number of dioxides crystallize with the rutile structure named after one of the mineral forms of TiO_2. Rutile is tetragonal with space group $P4_2/mnm$ of unit cell dimensions **a** = 4.594 Å, **c** = 2.958 Å. There are two Ti atoms located at 0, 0, 0 and $\frac{1}{2}, \frac{1}{2}, \frac{1}{2}$ and four O atoms at $\pm(x, x, 0; x + \frac{1}{2}, \frac{1}{2} - x, \frac{1}{2})$, where $x = 0.3053$. Its structure, depicted in Figure 4(d), consists of rectilinear chains of edge-shared $[TiO_6]$ octahedra joined by corner sharing to similar ribbons such that the orientation of adjacent ribbons differs by $\pi/2$ radians about the **c** axis. Projection along **a** suggests that the oxygen atoms approximate the hcp.

The oxygen framework shall be idealized to remove the puckering by flattening either the oxygen layers parallel to (100) or to (010) so that a perfect hcp arrangement is generated. The titanium atoms remain filling alternate rows of octahedral interstices parallel to **c**. Figure 7 shows the (100) layer of idealized rutile. Open circles represent the oxygen atoms in hcp arrangement, whereas solid circles denote the titanium atoms located above the oxygen layer but occupying alternate rows of octahedral interstices. Idealization of the model of rutile and its related structures in this way greatly facilitates visualization of the derived structures and CS.

The study of the homologous series of reduced oxides with structures derived from rutile displays several facets[4,20] in the understanding of the crystallographic and chemical behavior of

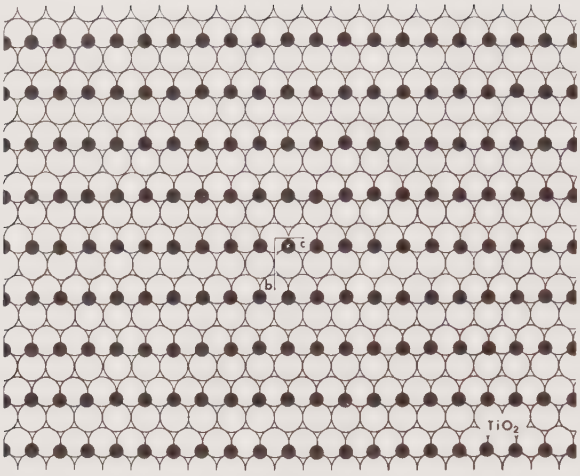

Fig. 7. A (100) layer of idealized rutile. (After Bursill and Hyde[4].)

Wadsley defects in solids. Nonstoichiometry of these compounds is accommodated by Wadsley defects even in very slightly reduced rutile.

Certain geometric operations form the basis of the structural principles which govern formation of the many types of CS and other planar faults. Figure 8 illustrates several possible operations. The left-hand models show the required patterns of vacant oxygen sites and the right-hand models show the structures after the operations are completed. Note that only one layer of anions plus cations is shown. To complete the three-dimensional structures, adjacent layers must be displaced by $\frac{1}{2}[11\bar{1}]_r$ of rutile (the subscript r refers to the rutile system). In every case, the displacement vector is $\frac{1}{2}[0\bar{1}1]_r$, precisely the vector between two oxygen atoms.

The first operation represented by $\frac{1}{2}[0\bar{1}1](011)$ is a special shear (Figure 8a). It involves no elimination of anions because the displacement vector is parallel to the shear plane across which it operates. Therefore this type of operation produces no change of stoichiometry. The "fault" is termed an antiphase boundary, APB. With an APB introduced, the connectivity of the $[TiO_6]$ octahedra remains unchanged; there are still six corner sharings to two edge sharings throughout. However, continued chains of edge-shared octahedra originally parallel to the **c** axis ($\mathbf{c}_r$ chains) are now broken into steps. If each step is denoted by A, the trace of the APB can be represented

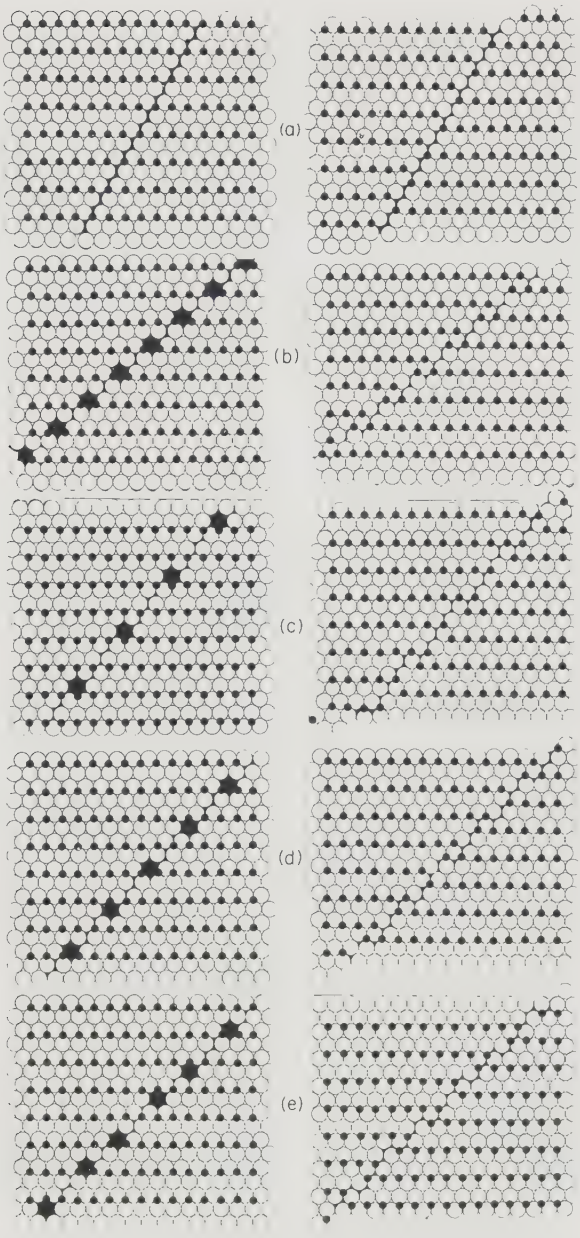

Fig. 8. Various APB and CS operations on idealized (100) layers. The left-hand models show the required pattern of vacant oxygen sites; the right-hand models show the structures after the operations are completed. In (a)–(e) the displacement vector is the same, $\frac{1}{2}[0\bar{1}1]$. (a) The APB (011). (b)–(e) The CS operations on (121), (132), (253), and (374) respectively. (After Bursill and Hyde[4].)

by

$$\cdots AAAAA \cdots$$

If the operation is repeated on every second (011) anion plane, the α-PbO_2 structure type, the high-pressure polymorph of rutile, is obtained. Repetition on every (011) anion plane generates rutile in a twin orientation.

The operation of $\frac{1}{2}[0\bar{1}1](121)$ (Figure 8b) creates a quite different type of fault. The **c** chains are folded back on themselves in a Z shape which shall be denoted by a Z. The trace of the CS in plane $(100)_r$ is therefore represented by

$$\cdots ZZZZZ \cdots$$

Each Z, consisting of an APB plus an extra "interstitial" cation, introduces one face-shared pair of $[TiO_6]$ octahedra normal to the layer. In fact, each of the $[TiO_6]$ octahedra located at this boundary is highly constrained by an environment of seven neighboring octahedra—three corner shared, three edge shared, and one face shared. Clearly, operations of this type cause an increase in the titanium-to-oxygen ratio. If the operation is repeated on one in every $2n$ anion planes along $\mathbf{c}_r$, the ordered Ti_nO_{2n-1} homologous series is obtained. The known members in the series are reported to have n ranging from three to ten. The member Ti_6O_{11} is represented in Figure 9. Each

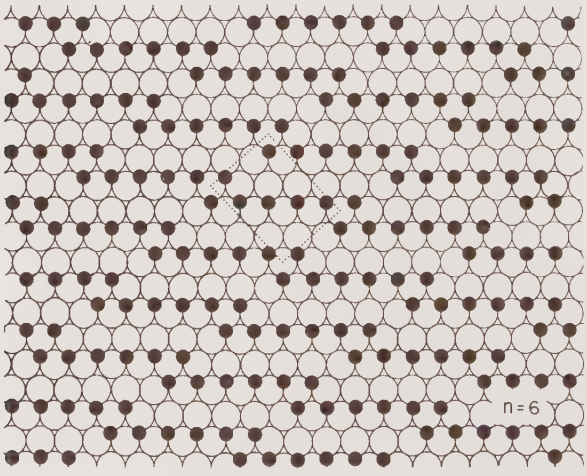

Fig. 9. Idealized (100) layer of (121) CS structure Ti_nO_{2n-1} with $n = 6$. (After Bursill and Hyde[4].)

member differs from the other only in the length of the edge-shared rutile-type chains. Vanadium oxides and ternary oxides of titanium and chromium also present homologous series in nearly the same composition range. They are V_nO_{2n-1} with $4 \leq n \leq 8$ and $Cr_2Ti_{n-2}O_{2n-1}$ with $6 \leq n \leq 11$. Structures of these members are reported to be isostructural with the corresponding titanium oxides.

In the case of $\frac{1}{2}[0\bar{1}1](132)$ (Figure 8c) the APB and (121)-type steps alternate along the trace of the CS plane. Following our notation, the trace can be described as

$$\cdots AZAZAZAZ \cdots$$

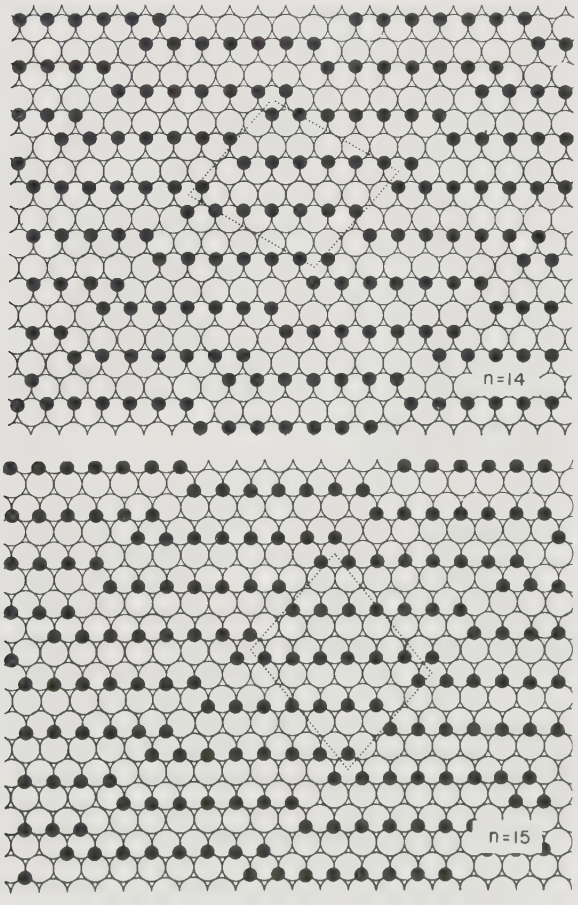

Fig. 10. Idealized (100) layers of (132) CS structure Ti_nO_{2n-1} with $n = 14$ and 15. (After Bursill and Hyde[4].)

Regular repetition at one in every $2n$ (132) anion planes along $\mathbf{c}_r$ yields another set of ordered structures Ti_nO_{2n-1}. Figure 10 shows two possible members of the series with $n = 14$ and 15. Depending on whether $n = 2k$ or $2k - 1$ (k being an integer), chains of the edge-shared octahedra $[TiO_6]$ originally parallel to $\mathbf{c}_r$ are joined together to form three types of continuing chains:

$$\cdots A\text{–}Z\text{–}A\text{–}Z\text{–}A \cdots \qquad \text{(type 1)}$$

$$\cdots Z\text{–}Z\text{–}Z\text{–}Z\text{–}Z \cdots \qquad \text{(type 2)}$$

$$\cdots A\text{–}A\text{–}A\text{–}A\text{–}A \cdots \qquad \text{(type 3)}$$

If n is even, only type 1 occurs; these identical chains are composed of subchains of $k = n/2$ edge-shared $[TiO_6]$. A dash (–) in type 1 represents a chain with k octahedral units. There are two different kinds of subchain terminations, one with A and the other with Z (heterogeneous). If n is odd ($2k - 1$), types 2 and 3 are present alternately joined together side by side. Those of type 2 are stepped by Z only and are composed of subchains with k units of $[TiO_6]$. On the other hand, those of type 3 are exclusively stepped by an APB; they are composed of subchains with length $k - 1$. The dashes for types 2 and 3 represent subchains of slightly different lengths and each type is terminated by the same kind of faulting step. However, the experimental observations suggest that structures with odd n do not occur (at least for $n \leq 22$) because the faulting steps are less uniformly distributed.

In the case of $\frac{1}{2}[0\bar{1}1](253)$ (Figure 8d) the sequence of steps along the trace of the CS plane becomes

$$\cdots AZZAZZAZZA \cdots$$

Two oxygens are removed per repeat unit along the CS plane. Regular repetition of the operation at one in every $2n$ (253) anion planes along $\mathbf{c}_r$ produces a new homologous series Ti_nO_{2n-2}. Representatives with $n = 24, 25$, and 26 are shown in Figure 11. The sequence of steps along the chains depends again on the character of n (i.e., whether $n = 3k$, $3k + 1$, or $3k - 1$, k being an integer). For $n = 3k$ the most uniform arrangement occurs; each subchain is composed of k numbers of edge-shared $[TiO_6]$ and the sequence along each chain runs

$$\cdots A\text{–}Z\text{–}Z\text{–}A\text{–}Z\text{–}Z\text{–}A \cdots \qquad \text{(type 4)}$$

For $n = 3k + 1$ the step sequence is similar to that of type 4 except that the homogeneous subchain intervals between two Z (terminating units are included) are $(k + 1)$ units—one octahedral unit longer than

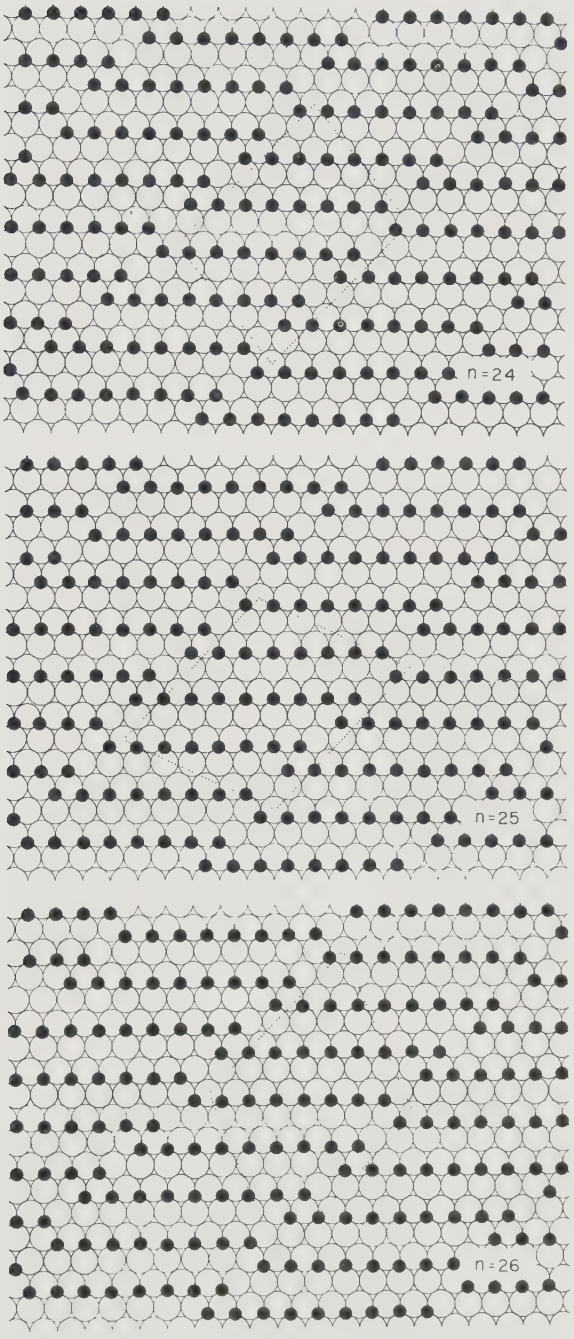

Fig. 11. Idealized (100) layers of (253) CS structure Ti_nO_{2n-2} with n = 24, 25, and 26. (After Bursill and Hyde[4].)

TABLE 1
Dependence of Faulting Z

Number of Z units	Step sequence along the trace	Resulting CS direction	Homologous series produced
0	$\cdots$AAAAAAAAAAAA$\cdots$	(011)	Ti_nO_{2n}
1	$\cdots$AZAZAZAZAZAZ$\cdots$	(132)	Ti_nO_{2n-1}
2	$\cdots$AZZAZZAZZAZZ$\cdots$	(253)	Ti_nO_{2n-2}
3	$\cdots$AZZZAZZZAZZZ$\cdots$	(374)	Ti_nO_{2n-3}
4	$\cdots$AZZZZAZZZZA$\cdots$	(495)	Ti_nO_{2n-4}
∞	$\cdots$ZZZZZZZZZZ$\cdots$	(121)	Ti_nO_{2n-1}

the heterogeneous subchain. When $n = 3k - 1$, two step sequences are present. They are identical to the two described in (132) CS structures for $n = 2k - 1$. The only difference is that the structures in this case are composed of two-thirds of type 2 and one-third of type 3.

It appears that the direction of the CS plane is a function of the step sequences along its trace. We can generalize the above results as in Table 1. The orientations (hkl) can be resolved into

$$(hkl) = p(121) + (011) = (p, 2p + 1, p + 1)$$

where p is an integer. The ordered structures resulting from periodic repetition of the CS have the stoichiometries Ti_nO_{2n-p}.

However, in contrast with the generalization given above, one or more consecutive APB's may occur, at least in principle, along the CS plane; this would yield a complementary set of sequences (Table 2).

TABLE 2
Dependence of Antiphase Boundaries (APB)

Number of APB's	Step sequence along the trace	Resulting CS direction
0	$\cdots$ZZZZZZZZZZ$\cdots$	(121)
1	$\cdots$ZAZAZAZAZAZ$\cdots$	(132)
2	$\cdots$ZAAZAAZAAZAAZ$\cdots$	(143)
3	$\cdots$ZAAAZAAAZAAAZ$\cdots$	(154)
4	$\cdots$ZAAAAZAAAAZAAAA$\cdots$	(165)
∞	$\cdots$AAAAAAAAAAAA$\cdots$	(011)

TABLE 3
Observable CS Planes with $(hkl) = p(121) + q(011)$

	p							
q	0	1	2	3	4	5	6	7	8
0		121	121	121	121	121	121	121	121
1		132	253	374	495	5, 11, 6	6, 13, 7	7, 15, 8	8, 17, 9
2		—	132	385	253	—	374	—	495
3		—	—	132	—	—	253	—	—
4		—	—	—	132	—	—	—	253
5		—	—	—	—	132	—	—	—
6		—	—	—	—	—	132	—	—
7		—	—	—	—	—	—	132	—
8		—	—	—	—	—	—	—	132

The orientations of the CS planes change and can be resolved into

$$(hkl) = (121) + q(011) = (1, 2 + q, 1 + q)$$

where q is an integer. Since the APB operation involves no elimination of anions, the ordered structures resulting from repetition of the CS have the stoichiometries Ti_nO_{2n-1}.

Obviously a completely general CS plane (hkl) can therefore be resolved into a linear combination of two basic components—an irreducible shear plane (121) and an APB (011). Mathematically, we have

$$(hkl) = p(121) + q(011) = (p, 2p + q, p + q)$$

The ordered structures have the generic formula Ti_nO_{2n-p} independent of the integer q. Table 3 lists some of the observable CS planes with $p, q \leq 8$.

Crystallographic shear planes are most easily characterized by means of electron diffraction coupled with lattice fringe imaging of intermediate resolution. Only CS plane with $q \leq 2$ (Table 3) have been actually observed. It should be stressed that all planes $(hkl) = p(121) + q(011)$ lie in the $[1\bar{1}1]$ zone and the ability to identify the indices of the CS plane depends upon the attainment of this zone. The stoichiometry of the ordered phase depends not only on the CS indices but also on their periodic separations, which are also determinable with certainty from the superlattice pattern in $[1\bar{1}1]$ zone. In the rutile system (CS)[1] the superlattice patterns become super-

lattice rows parallel to the reciprocal lattice vector $\mathbf{r}^*_{hkl}$; the indices (hkl) are, of course, referred to the basic rutile lattice. Along each superlattice row the diffraction spots are densely spaced with a separation corresponding to the interplanar spacing D. If there were no shear operation implying displacement of $\frac{1}{2}[0\bar{1}1]$, the interplanar spacing D would have been equal to n times d_{hkl}, where the parameter d_{hkl} is the corresponding interplanar spacing with indices specified by (hkl) in the regular TiO_2 structure. However, the shear operation shortens the interplanar spacing D by an amount corresponding to the CS plane. From elementary crystallography this quantity can easily be determined by the scalar product of the displacement vector and the reciprocal lattice vector of the CS plane:

$$\tfrac{1}{2}[0\bar{1}1] \cdot (hkl) = \tfrac{1}{2}[0\bar{1}1]\{p(121) + q(011)\} = \tfrac{1}{2}[0\bar{1}1] \cdot p(121) = -\tfrac{1}{2}p$$

The actual interplanar spacing should then be

$$D = d_{hkl}(n - \tfrac{1}{2}p)$$

This relationship illustrates how the stoichiometry of the ordered phases can be correlated with the experimental parameters.

Interesting results have been obtained from less ordered specimens in the series Ti_nO_{2n-1}.[21] For CS on $\{121\}$, epitaxial intergrowth of adjacent n values (7 with 8 and 8 with 9) has been observed in samples prepared by arc-melting titanium and titanium dioxide. Mixtures of this sort can produce compositions intermediate to those obtained from members of adjacent n's. For a CS on $\{132\}$, polysynthetic twinning is frequently displayed in the region of $10 \leq n \leq 36$; moreover, members having different CS planes may coexist together.

As in this series, Ti_nO_{2n-1}, the one with CS on (253) corresponding to Ti_nO_{2n-2}, also covers a relatively large composition range (i.e., $28 \leq n \leq 48$). In addition to the epitaxial intergrowth of adjacent n values, intermediate compositions can be generated through mixing various indices of CS planes along the trace. Such a trace sequence may, for instance, consist of alternate segments of (132) and (253) producing an apparent CS parallel to (385). The trace of the complex CS plane can be written as

$$\cdots|ZAZZA|ZAZZAZAZZA\cdots$$

Experimental observations of lattice images reveal that (385) CS planes (where $p = 3$, $q = 2$) are indeed segmented in this manner rather than having a "polarized" pattern such as $|ZZZAA|$. Likewise, more complex CS planes, for example ($p = 2$, $q = 3$), would take a

similar mixed mode:

$$\cdots|AZAAZ|AZAAZAZAAZ\cdots$$

Clearly, it is possible to invent perfectly ordered structures to accommodate any conceivable composition. With a continuous spectrum of compositions prepared from various types of mixed CS planes one may, in principle, be able to identify the composition of any specific CS plane.

2.2.2. The ReO_3- and MoO_3-Related Families

2.2.2.1. Introduction

Molybdenum trioxide and the corresponding isostructural tungsten trioxides present an interesting family of CS structures.[22,23] A description of these is greatly facilitated by regarding them as composed of cation polyhedra sharing corners or edges; face sharing is unknown in these structures. Although cation octahedra are the most frequently occurring type of coordination polyhedra, tetrahedra and pentagonal bipyramids are also found. When discussing CS in this system many of the oxides are classified with either the ReO_3 or the MoO_3 structure type.

There are only two members known in the binary system Mo–O: Mo_8O_{23} and Mo_9O_{26} related to ReO_3 and belonging to the series M_nO_{3n-1} corresponding to $n = 8$ and 9, respectively. In the ternary system Mo–W–O several more members corresponding to $n = 8$–12 and 14 have been observed. However, in the tungsten oxide system $W_{20}O_{58}$, $W_{40}O_{118}$, and $W_{50}O_{148}$ are the only known members of a similar series, M_nO_{3n-2}. The second family is based on a unique layer structure, MoO_3; it includes $Mo_{18}O_{52}$ and a related homologous series.

In addition to these there is a family based on a mixed polygonal network in which three-to-six-membered rings can be recognized. When these networks are stacked on top of each other to form three-dimensional structures the planar rings become tunnels running through the structures parallel to the short axis. However, CS has not been observed in these compounds.

2.2.2.2. The ReO_3-Related Family

The structures in an ReO_3-related family retain the basic ReO_3 connections throughout in all three crystallographic directions.

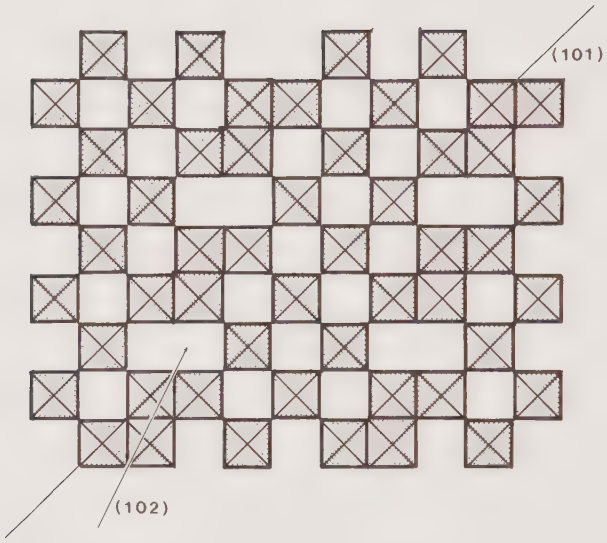

Fig. 12. The crystal structure of Mo_8O_{23} viewed along the short axis. (After Kihlborg[23].)

Distortion of the cation octahedra, although not as serious as in the other family, is still considerable. In any case it is profitable to view them as regular octahedra.

There are two ways of connecting ReO_3-type slabs to form the three-dimensional structures. In the first case the slabs are interconnected by mutual edge sharing between octahedra laying at the slab boundaries. Oxides with this type of structure are Mo_8O_{23} and Mo_9O_{26}, both of which belong to the homologous series Mo_nO_{3n-1} where $n = 8$ and 9. Figure 12 shows the structure of Mo_8O_{23} viewed along the short axis. In terms of the ReO_3 structure type, Mo_8O_{23} is formed by CS $\frac{1}{2}[10\bar{1}](102)$. The higher member in the same series, Mo_9O_{26}, can be produced by the same CS operator; the only difference is in the width of the basic slab. Other members produced in the same way might be expected; however, it is necessary to incorporate tungsten into the system in order to obtain homologues with $n > 9$. Known members in the mixed oxide systems correspond to $n = 8$–12 and 14. When tungsten becomes the major component, oxides with $n > 14$ have been observed but are difficult to characterize with X-ray analysis.

There is an obvious difficulty in identifying the CS plane indices. A more complete analysis of the CS structures, particularly those

accompanied by Wadsley defects, must rely on electron optical methods. In addition to the CS plane (102) which has just been discussed in connection with the Mo_8O_{23} structure, two other low-index shear planes are frequently encountered; they are (103) and (001), each with the same displacement vector $\frac{1}{2}[10\bar{1}]$. There is an exact analogy in the description of crystallographic shear between these ReO_3-related systems and those based on rutile. In the present case a permissible CS plane of indices ($h0l$) can be resolved into two basic components—an irreducible shear plane (001) responsible for the composition change and the (101) APB. The permissible CS planes are

$$(h0l) = p(001) + q(101) = (q, 0, p + q)$$

where p and q are positive integers or zero. The ordered structures therefore have the generic formula M_nO_{3n-p} independent of the coefficient q. For (102) CS, $p = 1$ and $q = 1$; for (103), $p = 2$ and $q = 1$; and for (001), $p = \infty$ and $q = 1$.

The indices $(p + q)$ and q are physically interpretable: The first quantity represents the number of edge-shared pairs of cation octahedra in unit periodicity and the second denotes the number of edge-sharing "groups" in the CS plane. For example, if $p = 3$ and $q = 2$, the CS plane is parallel to (205) and along this shear plane groups of four and six edge-shared octahedra alternate; each group when consisting of more than a pair of edge-shared octahedra appears in a finite zigzag slab.

Conceivably any intermediate CS plane ($h0l$) analogous to the CS planes (hkl) in the rutile-related system can be considered as a combination of the end members (101) and (001). The intermediate CS structures would be ordered intergrowths of columns of the primary structures MO_3 and M_nO_{3n-2}. For positive identification of any permissible ($h0l$) the zone [010] must be attained. The corresponding interplanar spacing between two successive CS planes would be

$$D = d_{h0l}(n - \tfrac{1}{2}p)$$

and there will be $(n - \frac{1}{2}p)$ superlattice spots along the reciprocal lattice vector $\mathbf{r}^*_{h0l}$.

The observations made by means of electron optical studies are equally interesting in the ReO_3-related systems. CS planes such as $\{102\}$ in slightly reduced WO_3 are observed aggregated into small parallel groups on four different orientations: (102), $(10\bar{2})$, (201), and $(20\bar{1})$. Coexistence of different CS planes is also possible, for example,

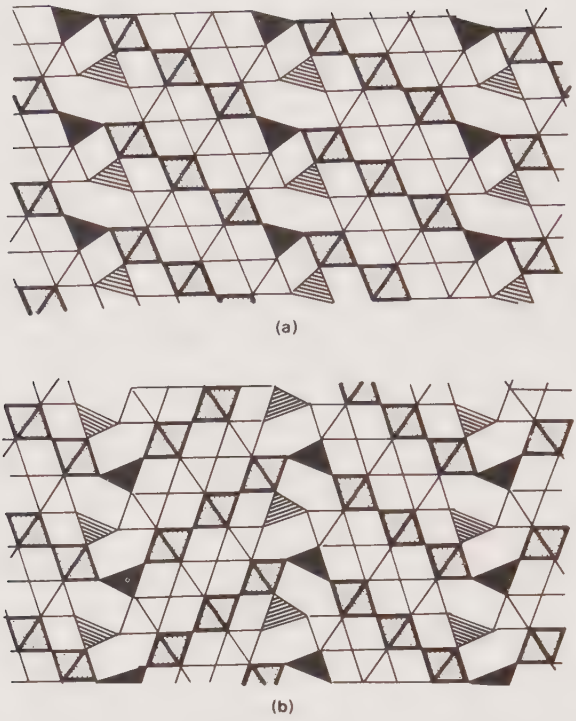

Fig. 13. The crystal structure of Mo_4O_{11}. (a) Monoclinic. (b) Orthorhombic. Slabs of ReO_3 type (see Figure 3) are connected by MoO_4 tetrahedra (black and heavily hatched at two levels, respectively). (After Kihlborg.[23])

in WO_3, (102) CS with $14 \leq n \leq 30$ is found together with (103) CS having $13 \leq n \leq 26$. Ternary tungsten oxides $(W, M)O_{3-x}$ with M = V, Nb, and Ta and $0 \leq x \leq 0.1$ display similar behavior.

In joining the ReO_3 slabs an alternative connection can be achieved through tetrahedra. This geometric variation is utilized by both polymorphic modifications of Mo_4O_{11}, monoclinic and orthorhombic (Figure 13). The essential difference between the two forms lies in the relative orientation of adjacent slabs. To denote the local orientation of the corner-shared octahedra $[001]_{ReO_3}$ is used. In the monoclinic form the orientations are invariant from one slab to the other. On the other hand, in the orthorhombic form the local $[001]_{ReO_3}$ changes its orientation from one slab to another producing an overall twofold screw axis along **a**.

The twofold screw axis originally present in each slab in the direction parallel to **b** is unaffected. These two nonintersecting ortho-

gonal screw axes generate (by group theory) a third screw axis, yielding the orthorhombic space group $P2_12_12_1$. It is theoretically possible to form a homologous series with this type of structure by varying the width of the slabs but such phases have not been observed. Perhaps polysynthetic twinning generated from these two polymorphic forms would be more likely to occur.

2.2.2.3. The MoO_3-Related Family

As pointed out earlier, a second family is based on the structure of MoO_3. It has orthorhombic symmetry with space group Pbnm and unit cell dimensions **a** = 3.96 Å, **b** = 13.86 Å, and **c** = 3.70 Å, $Z = 4$. The compound is generally regarded as having a layered structure. Two layers of octahedra sharing all equatorial corners as in ReO_3 are joined together by sharing edges to form a composite layer two octahedra thick. These composite layers of infinite dimensions (Figure 14) are parallel to the (010) plane and the successive layers are stacked such that each of the free apices in one layer pointing upward complete an "empty octahedron" with the tetragonal pyramidal hole present in the layer above.

Since the composite layer consists of two sublayers of ReO_3 type, the MoO_3 structure when projected on the (100) plane reveals zigzag chains of octahedra running in the [001] direction. Each octahedron has one corner unshared by other octahedra corresponding to an oxygen atom bonded to only one metal atom. In addition, two oxygen atoms are shared between two octahedra and three oxygen atoms are common to three octahedra, giving rise to the correct oxygen stoichiometry: $3 \times \frac{1}{3} + 2 \times \frac{1}{2} + 2 = 3$.

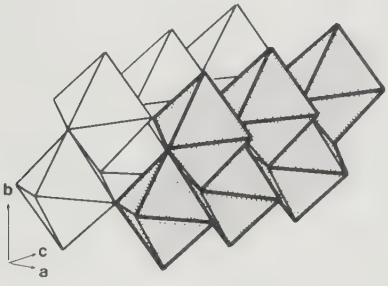

Fig. 14. The crystal structure of MoO_3 considered as built up of MoO_6 octahedra. (After Kihlborg.[23])

The oxygen framework of MoO_3 when visualized along the $[31\bar{3}]$ direction approximates a ccp arrangement although the distortion of the octahedral coordination around the molybdenum atom is considerable. If we assume the oxygen radius to be $r_O = 1.4$ Å, the unit cell dimensions of the idealized MoO_3 would be $\mathbf{a} = 2\sqrt{2}r_O = 3.06$ Å, $\mathbf{b} = 6\sqrt{2}r_O = 11.89$ Å, and $\mathbf{c} = 2\sqrt{3}r_O = 3.96$ Å^3. The oxygen framework is in strict close packing. The extent of oxygen packing may be expressed in terms of the unit cell volume divided by the number of oxygen atoms in the unit cell. This quantity, V/n, has the value 15.5 Å^3 for the ideal model and 16.91 Å for the actual structure.

$Mo_{18}O_{52}$ is triclinic[24] with space group $P\bar{1}$ and unit cell dimensions $\mathbf{a} = 8.15$ Å, $\mathbf{b} = 11.89$ Å, $\mathbf{c} = 21.23$ Å, $\alpha = 102.67^0$, $\beta = 67.82°$, and $\gamma = 109.97°$. The idealized structure can be derived from that of MoO_3 by dividing each composite layer into infinite, step-edged strips in the direction of [010] as shown in Figure 15. The width of the slab is determined by the number of octahedra within one zigzag chain (indicated by an arrow in Figure 15). In the case of $Mo_{18}O_{52}$ this number is 36. The chains are joined in the following manner: Six octahedra at each end of every zigzag chain share edges with another six octahedra of a chain from the neighboring slab with a total of 11 octahedral edges shared between two chains. It is conceivable that a sharp increase in edge sharing is energetically unfavorable due to electrostatic repulsion. In this event, any possible

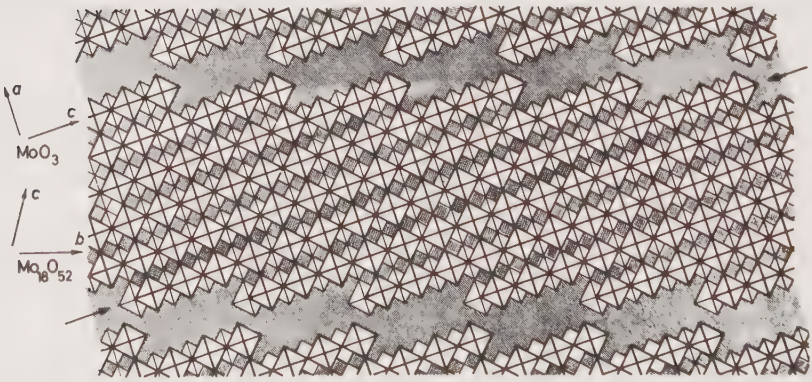

Fig. 15. An idealized MoO_3-type layer divided into strips of the type occurring in $Mo_{18}O_{52}$. One zigzag row of octahedra at two levels sharing edges is indicated by arrows. The orientation of the axes of MoO_3 and $Mo_{18}O_{52}$ is shown to the left. (With permission from Kihlborg.[24])

rearrangement of the metal atoms which tends to reduce this edge sharing would be favored. Indeed, in the real structure the molybdenum atom in the second outermost octahedron at the end of each chain moves into a tetrahedral site. As a result, there is a drastic reduction of ten in the number of edges shared between the 12 polyhedra joining the chains of two different strips; this gives a net increase of only one shared edge per 36 molybdenum atoms when going from MoO_3 to $Mo_{18}O_{52}$. Despite such a deviation from the idealized structure and the severe distortion of some octahedra, the oxygen framework still maintains an approximate ccp. The extent of oxygen packing, V/n, now has the value 17.11 Å^3, only slightly higher than that corresponding to MoO_3.

The ideal $Mo_{18}O_{52}$ structure can be regarded as a shear structure of MoO_3[17] with the CS operator $\frac{1}{6}[3\bar{1}0](35\bar{1})_{MoO_3}$.* The oxygen sites formally eliminated from MoO_3 and the resulting pattern of filled interstices in $Mo_{18}O_{52}$ are indicated in Figures 16(a) and 16(b). Note that the anion lattice is recovered after the shear operation. The unit cell transformation matrix from MoO_3 to $Mo_{18}O_{52}$ can be worked out as $/\frac{1}{2}, -\frac{1}{2}, -1/1, 0, 3/\frac{9}{2}, \frac{1}{6}, -3/$. Of the four close-packed planes, projection onto $(13\bar{1})$ is used because both the displacement vector and the **a** axis lie in this plane.

As may be recalled, each zigzag chain of the ideal $Mo_{18}O_{52}$ structure consists of 2×18 octahedra. If this number is varied infinitely, many hypothetical structures could be derived which differ only in the width of the basic strips. Such structures would form a homologous series Mo_nO_{3n-2} where $2n$ is the number of octahedra in a zigzag chain. In fact, the existence of four new members, $n = 19$–22, have recently been revealed by electron optical studies.

In considerably disordered samples Wadsley defects are observed in a variety of orientations $\{130\}$ and many of them are planar only over very restricted distances. It is also possible to vary the number of octahedra involved in edge sharing at each end of a zigzag chain. This is equivalent to changing the direction of the shear plane. If this number is designated $2m$, which is six in the case of $Mo_{18}O_{52}$, the more general formula Mo_nO_{3n-m+1} can be obtained.[24] Indices are referred to MoO_3 and the number n has the same physical meaning as before.

In spite of the possibly infinite number of CS structures, only three families of different m have been observed so far. In addition to

* The displacement vector is $[\frac{1}{2}\mathbf{a} - \frac{1}{7}\mathbf{b}]$ in the actual structure.

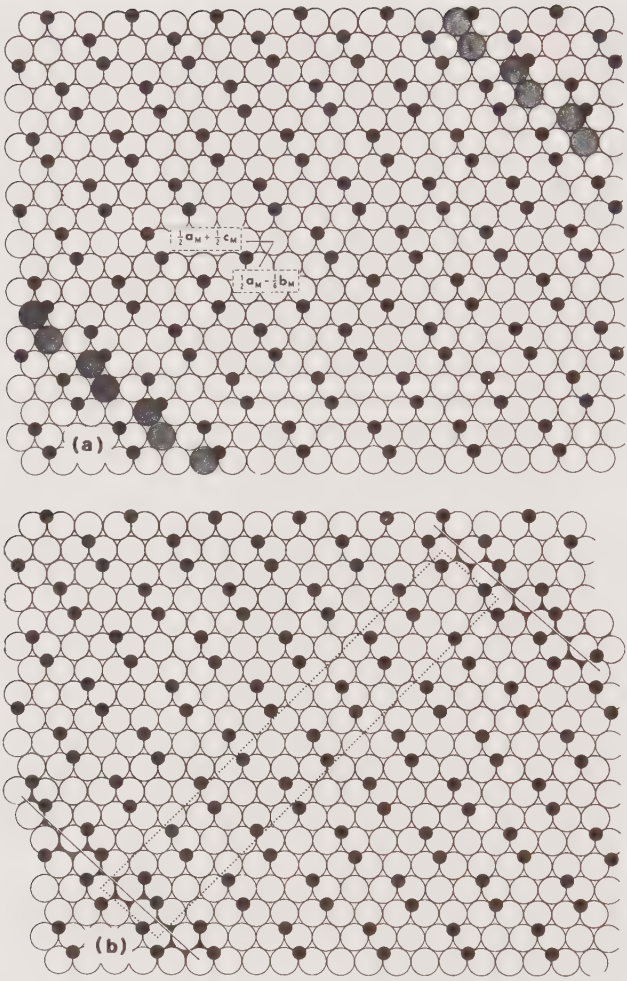

Fig. 16. Pattern of filled octahedral interstices in the ideal fcc anion lattices of (a) MoO_3 and (b) $Mo_{18}O_{52}$. Larger shaded circles in (a) indicate anion sites eliminated formally by the CS operation $\frac{1}{6}[3\bar{1}0](35\bar{1})$. (After Bursill.[17])

$Mo_{18}O_{52}$ (ζ phase) and four other members observed in recent electron optical studies ($n = 19$–22)[17] ($m = 3$), structures of two additional phases, ζ' and ζ'', are expected to be quite similar to that of ζ. They are, respectively, $Mo_{13}O_{38}$ ($m = 2$) and $Mo_{26}O_{75}$ ($m = 4$). It seems likely that these oxides are formed in a metastable state and the conditions governing their formation are not known.

2.3. Compounds Containing Two-Dimensional Crystallographic Shear

2.3.1. Introduction

The complex oxides and oxyfluorides of niobium all contain elements of the ReO_3 structure type but they are far more complex systems than those previously discussed. These structures can be derived from the parent NbO_2F (isomorphous with ReO_3) structure by CS on (100) and (010) planes, $(CS)^2$. In all cases the intersecting sets of CS planes subdivide the structures into blocks or columns, each of which retains the ReO_3-type structure. The blocks are joined by sharing octahedral edges and the structures differ only in the sizes of the blocks and the geometry of their corner junctions.

The CS concept and the block principle were progressively established by the structural solution of the shear compounds $TiNb_2O_7$,[25] $Ti_2Nb_{10}O_{29}$,[26] and *H*-Nb_2O_5.[27] These structures were determined by means of X-ray analysis of comparatively well-ordered single crystals; however, many materials of this kind are difficult, if not impossible, to prepare in a fully ordered state and in those cases X-ray techniques are of limited value. Recent application of high-resolution transmission electron microscopy to these systems has demonstrated that the CS planes can be observed directly and their arrangement, whether random or ordered, revealed.[13–15]

The niobium-based oxides and oxyfluorides are prepared at high temperature by solid-state reactions. They have at least one periodicity in the range of 3.8–3.9 Å corresponding to the length of the unit cell edge of NbO_2F, which is the distance between nearest-neighbor metal atoms or the length of the body diagonal of the regular coordination octahedron. Therefore they may all be viewed in projection down their short (3.8 Å) axes (Figure 3). The idealized octahedra are viewed as "black" squares in the plane of the paper. Blocks of finite size of ReO_3 are joined by sharing edges of outermost octahedra. As a result, the blocks are located on two levels perpendicular to the shortest axis, and hence are offset 1.9 Å (half the shortest cell edge). The oxygen atoms involved in the edge sharing are connected to three metal atoms rather than to two as in the remainder of the structure. Consequently, there is a reduction of the O/M ratio without alteration in the coordination number of metal atoms. The variety of structures results from the large number of ways blocks of varying dimensions can be joined.

The structures can be differentiated by the size of the blocks and by the block linkage or geometry at the block corners. These will be catalogued according to the block linkage. A small number, two, three,

or four octahedra at the outermost edge of the block, can share edges with others on the same level. Alternatively, if no grouping of this sort is achieved, a string of tetrahedral sites along the short axis is created which may be empty or filled with cations.

2.3.2. The Formulas of Block Structures

Compositions of members of this complicated system may be calculated using the general formula[28]

$$M_{mnp+1}O_{3mnp-p(m+n)+4}$$

if blocks centered about two levels perpendicular to the short axes of symmetry are all of the same size. The subscripts m and n designate the size of a block m by n corner-sharing octahedra. In $(CS)^1$ systems the homologous series formula requires only one variable, for instance, n in Mo_nO_{3n-1}, Mo_nO_{3n-2}, and Ti_nO_{2n-1}. Although it might appear that two parameters m and n would be sufficient to characterize the block series, this is not so in reality.

These structures are differentiated not only by the size of the blocks but also by the block linkage or geometry of the block corner, necessitating a third subscript p to complete the description. (a) When $p = 1$ the structure consists of isolated blocks with their outermost octahedra sharing no edges at the same level. (b) For $p = 2$ the blocks at the same level are joined in pairs by edge sharing. (c) For $p = \infty$ the blocks at the same level are joined by edge sharing to form either a strip or a sheet.

Since the structures of identical block size can be completely characterized by the three parameters m, n, and p, it is advantageous to have a compact notation for representing the block character. The most natural form is $(m \times n)_p$. Tables 4–7 list formulas and some compounds utilizing this notation. It is interesting to observe that the general formula converges to M_kO_{3k-1} for either p and m or p and n approaching infinity and the corresponding structure is reduced to a one-dimensional shear structure, $(CS)^1$. There are two known members in the series when $m \to \infty$ (Table 7), namely V_2O_5 and Nb_3O_7F. Of course, if k also becomes infinite, the ReO_3-type structure will result. In each of these tables (p fixed) the difference between the structural formulas of two successive members in the same series of m (m fixed) is $\alpha \cdot M_mO_{3m-1}$, where α is equal to p for all finite p and to unity when p becomes infinity. Since m and n are symmetric, the reverse also holds true.

TABLE 4
Homogeneous Block Structures with $(m \times n)_1$

m	n	Structural formula	Components	Representative (space group)	Isostructural compound
3	2	M_7O_{17}	$(3 \times 2)_1$	—	—
	3	$M_{10}O_{25}$	$(3 \times 3)_1$	PNb_9O_{25} ($I\bar{4}$)	VNb_9O_{25}, $AsNb_9O_{25}$
	k	$M_{3k+1}O_{8k+1}$	$(3 \times k)_1$	—	—
4	2	M_9O_{22}	$(4 \times 2)_1$	—	—
	3	$M_{13}O_{33}$	$(4 \times 3)_1$	$WNb_{12}O_{33}$ ($C2$)	$MoNb_{12}O_{33}$
	4	$M_{17}O_{44}$	$(4 \times 4)_1$	$W_3Nb_{14}O_{44}$($I\bar{4}$)	$Mo_3Nb_{14}O_{44}$
	k	$M_{4k+1}O_{11k}$	$(4 \times k)_1$	—	—
5	2	$M_{11}O_{27}$	$(5 \times 2)_1$	—	—
	3	$M_{16}O_{41}$	$(5 \times 3)_1$	$MoNb_{15}O_{40}F$ ($C2$)	$WNb_{15}O_{40}F$
	4	$M_{21}O_{55}$	$(5 \times 4)_1$	$W_5Nb_{16}O_{55}$ ($C2$)	—
	5	$M_{26}O_{69}$	$(5 \times 5)_1$	$W_8Nb_{18}O_{69}$ ($I\bar{4}$)	—
	k	$M_{5k+1}O_{14k-1}$	$(5 \times k)_1$	—	—
6	2	$M_{13}O_{32}$	$(6 \times 2)_1$	—	—
	3	$M_{19}O_{49}$	$(6 \times 3)_1$	—	—
	4	$M_{25}O_{66}$	$(6 \times 4)_1$	—	—
	5	$M_{31}O_{83}$	$(6 \times 5)_1$	—	—
	k	$M_{6k+1}O_{17k-2}$	$(6 \times k)_1$	—	—

TABLE 5
Homogeneous Block Structures with $(m \times n)_2$

m	n	Structural formula	Components	Representative (space group)	Isostructural compound
3	2	$M_{13}O_{30}$	$(3 \times 2)_2$	—	—
	3	$M_{19}O_{46}$	$(3 \times 3)_2$	—	—
	k	$M_{6k+1}O_{16k-2}$	$(3 \times k)_2$	—	—
4	2	$M_{17}O_{40}$	$(4 \times 2)_2$	—	—
	3	$M_{25}O_{62}$	$(4 \times 3)_2$	$TiNb_{24}O_{62}$ ($C2$)	$Nb_{25}O_{62}$, α-$ZrNb_{24}O_{62}$
	4	$M_{33}O_{84}$	$(4 \times 4)_2$	—	—
	k	$M_{8k+1}O_{22k-4}$	$(4 \times k)_2$	—	—
5	2	$M_{21}O_{50}$	$(5 \times 2)_2$	—	—
	3	$M_{31}O_{78}$	$(5 \times 3)_2$	$Nb_{31}O_{77}F$ ($C2$)	—
	4	$M_{41}O_{106}$	$(5 \times 4)_2$	—	—
	5	$M_{51}O_{134}$	$(5 \times 5)_2$	—	—
	k	$M_{10k+1}O_{28k-6}$	$(5 \times k)_2$	—	—
6	2	$M_{25}O_{60}$	$(6 \times 2)_2$	—	—
	3	$M_{37}O_{94}$	$(6 \times 3)_2$	—	—
	4	$M_{49}O_{128}$	$(6 \times 4)_2$	—	—
	5	$M_{61}O_{162}$	$(6 \times 5)_2$	—	—
	6	$M_{73}O_{196}$	$(6 \times 6)_2$	—	—
	k	$M_{12k+1}O_{34k-8}$	$(6 \times k)_2$	—	—

TABLE 6
Homogeneous Block Structures with $(m \times n)_\infty$

m	n	Structural formula	Components	Representative (space group)	Isostructural compound
3	2	M_6O_{13}	$(3 \times 2)_\infty$	—	—
	3	M_9O_{21}	$(3 \times 3)_\infty$	$TiNb_2O_7$ ($C2/m$)	$TiTa_2O_7$
	k	$M_{3k}O_{8k-3}$	$(3 \times k)_\infty$	—	—
4	2	M_8O_{18}	$(4 \times 2)_\infty$	—	—
	3	$M_{12}O_{29}$	$(4 \times 3)_\infty$	$Ti_2Nb_{10}O_{29}$ ($C2/m$, $Cmcm$)	$Nb_{12}O_{29}$; $(M, Nb)_{12}O_{29}$, M = Mg, Al, V, Fe, Co, Ni, Zn
	4	$M_{16}O_{40}$	$(4 \times 4)_\infty$	M-Nb_2O_5 ($14/mmm$); N-Nb_2O_5 ($C2/m$)	—
	k	$M_{4k}O_{11k-4}$	$(4 \times k)_\infty$	—	—
5	2	$M_{10}O_{23}$	$(5 \times 2)_\infty$	—	—
	3	$M_{15}O_{37}$	$(5 \times 3)_\infty$	$MgNb_{14}O_{35}F_2$ ($C2/m$)	—
	4	$M_{20}O_{51}$	$(5 \times 4)_\infty$	—	—
	5	$M_{25}O_{65}$	$(5 \times 5)_\infty$	—	—
	k	$M_{5k}O_{14k-5}$	$(5 \times k)_\infty$	—	—
6	3	$M_{18}O_{45}$	$(6 \times 3)_\infty$	—	—
	4	$M_{24}O_{62}$	$(6 \times 4)_\infty$	—	—
	5	$M_{30}O_{79}$	$(6 \times 5)_\infty$	—	—
	k	$M_{6k}O_{17k-6}$	$(6 \times k)_\infty$	—	—

TABLE 7
Homogeneous Block Structures with $(\infty \times n)_\infty$: One-Dimensional Shear Structures

m	n	Structural formula	Components	Representative (space group)	Isostructural compound
∞	2	M_2O_5	$(\infty \times 2)_\infty$	V_2O_5 ($Pnmm$)	R-Nb_2O_5
	3	M_3O_8	$(\infty \times 3)_\infty$	Nb_3O_7F ($Cmmm$)	—
	4	M_4O_{11}	$(\infty \times 4)_\infty$	—	—
	5	M_5O_{14}	$(\infty \times 5)_\infty$	—	—
	k	M_kO_{3k-1}	$(\infty \times k)_\infty$	—	—
	∞	MO_3	$(\infty \times \infty)_\infty$	ReO_3 ($Pm3m$)	—

2.3.3. Representations of Block Structures

The idealized structures of representatives with uniform block size[3] are illustrated in Figures 17–19. Figure 17 shows the structure of $WNb_{12}O_{33}$ composed of $(3 \times 4)_1$ blocks. The blocks are present at two levels with W tetrahedrally coordinated at the join of any four blocks. Figure 18 shows the structure of $TiNb_{24}O_{62}$, $(3 \times 4)_2$, where the blocks are joined by edges at the same level into pairs and the tetrahedral positions are located at the intersection of these double units. Figure 19 shows the third kind of uniform block structure, $(4 \times 4)_\infty$, illustrated by M-Nb_2O_5 and N-Nb_2O_5. The former has tetragonal symmetry with all four corners of the block in single edge-

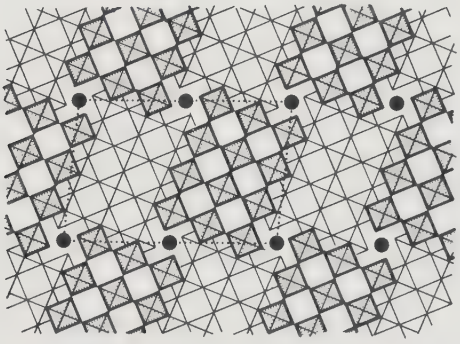

Fig. 17. A homogeneous $(3 \times 4)_1$ block structure, $WNb_{12}O_{33}$.

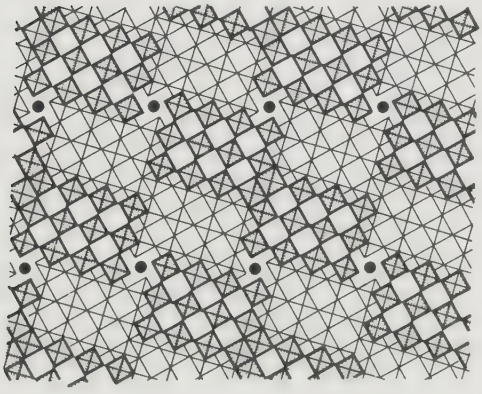

Fig. 18. A homogeneous $(3 \times 4)_2$ block structure, $TiNb_{24}O_{62}$.

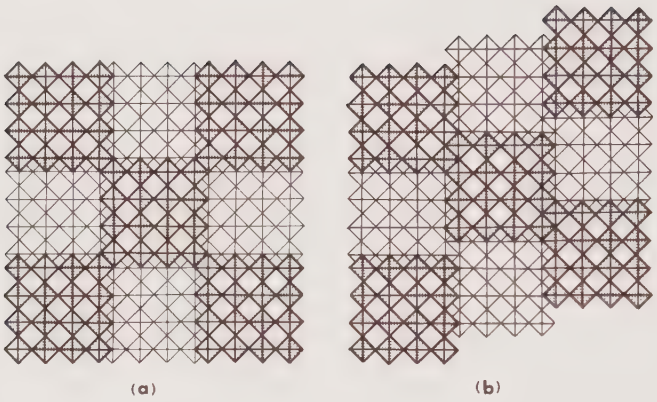

Fig. 19. Homogeneous $(4 \times 4)_\infty$ block structure: (a) M-Nb_2O_5. (b) N-Nb_2O_5.

sharing, whereas the latter is monoclinic with only two corners in triple edge-sharing.

The complexity extends beyond the variation of block size and linkage. Composite structures can be produced by ordered arrangement of two different block components at two levels. This is best illustrated by the structure of H-Nb_2O_5,[27] the high-temperature form of niobium oxide. In H-Nb_2O_5 the blocks centered about the two levels perpendicular to the short axis are of two kinds (Figure 20). At one level, where octahedra are heavily outlined, the block component is isolated and of one size $(4 \times 3)_1$; at the other level, where the blocks are joined by triple edge-sharing to form separate stepped strips,

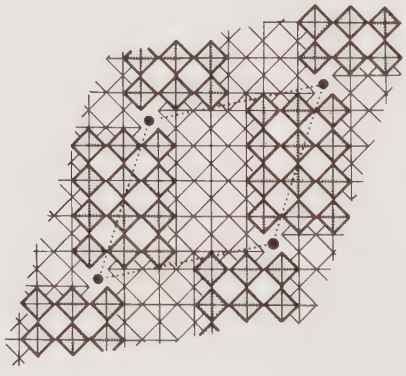

Fig. 20. The structure of H-Nb_2O_5 composed of interleaved layers of $(4 \times 3)_1$ and $(5 \times 3)_\infty$.

TABLE 8
Composite Structures Derived from Two Different Block Components at Two Levels

Phase	A	B	Sequence	Formation
H-Nb_2O_5	$(4 \times 3)_1$	$(5 \times 3)_\infty$	$\|\mathbf{AB}\|\mathbf{A}$	$(4 \times 3)_1 + (5 \times 3)_\infty$
$Nb_{22}O_{54}$	$(3 \times 3)_1$	$(4 \times 3)_\infty$	$\|\mathbf{AB}\|\mathbf{A}$	$(3 \times 3)_1 + (4 \times 3)_\infty$
$Nb_{34}O_{84}F_2$	$(5 \times 3)_1$	$(6 \times 3)_\infty$	$\|\mathbf{AB}\|\mathbf{A}$	$(5 \times 3)_1 + (6 \times 3)_\infty$

the component is $(5 \times 3)_\infty$. Blocks at the two levels are then joined together by edge sharing. Such a structure possesses open tunnels running parallel to the short axis but having alternate tetrahedral positions located in these tunnels filled by metal atoms. The periodic sequence of the block components is revealed in the direction (indicated by an arrow) perpendicular to the short axis. If A and B represent the block components $(4 \times 3)_1$ and $(5 \times 3)_\infty$ and alternate levels are denoted by boldface type, the periodic sequence becomes $|\mathbf{AB}|\mathbf{AB}\cdots$. The unit cell content is simply the summation of the two components present in the period. As an example, using the information given in Tables 4 and 6, one can easily obtain

$$A + B = (4 \times 3)_1 + (5 \times 3)_\infty = M_{13}O_{33} + M_{15}O_{37}$$
$$= M_{28}O_{70} = 14M_2O_5$$

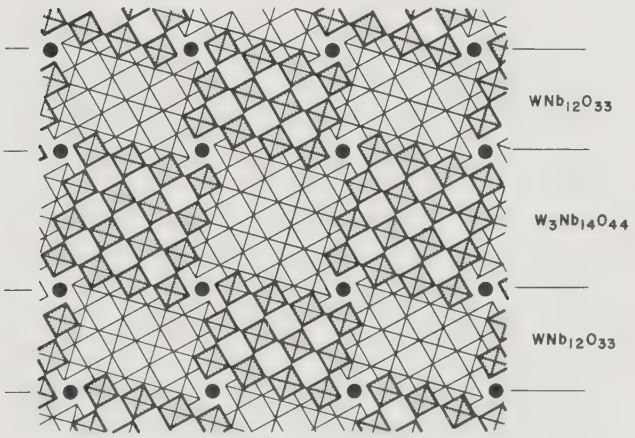

Fig. 21. $W_4Nb_{26}O_{77}$ as an intergrowth compound of the component structures $WNb_{12}O_{33}$ and $W_3Nb_{14}O_{44}$.

which is, indeed, the composition of the high-temperature form of niobium oxide.

The ultimate complexity of observed block structures is the ordered intergrowth of members of the basic block structures listed in Tables 4–6 and 8. Examples of this type of structure appear to be limited to the binary and ternary niobium oxides. In order to illustrate the structural principle involved, consider $W_4Nb_{26}O_{77}$ (Figure 21). It is the only member of this family for which a single-crystal structure determination has so far been completed.[29]

$W_4Nb_{26}O_{77}$ crystallizes in the monoclinic form, space group $C2$, with unit cell dimensions $\mathbf{a} = 29.74$ Å, $\mathbf{b} = 3.824$ Å, $\mathbf{c} = 25.97$ Å, and $\beta = 92.3°$. The structure contains two kinds of octahedral blocks, 4×3 and 4×4, with the tetrahedral junctions between any four containing the tungsten atoms. Therefore the block components are $(4 \times 3)_1$ and $(4 \times 4)_1$. Blocks of the same character are joined into continuous slabs parallel to the longer axis and perpendicular to the plane of the page as indicated. The two kinds of slabs are recognized fragments of $WNb_{12}O_{33}$ and $W_3Nb_{14}O_{44}$, respectively, from Table 4. The composition of the hybrid structure is the sum of the two components. Alternatively, the periodic sequence in the direction indicated by the arrow can be formulated as

$$|\mathbf{A}B|\mathbf{A}$$

where $\mathbf{A} = (4 \times 3)_1$ and $B = (4 \times 4)_1$.

Table 9 summarizes all the hybrid structures presently known. It is worth noticing that the block components utilized almost all possess a common block dimension of three except for $W_4Nb_{26}O_{77}$. The direction of the periodic sequence given as column six of Table 9 is perpendicular to the short axis and crosses the common block dimension. The sequence period in most cases is equal to a full unit cell translation. However, in the case of $Ti_2Nb_{76}O_{194}$ it is twice the unit cell translation.

The periodic sequence is in an interesting relationship with the overall structural formula. If the sequence and the block components participating in the sequence are known, the composition of the hybrid structure can be expressed as

$$\sum_j (a_j/\alpha_j)[(m \times n)_p]_j = \sum_j b_j[\mathrm{M}_{mnp+1}\mathrm{O}_{3mnp-p(m+n)+4}]_j \qquad (1)$$

The bracketed $(m \times n)_p$ with a subscript j represents the block component of the jth type and a_j is the number of such components

TABLE 9
Relationship of the Hybrid Structures and Their Block Components

Compound	Component structure	A	B	C	Sequence	Formation
$W_4Nb_{26}O_{77}$	$WNb_{12}O_{33} + W_3Nb_{14}O_{44}$	$(4 \times 3)_1$	$(4 \times 4)_1$	—	|**A***B***|**	A + B
$Ti_3Nb_{34}O_{91}$	$TiNb_{24}O_{62} + Ti_2Nb_{10}O_{29}$	$(4 \times 3)_2$	$(4 \times 3)_\infty$	—	|**AA*B*AA*B***|	A + B
$Ti_3Nb_{44}O_{120}$	$TiNb_{24}O_{62} + 2Ti_2Nb_{10}O_{29}$	$(4 \times 3)_2$	$(4 \times 3)_\infty$	—	|**A*B*BA*B***|	A + 2B
$WNb_{26}O_{68}$	$2WNb_{12}O_{33} + Nb_{28}O_{70}$	$(4 \times 3)_1$	$(5 \times 3)_\infty$	—	|**B*A*AA*A***|	3A + B
$WNb_{40}O_{103}$	$WNb_{12}O_{33} + Nb_{28}O_{70}$	$(4 \times 3)_1$	$(5 \times 3)_\infty$	—	|**B*A*AB*A*A*A***|	2A + B
$WNb_{68}O_{173}$	$WNb_{12}O_{33} + 2Nb_{28}O_{70}$	$(4 \times 3)_1$	$(5 \times 3)_\infty$	—	|**B*A*AB*A*BA*A*BA*A***|	3A + 2B
$Nb_{53}O_{132}$	$Nb_{25}O_{62} + Nb_{28}O_{70}$	$(4 \times 3)_2$	$(4 \times 3)_1$	$(5 \times 3)_\infty$	|**C*A*BA*A***|	A + B + C
$Nb_{47}O_{116}$	$Nb_{25}O_{62} + Nb_{22}O_{54}$	$(4 \times 3)_2$	$(3 \times 3)_1$	$(4 \times 3)_\infty$	|**B*A*CA*A***|	A + B + C
$Nb_{59}O_{147}F$	$Nb_{31}O_{77}F + Nb_{28}O_{70}$	$(5 \times 3)_2$	$(4 \times 3)_1$	$(5 \times 3)_\infty$	|**C*A*BA*A***|	A + B + C
$Nb_{65}O_{161}F_3$	$Nb_{34}O_{84}F_2 + Nb_{31}O_{77}F$	$(5 \times 3)_2$	$(5 \times 3)_1$	$(6 \times 3)_\infty$	|**B*A*CA*A***|	A + B + C
$Ti_2Nb_{76}O_{194}$	$2Nb_{25}O_{62} + Nb_{28}O_{70}$	$(4 \times 3)_2$	$(4 \times 3)_1$	$(5 \times 3)_\infty$	|**B*A*ACA*A***|	2A + B + C
β-$ZrNb_{24}O_{62}$	$Nb_{13}O_{33} + 3Nb_{25}O_{62} + Nb_{12}O_{29}$	$(4 \times 3)_1$	$(4 \times 3)_2$	$(4 \times 3)_\infty$	|**B*B*AB*B*BC*B***|	A + 3B + C
γ-$ZrNb_{24}O_{62}$	$Nb_{25}O_{62}$	$(4 \times 3)_2$	—	—	|**A*A*A*A*A*A*A*A***|	4A
$Nb_{97}O_{243}$	$Nb_{13}O_{33} + 3Nb_{28}O_{70}$	$(4 \times 3)_1$	$(5 \times 3)_\infty$	–	|**A*B*A*B*A*B*A*A*B*A*B*A*B*A***|	8A + 6B

over a sequence period; α_j is the same p-dependent coefficient given earlier and b_j is the number of corresponding component structures.

The simplified relationship is of significance when the reversed problem is considered. The stoichiometry of a composite or hybrid structure provides not only the kinds of block components and in turn the component structures it possesses, but also a positive idea of how these subunits are connected. This involves searching for the coefficients b_j and can be easily solved by computer once the formula of the component structures to be considered is stored in a memory bank. The solution, however, may not be unique. For example, $(4 \times 3)_1 + (5 \times 3)_\infty$ and $(4 \times 3)_\infty + (5 \times 3)_1$ offer the same composition $M_{28}O_{70}$ but one can eliminate the second possibility because of the poor fit of those units. If units are badly fitted in the block structure, fragments of the MoO_3 structure type can be recognized. The number of each kind of block component a_j is then equal to $\alpha_j b_j$. When all these coefficients are determined the periodic sequence and a structural model can be proposed.

2.4. Disorder in Block Structures

Single crystals of only a few of the hybrid structures have been prepared but the existence of many others can be detected by electron optical studies. It is conceivable that intergrowth may not be completely ordered. Two-component structures can be intergrown at random, creating nonperiodic regions. If the amounts of these two-component structures are uneven in a certain selected area, the minor phase is considered a fault component and its random appearance in the matrix of the other involves Wadsley defects. Such disordered intergrowths when present in a minute amount would not be detected by X-ray diffraction but would be revealed by electron microscopy. It should be emphasized again that no discontinuity is imposed on the structure when planar faults are introduced; their presence only slightly alters the stoichiometry of the overall material.

It is virtually impossible to find a well-ordered single crystal of any one of these complex phases because of the experimental difficulty of obtaining exact stoichiometry. In addition, a true equilibrium state might not be represented either because the components had not reached equilibrium at temperature or the equilibrium phase had disproportionated during cooling.

2.4.1. High-Resolution Electron Optical Techniques

Various types of Nb_2O_5-based systems have been examined at medium resolution and many defects observed but because of the limited resolution, complete characterization was not possible. Occasionally, conjectures from observations made at lower resolution level turn out to be inconclusive. For example, confusion[30] concerning polymorphic structures of β- and γ-$ZrO_2 \cdot 12Nb_2O_5$ required high-resolution electron optical techniques for clarification.

Recently with skillful use of the modern high-resolution electron optical techniques of imaging it has become possible to record image patterns which have a direct correlation to the structure. Regions of high electron density such as heavy metal atoms show up as dark spots, regions with low electron density associated with light atoms appear as gray spots, whereas tunnels or other regions of very low electron density appear as white spots. For example, in a 4×3 block of octahedra, there would be 4×3 gray spots enclosing 3×2 white dots. In addition, a region near tetrahedrally coordinated metal atoms which are surrounded with other metal atoms in the nearest octahedral positions appears as a black spot. The technique of lattice imaging uses many diffracted beams together with the undiffracted beam to form the bright-field image or, without the central beam, the dark-field image. In order to observe the one-to-one correlation, the thickness of the specimen must be less than 150 Å and the image recorded at about 900 Å underfocus. The arrangement of metal atoms revealed by the image should enable reliable trial structures to be proposed which could subsequently be refined using X-ray diffraction. Above all, the techniques yield detailed information about the precise nature of defects not obtainable by any other method.

2.4.2. Observed Disorder in *H*-Nb_2O_5-Related Structures

Direct observation of the planar defects in quenched *H*-Nb_2O_5 based on the metal atom positions by high-resolution electron microscopy has been reported.[15] Figure 22 shows a low-magnification image of a relatively well-ordered region which contains various types of defects. These defect lines or bands can be catalogued into four groups according to their crystallographic orientations. If the Greek letter $\boldsymbol{\delta}$ represents the defect direction, these four types of defects are represented as $\boldsymbol{\delta}[001]$, $\boldsymbol{\delta}[101]$, $\boldsymbol{\delta}[10\bar{1}]$, and $\boldsymbol{\delta}[100]$. The defect bands do not disappear within the crystal except when they intersect with other faults or, trivially, at the crystal edge.

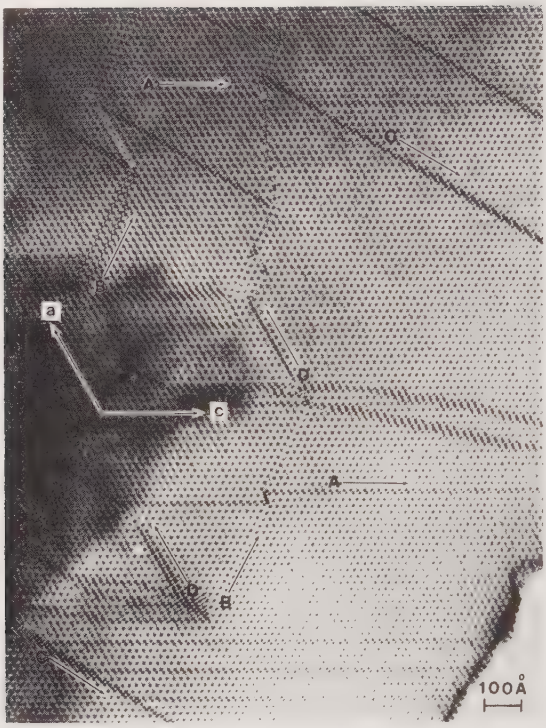

Fig. 22. Low-magnification, two-dimensional lattice image of a relatively ordered region of H-Nb_2O_5 showing four kinds of planar defects labeled A, B, C, and D. (With permission from Iijima.[15])

For convenience in presenting a block structure with or without defects, a simplified block diagram is normally used. All the structural components $(m \times n)_p$ can be simplified into $m \times n$ blocks. Blocks located at upper and lower levels are depicted respectively by heavy or light contours. Tetrahedral positions are shown as dots, each of which is surrounded by four blocks. Blocks joined by edge sharing are indicated by their close approach. Defect lines and bands are represented by rows of shaded blocks.

The first type of planar defect is $\delta[001]$, labeled as A in Figure 22. As may be recalled, the structure sequence of H-Nb_2O_5 can be expressed as **A***B***A***B***A***B*** where $A = (4 \times 3)_1$ and $B = (5 \times 3)_\infty$. A high-magnification image centered at one of those defect regions (Figure 23) reveals a sequence **A***B***A***A***B***A***B**, where two rows of A are adjacent. The inset represents the block diagram corresponding to the enclosed area in the lattice image photograph. A similar defect of the type

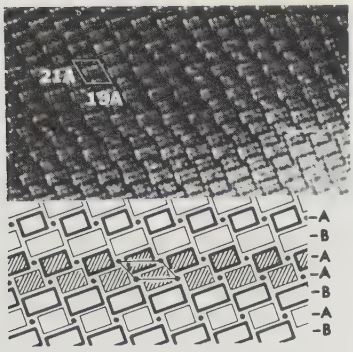

Fig. 23. High-magnification, two-dimensional lattice image of H-Nb_2O_5 showing defects of type A parallel to the **c** axis. Inset corresponds to the enclosed area. (With permission from Iijima.[15])

A*BA***A***BA* is also possible but rarely observed. The defects **δ**[001] may appear repeatedly at intervals of simple multiples of **a**. A periodic appearance of the defect bands with interval of 3**a** corresponds to |**A***BA***B***A***B***A***AB***A*|**A**, producing a superlattice of six unit cells of H-Nb_2O_5. It has a monoclinic unit cell in which **a** = 157.8 Å, **b** = 3.8 Å, **c** = 19.4 Å, and $\beta = 121°$. Using the scheme for determining the sequence, one can work out its composition:

$$8A + 6B = 8(4 \times 3)_1 + 6(5 \times 3)_\infty = 2(Nb_{97}O_{243})$$

The defects **δ**[101] (labeled B in Figure 22) reveal another extraordinary feature. Figure 24(a) and 24(b) show the high-magnification images of this type of defect. It consists of a single row of a component, either $(4 \times 3)_1$ or $(5 \times 3)_\infty$, parallel to [101] which is rotated by 90° with respect to the corresponding components in the host structure. Double rows of $(4 \times 3)_1$ and $(5 \times 3)_\infty$ and triple rows of $(4 \times 3)_1$, $(5 \times 3)_\infty$, and $(4 \times 3)_1$ have also been observed.[31] A consequence of this is a sudden shift of the arrays of tetrahedral positions along the **c** direction, but there is no interruption of the periodicity along **c***. Just as in an APB, these defects do not alter the stoichiometry. Moreover, if the blocks on one side of the defect boundary all change their orientation, formation of a twin will occur.

Defects of **δ**[10$\bar{1}$] type consist of block components different from those in the host structure, as may be seen in Figure 25, which shows a high-magnification image and the corresponding block

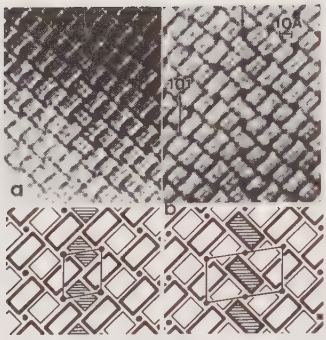

Fig. 24. Two-dimensional lattice images showing two types of defects of type *B*, **δ**[101] composed of (a) $(4 \times 3)_1$ blocks, (b) $(5 \times 3)_\infty$ blocks. (With permission from Iijima.[15])

diagram. It is obvious that the defect band is composed of only $(3 \times 3)_1$ blocks (the same structure as PNb_9O_{25}, whose unit cell is outlined in the model); however, the fault bands are interrupted by a row of $(4 \times 3)_1$ blocks (indicated by arrows).

Figure 26 shows an image of the fourth type of defect, **δ**[100] (indicated by arrows) and a block diagram corresponding to the enclosed area in the image. This defect consists of a row of $(5 \times 3)_2$ blocks parallel to the **a** axis; this block component is also different

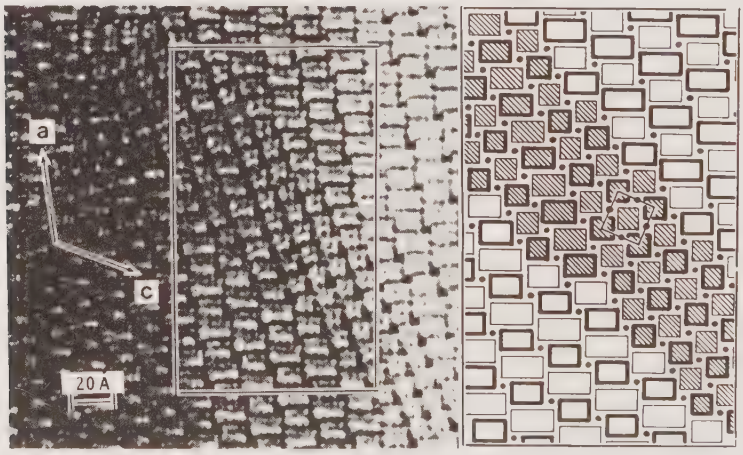

Fig. 25. Two-dimensional lattice images showing the type-*C* defect containing inserted $(3 \times 3)_1$ blocks characteristic of PNb_9O_{25} structure. (With permission from Iijima.[15])

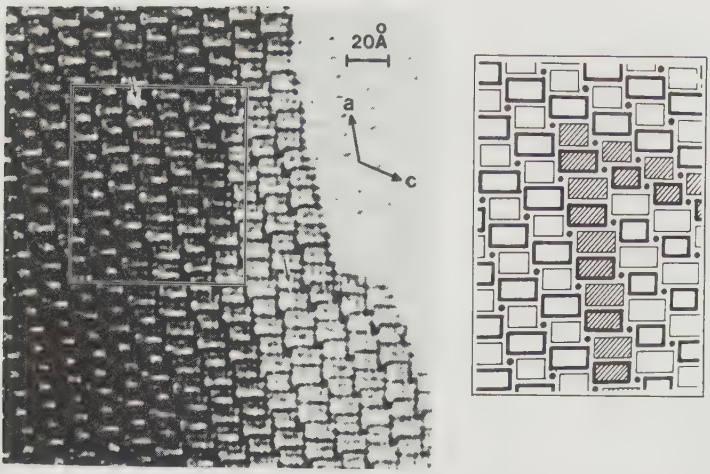

Fig. 26. Two-dimensional lattice showing the defect of type *D*, δ[100], which is annihilated by intersection with the type-*A* defect δ[001]. (With permission from Iijima, private communication.)

from the block components of the host structure. Note that this defect slab disappears at the point of its intersection with δ[001].

Quenched samples of *H*-Nb_2O_5 are considerably disordered. Nevertheless, each block shape shown in an image is still clearly distinguishable, indicating that the blocks are well ordered along the short axis. The better ordering along the **b** axis may be attributed to the extremely high diffusion rate of oxygen along this direction; this may also explain why only planar faults parallel to the **b** axis are formed.

Even in a heavily disordered region, locally ordered structures often appear. There are generally three types of variations observed. (The number here cannot be regarded as exhaustive since arrangements other than these three may be possible.) The compositions of all three are the same as that of the host. The first two types are simply rearrangements of the block components and therefore their composition remains the same. The first variation is associated with the defect δ[101]. When such defects occur periodically in every other row of $(5 \times 3)_\infty$ parallel to the [101] direction, a new polymorph of Nb_2O_5 is formed which has cell dimensions approximately **a** = 19 Å, **b** = 3.8 Å, **c** = 32 Å, and $\beta = 80°$. The second variation is an extreme case of the first. The defect δ[101] occurs in every row instead of every other row of $(5 \times 3)_\infty$, yielding another new polymorph. The third variation is an inclusion of *N*-Nb_2O_5 composed of $(4 \times 4)_\infty$. This

structural entity is not one of the components of the host. In addition,[31] single sheets of M-Nb_2O_5 [in slightly different connections of $(4 \times 4)_\infty$ blocks] have also been observed along $[10\bar{1}]$ without causing twinning. From these examples it may be concluded that even in a heavily disordered region locally ordered structures have a tendency to retain the same composition as that of the host structure.

2.5. Disorder in Systems Related to the Tetragonal Tungsten Bronze

At least ten distinct phases have been recognized in the binary system Nb_2O_5–WO_3. The difference between the structures arises from the two-dimensional variations in the arrangement of coordination octahedra. It has been known for some time that the pseudobinary compounds in the $Nb_2O_5 \cdot xWO_3$ system have block structures similar to H-Nb_2O_5 when $x < 0.48$ and belong to Magnéli phases when $x > 0.90$. On the other hand, when $0.64 < x < 0.78$ the octahedra are joined in a more complex manner, leaving tunnels of various shapes; these have been called tunnel structures.

In both the CS and tunnel structures the framework basically consists of octahedra sharing corners. Alteration of the overall O/M ratio is achieved by edge sharing of some octahedra in the CS structures and principally by filling some of the pentagonal tunnels with metal atoms in the tunnel structures.

The two binary compounds $4Nb_2O_5 \cdot 9WO_3$ and $2Nb_2O_5 \cdot 7WO_3$ have been most intensively studied. Both are related to the tetragonal tungsten bronze (TTB) structure. The structure of TTB is derived from the ReO_3 type by rotating 4×4 blocks by 45° about the short axis and reestablishing corner sharing such that triangular and pentagonal tunnels alternate around the perimeter as illustrated in Figure 27(a). Atoms may be accommodated in the pentagonal tunnels either systematically or randomly to produce nonstoichiometry.

The structure of $4Nb_2O_5 \cdot 9WO_3$ (Figure 27b) has been determined by X-ray analysis to be orthorhombic, $P2_12_12$ with unit cell dimensions $\mathbf{a} = 36.62$ Å, $\mathbf{b} = 12.25$ Å, and $\mathbf{c} = 3.94$ Å. It contains three TTB-type subcells with only one-third of the 12 pentagonal tunnels regularly occupied, approximating a hexagonal network.

Planar defects are also commonly observed in this system. An image taken from a faulted crystal at lower resolution is shown in Figure 28. The corresponding electron diffraction pattern inserted contains a square array of strong reflections due to the tetragonal subcell of TTB; however, each of the major axes of this subcell appears

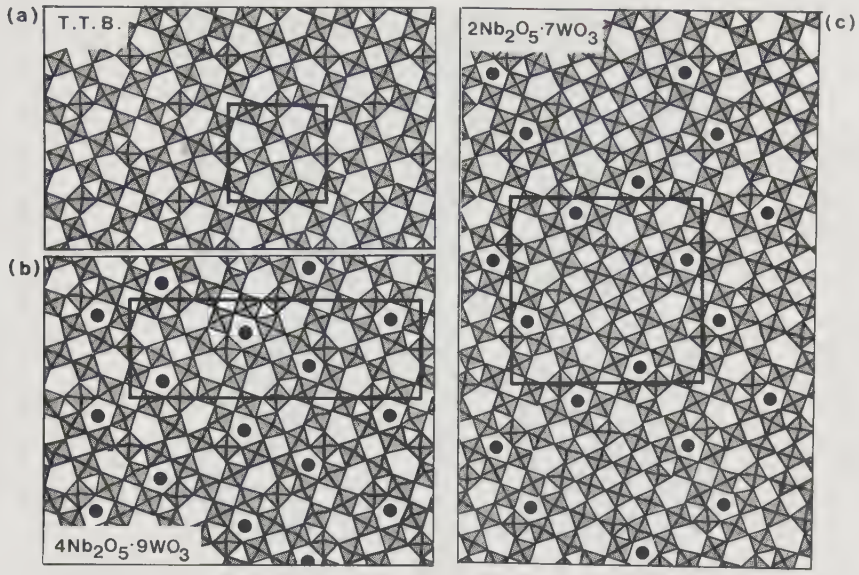

Fig. 27. Structural relationship among structures of: (a) Tetragonal tungsten bronze, (b) $4Nb_2O_5 \cdot 9WO_3$, (c) $2Nb_2O_5 \cdot 7WO_3$.

to be trebled, yet the complete absence of reflections within the squares defined by the subcell reflections does not correspond to any space group extinction condition. Such an inconsistency immediately suggests some form of twinning and this conclusion is confirmed directly by the lattice image. There are three distinguishable faults labeled *A*, *B*, and *C* composed of various block dimensions within the host structure consisting of 3 × 1 TTB subunits.

The defect marked *A* in Figure 28 can be written as $\delta[100]$* because it is parallel to the **a** axis of the $4Nb_2O_5 \cdot 9WO_3$ structure. It can be terminated anywhere in the structure. Figure 29 shows a high-magnification image corresponding to one of these areas. In interpreting such images, the filled pentagonal tunnels together with the neighboring octahedra are shown as large black patches, whereas the unfilled ones appear as large white circles; small circles in white imply the presence of the usual tetragonal tunnels. A group of five white patches (four larger ones at the corners and the smaller one at the center) is distinguishable and circled for clarity (Figure 29). The defect band is composed of 5 × 2 TTB subunits but the pentagonal tunnels are not filled in the same way as in the parent structure.

* Indices refer to the parent unit cell.

Fig. 28. Low-magnification, two-dimensional lattice image from a faulted crystal of $4Nb_2O_5 \cdot 9WO_3$ showing several kinds of defect boundaries. (With permission from Iijima, private communication.)

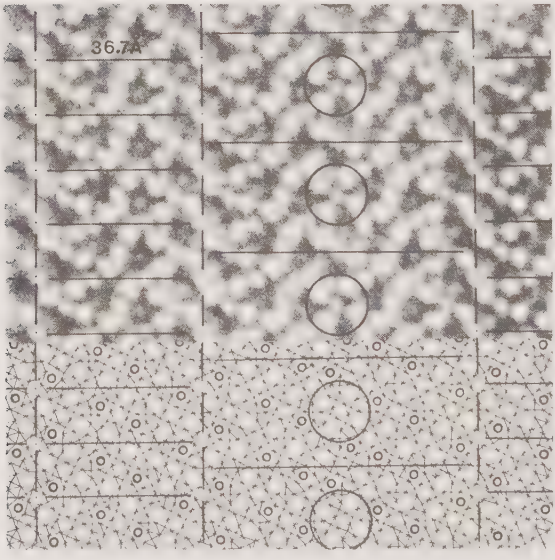

Fig. 29. A defect boundary $\delta[100]$ in $4Nb_2O_5 \cdot 9WO_3$. (With permission from Iijima, private communication.)

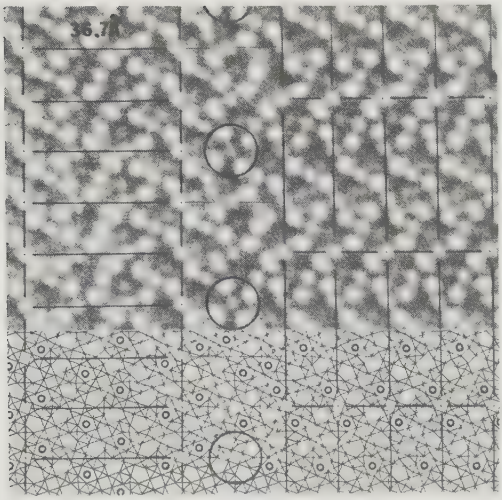

Fig. 30. A defect band at a twin boundary in $4Nb_2O_5 \cdot 9WO_3$. (With permission from Iijima, private communication.)

Of the 40 available tunnels in the supercell, 14 are occupied. This requires a decrease of the O/M ratio in the defect band. Notice that the TTB framework is not interrupted between the host structure and the defect domain. This also holds true in the other two kinds of defects.

The same defect type (labeled *B* in Figure 28) may have different kinds of functions; it can serve as a twin boundary, as Figure 30 shows.

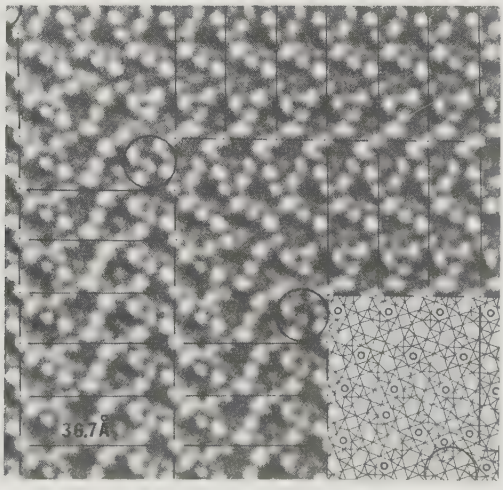

Fig. 31. The defect $\delta[130]$ in $4Nb_2O_5 \cdot 9WO_3$. (With permission from Iijima, private communication.)

The defect is composed of 3 × 2 TTB subunits. There are, in this case, nine out of 24 available pentagonal tunnels occupied, reducing the O/M ratio. The fundamental 3 × 1 unit cells on each side of the boundary are related by $\pi/2$ rotation.

The defect **δ**[130] is composed of 4 × 3 TTB subunits. Figure 31 shows a high-magnification image corresponding to such an area (labeled C in Figure 28). Similar to the $(m \times n)_\infty$ in the Nb_2O_5-based system, blocks of this size are all joined together by sharing one-fourth of their longest dimension (equivalent to a tetragonal cell edge of TTB) to form a stepped boundary parallel to [130]. The defect band becomes a twin boundary because the basic unit cells on each side of the boundary are rotated 90° with respect to each other. Of the 48 available tunnels in the supercell 15 of them are occupied; this corresponds to an increase of the O/M ratio.

Similar types of stepped boundaries are also found along the ⟨110⟩. The defect **δ**[110] is composed of 5 × 1 blocks all joined together by sharing two-thirds of **a** (equivalent to two TTB cell edges) to form the stepped boundary. The defect strip **δ**[1$\bar{1}$0] can intersect the equivalent **δ**[110] terminating the defect band. Contrary to the former case, **δ**[130], this boundary causes a decrease of the overall O/M ratio.

The framework or host structure of TTB is apparently continuous throughout the entire crystal. It is the selective redistribution of metal atoms in the available pentagonal tunnels that defines the size of the blocks participating in the formation of the defect boundary.

The structure of $2Nb_2O_5 \cdot 7WO_3$,[14] more complex than the previous one, is tetragonal with reported unit cell dimensions **a** = 24.26 Å and **c** = 3.92 Å. The unit cell contains four TTB-like subcells. Analogous to the derivation of the TTB from ReO_3, a 4 × 4 ReO_3 block is rotated to create 12 pentagonal tunnels in a unit cell. Again only one-third of them are occupied. This new structure can be regarded as a transition form between block structures based on ReO_3 and on TTB.

Unlike $4Nb_2O_5 \cdot 9WO_3$, the framework structure of $2Nb_2O_5 \cdot 7WO_3$ may be interrupted at the boundary and structural fragments of either form adopted. A defect band **δ**⟨100⟩ where the ReO_3 blocks are brought closer together than they are in the matrix may maintain the composition, giving rise to an antiphase boundary. Equivalent defect bands **δ**⟨100⟩ and **δ**⟨010⟩ may intersect and terminate each other (Figure 32). On the other hand, two slabs of the structure may be separated by a band of $2Nb_2O_5 \cdot 7WO_3$ only one-quarter of its normal

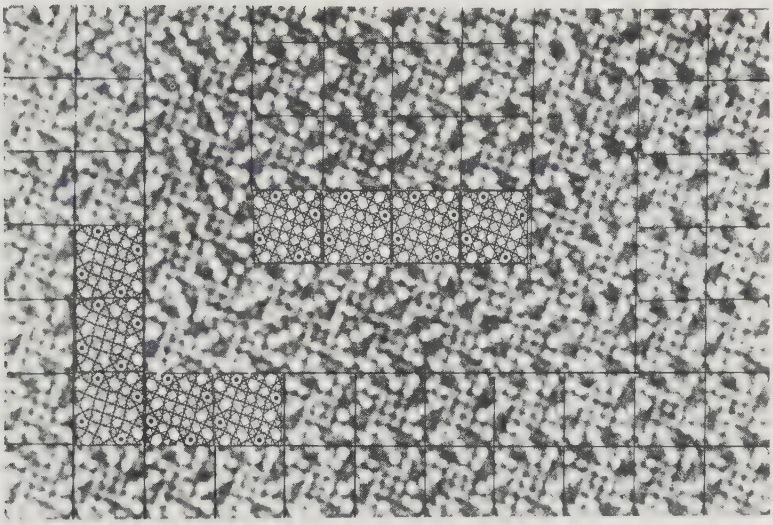

Fig. 32. A defect band $\delta\langle 100\rangle$ in which the concentration of the ReO_3 blocks is relatively increased. (With permission from Iijima, private communication.)

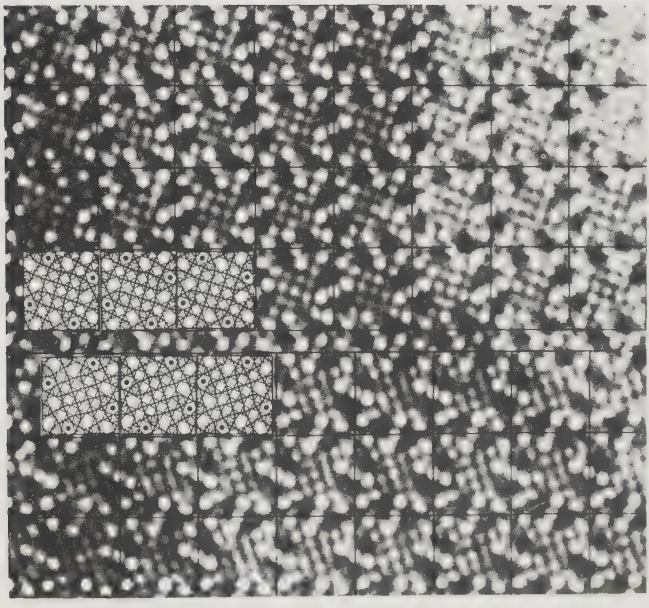

Fig. 33. A narrow defect band separating two regions of $2Nb_2O_5 \cdot 7WO_3$ related by a noncrystallographic glide plane. (With permission from Iijima, private communication.)

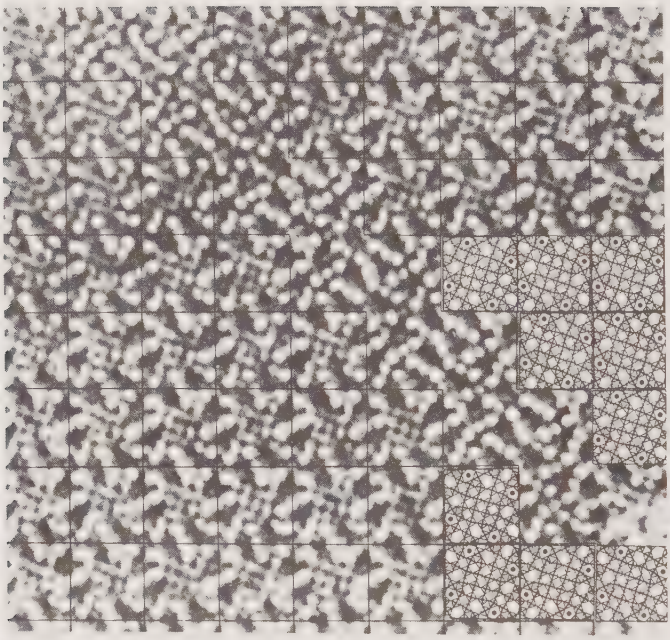

Fig. 34. A stepped boundary in $2Nb_2O_5 \cdot 7WO_3$ containing ordered blocks of $4Nb_2O_5 \cdot 9WO_3$. (With permission from Iijima, private communication.)

width. The two slabs are related by a local noncrystallographic glide symmetry with the same amount of translation. Figure 33 shows two types of unit cells marked by *A* and *C*; one is obviously a mirror image of the other. Stepped boundaries have also been observed, but the constituents are based only on the TTB host structure (Figure 34).

It may be noted that the fault boundaries are regions of compositional variation. It appears that in $4Nb_2O_5 \cdot 9WO_3$ nonstoichiometry results from a selective redistribution of metal atoms in the available pentagonal tunnels. However, in the $2Nb_2O_5 \cdot 7WO_3$ it is attained by adopting a wide variety of structural fragments of either form.

In disordered regions $4Nb_2O_5 \cdot 9WO_3$ and $2Nb_2O_5 \cdot 7WO_3$ can randomly coexist. There is no doubt that random occupation of the pentagonal tunnels with metal and oxygen atoms also plays a vital role in the nonstoichiometry.

3. The Fluorite-Related Structures

3.1. Introduction

In this section we shall discuss in some detail structures related to the fluorite type, including many having extended defects. This class of solids, based on the structure of CaF_2 (space group $Fm3m$), involves some compounds of nearly half of the elements. The most frequent occurrence is among the oxides of the rare earth and actinide elements. Table 10 is a selective list of examples of these solids.

TABLE 10
Selected Fluorite-Related Compounds

Fraction of occupied tetrahedral sites	Formula	Name of structure or phase	CN of O:M*	Element (compound) for which this phase is known
Variable net excess	M_4O_{9-x}	—	—	U
Variable net excess	MO_{2+x}	—	—	U
All	MO_2	Fluorite	4:8	Ce, Pr, Tb, Hf, Th, Pa, U, Np, Pu, Am, Cm, Bk
All	M_2O	Antifluorite	8:4	Li, Na, K, Rb
Variable deficiency	MO_{2-x}	α	—	Ce, Pr, U, Pu, Am, Cm, Bk
Variable deficiency	MO_{2-x}	CSZ	—	$Ca_{0.15}Zr_{0.85}O_{1.85}$
13/14	$M_{14}O_{26}$	γ	$4:6, 7_6, 8_7$	$Zr_5Sc_2O_{13}$
11/12	$M_{12}O_{22}$	β	—	Pr
10/11	$M_{11}O_{20}$	δ	—	Ce, Pr, Tb
9/10	$M_{10}O_{18}$	ε	—	Ce, Pr
8/9	M_9O_{16}	ζ	—	Ce, Pr
7/8	M_8O_{14}	Pyrochlore	$4:6_2, 8_2$	$La_2Ti_2O_7$
		—	$4:7_4$	Na_3UF_7
6/7	M_7O_{12}	ι	$4:6, 7_6$	Ce, Pr, Tb, $Zr_3Sc_4O_{12}$, WY_6O_{12}, UY_6O_{12}
5/6	M_6O_{10}	κ	$4:6_1, 7_2$	Sr_2UO_5, Cd_2UO_5
			$4:5, 7, 8$	La_2TiO_5, Pr
Variable excess	$MO_{1.5+x}$	σ	—	Ce, Pr, Tb, Pu, Am, Cm, Bk
3/4	M_4O_6	*C*-type sesquioxide	$4:6_2$	Mn, Pr, Pm-Lu, Y, Am, Cm
		Ideal $D5_5$	4:6	Bi, Sb
1/2	MX	Sphalerite	4:4	ZnS (no oxides), CuI, AgI
3/8	M_3X_4	Regular	—	β-Cu_2HgI_4, β-Ag_2HgI_4
3/8	M_3X_4	Random	—	α-Ag_2HgI_4, α-Cu_2HgI_4
1/3	M_3X_4	Random	—	γ-Ga_2Se_3
1/4	M_2O	HgI_2	4:2	HgI_2, SiS_2, Cu
1/8	MO_2	β-Cristobalite	2:4	Si, ($\frac{1}{2}Cu_2O$)

* Subscript indicates the relative number of atoms with the particular CN.

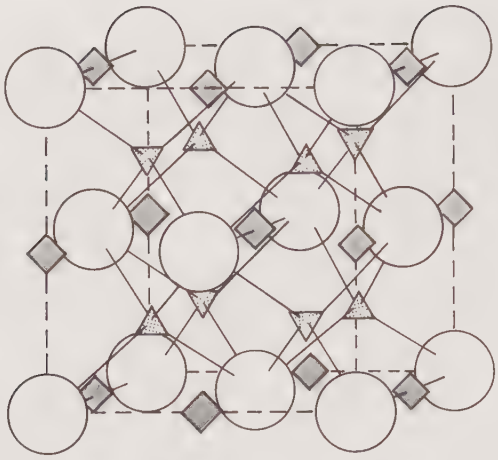

Fig. 35. A representation of the face-centered cubic arrangement of atoms indicating the position and type of interstitial sites. Triangles mark tetrahedral and squares locate octahedral sites.

There are many ways of visually representing the fluorite structure; each has its special appeal. One that is frequently encountered views one atomic network of a binary compound as in the cubic close-packed arrangement with the other atom occupying *all* the tetrahedral sites but none of the octahedral sites. When metal atoms are in the ccp arrangement the composition is MX_2 (M = metal atom, X = nonmetal atom). Figure 35 illustrates this arrangement if the circles represent metal atoms and triangles represent nonmetals.

On the other hand, one can consider the structure as consisting of oxygen atoms (X = O) in a simple cubic framework with the metal atoms occupying alternative cube centers in a three-dimensional checkerboard network of $[MO_8]$ coordination cubes sharing all edges.

In this view nonmetal-deficient structures may be represented as containing metal atoms with a CN of less than eight. There are advantages to this viewpoint and it has been utilized effectively to discuss the end members and ordered intermediate phases in the rare earth oxides,[32–35] as will be discussed in more detail below.

An analogous alternative approach is to consider the nonmetal coordination tetrahedra $[M_4X]$ in the fluorite structure as extended in all three directions sharing all edges. This arrangement of filled edge-sharing tetrahedra leaves edge-sharing octahedra empty. The

defect structures can then be represented simply as having some arrangement of empty tetrahedra. In this case one may focus on the filled coordination tetrahedra[36] or alternatively, as emphasized below, on the empty tetrahedra. The former approach is most effective in discussing broad classes of partially covalent compounds considered as consisting of layered slices of the edge-sharing tetrahedra of the fluorite structure of composition $(MX)_n^{n+}$ sandwiching anions of a wide variety,[37] by analogy to $(BiO)_n^{n+}$ structural chemistry. The structures assumed by compounds depend not only on efficient packing of spheres but also on the bonding characteristics of the specific atoms involved.

The architecture of the fluorite structure viewed from the point of view of the tetrahedral positions and their spatial relationships is illuminated if one views the face-centered cube as cut along all four $\{111\}$ planes.* This results in the formation of eight tetrahedra, one complete octahedron, and 12 polyhedra which are one-fourth of an octahedron. These polyhedral positions are indicated in Figure 35 by the triangles and diamonds.

It should be noticed that all tetrahedra and octahedra formed in this way have only $\{111\}$ faces. It will be useful later to observe that in this structure any particular tetrahedron may associate with another in only a few permissible ways to form a double tetrahedral unit: (a) A corner may be shared such that two edges, one in each tetrahedron, lie in a straight line in all six $\langle 110 \rangle$. This unit has a point group symmetry $2mm$ (C_{2v} in Schoenflies notation). (b) Edge-sharing may occur in each of the three $\langle 100 \rangle$ directions. This generates a unit with point group symmetry mmm (D_{2h}). (c) A double tetrahedron may be formed along each threefold axis of the tetrahedron in only one way. This occurs along the four $\langle 111 \rangle$ directions with point group symmetry $\bar{6}m2$ (D_{3h}). To facilitate reference to these geometries, the double tetrahedra shall be designated $U(C_{2v})$, $U(D_{2h})$, and $U(D_{3h})$, respectively. The distance between tetrahedral centers in the double unit increases in the order $U(D_{2h}) < U(C_{2v}) < U(D_{3h})$, as does the importance of this structural feature in oxides in the fluorite-related systems. If the vacancies are at the centers in the double tetrahedron, they result in edge, face-diagonal, or body-diagonal pairs in the $[MX_8]$ coordination cube, respectively.

It should be appreciated that isolated $(SiO_4)^{4-}$ tetrahedra but especially double tetrahedra of composition $(Si_2O_7)^{6-}$ of $U(C_{2v})$ and

* All indices in Section 3 shall refer to the fluorite structure unless otherwise specified.

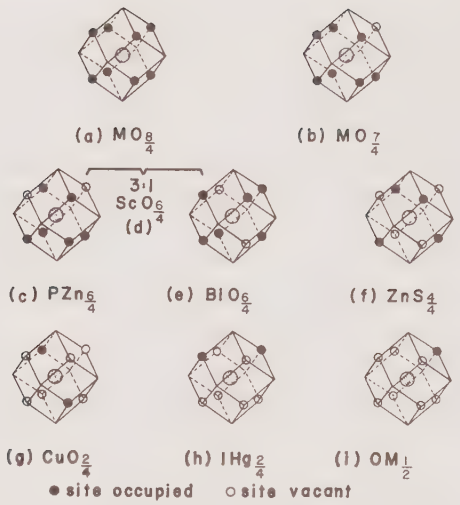

Fig. 36. Space-filling polyhedra of fluorite-related structures. (a) Fluorite. (b) Pyrochlore. (c) Zn_3P_2. (d) *C*-Type sesquioxide. (e) Bi_2O_3. (f) Sphalerite. (g) Cuprite. (h) HgI_2. (i) β-Cristobalite.

more often $U(D_{3h})$ type are the building blocks in the structure of silica and silicates. For example, a dense form of SiO_2 (coesite) consists of complex linkages of $U(C_{2v})$ groups, while the SiO_2 mineral β-cristobalite is a simple three-dimensional network of $U(D_{3h})$ groups.

An attractive alternative is to use SFP (Section 2.1.2) to represent fluorite-related structures[16] as shown in Figure 36. These diagrams emphasize the coordination of the metal atom in this case and illustrate structures resulting from the ordered removal of nonmetal atoms in the tetrahedral sites. The SFP facilitate visualization of the complimentary nature of the filled and empty tetrahedral sites. For example, one may observe just from the SFP representation in Figure 36 that the fluorite structure may be considered to be the superimposed sum of the V_2MO_6 (Bi_2O_3 structure) SFP and V_6MO_2 (Cu_2O structure), where V represents a vacant tetrahedral site. Indeed, if the complimentary Cu_2O structure of oxygen vacancies is subtracted from fluorite, the Bi_2O_3 structure results. This representation would be of much greater value if it were easier to visualize the extension to three-dimensional frameworks.

The idea of representing diamond, sphalerite, β-cristobalite, and fluorite, for example, as related by regular omissions or additions of atoms has been the basis of some useful crystal chemical representa-

tions.[38] The weakness of all these idealized treatments in not being exactly correct is surely more than compensated for by their demonstration of the striking interrelationships between structures.

As fundamental a concept as the unit cell is, its value in depicting complex defect structures is limited. It may, in fact, be true that this limitation is appropriate in that the unit cell concept, being a creation of perfect structure, may have reduced significance for the real structure of solids. To this extent, the larger views of void filling in closest-packing representation and infinite associations of coordination polyhedra or defect clusters are more useful concepts in considering substances having extended defects.

3.2. The Relationship between the Fluorite and Other Structures

To broaden the base of our consideration, it would be well to relate the fluorite structure to a number of others frequently observed. The basic structure types to be correlated are α-UO_3, CaF_2, La_2O_3 (*A*-type rare earth sesquioxide), and NaCl. A useful approach in this representation is to consider each member derived from its more oxidized predecessor by CS.[39]

The face-centered cubic unit cell of CaF_2 and NaCl may be represented as hexagonal with the transformation $/-\frac{1}{2}, 0, \frac{1}{2}/\frac{1}{2}, -\frac{1}{2}, 0$ $/1, 1, 1/$ and the highest symmetry of the subgroups from $Fm\bar{3}m$ would be $R\bar{3}m$. Both the α-UO_3 and La_2O_3 structure types are hexagonal with space group $P\bar{3}m1$.

The simplest hexagonal cell for the CaF_2 structure contains three units of CaF_2. The Ca atoms occupy the positions $0, 0, 0$; $\frac{2}{3}, \frac{1}{3}, \frac{1}{3}; \frac{1}{3}, \frac{2}{3}, \frac{2}{3}$. The oxygen atoms occupy positions $z = \frac{1}{4}$ above and below each Ca site. If the sites with x and y coordintes of $0, 0$ are labeled α for metal atoms and A for nonmetal atoms, those with $\frac{2}{3}, \frac{1}{3}$ are labeled β and B and those with $\frac{1}{3}, \frac{2}{3}$ are γ and C. The structures viewed as a series of atom layers along the **c** axis are shown in Table 11.

The table represents by arrows the progressive removal of a fraction of the close-packed basal planes of nonmetal atoms normal to the trigonal axis in a regular way, followed by collapse of the lattice and shear to restore the sequence of ccp of nonmetal planes (-*ABCABC*-) and cubic coordination of the metal atoms.

The sequence of metal planes is different among the four structural types but the nonmetal plane sequence is the same. The ideal CS displacement vectors are the same for each transformation, being the edge of the anion cube $\frac{1}{2}[001]$. It will be remembered that the Magnéli

TABLE 11
Layer Sequence and Crystallographic Shear Relationships among the α-UO_3, CaF_2, La_2O_3, and NaCl Structure Types*

	R_nO_{2n-2} (CaF_2, $n = \infty$)							
α-UO_3	∞	14	8	7	6	4	La_2O_3	NaCl
B	*B*	*B*	−1/4	−1/7	−1/6	−1/4	*B*	*B*
γ	γ						γ	γ
A	*A*	−1/7	*A*	−1/7	−1/6	−1/4	↓	↓
C	↓						↓	↓
B- -CS →	*C*	−1/7	*C*	−1/7	−1/6	−1/4- -CS →	*A*	*A*
γ	α						β	β
A	*B*	−1/7	−1/4	−1/7	−1/6	−1/4	*C*	↓
C	↓						↓	↓
B- -CS →	*A*	*A*	−1/4	−1/7	−1/6	−1/4	*B*- -CS →	*C*
γ	β						γ	α
A	*C*	*C*	*C*	−1/7	−1/6	−1/4	↓	↓
C	↓						↓	↓
B- -CS →	*B*	*B*	*B*	−1/7	−1/6	−1/4---CS →	*A*	*B*
γ	γ						β	γ
A	*A*	−1/7	−1/4	−1/7	−1/6	−1/4	*C*	↓
C	↓						↓	↓
B- -CS →	*C*	−1/7	−1/4	−1/7	−1/6	−1/4	*B*- -CS →	*A*
γ	α						γ	β
A	*B*	−1/7	*B*	−1/7	−1/6	−1/4	↓	↓
C	↓						↓	↓
B- -CS →	*A*	*A*	*A*	−1/7	−1/6	−1/4- -CS →	*A*	*C*
γ	β						β	α
A	*C*	*C*	−1/4	−1/7	−1/6	−1/4	*C*	↓
C	↓						↓	↓
B- -CS →	*B*	*B*	−1/4	−1/7	−1/6	−1/4	*B*- -CS →	*B*
γ	γ						γ	γ

* An eliminated anion layer is indicated by ↓. The CS operation is indicated by - - →.

phases are formed by a CS displacement of an edge of the nonmetal octahedron.

The CS sequentially increases the contact of the $[MO_8]$ cubes from corner and edge sharing in idealized α-UO_3, to all edge sharing in CaF_2, to edge and face sharing in idealized La_2O_3, to all face sharing in idealized NaCl. Whereas in the real α-UO_3 and CaF_2 structures the $[MO_8]$ polyhedra are unambiguous, in La_2O_3 one actually has $[MO_7]$ and in NaCl $[MO_6]$ coordination. In view of this the comparison may seem somewhat contrived but it does give insight into the structural relationships where no coherent view presently exists.

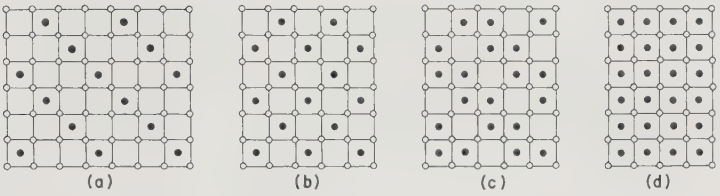

Fig. 37. Idealized projection of: (a) α-UO_3. (b) CaF_2. (c) La_2O_3. (d) NaCl(CsCl). Cations are solid circles centered within the simple cubic anion framework.

An alternative representation[40] relates the CaF_2 structure type on the one hand to the La_2O_3 (*A*-type) and Sm_2O_3 (*B*-type) structures on the other. In this case the simple cubic nonmetal atom framework is represented as stationary and CS is accomplished by metal atoms occupying interstitial positions as shown in Figure 37. In this way CS could produce a homologous series M_nO_{2n-1} having MO_2 slabs of varying thickness, as n changes, separated by the shear planes present in La_2O_3.

In reality it is the CsCl structure which is the "ideal" NaCl resulting from continued shear. These two structures are related to each other by an extension of CsCl in the $\langle 111 \rangle$ direction. The c/a ratios for the hexagonal unit cells are 1.225 for CsCl and 2.450 for NaCl. CsCl results from compression of the rhombohedral axis of NaCl by a factor of two with the concomitant change of the rhombohedral angle from 60° to 90°.

The foregoing discussion suggests that it might be possible to trace the mode of oxygen loss from α-UO_3 to TiO (MO_x, $3 \geq x \geq 1$) through a variety of oxides having structures which provide links in the structural sequence. This approach has already been anticipated in Tables 10 and 11.

3.3. Fluorite-Related Phases with Excess Oxygen

Loss of oxygen from α-UO_3 produces vacancies in its sublattice resulting in a lower coordination number of the metal atoms. Regions of U_3O_8-type structure may be formed as microdomains at some critical concentrations and these domains might grow at the expense of the α-UO_3 as reduction proceeds until stoichiometric U_3O_8, a superstructure of α-UO_3 with anion vacancies, is reached. It may be imagined that further reduction results in aggregation of oxygen vacancies on the $(0001)_h$ planes and crystallographic shear eliminates

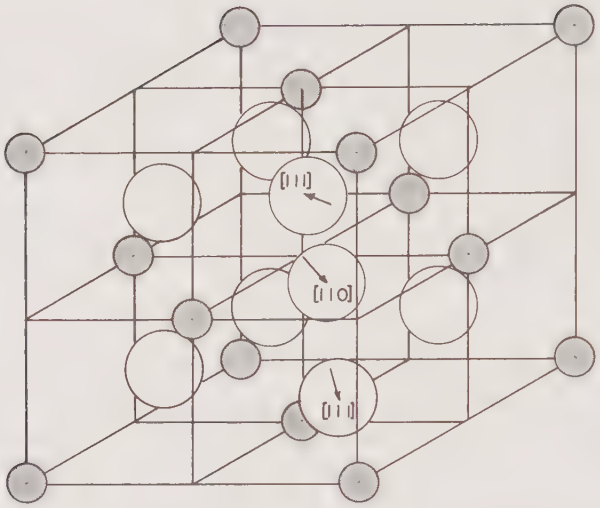

Fig. 38. Representation of the defect clusters occurring in UO_{2+x}. The extra oxygen is displaced about 1 Å from $\frac{1}{2}, \frac{1}{2}, \frac{1}{2}$ and two oxygens are displaced from normal tetrahedral sites as indicated.

the vacant sites in the transformation of $U_3O_8 \rightarrow U_4O_9$. U_4O_9 may be viewed as a superstructure of fluorite UO_2 with ordered extended defects consisting primarily of oxygen interstitials.[41] These extended defects are disordered in hyperstoichiometric UO_{2+x}.

The excess oxygen in UO_{2+x} is accommodated in a complex way. It has not been possible to give a unique solution to the problem of defect size and atomic arrangement; however, a plausible model consistent with the observed Bragg intensities has been proposed. Rather than the excess oxygen entering the fluorite unit cell at the $\frac{1}{2}, \frac{1}{2}, \frac{1}{2}$ position as originally supposed, it is off-center about 1 Å in the [110] direction. Consequently the two closest oxygens are displaced from their fluorite positions about the same distance in the [111] directions as shown in Figure 38. This extended defect (with reference to the fluorite structure) consists of a cluster of five point defects: three interstitial atoms in different kinds of sites and two oxygen vacancies. Such an extended defect appears to develop long-range order at lower temperatures when the composition essentially reaches U_4O_9. The complex does not have cubic symmetry and it is correlated in a complicated way to give the unsolved superstructure of U_4O_9 made up of $4 \times 4 \times 4$ fluorite subcells (576 oxygen atoms).

There is evidence that other hyperstoichiometric fluorite structures such as yttrium-doped calcium fluoride contain clusters very similar to those in UO_{2+x}.[42] In this case there is no indication of superlattice formation but broad, diffuse scattering confirms defect clusters.

3.4. The Fluorite-Related Homologous Series

The rare earth oxides, typified by praseodymium oxide, shall be the primary thread in the discussion of fluorite-related oxides MO_x ($1.5 \leq x \leq 2.0$). There are, however, many pseudobinary systems which possess fluorite-related oxides belonging, no doubt, to this structural family. They shall be discussed where they provide additional examples. It is not clear at present how many compositional and structural series exist in this range. The one to be discussed has members of formula M_nO_{2n-2} where examples are known for $n = 4$, 6–12, 14, and ∞.

Removal of oxygen from fluorite-related oxides leaves tetrahedral sites unoccupied. The high mobility of oxygen in these phases permits an ordered structure of low free energy to be formed rapidly at relatively low temperatures. The result is an ordered distribution of tetrahedral voids over the sum of such positions. In the structures of all known oxygen-deficient fluorite-related phases the voids are condensed in pairs as double tetrahedra, $U(D_{3h})$, and these condensed units themselves are ordered or further condensed depending on the composition.

3.4.1. The Iota and Gamma Phases

The only intermediate binary phase for which the structure is known is M_7O_{12} (ι phase) of space group, $R\bar{3}$. On the other hand, the ternary phases UY_6O_{12} and $Zr_3Sc_4O_{12}$ are isomorphous with Tb_7O_{12}. The structure of $Zr_5Sc_2O_{13}$ (γ phase) has been determined to have the same space group and a very closely related defect structure.[35,43,44]

In Figure 39 the known structures of the fluorite-related system under discussion are represented in projection on the (111) plane. This projects the stacking sequence of metal planes listed in Table 11 onto the (111) plane.

In Figure 39(a) the fluorite cell is shown projected along one of the threefold axes. The oxygen atoms (not shown) occupy positions

Fig. 39. Projections of the metal atom framework of several fluorite-related homologues along the hexagonal **c** axis. (a) Fluorite. (b) The iota and gamma phases. (c) Pyrochlore structure type. (d) The kappa phase. (e) The *C*-type sesquioxide. The Greek letters α, β, and γ represent the three levels in the ccp array. Boldface letters signify vertical strings of $U(D_{3h})$ units. Solid arrows indicate other $U(D_{3h})$ strings whose lengths correspond to the spacing between tetrahedral centers. Dashed lines indicate the projected distance between tetrahedral centers in the $U(C_{2v})$. Dotted lines outline a projected unit cell.

above and below each metal atom (the M–O distance for PrO_2 is 2.234 Å). This O–M–O unit with the other six-coordinating metal atoms is the $U(D_{3h})$ double tetrahedron. These units are separated by the vacant octahedral sites forming $U(D_{3h})$ *strings* in the $\langle 111 \rangle$ directions.

Similarly the structure of M_7O_{12} is represented in Figure 39(b) as a triple hexagonal cell. The two missing oxygen atoms from the fluorite composition form $U(D_{3h})$ double tetrahedral strings along the $\langle 111 \rangle$ direction of the cube perpendicular to the plane of the page. These threefold axes are marked with larger boldface symbols.

The unit cell in this projection is the same for the γ phase but the length of the **c** axis is twice that of ι phase. The doubled **c** axis results

from alternate filling of the $U(D_{3h})$ units along the strings. As may be seen from Figure 39(b), all the oxygens are missing from 1/7 of the rows of parallel and symmetrically placed strings in M_7O_{12} and half that number, or 1/14, are missing from $M_{14}O_{26}$, giving $MO_{2-(2/7)} = M_7O_{12}$ or $MO_{2-(2/14)} = M_{14}O_{26}$, respectively, as required.

The coordination number of the shared metal atom in the double tetrahedron is six; hence the strings in M_7O_{12} give unbroken rows of six-coordinated metal atoms surrounded by ones having seven coordination.

In $M_{14}O_{26}$ alternate metal atoms in the rows are eight-coordinated. The parameters for the fluorite-related phases are collected in Table 12.

TABLE 12
Unit Cell Parameters of Representative Fluorite-Related Phases

Phase	Symmetry and lattice parameters of pseudocells*	Symmetry and lattice parameters of true cells*
$MO_{2.00}$	—	FCC (fluorite), $Fm3m$
(PrO_2)		**a** = 5.393(2)
$M_{14}O_{26}$	—	Rhombohedral, $R\bar{3}$
($Zr_5Sc_2O_{13}$)		**a** = 8.00(5), α = 73.0(8)
$M_{12}O_{22}$	—	Monoclinic, $P2_1/n$
($Pr_{24}O_{44}$)		**a** = 6.687(4), **b** = 11.60(2)
		c = 15.47(0), β = 125.25(7)
$M_{11}O_{20}$	Triclinic	Triclinic
($Pr_{11}O_{20}$)	**a** = 5.47(3), **b** = 5.47(4), **c** = 5.47(5), $\alpha = \beta = \gamma \cong 90.09$	
($Tb_{11}O_{20}$)	—	**a** = 9.9, **b** = **c** = 6.5, α = 80.4, β = 90.0, γ = 83.7
$M_{10}O_{18}$	Triclinic	—
($Pr_{10}O_{18}$)	**a** = **b** = **c** = 5.482(0) $\alpha = \beta$ = 90.28, γ = 90.09	
M_9O_{16}	Triclinic	—
(Pr_9O_{16})	**a** = 5.47(8), **b** = 5.48(2) **c** = 5.49(6), α = 90.15 β = 90.50, γ = 90.91	
M_8O_{14}	—	Cubic, $Fd3m$
($Pr_2Ru_2O_7$)		**a** = 10.35(5)
M_7O_{12}	—	Rhombohedral, $R\bar{3}$
(Pr_7O_{12})		**a** = 6.74(1), α = 99.28
M_6O_{10}	—	Monoclinic $P2_1/c$
($Sr_8U_4O_{20}$)		**a** = 8.10(4), **b** = 5.66(1), **c** = 11.91(8), β = 108.9(8)
M_4O_6	—	BCC, $Ia3$
(C-type Pr_2O_3)		**a** = 11.15(2)

* **a**, **b**, **c** in Å; α, β, γ in degrees.

3.4.2. The Beta Phase

The unit cell of $Pr_{12}O_{22}$ (β phase) has been determined[45] and its relationship to the fluorite unit cell established by the transformation $/-\frac{1}{2}, -\frac{1}{2}, 1/-\frac{1}{2}, +\frac{1}{2}, 0/2, 2, 0/$. The volume is six times that of the subcell which contains four MO_2 units. Since 1/12 of the oxygens are missing, this gives a unit cell composition of $M_{24}O_{44}$. The four missing oxygens seem likely to be ordered as two $U(D_{3h})$ but the structure has not yet been determined.

3.4.3. The Delta Phase

When one oxygen in 11 is removed from MO_2, $M_{11}O_{20}$ (δ phase) is formed. The triclinic unit cell has been determined from electron diffraction patterns to be derived from the fluorite subcell by the transformation $/1, \frac{1}{2}, -\frac{3}{2}/\frac{1}{2}, 1, \frac{1}{2}/1, -\frac{1}{2}, \frac{1}{2}/$. The cell parameters for $Tb_{11}O_{20}$ are listed in Table 12. There are two oxygens missing in this unit cell, possibly as a $U(D_{3h})$, but the structure is not yet known.

3.4.4. The Epsilon Phase

The powder diffraction pattern of $Pr_{10}O_{18}$ (ε phase) has been indexed on a triclinic pseudocell with $\mathbf{a} = \mathbf{b} = \mathbf{c}$ and $\alpha = \beta \neq \gamma$ (see Table 12), which accounts satisfactorily for the strong lines of the powder diffraction pattern. Neither the true unit cell not the structure is known.

3.4.5. The Zeta Phase

The powder diffraction pattern of Pr_9O_{16} (ζ phase) has been indexed on a triclinic pseudocell with $\mathbf{a} \neq \mathbf{b} \neq \mathbf{c}$ and $\alpha \neq \beta \neq \gamma$ (see Tabel 12).

3.4.6. Pyrochlore Phases

Oxides of the composition M_8O_{14} belonging to the homologous series of *binary* compounds have not been observed. On the other hand, there are scores of pseudobinary compounds having the cubic pyrochlore structure with composition $A_2B_2O_7$. The space group for this ideal structure is *Fd*3*m*. In these compounds the A atom is larger than B with less disparity than exists in M^{3+}, M^{4+}, where M is the same element.

The ideal pyrochlore structure is generally considered to be fluorite-related by loss of 1/8 of the nonmetal atoms forming ordered $U(D_{3h})$ vacancy pairs occurring alternately along threefold axes as indicated in Figure 39(c). One of the $\langle 111 \rangle$ axes is indicated as before. This means parallel threefold axes are through each corner of the fluorite subcell. The cubic pyrochlore structure has a cell edge twice the basic fluorite unit. In this case the proximity of the half-filled strings results in an interpenetrating framework of $[VM_4]$ tetrahedra sharing all corners, resulting in tetrahedrally coordinated vacancy tetrahedra. This complimentary structure may be recognized as the β-cristobalite structure type where the silicon atoms correspond to the oxygen vacancies. There is another β-cristobalite type of interpenetrating framework consisting of the alternate filled $U(D_{3h})$ in the strings. If the oxygen in this latter framework were also removed, the interpenetrating complimentary framework would be Cu_2O type and one oxygen in four would have been removed. The remaining oxide has the composition M_2O_3 and the structure is that proposed for Bi_2O_3.[46] Neither of these structures is known in the binary rare earth oxides but they clearly belong to the same defect series type.

In terms of complimentary structures

$$(M_4O_8)_{\text{fluorite}} - (M_2O)_{\beta\text{-cristobalite}} = (M_4O_7)_{\text{pyrochlore}}$$

$$(M_4O_8)_{\text{fluorite}} - 2M_2O_{(Cu_2O)} = (M_4O_6)_{Bi_2O_3}$$

Space-filling polyhedra may be used to illustrate the relationship between these structures by noting in Figure 36 that (a) − (i) = (b) and (a) − (g) = (e).

In reality the pyrochlore structure often observed[47,48] may be designated $A_2B_2O_6O'$ ($Z = 8$) to emphasize the four crystallographically nonequivalent kinds of atoms. This structure may be considered as consisting of $[AO_8]$ and $[BO_6]$ coordination polyhedra sharing edges. The $[AO_8]$ polyhedra possess two A–O distances shorter than the other six, hence $[AO_2]$. It is convenient to consider the $[AO_2]$ and the $[BO_6]$ as two interpenetrating frameworks. In the $[AO_2]$ portion the A atom is in linear coordination while the oxygens associated with it are in tetrahedral coordination, the β-cristobalite structure type. As before this is one of the interpenetrating frameworks of the Cu_2O structure. The B_2O_6 residue of the structure consists of $[BO_6]$ coordination octahedra sharing edges such that each group is at the corner of a tetrahedron forming a unit having a point group symmetry T_d. These units are interlocked in a ccp arrangement.

It is possible to have defects in the oxygen sublattice of pyrochlore which result in the formation of a perovskite $A_2B_2O_6$ formed at high pressure and temperature. In this case the BO_3 framework becomes the ReO_3 type and the A atoms fit into all the all-anion octahedral sites. In the perovskite structure the A atoms are positioned around the B atoms at the corners of a cube, whereas the six A atoms around the B atom in the pyrochlore structure are in the same plane as B.

3.4.7. The Kappa Phase

The structure of Sr_2UO_5 has been determined[49] to have the space group $P2_1/c$ with $\mathbf{a} = 8.104$ Å, $\mathbf{b} = 5.661$ Å, $\mathbf{c} = 11.919$ Å, and $\beta = 108.985°$, and obviously belong to the fluorite-related system.[16] In this case the uranium atoms are all in $U(D_{3h})$ strings in the [111] and $[1\bar{1}1]$ directions in $(10\bar{1})$ planes and the strontium atoms are in two adjacent parallel planes (Figure 39d). The spacing of the $U(D_{3h})$ strings in the $(10\bar{1})$ plane is the same as in Bi_2O_3 (Figure 39c). However, the strings are equally spaced in the $(\bar{3}21)$ planes at the same interval as in M_7O_{12} (Figure 39b). The structure of Pr_6O_{10} is unknown but the powder diffraction pattern suggests a very close relationship to *C*-type Pr_2O_3.

There is another M_6O_{10} compound of formula La_2TiO_5[16] which ideally involves continuous zigzag ribbons of edge-sharing vacancy tetrahedra, $U(D_{2h})$, and hence does not fit into the family of fluorite-related oxides being discussed.

3.4.8. The Sesquioxides

One structure type of this composition (Bi_2O_3) has already been discussed (Figure 39c). It is generated if $U(D_{3h})$ strings are parallel and along the body diagonal of the $[MO_8]$ coordination cubes of all unit cells of the fluorite host lattice, producing intersecting strings in all $\langle 111 \rangle$ directions.

The *C*-type sesquioxide is an interesting variation of this connectivity. In this case also all the oxygen is missing in nonintersecting $U(D_{3h})$ strings in all four $\langle 111 \rangle$ directions. The closest approach of the strings is across face diagonals of the $[MO_8]$ coordination cubes, generating $U(C_{2v})$ double tetrahedra in three times the number of $U(D_{3h})$. The cubic unit cell is twice the cell edge of the fluorite subcell. The *C*-type structure is represented by comparison to others in Figure 39(e).

When the higher oxides of praseodymium are reduced to the sesquioxide at temperatures between 550 and 1000°C the *C* form is always obtained directly. It then transforms to the *A* form at a rate which increases rapidly with temperature. This would be achieved by a complex CS and the filling of all oxygen planes. The relationship between the *A*- and *B*-type rare earth sesquioxides has been discussed in Section 3.2.

3.4.9. Disordered Fluorite-Related Nonstoichiometric Phases

Many fluorite dioxides lose oxygen to form hypostoichiometric fluorite phases, frequently with a very wide composition range. This is true, for example, in MO_{2-x} (α phase) as listed in Table 10. The powder patterns of these phases have invariably been indexed as fluorite with a variable lattice parameter which increases with increasing vacancy concentration.

At present the structure of this phase is not known in any greater detail but it is generally believed to possess a great deal of short-range order at low temperatures which could involve $U(D_{3h})$ double tetrahedra randomly arranged in the four $\langle 111 \rangle$.

There is another phase of variable composition $MO_{1.5+x}$ (σ phase) which can be considered as hyperstoichiometric *C* type as listed in Table 10. In this case the concentration of oxygen vacancies is much higher than in the α phase and a different type of random behavior must exist. Indeed, the two nonstoichiometric phases are immiscible even at high temperatures not only in the binary compounds mentioned but in the pseudobinary phases as well.

3.4.10. Other Fluorite-Related Oxides

The sphalerite structure (ZnS) is closely related to the fluorite structure having half the nonmetal atoms removed. Figures 36(f) and 36(a) illustrate the relationship between their CN. No oxide has this structure. In terms of nonmetal vacancies, all are missing in alternating criss-crossed continuous strings of $U(C_{2v})$ in the $[1\bar{1}0]$ and $[110]$ directions, making a two-dimensional network of alternatively filled and empty rows. A similar operation along $[101]$ or $[10\bar{1}]$ generates similar linkages in the third direction. Of course, the fluorite-related structure complimentary to sphalerite is sphalerite.

The fluorite-related oxides having O/M less than unity have been previously dealt with as complimentary structures of MO_x ($1.5 \leq x \leq 2.0$) and have been depicted as SFP in Figure 36.

4. Extended Defects in the NaCl Structure Type

There are a number of nonstoichiometric monoxides usually said to be of the rocksalt structure type. Of these, TiO and VO are to be clearly distinguished from $Mn_{1-x}O$, $Fe_{1-x}O$, $Co_{1-x}O$, and $Ni_{1-x}O$. As will be seen, the structures of most of these phases are probably not of the NaCl structure type because of ordering of defects. The structures of TiO, VO, and $Fe_{1-x}O$ shall be discussed.

4.1. Nonstoichiometry and Defect Structure of Titanium and Vanadium Monoxides

4.1.1. The Titanium Monoxide Phase

A single-phase region exists in the $TiO_{1+x}(-0.16 \leq x \leq 0.30)$ system at temperatures below 990°C. At higher temperatures the range is larger. The stoichiometry is achieved with varying proportions of both metal and nonmetal vacancies always occurring together; 15% of each are present in TiO. At $TiO_{0.84}$ the metal sublattice is almost perfect, while at $TiO_{1.30}$ the oxygen sublattice is virtually complete. This is not to imply that the vacancies occur at random. On the contrary, it is known that they are highly ordered at long range below 990°C and probably have a good deal of short-range order above that temperature.

4.1.2. Ordered Phases

The lattice parameter of the rocksalt type unit cell is $\mathbf{a}_0 = 4.182$ Å. Annealed samples of TiO show superstructure in their X-ray or electron diffraction patterns.[50] A monoclinic cell of space group $A2/m$ and lattice parameters $\mathbf{a} = 5.855$ Å $\simeq \mathbf{a}_0\sqrt{2}$, $\mathbf{b} = 9.340$ Å $\simeq \mathbf{a}_0\sqrt{5}$, $\mathbf{c} = 4.142$ Å $\simeq \mathbf{a}_0$, and $\gamma = 107°32' \simeq \cos^{-1}(-1/\sqrt{10})$ describes the crystal. The corresponding distorted cubic unit cell would have $\mathbf{a} = 4.200$ Å, $\mathbf{b} = 4.143$ Å, and $\mathbf{c} = 4.142$ Å with $\gamma = 89°9'$.

The unit cell of the ordered phase contains 12 each of metal and nonmetal sites with 16.7% vacancies in each. Half the titanium and half the oxygen atoms are missing alternately in every third $(100)_c$ plane of the original cubic cell (see Figure 40). This results in slightly greater

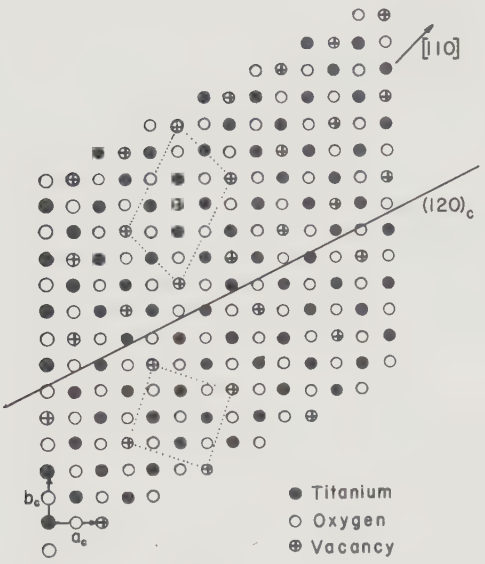

Fig. 40. Arrangement of atoms near the interface plane of the alternate plates in ordered $TiO_{1.19}$. Upper half of the figure is ordered TiO type and lower half the ordered $TiO_{1.25}$: dotted lines indicate the projected unit cells. (After Watanabe.[50])

spacing for this $(110)_c$ than that of other $\{110\}$ and hence the monoclinic distortion. This structure is capable of nonstoichiometry in the range $TiO_{0.9}$–$TiO_{1.1}$. At lower oxygen contents ($TiO_{0.7}$–$TiO_{0.9}$) a superlattice cell involving six each of Ti and O atoms appears. This unit cell is orthorhombic with space group $I222$ with $\mathbf{a} = \mathbf{a}_0/\sqrt{2}$, $\mathbf{b} = 3\mathbf{a}_0/\sqrt{2}$, and $\mathbf{c} = \mathbf{a}_0$. It is assumed that ordered oxygen vacancies occur on every third $(110)_c$ plane but with random Ti vacancies which are of very low concentration at this composition.

The structure of the ordered $TiO_{1.25}$ is tetragonal with $\mathbf{a} = \mathbf{a}_0'\sqrt{10}/2 = 6.594$ Å and $\mathbf{c} = \mathbf{a}_0' = 4.171$ Å with space group $I4/m$, where $\mathbf{a}_0'$ is the cell parameter of the low-temperature cubic form. The filled unit cell would have ten each of Ti and O atoms but the correct symmetry is observed if two titanium atoms are missing from the tetragonal cell (see Figure 40). This also gives the correct stoichiometry.

In this case the complimentary vacancy structure is that of the Ni_4Mo structure type where the Ti atoms correspond to Ni and the four-coordinated vacancies to Mo.

4.1.3. Disordered Phases

As in the fluorite-related homologous series and their disordered counterparts (α and σ phases of Table 10), the vacancies appear to have become a palpable part of the structure, which remains closely related to the NaCl type; hence ordered members of the series can intergrow with low energy boundaries.

Electron miscroscopic diffraction studies[50] have shown that intermediate compositions are accommodated at low temperatures by the intergrowth of $TiO_{1.00}$ and $TiO_{1.25}$, each a completely ordered material capable of intergrowth as shown in Figure 40.

4.1.4. The Vanadium Monoxide Phase

Compositionally the vanadium and titanium monoxide phases have much in common. The range of existence of VO_{1+x} ($-0.14 < x < 0.25$) has been determined.[51] Stoichiometric VO contains about 16% vacancies of each type ($V_{0.84}O_{0.84}$).

Evidence for order–disorder transitions were found[52] in an annealed single-crystal specimen of composition near $VO_{1.30}$. The ordered phase at low temperature is suggested as a superstructure of $V_{52}O_{64}$, which had previously been proposed as the ordered structure.[53] In addition to the normal octahedrally coordinated V and O positions, the structure contains interstitial tetrahedral sites filled with vanadium but with tetrahedrally coordinating atom sites vacant. The extra vanadium atoms were then removed from a larger superlattice containing 320 oxygen atoms.

The fact that the rocksalt structure type of vanadium and titanium oxides have about the same composition at high temperatures but are practically immiscible suggests that the free-energy difference between their defect structures having only short-range order is appreciable.

4.2. The Defect Structure of $Fe_{1-x}O$

A classical problem in the structure of materials having extended defects is that of wüstite. This phase of approximate rocksalt structure type, often called the FeO phase, does not contain the stoichiometric composition in its phase field at ordinary pressures. The phase diagram of wüstite in the composition range between about $Fe_{0.953}O$ and $Fe_{0.825}O$ is well known. Since the ideal structure would contain Fe and O in a 1 : 1 ratio, it must be highly defective. As a matter of fact,

a study of certain thermodynamic properties of wüstite has suggested the phase field should be divided into three regions.[54]

Recent studies of the defect structure of wüstite and $Mn_{1-x}O$ seem to be converging upon the same type of defect cluster. In the wüstite study[55] single crystals were adjusted to a composition of $Fe_{0.902}O$. Detailed comparisons of peak profiles and structure factors with what would be expected from model structures were made. Satisfactory agreement was found with a defect cluster the size of one fcc unit cell (Figure 41). In the idealized cluster the metal atoms of the unit cell are all moved from their octahedral positions, leaving 13 vacancies at octahedral sites. Four metals are located in four of the eight interstitial tetrahedral sites. This unit cell corresponds to an antisphalerite structure. The composition of this isolated cluster is FeO. It must be surrounded by a region of net positive charge, since it would be intrinsically negative.

The cluster is not a unit of the magnetite structure as had been suggested earlier,[56] nor is it a unit of spinel. The clusters are ordered only in quenched specimens. Diffuse neutron scattering measurements indicate multiclusters formed from groups of the clusters just described. Quadrupole splitting has been observed in the Mössbauer spectra,[57] suggesting some distortion of the ideal cluster and perhaps even some modification of it.

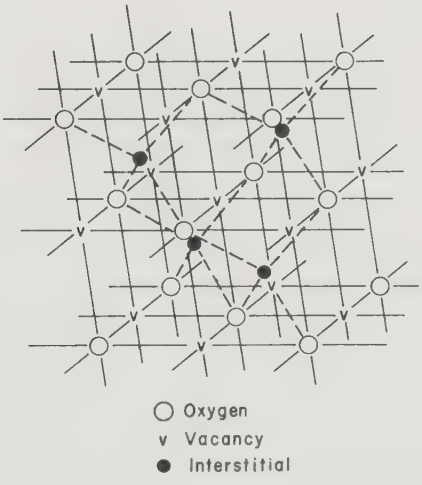

Fig. 41. The defect cluster in wüstite. One fcc unit cell is shown.

5. Stoichiometry and Structure of Highly Conducting Solid Electrolytes

The crystal structures of certain ionic conductors are unusual and permit extreme mobility of atoms at easily accessible temperatures. Materials with high atom mobility are potentially of great practical use as solid electrolytes in a wide variety of scientific and engineering applications (see Chapter 6, Volume 4). Useful materials seem to be divided into three categories: (a) Those in which oxygen is mobile at high temperatures, such as calcia or yttria-stabilized zirconia; (b) those in which alkali metal or silver ions are mobile at moderate temperatures, as in β-alumina; and (c) those in which silver, mercury, or copper ions migrate at relatively low temperatures, such as in the halides or chalcogenides.

5.1. The Structure of Calcia-Stabilized Zirconia

When about 15% CaO is added to monoclinic ZrO_2 and the mixture sintered at 2000°C only the cubic reflections are detected in Debye–Scherrer X-ray patterns. Single crystals are grown by the Verneuil method without change in composition. This anion-deficient, fluorite-related phase is historically the most important of the high-temperature anionic conductors. It has usually been called calcia-stabilized zirconia, CSZ.

It is clear that the unusual transport properties are due to the oxygen vacancies and to the positional disorder of oxygen. The transport number for oxygen ions is unity, with negligible cation or electronic conductivity above about 1000°C.

When CSZ is cooled from above 1200°C it is found in a disordered form in which Ca and Zr ions occupy the cation sites and oxygen ions and vacancies occupy the anion sites.[58] In addition, there is a positional disorder of the oxygen due to random displacements within their tetrahedral site. The statistical disorder results in observed diffuse neutron scattering.

Although pycnometric density measurements indicated a 1.5% occupancy of the vacant interstitial sites of the CaF_2 structure, the X-ray measurements did not have the necessary sensitivity to detect it. On the other hand, the neutron scattering measurements are in agreement with a disordered structure of eight fractional oxygens about each metal atom of the $[MO_8]$ coordination cube if the oxygens are statistically displaced within their $[OM_4]$ coordination tetrahedra

Fig. 42. Schematic drawing illustrating growth of ordered domains of deformed oxygen polyhedra. Solid circles are cations; oxygens are now shown, but are at the corners of the coordination figure. (After Carter and Roth.[58])

along the ⟨111⟩ directions. The average displacement is about 0.2 Å and is almost independent of composition.

When CSZ is aged at about 1000°C the diffuse neutron scattering due to disorder gives way to additional sharp peaks not allowed from the fluorite structure. This is interpreted as metal atoms remaining in fluorite positions but having an ordered but distorted oxygen framework approaching the Zr–O intervals characteristic of monoclinic ZrO_2. The disorder–order transition is seen to be the differentiation of the disordered region into ordered domains of deformed oxygen polyhedra (Figure 42). The distortion of the $[MO_8]$ coordination cube is as though a pair of opposite face diagonals of the cube were squeezed, producing two rhombic faces with the acute angles across the body diagonal from the obtuse corner. No knowledge of the ordering of Ca and O exists, since a supercell was not observed.

5.2. The Structure of Some Beta-Aluminas

Beta-alumina was originally believed to be a polymorph of alumina but later was indicated to be $Na_2O \cdot 11Al_2O_3$ (often written $NaAl_{11}O_{17}$) but usually appears to be nonstoichiometric. There are at least three sodium beta-aluminas: β, β', and β''. Only the first shall be discussed since it is the material most completely described. Reviews of the history, useful properties, and promise of these remarkable materials, sometimes termed superionic conductors, have been written.[59–61]

Beta-alumina usually refers to a large family of isomorphs with a generic formula of $AM_{11}O_{17}$, where A may be Na, K, Rb, or Ag and M may be Al, Fe, or Ga. Most structural work on these compounds has been done on the sodium and the silver compounds on which structural refinements have been made.[62,63]

5.2.1. Sodium Beta-Alumina

The structure of sodium β-alumina is hexagonal, space group $P6_3/mmc$ with $\mathbf{a} = 5.594$ Å, $\mathbf{c} = 22.603$ Å, and an observed density of 3.253 g/cm^3. The average unit cell composition is $Na_{2.46}Al_{22}O_{34.23}$. It is a layer structure consisting of "spinel blocks" (having a structure similar to $MgAl_2O_4$) separated by a thin layer containing all the alkali metal atoms. This thin region is a basal mirror plane at $z = \frac{1}{4}$ and $\frac{3}{4}$. The spinel block consists of a distorted ccp arrangement of oxygens with two different Al atoms in octahedral sites and two others in tetrahedral sites. Distortions from ideal octahedral and tetrahedral coordination in these spinel blocks are almost unchanged as the composition of the mirror plane is changed.

Figure 43(a) shows a section of the structure of β-alumina in the $(2\bar{1}0)$ plane. Half the repeat distance is seen to be about 11.23 Å, while the width of the mirror plane regions is about 4.76 Å. The arrangement of the atoms in the mirror plane which is perpendicular to the **c** axis is shown in Figure 43(b). The radii shown for the atoms are proportional to the usual ionic radii, illustrating the relatively loose packing in this plane. The lightly shaded circle represents a frequently occupied position of Ag in the silver β-alumina to be described later.

As has been mentioned, these compounds are usually nonstoichiometric. The composition of the crystal whose parameters were given above contained 23% excess sodium over the "ideal" composition. The Na positions indicated as heavily shaded circles in

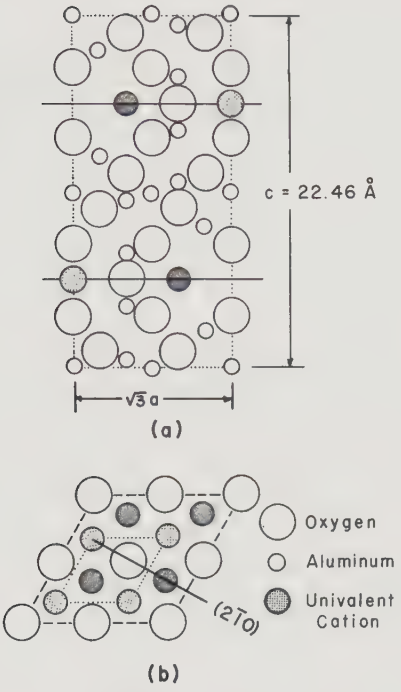

Fig. 43. (a) The structure of β-alumina in the $(2\bar{1}0)$ plane. All the nonequivalent atomic positions are represented in this section. (b) The atomic arrangement in the mirror plane at $z = \frac{1}{4}, \frac{3}{4}$. The special positions b and d (lightly and heavily shaded circles, respectively) are statistically occupied by the univalent metal atoms.

Figure 43(b) are only 75% occupied at room temperature and the distribution of electron density around the site is very broad and triangular. The remaining Na atoms are located in elongated ellipsoids centered near positions halfway between the oxygens.

The charged balance required by the excess sodium has been suggested to be achieved in sodium β-alumina by aluminum vacancies in the spinel block adjacent to the mirror plane. The question has not been entirely settled, however, since increased oxygen content is favored in the case of silver β-alumina.[63] It is possible, of course, that electroneutrality is achieved in different ways in these two cases.

5.2.2. Silver Beta-Alumina

Crystals of silver β-alumina prepared by Ag exchange when sodium β-alumina is submerged in molten $AgNO_3$ at 370°C for several days have been studied by X-ray and electron diffraction.[63,64] They are hexagonal, space group $P6_3/mmc$ with **a** = 5.595 Å, **c** = 22.448 Å, an average composition $Ag_{2.4}Al_{22}O_{34.2}$, and a density of 3.813 g/cm^3. The spinel block is virtually as described above. The atomic arrangement in the mirror plane containing the univalent atom is, however, very different.

The silver atoms are distributed statistically over the special positions *b* (lightly shaded circles) and *d* (heavily shaded circles) in the basal mirror plane (Figure 43) with an average of 43% occupancy of the *b* sites and 84% of the *d* sites. The best agreement with observed diffraction data was obtained when the excess oxygen was placed between the two Ag atoms. Silver atoms are actually displaced from the $\bar{6}$ axis and there are bulges of electron density about the *d* position. This is to say that there is considerable disorder in the mirror planes, which accounts for the high mobility of cations.

A domain model has been suggested to account for the nonstoichiometry in silver β-alumina.[63] It is assumed that both types of silver atoms are distributed in domains of stoichiometric composition $AgAl_{11}O_{17}$. Nonstoichiometry results from a high concentration of silver in the domain boundary. The domains coexist in what appears to be a single crystal but which in fact is a syntactic intergrowth of the two types of domains. One domain has silver in the *d* positions and the other in the *b* positions. The domain boundary is then seen to contain 1.5 or 2.0 silver atoms per spinel block. In the latter case the arrangement is that in the β''-alumina structure. It is proposed that this domain model could equally well explain nonstoichiometry in sodium β-alumina. The structure of an actual specimen would depend upon its thermal history.

5.3. The Structure of Halide and Chalcogenide Solid Electrolytes

A review[65] of halide and chalcogenide solid electrolytes suggests their unusual characteristics. Among this group of solid electrolytes are some with fluorite-related structures as indicated in Table 10. At 250°K the conductivity of NaCl is about 10^{-18}/ohm-cm whereas that for $RbAg_4I_5$ at the same temperature is about 10^{-1}/ohm-cm. This difference of 10^{17} between these alkali-containing halides is only

partly accounted for by the differences in melting points. The iodide is one of a class of superionic conductors based on the halides and chalcogenides of copper and silver which have been studied for years.

It has been known for about forty years that a characteristic of these types of solid electrolytes is the existence of a more or less rigid anion framework with partial occupancy of the available cation sites in the structure by the Cu or Ag atoms. The conductivity of some of these solids is comparable to aqueous electrolyte solutions of reasonable concentration even at room temperature. A marked feature of these superionic conductors is a low temperature coefficient of resistivity so that they retain reasonably high conductivities to low temperatures.

5.3.1. Body-Centered Cubic Arrangement of Anions

In the bcc anion framework of α-AgI there are 12 face-sharing tetrahedra per unit cell. It is believed that the high mobility of Ag is due to occupancy of not only the tetrahedral sites but also of the face-shared and the octahedral sites to give a quasimolten state for the silver component.

Other compounds also have this structure with some modification of the site occupancy. For example, in α-Ag_2Se there appears to be a preference of silver for occupancy of the tetrahedral sites. The high-temperature Ag_3SI is very similar, with random occupancy of the anion sites by S and I. Compositional differences of compounds with this anion substructure demand different silver occupancy, i.e., two for halides, three for α-Ag_3SI, and four for α-Ag_2S.

In some compounds of two different anions, such as in β-Ag_3SI and Ag_3SBr, space group $Pm3m$, ordering occurs and the (0, 0, 0) position is occupied by I^- (or Br^-) and the S^{2-} ion is located at the center $(\frac{1}{2}, \frac{1}{2}, \frac{1}{2})$. The three silver ions are situated on the 12(h) tetrahedral interstices. These sites are the same as in α-Ag_3SI for $x = \frac{1}{4}$ but for $x = \frac{1}{2}$, 12(h) sites collapse into 3(c) sites of the ideal anti-perovskite structure.

5.3.2. Face-Centered Cubic Arrangement of Anions

In this case we have the arrangement of interstices characteristic of the fluorite structure discussed in detail above (see Figure 35). It was first suggested that in α-Ag_2HgI_4 the three cations are distributed over the four tetrahedral sites occupied in the sphalerite

structure. Later work indicated that all eight of the tetrahedral sites are partially occupied.

For the other compounds of this structure with similar properties a variety of occupancy patterns of the various interstitial positions has been suggested but the work has been semiquantitative and on polycrystalline specimens. It is likely that when more quantitative occupancy factors are determined they may show more differentiation between the crystallographically different sites.

5.3.3. Structures of Compounds MAg_4I_5

Structures of compounds with this formula with M = Rb, K, and NH_4 have been recently determined to belong to the enantiomorphic cubic space groups $P4_132$ and $P4_332$ with $Z = 4$. The arrangement of the I atoms is similar to the Mn atom positions of β-Mn. There are 56 tetrahedral interstices for the 16 Ag^+ ions of the unit cell. There are three sets of sites: one 8(*c*) and two 24(*e*). The two latter sets share faces with each other as well as with the former. The M^+ ions are located in distorted I^- octahedra. In $RbAg_4I_5$, which has been most thoroughly studied, the fractional occupancy is far from random and is 0.11 for the 8(*c*) and 0.39 and 0.23 for the two 24(*e*) positions at room temperature.

The shared tetrahedral faces are believed to be the path of Ag^+ transport in these related structures. There are zigzag channels through the iodine framework. It is this feature in the superionic conductors which accounts for their high conductivity even to low temperatures. The structure $[(CH_3)_4N]_2Ag_{13}I_{15}$ has similar interlinked face-sharing tetrahedral channels[66] and exhibits similar superionic conductivity.

Acknowledgment

Deep appreciation is felt for the special help in the preparation of this manuscript of Marguerite Jones, whose careful syntactic reading, and Drs. Sumio Iijima and Peter Kunzmann, whose critical reading, prevented the appearance of more errors than might otherwise exist. The United States Atomic Energy Commission, through its continuing support of our interest in the oxides, catalyzed this effort.

References

1. A. Magnéli, Structures of the ReO_3-type with recurrent dislocations of atoms: Homologous series of molybdenum and tungsten oxides, *Acta Cryst.* **6**, 495–500 (1953).
2. A. D. Wadsley, Inorganic non-stoichiometric compounds, in *Non-Stoichiometric Compounds* (L. Mandelcorn, ed.), pp. 98–209, Academic, New York (1964).
3. A. D. Wadsley and S. Andersson, Crystallographic shear and the niobium oxides and oxide fluorides in the composition region MX_x, $2.4 < x < 2.7$, in *Perspectives in Structural Chemistry* (J. D. Dunitz and J. A. Ibers, eds.), Vol. 3, pp. 1–58, Wiley, New York (1970).
4. L. A. Bursill and B. G. Hyde, Crystallographic shear in the higher titanium oxides: Structure, texture, mechanisms and thermodynamics, in *Progress in Solid State Chemistry* (H. Reiss and J. O. McCaldin, eds.), Vol. 7, pp. 177–251, Pergamon, Oxford (1972).
5. R. J. D. Tilley, Crystallographic shear in inorganic oxides, *Int. Rev. Sci.*: *Inorg. Chem., Ser. One* **10**, 279–313 (1972).
6. G. Andersson, Studies on vanadium oxides. I. Phase analysis, *Acta Chem. Scand.* **8**, 1599–1606 (1954).
7. S. Andersson and L. Jahnberg, Crystal structure studies on the homologous series Ti_nO_{2n-1}, V_nO_{2n-1}, and $Ti_{n-2}Cr_2O_{2n-1}$, *Ark. Kemi* **21**, 413–426 (1963).
8. L. Kihlborg, The structural chemistry of the higher molybdenum oxides, *Ark. Kemi* **21**, 471–495 (1963).
9. A. D. Wadsley, Crystallographic shear and planar faults in solids, in *Reactivity of Solids, Proc. 6th Int. Symp.*, pp. 1–15, Wiley, New York (1969).
10. S. Amelinckx and J. Van Landuyt, The use of electron microscopy in the study of extended defects related to nonstoichiometry, in *The Chemistry of Extended Defects in Non-Metallic Solids* (L. Eyring and M. O'Keeffe, eds.), pp. 295–322, North-Holland, Amsterdam (1970).
11. J. G. Allpress, The application of electron optical technique to high temperature materials, in *Proc. 5th Materials Res. Symp.* (R. S. Roth and S. J. Schneider, Jr., eds.), pp. 87–111, National Bureau of Standards Special Publication 364 (1972).
12. J. M. Cowley, Crystal structure determination by electron diffraction, in *Progress in Materials Science* (B. Chalmers and W. Hume-Rothery, eds.), Vol. 13, No. 6, pp. 269–321, Pergamon, Oxford (1967).
13. S. Iijima, High-Resolution electron microscopy of crystal lattice of titanium–niobium oxide, *J. Appl. Phys.* **42**, 5891–5893 (1971).
14. S. Iijima, Structure analysis from high resolution EM images, in *Proc. 30th Electron Microscopy Soc. Am.* (C. J. Arceneaux, ed.), pp. 556–557, Claitor Publishing (1972).
15. S. Iijima, Direct observation of lattice defects in H–Nb_2O_5 by high resolution electron microscopy, *Acta Cryst.* **A29**, 18–24 (1973).
16. E. W. Gorter, Classification, representation and prediction of crystal structures of ionic compounds, *J. Solid State Chem.* **1**, 279–305 (1970).
17. L. A. Bursill, Electron microscope study of an homologous series of shear structures based on molybdenum trioxides, *Acta Cryst.* **A28**, 187–191 (1972).
18. S. Andersson and J. Galy, Wadsley defects and crystallographic shear in hexagonally close-packed structures, *J. Solid State Chem.* **1**, 576–582 (1970).

19. I. E. Grey and A. F. Reid, Shear structure compounds $(Cr, Fe)_2Ti_{n-2}O_{2n-1}$ derived from the α-PbO_2 structure type, *J. Solid State Chem.* **4**, 186–194 (1972).
20. L. A. Bursill, B. G. Hyde, and D. K. Philp, New crystallographic shear families derived from the rutile structure and the possibility of continuous ordered solid solution, *Phil. Mag.* **23**, 1501–1513 (1971).
21. O. Terasaki and D. Watanabe, Electron microscopic study on the structure of Ti_nO_{2n-1} $(4 \leq n \leq 10)$ phases, *Japan J. Appl. Phys.* **10**, 292–303 (1971).
22. L. Kihlborg, The crystal chemistry of molybdenum oxides, in *Nonstoichiometric Compounds* (R. F. Gould, ed.), pp. 37–45, Advances in Chemistry Series, American Chemical Society, Washington, D.C. (1963).
23. L. Kihlborg, The structural chemistry of the higher molybdenum oxides, *Ark. Kemi* **21**, 471–495 (1963).
24. L. Kihlborg, The crystal structure of $Mo_{18}O_{52}$ and the existence of homologous series of structures based on MoO_3, *Ark. Kemi* **21**, 443–460 (1963).
25. A. D. Wadsley, Mixed oxides of titanium and niobium. I, *Acta Cryst.* **14**, 660–664 (1961).
26. A. D. Wadsley, Mixed oxides of titanium and niobium. II. The crystal structures of the dimorphic forms of $Ti_2Nb_{10}O_{29}$, *Acta Cryst.* **14**, 664–670 (1961).
27. B. M. Gatehouse and A. D. Wadsley, The crystal structure of the high temperature form of niobium pentoxide, *Acta Cryst.* **17**, 1545–1554 (1964).
28. R. S. Roth and A. D. Wadsley, Multiple phase formation in the binary system Nb_2O_5–WO_3. IV. The block principle, *Acta Cryst.* **19**, 42–47 (1965).
29. S. Andersson, W. G. Mumme, and A. D. Wadsley, Multiple phase formation in the binary system Nb_2O_5–WO_3. V. The structure of $W_4Nb_{26}O_{77}$, an ordered intergrowth of the adjoining compounds $WNb_{12}O_{33}$ and $W_3Nb_{14}O_{44}$, *Acta Cryst.* **21**, 802–808 (1966).
30. N. C. Stephenson, J. P. Beale, and D. C. Craig, The structure and intergrowth of the polymorphic forms of $ZrO_2 \cdot 16Nb_2O_5$, in *Proc. 5th Materials Res. Symp.* (R. S. Roth and S. J. Schneider, Jr., eds.), pp. 165–182, National Bureau of Standards Special Publication 364 (1972).
31. J. S. Anderson, J. M. Browne, and J. L. Hutchison, Electron microscopy of the niobium oxides. I. Twinning and defects in H–Nb_2O_5, *J. Solid State Chem.* **5**, 419–431 (1972).
32. B. G. Hyde and L. Eyring, On phase equilibria and phase reactions in TbO_x–O_2 and related systems, in *Rare Earth Research III* (L. Eyring, ed.), pp. 623–664, Gordon and Breach, New York (1965).
33. J. O. Sawyer, B. G. Hyde, and L. Eyring, Fluorite-related homologous series in the rare earth oxides, *Bull. Soc. Chim. Fr.* **1965**, 1190–1199.
34. B. G. Hyde, D. J. M. Bevan, and L. Eyring, A structural model of the rare earth oxides RO_x (R = Ce, Pr, Tb; $1.5 < x < 2.0$), in *Proc. Int. Conf. Electron Diffraction and Crystal Defects, Melbourne, 1965*, IIC-4.
35. M. R. Thornber, D. J. M. Bevan, and J. Graham, Mixed oxides of the type MO_2 (fluorite)–M_2O_3. III. Crystal structures of the intermediate phases $Zr_5Sc_2O_{13}$ and $Zr_3Sc_4O_{12}$, *Acta Cryst.* **B24**, 1183–1190 (1968).
36. P. E. Caro, OM_4 Tetrahedra linkages and the cationic group $(MO)_n^{n+}$ in rare earth oxides and oxysalts, *J. Less-Common Metals* **16**, 367–377 (1968).
37. P. Caro, Anion centered coordination polyhedra and related physical properties in rare earth oxides and oxysalts, in *Proc. 5th Materials Res. Symp.* (R. S. Roth and

S. J. Schneider, Jr., eds.), pp. 367–383, National Bureau of Standards Special Publication 364 (1972).
38. F. S. Galasso, *Structure and Properties of Inorganic Solids*, Pergamon, Oxford (1970).
39. B. G. Hyde, Crystallographic shear relations between the structure types α-UO_3, CaF_2, La_2O_3 and NaCl and a correlation of some lanthanide and actinide oxide structures, *Acta Cryst.* **A27**, 617–621 (1971).
40. L. Eyring and B. Holmberg, Ordered phases and nonstoichiometry in the rare earth oxide system, in *Advances in Chemistry Series*, No. 39 (R. F. Gould, ed.), pp. 46–57, American Chemical Society, Washington, D.C. (1963).
41. B. T. M. Willis, Structures of UO_2, UO_{2+x} and U_4O_9 by neutron diffraction, *J. Phys. Rad.* **25**, 431–439 (1964).
42. A. K. Cheetham, B. E. F. Fender, D. Steele, R. I. Taylor, and B. T. M. Willis, Defect structure of fluoride compounds containing excess anions, *Solid State Commun.* **8**(3), 171–173 (1970).
43. N. C. Baenziger, H. A. Eick, H. S. Schuldt, and L. Eyring, Terbium oxides. III. X-Ray diffraction studies of several stable phases, *J. Am. Chem. Soc.* **83**, 2219–2223 (1961).
44. S. F. Bartram, Crystal structure of the rhombohedral $MO_3 \cdot 3R_2O_3$ compounds (M = U, W or Mo) and their relation to ordered R_7O_{12} phases, *Inorg. Chem.* **5**, 749–754 (1966).
45. M. Z. Lowenstein, L. Kihlborg, K. H. Lau, J. M. Haschke, and L. Eyring, Growth and X-ray studies of single crystals of higher oxides of praseodymium and terbium, in *Proc. 5th Materials Res. Symp.* (R. S. Roth and S. J. Schneider, Jr., eds.), pp. 343–351, National Bureau of Standards Special Publication 364 (1972).
46. A. F. Wells, *Structural Inorganic Chemistry*, Oxford Press, Oxford (1962).
47. A. W. Sleight, New ternary oxides of mercury with the pyrochlore structure, *Inorg. Chem.* **7**, 1704–1708 (1968).
48. A. W. Sleight and R. J. Bouchard, Precious metal pyrochlores, in *Proc. 5th Materials Res. Symp.* (R. S. Roth and S. J. Schneider, Jr., eds.), pp. 227–232, National Bureau of Standards Special Publication 364 (1972).
49. B. O. Loopstra and H. M. Rietveld, Structure of some alkaline-earth-metal uranates, *Acta Cryst.* **B25**, 787–791 (1969).
50. D. Watanabe, O. Terasaki, A. Jostsons, and J. R. Castles, Electron microscopic study on the structure of low temperature modification of titanium monoxide phase, in *The Chemistry of Extended Defects in Non-Metallic Solids* (L. Eyring and M. O'Keeffe, eds.), pp. 238–258, North-Holland, Amsterdam (1970).
51. H. Reuther and G. Brauer, Über das kubische vanadiummonoxid, *Z. Annorg. Allg. Chem.* **384**, 155–159 (1971).
52. P. S. Bell and M. H. Lewis, Non-stoichiometric vacancy order in vanadium monoxide, *Phys. Stat. Sol.* (*a*) 7, 431–439 (1971).
53. B. Andersson and J. Gjønnes, Ordered phases in the monoxide region of the vanadium–oxygen system, *Acta Chem. Scand.* **24**, 2250–2252 (1970).
54. P. Vallet and P. Raccah, Sur les limites du domaine de la Wüstite solide et le diagramme general qui en resulte, *Compte. Rend.* **258**, 3679–3682 (1964).
55. F. Koch and J. B. Cohen, The defect structure of $Fe_{1-x}O$, *Acta Cryst.* **B25**, 275–287 (1969).

56. W. L. Roth, Defects in the crystal and magnetic structures of ferrous oxide, *Acta Cryst.* **13**, 140–149 (1960).
57. G. Shirane, D. E. Cox, and S. L. Ruby, Mössbauer study of isomer shaft, quadrupole interaction and hyperfine field in several oxides containing Fe^{57}, *Phys. Rev.* **125**, 1158–1165 (1962).
58. R. E. Carter and W. L. Roth, Conductivity and structure in calcia-stabilized zirconia, in *Electrochemical Force Measurements in High Temperature Systems* (C. B. Alcock, ed.), pp. 125–144, Institution of Mining Engineers, London (1968).
59. J. T. Kummer, β-Alumina electrolytes, in *Progress in Solid State Chemistry* (H. Reiss and J. O. McCaldin, eds.), pp. 141–175, Pergamon, Oxford (1972).
60. R. C. DeVries and W. L. Roth, Critical evaluation of the literature data on beta alumina and related phases: I. Phase equilibria and characterization of beta alumina phases, *J. Em. Ceram. Soc.* **52**, 364–369 (1969).
61. M. S. Wittingham and R. A. Huggins, Beta alumina—prelude to a revolution in solid state electrochemistry, in *Proc. 5th* Materials Res. Symp. (R. S. Roth and S. J. Schneider, Jr., eds.), pp. 139–154, National Bureau of Standards Special Publication 364 (1972).
62. C. R. Peters, M. Bettman, J. W. Moore, and M. D. Glick, Refinement of the structure of sodium β-alumina, *Acta Cryst.* **B27**, 1826–1834 (1971).
63. W. L. Roth, Stoichiometry and structure of the super ionic conductor silver beta-alumina, *J. Solid State Chem.* **4**, 60–75 (1972).
64. W. L. Roth, Observation in the electron microscope of lattice planes and migration of silver in beta alumina, in *Proc. 5th Materials Res. Symp.* (R. S. Roth and S. J. Schneider, Jr., eds.), pp. 129–138, National Bureau of Standards Special Publication 364 (1972).
65. H. Wiedersich and S. Geller, Properties of highly conducting halide and chalcogenide solid electrolytes, in *The Chemistry of Extended Defects in Non-Metallic Solids* (L. Eyring and M. O'Keeffe, eds.), pp. 629–650, North-Holland, Amsterdam (1970).
66. S. Geller and M. D. Lind, Crystal structure of the solid electrolyte $[(CH_3)_4N]Ag_{13}I_{15}$, *J. Chem. Phys.* **52**, 5854–5861 (1970).
67. S. Andersson, in *The Chemistry of Extended Defects in Non-Metallic Solids* (L. Eyring and M. O'Keefe, eds.), North-Holland, Amsterdam (1970).

4

*Interstitial Phases**

A. L. Bowman and N. H. Krikorian
Los Alamos Scientific Laboratory—University of California
Los Alamos, New Mexico

1. Introduction

The terms "interstitial compound" and "interstitial phase" are commonly applied to the compounds of the transition metals with the light nonmetals hydrogen, boron, carbon, nitrogen, and, sometimes, oxygen, silicon, phosphorus, and sulfur. The alternate term "hard metals" has been used for the compounds with boron, carbon, nitrogen, and silicon. The latter description refers to the properties of metallic luster and conductivity, coupled with high hardness, while the "interstitial" descriptions are derived from a consideration of the crystal structures of these compounds. Both types of definition refer to compounds that may be considered as intermediate between intermetallic compounds, or alloys, and inorganic (nonmetallic) compounds, with some of the properties of each class.

The term "Einlagerungstruktur" (interstitial structure) was proposed by Hägg in 1931[1] to describe the crystal structures of some of the transition metal carbides, nitrides, and hydrides. Hägg found from a study of the available literature on binary systems of metals with the elements H, B, C, and N that these light nonmetals formed, with the transition metals, phases of a metallic nature, based on their luster and electrical conductivity. He further concluded, from the X-ray structure data, that the radius ratio R of nonmetal to metal

* Work performed under the auspices of the U.S. Atomic Energy Commission. The Government and its authorized representatives have unrestricted right to reproduce in whole or in part this article under any copyright secured by the publisher.

atom is an important factor in determining the crystal structures of these phases. When the radius ratio was less than 0.59 the observed structures could be described as the packing of the nonmetal atoms into the interstitial holes of very simple metal atom lattices, which are in almost all cases identical with the most common lattices of pure metals. When the radius ratio was greater than 0.59 the structures were complicated. It was recognized that the oxygen atom was small enough for consideration, but oxides were not studied because of their usual ionic nature.

No borides were known with $R < 0.59$ at the time of Hägg's original study. Since that time the structures of many new boride phases have been determined, with R ranging from 0.5 to 0.7. None of these borides was found to have a simple interstitial structure, although the AlB_2 structure type common to most diborides is quite similar to the WC type of interstitial structure. The metallic properties that were originally considered by Hägg are also found in the transition metal silicides, but like the borides, these crystallize in complex structures, with $R > 0.6$ in all cases.

The term "hard metals" has been used to describe compounds between a transition metal of the fourth to sixth groups and a small nonmetal atom which are characterized by high hardness, high melting point, and metallic bonding.[2] This classification includes carbides, nitrides, borides, and silicides.

Goldschmidt[3] has defined an interstitial alloy as one in which the metal–metal atom bond remains the dominant one, and in which the nonmetal atoms are sufficiently small to be accommodated with at most a limited degree of distortion from metal-type symmetry. This definition, which tends to emphasize the metallic bonding, allows the inclusion of the borides and silicides, some oxides, and perhaps phosphides and sulfides. It will be seen from the discussion in Section 3.9 that this definition does not agree with present theories of bonding in interstitial phases.

An interstitial phase will be defined here as any phase that has an interstitial structure. This simple definition will include most of the hydrides, carbides, and nitrides of the transition metals (groups three through eight), as well as the solutions hydrogen, carbon, and nitrogen in the metals. The solutions of oxygen in these metals are also interstitial in nature, and some of the lower oxides have interstitial structures and metallic properties. Many ternary compounds of these elements may also be considered as interstitial phases. This discussion will be limited to the systems with hydrogen, carbon, and nitrogen as

the nonmetal, and will include a few compounds with complex structures. It should be noted again that boron and silicon form phases with the transition metals that are very similar to the carbides and nitrides with regard to their physical properties, but which have complex crystal structures.

The crystal chemistry of the interstitial phases will be examined from the viewpoint of the packing of the small nonmetal atoms into the interstices of the close-packed metal lattices. The existing data on the ordering of the light atoms (or of the vacancies) will be reviewed. The properties of these materials will be discussed with the emphasis on their melting points and hardness, typical of covalent bonding, and their electrical resistivity and superconductivity, which are metallic in nature. The thermodynamic properties and thermal expansion behavior will also be noted briefly. Finally, the recent theories on bonding in these "almost" metals will be considered.

It should be emphasized here that the interstitial compounds are very difficult to study experimentally. They are difficult to prepare, requiring high temperatures for the carbides and high temperature and/or high pressure for the nitrides and hydrides. Many of their properties are very sensitive to composition or to impurities, particularly those impurities that are the hardest to avoid. Many experiments are of no value because the phase composition is not defined, or the levels of important impurities are not specified. Crystal structure determinations are best done on single crystals, but these are difficult or impossible to obtain for most interstitial compounds. Thus the structures have been based on powder data, with the nonmetal atoms located by neutron diffraction.

Several recent reviews provide more detailed information on interstitial compounds. The carbides and nitrides of groups 4–6 and thorium, uranium, and plutonium have been critically reviewed by Storms.[4,5] This work has been extended by Toth.[6] The interstitial hydrides have been thoroughly reviewed by Mueller *et al.*[7] The borides, silicides, and phosphides have been discussed in detail by Aronsson *et al.*[8] A recent review[9] provides up-dated information on most of these systems.

2. Crystallography of Interstitial Phases

The crystal structures of the interstitial carbides, nitrides, and hydrides may be described generally on the basis of a close-packed

metal sublattice, with the nonmetal atoms occupying interstitial positions (holes).

2.1. Geometrical Basis of Close Packing

The close-packing concept is based on spheres of equal size, which may be packed in a planar layer, as shown in Figure 1. Each sphere is surrounded by six others at the apices of a regular hexagon. A second, similar layer may be placed on top of the initial *A* layer in either of the two equivalent positions labeled *B* and *C*. If the second layer is placed at *B*, then the third layer may be positioned at either *A* or *C*, and so on. Many metal structures may be regarded as close packed, with layer sequences $AB\cdots$ (hexagonal close packed, e.g., titanium); $ABC\cdots$ (cubic close-packed, e.g., scandium); $ABAC\cdots$ (double hexagonal close packed, e.g., lanthanum); and $ABABCBCAC\cdots$ (e.g., samarium). An alternate method of describing these packing sequences denotes a layer by *h* if the two adjacent layers are of the same type and by *c* if they are different (Jagodzinski–Wyckoff notation). Thus hexagonal close-packing is *h*, the lanthanum type is *hc*, and the samarium type is *hhc*.

The cubic close packing is unique in possessing cubic symmetry. The unit cell, or repeat unit, of this structure is a cube with spheres (or atoms) at the corners and at the centers of the faces, hence face-centered cubic (fcc). The normal to the close-packed layers extends in the direction of the body diagonal of the cube. All other close-packed structures have either hexagonal or trigonal symmetry, with the symmetry axis normal to the layers.

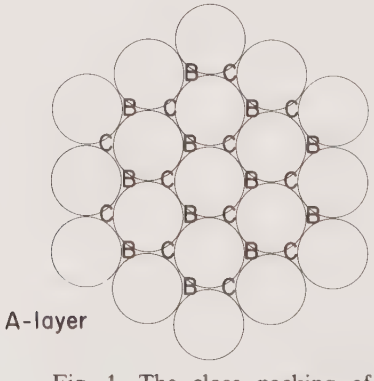

Fig. 1. The close packing of spheres in a plane.

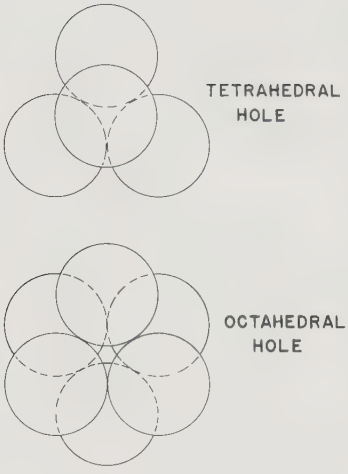

Fig. 2. Tetrahedral and octahedral holes in a close-packed array.

The interstices between the atoms are of two kinds, tetrahedral and octahedral, so named because of the coordination polyhedra formed by the close-packed atoms (Figure 2). The coordination polyhedron of an atom is defined here as the polyhedron whose vertices are the nearest-neighbor atoms of the other kind. There are one octahedral and two tetrahedral interstices, or holes, per metal atom in a close-packed lattice. The largest spheres that will fit into the holes have radii of $0.414r$ in the octahedral holes and $0.225r$ in the tetrahedral holes, where r is the radius of the close-packed atoms.

The third common metal structure, in addition to the hcp and the fcc, is the body-centered cubic structure (bcc), which has an atom at the corner and one at the center of a cube. This structure may also be considered as face-centered tetragonal, with $c/a = \sqrt{2}/2$. It is thus seen to be a fcc cell compressed along the c axis, as shown in projection in Figure 3. There are six tetrahedral holes per metal atom in this structure, with the positions shown in Figure 3. The tetrahedral coordination is regular, with the radius of the hole equal to $0.291r$, as compared with $0.225r$ in the close-packed structures. The distance between holes is only $0.815r$, however, compared with $\sqrt{2}r$ in the close-packed structure. The octahedral holes are very badly distorted, with a minimum radius of only $0.155r$. The metal atom radius is taken as one-fourth the body diagonal in this case.

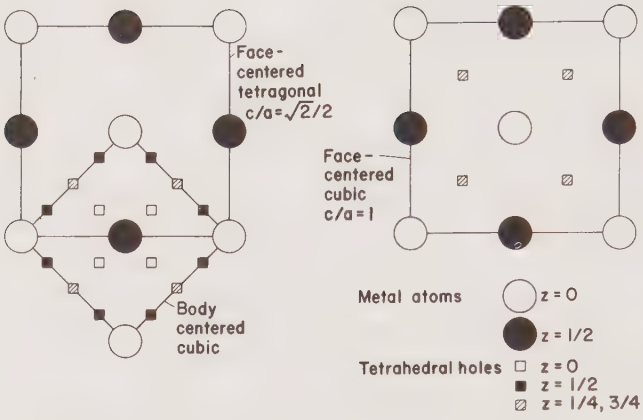

Fig. 3. The fcc and bcc unit cells in the xy plane. The z axis is $\sqrt{2}$ longer in the fcc cell.

The very useful concept of close-packed structures can be extended by allowing distortion of the lattice. The lattice may be distorted by (1) a deviation in the interlayer distance from the ideal value of $1.63r$, (2) a nonideal packing of adjacent layers, or (3) a distortion of the layers which might arise from missing atoms or from nonplanar packing in the layer. The first type of distortion occurs in most noncubic close-packed structures. The most extreme packing sequence occurs when adjacent layers are in identical positions, i.e., $AA\cdots$ packing. The holes between such layers are trigonal prisms, with two holes per metal atom. This structure does not exist in a pure metal, but does occur in a few interstitial phases. The bcc structure could be considered as an extremely distorted hcp type with distorted layers [the (110) planes, with nonhexagonal symmetry] that are packed imperfectly. This description does not appear to be useful, and will not be used.

2.2. The Radius Ratio

The radius ratio concept suggested by Hägg[1] can be derived directly from the preceding geometric considerations. A metal lattice of close-packed, perfect, hard spheres of radius r can accommodate similar interstitial atoms of radius $0.225r$ in tetrahedral holes and atoms of radius $0.414r$ in octahedral holes. Thus a limiting radius ratio (r_X/r_M) of 0.414 should be expected in interstitial structures made up of hard spheres. The real atoms are of course not hard spheres,

and the interatomic distances in the interstitial phases are such that usually $d_{M\text{-}M} > 2r_M$ and $d_{M\text{-}X} < r_M + r_X$. Thus the radius ratios noted above appear to be more nearly the lower limits, with tetrahedral occupancy from $0.2r$ to $0.4r$, and octahedral occupancy from $0.4r$ to $0.6r$.

2.3. Crystal Structures of Interstitial Phases

The crystal structures of the interstitial phases may be conveniently described and compared by defining (1) the layer sequence of the close-packed metal lattice, including any distortion, and (2) the types of holes that are filled, the level of occupancy, and whether the vacancies are ordered.

2.3.1. The Metal Lattices

The known interstitial carbide phases are shown in Figure 4, with the carbides with complex structures separated on the sides. The interstitial nitrides are shown in similar fashion in Figure 5, and the hydrides in Figure 6. The Jagodzinski–Wyckoff symbols (*h*, *c*, *hcc*,

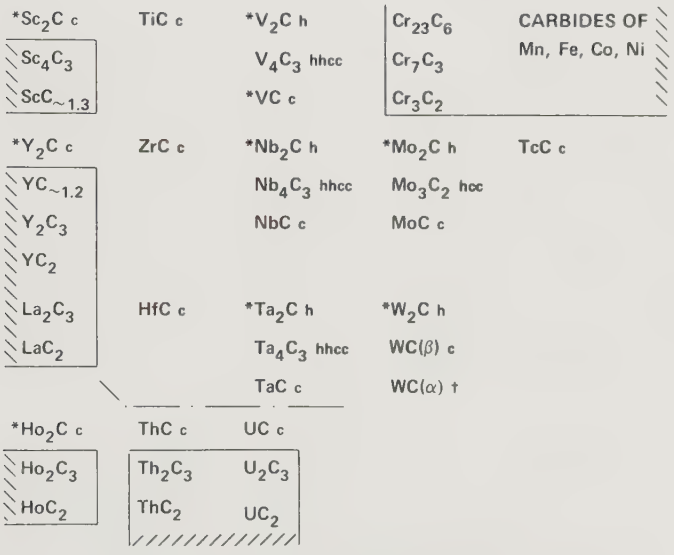

Fig. 4. The interstitial carbides. The close-packed structures are indicated by their Jagodzinski–Wyckoff symbol. (*) These phases have a well-established ordered vacancy structure. (†) $AA\cdots$ stacking sequence.

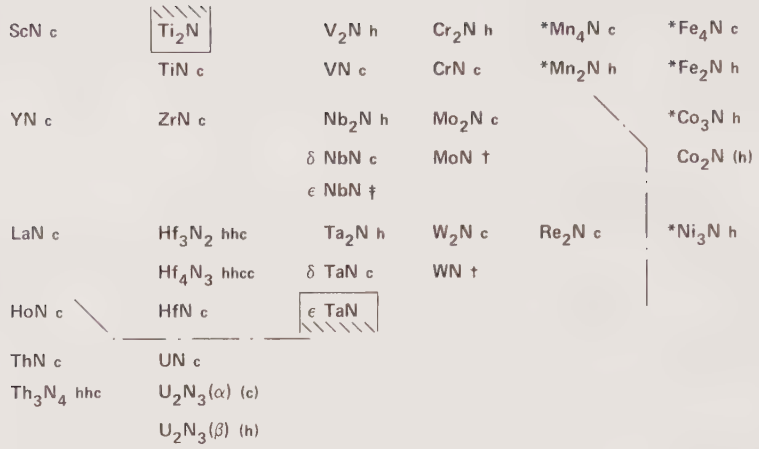

Fig. 5. The interstitial nitrides. The close-packed structures are indicated by their Jagodzinski–Wyckoff symbol. Distorted lattices are shown in parentheses. (*) These phases have an ordered vacancy structure. (†) *AA* ··· stacking sequence. (‡) *AABB* ··· stacking sequence.

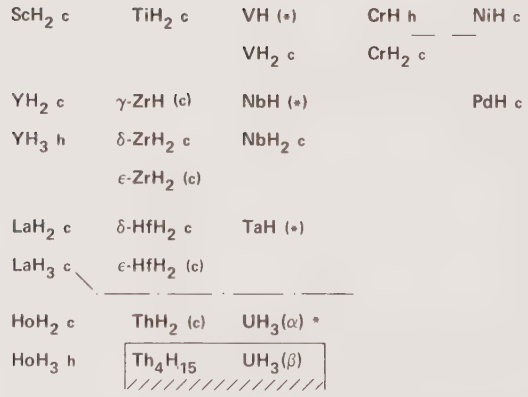

Fig. 6. The interstitial hydrides. The close-packed structures are indicated by their Jagodzinski–Wyckoff symbol. (*) Body-centered cubic lattice. Distorted lattices are shown in parentheses.

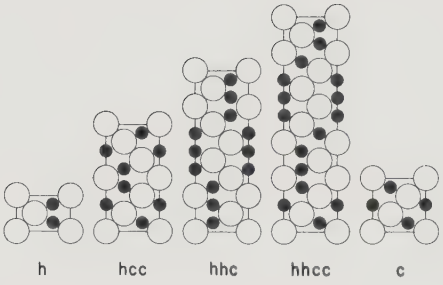

Fig. 7. The known close-packed interstitial structures. The (110) plane. The filled circles are the octahedral holes.

etc.) for the metal lattices are noted for each close-packed or interstitial phase. The observed stacking sequences are shown in Figure 7 as projections of the (110) planes, with large, open circles for the metal atom positions and small, filled circles for the octahedral holes.

The tabulation of interstitial carbides, nitrides, and hydrides in Figures 4–6 is intended to include those compounds whose existence as stable binary phases is well established. Some compounds are included that can only be prepared under high pressure, such as Th_2C_3[10] and δ-TaN.[11] A few metastable phases are also included, such as NiH and γ-ZrH. The carbides V_4C_3, Nb_4C_3, and Ta_4C_3 have never been obtained in pure form, and may also be metastable. Their actual composition also appears to be closer to M_3C_2 than to M_4C_3. Many other compounds have been reported but have not been confirmed as pure binary phases. Some of these are actually ternary phases, requiring the presence of an impurity in order to be formed, while others may be metastable binary phases. Several molybdenum carbides have been reported, for example, which are almost certainly oxycarbides, for they are obtained only when the material contains large amounts of oxygen.[5] A large number of tungsten nitrides have been observed only with electron diffraction studies of thin films.[12] There is no evidence that any of these phases can exist in a bulk sample.

2.3.2. The Nonmetal Positions

The interstitial carbides and nitrides are formed in most cases with the nonmetal atom (carbon or nitrogen) in the octahedral holes. The higher nitrides of thorium and uranium ($N/M > 1$) include nitrogen in tetrahedral holes. The structures of Th_3N_4 (*hcc*)[13] and

β-U_2N_3 (*h*, distorted)[14] have an ordered mixture of tetrahedral and octahedral nitrogen atoms. The α-U_2N_3 phase has the *A*-type sesquioxide structure[15] with a distorted *c*-type packing and three-fourths of the tetrahedral holes filled in an ordered manner.

The interstitial hydrides, on the other hand, are formed with the hydrogen atoms in the tetrahedral holes, with the exception of CrH, NiH, and PdH, which have their hydrogen atoms in octahedral holes. The rare earth metals also form trihydrides, MH_3, with both kinds of holes completely filled.

The maximum interstitial composition of a close-packed phase with octahedral sites occupied would seem to correspond to the formula MX. However, this ideal composition is approached only with the *c*-type of stacking, while the maximum interstitial composition of the *h*-type phases is M_2X. It has been suggested that where two interstitial sites are located above each other in the (110) plane (which occurs with each *h* layer) only one site can be occupied.[16] Following this argument, which is valid for the *h*-type stacking, and assuming complete occupation of sites adjacent to a *c* layer, maximum interstitial compositions can be defined as M_2X for *h*, M_3X_2 for *hcc* and *hhc*, M_4X_3 for *hhcc*, and MX for *c*. These compositions must be considered as an upper limit which need not be reached. The composition M_2X appears to be the approximate upper limit for all the *h*-type phases, while among the *c*-type phases, VC, MoC, WC, NbN, and TaN are always deficient in carbon or nitrogen (only VC and NbN are stable at room temperature). The *c*-type carbides of scandium, yttrium, and the rare earths have a maximum composition M_2C at low temperature ($< 1000°$) but form a continuous solid solution field with the dicarbides at higher temperatures. The phases with mixed stacking sequences (M_3X_2 and M_4X_3) all appear to be deficient in carbon or nitrogen.

2.3.3. Ordered Vacancy Structures

The close-packed carbides and nitrides thus tend to have large percentages (up to $\sim 65\%$) of their interstitial sites vacant. Even the *c*-type phases with composition MX have, in most cases, large ranges of homogeneity based on interstitial vacancies. These vacancies can be either ordered or random in the *c*- and *h*-type structures. Ordered vacancy structures have been identified in the *c*-type vanadium carbide at V_8C_7 (cubic)[17] and V_6C_5 (trigonal).[18] The VC phase has only random vacancies above $\sim 1200°$. The M_6C_5 ordered structure

TABLE 1
The Ordered M_2C Phases

Compound	Structure type	Ref.
V_2C	ζ-Fe_2N	22
Nb_2C	α-Nb_2C	23
Ta_2C	CdI_2 (*C*6)	24
Mo_2C	ζ-Fe_2N	25
W_2C	ε-Fe_2N	26
Sc_2C	$CdCl_2$ (*C*19)	27
Y_2C	$CdCl_2$ (*C*19)	27
Tb_2C	$CdCl_2$ (*C*19)	28
Ho_2C	$CdCl_2$ (*C*19)	29

has also been reported for NbC and TaC.[19] A different cubic ordered structure has been reported for Ti_2C and Zr_2C.[20] This structure may be stabilized by the presence of hydrogen. Another cubic ordered structure has been suggested for Th_4C_3.[21] Ordered vacancy structures have been observed in all of the M_2C carbides, including the

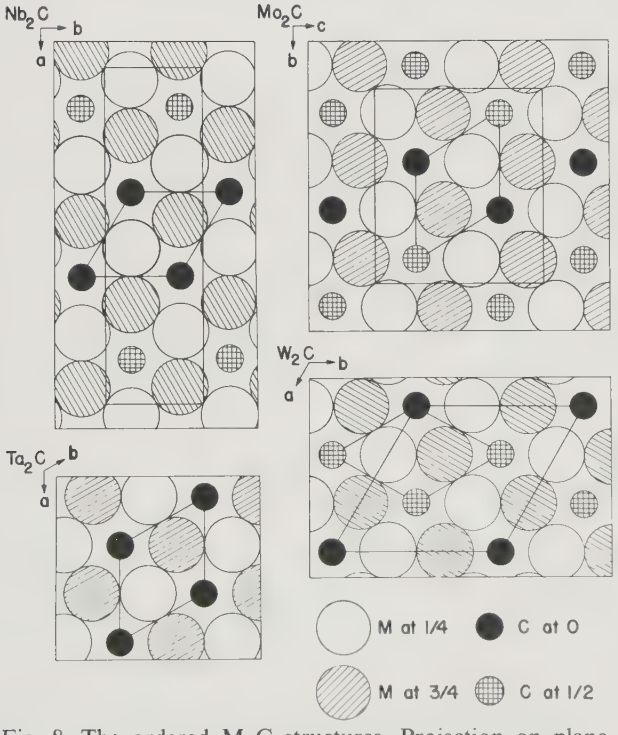

Fig. 8. The ordered M_2C structures. Projection on plane perpendicular to the *c* axis.

c type of the third group metals. These structures are listed, and the references cited, in Table I. The structures of the ordered *h*-type M_2C carbides are shown in Figure 8 as projections in the plane perpendicular to the *c* axis (V_2C has the same structure as Mo_2C). The *c*-type M_2C compounds have the same vacancy arrangement as Ta_2C, with alternate C planes completely filled. It appears that all of the M_2C carbides are transformed to the corresponding random vacancy structures at temperatures ranging from $\sim 600°$ to over 2000°. The transformations of Mo_2C[30] and Ta_2C[31] have been studied with high-temperature neutron diffraction. It seems probable that similar vacancy ordering occurs in the nitrides, but very few experimental data are available. An ordered vacancy structure (which is probably ε-Fe_2N type) has been reported for Cr_2N[32] based on X-ray diffraction data. The ordered vacancy structures of the iron nitrides have been studied thoroughly with X-ray diffraction.[33] These results should probably be confirmed with neutron diffraction experiments.

The intermediate phases with mixed stacking sequences have two different kinds of carbon sites, those that are adjacent to an *h* layer (*H*), and those that are not (*C*). There are thus three possible types of vacancy arrangement, random distribution over all sites, random distribution over *H* sites with *C* sites filled (partial ordering), and ordered arrangement among specific sites (more probably *H* sites), as well as possible intermediate states. The neutron diffraction pattern of Mo_3C_2 obtained at 1750°[34] appears to agree better with the calculated random vacancy pattern than with the partially ordered vacancy pattern, while the completely ordered structure is not possible. The neutron diffraction patterns of Ta_4C_3 also do not appear to be consistent with even partial ordering, although an ordered structure has been proposed from an electron diffraction study.[35]

The problem of ordered vacancies in the hydrides has been much more difficult to resolve experimentally. The metastable γ-ZrH has an ordered filling of one-half the tetrahedral sites in a *c*-type lattice.[36] The group V hydrides VH, NbH, and TaH have tetrahedral hydrogens in a distorted body-centered cubic metal lattice. The first neutron diffraction studies of VH and TaH suggested at least a partial ordering of the hydrogen atoms on the tetrahedral sites.[37] Subsequent studies over a wide temperature range showed an identical ordered structure for VH, NbH, and TaH, which would be transformed to a random structure at higher temperatures.[38] Additional ordered structures were found for Nb_4H_3 and Ta_2H.

2.3.4. Distorted Close-Packed Structures

Several compounds listed in Figures 4–6 that are not close packed or bcc can be considered to be distorted interstitial-type phases. The dicarbides of the group three metals may be considered to be *c*-type structures with C_2 interstitials (C–C distance of ~ 1.3 Å). At high temperatures the metal lattices are cubic, and the C_2's are oriented randomly to give a true interstitial phase.[39–41] The C_2 alignment is transformed at lower temperatures to an ordered form, with a distortion of the metal lattice. Four distinct structures are known; ThC_2 (β) (tetragonal, stable only between 1430 and 1480°, with C_2's randomly oriented in a plane),[41] ThC_2 (α) (monoclinic, with a totally ordered C_2 arrangement),[41] UC_2 (α) (tetragonal, CaC_2 type, formed also by YC_2 and all of the rare earths except Lu), and an unknown low-symmetry structure, stable at lower temperatures, formed by the rare earths from terbium through lutetium.[42] The sesquicarbides also have C_2's as the interstitial, but the metal lattice is very badly distorted from close packing. The Ti_2N structure may be considered as a distorted *h* type, with 50 % ordered filling of octahedral sites.[43]

2.3.5. Metal Atom Vacancies

The consideration of vacancies in interstitial phases may be limited in most cases to vacant interstitial sites, with the metal lattice sites assumed to be completely filled. This assumption has been verified experimentally for many interstitial phases, but it is not valid for the *c*-type nitrides of titanium, zirconium, hafnium, and niobium. Metal atom vacancy levels have been reported at 7 % for ZrN[44] and δ-NbN[45] and 13 % for HfN.[46] It appears that complete filling of the interstitial sites in these compounds occurs at the high nitrogen phase boundary.

2.3.6. Metal–Interstitial Solutions

The interstitial compounds thus appear as solutions of carbon, nitrogen, or hydrogen in a metal lattice that is different in most cases from that of the pure metal. The carbon atoms are always found in octahedral holes, nitrogen usually in octahedral holes, and hydrogen usually in tetrahedral holes. The interstitial atoms will also dissolve in the metals without change of metal structure, but in most cases to a very limited degree. The solubility of carbon and nitrogen is greater

in the close-packed metals, and hydrogen is more soluble in the body-centered cubic metals. Thus large carbon solubility is observed for thorium (cubic close-packed) (Figure 12, see Section 3.1) and yttrium (hexagonal close-packed) (Figure 9). A large nitrogen solubility is observed in the hexagonal close-packed forms of titanium, zirconium, and hafnium (Figure 11). The solubility of hydrogen is found to be largest in the body-centered cubic forms of titanium, zirconium, and hafnium and in vanadium, niobium, and tantalum (also bcc) (Figure 13). The interstitial atoms are assumed to be randomly distributed in these solutions, but ordered structures have been reported for nitrogen[47] and carbon[48] in tantalum. The austenite–martensite transformation in the Fe–C and Fe–N systems has been shown to involve a partial ordering of the random solution.[33b,49] It is at least possible that other ordered solutions may exist.

The dilute solutions of oxygen in the transition metals are also interstitial in nature, and are very similar to the solutions of carbon and nitrogen.

2.4. Polymorphism in Interstitial Compounds

A compound is described as polymorphic if it forms two or more crystalline phases differing in their atomic arrangement. An interstitial compound would thus be polymorphic if it existed with different metal lattices, or with different kinds of interstitial packing.

The first type of polymorphism, two different metal lattices, is found in only a few interstitial compounds. This transformation may be described for WC ($AA, \cdots \rightarrow$ *c*-type packing), NbN ($AABB \cdots \rightarrow$ *c* type), TaN (ε-TaN $\rightarrow$ *c* type) and U_2N_3 (*c* type $\rightarrow$ *h* type). The phase diagrams of these systems (Figures 10–12) suggest that the transformations involve a significant change in composition, and are thus not truly polymorphic.

The true cases of polymorphism in interstitial phases occur in the interstitial packing, in particular with regard to ordered vacancies. The order–disorder transformation has been observed for all of the known ordered phases, as noted previously. Also, in the ordered structures the metal lattices are found to be slightly distorted. The dicarbides also undergo a similar order–disorder transformation with respect to the alignment of the C_2 groups. The hydrogen atoms in palladium hydride change from octahedral sites at room temperature to a partial occupancy of tetrahedral sites at 4.2°K.[50]

2.5. Ternary Interstitial Phases

Two types of ternary interstitial phases can be considered; those with two different metals ($M^IM^{II}X$) and those with two nonmetals (MCN, MCH, MNH). The first type of ternary phase has a metal lattice with two different kinds of metal atoms which may be mixed randomly or in an ordered arrangement. Ternary carbides, nitrides, and hydrides are known as solid-solution systems, such as (Ta,Nb)C and (Zr,Hf)N, both with *c*-type packing and octahedral interstitial atoms, and $(Ti,Zr)H_2$, with *c*-type packing and tetrahedral hydrogen atoms. Each of these ternary phases is structurally the same as its two binary phases. In systems where complete solid solubility does not occur, ternary phases may be formed with different metal lattices. Compounds are known such as Ta_2VC_2,[51] with hcc packing and a random arrangement of metal atoms, U_2IrC_2,[52] with a distorted *c*-type packing, and the perovskite-type phases with the $AuCu_3$-type metal lattice (*c* type).* The last two structures have ordered arrangements of the metal atoms. The vacant interstitial sites tend to be ordered when the metal atoms are ordered and random when the metal lattice is random. The rare earth metal–nickel and –cobalt compounds of the $LaNi_5$ type have been found to form ternary hydrides with the metal lattice unchanged.[54] An ordered hydrogen arrangement has been reported for $PrCo_5D_4$,[55] while $LaNi_5D_7$ is only partially ordered.[56]

The ternary M(C, N) or carbonitride phases exist in most cases as solid solutions of the two binary phases, with carbon and nitrogen both occupying octahedral sites, presumably randomly mixed. The ThCN phase is an exception, having a distorted *h*-type metal lattice with alternating layers of C_2's in octahedral sites and N's in tetrahedral sites.[57]

The ternary carbohydride [M(C,H)] and nitrohydride [M(N,H)] phases are normally found with hydrogen in tetrahedral holes and carbon or nitrogen in octahedral holes. The simplest type of ternary hydride phase is formed by the addition of hydrogen to a carbide or nitride with vacant interstitial sites. The hydrogen atoms have been reported to fill octahedral holes at random in $ZrC_{1-x}H_y$,[58] and to fill both tetrahedral and octahedral sites in $ThC_{1-x}H_y$.[59] In addition to these solutions of hydrogen in an existing carbide phase, ternary carbohydride phases with *h*-type packing have been reported for Ti

* The perovskite-type carbides and nitrides are reviewed by Toth,[6] pp. 54–56, and Stadelmaier.[53]

and Hf,[60] Zr,[58] and Y.[61] These phases appear to have the composition M_2CH_2, with alternating layers of octahedral carbon and tetrahedral hydrogen. Hexagonal nitrohydrides have also been reported for Ti[61] and Zr.[58] A thorium carbohydride is known of composition $Th_3C_2H_2$, with hcc packing, isomorphous with Th_3N_4.[61]

The ternary interstitial phases are thus a simple extension of the binary phases from a structural standpoint. The only additional consideration is whether the third kind of atom is included in a random or ordered manner. The effect of oxygen should also be noted. While only a few oxides may be considered as interstitial phases, oxygen dissolves readily into available octahedral holes to form oxycarbides and oxynitrides. These may exist with the same metal lattice as the carbide or nitride or with a totally different lattice.*

3. Properties of Interstitial Phases

The physical properties of the interstitial phases may be classed as metallic (electrical, magnetic, superconducting, and thermal expansivity and conductivity) and nometallic (melting point, hardness and mechanical behavior). The carbides, nitrides, and hydrides tend to be quite similar with respect to their metallic properties but exhibit marked differences in their nonmetallic properties. While these materials are very interesting and have several potentially useful properties, the main commercial application has been in carbide cutting tools and wear-resistant parts. The carbides also have a potential use as high-temperature structural materials. The nitrides are also hard materials, but not as hard as the carbides, and are at present of little commercial value. The hydrides are used almost exclusively as a solid hydrogen storage medium, either for a long-term container in nuclear reactor applications or for a convenient source of atomic hydrogen or hydrogen gas.

3.1. Phase Diagrams

The approximate phase diagrams of several binary systems of transition metals with carbon, nitrogen, and hydrogen are presented in Figures 9–13. The Y–C system (Figure 9A) is essentially a composite

* Several reported carbides of molybdenum are almost certainly oxycarbides with their own metal lattice (p. 126 of Ref. 5), as noted in Section 2.3.1.

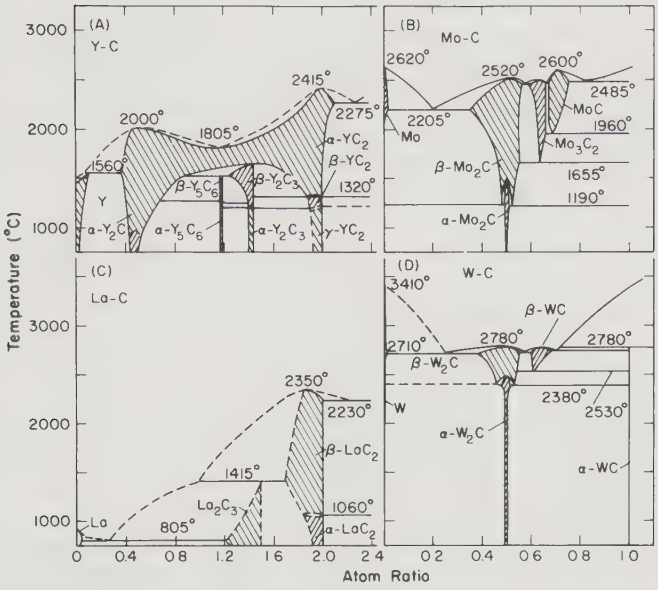

Fig. 9. Phase diagrams of the Y–C, Mo–C, La–C, and W–C systems. (From Refs. 9 and 62–64.)

from Carlson and Paulson[62] and Storms.[63] The La–C system (Figure 9C) is from Spedding *et al.*,[64] with a later determination of the LaC_2–C eutectic and LaC_2 transformation temperatures.[65] The other carbide and nitride systems (Figures 9B, 9D, and 10–12) have been compiled by Storms[9] from available experimental data, with minor modifications by the authors. The hydride systems (Figure 13) are from Mueller *et al.*[7] The metal–carbon phase diagrams depict the phases that may be found under high-vacuum conditions, ignoring the effect of the vapor phase. This is a valid treatment except at very high temperatures, where the vapor pressure becomes significant, and sample composition may change with time. The nitride and hydride phase diagrams show the phases that will exist under the equilibrium pressure of nitrogen or hydrogen. The isobar for 1 atm of gas pressure is shown on the diagrams. Phases above or to the right of this line will exist in equilibrium only at pressures greater than 1 atm. Note, however, that the 150 atm isobar is estimated for the Nb–N system and the 5 atm isobar for the Ta–N system in order to show more clearly the nature of the $\delta \rightarrow \varepsilon$ phase transition in these systems. Note also that two different temperature scales are used for the Nb–N diagram.

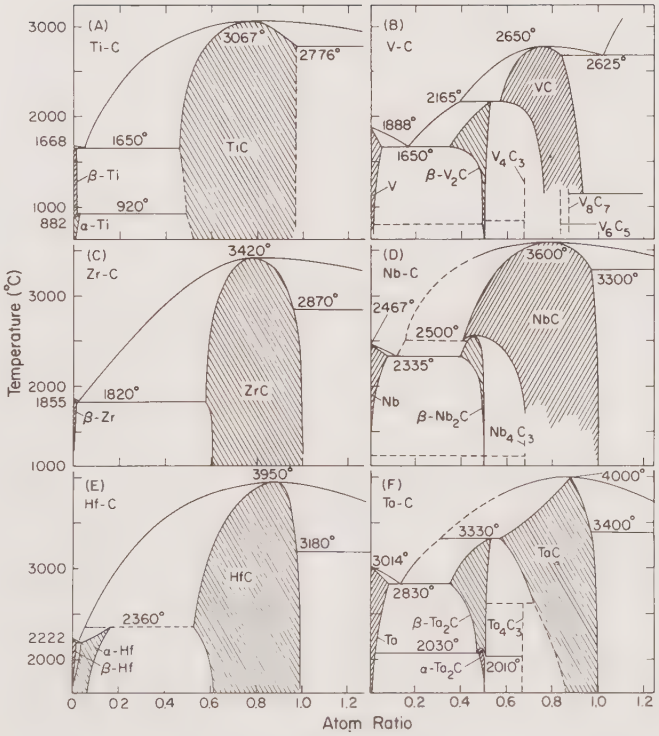

Fig. 10. Phase diagrams of the Ti–C, V–C, Zr–C, Nb–C, Hf–C, and Ta–C systems. (From Ref. 9.)

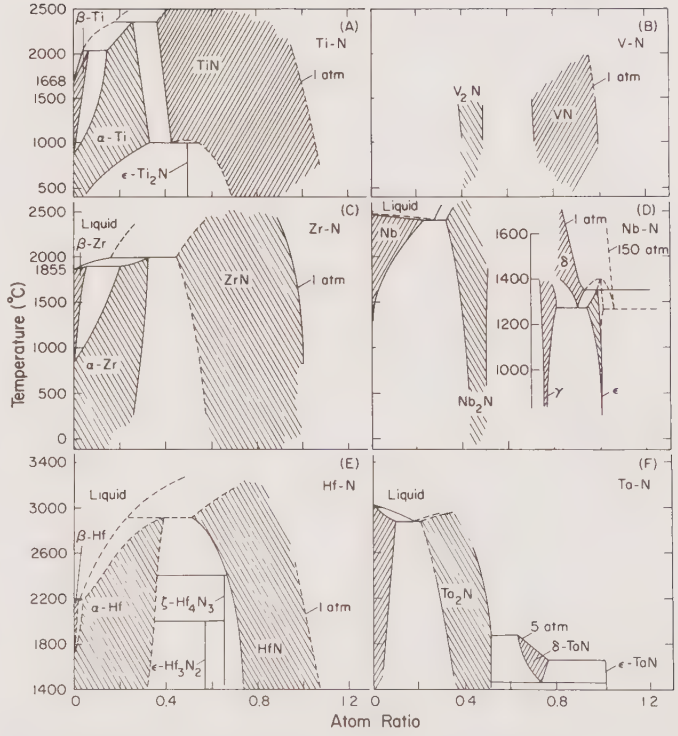

Fig. 11. Phase diagrams of the Ti–N, V–N, Zr–N, Nb–N, Hf–N, and Ta–N systems. (From Ref. 9.) Note that two different temperature scales are used for the Nb–N diagram (D.)

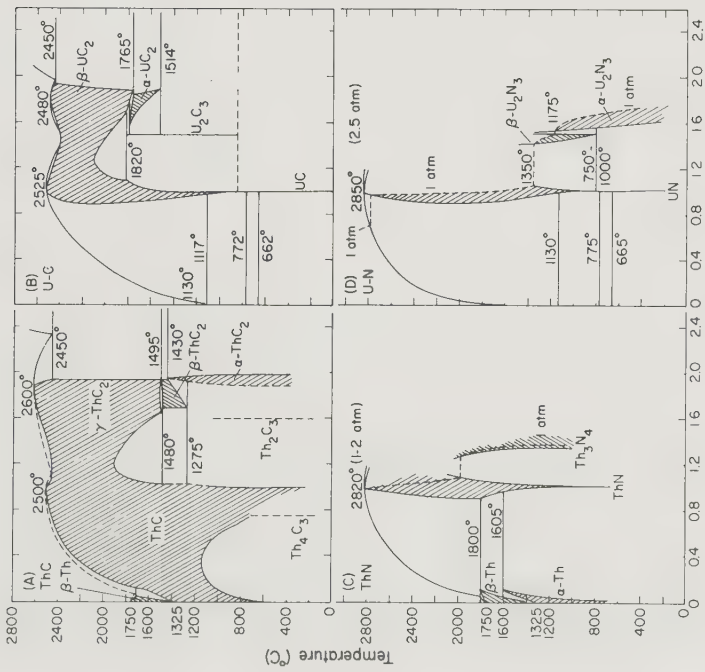

Fig. 12. Phase diagrams of the Th–C, U–C, Th–N, and U–N systems. (From Ref. 9.)

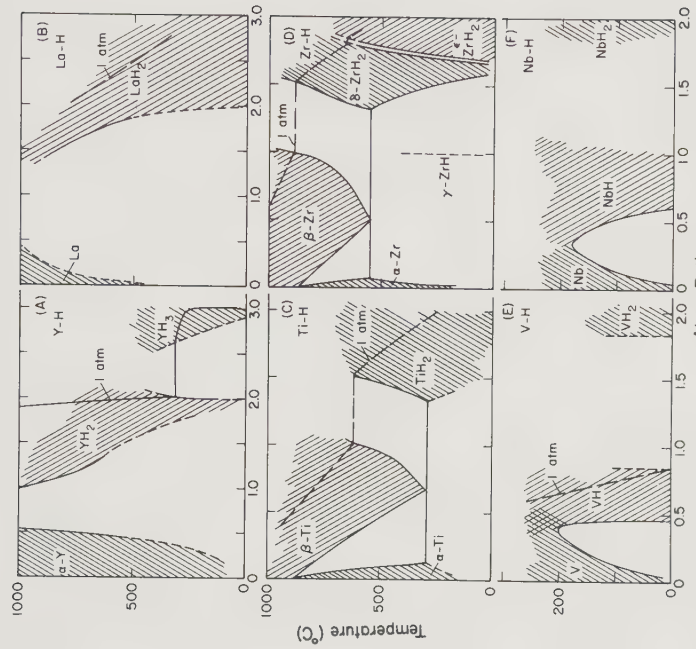

Fig. 13. Phase diagrams of the Y–H, La–H, Ti–H, Zr–H, V–H, and Nb–H systems. (From Ref. 7.)

TABLE 2
Melting Points of Interstitial Compounds*

YC_2	2415	MoC	2600
LaC_2	2350	WC	2780
TiC	3065	VC	2650
ZrC	3420	NbC	3600
HfC	3950	TaC	4000
ThC	2500	ThN	2820[66,67]
UC	2525	UN	2850[68,69]

* Data from Refs. 3, 5, and 9 except where noted.

3.2. Melting Points

The melting points of the interstitial carbides are shown in Table 2. Only the highest-melting carbide of each metal is listed. There are no interstitial nitrides or hydrides that are known to melt congruently under a pressure of less than 1 atm. The congruent melting temperatures of ThN (2 atm)[66,67] and UN (2 atm)[68,69] have been determined and are included in Table 2. Although the true melting points of the other nitrides have not been determined experimentally, they may be estimated with respect to the melting points of the corresponding carbides. From reported values which were determined at 1 atm or less and thus must be too low, ΔT_m (nitride versus carbide) can be estimated at $+300°$ for group III metals, 0° for group IV, and $-400°$ for group V. The congruent melting temperature of the carbides is always displaced from the stoichiometric composition, as can be seen from the phase diagrams (Figures 9–11). This is probably also the case with the nitrides and the hydrides.

The very refractory nature of the interstitial carbides can be shown conveniently by comparing their melting points with those of the parent metals. The ratio of melting point of metal to melting point of carbide (in °K) is plotted versus period of the periodic table in Figure 14. Each group is shown as a separate curve, with the lanthanide metals plotted at regular spacing between scandium and lanthanum. If this melting-point ratio is indeed a measure of the stability of the carbide with respect to the metal, then these curves suggest a fairly regular dependence on group number, with WC, ThC, UC, and YbC_2 showing the only significant deviations. The group III data are based on the MC_2–C eutectic temperatures,[65,70] since the melting points of the carbides have been determined only for LaC_2 and YC_2.

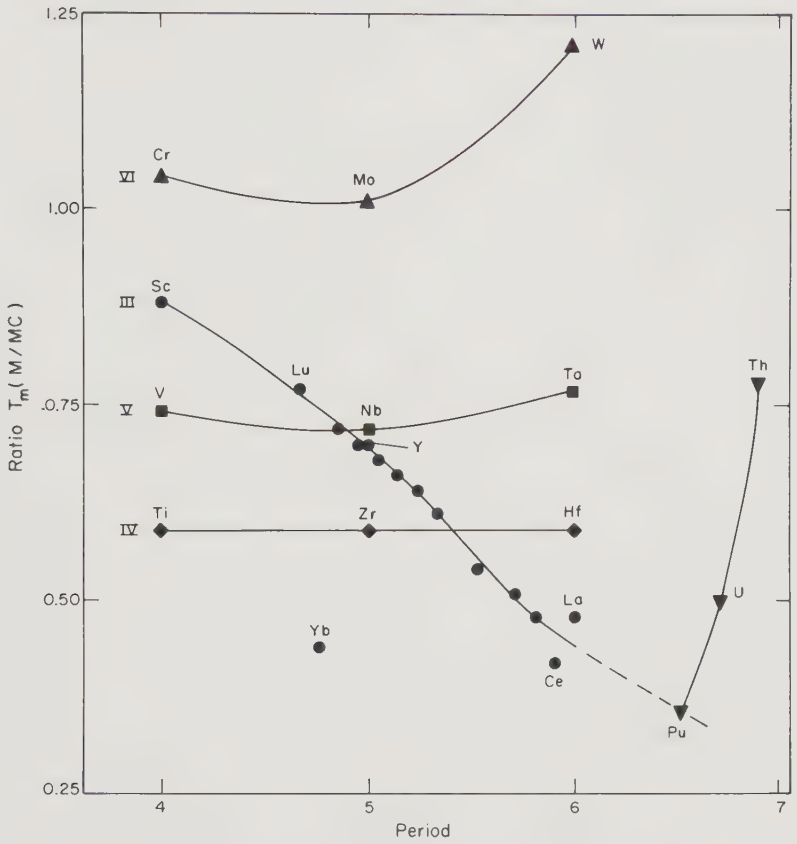

Fig. 14. The ratio of melting points of metal versus carbide shown as a function of the period in the periodic table. Each group is represented by a separate curve, with the lanthanides plotted from Lu to La in such a manner that Y falls between Er and Ho.

3.3. Thermodynamic Properties

The complete thermodynamic definition of an interstitial phase requires data on the low-temperature heat capacity, high-temperature heat content, and either the enthalpy or free energy of formation. Furthermore, these data are needed as a function of composition across the range of homogeneity. The heat of formation of the interstitial carbides can be determined experimentally in most cases from a calorimetric heat of combustion. The most common experimental information for nitrides and hydrides is the measurement of the equilibrium gas pressure (nitrogen or hydrogen) as a function of temperature and composition. The free energy of formation has also

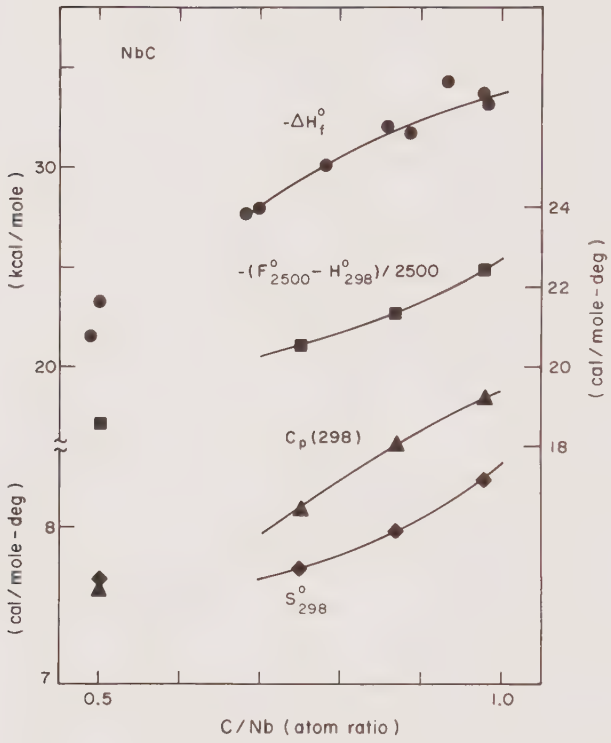

Fig. 15. The thermodynamic properties of niobium carbide. S_{298}° and $C_p(298)$ are on the cal/mole-deg scale on the left, $-(F_{2500}^\circ - H_{298}^\circ)/2500$ is on the scale on the right, and $-\Delta H_f^\circ$ is on the kcal/mole scale.

been determined, with limited success, from vapor–solid equilibrium measurements and from electrochemical cells. The measurement of the vapor pressure has been applied to the interstitial carbides in recent years with excellent results. The combination of vapor pressure data with the heat of combustion and thermal data provides an experimental measurement of the randomization entropy of the vacancies.

The niobium–carbon system has been studied the most completely, with the low-temperature heat capacity,[71] high-temperature heat content,[72,73] heat of combustion,[74–76] and vapor pressure[77] known as functions of composition across the range of homogeneity of the NbC phase. The variation of S_{298}°, $-\Delta H_f^\circ(298°K)$, and $-(F_{2500}^\circ - H_{298}^\circ)/2500$ with composition is shown in Figure 15, and the variation of the activity of Nb and C at 2500°K is shown in Figure 16. These data may be combined to give an entropy of random-

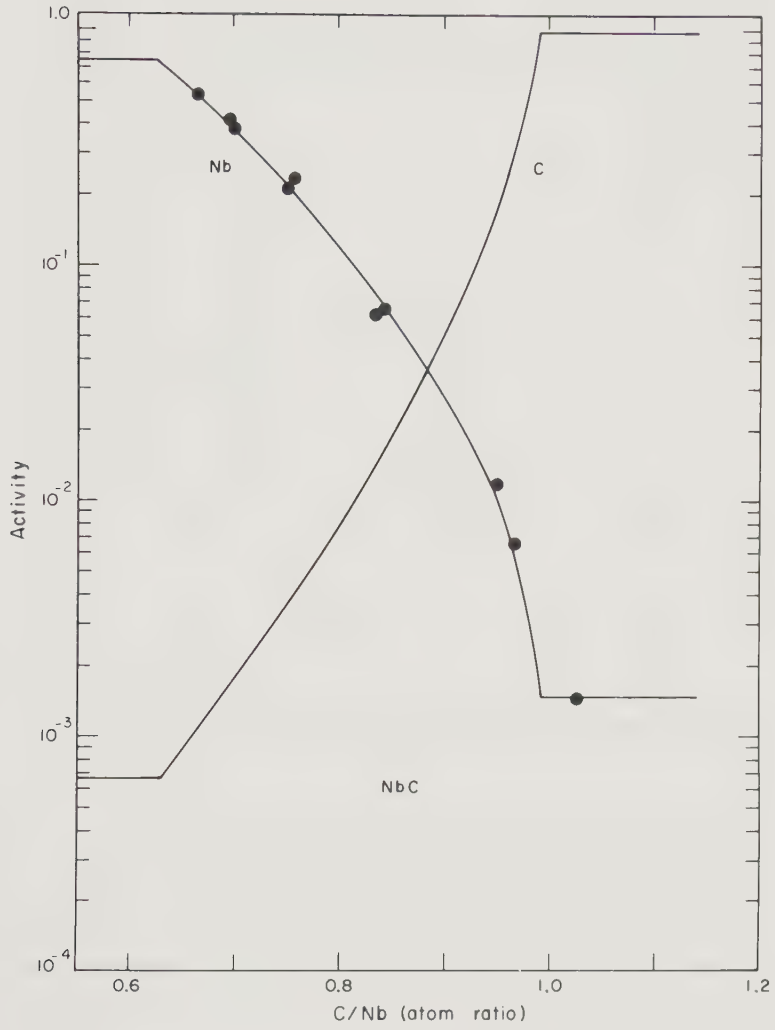

Fig. 16. The thermodynamic activities at 2500°K of Nb and C in niobium carbide. (From Ref. 77.)

ization of vacancies that is smaller than the value calculated for a completely random vacancy model.[77] This is in at least qualitative agreement with the result of a long-wavelength neutron scattering experiment, which shows a definite short-range ordering of vacancies.[78]

The standard heat of formation has been determined for many of the interstitial phases for at least one composition. Selected values

TABLE 3
Standard Heats of Formation of Interstitial Compounds*

Ce_2C_3	21.1[79]	UN	70	ScH_2	50
CeC_2	23.2[79]	U_2N_3	84	YH_2	54.3
ThC	29.6			YH_3	65
ThC_2	29.7			LaH_2	49.6
UC	23.3			ThH_2	35
U_2C_3	21.7[80]			UH_3	30.3
UC_2	20.0				
TiC	44.1	TiN	80	TiH_2	29.5
ZrC	47.0	ZrN	87	$ZrH_{1.5}$ (δ)	33.7
HfC	50.1	HfN	88	ZrH_2 (ε)	39.0
V_2C	16.5	VN	52	V_2H	4
VC	24.5	Nb_2N	30	Nb_2H	5
Nb_2C	23.3	NbN	57	Ta_2H	4
NbC	33.6	Ta_2N	32		
Ta_2C	24.9	TaN	60		
TaC	34.1				
Mo_2C	5.5	Cr_2N	13.7[81]		
Mo_3C_2	3.0	CrN	25.0[81]		
W_2C	3.2	Mo_2N	10		
WC	9.7				

* $-\Delta H_{298}$ expressed as kcal/g-atom of metal. The carbide and nitride data are from Storms[4,5] except where noted, and the hydride data are from Mueller *et al.*[7]

are summarized in Table 3. The carbide data are primarily from heats of combustion, and the hydride data are from equilibrium pressure measurements, while the nitride data are from both kinds of experiments. The $\Delta H°$ values of the carbides are known to within 1 kcal in most cases, while the uncertainties of the nitride and hydride values are generally much larger. The low-temperature heat capacity and high-temperature heat content data are available for most of the carbides and a few of the nitrides and hydrides, but generally not as a function of composition.

3.4. Hardness

The most significant property of the interstitial carbides, from the standpoint of commercial application, is their very high hardness. Even with the obvious importance of this property, there is still much work needed to study the variables affecting the hardness. Hardness measurements are usually performed on a single grain of a polycrystalline sample, using a Knoop indenter under an appropriate load.

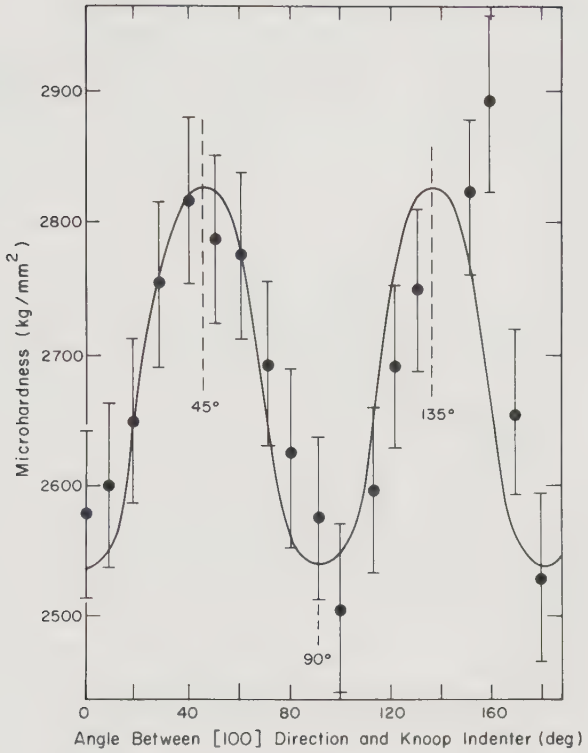

Fig. 17. The variation of the measured microhardness of titanium carbide with change in the angle between sample and indenter. (From Ref. 82.)

The measured hardness has been shown to vary with the angle between the indenter and the crystal face.[82] The results of an experiment with a single crystal of TiC are shown in Figure 17. It seems probable that the measured hardness should also be different for different crystal planes. It is now well understood that hardness will vary with composition across an interstitial phase. The results of three different studies of TiC are shown in Figure 18, with the effect of added oxygen also shown as an increase in hardness. The variation of hardness with a change of composition in ZrC, HfC,[84] and VC[85] is similar to that of TiC, while NbC and TaC show an increase in hardness with a decrease in carbon content.[85,86] It has been suggested that the TaC hardness reaches a maximum value at $TaC_{0.83}$,[86] but this may be a result of the existence of two phases at lower carbon content.

The anisotropic hardness of hexagonal WC has been measured on a single crystal, with values of 2100 kg/mm^2 for the (001) plane,

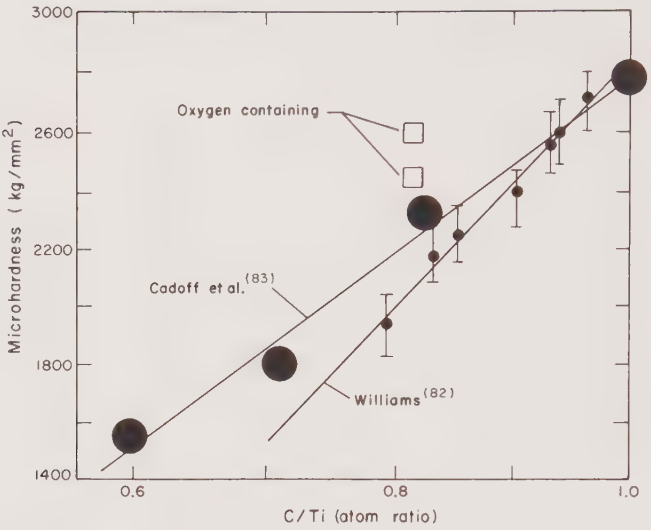

Fig. 18. The variation of the microhardness of titanium carbide with change in composition. The effect of oxygen on the microhardness is shown by the open squares.

1080 kg/mm^2 for (100), and 1060 kg/mm^2 for (101).[87] The hardness of Mo_2C and Mo_3C_2 has been studied as a function of crystal orientation and annealing temperature.[88] The hardness was found to decrease with increase in annealing temperature up to 2000°C, after which the hardness began to increase. This effect was explained by the precipitation and dispersion of Mo and Mo_3C_2.

TABLE 4
Hardness of Interstitial Compounds*

YC_2	400	ThC	850	UC	650
LaC_2	215	ThC_2	600	U_2C_3	1100
				UC_2	500
TiC	2900	ZrC	2600	HfC	2500
V_2C	1800	Nb_2C	2050	Ta_2C	1300
VC	3000	NbC	1700	TaC	1400
Cr_3C_2	1300	Mo_2C	1650	WC	2200
				UN	580
TiN	2100	ZrN	2000	HfN	1600
V_2N	1900	Nb_2N	1700	Ta_2N	1200
TiH_2	250	$ZrH_{1.5}$ (δ)	250	ZrH_2 (ε)	150

* In kg/mm^2. Data from Refs. 2–7, 9, 84, and 85.

It is apparent that the hardness of an interstitial phase cannot be defined by a single number, but rather by a range of values depending on several variables. This is equally true for the softer nitrides and hydrides. Typical values of the hardness of interstitial phases are shown in Table 4, but these must be considered as approximate, with a wide range possible for each phase.

3.5. Thermal Expansion

The increasing use of interstitial compounds as high-temperature structural materials has made necessary a knowledge of their thermal expansion behavior. The thermal linear expansion can normally be defined by a quadratic function of temperature of the form

$$\Delta l/l = 1 + \alpha_0(t - 25) + \alpha_1(t - 25)^2$$

with $\alpha_0 \sim 10^{-5}/°C$ and $\alpha_1 \sim 10^{-9}/°C^2$. An average coefficient of thermal expansion is then defined by

$$\bar{\alpha} = \alpha_0 + \alpha_1(t - 25)$$

which will obviously vary with temperature. The thermal expansion of the interstitial phases may then be examined by comparing $\bar{\alpha}$ defined at the same temperature. This is done in Table 5, where values at

TABLE 5
Thermal Expansion of Interstitial Phases*

	Metal	Carbide	Nitride	Hydride
Y	—	7.0	—	16
La	9	8.4	—	—
Th	12.4	11.0	—	—
U	16.0	12.0	9.4	—
Ti	9.3	7.9	8.6	—
Zr	7.1	7.3	7.6	13
Hf	5.8	6.8	6.2	—
V	10.0	8.4	8	—
Nb	8.0	6.9	9	—
Ta	7.0	6.6	5	—
Cr	10.8	10.2	—	—
Mo	6.0	6.0	—	—
W	4.5	5.0	—	—

* $\bar{\alpha} \times 10^6/°C$ for $T = 25$–$1000°C$. Data are derived from Refs. 2–7 and 89–111.

1000°C are listed for the metals, monocarbides, and mononitrides and for ZrH_2 and YH_2.

The available thermal expansion data are from dilatometric and diffraction experiments, with the diffraction data generally showing much better agreement among different investigators. The carbides of groups IV and V have been studied as a function of composition with conflicting conclusions.[107–111] It would seem that there is no well-established variation of $\bar{\alpha}$ with change of composition for any interstitial phase, and it is best to assume a constant $\bar{\alpha}$ for any given compound.

3.6. Electrical Resistivity

The interstitial phases are metallic conductors, that is, they are good conductors at room temperature with the electrical resistivity ρ increasing with increasing temperature. The electrical properties of the carbides and nitrides have been reviewed recently by Storms[9] and those of the hydrides by Libowitz.[9] The resistivities of the interstitial phases are compared with those of the metals in Table 6.

TABLE 6
Electrical Resistivity of Interstitial Compounds*

	Metal	Carbide	Nitride	Hydride
Y	65	30†	—	20
La	57	45†	—	40
Th	20	25	20	—
U	30	30	149	—
Ti	46	50	27	120†
Zr	50	43	21	25†
Hf	37	37	33	—
V	23	76	85	—
Nb	16	40	80	—
Ta	13	18	130	—
Cr	16	75‡	80§	—
Mo	6	57§	—	—
W	5	20	—	—

* ρ in $\mu\Omega$-cm at 25°C. Except where noted, all compounds are the MX phase. Data from Refs. 2–7, 9, 89, 102, and 103.

† MX_2.

‡ M_3X_2.

§ M_2X.

The cubic carbides and nitrides generally have a resistivity at the stoichiometric composition that is approximately that of the pure metal. The resistivity increases with a decrease in content of nonmetal (or increase in the number of vacancies). The resistivity also tends to increase sharply with an increase in metal atom vacancies in the cubic nitrides. This has been demonstrated in the Nb–N system, where ρ increases from $\sim 90\,\mu\Omega$-cm at $NbN_{1.0}$ to $\sim 270\,\mu\Omega$-cm at $NbN_{1.05}$.[112] The higher nitride of thorium, Th_3N_4, has been found to be a semiconductor.[113]

The resistivities of the interstitial hydrides are also very close to those of the metals, but the variation with change of hydrogen content differs among groups. Thus the resistivity of cerium hydride increases from $\sim 100\,\mu\Omega$-cm at $CeH_{2.0}$ to $\sim 1000\,\mu\Omega$-cm at $CeH_{2.7}$, but at higher hydrogen compositions the material becomes a semiconductor.[114] The tetragonal zirconium and titanium hydrides show an increase in ρ with decrease in hydrogen content, while the resistivities of cubic δ-ZrH_2 and the group V hydrides increase with increasing hydrogen content. The resistivity of palladium hydride passes through a maximum at $PdH_{0.74}$, with a value about twice that of palladium metal.

3.7. Superconductivity

The interstitial phases are in many cases superconducting at low temperatures, with some of the highest critical transition temperatures T_c known. The highest values of T_c have been obtained with intermetallic compounds with the $A15$ (β-W type) structure and with interstitial phases with the $B1$ (NaCl type) or $D5_c$ (Pu_2C_3 type) structures. The T_c values of known superconducting interstitial phases are listed in Table 7. The complex-structured Th_4H_{15} is the only hydride known to be superconducting.[115]

The variation of T_c with change of composition of an interstitial phase has been studied for δ-NbN,[112] NbC and TaC,[123] VN and TiN,[124] and HfN.[45] The variation of T_c in NbC and TaC is shown in Figure 19. In addition to the effect of vacancies, dissolved oxygen is also known to lower the T_c, but the magnitude of this effect has not been determined quantitatively. The value of T_c always increases with increasing lattice parameter in the c-type carbides and nitrides.

The highest values of T_c in interstitial phases have been obtained in ternary systems, with $T_c = 17.8°$ in Nb(C, N)[125] and $T_c = 17.0°$ in $(Y, Th)_2C_3$[126] among the highest known. The variation of T_c with

TABLE 7

Superconducting Critical Temperatures (in °K) of Interstitial Compounds*

Y_2C_3	11.5[116]	YC_2	3.88[119]		
La_2C_3	11.0[117]	LaC_2	1.44[120]		
Th_2C_3	4.1[118]			ThN	3.2[121]
				Th_4H_{15}	8.2[115]
TiN	5.49	ZrN	10.0	HfN	8.83
		NbC	11.2[122]	TaC	10.5[122]
VN	8.5	δ-NbN	17.3		
α-Mo_2C	4.05	Mo_2N	5.0	α-W_2C	2.74
Mo_3C_2	8.0	MoN	12.0	β-WC	10.0
MoC	14.3				

* Data from Toth[6] except where noted.

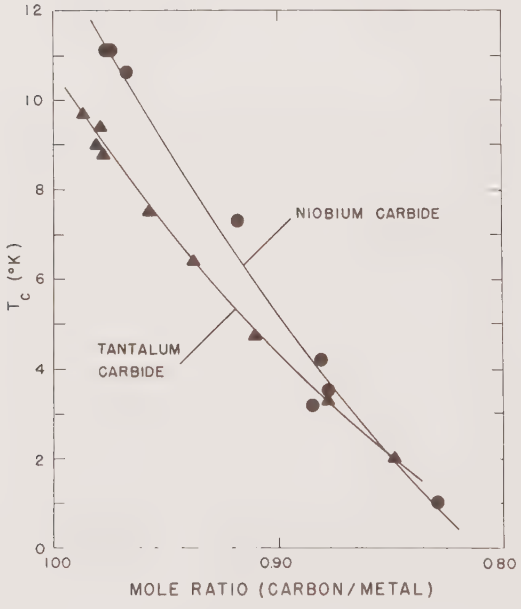

Fig. 19. The variation of the superconducting critical temperature of niobium carbide and tantalum carbide with change in composition. (From Ref. 123.)

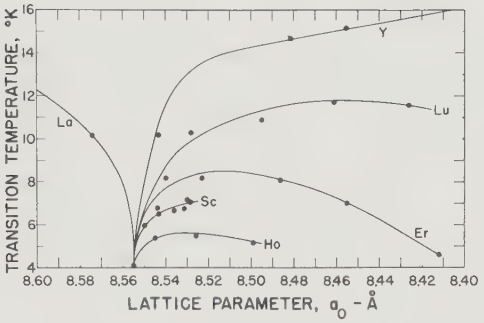

Fig. 20. The variation of the superconducting critical temperature of ternary $(Th, M)_2C_3$ phases with change of lattice parameter (M = Sc, Y, La, Ho, Er, Lu). (From Ref. 121.)

lattice parameter is shown in Figure 20 for several ternary sesquicarbides with thorium.

3.8. Diffusion

The problem of diffusion in binary carbides has been reviewed by DePoorter and Wallace.[127] It is noted that the metal self-diffusion coefficients are independent of the carbon content, while the carbon diffusion increases with decrease in carbon content. The carbon diffusion is much higher than that of the metal, for example, 10^4 times higher at 2000° for TiC. It is suggested that diffusion occurs separately and independently on each sublattice and takes place through a vacancy mechanism. In the metal sublattice, only thermal vacancies exist, while structural vacancies are the dominant factor in the carbon sublattice.

The experimental data on diffusion in carbides are very limited, and in some cases almost certainly are in error from grain boundary diffusion effects. Nevertheless, the qualitative view described above is generally confirmed by the available data. There are essentially no data on diffusion in nitrides and hydrides but it seems reasonable to assume an equivalent picture. It is probable that the metal diffusion is much higher in the cubic nitrides with significant metal atom vacancies.

3.9. Bonding

The nature of the bonding in the interstitial phases is still not fully understood. The recent theories of bonding for carbides and nitrides

agree on the existence of strong metal–metal and metal–nonmetal bonds, but disagree with each other in the details. The band structure and bonding in TiC have been developed by Lye[128–130] using the LCAO method. In this model the metal–metal interactions are similar to those in the transition metals but are strengthened by the effect of carbon–atom core potentials in regions of overlap between metal orbitals and by a transfer of electrons from the carbon to metal orbitals. Additional bonding, with a substantial covalent character, is derived from the metal–carbon and carbon–carbon interactions. An ionic component is present as a result of the charge transfer, but contributes little to the total cohesive energy. The calculations of Ern and Switendick[131] using the augmented plane wave method also emphasize metal–metal and metal–nonmetal bonding, but result in a band structure for TiC that differs from that of Lye. The available experimental data do not permit a conclusive choice between the two models. The calculations on TiN[131] show less hybridization than for TiC, and indicate electron transfer from Ti to N, but are generally similar to the results for TiC.

The general picture of bonding in interstitial hydrides is similar, but the nature of the metal–nonmetal interactions must differ considerably from that found in the carbides and nitrides. It has been suggested by Libowitz[9] that the rare earth hydrides are essentially anionic, with some covalent character, while the other interstitial hydrides are metallic and are best described by a screened proton model.

4. Summary

An interstitial phase is defined here as any phase that has an interstitial structure.[1] This includes most of the hydrides, carbides, and nitrides of the transition metals (groups three through eight), as well as the solutions of H, C, and N in these metals. The crystal structures of these phases may be described generally on the basis of a close-packed metal sublattice, with the nonmetal atoms occupying interstitial positions (holes). These phases typically have wide ranges of homogeneity, resulting from partial filling of the available interstitial holes. The vacancies may be either ordered or random, with the possibility of an order–disorder transformation. The physical properties of these phases are generally similar to those of the pure metals, but with much higher hardnesses and melting points. This is consistent with recent theories of bonding in interstitial phases, which

show metal–metal interactions similar to those in the metals coupled with strong, partly covalent, metal–nonmetal bonds. The significance of the metal–nonmetal bond is apparent from the strong dependence on composition of many of the properties of the interstitial phases.

References

1. G. Hägg, Eigenschaften der Phasen von Übergangselementen in binären Systemen mit Bor, Kohlenstoff und Stickstoff, *Z. Phys. Chem. Abt. B* **6**, 221–232 (1930); Gesetzmässigkeiten im Kristallbau bei Hydriden, Boriden, Carbiden und Nitriden der Übergangselemente, *Z. Phys. Chem. Abt. B* **12**, 33–56 (1931).
2. P. Schwarzkopf and R. Kieffer, *Refractory Hard Metals*, Macmillan, New York (1953).
3. H. J. Goldschmidt, *Interstitial Alloys*, Butterworths, London (1967).
4. E. K. Storms, A Critical Review of Refractories, Los Alamos Scientific Laboratory Report LA-2942 (August 1964).
5. E. K. Storms, *The Refractory Carbides*, Academic, New York (1967).
6. L. E. Toth, *Transition Metal Carbides and Nitrides*, Academic, New York (1971).
7. W. M. Mueller, J. P. Blackledge, and G. G. Libowitz (eds.), *Metal Hydrides*, Academic, New York (1968).
8. B. Aronsson, T. Lundström, and S. Rundqvist, *Borides, Silicides and Phosphides*, Wiley, New York (1965).
9. E. K. Storms, Phase relationships and electrical properties of refractory carbides and nitrides, pp. 37–78; G. G. Libowitz, Solid state properties of metallic and saline hydrides, pp. 79–116; H. Nowotny, Silicides and borides, pp. 151–188; in *Solid State Chemistry*, Vol. 10 (L. E. J. Roberts, ed.), Butterworths, London (1972).
10. M. C. Krupka, High pressure synthesis of thorium sesquicarbide: A new actinide carbide, *J. Less-Common Metals* **20**, 135–140 (1970).
11. R. Kieffer, P. Ettmayer, M. Freudhofmeier, and J. Gatterer, Über das kubische Tantalmononitrid mit B-1 Struktur, *Monatsh. Chem.* **102**, 483–485 (1971).
12. V. I. Khitrova and Z. G. Pinsker, Chemical crystallography of tungsten nitrides and of some other interstitial phases, *Soviet Phys.—Crystallography* **6**, 712–719 (1961).
13. A. L. Bowman and G. P. Arnold, The crystal structure of Th_3N_4, *Acta Cryst.* **B27**, 243–244 (1971).
14. D. A. Vaughan, X-Ray diffraction study of the nitrides of uranium, *Trans. AIME* **206**, 78–79 (1956).
15. R. E. Rundle, N. C. Baenziger, A. S. Wilson, and R. A. McDonald, The structures of the carbides, nitrides and oxides of uranium, *J. Am. Chem. Soc.* **70**, 99–105 (1948).
16. E. Parthé and K. Yvon, On the crystal chemistry of the close packed transition metal carbides. II. A proposal for the notation of the different crystal structures, *Acta Cryst.* **B26**, 153–163 (1970).
17. C. H. de Novion, R. Lorenzelli, and P. Costa, Existence d'une surstructure dans le carbure de vanadium VC_{1-x}, *Compt. Rend. Ser. B.* **263**, 775–778 (1966); A. W. Henfrey and B. E. F. Fender, Neutron-diffraction investigation of V_8C_7, *Acta Cryst.* **B26**, 1882–1883 (1970).

18. J. D. Venables, D. Kahn, and R. G. Lye, Structure of the ordered compound V_6C_5, *Phil. Mag.* **18**, 177–192 (1968).
19. J. D. Venables and M. H. Meyerhoff, Ordering effects in NbC and TaC, in *Solid State Chemistry* (R. S. Roth and S. J. Schneider, Jr., eds.), National Bureau of Standards Special Publication 364, Washington, D.C. (July 1972).
20. H. Goretzki, Neutron diffraction studies on titanium–carbon and zirconium–carbon alloys, *Phys. Stat. Sol.* **20**, K141–K143 (1967).
21. R. Lorenzelli and I. de Dieuleveult, Existence d'une surstructure dans le carbure de thorium sous-stoechiometrique: $ThC_{0.76}$, *J. Nucl. Mater.* **29**, 349–353 (1969).
22. K. Yvon, W. Rieger, and H. Nowotny, Die Kristallstruktur von V_2C, *Monatsh. Chem.* **97**, 689–694 (1966).
23. K. Yvon, H. Nowotny, and R. Kieffer, Die Kristallstruktur der Subcarbide von Übergangsmetallen, *Monatsh. Chem.* **98**, 34–44 (1967).
24. A. L. Bowman, T. C. Wallace, J. L. Yarnell, R. G. Wenzel, and E. K. Storms, The crystal structures of V_2C and Ta_2C, *Acta Cryst.* **19**, 6–9 (1965).
25. E. Parthé and V. Sadagopan, The structure of dimolybdenum carbide by neutron diffraction technique, *Acta Cryst.* **16**, 202–205 (1963).
26. K. Yvon, H. Nowotny, and F. Benesovsky, Zur Kristallstruktur von W_2C, *Monatsh. Chem.* **99**, 726–729 (1968).
27. M. Atoji and M. Kikuchi, Crystal structures of cubic and trigonal yttrium hypocarbides; a dimorphically interphased single-crystal study, *J. Chem. Phys.* **51**, 3863–3872 (1969).
28. M. Atoji, Magnetic and crystal structures of the trigonal Tb_2C, *J. Chem. Phys.* **51**, 3872–3876 (1969).
29. G. L. Bacchella, P. Mériel, M. Pinot, and R. Lallement, Etude par diffraction de neutrons de Ho_2C, *Bull. Soc. Fr. Mineral. Cristallogr.* **89**, 226–228 (1966).
30. A. L. Bowman, G. P. Arnold, and T. C. Wallace, The kinetics of the solid-state transformation of Mo_2C, 1969 Southwest Regional Meeting, American Chemical Society, Tulsa, Oklahoma (December 1969).
31. A. L. Bowman, N. H. Krikorian, and N. G. Nereson, The order–disorder transformation of Ta_2C, *Étude de Transformations Cristallines à Haute Température au-dessus de 2000K*, pp. 193–197, Centre National de la Recherche Scientifique, Paris (1972).
32. S. Eriksson, Röntgenunders ökningar över systemet järnkrom-kvave, *Jernkontorets Ann.* **89**, 530–543 (1934), as described in *Strukturbericht* **3**, 586–587 (1933–1935).
33. (a) K. H. Jack, Binary and ternary interstitial alloys: I. The iron–nitrogen system: the structures of Fe_4N and Fe_2N, *Proc. Roy. Soc. Ser. A*, **195**, 34–40 (1948); (b) The iron–nitrogen system: the preparation and the crystal structures of nitrogen–austenite (γ) and nitrogen–martensite (α'), *Proc. Roy. Soc. Ser. A* **208**, 200–215 (1951); (c) The occurrence and the crystal structure of α''-iron nitride; a new type of interstitial alloy formed during the tempering of nitrogen martensite, *Proc. Roy. Soc. Ser. A* **208**, 216–224 (1951); (d) The iron–nitrogen system: The crystal structures of ε-phase iron nitrides, *Acta Cryst.* **5**, 404–411 (1952).
34. A. L. Bowman, N. H. Krikorian, G. P. Arnold, and N. G. Nereson, A high-temperature neutron diffraction study of the molybdenum–carbon system, to be published (1973).
35. J. L. Martin, A. Rocher, B. Jouffrey, and P. Costa, Electron diffraction patterns of the (Ta, C) ζ phase, *Phil. Mag.* **24**, 1355–1364 (1971).

36. S. S. Sidhu, N. S. Satya Murthy, F. P. Compos, and D. D. Zauberis, Neutron and X-ray diffraction studies of nonstoichiometric metal hydrides, in *Symp. on Nonstoichiometric Compounds, Washington, D.C., 1962* (Advances in Chemistry Series, No. 39), pp. 87–98, American Chemical Society, Washington (1963).

37a. B. W. Roberts, Neutron diffraction study of VD_x, *Phys. Rev.* **100**, 1257 (1955).

37b. W. E. Wallace, Neutron diffraction data for Ta_2D and the probable arrangement of the deuteriums in two of its polymorphic varieties, *J. Chem. Phys.* **35**, 2156–2164 (1961).

38a. V. A. Somenkov, A. V. Gurskaya, M. G. Zemlyanov, M. E. Kost, N. A. Chernoplekov, and A. A. Chertkov, Neutron scattering study of structure and phase transitions in niobium hydrides and deuterides, *Soviet Phys.—Solid State* **10**, 1076–1081 (1968).

38b. V. A. Somenkov, M. G. Zemlyanov, M. E. Kost, N. A. Chernoplekov, and A. A. Chertkov, Study of ordering of interstitial atoms in solid solutions of hydrogen in metals of group V, *Soviet Phys.—Dokl.* **13**, 669–671 (1969).

38c. V. A. Somenkov, A. V. Gurskaya, M. G. Zemlyanov, M. E. Kost, N. A. Chernoplekov, and A. A. Chertkov, Neutron-diffraction study of the structure and phase transformations of tantalum hydrides and deuterides, *Soviet Phys.—Solid State* **10**, 2123–2127 (1969).

38d. V. A. Somenkov, V. F. Petrunin, S.Sh. Shil'shtein, and A. A. Chertkov, Neutron-diffraction study of the decomposition and ordering in the niobium–hydrogen system, *Soviet Phys.—Crystallography* **14**, 522–530 (1970).

38e. V. F. Petrunin, V. A. Somenkov, S.Sh. Shil'shtein, and A. A. Chertkov, The structure of Ta_2D, *Soviet Phys.—Crystallography* **15**, 137–139 (1970).

39. A. L. Bowman, G. P. Arnold, W. G. Witteman, T. C. Wallace, and N. G. Nereson, The crystal structures of UC_2, *Acta Cryst.* **21**, 670–671 (1966).

40. A. L. Bowman, N. H. Krikorian, G. P. Arnold, T. C. Wallace, and N. G. Nereson, The crystal structures of LaC_2, *Acta Cryst.* **B24**, 459–460 (1968).

41. A. L. Bowman, N. H. Krikorian, G. P. Arnold, T. C. Wallace, and N. G. Nereson, The crystal structures of ThC_2, *Acta Cryst.* **B24**, 1121–1123 (1968).

42. M. C. Krupka, N. H. Krikorian, and T. C. Wallace, Polymorphism in heavy rare earth dicarbides at high pressures and temperatures, in *Proc. 7th Rare Earth Research Conf., Coronado, California October 1968.*

43. B. Holmberg, Structural studies on the titanium–nitrogen system, *Acta Chem. Scand.* **16**, 1255–1261 (1962).

44. M. E. Straumanis, C. A. Faunce, and W. J. James, The defect structure and bonding of zirconium nitride containing excess nitrogen, *Inorg. Chem.* **5**, 2027–2030 (1966).

45. A. L. Giorgi, E. G. Szklarz, and T. C. Wallace, Anomalous superconducting properties of carbides and nitrides of group IVa and Va elements, *Proc. Brit. Ceram. Soc.* **10**, 183–193 (1968).

46. G. Brauer and H. Kirner, Drucksynthese von Niobnitriden und Konstitution von δ-NbN, *Z. Anorg. Allgem. Chem.* **328**, 34–43 (1964).

47. D. P. Seraphim, N. R. Stemple, and D. T. Novick, Phase instability in dilute interstitial solid solutions of nitrogen in tantalum, *J. Appl. Phys.* **33**, 136–141 (1962).

48. R. E. Villagrana and G. Thomas, Interstitial ordering of carbon in tantalum, *Phys. Stat. Sol.* **9**, 499–518 (1965).

49. N. J. Petch, The positions of the carbon atoms in martensite, *J. Iron Steel Inst. (London)* **147**, 221–227 (1943); H. Lipson and A. M. B. Parker, The structure of martensite, *J. Iron Steel Inst. (London)* **149**, 123–141 (1944).
50. G. A. Ferguson, Jr., A. I. Schindler, T. Tanaka, and T. Morita, Neutron diffraction study of temperature-dependent properties of palladium containing absorbed hydrogen, *Phys. Rev.* **A137**, 483–487 (1965).
51. E. Rudy, The crystal structure of Ta_2VC_2, *J. Less-Common Metals* **20**, 49–55 (1970).
52. A. L. Bowman, G. P. Arnold, and N. H. Krikorian, The crystal structure of U_2IrC_2, *Acta Cryst.* **B27**, 1067–68 (1971).
53. H. H. Stadelmaier, Metal-rich metal–metalloid phases, in *Developments in the Structural Chemistry of Alloy Phases* (B. C. Giessen, ed.), pp. 141–180, Plenum, New York (1969).
54. H. Zijlstra and F. F. Westendorp, Influence of hydrogen on the magnetic properties of $SmCo_5$, *Solid State Commun.* **7**, 857–9 (1969); J. H. van Vucht, F. A. Kuijpers, and H. C. A. M. Bruning, Reversible room-temperature absorption of large quantities of hydrogen by intermetallic compounds, *Philips Res. Repts.* **25**, 133–140 (1970).
55. F. A. Kuijpers and B. O. Loopstra, Magnetic structure of $PrCo_5D_4$, *J. Phys. (Paris)* **32**, C657–58 (1971).
56. A. L. Bowman, J. L. Anderson, and N. G. Nereson, A neutron-diffraction study of $LaNi_5D_7$, *Proc. 10th Rare Earth Research Conf., Carefree, Arizona*, pp. 485–489 (1973).
57. R. Benz, G. P. Arnold, and W. H. Zachariasen, ThCN crystal structure, *Acta Cryst.* **B28**, 1724–27 (1972).
58. K. Yvon, H. Nowotny, and R. Kieffer, Zur Kristallstruktur der Carbohydride von Übergangsmetallen, *Monatsh. Chem.* **98**, 2165–2172 (1967).
59. G. Lobier and D. Rossier, Structural study of the thorium carbohydrides by X-rays and proton nuclear magnetic resonance: Evidence for vacancy induced hydrogen position correlations, *Acta Cryst.* **B26**, 945–953 (1970).
60. H. Goretzki, E. Ganglberger, H. Nowotny, and H. Bittner, Zum Problem der Carbohydride, *Monatsh. Chem.* **96**, 1563–66 (1965).
61. G. Lobier, Contribution a l'etude de l'insertion de l'hydrogene dans les carbures, nitrures et sulfures des elements de transition, Commis. Energ. At. (Fr.) Rapport, CEA-R-4065 (1970).
62. O. N. Carlson and W. M. Paulson, The yttrium–carbon system, *Trans. AIME* **242**, 846–852 (1968).
63. E. K. Storms, The vaporization behavior of the defect carbides. II: The Y–C system, *High Temp. Sci.* **3**, 99–122 (1971).
64. F. H. Spedding, K. Gschneidner, Jr., and A. H. Daane, The lanthanum–carbon system, *Trans. AIME* **215**, 192–199 (1959).
65. N. H. Krikorian, T. C. Wallace, and M. G. Bowman, Phase relationships of the high carbon portion of lanthanide–carbon systems, in *Propriétés Thermodynamiques Physiques et Structurales des Derives Semi-Metalliques*, pp. 489–498, Centre National de la Recherche Scientifique, Paris (1967).
66. W. M. Olson and R. N. R. Mulford, The decomposition pressure and melting point of thorium mononitride, *J. Phys. Chem.* **69**, 1223–26 (1965).
67. R. Benz, C. G. Hoffman, and G. N. Rupert, Some phase equilibria in the thorium–nitrogen system, *J. Am. Chem. Soc.* **89**, 191–197 (1967).

68. W. M. Olson and R. N. R. Mulford, The decomposition pressure and melting point of uranium mononitride, *J. Phys. Chem.* **67**, 952–954 (1963).
69. R. Benz and M. G. Bowman, Some phase equilibria in the uranium–nitrogen system, *J. Am. Chem. Soc.* **88**, 264–268 (1966).
70. N. H. Krikorian, A. L. Bowman, M. C. Krupka, and G. P. Arnold, The preparation and crystal structure of Sc_4C_3, *High Temp. Sci.* **1**, 360–366 (1969).
71. T. A. Sandenaw and E. K. Storms, Heat capacities of $NbC_{0.702}$, $NbC_{0.825}$, $NbC_{0.980}$ and Nb_2C below 320°K, *J. Phys. Chem. Solids* **27**, 217–218 (1966).
72. L. S. Levinson, High temperature heat content of niobium carbide and of tantalum carbide, *J. Chem. Phys.* **39**, 1550–1 (1963); Erratum, *J. Chem. Phys.* **42**, 3342 (1965).
73. P. V. Gel'd and F. G. Kusenko, Heat content and specific heats of niobium oxides at elevated temperatures, *Izv. Akad. Nauk SSSR, Otd. Tekh. Nauk, Met. Topl.* **2**, 79–86 (1960).
74. E. J. Huber, Jr., E. L. Head, C. E. Holley, Jr., E. K. Storms, and N. H. Krikorian, The heats of combustion of niobium carbides, *J. Phys. Chem.* **65**, 1846–1849 (1961).
75. F. G. Kusenko and P. V. Gel'd, Heats of formation of niobium oxides and carbides, *Izv. Sib. Otd. Akad. Nauk SSSR* **2**, 46–52 (1960).
76. A. N. Kornilov, I. D. Zaikin, S. M. Skuratov, and G. P. Shveikin, Standard heats of formation of niobium carbide present in the NbC phase, *Zh. Fiz. Khim.* **40**, 1070–1076 (1966).
77. E. Storms, B. Calkin, and A. Yencha, The vaporization behavior of the defect carbides. I: The Nb–C system, *High Temp. Sci.* **1**, 430–455 (1969).
78. A. W. Henfrey and B. E. F. Fender, unpublished work, cited in *Solid State Chemistry*, Vol. 10, p. 263 (L. E. J. Roberts, ed.), Butterworths, London (1972).
79. F. B. Baker, E. J. Huber, Jr., C. E. Holley, Jr., and N. H. Krikorian, Enthalpies of formation of cerium dioxide, cerium sesquicarbide, and cerium dicarbide, *J. Chem. Thermodyn.* **3**, 77–83 (1971).
80. E. J. Huber, Jr., C. E. Holley, Jr., and W. G. Witteman, Enthalpy of formation of uranium sesquicarbide, *J. Chem. Thermodyn.* **1**, 579–587 (1969).
81. T. Mills, Thermodynamic relations in the chromium–nitrogen system, *J. Less-Common Metals* **26**, 223–234 (1972).
82. W. S. Williams, Brittle-ductile behavior of the transition metal carbides, in *Propriétés Thermodynamiques Physiques et Structurales des Derives Semi-Metalliques*, pp. 181–190, Centre National de la Recherche Scientifique, Paris (1967).
83. I. Cadoff, J. P. Nielsen, and E. Miller, Properties of arc-melted vs. powder metallurgy titanium carbide, in *Plansee Proceedings 1955* (F. E. Benesovsky, ed.), pp. 50–55, Pergamon, London (1956).
84. L. Ramqvist, Variation of lattice parameter and hardness with carbon content of group 4b metal carbides, *Jernkontorets Ann.* **152**, 517–523 (1968).
85. L. Ramqvist, Variation of hardness, resistivity and lattice parameter with carbon content of group 5b metal carbides, *Jernkontorets Ann.* **152**, 465–475 (1968).
86. G. Santoro, Variation of some properties of tantalum carbide with carbon content, *Trans. AIME* **227**, 1361–1368 (1963).
87. T. Takahashi and E. J. Freise, Determination of slip systems in single crystals of tungsten monocarbide, *Phil. Mag.* **12**, 1–8 (1965).

88. F. W. Vahldiek, S. A. Mersol, and C. T. Lynch, Investigation of Single-Crystal Dimolybdenum Carbide, U.S. Air Force Tech. Report AFML-TR-66-268 (1966).
89. Y. S. Touloukian (ed.), *Thermophysical Properties of High Temperature Materials*, Macmillan, New York (1967).
90. R. O. Elliott and C. P. Kempter, Thermal expansion of some transition metal carbides, *J. Phys. Chem.* **62**, 630–31 (1958).
91. J. J. Gangler, Some physical properties of eight refractory oxides and carbides, *J. Am. Ceram. Soc.* **33**, 367–374 (1950).
92. C. R. Houska, Thermal expansion of certain group IV and group V carbides at high temperatures, *J. Am. Ceram. Soc.* **47**, 310–311 (1964).
93. S. J. Grisaffe, Thermal expansion of hafnium carbide, *J. Am. Ceram. Soc.* **43**, 494 (1960).
94. V. N. Paderno, Physical properties of hafnium carbide samples prepared by powder metallurgical methods, *Izv. Akad. Nauk SSSR, Otd. Tekh. Nauk, Met. Topl.* **6**, 176–178 (1962).
95. H. Nowotny and E. Laube, The thermal expansion of high-melting phases, *Planseeber. Pulvermet.* **9**, 54–59 (1961).
96. C. K. Jun and P. T. B. Shaffer, Thermal expansion of niobium carbide, hafnium carbide and tantalum carbide at high temperatures, *J. Less-Common Metals* **24**, 323–327 (1971).
97. J. H. Richardson, Thermal expansion of three group IVA carbides to 2700°C, *J. Am. Ceram. Soc.* **48**, 497–499 (1965).
98. G. V. Samsonov, I. B. Paderno, and A. D. Panasiuk, Des composés definis et des domaines d'homogéneité des metaux de transition, *Rev. Hautes Temper. et Refract.* **3**, 179–184 (1966).
99. A. L. Bowman, N. H. Krikorian, and N. G. Nereson, The variation of lattice parameter of UC–ZrC solid solutions with temperature and composition, in *AIP Conf. Proc. No. 3, Thermal Expansion—1971* (M. G. Graham and H. E. Hagy, ed.), pp. 119–130, American Institute of Physics, New York (1972).
100. C. P. Kempter and M. R. Nadler, Thermal expansion of tantalum monocarbide to 3020°C, *J. Chem. Phys.* **43**, 1739–1742 (1965).
101. C. R. Houska, Thermal expansion and atomic vibration amplitudes for TiC, TiN, ZrC, ZrN, and pure tungsten, *J. Phys. Chem. Solids* **25**, 359–366 (1964).
102. G. V. Samsonov and T. S. Verkoglyadova, Physical properties of transition metal nitrides, *Dokl. Akad. Nauk SSSR* **142**, 608–611 (1962).
103. G. N. Makarenko, L. T. Pustovoit, V. L. Yupko, and B. M. Rud', The nature of the chemical bond in dicarbides of the rare-earth metals, *Izv. Akad. Nauk SSSR, Neorg. Mater.* **1**, 1787–1790 (1965).
104. R. Mendez-Penalosa and R. E. Taylor, Thermal expansion of uranium sesquicarbide, *J. Am. Ceram. Soc.* **47**, 416–17 (1964).
105. A. L. Bowman, G. P. Arnold, W. G. Witteman, and T. C. Wallace, Thermal expansion of uranium dicarbide and uranium sesquicarbide, *J. Nucl. Mater.* **19**, 111–112 (1966).
106. T. Satow, Electrical resistivity, magnetic susceptibility, and thermal expansion of thorium monocarbide, *J. Nucl. Mater.* **21**, 343–344 (1967).
107. G. V. Samsonov and V. Ya. Naumenko, Thermal expansion of carbides of the transition metals of group IV–V in their homogeneity range, *Teplofiz. Vys. Temp.* **8**, 1093–1095 (1970).

108. A. L. Bowman, N. H. Krikorian, and N. G. Nereson, Thermal expansion of ZrC and ZrN, To be published (1973).
109. E. K. Storms and C. P. Kempter, Thermal expansion of some vanadium carbides, *J. Chem. Phys.* **42**, 2043–2045 (1965).
110. C. P. Kempter and E. K. Storms, Thermal expansion of some niobium carbides, *J. Less-Common Metals* **13**, 443–447 (1967).
111. R. J. Fries and L. A. Wahman, Effect of stoichiometry on thermal expansion of TaC_x, *J. Am. Ceram. Soc.* **50**, 475–477 (1967).
112. H. Rögener, Zur Supraleitung des Niobnitrids, *Z. Phys.* **132**, 446–467 (1952).
113. A. B. Auskern and S. Aronson, Electrical properties of thorium nitrides, *J. Chem. Phys. Solids* **28**, 1069–1071 (1967).
114. G. G. Libowitz and J. G. Pack, Electrical resistivities of nonstoichiometric cerium hydride single crystals, *J. Chem. Phys.* **50**, 3557–3560 (1969).
115. C. B. Satterthwaite and I. L. Toepke, Superconductivity of hydrides and deuterides of thorium, *Phys. Rev. Lett.* **25**, 741–743 (1970).
116. M. C. Krupka, A. L. Giorgi, N. H. Krikorian, and E. G. Szklarz, High pressure synthesis and superconducting properties of yttrium sesquicarbide, *J. Less-Common Metals* **17**, 91–98 (1969).
117. A. L. Giorgi, E. G. Szklarz, M. C. Krupka, and N. H. Krikorian, Occurrence of superconductivity in lanthanum sesquicarbide, *J. Less-Common Metals* **17**, 121–123 (1969).
118. A. L. Giorgi, E. G. Szklarz, N. H. Krikorian, and M. C. Krupka, Preparation and superconductivity of the sesquicarbide phase in the lanthanum–thorium–carbon system, *J. Less-Common Metals* **22**, 131–135 (1970).
119. A. L. Giorgi, E. G. Szklarz, M. C. Krupka, T. C. Wallace, and N. H. Krikorian, Occurrence of superconductivity in yttrium dicarbide, *J. Less-Common Metals* **14**, 247 (1968).
120. A. L. Giorgi, Private communication (1973).
121. A. L. Giorgi, E. G. Szklarz, and M. C. Krupka, Superconductivity of various ternary thorium compounds, in *AIP Conf. Proc. No. 4, Superconductivity in d- and f-Band Metals* (D. H. Douglass, ed.), pp. 147–153, American Institute of Physics, New York (1972).
122. A. L. Bowman, A. L. Giorgi, and E. G. Szklarz, Superconductivity of TaC and NbC in the presence of carbon, To be published (1973).
123. A. L. Giorgi, E. G. Szklarz, E. K. Storms, A. L. Bowman, and B. T. Matthias, Effect of composition on the superconducting transition temperature of tantalum carbide and niobium carbide, *Phys. Rev.* **125**, 837–838 (1962).
124. L. E. Toth, C. P. Wang, and C. M. Yen, Superconducting critical temperatures of nonstoichiometric transition metal carbides and nitrides, *Acta Met.* **14**, 1403–1408 (1966).
125. N. Pessall, R. E. Gold, and H. A. Johansen, A study of superconductivity in interstitial compounds, *J. Phys. Chem. Solids* **29**, 19–38 (1968).
126. M. C. Krupka, A. L. Giorgi, N. H. Krikorian, and E. G. Szklarz, High pressure synthesis of yttrium–thorium sesquicarbide: A new high-temperature superconductor, *J. Less-Common Metals* **19**, 113–119 (1969).
127. G. L. De Poorter and T. C. Wallace, Diffusion in binary carbides, in *Advances in High Temperature Chemistry* (L. Eyring, ed.), Vol. 4, pp. 107–135, Academic, New York (1971).

128. R. G. Lye and E. M. Logothetis, Optical properties and band structure of titanium carbide, *Phys. Rev.* **147**, 622–635 (1966).
129. R. G. Lye, Band Structure and Bonding in Titanium Carbide, Research Institute for Advanced Studies Technical Report 66-8 (1966).
130. R. G. Lye, A simple model for the stability of transition metal carbides, in *Solid State Chemistry* (R. S. Roth and S. J. Schneider, Jr., eds.), pp. 567–582, National Bureau of Standards Special Publication 364 (1972).
131. V. Ern and A. C. Switendick, Electronic band structure of TiC, TiN, and TiO, *Phys. Rev.* **137A**, 1927–1936 (1965).

5

Inorganic Amorphous Solids and Glass-Ceramic Materials

D. R. Uhlmann
Department of Metallurgy and Materials Science
Center for Materials Science and Engineering
Massachusetts Institute of Technology
Cambridge, Massachusetts

1. Introduction

A liquid can solidify in either of two ways: It can form a crystalline solid, in which the molecules are regularly arranged on a lattice; or it can form an amorphous solid, called a glass, in which the molecular array is characterized by the absence of long-range order.

To appreciate the distinction between these processes, let us consider the variation with temperature of an extensive parameter, such as the volume, which is used to describe a material (see Figure 1). As the liquid is cooled from a high temperature where the liquid is thermodynamically stable, a temperature is reached below which the crystalline solid is stable. This temperature, designated T_E, is the melting point. At any temperature less than T_E, transformation of liquid to crystal will decrease the free energy of the system.

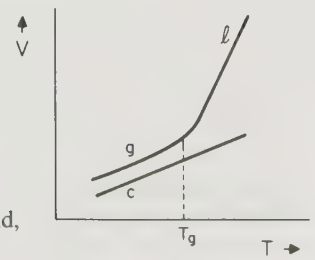

Fig. 1. Volume–temperature curves (schematic) for liquid, glass, and crystal.

The crystallization process is, however, a discontinuous one and requires the formation of nuclei of the new phase. For this reason, all liquids can be supercooled, at least to some extent, below their respective melting points without the occurrence of crystallization. Under such conditions, the liquid can persist in a state of metastable equilibrium.

When most liquids are cooled in bulk form, the maximum range of supercooling is limited to some small fraction of the melting temperature; upon further cooling, nucleation and growth of the crystalline phase are observed. Some liquids, however, can be supercooled indefinitely (assuming reasonable cooling rates) without the occurrence of detectable crystallization. Under such circumstances, the liquid will continue along a cooling curve such as that labeled *lg* in Figure 1.

As the liquid is cooled without crystallizing, a region of temperature will be reached in which a bend appears in the volume–temperature relation. In this region, the viscosity of the material has increased to a sufficiently high value, typically about 10^{12}–10^{13} P, that the sample exhibits solidlike behavior and is termed a glass. At temperatures below the bend, the slope of the volume–temperature curve is smaller than that of the liquid and is usually similar to that of the crystal. The region of the bend, designated T_g in Figure 1, is termed the glass transition region.

While the structural states of supercooled liquids represent metastable equilibrium states, those of glasses should be regarded as thermodynamically unstable configurations. While they may persist over extended periods for kinetic reasons, they will change continuously with time toward other amorphous configurations having lower free energies until the equilibrium liquid state characteristic of the particular temperature is reached (or until the crystalline phase is formed).

It is often convenient to speak of the structure of a particular glassy material. It must be recognized, however, that characterizations of glass structure are meaningful only within certain limits. These are illustrated by the volume–temperature relations shown in Figure 2, where the glass transition temperatures and the specific volumes of the glasses produced are seen to increase with increasing cooling rate. Specification of the temperature would clearly be insufficient for specifying the state of the glass—as, for example, at temperature T, the specific volume could be V_1, V_2, or V_3, depending on the cooling rate used to form the glass. For typical glass-forming materials,

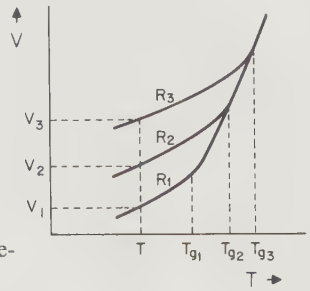

Fig. 2. Volume–temperature curves (schematic) corresponding to different cooling rates $R_1 < R_2 < R_3$.

specific volumes obtainable by variations in cooling rate are in the range of a few percent; and only within such a range can the structure of a glassy material be specified without also specifying its thermal history.

With this general qualification, we shall in the following sections consider the structure of glasses on three scales: (1) the scale of local atomic arrangements, 2–10 Å; (2) the scale of submicrostructure, 30 to a few thousand Å; and (3) the scale of microstructure and macrostructure, microns to millimeters or more. We shall also consider the electronic structure of glasses, the conditions required for glass formation, and glass–ceramic materials. Transformations in inorganic glasses are discussed in detail elsewhere in this series (Volume 5, Chapter 10).

2. Atomic Structure of Glasses

The distinguishing structural characteristic of glasses is the absence of long-range order. This does not, however, imply the absence of short-range order (on a scale of a few angstroms). Such short-range order is usefully described in terms of an atom-centered coordinate system, and is frequently represented in terms of radial distribution functions and correlation functions.

The radial distribution function $\rho(R)$ is defined as the atom density in a spherical shell of radius R from the center of a typical atom in the glass. The radial distribution functions for some Ni–P glasses, determined from X-ray diffraction studies, are shown in Figure 3. Modulations are observed in the radial density of atoms for interatomic separations of the order of a few angstroms, while for larger distances the actual atom density approaches the average atom density ρ_0. Such modulations in the radial density function may be taken as constituting the structure of the glass, and the scale on which

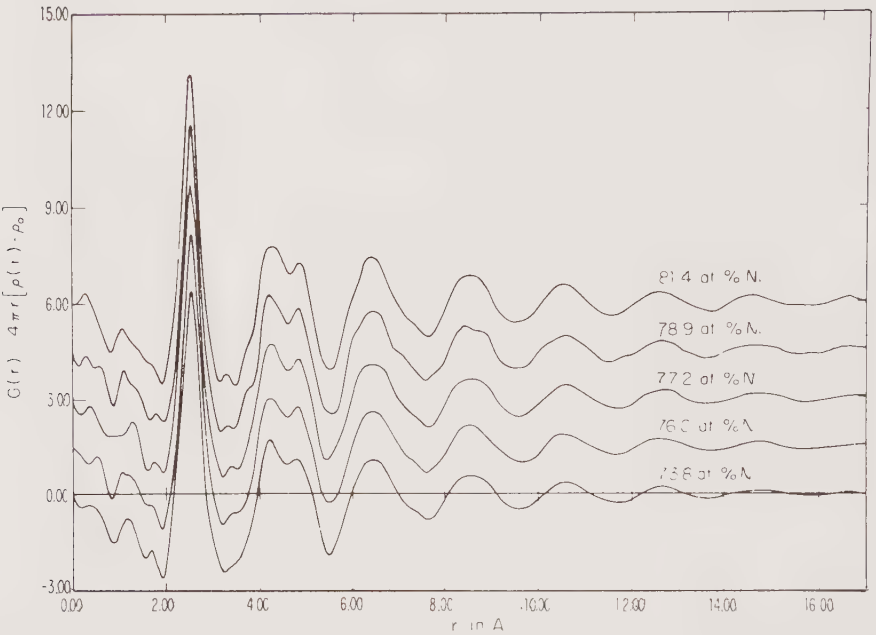

Fig. 3. Radial distribution functions for nickel–phosphorous glasses. (After Cargill.[1])

they are observed represents the scale of short-range order in the materials.

2.1. Models of Glass Structure

Several models have been suggested to represent the structure of glasses. These include the following.

2.1.1. Crystallite Model

The diffraction patterns from glasses often exhibit broad peaks centered in the range where strong peaks are seen in the diffraction patterns of the corresponding crystals. This is shown in Figure 4 for the case of SiO_2. Such observations led[3,4] to the suggestion that glasses are composed of assemblages of small crystals, termed crystallites; and the observed breadths of the glass diffraction patterns were then associated with particle size broadening.

2.1.2. Random Network Model

Glasses have also been viewed[2,5] as three-dimensional arrays in which no unit of the structure is repeated at regular intervals. In the

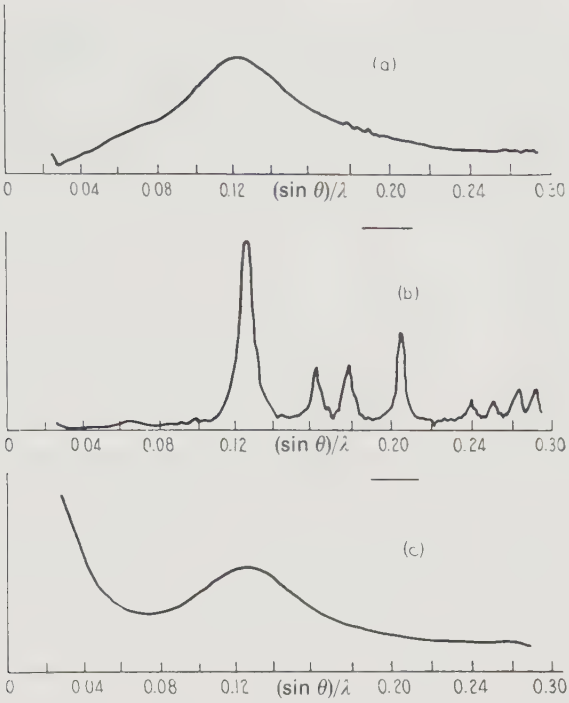

Fig. 4. X-ray diffraction patterns from (a) SiO_2 glass, (b) crystalline cristobalite, and (c) silica gel. (After Warren and Biscoe.[2])

case of oxide glasses, these arrays would consist of networks of oxygen polyhedra, in practice triangles and tetrahedra. The "network-forming" cations (such as Si, B, Al, and P) are those that occupy the centers of oxygen triangles or tetrahedra, while the "network-modifying" cations (such as the alkali and alkaline-earth ions) are those that disrupt the networks. In the case of multicomponent glasses, the network modifiers are viewed as randomly distributed through the structure, located in the immediate vicinity of certain anions or anion groups (e.g., singly bonded oxygens or BO_4 tetrahedra).

2.1.3. Models Based on Pentagonal Symmetries

Several models based on non-space-filling structural units have been proposed. In perhaps the most familiar of these, the structure of glassy SiO_2 is regarded as consisting of pentagonal rings of SiO_4 tetrahedra.[6] From a given tetrahedron, the rings extend in six

directions to include the six edges and form 12-sided regular cavities. Because of their fivefold symmetry, these dodecahedral cages cannot be extended in three dimensions without strain. Similar models have been suggested for the structures of alkali silicate glasses; and related models based on structural elements having fivefold symmetry have also been suggested for simple hard-sphere liquids and glasses (e.g., Refs. 7–9).

2.1.4. Paracrystal or Micelle Models

Glasses have also been viewed (e.g., Refs. 10, 11) as composed of "micelles" or "paracrystals" characterized by a degree of order intermediate between that of a perfect crystal and that of a random array. This order is sometimes described as a propagation of errors in the distances between atoms from what they would be in a crystalline lattice. The paracrystalline grains may themselves be arranged in arrays with differing degrees of order.

2.2. Structure of Oxide Glasses

Information about glass structure has been provided by a variety of experimental techniques, including X-ray, neutron, and electron diffraction, nuclear magnetic resonance and electron-spin paramagnetic resonance spectroscopy, Mössbauer absorption, infrared and Raman spectroscopy, etc. Of these, the most widely used has been X-ray diffraction. The results of such studies provide information with which any proposed structural model must be consistent, and indicate which of several suggested models provides the most satisfactory description of the data, rather than uniquely establish a particular model as the best representation of the structure.

Recent advances in experimental techniques and in means of analyzing data appear to have opened a new era of glass diffraction studies. The experimental advances include the use of double crystal monochromators or fluorescence detectors to reduce or eliminate Compton scattering from the measured intensity (e.g., see discussion in Ref. 12). The analytical development involves using crystal chemical information and calculating pair functions expected on the basis of different structural models, rather than assuming a similar variation of scattering factors with scattering angle for different atoms and carrying out a Fourier transform (e.g., see discussion in Ref. 13).

To date, these advances have been applied to only two simple glasses, SiO_2 and B_2O_3. In the case of SiO_2, the early discussion between proponents of the crystallite and random network models of glass structure was generally decided in favor of the random network model, based largely on the arguments advanced by Warren: From the width of the main diffraction maximum in the glass diffraction pattern, the crystallite size in SiO_2 was estimated as about 7–8 Å. Since the size of a unit cell of cristobalite is also about 8 Å, the crystallites, if present, would be only a single unit cell in extent, and these can hardly be regarded as crystallite arrays. Further, since there is no marked small-angle scattering from fused silica (Figure 4), if crystallites of more reasonable size are present, they must be connected by material which has a density similar to that of the crystallites.

To illustrate the improvements provided by new experimental techniques, Figure 5a shows the original radial distribution determined for fused silica,[14] to be compared with the results of a recent investigation[15] shown in Figure 5b. The second and third peaks—which correspond respectively to oxygen–oxygen and silicon–silicon

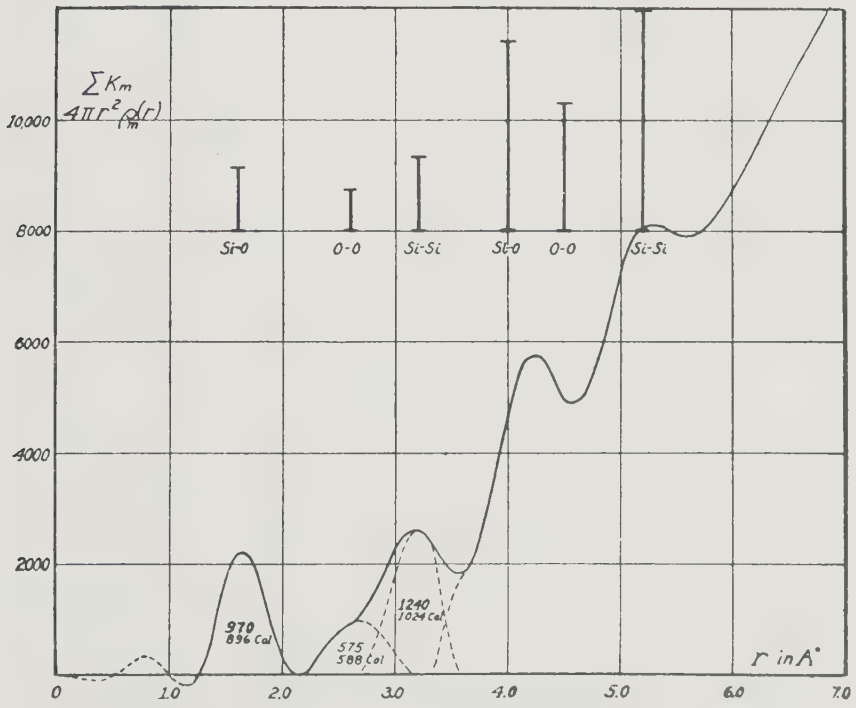

Fig. 5a. Radial distribution function of fused silica determined in Ref. 14.

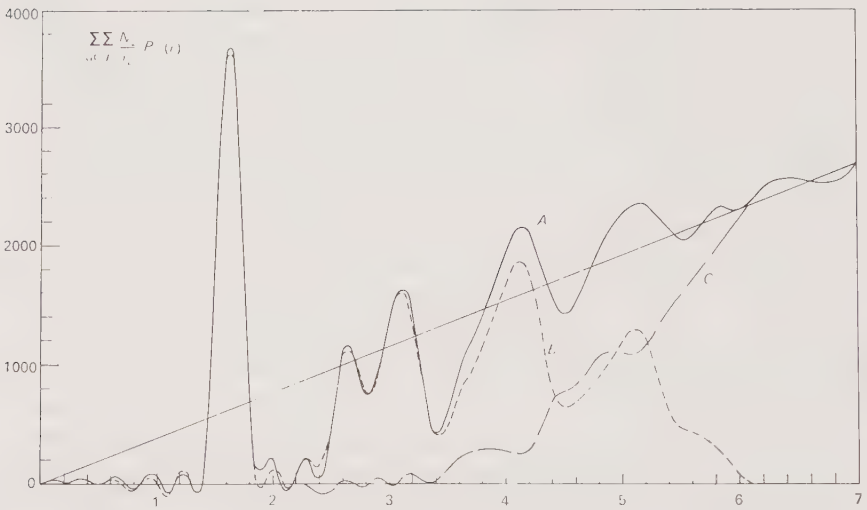

Fig. 5b. Pair function of fused silica determined in Ref. 15. Curve A is the measured curve; curve B is the sum of the first six contributions: Si–O, O–O, Si–Si, Si–Second O, O–second O, Si–second Si; curve C is the difference, A − B.

distances in the glass—are clearly resolved in the new results, whereas they overlap significantly in the original data. The recent results indicate that the Si–O–Si bond angles in this material are distributed over a broad range, from about 120 to 180°, centered about 145°. This range is much broader in the glass than in crystalline cristobalite, whereas the Si–O and O–O distances are nearly as uniform in the glass as in the crystal.

The essential randomness of the glass structure is a result of the variation in Si–Si distances (the Si–O–Si bond angles). The assumption of complete randomness beyond such a joining of the tetrahedra results in a satisfactory description of the experimental data (see Figure 5b). Such a description is superior to that provided by the pentagonal dodecahedron model or a model based on cristobalite crystallites. The resolution of the data is not, however, sufficient to establish that the structure is random beyond the linking between tetrahedra; and some preference for edge-to-face sharing of tetrahedral units may be present in the glass.

The structure of fused silica seems, then, to be well described by a random network of SiO_4 tetrahedra with significant variability occurring in Si–O–Si bond angles. Such a random network is, however, not a uniform network; and local variations in density and structure are still expected. The extent of such fluctuations can be

determined from the intensity of small-angle X-ray scattering. This has been done for SiO_2, and the experimental values of the density fluctuations are found to be within a factor of two of those expected from the thermodynamic fluctuation theory for liquids applied to SiO_2 at its glass transition temperature.[16,17]

Little is known in satisfactory detail about the structure of silicate glasses containing sizable concentrations of alkali or alkaline earth oxides. Almost nothing is known about the cation distributions and cation environments in such glasses; and little is known about the effect of the alkali or alkaline earth oxides on the silicon–oxygen framework beyond their breaking up the network with the formation of singly bonded oxygens.

In crystalline silicates, the SiO_4 tetrahedra are found in a variety of configurations depending on the oxygen-to-silicon ratio. These are indicated in Table 1. Such configurations can also occur in glasses of the corresponding compositions (and mixtures of these configurations in glasses of intermediate compositions); but firm evidence for their presence as the structural units of the glasses remains to be provided. The formation of three-dimensional silicate networks requires at least two bridging oxygens per tetrahedron. In the case of simple alkali or alkaline earth silicate glasses, this implies the absence of networks for oxygen-to-silicon ratios greater than three.

The results of both X-ray diffraction and nuclear magnetic resonance investigations of glassy B_2O_3 indicate a structure composed of BO_3 triangles. Random networks of such triangles and arrays of the triangles in boroxyl configurations have been variously suggested to represent the structure,[18] but the most satisfactory agreement with experimental data seems to be provided by a structural model based on a distorted version of the crystal structure, in which

TABLE 1
Structural Units Observed in Crystalline Silicates

Silicon–oxygen groups	Structural units	Examples
SiO_2	Three-dimensional network	Quartz
SiO_4O_{10}	Sheets	Talc
Si_4O_{11}	Chains	Amphiboles
SiO_3	Chains	Pyroxenes
	Rings	Beryl
Si_2O_7	Tetrahedra sharing one oxygen ion	Pyrosilicates
SiO_4	Isolated orthosilicate tetrahedra	Orthosilicates

the triangles are linked in the form of ribbons.[19] The suggested distortions would destroy the essential symmetry of the crystal; and the notion of discrete crystallites embedded in a matrix would still not be applicable.

The addition of alkali or alkaline earth oxides to B_2O_3 results in the formation of BO_4 tetrahedra. The fraction of 4-coordinated borons increases with the concentration of alkali oxide as shown in Figure 6. The smooth curve in the figure represents each of the added oxygens converting two triangles to tetrahedra. For alkali oxide additions smaller than about 30%, nearly all the added oxide converts BO_3 triangles to BO_4 tetrahedra, while for larger additions singly bonded oxygens are apparently produced in sizable numbers.

In phosphate glasses, the most common structural units are chains or rings of PO_4 tetrahedra; the changes in average chain length with variations in the P_2O_5 concentration have been determined in chromatographic studies.[21] Because of the difference in charge between the phosphorus and silicon cations, the structure of phosphate glasses bears a relation to silicate glasses richer in modifier oxides than the metasilicate. With other additions, such as aluminum oxide, it is possible to simulate the characteristics of network-based silicate glasses.

The structure of glassy GeO_2 is less well known than that of SiO_2, but appears to be composed of GeO_4 tetrahedra, with a mean Ge–O–Ge bond angle of about 134°. Upon adding alkali oxide, at least up to molar concentrations of 15–30%, GeO_6 octahedra are apparently formed (unlike the silicate analog where singly bonded

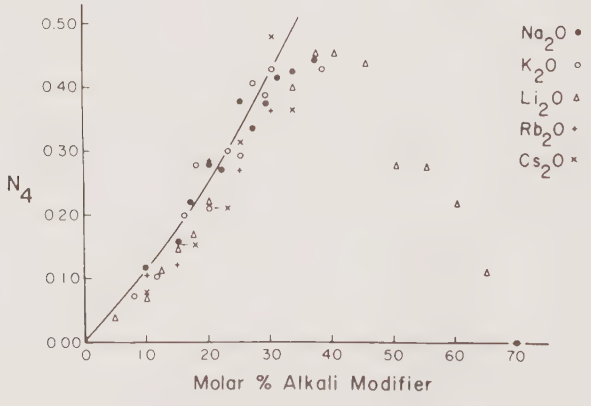

Fig. 6. Fraction N_4 of 4-coordinated boron atoms in alkali borate glasses. (After Bray.[20])

oxygens are produced). For larger additions of modifier oxides to GeO_2, a return to tetrahedral coordination with the formation of singly bonded oxygens is indicated. These suggestions for the structure of germanate glasses other than GeO_2 itself are, however, based on property measurements rather than diffraction data; more direct structural investigations are clearly indicated.

In alkali aluminosilicate glasses, such as those used in ion-exchange applications, the aluminum ions are believed to occupy the central positions in AlO_4 tetrahedra, with the alkali ions occupying nearby positions for local charge compensation. In this way, the aluminum ions can be regarded as re-forming the networks of the alkali silicate glasses.

The local environments of transition metal ions and rare earth ions in glasses have been investigated using techniques such as electron spin paramagnetic resonance; optical, infrared, and Raman absorption; and Mössbauer absorption. A striking example of the power of combining information from different techniques is provided by an investigation of the state of the Fe^{3+} ion in glasses,[22] where it was concluded that this ion is predominantly tetrahedrally coordinated in silicate glasses and octahedrally coordinated in phosphate glasses.

In general the structural states of transition metal and rare earth ions have been found to depend on the concentration of the ions in the glasses; for example, pairing appears to be a significant factor in phosphate glasses for Cr^{3+} at concentrations as low as 1%.[23] For a detailed discussion of these and other aspects of the structural states of transition metal ions in glasses, see Ref. 24.

2.3. Structure of Nonoxide Glasses

The structures of a sizable number of nonoxide glasses have been determined, and the interested reader is referred to Ref. 25 for a recent bibliography of such structural studies. In the present section we shall consider the salient structural features of several representative materials, namely glasses of selenium, silicon, and germanium, and nickel–phosphorus alloys.

The structure of glassy selenium has been the subject of several investigations, utilizing X-ray diffraction data[26] as well as property measurements[27,28] to infer the structural features. Long polymer chains and eight-member rings in various proportions have been suggested as the structural elements of this material. A ring component of 30–50% has been inferred from data on viscosity,[27] dissolution

behavior,[27] and Raman scattering.[28] When samples of amorphous selenium are held in the appropriate temperature range for periods of time, crystallization to the hexagonal form (which consists entirely of chains) is observed.

In the case of both glassy silicon[29] and glassy germanium,[30] the basic tetrahedral arrays of the crystalline form are also present in the glass: The nearest-neighbor peak in the radial distribution function of the glass occurs at very nearly the same distance as in the crystals; the area of this peak corresponds to about four nearest neighbors; and the broadened second peak also occurs at very nearly the same distance as in the crystal. The first clear differentiation between the crystal and amorphous forms is provided by the third-neighbor peak, which is poorly defined for the amorphous material but is about as large as the second peak for the crystalline form.

A number of models have been suggested to account for the structure of amorphous silicon and germanium, including crystallites, layered structures, mixtures of pentagonal rings with boat and chair types of hexagonal rings, and random networks. Of these, Polk's description[31] in terms of a random network seems the most satisfactory, since it can represent well the observed density deficit between crystalline and glassy structures of a few percent and can also describe closely the measured radial distribution functions. In this model, all bonds are included in at least one five- or six-member ring; but these rings are distorted from their symmetric shapes. The six-number rings occur in a continuous range of shapes, rather than in simple boat or chair configurations. The essential randomness of the structure results from variations in the tetrahedral bond angle and rotation about bonds.

The principal objection to this model is provided by recent electron microscope observations on amorphous germanium films.[32] In this study, a high-resolution lattice imaging technique indicated regular fringes corresponding to approximately the close-packed interplanar spacings of the crystalline forms in regions of about 14 Å in extent. Such fringes are usually associated with the presence of crystalline arrays and would not be expected for a random array of the type suggested by Polk. The fringes could arise from astigmatism in the lens system of the electron microscope or from other instrumental problems; but the results are sufficient to introduce caution into any specification of the structural state of glassy silicon and germanium.

The structures of electrodeposited nickel–phosphorus alloy glasses containing 73.8–81.4 mole % Ni have been determined using

X-ray diffraction techniques.[1,33] Fortunately, the scattering factors for Ni and P vary in a similar manner with $(\sin\theta)/\lambda$; hence the proportionality-of-scattering factors approximation used in obtaining the radial distribution functions from intensity data should not impose significant limitations on the results.

The diffraction results indicate that the glasses have a short-range order which is better defined than that of the liquid noble metals at temperatures above their melting points. From the forms of the radial distribution functions, shown in Figure 3, combined with density data, it was suggested that the glasses have a continuous structure rather than one composed of small, highly-ordered regions separated by internal boundaries. The experimentally determined radial distribution functions were compared with those calculated[34] for a dense, random packing of hard spheres; the agreement was remarkably good, even to a description of the split second peak in the radial distribution function.

2.4. Effects of Pressure, Thermal History, and Irradiation

In contrast to the behavior of crystalline materials, when glasses are subjected to high-pressure treatment they often show sizable increases in density after the pressure has been removed. Increases in density as large as 15–20% have been observed for both SiO_2 and B_2O_3,[35,36] and even higher densifications are in principle obtainable since these values were obtained by high-pressure treatment of glasses, whereas data obtained on other materials (e.g., Ref. 37) indicate that maximum densification is achieved by pressurization treatment in the vicinity of the glass transition at pressure.

These increases in density will in many cases persist indefinitely at room temperature (atmospheric pressure) but will anneal out at higher temperatures at rates which depend on the material and the manner in which it was compacted. The observed densification generally increases with increasing extent of shear present in the pressurizing apparatus,[36] but even under isostatic conditions permanent densification can be obtained.[38]

The magnitudes of the densifications obtainable by high-pressure treatment of oxide glasses can be usefully compared with density changes obtainable by changes in cooling rate (recall Figure 2). In the case of B_2O_3, the difference in the volume thermal expansion coefficient between liquid and glass is about $5.5 \times 10^{-4}°C^{-1}$.[39] Hence a decrease in the glass transition temperature of some 360°C would be

required to produce a 20% increase in the density of the glass from its usual value. Such a decrease in T_g is physically unattainable.

Even when equal densifications are obtained by high-pressure treatment and by slow cooling, however, the structural details and thermodynamic stabilities of the two materials are expected to be different. Experiments carried out on a polymeric glass have indicated[40] that treatment in the glass transition region at pressure produces samples with somewhat smaller heat contents than glasses prepared at atmospheric pressure, while high-pressure treatment in the glassy state produces materials with similar heat contents to glasses formed at atmospheric pressure. The resistance to annealing of densified glasses made in the region of T_g at pressure is notably larger than that of glasses made by pressurization in the glassy state.

The infrared spectra of densified glasses are in all cases similar to those of uncompacted glasses, although in some cases a broadening and weakening of the major absorption bands is noted. These findings, together with the results of other studies (e.g., NMR studies of borate glasses), indicate the absence of significant change in the basic coordination polyhedra of silicate, borate, or germanate glasses on densification.[41] Little direct information is available on the structural changes involved in densification. In the only X-ray diffraction study carried out on such material,[19] the radial distribution function of a B_2O_3 glass isostatically compacted by 4.4% was found to be quite similar to that of an uncompacted glass.

Density increases of 2–3% can be obtained by subjecting fused silica to fast neutron doses in the range of 10^{19}–10^{20} nvt. Highly disordered material of very nearly the same density is produced by subjecting crystalline quartz to similar neutron doses. The precise nature of the structural changes involved in such densification have not been satisfactorily elucidated, but seems to involve smaller silicon–oxygen–silicon bond angles. (See Ref. 42 for a discussion of these and other effects of radiation on glasses.)

3. Submicrostructure of Glasses

3.1. Introduction

Following the classic work of Warren in the 1930's, the random network model became widely accepted as the best representation of glass structure, and glasses were regarded as homogeneous materials. At the same time, it was recognized that structural hetero-

geneities provided the basis of the commercial Vycor process and that stable liquid–liquid immiscibility occurred in several glass systems.

Since the introduction of electron microscopy in the 1950's, structures on a scale of 30 to a few hundred Å have been observed in many glass systems, including silicates, borates, germanates, chalcogenides, and fused salts. Because of their scale, below that resolvable in the light microscope, these are termed submicrostructures. They result from a process of phase separation in which an initially homogeneous liquid separates into two or more liquid phases on cooling into a miscibility gap.

To illustrate the characteristics of submicrostructure in glasses, consider the system $BaO–SiO_2$, whose metastable miscibility gap is

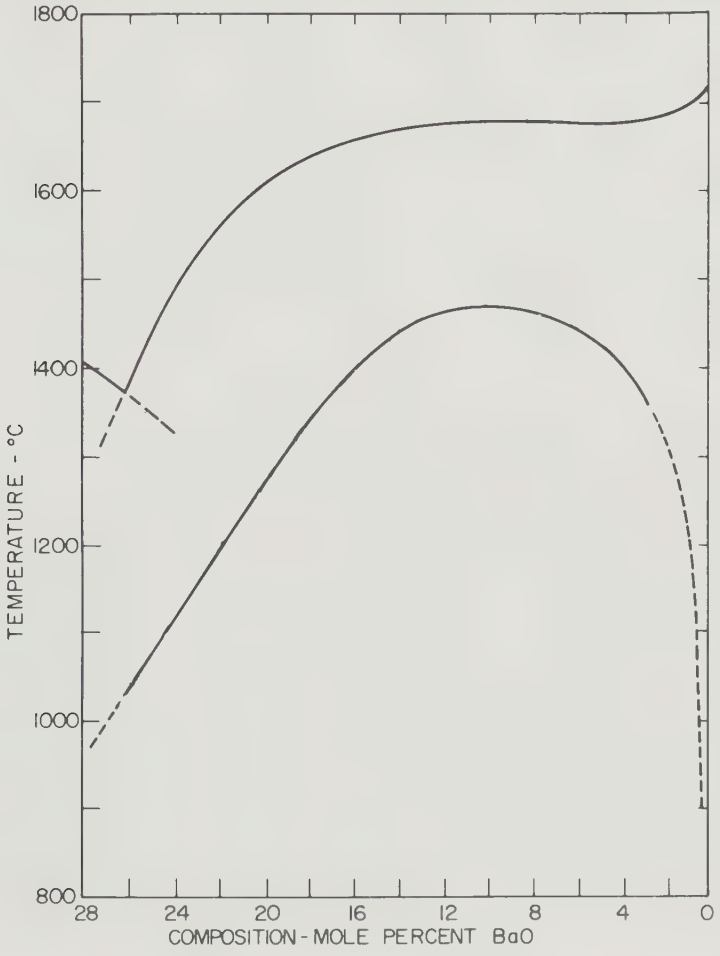

Fig. 7a. Miscibility gap in the system $BaO–SiO_2$. (After Seward *et al.*[43])

shown in Figure 7a. For compositions near the SiO_2-rich side of the gap, such as the 4 mole % BaO composition, the submicrostructure consists of discrete spherical particles of a BaO-rich phase embedded in a continuous matrix of a SiO_2-rich phase (Figure 7b). For compositions near the BaO-rich side of the miscibility gap, such as the 24% BaO composition, the submicrostructure consists of spherical SiO_2-rich particles embedded in a continuous BaO-rich matrix (Figure 7c). For compositions near the center of the gap, such as the 10% BaO composition, the submicrostructure often consists of two phases, each of which is three-dimensionally interconnected (Figure 7d). In Figures 7b–7d, both phases are amorphous as determined from electron diffraction.

The system BaO–SiO_2 was chosen because of the large difference in electron and atom density between the phases into which the system separates; this difference in density is reflected in the significant contrast between the phases seen in the electron micrographs. A similar

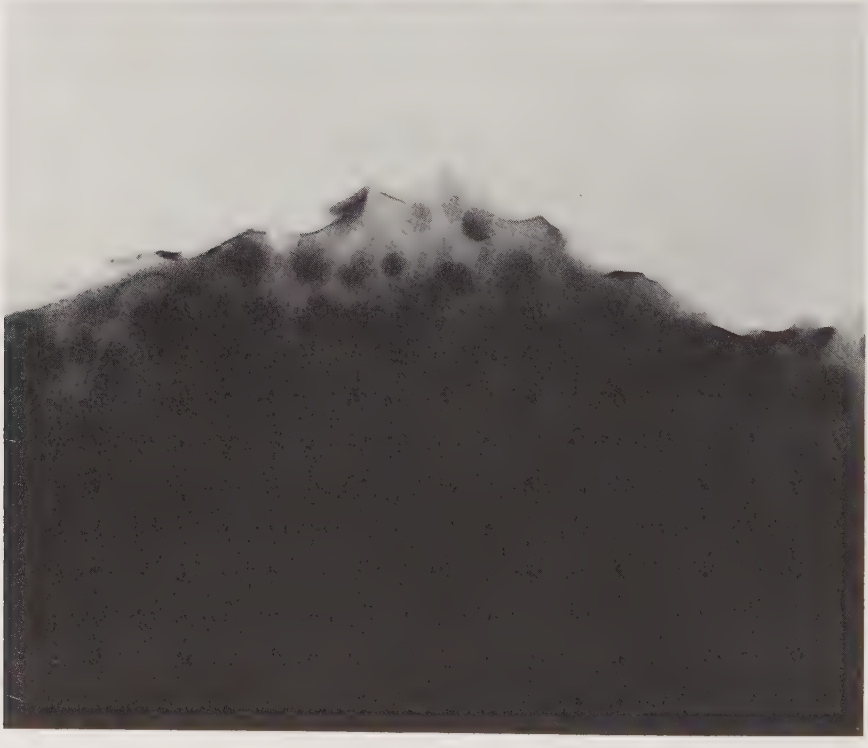

Fig. 7b. Direct transmission electron micrograph of 0.04 BaO–0.96 SiO_2. (After Seward *et al.*[43])

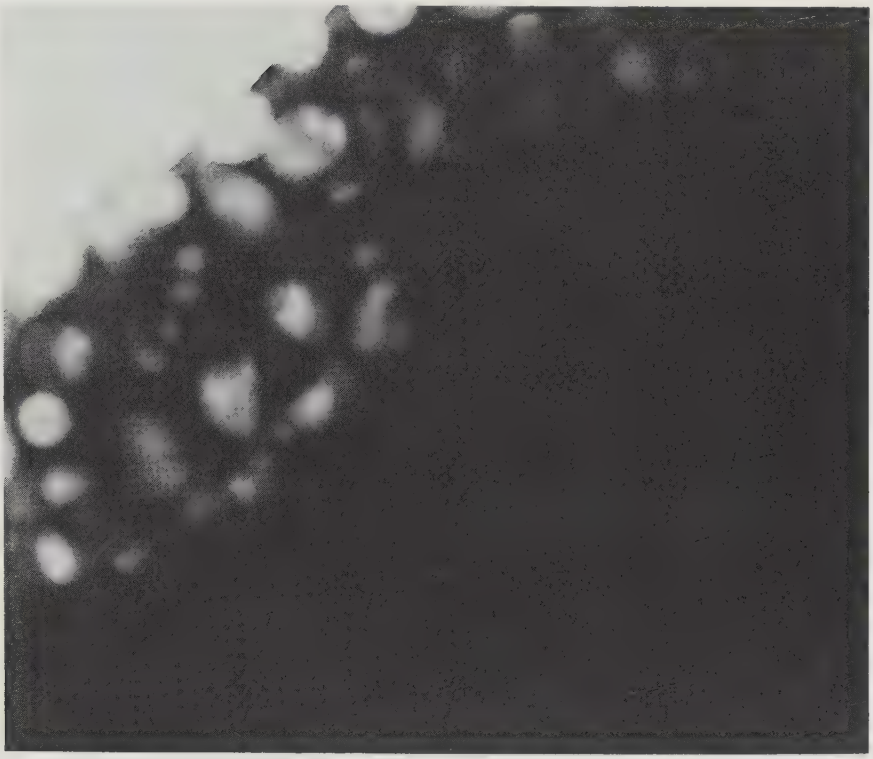

Fig. 7c. Direct transmission electron micrograph of 0.24 BaO–0.76 SiO_2. (After Seward *et al.*[43])

variation in submicrostructural features is, however, expected in most systems as miscibility gaps are traversed.

As indicated above, liquid–liquid immiscibility is a common feature of many glass-forming systems. Of the alkali silicates, metastable miscibility gaps are found in the Li_2O–SiO_2[44,45] and Na_2O–SiO_2[45,46] systems. A metastable gap is found in the BaO–SiO_2 system (Figure 7a); stable gaps are found in all other alkaline earth silicate systems[47] as well as in all alkaline earth borate systems.[47] Miscibility gaps—metastable in all cases—are also found in each of the alkali borate systems[48] and ranges of immiscibility have been determined in the commercially important systems Na_2O–B_2O_3–SiO_2[49] and NaO–CaO–SiO_2,[50] as well as in the TiO_2–SiO_2[47] and PbO–B_2O_3[51] systems.

The occurrence of immiscibility is then a common feature of oxide systems, and it can no longer be assumed *a priori* that a given optically transparent glass is homogeneous on a scale of 30 to a few hundred Å. In many cases, such a determination can only be effected by sensitive

Fig. 7d. Direct transmission electron micrograph of 0.10 BaO–0.90 SiO_2. (After Seward *et al.*[43])

property measurements or by careful electron microscope or small-angle X-ray scattering studies, since the scale on which submicrostructural features can occur may preclude visual or microscopic detection. In other cases, liquid–liquid phase separation can produce a visible opacity which may incorrectly be associated with crystallinity.

Among chalcogenide systems, the occurrence of liquid–liquid immiscibility is also widespread (e.g., Refs. 52, 53). In few if any cases, however, have the miscibility gaps been mapped out, and lack of information in this area limits significantly the discussion of many properties of the glasses. Phase separation has also been observed in a number of fused salt and salt water systems (e.g., Ref. 54).

Submicrostructural features have in some cases been reported for single-component as well as multicomponent glasses. In a recent study,[55] however, such features were found to be absent in the case of a single-component glass, fused silica, in which they had previously

been reported. The structure of this material on a scale of 30 Å and larger has been examined in considerable detail and heterogeneities on a scale 30–100 Å are sometimes seen. When seen, however, the heterogeneities are found to depend on the technique used to prepare the electron microscope sample, and are not changed by extended heat treatment of the bulk glass in its transition region.

On reviewing the sources of contrast in the electron microscope, it has been shown[55] that the variations in density and internal potential needed to explain the heterogeneities occasionally seen in fused silica exceed those expected from fluctuation theory or observed experimentally in small-angle X-ray scattering studies. It seems likely, therefore, that the observed heterogeneities sometimes seen in electron microscope studies of single-component glasses are associated with surface effects and cannot be taken as structural characteristics of the bulk glasses.

In cases where glasses are prepared without passing through the liquid state, as in specimens prepared by condensation from the vapor onto a cold substrate, voids can form an important submicrostructural feature of the material. An interesting example of this is provided by vapor-deposited germanium or silicon films, whose overall densities often differ from the crystal densities by more than the few percent cited in Section 2.3 (values for the density deficit of 10–30% are typical). The origin of this discrepancy lies in the presence of pores or other low-density regions in the glassy samples. Small-angle X-ray scattering data on thick evaporated germanium films have indicated anisotropic low-density regions with approximate linear dimensions of 22 and 46 Å in the film plane and 2200 Å normal to the film plane.[56] Other pore morphologies have been indicated in other investigations; the suggested variability may well reflect differences in film thickness and deposition conditions.

3.2. Spinodal Decomposition vs. Nucleation Growth Coalescence

In many respects, the most interesting submicrostructural features of glasses are those of the type shown in Figure 7d, in which two phases are both three-dimensionally interconnected. Such structures are often observed when there is a large volume fraction of both phases, and are frequently taken as indicative of phase separation by a spinodal decomposition process. In such a process, phase separation takes place by changes which are, at least initially, small in degree and large in spatial extent. The salient features of this process are discussed in detail in Chapters 2 and 3 of Volume 5.

Within the spinodal region of a miscibility gap, i.e., for composition and temperature ranges where $\partial^2 f/\partial c^2 < 0$ (f is the specific free energy of a uniform solution of composition c), a homogeneous solution is unstable against infinitesimal fluctuations in composition provided these occur on a sufficiently large scale that there is no thermodynamic barrier to their growth. When a specimen is quenched from a temperature above a miscibility gap and held at a temperature within the spinodal, some components of the original distribution of fluctuations will grow in amplitude with time while others will shrink. The kinetics of this process have been described in a series of classic papers by Cahn and his associates (e.g., Refs. 57–62), which indicate that—at least during the initial stages of decomposition—the phase separation process will be dominated by fluctuations of a wavelength, or narrow range of wavelengths, which grow most rapidly. Microstructures calculated on this basis for the central region of a miscibility gap indicate[59] morphologies in which both of two phases are three-dimensionally interconnected (Figure 8).

Since such interconnected submicrostructures are often seen in experimental studies of phase separation when both phases occupy large volume fractions (near the central portions of miscibility gaps), their identification with a spinodal mechanism seems natural. It should be noted, however, that the theory used in the microstructure calculations was a relatively simple linearized theory. Inclusion of the most important higher order terms in the appropriate diffusion equation seems to result in a sharpening of interfaces and a breaking off of connectivity,[60] but the morphological implications of all the terms have not been explored in satisfactory detail.

An alternative explanation for the formation of interconnected submicrostructures involves the coalescence of second-phase particles which are present in large concentrations. Support for this view is provided by calculations[63] in which a random array of point nuclei begin simultaneously to grow at a constant rate until they occupy a specified volume fraction. When this volume fraction is high, appreciable connectivity is seen in calculated cross sections through the array (Figure 9).

It has been pointed out, however, that overlapping diffusion fields in the region of approach between growing particles should reduce the diffusive flux to the region and limit further growth. Calculations in which surface tension effects are neglected indicate, in fact, that such interference can completely prevent coalescence and result in flattened particles rather than interconnected structures.[64]

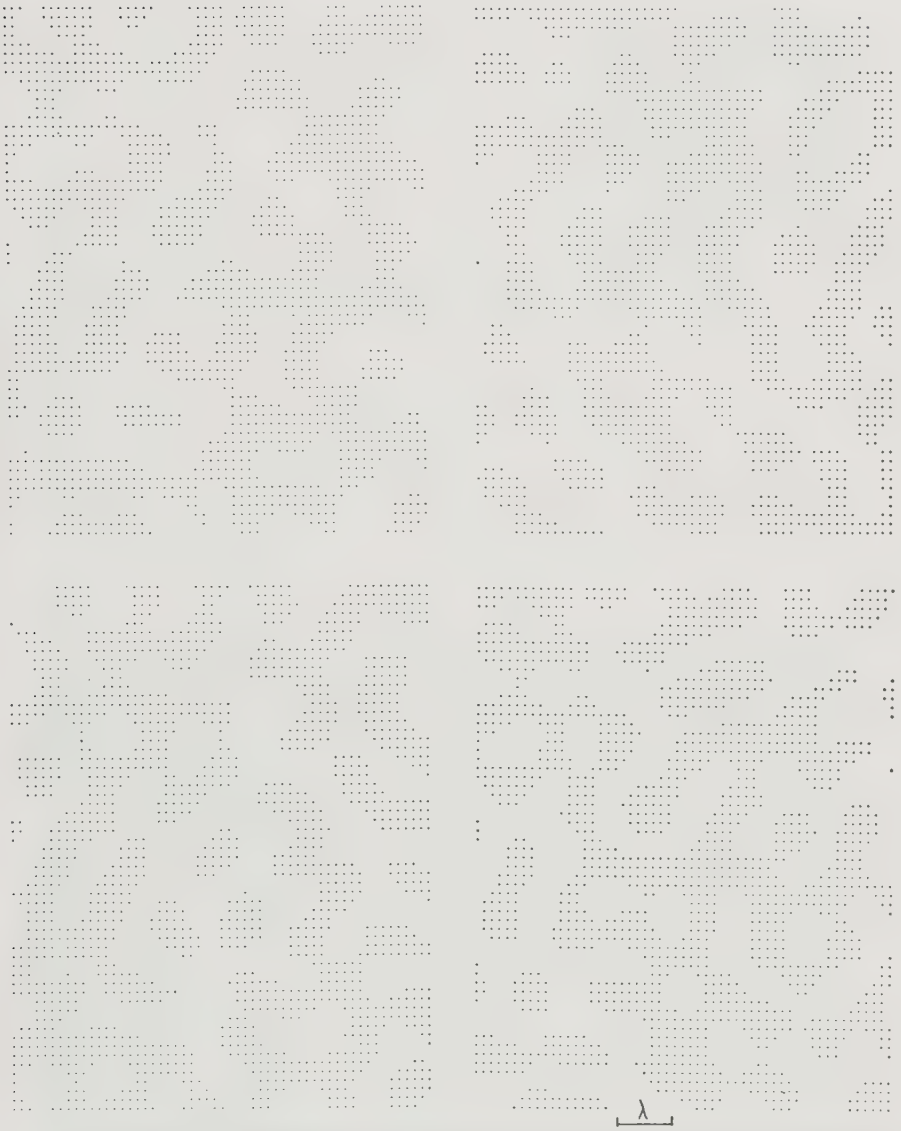

Fig. 8. Succession of computed sections through a two-phase structure in which both phases occupy a volume fraction of 50%. (After Cahn.[59])

When surface tension effects are considered, a number of mechanisms are possible which would permit coalescence in reasonable times despite interparticle interference.[65] These mechanisms include: (1) enhanced diffusion to the flattened region of approach between particles, driven by capillarity; (2) diffusion in the region of approach

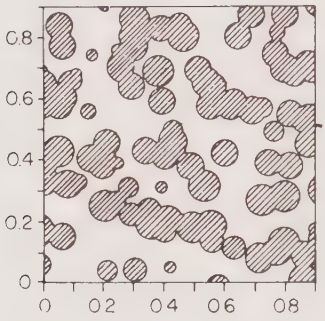

Fig. 9. Computed section through three-dimensional array of equal spheres (radius $r = 0.05$). (After Haller.[63])

driven by a surface energy which decreases with decreasing separation; and (3) nucleation of necks joining the particles. Each of these mechanisms should only be effective when the particles have approached within some small separation, of the order of 10 Å. This condition can result directly from the growth process, and may be enhanced by Brownian motion of the particles. Coalescence will be most likely when copious nucleation results in many small (30–100 Å in diameter) second-phase particles occupying a large volume fraction.

Interconnected submicrostructures can, then, result from either a spinodal decomposition process in which higher order terms in the diffusion equation are unimportant or from the coalescence of discrete second-phase particles. In the latter case the particles may form by a spinodal decomposition process where higher order terms are important (as those arising from the composition dependence of the bulk free energy or of the mobility), or by a nucleation and growth process.

Small-angle X-ray scattering studies of phase separation in glass-forming systems (e.g., Refs. 66–69) have indicated qualitative agreement with some of the predictions of the early-stage theory of spinodal decomposition. In detail, however, no such study has produced data in full agreement with the theory. The development of interconnected submicrostructures by the formation, growth, and coalescence of discrete second-phase particles has been observed in one electron microscope study[70] and is implied by the morphological observations in another.[71]

Upon annealing, interconnected submicrostructures sometimes coarsen while retaining a high degree of connectivity,[72] and in other cases coarsen with a breakup of the connectivity.[43] Such breakup may be responsible for the discrete-particle submicrostructures, occupying large volume fractions, which are sometimes seen instead

of the interconnected structures in compositions near the central regions of miscibility gaps. An example of such a discrete-particle submicrostructure, from the system $PbO–B_2O_3$, is shown in Figure 10.

The observed formation of discrete-particle structures from interconnected structures, and of interconnected structures from discrete-particle structures, together with the variations in phase morphologies noted in different systems, emphasize that caution must be employed in inferring phase separation mechanisms from morphological observations.

The complexity of phase separation phenomena is further illustrated by the occurrence of secondary phase separation in many systems. This phenomenon develops when phases which have originally separated at a relatively elevated temperature become supersaturated with respect to the other phases as the temperature is lowered. It results in submicrostructures in which finer-scale structures are found within the primary phase separation structures. Such

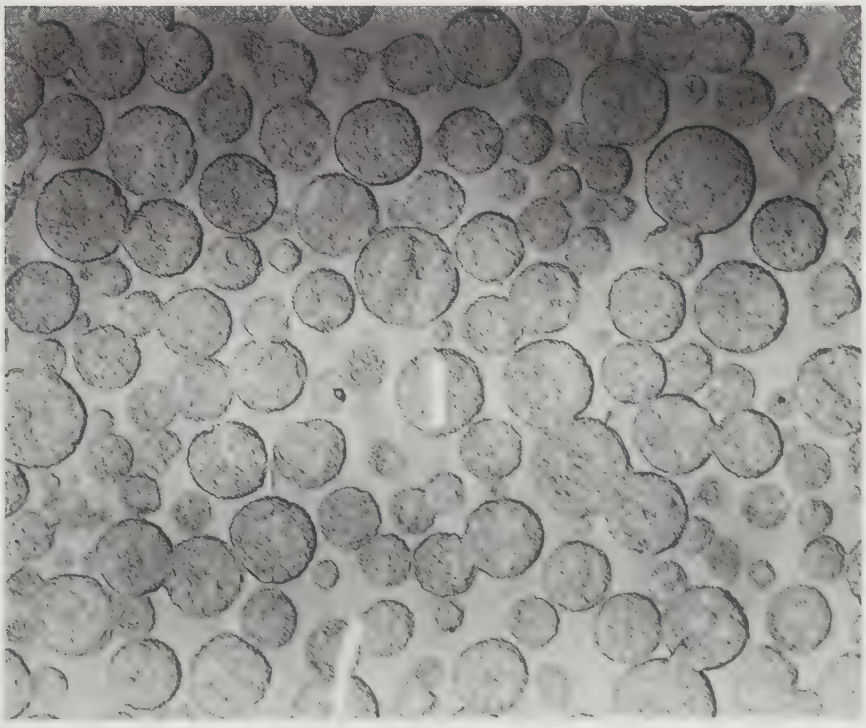

Fig. 10. Discrete-particle submicrostructure in 0.11 PbO–0.89 B_2O_3 glass. (After Shaw and Uhlmann.[73])

secondary structures are usually not observed near the interphase boundaries of the primary structure, since chemical equilibrium can be maintained to lower temperatures in these regions. The extent of secondary phase separation depends upon details of the system, such as the shape of the miscibility gap and the mobility–temperature relation, as well as upon the thermal history of the specimens (e.g., Refs. 74–76).

4. Electronic Structure of Glasses

4.1. Introduction

The electronic properties of crystalline materials have been the subject of intensive scientific and technological interest for the past several decades. More recently, the electronic structure and properties of disordered systems have received wide attention. These subjects are discussed in detail in Chapter 2 of Volume 1 as well as in Chapters 4 and 5 of Volume 2. The present discussion is therefore intended only as a brief summary of some of the salient features of the electronic structure of glasses, and follows the approach of a noteworthy recent review.[77]

4.2. Density of States

Since the short-range order in most glasses is similar to that in corresponding crystals, many of the features of the density of states of the crystals will also be found in the glasses. The glass density of states will, however, be characterized by a smoothing out of sharp features found in the crystals, and in the case of glassy semiconductors by a quasi energy gap where the density of states is much lower than in the valence and conduction bands. In the case of transparent glasses, a real gap (or at least a very deep minimum) will be found in the state density.[78] The expected difference between the densities of states for the crystalline and glassy forms of a material are shown schematically in Figure 11.

As shown in the figure, a finite state-density is expected within the quasi gap for all real glasses. These states are believed to be localized in space (perhaps associated with defects or fluctuations in the materials) and are characterized by very low mobility at low temperature.[77] Within the valence and conduction bands, electronic states are expected to be localized near the band edges, while those in the centers

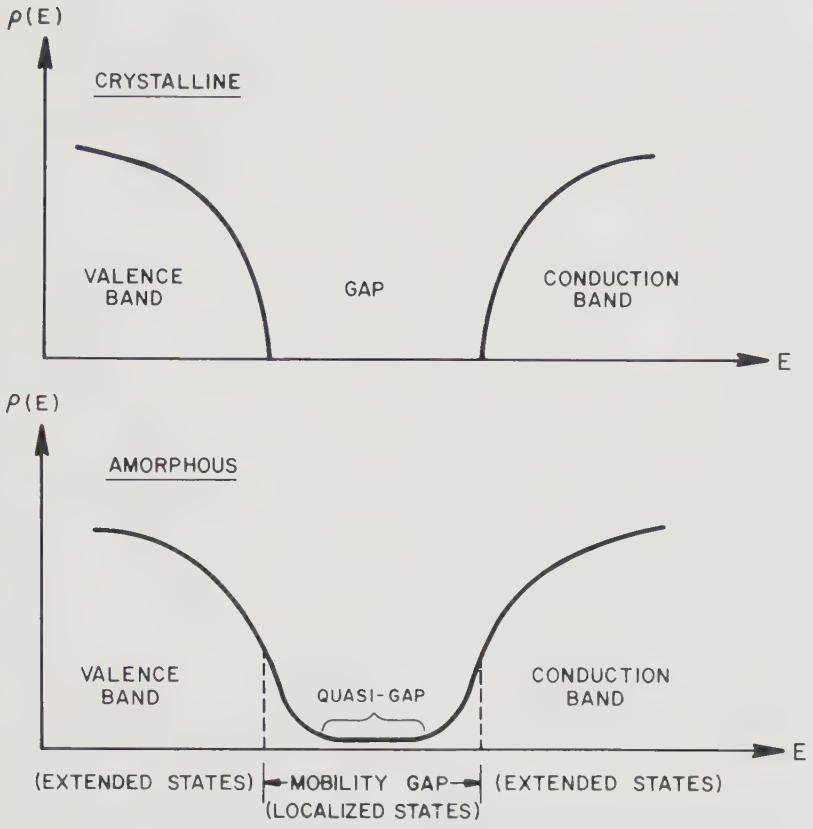

Fig. 11. Density of states for crystalline and glassy semiconductors (schematic). (After Ehrenreich *et al.*[77])

of the bands are very likely extended throughout the glass. Such extended states should have a much higher mobility than those in the quasi gap; the transition between these states and the states of low mobility is called the mobility edge.

In considering such energy gaps, it is instructive to recall the case of glassy silicon and germanium, whose structures lack long-range order (Section 2.3) but whose energy gaps are shown by measurements of optical properties (e.g., Ref. 79) to be qualitatively similar in many respects to those of the crystalline forms. The existence of such gaps in the glasses presents some interesting theoretical problems since great emphasis is placed in the familiar theories of solids on the importance of long-range order in producing band gaps. Recent calculations[80,81] on clusters of atoms of various sizes have yielded an approximate density of states with a quasi gap clearly indicated. With increasing

cluster size, the density of states in the quasigap region was found to decrease. These results suggest that the presence of quasi gaps in the densities of states for glasses can (at least in some cases) be associated with short-range order effects; the qualitative similarity in the optical gap of glassy and crystalline silicon or germanium then reflects similarities in the short-range order in the materials.

Significant variability is noted in the optical properties of glassy silicon and germanium as reported in different investigations. In some cases (e.g., Ref. 82), the data indicate gradual band edges in as-deposited films, which sharpen during annealing below the temperature range where crystallization is observed. In other cases (e.g., Ref. 83), sharp edges are observed in as-deposited films, with the apparent optical gaps (0.55 eV for Ge and 0.8 eV for Si) being appreciably smaller than those indicated in other studies (1.1 eV for Ge and 1.6 eV for Si). One source of this variability in the optical properties of glassy Si and Ge may be the oxygen content of the films, since the presence of oxygen has been shown[84] to sharpen and shift the band edges in glassy Ge. For further discussion of this point, see Refs. 85 and 86.

Discussions of the transport properties of electronic conducting glasses most often employ the density of states functions with analyses similar to those used in describing conduction in heavily doped crystalline semiconductors. Two contributions to the conductivity of such glasses are then identified: (1) a free carrier contribution from electrons or holes which are excited thermally into the extended states of high mobility; and (2) a hopping contribution from thermally activated tunneling between localized states. Theoretical treatments of these processes have yielded at least qualitative agreement with experimental data on the transport properties of many semiconducting glasses. In some cases, however, the agreement may be merely fortuitous because of the occurrence of phase separation or crystallization on a fine scale in the materials.

5. Glass Formation

As should be apparent from the discussion in Sections 2 and 3, glass formation is not restricted to covalently bonded oxides, but is found in ionic, metallic, van der Waals, and hydrogen-bonded materials as well. Experience indicates, in fact, that nearly any liquid will form a glass if cooled to a sufficiently low temperature without the occurrence of crystallization; the question of glass formation is

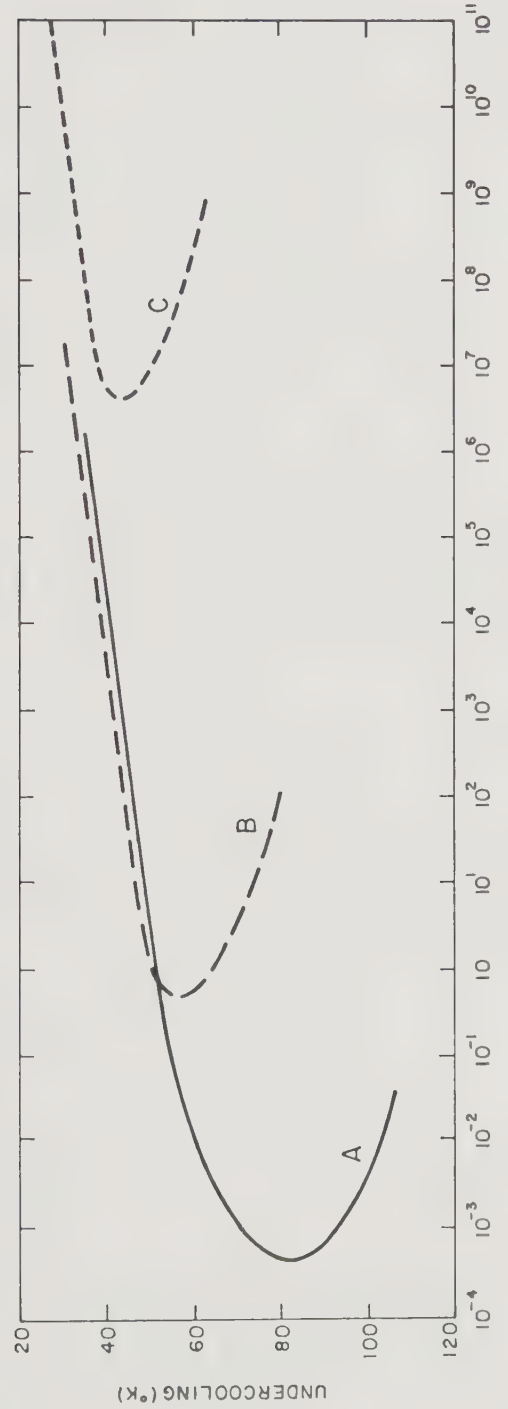

Fig. 12. Time–temperature–transformation curves for salol-like materials having various melting points and a volume fraction crystallized of 10^{-6}. (A) $T_E = 356.6°K$; (B) $T_E = 316.6°K$; and (C) $T_E = 276.6°K$. (After Uhlmann.[88])

not *whether* a given liquid is a glass-former, but *how fast* it must be cooled to avoid detectable crystallization.

In estimating critical cooling rates for various liquids, it is useful to construct time–temperature–transformation (T-T-T) curves corresponding to some barely detectable degree of crystallinity—such as a volume fraction of crystals of 10^{-6}. Such curves, examples of which are shown in Figure 12, can be constructed from calculated or measured values of the nucleation frequency and growth rate of crystals at various temperatures. For homogeneous nucleation and interface-controlled growth, for example, the fraction crystallized X can be related to the nucleation frequency per unit volume I_v and the growth rate u as[87]

$$X \approx \tfrac{1}{3}\pi I_v u^3 t^4 \tag{1}$$

The noses in the T-T-T curves result from a competition between the driving force for crystallization, which increases with decreasing temperature, and the atomic mobility, which decreases with decreasing temperature. The critical cooling rates for glass formation can be estimated from the relation

$$(dT/dt)_c \approx \Delta T_n/\tau_n \tag{2}$$

where ΔT_n is the undercooling and τ_n is the time at the nose of the T-T-T curve. The cooling rates estimated in this way will be insensitive to the assumed barely detectable fraction of crystals [see Eq. (1)], but will depend significantly upon the density of nucleating heterogeneities of various potencies in the liquid.

A kinetic treatment of this kind has been applied to a number of liquids of various types.[88] The results indicate that the material characteristics most favorable for glass formation are a large viscosity at the melting point or liquidus temperature and/or a viscosity which increases strongly with falling temperature below the melting point.

The familiar oxide glass-formers are usually characterized by large viscosities at their melting points or liquidus temperatures. In contrast, organic glass-formers usually have much smaller viscosities at their melting points, but the viscosities of such organic liquids increase much more rapidly with falling temperature below the melting points. These variations in flow behavior are reflected in the data shown in Fig. 13. In the viscosity range about 10^7 P, for example, the viscosity of a typical oxide glass-former increases by two orders of magnitude in a temperature interval of about 100–150°C, while that

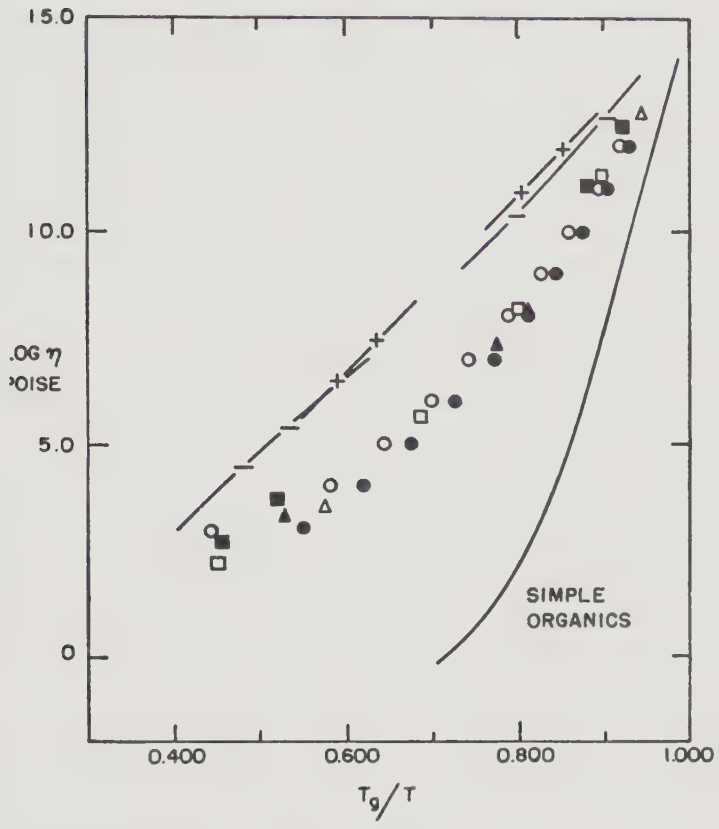

Fig. 13. Viscosity vs. reduced temperature T_g/T relations for various liquids. +, SiO_2; —, GeO_2; △, ▲, B_2O_3; ■, $K_2O{\cdot}2SiO_2$; □, $Na_2O{\cdot}2SiO_2$; ○, NBS standard soda lime silicate glass; ●, NBS standard lead silicate glass. (After Laughlin and Uhlmann.[89])

of a typical organic increases by the same factor in a temperature interval of only 10°C.

Within a given class of materials having similar viscosity–temperature relations, glass formation is favored by low melting points. This is illustrated by curves A and C in Figure 12, which were constructed for hypothetical materials with the same viscosity vs. temperature relation and other material properties as salol, but with melting points 40°C higher and 40°C lower than salol (316.6°K). The viscosities at the respective melting points differ overall by a factor of about 40 (0.03, 0.08, and 1.15 P for curves A, B, and C), while the estimated cooling rates for glass formation differ by some ten orders of magnitude (2×10^4, 10, and 10^{-6}°C sec^{-1} for curves A, B and C).

The observed ease of glass formation in the regions of composition near eutectics may in part reflect similar factors—namely the eutectic regions correspond to lowered liquidus temperatures, and hence to lower temperatures of maximum crystallization kinetics and higher viscosities at these temperatures. The preferred character of low-lying eutectics over shallow eutectics for forming glasses can be directly related to these considerations. Also contributing to glass formation in eutectic regions is the material transport required for crystallization of the two-phase equilibrium structures, which results in lowered growth rates.

A variety of other models have been suggested to describe the degree of ease with which various liquids can form glasses. Perhaps the most celebrated is that advanced by Zachariasen,[5] who considered that glass formation would be favored when the differences in energy between crystal and glass are small. On this basis, he suggested four rules for forming random networks of oxygen polyhedra: (1) Each oxygen ion should be linked to not more than two cations; (2) the coordination number of oxygen ions around the central cation should be four or less; (3) oxygen polyhedra share corners, not edges or faces; and (4) at least three corners of each polyhedron should be shared.

Other models have suggested correlations between the glass transition temperature T_g and the melting point, or between T_g and the heat of vaporization. None is capable, however, of representing the behavior of the wide variety of glass-forming liquids, and it seems preferable to relate glass-forming ability to the material parameters which determine the kinetics of crystal nucleation and growth.

The compositions of a variety of commercial glasses are shown in Table 2. Of these, more than 90% of annual U.S. glass production is represented by a rather narrow range of Na_2O–CaO–SiO_2 compositions used in containers, sheet, plates, and light envelopes. The glasses are melted in large, refractory-lined furnaces, called tanks, in a continuous operation where molten glass is withdrawn from one end and raw materials are added at the other.

6. Macrostructure of Glasses

Much of the discussion of the properties of glasses assumes, implicitly or explicitly, that they are simple homogeneous materials. It has been noted in the preceding sections, however, that many

TABLE 2
Approximate Compositions of Some Commercial Glasses*

Glass	SiO_2	Al_2O_3	Fe_2O_3	CaO	MgO	BaO	Na_2O	K_2O	SO_4	F_2	ZnO	PbO	B_2O_4	Sc	CdO	CuO
Container flint	72.7	2.0	0.06	10.4	—	0.5	13.6	0.4	0.3	0.2	—	—	—	—	—	—
Container amber	72.5	2.0	0.1	10.2	—	0.6	14.4	0.2	S – 0.02	0.2	—	—	—	—	—	—
Container flint	71.2	2.1	0.05	6.3	3.9	0.5	15.1	0.4	0.3	0.1	—	—	—	—	—	—
Window	72.0	1.3	—	8.2	3.5	—	14.3	0.3	0.3	—	—	—	—	—	—	—
Plate	71.6	1.0	—	9.8	4.3	—	13.3	—	0.2	—	—	—	—	—	—	—
Ruby selenium	67.2	1.8	0.03	1.9	0.4	—	14.6	1.2	S – 0.1	0.4	11.2	—	0.7	0.3	0.4	—
Ruby	72.0	2.0	0.04	9.0	—	—	16.6	0.2	—	Tr	—	—	—	—	—	0.05
Borosilicate	76.2	3.7	—	0.8	—	—	5.4	0.4	—	—	—	—	13.5	—	—	—
Fiber glass	54.5	14.5	0.4	15.9	4.4	—	0.5	—	—	0.3	—	—	10.0	—	—	—
Lead tableware	66.0	0.9	—	0.7	—	0.5	6.0	9.5	—	—	—	15.5	0.6	—	—	—
Lead technical	56.3	1.3	—	—	—	—	4.7	7.2	—	—	—	29.5	0.6	—	—	—
Lamp bulb	72.9	2.2	—	4.7	3.6	—	16.3	0.2	0.2	—	—	—	0.2	—	—	—
Heat absorbing	70.7	4.3	0.8	9.4	3.7	0.9	9.8	0.7	—	Tr	—	—	0.5	—	—	—

* After Tooley.[90]

glasses are phase-separated on a scale of 30 to a few hundred Å, and that all glasses are characterized by fluctuations in density or composition.

On a scale observable with light microscopy or with the naked eye, the uniformity of glasses depends upon the type of glass, its intended application, and the way it was prepared. Among commercial glasses, the two limiting cases may be those of container glasses, which are melted at the maximum throughput obtainable with reasonable homogeneity, and optical glasses, whose indices of refraction can be uniform to better than one part in 10^6 across a 2.5 cm section.

The uniformity of glass on this scale of macrostructure depends on a number of factors in addition to composition. These include the specific batch raw materials used in the melting, the throughput (the rate at which glass is removed from the tank relative to the size of the tank), the nature of the tank lining (platinum vs. ceramic), the highest melting phases which are likely to be retained in the melt, and the service life of the refractories.

In the manufacture of optical glass, relatively high-purity batch raw materials are used, very refractory compositions are avoided, and the melting is usually carried out in platinum-lined tanks or pots. In other applications, however, a tradeoff may be effected between uniformity and other characteristics of the material. The most common tradeoff is that between uniformity and throughput; in other cases, such as the preparation of laser glasses, the tradeoff is between uniformity and the elimination of small metallic inclusions.

Among the common types of imperfections found in glasses, the following should be noted: (1) *cord*: attenuated glassy inclusions with properties different than those of the surrounding glass; (2) *striae*: cord of low intensity, of greatest concern in the preparation of optical

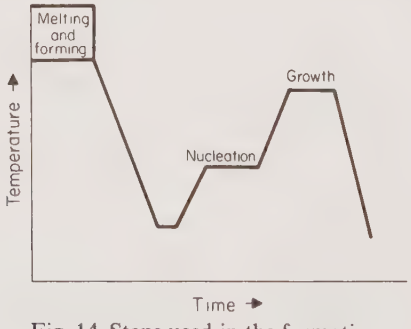

Fig. 14. Steps used in the formation of glass-ceramic bodies (schematic).

glass; (3) *stone*: small crystalline imperfections in the glass, generally resulting from melting for insufficiently long periods of time; and (4) *seed*: small gaseous inclusions in the glass. Of these, the one which is most frequently important in technological applications is the occurrence of seed, whose elimination provides the effective limitation on the throughput which can be obtained with many glass-melting operations.

7. Glass-Ceramic Materials

Glass-ceramic materials, such as the commercial products Corning Ware,* Centura Ware,* and CER-VIT,† consist of a large volume fraction of crystals (typically 95–98 % or more) with a small amount of glass forming a pore-free composite. They are produced by the controlled crystallization of glasses, using steps such as those outlined in Figure 14.

In fabricating these materials, the glass is melted and bodies of desired shapes are formed using conventional techniques which can be highly automated and efficient. To obtain the desired number of small (0.1–1 μm) crystals distributed throughout the volume of the specimens, a uniform density of nuclei of the order of 10^{12}–10^{15} cm^{-3} is required. Such copious nucleation is provided by adding appropriate nucleating agents to the batch during melting and carrying out a suitable heat treatment. The most commonly used nucleating agents are TiO_2 and ZrO_2 (or combinations of both); but P_2O_5, the Pt-group and noble metals, and fluorides can also be used in many applications.

The metal nucleating agents are effective in forming a crystalline nucleating phase (the metal) by a precipitation process. The oxide nucleants seem to be effective in first promoting a phase separation process, which provides a fine dispersion of second-phase material that subsequently forms a crystalline nucleant phase.

After the nucleation treatment is carried out—often in a region of temperature where the viscosity is about 10^{11}–10^{12} P and hence where the rate of crystal growth is small—the material is heated further to effect the growth of the major crystalline phases. Such growth takes place during the heating process as well as during any hold at the maximum growth temperature. The latter temperature is

* Trademark of Corning Glass Works.
† Trademark of Owens–Illinois Inc.

selected on the basis of several considerations, such as: (1) crystal growth kinetics; (2) combination of phases desired; (3) deformation of material; (4) transformation temperatures in crystalline phases; (5) redissolution of crystalline phases, etc. The maximum growth temperature and the time for which the material is held there (which can be brief) depend therefore upon the composition and the properties desired in the final bodies.

After the crystallization treatment is carried out, the glass-ceramic bodies are cooled to ambient and given whatever additional processing treatments are desired. Such treatments may include the application of compressive glazes or ion-exchange strengthening. The final bodies usually consist of two or more crystalline phases (often more than two), occupying a preponderant volume fraction, imbedded in a glass phase (or phases) of very small volume fraction whose composition is in general poorly specified.

7.1. Commercial Glass-Ceramic Systems

Glass-ceramic materials are presently available in a number of systems, including the following.

(1) Li_2O–Al_2O_3–SiO_2. Glass-ceramics in this system, which is the most important commercially, are designed for very small thermal expansion coefficients (among the smallest known for any material) and hence very high resistance to thermal shock. They are used in applications such as home cookware, stove tops, telescope mirror blanks, and the like. The important crystalline phases in the system are β-spodumene ($Li_2O \cdot Al_2O_3 \cdot 4SiO_2$), which has a small expansion coefficient, and β-eucryptite ($Li_2O \cdot Al_2O_3 \cdot 2SiO_2$), which has a negative volume expansion coefficient. Different phase assemblages, characterized by different properties, can be produced by using TiO_2 and ZrO_2 in different proportions as the nucleating agent, as well as by varying the composition and heat treatment schedule. The composition of a commercial glass-ceramic material in this system is about as follows (in wt%): Li_2O (3), Al_2O_3 (18), SiO_2 (70), TiO_2 (5), and alkaline earth and other alkali oxides (4).

(2) MgO–Al_2O_3–SiO_2. Glass-ceramics in this system are designed for high mechanical strength, for high-temperature use, and for high electrical resistivity. The most important crystalline phase in this system is α-cordierite ($2MgO \cdot 2Al_2O_3 \cdot 5SiO_2$), which has exceptionally high elastic moduli. The composition of a glass-ceramic material

in the system is about as follows: MgO (13), Al_2O_3 (30), SiO_2 (47), and TiO_2 (10). They have been used in a number of applications, ranging from nose cones and shields for missiles to ceramic ball bearings.

(3) *Na_2O–BaO–Al_2O_3–SiO_2*. Glass-ceramics in this system are characterized by relatively high thermal expansion coefficients (in the range of $80 \times 10^{-7}°C^{-1}$). The important crystalline phases are nepheline ($Na_2O \cdot Al_2O_3 \cdot 2SiO_2$) and celsian ($BaO \cdot Al_2O_3 \cdot 2SiO_2$). The composition of a glass-ceramic material in this system is about as follows: Na_2O (13), BaO (9), Al_2O_3 (29), SiO_2 (41), and TiO_2 (7). Their most important use is in break-resistant home tableware. In this application, the glass-ceramic bodies are provided with a compressive glaze coating. This glaze is characterized[91] by a smaller thermal expansion coefficient than the underlying glass-ceramic; hence, after cooling, the surfaces of the coated pieces are placed in a state of compressive stress which increases the strength of the bodies.

(4) *K_2O–MgO–Al_2O_3–SiO_2*. Glass-ceramics in this system, generally formed with small concentrations of B_2O_3 and fluoride, are designed for ease of machinability. The most important crystalline phase is a fluoride mica ($KMg_3 \cdot AlSi_3 \cdot O_{10} \cdot F_2$) and its solid solutions. The composition of a glass-ceramic material in this system is about as follows: K_2O (10), MgO (15), Al_2O_3 (15), SiO_2 (47), B_2O_3 (7), and F (6). The machinability of the crystallized bodies, which have useful electrical and thermal properties, depends[92] upon the precipitation in large volume fractions of sheet silicates (micas) having large aspect ratios. Under these conditions, the contact or interlocking of the crystals together with their marked basal cleavage results in a detachment of individual crystals or small groups of crystals and a localized flaking or pulverization of the material.

(5) *Li_2O–MgO–Al_2O_3–SiO_2*. Glass-ceramics in this system are designed for low thermal expansion coefficients combined with optical transparency and ease of chemical strengthening. The important crystalline phase in this regard is a stuffed β-quartz solid solution, and the most attractive compositions range about the following: Li_2O (2), MgO (4), Al_2O_3 (19), SiO_2 (71), and ZrO_2 (4).

Transparency in glass-ceramic materials is achieved[93] by carrying out the crystallization so that the crystal size is below that at which scattering of visible wavelengths is effective, or so that the refractive index difference between crystals and glass and between different orientations of the crystals is small. Ion-exchange strengthening is carried out at elevated temperatures in fused salt baths. For the

stuffed β-quartz solid solutions described above, the exchange is between K^+ ions in the bath and Li^+ ions in the β-quartz. Such exchange produces a surface compression, and hence higher strength, by a crowding mechanism. In the chemical strengthening of other glass ceramics, however; the surface compression may be produced by differences in thermal expansion coefficient between exchanged layers and base glass[94] or by transformation of crystalline phases in the exchanged layer to other crystalline phases of higher specific volumes.[95]

7.2. Microstructural Features and Properties

Many of the desirable properties of glass-ceramic materials are associated with a number of microstructural features. These include the following.

(1) *Absence of porosity.* This is primarily related to the fact that the volume changes involved in crystallization can be accommodated by flow, in contrast to the porosities of 5–10% or more which are usually found in ceramic bodies formed by powder processing techniques.

(2) *Very small crystal size.* This is associated with the copious internal nucleation attainable with selected additions to the batch and appropriate heat treatments. The crystal sizes in glass-ceramic bodies are often less than 1 μm, in contrast with the crystal or grain sizes found in conventional crystalline ceramics of 5–50 μm or more.

(3) *Uniform distribution of randomly oriented crystals.* This is also a result of the nucleation and growth treatments, and is in contrast with the nonuniform, oriented crystallinity which results from devitrification of conventional glasses.

(4) *Wide and continuous variation of phase assemblages.* This represents the essential feature of the glass-ceramic concept—namely the achievement of desired combinations of properties by systematic variations of the chemistry and microstructure of materials having both glassy and crystalline phases.

The properties of glass-ceramic materials can only be related to those of the individual phases within the framework of various treatments of composite materials. Their densities lie in the range of conventional glasses and crystalline ceramics (2.4–5.8 g/cm^3), and their moduli lie in the same range as many glasses (10–20 $\times$ 10^6 psi). Under ambient conditions, they behave as brittle, elastic solids and fail by the propagation of flaws. Their practical strengths without surface

treatments are higher than those of most glasses, and can be as high as 20–30 $\times$ 10^3 psi or more. In some cases, strengths comparable to those of ordinary glasses can be maintained to temperatures of 800°C or more. Their susceptibility to surface damage seems to be less than that of most glasses, and their chemical durabilities are often excellent (depending primarily upon the amount and composition of the residual glass which is present). Their abrasion resistance and hardness are generally much superior to those of conventional glasses.

The thermal expansion coefficients of glass-ceramic materials in different systems have been reported as large as 160 $\times$ 10^{-7}°C^{-1} and as strongly negative as -35×10^{-7}°C^{-1}. With appropriate control of composition and crystallization treatment in the Li_2O–Al_2O_3–SiO_2 system, values smaller than 5 $\times$ 10^{-8}°C^{-1} can be obtained. Such materials have, of course, exceptional resistance to thermal shock.

The conduction process in most glass-ceramic materials involves the motion of cations, particularly the alkali ions; and hence their conductivities increase with increasing temperature. The conductivity decreases during the crystallization process, and the conductivities of glass-ceramics can be smaller than those of the glasses from which they are derived by factors of more than 10^4. The dielectric losses of glass-ceramics are generally smaller than those of the parent glasses, and loss factors smaller than 2 $\times$ 10^{-3} at 10^6 Hz and 20°C can be obtained. Their dielectric breakdown strengths can be significantly larger than those of conventional glasses and ceramics, and values approaching 50 kV/mm have been obtained.

There have been few systematic investigations of the relation between the microstructure and properties of glass-ceramic materials; indeed, in relatively few cases have the microstructures (submicrostructures) been characterized in sufficient detail for meaningful conclusions to be reached. In the processing area, even the role of the oxide nucleants remains to be suitably elucidated. For more detailed discussions of available information in these areas, the reader is referred to Refs. 96 and 97.

8. Concluding Discussion

In the preceding sections, the structural characteristics of glasses and glass-ceramic materials have been examined and the conditions for glass formation have been developed. On the scale of local atomic arrangements, recent advances in experimental and analytical tech-

niques have opened new opportunities for obtaining structural information about glasses. The results are consistent with a random network model for SiO_2 and with a distorted ribbon structure for B_2O_3. On the scale of submicrostructure, liquid–liquid immiscibility has been found to be widespread in glass-forming systems; many glasses which are homogeneous on a scale of light microscopy may be heterogeneous on a scale of 30 to a few hundred Å. In the case of glasses formed from the vapor or from solution, void structures of various forms can represent important submicrostructural features. On the scale of macrostructure, it has been noted that many glasses have gas bubbles, unmelted crystalline fragments, or regions of notable compositional inhomogeneity. On the scale of electronic structure, it has been shown that long-range order is not required for a quasi gap to appear in the density of states, but that a finite state density is expected in such a quasi gap for all real glasses. The forms of the band edges and the magnitudes of the gaps can, at least in the case of glassy silicon and germanium, depend significantly upon the conditions used to form the glasses.

In brief, then, the structures of glasses are complex on any scale where information can reliably be obtained. The concept of glass as a simple homogeneous state of matter is a simplification only exceeded by the notion of crystalline materials as perfect single crystals.

References

1. G. S. Cargill, *J. Appl. Phys.* **41**, 12 (1970).
2. B. E. Warren and J. Biscoe, *J. Am. Ceram. Soc.* **21**, 49 (1938).
3. J. T. Randall, H. P. Rooksby, and H. S. Cooper, *J. Soc. Glass Technol.* **14**, 219 (1930).
4. N. Valenkov and E. A. Porai-Koshits, *Z. Krist.* **95**, 195 (1937).
5. W. H. Zachariasen, *J. Am. Chem. Soc.* **54**, 3841 (1932).
6. L. W. Tilton, *J. Res. NBS* **59**, 139 (1957).
7. F. C. Frank, *Proc. Roy. Soc.* **A 215**, 43 (1952).
8. J. D. Bernal, *Nature* **185**, 68 (1960).
9. B. G. Bagley, *Nature* **208**, 674 (1965).
10. R. Hosemann and S. N. Bagchi, *Direct Analysis of Diffraction by Matter*, North Holland, Amsterdam (1962).
11. J. Zarzycki and R. Mezard, *Phys. Chem. Glasses* **3**, 163 (1962).
12. B. E. Warren and R. L. Mozzi, *J. Appl. Cryst.* **3**, 59 (1970).
13. B. E. Warren, *X-Ray Diffraction*, Addison Wesley, Reading, Massachusetts (1969).
14. B. E. Warren, H. Krutter, and O. Morningstar, *J. Am. Ceram. Soc.* **19**, 202 (1936).
15. R. L. Mozzi and B. E. Warren, *J. Appl. Cryst.* **2**, 164 (1969).
16. A. M. Levelut and A. Guinier, *Bull. Soc. Franc. Miner. Crist.* **90**, 445 (1967).

17. A. Pierre, D. R. Uhlmann, and F. N. Molea, *J. Appl. Cryst.* **5**, 216 (1972).
18. R. L. Mozzi and B. E. Warren, *J. Appl. Cryst.* **3**, 251 (1970).
19. F. M. Dunlevey and A. R. Cooper, *Bull. Am. Ceram. Soc.* **51**, 374 (1972).
20. P. J. Bray, in *Interaction of Radiation with Solids*, Plenum Press, New York (1967).
21. A. E. R. Westman, in *Modern Aspects of the Vitreous State*, Vol. 1, Pergamon Press, New York (1961).
22. C. R. Kurkjian and E. A. Sigety, *Phys. Chem. Glasses* **9**, 73 (1968).
23. R. J. Landry, J. T. Fournier, and C. G. Young, *J. Chem. Phys.* **46**, 1285 (1967).
24. T. Bates, in *Modern Aspects of the Vitreous State*, Vol. 2, Pergamon Press, New York (1965).
25. J. K. Hendren, *Am. J. Phys.* **40**, 1343 (1972).
26. R. Kaplow, T. A. Rowe, and B. L. Averbach, *Phys. Rev.* **168**, 1068 (1968).
27. J. Schattmiller, M. Tabak, G. Lucovsky, and A. Ward, *J. Non-Cryst. Solids* **4**, 80 (1970).
28. A. T. Ward, *J. Phys. Chem.* **74**, 4110 (1970).
29. J. F. Graczyk and S. C. Moss, in *Proceedings of 10th International Conference on the Physics of Semiconductors*, A.E.C. Div. Tech. Info., Oak Ridge (1970), p. 658.
30. N. J. Shevchik and W. Paul, *J. Non-Cryst. Solids* **8–10**, 381 (1972).
31. D. E. Polk, *J. Non-Cryst. Solids* **5**, 365 (1971).
32. M. L. Rudee and A. Howie, *Phil. Mag.* **25**, 1001 (1972).
33. G. S. Cargill, *J. Appl. Phys.* **41**, 2248 (1970).
34. J. L. Finney, *Proc. Roy. Soc.* (*London*) **A 319**, 479 (1970).
35. D. R. Uhlmann, J. F. Hays, and D. Turnbull, *Phys. Chem. Glasses* **8**, 1 (1967).
36. J. D. Mackenzie, *J. Am. Ceram. Soc.* **46**, 461 (1963).
37. R. M. Kimmel and D. R. Uhlmann, *J. Appl. Phys.* **41**, 2917 (1970).
38. W. Poch, *Phys. Chem. Glasses* **8**, 129 (1967).
39. M. E. Spaght and G. S. Parks, *J. Phys. Chem.* **38**, 103 (1934).
40. R. M. Kimmel and D. R. Uhlmann, *J. Appl. Phys.* **42**, 4917 (1971).
41. S. Sakka and J. D. Mackenzie, *J. Non-Cryst. Solids* **1**, 107 (1969).
42. E. Lell, N. J. Kreidl, and J. R. Hensler, in *Modern Aspects of the Vitreous State*, Vol. 3, Pergamon Press, New York (1967).
43. T. P. Seward, D. R. Uhlmann, and D. Turnbull, *J. Am. Ceram. Soc.* **51**, 278 (1968).
44. Y. Moriya, D. H. Warrington, and R. W. Douglas, *Phys. Chem. Glasses* **8**, 19 (1967).
45. N. S. Andreev, D. A. Goganov, and E. A. Porai-Koshits, in *Structure of Glass*, Vol. 3, Plenum Press, New York (1964).
46. J. J. Hammel, in *Proceedings of VII International Congress on Glass*, Institut National de Verre, Charleroi (1966).
47. E. M. Levin, C. R. Robbins, and H. F. McMurdie, *Phase Diagrams for Ceramists*, American Ceramic Society, Columbus (1964).
48. R. R. Shaw and D. R. Uhlmann, *J. Am. Ceram. Soc.* **51**, 377 (1968).
49. W. Haller, D. H. Blackburn, F. E. Wagstaff, and R. J. Charles, *J. Am. Ceram. Soc.* **53**, 34 (1970).
50. D. G. Burnett and R. W. Douglas, *Phys. Chem. Glasses* **11**, 125 (1970).
51. J. Zarzycki and F. Naudin, *Phys. Chem. Glasses* **8**, 11 (1967).
52. S. V. Phillips, R. E. Booth, and P. W. McMillan, *J. Non-Cryst. Solids* **4**, 510 (1970).
53. G. V. Bunton, *J. Non-Cryst. Solids* **6**, 72 (1971).
54. A. J. Easteal and C. A. Angell, *J. Chem. Phys.* **56**, 4231 (1972).

55. T. P. Seward and D. R. Uhlmann, in *Amorphous Materials*, Wiley, New York (1972).
56. G. S. Cargill, *Phys. Rev. Letters* **28**, 1372 (1972).
57. J. W. Cahn, *Acta Met.* **9**, 795 (1961).
58. M. Hillert, *Acta Met.* **9**, 525 (1961).
59. J. W. Cahn, *J. Chem. Phys.* **42**, 93 (1965).
60. J. W. Cahn, *Acta Met.* **14**, 1685 (1966).
61. J. E. Hilliard, in *Phase Transformations*, American Society for Metals, Metals Park (1970).
62. H. E. Cook, *Acta Met.* **18**, 297 (1970).
63. W. Haller, *J. Chem. Phys.* **42**, 686 (1965).
64. M. Goldstein, *J. Crystal Growth* **3–4**, 594 (1968).
65. R. W. Hopper and D. R. Uhlmann, *Disc. Faraday Soc.* **50**, 166 (1970).
66. G. F. Nielson, *Phys. Chem. Glasses* **10**, 54 (1969).
67. J. Zarzycki and F. Naudin, *J. Non-Cryst. Solids* **1**, 215 (1969).
68. M. Tomozawa, R. K. MacCrone, and H. Herman, *Phys. Chem. Glasses* **11**, 136 (1970).
69. G. F. Nielson, *Phys. Chem. Glasses* **13**, 70 (1972).
70. T. P. Seward, D. R. Uhlmann, and D. Turnbull, *J. Am. Ceram. Soc.* **51**, 634 (1968).
71. J. F. MacDowell and G. H. Beall, *J. Am. Ceram. Soc.* **52**, 17 (1969).
72. T. H. Elmer, M. E. Nordberg, G. B. Carrier, and E. J. Korda, *J. Am. Ceram. Soc.* **53**, 171 (1970).
73. R. R. Shaw and D. R. Uhlmann, *J. Non-Cryst. Solids* **1**, 474 (1969).
74. W. Vogel, *Silikattech.* **15**, 383 (1964).
75. E. A. Porai-Koshits and V. I. Averjanov, *J. Non-Cryst. Solids* **1**, 29 (1968).
76. R. R. Shaw and J. F. Breedis, *J. Am. Ceram. Soc.* **55**, 422 (1972).
77. H. Ehrenreich *et al.*, *Fundamentals of Amorphous Semiconductors*, National Materials Advisory Board Publication NMAB-284, NMAB, Washington (1971).
78. N. F. Mott, *Disc. Faraday Soc.* **50**, 7 (1971).
79. R. Grigorovici and A. Vancu, *Thin Solid Films* **2**, 105 (1968).
80. T. C. McGill and J. Klima, *J. Phys. C* **3**, 163 (1970).
81. T. C. McGill and J. Klima, *Phys. Rev. B* **5**, 1517 (1972).
82. M. L. Theye, *Mat. Res. Bull.* **6**, 103 (1971).
83. T. M. Donovan, W. E. Spicer, J. M. Bennett, and E. J. Ashley, *Phys. Rev. B* **2**, 397 (1970).
84. M. Zavetova, S. Koc, and J. Zemek, *Czech. J. Phys. B* **22**, 1812 (1972).
85. S. C. Moss and D. Adler, *Comments on Solid State Physics* **5**, 47 (1973).
86. A. Adler and S. C. Moss, *Comments on Solid State Physics* **5**, 63 (1973).
87. M. Avrami, *J. Chem. Phys.* **7**, 1103 (1939).
88. D. R. Uhlmann, *J. Non-Cryst. Solids* **7**, 337 (1972).
89. W. T. Laughlin and D. R. Uhlmann, *J. Phys. Chem.* **76**, 2317 (1972).
90. F. V. Tooley, *Handbook of Glass Manufacture*, Ogden Publishing Co., New York (1953).
91. D. A. Duke, J. E. Megles, J. F. MacDowell, and H. F. Bopp, *J. Am. Ceram. Soc.* **51**, 98 (1968).
92. G. H. Beall, in *Advances in Nucleation and Crystallization in Glasses*, American Ceramic Society, Columbus (1972).
93. G. H. Beall and D. A. Duke, *J. Mat. Sci.* **4**, 340 (1969).

94. G. H. Beall, B. R. Karstetter, and H. L. Rittler, *J. Am. Ceram. Soc.* **50**, 181 (1967).
95. D. A. Duke, J. F. MacDowell, and B. R. Karstetter, *J. Am. Ceram. Soc.* **50**, 67 (1967).
96. P. W. McMillan, *Glass-Ceramics*, Academic Press, New York (1964).
97. A. I. Berezhnoi, *Glass-Ceramics and Photo-Sitalls*, Plenum Press, New York (1970).

6

The Morphology of Crystalline Synthetic Polymers

F. Khoury and E. Passaglia
Institute for Materials Research
National Bureau of Standards
Washington, D.C.

1. Introduction

1.1. General and Historical

Crystalline organic high polymers in their solid state have very complex morphologies. This is due to the chainlike nature of their constituent molecules, which leads to crystallization behavior and morphologies that are in most aspects only rarely encountered in more traditional "small molecule" solids, and in other aspects are unique to polymers. Moreover, this chainlike nature leads to a wealth of phenomena and a rich diversity of morphological behavior that is, on the one hand, a boon to the experimentalist, for it provides an almost endless source of study, and, on the other hand, a source of despair for those who, like ourselves, attempt to summarize the behavior of these materials. There is a real danger that too great a preoccupation with the details of the morphology of one or two individual polymers will both obscure important aspects of behavior common to all polymers and also mislead the reader into perceiving a simplicity that in fact does not exist.

The morphology of polymers has been studied for a very long time indeed. In fact, fibers of naturally occurring polymers were some of the first materials used for x-ray diffraction studies.* Such studies

* The interested reader is referred to an early book by Astbury,[1a] which includes a bibliography of x-ray diffraction studies carried out in the 1920's and early 1930's on fibrous proteins, cellulosic fibers, and natural rubber. A summary of early work on cellulosic fibers can also be found in a book by Hermans.[1b]

(and others as well, as will become apparent below) indicate that polymers do not attain complete crystalline order. Moreover, crystals of macroscopic size cannot be produced for the majority of polymers of interest. Thus spots in x-ray diffraction patterns are broad and diffuse, densities are intermediate between those of the crystal and those of the liquid, heats of fusion are low, melting points are broad, etc. All macroscopic properties indicate that bulk polymers consist of either microcrystals with a large degree of imperfection, or of an intimate mixture of microscopic crystalline and amorphous phases.

In fact, for many years, the latter was the accepted view of polymer morphology. The state of the bulk polymer was regarded as that of crystals of the order of several hundred angstroms in size imbedded in an amorphous matrix. The polymer chains (which in a typical polymer are 0.1–10 μm in length) were viewed as threading their way through more than one crystallite via intermediate armorphous regions, so that the crystals were considered to be parallelepipeds connected together by the chains which threaded through them. This so-called "fringed-micelle"[2] model of polymer structure was the accepted view for many years, and indeed, this model was quite successful for explaining the bulk macroscopic properties of polymers.

In the mid 1940's[3] it was found that synthetic polymers crystallized from the melt formed complex but ordered aggregates called "spherulites" in which the constituent crystalline units are arrayed in a spherically symmetric fashion (hence their name). Such spherical aggregates were not unknown in nonpolymeric materials (see Section 4.2), but the explanation of the structure of polymer spherulites on the basis of the fringed micelle model proved to be difficult.

Then, in the mid-1950's it was discovered[4–7] that single crystals of polyethylene could be grown from solution, and it may be said that the modern study of polymer morphology began with that discovery. We shall subsequently see that, as proposed by Keller,[6] this discovery necessitated that a single molecule thread many times through the same crystal, which it does by folding in the crystal surface.* This led to the modern view of "chain-folded" polymer crystallization.

* It should be noted that the possible incidence of crystallization involving chain folding in polymers had been invoked by Storks[8] many years earlier, in 1938, to account for the nature of the molecular orientation in thin, solution-cast films of the polymer gutta percha [*trans*-1,4-poly(2-methyl-butadiene)] which occurs in nature. This suggestion, however, was not followed up and did not receive attention until Keller revived the concept and unequivocally established the occurrence of chain folding in his landmark paper on microscopic solution-grown crystals of polyethylene.[6]

At approximately the same time in history, methods for the production of so-called stereoregular polymers were developed[9,10] and a large number of new crystallizable polymers became available for study. These two discoveries, coupled with the coincident perfecting and proliferation of the electron microscope as a research tool during the same period, led to a veritable explosion in the study of the solid state of polymers, spurred in part by the economic importance of the new stereoregular polymers.

1.2. Scope of the Chapter

We shall in the main be concerned with developments since the mid-1950's. Closely related to polymer morphology is the subject of crystallization kinetics, which has also been intensively investigated in this same period, but we shall not be concerned with this topic, since it is covered by Hoffman, Davis, and Lauritzen[11] elsewhere in this Treatise. Moreover, to attempt a comprehensive review of all the work in polymer morphology carried out during this period of time would be impossible. A mere listing of all the papers in polymer morphology would take most of our alloted space.

This chapter is written for the nonspecialist, and our intent is to give the main thrust of what is known at this time about the main features of polymer morphology.

The chapter is divided into three main sections:

1. Crystallinity in polymers, in which we give some of the requisites on polymer chains necessary for crystallization.
2. Crystallization from dilute solution, in which we describe some of the more characteristic morphological forms polymers exhibit when they crystallize from solution.
3. Crystallization from the melt, in which we include the topic of crystallization under pressure.

We concern ourselves only with synthetic polymers, and omit the subject of natural polymers.

Other reviews are, of course, available. The book by Geil[12] remains an invaluable source of detail, and a useful recent book is that by Wunderlich.[13] There are numerous shorter reviews. An early review by Keller[14] summarizes very well the state of knowledge up to 1958, and subsequent reviews also by Keller provide a good historical account of the development of knowledge in this field.[15–17] The two reviews by Keith are particularly valuable for their discussion

of crystallization from the melt.[18,19] The first of these is now somewhat old, but the main arguments are still sound. Among other reviews we especially note those by Ingram and Peterlin,[20] Rees and Bassett,[21] and Fava.[22] All of these reviews have been of considerable help in the preparation of this chapter.

2. Crystallinity in Polymers

Since we are concerned only with crystalline polymers, in this section we consider the requirements on polymer chains for crystallization to be possible, several important and unique features of polymer crystal structures, and the extent to which polymers crystallize.

2.1. Requisites for Crystallization

As will be seen, synthetic polymers crystallize by their constituent chains packing parallel to one another in an ordered manner. Thus, in order for this to be feasible in polymers, the polymer chains must possess a linear structure. Even linear polymers must, however, have sufficient regularity in order to crystallize,* or, to put it more precisely, whatever irregularity is present must not cause such an increase in crystal free energy that crystallization is precluded. We therefore now address ourselves to the question of regularity in polymer chains. This regularity is of two types, which are designated as chemical regularity and stereoregularity.

2.1.1. Chemical Regularity

A linear polymer chain is a linked succession of units, the monomers. If these units are all the same, as represented schematically by the sequence

-A-A-A-A-A-A-A-A-A-

then complete chemical regularity exists, and this is called a homopolymer. We list in Table 1 several homopolymers and their respective chemical repeat units. We shall have occasion to refer to several of these polymers in the remainder of this chapter. The units A may be simple or quite complex. In the simplest polymer, polyethylene, they are simply $-CH_2-$ units, whereas in the very important

* As will become apparent below, however, complete regularity is not always essential.

TABLE 1
Polymers Mentioned in This Chapter

Name	Chemical repeat unit
1. Polyethylene	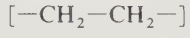
2. Polypropylene	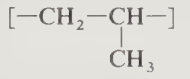
3. Poly(4-methylpéntene-1)	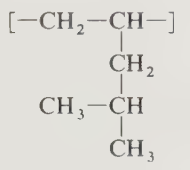
4. Polybutene-1	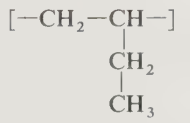
5. Polystyrene	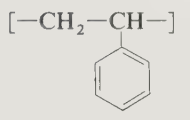
6. Polyoxymethylene	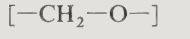
7. Poly(ethylene oxide)	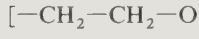
8. Polychlorotrifluoroethylene	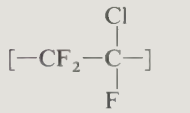
9. Polytetrafluoroethylene	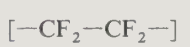
10. Poly(vinyl chloride)	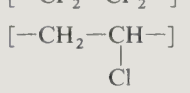
11. Polyacrylonitrile	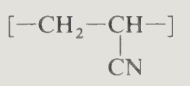
12. Poly(ethylene adipate)	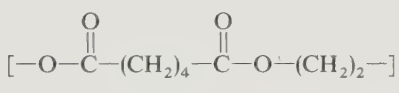
13. Poly(glutamic acid)	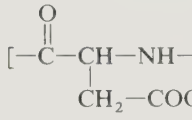
14. Poly(hexamethylene adipamide) (nylon 6.6)	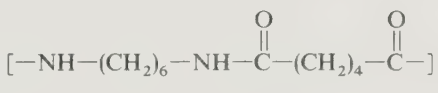

Table 1—*continued*

Name	Chemical repeat unit
15. Poly(ethylene terephthalate)	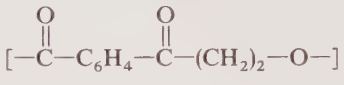
16. Poly(vinylidene fluoride)	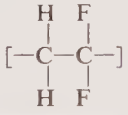

polymer, poly(hexamethylene adipamide) (nylon 6.6), the chemical repeat unit is

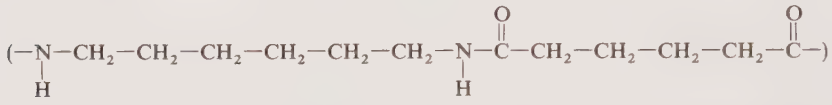

Whatever the complexity of the repeating unit, any polymer possessing the regularity represented by this scheme has sufficient chemical regularity to crystallize, provided irregularities of a stereochemical nature (see below) do not prevent crystallization.

Many important polymers do not, however, have complete chemical regularity. In some cases irregularity is intentionally introduced, and in other cases it is accidental.

When chemical irregularity is intentionally introduced we have what is called a copolymer. In a so-called "random" copolymer two (or more) monomers are polymerized together, so that the resulting structure may be represented schematically as A-B-A-A-A-B-B-A-B-A-A-B-B-, where A and B represent the two types of monomer unit, and the arrangement is meant to be random. In fact, if f_A and f_B represent, respectively, the fraction of A units and the fraction of B units in the chain, and f_{AB}, f_{BA}, f_{AA}, and f_{BB} represent, respectively, the fractions of AB, BA, AA, and BB sequences in the chain, the conditions for complete randomness are

$$f_{AB} = f_{BA} = f_A f_B$$
$$f_{AA} = f_A f_A, \qquad f_{BB} = f_B f_B$$

These conditions are rarely completely obeyed,[23] for the probability

(or rate) of addition of A to B (or B to A) in the polymerization process is not always the same as the probability of addition of A to A (or B to B), and the study of the irregularity of this type of polymer is the subject of an extensive literature.[24] Nevertheless, for the synthetic polymers of interest to us the departures from complete randomness are not large, and for our purposes random copolymers may be considered truly random.

While random copolymers generally do not crystallize, crystallization in them is not always precluded.[25–27] Their ability to crystallize is governed most importantly by the relative fractions of the two different monomers which make up the chains (being greatest when one of the fractions is very small), and by the chemical and structural similarity of the two monomers. We shall have occasion to consider aspects of the crystallization of random copolymers in Section 3.4.6.3(a).

Copolymers need not be random. Using our previous notations, the arrangement in a copolymer may be as follows:

-A-A-A-A-A-A-A-B-B-B-B-B-A-A-A-A-

this is, the polymer chain is made up of subchains of A units and B units linked at their ends. This type of polymer is called a block copolymer.

Such a block copolymer would superficially appear to have all the chemical regularity necessary for crystallization. This would be true if all the A subchains were of the same length, and all the B subchains were of the same length. Unfortunately, this is not usually the case in practice. The A and B subchains are not completely monodisperse, and irregularity in these polymers exists due to the varying lengths of the A and B subchains in the total chains. However, in some special cases it has been possible to prepare block copolymers whose chains consist of two or three subchains having fairly narrow length distributions. The manifestation of crystallization in such block copolymers has been established.[28–33] The crystallization and morphology of such block copolymers, namely two block copolymers in which the chains consist of one poly(ethylene oxide) and one polystyrene subchain, have been studied extensively.[31–33] We shall have occasion to refer to these latter studies in due course in Section 3.4.6.2.

Accidental chemical irregularity occurs due to uncontrollable vagaries in the polymerization process. An important type of such irregularity occurs in polyethylene, a polymer of great commercial

importance, and of basic importance in morphology studies. In this polymer, occasional paraffinic side branches are introduced during the polymerization process, so that the polymer may be represented schematically by the sequence

The B units are spaced randomly down the chain, and while we have drawn them as being the same, the evidence is that these pendant groups are chemically different, i.e., B = CH_3, C_2H_5, etc. The amount of such irregularity is very strongly dependent on the polymerization process, and has a very pronounced effect on the crystallinity attainable. Thus, for example, polyethylene polymerized by the high-pressure process (so-called branched polyethylene) has about three pendant groups per 100 chain units and attains a degree of crystallinity (see below) of 40–50%,[34] whereas low-pressure polyethylene (so-called linear polyethylene), polymerized by any of several catalytic processes, has about three pendant groups per 1000 chain units and attains a degree of crystallinity as high as 90–95%.[34]*

Another type of accidental chemical irregularity arises from "head-to-head" addition as compared to "head-to-tail" sequences in addition polymers (Ref. 35, Chapter 6; Ref. 36, p. 54). In such polymers, the monomer unit may be either of the following two types:

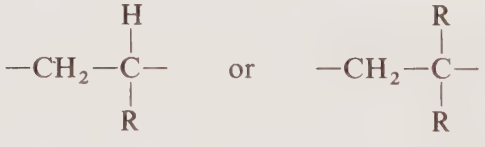

Complete head-to-tail addition leads to following structures:

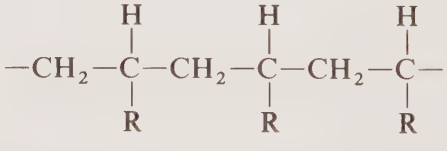

* Branched polyethylene will be referred to as such in this chapter, in order to distinguish it from linear polyethylene, to which we shall refer simply as polyethylene.

or

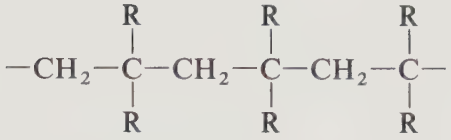

and this is by far the dominant mode of addition in these polymers. However, an occasional head-to-head sequence in an otherwise head-to-tail structure can occur, and the resulting structure may be represented schematically as follows:

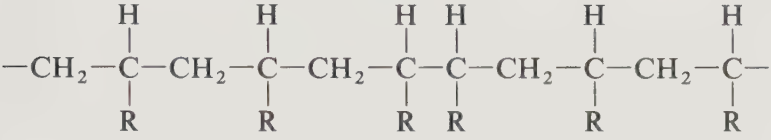

or

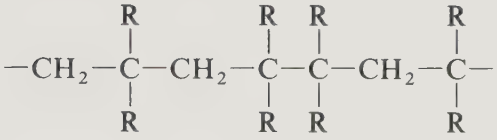

Thus the head-to-head sequence may be thought of as a switch from a head-to-tail sequence to a tail-to-head sequence. This is a common type of irregularity among addition polymers prepared by free-radical synthesis (Ref. 35, Chapter 4), but the fraction of head-to-head sequences as compared to head-to-tail sequences is generally small. In the case where there are two identical pendant R groups on the monomer unit, crystallization is not precluded by the occurrence of relatively infrequent head-to-head sequences although, as indicated by Lando and Doll,[37] [in the case of poly(vinylidene fluoride), in which R is a fluorine atom] such sequences may influence the conformation of the chains in the crystal lattice. When there is only one R group on the monomer unit, or if there are two different R groups, the ability of the chains to crystallize is governed primarily by an aspect of the stereoregularity of the chains other than the incidence of head-to-head attachments, as will become evident in the following section.

2.1.2. Stereoregularity

In polymers that do not have pendant side groups, chemical regularity is the only regularity necessary for crystallization. However, if the polymers contain pendant side groups, then the carbon atom to which the pendant group is attached is an asymmetric carbon atom, and the possibility of stereoisomerism occurs. In order for these polymers to crystallize, they must, generally speaking, be stereoregular, and we now discuss this.

The importance of the stereoregularity of polymers for crystallization was recognized for many years, but it was not until 1955 that Ziegler[9] and Natta[10] showed how to synthesize addition polymers with stereoregularity, and this discovery led to a profusion of new addition polymers that crystallize. Stereoregular polymers have become of immense economic importance and have provided an inexhaustive and rich source for scientific study.

A scientifically important and much studied class of these addition polymers is made up of the vinyl hydrocarbon polymers. The concept of stereoregularity in these polymers is best described with reference to a diagram (Figure 1). As shown in Figure 1, vinyl addition polymers consist of a backbone of carbon atoms, with pendant groups R attached to alternate carbon atoms. The group R identifies the polymer. For example, for polypropylene, R is $-CH_3$; for polystyrene, R is $-C_6H_5$; for poly(4-methylpentene-1), R is

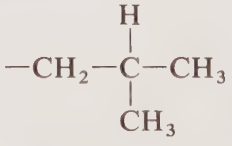

Three different chains are possible for these types of polymer, and we now describe these chains with reference to Figure 1. If the backbone carbon atoms are arranged in zigzag conformation, the zigzag of these carbon atoms defines a plane. The hydrogen atoms and the pendant groups that are attached to the backbone carbon atoms lie in planes that are at right angles to the plane of the zigzag. Now, fixing attention on the pendant groups, it will be noticed that each group may be attached in two different ways: It may be either to the right or the left of the plane of backbone carbon atoms. Using the designations developed originally by Natta and co-workers (see, e.g., Ref. 38), if these groups are randomly placed to the left or the right of the backbone carbon plane, the structure is obviously irregu-

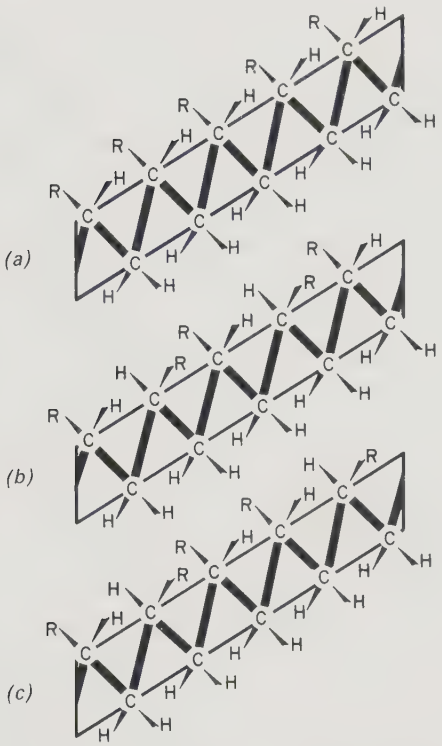

Fig. 1. An illustration of the chain configuration in (a) isotactic, (b) syndiotactic, and (c) atactic polymers. In this illustration, the backbone carbon atoms define a plane. In the isotactic chain (a), the pendant substituent groups (denoted by R) are all on one side of this plane, in the syndiotactic chain (b) they are alternately on the right and left side, and in the atactic chain (c) they are randomly on the right and left.

lar and is called *atactic*. Except in rare cases (see Section 2.2.1.3) chains with such an irregular configuration do not crystallize. If all the pendant groups are on one side, the structure is called *isotactic* and has the necessary configurational regularity for crystallization. If the pendant groups are alternately left and right of the backbone plane, the structure is called *syndiotactic*, and again has the requisite regularity for crystallization. The great discovery of Natta and Ziegler was that of learning how to synthesize these isotactic and syndiotactic polymers. The isotactic polymers are by far the more common.

These different chain configurations clearly form a type of stereoisomerism. In fact, and although the following concept and notation have been criticized (Ref. 36, p. 56), if we consider that each of the carbon atoms with a pendant group may have either a *d* (dextro) or *l* (levo) configuration, then the atactic polymer can be considered a random sequence of *d* and *l*, the isotactic a sequence of all *d* or all *l*, and the syndiotactic a regular alternation of *d* and *l*. Although this is at least a useful means of characterization of these structures, it should not be assumed that we mean that these centers are truly asymmetric and thus that the chains are necessarily optically active.[36] As Bovey[36] has pointed out, if the chain ends are neglected, these centers are actually pseudosymmetric, and give rise to no optical activity, either actual or potential. Thus, for example, neglecting chain ends (which in any case have a negligible effect) an isotactic sequence is obviously superposable on its mirror image, and has translational symmetry but no symmetry axes. A syndiotactic sequence has translational symmetry and, if it has an even number of carbon atoms, has a twofold symmetry axis. If it contains an odd number of carbon atoms, it has a mirror plane. To discuss this topic further and to discuss the other types of possible stereoisomers would take us too far afield. For our purposes it is sufficient to note that generally atactic polymers do not crystallize, whereas isotactic and syndiotactic ones do, although, as will be seen, they give quite different crystal structures.

It should be noted that, in practice, there are some atactic chains produced along with the stereoregular chains in the polymerization process.

2.1.3. Molecular Weight

In normal synthetic polymers, the molecules do not all have the same molecular weight. Hence there is a distribution of molecular lengths, and often this distribution is very broad. This obviously is an important source of irregularity, for all other considerations aside, it precludes crystallization of the mode found in *n*-paraffins (see Section 2.2.2). The polymers of interest in morphology have molecular weights that range from 10^4 to 10^6, and contain lengths (that is, the length of the fully extended molecule) that range from 0.1 to 10 μm. This range of lengths is often found in the same sample unless special care is taken to prepare specific molecular weight fractions.

2.2. Polymer Crystal Structures

It is not our intent in this section to give a comprehensive description of polymer crystal structures or to dwell on the methods by which they are determined. An extensive compilation of unit cell parameters, space groups, and chain conformations in crystalline polymers has been made by Miller,[39,40] and the methods for determining polymer crystal structures are the subject of two recent comprehensive monographs.[41,42] In addition, a collection of crystal structures of many polymers prepared by stereospecific polymerization is given by Natta and Danusso.[43] Our aim here is to present some polymer crystal structures that will be useful in our subsequent discussion and to discuss some unique features of polymer crystal structures.

We must, however, say a few words about the difficulty of determining polymer crystal structures. Polymer single crystals generally cannot be obtained of sufficient size to make the traditional techniques of x-ray structure determination, such as precession and Wiessenberg camera methods, applicable.* The best that can usually be done is to use drawn fibers which give diffraction patterns that closely approximate single-crystal rotation patterns. In these fibers the molecular chains are aligned preferentially along the fiber axis, and therefore from measurements of the layer line spacings the repeat distance along the chain may be deduced. In favorable cases this, in turn, gives an immediate clue as to the chain conformation. Moreover, the unit cell parameters may also be obtained from these fiber patterns, as well as the space group. To obtain the full structure, trial structures are developed on the basis of the chemical character of the polymer, bond lengths and angles, etc., and the intensities calculated from these trial structures are compared to those observed. Fortunately, in most cases, the chain conformation is determined primarily by intrachain potential energies, and bond dimensions and angles are not greatly affected by lateral packing. Even under favorable conditions, however, the diffuseness of the x-ray patterns resulting from the imperfect order in the polymer leads to a limitation on the resolution of the resulting structure. For more details, the reader is referred to advanced treatments.[41,42]

* Exceptions are the special case of some polymers prepared by the process of solid-state polymerization in macroscopic crystals of the monomer or a cyclic oligomer, such as, for example, the preparation of polyoxymethylene from trioxane.[44]

Sometimes electron diffraction is useful in determining crystal structures. As will be seen in due course, polymer single crystals of microscopic size can often be grown from solution. Information on the nature of the lateral packing of the chains can be obtained from electron diffraction patterns given by these crystals. Full structural determination, however, requires the use of x-ray methods as discussed above.

It should be noted that many polymers exhibit polymorphism. This can manifest itself in several ways. First, the polymer may exhibit different crystal structures depending on the conditions of crystallization.[45] Second, spherulites (see Section 4.3.1) of different polymorphic forms of a polymer may form in the same polymer sample.[46,47] Third, a polymer sample may undergo a change or partial change in crystal structure when it is deformed.[48]

2.2.1. Representative Crystal Structures

Detailed descriptions of the unit cell structures of polymers can be found in several places (Ref. 13, pp. 95–177; Refs. 41–43). However, in this section we give a few representative crystal structures of some polymers which we shall have occasion to discuss later.

2.2.1.1. Polyethylene

This is the most studied of all polymers and (somewhat unfortunately) in some respects its morphological behavior has been taken to be representative of most polymers. Its unit cell structure[49] is shown in Figure 2. It is orthorhombic, with dimensions $a = 7.36$ Å, $b = 4.92$ Å, and $c = 2.54$ Å. The space group is *Pnam*. The chains have a planar zigzag conformation, and two of them pass through a unit cell, which contains four $-CH_2-$ groups.

2.2.1.2. Vinylic Hydrocarbon Polymers

By this class of polymer we mean those that have the chemical structure $(CH_2-CHR)_n-$ where R is any hydrocarbon group. It is in this class of polymer that the distinction among atactic, isotactic, and syndiotactic structures achieves its important effect.

The crystal structures of these polymers have been the subject of numerous studies, foremost among them being those of Natta and his co-workers.[43] An attempt even to summarize these studies would take us too far afield. The isotactic polymer chains generally

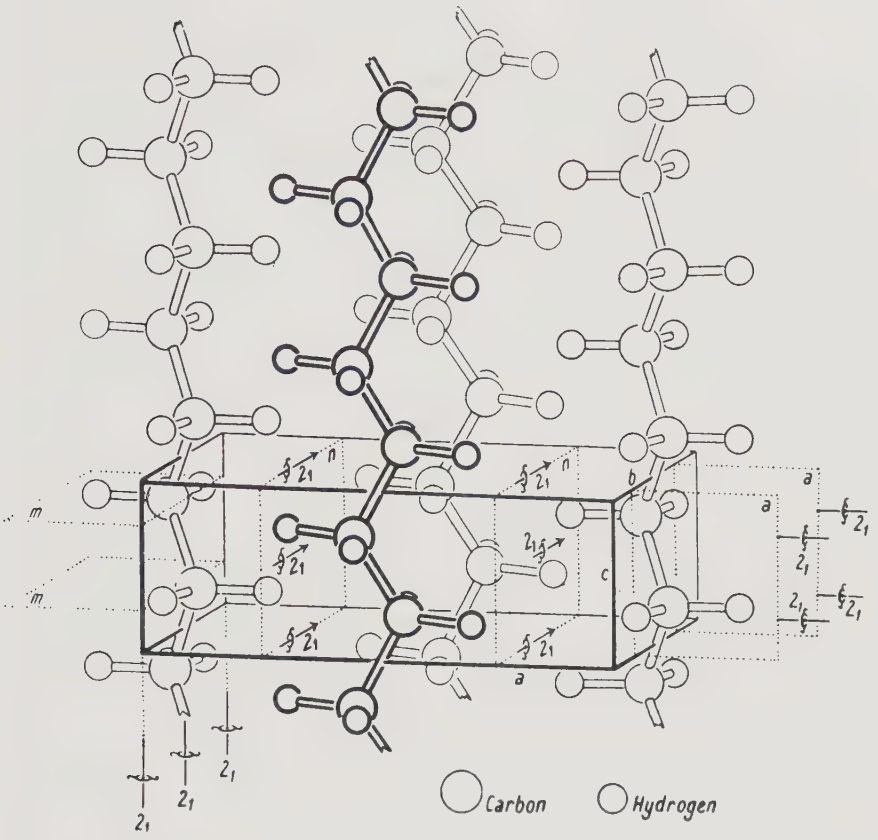

Fig. 2. The orthorhombic unit cell of polyethylene. Two chains thread their way through the cell with their long axis parallel to the *c* axis of the cell. (From Bunn,[50] reprinted with permission of the Oxford University Press.)

form helices, whereas the syndiotactic chains form either planar zigzags or helices. Below we shall describe briefly the crystal structures of three polymers, which polymers we shall have occasion to discuss subsequently: polypropylene, polystyrene, and poly(4-methylpentene-1).

Polypropylene is, chemically, the simplest of this class of polymer, and a polymer of immense economic and scientific importance. Both isotactic and syndiotactic forms are known, although the latter form is rare and, to our knowledge, has not been the subject of any morphological studies.

Isotactic polypropylene crystallizes in various polymorphic forms,[39,40] the most common of which is monoclinic.[51] In it the

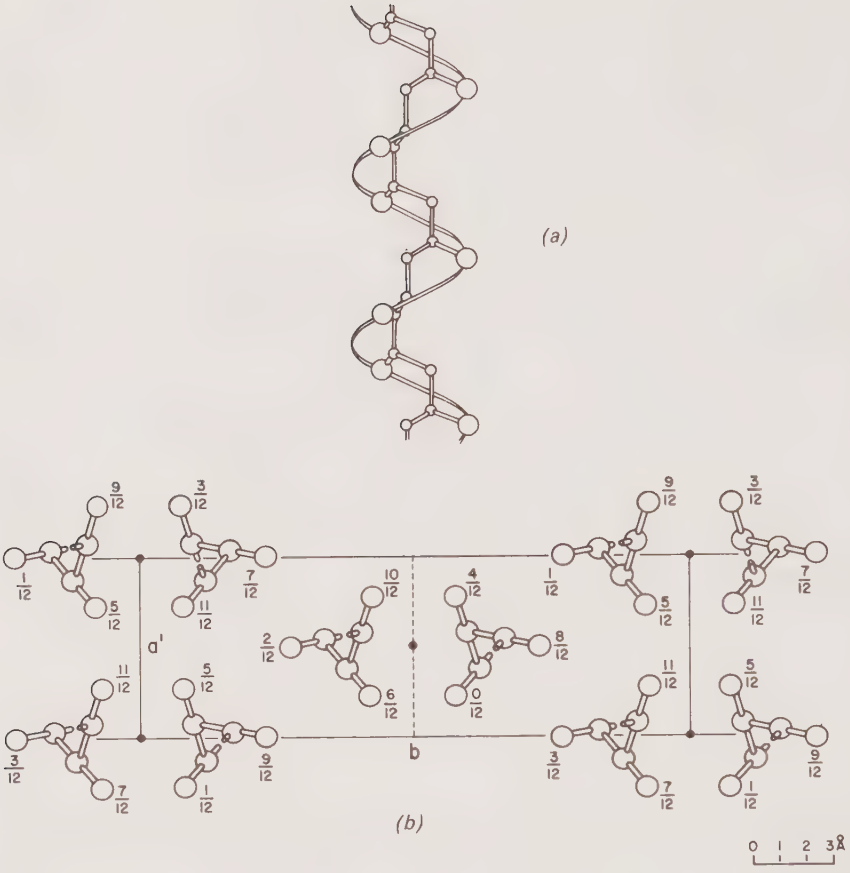

Fig. 3. (a) Illustration of the 3/1 helical conformation of isotactic polypropylene chains. Small circles are the backbone carbon atoms, large circles represent methyl branches. (After Natta and Corradini.[56]) (b) A projection along the *c* axis of the monoclinic unit cell of isotactic polypropylene. Four 3/1 helical chains (two right-handed and two left-handed) pass through the unit cell with their long axis parallel to the *c* axis of the cell. The circles represent the backbone and side branch carbon atoms. The numbers refer to the elevations of the side group carbon atoms relative to the basal (001) plane. The axis a' ($= a \cos 9°20'$) is a projection of the *a* axis on the plane normal to the *c* axis. (After Natta and Corradini.[51])

chains are in a 3/1 helical conformation (i.e., three monomer units per turn). Four chains pass through the unit cell; both right- and left-handed helices are in the structure in equal numbers. A polypropylene chain in a 3/1 helical conformation is shown in Figure 3(a) and a projection of the polypropylene unit cell along the chain axes

is shown in Figure 3(b). The lattice dimensions are $a = 6.65$ Å, $b = 20.9$ Å, $c = 6.50$ Å and the angle β is 99°, 20′.

The syndiotactic polypropylene structures are reported as orthorhombic and hexagonal.[39,40] While syndiotactic polypropylene is not common, and will not be discussed further in this chapter, we illustrate in Figure 4 the chain conformation in syndiotactic polypropylene,[52] for a comparison of this conformation with Figure 3(a) vividly illustrates the effect of chain configuration (i.e., different types of stereoregularity) on chain conformation.

The next polymer we mention is isotactic polystyrene. As in polypropylene, the chains form a 3/1 helix, but the structure is rhombohedral with space group $R\bar{3}_C$.[53] Six chains pass through the

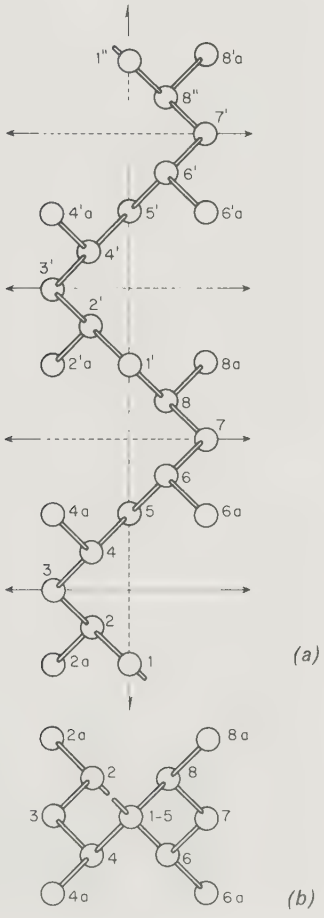

Fig. 4. (a) Side and (b) end views of the conformation of a syndiotactic polypropylene chain. Only the carbon atoms are shown. The identity (repeat) period along the chain axis corresponds to four monomer units. The main chain has a twofold screw axis parallel to the chain axis and there are two twofold symmetry axes normal to the chain itself. (After Natta.[52])

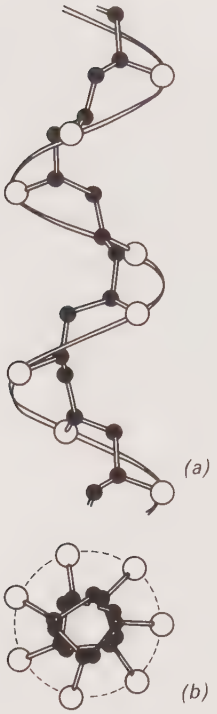

Fig. 5. An illustration of the 7/2 helical conformation of the chains in poly(4-methylpentene-1) as seen (a) at right angles to the helix axis and (b) along that axis. Two right-handed and two left-handed helices pass through the unit cell.[54,55] Filled circles are backbone carbon atoms, large circles represent positions of attachment of the side branches. (After Natta and Corradini.[56])

unit cell, and both left- and right-handed helices are present in equal numbers. The lattice dimensions are $a = b = 22.0$ Å and $c = 6.62$ Å, the repeat distance along the chain being approximately the same as in polypropylene.

The last polymer of this group we want to mention is poly(4-methylpentene-1). This is known only in its isotactic modification. This polymer also exhibits polymorphism.[39,40] The most common crystal structure, which is referred to as modification one, is tetragonal,[54] with $a = b = 18.6$ Å and $c = 13.8$ Å. The space group is apparently $P\bar{4}$.[54,55] In this case the chains have a 7/2 helical conformation, and the difference between this conformation and that shown by the previous two isotactic polymers has been attributed to the fact that in this polymer the carbon atom of the side chain adjacent to the backbone is unsubstituted.[56] The helical character of poly(4-methylpentene-1) chains is shown in Figure 5. Four chains pass through the unit cell; right-handed and left-handed helices are in equal numbers in the structure.

2.2.1.3. Polychlorotrifluoroethylene

This is one of a class of polymer that may be considered as polyethylene in which one or more of the hydrogen atoms have been regularly replaced by halogen atoms. The chemical structure of the polymer chain is

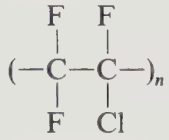

This polymer has an interesting feature. The structure is very nearly atactic.[57] Nevertheless the polymer crystallizes, but in a manner that is not completely perfect. The chain itself is a rather lazy spiral, but the helical pitch is not well defined, it being variously reported as a 14/1[58] and a 17/1 helix.[59,60] According to a recent paper by Mencik,[61] the chains have an average of 16.8 monomer units in one turn (equal to the *c*-axis spacing). As would be expected, the chains are packed side by side in a hexagonal array with the *a* axis[58–61] equal to 6.3–6.5 Å, but the space group is unknown. Thus the packing is similar to the packing that would be expected for irregularly "knobby" cylinders, the knobs being the chlorine atoms. We have thus in this polymer, which has been the subject of several important property–crystallinity[62,63] studies, a case in which an atactic polymer crystallizes. This is not the usual mode of behavior for atactic polymers, which almost universally do not crystallize because the steric hindrances between successive substituent groups cause the chain to adopt a random conformation that cannot be overcome by the energy of crystallization.

2.2.1.4. Poly(hexamethylene adipamide)

This is a member of the class of polymers called polyamides[64,65] and known generically as nylons. The important members of this large and very significant class of polymer have no pendant side groups, so that questions of tacticity are obviated. However, due to the presence of amide linkages in the main backbone, hydrogen bonding between chains occurs, so that interchain interactions play an important part in determining the crystal structure. This is illustrated in Figure 6 by the crystal structure[66] of poly(hexamethylene

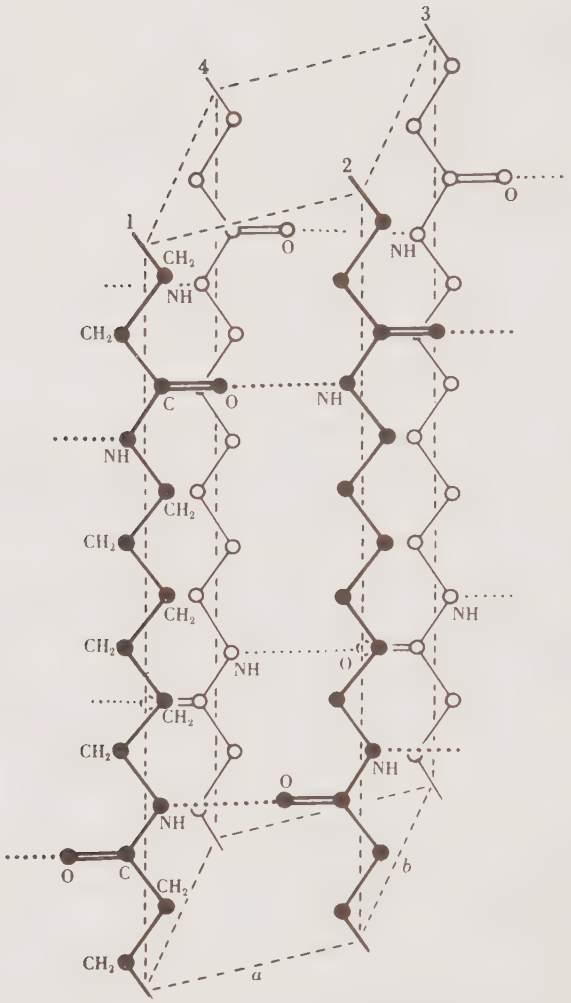

Fig. 6. Illustration of the triclinic unit cell of poly-(hexamethylene adipamide) as determined by Bunn and Garner.[66] (Reprinted with permission of the Royal Society, London.)

adipamide), or nylon 6.6, the monomer unit of which is given in Section 2.1.1.

The crystal structure is such that the maximum possible number of hydrogen bonds are formed between adjacent chains which lie along the *a*-axis direction relative to one another (e.g., chains 1 and 2 in Figure 6). This feature leads to a hydrogen-bonded, sheetlike arrangement of the chains. The unit cell is triclinic and centrosym-

metric. The unit cell parameters are $a = 4.9$ Å, $b = 5.4$ Å, $c = 17.2$ Å, and $\alpha = 48°$, $\beta = 77°$, $\gamma = 63.5°$.

2.2.2. A General Characteristic of Polymer Lattices

As can be seen from the above crystal structures, polymer crystals have an important aspect in common, and that is that one molecule partakes of many unit cells.* This has an important bearing on the possible structures of the surfaces of polymer crystals that are not parallel to the chain axis. Unlike the situation with smaller organic molecules, or with inorganic materials and metals, these surfaces cannot be considered as cleavage planes of the polymer crystal lattice. For cleavage to occur along these planes, primary chain bonds would have to be broken. At these surfaces the chains may fold back, as in the chain-folded view of polymer structure, or have a bundlelike surface, as in the historically important but now largely discredited fringed micelle model of polymer crystals. Whatever the view, the important point is that those surfaces of a polymer crystal that are intercepted by polymer molecules are not cleavage planes of the crystal lattice. This has an important bearing on the definition of surface free energy, which is a topic that is developed at length by Hoffman, Davis, and Lauritzen elsewhere in this Treatise.[11]

This difference between polymer crystals and crystals of smaller molecules is best illustrated by a comparison between the structures of polyethylene and *n*-paraffins. The latter are homologs for polyethylene, and the subcell structure of the orthorhombic modifications of these materials is the same as the unit cell of polyethylene. However, the full unit cell of the *n*-paraffins contains the total molecular length. The structure of an orthorhombic *n*-paraffin is given in Figure 7.[67] It can be seen in this structure that the planes that contain the methyl groups [(001) or (002) planes] are normal to the chain axes, and are cleavage planes, in contrast with the (001) planes in polyethylene, which are not cleavage planes.

2.3. Degree of Crystallinity

Even the presence of complete chemical and geometric regularity does not ensure that a synthetic polymer will be completely crystal-

* We shall see in Section 4.3.3 that in polycrystalline aggregates a molecule can in fact participate in more than one crystallite.

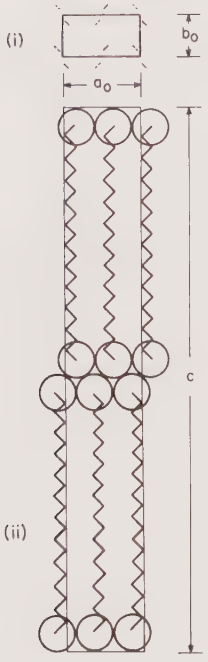

Fig. 7. The structure of the orthorhombic unit cell of the normal paraffin n-$C_{23}H_{48}$[67] as seen (i) along the long axis of the chains (c axis of the unit cell) and (ii) at right angles to the c axis. The subcell structure is the same as in polyethylene (Figure 2). The (001) and (002) planes in this n-paraffin lattice are cleavage planes, whereas in the case of the polyethylene lattice they are not. (Diagrams after Smith.[67])

line. Various forms of disorder, the nature of which will become apparent in the remainder of this review, arise due to the long-chain nature of polymer molecules and the resulting complexity of the crystallization process. The disorder is far greater than would be caused by the customary dislocations and vacancies found in small-molecule crystalline solids. In fact, solid polymers (and this includes single crystals grown from solution) have bulk properties intermediate between those of the completely crystalline material (when these can be known) and those of the completely amorphous material. The bulk properties we have in mind are those such as density, heat of fusion, x-ray scattering, etc.

Because of this fact it has become customary to characterize the solid state of a polymer by the "degree of crystallinity." The basis for this concept is an idealized and almost certainly oversimplified view of the structure of a solid polymer. In this view, the polymer is considered as a material which consists of a portion called the amorphous phase, which has all the properties of a true amorphous phase at the given temperature and pressure, and a portion called the crystalline phase, which has all the properties of the perfect crystalline phase at that temperature and pressure. Thus the solid polymer is viewed as a mixture of coexisting crystalline and amorphous phases. In this view,

the degree of crystallinity is taken as the weight fraction (or weight percentage) of crystalline material. Then the measurement of a property for the polymer and a knowledge of the value of that property for the completely amorphous and completely crystalline* material permits one to calculate the degree of crystallinity χ. The properties commonly used to determine a degree of crystallinity are density, heat of fusion, x-ray scattering, infrared absorption, nuclear magnetic resonance linewidth, etc. Each of these properties gives somewhat different values for χ, but generally will order samples with varying χ in the same sequence. To discuss these differences in detail would take us too far afield. The interested reader is referred to the literature.[68]

Our point here is that, with perhaps the single exception of polyethylene crystallized under pressure,[69] in which case χ is very nearly unity, the values obtained for χ range from less than 0.5 to 0.95. Even single crystals of polyethylene, the most studied of polymers, give values of χ at most 0.9.[70–74] Thus, on the basis of the measurement of bulk properties, polymers do not show the properties expected of a completely crystalline material.

The values of χ attained are very much dependent on the nature of the polymer and its thermal treatment. Thus, for example, branched polyethylene synthesized by the high-pressure process has values of χ that range around 0.5,[34] whereas linear polyethylene has values as high as 0.95.[34] In poly(chlorotrifluoroethylene) values of χ ranging from 0.38 to 0.8 can[62] be obtained depending on thermal treatment, and similar ranges can be obtained for polypropylene.[75]

The view that pictures a polymer as consisting of coexisting crystalline and amorphous phases is, of course, far too simple. There are various degrees of disorder possible. Hosemann[76] has developed a theory of disorder in polymer crystal lattices, but a description of it is far beyond the scope of this review. Whatever the true state of affairs in polymers, the value of χ attained in them indicates that compared to traditional crystalline materials, they contain considerable disorder.

3. The Morphology of Polymers Crystallized from Solution

3.1. Preliminary Remarks

Polymers exhibit a variety of different habits when they are crystallized from solution. These habits range from relatively simple

* For some properties, such as heat of fusion, this is hard to obtain.

single crystals, which are usually grown from dilute solutions at high temperatures (low undercooling), to complex spherulitic aggregates, which are formed when crystallization takes place from concentrated solutions. Most studies of the morphology of polymers crystallized from solution have been aimed at characterizing the habits they exhibit when they are crystallized from relatively dilute solutions (typically solutions containing less than 0.1 g of polymer in 100 g of solvent). This section will de devoted to summarizing the outcome of such studies. Later we shall have occasion to consider briefly observations stemming from the relatively fewer detailed studies of the crystallization of polymers from concentrated solutions (Section 4.3.2.3).

Before proceeding with a description and discussion of the morphological characteristics of polymers crystallized from dilute solutions it is appropriate to dwell, briefly, on some aspects of the experimental procedures which are involved in crystallizing polymers from solution, as well as on some aspects of the techniques used to study the morphology of solution-crystallized polymers.

3.2. Crystallization Procedures, with Comments on Polydispersity in the Molecular Weight of Polymers and the Incidence of Fractionation during Crystallization

The simplest and most common method which is used to crystallize polymers from solution is to select an appropriate solvent in which the polymer that is to be studied dissolves readily at a high temperature but in which it is insoluble at room temperature. After dissolving the polymer in the hot solvent the resulting solution is then cooled and allowed to crystallize at lower temperatures. By using this method, it is possible to crystallize individual polymers isothermally over a reasonably wide temperature range (about 20°C or so). It may be noted that in the earliest studies of the crystallization of polymers from solution the hot solutions were simply allowed to cool continuously to room temperature. It soon became evident, however, that the crystallization habits that polymers exhibit vary with the crystallization temperature (other things being equal, i.e., solvent, polymer concentration). Consequently, since, generally speaking, crystallization does not proceed to completion and some polymer remains in solution in the mother liquor (particularly at low undercoolings) even after extended periods, it may then be necessary in certain circumstances to either filter the hot preparations[77,78] or

to exchange the mother liquor with fresh solvent which has been previously preheated to the same temperature in order to prevent or minimize the occurrence of further crystallization in a modified form when the preparation is ultimately allowed to cool to room temperature.[79,80] It should be noted that fractionation according to molecular weight, i.e., chain length, occurs during the crystallization of polymers from solution[81–84] and that the chains of shorter length tend to remain in solution more readily than longer ones.* The manifestation of fractionation during the crystallization of polymers from solution is a phenomenon that has been receiving increasing attention in recent years due to its potential as a useful technique to prepare different molecular weight fractions of a polymer and also because an understanding of this phenomenon should in principle provide a basis for predicting the molecular weight composition of crystals or crystalline aggregates grown from solutions containing polymer having a known distribution of chain lengths.[83]

An important refinement in crystallization procedure has been developed in recent years.[90–96] In this so-called "self-seeding procedure" the longest chains play a vital role in the initiation of crystal growth. By a judicious application of this procedure preparations consisting of solution-grown crystals of uniform and predictable sizes and habits have been obtained.[90–93] The potential application of "self-seeded" crystallization for the molecular weight characterization of polymers has also been explored.[94–96]

3.3. Optical and Electron Microscopy, with Comments on the Susceptibility of Polymers to Electron Irradiation

The crystals or more complex crystalline aggregates which are formed when polymers are crystallized from solution are, generally speaking, microscopic in size and the characterization of their morphologies requires the combined use of optical and electron microscopy. A brief but comprehensive summary of the various optical and electron microscopic techniques that have been used in characterizing the habits that polymers exhibit when they are crystal-

* We refer here only to fractionation during crystallization in unstirred solutions. Fractionation is enhanced by stirring. This latter effect and the special morphological consequences of crystallization in stirred polymer solutions will not be dwelt on in this chapter. Studies of these aspects were pioneered by Pennings *et al.*[85–87] in the case of polyethylene in particular. Among other polymers which have been studied with respect to the influence of stirring on fractionation and morphology are isotactic polystyrene[88] and polyvinyl alcohol.[89]

lized from solution has been given by Keller in a relatively recent review on polymer crystals.[15] The best combination of optical and electron microscopic methods of examination varies depending on the type of object being studied. We shall not dwell on the subject of optical microscopy except to point out that phase-contrast optical microscopy may be singled out as invaluable in two major respects in the study of the crystallization habits that polymers exhibit, namely in the characterization of the three-dimensional shapes of objects, by examining them while they are in suspension in liquid, and in the scanning of the populations of objects after they have been deposited and allowed to dry on glass slides. We shall have occasion to indicate or illustrate in appropriate context in succeeding sections how optical microscopy involving the use of either phase-contrast or dark-field optical methods has been brought to bear in the characterization of various aspects of the crystallization habits that polymers adopt when they are crystallized from solution. The ensuing portion of this subsection is devoted to comments concerning the application of electron microscopy and comments on the susceptibility of polymers to electron irradiation.

Obviously, direct examination in the transmission electron microscope is limited to those species of objects grown from solution that are thin enough to be sufficiently "transparent" to the electron beam. The simplest lamellar polymer crystals (see Section 3.4), which are typically ~ 100 Å thick, present no problem in this respect, but replicating techniques must be resorted to in the case of thick objects (Ref. 12, pp. 69–71; Refs. 97–99). Although in such cases the fine structural information which is obtained from an examination of the replicas in the electron microscope is limited to the morphological characteristics of the exterior of the objects, important inferences can usually be derived therefrom concerning the internal structure of the objects.

As for the direct examination of the thinner objects such as the simple single crystals mentioned above, the major problem that arises is the fact that polymers are susceptible to electron irradiation damage. For an excellent tour d'horizon and extensive bibliography on the topic of radiation damage in the context of the application of electron microscopy to the study of polymer morphology, the reader is referred to a recent concise article by Grubb and Keller[100] on the subject of the effect of beam-induced radiation damage in polymers on the images formed in the electron microscope. We shall confine ourselves here to some general comments concerning the well-

established fact that the crystallinity in polymers is destroyed in the course of usual electron microscopy. Briefly, inelastic interactions between irradiating electrons and the long-chain molecules in polymers result in two types of permanent chemical changes, namely chain scission and cross-linking.[101]

In some polymers, such as polyoxymethylene, chain scission is the dominant reaction; the polymer chains revert to volatile monomer and little is left of the crystals after irradiation.[102] A replica of the crystals is, however, preserved when they are coated with metal (as in the usual shadowing procedures used in electron microscopy) prior to irradiation.[80,103,104] In other polymers, of which polyethylene is an example, cross-linking is the dominant reaction, in which case the internal structure of the crystals is transformed into a disordered (amorphous) and intractable three-dimensional network of chemically cross-linked chains. The crystals, however, retain their preirradiated shapes.* Other examples of polymers that belong to the latter class and to which we shall have occasion to refer later in this section are isotactic poly(4-methylpentene-1),[54,79,102] isotactic polystyrene,[106,107] isotactic polypropylene,[108–110] polychlorotrifluoroethylene,[60,111,112] and the polyamides.[113]†

As a consequence of the damage caused by the electron beam, the diffraction patterns exhibited by polymer crystals or crystalline aggregates degenerate progressively and eventually disappear,[114–120] as do all the features in the electron images (both bright field and dark field) that depend on diffraction (elastic scattering) by the crystal lattice. Among these features are variations in contrast due to variations in lattice orientation in different portions of the crystals, moiré patterns, dislocations, and dislocation networks.[102,114,121–126] Thus, although information concerning the habits of crystals can be derived from an examination of samples previously shadowed even after they have been damaged by the electron beam as indicated above, special precautions are necessary in order to preserve the diffraction dependent features of the crystals, since the detection and characterization of these features require the preservation of the lattice in an intact form long enough so as to allow them to be

* See Ref. 12, pp. 79–188. In the case of polyethylene this applies when the crystals have been deposited on the usual carbon film substrate, but not on a collodion substrate.[105]

† Even in cases where the polymer does not volatilize, it is common to shadow the crystals with evaporated metals in order to enhance the visibility of the lateral shapes of the crystals as well as their surface topography.

recorded photographically. The lifetime of these features can be increased by use of low current densities and high beam voltages. There are, however, practical limits to how low the current density can be since if it is too low, not only are long photographic exposures required, but, in addition, visual observation of the samples and hence focusing the images become all the more difficult. As for higher beam voltages, damage is slower the higher the voltage, but elastic scattering and hence image contrast are reduced the higher the voltage and, moreover, the photographic efficiency of electron image plates is also reduced, thus requiring longer exposures.[100,127,128]

Despite the difficulties presented by the susceptibility of polymers to damage by electrons, it has been possible by operating conventional 100-kV electron microscopes at 80 or 100 kV and at low current densities to preserve polymer crystals unimpaired long enough (several minutes) not only to record photographically electron diffraction patterns but also to record dark-field and bright-field diffraction contrast images, moiré patterns, and dislocations.[102,114,121–126] On the whole, however, the recording of diffraction contrast effects, dislocations, etc. has been limited for the most part to low magnifications, usually $\times 5000$ or less, because of the low current densities which have to be used. This is a limitation which may be overcome, however, by use of image intensifiers.[129] The newly developed technique of transmission scanning electron microscopy[130,131] also looms promising in this respect, although its application to polymer crystals remains to be exploited.

3.4. Polymer Crystals

3.4.1. Introductory Remarks

When polymers crystallize from dilute solution, they usually do so in the form of individual microscopic crystals that exhibit varying degrees of morphological complexity depending on the particular polymer and the conditions of crystallization. In the space available, we cannot present an exhaustive review of the growth habits exhibited by the vast number of polymers whose crystallization habits have been studied in varying detail. However, we shall use as examples various polymers that serve to illustrate the growth and morphological features that polymer crystals have in common. Some of these examples will also serve to illustrate that, in some respects, individual

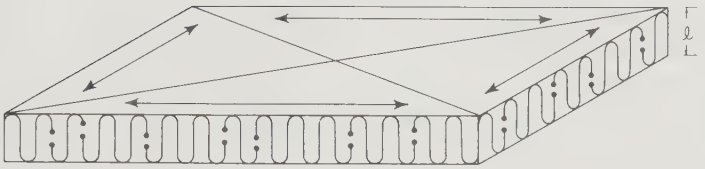

Fig. 8. A drawing of an idealized lamellar chain-folded polymer crystal. The lines on the surface of the crystal delineate four sectors or fold domains. The arrows in each sector indicate the orientation of the planes along which the molecules are folded (the fold planes). In this model the folds in the chains are considered to be sharp, and the fold period regular. The chain ends are also viewed as being incorporated into the crystal.

polymers often exhibit peculiar and indeed idiosyncratic behavior. It will become apparent that the single unique feature common to the crystallization of the overwhelming majority of synthetic polymers is that of chain folding.

The simplest entity obtained when polymers are crystallized from dilute solution is the monolayered crystal. An idealized representation of a monolayered polymer crystal is depicted in Figure 8. Although simplified in many respects, this rendition of a planar lamellar crystal serves as a useful model for introducing some of the fundamental features which characterize the growth and morphology of polymer crystals.

Generally speaking, the lateral dimensions of polymer crystals grown from solution fall in the range 1–50 μm. The habit of the crystals is characteristically lamellar. The thickness (l in Figure 8) of the monolayered crystals varies depending on the degree of undercooling at which crystallization takes place (other things being equal, e.g., solvent, concentration) and is usually in the range $\sim$50–150 Å. A general feature concerning the thickness of the lamellae, which was first reported by Keller and O'Connor[115] in the case of polyethylene, is that they are thicker the higher the temperature of crystallization (Ref. 12, pp. 87–90; Ref. 13, pp. 194–204; Ref. 132). Furthermore, the long axis of the planar zigzagged or helical polymer chains is most frequently found to be oriented at right angles or nearly at right angles to the upper and lower surfaces of the lamellae. In some instances (e.g., in nylon 6.6 crystals[133] and in some species of polyethylene crystals; see Section 3.4.2) the chains are tilted relative to these surfaces, although by not more than $\sim$45°.

The necessity to reconcile the fact that monolayered crystals are only about 100 Å thick with the fact that the extended length of their constituent molecules is several thousand angstroms and that the *c* crystallographic axis is inclined by at most $\sim 45°$ to the surface of the lamellae has led to the acceptance of the by now well-established fact, originally established by Keller in the case of polyethylene,[6] that the molecules in the lamellae are folded back and forth between the upper and lower surfaces (the so-called fold surfaces) of the lamellae, as shown schematically in Figure 8.

These introductory remarks serve to emphasize a fundamental feature of the habits of polymer crystals, namely their characteristically lamellar character. This feature is an inherent consequence of the fact that the polymer chains adopt a folded conformation during the process of crystallization. As originally envisaged, the lateral growth of polymer lamellae was viewed as involving the apposition of fresh molecules in a regularly folded conformation along the lateral growth faces of the crystals, as shown in Figure 8. One feature concerning the folding of the chains which was originally postulated was that the folds are tight, the implication being that the apposition of the chain molecules in a folded conformation along the lateral faces of the lamella involved adjacent reentry as shown in Figure 8 as distinct from nonadjacent reentry (see discussion in Section 3.4.5). Various aspects concerning chain folding in polymer crystals have been the subject of much debate in recent years. Stated in question form, these aspects are: (a) Are the folds in the chains tight or loose? (b) Is the fold period at a given growth temperature regular or not? (c) To what extent does nonadjacent reentry manifest itself, if it does manifest itself at all? (d) Are the chain ends incorporated in the interior of the lamellae or are they excluded and exist as dangling "cilia" at the fold surfaces of the lamellae? We shall not dwell on these various questions at this stage. They will be discussed in Section 3.4.5. It suffices for the present to bear in mind that the thickness of a lamella is governed by the average fold period in its constituent molecules, and that, as evidenced experimentally from (a) a measure in the electron microscope of the lengths of the shadows cast about the periphery of the lamellae when they are shadowed with metal, and (b) from small-angle x-ray diffraction patterns obtained from mats consisting of lamellae oriented with their fold surfaces parallel to the plane of the mat with the incident x-ray beam also oriented parallel to the plane of the mat, the thickness of the lamellae is greater the

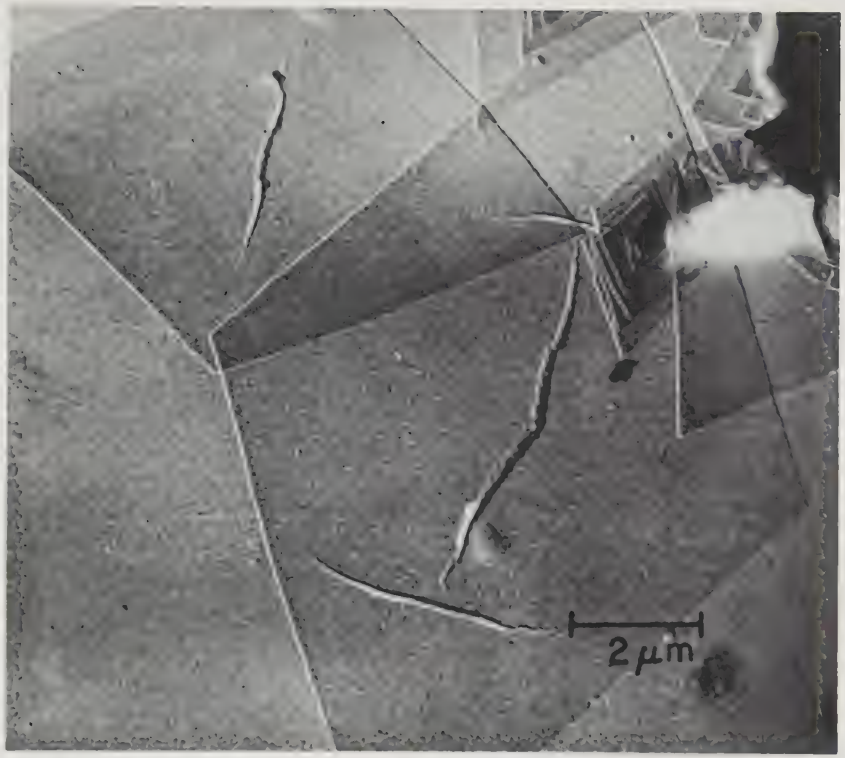

Fig. 9 (a) Electron micrograph of two solution-grown polyethylene crystals which exhibit a lozengelike lateral habit [104] (Picture courtesy of D. H. Reneker and P. H. Geil, reprinted with permission of The American Institute of Physics.) (b) Schematic representation of the type of crystal shown in (a) with the lateral growth faces and sector boundaries indicated. The planes along which folding occurs are parallel to the double-headed arrows in the sectors.

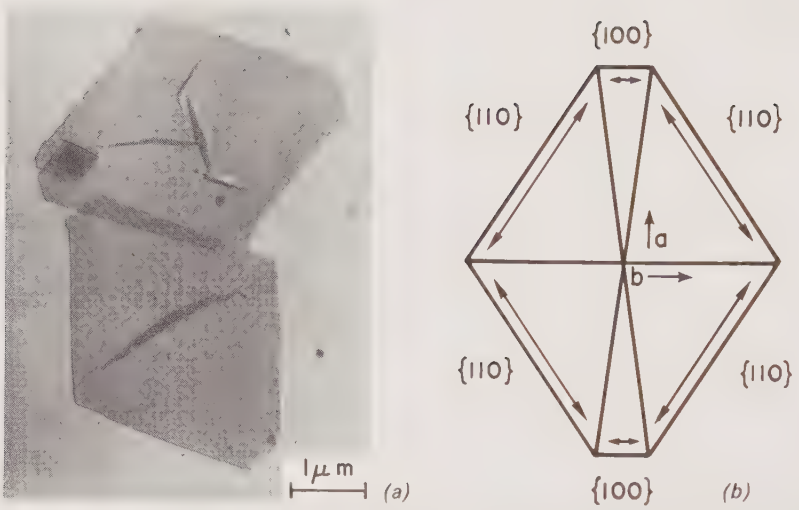

Fig. 10. (a) Electron micrograph of solution-grown polyethylene crystals which exhibit a truncated lozenge lateral habit.[90] (Photograph courtesy A. Keller, reprinted with permission of John Wiley and Sons, Inc.) (b) Schematic representation of the type of crystal shown in (a) with lateral growth faces and sector boundaries indicated. Planes along which folding occurs are parallel to the double-headed arrows.

higher the crystallization temperature, indicating that the average fold period is also correspondingly greater.

Although there are many exceptions (e.g., polyacrylonitrile and polychlorotrifluoroethylene; see Section 3.4.4.3), solution-grown, chain-folded lamellar crystals of many crystallizable synthetic polymers when grown at low undercooling exhibit well-defined lateral growth shapes which reflect the symmetry of the unit cell of the polymer. Such crystals are bound laterally by smooth or essentially smooth low-index growth faces. Thus, for example, in the case of polyethylene (orthorhombic unit cell) the crystals exhibit (depending on the crystallization temperature) a lozenge-like or a truncated lozenge-like lateral shape as shown in Figures 9(a) and 10(a), respectively.[104,134–138] As indicated in Figure 9(b), and as determined from electron diffraction patterns, the lateral growth faces in the lozenge-like crystals are {110} faces, whereas in the case of the truncated type of crystal (shown in Figure 10a), the longer faces are {110} and the shorter faces are (100), as indicated in Figure 10b.*

* It may be noted that the higher the temperature at which polyethylene crystals are formed, the more pronouncedly truncated they are. At high enough temperatures the {100} faces become longer than the {110} faces.[139,140]

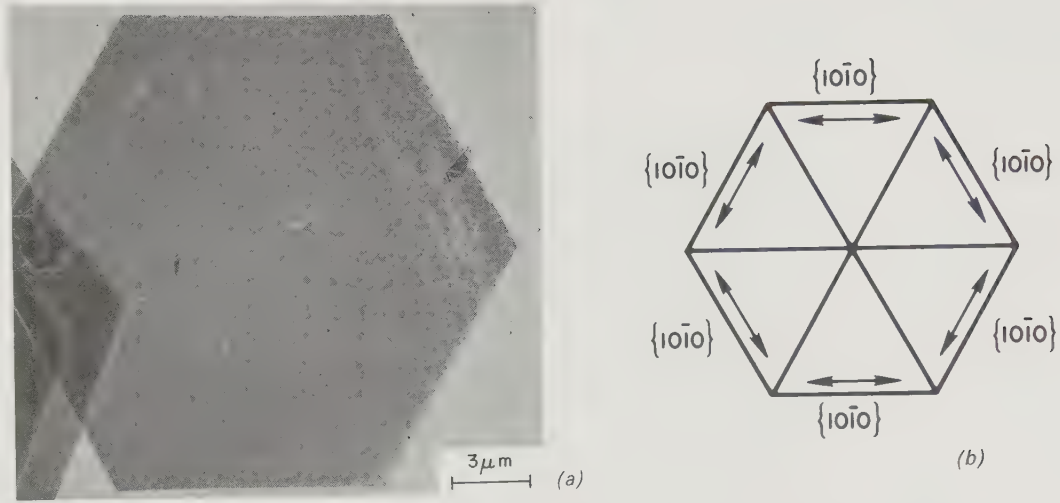

Fig. 11. (a) Electron micrograph of a polyoxymethylene crystal grown from 0.02% solution in orthodichlorobenzene at 140°C (from Khoury and Barnes[80]). (b) Schematic representation of the type of crystal shown in (a) with lateral growth faces, sector boundaries, and orientation of fold planes indicated.

Fig. 12. (a) Phase-contrast optical micrograph of a crystal of poly(4-methylpentene-1) grown at 90°C from 0.1 % solution in an equivolume mixture of xylene and amyl acetate. (b) Electron micrograph depicting a corner (arrow) of a crystal such as that shown in (a). Note the essentially smooth lateral edges. (From Khoury and Barnes[279]) (c) Schematic representation of type of crystal shown in (a) and (b) with lateral growth faces, sector boundaries, and the orientation of the fold planes indicated.

In the case of polyoxymethylene crystals (hexagonal unit cell[141]) the simplest lamellar crystals are hexagonally shaped, as shown in Figure 11, and are bound laterally by $\{10\bar{1}0\}$ faces.[102–104] As a final example, we cite poly(4-methylpentene-1), whose simplest crystals, as shown in Figure 12, are square, in accordance with its tetragonal unit cell.[54] These crystals are bound laterally by $\{100\}$ growth faces, as indicated in Figure 12(c).[54,102] It may be noted that in contrast with Figures 9(a), 10(a), and 11(a), which are electron micrographs, Figure 12(a) is an optical micrograph taken with phase-contrast optics. Our purpose in interjecting this optical micrograph is to illustrate the fact that phase-contrast optical microscopy is a most useful tool for surveying rapidly the nature of polymer crystals grown from solution prior to resorting to more detailed electron microscopic studies. All that is required is to deposit a droplet of the preparation (containing the crystals in suspension) on a glass slide and allowing the solvent to evaporate. The thin crystals are barely if at all visible in the optical microscope using conventional optics. They are readily seen, however, when phase-contrast optics are used, as evidenced in Figure 12(a). An interference optical microscope can also be used for

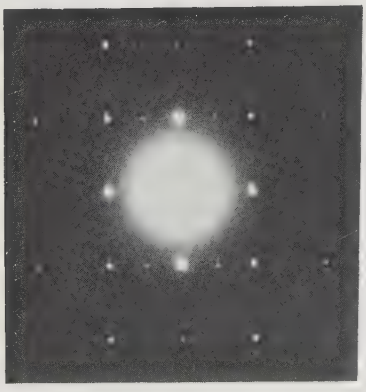

Fig. 13. Electron diffraction pattern obtained from a crystal of poly(4-methylpentene-1) similar to those shown in Fig. 12. The spots correspond to diffraction from $\{hk0\}$ planes, indicating that the molecules are normal or very nearly normal to the surface of the lamellae. The four strong inner spots are reflections from the $\{200\}$ planes.

the same purpose, and such an instrument has an added advantage in that it can be used to measure the thickness of the lamellae.[142] Figure 12(b) is an electron micrograph showing a corner of a crystal of the type shown in Figure 12(a). Figure 13 is an electron diffraction pattern obtained from a crystal such as those shown in Figure 12.

3.4.2. Sectorization in and the Three-Dimensional Shapes of Lamellar Polymer Crystals

Having pointed out in the previous section that two basic features of polymer crystals, namely their lamellar character and the thickness of the lamellae, are directly associated with the incidence of chain folding, we pass on to a consideration of a third feature which is also associated with (or, perhaps more accurately, which is a consequence of) the incidence of chain folding in polymer crystallization. As we have pointed out, the lateral growth of the lamellae occurs by the folding of fresh molecules along the sides of the lamellae. As a result of this manner of growth, the lamellae are inherently subdivided into a number of distinct sectors which are distinguished from one another by the fact that the molecules in each sector are folded along planes parallel to the particular lateral crystal face that subtends the sector. Clearly, as shown schematically in Figures 9(b), 10(b), 11(b), and 12(c), the sector boundaries in the lamellae are defined by the lines joining the corners and the center of the lamellae. The arrows in these figures identify respectively the orientation of the planes along which the molecules are folded in the lozenge-shaped [fold planes {110}] and truncated lozenge-like [fold planes {110} and {200}] polyethylene crystals; in the hexagonal crystals of polyoxymethylene [fold planes $\{10\bar{1}0\}$]; and in the tetragonal crystals of poly(4-methylpentene-1) [fold planes {200}]. The different sectors in chain-folded lamellae are often referred to as fold domains,* a term originally coined by Geil and Reneker.[143] It can be noted in this connection that cleavage occurs between the planes along which the molecules are folded (the fold planes) in the constituent sectors in chain-folded lamellae, i.e., the fold planes in each sector are cleavage planes. This feature, which, as indicated by Keller,[144] was first noticed by Fischer and subsequently by others,[145,146] and which is illustrated in the case of a polyethylene crystal in Figure 14(a) and in a crystal of poly(4-methylpentene-1) in Figure 14(c) (see region marked

* The terms "fold domain" and "sector" will be used synonymously in this chapter.

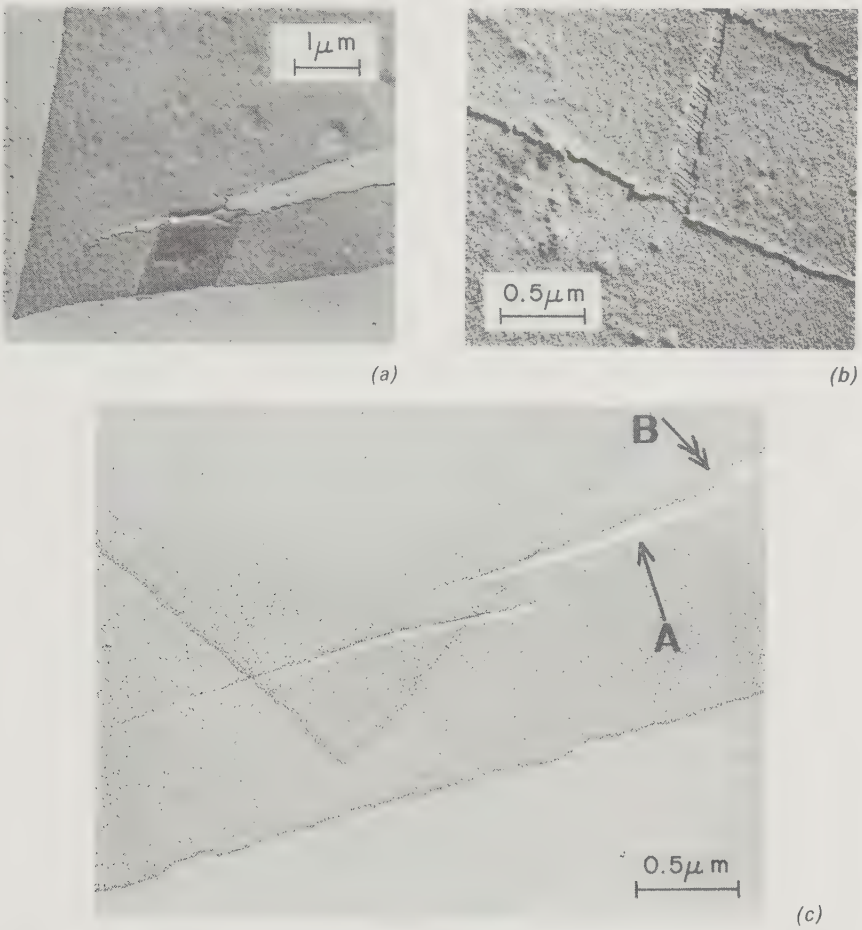

Fig. 14. (a) Electron micrograph showing a crack parallel to the {110} fold planes in a portion of a polyethylene crystal. Note absence of fibrils.[145] (b) Electron micrograph showing a crack which traverses the {110} fold planes in a portion of a polyethylene crystal. Note the fibrils which traverse the crack.[145] (c) Region near an edge of a four-sectored lamella of poly(4-methylpentene-1). Arrow A points to a portion of a crack that runs parallel to the {200} fold planes, which are parallel to the edge of the crystal. No fibrils traverse this portion of the crack. Arrow B points to fine fibrils in the portion of the crack that intersects these planes. (From Khoury and Barnes.[79]) (Photographs (a) and (b) courtesy of V. F. Holland, reprinted with permission of John Wiley and Sons, Inc.)

A), contrasts with the fact that cracks that intersect the fold planes are transversed by thin fibrils (Ref. 12, pp. 450–452; Refs. 145–148), as can be seen in the polyethylene crystal shown in Figure 14(b) and in region B of the poly(4-methylpentene-1) crystal shown in Figure

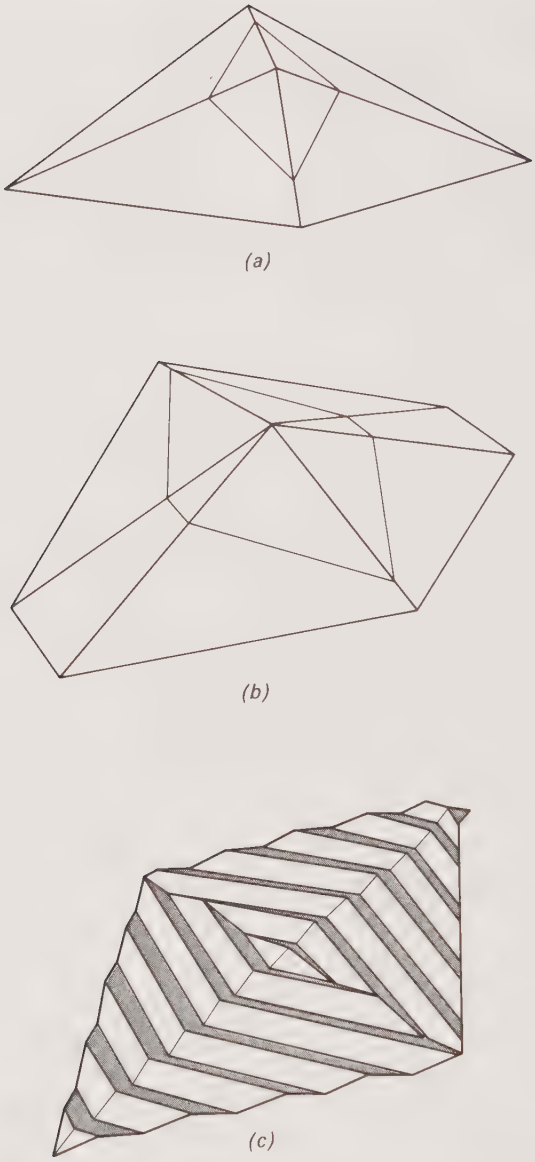

Fig. 15. Schematic representations of nonplanar polyethylene crystals in which the fold surfaces of the sectors which are bounded by {110} growth faces are taken to be {312}. (After Bassett, Frank, and Keller.[137]) (a) Four-sectored pyramidal crystal bounded by {110} growth faces. The lines drawn within the sectors represent the trace of the intersection of the surface of the pyramid with a plane normal to the pyramid axis. (b) Six-sectored hollow pyramidal crystal of polyethylene bounded laterally by {110} (longer) and {100} (shorter) lateral growth faces. The lines drawn within the sectors represent the trace of the intersection of the surface of the pyramid with a plane normal to the pyramid axis. (c) Corrugated crystal bounded laterally by {110} growth faces.

14(c). This latter feature is attributable to the "pulling out" and, at any rate, partial unzipping of folded molecules. The fact that in chain-folded lamellae the planes in each sector (fold domain) that are parallel to the lateral face that subtends the sector are cleavage planes is one of the many features that substantiates the fact that chain folding occurs preferentially along the lateral growth faces and that the crystals consist of distinguishable fold domains. Additional features associated with and reflecting upon the sectorized character of polymer crystals are pointed out below.

For the sake of simplicity in introducing the phenomenon of chain folding, the drawing of the monolayered crystal shown in Figure 8 depicted the lamella as being flat. It also depicted the stems of the molecules as being normal to the "fold surfaces." In actuality, monolayered polymer crystals are often not planar. For example, polyethylene crystals adopt, inter alia, hollow pyramidal shapes. A model due to Bassett, Frank, and Keller[137] of a hollow pyramidal crystal of polyethylene is shown in Figure 15(a). If viewed along a direction parallel to the pyramid axis, such a crystal, in which the molecules are folded along {110} planes, would exhibit a lozenge-shaped profile. The stems of the molecules throughout the crystal are oriented parallel to the pyramid axis (the *c* axis of the crystal); they are therefore inclined to the sloping faces of the pyramid. The magnitude of the inclination of the sloping faces of the pyramid relative to the stems is the same throughout the crystal; its direction in the different sectors differs, however. This latter feature reflects in itself the sectored character of such a chain-folded crystal. The hollow pyramidal character of polyethylene crystals has been attributed to the incidence of regular staggering between the levels of the folds in successive fold planes in each sector. Figure 15(b) represents a model[137] of a hollow pyramidal crystal of polyethylene whose base is six-sided and which corresponds to the truncated type of crystal shown in Figure 10(a). Figure 15(c) represents a corrugated crystal resulting from reversals in the direction of staggering of the chain folds.

The occurrence of fold staggering in polyethylene crystals has been attributed to the bulkiness of the chain folds, the view being that the apposition of folds side by side in a staggered fashion rather than level with one another tends to minimize steric interactions between neighboring folds. The extent of the staggering is such that crystallographic registry is maintained between the stems of the molecules in the interior of the crystals. For detailed discussions on

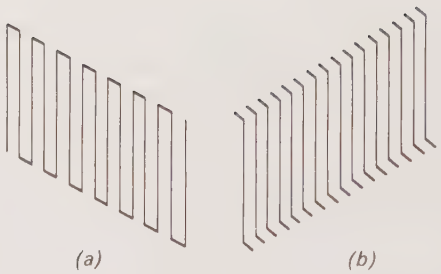

Fig. 16. Illustration of fold staggering in nonplanar polyethylene crystals. (After Keller[144].) (a) Staggering of the folds in an individual fold plane. A view at right angles to the plane. (b) Staggering of the folds in successive fold planes in a sector. The planes are viewed edge-on in this diagram.

the phenomenon of regular fold staggering and its origins in polyethylene crystals the reader is referred to papers by Niegisch and Swan,[135] Reneker and Geil,[104] and Bassett *et al.*[136–138] and to reviews on this subject by Geil (Ref. 12, pp. 108 139) and Keller.[15,144] We will simply indicate here that according to Bassett, Frank, and Keller,[137,138] both in-plane and interplane fold staggering can occur in the {110} fold sectors* of polyethylene crystals, whereas only interplane staggering occurs in the {100}† sectors in such truncated pyramidal crystals as that depicted by the model shown in Figure 15(b). A schematic cross-sectional representation of regular staggering between successive folds along individual fold planes (in-plane fold staggering) is depicted in Figure 16(a); staggering between the folds in successive fold planes (interplane fold staggering) in a hollow pyramidal crystal is depicted in Figure 16(b).[144] In the case of the model shown in Figure 15(a) the surface of the {110} sectors are parallel to the {312} lattice planes. The angle between the normal to these surfaces and the *c* axis of the crystal (the pyramid axis) is 29°. In the case of the truncated type of crystal shown in Figure 15(b) the surfaces of the {110} sectors are also parallel to the {312} lattice planes, whereas the surfaces of the {100} sectors are closely parallel to the {201} lattice planes. Turning to the case of the model of a

* That is, the sectors in which the molecules are folded along {110} planes.
† That is, the sectors in which the molecules are folded along {200} planes.

Fig. 17. Phase-contrast optical micrograph of several nonplanar crystals of polyethylene which had collapsed onto the substrate upon drying. Pleats formed during the drying are indicated by arrows. Similar pleats can be seen, for example in Figure 9.

four-sectored corrugated type of polyethylene crystal, shown in Figure 15(c), in which reversals in stagger occur within each sector, the slanting surface facets are shown as being parallel to the {312} lattice planes.[137] It should be noted, however, that they have been found in actuality to be parallel to the {314} lattice planes.[138]

It should be mentioned that the determination of the as-grown shapes of nonplanar monolayered polymer crystals (and indeed multilayered crystals, see Section 3.4.3) is complicated in some measure by the fact that because they are very thin they readily collapse under the influence of forces due to surface tension when they are deposited and allowed to dry on a flat substrate, as is necessary for examining them in the electron microscope. Thus, for example, the substantial pleats which may be seen in the central portions of the crystals shown in Figures 9(a) and 10(a) and which can also be seen in the optical phase-contrast micrograph shown in Figure 17, are a consequence of the collapse of the crystals. Characterization of the as-grown shapes

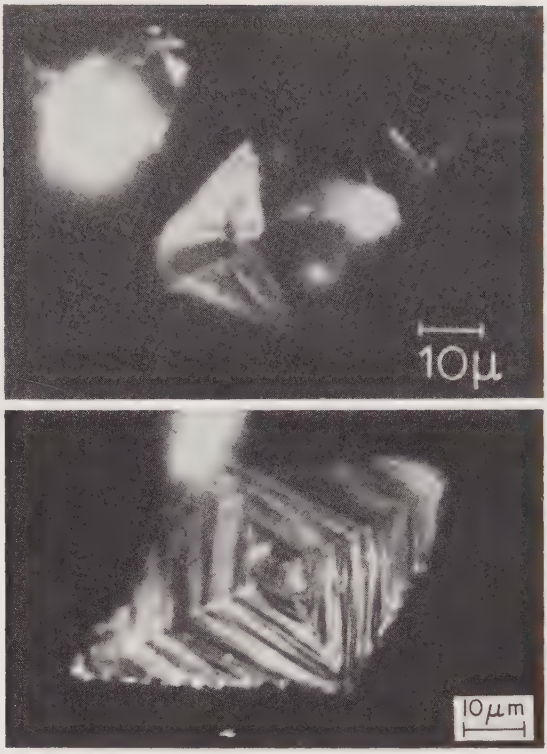

Fig. 18. (a) Dark-field optical micrograph showing a hollow pyramidal crystal of polyethylene akin to the type depicted in Figure 15(b). The crystal is in suspension in liquid.[137] (b) Dark-field optical micrograph showing a corrugated crystal akin to the type shown in Figure 15(c). The crystal is in suspension in liquid.[137] (Courtesy A. Keller, reprinted with permission of Taylor and Francis Ltd., London.)

of nonplanar polymer crystals involves, as exemplified by the detailed studies of Bassett *et al.*[136–138] on polyethylene crystals, and as summarized by Keller,[15] the judicious combination of electron microscopy (electron diffraction, bright-field and dark-field imaging) on collapsed or partially collapsed crystals, and optical microscopy (dark-field illumination or phase-contrast optics), which is used for examining the crystals in the uncollapsed state in different perspectives while they are in suspension in liquid. Dark-field optical micrographs due to Bassett, Frank, and Keller[137] of a hollow pyramidal crystal akin to the model in Figure 15(b) and a corrugated crystal akin to the model in Figure 15(c) are shown in Figures 18(a) and 18(b),

respectively. In these micrographs the crystals are seen as they appear in the uncollapsed state in suspension in liquid.

In addition to the fact that the formation of hollow pyramidal or corrugated polyethylene crystals such as the ones described above clearly reflects the sectored character of these crystals—which morphological feature is, as indicated earlier, a consequence inherent in the phenomenon of chain folding which underlies the formation of polymer crystals—the nonplanar character of the crystals represents in itself yet another morphological consequence of chain folding, due in this case to the bulkiness of the chain folds. In fact, as pointed out earlier, departure from planarity in chain-folded monolayered crystals due to the bulkiness of the chain folds is not an uncommon feature. It is not, however, necessarily associated with the occurrence of regular fold staggering. We shall return to this matter in due course following a brief indication of yet another feature, exemplified in four-sectored lamellae of poly(4-methylpentene-1)[102] and six-sectored lamellae of polyoxymethylene[102] as well as in polyethylene crystals,[15,149] namely the distortion of the unit cell in each of the constituent sectors in the crystals. This feature is also attributable to the bulkiness of the chain folds.

Confining ourselves for the present to the case of poly(4-methylpentene-1), whose unit cell, as pointed out earlier, is tetragonal[54] ($a = b \neq c$, where c is parallel to the axis of the chains), and referring to Figure 12(c), which represents the c-axis projection of a four-sectored crystal of that polymer, it was pointed out earlier that such crystals are bound laterally by {100} faces. The chain molecules in each sector are folded along the {200} planes, which are parallel to the {100} face that subtends each sector. These planes, which are identified in Figure 19 by the thick lines in each sector, will henceforth be referred to as the $\{200\}_f$ planes in order to distinguish them from the orthogonal set of $\{200\}_{nf}$ planes (thin lines in each sector in Figure 19). Ideally, the spacing $d_{\{200\}_f}$ between the $\{200\}_f$ planes in each sector should be equal to the spacing $d_{\{200\}_{nf}}$ between the $\{200\}_{nf}$ planes in each sector. An analysis due to Bassett[102] of moiré patterns exhibited in dark-field electron micrographs of poly(4-methylpentene-1) crystals, which consisted of two overlapping four-sectored, chain-folded layers which were slightly rotated relative to one another about the normal (i.e., the c axis) to the layers, has indicated that there is a difference of $\sim 0.1\,\%$ between $d_{\{200\}_f}$ and $d_{\{200\}_{nf}}$ in each sector in the four-sectored, chain-folded lamellae of this polymer. This disparity in spacing has been attributed to the

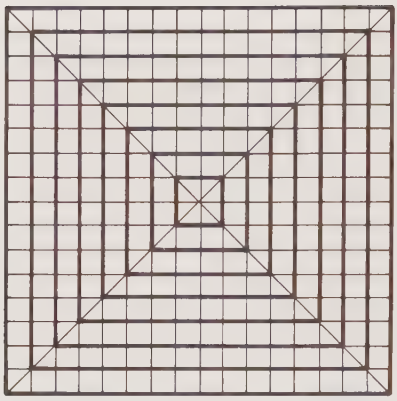

Fig. 19. Schematic representation of a four-sectored crystal of poly(4-methylpentene-1) showing the {200} fold planes and the {200} non-fold planes in each sector. Although the spacings between these two sets of planes in each sector should ideally be equal, the spacing between the fold planes differs by 0.1% from that between the non-fold planes. This has been attributed to the bulkiness of the chain folds.[102]

bulkiness of the chain folds.[102] Similarly, an analysis (also due to Bassett)[102] of moiré patterns exhibited by bilayered crystals of polyoxymethylene, whose constituent layers were six-sectored and rotationally displaced relative to one another, has indicated that the spacing $d_{\{10\bar{1}0\}_f}$ between the $\{10\bar{1}0\}_f$ planes in each sector and the spacing $d_{\{10\bar{1}0\}_{nf}}$ between the other two sets of $(10\bar{1}0)_{nf}$ planes in each sector differ by $\sim 0.3\%$, which difference is also attributable to the bulkiness of the chain folds. In addition, Keller has reported that a sector-by-sector exploration of the electron diffraction patterns exhibited by certain truncated crystals of polyethylene indicated, in effect, that there is a disparity in spacing between the $\{110\}_f$ and the $\{110\}_{nf}$ planes in the $\{110\}$ sectors in these crystals.[15] Bassett has also deduced from moiré patterns the existence of a unit cell distortion in the constituent sectors of polyethylene crystals.[149]

The systematic character of the distortions of the unit cell in each sector resulting from the differences in spacing indicated above

between families of planes that would ideally exhibit equivalent spacings, but whose spacings differ in actuality according to whether or not they are fold or nonfold planes, evidences in itself the sectored character of the crystals. These unit cell distortions, which are attributable to the bulkiness of the chain folds, are also of interest in another connection, which was mentioned earlier, namely the fact that the manifestation of nonplanarity in polymer crystals need not necessarily result from or involve regular fold staggering. Four-sectored lamellae of poly(4-methylpentene-1) are a case in point, and we now discuss this.

As originally indicated by Bassett *et al.*,[150] these crystals are not perfectly flat. Their departure from planarity is, however, extremely small (see below). Indeed, examination of such crystals in different

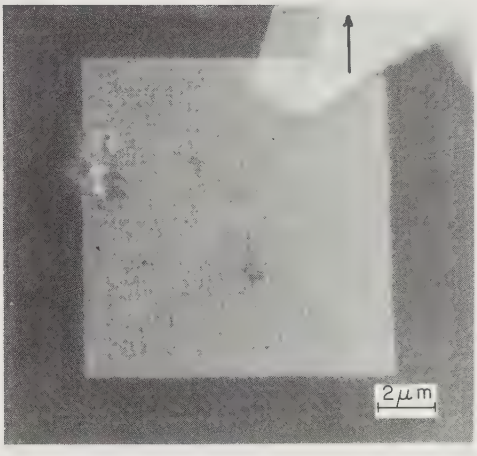

(a)

(b)

Fig. 20. (a) Dark-field electron micrograph of a four-sectored crystal of poly(4-methylpentene-1). The planes imaged in this micrograph are the {200} planes parallel to the arrow. (From Khoury and Barnes.[79]) (b) Schematic representation identifying the individual sectors in (a). (See text.)

perspectives under the optical microscope while they are in suspension in liquid reveals no resolvable departure from planarity.[79,150] The deduction due to Bassett *et al.*[150] that such four-sectored lamellae are not perfectly planar stems from the diffraction contrast characteristics exhibited by these crystals in dark-field electron micrographs formed by imaging the {200} planes.[102,150] A dark-field electron micrograph of a four-sectored monolayer crystal of poly(4-methylpentene-1) is shown in Figure 20(a). The {200} planes that were imaged in this case were those that run vertically in the field of view as indicated by the arrow in the top right-hand corner of the micrograph. The four-sectored character of the crystal is clearly revealed in this dark-field image, in which it can be readily seen that the upper and lower sectors (s_1 and s_2, Figure 20b), in which the {200} planes that were imaged are not fold planes, are darker than the other two sectors (s_3 and s_4, Figure 20b), in which the {200} planes that are imaged are fold planes. The contrast in appearance between the pairs of sectors would be reversed if the {200} planes running horizontally in Figure 20(a) had been imaged. Briefly, these systematic variations in diffraction contrast, which have been attributed to a slight tilting of the molecular stems in each sector about a direction normal to the corresponding outer edge (i.e., the {100} growth face) that subtends each sector, have been adduced as evidence that the crystals as-grown possess a slight "conicalness" in shape[150] (see also discussion in Ref. 79). This latter feature has been attributed to a slight buckling of those crystals, which arises as a result of stresses that occur in the lattice at the sector boundaries where the mismatch in spacing between the $\{200\}_f$ planes in one sector and the $\{200\}_{nf}$ planes in adjoining ones must be accommodated, as well as due to stresses at the fold surfaces.[79,150] Assuming that $d_{\{200\}_f} > d_{\{200\}_{nf}}$ in the sectors,* and given that these interplanar spacings differ by $\sim 0.1\%$,[102] it can be roughly "reconstructed" that the resulting buckled lamella, as grown, would be slightly conical in character (one visualizes a cone which is slightly rounded at the apex, with the stems of the molecules oriented normal to the surface throughout) and have an angle of elevation of $\sim 2°$,[79,150] which is small enough to escape resolution under the optical microscope when the crystals are examined in suspension in liquid.

* It is not possible to distinguish from the moiré patterns exhibited by bilayer crystals which of these spacings is the larger. All that can be derived from the patterns is the difference in magnitude between $d_{\{200\}_f}$ and $d_{\{200\}_{nf}}$.

Summarizing the remarks presented in the preceding paragraphs concerning the origins of the nonplanar character of monolayered polymer crystals, we see that the departure from planarity in the crystals is attributable to the bulkiness of the chain folds. Nonplanarity may result either as a consequence of the incidence of the regular staggering of the folds, or as a consequence of slight buckling associated with a distortion (due to the folds) of the unit cell in the constituent sectors of the crystals, or as a consequence of both these effects acting together. In this last case, which probably obtains in polyethylene hollow pyramidal crystals (see, e.g., Ref. 150), the nonplanarity due to fold staggering is overwhelmingly greater than that due to unit cell distortion. In addition to poly(4-methylpentene-1), six-sectored crystals of polyoxymethylene of the type shown in Figure 11 are another example in which slight nonplanarity is attributable to buckling associated with the incidence of unit cell distortion caused by bulkiness of the chain folds.[80]

3.4.3. Multilayered Crystals

We have confined ourselves in the examples illustrated and discussed above to a description of monolayered polymer crystals, i.e., crystals that are one chain-folded layer thick. Such crystals are typically formed at low undercoolings from dilute solutions. As we have pointed out, the thickness of such chain-folded polymer lamellae usually falls in the range 50–150 Å and is governed by the conditions of undercooling that prevail during their growth in that they are thicker (i.e., the fold period is larger), the smaller the undercooling. It should be emphasized, however, that while the thickness of *individual* chain-folded polymer lamellae grown from solution at a given undercooling is inherently limited by the incidence of chain folding, the growth of polymer crystals is not restricted to lateral (two-dimensional) propagation. Thus the formation of "multilayered" crystals consisting of several superposed chain-folded layers (which layers are all of equal thickness) is also frequently observed at low undercoolings. Indeed the formation of monolayered and multilayered polymer crystals from dilute solutions in one and the same preparation at low undercoolings is not unusual. It should be pointed out, however, that the formation of multilayered crystals is particularly characteristic of growth at high undercoolings, which, as we shall see in Section 3.4.4.2, also favor the manifestation of dendritic habits.

Confining ourselves for the present to the formation of multilayered crystals at low undercoolings, it can be noted that the formation of additional chain-folded layers upon the basal layer in multilayered crystals usually originates from screw dislocations situated at or near the center of the basal layer. Through the agency of these dislocations, whose Burgers vector is parallel to the stems of the folded molecules and is equal to the fold period, the overgrowth layers evolve upon the fold surfaces of the basal layer either as spiraling ramps (growth from a single or several vicinal screw dislocations having the same hand) or as successive "closed" terraces (growth from a pair of vicinal screw dislocations of opposite hand). These patterns of development of additional chain-folded layers in polymer crystals through the agency of screw dislocations are akin to those manifested in crystals of nonpolymeric materials.[151] Examples of multilayered crystals of polyoxymethylene are shown in Figure 21. It should be noted that, as in the case of monolayered crystals, the consecutive chain-folded layers in multilayered polymer crystals are also sectored in character.

Various aspects of the formation of multilayered polymer crystals through the agency of screw dislocations have been described and discussed by several authors.[103,152-154] Among these aspects are (1) the fact that whereas consecutive terraces in multilayered crystals of a given polymer are in crystallographic registry in some crystals, they are irregularly or regularly rotated relative to one another in other crystals of the same polymer,[153] and (2) the fact that "splaying" between layers is manifested in some crystals but not in others.[153,154]

We shall only dwell briefly on the two features mentioned above, which have been observed to occur variously in some multilayered crystals, namely the incidence of "splaying" between their constituent terraces and the occurrence of regular rotations between consecutive terraces relative to one another. This latter feature has been discussed in some detail with particular reference to some chain-folded multilayered crystals formed from solutions of relatively low-molecular-weight polyethylene in xylene, in which case terrace rotation was manifested most frequently and dramatically, as illustrated in the electron micrograph of a so-called "four-leaf"-type crystal shown in Figure 22 due to Keller and Mitsuhashi.[153] Briefly, examination under the phase-contrast optical microscope of the "four-leaf" type of crystals in edge-on perspective while they were in suspension in liquid showed that they were constituted of two stacks of overlapping terraces

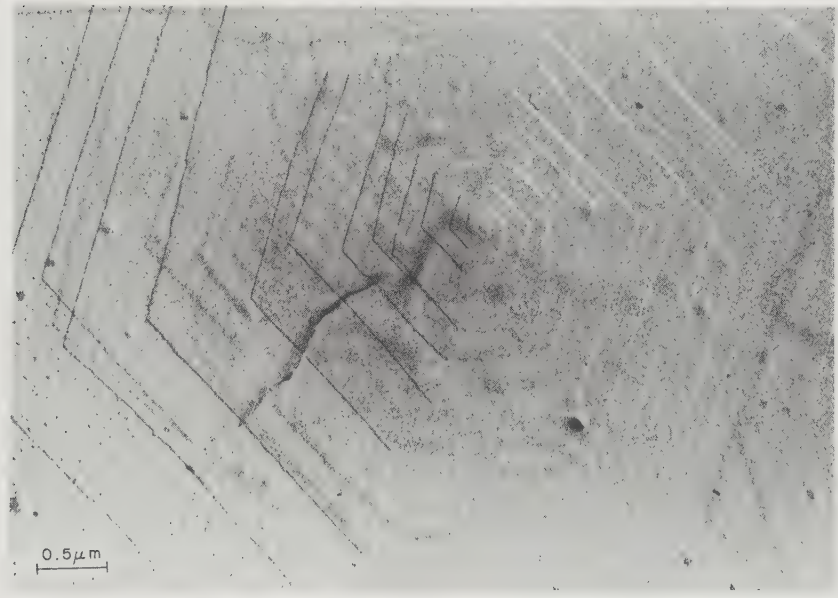

(a)

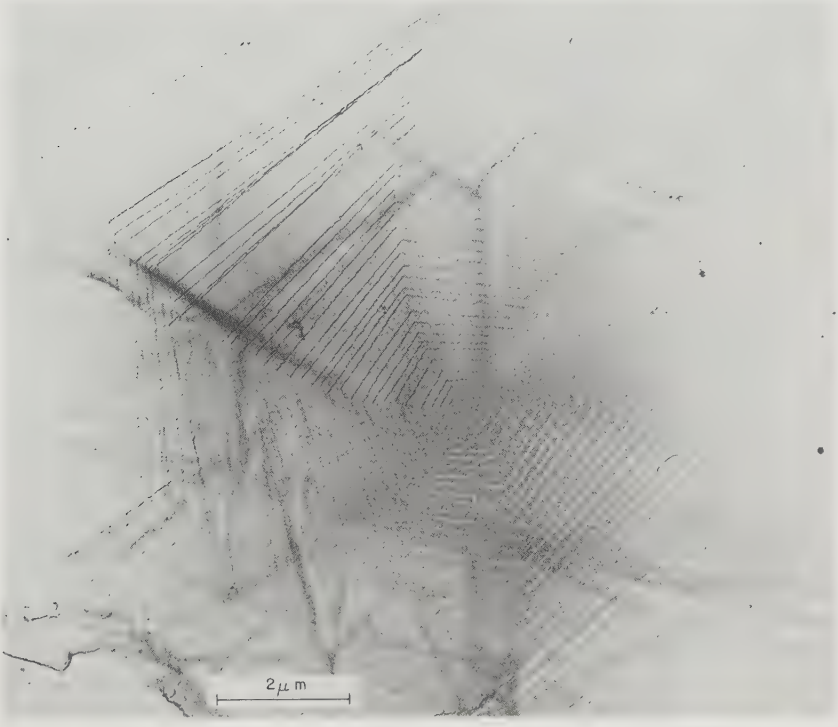

(b)

Fig. 21. Electron micrographs of multilayered crystals of polyoxymethylene showing spiral-like development of successive layers through the agency of screw dislocations. Note the rotation of successive layers in (b). (From Khoury and Barnes.[80])

Fig. 22. Electron micrograph of a replica of a multilayered crystal of polyethylene with the successive layers rotated relative to one another[153]; Keller has called these crystals "four-leaf" crystals. (Photograph courtesy A. Keller, reprinted with permission of Dietrich Steinkopff Verlag, Darmstadt.)

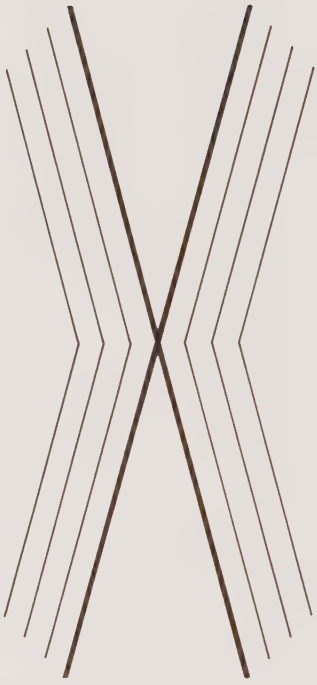

Fig. 23. Schematic representation of an edge-on view depicting the incidence of splaying in a multilayered crystal such as that shown in Figure 22. (From Keller,[153] reprinted with permission of Dietrich Steinkopff Verlag, Darmstadt.)

splaying outward from a common center as two shallow cones in contact at their apices, as depicted schematically in Figure 23. Considerations have been advanced by Keller[153] to the effect that the occurrence of splaying between the two stacks of terraces (as distinct from more complex forms of splaying[154]) and the incidence of regular terrace rotation of the type illustrated above are interrelated features. Keller has proposed a mechanism concerning how these two features arise, which invokes shear transformation in the terraces

following primary growth. It should be noted in this connection that the absence of both splaying and regular terrace rotations in other multilayered crystals formed in the same polyethylene preparations that yielded the type of crystals shown in Figure 22 was adduced as evidence supporting the view that splaying and terrace rotation are indeed interrelated features.[153] For additional details concerning a discussion of their origins and the variations in their manifestation the reader is referred to Keller's paper, in which unanswered aspects concerning the manifestation of splaying are also pointed out.[153]

The type of multilayered crystal we have described above consists of numerous consecutive folded chain terraces which developed through the agency of screw dislocations situated at and/or close to the center of the crystals, i.e., the dislocations were either present in the original nucleus from which the crystals evolved or were generated during the early stages of the subsequent growth of the nucleus. As we shall see in due course (Section 3.3.4.2), this contrasts with the case of, for example, dendritic crystals grown at relatively high undercoolings, in which new screw-dislocation-like defects giving rise to new terraces are generated at the periphery of the developing crystals throughout their growth.

3.4.4. Aspects of the Diversity of the Lateral Growth Habits and Sectored Characters of Chain-Folded Crystals

3.4.4.1. Introductory Comments

The scope of our description of the growth habits and morphologies of solution-grown, chain-folded polymer crystals has so far been limited to relatively simple examples of monolayer and multilayered crystals in which the lamellae were bound laterally by smooth, low-index growth faces and exhibited simple polygonal lateral shapes free of reentrant corners. These latter two features are not to be construed as being generally characteristic features of polymer crystal lamellae. For example, (a) crystals of linear polyethylene exhibit dendritic lateral modes of development when they are grown at high undercoolings,[70,77,143,155] (b) lamellae of polyacrylonitrile exhibit finely serrated and somewhat irregular elliptical outlines irrespective (as far as is known) of the conditions of undercooling at which growth takes place,[156–159] and (c) whereas lamellae of isotactic polystyrene exhibit regular hexagonal shapes when they are

grown from a poor solvent,[107] crystallization from good solvents yields lamellae that, although they are basically hexagonal in shape, exhibit rounded and irregular outlines.[106] These diversities (and others) in the lateral growth habits exhibited by lamellar polymer crystals and their implications will be briefly considered and discussed in subsequent subsections. The formation and characteristics of lamellar crystals exhibiting dendritic lateral modes of growth are described in Section 3.4.4.2. The manifestation of "irregular" lateral growth habits and their origins are the subjects of Section 3.4.4.3.

3.4.4.2. Dendritic Lateral Growth Habits

As the temperature at which polyethylene crystals are grown from xylene solutions is decreased (other factors being kept equal, i.e., the molecular weight of the polymer, its concentration, the solvent used), the lateral growth habit of the crystals changes progressively until eventually the development of (100) faces is totally suppressed and four-sectored, lozenge-shaped crystals bound laterally by (110) faces are formed. Crystallization at even lower temperatures leads to further changes in the lateral growth habit of polyethylene crystals. Thus at sufficiently high undercoolings a distinct change occurs from the aforementioned lozenge habit to dendritic habits. Various aspects of the formation and growth characteristics of dendritic crystals of polyethylene have been described and discussed in several papers, notably by Geil and Reneker,[143] Bassett and Keller,[77] Fischer and Lorenz,[70] Wunderlich *et al.*,[155] and Keith.[160] We shall not attempt to describe in what follows differences in detail between the various species of polyethylene dendrites formed at different undercoolings from different solvents. Rather, we shall limit ourselves to indicating in broad terms those growth features that distinguish polyethylene dendrites from the simpler polyethylene crystals described in Sections 3.4.1 and 3.4.2. We shall, however, illustrate and discuss these features with reference to rather simple polyethylene dendrites grown from dilute solutions of the polymer in xylene. It bears noting in this latter connection that the transition in lateral crystal habit from lozenge-shaped to dendritic growth in the case of crystallization from xylene occurs at a lower temperature the lower the molecular weight of the polymer and, broadly speaking, manifests itself at $\sim 80°C$ for samples whose molecular weight is greater than 10,000.[155]

Polyethylene dendrites are usually multilayered. Before dwelling specifically on the characteristics of dendrites grown from xylene

solutions, the following growth features that distinguish the habits of polyethylene dendrites in general from the habits exhibited by the simpler crystals of polyethylene discussed earlier may be noted. (a) The periphery of the constituent lamellae in the dendrites is distinctly microfaceted. (b) The nucleation of new fold planes (i.e., new strips of folded molecules) at the periphery of the lamellae occurs preferentially at protruding corners. (c) During the course of the development of the microfaceted basal lamella, screw-dislocation-like defects are generated intermittently at the periphery of the lamella. These defects, which are generated at reentrant corners, act as sources from which additional chain-folded terraces develop in a spiral fashion upon both surfaces of the basal lamella. These three features, which are interrelated, are discussed briefly below with reference to their manifestation in dendrites grown from xylene solutions.

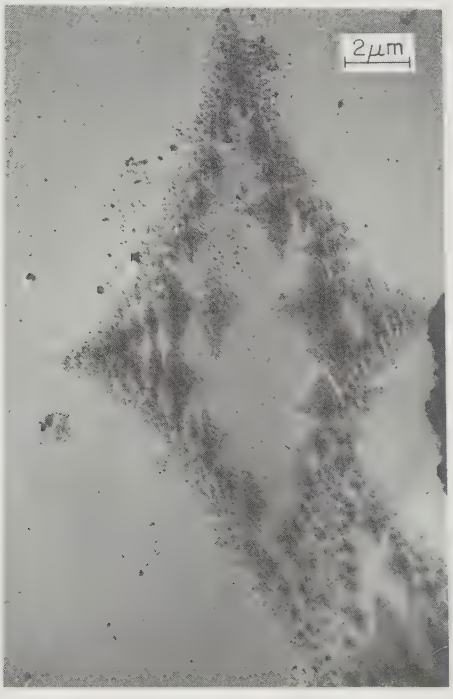

Fig. 24. Electron micrograph of a dendritic crystal of polyethylene.[77] (Photograph courtesy A. Keller, reprinted with permission of Taylor and Francis Ltd., London.)

An example of a dendritic crystal of polyethylene grown from xylene is shown in Figure 24, and a portion of another dendritic crystal also grown from xylene is shown in Figure 25(a), in which part of the microfaceted periphery of the basal lamella (see arrows *B*) can be clearly seen, as can terraces which evolved through the agency of screw-dislocation-like defects in the basal lamella. A view at higher magnification of the region outlined in Figure 25(a) is shown in Figure 25(b), in which the microfaceted character of the periphery of the larger terraces which developed upon the basal lamella can be clearly seen (e.g., arrows *C* and *D*).

An idealized schematic representation of the lateral habit of a relatively simple type of dendritic lamella of polyethylene of the type grown from xylene is depicted in Figure 26(a) (*E″F″G″H″*), where it is shown in relation to the four-sectored lozenge habit (*EFGH*) exhibited by lamellae formed at relatively lower undercoolings. The reentrant and protruding corners at the periphery of dendritic lamellae grown from xylene are subtended by {110} facets[77,143] (and in some cases apparently by {310} facets[77]) along which the polymer chains fold. Consequently, each microfacet subtends a microsector (fold domain) in the interior of the lamella, in which microsector the molecules are folded along the {110} (or perhaps sometimes {310}) planes that are parallel to the microfacet. In short, one of the consequences of the incidence of microfaceting is that dendritic lamellae possess a multisectored fine structure,[77,143] i.e., they consist of a multiplicity of fold domains as shown in Figure 26(a) in contrast with the four-sectored character of the lozenge-shaped lamellae.

In addition to the incidence of microfaceting, the lateral habit of dendritic lamellae grown from solutions of polyethylene in xylene is characterized by the manifestation of preferential growth parallel to the *a* axis (i.e., the [100] direction). The ratio of the principal axes (i.e., the ratio of the length of the longer dendrite diagonal, which is parallel to [100], to the length of the shorter diagonal, which is parallel to [010]) is greater than the ratio of the corresponding diagonals in the four-sectored lozenges in which the axial ratio is equal to a/b ($=1.495$), where $a = 7.36$ Å and $b = 4.92$ Å are the unit cell axes.[49] Thus, for example, the ratio of the lengths of the longer and shorter diagonals in the dendritic crystal shown in Figure 24 is ~ 1.7, and in the case of the larger dendritic terraces in Figure 25(a) the ratio is ~ 2.2.

Another characteristic, which we pointed out earlier, concerning the development of dendritic crystals of polyethylene is that screw-

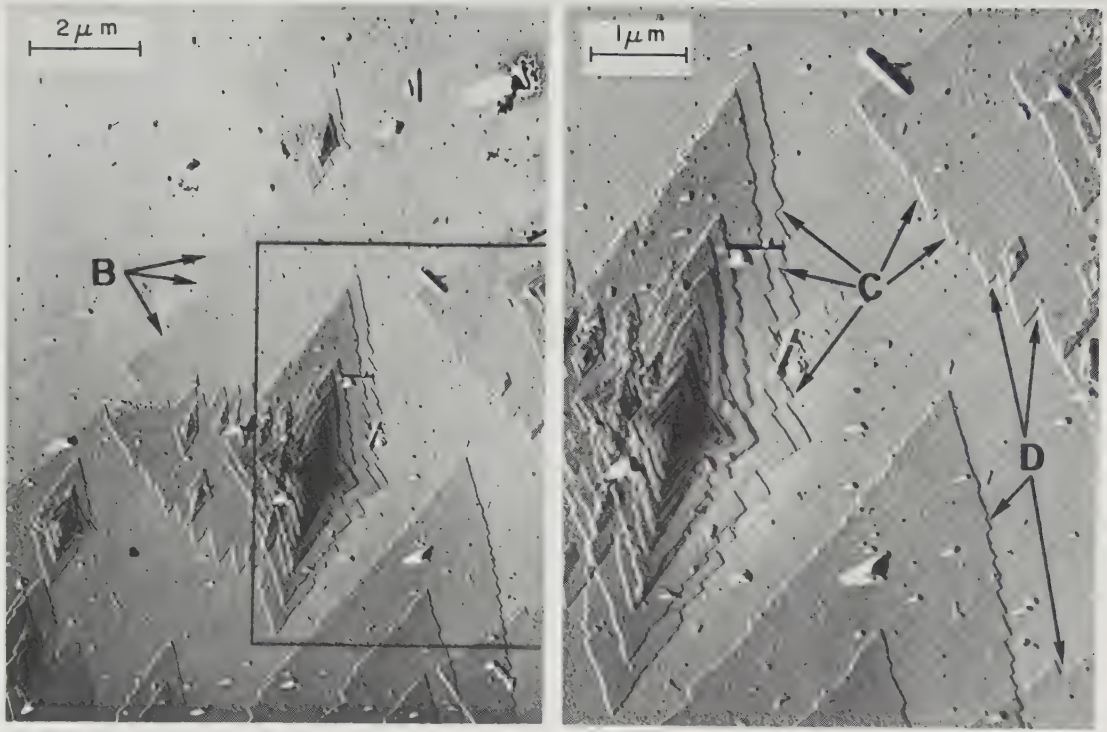

Fig. 25. (a) Electron micrograph of a portion of a dendritic crystal of polyethylene.[161] Arrows B point to microfaceted periphery of the basal lamella. The formation upon the basal lamella of additional terraces which developed through the agency of screw dislocations can also be seen. (b) A view at higher magnification of the region outlined in (a). Arrows C and D point to microfaceting at the sides of some of the larger terraces which developed upon the basal lamella.

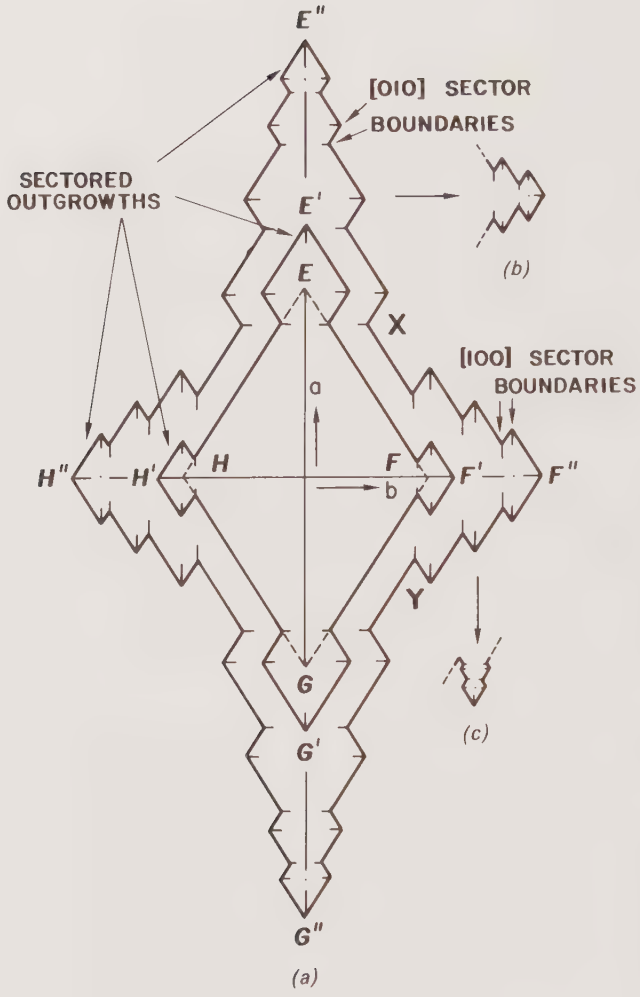

Fig. 26. (a) Schematic representation of the development of a multisectored dendritic lamella of polyethylene. *EFGH* represents a four-sectored, lozenge-shaped precursor crystal growing under conditions which favor the preferential nucleation of new fold planes at its corners, resulting in the development of sectored outgrowths (E', F', G', H') at these corners. $E''F''G''H''$ is an idealized rendition of the microfaceted profile and the multisectored character of the dendrite resulting from the successive generation of new sectored outgrowths at the four leading corners of the developing lamella. (b, c) Development of new sectored outgrowths from subsidiary corners at the periphery (e.g., along $E''X$, $F''Y$) of the dendritic lamella. (See text.)

dislocation-like defects giving rise to the development of spiral terraces on both sides of the basal lamella are generated intermittently at reentrant corners at the periphery of the lamella throughout the course of its growth. This contrasts with the multilayered crystals described previously (Section 3.4.3), in which the occurrence of screw dislocations giving rise to the formation of additional terraces upon the basal lamella only occurred in its initially formed central region. Some considerations which have been advanced concerning the cause(s) of the generation of screw-dislocation-like defects at the reentrant corners of the dendritic lamellae of polyethylene are indicated below.

There exists a body of evidence[77,143,160] which indicates that the folds in the constituent microsectors in multisectored dendritic lamellae of polyethylene are staggered, as is the case in the constituent sectors of the simpler polyethylene pyramidal crystals discussed in Section 3.4.2. On the basis of this evidence it can be readily concluded that dendritic lamellae possess in the uncollapsed state a complex puckered surface due to the differences in the direction of inclination of the surface of the lamella from one microsector to the next. Bassett and Keller[77] and Keith[160] have pointed out that there is an ideal orientation for the boundary between any pair of adjacent microsectors (i.e., microsectors subtended by contiguous microfacets) that allows the inclined surfaces of the microsectors to meet in register. This ideal orientation is [010] for microsectors in region ($E''X$) in Figure 26(a) and [100] in region ($F''Y$) in the same figure. If the boundary between microsectors departs from one or the other of these ideal orientations, a ledge will be generated which acts as a nucleus from which new terraces develop in a spiral-like fashion.[77,160] The occurrence of deviations in the orientation of the boundary between microsectors from the ideal orientations, and hence the creation of ledges which promote the development of new chain-folded terraces, has been attributed to imbalances in the outward growth of contiguous microfacets which subtend reentrant corners. This matter has been discussed at some length by Keith,[160] whose paper should be consulted for further details. The reader is also referred to a paper by Geil and Reneker[143] in which other possible ways that screw-dislocation-like defects may be generated at the periphery of dendritic chain-folded lamellae are considered.

The transition from the lozenge habit to dendritic growth that occurs at high enough undercoolings evidences that under these conditions diffusion becomes a controlling factor in the lateral

development of the lamellae, in contrast to growth at low undercoolings, which is controlled by nucleation processes.[11,162–166] In diffusion-controlled growth, crystal geometry is a factor that influences the pattern of subsequent growth. Growth tends to occur preferentially at "protruding" corners at the periphery of the lamellar substrate due to the closer accessibility of these corners to oncoming molecules as well as due to the more rapid dissipation of heat (of crystallization) from the corners to the surrounding medium.[77,143] The microfaceted character of the periphery of the dendritic lamellae is a direct consequence of the fact that new fold planes are nucleated preferentially at the leading corners of the developing lamellae (e.g., $E \ldots E''$, $F \ldots F''$, in Figure 26a), which preferential nucleation results in the development of new sectored outgrowths at these corners, as pointed out in Figure 26(a). At sufficiently high undercoolings the subsidiary protruding corners at the sides of the dendrite, e.g., along

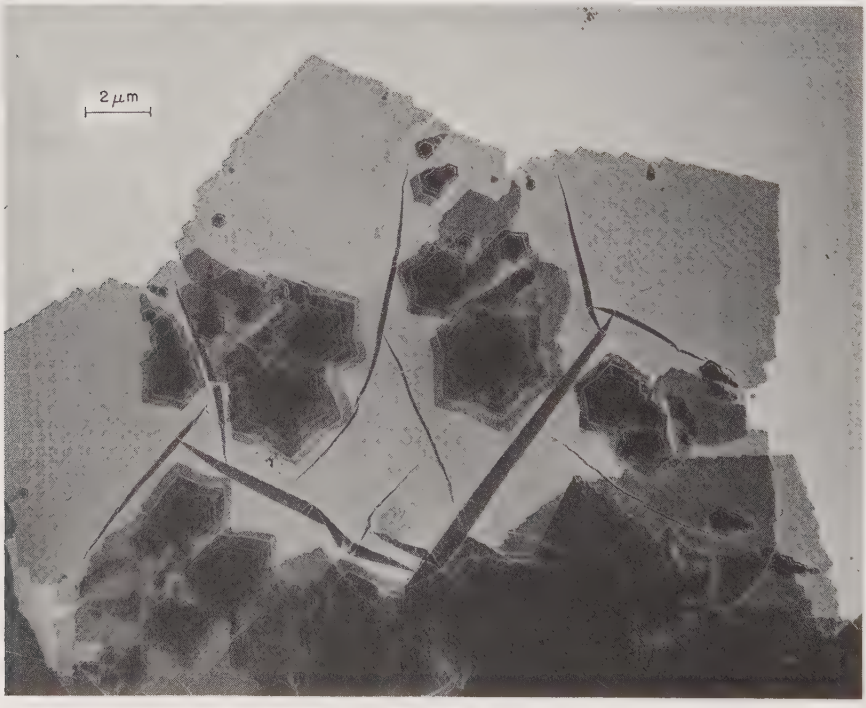

Fig. 27. Electron micrograph of a star-shaped dendritic crystal of polyoxymethylene grown from a 0.02% solution in orthodichlorobenzene cooled to 114°C. (From Ref. 80.)

($E''X$) and ($F''Y$), also become sites of preferential nucleation, with the result that new sectored outgrowths also develop about these corners, as depicted schematically in Figures 26(b) and 26(c), respectively (see, e.g., Ref. 143).

It is fair to say that the number of well-documented cases of polymers whose crystals exhibit simple lateral polygonal habits at low undercoolings and distinctly dendritic habits at high undercoolings is limited. The case of polyoxymethylene is well documented.[80,104] An example of a dendritic crystal of polyoxymethylene is shown in Figure 27. The microfaceted character of the basal lamella and its starlike overall profile are evident, as are the several families of terraces originating from screw-dislocation-like defects generated at the periphery of the basal lamella during its growth. These features contrast with the hexagonal habit of lamellae grown at relatively low undercoolings (Figure 11), as well as with the nature of the multilayered crystals formed at low undercoolings (Figure 21). The manifestation of dendritic growth in cellulose triacetate crystals has been reported by Manley,[167] and incipient dendritic growth in a 6 nylon crystal appears in a photomicrograph by Geil (see Figure 2 in Ref. 113).

3.4.4.3. Irregular or Ill-Defined Lateral Growth Habits in Chain-Folded Polymer Crystals

We mean by "irregular" or "ill-defined" lateral growth habits that the lamellar crystals either do not exhibit simple geometric lateral shapes, i.e., they are not bounded laterally by smooth, well-defined growth faces, nor, alternatively, do they exhibit crystallographically distinguishable microfaceting. There are, in fact, numerous examples in the literature of solution-grown polymer crystals whose periphery is rounded in character and is often serrated on such a fine scale that the occurrence of crystallographically distinguishable microfaceting, if any, is difficult to ascertain with any confidence. In several instances the manifestation of irregular lateral habits is found even in crystals formed under conditions that favor slow growth. Among the polymers whose solution-grown, chain-folded lamellae exhibit irregular or ill-defined lateral growth habits are various homopolymers having low tacticity, such as free radical polymerized polyacrylonitrile[156-159] (see Figure 28), polychlorotrifluoroethylene[60,111,112] (see Figure 29), and polyvinylchloride.[168] Irregular lateral growth habits are also exhibited by branched

Fig. 28. Electron micrograph depicting several oblong lamellar crystals of polyacrylonitrile.[156] Note ill-defined nature of the lateral shape of the crystals. (Photograph courtesy V. F. Holland, reprinted with permission of Interscience Publishers.)

polyethylene,[169,170] randomly chlorinated polyethylene,[171,172] and random copolymers of ethylene with either propylene or butene-1.[173,174] In view of the variously irregular nature of the configuration of the chains in all these polymers, it is not unreasonable to attribute the irregular lateral habits exhibited by their crystals as being an inherent consequence of the configurational irregularities in their constituent chains, due to the influence of these irregularities upon the packing of the chain stems side by side and/or the manner in which the molecules fold. It should be noted, however, that the formation of irregularly shaped lamellae is not limited to polymers whose constituent chains are either highly branched or possess poor tacticity. Isotactic polystyrene is an interesting example in this regard. Thus when this polymer is crystallized from a poor solvent[107] it does so in the form of simple hexagonal crystals such as that shown in Figure 30(a), whereas when it is crystallized from good solvents (at growth rates which are much slower than those associated with the

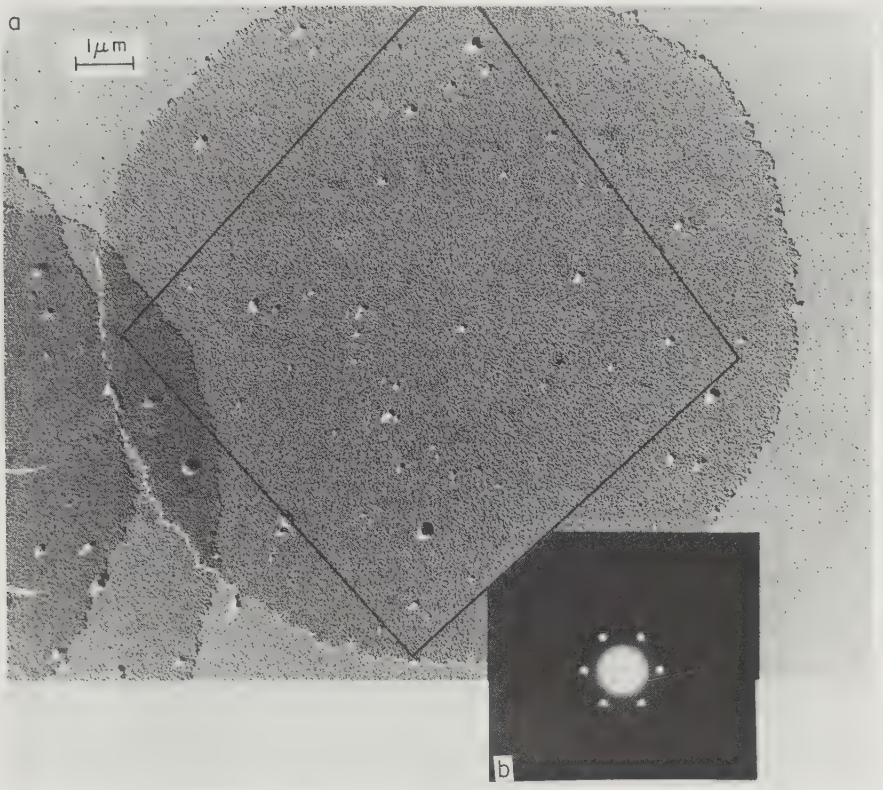

Fig. 29. (a) Electron micrograph of a single crystal of polychlorotrifluoroethylene grown from a 0.1% solution in low-molecular-weight polychlorotrifluoroethylene oil at 110°C. Note disklike overall profile and finely serrated character of the periphery. (b) Selected-area electron diffraction pattern obtained from the region outlined in (a). The six sharp spots are $\{10\bar{1}0\}$ reflections. The faint, continuous outer ring is from the gold layer which was evaporated upon the crystal. (From Barnes and Khoury.[112])

formation of the regular type of crystal shown in Figure 30a) the crystals exhibit somewhat rounded overall shapes and a finely serrated periphery[106,107] as shown in Figure 30(b). It may also be noted in this connection that Jones *et al.*[175] have crystallized isotactic polystyrene from solution over a wide range of undercoolings and report that the lamellae, although basically hexagonal, were somewhat rounded and had irregular outlines.

The gist of the preceding remarks is that the origins of the manifestation or irregular lateral growth habits even under conditions of slow growth in polymer chain-folded crystals may differ from polymer to polymer. It is a phenomenon which, viewed in broad

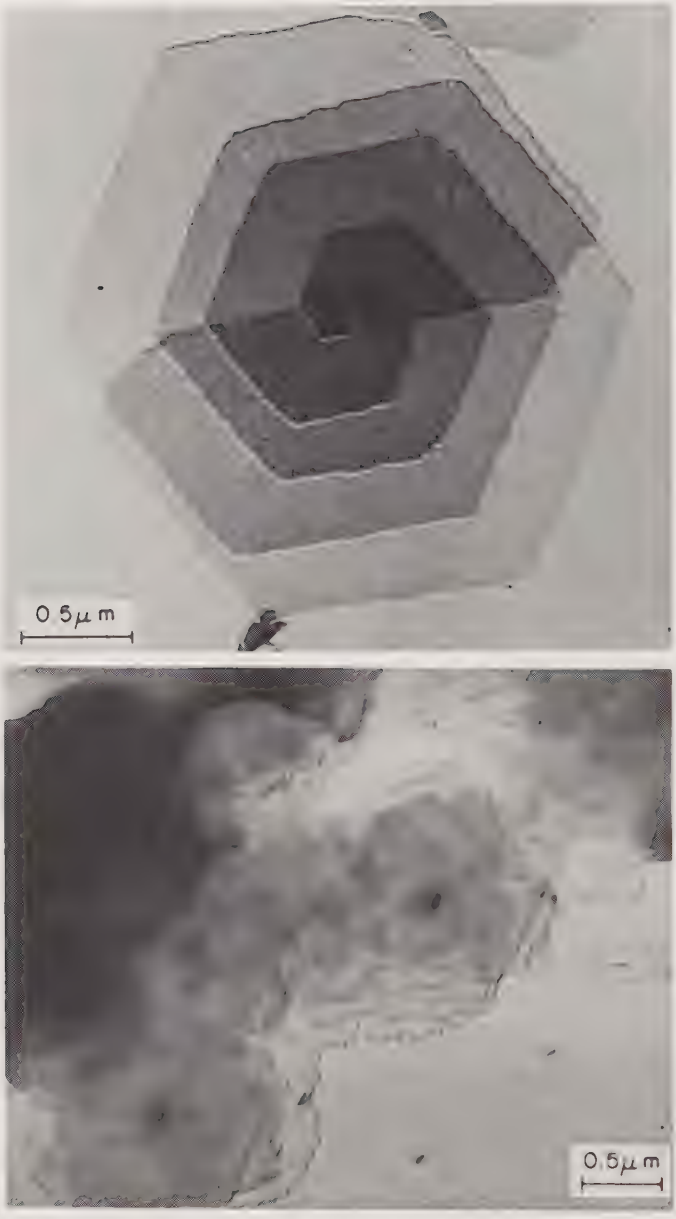

Fig. 30. (a) Electron micrograph of a single crystal of isotactic polystyrene grown at 190°C from solution in atactic polystyrene.[107] (Photograph courtesy H. D. Keith, reprinted with permission of John Wiley and Sons, Inc.) (b) Electron micrograph of single crystal of isotactic polystyrene grown at 100°C from solution in trimethylbenzene for about 2000 hr.[106] Note irregular lateral shapes of the lamellae in comparison with the crystal shown in (a). (Photograph courtesy R. St. John Manley, reprinted with permission of John Wiley and Sons, Inc.)

perspective, needs to be investigated further concerning possible distinctions which can be made as to the extent of its dependence, on the one hand, on the intrinsic configurations of the polymer molecules and, on the other hand, on molecular weight (chain length), on the nature of polymer–solvent interactions, and on solvent viscosity. Among the other aspects which remain to be clarified with regard to the formation of lamellae exhibiting irregular lateral habits are the following: (a) How do the molecules fold at the periphery of the crystals? (b) What is the interrelationship between the manner in which the chain molecules are apposed in a folded conformation at the periphery of the lamellae and the irregular habit exhibited by the lamellae? (c) What is the fold-domain structure in the lamellae? Some brief comments concerning these three interrelated features will be advanced in due course in Section 3.4.6.

3.4.5. Comments Concerning the Nature of the Fold Surfaces in Solution-Grown Polymer Crystals with Particular Reference to Linear Polyethylene

Measurements of, inter alia, the density[70–74,176] of solution-grown crystals of linear polyethylene, such as the ones described in Section 3.4.2, indicate that the crystals are only 75–90% crystalline (see also Refs. 16 and 17). In short, the crystals contain an appreciable amount of disorder corresponding to the presence of an "amorphous" content of 25–10%. It is generally accepted that the disorder in the crystals occurs predominantly at the fold surfaces[16,17] and the view which has emerged is that the chain-folded lamellae consist of a central crystalline core (where the density is equal to or very closely equal to the unit cell density) "sandwiched" between two disordered surface regions which contain the chain folds, and which have a lower average density than the core. There has, however, been considerable debate and controversy concerning the origins and nature of the disorder at the fold surfaces of the crystals. It is not our intention to dwell in any detail on the various techniques and numerous investigations which have been brought to bear, and the conflicting conclusions which have been derived therefrom, concerning the origins or nature and extent of disorder at the fold surfaces in polyethylene crystals. This important and controversial topic has been discussed extensively by Keller in recent reviews,[16,17] to which the reader is referred to for a comprehensive examination of this issue. We shall confine

ourselves for the most part to pointing out some of the different ways in which it has been suggested that disorder occurs at the fold surfaces of the crystals, and some of the conclusions that have been advanced concerning this matter, which is the subject of continuing investigation.

Borrowing from the models upon which kinetic theories of chain-folded polymer crystal growth have been based[162–166] (see also review in Ref. 11), we note that two processes underlie the apposition of successive strips or planes (sometimes referred to as ribbons) of folded molecules along the sides of a developing lamella, namely the initiation of the strips, which is induced by the formation of two-dimensional surface nuclei at the periphery of the lamella, and the propagation of the strips along the sides of the lamella. The nucleation of a strip is envisaged to result from the deposition of a single chain (or a portion thereof) in a folded conformation at the periphery of the lamella. Each such nucleus constitutes the "beginning" of a strip, which then proceeds to propagate along the sides of the lamella by the addition of fresh molecules in a folded conformation at both extremities of the nucleus. It is self-evident that minimal disorder and surface roughness at the fold surfaces of a lamella will occur if, as depicted schematically in Figure 8, the fold period l is constant, the end portions of the chains are incorporated in the crystal (as distinct from remaining as dangling cilia at the surface of the crystal; see Figure 31), and if the ends of neighboring chains in each strip are correctly juxtaposed such as to simulate "continuity" between the chains in each strip. The essential feature of this idealized model is that the folds in the lamella are packed in a regular fashion and the fold surface is "smooth." The other important feature is the adjacently reentrant manner in which the molecules are folded in each successive strip in the lamella.

Various possibilities have been invoked to account for the incidence of disorder at the fold surfaces of polyethylene crystals. Among these possibilities are: the exclusion of the end portions (or indeed longer portions) of the chains from the crystal interior, leading to cilia dangling from the fold surfaces of the lamellae; fluctuations in the fold period about a mean value (which increases of course with increasing crystallization temperatures); loose loops; and nonadjacent reentry. These factors are considered briefly below. We shall start with some comments concerning ciliation and nonadjacent reentry.

Briefly, Keller,[16] referring to suggestions by F. C. Frank, has indicated that the probability that the idealized juxtaposition of the ends of neighboring molecules in the strips of folded molecules will occur (see Figure 8) is small and that the attachment of a new chain to the extremity of a developing strip is more likely to occur elsewhere along the contour of the depositing chain. As a result there will usually be two chain portions capable of folding along the strip (Figure 31a), one of which will do so while the other will be left dangling as a cilium (Figure 31b). A more complicated variation of the situation depicted in the latter figure is shown in Figure 31(c), which represents the occurrence of cilia as a consequence of the attachment of a fresh molecule along a strip before the preceding molecule has completed its deposition. The possibility that a long cilium may reenter and fold further downfield along the same strip from which it was initially excluded can also be envisioned (Figure 31d). We refer to this latter possibility as intrastrip nonadjacent reentry. Finally, insofar as ciliation is concerned, the occurrence of cilia may also be envisaged to occur in the case of the incidence of multiple nucleation, e.g., when the initiation of a new strip of folded molecules occurs simultaneously at different places along the periphery of a lamella. In such cases, parts of chains may be envisaged to be exluded from the developing strip as dangling cilia when abuttal occurs between portions of the strip which have propagated toward one another from neighboring nuclei.

Evidence has been adduced by Keller and Priest[177] and Bank and Krimm[178] that cilia do occur at the surfaces of solution-grown polyethylene crystals. According to Keller and Priest,[177] about 90% of the chain ends occur at the fold surfaces of the crystals. The matter of the incidence of ciliation is of interest in two respects. First, it is clear that the exclusion of cilia from the interior of the crystals would be a feature contributing to fold surface disorder or roughness. This also applies in the case of the type of nonadjacent intrastrip reentry of cilia shown in Figure 32(d). Second, the incidence of cilia also carries some important implications with regard to the lateral growth of the lamellae since a long cilium dangling from a completed strip of folded molecules (e.g., Figure 31e) could conceivably fold outwards and then upon that strip, thus nucleating a new strip (Figure 31f) either on its own, if the cilium is sufficiently long to contribute several stem lengths, or by being stabilized by the accretion of a fresh molecule from the solution.[16,166] It should also be noted

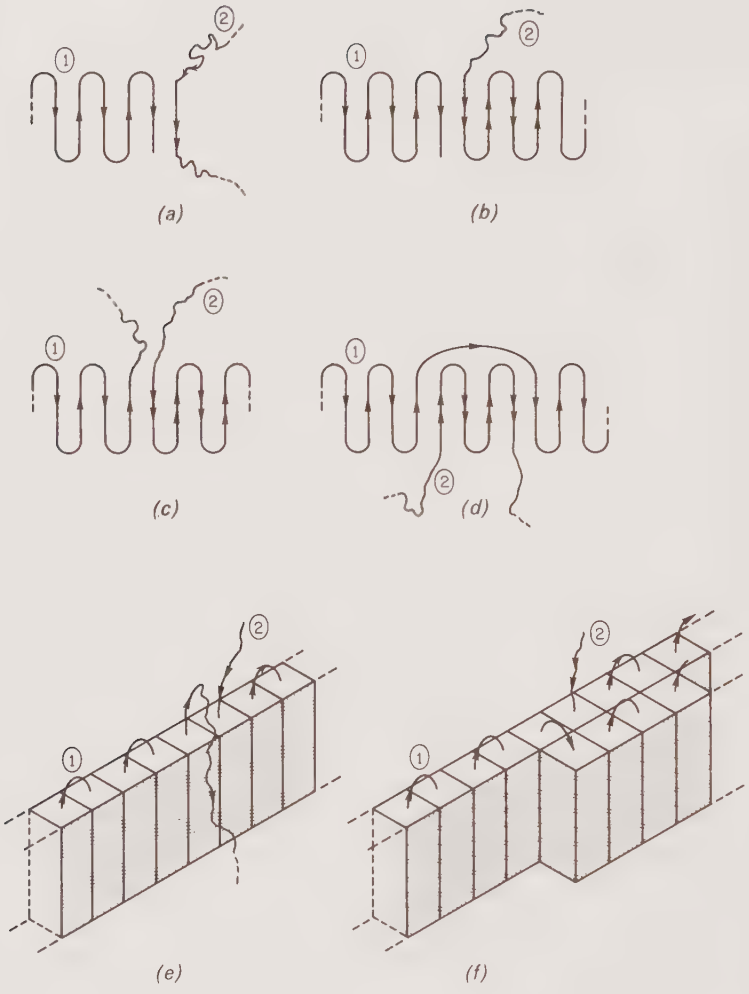

that the partaking of cilia in the lateral growth of the lamella need not necessarily be limited to the nucleation of new strips. Thus it may be envisaged that a cilium dangling from a completed strip might well fold along the next strip when the latter "passes by" the cilium[16] (Figure 31g). We shall refer to the situations depicted in Figures 31(f,g) as instances of interstrip adjacent reentry in order to distinguish them from reentry between nonadjacent strips, such as is envisaged in Flory's[179] random reentry with irregular folding model (the so-called "switchboard model"), which is depicted in Figure 32.

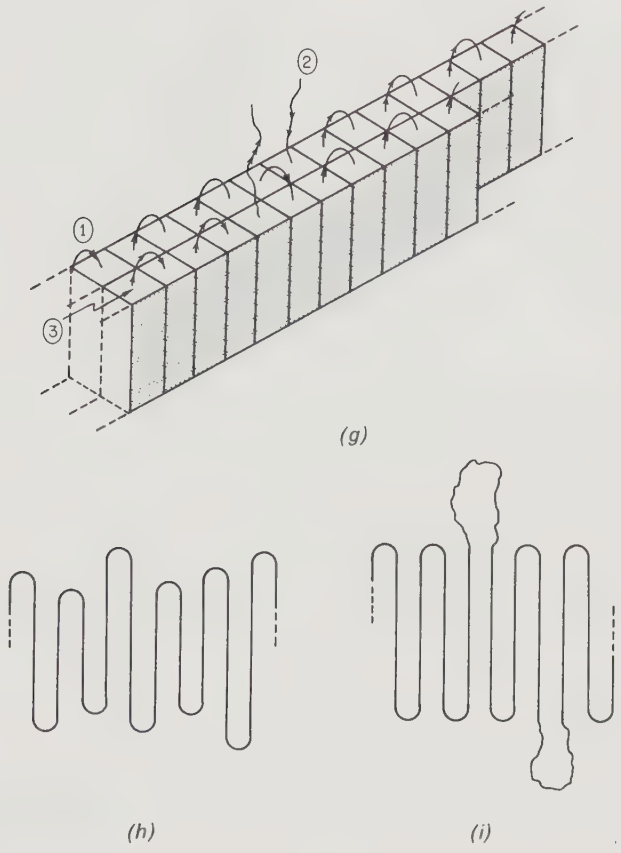

Fig. 31. Illustration of some different ways in which folding and the incidence of ciliation can occur at the periphery of chain-folded lamellae. The numbers in (a)–(g) identify different chains whose traces are delineated by a corresponding number of arrowheads assigned to each chain. See text. (In part after Keller[16].)

The distinctly sectored character of polyethylene single crystals, such as those described in Section 3.4.2, argues against the aforementioned random reentry (switchboard) model, and also indicates that the incidence, if any, of interstrip adjacent reentry and reentry between nonadjacent strips is minimal in comparison with intrastrip adjacent reentry (Figures 31a–c). In contrast, the exclusion of cilia from the interior of the crystals and some intrastrip nonadjacent reentry (Figure 31d) are not incompatible with the distinctly sectored character of the crystals, nor are the following additional features,

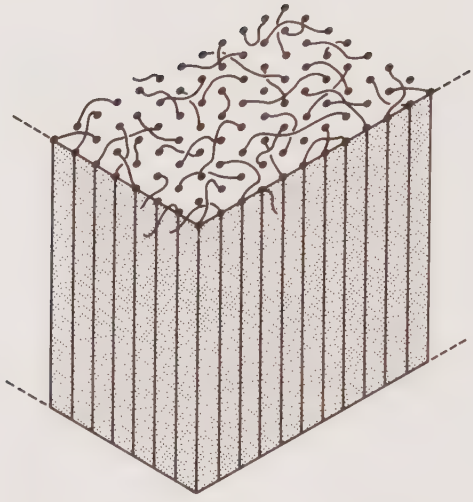

Fig. 32. Random reentry with irregular folding model of chain-folding, sometimes referred to as the switchboard model. (After Flory.[179])

which have also been invoked to account for the incidence of disorder at the fold surfaces of the crystals: the occurrence of sharp (adjacently reentrant) folds but with fluctuations in fold period (see Figure 31h) as predicted by theory,[165] and the occurrence of loose folds with intrastrip adjacent reentry (Figure 31i). A puzzling question arises, however, in this connection: How can these various types of "disorder" at the fold surfaces of the lamellae be reconciled with the fact that the crystals are hollow pyramidal? This question stems from (a) the difficulty of accounting for the hollow pyramidal nature of the crystals in terms other than its being due to regular fold staggering (see Section 3.4.2) and (b) the fact that it is difficult to imagine how regular fold staggering could occur if the steric interactions between neighboring folds about the surfaces of the lamellae were not "uniform." In other words, one is faced with the problem of reconciling the existence of disorder at the fold surfaces of the lamellae with the attribution of the hollow pyramidal habits of the crystals to regular fold staggering, where the latter feature entails the presumption that there exists a pervading uniformity in the steric interactions between folds at the surfaces of the lamellae. This paradoxical problem remains

to be resolved rigorously, as will become even more evident from the additional aspects of the occurrence and nature of disorder at the fold surfaces of polyethylene crystals, which are summarized below.

We have already pointed out that studies due to Keller and Priest[177] and Bank and Krimm[178] have indicated that cilia do occur at the fold surfaces of the crystals. Furthermore, infrared spectroscopy studies of linear polyethylene and poly(ethylene-d_4) [i.e., $(-CD_2-)_x$] mixed crystals by Bank and Krimm[180] and Krimm and Ching[181] and etching studies by Williams *et al.*[182] have led these authors to the conclusion that intrastrip adjacent reentry is the predominant manner in which folding occurs in the polyethylene crystals. Subsequent etching studies reported by Priest[183] and Keller *et al.*,[184,185] while indicating that adjacently reentrant folds are predominant, have led to the conclusion that fluctuations in fold period contribute substantially to the disorder nature of the fold surfaces in the crystals. Fluctuations of up to ~ 20 Å between the levels of the folds situated at either of the "fold surfaces" in the lamellae were deduced.[185] Furthermore, it has also been adduced from the results of these etching studies that the distribution, according to depth, of the folds at either surface of the lamellae is not uniform.[185] For example, as has been summarized by Keller,[17] it can be deduced that 65% of the folds in a lamella which is 150 Å thick occur within 8–14 Å from the surface, 10–15% occur at higher depths, i.e., down to 20–30 Å, and the remainder of the folds occur closer to the surfaces. The suggestion has also been made that the folds tend to be "looser" the further they are situated from the crystalline core of the lamellae.[17] This latter feature, coupled with the fluctuations in fold height indicated above, should lead to a progressive diminution in density on proceding outward in the surface layers between which the central crystalline core of each lamella is "sandwiched." This differs, however, from the *two-phase* model of polyethylene crystals favored by Fischer and collaborators,[70,186–190] whose investigations in this connection include the measurement of the absolute intensity of the low-angle x-ray patterns obtained from mats of single crystals,[187–189] as well as the determination of the density and the enthalpy of the crystals.[70,190] The results of these investigations have been adduced as evidence supporting the "two-phase" model, in which the lamellae are viewed as consisting of a central core, whose density corresponds closely to the ideal value calculated from the unit cell of polyethylene, which core is sandwiched between two surface layers in which the

density is equal or almost equal to the density of amorphous polyethylene, that is, the density of supercooled molten polyethylene extrapolated to room temperature (see, e.g., Refs. 187–190).

In summary, the current situation, as we see it, concerning the disordered regions in crystals of polyethylene grown from solution is as follows. There is general agreement that the crystals consist of a central core whose density is equal to or very nearly equal to the unit cell density, and that this central core is sandwiched between two disordered regions (fold surface regions). There remains some divergence of opinion, however, as to whether (a) the degree of disorder on either side of the central core increases progressively and, accordingly, the density tends to the amorphous density, the closer one approaches the outer reaches of the fold surfaces of the lamellae, or (b) the delineation between the crystalline core and the disordered surface regions is a sharp one, i.e., there is a sharp transition from crystalline core to amorphous surface regions. Whichever the case may be (and the difficulties facing the solution of this aspect of the fine structures of the crystals cannot be overemphasized), there are two factors which should be borne in mind. The first factor is that the most obvious two-phase model is the random reentry with irregular fold model (switchboard model). This latter model is incompatible with the sectored character of the crystals. The second factor is that the occurrence of disorder at the fold surfaces of the lamellae remains to be reconciled with the attribution of the hollow pyramidal habits exhibited by the crystals to the incidence of regular fold staggering. In this connection Hoffman has recently suggested that the occurrence of disorder at the fold surfaces of polyethylene crystals may be due to the presence of a disordered layer of adsorbed molecules at these surfaces.[11] This interesting possibility, which lends itself to detailed experimental study, remains to be probed directly.

3.4.6. Additional Aspects of the Nature of Chain Folding, the Fold Surfaces, and the Lateral Growth Habits of Polymer Crystals

3.4.6.1. Preliminary Comments

We have in previous sections variously touched upon the following aspects of the morphology of polymer crystals: (i) chain folding and the regularity or otherwise of the folds and fold surfaces in chain-folded lamellae, and (ii) the interrelationships between chain folding, sectorization, and the lateral growth habits of chain-folded

lamellar crystals. Our intention in this section is to summarize or comment briefly upon observations concerning these two aspects of the morphology of polymer crystals with reference to additional factors and/or features which we have not dwelt on so far.

3.4.6.2. On Aspects of the Nature of Folding and the Fold Surfaces in Polymer Crystals

We have confined our earlier remarks concerning the regularity of chain folding and the nature of the fold surfaces in polymer crystals to the case of crystals of polyethylene (Section 3.4.5), which have been studied in most detail in this connection. We wish now to consider briefly the case of the aliphatic polyamides and that of ethylene oxide–styrene two-block copolymers (PEO–PS). The polyamides are of particular interest because of the incidence of hydrogen bonding between the amide groups in neighboring chains, which imposes restrictions upon the manner in which the chains fold if correct registry between the amide groups in adjoining chains is to be maintained. This aspect has been the subject of several recent investigations.[191–196] The two-block copolymers of PEO–PS are of interest because their constituent chains consist of one portion (the PEO) which is intrinsically capable and indeed does undergo crystallization (see below), whereas the other portion of each chain (the PS) is atactic and does not. The aspects of interest in this case are how is the crystallization of the PEO affected by the presence of a large chemical "defect" attached at one end of each PEO chain, and what is the fate of the PS portion of each chain when the PEO part undergoes crystallization? The morphology of PEO–PS two-block copolymers has been investigated in detail.[31,32] We shall summarize the findings of these latter studies following a consideration of chain folding in the aliphatic polyamides.

By way of background to chain folding in solution-grown crystals of the aliphatic polyamides, some comments concerning the juxtaposition of neighboring stems in correct registry relative to one another in polyethylene lamellae during the process of folding are pertinent. Chemically and structurally speaking, polyethylene, which has served as a model for the study of various aspects of chain folding, is in fact the simplest model polymer for the following reasons. First, the chains are chemically homogeneous. Second, the interactions between adjoining chains in the polyethylene lattice are van der Waals forces. Third, the crystallographic repeat in the direction of

the chains, which is 2.54 Å and corresponds to two $-(CH_2)-$ units, is considerably smaller than the usual range of thicknesses (~ 100 Å) exhibited by polyethylene lamellae grown from solution. In view of these three factors, the juxtaposition of adjoining stems parallel to one another in correct crystallographic registry during the process of the folding of the chains at the periphery of the crystals is achieved relatively easily. Because of the chemical homogeneity of the chains, there are no specific interactions between special chemical groups in the chains, and furthermore the adjustments in the chain direction which are necessary for correct registry to be achieved between the $-(CH_2)-$ groups in adjacent stems are relatively small. The aliphatic polyamides $[-HN(CH_2)_XNH{\cdot}OC(CH_2)_{Y-2}CO-]_n$ (type XY) and $[-HN(CH_2)_ZCO-]_n$ (type Z) are in distinct contrast with polyethylene in these two respects.

Broadly speaking, the chains in polyamide lattices tend to array themselves such that the maximum possible degree of coupling (hydrogen bonding) is achieved between the amide groups on adjacent chains. For example, in the case of type XY polyamides, the maximum extent of hydrogen bonding possible is governed by the number (odd or even) of $-CH_2-$ groups between successive amide groups in the chains.[197-199] We take as an example the case of poly(hexamethylene adipamide) (nylon 6.6,* Table 1). The unit cell of this polymer is triclinic (see Figure 6).[66] The chemical repeat unit, which corresponds to the crystallographic repeat (i.e., the c axis of the unit cell) in the direction of the chains, is 17.2 Å. Furthermore, the lateral packing of the chains in the lattice is such that each amide group in a given chain stem is aligned with an amide group on a neighboring chain stem lying in the same (010) plane such that hydrogen bonding occurs between all the paired amide groups in successive chain stems situated in the same (010) plane. This is shown schematically in the three-dimensional perspective of the nylon 6.6 unit cell shown in Figure 6; it is also depicted in the plan view of an (010) lattice plane illustrated in Figure 33(a). This hydrogen-bonded, sheetlike character of the nylon 6.6 lattice [in which the interactions between the chains in adjoining (010) planes are weak van der Waals interactions] is also found in other aliphatic polyamides. As we have

* A two-number convention is used to differentiate between different type XY polyamides. The number X gives the number of backbone carbon atoms in the diamine $[-HN(CH_2)_XNH-]$ part of the chemical repeat unit. The second number Y gives the total number of backbone carbon atoms in the diacid $[-OC(CH_2)_{Y-2}CO-]$ part of the repeat unit.

pointed out earlier, however, the number of hydrogen bonds that can be formed between chains will vary according to the number of $-(CH_2)-$ groups between successive amide groups along the chains. In the case of the nylon 6.6 lattice all the amide groups are involved in hydrogen bonding and the arrangement of the chains side by side in (010) planes is such that the diacid (A) and diamine (B) portions of the chemical repeat unit in a given chain are paired with the diacid and diamine portions, respectively, in neighboring chains, as indicated in Figure 33(a).

Among the questions which arise in the case of chain folding in nylon 6.6 in particular and aliphatic polyamides in general is: How is the fold period in lamellar crystals of such polymers influenced by the length of the chemical repeat unit in the chains and the occurrence of hydrogen bonding between specific groups in neighboring chains? This question has been addressed in several investigations recently reported in a series of papers[191–196] on the thickness of chain-folded lamellae of several polyamides of both type *XY* and type *Z* which have been crystallized from solution at different temperatures. In most cases the polymers crystallized in the form of sheaflike aggregates consisting of chain-folded lamellae. The preparations were filtered and the resulting mats were used as samples for the determination of the thickness of the lamellae using x-ray diffraction techniques. It may be noted in anticipation of what follows that the lamellae in the mats were preferentially oriented with their fold surfaces parallel to the plane of the mats. Space limitations do not permit us to do full justice to the results of these studies, nor do they permit us to dwell on related experimental details and problems concerning effective removal of residual solvent from the mats. The interested reader is referred to the original series of papers.[191–196] We shall confine ourselves mostly here to the case of nylon 6.6, which has been studied in greatest detail. We shall, however, indicate some of the conclusions derived from the study of other polyamides.

Data on the thickness of lamellae of nylon 6.6 grown from solution (mostly from 1,4-butanediol) are given in all the above-mentioned papers.[191–196] Dreyfuss and Keller[191] established that the fold surfaces (or basal plane) of the lamellae were parallel to the (001) planes in the lamellae. Consequently a comparison of the thickness of the lamellae with the spacing of the (001) crystal planes provided a direct indication of how many chemical repeats along the chains are accommodated within the lamellae between each successive fold in

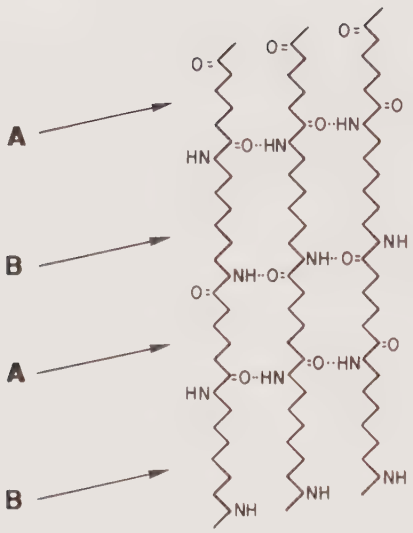

(a)

Fig. 33. (a) Schematic representation of neighboring hydrogen-bonded chains in the same (010) plane in the lattice of nylon 6.6. Note the alignment of the diacid

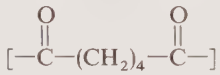

(A)

and the diamine

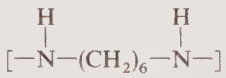

(B)

portions of the chemical repeat units (AB) in the adjoining chains. (b) Schematic representation of chain folding along an (010) plane, with folding occurring at the diacid portion A of every fourth chemical repeat unit along the chain such that maximum hydrogen bonding is achieved between neighboring stems as is the case in (a). The length of the stems between successive folds corresponds to $3\frac{1}{2}$ chemical repeat units. (c) Same as in (b) but with folding occurring at the diamine portions of the chain.

the molecules when account was taken of the inclination of the chains relative to the (001) planes. Precautions had to be taken, however, to ensure that the solvent was effectively removed from the mats obtained by filtration, or otherwise higher values are obtained for the lamellar thickness. Thus, in the case of samples crystallized from 1,4-butanediol at 120°C the lamellar thickness obtained from mats

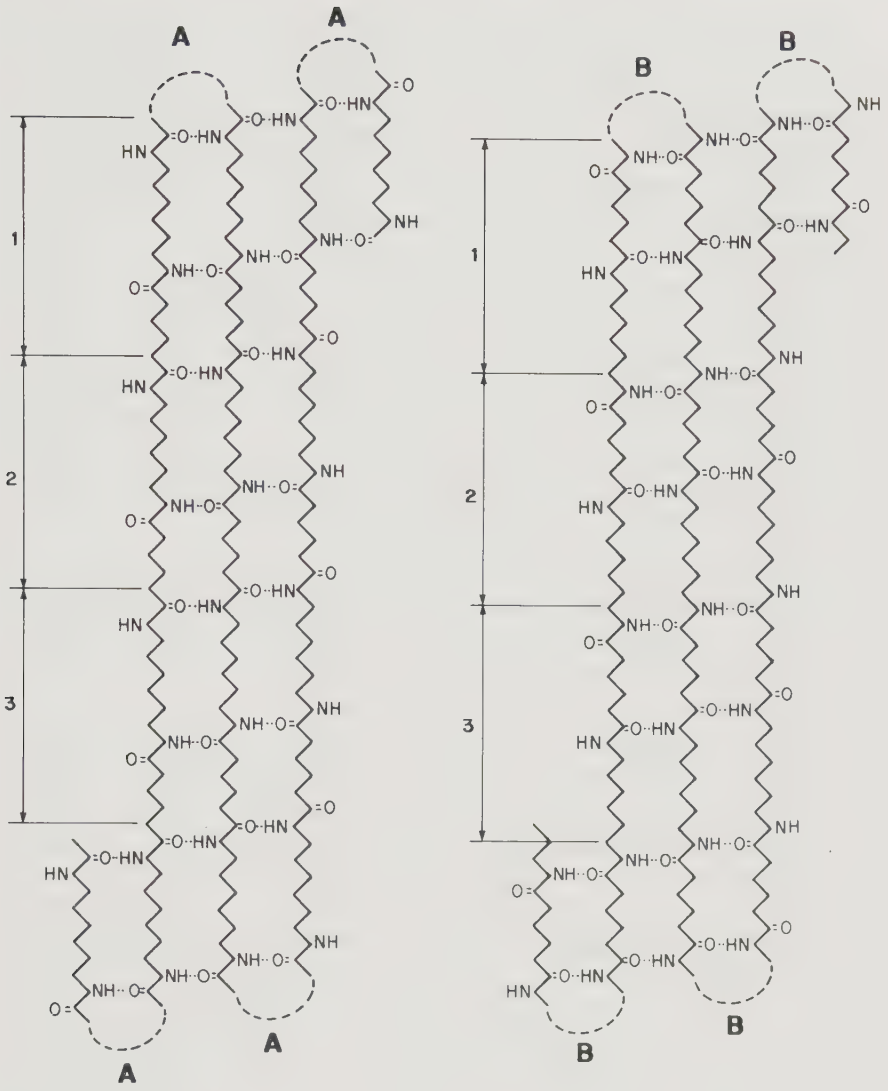

(b) *(c)*

prepared by filtration was found to be in the range 56–59 Å. Upon subjecting the mats to subsequent heat treatment at 230°C the long period diminished to 53–54 Å ($= L_x$). The decrease in spacing was attributed to removal of residual solvent and consequently to the diminution of gaps between superposed lamellae. The point of interest is that the ratio R of these smaller spacings to the measured spacings

of the (001) planes d_{001} was very close to 4. Indeed, Dreyfuss and Keller[191,195] have found that both L_x and the ratio $R = 4$ $(= L_x/d_{001})$ were insensitive to the temperature at which the lamellae were grown for a large temperature range, namely 70–120°C. We shall return later to this latter matter (which is in contrast with the variation of lamellar thickness with crystallization temperature exhibited by many polymers) and to observations obtained from nylon samples crystallized at higher temperatures. Confining ourselves to the data already mentioned, the fact that R was apparently constant and equal to 4 suggested in itself that the folds in the lamellae were located at chemically equivalent positions along any given molecule. Accordingly, two plausible models for the lamellae were originally considered.[191] These models [or more accurately, plan views of the (010) planes in the models] are depicted in Figures 33(b) and 33(c), respectively. In both models the nylon 6.6 lattice is preserved. In each case the stems that are inclined to the lamellar surface are $3\frac{1}{2}$ chemical repeat units long and the remainder of the lamellar thickness (i.e., the remaining thickness, which is equivalent to $\frac{1}{2}$ chemical repeat unit) is apportioned to the folds. The assumption that folding occurs along the (010) planes in the lamellae is implicit in these models.*

The difference between the two models is that in one case (Figure 33b) folding occurs about the diacid [$-OC(CH_2)_4CO-$] portion of every fourth chemical repeat unit along the chains, whereas in the other (Figure 33c) folding occurs about the diamine [$-NH(CH_2)_6NH-$] portion of every fourth repeat unit. In both cases each fold is bridged by a hydrogen bond. Of these two possibilities, it might seem that the availability of six $-(CH_2)-$ groups to form a diamine fold would favor such a fold over a diacid fold involving only four $-(CH_2-$ groups. Indeed, prior to the above mentioned x-ray studies, Koenig and Agboatwalla[200] had concluded on the basis of infrared band assignments for nylon 6.6 that the folds in solution-grown crystals were diamine folds and had also illustrated a model of such a fold. However, an examination by Dreyfuss, Keller, and Willmouth[192] of combined wide-angle and low-angle x-ray patterns obtained from crystal mats similar to the ones mentioned earlier (with refererence to work by Dreyfuss and Keller[191]) revealed some subsidiary maxima between the maxima corresponding to L_x

* Whether folding also occurs along other ($hk0$) planes [e.g., (100), (110)] in lamellae of nylon 6.6 remains an open question, a discussion of which is beyond the scope of this chapter.

and d_{001} as well as between the maxima corresponding to $d_{(001)}$ and $d_{(002)}$. A structural analysis by Atkins, Keller, and Sadler[193] of the "diacid" and "diamine" fold models of lamellae for which $R = 4$ (i.e., total thickness corresponds to $3\frac{1}{2}$ repeat units plus folds) has revealed, surprisingly, that of the two models the intensities (or structure amplitudes) of the subsidiary maxima calculated for the "diacid" model agreed more closely with the observed intensities. In short, the conclusion derived by Atkins *et al.*[193] from the x-ray studies is that the folds in the above-mentioned nylon 6.6 lamellae are diacid folds (Figure 33b). The different conclusion derived from the infrared band assignments which we alluded to earlier remains to be reconciled with this result (or vice versa). We shall not dwell on the matter of diacid or diamine folds further, other than to point out that models for the folds in nylon 6.6 have also been considered on the basis of the structures of cyclic oligomers.[201]

For our present purpose the important factors which emerge from the x-ray studies mentioned above are that the folds in the particular nylon 6.6 crystals which were studied are apparently sharp, hairpin-like folds which occur at chemically equivalent positions along the chains, and that the folds consist of approximately one-half a chemical repeat unit. Two points bear noting in connection with these results when one examines the possibility of the occurrence of any loose folds and/or fluctuations in fold period (with hairpin folds) in the nylon 6.6 lamellae. First, given that the lattice structure is maintained, and given that the length of the chain stems is fixed ($3\frac{1}{2}$ repeat units in the case mentioned above), then any loose folds would have to be $n + \frac{1}{2}$ chemical repeat units long, where n is an integral number. Second, if fluctuations in stem length were to occur with the lattice structure still being maintained, these fluctuations, and hence the fluctuations in fold period (with hairpin folds), would have to occur in "quantum" jumps corresponding to an integral number n of repeat units, and the corresponding fluctuations in the local thickness of a lamella would correspond to nd_{001}. The x-ray data (both low angle and wide angle) referred to above have been adduced as evidence arguing against any significant occurrence of loose folds or fluctuations in fold period. One might therefore expect that the density (or "crystallinity") of the crystals is high. This is apparently not the case, as we shall see later. Before dwelling on this latter point, however, it is appropriate to consider briefly observations concerning the effect of crystallization temperature on the thickness L_x of nylon 6.6 lamellae.

We have already pointed out that according to Dreyfuss and Keller,[195] the thickness of the solution-grown lamellae was insensitive to crystallization temperature in the range 70–120°C and that in that range the ratio $R = L_x/d_{001}$ is equal to 4. Interestingly, the same workers have found that crystallization at 155°C leads to the formation of lamellae for which $R = 5$ ($L_x = 65$ Å), which corresponds to a "quantum jump" in thickness between 120 and 155°C equivalent to one additional chemical repeat unit in the stems of the folded molecules. This increase is consistent with the maintenance of the lattice structure within the lamellae. However, lamellae grown at 130, 140, 145, and 150°C yielded R values of 4.1, 4.3, 4.8, and 4.8, respectively,[195] which implies that nonintegral values of R may be possible, although this may be subject to problems associated with preparing suitably compact mats from which to obtain the measurements. It is of interest to note in this connection the results of Hinrichsen,[202] who has determined the thickness of chain-folded lamellae of nylon 6.6 grown from solution at different temperatures in the range of 80–145°C. The thickness of the lamellae was found to remain essentially constant, ~ 54 Å, for crystallization in the range 80–135°C, whereas those grown at 145°C were 60 Å thick. In short, the observations of both Dreyfuss and Keller[195] and Hinrichsen[202] suggest that whereas the smallest thickness which has been observed in chain-folded lamellae of this polymer corresponds to an integral multiple (namely 4) of the (001) lattice spacing and does not vary over a wide temperature range, there apparently exists a tendency for the lamellae to be thicker when grown at sufficiently higher temperatures and that increases in thickness, which are smaller than d_{001} and not necessarily equal to $(\frac{1}{2})d_{(001)}$,* apparently do occur (see tabulated data in Ref. 195). This indicates that, under certain conditions at any rate, the maximum number of hydrogen bonds may not be formed between the molecular stems in the lamellae. It is important to note in this connection that in addition to measuring the lamellar thickness, Hinrichsen[202] also measured the densities of the crystals formed at different temperatures and found that the crystallinity of

* It can be noted that maximum hydrogen bonding between chains would be achieved if the straight stems in the lamellae were four chemical repeat units long (as compared to $3\frac{1}{2}$ in the models shown in Figures 33b,c). As pointed out by Dreyfuss and Keller,[191] however, the occurrence of an integral number of chemical repeat units in the straight stems would lead to an alternation of an acid fold followed by an amine fold in the chains, with the result that these different folds will occur at opposite fold surfaces of the lamellae.

the lamellae increased progressively from about 40% in crystals grown at 80°C to about 60% in crystals formed at 145°C.

Two features are noteworthy. The first is that even though the lamellar thickness remained essentially constant with $R = 4$ in the crystals grown at temperatures between 80 and 135°C, there was a 10% difference in crystallinity between crystals grown at the extremes of this temperature range. The second feature is that the crystallinity of the lamellae formed over the whole temperature range (up to 145°C) is evidently low. It may be noted in this latter connection that Hinrichsen reports a density of 1.172 for crystals grown at 120°C, for which R is also equal to 4. Atkins *et al.*[193] report a density of 1.18 g/cm^3 for crystals grown at 120°C, for which $R = 4$ and which, as we pointed out earlier, exhibited satellite reflections in x-ray diagrams which were interpreted as being consistent with regular hairpin folding with "diacid" in the folds. Based on the values used by Hinrichsen[202] for the density of purely crystalline polymer (1.233 g/cm^3) and that of the polymer in the amorphous state (1.1198 g/cm^3), then the densities of the lamellae grown at 120°C by Atkins *et al.*.[193] and Hinrichsen[202] are found to correspond to crystallinities of 56% and 49%, respectively. This difference in density notwithstanding, the fact remains that they are both extremely low. Thus, as pointed out by Hinrichsen,[202] on the one hand the low crystallinities of the crystals indicate that there is substantial "amorphous" disorder in the crystals which can be interpreted as their having a two-phase (crystalline–amorphous) structure. On the other hand, the occurrence of the aforementioned satellite reflections in x-ray diffraction patterns is evidence of highly regular folding.[193] One is led to conclude that the disordered regions in the crystal do not occur at the fold surfaces. Thus the occurrence of substantial disorder in nylon 6.6 crystals remains to be explained or reconciled satisfactorily. An important uncertainty to be resolved is the value of the density of amorphous nylon 6.6. In contrast with the value of 1.1198 g/cm^2 given by Hinrichsen, Starkweather and Moynihan[203] had previously deduced a value of 1.069 g/cm^2 for the amorphous density. On the basis of this latter value the crystallinities of the crystals grown at 120°C by Atkins *et al.*[193] and Hinrichsen[202] would be 66% and 71% respectively instead of 49% and 56%. Even if one accepts the higher values for the crystallinities based on an amorphous density of 1.069 g/cm^2, the nature of the disorder in the crystals (corresponding to an "amorphous" content of 29% to 34% remains to be accounted for in the light of the x-ray

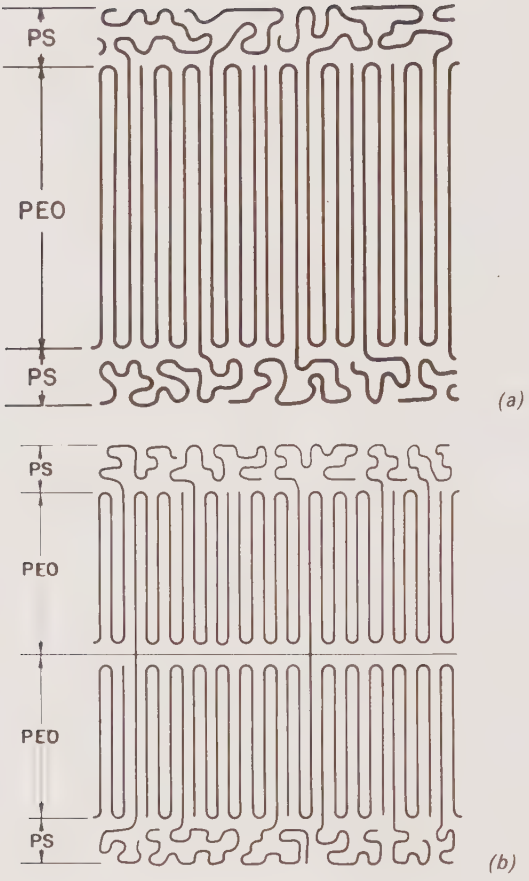

Fig. 34. Edge-on cross-sectional models of crystals of two-block copolymers of ethylene oxide and styrene (PEO–PS), showing the chain-folded character of the PEO crystalline core of the crystals and the occurrence of the amorphous (PS) portions of the chains at the surfaces of the crystals. (a) A monolayer crystal, (b) a bilayer crystal. (After Lotz and Kovacs.[31])

diffraction studies mentioned earlier.[193] Again it should be noted in this context that the planes along which the molecules fold in nylon 6.6 crystals still remain to be satisfactorily determined.

Finally, insofar as our comments on the polyamides are concerned, it should be pointed out that the formation from solution of lamellar crystals whose thickness corresponds to an integral number of chemical repeat units along the folded chains is not peculiar to

nylon 6.6. It has been observed in broad series of type XY and type Z polyamides. An extensive survey and analysis has been given by Dreyfuss,[196] who discusses the relationship between hydrogen bonding and the fold period in polyamides in detail. The matter of the occurrence, or otherwise, of disorder in crystals of these other polyamides remains to be pursued in detail.

We now turn to some brief comments on the nature of chain-folded lamellar crystals of two-block copolymers whose constituent chains consist of one block of crystallizable poly(ethylene oxide) (PEO) and one block of noncrystallizable (atactic) polystyrene (PS). The crystallization of a series of such copolymers in which the weight fraction of PS varied from 0.28 to 0.88 has been studied in detail by Lotz *et al.*[31,32] Briefly, fractionation according to composition (weight fraction of PS) manifests itself during the crystallization of individual copolymers. Only that fraction of the chains having an appropriate PS–PEO ratio precipitates in the form of crystals. Crystals in which the weight ratio of PS was between 20% and 55% have been formed. Furthermore, electron diffraction patterns obtained from such crystals are consistent with the pure PEO lattice structure. This latter feature, as well as others we will not go into here, leaves little room for appreciable lattice imperfections due to the amorphous PS, which noncrystallizable component is excluded from the lattice and lies on the top and bottom of the chain-folded monolayer lamellar crystals as suggested by Lotz *et al.*[31,32] A schematic representation, after Lotz and Kovacs,[31] of the crystalline chain-folded PEO core of such copolymer lamellae with a highly disordered (amorphous) PS layer on opposite (fold) surfaces is shown in Figure 34(a). The formation of bilayered crystals, in which the disposition of the two chain-folded PEO layers and the amorphous PS is as depicted in Figure 34(b), has also been discussed.[31] We shall not dwell on this latter aspect, however. We confine ourselves to pointing out the following two main morphological features of PEO–PS two-block copolymers. The first is that the crystals of these copolymers exemplify definite cases of the formation of chain-folded lamellae in which there exists an amorphous (if albeit chemically different) layer at opposite surfaces of the crystalline chain-folded core. The second feature is that lamellar crystals of the PEO–PS two-block copolymers exhibit regular polygonal lateral habits as illustrated in Figure 35. Indeed a variety of well-defined polygonal lateral habits have been observed which are similar to habits exhibited by crystals of PEO homopolymer (see Refs. 31, 32, and 93 for comparison). In short, within the constitutional bounds

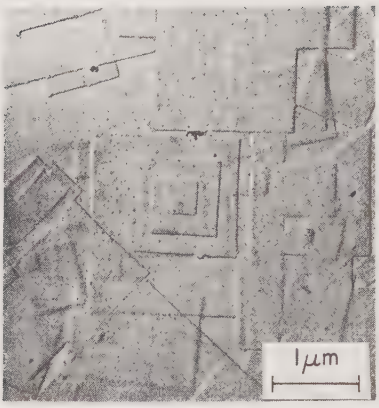

Fig. 35. Electron micrograph showing well-defined square lateral habit of the constituent lamellae in a multilayered crystal of a two-block copolymer of ethylene oxide and styrene.[32] (Reprinted with permission of Dietrich Steinkopff Verlag, Darmstadt.)

indicated above the presence of the PS as a chemical and steric chain imperfection does not disrupt the folding of the PEO portions of the block copolymer chains, nor does it disrupt the lateral mode of growth of the crystals. This latter feature is in marked contrast to the case of random copolymers, which, as we pointed out in Section 3.4.4.3 with reference to, for example, ethylene–propylene and ethylene–butene-1 copolymers, exhibit irregular lateral growth habits. We shall return to this contrast between the lateral habits of two-block and random copolymers briefly in the next subsection.

3.4.6.3. On Aspects of the Lateral Growth Habits of Polymer Crystals

There are two topics we wish to touch on briefly in this subsection. First, although we have already dwelt on the subject in Section 3.4.4.3, we wish to advance some additional comments on the manifestation of irregular lateral growth habits in chain-folded crystals grown from solution. As will become evident, these comments derive in part from factors or observations which were introduced or described in Section 3.4.5. This is the reason for delaying further consideration of matters concerning irregular lateral growth habits to this stage. Second, we wish to dwell briefly on the formation of some lath-shaped, chain-folded polymer crystals with reference to some views which have been advanced concerning the manner in which the molecules are apposed in a folded manner at the lateral faces of such crystals during growth. Our purpose in dwelling on these latter

views is that, if correct, they represent a radical departure in the manner in which chain molecules fold at the periphery of a growing lamella from that which occurs in simple sectored crystals such as those of polyethylene, polyoxymethylene, and poly(4-methylpentene-1).

(a) *On the Manifestation of Irregularity in the Lateral Habits of Chain-Folded Crystals.* We pointed out at the end of Section 3.4.6.2 that the regular lateral growth habits exhibited by ethylene oxide–styrene two-block copolymer crystals is in marked contrast with the irregular lateral habits exhibited by lamellae of crystallizable random copolymers, such as, for example, ethylene–propylene copolymers, in which the preponderance of monomer units in the chains are $[-CH_2-CH_2-]$ and a relatively minor number of comonomer units are

$$[-CH_2-\underset{\displaystyle CH_3}{\underset{|}{CH}}-]$$

As summarized in general terms in a paper by Sanchez and Eby,[204] a central issue in the crystallization of random copolymers in which the minor constituent comonomer units are stereochemically quite different from the main constituent monomer units along the chains is whether the minor units are incorporated (e.g., as point defects) in the crystal lattice of the major component units upon crystallization, or whether they are in fact preferentially excluded from the crystal lattice as assumed in Flory's theory of copolymer crystallization.[205] It is implicit in this latter view that, in the case of chain-folded lamellae of random copolymers, the minor constituent comonomer units would be primarily situated at the fold surfaces and that the exclusion of these units would contribute to fluctuations in fold period and hence to fold surface roughness. The issue of the incorporation or preferential rejection of comonomer units from the crystal lattice of the major component in random copolymers is also important to an understanding of the manifestation of irregular lateral growth habits in crystals of such copolymers. For the sake of simplicity, we shall confine ourselves here to some brief comments on random ethylene–propylene copolymers, in which propylene is the minor constituent. We use these as examples to illustrate some of the considerations which arise concerning the manifestation of irregular lateral growth habits in random copolymer crystals. In what follows, we shall refer

to the ethylene–propylene copolymers as methyl-branched copolymers of polyethylene.

Chain-folded crystals of such copolymers containing up to 28 methyl branches/1000 carbon atoms have been grown from solution.[173,174] The crystals exhibited the polyethylene unit cell structure, except that the *a* axis of the cell tended to be larger than that in polyethylene and all the more so the higher the methyl branch content. In addition, the "degree of crystallinity" of the crystals decreased as the number of branches in the chains increased. Furthermore, as is the case for linear polyethylene, the lamellae were thicker the higher the crystallization temperature. The irregularity in the lateral habits of copolymers containing 17 and 28 methyl branches per 1000 carbon atoms has been demonstrated by Kawai *et al.*[174] and Holdsworth and Keller,[173] respectively (see, e.g., Figure 36). These authors concluded that an appreciable proportion of methyl branches was incorporated in the core of the lamellae (see also Refs. 206–208). As we pointed out in a previous section, the details of the lateral propagation of such crystals remain to be determined. The irregular character of their lateral growth habits suggests imperfect reentry (e.g., excessive interstrip reentry as compared to any which may occur in the case of polyethylene) during the folding of the chains as one possible contributing factor which one might associate with the occurrence of methyl branches at the folds. This matter, and the influence of methyl branches occurring in the core of the lamellae on the lateral growth of the crystals, remain to be elucidated.*

Finally, it must be borne in mind that, as was pointed out in Section 3.4.4.3 with reference to isotactic polystyrene, the manifestation of irregular lateral habits does also occur under certain circumstances in the case of this stereoregular homopolymer. While this feature also remains to be fully elucidated, a possible molecular mechanism involving what would in essence be excessive interstrip reentry may be pointed out. We refer in this connection to a lateral growth regime whose possible manifestation was originally considered in general

* Two features should be noted in this connection. The first is that the departures exhibited by these copolymers from the regular lateral growth habits exhibited by crystals of polyethylene is accentuated the larger the number of methyl branches (e.g., compare Figure 36a shown here with Figure 1a in Ref. 173). The second is that the reflections obtained in electron diffraction patterns from crystals of the copolymers containing a substantial number of methyl branches are distinctly arced, as can be seen in Figure 36b. The interrelationship between this latter feature and the fold domain structure in the crystals remains to be fully elucidated.

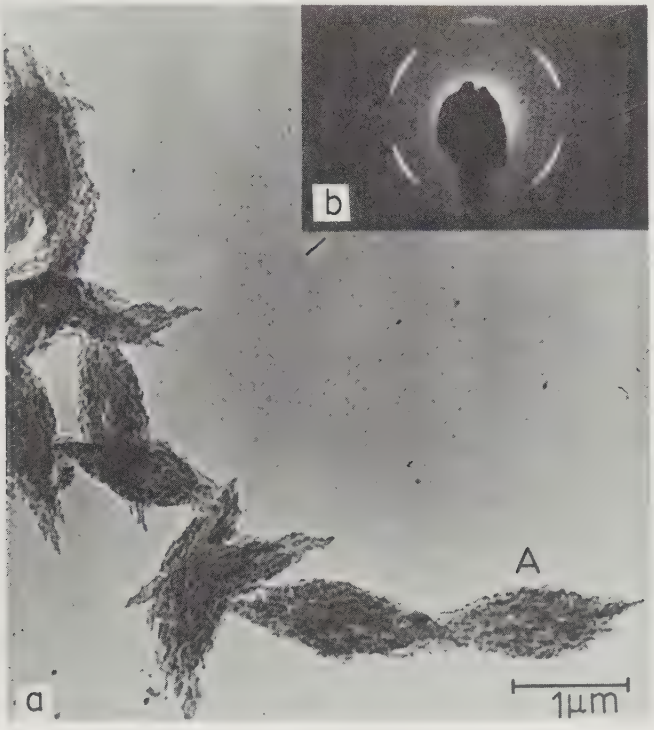

Fig. 36. (a) Electron micrograph of crystals of a random ethylene–propylene copolymer (27.9 methyl branches per 1000 carbon atoms). A crystal in the orientation of crystal A would give rise to an electron diffraction pattern such as that shown in the inset (b). Growth is fastest in the *b*-axis direction in these crystals.[173] (Photograph courtesy A. Keller, reprinted with permission of John Wiley and Sons, Inc.)

terms by Sanchez and DiMarzio[166] and has subsequently been developed by Lauritzen and Hoffman.[209] In this regime (regime II),[209] which is also discussed in detail by Hoffman *et al.*[11] elsewhere in this Treatise, it is envisaged that the rate of formation of surface nuclei along the sides of a developing lamella is relatively large as compared to the rate at which the molecules fold along the sides of the lamella. The situation may be imagined in which the number of monomolecular nuclei is so large such as to result in excessive abutment between nuclei as they spread along the sides of the lamella, thus leading in turn to excessive interstrip reentry (see, for example, Figure 25, Ref. 11), which feature we speculate might well result in the

manifestation of an irregular lateral habit. Pending a detailed characterization of the nature of sectorization in the particular species of isotactic polystyrene crystals which exhibit ill-defined outlines, this possibility remains somewhat conjectional at this stage; it certainly merits further investigation, not only in the case of isotactic polystyrene, but also in other cases, such as the copolymer crystals mentioned earlier, in which the manifestation of irregular lateral growth habits might be due, in part at any rate, to excessive surface nucleation.

(b) *On the Formation of Lath-Shaped, Chain-Folded Polymer Crystals.* Solution-grown, chain-folded lamellar crystals of some polymers exhibit lath-shaped habits. Polypropylene[108–110] crystallized in its α-monoclinic crystalline modification and barium poly-L-glutamate[210] crystallized in the β-crystalline modification are two such polymers. Our reason for bringing up the topic of the formation of the lath-shaped crystals of the above-mentioned polymers is to acquaint the reader with the view, which has been advanced by Sauer *et al.*[108] in the case of polypropylene and with the possibility con-

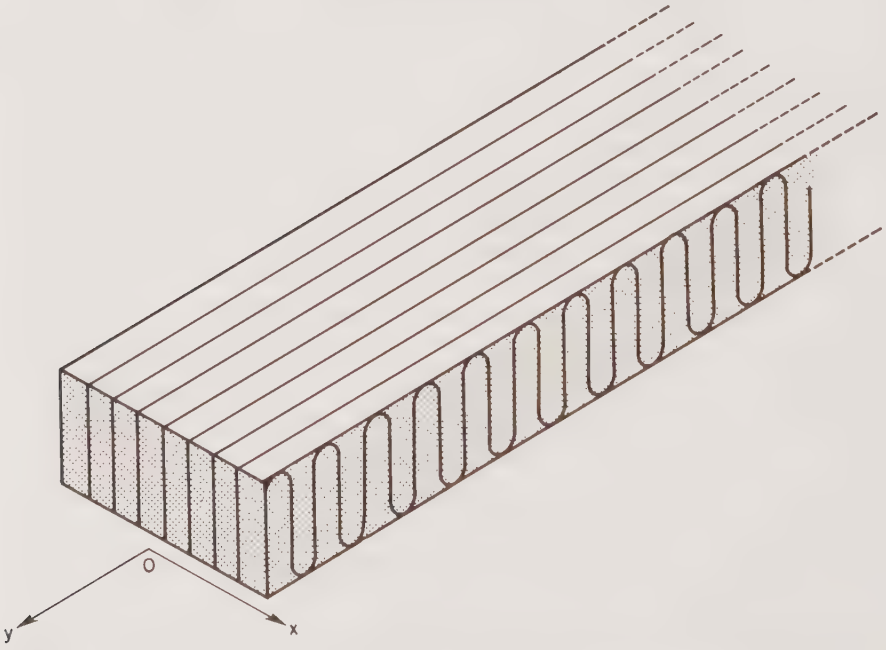

Fig. 37. Illustration of a lath-shaped lamella in which the chains are depicted as being folded only along planes parallel to the long axis *Oy* of the lath.

sidered by Keith *et al.*[210] in the case of barium poly-L-glutamate, that the chain molecules in the laths are folded along the set of planes parallel to the long axis and the long lateral faces of the lamella, as shown schematically in Figure 37. In other words, each lath consists of a single fold-domain. It is implicit in this view that the chains which accrue at the extremity of the lath do not fold parallel to the narrow side of the lath, i.e., along Ox in Figure 37, but that they actually fold into the surrounding solution, i.e., parallel to Oy, which is the direction of most rapid propagation in the crystal. This mode of growth is in distinct contrast with that which prevails more generally among polymer crystals. Even in the case of regime II[11,209] type of growth mentioned earlier, folding does not exclusively occur "into" the solution.

If one accepts that the molecules are indeed folded only along the planes that are parallel to the long axis of the lath-shaped crystals mentioned above, then the evident question is: Why is this so? This is an aspect which remains to be resolved, and it is not our intention to dwell in any length on the many possibilities and queries which can be or have been envisaged. There is little that has been published on this matter. We shall confine ourselves to some brief comments.

In the case of polypropylene it should be pointed out that the suggestion that folding occurs only along the planes parallel to the long axis of the laths stems from an observation reported by Sauer *et al.*[108] on deformed laths. According to these workers, the laths split "cleanly" along a direction parallel to the long axis of the lath, i.e., no traversing fibrils resulting from the pulling out of material are observed in fractures parallel to the long axis of the laths. In contrast, cracks which develop at right angles to the long axis of the laths are traversed by fibrils.[108,211] The planes that are parallel to the long axis of the laths are the (040) planes, and the unit cell structure of α-monoclinic polypropylene[51] is such that the hand of the helical stems in successive (040) planes as one proceeds across the lath (i.e., in a direction parallel to Ox in Figure 37, which corresponds to the b-axis direction in the crystal) alternates from left-handed to right-handed from one plane to the next. It was initially conjectured[108] that the folding of chains along the (040) planes and the occurrence of preferential growth parallel to these planes in the laths is favored because, inter alia, such folding does not involve any change in the handedness of successive stems along each (040) plane. This view was subsequently discounted by Morrow and Newman[212] insofar as any influence the folding might have in determining the

preferential growth direction in the laths, since it was observed that α-monoclinic crystals of very low-molecular-weight polypropylene, in which the chains were so short that they did not fold, also exhibited a lathlike habit in which the (040) planes were also oriented parallel to the long axis of the laths. The manifestation of such preferential growth parallel to the (040) planes in the latter laths also remains to be explained. Finally, we point out that it is puzzling that in the case of some chain-folded laths of polypropylene (e.g., Figure 5a, Ref. 109) the extremity of the lath is smooth and straight-edged and makes an angle of about 73° with the long axis of the lamella, which orientation corresponds to that of the (110) planes in the lath.* Ordinarily, this feature would be taken as indicating the occurrence of folding along such planes. This feature needs to be borne in mind, because if chain folding in such laths only occurs along the (040) planes, then one would be led to conclude that the accretion of molecules at the extremity of such laths and folding "into the solution" must occur in a highly systematic sequential fashion from one side of the lath to the other. There are clearly interesting grounds for further investigations into the nature of folding in α-monoclinic polypropylene crystals.

Turning to the case of barium poly-L-glutamate,[210] it is of interest to note that the long lateral faces of the laths are parallel to the (001) lattice planes in which neighboring stems in each plane are hydrogen-bonded to one another. These planes are usually referred to as the hydrogen-bonded sheets, and Keith *et al.*[210] have indicated that it is much more likely for the polymer chains to fold within these hydrogen-bonded sheets than across them. This could imply another possible instance of "folding into the solution." This should not be construed as indicating that the preferred direction of growth and the direction of folding of the chains are always parallel to the direction of hydrogen bonding in polymers possessing hydrogen-bonded, sheetlike lattice structures. Calcium poly-L-glutamate β crystals are a case in point. Thus, as indicated by Keith *et al.*[210] chain-folded lamellae of this latter polymer, although not possessing the morphological regularity of the barium poly-L-glutamate laths, do nevertheless exhibit a preferential direction of growth, which is, however, at right angles to the hydrogen-bonded sheets ((001) planes) along which the molecules are presumed to be folded. In short, in the case of calcium poly-L-glutamate, not only are the hydrogen-bonded

* While this feature is not a common feature of all polypropylene laths, it should be noted that examples other than the one mentioned here have been observed.[213]

sheets oriented at right angles to the preferred growth direction in the crystals, but so is the direction of folding of the molecules as envisaged by Keith *et al.*[210] (see Figure 2, Ref. 210).

3.4.7. On the Conformations (Three-Dimensional Shapes) of Chain-Folded Polymer Crystals: The Formation of Curved Crystals

The formation of chain-folded lamellar crystals that are not flat has already been mentioned and discussed briefly in Section 3.4.2, where we referred specifically to the hollow pyramidal character of some species of polyethylene crystals and to the incidence of a slight buckling (conicalness) in simple four-sectored crystals of poly(4-methylpentene-1) and in six-sectored crystals of polyoxymethylene. The manifestation of departures from planarity in chain-folded polymer crystals is certainly not limited to these specific examples. Thus Bassett *et al.*[138] have observed that some crystals of polyethylene that exhibit a truncated lozengelike lateral habit are essentially chair-shaped. Furthermore, instances of the formation from dilute polymer solutions of chain-folded polymer crystals that exhibit pronounced curved lamellar habits have also been reported. For example, Holland and Miller[45] have pointed out that chain-folded crystals of orthorhombic poly(butene-1) are rolled up in a scroll-like manner, and a similar observation has been reported by Geil[113] in the case of some crystals of nylon 6.6. The incidence of curvature in such crystals of poly(butene-1) and nylon 6.6 remains to be accounted for, as is also the case for hollow bowl-shaped crystals of poly(vinylidene fluoride) observed by Sakaoku and Peterlin.[214] The formation of curved polymer crystals from solution has been observed and examined in detail in the case of poly(4-methylpentene-1),[79] polyoxymethylene,[80] and polychlorotrifluoroethylene.[112] These studies, in which all three polymers were crystallized from dilute solutions at different temperatures, revealed an interesting phenomenon which was first observed in the case of P4MP and was subsequently also found to be exhibited by POM and PCTFE.* Thus, summarizing in broad terms, the following effect of crystallization temperature on the conformation (overall three-dimensional shape) of the crystals was observed in all three polymers: It was found that

* For the sake of brevity in the remainder of this section we shall refer to poly(4-methylpentene-1), polyoxymethylene, and poly(chlorotrifluoroethylene) by P4MP, POM, and PCTFE, respectively.

whereas the lamellar crystals formed at high temperatures (low undercoolings) were planar (in the case of PCTFE[112]) or very nearly so (in the case of P4MP[79] and POM[80] the crystals were very slightly buckled), at lower temperatures multilayered crystals were formed which were distinctly curved (dished) and all the more pronouncedly so the lower the crystallization temperature. Indeed, at the lowest crystallization temperatures investigated, the crystals were hollow bowl-shaped and had a radius of curvature in the range 2–5 μm. A brief description of some of the observations derived from these studies on the crystal habits of P4MP, POM, and PCTFE is presented below in addition to a very brief outline of a working hypothesis or model which has been suggested concerning the incidence of curva-

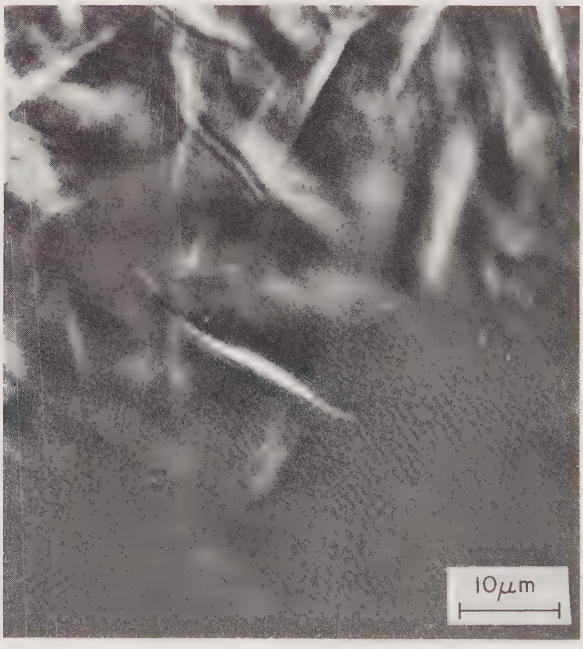

Fig. 38. Optical phase-contrast micrograph showing a crystal (center of picture) of poly(4-methylpentene-1) grown at 90°C from a 0.1% solution in an equivolume mixture of xylene and amyl acetate. This crystal, which is in suspension in liquid and is viewed edge-on, is similar to the four-sectored crystals shown in Figures 12 and 20. Note the essentially straight character of the edge-on profile of the crystal. (From Khoury and Barnes.[79])

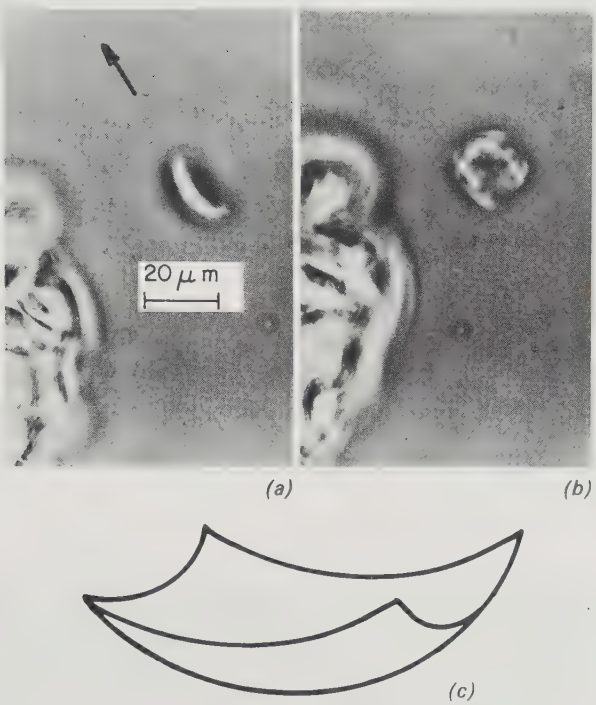

Fig. 39. (a, b) Two views under the optical microscope (phase contrast) of a multilayered crystal of poly(4-methylpentene-1) grown at 80°C from a 0.1% solution in an equivolume mixture of xylene and amyl acetate. The crystal is in suspension in liquid. (a) An edge-on view of the crystal. Note its crescent-like profile. (b) The same crystal after it had rotated through ~90° about an axis (arrow) oriented at ~30° with respect to the vertical in the field of view. (c) Schematic representation of the distinctly curved (dished) overall shape of this type of crystal. (From Ref. 79.)

ture and its variation in crystals of these polymers according to the crystallization conditions.

While electron microscopy was used to examine the fine structures of the crystals formed at different temperatures, optical microscopy was used to examine the as-grown (uncollapsed) shapes of the crystals. The differences in curvature between the crystals formed at different temperatures were readily detected by examining the crystals in various perspectives while they were in suspension in liquid, using an optical microscope equipped with phase-contrast optics. Figures 38–40 are optical micrographs of crystals of P4MP formed at

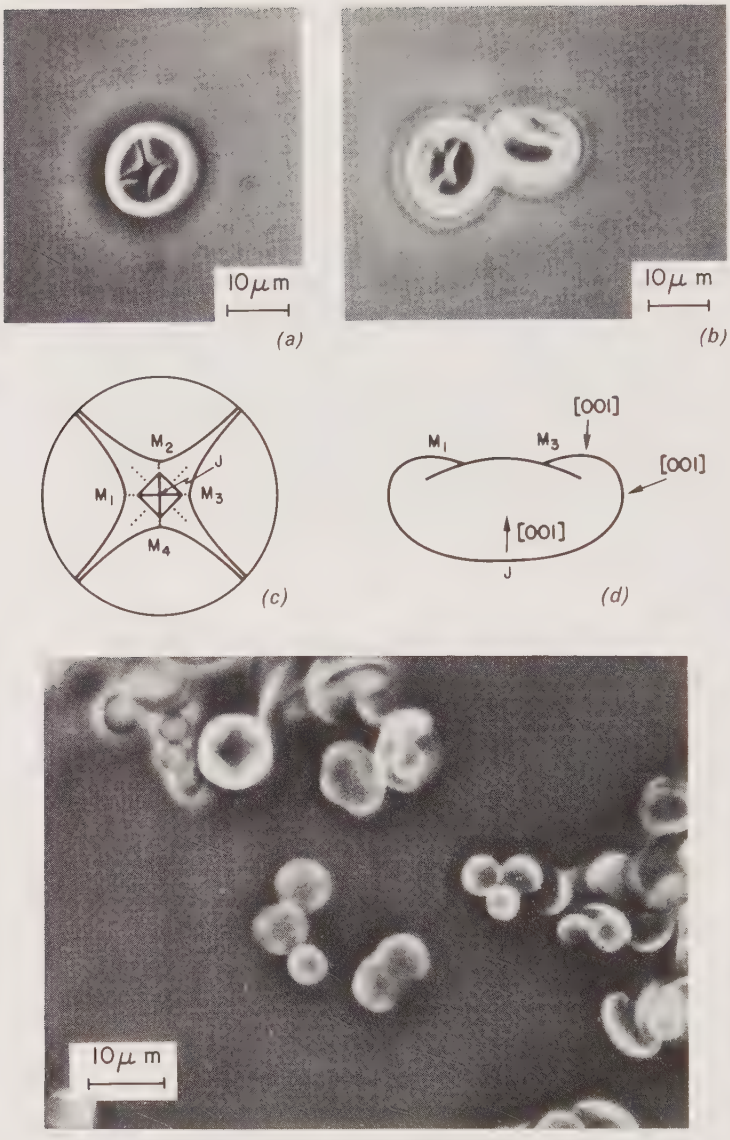

Fig. 40. (a, b) Three different views under the optical microscope (phase-contrast optics) of the fourfold symmetric, multilayered, hollow bowl-shaped crystals of poly(4-methyl-pentene-1) formed upon cooling a 0.1% solution in an equivolume mixture of xylene and amyl acetate to 70°C. The crystals are in suspension in liquid. (a) A view of a crystal as seen along its central axis. (b) The crystal in the lower portion of the picture is seen edge-on. (c, d) Schematic representations of the overall shape of these hollow bowl-shaped crystals as seen along and at right angles to their central axis, respectively. The overall shape of such bowls in relation to the lateral habit of the essentially flat, four-sectored crystals formed at 90°C is shown in (c). (e) A view under the optical microscope (phase-contrast optics) of numerous hollow bowl-shaped crystals of poly(4-methyl-pentene-1) formed upon cooling a 0.1% solution to 50°C. These crystals, which are similar in shape but have smaller radii than those shown in (a) and (b) are in suspension in liquid; see text. (From Ref. 79.)

temperatures in the range 90–50°C from 0.1 % solutions of the polymer in equivolume mixtures of xylene and amyl acetate.[79] The simplest crystals formed at 90°C were four-sectored monolayered crystals of the type illustrated in Sections 3.4.1 and 3.4.2 (e.g., Figures 12, 14c, and 20) as well as multilayered crystals whose constituent lamellae were four-sectored. As shown in Figure 38, such square, four-sectored lamellar crystals exhibit an essentially linear profile when they are viewed edge-on while in suspension in liquid. This illustrates that although the four-sectored lamellae are not perfectly flat, their departure from planarity is indeed very small, as was indicated in Section 3.4.2. In contrast, as illustrated by the examples shown in Figures 39 and 40, the crystals formed at 80, 70, and 50°C exhibit distinctly curved but nonetheless fourfold symmetric shapes. Two different views of an example of the multilayered P4MP crystals formed at 80°C are shown in Figures 39(a) and 39(b). Figure 39(a) represents an edge-on view of the crystal, whose crescent-like profile when viewed in this perspective clearly reveals the distinctly dished character of the crystal. Figure 39(b) represents the same crystal after it had rotated through $\sim 90°$ about an axis (arrow in Figure 39a) oriented at $\sim 30°$ to the vertical in the field of view. In this latter perspective the crystal may be seen to exhibit an essentially square peripheral profile which is, however, rounded at the corners. This latter feature is due to the fact that all four corners of the crystal are upturned (or downturned as the case may be) as depicted in the schematic representation, which is shown in Figure 39(c), of the overall dished shape of such crystals. The radius of curvature of the crystals was estimated to be roughly 15 μm, which is appreciably larger than that found in the hollow bowl-shaped crystals which were formed in solutions cooled to 70 and 50°C, respectively. Three perspectives of the fourfold symmetric hollow bowl-shaped crystals of P4MP, which were formed upon cooling a solution to 70°C, are shown in Figures 40(a) and 40(b). Figure 40(a), which represents a hollow bowl as seen almost along its central axis, illustrates two features. First, when viewed along their central axis, these curved crystals exhibit an essentially circular outline (radius 6–7.5 μm), and second, the "tetracuspid" character of the open end (rim) of these hollow bowls can also be clearly seen. The lower crystal in Figure 40(b) is oriented with its central axis in the plane of the field of view, whereas the orientation of the upper crystal in Figure 40(b) is intermediate between the other two crystals in Figures 40(a) and 40(b). Schematic representations of such fourfold symmetric, hollow

bowl-shaped crystals as seen along and at right angles to their central axis are depicted in Figures 40(c) and 40(d), respectively. Furthermore, the relationship between the habit of these hollow bowls (whose wall is several chain-folded lamellar layers thick) in relation to that of the essentially flat, four-sectored lamellae formed at 90°C is also shown in Figure 40(c). Briefly the following features are noteworthy: (a) The orientation of the axis of the chain molecules (i.e., the *c* axis or [001]) is normal to the lamellar wall and changes progressively through 180° or more upon proceeding along the four symmetrically disposed longitudinal paths traced from the pole (*J*) to the leading extremities M_{1-4} at the rim of the hollow bowls; (b) notwithstanding this pronounced change in the orientation of the axis of the molecules, these crystals exhibit a fourfold symmetric mode of development which is indicative in itself of an overall coherence in the manner in which these crystals grow.

At crystallization temperatures below 70°C hollow bowl-like crystals were formed whose shapes were similar to those formed at 70°C but whose radius of curvature was smaller the lower the growth temperature. Examples of hollow bowl-shaped crystals formed in a solution cooled to 50°C are shown in Figure 40(e). Under the conditions of high supercooling which prevailed in this latter case the onset of crystallization occurred before temperature equilibrium was attained at 50°C, and the overall curvature of the crystals was correspondingly more pronounced the lower the temperature at which they started growing. The radius of the bowls varied in the range 2.5–5 μm.

Figures 38–40 clearly illustrate the manifestation of increasing curvature in P4MP crystals the lower the crystallization temperature. It is important to note that this trend was not the only effect caused by increasing undercooling on the morphology of the crystals. Thus, in contrast with the nearly planar crystals formed at 90°C, which are four-sectored and are bounded laterally by smooth or essentially smooth {100} lateral faces (see Figures 12, 14, 20), the sides of the constituent lamellae in the distinctly curved crystals grown at lower temperatures were distinctly microfaceted, as can be seen in the electron micrograph shown in Figure 41 of a curved crystal formed at 80°C, i.e., of the type of crystal illustrated in Figure 39. Correspondingly, the lamellae in these crystals were multisectored as a result of the accretion and folding of molecules along leading and reentrant {100} microfacets during growth. Briefly, the lateral propagation of the lamellae in the curved crystals was characterized by the

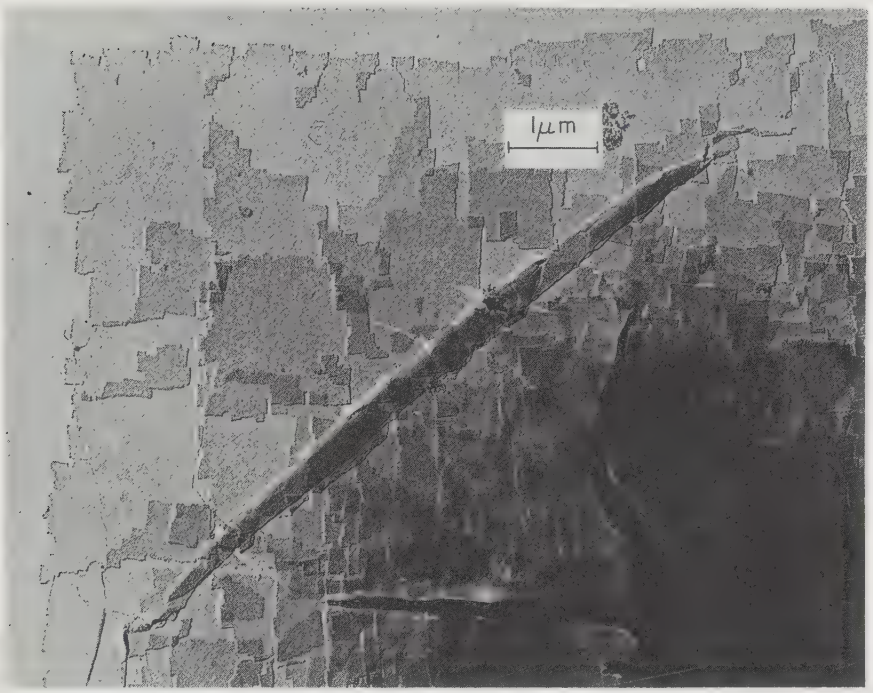

Fig. 41. Electron micrograph of a portion including a corner of the basal lamella and showing the superimposed lamellae in a multilayered crystal of poly(4-methylpentene-1) of the type shown in Figure 39, which grew from a 0.1% solution at 80°C. Note the distinctly microfaceted character of the periphery of the basal and the other lamellae. The occurrence of the pleats in the interior of the crystal is a consequence of the collapse of the curved crystal upon the substrate during drying. (Similar examples are shown in Ref. 79.)

development at their periphery of successive arrays of new sectored outgrowths bounded by {100} facets. Furthermore, examination of the peripheral characteristics of constituent lamellae in the curved crystals indicated that the lower the temperature at which growth occurred, the smaller were the lateral dimensions attained by growing sectored outgrowths before new ones developed therefrom. In other words, the lower the temperature at which growth occurred, the more finely multisectored were the lamellae.

We turn now very briefly to the case of POM.[80] The effect of increasing supercooling on the shapes (curvature) of lamellar crystals formed at different undercoolings as well as on the sectored character of the lamellae was found to be akin to that observed in the case of P4MP. Figure 11 represents a six-sectored lamellar crystal bounded

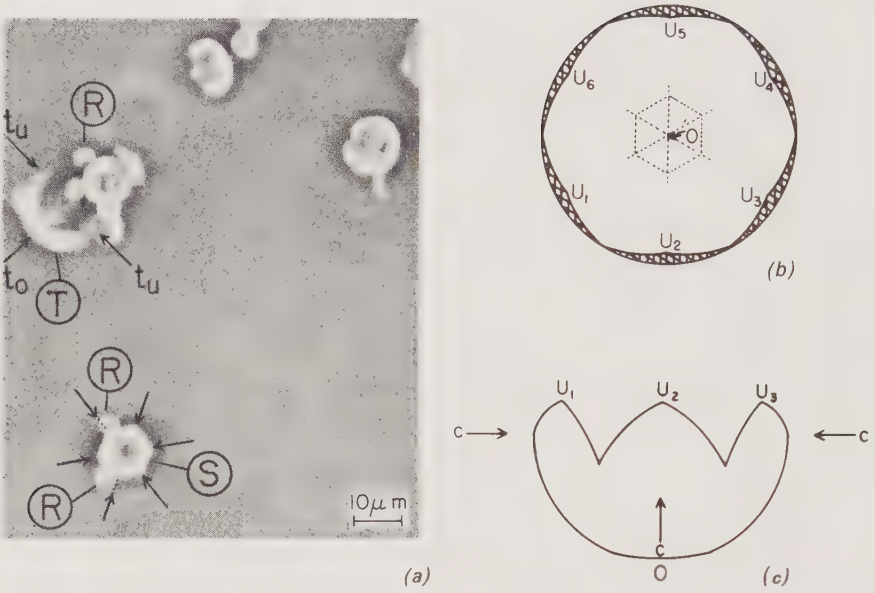

Fig. 42. (a) Phase-contrast optical micrograph of multilayered hollow bowl-shaped crystals of polyoxymethylene of different sizes grown upon cooling a 0.02 % solution in orthodichlorobenzene to 80°C. The crystals are in suspension in liquid. The larger bowl *T* and the intermediate-sized bowl *S* are oriented with their central axis of sixfold symmetry in the plane and at right angles to the plane of the field of view, respectively. Several smaller bowls, which are denoted *R*, can also be seen. (b, c) Schematic representations of the sixfold symmetric overall shape of the type of hollow bowls shown in (a) as seen along and at right angles to the central axis, respectively. The relationship between the overall shape of such bowls and the nearly flat hexagonal crystals formed at 140°C (e.g., Figure 11) is indicated in (b). The arrows t_0 and t_u appended to crystal *T* in (a) are normal to the surface of the bowl at its pole and at its rim, respectively, and the six arrows about the bowl *S* point to the regions of larger projected thickness in that crystal, which regions correspond to the hatched areas U_{1-6} in (b). (From Khoury and Barnes.[80])

by $\{10\bar{1}0\}$ growth faces and grown at 140°C from a 0.02 % solution of polyoxymethylene in orthodichlorobenzene. As was pointed out at the end of Section 3.4.2, such crystals are only very slightly buckled. They exhibit under the optical microscope an essentially linear profile when they are viewed edge-on while in suspension in liquid (see Figure 6, Ref. 80). This contrasts with the perceptibly dished character which the sixfold symmetric dendritic multisectored crystals such as that shown in Figure 27 exhibited when viewed in suspension in liquid under the optical microscope (see Figure 24, Ref. 80). Their overall radius of curvature was estimated to be 20–30 μm. Such crystals were

formed upon cooling a 0.02% solution in orthodichlorobenzene to 114°C. The pronounced pleats, which can be seen in Figure 27, and which result from the collapse of the crystals upon the substrate, clearly reflect the nonplanar as-grown character of these crystals. At lower temperatures multilayered hollow bowl-shaped crystals exhibiting sixfold symmetric overall shapes and modes of development were formed. Figure 42(a) is an optical micrograph showing randomly oriented, hollow bowl-shaped crystals grown in a 0.02% solution cooled to 80°C. The radii of the bowls in this micrograph vary in the range 2–8 μm. This variation is due to the fact that the onset of crystallization occurred well before temperature equilibrium was attained at 80°C, and the overall curvature of the crystals was correspondingly all the more pronounced and the sectored character of the lamellae all the more fine, on average, the lower the temperature at which growth took place. Schematic representations of the sixfold symmetric shape of these hollow bowl-like crystals as seen along their central axis, as well as at right angles to that axis, are shown in Figures 42(b) and 42(c), respectively. The sixfold symmetric shape and pattern of development of these bowls, which are characterized by a change of $\sim 90°$ in the orientation of the axis of the chain molecules (the *c* axis) on proceeding from the pole (*O*) of the crystals along the six longitudinal paths OU_{1-6}, is shown in Figure 42(b) in relation to the habit of the essentially flat, six-sectored lamellar crystals formed at 140°C.

Finally, insofar as this brief summary of the phenomenological observations of the effect of supercooling on lamellar curvature is concerned, we turn to the case of PCTFE.[112] Figure 29(a) is an example of the apparently planar, disk-shaped monolayer crystals formed at low undercoolings (crystallization temperature 110°C) from 0.1% solutions of the polymer in PCTFE oil. Planar multilayered crystals were also formed under the same conditions. The planar character of the crystals formed at 110°C contrasts with the crystals grown at intermediate undercoolings (crystallization temperatures 105 and 100°C), under which conditions curved-watchglass-shaped multilayered crystals were formed (Figures 43a, b) as well as multilayered crystals which are most easily described as double watchglasses (Figure 43c), i.e., they are like two watch glasses which have been placed in contact back to back. The latter crystals consist of two sets of lamellae which are curved in opposite directions. At higher undercoolings crystals were formed which had essentially hollow spherical shapes (radius ~ 4 μm), as well as aggregates consisting of intricate arrays of curved lamellae, which aggregates reflected a

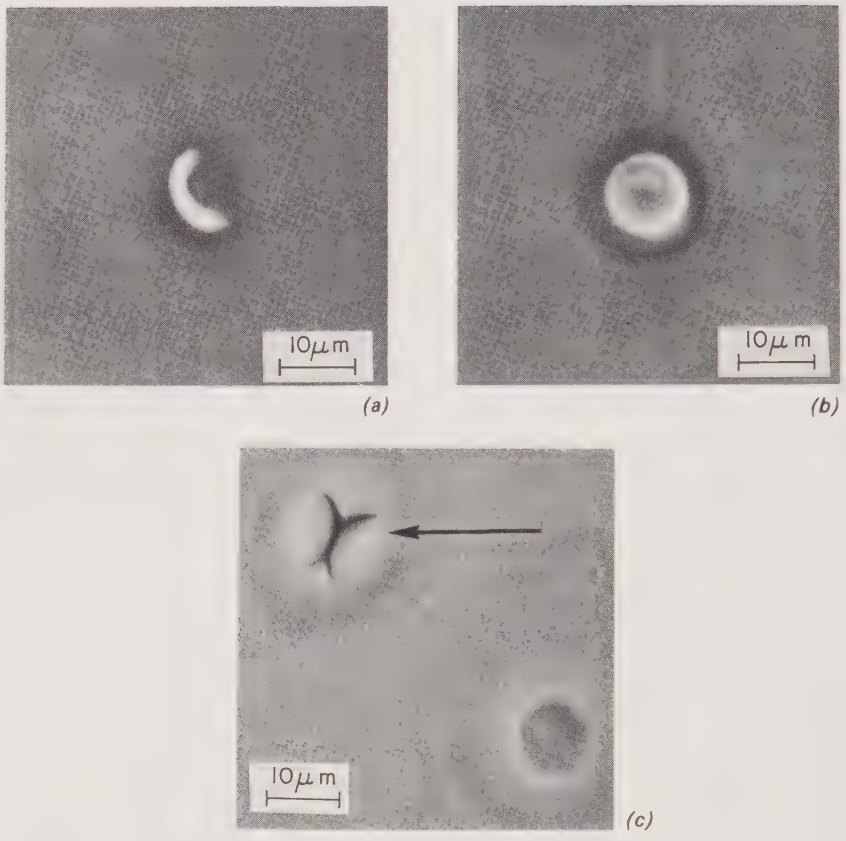

Fig. 43. (a) Phase-contrast optical micrograph showing an edge-on view of a watchglass-shaped crystal of polychlorotrifluoroethylene grown at 105°C from a 0.1% solution in low-molecular-weight polychlorotrifluoroethylene oil. (b) The same crystal seen along its central axis. (c) Edge-on view of a double watchglass type of crystal (arrow) grown under the same conditions. The crystals in (a), (b), and (c) are in suspension in liquid. (From Barnes and Khoury.[112])

frequent tendency for new curved lamellae to be curved in a direction opposite to that of the parent lamellae from which they evolved.[112] Although the variation in curvature between the curved crystals of PCTFE formed at different undercoolings (in the temperature range 90–105°C) was not as marked over the temperature range studied as the variations in curvature observed in the cases of P4MP and POM, the overall trend in the effect of undercooling on the curvature of PCTFE crystals parallels that observed in these other two polymers. An important difference between the effect of undercooling on the morphology of crystals of P4MP and POM on the

one hand and crystals of PCTFE on the other hand must, however, be pointed out. This difference is in the effect of undercooling on the lateral habit and correspondingly on the sectored character of the lamellae formed at different temperatures. In the case of P4MP and POM the essentially planar crystals formed at low undercoolings were four-sectored and six-sectored, respectively, and were bound laterally by smooth growth faces, whereas the lamellae in the curved crystals formed at higher undercoolings exhibited distinctly microfaceted lateral habits; they were correspondingly multisectored, and all the more pronouncedly so the higher the undercooling. In the case of PCTFE, however, the periphery of the lamellae in both the flat and the curved crystals was finely serrated, as is the case of the crystal shown in Figure 29. No crystallographically distinguishable microfaceting could be resolved unequivocally in the crystals formed at any of the different undercoolings, nor could any differences in sectorization be established between the lamellae in the various crystals formed in the temperature range studied.

In summary, although there is a distinct phenomenological similarity between the effect of undercooling on the curvature of crystals of P4MP, POM, and PCTFE, in that the crystals in all three cases were all the more pronouncedly curved the lower the crystallization temperature, there exists a basic difference between the effect of supercooling on the fine structures (sectored character) of chain-folded lamellae of P4MP and POM in comparison with PCTFE.

A possible explanation of why it is that P4MP and POM crystals are more pronouncedly curved the lower the crystallization temperature has been advanced as a working hypothesis and has been discussed in detail.[79,80] We shall confine ourselves here to a bare outline. The interested reader is referred to the original papers, in which the conjectural nature of this hypothesis as well as the undetermined role of a number of possible factors which might underlie the manifestation of curvature and its enhancement with lower crystallization temperature are pointed out and discussed. The thrust of this hypothesis is conveyed by the model shown in Figure 44, in which P4MP[79] is used as an example. The first and basic premise upon which this hypothesis is based is that successive sectored outgrowths which develop at the periphery of a multisectored lamella of P4MP or POM growing at a sufficiently high undercooling are possessed of a slight intrinsic conicalness with an angle of inclination θ of a few degrees, as are simple four-sectored lamellae ($\theta \simeq 2°$)[79] and six-sectored lamellae ($\theta \simeq 4.5°$)[80] of these polymers, respectively (see

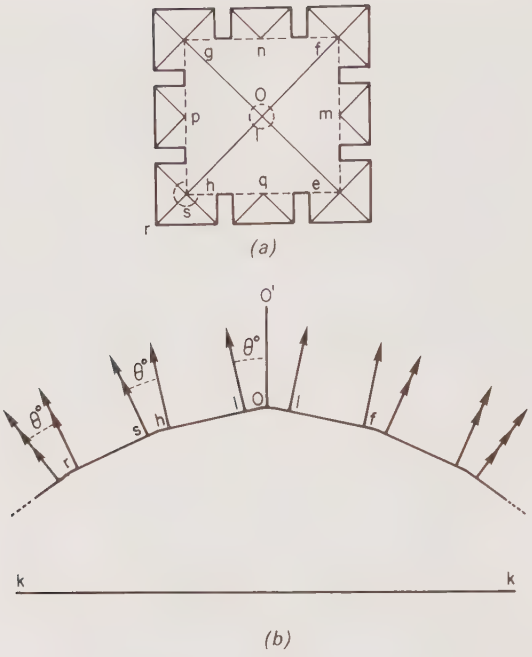

Fig. 44. (a) Plan view representing sectored outgrowths developing at the periphery of a four-sectored precursor lamella of poly(4-methylpentene-1). (b) Edge-on view of a diagonal cross section of the developing multisectored crystal depicted in (a), showing suggested incremental contribution of sectored outgrowths to the overall curvature of the lamella; see text and Ref. 79.

Section 3.4.2, where attribution of this feature to buckling under the influence of the bulkiness of chain folds was pointed out). The second premise of the hypothesis is that in the case of multisectored lamellae the intrinsic slight conicalness of sectored outgrowths is considered to contribute, in a cumulative manner, to the overall curvature of the lamellae, i.e., the development of successive arrays of sectored outgrowths at the periphery of a multisectored lamella is correspondingly accompanied by successive increases in inclination of θ at the periphery of the developing layer as indicated schematically in Figure 44. On the basis of these two premises it is envisaged that the overall curvature of multisectored lamellae will be (cumulatively) more pronounced the greater the frequency (per unit path length from the center of the lamella to its periphery) at which new sectored outgrowths

develop from preceding ones, i.e., the more finely multisectored is the character of the lamella. This conjecture is qualitatively consistent with the fact that the lamellar crystals of P4MP and POM tended to be all the more finely multisectored and were correspondingly all the more pronouncedly curved the lower the crystallization temperature. As was pointed out earlier, however, there are numerous additional factors (which we will not attempt to dwell on here) which could also contribute to the incidence of curvature in the crystals; the roles of these factors remains undetermined, however.[79,80] The case of the incidence of curvature and its variation in PCTFE crystals is at this stage very much of an open problem. For a discussion of the formation of curved crystals of PCTFE in the light of the working hypothesis outlined above for P4MP and POM, the reader is referred to the original paper.[112]

The phenomenon described above of curved crystal formation as exhibited by P4MP, POM, and PCTFE will be briefly considered in a broader context in Section 4.3.2.3 on the nature of the early stages of evolution of spherulites.

3.4.8. Twinned Polymer Crystals

Twinned crystals are edifices composed of two (or more, in which case the edifice is referred to as a multiple twin) identical single-crystal lattices united in a definite and regular manner other than parallelism. Twinning introduces an element of symmetry into the crystalline edifice which is not present in the untwinned crystal lattice, in that the lattices of the individual components in a twinned crystal are symmetrically disposed to one another relative to either an axis and/or a plane common to both component lattices.

The formation of twinned crystals, which is a well-known phenomenon in the crystallization of low-molecular-weight compounds, is also encountered in polymers. The formation of growth twins from solution has been observed in the case of several polymers, among which are polyethylene,[92,115,161,215–217] poly(ethylene oxide),[93] block copolymers composed of one poly(ethylene oxide) and one polystyrene block,[31,32] polyacrylonitrile,[218] and isotactic polypropylene.[99,108–110,219]

With the notable exception of a particular prolific mode of twinning in the case of polypropylene,[99,108–110] which we shall discuss separately in the next paragraph, twinned chain-folded polymer crystals have one feature in common, which the examples of

b1
a1
134.8°
112.6°
TWIN BOUNDARY
b2
112.6°
123.7°
a2
(a)
(b)
0·5μm

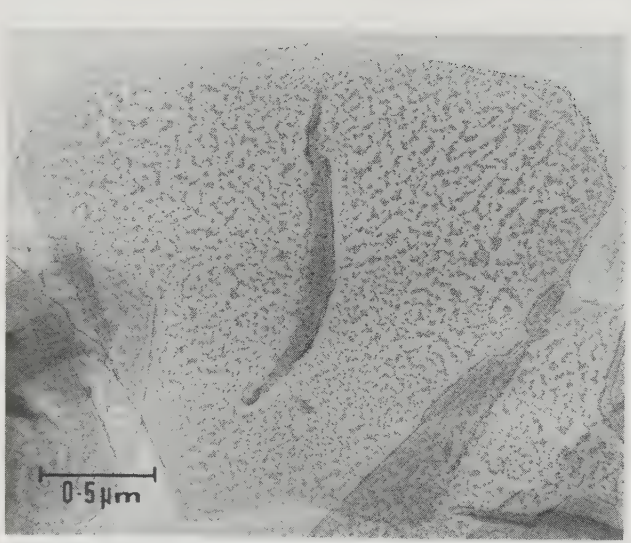

(c)

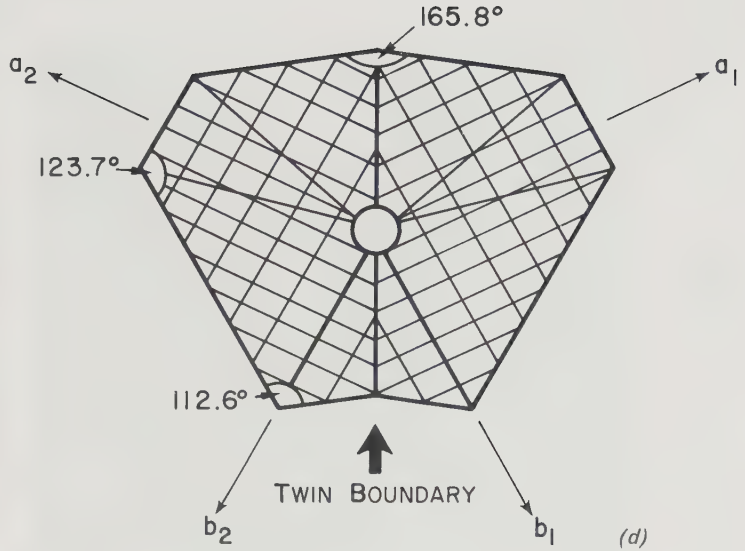

(d)

Fig. 45. (a) Electron micrograph of a shield-shaped {110} twinned crystal of polyethylene. (b) Schematic representation after Blundell and Keller[92] of the crystal shown in (a), depicting the {110} twin boundary and the orientation of the twin lattices relative to one another. (c) Electron micrograph of a {310} twinned crystal of polyethylene. (d) Schematic representation after Blundell and Keller[92] of the crystal shown in (c), depicting the {310} twin boundary and the orientation of the twin lattices relative to one another. [Photographs (a) and (c) courtesy of A. Keller, reprinted with permission of Marcel Dekker, Inc.]

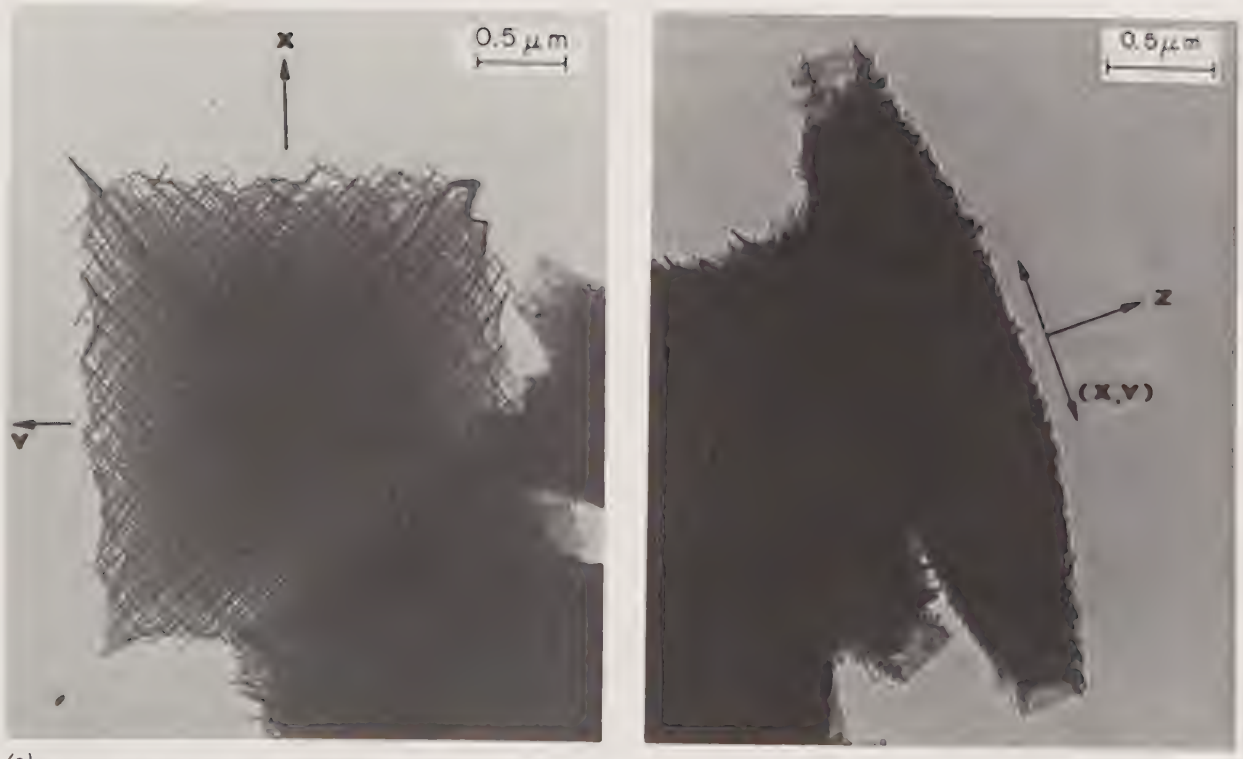

(a) (b)

Fig. 46. (a) Electron micrograph of a twinned crystal of isotactic polypropylene consisting of a cross-hatched array of chain-folded lamellae which are oriented with their fold surfaces normal to the x, y plane of the object and which traverse that plane diagonally. (b) Electron micrograph showing edge-on view (i.e., parallel to the x, y plane) of a similar twinned crystal. Lamellar structural units can be seen protruding from the two extremities of the crystal. (From Khoury.[75])

twinned crystals of polyethylene shown in Figure 45 serve to illustrate, namely the orientation of the chain molecules is unique throughout the twinned edifice (i.e., the stems of the chains in one component region are parallel to those in its twin). The twin plane in twinned crystals of polyethylene is most frequently {110}. The crystal depicted in Figure 45(a) is a "shield"-shaped {110} twin, whereas Figure 45(c) represents a {310} twinned crystal of polyethylene. The twin boundaries in these crystals are identified in Figures 45(b) and 45(d), respectively. "Triplets" (multiple twins) with {110} and {310} twin boundaries have also been observed.[92]

Isotactic polypropylene exhibits a unique type of twinning when it is crystallized in its most common α-monoclinic modification (see Section 2.2.1). Thus in contrast with other polymers (as well as polypropylene in some instances[219]), in which the stems of the folded molecules are all parallel to one another throughout the twinned lamellar edifices, isotactic polypropylene exhibits a prolific mode of twinning which leads to the formation of twinned crystals of the type shown in Figure 46. Confining ourselves at first to the morphological characteristics of these crystals, their overall shape (envelope) approximates that of a rectangular parallelepiped (Cartesian axes x, y, z, where $x/y \simeq 1.1$ and $y > 2z$). Figures 46(a) and 46(b) represent two such crystals viewed along and at right angles to the z axis, respectively. They consist of a dense network of monolayer

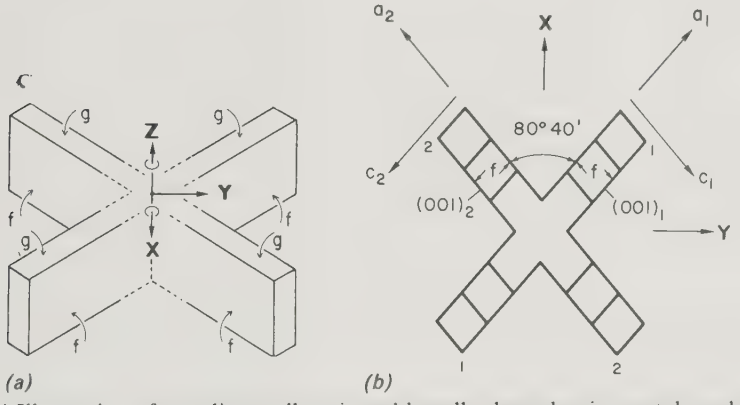

Fig. 47. (a) Illustration of two diagonally oriented lamellar branches in crystals such as those shown in Figure 46. The fold surfaces, (001), in the lamellae and the (010) lateral growth faces are denoted *f* and *g*, respectively. (b) Interrelationship between the unit cell orientation in the different diagonally oriented branches relative to one another. The branches are shown as seen along the normal to the *x*, *y* plane, which direction corresponds to the orientation of the *b* axis in all the branches; the fold surfaces are denoted *f*. (From Ref. 99.)

chain-folded branches which traverse the object diagonally with respect to its rectangular x, y cross section with their fold surfaces oriented at right angles to that cross section. Figure 47(a) serves to convey this latter feature. In short, the thin, diagonally oriented structural units which can be seen in Figure 46(a) are chain-folded lamellae being viewed edge-on. The lamellar character of these units is revealed in Figure 46(b), where lamellae can be seen protruding from the two extremities of the twinned crystal. The relationship between the respective orientations of the stems of the folded molecules in the two families of diagonally oriented lamellar branches relative to one another is shown schematically in Figure 47(b).[99] The fold surfaces in all the branches are {001} and, as indicated above, are oriented normal to the x,y cross section of the twinned edifice, as is the orientation of the b crystallographic axis in all the branches. The development of this species of twinned crystal is characterized by repeated and prolific development of daughter lamellar branches from parent branches, the dihedral angle between parent and daughter branches being nearly 90° (actually 80° 40′ as shown schematically in Figure 47b). The angle between the c crystallographic axis (the axis of the chains) in parent and daughter branches is also 80° 40′. In short, the orientation of the lattice in a parent branch relative to an offspring branch is such that the c axis in the parent branch is oriented parallel to the a axis in the offspring and vice versa. This mode of twinning is highly surprising since it violates a fundamental feature of the crystal structure of polymers and of polymer crystal growth processes, namely that crystallization involves the packing of chains parallel to one another. This tenet clearly does not hold at the interface between the twinned branches in the above-mentioned crystals of polypropylene. The specificity of the type of twinning that underlies the branching process is therefore highly unusual. Briefly, the speculation was originally advanced that the initiation of a daughter branch from a parent branch resulted from the epitaxial laying down of individual molecules in a regularly folded conformation upon the fold surfaces (i.e., the {001} faces, denoted f in Figure 47) of the parent branch such that the segments of the folded molecules lie parallel to the latter surfaces.[99] Subsequent evidence due to Padden and Keith[109,110] indicated that branching (twinning) originates at the {010} faces of parent lamellae (denoted g in Figure 47a): A detailed discussion of the origin of the unusual type of twinning exhibited by polypropylene is beyond the scope of the present chapter. For recent developments the reader is referred to a paper by Padden and

Keith[110] in which this phenomenon and its epitaxial origins are considered at length. For our present purposes it suffices to point out that, viewed in the overall context of the morphology of isotactic polypropylene in particular and the morphology of polymers in general, this unusual mode of twinning which polypropylene exhibits is more than a mere curiosity. It manifests itself prolifically when this polymer is crystallized from solution as well as from the melt and underlies many of the unusual morphologies (Ref. 12, pp. 215–220; Refs. 99, 108–110, 220, 221) which distinguish polypropylene from other "normal" polymers. In short, the unique type of twinning exhibited by isotactic polypropylene is not an insignificant aspect of the comparative morphological phenomenology of polymers.

We have confined our summary of the manifestation of twinning in polymer crystals to the case of "growth twins," i.e., twinned crystals which developed as such. It may be noted that the manifestation of twinning as a result of deformation has been observed to occur when single crystals of polyethylene are deformed.[48,222] The topic of deformation- or stress-induced twinning is, however, beyond the scope of this chapter.

4. The Morphology of Polymers Crystallized from the Melt

4.1. Preliminary Remarks

As might be deduced from the discussion of the crystallization of polymers from solution, the morphology of polymers crystallized from the melt has many complex features associated with it. All the characteristics of crystals grown from solution, such as chain folding, fold staggering, multisectorization, irregular fold surfaces, etc., also obtain in crystallization from the melt. In fact, under special circumstances, lamellar single crystals have been grown from the melt. In addition, somewhat more complex multilayered entities (called "hedrites" or "axialites") that have many of the features of single crystals have also been grown. These are discussed in Section 4.3.2.3. However, polymers crystallize from the melt most commonly in the form of spherulites, which, as we shall see, are spherically symmetric arrays of chain-folded lamellae. The study of the morphology of polymers crystallized from the melt is therefore predominantly concerned with the determination of the fine structure of spherulites and of the mechanism of their growth. As a result, we shall be

concerned with these two topics in what follows. In Section 4.4 we shall briefly discuss the morphology of polymers crystallized from the melt under pressure, which, as we shall see, exhibits some rather special and unusual features.

4.2. General Comments on Spherulites and Their Structures

As pointed out above, the dominant morphological entity formed when polymers crystallize from the melt is the spherulite, and crystallization to form spherulites is called "spherulitic crystallization." In nonpolymeric materials, in contrast, spherulitic crystallization is confined to some rather special systems. Where it seems to occur most readily is in viscous media and from melts that are relatively impure. It has been observed in minerals[223–225] and has been studied rather extensively in the crystallization of organic compounds mixed with additives to increase the melt viscosity.[226 228] The occurrence of this mode of crystallization in impure melts of high viscosity is important and we shall return to it later, for it forms the basis of the theory of spherulitic crystallization of Keith and Padden,[228–230] which we discuss in Section 4.3.2.2.

As their name suggests, spherulites are spherical aggregates of crystals, and in Figure 48 we show, in diametral section, an example of a large spherulite of the mineral barite. As can be seen, the aggregate consists of a radiating array of fibrillar structural units, so that the overall structure is morphologically spherically symmetric, suggesting that the crystal organization within the spherulite also possesses spherical symmetry. Spherulites in polymers look superficially the same as this spherulite, but there are differences, and we now proceed to discuss polymeric spherulites.

Spherulites in polymers are generally far smaller than the spherulite shown in Figure 48, and indeed are usually microscopic in size. It is pertinent to point out in this connection that polymer melts can be undercooled quite extensively, with undercoolings of over 25°C not being uncommon. The size of the spherulites grown is generally dependent on the magnitude of the undercooling, since at high undercoolings more spherulites are nucleated per unit volume. Although in special cases spherulites a few millimeters in diameter have been grown, they are usually of the order of 100 μm or less in diameter. Examples of spherulites observed in thin films under the optical microscope with crossed polarizers (see next section) are shown in Figure 49. In Figure 49(a), the spherulites are dispersed in

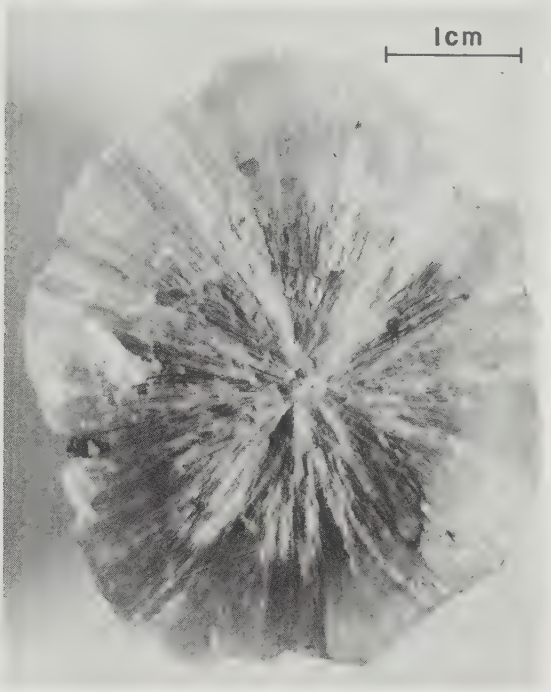

Fig. 48. A diametral section of a spherulite of the mineral barite. Note the radiating fibrillar structure.

uncrystallized polymer and exhibit a circular outline. In Figure 49(b), we show spherulites which have grown until they impinged upon their neighbors. The boundaries between the spherulites that are nucleated simultaneously are straight. When the spherulites are nucleated at different times so that they are different in size when impinging on one another, their boundaries are hyperbolas as a consequence of the fact that the radius of the spherulites increases linearly with time during growth (see Section 4.3.2.1). It will be noticed that each spherulite exhibits an extinction cross centered at the spherulite center with the arms of the cross oriented parallel to the vibration directions of the polarizer and analyzer of the microscope. The origin of these patterns will be described in the following section. The overall radiating fine texture usually exhibited by spherulites is readily discernible in Figure 49(b), and is generally all the more evident the lower the undercooling at which crystallization occurs.

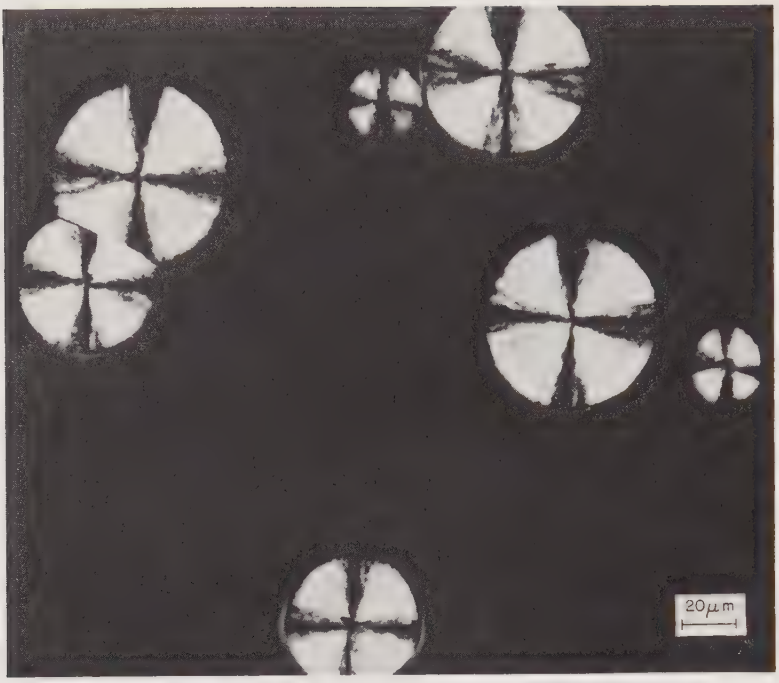

Fig. 49. Spherulites grown in thin films viewed between crossed polarizers in the optical microscope. (a) Spherulites of poly(hexamethylene sebacamide) (nylon 6.10). The black background is uncrystallized polymer. The arms of the black extinction crosses are parallel to the polarizer and analyzer vibration directions. (b) Large spherulites in poly(ethylene oxide) after completion of growth. Note their radiating fine structure. The boundary between spherulites that are nucleated simultaneously is straight; it is, however, curved when neighboring spherulites are nucleated at different times.

4.3. The Fine Structure of Polymer Spherulites

4.3.1. Experimental Observations on Fully Grown Spherulites

Polymer spherulites have generally been studied in thin films, i.e., films that are thin in comparison with the diameter of the spherulite. Such films are conveniently prepared by melting a small amount of polymer between microscope cover slips and crystallizing the polymer at the desired temperature either on the microscope hot stage or in a temperature bath. These films can also be cast from a solution of the polymer in an appropriate solvent, after which the solvent is allowed to evaporate and the film is melted and then allowed to crystallize. In essence, studying these films amounts to studying a diametral section of three-dimensional spherulites. In addition, fracture surfaces of three-dimensional spherulites grown in bulk polymer samples have also been studied, and a comparison of the results obtained from such studies (and others on bulk polymer samples) with the results obtained from the study of spherulites grown in thin films indicates that the latter are indeed accurate representations of the diametral sections of three-dimensional spherulites.

The thin films can be viewed in the polarizing microscope; surface replicas can be made for examination in the electron microscope; in the favorable case of especially thin films, they can be studied by transmission electron microscopy; in recent years, the thin films have been studied by the scanning electron microscope; and when the spherulites are large enough, microbeam x-ray diffraction studies of selected regions of the spherulite can be carried out. In addition, bulk samples of polymer crystallized from the melt can be studied by low-angle x-ray diffraction with important results for the interpretation of spherulite morphology, as we will discuss below. We shall discuss the results of the application of some of these various techniques during the remainder of this section. It is convenient for our purposes to begin with the microbeam x-ray studies.

The microbeam x-ray diffraction technique has been extremely useful in studies of spherulite structure and was apparently first used by Herbst[231] for polyamides. Subsequently it was used by numerous investigators to study a wide variety of polymers, among which we mention polyethylene (Point,[232] Keller,[233] Fujiwara[234]), poly(ethylene adipate) (Point[235]), poly(ethylene terephthalate) (Keller[233]), polyamides (Keller,[233] Mann and Roldan-Gonzales,[236] and Magill[237]), and poly(ethylene oxide) (Baltá Calleja, Hay, and

Keller[238]). In these studies, a very fine and well-collimated beam is used to "illuminate" only a small portion along a radius of a spherulite diametral section. The resulting diffraction pattern then gives the molecular orientation with respect to the radial direction, and this is the most important result of the application of this technique.

These diffraction studies have shown that in polymeric spherulites the unit cell orientation is such that the molecular chains are normal to the radial direction, or nearly so, and that a particular crystallographic direction is parallel to the radius, and this clearly demonstrates the spherical symmetry of the spherulite. In many cases, such as polyethylene (for which the radial direction is the *b* crystallographic axis) the molecular chains are normal to the radius[232-234]; in other polymers this is not strictly true, but to our knowledge no polymer (other than in the case of some species of polypropylene spherulites)* is known for which the molecular axis makes an angle of less than 60° with the radius. For obvious reasons, the molecular orientation in spherulites is said to be "tangential."

It may be noted that this "tangential" orientation was known before the discovery of chain-folded polymer crystals, and for many years defied satisfactory explanation. In particular, it was difficult to explain tangential orientation along with the radiating fibrillar habit mentioned above (and to be discussed in more detail below) on the basis of the fringed micellar view of polymer crystallization. As will become apparent during the remainder of this section, tangential orientation is readily explained on the basis of the chain-folded nature of polymer lamellar crystals and the organization of the lamellae in a spherulite.

We next take up the subject of the study of spherulites by the polarizing microscope. This is the most common of the methods used to study spherulites, and historically the oldest.[3] A great deal has been learned about the grosser features of spherulite structure from its application, and, when coupled with the fine details observed by electron microscopy, it serves to give a unified picture of the structure of polymer spherulites.

* Twinning akin to that discussed in Section 3.4.8 occurs in some species of spherulites of the α-monoclinic form of polypropylene. This twinning leads to the development of daughter lamellar branches at right angles or nearly so to radially oriented lamellae in which the chains are at right angles to the radius. The chain molecules in the daughter branches are oriented with the chains parallel to the radius (see Binsbergen and De Lang[221]).

The utility of the observations with the polarizing microscope stems from the fact that polymer crystals are anisotropic with respect to their optical properties. The polarizability in the direction of the chain axis is usually different from that normal to the chain direction (see, e.g., Bunn and Daubeny[239] and Keedy *et al.*[240]). Consequently, the refractive index for light polarized with its electric vector along the chain axis is different from the refractive index for light polarized with its electric vector normal to the chain axis. Of course, the refractive index in the latter case may depend upon the actual direction of the electric vector, so that in general the refractive index ellipsoid is not an ellipsoid of revolution and the material is biaxial. In the more symmetric cases (tetragonal, hexagonal, rhombohedral) the ellipsoid is one of revolution and the material is uniaxial. No cases are known in which the optical properties are isotropic (i.e., the refractive index ellipsoid is a sphere) except for the case of poly(4-methylpentene-1), where it apparently occurs adventitiously at 50°C.[241,242]

When spherulitic films of such optically anisotropic polymers are viewed between crossed polarizer and analyzer under an optical microscope, certain characteristic extinction features are seen, and the interpretation of these extinction features has had an important bearing on the determination of the structure of spherulites. The simplest and most common extinction pattern that is observed is an extinction cross oriented with its arms parallel to the polarizer and analyzer vibration directions. Examples of this have already been seen in Figure 49. An important feature of this pattern (and others that we shall show later) is that as the specimen is rotated between the polarizer and analyzer, the pattern remains fixed in orientation. Historically, this fact, which clearly illustrates the spherical symmetry of the spherulite, was known before the study of spherulites by microbeam x-ray techniques.

The quantity of interest in these studies is the birefringence, defined as the difference between the refractive index for light polarized with its electric vector along the radial direction of the spherulite and the refractive index for light polarized with its electric vector normal to the radial direction. As we have noted above, microbeam x-ray diffraction studies show that the molecular chains are usually normal to the radius, or nearly so, and that one crystallographic direction is parallel to the radial direction. The birefringence gives a measure of the difference in refractive index for light polarized along the crystal direction, which is radial, and the *average* of the refractive indexes for light polarized so that its electric vector

is normal to this direction. In favorable cases the sign and magnitude of this quantity can provide information on the molecular orientation. For example, Bunn and Alcock[3] determined that spherulites of polyethylene were negatively birefringent. They knew from studies on drawn fibers, in which x-ray diffraction had shown that the molecular orientation was along the axis of the fiber, that the refractive index for light polarized parallel to the molecular chains is higher than the average refractive index for light polarized normal to this direction From this, the crystal structure of polyethylene (which is orthorhombic[49,50] but almost hexagonal), and the negative birefringence of the spherulites, they were able to deduce the tangential orientation of the molecular chains. However, in other cases, as, for example, the polyamides, the determination of molecular orientation from birefringence is fraught with ambiguities.[66] The use of birefringence to determine molecular orientation depends upon crystal symmetry and on the magnitude of the principal refractive indices. However, in almost all cases, all that can be determined is that the molecular chains are "tangential"; the crystallographic direction that is parallel to the radius cannot be determined as it can by the microbeam x-ray studies.

Referring again to Figure 49(b), there is another characteristic of the spherulites that should be considered. This is the fact we mentioned earlier that they exhibit a radiating fine texture, which suggests that spherulites possess a "fibrillar" morphology that is superficially similar to the truly fibrillar nature of the mineral spherulite shown in Figure 48. Now, the word "fibril" implies a structure with one dimension that is very long compared to the other two, these two being approximately equal. It thus implies that the transverse cross section of the fibril is approximately equiaxed, indeed that the fibril is pencil-like. As we shall see later when considering the results of electron microscope observations, these apparently fibrillar structures in polymer spherulites are in fact highly elongated, chain-folded lamellae or, at most, stacks of elongated lamellae. They are thus not "fibrils" in the traditional sense, but we shall continue to use the term for lack of a more suitable wieldy one.

As summarized by Keller in his early review,[14] this radiating fibrous texture was recognized in the earliest investigations of polymer spherulite morphology, although the nature of the radiating structural entities (fibrils) was not known. In fact, as mentioned earlier, this fibrillar character and the tangential orientation of the molecular chains were hard to account for before the discovery of chain folding

and the recognition that the radiating structural entities are elongated, chain-folded lamellae.

Continuing our discussion of the extinction patterns observed in the optical microscope, it was first discovered by Keller[243] and subsequently observed by others (see, e.g., Ref. 14) that in some cases polymer spherulites exhibit more complex extinction patterns. These are of four types: (1) a pattern in which, in addition to the extinction cross, concentric extinction rings with a regular periodicity are seen, (2) a pattern similar to the previous one, but with the rings paired so that there is a double periodicity (3) a pattern in which the extinction cross is replaced by a zigzag, and (4) a pattern which can best be described with reference to Figure 50, where we illustrate it in spherulites of polyethylene. In these spherulites, concentric extinction rings are seen. Along the vertical and horizontal directions, where

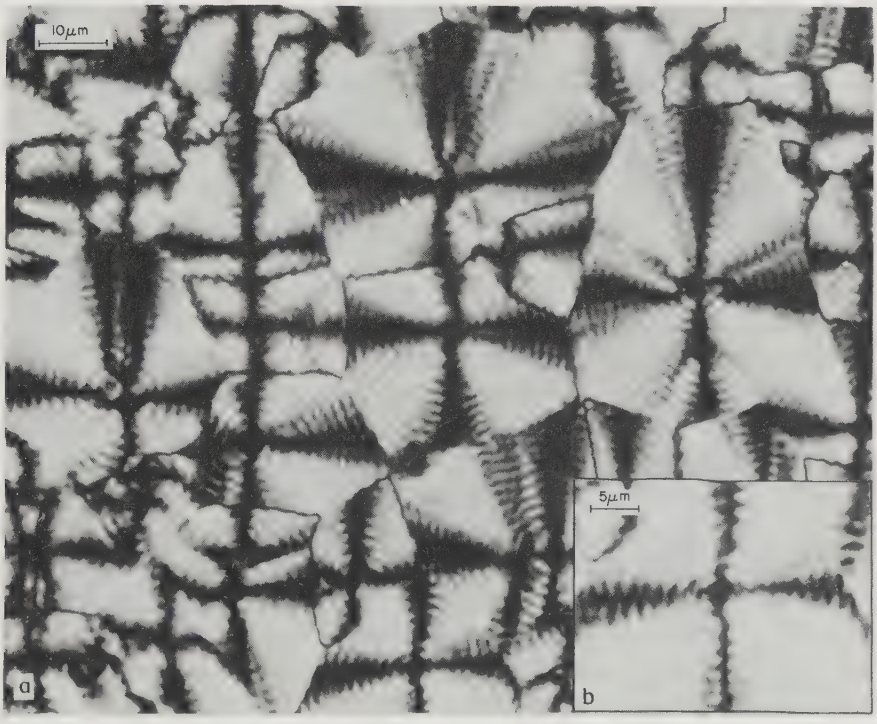

Fig. 50. (a) Ringed spherulites in a thin film of polyethylene viewed between crossed polarizers in the optical microscope. Note the zigzag pattern in the arms of the extinction crosses; this is seen more clearly at higher magnification and in lighter print in the inset (b). The origin of this pattern is described in the text.

the extinction cross would normally appear, the rings are connected by extinction lines that get longer as the distance from the center of the spherulite increases, giving somewhat the appearance of a zigzag. We shall return to this pattern and its explanation shortly.[244,245] For examples of the other patterns the reader can refer to Keith and Padden[245] for an example of the first type in polyethylene; to Point[235] for an example of the second type in poly(ethylene adipate); and to Keller[243] for an example of the third type.

Keller[243] and Point[232,235] originally suggested that these complex extinction patterns were caused by a periodic variation of the orientation of the constituent birefringent structural units along the radius.* Subsequently, in papers that appeared simultaneously, these various patterns were fully analyzed and explained by Keith and Padden,[244,245] Price,[246] and Keller[247] and the explanation hinged upon a remarkable feature of those spherulites that show the more complex types of extinction patterns. The explanation (substantiated by electron microscopic observations) shows quite unambiguously that the crystal orientation rotates about the radius in progressing from the center of the spherulite outward. As we shall subsequently see, this is due to the fact that the fibrils twist about their long axes as they grow. Even more remarkable, neighboring fibrils twist with the same period and the same phase, that is, they twist cooperatively. The hand, however, may be different along different radial paths, and at rather well-defined radial boundaries the hand changes discontinuously from the right to left.[245]

Clearly, in a uniaxial material, when all the fibrils lie in the plane of the specimen and twisting occurs about an axis normal to the optical axis, rings of a single periodicity will occur along with an extinction cross. In a biaxial material, when twisting occurs about an axis that is normal to the plane containing the two optical axes, rings with a double periodicity occur, giving the second type of pattern. If the crystal orientation with respect to the radius is such that twisting occurs about an axis that is not normal to the optic axis (uniaxial) or that is not normal to the plane of the two optic axes (biaxial), the third type of pattern listed above is obtained.

The origin of the pattern shown in Figure 50 involves somewhat more subtle considerations. Zigzag patterns of this kind develop from the first type of pattern when the twisting fibrils do not lie in the

* This has been previously suggested and discussed many years earlier by, for example, Wallerant[226] in the case of nonpolymeric spherulites.

plane of the specimen, as would be accomplished by tilting the specimen in the microscope stage, or when viewing a nondiametral section of a polymer spherulite. They can also occur in spherulites grown on the microscope hot stage because of small temperature gradients across the film.[245] In this tilted orientation the pattern of concentric rings in the first type of pattern degenerates into a four-armed spiral, but the individual arms of the spiral cannot be resolved except along the polarizer and analyzer vibration directions.[232,235] For more details the reader is referred to the original literature.[232,235,244–247]

Cooperative twisting and the resulting complex extinction patterns have been observed in various polymers, among which we have already mentioned polyethylene, poly(ethylene adipate), and poly(ethylene terephthalate), and while it has been extensively studied, its origins remain one of the unsolved problems of polymer morphology. In the same polymer it sometimes occurs and sometimes does not. For example, in poly(ethylene adipate), Point[232,248] found that at relatively high undercoolings, ringed spherulites were formed, while at higher temperatures, unringed, positively birefringent spherulites were formed. This was substantiated by Takayanagi and Yamashita,[249] who found in addition that, at lower crystallization temperatures than those attained by Point, negatively birefringent, unringed spherulites were formed. Isotactic polypropylene when crystallized in its less common hexagonal crystal structure gives ringed spherulites of the first type we listed earlier, while when crystallized in the more common monoclinic structure gives unringed spherulites,[46,47] which, it has been subsequently found, exhibit exceptionally complex fine structures (see, for example, Figure 1 in Ref. 109 and Figure 12 in Ref. 221), as might be expected for a polymer whose solution-grown crystals exhibit the complex twinning morphology discussed in Section 3.4.8.

The period of the twist (ring spacing) depends upon the temperature of crystallization[232] being smaller the lower the temperature.[243,250] For polyethylene, the ring spacing, and hence the period of the twist, varies from about 1 μm to some tens of micrometers. Figure 51 shows an example of this change in period with temperature for polyethylene spherulites that were crystallized while the polymer was being cooled.[251] Various mechanisms have been proposed to explain twist[252–257] but it is fair to say that none of them can account convincingly for the experimental findings.

Electron microscope studies bear out the results of the optical and x-ray investigations and give more insight into the nature of the

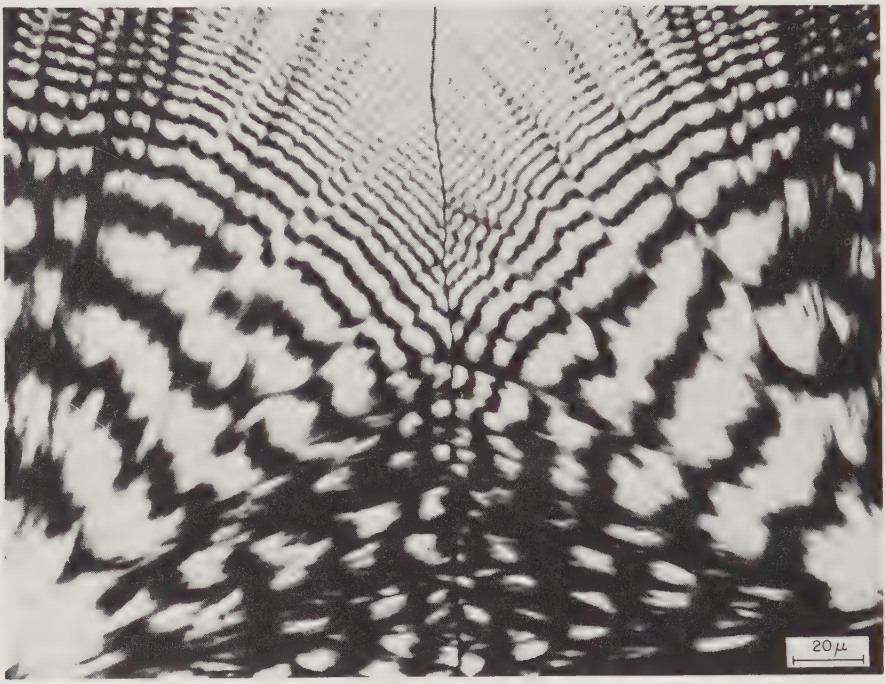

Fig. 51. Portions of two spherulites in a thin film of polyethylene crystallized while cooled continuously from the melt. The centers of the spherulites are close to the bottom corners of the picture. Note the decrease in ring spacing as the radial distance from the spherulite centers increases. The undercooling increased as the radial distance from the centers increased and this led to the decrease in the ring spacings.[251] (Photograph courtesy F. J. Padden Jr., reprinted with permission of John Wiley and Sons, Inc.)

fibrils. As mentioned earlier, these studies can be made on very thin films by direct transmission; on replicas of the free surface of a specimen crystallized in the form of a thin film*; or on replicas obtained from fracture surfaces. The second of these is commonly used, and when a replica obtained in this way is examined in the electron microscope, a result like that illustrated in Figure 52 is obtained. This replica was obtained from a spherulite of polyethylene that under the optical microscope showed extinction rings, i.e., it demonstrated twisting.

This figure shows that the spherulite consists of ribbonlike lamellae that twist cooperatively about the radial direction. Fischer[7]

* In such cases the replicated surface is a diametral section of the spherulite.

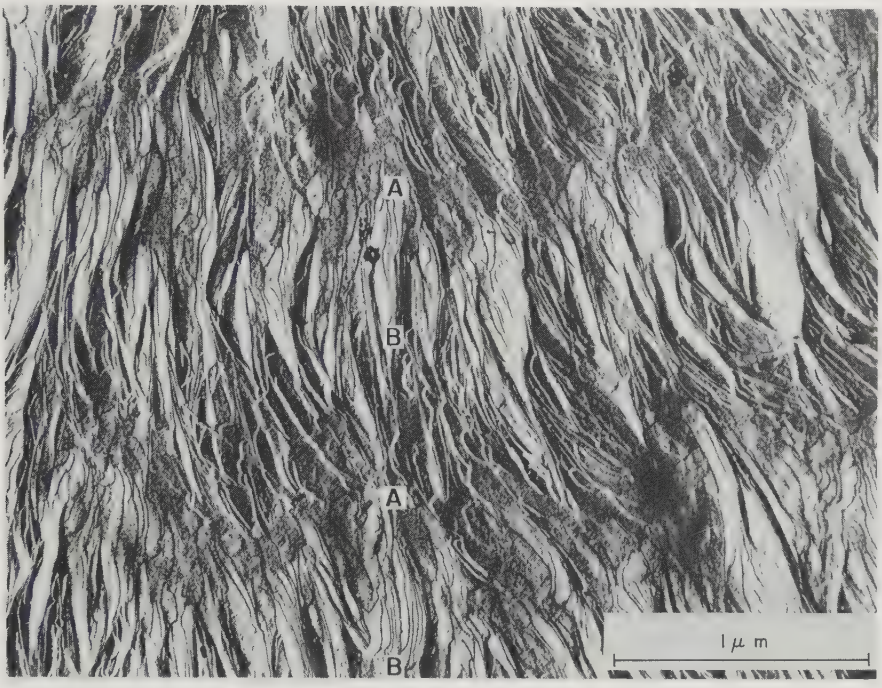

Fig. 52. An electron micrograph of a replica of the free surface of a thin film of polyethylene crystallized from the melt. The view shows a portion of a spherulite whose center is above the figure. This figure clearly illustrates the lamellar character of the radiating structural units. This spherulite is of the type that exhibits extinction rings. Note the difference in appearance between the regions marked *A*, where the lamellae are oriented preferentially flat-on, and the regions marked *B*, where they are oriented preferentially edge-on. (Photograph courtesy F. J. Padden, Jr.)

was the first to point out the lamellar morphology of polymer spherulites, and he also pointed out that the period of twist as seen in such electron micrographs corresponds to the periodicity of the extinction rings seen in the optical microscope.[7] The edges of the lamellae are seen as steps running approximately in the radial direction. When viewed on edge, the lamellae are seen to be densely packed, and when seen in plan view, they appear relatively broad and flat.

The same method can be used to study spherulites that do not show evidence of a twisting orientation, and Figure 53 shows an electron micrograph of the replica of a free surface of a diametral section of a spherulite of poly(4-methylpentene-1). The area shown is a region along the radius of the spherulite. This micrograph has many

Fig. 53. An electron micrograph of a replica of the free surface of a thin film of poly(4-methylpentene-1) crystallized from the melt. The view is along a radial portion of a spherulite whose center is off the left-hand portion of the photograph. The radiating lamellar structure is readily apparent.

features in common with the micrograph shown in Figure 52, although there is no regular twisting. Lamellae whose edges run generally in the radial direction can be seen. In regions where they are viewed edge-on they are seen to be densely packed.

Replication has been used to study other polymers (Ref. 12, pp. 232–304) and the preponderance of the evidence is that polymer spherulites consist of a radial array of elongated lamellae.

We now discuss the evidence that these lamellae are in fact chain-folded lamellae. Chain-folded lamellae with their broad faces generally parallel to the radius, as are the lamellae in the two examples given above, would, of course, be consistent with the tangential orientation of molecular chains in spherulites, but this of itself does not prove the presence of chain folding.

Further, albeit indirect, evidence of chain folding comes from the measurement of the thickness of the lamellae and its variation with temperature of crystallization. The thickness of the lamellae can be determined directly from electron micrographs of metal shadowed replicas of the fracture surfaces or the free surfaces of polymer samples. The thickness of the lamellae can also be measured by small-angle x-ray diffraction. Although there are, as we shall indicate briefly in the following, difficulties concerning the measurement of lamellar thickness by these different methods, the results indicate conclusively that the thickness of the lamellae in polymer samples crystallized from the melt under normal conditions (i.e., at atmospheric pressure) is usually of the order of a few hundred angstroms. Except for very low-molecular-weight fractions, this range of dimensions is considerably smaller than the usual lengths of polymer chains and is thus consistent with the occurrence of chain folding. In addition, an important aspect of the measurement of lamellar thickness is the determination of the effect of the temperature of crystallization or undercooling on the lamellar thickness. As is the case for lamellae grown from solution, the thickness of the lamellae in melt-grown spherulites increases as the degree of undercooling is decreased, which lends further support to the now well accepted fact that the lamellae in the spherulites are chain-folded. We shall not attempt to list the polymers for which lamellar thickness data as a function of undercooling are available. Some data are given by Geil (Ref. 12, pp. 232–304) and a bibliography and compilation of such data for polyethylene are given by Wunderlich (Ref. 13, p. 195), and further data can be found in papers we refer to in the next paragraph.

A detailed discussion of the problems related to the measurement of lamellar thickness from electron micrographs or from small-angle x-ray diffraction patterns is beyond the scope of this chapter. Various aspects have been discussed by, among others, Geil,[258] Reinhold *et al.*,[259] Illers and Hendus,[260] Crist,[261] Crist and Morosoff,[262] Vonk and Kortleve,[263] and Kortleve and Vonk[264]; these papers are sources of an extensive bibliography. We shall limit ourselves here to some brief comments.

As pointed out by Geil[258] concerning lamellar thickness measurements from shadow lengths in electron micrographs of surface replicas, uncertainties arise because the inclination of the lamellae relative to the surface is usually not accurately known. In special cases in which the lamellae are normal to the surface, as,

for example, in the work of Brown and Eby,[265] the lamellar thickness can be estimated in an alternative way by counting the number of lamellae that intersect the surface within a given distance. Concerning the small-angle x-ray diffraction measurements, a stack of lamellae would be expected to exhibit diffraction according to Bragg's law at an angle corresponding to the thickness of the lamellae. However, the degree of order between lamellae and/or the manner in which they are stacked are apparently not sufficient to yield sharply defined maxima in small-angle x-ray diffraction patterns. Instrumental factors (e.g., slit smearing) also contribute to the diffuseness of the patterns. Often the intensity maxima occur as shoulders on a background of intense diffuse scatter.[258,262,264] In some cases one intensity maximum is observed, whereas in others two maxima are observed which correspond (using Bragg's law) to spacings which are roughly in the ratio of 2:1, although the deviation from this ratio can be appreciable,[258,262,264] thus giving rise to the question of whether or not these two maxima are first and second orders of diffraction corresponding to the lamellar thickness. There has been divergence of opinion on this matter. It suffices for our present purposes to point out briefly that explanations of this problem have been advanced in terms of deviations from Bragg's law due to imperfect periodicity in lamellar stacking.[259,261–264] In addition, the importance of applying appropriate corrections in order to derive accurate spacings from the experimental data has been emphasized.[262,264] The problems of determining lamellar thickness in melt-crystallized polymers notwithstanding, the fact remains that the experimental results confirm that the lamellae are considerably thinner than the length of their constituent molecules, which is consistent with the incidence of chain folding, except in the case of low-molecular-weight fractions as found, for example, by Anderson,[266] who studied the morphology of fracture surfaces of polyethylene samples having different molecular weights.

Perhaps the most direct evidence for the presence of chain-folded lamellae comes from the digestion experiments of Palmer and Cobbold[267] and Keller and Sawada[268] on polyethylene. In these experiments samples of the polymer crystallized in spherulitic form were digested with fuming nitric acid. As a result of this treatment the polymer could be easily broken up into microscopic fragments. These fragments were then observed in the electron microscope, and electron diffraction patterns obtained from them. It was found in these experiments that the fragments are lamellar in appearance, and

the chain molecules had approximately similar orientations relative to the surface of the fragments as the chain molecules have with respect to the surface of chain-folded lamellae grown from solution.[267,268] Some of the fragments retain the twist they possessed in the spherulites, so that they look like small, stubby propellers.[268] The molecules in the fragments are not chain-folded, for in these digestion experiments attack occurs at and is essentially confined to the fold surfaces, which are in fact digested away. Nevertheless, the interiors of the lamellae are unaffected and the experiments provide strong evidence that in the untreated solid polymer, the lamellae in the spherulites existed as chain-folded crystals. The experiments also show that the lamellae are relatively long and narrow, a morphology that may be termed "lathlike."

There is other evidence that the lamellae seen in electron micrographs such as those shown in Figures 52 and 53 are chain-folded lamellae. Briefly, this evidence comes from electron diffraction patterns obtained from fragments detached from the spherulite when making replicas of the type used to obtain micrographs such as those illustrated in Figures 52 and 53 (Ref. 12, p. 253), indirect evidence from electron microscopic observations of replicas from fracture surfaces,[266] and finally indirect evidence coming from the increase of the thickness of the lamellae (i.e., an increase in the fold period) when annealed at temperatures above crystallization temperature,[186,258,260,269,270] which we shall have occasion to return to in Section 4.4 in discussing crystallization under pressure.

Summarizing all the results we have outlined above, we come to the following picture of polymer spherulites. They consist of radial arrays of chain-folded lamellae that are highly elongated in the radial direction. The fold surfaces of the lamellae are parallel to the radius. The chain molecules are oriented preferentially at right angles to the radius and one crystallographic axis is oriented preferentially along the radius. Normal to the radius, the lamellae cannot be in exact crystallographic registry, or spherical symmetry could not be maintained; nevertheless, there does appear to be some correlation in this direction, as observed in electron micrographs, so that stacks of lamellae have somewhat the appearance of fibrils and give low-angle x-ray diffraction patterns corresponding to the thickness of the lamellae. In some polymers the lamellae twist cooperatively, in other polymers they do not, whereas in yet other polymers the lamellae sometimes twist and sometimes do not, depending on the conditions of crystallization.

4.3.2. The Evolution of Spherulite Structures

As we pointed out in the preceding section, the evidence from observations with the optical and electron microscopes and from x-ray diffraction studies indicates that polymer spherulites consist of a spherically symmetric (radiating) array of ribbonlike structural units which are long, narrow, and thin lamellae that are oriented with their long dimension, and a corresponding crystallographic direction, preferentially parallel to the radial direction in the spherulite. In the present section we shall be concerned with the question of how the spherulite structure evolves during the solidification process. Primarily, we are concerned with how the radial ribbonlike structural units are developed, and how they multiply to fill space. Our discussion is divided into three main sections.

1. A discussion of the overall kinetics of spherulitic crystallization in polymers, in which we introduce the evidence for so-called "secondary crystallization," which indicates that after a spherulite is essentially fully grown, slow processes continue that lead to an increase in the density of the bulk sample.

2. A discussion of the theory of spherulite growth of Keith and Padden.[228–230] This theory, which is a general one and not specific to polymers, is concerned with the basic questions of the development of the radiating fibrillar habit of spherulites.

3. A discussion of the early stages of spherulite evolution. This will introduce the topic of "axialites" or "hedrites," which are considered to be structures of an intermediate stage between the original nucleus from which the spherulite grows and the full-fledged spherulite.

In the main this will complete our discussion of spherulite morphology, except for the related topic of "intercrystalline links" and "tie molecules." We discuss this topic in Section 4.3.3, where the evidence for individual molecules being incorporated in adjacent lamellae will be presented.

4.3.2.1. The Overall Kinetics of Spherulitic Crystallization in Polymers

In this section we deal with some aspects of spherulitic crystallization that are important to the understanding of the morphology of polymers. We are primarily interested in indicating the evidence for "secondary crystallization."

The kinetics of polymer crystallization can be divided into three aspects: (1) The overall kinetics of the transformation of liquid to solid. (2) The radial growth rate of the spherulites. (3) The molecular details of the kinetic processes that occur at the growing crystal face—what are called the interfacial kinetics.

Item 3 is discussed in detail by Hoffman, Davis, and Lauritzen[11] elsewhere in this Treatise and we therefore need not dwell on it here. We confine ourselves to items 1 and 2.

What one is concerned with in studying the overall kinetics of conversion of liquid to solid is the kinetics of the development of the crystallinity χ. Avrami[271] has shown that the functional dependence of χ on time t is given by the expression

$$\chi = 1 - \exp(-Kt^n)$$

In this expression K contains terms pertaining to rates of nucleation, and n is a constant whose value determines the types of processes occurring in nucleation and growth. Thus, if nuclei are born sporadically in time, n takes on the value 2, 3, or 4 depending upon whether the nuclei initiate one-, two-, or three-dimensional growth, respectively. If all nuclei are operative at $t = 0$, n takes on the value 1, 2, or 3 for the corresponding modes of growth.*

For polymer spherulitic crystallization and for relatively low values of χ (determined most commonly dilatometrically)† n is found to be constant and to have a value between 3 and 4,‡ which indicates that the growth is three dimensional and that some of the nuclei are born simultaneously while others are born sporadically in time. However, for higher values of χ (and at this stage the outer peripheries of the spherulites have usually impinged upon one another) the value of n drops drastically, and the crystallization proceeds much more slowly during the early stages. This stage is generally termed "secondary crystallization,"[273–278] and this indicates that after the spherulites are essentially full-sized in the sense that they have grown until they have impinged upon one another, some other but slower process or processes that lead to increases in density continue. What Keith and Padden envisage these processes to be will be described below during our discussion of their theory of spherulitic crystallization.

*It has been pointed out to us by J. I. Lauritzen, Jr. that for $n = 1$ or 2 the Avrami equation applies only for small values of χ.

† As pointed out by Price,[272] corrections to the Avrami equation must be made when the conversion from liquid to solid does not take place at constant volume.

‡ References concerning this can be found in a paper by Peterlin.[273]

The radial growth rate of spherulites has been the subject of numerous investigations. With the exception of cases in which rather significant amounts of noncrystallizable impurity were added in a deliberate attempt to influence the growth kinetics,[230] all the experiments indicate quite unambiguously and uniformly that the spherulites grow such that the radius increases at a rate which is proportional to the time, i.e., $r \sim t$ (e.g., see Ref. 249). This is very instructive, because it shows that radial diffusion processes cannot be the rate-controlling step in spherulite growth, for then the radial growth rate would be proportional to the square root of time, i.e., $r \sim t^{1/2}$. This linear growth rate must mean that the nucleation process occurring at the growing tips of the radial lamellae must be the rate-controlling step in the growth of spherulites.

Thus there are two aspects of the kinetics of the crystallization of polymers that are of concern to us. In one, the so-called "secondary crystallization," there is evidence of very slow, long-term processes that continue to increase the density of the material and thus the crystallinity. These appear to occur after the spherulites are fully formed. The second aspect is that the radial growth rate of the spherulites is linear in time, so that the overall growth process is not controlled by diffusion.

Now, with our previous account of spherulite structure, and with these brief words about the overall kinetics of spherulitic crystallization in polymers, we proceed to discuss the Keith–Padden theory[228–230] of spherulite development. While it is phenomenological and semiquantitative, it is nevertheless the most comprehensive theory of spherulite morphology available.

4.3.2.2. The Keith–Padden Theory of Spherulite Development

As we shall discuss in more detail below, a spherulite begins as an entity, presumably a single crystal nucleus. This crystalline entity must then develop into the spherically symmetric structure that is the spherulite. Since the final structure is one composed of radiating fibrils,* the original nucleus must develop a fibrillar habit. Moreover, in order that the fibrils fill space with what appears to be uniform density, they must proliferate, and therefore must "branch." This

* In what follows, we use the term "fibril" because it is the term used by Keith and Padden, whose theory is applicable to nonpolymeric materials as well as polymers.[228] When applying this term to polymers it should be considered with the qualifications noted on p. 448.

"branching" is at low angles and is thus noncrystallographic. For these reasons, any theory of spherulitic crystallization must account for two observations: (1) the development of a fibrillar habit and (2) the occurrence of low-angle noncrystallographic "branching."

Keith and Padden[228 230] explain the occurrence of both these phenomena from the viewpoint that among the systems known to form spherulites, polymers fall into the class having high melt viscosities and relatively impure melts. In the case of polymers, the "impurities" in the melt are considered to be low-molecular-weight fractions of the polymer, or, in those polymers where stereoregularity is important, atactic chains. Now, as is well known in non-spherulite-forming materials, the presence of impurities may in some cases cause constitutional undercooling[279,280] and a consequent degeneration of a planar growth front into a cellular growth front. This cellulation is caused by the presence at the growth front of an impurity-rich layer of width approximately $\delta = D/G$, where D is the diffusion constant and G the growth rate. Because of this impurity-rich layer, and with appropriate temperature gradients in the solid and liquid, constitutional undercooling may exist. When it does exist, a perturbation in the growth front will be stable, because a protuberance in the growth front will reach out into liquid of relatively higher undercooling and hence will grow more rapidly at its tip. In the process, impurity species are rejected from the growth tip, and diffuse laterally away from it, forming the well-known cellulation patterns seen in metals.[281] The width of one of these cells is also approximately equal to δ.

In polymers the situation is somewhat more complicated. In these materials, as demonstrated by the kinetics of spherulitic growth, the growth rate is not controlled by the diffusion of latent heat or material, but rather by the nucleation processes occurring at the tips of the growing radial fibrils. Nevertheless, while not playing a controlling role in the growth kinetics, according to Keith and Padden an impurity-rich layer occurs at the growing interface, and the value of δ plays the role in controlling the morphology. Also, and quite important, for these materials δ is quite small, for, although G may be small, so is D, because these materials have high melt viscosities (Keith and Padden estimate δ to be typically of the order of 10^{-4} cm, although it can vary greatly depending on the experimental conditions). Thus, in the hypothetical case of a planar growth front of a polymer crystal in a polymer melt, there is essentially constant temperature in solid and liquid (the evidence coming from the growth rate kinetics), and a very thin, impurity-rich layer at this interface, due to the very

small value of δ. This layer causes constitutional undercooling and because of its thinness, the gradient of undercooling is very steep. That is to say, if ΔT is the undercooling, and x is the direction normal to the growing surface, $d(\Delta T)/dx$ is very large, and hence any perturbation in the growth front is highly stable. The growth front therefore degenerates into a series of fibrils each of approximate width $\delta = D/G$, and this is the mechanism by which a planar growth front degenerates into fibrils. Moreover, the material between the fibrils now consists of anything that corresponds to an impurity. This, as the case may be, can be low-molecular-weight chains, partly stereoregular chains, atactic chains, etc. This material, when it can crystallize, will do so at a slower rate than that of the parent fibrils and is viewed, in this theory, as the source of the secondary crystallization discussed above.*

The foregoing explains the origin and the development of the fibrillar habit and gives a plausible basis for the existence of secondary crystallization. However, as discussed at the beginning of this section, the formation of fibrils is only one of the necessary conditions for the occurrence of spherulitic crystallization. The other is low-angle branching, and we now mention how Keith and Padden address this subject. Their argument here is somewhat less specific than their arguments on the origins of the fibrillar habit of the constituent structural units in spherulites. Basically they argue that with a very small value of δ, as occurs in spherulite-forming melts, any singularity at the growth face will continue to grow only if it is of the order of δ in size. If it is larger, it will be broken down by the cellulation process described above and if it is any smaller, it will be "swallowed up by other topographic features of more propitious size." Thus Keith and Padden consider that surface singularities (and by this they mean primarily misaligned surface nuclei) will be persistent if and only if they are of the order of δ in size. Moreover, since the probability of getting a stable, noncrystallographic misaligned surface nucleus will increase as δ decreases, the incidence of small-angle, noncrystallographic branching will increase as δ decreases.

In summary, Keith and Padden account for the development of the spherulite structure on the basis of impurity segregation and the concomitant occurrence of cellulation. In the case of polymers, impurities are low-molecular-weight material, atactic species, etc., as well as any chemically different material. Cellulation provides the mechanism by which fibrillation occurs, and the size of the fibrils is

* There are other factors that contribute to secondary crystallization (see, for example, Peterlin[273]).

determined by the magnitude of the parameter δ. Moreover, the magnitude of this parameter controls the extent of low-angle branching, and hence the proliferation of new fibrils, with the extent of branching increasing as δ decreases. Thus, as δ decreases, it would be expected that the texture of the spherulite would become finer, i.e., it would become composed of more densely packed and finer fibrils. Conversely, as the experimental conditions are changed so that δ is increased, the texture of the spherulite would become coarser, so that the spherulite would be composed of thicker, less densely packed fibrils.

Keith and Padden support the contentions made in their theory of spherulitic growth by an extensive series of experimental observations. We cannot, obviously, in our limited space give a complete account of these experiments. For a detailed accounting the reader is referred to the original papers.[228–230] Briefly we can say, however, that their experiments were designed, as would be expected, to demonstrate the effect of changing δ on the width of the radial fibrils and the incidence of low-angle, noncrystallographic branching. Moreover, they are concerned with the effect of impurity segregation, and how these impurities give rise to the differences noted above in the texture of the spherulites—what Keith and Padden call "compactness" and "coarseness" of texture.

The existence of segregation of noncrystallizable and low-molecular-weight polymer chains during the process of spherulite growth has been clearly demonstrated. For example, by growing isotactic polypropylene spherulites from a mixture of isotactic polypropylene and ^{14}C-tagged atactic polypropylene, Keith and Padden[229] showed by autoradiography of the resulting spherulites that the noncrystallizable atactic material was segregated at the interspherulite boundaries and also between some of the coarser fibrous arms of the spherulites. It can also be noted in this connection that Anderson,[266] by studying fracture surfaces of unfractionated linear polyethylene, obtained evidence indicating the occurrence of fractionation during spherulite growth. The lower molecular weight material crystallized with a different lamellar texture from that of the bulk of the polymer.

A quantitative evaluation of the effect of δ on the lateral size of the fibrils—a factor which Keith and Padden call by the term "coarseness"—is obviously quite difficult. The magnitude of δ can be changed by adding diluent, changing the molecular weight, which changes principally D, or by changing temperature, which changes both D and G. The value of D increases monotonically with tempera-

ture, but G increases as the temperature decreases from the melting point, reaches a maximum at some temperature below the melting point, and then decreases as the temperature is further lowered (see Ref. 11). The value of δ may therefore increase or decrease with temperature, depending upon the specific temperature range and polymer in question, although usually δ will increase with temperature. Thus Keith and Padden[229] systematically studied isotactic polystyrene spherulites under conditions in which δ was varied either by changing G or by changing D. In all cases, an increase in δ led to a "coarser" structure, supporting their hypothesis that the lateral size of the fibrils is governed by the value of δ. A particular case is shown in Figure 54, which illustrates spherulites of isotactic polystyrene grown in a blend of isotactic and atactic polystyrene at two different temperatures at which the growth rates were the same, i.e., the two temperatures were on either side of the maximum mentioned above. Since D increases monotonically with temperature, δ is larger at the higher of the two temperatures. The increase in coarseness at the higher temperature is apparent.

In nonpolymeric systems, Lofgren[282] has recently shown a similar dependence of the lateral dimension of the fibrils upon crystallization temperature in spherulites of the mineral rhyolite. However, in another nonpolymeric substance, 1,3,5-tri-α-naphthylbenzene, spherulites were obtained at high undercooling in what was ostensibly a very pure material[283] and the requirement of impurities for the occurrence of spherulitic crystallization has been questioned.[15,283]

The Keith and Padden theory of spherulite evolution generally accounts for the main features of spherulitic crystallization. It gives a satisfactory rationale for the variation in spherulite morphology with temperature and with the presence of "impurities." Its identification of δ as the important quantity in determining spherulite morphology is important in that it brings the behavior of polymers into closer correspondence with the behavior of more typical crystalline materials. The reader should recognize, however, that the theory does not specifically take into account that feature of polymers that is specifically polymeric, namely the existence of a lamellar habit. Thus it is easy to see by the theory of Keith and Padden how a growing crystal of polymer, being a broad, flat sheet, may cellulate and form elongated, thin lamellae in the plane of the sheet. It does not purport to provide a mechanism for cellulation in the direction normal to the plane of the sheet, and indeed, cellulation in this direction need hardly be invoked, for the thickness of the growing lamella is deter-

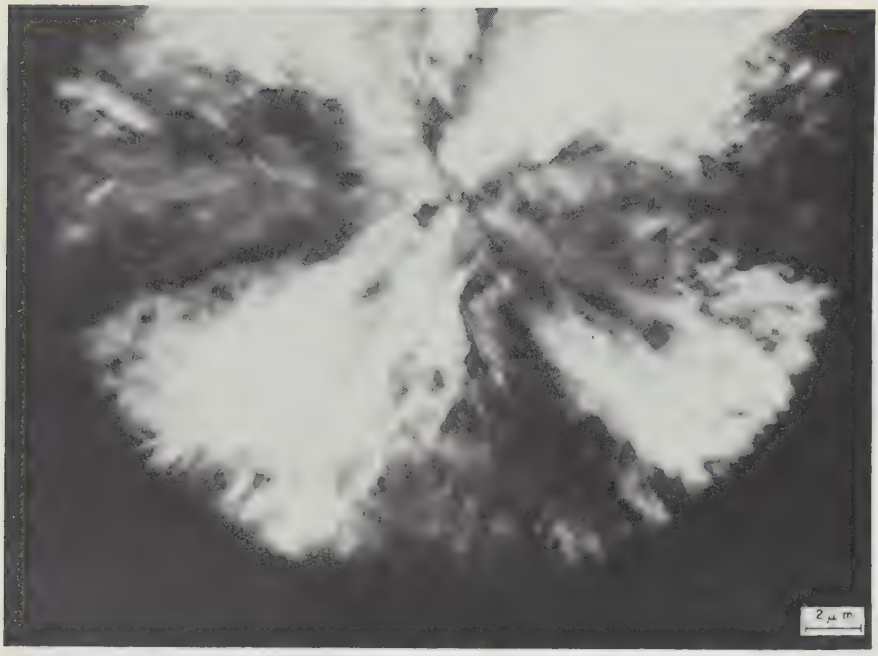

(a)

(b)

Fig. 54. Illustration of the effect of growth temperature on the texture of spherulites as seen under the optical microscope between crossed polarizer and analyzer. The spherulites are of isotactic polystyrene formed in a blend of this polymer with 75% of atactic polystyrene at (a) 165°C and (b) 200°C. At these two temperatures the spherulites had the same growth rates. Note the increase in coarseness of the spherulite texture with increase in growth temperature.[229] (Photographs courtesy F. J. Padden, Jr., reprinted with permission of the American Institute of Physics.)

mined by interfacial kinetic considerations and is already far smaller than δ. Moreover, the theory as such leaves out of detailed consideration those possible origins of "low-angle branching" that are peculiarly polymeric. This results primarily from the occurrence of growth spirals and the concomitant existence of splaying discussed in Section 3.4.3 and the possible influence of crystal curving caused by distortion of the lamellae due to the bulkiness of folds discussed in Section 3.4.2. These aspects will be discussed in more detail at the end of the next section.

4.3.2.3. On the Nature of the Early Stages of Evolution of Polymer Spherulites

It is very important to note that polymer spherulites do not grow in a spherically symmetric fashion from the moment of inception; rather, they evolve from simpler transitional precursor structures and the elucidation of how and why these structures evolve into spherulites as they grow larger is of central importance to an understanding of the origins and mechanism of evolution or formation of spherulites in polymers. Much has been learned during the last two decades about the nature of the early stages of the growth of polymer spherulites; there remain, however, some important aspects which it is fair to say still remain somewhat blurred. Our purpose in this section is to (a) summarize some of the salient morphological features which often characterize the early stages of growth of spherulites, (b) summarize current views concerning the nature of the early transitional stages of evolution of spherulites, and (c) point out some of the more significant aspects of general consequence (i.e., aspects other than those peculiar to individual polymers) that remain to be fully clarified.

The development of a sheaflike precursor during the early stages of the growth of polymer spherulites is a feature which is very commonly observed in polymer spherulite growth studies. This feature (which is not peculiar only to polymer spherulites) has been known since the earliest investigations on the morphology of polymer spherulites, which anteceded the discovery of chain folding in polymer crystallization. The then prevailing view was that the sheaflike precursors were akin in shape to a sheaf of wheat and consisted of a cylindrically symmetric or twisted bundle of fibrillar structural units (see, for example, the reviews by Keller[14,15]). Subsequent studies, which followed upon the discovery of chain folding led to the realization, first pointed out by Bassett, Keller, and Mitsuhashi,[98] that at an

early stage in growth these seemingly sheaflike precursors are multilayered, chain-folded structures akin to the crystalline objects which have been variously and collectively referred to as axialites and/or hedrites and which are formed when polymers are crystallized from concentrated solutions under certain circumstances as well as from the melt at low undercoolings, i.e., at temperatures above the wide range in which the evolution of spherulites prevails.* Broadly speaking, axialites/hedrites (we shall hereafter use the term hedrite) are multilayered, chain-folded crystals whose constituent superposed lamellae, which are bound laterally by low-index faces, splay or diverge progressively relative to a reference plane. When viewed along that plane these crystals exhibit a sheaflike appearance (their constituent lamellae are viewed edge-on in this perspective), whereas when viewed at right angles to that direction they exhibit a polygonal profile which corresponds to the lateral habit (e.g., hexagonal, tetragonal) of the constituent lamellae, which are being viewed essentially "flat-on" in this latter perspective (see Figures 55 and 56). The causes of the progressive evolution from such transitional multilayered precursor crystals, of a spherically symmetric array of long, narrow, ribbonlike chain-folded lamellae have been considered and discussed by Keith.[285] In an extension of the theory of spherulite growth discussed in the preceding section, Keith [285] addressed the uniquely polymeric aspects of polymer spherulite precursors.

According to Keith,[285] the transitional multilayered hedrite structures which develop during the early stages in the growth of spherulites, and the spherulitic structures into which they ultimately evolve, represent respectively successive stages in the evolution of an initially formed lamellar chain-folded single crystal which degenerates progressively as it grows under the influence of impurities rejected at its lateral growth fronts. Keith's interpretative accounting of the mechanism of the evolution of a single crystal through the hedrite transitional stage of development to the ultimate spherulite will be summarized below, where it will be discussed with reference to the idealized schematic representation of successive stages in the evolution of a spherulite depicted in Figure 55. We shall start with some

* The term "axialite" was first coined by Bassett, Keller, and Mitsuhashi[98] to apply to multilayered objects grown in relatively concentrated solutions of polyethylene in xylene. The lamellae in these objects diverge apparently from a central axis and the objects exhibit polygonal or sheaflike appearances, depending on the direction in which they are viewed. The term "hedrite" was first coined by Geil[284] to distinguish polygonal objects formed in melt-crystallized polymers from the more common spherulites. Geil subsequently extended his definition of a "hedrite" to include axialites (Ref. 12, pp. 189–211).

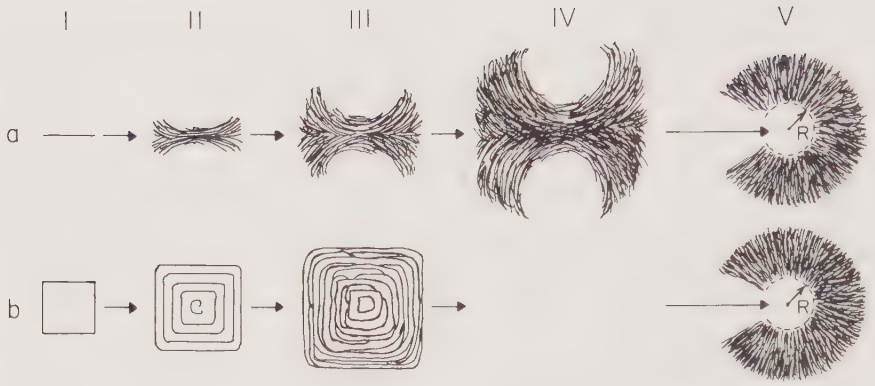

Fig. 55. Schematic representation of successive stages in the development of a spherulite (column V) from a chain-folded precursor crystal (column I). Rows (a) and (b) represent, respectively, edge-on and flat-on views of the evolution of the crystal, through transitional hedritic stages in growth (columns III and IV), to a spherulite. The successive stages in growth are not drawn to scale relative to one another. See text for comments on region *R* in column V, and for blank space in column IV, row b. Note that the stages of growth shown in columns I and IV occur within the central region (radius *R*) of the spherulite.

comments concerning the latter "reconstruction" or model of the development of a spherulite.

Column I (Figure 55) shows a chain-folded, monolayered, single-crystal precursor as seen edge-on (column I, row a) and flat-on (column I, row b). Corresponding cross-sectional representations (i.e., edge-on and flat-on, respectively) of the development of this precursor crystal as it evolves progressively into a spherulite consisting of a radiating array of ribbonlike, chain-folded lamellae (column V) are shown in columns II–IV, where columns II and III represent the intermediate multilayered hedrite stages in the development of the spherulite (see below for comments concerning the blank space in row b, column IV). As indicated in Figure 55, column V, the precursor (column I) and the intermediate stages of development (II–IV) occur within a radial span *R* beyond which growth progresses in a spherically symmetric fashion. It is pertinent to note at this juncture that the higher the crystallization temperature (and hence the slower the growth rate) the larger the radial span *R* within which the transformation from single-crystal to spherically symmetric (spherulitic) propagation is attained. Indeed at high enough crystallization temperatures neighboring transitional structures (such as those shown in columns II to IV) developing, for example, in a thin polymer film, impinge and hence stop growing further well before they attain the spherically

symmetric growth stage. Thus, by a judicious choice of crystallization conditions it is possible to obtain fully crystallized thin polymer films in which the constituent structures represent intermediate stages in the evolution of spherulites. The morphological characteristics of the intermediate stages of evolution of spherulites have been derived from a variety of optical and electron microscopic studies, but particularly so from electron microscopic examinations of replicas of such thin films. When the films are thin enough the development of the intermediate structures in the direction normal to the film is also highly restricted. In short, the structures in these thin films correspond in essence to thin central sections of the intermediate structures. Due to the random orientations of the transitional prespherulitic structures in the films, one obtains, by replicating the film surface, reproductions of the morphology corresponding to different central or near-central cross sections of the structures, i.e., ranging from "edge-on" (row a, Figure 55) to "flat-on" cross sections (row b, Figure 55).

This is illustrated by the replicas of poly(4-methylpentene-1) hedrites shown in Figures 56(a) and 56(b), respectively. These structures represent a stage in spherulite development which corresponds approximately to that depicted schematically in column III of Figure 55. As depicted in Figure 55 (column III, row b) and as can be readily judged from the replica of the flat-on cross section shown in Figure 56(b), the hedrite consists of a stack of superimposed lamellae which exhibit vestiges of a tetragonal lateral habit. Note the absence of any radiating fine texture emanating from the center of the structure as seen in this perspective. As can be seen from the replica of the edge-on cross section shown in Figure 56(a), the developing multilayered hedrite exhibits a distinctly sheaflike appearance in this latter perspective, in which the constituent lamellae are oriented preferentially edge-on with respect to the field of view. It is evident from Figure 56(a) that as growth proceeds, the lamellae that develop on either side of the central plane of reference *AB* fan progressively outward and away from that plane as the structure grows larger. The point to note here is that this fanning out (which becomes more and more pronounced as growth progresses) occurs even before any semblance of a radiating morphology manifests itself in corresponding flat-on cross sections. In short, the fanning out of the lamellae seemingly occurs before the lateral habit of the lamellae degenerates to the "fibrillar" lamellar habit characteristic of the spherulitic stage of growth. We shall return to this point and to the matter of the

(a)

(b)

Fig. 56. Two electron micrographs of replicas of hedrites formed in the same melt-crystallized thin film of poly(4-methylpentene-1). (a) An edge-on view of a hedrite. Note the distinctly lamellar character and the "sheaflike"arrangement of the lamellae. (Compare with Figure 55, column III, row a.) (b) A plan view of a hedrite. Note the degenerate overall square outline of the object, whose lamellar texture is evident. (Compare with Figure 55, column III, row b.)

origins of the fanning out process later. The main features to bear in mind at this point concerning the early stages of spherulitic growth are that (a) following the genesis of a monolayered single crystal additional chain-folded layers develop thereupon, presumably (but not necessarily exclusively) through the agency of screw dislocations, and (b) the constituent layers in the resulting structures fan out progressively in the manner depicted in Figure 55 (row a, columns II–IV).

The "features" concerning the nature of the early stages of growth of spherulites which we have summarized in the preceding paragraphs must of course be reconciled with the radiating fibrillar fine texture which is characteristic of the more advanced spherically symmetric stages of the growth of spherulites. Clearly, as pointed out by Keith,[285] a distinct change in the lateral growth habit of the lamellae must occur during the course of the development of the spherulite. The change in the habit of the lamellae from the polygonal single crystal habit which prevails early in the growth of the spherulite to the eventual fibrillar habit has been explained by Keith as being a consequence of the manifestation of cellulation at the periphery of the polygonal lamellae during the early stages of evolution of the spherulites. As pointed out in the preceding section, the incidence of cellulation is attributed to the diffusional segregation of impurities at the lateral growth faces of the lamellae. According to Keith,[285] the occurrence of cellulation gives rise to extensive crystalline imperfection in the growing single crystal lamellae, particularly at the boundary between adjoining "cells." This latter feature forebodes the onset of fibrillar growth.

Cellulation leading to a fibrillar habit does not account in itself for the evolution of a spherulitic aggregate. While, as has been discussed by Keith and Padden,[228–230] the incidence of low-angle noncrystallographic branching along with the establishment of the fibrillar habit during the course of the development of spherulites is one of the factors which contributes to the ultimate spherical symmetry of these aggregates, significant divergences in orientation, which contribute to the ultimate sphericity of the aggregates, apparently occur before the onset of fibrillar growth and the subsequent continued proliferation of new fibrils via low-angle noncrystallographic branching. That this is so is evidenced, for example, by the fact that (a) pronounced deviations in orientation occur in the transitional hedrite structures, as evidenced by the sheaflike character of these structures when they are viewed edge-on (Figure 56a), and the corresponding absence of a radiating fine texture when they are viewed flat-on (Figure 56b).

This brings us to the question of what causes the lamellae in hedrites to diverge or fan outward as they do. Interlamellar splaying (e.g., akin in origin to the type of splaying mentioned in Section 3.4.3) is a possible contributing factor.[15,285] Repeated splaying would, however, have to be invoked to account for the continuing manner in which the constituent lamellae fan outward. An additional possibility which has been suggested[286] is that the lamellae are actually intrinsically curved and that sheaving in hedrites is a feature which is related to the phenomenon of curved polymer crystal formation mentioned in Section 3.4.7. The observation that solution-grown lamellar crystals of poly(4-methylpentene-1), polyoxymethylene, and polychlorotrifluoroethylene are all the more pronouncedly curved the lower the crystallization temperature is of interest in this connection in view of the fact that the rate of change in orientation of the sheaving lamellae in the transitional hedrite stage in the growth of spherulites is also more pronounced the lower the crystallization temperature. This suggests that the phenomenon of curved crystal formation referred to above is related to and manifests itself in the sheaving morphology associated with the hedrite stage in the evolution of spherulites, but we shall not pursue this matter further since it remains speculative at this time. It suffices for our present purpose simply to point out that two basic aspects of the early stages of growth of spherulites remain to be elucidated. These are (a) what are the origins of sheaving, and (b) when does the onset of cellulation and the fibrillar habit occur in relation to the manifestation of sheaving during the early stages of spherulitic growth (hence the blank space in column IV, row b in Figure 55)?

4.3.3. Tie Molecules and Intercrystalline Links

We have seen that polymers crystallized from the melt under ordinary circumstances consist of spherulites, which in turn consist of a radiating array of chain-folded lamellar crystals. There is evidence that suggests the presence in the regions between fibrils (stacks of lamellae) of either low-molecular-weight or less stereoregularly perfect material.

It was recognized for some time that this view of the structure of bulk polymers is too simple in that it would not account for the mechanical properties of crystalline polymers. These materials are generally quite tough and show a great deal of plastic deformation when subjected to a tensile stress. A morphology which consists of

essentially "unlinked" spherulites, which in turn consist of lamellae that are connected only at their points of origin and at the sites of the low-angle branching previously discussed, is inconsistent with such mechanical properties. Such a structure would be expected to fail at the interspherulite boundaries, and the poor connectivity between the lamellae within spherulites would lead to a mode of deformation different from that which is observed.[251] Thus it was suggested[251] long ago that the constituent lamellae of the spherulites were probably held together by chain molecules which were partly imbedded in one lamella and partly in another. These molecules were termed "tie molecules." Evidence for the existence of these tie molecules was provided by Keith, Padden, and Vadimsky,[287] Davis,[288] and Clark[289] and more recently by the swelling experiments of Hase and Geil[290,291] and Rybnikar and Geil.[292] The subject has been reviewed by Keith, Padden, and Vadimsky[293] and here we give only a cursory account of their observations.

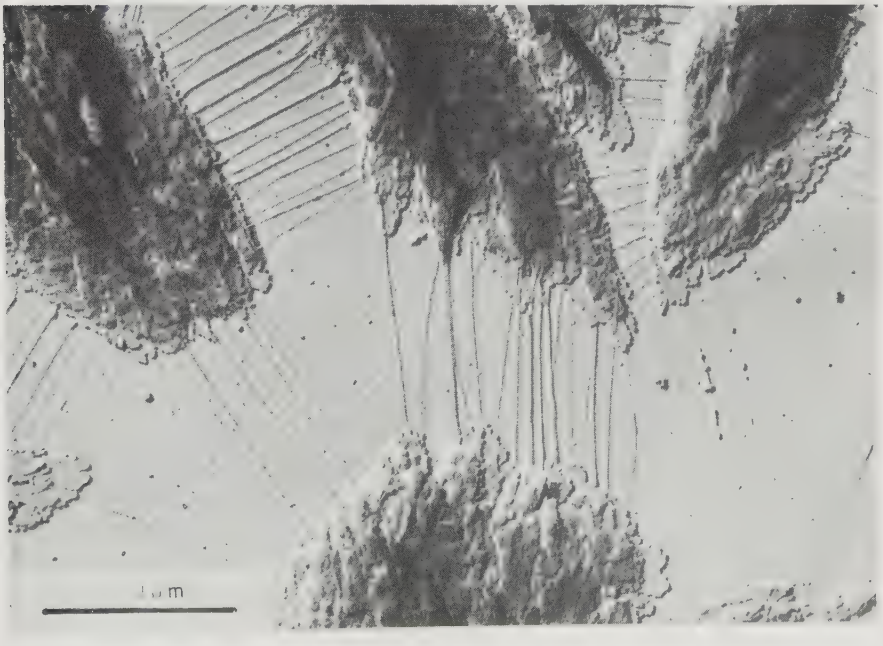

Fig. 57. Intercrystalline links between the lateral edges of lamellae in spherulites of polyethylene grown from a solution in dotriacontane. This electron micrograph was taken after the dotriacontane was dissolved. The links are crystalline with the *c* axis along their long dimension.[287] (Photograph courtesy H. D. Keith, reprinted with permission of the American Institute of Physics.)

Fig. 58. Intercrystalline links between the broad surfaces of polyethylene lamellae grown epitaxially on an uniaxially oriented poly(ethylene teraphthalate) film. On this substrate the lamellae grew with their lateral edges in contact with the substrate. The lamellae were grown from solution in dotriacontane, which solvent was subsequently dissolved prior to the preparation of this electron micrograph.[293] (Photograph courtesy H. D. Keith, reprinted with permission of the American Institute of Physics.)

Keith, Padden, and Vadimsky[287] grew two-dimensional spherulites of polyethylene using the long-chain paraffin n-$C_{32}H_{66}$ as a diluent. Being essentially a low-molecular-weight homolog of polyethylene, this material does not change the mode of growth of polyethylene. As we would expect from the previous discussion, the spherulites grown under these conditions have an open, coarse texture. Now, after growth, the paraffin was dissolved away and the resulting structure viewed electron microscopically. What was observed was a profusion of links bridging the *lateral* faces of the lamellae and the boundaries between spherulites. A typical and particularly striking example is shown in Figure 57. These links, which were termed "intercrystalline links" by Keith *et al.*[287] strongly support the evidence of interlamellar tie molecules.

In subsequent experiments[293] these same investigators were able to demonstrate the existence of intercrystalline links between the fold surfaces of the lamellae by crystallizing polyethylene epitaxially from the same paraffinic system on oriented sheets of poly(ethylene terephthalate). On this material the polyethylene lamellae grow on the substrate edge-on, so that the spaces between the broad faces of the lamellae are available for microscopic examination. Intercrystalline links between these broad surfaces are shown in Figure 58. Such links had previously been seen by Davis in slightly deformed samples of polyoxymethylene,[288] but due to the deformation, it could not be unambiguously concluded that they were a growth feature and not a result of the deformation. Their occurrence is, however, indicative of the existence of molecular ties between lamellae, as is also indicated by the observations of Hase and Geil[290,291] and Rybinkar and Geil[292] on swollen samples of poly(4-methylpentene-1). The experiments of Keith, Padden, and Vadimsky clearly support the view that tie molecules are indeed a feature of spherulite structure, and while the systems used to make their observations possible are somewhat specialized, there is no reason to believe that these observations cannot be extrapolated directly to crystallization from the undiluted melt.

While it is not our intention to discuss in detail the observations of Keith, Padden, and Vadimsky,[287,293] we summarize their conclusions, for certain aspects of the observations have a bearing on the growth processes occurring in spherulites. Selected-area electron diffraction indicates that the intercrystalline links are crystalline, and that the c crystallographic axis is parallel to the long axis of the link. This indicates, as proposed by these authors, that, at least in the system they investigated, the link grows by one molecule crystallizing with one end in one lamella and its other end in another lamella. Crystallization proceeds in both lamellae by the normal chain-fold mechanism until the molecule is drawn taut between the two lamellae. This taut molecule then acts as a substrate (or nucleus) for the crystallization of other molecules on it.

The trouble with this view is that subsequent crystallization of molecules in what is basically an extended chain conformation onto the original tie molecule is an energetically unfavorable process. The subsequent molecules would much prefer to fold (see the chapter elsewhere in this Treatise by Hoffman, Davis, and Lauritzen[11]). Since chain-folded structures are not observed in these intercrystalline links, Keith, Padden, and Vadimsky[293] were led to the view that the

crystallization processes occurring in the vicinity of the link require a flow of fluid in the narrow channel in which the link finds itself. This flow orients the molecules in the melt and favors the growth of extended-chain crystals (basically the flow raises the free energy of the melt). While basically sound, this explanation suffers from the fact that such orientation would lead to an increase in lamellar thickness in the neighborhood of the link, which is not observed, but this is a detail that should not obscure the main result. For all practical purposes these experiments and those of the other investigators mentioned above demonstrate the occurrence of tie molecules in polymer spherulites and thus provide a consistent basis for the explanation of the mechanical properties of polymers that a simpler view of spherulite structure would not provide.

Other mechanisms for the incorporation of tie molecules in lamellae are discussed by Clark,[289] after Reneker.

4.4. Crystallization under Pressure

Pressure raises the melting point of synthetic polymers and many other organic compounds approximately 0.02°K/atm. Thus the application of moderate pressures (on the order of a few thousand atmospheres) allows crystallization to be carried out at temperatures substantially higher than can be achieved by crystallization at 1 atm. Under these conditions of higher pressures and temperatures, some novel morphological features are observed in polymers, and in this section we shall summarize these features with particular reference to polyethylene, which, as usual, has been studied in most detail. The morphology and crystallization behavior under pressure has been studied for polyethylene,[69,294–307] polytetrafluoroethylene,[308] and polychlorotrifluoroethylene.[60] In all cases, the salient morphological features observed are lamellae of considerably greater thickness than those obtained by crystallization at 1 atm. These lamellae have been termed "extended chain lamellae," although the term "chain-extended lamellae" has been applied to the case of polyethylene crystallized under special conditions of temperature and pressure[302–306] for reasons that will become apparent in the remainder of the discussion, which we limit to polyethylene. The bulk of the work has been carried out by Wunderlich, Bassett, and their associates, and for the many details that we cannot hope to cover, the reader is referred to the original papers, which are included in the references given above and which serve as sources for additional bibliography.

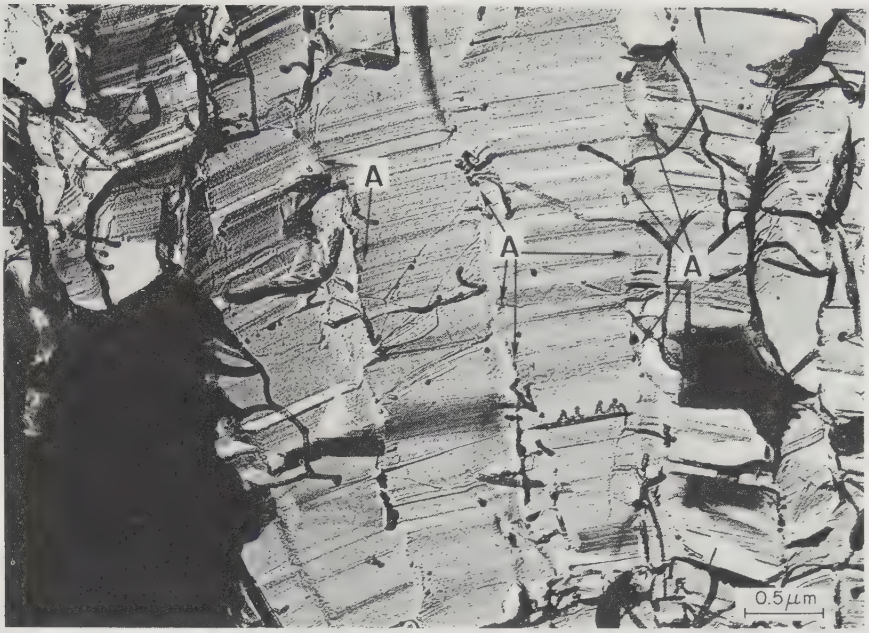

Fig. 59. An electron micrograph of a fracture surface of polyethylene crystallized under pressure. The *c* crystallographic axis is parallel to the fine striations, and the arrows *A* denote the traces of the surfaces of the lamellae on the plane of the specimen. The thickness of these lamellae is immense when compared with material crystallized at atmospheric pressure. (Cf. Figures 52 and 53.)

When polyethylene is crystallized under pressure, different morphologies are observed, depending on the temperature, pressure, and corresponding undercooling. These morphologies range from spherulitic or incipient spherulitic structures[69,302,306] to objects which have been termed "cigarlike"[307] and which Bassett has recently indicated are in fact thick lamellae seen edge-on.[306]

When samples of bulk material crystallized under pressure are fractured and replicas of the fracture surface are observed in the electron microscope, a novel morphology of the type shown in Figure 59 is typically observed. This was first observed by Geil *et al.*[294] Selected-area electron diffraction indicates that the axes of the chain molecules are oriented parallel to the fine striations seen in such photographs,[294] and hence this indicates that what is observed are fractured lamellae seen edge-on. The broad lamellar surfaces are normal to the plane of the photograph and are designated by the *A* in Figure 59. The interesting feature is that the thickness of these

lamellae is immense (thicknesses over 1 μm are often observed) compared to that of normal chain-folded lamellae formed at atmospheric pressure. This can be readily seen by comparing Figure 59 with Figure 52, and a comparison of these two figures illustrates the decidedly different morphology obtained in crystallization under pressure.

The thickness of the lamellae depends upon the molecular weight, the temperature, and the pressure during crystallization. According to Bassett and Turner,[304] the thickness of the lamellae increases with crystallization temperature at a given pressure, with crystallization pressure at constant supercooling, and with molecular weight (in the range 2×10^4 to 5×10^4) for crystallization at the same temperature and pressure.

Despite the fact that this type of morphology has been termed "extended chain" crystallization, the evidence strongly suggests that the lamellae are not composed of truly extended chains. Prime and Wunderlich[296] made a comparison of the length distribution of the lamellae with the weight-average distribution of molecular weight of the polymer, which indicated that while there is approximate correspondence between the peaks of the molecular weight and lamellar thickness distributions, and close similarity on the low-molecular-weight and low-lamellar-thickness ends of the distributions, there is a great dissimilarity on the high-molecular-weight end. The long end of the lamellar thickness distribution has a much sharper cutoff than the molecular weight distribution, which is to say, there are relatively fewer thick lamella than there are long molecules, and there are no lamellae with a thickness corresponding to the longest of the molecular chains. This strongly suggests that even in samples crystallized at the highest pressures and for the longest times, chain folding occurs for at least the longest molecules in the sample.

It is appropriate at this point to discuss how such an "extended chain" morphology could arise. Since the lamellar thickness is determined primarily by the undercooling, and the undercoolings in pressure crystallization are comparable to those used in crystallization at atmospheric pressure, one would be led to expect chain-folded lamellae of thickness comparable to those obtained under normal conditions. Since, as we have seen, the average thickness is approximately that of the average extended chain length, some additional process must be operative. According to Wunderlich and Davidson,[295] this process is very likely "thickening." That is, the lamellae form originally by the chain-fold mechanism at a thickness

determined by the undercooling. Now, these are, of course, metastable, for the stable crystal is one with a thickness equal to the extended length of the molecules and under certain conditions, the thickness of the lamellae can increase. For example, the thickness of the lamellae of polymers crystallized at atmospheric pressure increases upon annealing at temperatures above the crystallization temperature due to an increase in the fold period[269,270] and the rate of this process increases as the temperature increases.[186,273] Indeed, Hoffman and Weeks[309] even found that thickening occurs during isothermal crystallization from the melt at atmospheric pressure. However, the kinetics of the thickening process is such that thickening occurs slowly, being approximately linear in the logarithm of time. Thus, at the temperatures attainable at atmospheric pressure, thicknesses greater than a few hundred angstroms cannot be obtained, and the crystals remain chain-folded. At the higher temperatures attainable in crystallization under pressure, the thickening process is greatly increased in rate, and thus while the crystals are formed originally as chain-folded crystals, they thicken until they reach the thickness of "extended chain" crystals.

Bassett, Block, and Piermarini[306] have recently shown the existence of a new phase in polyethylene at elevated temperatures and pressure. Bassett and Turner[303] were led to postulate the existence of this phase by the differential thermal analysis and dilatometric study of the melting behavior of samples of polyethylene crystallized under pressure. The existence of this phase, which is deduced to be hexagonal, was demonstrated by x-ray diffraction studies under pressure.[306] This phase coexists with the normal orthorhombic phase and the liquid (at a triple point) at approximately 220°C and a pressure of 3.5 kbar. At higher pressures, the orthorhombic phase transforms to this hexagonal phase before melting. Conversely, during crystallization, at pressures above 3.5 kbar, and at low undercoolings, crystallization into the hexagonal phase takes place, with subsequent transformation to the orthorhombic phase when the temperature is lowered.

Indeed, Bassett *et al.* (e.g., see Refs. 303–306) have used the term "chain-extended" to denote polyethylene that has been crystallized via this intermediate phase. In this view, chain-folded crystallization occurs when the melt is transformed directly to the orthorhombic solid, and "chain-extended" polyethylene involving chain folding and subsequent rapid thickening results when the intermediate phase intervenes in crystallization. This leads Bassett and Turner[305] to

the conclusion that "chain-extended" crystallization can only occur in polyethylene, and in the absence of evidence for an intermediate phase, "chain-extended" crystallization cannot occur in other polymers. This view is too new to have received discussion. For further details on the possible mechanisms for the formation of "extended-chain" or "chain-extended" polyethylene, the reader is referred to the extensive original literature.

5. Concluding Remarks

In this chapter we have attempted to give an overview of the salient aspects of the broad subject of the morphology of crystalline synthetic polymers. We have addressed our remarks primarily to those who have little or no familiarity with this field but who wish to learn about it in sufficient depth to recognize the important problems in it and actively pursue them. We have in essence attempted to do two things.

First, we have tried to show that despite a wealth of seemingly disparate phenomena which are exhibited by individual polymers, there are many unifying concepts and features which characterize the morphology of most crystalline synthetic polymers. These main concepts or features are the influence of chain regularity on the crystallizability of polymers, the almost universal occurrence of chain folding during crystallization, and the consequent lamellar character of the morphology of these materials, be they crystallized in the form of single crystals, as is common from dilute solution, or in the form of spherulites, as is common in crystallization from the melt.

Second, in discussing the various topics we have covered, we have attempted to identify or point out some (but certainly not all) of the outstanding problems in these areas. Among these is the detailed characterization of the nature of the fold surfaces in polymer crystals, which includes several aspects, namely the disposition of chain ends, the sharpness or looseness of the chain folds, and fluctuations in fold period. Additional problematic topics which we have pointed out are: the origins of the manifestation of irregular lateral growth habits in polymer crystals, the sectorized character of such crystals, and the manner in which the chains fold at the periphery of these crystals; the causes of the formation of variously curved polymer crystals, which encompasses the manifestation of cooperative twisting in the constituent lamellae in some species of melt-grown spherulites; and a detailed understanding of the nature of the early stages of evolution

of spherulites, in particular the mechanisms by which axialite–hedrite precursors evolve progressively into spherulites.

Because of limitations in space we have had perforce to omit many topics from discussion and to treat other topics rather briefly. Thus our discussion of the morphology of random copolymers has been limited, and we have made only passing reference to the vast topic of disorder in melt-crystallized polymers. Furthermore, our discussion of annealing has been sketchy and superficial. In addition, we have not discussed the specialized and commercially very important topic of the morphology of drawn polymer fibers and films and the mechanisms by which the fine structure of these highly oriented materials is derived from that of the native polymer during deformation. In related topics, we have not discussed the morphology of polymers crystallized during deformation or under the influence of hydrodynamic flow. Among other topics we have omitted is the morphology of polymers in their as-polymerized state, which encompasses the subject of the morphology of polymers prepared by polymerization in the solid state. Finally, we have not treated the very large topic of the effect of morphology on the physical properties of polymers, such as melting point, internal friction, dielectric properties, etc.

Despite these omissions, we hope that we have provided the uninitiated reader with an introduction to the field of the morphology of crystalline polymers that is sufficiently unified and detailed in its perspectives to serve usefully as a background to enable him to understand and place in context all the topics we have omitted, and we hope we have been able to communicate some of the beauty and excitement of the field and the intellectual challenges still remaining.

Acknowledgments

We wish to thank Drs. S. R. Coriell, G. T. Davis, J. D. Hoffman, H. D. Keith, J. I. Lauritzen, Jr., F. J. Padden, Jr., and D. H. Reneker for the benefit of many helpful comments and suggestions.

References

1. (a) W. T. Astbury, *Fundamentals of Fiber Structure*, Oxford University Press (1933); (b) P. H. Hermans, *Physics and Chemistry of Cellulose*, pp. 1–40, Elsevier, New York (1949).

2. C. W. Bunn, in *Fibers from Synthetic Polymers* (R. Hill, ed.), pp. 240–300, Elsevier, New York (1953).
3. C. W. Bunn and T. C. Alcock, The texture of polyethylene, *Trans. Faraday Soc.* **41**, 317–325 (1945).
4. R. Jaccodine, Observations of spiral growths in ethylene polymers, *Nature* **176**, 305–306 (1955).
5. P. H. Till, Jr., The growth of single crystals of linear polyethylene, *J. Polymer Sci.* **24**, 301–306 (1957).
6. A. Keller, A note on single crystals in polymers: Evidence for a folded chain conformation, *Phil. Mag.* **2**, 1171–1175 (1957).
7. E. W. Fischer, Stufen und spiralförmiges Kristallwachstum bei Hochpolymeren, *Z. Naturforsch.* **12a**, 753–754 (1957).
8. K. H. Storks, An electron diffraction examination of some linear high polymers, *J. Am. Chem. Soc.* **60**, 1753–1761 (1938).
9. K. Ziegler, Folgen und Werdegang einer Erfindung (Nobel Prize Address), *Angew. Chem.* **76**, 545–553 (1964).
10. G. Natta, Von der stereospezifischen Polymerisation zur asymmetrischen autokatalytischen Synthese von Makromolekülen (Nobel Prize Address), *Angew. Chem.* **76**, 553–566 (1964).
11. J. D. Hoffman, G. T. Davis, and J. I. Lauritzen, Jr. This Treatise Vol. 3, Chapter 7.
12. P. H. Geil, *Polymer Single Crystals*, Wiley, New York (1963).
13. B. Wunderlich, *Macromolecular Physics:* Vol. 1, *Crystal Structure, Morphology, Defects*, Academic Press, New York (1973).
14. A. Keller, in *Growth and Perfection of Crystals* (R. H. Doremus, B. W. Roberts, D. Turnbull, eds.), pp. 499–528, Wiley, New York (1958).
15. A. Keller, Polymer crystals, *Rep. Prog. Phys.* **31**(Part 2), 623–704 (1968).
16. A. Keller, Solution grown polymer crystals: A survey of problematic issues, *Kolloid Z. Z. Polymere* **231**, 386–418 (1969).
17. A. Keller, in *MTP International Review of Science*, Vol. 8, *Macromolecular Science* (C. E. H. Bawn, ed.), pp. 105–158, Butterworths, London (1972).
18. H. D. Keith, in *Physics and Chemistry of the Organic Solid State* (D. Fox, M. M. Labes, and A. Weissberger, eds.), pp. 461–542, Interscience, New York (1963).
19. H. D. Keith, Crystallization of polymers from the melt, and the structure of bulk semicrystalline polymers, *Kolloid Z. Z. Polymere* **231**, 421–428 (1969).
20. P. Ingram and A. Peterlin, in *Encyclopedia of Polymer Science and Technology* (H. F. Mark and N. G. Gaylord, eds.), Vol. 9, pp. 204–274, Interscience, New York (1968).
21. D. V. Rees and D. C. Bassett, The texture of crystalline polymers: A brief review, *J. Mater. Sci.* **6**, 1021–1035 (1971).
22. R. A. Fava, Polyethylene crystals, *J. Polymer Sci. D: Macromolecular Reviews* **5**, 1–108 (1971).
23. G. E. Ham, in *Copolymerization* (G. E. Ham, ed.), pp. 1–65, Interscience, New York (1964).
24. G. E. Ham (ed.), *Copolymerization*, Interscience, New York (1964).
25. A. J. Yu and R. D. Evans, Isomorphous replacement in copolyamide systems: Adipic and terephthalic acids, *J. Polymer Sci.* **42**, 249–257 (1960).

26. M. Levin and S. C. Temin, Isomorphous replacement in a copolyamide system, *J. Polymer Sci.* **49**, 241–246 (1961).
27. R. K. Eby, A copolymer with lamellar morphology, *J. Res. Nat. Bur. Std. (U.S.)* **68A**, 269–272 (1964).
28. A. Skoulios and G. Finaz, La structure des colloides d'association. VII. Caractère amphipatique et phases mésomorphes des copolymères séquencés styrolène–oxide d'éthylène, *J. Chim. Physique* **59**, 473–480 (1962).
29. R. Perret and A. Skoulios, Etude de la cristallisation des copolymères triséquencés poly-ε-caprolactone/polyoxyéthylène/poly-ε-caprolactone. I. Copolymères dont les séquences ont des longueurs très inégales. *Makromol. Chemie* **162**, 147 162 (1972).
30. R. Perret and A. Skoulios, Etude de la cristallisation des copolymères trisequencés poly-ε-caprolactone/polyoxyéthylène/poly-ε-caprolactone. II. Copolymères dont les séquences ont des longueurs voisines, *Makromol. Chemie* **162**, 163–177 (1972).
31. B. Lotz and A. J. Kovacs, Propriétés des copolymères biséquencés polyoxyéthylène–polystyrène. I. Preparation, composition et étude microscopique des monocristaux, *Kolloid Z. Z. Polymere* **209**, 97–114 (1966).
32. B. Lotz, A. J. Kovacs, G. A. Bassett, and A. Keller, Properties, of copolymers composed of one poly(ethylene oxide) and one polystyrene block. II. Morphology of single crystals, *Kolloid Z. Z. Polymere* **209**, 115–128 (1966).
33. A. J. Kovacs, J. A. Manson, and D. Lévy, Propriétés des copolymères biséquencés polyoxyéthylène–polystyrène. III. Cinétique de croissance des monocristaux en solution, *Kolloid Z. Z. Polymere* **214**, 1–23 (1966).
34. E. Passaglia and H. K. Kevorkian, The heat capacity of linear and branched polyethylene, *J. Appl. Polymer Sci.* **7**, 119–132 (1963).
35. P. J. Flory, *Principles of Polymer Chemistry*, Cornell University Press, Ithaca, New York (1953).
36. F. A. Bovey, *High Resolution NMR of Macromolecules*, Academic, New York (1972).
37. J. B. Lando and W. W. Doll, The polymorphism of poly(vinylidene fluoride). I. The effect of head-to-head structure, *J. Macromol. Sci.—Phys.* **B2**, 205–218 (1968).
38. G. Natta and F. Danusso, Nomenclature relating to polymers having sterically ordered structures, *J. Polymer Sci.* **34**, 3–11 (1959).
39. R. L. Miller, in *Polymer Handbook* (J. Brandrup and E. H. Immergut, eds.), Chapter III, pp. 1–59, Interscience, New York (1966).
40. R. L. Miller, in *X-ray Diffraction Methods in Polymer Science*, L. E. Alexander, pp. 473–523, Wiley–Interscience, New York (1969).
41. L. E. Alexander, *X-ray Diffraction Methods in Polymer Science*, Wiley–Interscience, New York (1969).
42. M. Kakudo and U. Kasai, *X-Ray Diffraction by Polymers*, Elsevier, New York (1972).
43. G. Natta and F. Danusso (eds.), *Stereoregular Polymers and Stereospecific Polymerizations*, Vols. 1 and 2, Pergamon Press, New York (1967).
44. Y. Chatani, T. Uchida, H. Tadakoro, K. Hayashi, M. Niskii, and S. Okamura, X-ray crystallographic study of solid state polymerization of trioxane and tetraoxymethylene, *J. Macromol. Sci.—Phys.* **B2**, 567–590 (1968).

45. V. F. Holland and R. L. Miller, Isotactic polybutene-1 single crystals: Morphology, *J. Appl. Phys.* **35**, 3241–3248 (1964).
46. F. J. Padden, Jr. and H. D. Keith, Spherulitic crystallization in polypropylene, *J. Appl. Phys.* **10**, 1479–1484 (1959).
47. H. D. Keith, F. J. Padden, Jr., N. M. Walter, and H. W. Wyckoff, Evidence for a second crystal form of polypropylene, *J. Appl. Phys.* **30**, 1485–1488 (1959).
48. H. Kiho, A. Peterlin, and P. H. Geil, Polymer deformation. VI Twinning and phase transformation of polyethylene single crystals as a function of stretching direction, *J. Appl. Phys.* **35**, 1599–1603 (1964).
49. C. W. Bunn, The crystal structure of long-chain normal paraffin hydrocarbons. The "shape" of the CH_2 group, *Trans. Faraday Soc.* **39**, 482–491 (1939).
50. C. W. Bunn, *Chemical Crystallography*, p. 233, Oxford University Press (1949).
51. G. Natta and P. Corradini, Structure and properties of isotactic polypropylene, *Nuovo Cimento* **15**(Suppl. No. 1), 40–51 (1960).
52. G. Natta, Progress in stereospecific polymerization, *Makromol. Chemie* **35**, 94–131 (1960).
53. G. Natta, P. Corradini, and I. W. Bassi, Crystal structure of isotactic polystyrene, *Nuovo Cimento* **15**(Suppl. No. 1), 68–95 (1960).
54. F. C. Frank, A. Keller, and A. O'Connor, Observations on single crystals of an isotactic polyolefin: Morphology and chain packing in poly(4-methylpentene-1), *Phil. Mag.* **4**, 200–214 (1959).
55. I. W. Bassi, O. Bonsignori, G. P. Lorenzi, P. Pino, P. Corradini, and P. A. Temussi, Structure and optical activity of a crystalline modification of isotactic poly-(S)-4-methyl-1-hexene, *J. Polymer Sci. A-2* **9**, 193–208 (1971).
56. G. Natta and P. Corradini, General considerations on the structure of crystalline polyhydrocarbons, *Nuovo Cimento* **15**(Suppl. No. 1), 9–39 (1960).
57. G. V. D. Tiers and F. A. Bovey, Polymer NMR spectroscopy. VII. The stereochemical configuration of polytrifluorochloroethylene, *J. Polymer Sci.* **A1**, 833–841 (1963).
58. H. S. Kaufman, X-ray examination of polychlorotrifluoroethylene, *J. Am. Chem. Soc.* **75**, 1477–1478 (1953).
59. E. L. Gal Perrin, S. S. Dubov, E. V. Volkova, and M. P. Mlenick, The crystal structure of poly-trifluorochloroethylene, *Soviet Phys.—Cryst.* **9**, 81–83 (1964).
60. Y. Miyamoto, C. Nakafuku, and T. Takemura, Crystallization of polychlorotrifluoroethylene, *Polymer J. (Japan)* **3**, 122–128 (1972).
61. Z. Mencik, Crystal structure of polychlorotrifluoroethylene, *J. Polymer Sci.: Polymer Phys. Ed.* **11**, 1585–1599 (1973).
62. A. H. Scott, D. J. Scheiber, A. J. Curtis, J. I. Lauritzen, Jr., and J. D. Hoffman, Dielectric properties of semi-crystalline polychlorotrifluoroethylene, *J. Res. Nat. Bur. Std. (U.S.)* **66A**, 269–305 (1962).
63. J. M. Crissman and E. Passaglia, Mechanical relaxation in polychlorotrifluoroethylene, *J. Polymer Sci. C* **14**, 237–245 (1966).
64. R. Hill and E. E. Walker, Polymer constitution and fiber properties, *J. Polymer Sci.* **3**, 609–630 (1948).
65. R. W. J. Reynolds, in *Fibers from Synthetic Polymers* (R. Hill, ed.), pp. 115–144, Elsevier, New York (1953).
66. C. W. Bunn and E. V. Garner, The crystal structure of two polyamides ('Nylons'), *Proc. Roy. Soc. (London)* **A189**, 39–68 (1947).

67. A. E. Smith, The crystal structure of normal paraffin hydrocarbons, *J. Chem. Phys.* **21**, 2229–2231 (1953).
68. R. L. Miller, in *Encyclopedia of Polymer Science and Technology* (H. F. Mark, N. G. Gaylord, and N. M. Bikales, eds.), Vol. 4, pp. 449–528, Interscience, New York (1966).
69. T. Davidson and B. Wunderlich, Extended chain crystals II. Crystallization of polyethylene under elevated pressure, *J. Polymer Sci. A-2* **7**, 2051–2059 (1969).
70. E. W. Fischer and R. Lorentz, Über Fehlordnungen in Polyäthylen-Einkristallen, *Kolloid Z. Z. Polymere* **189**, 97–110 (1963).
71. J. B. Jackson, P. J. Flory, and R. Chiang, Thermodynamic stability of solution crystallized polyethylene, *Trans. Faraday Soc.* **59**, 1906–1917 (1963).
72. G. M. Martin and E. Passaglia, Density of polyethylene crystals grown from solution, *J. Res. Nat. Bur. Std.* (*U.S.*) **70A**, 221–224 (1966).
73. D. A. Blackadder and P. A. Lewell, The density of polyethylene single crystals, *Polymer* **9**, 249–263 (1968).
74. R. K. Sharma and L. Mandelkern, The density of polyethylene crystallized in the bulk and from dilute solution, *Macromolecules* **2**, 266–271 (1969).
75. E. Passaglia and G. M. Martin, Dependence of mechanical relaxation on morphology in isotactic polypropylene, *J. Res. Nat. Bur. Std.* (*U.S.*) **68A**, 519–527 (1964).
76. R. Hosemann, The paracrystalline state of synthetic polymers, *Crit. Rev. in Macromol. Sci.* **1**, 351–397 (1972).
77. D. C. Bassett and A. Keller, On the habits of polyethylene crystals, *Phil. Mag.* **7**, 1553–1584 (1962).
78. A. Nakajima and F. Hamada, Influence of crystallization conditions on single crystal formation, *Pure Appl. Chem.* **31**, 1–49 (1972).
79. F. Khoury and J. D. Barnes, The formation of curved polymer crystals: Poly-(4-methylpentene-1), *J. Res. Nat. Bur. Std.* (*U.S.*) **76A**, 225–252 (1972).
80. F. Khoury and J. D. Barnes, The formation of curved polymer crystals: Polyoxymethylene, *J. Res. Nat. Bur. Std.* (*U.S.*) **78A**, 95–127 (1974).
81. T. Kawai and A. Keller, Some effects of molecular fractionation during single crystal growth of polyethylene, *J. Polymer Sci. B* **3**, 333–337 (1964).
82. R. Koningsveld and A. J. Pennings, Crystallization fractionation of polymers, *Rec. Trav. Chim.* **83**, 552–555 (1964).
83. D. M. Sadler, Fractionation during crystallization, *J. Polymer Sci. A-2* **9**, 779–799 (1971).
84. I. C. Sanchez and E. A. DiMarzio, Dilute solution theory of polymer crystal growth, fractionation effects, *J. Res. Nat. Bur. Std.* (*U.S.*) **76A**, 213–223 (1972).
85. A. J. Pennings, Fractionation of polymers by crystallization from solutions. II, *J. Polymer Sci. C*, **16**(3), 1799–1812 (1967) (paper presented IUPAC Int. Symp. on Macromolecular Chemistry, Prague, 1965).
86. A. J. Pennings and A. M. Kiel, Fractionation by crystallization from solution, III. On the morphology of fibrillar polyethylene crystals grown in solution, *Kolloid Z. Z. Polymere* **205**, 160–162 (1965).
87. A. J. Pennings, J. M. M. A. Van der Mark, and A. M. Kiel, Hydrodynamically induced crystallization of polymers from solution. III. Morphology, *Kolloid Z. Z. Polymere* **237**, 336–358 (1970).

88. A. G. Wikjord and R. St. John Manley. Fibrillar crystals of isotactic polystyrene. 1. Morphological aspects, *J. Macromol. Sci.—Phys.* **B4**, 397–412 (1970).
89. S. Matsuzawa, K. Yamaura, and H. Yanagisawa, Stress induced crystallization of poly(vinyl alcohol) from its aqueous solution under steady-state flow, *Kolloid Z. Z. Polymere* **250**, 20–26 (1972).
90. D. J. Blundell, A. Keller, and A. J. Kovacs, A new self-nucleation phenomenon and its application to the growing of polymer crystals from solution, *J. Polymer Sci. B* **4**, 481–486 (1966).
91. D. J. Blundell and A. Keller, Nature of self-seeding polyethylene crystal nuclei, *J. Macromol. Sci.—Phys.* **B2**, 301–336 (1968).
92. D. J. Blundell and A. Keller, Controlled crystal growing procedures in polyethylene involving self-seeding: Some novel twinning habits, *J. Macromol. Sci.—Phys.* **B2**, 337–359 (1968).
93. A. J. Kovacs, B. Lotz, and A. Keller, Multiple twinning in polyethylene oxide single crystals—A scheme for the formation of growth twins from self-seeding nuclei, *J. Macromol. Sci.—Phys.* **B3**, 385–425 (1969).
94. A. Keller and F. M. Willmouth, Self-seeded crystallization and its potential for molecular weight characterization. I. Experiments on broad distributions, *J. Polymer Sci. A-2* **8**, 1443–1456 (1970).
95. A. Keller and D. M. Sadler, Self-seeded crystallization and its potential for molecular weight characterization. II. Experiments on narrow fractions, *J. Polymer Sci. A-2* **8**, 1457–1465 (1970).
96. S. H. Carr, A. Keller, and E. Baer, Relationship between self-seeded and epitaxial crystallization from polymer solutions: A potentially new method for molecular weight separation and a new decoration method for alkali halides, *J. Polymer Sci. A-2* **8**, 1467–1490 (1970).
97. D. C. Bassett, Surface detachment from polyethylene crystals, *Phil. Mag.* **6**, 1053–1056 (1961).
98. D. C. Bassett, A. Keller, and S. Mitsuhashi, New features in polymer crystal growth from concentrated solutions, *J. Polymer Sci. A* **1**, 763–788 (1963).
99. F. Khoury, The spherulitic crystallization of isotactic polypropylene from solution: On the evolution of monoclinic spherulites from dendritic chain-folded crystal precursors, *J. Res. Nat. Bur. Std. (U.S.)* **70A**, 29–61 (1966).
100. D. T. Grubb and A. Keller, Beam induced damage in polymers and its effect on the image formed in the electron microscope, in *Proc. 5th European Congress on Electron Microscopy*, pp. 554–560, Institute of Physics, London (1972).
101. A. Chapiro, *Radiation Chemistry of Polymeric Systems*, p. 352, Insterscience, Publishers, New York (1962).
102. D. C. Bassett, On moiré patterns in the electron microscopy of polymer crystals, *Phil. Mag.* **10**, 595–615 (1964).
103. P. H. Geil, Jr., N. K. J. Symons, and R. G. Scott, Solution grown crystals of an acetal resin, *J. Appl. Phys.* **30**, 1516–1517 (1959).
104. D. H. Reneker and P. H. Geil, Morphology of polymer crystals, *J. Appl. Phys.* **31**, 1916–1925 (1960).
105. D. T. Grubb, A. Keller, and G. W. Groves, Origin of contrast effects in the electron microscopy of polymers. Part 1: Polyethylene single crystals, *J. Mater. Sci.* **7**, 131–141 (1972).

106. P. Blais and R. St. John Manley, Crystallization of isotactic polystyrene from solution, *J. Polymer Sci. A-2* **4**, 1022–1024 (1966).
107. H. D. Keith, R. G. Vadimsky, and F. J. Padden, Jr., Crystallization of isotactic polystyrene from solution, *J. Polymer Sci. A-2* **8**, 1687–1696 (1970).
108. J. A. Sauer, D. R. Morrow, and G. C. Richardson, Morphology of solution-grown polypropylene crystal aggregates, *J. Appl. Phys.* **36**, 3017–3021 (1965).
109. F. J. Padden, Jr. and H. D. Keith, Crystallization in thin films of isotactic polypropylene, *J. Appl. Phys.* **37**, 4013–4020 (1966).
110. F. J. Padden, Jr. and H. D. Keith, Mechanism for lamellar branching in isotactic polypropylene, *J. Appl. Phys.* **44**, 1217–1223 (1973).
111. V. A. Kargin, N. F. Bakeev, and L. Li-Shen, Investigation of polychlorotrifluoroethylene monocrystals (in Russian), *Vysokomol. Soedin.* **3**, 1100–1101 (1961).
112. J. D. Barnes and F. Khoury, The formation of curved polymer crystals: Polychlorotrifluoroethylene, *J. Res. Nat. Bur. Std. (U.S.)* **78A**, 363–373 (1974).
113. P. H. Geil, Nylon single crystals, *J. Polymer Sci.* **44**, 449–458 (1960).
114. A. W. Agar, F. C. Frank, and A. Keller, Crystallinity effects in the electron microscopy of polyethylene, *Phil. Mag.* **4**, 32–55 (1959).
115. A. Keller and A. O'Connor, Study of single crystals and their associations in polymers, *Disc. Faraday Soc.* **25**, 114–121 (1958).
116. A. Keller, Electron microscope—electron diffraction investigations of the crystalline texture of polyamides, *J. Polymer Sci.* **36**, 361–387 (1959).
117. K. Kobayashi and K. Sakaoku, The changes of polymer crystals due to irradiation with electrons accelerated at various voltages, *Bull. Inst. Chem. Res. Kyoto Univ.* **42**, 473–493 (1964).
118. H. Orth and E. W. Fischer, Änderungen der Gitterstruktur hochpolymerer Einkristalle durch Bestrahlung in Electronenmicroskop, *Makromol. Chem.* **88**, 188–214 (1965).
119. R. W. Ditchfield, D. T. Grubb, and M. J. Whelan, Electron energy loss studies of polymers during radiation damage, *Phil. Mag.* **27**, 1267–1280 (1973).
120. E. L. Thomas and S. L. Sass, On the orthorhombic to hexagonal phase transformation in polyethylene single crystals, *Makromol. Chem.* **164**, 333–341 (1973).
121. V. F. Holland, Dislocations in polyethylene single crystals, *J. Appl. Phys.* **35**, 3235–3241 (1964).
122. V. F. Holland, P. H. Lindenmeyer, R. Trivedi, and S. Amelinckx, Contrast effects at dislocation networks in very thin polyethylene single crystals observed in the electron microscope, *Phys. Stat. Sol.* **10**, 543–569 (1965).
123. D. C. Bassett, On fold surfaces of polymer crystals, *Phil. Mag.* **17**, 37–50 (1968).
124. N. Niinomi, K. Abe, and M. Takayanagi, Mechanism of formation of the interlamella dislocation network in polyethylene single crystals, *J. Macromol. Sci.—Phys.* **B2**, 649–661 (1968).
125. D. M. Sadler and A. Keller, Polyethylene crystals with dislocation networks: Their origin, structure, and relevance to polymer crystallization, *Kolloid Z. Z. Polymere* **239**, 641–654 (1970).
126. J. Peterman and H. Gleiter, Direct observation of dislocations in polyethylene crystals, *Phil. Mag.* **25**, 813–816 (1972).

127. L. E. Thomas, C. J. Humphreys, W. R. Duff, and D. T. Grubb, Radiation damage of polymers in the million volt electron microscope, *Radiation Effects* **3**, 89–91 (1970).
128. D. T. Grubb and G. W. Groves, Rate of damage of polymer crystals in the electron microscope: Dependence on temperature and beam voltage, *Phil. Mag.* **24**, 815–828 (1971).
129. E. L. Thomas and S. Danyluk, A channelplate image intensifier for the electron microscope, *J. Phys. E: Sci. Instrum.* **4**, 843–844 (1971).
130. D. R. Clarke, Review: Transmission scanning electron microscopy, *J. Mater. Sci.* **8**, 279–285 (1973).
131. A. V. Crewe, Scanning transmission electron microscopy, *J. Microscopy* **100**, 247–259 (1974).
132. R. L. Miller, Polymer crystal formation: On an analysis of the dilute solution lamellar thickness–crystallization temperature data for polyethylene, *Kolloid Z. Z. Polymere* **225**, 62–69 (1968).
133. V. F. Holland, Morphology and electron diffraction of nylon 66 single crystals, *Makromol Chem.* **71**, 204–206 (1964).
134. D. C. Bassett, F. C. Frank, and A. Keller, Evidence for distinct sectors in polymer single crystals, *Nature* **184**, 810–811 (1959).
135. W. D. Niegisch and P. R. Swan, Hollow pyramidal crystals of polyethylene and a mechanism of growth, *J. Appl. Phys.* **31**, 1906–1910 (1960).
136. D. C. Bassett and A. Keller, Some new habit features in crystals of long chain compounds. Part II. Polymers, *Phil. Mag.* **6**, 345–358 (1961).
137. D. C. Bassett, F. C. Frank, and A. Keller, Some new habit features in crystals of long chain compounds. Part III. Direct observations of unflattened monolayer polyethylene crystals, *Phil. Mag.* **8**, 1739–1751 (1963).
138. D. C. Bassett, F. C. Frank and A. Keller, Some new habit features in crystals of long chain compounds. Part IV. The fold surface geometry of monolayer polyethylene crystals and its relevance to fold packing and crystal growth, *Phil. Mag.* **8**, 1753–1787 (1963).
139. T. Kawai and A. Keller, On the effect of the crystallization temperature on the habit and fold length of polyethylene single crystals, *Phil. Mag.* **11**, 1165–1177 (1965).
140. B. Valenti and E. Pedemonte, Sulla morfologia di cristalli singoli di polietilene, *La Chimiva e l'Industria* **54**, 112–116 (1972).
141. G. A. Carazzolo, Structure of the normal crystal form of polyoxymethylene, *J. Polymer Sci. A* **1**, 1573–1583 (1963).
142. P. Sullivan and B. Wunderlich, The interference microscopy of crystalline linear high polymers, *SPE Trans.* **4**, 113–119 (1964).
143. P. H. Geil and D. H. Reneker, Morphology of dendritic polyethylene crystals, *J. Polymer Sci.* **51**, 569–582 (1961).
144. A. Keller, Crystal configurations and their relevance to the crystalline texture and crystallization mechanism in polymers, *Kolloid Z. Z. Polymere* **197**, 98–115 (1964).
145. P. H. Lindenmeyer, Crystallization in polymers, *J. Polymer Sci. C* **1**, 5–39 (1963).
146. D. H. Reneker, Localized deformation of lamellar polyethylene crystals, *J. Polymer Sci. A* **3**, 1069–1077 (1965).

147. K. Haas and P. H. Geil, Polymer deformation. XI. Biaxial deformation of polyethylene crystals, *J. Polymer Sci. A-2* **4**, 289–298 (1966).
148. H. Gleiter and J. Peterman, Deformation of substrate-free polyethylene single crystals, *J. Polymer Sci. B* **10**, 877–881 (1972).
149. D. C. Bassett, A note on sector boundaries in polymer crystals, *Phil. Mag.* **12**, 907–914 (1965).
150. D. C. Bassett, F. R. Dammont, and R. Salovey, On the morphology of polymer crystals, *Polymer (London)* **5**, 579–588 (1964).
151. F. C. Frank, Crystal growth and dislocations, *Adv. Phys.* **1**, 91–109 (1952).
152. W. J. Barnes and F. P. Price, Morphology of polymer crystals: Screw dislocations in polyethylene, polymethylene oxide and polyethylene oxide, *Polymer (London)* **5**, 283–292 (1964).
153. A. Keller, Regular rotation of growth terraces in polymer single crystals, *Kolloid Z. Z. Polymere* **219**, 118–131 (1967).
154. S. Mitsuhashi and A. Keller, The morphology of multilayer polymer crystals, *Polymer (London)* **2**, 109–112 (1961).
155. B. Wunderlich, E. A. James, and S. W. Shu, Crystallization of polyethylene from *o*-xylene, *J. Polymer Sci. A* **2**, 2759–2769 (1964).
156. V. F. Holland, S. B. Mitchell, W. L. Hunter, and P. H. Lindemeyer, Crystal structure and morphology of polyacrylonitrile in dilute solution, *J. Polymer Sci.* **62**, 145–151 (1962).
157. J. J. Klement and P. H. Geil, Growth and drawing of polyacrylonitrile crystals grown from solution, *J. Polymer Sci. A-2* **6**, 1381–1399 (1968).
158. G. N. Patel and R. D. Patel, Single crystals of polymers by thin film formation, *J. Polymer Sci. A-2* **8**, 47–59 (1970).
159. G. Hinrichsen and H. Orth, Zur Structur Verstrekter Folien und Fäden sowie aus Verdünnten Lösungen Hergesteller Einkristalle aus Polyacrylnitril, *Kolloid Z. Z. Polymere* **247**, 844–850 (1971).
160. H. D. Keith, Habits of polyethylene crystals grown from paraffinic solvents and from the melt, *J. Appl. Phys.* **35**, 3115–3126 (1964).
161. F. Khoury and F. J. Padden, Jr., On the growth habits of twinned crystals of polyethylene, *J. Polymer Sci.* **47**, 455–468 (1960).
162. J. I. Lauritzen, Jr. and J. D. Hoffman, Theory of formation of polymer crystals with folded chains in dilute solution, *J. Res. Nat. Bur. Std. (U.S.)* **64A**, 73–102 (1960).
163. F. P. Price, The growth habit of single polymer crystals, *J. Polymer Sci.* **42**, 49–56 (1960).
164. F. C. Frank and M. Tosi, On the theory of polymer crystallization, *Proc. Roy. Soc.* **263A**, 323–339 (1961).
165. J. I. Lauritzen, Jr. and E. Passaglia, Kinetics of crystallization in multicomponent systems: II. Chain-folded polymer crystals, *J. Res. Nat. Bur. Std. (U.S.)* **71A**, 261–275 (1967).
166. I. C. Sanchez and E. A. DiMarzio, Dilute solution theory of polymer crystal growth: A kinetic theory of chain folding, *J. Chem. Phys.* **55**, 893–907 (1971).
167. R. St. Manley, Growth and morphology of single crystals of cellulose triacetate, *J. Polymer Sci. A* **1**, 1875–1892 (1963).
168. A. Nakajima and S. Hayashi, Single crystals of polyvinyl chloride polymerized at various temperatures, *Kolloid Z. Z. Polymere* **228**, 12–17 (1969).

169. R. Eppe, E. W. Fischer, and H. A. Stuart, Morphologische Strukturen in Polyäthylenen, Polyamiden und andern Kristallisierenden Hochpolymeren, *J. Polymer Sci.* **34**, 721–740 (1959).
170. P. H. Geil, Lamellar crystallization of low density polyethylene, *J. Polymer Sci.* **51**, S10–S14 (1961).
171. H. G. Kilian and E. W. Fischer, Morphologische Struktur von Copolymeren des Äthylens abhängig von den Gegebenheiten des Molekülbaues, *Kolloid Z. Z. Polymere* **211**, 40–52 (1966).
172. R. J. Roe, H. F. Cole, and D. R. Morrow, in *Advances in Polymer Science and Engineering* (K. D. Pae, D. R. Morrow, Y. Chen, eds.), pp. 27–41, Plenum, New York (1972).
173. P. J. Holdsworth and A. Keller, The crystallization of ethyl and methyl branched copolymers of polyethylene from dilute solution, *J. Polymer Sci. B* **5**, 605–612 (1967).
174. T. Kawai, K. Ujihara, and H. Maeda, Fold structure of solution grown crystals of alkyl-branched copolymers of polyethylene, *Makromol. Chem.* **132**, 87–111 (1970).
175. D. H. Jones, A. J. Latham, A. Keller, and M. Girolamo, Fold length of single crystals of polystyrene: A conflict with crystallization theories at high supersupercoolings, *J. Polymer Sci.: Polymer Phys. Ed.* **11**, 1759–1767 (1973).
176. L. Mandelkern, in *Progress in Polymer Science* (A. D. Jenkins, ed.), Vol. 2, pp. 165–200, Pergamon, New York (1970).
177. A. Keller and J. D. Priest, Experiments on the location of chain ends in monolayer single crystals of polyethylene, *J. Macromol. Sci.—Phys.* **B2**, 479–495 (1968).
178. M. I. Bank and S. Krimm, Infrared study of lamellar linking by cilia in polyethylene single crystal mats, *J. Appl. Phys.* **40**, 4248–4253 (1969).
179. P. J. Flory, On the morphology of the crystalline state in polymers, *J. Am. Chem. Soc.* **84**, 2857–2867 (1962).
180. M. I. Bank and S. Krimm, Mixed crystal infrared study of chain folding in crystalline polyethylene, *J. Polymer Sci. A-2* **7**, 1785–1809 (1968).
181. S. Krimm and J. H. C. Ching, Infrared spectra of polyethylene–poly(ethylene-d_4) mixed crystal systems, *Macromolecules* **5**, 209–211 (1972).
182. T. Williams, J. D. Blundell, A. Keller, and I. M. Ward, Gel permeation chromatographic studies of the degradation of polyethylene with fuming nitric acid. I. Single crystals, *J. Polymer Sci. A-2* **6**, 1613–1619 (1968).
183. D. J. Priest, Fold surface of polyethylene single crystals as assessed by selective degradation. I. Ozone degradation method, *J. Polymer Sci. A-2* **9**, 1777–1791 (1971).
184. A. Keller and Y. Udagawa, Fold surface of polyethylene crystals as assessed by selective degradation studies. II. Refinements of the nitric acid degradation method, *J. Polymer Sci. A-2* **9**, 1793–1805 (1971).
185. A. Keller, E. Martucelli, D. J. Priest, and Y. Udagawa, Fold surface of polyethylene single crystals as assessed by selective degradation studies. III. Application of the improved techniques to single crystals, *J. Polymer Sci. A-2* **9**, 1807–1837 (1971).
186. E. W. Fischer and G. F. Schmidt, Long periods in drawn polyethylene, *Angew. Chem. Int. Ed.* **1**, 488–499 (1962) [*Angew Chem.* **74**, 551–562 (1962)].

187. E. W. Fisher, H. Goddar, and G. F. Schmidt, A remark on the surface structure of polyethylene single crystals, *J. Polymer Sci. B* **5**, 619–624 (1967).
188. E. W. Fischer, H. Goddar, and R. Salovey, Effect of filtration conditions on the apparent density of the intercrystalline layers of polyethylene single crystal mats, *J. Polymer Sci. B* **7**, 307–311 (1969).
189. E. W. Fischer and F. Kloos, Proof of the existence of a glass transition in the surface layers of polyethylene single crystals, *J. Polymer Sci. B* **8**, 685–693 (1970).
190. E. W. Fischer and G. Hinrichsen, Schmelz- und Rekristallisationsvorgänge bei Polyäthylen-Einkristallen. IV. Schmelzenthalpie und Grenzflächenenergie von Polyäthylen-Einkristallen, *Kolloid Z. Z. Polymere* **247**, 858–866 (1971).
191. P. Dreyfuss and A. Keller, Chain folding in polyamides: A study of nylons 6.6, 6.10, and 6.12 as crystallized from solution, *J. Macromol. Sci.—Phys.* **B4**, 811–836 (1970).
192. P. Dreyfuss, A. Keller, and F. M. Willmouth, Novel diffraction effects in the combined wide-angle and low-angle x-ray diffraction patterns of solution-grown nylon crystals, *J. Polymer Sci. A-2* **10**, 857–861 (1972).
193. E. D. T. Atkins, A. Keller, and D. M. Sadler, Structure analysis of chain-folded lamellar polyamide crystals from x-ray diffraction, *J. Polymer Sci. A-2* **10**, 863–875 (1972).
194. A. F. Burmester, P. Dreyfuss, P. H. Geil, and A. Keller, On the annealing of polyamide crystal mats, *J. Polymer Sci. B* **10**, 769–775 (1972).
195. P. Dreyfuss and A. Keller, Invariance of the long spacing–crystallization temperature dependence of polyamides precipitated from solution, *J. Polymer Sci.: Polymer Phys. Ed.* **11**, 193–200 (1973).
196. P. Dreyfuss, Survey of the long spacing of polyamides crystallized from solution, *J. Polymer Sci.: Polymer Phys. Ed.* **11**, 201–216 (1973).
197. C. W. Bunn, in *Fibers from Synthetic Polymers* (R. Hill, ed.), pp. 311–314, Elsevier, New York (1953).
198. W. P. Slichter, Molecular motion in polyamides, *J. Polymer Sci.* **35**, 77–92 (1958).
199. W. P. Slichter, Crystal structures in polyamides made from ω-amino acids, *J. Polymer Sci.* **36**, 259–266 (1959).
200. J. L. Koenig and M. C. Agboatwalla, Infrared studies of chain folding in polymers. V. Polyhexamethylene adipamide, *J. Macromol. Sci.—Phys.* **B2**, 391–420 (1968).
201. L. E. Alexander, Chain folding conformations in polyamides: Models from the structures of cyclic oligomers, *J. Polymer Sci. B* **10**, 759–767 (1972).
202. G. Hinrichsen, Untersuchungen zu Struktur und Eigenschaften der Polyamide. 2. Einkristalle aus Polyamid 6.6, *Makromol. Chem.* **166**, 291–306 (1973).
203. H. W. Starkweather and R. E. Moynihan, Density, infrared absorption, and crystallinity in 6.6 and 6.10 nylons, *J. Polymer Sci.* **22**, 363–368 (1956).
204. I. C. Sanchez and R. K. Eby, Crystallization of random copolymers, *J. Res. Nat. Bur. Std. (U.S.)* **77A**, 353–358 (1973).
205. P. J. Flory, Theory of crystallization in copolymers, *Trans. Faraday Soc.* **51**, 848–857 (1955).
206. P. J. Holdsworth, A. Keller, I. M. Ward, and T. Williams, Investigations of the structure of ethylene–propylene and ethylene–butene copolymer crystals. Part I. The molecular weight distribution of degraded copolymer crystals, *Makromol. Chem.* **125**, 70–81 (1969).

207. P. J. Holdsworth and A. Keller, Investigations of the structure of ethylene–propylene and ethylene–butene copolymer crystals. Part II. The removal of branches by nitric acid, *Macromol. Chem.* **125**, 82–93 (1969).
208. P. J. Holdsworth and A. Keller, Investigations of the structure of ethylene–propylene and ethylene–butene copolymer crystals. Part III. The effects of nitric acid on the physical properties of single crystal mats of ethylene copolymers, *Makromol. Chem.* **125**, 94–107 (1969).
209. J. I. Lauritzen, Jr. and J. D. Hoffman, Extension of theory of growth of chain-folded polymer crystals to large undercoolings, *J. Appl. Phys.* **44**, 4340–4352 (1973).
210. H. D. Keith, G. Giannoni, and F. J. Padden, Jr., Single crystals of poly(L-glutamic acid), *Biopolymers* **7**, 775–792 (1969).
211. P. Cerra, D. R. Morrow, and J. A. Sauer, Deformation of polypropylene single crystals, *J. Macromol. Sci.—Phys.* **B3**, 33–51 (1969).
212. D. R. Morrow and B. A. Newman, Crystallization of low-molecular-weight polypropylene fractions, *J. Appl. Phys.* **39**, 4944–4950 (1968).
213. F. J. Padden, Jr. and H. D. Keith, Private communication
214. K. Sakaoku and A. Peterlin, Poly(vinylidene fluoride) single crystals, *J. Macromol. Sci.—Phys.* **B1**, 401–406 (1967).
215. C. Sella and J. J. Trillat, Structures périodiques dans les polyéthylènes, *Compt. Rend.* **248**, 410–413 (1959).
216. R. D. Burbank, Molecular structure in crystal aggregates of linear polyethylene, *Bell System Tech. J.* **39**, 1627–1663 (1960).
217. J. C. Wittman and A. J. Kovacs, Vielartige Zwillinge in Polyäthylene-Einkristallen, *Ber. Bunsenges. Phys. Chem.* **74**, 901–904 (1970).
218. R. M. Gohil, K. C. Patel, and R. D. Patel, Twinning in polyacrylonitrile, *Makromol. Chem.* **169**, 291–300 (1973).
219. M. Kojima, Morphology of polypropylene crystals. II. Twinning of lamellar crystals, *J. Polymer Sci. A-2* **5**, 615–622 (1967).
220. G. W. Bailey, Electron microscope studies on polyethylene and polypropylene, *J. Polymer Sci.* **62**, 241–249 (1962).
221. F. L. Binsbergen and B. G. M. De Lang, Morphology of polypropylene crystallized from the melt, *Polymer* **9**, 23–40 (1968).
222. P. Allan, E. B. Crellin, and M. Bevis, Stress-induced twinning and phase transformations in polyethylene single crystals, *Phil. Mag.* **27**, 127–145 (1973).
223. W. Cross, Constitution and origin of spherulites in acid eruptive rocks, *Bull. Phil. Soc. Washington* **11**, 411–443 (1891).
224. A. Johannsen, *A Descriptive Petrography of Igneous Rocks*, University of Chicago Press, Chicago, Illinois (19).
225. J. P. Iddings, Spherulitic crystallization, *Bull. Phil. Soc. Washington* **11**, 445–463 (1891).
226. F. Wallerant, Sur les enroulements hélicoïdaux dans les corps cristalisés, *Bull. Soc. Fr. Mineral.* **30**, 43–60 (1907).
227. F. Bernauer, *Gedrillte Kristalle*, Bornträger, Berlin (1929).
228. H. D. Keith and F. J. Padden, Jr., A phenomenological theory of spherulitic crystallization, *J. Appl. Phys.* **34**, 2409–2421 (1963).
229. H. D. Keith and F. J. Padden, Jr., Spherulitic crystallization from the melt. I. Fractionation and impurity segregation and their influence on crystalline morphology, *J. Appl. Phys.* **35**, 1270–1285 (1964).

230. H. D. Keith and F. J. Padden, Jr., Spherulitic crystallization from the melt. II. Influence of fractionation and impurity segregation on the kinetics of crystallization, *J. Appl. Phys.* **35**, 1286–1296 (1964).
231. M. Herbst, Röntgenographische Untersuchung an Sphärolithen in Polyamid-Spritzgussmassen, *Z. Electrochem.* **54**, 318–320 (1950).
232. J. J. Point, Enroulement hélicoïdal dans les sphérolithes de polyéthylène, *Bull. Acad. Roy. Belg.* **41**, 982–990 (1955).
233. A. Keller, The spherulitic structure of crystalline polymers, Part II. The problem of molecular orientation in polymer spherulites, *J. Polymer Sci.* **17**, 351–364 (1955).
234. Y. Fujiwara, The superstructure of melt-crystallized polyethylene. I. Screwlike orientation of unit cell in polyethylene spherulites with periodic extinction rings, *J. Appl. Polymer Sci.* **4**, 10–15 (1960).
235. J. J. Point, Sphérolithes de polyadipate de glycol, *Bull. Acad. Roy. Belge.* **39**, 435–441 (1953).
236. J. Mann and L. Roldan-Gonzalez, Orientation in nylon spherulites: A study by x-ray diffraction, *J. Polymer Sci.* **60**, 1–20 (1962).
237. J. H. Magill, Formation of spherultes in polyamide melts: Part III. Even–even polyamides, *J. Polymer Sci. A-2* **4**, 243–265 (1966).
238. F. J. Baltá Calleja, I. L. Hay, and A. Keller, Diffraction effects in single crystals and spherulites of poly(ethylene oxide), *Kolloid Z. Z. Polymere* **209**, 128–135 (1966).
239. C. W. Bunn and R. de P. Daubeny, The polarizabilities of carbon–carbon bonds, *Trans. Faraday Soc.* **50**, 1173–1177 (1954).
240. D. A. Keedy, J. Powers, and R. S. Stein, A theoretical calculation of the birefringence of polypropylene crystals, *J. Appl. Phys.* **31**, 1911–1915 (1960).
241. F. L. Saunders, Observations on spherulite structure in poly(4-methylpentene1-), *J. Polymer Sci. B* **2**, 755–760 (1964).
242. I. Kirshenbaum, R. B. Isaacson, and W. C. Feist, The effect of molecular motion on the birefringence–temperature curve of poly(4-methylpentene-1), *J. Polymer Sci. B* **2**, 897–901 (1964).
243. A. Keller, Morphology of crystallizing polymers, *Nature* **169**, 913–914 (1952).
244. H. D. Keith and F. J. Padden, Jr., The optical behavior of spherulites in crystalline polymers. Part I. Calculation of theoretical extinction patterns in spherulites with twisting crystalline orientation, *J. Polymer Sci.* **39**, 101–122 (1959).
245. H. D. Keith and F. J. Padden, Jr., The optical behavior of spherulites in crystalline polymers. Part II. The growth and structure of the spherulites, *J. Polymer Sci.* **39**, 123–138 (1959).
246. F. P. Price, On extinction patterns of polymer spherulites, *J. Polymer Sci.* **39**, 139–150 (1959).
247. A. Keller, Investigations on banded spherulites, *J. Polymer Sci.* **39**, 151–173 (1959).
248. J. J. Point, Structure fibreuse et phénomènes de cristallisation rayonnante dans les hauts polymères sphérolithiques, *Bull. Acad. Roy. Belg.* **41**, 974–981 (1955).
249. M. Takayanagi and T. Yamashita, Growth rate and structure of spherulites in fractionated poly(ethylene adipate), *J. Polymer Sci.* **22**, 552–555 (1956).
250. P. H. Lindenmeyer and V. F. Holland, Relationship between molecular weight, radial growth rate, and the width of extinction bands in polyethylene spherulites, *J. Appl. Phys.* **35**, 55–58 (1964).

251. H. D. Keith and F. J. Padden Jr., Deformation mechanisms in crystalline polymers, *J. Polymer Sci.* **41**, 525–528 (1959).
252. H. D. Keith and F. J. Padden, Jr., Note on the origin of twisting orientation in fibrillar crystals, *J. Polymer Sci.* **51** (Issue 156), S4–S7 (1971).
253. J. D. Hoffman and J. I. Lauritzen, Jr., Crystallization of bulk polymers with chain folding: Theory of growth of lamellar spherulites, *J. Res. Nat. Bur. Std. (U.S.)* **65A**, 297–336 (1961).
254. J. R. Burns, Mechanism for twisting in polyethylene spherulites, *J. Polymer Sci. A-2* **7**, 593–600 (1969).
255. S. Sato and T. Seto, Effect of crystallization temperature on the period of lamellar twist in polymer spherulites, *Rep. Prog. Polymer Phys. Japan* **12**, 161–164 (1969).
256. J. M. Schultz and D. R. Kinloch, Transverse screw dislocations: A source of twist in crystalline polymer ribbons, *Polymer (London)* **10**, 271–278 (1969).
257. P. D. Calvert and D. R. Uhlmann, Surface stresses and crystal twisting in hippuric acid and in polymers, *J. Polymer Sci.: Polymer Phys. Ed.* **11**, 457–465 (1973).
258. P. H. Geil, Small angle x-ray scattering from bulk crystalline polymers, *J. Polymer Sci. C* **13**, 149–163 (1966).
259. C. Reinhold, E. W. Fischer, and A. Peterlin, Evaluation of small-angle x-ray scattering of polymers, *J. Appl. Phys.* **35**, 71–74 (1964).
260. K. H. Illers and H. Hendus, Lamellendicke und Röntgen-Kleinwinkel-Perioden von Polyäthylen, *Kolloid Z. Z. Polymere* **218**, 56–58 (1967).
261. B. Crist, Small angle x-ray scattering of semicrystalline polymers. I. Review of Existing models, *J. Polymer Sci.: Polymer Phys. Ed.* **11**, 635–661 (1973).
262. B. Crist and N. Morosoff, Small angle x-ray scattering of semicrystalline polymers. II. Analysis of experimental scattering curves, *J. Polymer Sci.: Polymer Phys. Ed.* **11**, 1023–1045 (1973).
263. C. G. Vonk and G. Kortleve, X-ray small-angle scattering of bulk polyethylene, *Kolloid Z. Z. Polymere* **220**, 19–24 (1967).
264. G. Kortleve and C. G. Vonk, X-ray small-angle scattering of bulk polyethylene, *Kolloid Z. Z. Polymere* **225**, 124–131 (1968).
265. R. G. Brown and R. K. Eby, Effect of crystallization conditions on polyethylene: Lamellar thickness, melting temperature, and density, *J. Appl. Phys.* **35**, 1156–1161 (1964).
266. F. R. Anderson, Morphology of isothermally bulk-crystallized linear polyethylene, *J. Appl. Phys.* **35**, 64–70 (1964).
267. R. P. Palmer and A. J. Cobbold, The texture of melt crystallized polyethylene as revealed by selective oxidation, *Makromol. Chemie* **74**, 174–189 (1964).
268. A. Keller and S. Sawada, On the interior morphology of bulk polyethylene, *Makromol. Chemie* **74**, 190–221 (1964).
269. I. C. Sanchez, J. P. Colson, and R. K. Eby, Theory and observations of polymer crystal thickening, *J. Appl. Phys.* **44**, 4332–4339 (1973).
270. E. W. Fischer, Effect of annealing and temperature on the morphological structure of polymers, *Pure and Appl. Chem.* **31**, 113–131 (1972).
271. M. Avrami, Kinetics of phase change I. General theory, *J. Chem. Phys.* **7**, 1103–1112 (1939); Kinetics of phase change II. Transformation–time relations for random distribution of nuclei, *J. Chem. Phys.* **8**, 212–224 (1940).
272. F. P. Price, Some comments on the "Avrami" equation, *J. Appl. Phys.* **36**, 3014–3016 (1965).

273. A. Peterlin, Secondary crystallization and annealing of polyethylene, *J. Appl. Phys.* **35**, 75–81 (1964).
274. A. J. Kovacs, Cinétique de crystallization du polyéthylène, *Ric. Sci.* **25** (Suppl. A: Papers given at IUPAC Int. Symp. Macromol. Chem., Milan–Turin, 1954), pp. 668–685 (1955).
275. H. G. Zachmann and H. H. Stuart, Schmelz- und Kristallisationserscheinungen bei Makromolekularen Substanzen. IV. Haupt- und Nachkristallisation von Terylen aus dem Glaszustand, *Makromol. Chemie* **41**, 131–147 (1960); Schmelz- und Kristallisationserscheinungen bei Makromolekularen Substanzen. V. Partielles Schmelzen und Neuekristallisieren von Terylen, *Makromol. Chemi* **41**, 148–173 (1960).
276. F. Rybnikar, Secondary crystallization of polymers, *J. Polymer Sci.* **44**, 517–522 (1960).
277. F. Rybnikar, Mechanism of secondary crystallization in polymers, *J. Polymer Sci. A* **1**, 2031–2038 (1963).
278. J. M. Schultz and R. D. Scott, Temperature dependence of secondary crystallization in linear polyethylene, *J. Polymer Sci. A-2* **7**, 659–666 (1969).
279. W. A. Tiller, K. A. Jackson, J. W. Rutter, and B. Chalmers, The redistribution of solute atoms during the solidification of metals, *Acta Met.* **1**, 428–437 (1953).
280. R. L. Parker, Crystal growth mechanisms: Energetics, kinetics and transport, in *Solid State Physics*, Vol. 25, p. 260 (D. Turnbull and F. Seitz, eds.), Academic, New York (1970).
281. J. W. Rutter and B. Chalmers, A prismatic substructure formed during solidification of metals, *Can. J. Phys.* **31**, 15–39 (1953).
282. G. Lofgren, Spherulitic texture in glassy and crystalline rocks, *J. Geophys. Res.* **76**, 5635–5640 (1971).
283. J. H. Magill and D. J. Plazek, Physical properties of aromatic hydrocarbons. II. Solidification behavior of 1,3,5-tri-α-naphthylbenzene, *J. Chem. Phys.* **46**, 3757–3769 (1967).
284. P. H. Geil, Polyhedral structures in polymers grown from the melt, in *Growth and Perfection of Crystals* (R. H. Doremus, B. W. Roberts, and D. Turnbull, eds.), pp. 579–585, Wiley, New York (1958).
285. H. D. Keith, On the relation between different morphological forms in high polymers, *J. Polymer Sci. A* **2**, 4339–4360 (1964).
286. F. Khoury and J. D. Barnes, Phenomenon of curved-crystal formation and the evolution of spherulitic structures in polymers, *Bull. Am. Phys. Soc.* **11**, 248 (FA 11) (1966).
287. H. D. Keith, F. J. Padden, Jr., and R. G. Vadimsky, Intercrystalline links in polyethylene crystallized from the melt, *J. Polymer Sci. A-2* **4**, 267–281 (1966).
288. H. A. Davis, Interlamella ties, *J. Polymer Sci. A-2* **4**, 1009–1010 (1966).
289. E. S. Clark, Molecular orientation in injection molded acetal homopolymer, *SPE J.* **23**(7), 46–49 (1967).
290. Y. Hase and P. H. Geil, Swelling, deformation and retraction of poly(4-methylpentene-1). I. Morphological observations, *Polymer J. (Japan)* **2**, 560–580 (1971).
291. Y. Hase and P. H. Geil, Swelling, deformation, and retraction of poly(4-methylpentene-1). II. Mechanical properties in the swollen state, *Polymer J. (Japan)* **2**, 581–592 (1971).

292. F. Rybnikar and P. H. Geil, Lamellar structure of isothermally crystallized poly(4-methylpentene-1), *J. Macromol. Sci.—Phys.* **B7**, 1–17 (1973).
293. H. D. Keith, F. J. Padden and R. G. Vadimsky, Intercrystalline links: Critical evaluation, *J. Appl. Phys.* **42**, 4585–4592 (1971).
294. P. H. Geil, F. R. Anderson, B. Wunderlich, and T. Arakawa, Morphology of polyethylene crystallized from the melt under pressure, *J. Polymer Sci. A* **2**, 3707–3720 (1964).
295. B. Wunderlich and T. Davidson, Extended chain crystals. I. General crystallization conditions and review of pressure crystallization of polyethylene, *J. Polymer Sci. A-2* **7**, 2043–2050 (1969).
296. R. B. Prime and B. Wunderlich, Extended chain crystals. III. Size distribution of polyethylene crystals grown under elevated pressure, *J. Polymer Sci. A-2* **7**, 2061–2072 (1969).
297. R. B. Prime and B. Wunderlich, Extended chain crystals. IV. Melting under equilibrium conditions, *J. Polymer Sci. A-2* **7**, 2073–2089 (1969).
298. R. B. Prime, B. Wunderlich, and L. Melillo, Extended chain crystals. V. Thermal analysis and electron microscopy of the melting process in polyethylene, *J. Polymer Sci. A-2* **7**, 2091–2097 (1969).
299. C. L. Gruner, B. Wunderlich, and R. C. Bopp, Extended chain crystals. VI. Annealing of polyethylene under elevated pressure, *J. Polymer Sci. A-2* **7**, 2099–2113 (1969).
300. B. Wunderlich and L. Melillo, Morphology and growth of extended chain crystals of polyethylene, *Makromol. Chem.* **118**, 250–264 (1968).
301. M. Yasuniwa, C. Nakafuku, and T. Takemura, Melting and crystallization process of polyethylene under high pressure, *Polymer J. (Japan)* **4**, 526–533 (1973).
302. D. C. Bassett, B. A. Khalifa, and B. Turner, Chain-extended crystallization of polyethylene, *Nature, Phys. Sci.* **239**, 106–108 (1972).
303. D. C. Bassett and B. Turner, Chain-extended crystallization of polyethylene: Evidence for a new, high pressure phase, *Nature, Phys. Sci.* **240**, 146–148 (1972).
304. D. C. Bassett and B. Turner, On chain-extended and chain-folded crystallization of polyethylene, *Phil. Mag.* **29**, 285–307 (1974).
305. D. C. Bassett and B. Turner, On the phenomenology of chain-extended crystallization in polyethylene, *Phil. Mag.* **29**, 925–955 (1974).
306. D. C. Bassett, S. Block, and G. J. Piermarini, A high pressure phase of polyethylene and chain extended growth, *J. Appl. Phys.* **45**, 4146–4150 (1974).
307. J. F. Jackson, T. S. Hsu, and J. W. Brasch, Direct microscopic observations of the crystallization process of polyethylene at high pressure: Acicular bladed crystals, *J. Polymer Sci. B* **10**, 207–224 (1972).
308. L. Melillo and B. Wunderlich, Extended chain crystals. VIII. Morphology of polytetrafluoroethylene, *Kolloid Z. Z. Polymere* **250**, 417–425 (1972).
309. J. D. Hoffman and J. J. Weeks, X-ray study of isothermal thickening of lamellae in bulk polyethylene at the crystallization temperature, *J. Chem. Phys.* **42**, 4301–4302 (1965).

7

The Rate of Crystallization of Linear Polymers with Chain Folding

John D. Hoffman, G. Thomas Davis, and John I. Lauritzen, Jr.

Institute for Materials Research
National Bureau of Standards
Washington, D.C.

1. Introduction

1.1 Aims and Objectives

Under a variety of circumstances commonly encountered in practice linear macromolecules crystallize into the form of thin platelets whose large upper and lower surfaces consist of an array of molecular folds. We refer to these as "chain-folded crystals" or "chain-folded lamellae," the latter term usually being reserved for folded structures in polymers crystallized from the melt. The theory of the rate of formation of these platelets will be outlined, and the prediction and origin of the thin dimension given. The thin dimension of the crystal platelets is determined by kinetic factors, and the elucidation of the kinetics of growth is therefore of importance in polymer morphology on both a molecular and a macroscopic scale.

Interest in crystallization of linear polymers with chain folding has several origins. First, many synthetic organic polymers such as polyethylene and nylon are crystalline and exhibit chain folding, and their physical (and even chemical) properties often depend critically on the nature of the crystals that largely comprise their bulk. Second, systems of biological origin are frequently polymeric in character, and some of these or their prototypes or derivatives crystallize with

chain folding. Examples here are natural rubber, cellulose triacetate, the salts of poly(L-glutamic) acid, and probably the DNA of many organisms. Third, some inorganic materials, such as liquid selenium, have polymeric character, and under certain circumstances crystallize in the chain-folded mode. Fourth, the crystallization of polymers is of intrinsic interest in the purely scientific sense, a revised version of surface nucleation theory achieving a surprising degree of success in explaining or predicting observed crystallization phenomena. It is the latter point that will be given the greatest attention in this work.

For the most part the crystals formed by linear polymers belong to the class of molecular crystals, i.e., the forces that hold the body of the crystal intact are of the van der Waals type. Usually the predominant term in the crystal attraction energy involves London forces, with dipole–dipole and hydrogen bond forces being present if the appropriate chemical groups giving rise to these happen to exist in the substance. [In a few cases ionic bonds play a role in stabilizing polymer crystals, for example, as in the Ca and Ba salts of the polyelectrolyte poly(L-glutamic acid).] In this sense polymer crystals are similar to ordinary molecular crystals consisting of small molecules. There exists, however, an important difference. Small molecules are incorporated one after another into molecular crystals, producing entities of macroscopic size in three dimensions. In contrast, under many conditions linear macromolecules crystallize by forming platelets of the order of 50–200 Å thick, where the remaining two dimensions are very large in comparison with this thickness. Thus one dimension of the polymer crystal does *not* grow during the crystallization process. One is thus confronted at the outset with a major difference between polymeric molecular crystals and nonpolymeric molecular crystals, which not only has far-reaching effects on the properties of polymers, but which also stands as a challenge to crystal growth-rate theories. To anticipate data and a theoretical treatment to be outlined in the body of this chapter, the thin dimension of a chain-folded crystal or lamella is closely associated with the dimension of a surface nucleus of critical size.

It is of interest that chain-folded crystals in a number of ways behave in a manner contrary to some of the usual "rules" and expectations associated with crystal growth in general, though for reasons that are fairly obvious on due consideration. For instance, screw dislocations, though they exist in polymer crystals, play a relatively minor role in the fundamental crystal growth process, and there is at present no known example where screw-dislocation growth is the

rate-determining step. Also, polymer crystals do *not* show their most rapid growth on the highest energy surface; the chain-folded surface has by far the highest surface free energy in the crystal, yet it is just this surface that usually does not grow at all. Another interesting point is that polymers, especially when crystallized from the melt, exhibit a persistent and frequently large (often 10–70 %) noncrystalline component even after prolonged storage at a temperature where crystallization was initially quite rapid. This phenomenon, which is an apparent violation of Gibbs' phase rule, is not a result of impurities, and has no analog in molecular crystals consisting of small molecules; the system is actually not in equilibrium. The peculiarities enumerated above arise from the long-chain character of the polymer molecule.

In contrasting polymer crystal growth with growth of other materials from an experimental viewpoint it is found that studies on polymers have some advantages and disadvantages peculiar to themselves. Preparation, and especially the characterization, of polymers is frequently a difficult problem compared with a simple organic or inorganic crystalline system. The molecular weight of such a compound is known and fixed and need not be determined for each new sample, but the molecular weight and molecular weight distribution of a polymer can vary from one sample to another and are often important parameters in its behavior. Nevertheless, with sufficient effort an adequate characterization can be obtained. From the standpoint of obtaining accurate isothermal crystallization rates over a wide range of temperature, polymers are endowed with great advantages. Because of the optical anisotropy of the crystalline regions and the transparency of the uncrystallized regions in many polymers, growth rates can usually be measured by optical microscopy using crossed Nicol prisms and a temperature-controlled hot stage. Also, because of their high viscosity and high surface energy, the crystallization is often quite slow both at low temperatures and near the melting point, and it is therefore frequently possible to measure the isothermal crystallization rate over a very wide range of temperature.† In one case to be cited in detail later (isotactic polystyrene) an isothermal crystallization range of 100°C was obtained,

† Because of the relatively slow growth rate of crystals in polymers near the melting point, a temperature range can always be found in this region where growth is not limited by heat transfer. Growth that is so limited is in any case easily recognized. In a number of polymers the growth rate is slow enough at all temperatures to preclude the effects of heat transfer, and in such polymers accurate growth rates can be obtained over a considerable range of undercooling (see Section 4.2).

and even this could have been extended had it been thought useful. In principle, sufficient data can be obtained on a number of polymers consistent with the requirements of a rigorous test of crystallization theories. This experimental boon, however, is compensated somewhat by what must appear to the uninitiated as a trivial problem: It is frequently difficult to definitely establish the exact melting point T_m^0 of a polymer. There is therefore some uncertainty in the undercooling $\Delta T = T_m^0 - T$ that corresponds to a crystallization experiment carried out isothermally at a temperature T. (Theories are usually expressed in terms of ΔT.) This difficulty arises from the fact that chain-folded polymer crystals are naturally formed in a very thin state, and the fact that thin crystals with high surface free energies melt far below T_m^0. The thin dimension of the chain-folded crystal has a tendency to maintain itself because of the folds, even in annealing experiments, so it is difficult to completely erase this effect experimentally. Thin polymer crystals that melt 10–20°C below T_m^0 are well known. However, there are ways to narrow the uncertainty in T_m^0 and these will be described.

In summary, our main aim is to present a basic picture of the rate of growth of chain-folded polymer crystals and of the lamellar thickness that naturally attends this growth rate. We will also take the opportunity to point out some of the properties, such as the unusual melting behavior of polymers, that arise from these considerations. Other than to deal with the basic morphological entity, i.e., the chain-folded crystal or lamella itself, we will not become deeply involved in such details of polymer morphology as dendritic growth, noncrystallographic branching, twinning, serrated crystal edges, detailed origin of spherulites, or the like. These have been covered elsewhere,[1] most recently in this treatise.[2]

1.2. Nature of Crystallizable Linear Macromolecules

The basic nature of macromolecules that can crystallize has been described in some detail in this treatise by Khoury and Passaglia,[2] and we therefore confine ourselves here to a brief discussion of certain key points that are essential to the understanding of the theoretical and experimental depositions to follow. This discussion will be helpful in defining the scope of what is attempted, and will also serve as a useful reminder of the pertinent characteristics of crystallizable macromolecules.

Our considerations are restricted to the case of linear macromolecules. A macromolecule of this type is a long, more or less

flexible chain, consisting of a set of concatenated monomer units held together by covalent chemical bonds. The flexibility is known from the fact that polymer chains of sufficient contour length approximate a random coil in dilute solution,[3] as is clearly evident from light scattering and other data. In sufficiently dilute solution, the molecules show little or no interpenetration. The entropy S of the random-coil molecule on a per molecule basis is very large because of the numerous configurations Ω the flexible chain can assume ($S = k \ln \Omega$), and this entropy is greatly reduced upon crystallization of the molecule. (Bulk polymers in the molten state are usually assumed to be largely in an approximately random coil state also, with considerable interpenetration of the molecules.†)

There is almost always a distribution of molecular lengths, corresponding to a distribution of molecular weights. The distribution of molecular weights has an interesting significance in crystallization in that at a given temperature below T_m^0, the larger molecules tend to crystallize more rapidly than the shorter ones. In some cases, this leads to a separation of molecules on a molecular weight basis during the act of crystallization,[4] the small ones concentrating but not crystallizing near the growing crystal boundary. We do not treat the topic of the effect of molecular weight or molecular weight distribution on crystallization in detail in this chapter, but instead deal primarily with those cases where the chain length is large enough so that the crystallization is relatively insensitive to changes in chain length. A brief summary of the effect of chain length is given in Section 3.6.

Another important consideration in characterizing polymers, especially with regard to crystallization properties, is stereoregularity, which leads in turn to questions regarding the "tacticity" of the polymer chain. Tacticity concerns the symmetry of the groups on one monomer unit in the chain with respect to those of neighboring units, e.g., the placement in the stereochemical sense of the R group in successive units in the vinyl polymer ($-CH_2CHR-$). Usually, the

† Investigations are currently being carried out in various laboratories using techniques such as neutron diffraction to obtain information on the nature of linear polymers in the molten state. The preliminary results suggest the approximate validity of the random coil model. The topic of the conformation of polymer molecules in solution has been extensively studied both from an experimental and a theoretical standpoint, and evidence for the random coil model, as governed largely by intrachain potentials, and as perturbed by such effects as excluded volume, is outstandingly strong and convincing. Comprehensive summaries exist, as, for example, in the book by Flory.[3]

random spatial array of substituents such as R in an atactic polymer prevents crystallization, but the isotactic or syndiotactic forms can be crystallized to a rather high degree (usually 50% or more). (The effect of atacticity in preventing crystallization must not be overdrawn. For example, if hydrogen and deuterium are randomly substituted in the atactic mode on a carbon backbone, the resulting polyethylene molecules crystallize in much the same manner as the pure hydrogenated or pure deuterated substance. Atacticity is most effective in preventing crystallization when the substituent groups are of different size.) When R is the phenyl ring, $-C_6H_5$, the polymer is polystyrene, which will be discussed in some detail later. Atactic polystyrene is that commonly found in commerce and does not crystallize at all.[5] Isotactic polystyrene has been synthesized using special catalysts and its crystallization behavior has been studied rather extensively.[6–8] We shall confine ourselves here either to cases where stereoregularity is high and crystallization well developed, or cases such as polyethylene where stereoregularity is not a basic problem. Fortunately, this covers many materials of both basic and practical interest.

Other chain irregularities may occur that affect crystallization behavior. For example, one of the units may occasionally go in the chain in a reversed position ("head-to-head" as opposed to "head-to-tail" polymerization). Another example involves copolymers. One may have a copolymer consisting of inherently crystallizable units A and B of different size giving a polymer such as –ABBABBBA–. Assuming that only like units can crystallize together, e.g., –AAAA– with –AAAA–, but not –AAAA- with –BBBB–, the mean sequence length of A and B becomes important, and the polymer must solve a "parking" problem in order to crystallize. A few "wrong" units can often be tolerated in a polymer crystal as defects, but this has its limits. Interesting work on this problem has been carried out, for instance, by Bolz and Eby,[9] who have shown that up to 7 mole % of side-chain $-CF_3$ units can be accommodated into $(-CF_2-CF_2-)_n$ crystals, causing an expansion of the host lattice. Finally, we mention block copolymers. Here one may have a long sequence of X units connected to a similar sequence of Y units, forming an –XXXXXYYYYY– polymer. If the –XXX– polymer is crystallizable, and the –YYY– polymer is not, say for reasons of atacticity, the two sections of the polymer will often separate into two microphases, the crystalline one exhibiting chain folding on being undercooled. All these situations occur in real systems, but lie outside the scope of this chapter. Further details and references concerning the effects of tacticity and copolymeric char-

acter on crystallization of polymers are given in the chapter by Khoury and Passaglia.[2]

We turn now to a description of the nature of polymer crystals in order to set the stage for the main discussion concerning their growth.

1.3. Chain-Folded Crystals from Bulk and Dilute Solution

1.3.1. Background

A totally new picture of the nature of polymer crystals began to form in the years 1957–1960. Before that time what was known was essentially as follows. It was known that the unit cell (or more correctly the subcell) of some polymer crystals in the bulk phase was the same as that for the corresponding molecules of low molecular weight. For instance, in a classic work, Bunn[10] showed that the unit subcell in polyethylene was very nearly identical to that of the orthorhombic form of the *n*-paraffins. It was also known that polymer crystals were small; X-ray line broadening measurements generally suggested dimensions of the order of several hundred angstroms. Typical though broad melting behavior was known to occur for some polymers through calorimetric and dilatometric studies, and at the same time it was recognized that other polymers did not crystallize at all. Many polymers were known to be "semicrystalline," i.e., they acted over a range of temperature as if they had both a liquid and a crystalline component. Crystalline objects called "spherulites" were well known in bulk polymers, and it was understood, for instance through the work of Point[11] and Bunn and Alcock (see Section 1.3.3), that the chain axes were perpendicular to the spherulite radius. However, the lamellar texture of spherulites was unrecognized prior to 1957 and chain-folding was not considered in the models proposed to explain their fine structure. Accordingly, the early models of spherulite structure possessed serious deficiencies. Meanwhile, no viable model of the growth of spherulites was extant. The existence of polymer single crystals obtained by crystallization from dilute solution was uncovered in 1955,[12] but the basic molecular nature of these crystals was not understood—nor was there a convincing model of growth or an explanation of their thinness—and their true importance remained unrecognized. The situation was ripe for the intervention of significant experimental discoveries and unifying themes.

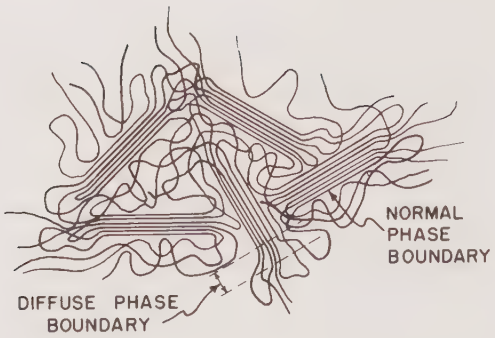

Fig. 1. Fringed micelle model (schematic).

Much of what was known up to 1957 concerning crystallinity in polymers was interpreted using a representation known as the "fringed micelle model," which is sketched in Figure 1. While considered inappropriate or at least incomplete as a general picture of polymer crystallization in terms of what is known now, the fringed micelle model had certain facts to support it. One key feature in the fringed micelle model is that one molecule participates in more than one crystallite. This seemed logical from the fact that the molecular contour length (often 5000 Å or more) was much larger than the known crystallite size. With one notable exception, no one seems to have thought of folding the chain back into the crystal (with an occasional intercrystallite excursion) to accommodate the same facts. Also, the mechanical strength of semicrystalline polymers in bulk implied some molecular connection between the crystallites. This particular point is not entirely misplaced; such "interlamellar links" and "intercrystalline links," as they are now called, do exist between the chain-folded entities when the polymer is crystallized from the melt or concentrated solution. Intercrystalline and interlamellar links have been found experimentally by Keith, Padden, and Vadimsky[13] between chain-folded lamellae in polyethylene by cocrystallizing with a material that can later be extracted. Electron micrographs showing the existence of such links is shown in Figure 2.† The exception to

† The term "intercrystalline link" is used here to denote a long molecular interconnection between the edges of widely separated stacks of chain-folded lamellae as shown in Figure 2(a). The term "interlamellar link" is used to denote the shorter link that connects adjacent lamellae within a stack (Figure 2b). Both types of link arise from fundamentally the same cause, i.e., a polymer molecule of sufficient length occasionally becomes involved in crystallization on more than one lamella. The "links" observed in the micrographs are of the order of 50 Å in diameter and therefore must consist of a number of chains, presumably forced to crystallize about a central one in a fibrillar habit as a result of crystallization-induced orientation.

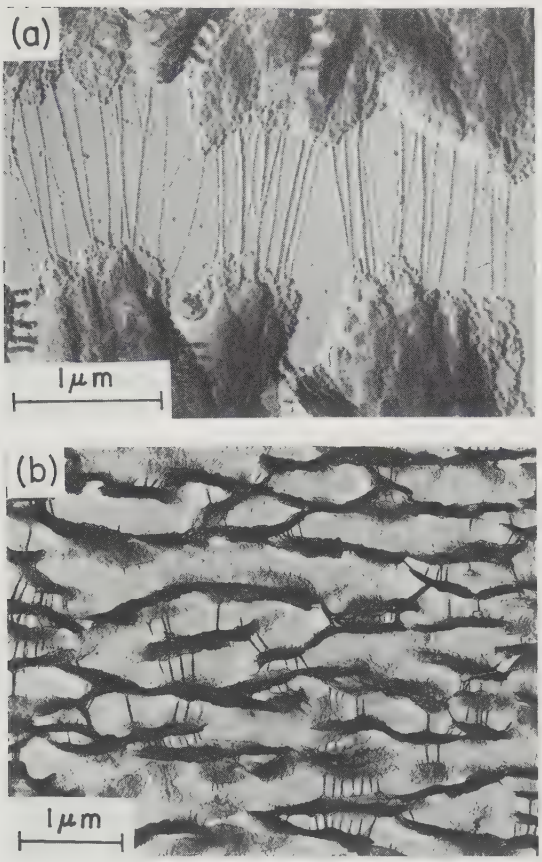

Fig. 2. Intercrystalline and interlamellar links in polyethylene. (a) Intercrystalline links in polymer of M.W. = 726,000 crystallized in presence of 50% n-$C_{32}H_{66}$ which was then extracted with xylene at room temperature. Links connect chain-folded lamellae in different crystalline aggregates. (b) Interlamellar links in polymer of M.W. = 227,000 crystallized epitaxially on oriented Mylar film from 25% solution in n-$C_{32}H_{66}$. (Reprinted with permission of *J. Appl. Phys.*[13]; electron micrographs courtesy of Drs. H. D. Keith, F. J. Padden, Jr., and R. G. Vadimsky.)

the general acceptance of the fringed micelle model prior to 1957–1960 is due to Storks,[14] who suggested chain folding in 1938 in *trans*-1,4-poly(isoprene) (gutta percha) on the basis of what must now be regarded as sound experimental facts and reasoning. The idea was not actively pursued at the time partly because electron microscopy did not either then or for some time thereafter exist as a practical tool.

As we see it now, there should have been some reservations about the fringed micelle model, entirely apart from the fact that it was difficult to reconcile some of the properties of spherulites with it.[2] One questionable feature of the fringed micelle or "bundlelike" model is that it demands a very thick phase boundary where the polymer molecules emanate from the ordered crystal out through the fringed end into the disordered liquid (Figure 1). This thick and diffuse phase boundary is necessitated by the fact that chain molecules with covalent bonds extend through the region of the bundle ends, requiring a slow change in energy, entropy, and density as a traverse is made from the crystal interior out through the bundle end into the liquid. It is impossible in this situation to go from a true crystal density to a normal liquid density in a few angstrom units as it is at a normal phase boundary, where chain molecules do not go through the boundary. This circumstance does not exist between a crystal and its own liquid on such a scale elsewhere in nature, and would lead to high surface free energies (and cumulative strain) at the bundle ends.[15] While the surface free energy associated with a chain-folded surface is often fairly high for a molecular crystal (usually 30–100 ergs/cm^2), it is not subject to cumulative strain, and it has been proposed that the corresponding surface free energy for a sufficiently large, bundlelike nucleus would be even higher.[15,16] This situation leads to the favoring of nucleation-controlled growth with chain folds on a *kinetic* basis.[15,16] The second feature of the fringed micelle that has always concerned us is that it was used to explain the low crystallinity of some bulk polymers on an *equilibrium* basis. Excluding cases where tacticity and other such chain imperfections were the cause of the low degree of crystallinity, incompleteness of crystallization in a chemically pure substance below its melting point has generally appeared to us to be a matter of kinetics rather than of equilibrium.

1.3.2. The Advent of Chain Folding: Polymer Single Crystals

The aforementioned abrupt change in outlook on the nature of polymer crystals resulted from the careful work of Keller[17] in 1957 following an earlier lead by Jaccodine[12] who showed that polyethylene molecules could form single crystals from dilute solution. Based on his studies of the properties of such crystals, Keller concluded that the polymer molecules in the crystals were folded back upon themselves. The evidence from which he drew his conclusions was supported by similar, independent observations of Fischer[18] and Till.[19]

It is of interest to indicate the nature of the experiments and the logic leading to the postulate of chain folding in single crystals. If a sample of high-molecular-weight linear polyethylene is dissolved in hot xylene (~135°C) in the range of concentration from 0.005 to 0.1% and the solution cooled to anywhere in the range of 75–85°C, the polymer crystallizes in the form of thin platelets. An electron micrograph and a typical electron diffraction pattern of crystals from such a preparation[20] are shown in Figure 3.

Knowing the crystal structure of polyethylene from the work of Bunn,[10] the electron diffraction experiments on crystals formed in the general manner described above proved beyond any doubt that the polymer chain axes in the body of the crystals were essentially *perpendicular* to the large, flat faces of the crystal. Such a result was totally unexpected. The thickness of the crystals was in the vicinity of 110–140 Å, and this was far less than the contour length of the molecules in the preparation, the latter being at least 2000 Å on the average. On the basis of such information, Keller concluded that the

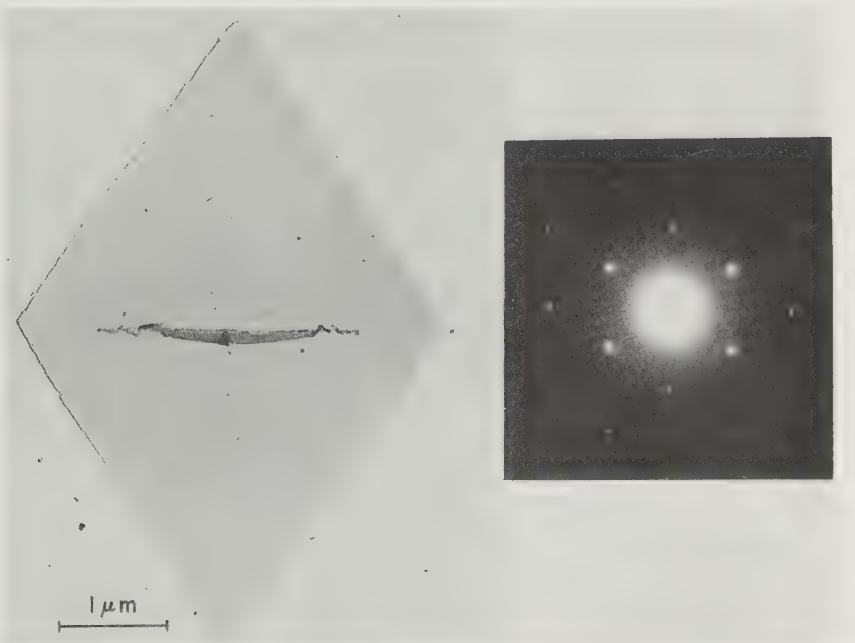

Fig. 3. Electron micrograph and electron diffraction pattern of polyethylene single crystal. Electron micrograph (left) of crystal from xylene. Crystal is ~130 Å thick. Electron diffraction pattern (right) shows that chain axes are perpendicular to large, flat faces of the crystal. (Courtesy of Dr. W. D. Niegisch; reprinted with permission of *J. Appl. Phys.*[20])

upper and lower surfaces of the single crystals consisted of chain folds (Figure 4). A series of critical experiments followed this discovery, and it has become increasingly clear that the model for single crystals with chain folds is correct in its basic points.

In well-formed single crystals of polyethylene of the diamond-shaped variety shown in Figure 3, studies show that fracture[21] occurs readily along the planes shown diagrammatically in Figure 4. Also, these crystals consist of four sectors,[22] as has been shown by dark-field electron microscopy (Figure 5). The sectorization is also shown clearly in Figure 6, where a large polyethylene single crystal,

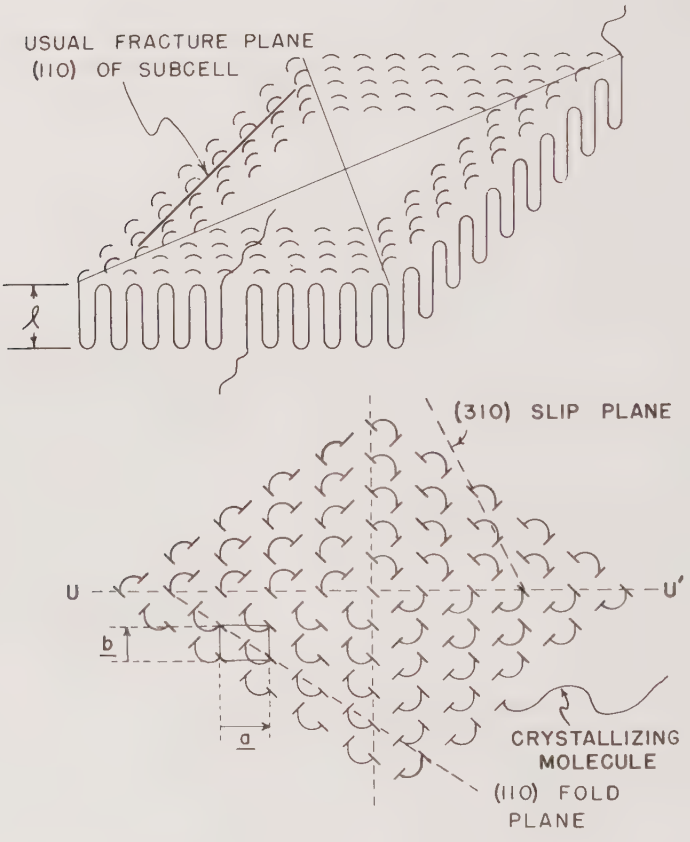

Fig. 4. Chain-folded polyethylene single crystal (schematic). The orthorhombic subcell with dimensions **a** and **b** typical of many of the *n*-paraffins is shown in the lower diagram.

Fig. 5 Electron micrograph of polyethylene single crystal in normal illumination (left) and dark-field illumination (right). In dark-field illumination only electrons diffracted from a given set of planes—in this case {110}—are selected to form the image. Sectorization consistent with Figure 4 is apparent. (Courtesy of Dr. W. D. Niegisch, reprinted with permission of *J. Appl. Phys.*[29])

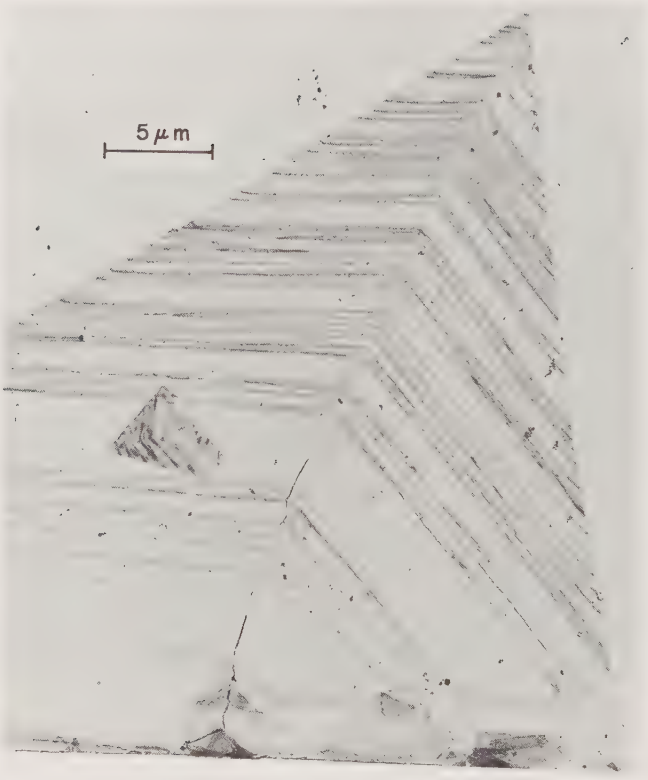

Fig. 6. Electron micrograph of large polyethylene single crystal collapsed on substrate. Crystal exhibits (310) slip planes (cf. Figure 4) and clearly demonstrates sectorization. The rather large lateral dimensions result from the use of low-molecular-weight polymer. (Courtesy of Dr. F. Khoury.)

which was originally a wide-based hollow pyramid,† has been collapsed onto a substrate developing slip planes in each sector corresponding to the (310) crystal planes (cf. Figure 4). These facts point with considerable strength to the correctness of the postulate that such a crystal is built up in a regular way by molecules attaching themselves to the edge of the crystal as shown in Figure 4 with the folds situated in a plane parallel to each edge of the crystal.

In the case of polyethylene single crystals formed from mixtures of deuterated and the normal hydrogen-bearing chains, Bank and

†The diamond-shaped polyethylene single crystals are actually hollow pyramids with an apex angle that is typically 19°. When flattened onto a substrate the crystal usually buckles, forming a section of double thickness, as seen in Figures 3 and 5 as the dark strip. In others it splits along the line U–U′ depicted in Figure 4. In the case of large crystals the flattening process can lead to slip planes such as the (310) planes apparent in Figure 6.

Krimm[23] have been able to show conclusively by a detailed analysis of the infrared spectra that the predominant type of folding involves reentry of the emergent stem into an *adjacent* position on the crystal face ("adjacent reentry"),[16] as illustrated in Figure 4. A similar conclusion also applies to the case of melt-crystallized polyethylene,[23] although the fold plane is apparently different.

In the theoretical development to be outlined later we employ the approximation of adjacent reentry for purposes of obtaining a reasonably simple treatment. The existence of intercrystalline and interlamellar links shows that nonadjacent reentry must certainly occur to some extent in melt-crystallized polymers. In crystallization from the melt the intervention of a "strange" molecule is certainly bound to occur occasionally before a molecule already on the substrate completes its folding process on the substrate. Such an act creates in effect a long cilium, and sets the stage for nonadjacent reentry in the growth plane as well as intercrystalline and interlamellar links. Doubtless, a detailed theory can be devised to take the formation of these links during the crystallization process into account, but this has not yet been accomplished. Meanwhile the theory with strictly adjacent reentry will prove to be quite adequate as regards the prediction of the growth rate and the lamellar thickness for the case of crystallization from both the melt and dilute solution.

The density of polyethylene single crystals is somewhat lower than the theoretical crystal density ($\rho = 1.003\ \text{g/cm}^3$ at 25°C) calculated from the dimensions of the unit subcell. The observed values[24] are around $\rho = 0.97\ \text{g/cm}^3$ at 25°C, the exact value depending on the temperature of preparation and other factors. The observation of this low density has led to considerable discussion and experimentation,[25,26] but it is now commonly supposed that a portion of this density defect is associated with a slight roughness or irregularity of the chain-folded surface (Figure 7). Keller and coworkers[27] have shown by experiments in which the chain stems in chain-folded polyethylene single crystals were isolated after selective scission of the folds with ozone that the original crystals possessed a distribution of stem lengths corresponding to a somewhat rough fold surface. Probably some nonadjacent reentry "mistakes" occur in the growth plane, and some cilia are thought to protrude from the surface. These probably contribute to the density defect. Some investigators attribute practically the entire density defect in single crystals to surface roughness in the form of long loose folds ("loops"), while others attribute it to an "amorphous" surface zone arising mostly from nonadjacent reentry on a large scale. Below we shall present an

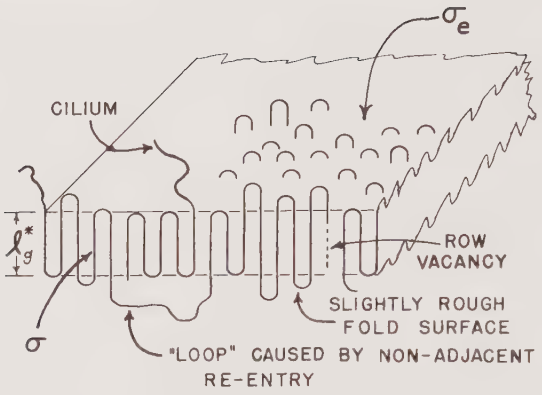

Fig. 7. Possible departures from strictly regular folding and defects in a single crystal (schematic).

alternative possibility to account for a considerable portion of the density defect.

While there is no doubt that the actual density of polyethylene single crystals as measured in the presence of solvent is substantially lower than the theoretical crystal density, it is not entirely clear that this must be interpreted in all instances as proving the existence of an "amorphous" surface layer that is truly a part of the fold zone, or alternatively, as proving fold surface roughness on a considerable scale. In fact, there are clear indications that the fold surface might be rather regular in some cases. For example, Geil[1] (pp. 125–139) has summarized results of a number of workers that suggest that the fold surfaces in various types of pyramidal polyethylene single crystals correspond to specific crystal planes consisting of a regular array of folds. Note, however, that such crystals have a density defect implying (in the customary interpretation) a rough fold surface or an "amorphous" surface zone. One possible resolution to this apparent contradiction is that the fold surface itself may in some cases be rather smooth, the "amorphous" layer actually consisting of *independent* polymer chains that are *physically adsorbed* on the fold surface. While the experimental situation may well vary from one case to another and even suggests different results regarding the fold surface roughness, the theories of growth are capable of predicting either quite smooth or slightly rough surfaces, depending on the physical approximations used.

Evidence has recently been given, which will be discussed in some detail later, that implies that surface adsorption (i.e., physical adsorption) of the polymer molecules takes place prior to their actual crystallographically coherent attachment to the substrate.[28] We

would expect physical adsorption to occur in such a way that a layer of less than crystal density consisting of adsorbed polymer molecules would exist on the surfaces of the crystals. This layer would be highly persistent near the melting point, where the rate of crystallization is essentially zero. This layer could contribute to a density defect in single crystals near the melting point, and could lead to a similar effect in bulk polymers. It is well known that a polymer molecule adsorbed onto a foreign surface from dilute solution forms a set of loops attached at a number of points to the substrate so that the adsorbed molecule resembles a two-dimensional random walk[29 33] with "excluded" area (or a highly flattened three-dimensional one with some excluded volume), and we can discern no reason why this model would not hold for a polymer molecule adsorbed on its own crystal from dilute solution in the region where the crystallization rate was nil.† Similarly, we would anticipate the formation of a similar set of constrained loops for a polymer molecule adsorbed from the melt onto its own crystal. In this case no significant concentration gradient would occur, but the conformation, energy, and entropy of such an "adsorbed" molecule would still bear a strong resemblance to one adsorbed from dilute solution.‡ It is also worth mentioning that the rate of desorption of polymer molecules from

† Several fates are possible for a physically adsorbed layer of polymer molecules on a polymer crystal in dilute solution. As noted above, an adsorbed molecule would simply stay on the fold surface and lateral surface of the crystal when the crystallization rate was essentially zero. In the normal crystallization range, molecules will continuously arrive at the crystal surfaces and become adsorbed there and at the same time others already on the surface will migrate to the site of crystallization. Then in one extreme (slow adsorption and rapid migration and crystallization) there could be but few adsorbed molecules, and in the other (rapid adsorption and slow migration and crystallization) the surface could have practically the steady-state concentration of adsorbed molecules. Quenching of such systems could lead to single crystals that had a quasi-liquidlike adsorbed layer of molecules on the fold surface that could not be crystallized, and which might show such effects as a density defect and a glass transition. This whole topic deserves further attention.

‡ Our use of the term "physical adsorption" to describe a molecule attached to a substrate at numerous points so that it resembles a two-dimensional random walk or a flattened three-dimensional one corresponds to the normal usage of this term in both dilute and concentrated polymer solutions, where a concentration gradient occurs near the surface. Above we have extended the term "physical adsorption" to cover the quite similar configurational entropy situation that must be expected to occur at the interface between a pure liquid or subcooled liquid and its own crystal despite the absence of a significant concentration gradient. This extension is probably not as radical as it may seem in the case of real bulk polymers, with a normal molecular weight distribution, since in these it is well known that the shorter molecules accumulate without crystallizing near the crystal growth boundary. In such cases the situation at the crystal surface resembles that of a moderately concentrated solution where the term "physical adsorption" preserves its customary meaning.

surfaces is usually extremely slow compared to the rate of adsorption,[34] which means that any adsorbed layer formed on the lateral or fold surface would tend to be extremely persistent. Recent evidence for the existence of a thin amorphous adsorbed layer that is not an integral part of the fold surface in single crystals of several polymers is cited in Section 4.3.3. (See Note Added in Proof, page 583.)

The appearance of polymer single crystals with chain folds from dilute solution is by no means a phenomenon unique to polyethylene. Figure 8 shows the repeating monomer units for some of the polymers for which suitable evidence of chain folding has been found.[35-53] (The latter usually consists of a proof by electron diffraction that the chains in single crystals are more or less perpendicular to the large, flat faces of the crystal, and that the contour length of the molecules considerably exceeds the thickness of the crystal.) An electron micrograph of a crystal of isotactic poly(4-methyl-pentene-1), which crystallizes in the tetragonal system, is shown in Figure 9. Synthetic polypeptides exemplified by the calcium and barium salts of poly(L-glutamic acid) shown in Figure 10 can be crystallized in a chain-folded configuration.[48] Sonically degraded salmon sperm DNA has been made to crystallize in a chain-folded configuration[54] and it may not be unreasonable to suppose that the DNA of viruses such as T-2 bacteriophage shown in Figure 11[55] crystallize with chain folds when packed into the intact head of the virus.[56] The phenomenon of crystallization with chain-folding is clearly a very common one.

From what we now know, it is worth indicating the basic conditions for forming a chain-folded crystal from a linear polymer. The first condition is that the chain be regular enough to be inherently crystallizable, i.e., that it possess no structural features such as atacticity that prevent crystallization. A second condition is that the molecule be long enough to recover in the free energy of crystallization the free energy expended in the chain fold. The short *n*-paraffins containing 16–94 carbon atoms do not fold, but polyethylene, with a molecular weight corresponding to about 123 carbon atoms, has recently been made to crystallize with one fold per molecule by quenching.[57,58] Similar studies on crystal thickness and molecular length have been made on oligomers of polyamides,[59] polyurethanes[41] and poly(oxyethylene).[60] A third requirement (actually a corollary of the second) is that the chain have a reasonable degree of flexibility so that a fold can be formed without the expenditure of too much work. The existence of rotatable bonds such as –C–C–, C–O–C, Si–O–Si, or –CO–NH–C– in sequences of sufficient length between

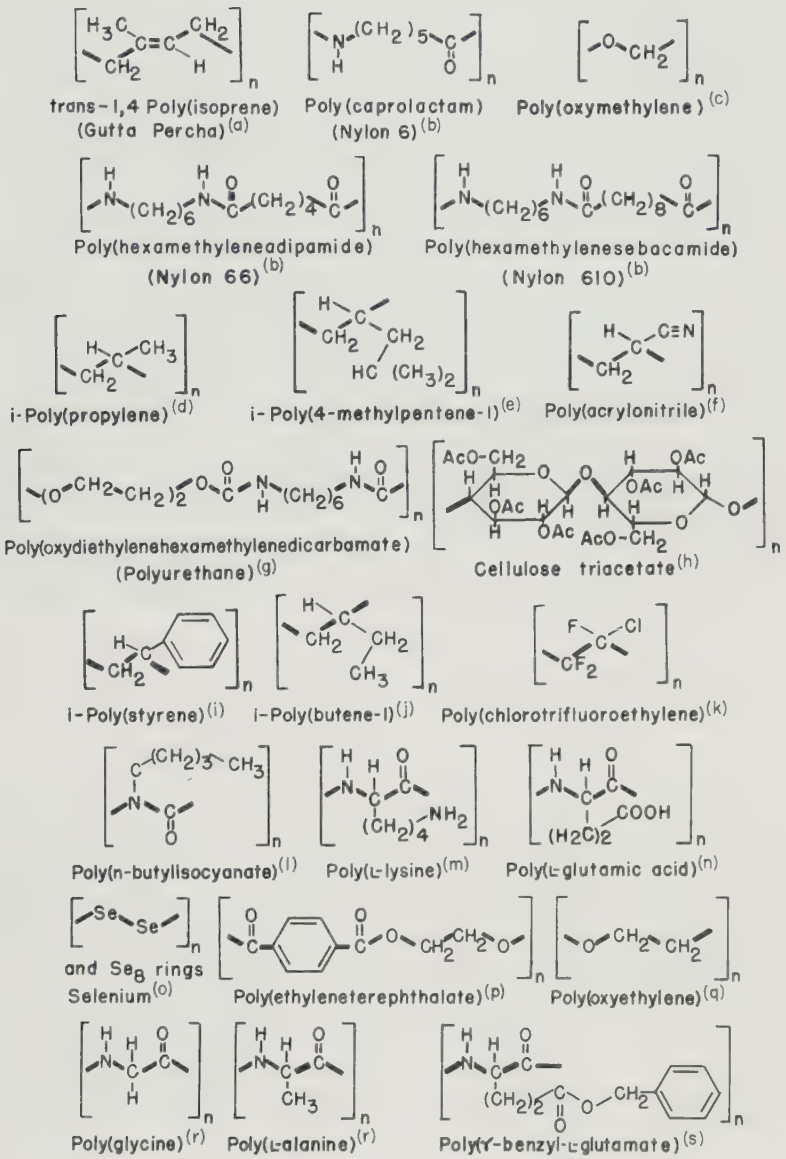

Fig. 8. Some polymers that form chain-folded single crystals (partial list). Heavy solid line indicates main-chain backbone. Names in parentheses are common names. a = Ref. 14, b = Ref. 35, c = Ref. 36, d = Refs. 37, 38, e = Ref. 39, f = Ref. 40, g = Ref. 41, h = Ref. 42, i = Ref. 43, j = Ref. 44, k = Ref. 45, l = Ref. 46, m = Ref. 47, n = Ref. 48, o = Ref. 49, p = Ref. 50, q = Ref. 51, r = Ref. 52, s = Ref. 53.

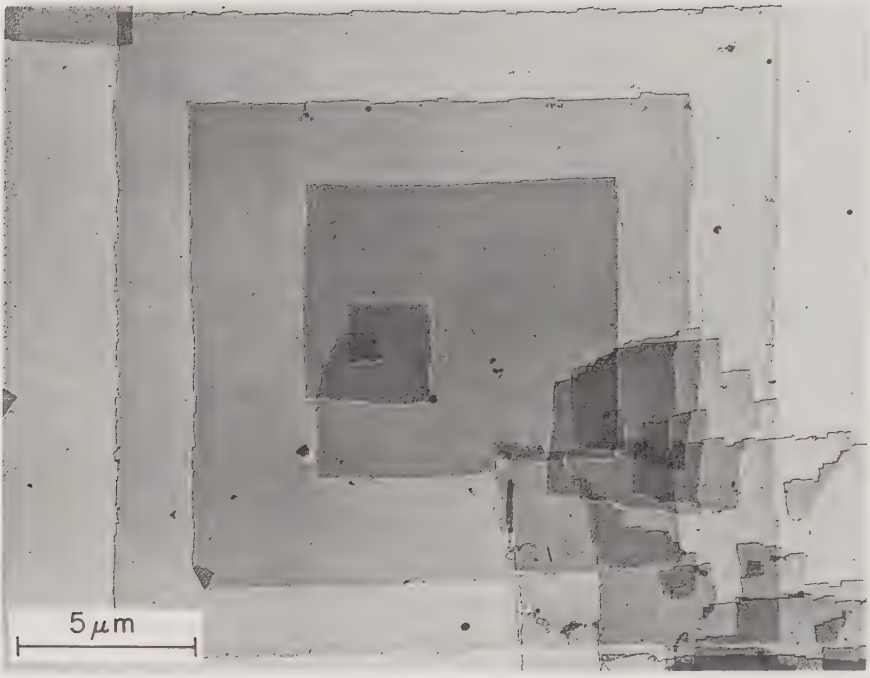

Fig. 9. Electron micrograph of chain-folded crystal of poly(4-methylpentene-1). Grown from 0.01% solution of equivolume mixture of xylene and amyl acetate at 90°C. Platelet is about 140 Å thick, and polymer chain axes are perpendicular to large face of crystal. (Courtesy of Dr. F. Khoury.)

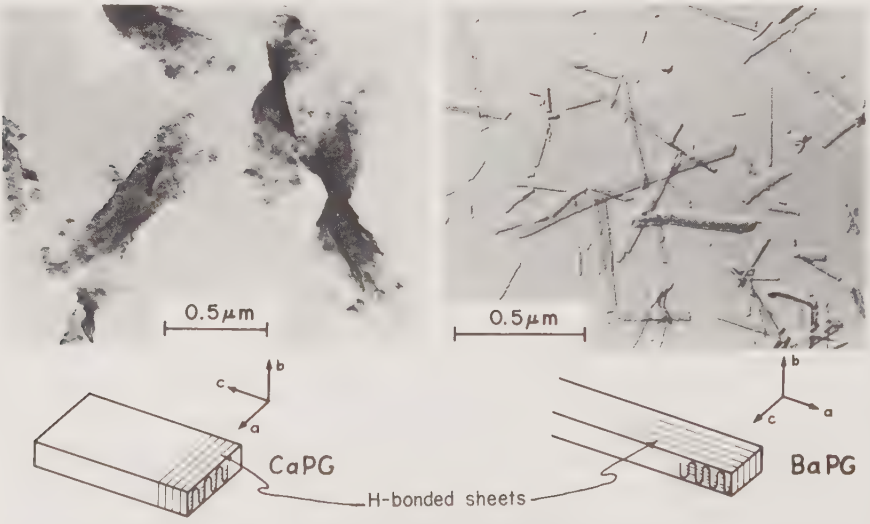

Fig. 10. Folded chain crystals of Ca and Ba salts of poly(L-glutamic acid). Diagrams show orientation of chains in platelike crystals. (Electron micrographs and diagrams courtesy of Drs. H. D. Keith, G. Giannoni, and F. J. Padden, Jr; reprinted with permission of John Wiley and Sons, Inc.[48])

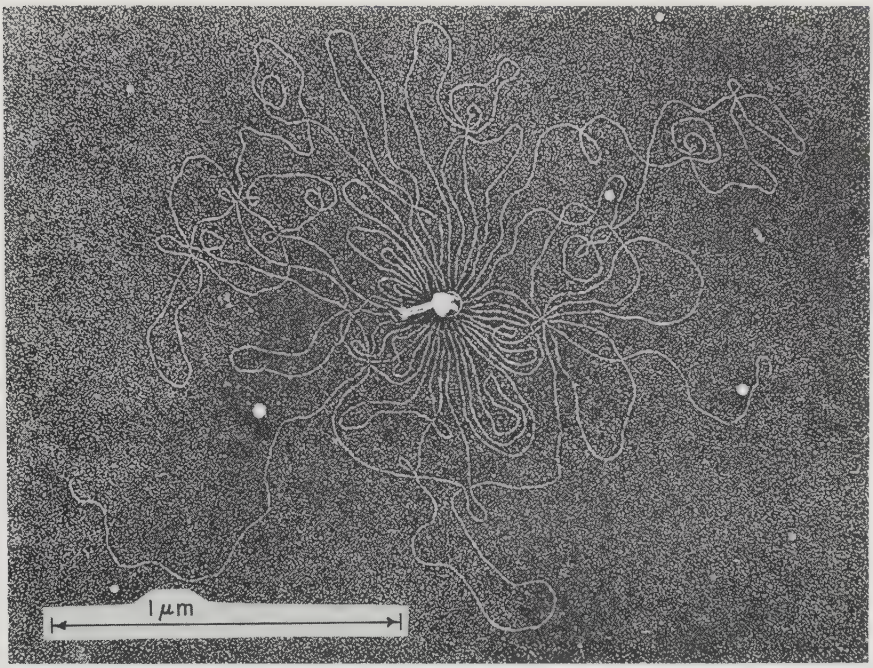

Fig. 11. Electron micrograph of osmotically shocked *T*-2 *E. coli* bacteriophage. Long chain is single DNA molecule that was encased in capsule in center of micrograph prior to osmotic shock. Encapsulated molecule is believed to have been in folded configuration. (Courtesy of Dr. A. K. Kleinschmidt; reprinted with permission of Elsevier Publishing Co.[55])

otherwise stiffer units in the main chain backbone is evidently enough to ensure the ability to form chain folds. Thus, polymers such as poly(ethylene terephthalate)[50] (Figure 12a), with the stiff phenyl ring but the flexible $-O-CH_2-CH_2-O-$ linkage, and poly(-p-xylylene)[61] (Figure 12b), with phenyl rings separated by the flexible $-CH_2-CH_2-$ linkage, exhibit single crystals with chain folds. The existence of certain substituents may lead to steric hindrance or special interactions and render a chain that would otherwise be flexible to behave as if it were extremely stiff in certain solvents, but even this need not prevent chain folding. For example, poly(isobutylcyanate) in solution in CCl_4 behaves much like a rigid rod,[62] yet it, too, crystallizes with chain folds when it is precipitated from solution by addition of a polar liquid.[46] Examples of polymers that evidently cannot fold include the poly(*p*-phenylenes)[63] (Figure 12c), in which the C-C bond between phenyl groups is coplanar with the adjacent rings and rotation only results in motion about the chain axis, producing in effect an excessively stiff chain. The so-called "ladder polymers" such as

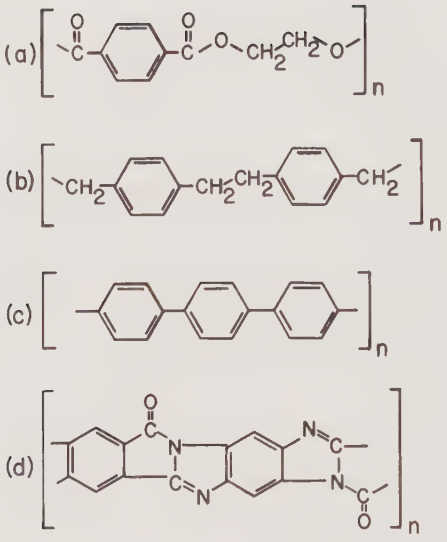

Fig. 12. Examples of foldable and nonfoldable polymer chains. (a) poly(ethyleneterephthalate); –C–O–CH_2–CH_2–O–C– linkage is flexible, and polymer crystallizes with chain folding. (b) Poly(*p*-xylylene); –CH_2–CH_2– linkage is flexible, and polymer crystallizes with chain folding. (c) Poly(*p*-phenylene); rigid and does not fold. (d) Poly(imidazopyrrolone); rigid and does not fold.

poly(imidazopyrrolone)[64] (Figure 12d), in which the chain is composed of condensed ring structures, does not have any flexible bonds along the molecular axis which allow the molecule to fold. The triple-stranded tropocollagen molecule[65] is probably too stiff to form chain folds. Nevertheless, a significant number of linear polymers of general interest exhibit the chain-folding phenomenon on crystallization under appropriate conditions.

Before discussing bulk polymers, it is important to mention that the initial lamellar thickness for single crystals generally depends on the undercooling at which the crystal is formed, the crystals being thicker the smaller the undercooling. This fact, together with the well-known negative temperature coefficient of the growth rate near the melting point, prompted Lauritzen and Hoffman to attempt to explain the thickness and growth rate of these crystals in terms of a modified form of nucleation theory.[66] Simultaneously, and for

essentially the same physical reasons, Price[67] also applied nucleation theory to the problem. The original suggestion that a nucleus might control the size of the fold period was made by Keller and O'Connor.[68]

1.3.3. Chain-Folded Lamellar Crystals in Bulk Polymers

Highly crystallizable, flexible linear polymers in bulk commonly crystallize in the form of *spherulites*, though other types of objects such as *axialites* are known. Figure 13(a) shows spherulites found in Nylon 6-10, and Figure 13(b) depicts the spherulites found in a polyethylene fraction upon quenching from the melt to room temperature. Figures 13(c) and 13(d) show the spherulites and axialites that appear in the same polyethylene fraction at different isothermal growth

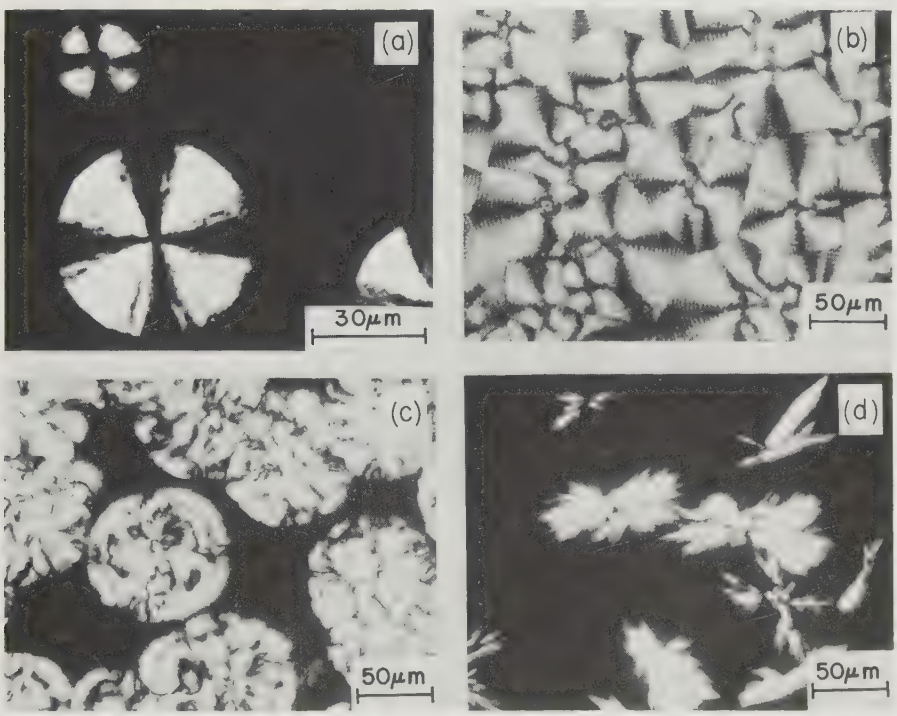

Fig. 13. Spherulites in melt-crystallized nylon 6-10 and polyethylene (optical micrographs, crossed Nicols). (a) Nylon 6-10 grown near 200°C (optical micrograph courtesy of Dr. F. Khoury). (b) Intersecting ringed spherulites in polyethylene fraction with M.W. = 42,000 formed by rapid quenching of melt to room temperature. (c) Spherulites in the same polyethylene specimen grown isothermally at 124.3°C. (d) Axialites in the same polyethylene specimen grown isothermally at 128°C. (Polyethylene micrographs courtesy of Drs. G. S. Ross and L. J. Frolen.)

temperatures. (The growth rate of these objects is discussed in Section 4.) The presence of spherulites in synthetic polymers was first reported by Bunn and Alcock,[69] who also showed by birefringence measurements that the polymer chain axes were perpendicular to the spherulite radius. Further early work on their structure was performed by Point.[11] The theory of the optical extinction patterns of spherulites is to be found in a set of interesting papers published simultaneously.[70–73]

The structure of spherulites has been the subject of intensive study,[69–75] and with rare exceptions the following summary holds for these and related structures. This summary has been taken from many papers that are reviewed in more detail by Geil,[1] Khoury and Passaglia,[2] and Keller.[73] Spherulites and related objects consist principally of chain-folded lamellae radiating from a central point (Figure 14). Fischer[18] was the first to clearly show the existence of the lamellar structures in melt-crystallized polymers. A spherulite

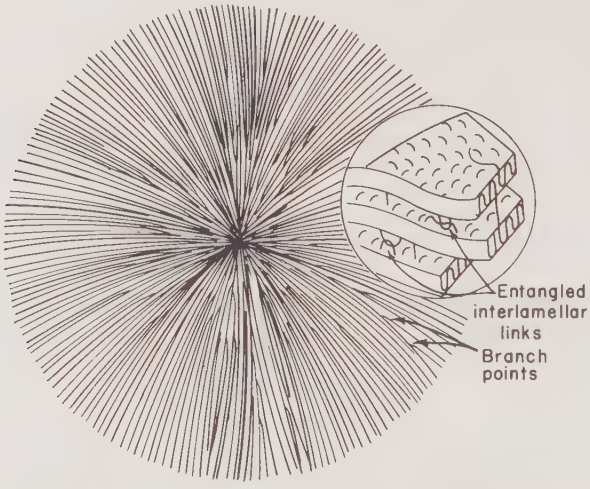

Fig. 14. Polymer spherulite with chain-folded lamellae (schematic). Spherulite consists of chain-folded lamellae radiating from central point. Polymer chain axes in lamallae are more or less perpendicular to radius of spherulite. Branching causes spherulite to become spherical in shape after sufficient growth. Noncrystallizable material (not shown) when present accumulates between lamellae and at outer boundary. Twist of lamellae when present causes rings in optical extinction patterns [cf. Figure 13(b)]. Interlamellar links [cf. Figure 2(b)] and entanglements can cause incomplete crystallization in high-molecular-weight polymer.

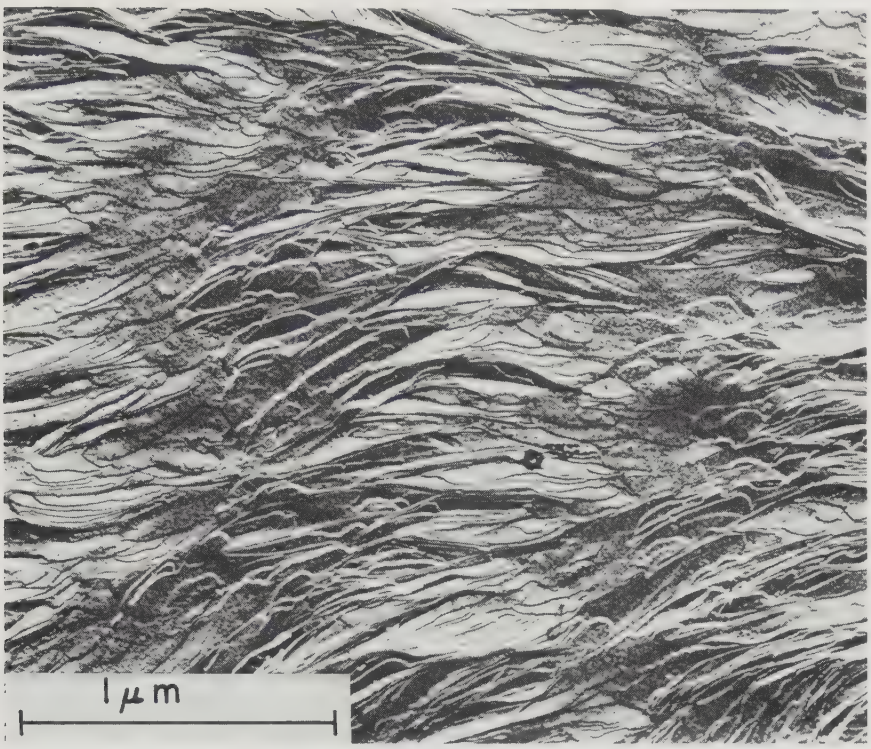

Fig. 15. Lamellar structure in melt-crystallized polyethylene. Electron micrograph of replica from melt-crystallized thin film showing lamellae ~150 Å thick. Growth was from left to right; center of spherulite is not shown. The lamellae show a gradual twist, resulting in the two dark, diffuse, vertical bands. (Micrograph courtesy of Frank J. Padden, Jr.)

becomes a three-dimensional spherical object by virtue of the fact that the lamellae occasionally branch (Figure 14). Note that the polymer chain axes in the spherulite are approximately perpendicular to the radius of the spherulite; this property of polymeric spherulites is readily deduced from the optical extinction patterns and from microbeam X-ray[76,77] investigations. Sometimes a lamella in a fractured spherulite can be traced all the way from the center of the spherulite to the spherulite boundary. Figure 15 shows the lamellar structure in a replica of the surface of a film of bulk polyethylene. Many of the polymers shown in Figure 8 exhibit spherulites or related objects that possess a typical lamellar texture when crystallized from the melt. In some cases it has been possible to show that the chains are perpendicular to the large, flat faces of the lamellae,[78–80] leading to the same direct argument for chain folding as was employed for single crystals. [Recall also that Bank and Krimm[23] have demonstrated

the predominance of the adjacent reentry type of chain folding in melt-crystallized polyethylene.] The main point here is that *the principal crystalline unit in a melt-crystallized linear polymer is ordinarily a thin chain-folded lamella similar in general character to a single crystal as regards the site of the folds and its thickness.*†

Subsequently, it will be shown that the surface free energy of polyethylene single crystals and melt-crystallized polyethylene are quite similar, which implies a considerable similarity in the basic nature of the fold surfaces in the two cases.

Special features appearing in melt-crystallized polymers are the intercrystalline links (Figure 2a) and the interlamellar links (Figures 2b and 14) mentioned earlier, and a boundary layer of noncrystallizable or slowly crystallizing "impurities" at the growth front.[74] These "impurities" may be either polymer of low-molecular-weight, atactic material, highly branched polymer, or adventitious foreign material such as residual solvent. The intercrystalline and interlamellar links are the only features that are in any way reminiscent of the fringed micelle model. These links arise when a molecule crystallizing from the melt nucleates on two different lamellae. They do not occur to any significant extent in crystallization from dilute solution.

It is convenient at this point to discuss briefly the incomplete crystallinity or "semicrystalline" character of linear polymers when crystallized from the melt. This discussion is occasioned by the fact that crystallization in a chemically pure substance that appears to cease far short of completion, even though the initial rate is readily measurable at the same temperature, is a situation not ordinarily encountered by investigators interested in the growth of crystals of pure substances consisting of small atoms or molecules, and accordingly requires some clarification.

Even when crystallized from the melt for a very long time, and in the absence of any chain defects that would prevent complete crystallization, a polymer crystallized in a manner conducive to the chain-folded mode frequently shows some evidence of the presence of a noncrystalline component. This shows up, for example, in the thermodynamic,[5,81–84] mechanical,[85,86] and dielectric properties,[86] where responses characteristic of the (sometimes abnormal) undercooled liquid phase are clearly evident. It is not uncommon to have from 10 to 70% by weight of such material in the polymer. Thus the polymer acts to an approximation as a two-phase system (crystal +

† An exception to this statement is noted in Section 1.3.4, where the fibrillar crystals produced under high mechanical stress are mentioned.

glass, or crystal + subcooled liquid) over a wide range of temperature. This behavior would of course be in contradiction to the phase rule if the phases were in equilibrium. There is strong evidence that the two phases are *not* in thermodynamic equilibrium. Even at the "last" stages of the crystallization process, where the degree of crystallinity has apparently reached its "limiting" value and the spherulites have long since fully impinged on each other, a slow increase in density (sometimes called "stage 2" crystallization) indicative of continued crystallization still occurs. Typical examples of this may be found in poly(chlorotrifluoroethylene),[81] polyethylene,[83] and natural rubber.[84] Also, a state of nonequilibrium is implied by the fact that the melting point of lamellar crystals in a semicrystalline polymer frequently increases on prolonged storage (see Section 2.2). Polymers can be successfully treated as two-phase systems in a state of torpid equilibrium if the measurement system used to detect the crystalline and noncrystalline regions is rapid compared with any change of crystallinity with time.

To what is the noncrystalline component in a melt-crystallized polymer due? When the degree of crystallinity is substantially less than about 85–90%, and excluding the presence of uncrystallizable material of low molecular weight or atactic material, the answer must to a considerable extent be concerned with the interlamellar links. (We assume that the 10–15% remainder of the material is partly due to a "rough" fold surface, cilia, and a certain amount of adsorbed polymer molecules.† As will be seen, some of this remainder is a result of the work of chain folding when crystallinity measurements are based on heat of fusion data.) In a material of moderate chain length, one molecule will occasionally crystallize onto two lamellae. As the chain length is increased, a larger number of difficultly resolvable entanglements will occur in the region between the lamellae as the interlamellar links form (Figure 14). This picture leads to the concept that, other things being equal, the maximum degree of crystallinity attainable for practicable times of crystallization will decrease as the molecular weight is increased. That this effect occurs can be seen in the "limiting" density measurements obtained on melt-crystallized polyethylene by Ergoz, Fatou, and Mandelkern.[87] The "limiting" degree of crystallinity calculated from these data if 80–85% when the molecular weight is 10^4–10^5 (contour length 9×10^2 to 9×10^3 Å) but it falls to below 40% for samples whose molecular weight is above 10^6

† A calculation shows that 1 cm^3 of bulk polyethylene with 150-Å-thick lamellae contains roughly 133 m^2 of fold surface.

(contour length of 9×10^4 Å). In our view, this decrease in crystallinity from 80–85% to 40% must be associated with a large increase in the number of interlamellar links and irresolvable entanglements of the type shown in Figure 14. Further data and interpretation on this point may be found elsewhere.[88] Interestingly, the interlamellar links and concomitant entanglements in the interlamellar noncrystalline regions apparently do not strongly affect the temperature dependence of the initial rate of crystallization at moderate molecular weights. As will be seen in Section 4, the nucleation constant K_g for polyethylene grown in dilute solution is quite similar to the corresponding constant for axialites grown from the melt. Nevertheless, one must be reconciled to the possibility that at exceedingly high molecular lengths—say 10^7 Å or higher—the extent of crystallization even after prolonged isothermal storage may be quite low, and the initial rate of crystallization as measured by K_g somewhat perturbed.

One final point remains to be made on the interpretation of the "degree of crystallinity" so widely used by investigators working with polymers. This point is that the quantity $1 - \chi$, where χ is the "degree of crystallinity," is *not* always an accurate measure of the mass fraction that is actually noncrystalline in the sense of "liquidlike," especially when χ is about 0.90–0.95 or larger. Here we assume that χ has been determined from a thermodynamic expression such as $\chi = (H_l - H_s)/(H_l - H_c)$ or $\chi = (\bar{V}_l - \bar{V}_s)/(\bar{V}_l - \bar{V}_c)$, where H is the enthalpy and $\bar{V}$ the specific volume; the subscript s refers to sample, c to the pure crystalline phase, and l to the liquid or subcooled liquid phase. The reason that $1 - \chi$ may not accurately reflect the fraction of liquidlike noncrystalline material when χ is large is that the folded crystal surfaces themselves have an enthalpy content, and possibly a density defect due to roughness, that contributes to $1 - \chi$ even though this contribution clearly is a crystal property (crystal = crystal interior + fold surface). This portion of $1 - \chi$ is not liquidlike in that it cannot have the typical relaxational responses of a subcooled liquid. Heat of melting and specific volume measurements on single crystals of polyethylene[24,89,90] formed in dilute solution give a χ value of close to 0.85–0.90. In this case the truly noncrystalline (liquidlike) component $1 - \chi$ is not 0.10–0.15, but considerably less. A substantial part of the aforementioned contribution of 0.10–0.15 to $1 - \chi$ is in our view more properly interpreted for single crystals as relating to the properties of the fold surface, including any disorder, this surface being viewed as part of the crystal. Such a contribution will also occur in bulk polymer, the appearance of the truly noncrystalline or liquidlike component beginning when χ falls below 0.90–0.95.

Even a crystal with a completely regular fold surface can exhibit a χ value below unity. The simplest illustration arises when the degree of crystallinity χ is based on measurement of the heat content of the crystals. If it is assumed that a regular fold in a polyethylene single crystal requires 5 kcal/mole (see Section 2.3), and the $-CH_2-$ units have a heat of fusion of 1 kcal/mole, then a crystal 135 Å thick is predicted to have $\chi = 0.95$ or $1 - \chi = 0.05$, even when no liquidlike or disordered phase is present whatsoever. The introduction of some roughness or disorder in the fold domain would increase $1 - \chi$, again without any true liquidlike phase being present. The introduction of the concept of slight surface roughness could also lead to a degree of crystallinity based on specific volume determinations that was somewhat below unity even though no true liquidlike component was present.

In most discussions $1 - \chi$ is called the "amorphous" fraction of the polymer, but it is seen from the foregoing that the term "amorphous" in this case covers two broadly different effects: (1) density defects and heat content stored in the zone of the chain-folded surface, this zone being viewed as a somewhat disordered part of the crystal, and (2) polymer chains lying outside the chain-folded lamellae, partly in the form of interentangled interlamellar links, which have thermodynamic and relaxational properties at least roughly approximating that of the subcooled liquid. Probably physically adsorbed molecules, long cilia, and long nonadjacent reentry loops can be classified, in an approximate sense at least, in this latter category also. In effect, the interlamellar links and the corresponding entanglements in a melt-crystallized polymer of high molecular weight hold part of the polymer prisoner between the lamellae, and condemn it to nearly eternal servitude in a state exhibiting thermodynamic and relaxational responses fairly similar to those one would normally associate with the subcooled liquid at the same temperature. Certain abnormalities are to be expected in such confined material, for example, a glass transition temperature that is somewhat different than that for the normal and unconfined subcooled liquid phase.[86]

Spherulites and axialites are almost always initiated at a heterogeneity, and usually reappear at precisely the same place when a sample is melted out and then recooled to a temperature where crystallization can occur again. The number of spherulites per unit volume is usually reduced by heating the specimen to increasingly higher temperatures above T_m^0 prior to crystallization. (A theory of heterogeneous nucleation that can be used to explain[81] these effects has been advanced by

Turnbull.[91]) Following this heterogeneous initiation, the radius of the spherulite generally increases linearly with time (*lineal growth*). Homogeneous nucleation can be obtained in bulk polymers, but usually only after the application of very specialized techniques.[92,93] Homogeneous nucleation will be discussed briefly toward the end of the chapter.

From the foregoing it is clear that under appropriate conditions of undercooling, many flexible linear molecules that do not contain built-in chain defects will crystallize in a chain-folded mode from both the pure polymeric liquid state and from dilute solution. The conditions are so broad and so readily attainable that one can state that this mode of crystal formation is a natural one, and calls for a generalized treatment and theoretical analysis. Before going on to give such an analysis, it may be useful to indicate what has to be done with an inherently crystallizable flexible macromolecule to *avoid* getting chain folding.

1.3.4. Real and Apparent Departures from Chain Folding: Fibrils and Extended-Chain Crystals

One basic answer to the question of preventing chain folding in an undercooled system of inherently crystallizable linear polymer molecules seems to be to apply very strong mechanical forces during the crystallization process to achieve strong orientation. A few examples will suffice to illustrate this point. Pennings[94] has shown that when polyethylene is crystallized from a slightly undercooled solution in xylene with very rapid stirring, long *fibrils* with a diameter of roughly 50–100 Å are formed. The structure of these fibrils is not known precisely, but the basic fibrillar unit is certainly not highly folded in the sense of having a large number of folds per unit volume. In any event, when the stirring is stopped, chain-folded structures promptly use the fibril as a nucleus, forming recognizable chain-folded lamellar nodules ("kebabs") on the fibril in profusion.† This formation of folded structures of course shows that the natural mode of polymer crystallization in the absence of stress (or more correctly the absence of orientation resulting from stress) is indeed the folded one: Where stress is absent, the fibril nucleates folded structures from

† The resultant structure is usually called a "shish-kebab," where "shish" = fibril and "kebab" = chain-folded nodule on fibril. It is interesting to note the degree to which biological (and now gastronomical) terminology has permeated the field of polymer crystallization.

solution, not more fibrillar material.[95] This type of two-stage crystallization has been proposed to account for the structures seen in stress-induced crystallization in polyethylene film.[96] A similar set of phenomena occur when crystallization is induced in rubber by stretching[96–98]: Fibrils form first, and these are then "decorated" with chain-folded nodules. The fibrils that grow on straight interlamellar links as described by Keith and co-workers[95] also appear to be limited in their radial growth, and promptly become sites for the growth of chain-folded structures when additional polymer is introduced. In this case, the mechanical force that induces the straight chain on which the fibril originated arises from the free energy of crystallization.† In general, the facts appear to support the concept that fibril formation represents a true exception to chain folding.

So-called "extended-chain" material can be produced in certain polymers such as polyethylene by crystallization at high pressures and temperatures.[99] It has been proposed that this form begins its existence as a folded crystal, which then undergoes thickening during the annealing process, producing a very thick lamella in which the molecules are presumably still mostly folded.[100] Alternatively, it has been suggested that "extended-chain" material may be the result of a type of crystal growth not involving folds that competes with chain folding at high pressures and whose existence requires a separate theory for formation directly from the melt.[101] This latter view, however, appears to have been successfully challenged[102] (see also Section 2.2) with the result that extended-chain crystallization should probably not be regarded as an exception to chain folding. Elsewhere in this treatise, Khoury and Passaglia have summarized the evidence which indicates that "extended-chain" lamellae actually contain chain folds.[2] Thermodynamically, "extended-chain" crystals represent a closer approach to equilibrium than thin, folded crystals, by virtue of the fact that the extended-chain type are much thicker. (The subcell of the extended-chain polymer is essentially identical to that of the folded type.) Nevertheless, when extended-chain polymer is used as a nucleating surface for further crystallization of polyethylene at ordinary pressures, the crystals that form are of the thin, chain-folded type, and not the thick extended-chain variety.[103]

---

† The authors are indebted to Dr. H. D. Keith for helpful discussions on this topic, and in particular for pointing out that the growth of chain-folded structures on tensed chains or fibrils between lamellae shows that the natural mode of crystallization in the absence of stress is that with chain folding.

The considerations noted above point to the fact that the basic explanation of the existence of thin chain-folded crystals must involve kinetic considerations, since in the absence of stress, this type of crystal forms even when the substrate is of a thermodynamically more stable character.

2. Thermodynamic Preliminaries and Work of Chain Folding

2.1. Fold Surface Free Energies from Melting Point and Crystal Thickness Data

It is necessary in developing a theory of crystal growth to know the thermodynamic driving force for crystallization, and it is also important in a theory involving surface nucleation to establish as firmly as possible the surface free energies that determine the nucleation rate. Usually the latter is done strictly from kinetic data, but in the case of polymers the fact that the crystals are exceedingly thin provides an opportunity to determine one of the principal surface free energies from strictly thermodynamic considerations.

The free energy of formation of a single chain-folded crystal may be set down in the manner of Gibbs as

$$\Delta\phi_{\text{crystal}} = 4xl\sigma + 2x^2\sigma_e - x^2l(\Delta f) \tag{1}$$

where l is the thin dimension of the crystal, x the large dimension, σ_e the fold surface interfacial free energy, and σ the lateral surface interfacial free energy (see Figure 16). Equation (1) may be regarded as the defining relation for σ and σ_e. While we have used the terminology "surface interfacial free energy" (usually contracted to "surface free energy") that would be appropriate for normal molecular crystals,

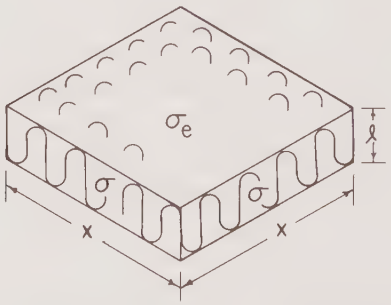

Fig. 16. Thin chain-folded crystal showing σ and σ_e (schematic).

it should be noted that the surface free energies for chain-folded polymer crystals involve certain conceptual differences from the normal case. In the normal molecular crystal some molecules will be in the interior of the crystal and some will be on the surface. In the chain-folded polymer crystal each polymer molecule will have monomer units in the "interior" of the crystal, but will have other monomer units in the chain-folded surface as well. If this fact is borne in mind, Eq. (1) defines σ and σ_e in an unambiguous manner. The quantity Δf is the bulk free energy of fusion, which can be approximated near the melting point by assuming that the heat of fusion is independent of temperature:

$$\Delta f = \Delta h_f - T\Delta S_f = \Delta h_f - T(\Delta h_f)/T_m^0 = \Delta h_f(\Delta T)/T_m^0 \qquad (2)$$

Here Δh_f is the heat of fusion per unit volume of crystal, T_m^0 the melting point of a crystal with very large l, and ΔT the undercooling $T_m^0 - T$. At the melting point of the crystal $\Delta\phi_{\text{crystal}} = 0$, and one finds for $x \gg l$ that

$$T_m = T_m^0[1 - 2\sigma_e/(\Delta h_f)l] \qquad (3)$$

Equation (3) shows that the observed melting point T_m for a thin platelet is depressed below that of an infinite crystal by an amount $2T_m^0\sigma_e/(\Delta h_f)l$. Thus by plotting T_m versus $1/l$ one finds the slope is $-2\sigma_e T_m^0/\Delta h_f$ and the intercept is T_m^0. Hence if Δh_f is known, σ_e can be determined. This method is readily applicable to polymer crystals because the very small value of l leads to a large depression of the melting point. When dealing with dissolution, T_m^0 in Eq. (3) is replaced by T_d^0, the dissolution temperature.

Huseby, Bair, and Salovey have carried out the required measurements of thickness and dissolution temperature[104] or melting point[105] for polyethylene single crystals. The thin crystals are metastable from the thermodynamic viewpoint, and spontaneously slowly increase in thickness near the melting point, i.e. the crystals try to gain stability by getting rid of the chain folds in which the high surface free energy σ_e resides. To minimize thickening, these authors used rapid melting techniques, and subjected the crystals to a weak gamma-ray dosage to induce moderate cross-linking. The results are shown in Figure 17. Equation (3) is obeyed within experimental error and a value of $\sigma_e = 93 \pm 8$ ergs/cm^2 is found for both dried single crystals and single crystals in a suspension of solvent. The value of T_m^0 is about 146°C for dried single crystals, and the dissolution temperature

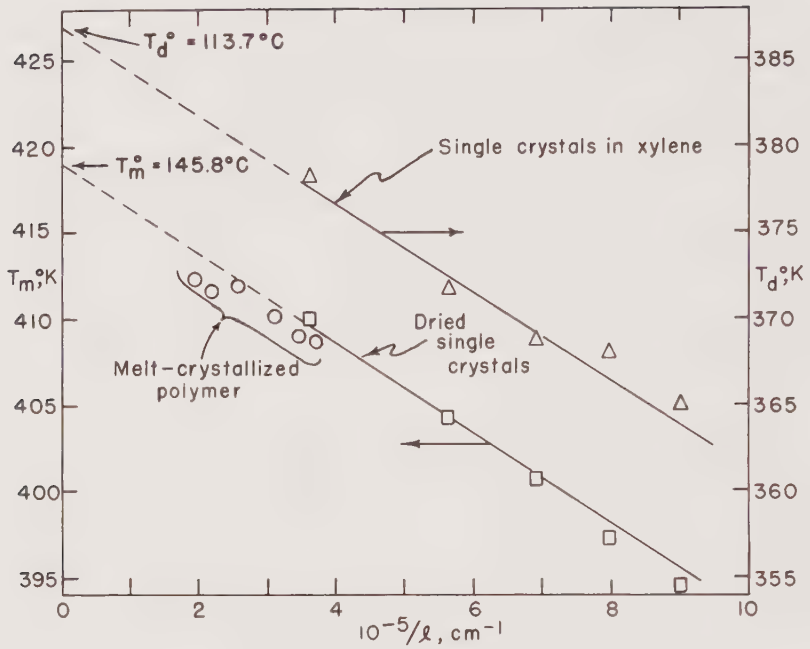

Fig. 17. T_m versus $1/l$ and T_d versus $1/l$ plots for polyethylene. Dried single crystals and single crystals in xylene, data of Huseby and Bair[104]; melt-crystallized polymer, data of Brown and Eby.[109] These plots show thermodynamic similarity of the fold surface in melt-crystallized and solution-grown crystals.

T_d^0 is about 114°C (xylene).† These authors and others[106,107] have also given results for other solvents, and the value of σ_e remains in most cases in the region just quoted. Also, Bair and Salovey[108] showed that l, and by inference σ_e, is approximately independent of molecular weight in the moderate to high range, by studies on fractions with viscosity-average molecular weights ranging from 2×10^4 to 2×10^6.

Also shown in Figure 17 are the melting point data obtained by Brown and Eby[109] on bulk polyethylene. Rapid melting was used. (Only l values obtained by electron microscopy were employed in the plot; low angle X-ray diffraction results on melt-crystallized polyethylene exhibit uncertainties that are as yet unexplained, and are not

† The dissolution temperature of a polymer is ordinarily insensitive to the polymer concentration at dilutions of 0.1% or less. The value of σ_e is rather insensitive to the type of solvent present, because the principal contribution to this quantity is the work of chain folding, which arises mainly from the potential energy associated with the chain conformation in the fold.

fully reliable as a measure of the absolute value of l.) It is clear that there is little difference between dried single crystals and bulk polyethylene as regards the melting point depression for a given value of l, which implies that σ_e and T_m^0 are essentially the same in the two cases. As was observed earlier, the results for σ_e suggest a considerable thermodynamic similarity between fold surfaces of polyethylene single crystals from dilute solution and dried single crystals from the same source. Later it will be shown by analysis of data on the rate of crystallization that $\sigma\sigma_e$ is quite similar for melt-crystallized polyethylene and single crystals, which further reinforces this point.

The significance of the results outlined above is first that the average character of the fold surface of single crystals in the presence of solvent, dried single crystals, and bulk polymer is similar from a thermodynamic viewpoint. Thus the fold surface is the common ground despite large differences in macroscopic morphology. This was to be anticipated from the discussion on the nature of single crystals and lamellae in bulk polymers given earlier. The second point is that the data and references cited also serve to emphasize the enormous depression of the melting point occasioned by the small size of the l dimension of the crystals in chain-folded polymers.

2.2. Melting Behavior

At this point it is convenient to clarify certain aspects of the behavior of the melting point of linear polymers in bulk, taking account of the fact that the chain-folded lamellae may thicken somewhat after their original formation.

Later in this chapter it will be shown by application of a revised version of surface nucleation theory that the *initial* thickness l_g^* of a chain-folded lamella, which is kinetically determined, is of the form

$$l_g^* = (2\sigma_e/\Delta f) + \delta l = [2\sigma_e T_m^0/\Delta h_f(\Delta T)] + \delta l \tag{4}$$

Here δl is a quantity that is only a weak function of the undercooling near the melting point, which is the region of interest here. For present purposes δl may be regarded as a constant in the units of length, and for most polymers it is 10–40 Å. Observe that the initial thickness is a function of the undercooling, Eq. (4) being in general of the form

$$l_g^* \cong (C_1/\Delta T) + C_2 \tag{5}$$

where C_1 and C_2 are approximately constant.

If one now inserts l_g^* from Eq. (4) for l in Eq. (3), and recalls that $T_m^0 = T_x + \Delta T$, one finds that the melting point is[110]

$$T_m = T_x + \Delta T\left\{1 - \frac{1}{1 + \delta l(\Delta h_f)(\Delta T)/2\sigma_e T_m^0}\right\} \tag{6}$$

A little consideration then shows that for a crystal formed at some finite undercooling ΔT the melting point of an unthickened crystal on reheating is somewhat above the temperature T_x at which the crystal was formed, because δl is small and greater than zero. This corresponds to what is observed for unthickened crystals. Notice also that when δl is zero, $T_m = T_x$, so it is clear that the condition $\delta l > 0$ is required to allow the crystal to grow. We shall return to this point.

Consider now the melting point of a polymer that is crystallized in a region where thickening occurs. Polyethylene is used for purposes of illustration. Below 90°C (near the maximum practicable temperature for forming crystals from xylene) the rate of thickening is virtually zero, so crystals formed in dilute solution show little or no such isothermal thickening effect during the crystallization process. At higher temperatures the rate of thickening becomes measurable[111–113] and for a time at least has the form $l(t) = l_g^* + B \log t$, where t is the age of the crystal.[16,112,113] The value of B is essentially zero below 90°C, but rises with increasing temperature to a value of roughly 100 Å per decade at 120°C. In any case, thickening will occur at the temperatures (about 124–131°C) where isothermal crystallization from the melt is conveniently attained. Suppose that we now make the simplified assumption that on the average the thickness achieves a "final" value at the end of a crystallization experiment that is γ times larger than the initial thickness l_g^*:†

$$l = \gamma l_g^* \tag{7}$$

Insertion of this into Eq. (3) leads to[16,66]

$$T_m = T_m^0[1 - (1/\gamma)] + (T_x/\gamma) \qquad \text{(thickened crystals)} \tag{8}$$

for the case where $2\sigma_e/\Delta f \gg \delta l$, which is a fair approximation for

† Reference 66 gives Eq. (8) for the special case $\gamma = 2$. The derivation for general γ is given in Ref. 115.

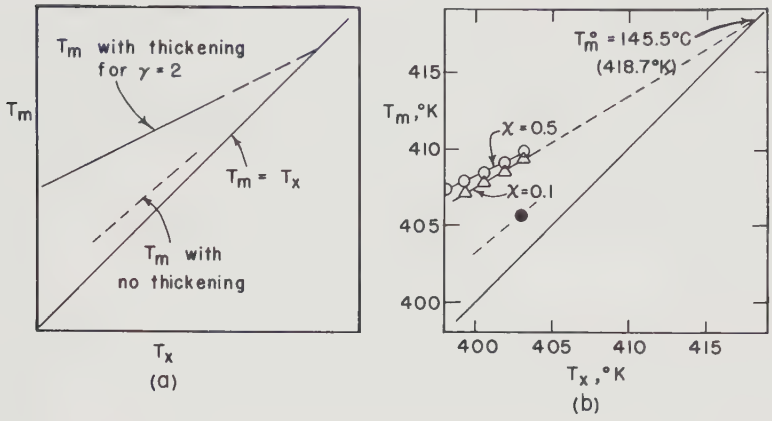

Fig. 18. T_m versus T_x plots for polymers with and without lamellar thickening during isothermal crystallization. (a) Schematic diagram showing T_m for no thickening, and case where thickening doubles the original thickness ($\gamma = 2$). (b) Data for melt-crystallized polyethylene from Ref. 112, showing "first" melting, i.e., no significant thickening (solid circle), and T_m versus T_x data for samples where the original thickness approximately doubled during isothermal crystallization to degrees of crystallinity of $\chi = 0.1$ and 0.5. These results show the tendency of a chain-folded polymer to "remember" its crystallization temperature.

crystals formed at low undercoolings. This expression suggests that the melting point of a polymer that has thickened by a factor γ during the crystallization process at T_x is approximately a linear function of its temperature of crystallization! This is shown schematically in Figure 18(a), which shows a plot of T_m against T_x for thickened and unthickened crystals using Eqs. (6) and (8). In some cases an upward curvature in T_m versus T_x data must be expected as a result of an increase of γ at higher temperatures that is caused by an increased thickening rate.

Figure 18(b) shows results from experiments on bulk polyethylene[112] that exhibit the effect of thickening during crystallization. The value of γ obtained from the slope is close to two. The thickening process in melt-crystallized polyethylene near 128°C has been observed directly by low-angle X-ray measurements and melting point measurements as a function of time.[111,112] For example, in the low-angle X-ray experiments of Hoffman and Weeks on melt-crystallized polyethylene[111] the lamellae started at $l_g^* \cong 135$ Å, and at long times exhibited a thickness of 270–300 Å, i.e., the initial thickness was about doubled. This is consistent with the value $\gamma \cong 2$

determined from the T_m versus T_x plot shown in Figure 18(b).† It is also of interest to note the work of Wood and Bekkedahl[114] on natural rubber published in 1946, which shows that they recognized a difference between a low "first melting" point of some crystals and a higher melting point of other (thickened) crystals, and in fact described these effects on a plot of T_m versus T_x. The approximate theory outlined above is consistent with their results. The γ value for other polymers often differs from that exhibited by polyethylene.[115,116]

We are now in a position to clear up some heretofore rather mysterious points concerning the melting behavior of linear polymers. Because in early experiments polymers did not appear to act as if they had a "fixed" melting point, they had laid upon them the curse of not obeying the laws of thermodynamics. Nothing could be further from the truth once it is understood that the chain-folded crystal, once formed, has a strong tendency to maintain the fold period; only a complicated and often slow process allows thickening, and thickening by a factor of no more than two to five times the initial value is common. The initial fold period is, by the kinetic theory of nucleation, smaller the lower the crystallization temperature, according to Eqs. (4) or (5). Therefore, through the thermodynamic relation given in Eq. (3), one must expect the thin crystals formed at a low crystallization temperature to melt lower on warming than the thick ones formed at a high crystallization temperature.‡ Hence the prediction

† Near and below 128°C melt-crystallized polyethylene appears to thicken in stages.[111,112] The first stage follows an expression of the form $l(t) = l_g^* + B \log t$ from l_g^* to 270 Å. This amounts to a doubling of the original thickness. This is followed by a second and considerably slower thickening process which appears to obey the relation $l(t) = 270\ \text{Å} + B' \log t$, where $B' < B$.[111] Thus any reasonably long crystallization time near and below 128°C has a tendency to give $\gamma \cong 2$. At crystallization temperatures near 130°C the slower second stage appears to be absent.[112]

‡ The lamellae in a polymer crystallized from the subcooled melt at a low crystallization temperature T_1 are sometimes so thin that they melt out on rewarming at a temperature T_2 where crystallization can still occur. According to Eq. (4), the new lamellae formed at T_2 will be thicker than those formed at T_1. Under these circumstances the lamellae will appear to grow in thickness on warming even though isothermal thickening is not observed at T_1 or T_2.[15] If not properly understood, this effect could mislead one into supposing that the chain-folded lamellar thickness in such cases depended on the ambient temperature rather than the undercooling at which the crystals were formed. Usually a volume increase corresponding to the "melting" process is discerned just as one warms from T_1 to T_2, followed by an isothermal decrease of volume resulting from crystallization at T_2. (It may be speculated that in some instances the increase in volume on warming from T_1 to T_2 may not correspond to a complete melting of the crystal to a state characteristic of the normal subcooled liquid at T_2, since formation of a disordered state resembling a mobile surface layer may suffice—see the discussion of the role of physically adsorbed molecules in crystallization in Section 3.)

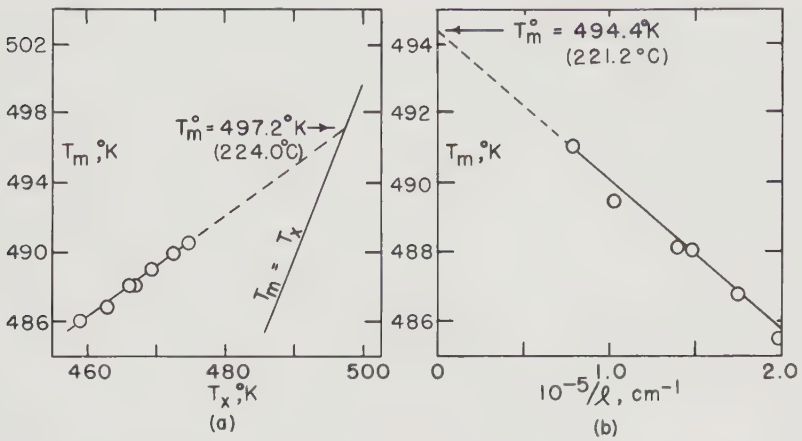

Fig. 19. Extrapolations used to estimate T_m^0. (a) T_m versus T_x plot for melt-crystallized poly(chlorotrifluoroethylene) according to Ref. 115. Specimens were of low crystallinity ($\chi = 0.1$) and rapid melting was used. A value of $T_m^0 = 224°C$ is indicated. The value of γ is 3.4. (b) T_m versus $1/l$ plot for melt-crystallized poly(chlorotrifluoroethylene). Lamellar thickness determined by low-angle X-ray diffraction by Dr. P. H. Geil, reported in Ref. 16. A value of $T_m^0 = 221.2°C$ is estimated. The same samples were used in both investigations. From the slope, $\sigma_e = 40.3$ ergs/cm^2. If the line in (b) is forced to pass through $T_m^0 = 224°C$, σ_e would be 57.3 ergs/cm^2.

that, in general, the lower the crystallization temperature, the lower the melting point. Thickening in general simply reduces this effect, but does not ordinarily eradicate it. The melting point of the crystal of infinite l, which we call T_m^0, can be obtained by extrapolation to $1/l = 0$ in Eq. (3) or the intersection of the experimental line with the line $T_m = T_x$ in Figure 18, which is equivalent to an extrapolation to infinite l. A comparison of T_m versus T_x and T_m versus $1/l$ using data for poly(chlorotrifluoroethylene)[115] is shown in Figure 19. We regard the extrapolation of T_m versus $1/l$ data as probably a more reliable way of estimating T_m^0, since some curvature is inherent in the exact form of Eq. (8) if γ is not strictly a constant at various crystallization temperatures, this curvature usually tending to give a slightly high value of T_m^0. However, in using the T_m versus $1/l$ method, suitable steps must be taken to minimize thickening in the melting run after l has been established, since such thickening will lead to melting points higher than those that correspond to l, and thus yield a slightly low value of T_m^0 and σ_e because the thickening tends to be more prominent for small l. These extrapolations are of some importance to those interested in testing theories of crystallization in polymers, since the undercooling is measured from T_m^0. Above a

molecular weight of roughly 5×10^4 the value of T_m^0 is usually practically independent of the molecular weight.

From a thermodynamic viewpoint, the melting of a thin platelet or lamella at T_m represents a conversion according to Eq. (3) of a crystal in a metastable state to a slightly subcooled liquid also in a metastable state. Thermodynamics can be applied to phase transitions between two metastable states provided that neither of these states is changing within itself in the time frame of the experiment under consideration. The melting of polymers obeys the laws of thermodynamics, but metastable states are involved in the equilibria.

The foregoing treatment also indicates one of the main reasons that polymers crystallized in the chain-folded scheme tend to have a rather broad melting range. As a result of the varying ages of the thickened crystallites, and the fact that there is an inherent initial distribution of lamellar thickness skewed about l_g^* (see Section 3.3), there will be a distribution of melting points. This broad melting range has nothing to do with "impurities" in the usual sense. Even an isothermally crystallized fraction with a sharp distribution of molecular weights would show a melting range if it were crystallized in the region where chain-folding occurred. Nonisothermal crystallization will lead to an even broader melting range.

One other point is of interest. The implication in the foregoing discussion is that the most stable crystal (assuming a sharp fraction) of a polymer would be one where all the chains lay side by side with the chain ends all together on the surface as in an *n*-paraffin, and which had *no* chain folds, and *no* noncrystalline component. This is precisely what we intended to imply. It is such a crystal that would melt at T_m^0.

Crystallization at high temperatures can be accomplished by application of high pressures, which increases the melting point according to the Clausius Clapeyron equation. In the case of polyethylene this can result in polymer that is largely in the so-called "extended-chain" form. The "lamellae" are extremely large, the average thickness frequently lying in the range 1500–3000 Å.[117] As mentioned earlier, this is probably material that has nucleated and grown in its early stages in the chain-folded mode, and which has undergone extensive thickening.[100,102,117]† In this extreme the

† Studies by Bassett and Turner[102] have indicated that an "intermediate" crystalline phase exists in the phase diagram of polyethylene in the vicinity of 240°C and at pressures exceeding about 4 kbar, which is the region where extended-chain polymer is typically formed. Recent x-ray work (to be published in *J. Appl. Phys.*) by Prof.

thickening process removes a substantial fraction of the folds, leaving perhaps one or two per molecule, and produces higher and sharper melting crystals than are found in crystallization of similar polymers carried out at 1 atm.[118] Defects in the form of row vacancies resulting from chain ends and residual chain folds must be certainly expected to occur in such crystals in sufficient concentration to lower the observed melting point below T_m^0. The highest melting point achieved so far for pressure-crystallized polyethylene in the extended-chain form is 141.4°C,[118] and T_m^0 is known to be about 146°C (see Section 4.2). Polyethylene that is crystallized from the melt under normal conditions, which contains fairly thin chain-folded lamellae, exhibits melting points in the range of about 132–139°C, depending on the crystallization temperature and the annealing time.

2.3. Interpretation of σ_e in Terms of Fold Structure

Having seen how σ_e for polyethylene can be determined by thermodynamic means to be 93 ± 8 ergs/cm^2, we must now ask how this value is to be interpreted in molecular terms. By reference to Figure 20, it is seen that each chain fold contributes an area of $2ab = 2A_0$ to the fold surface, where A_0 is the cross-sectional area of each chain. Therefore[66]

$$\sigma_e = (q/2A_0) + \sigma_{e0} \tag{9}$$

where q is the work required to form the fold by bending the polymer chain back upon itself in the appropriate configuration. The term σ_{e0} is the value the surface free energy would assume if no work were required to form the fold. In one approximation we would assume

---

Bassett and Drs. G. Piermani and S. Block at the National Bureau of Standards using a diamond anvil pressure cell has confirmed the existence of the intermediate phase, and suggests that the molecules exhibit hexagonal packing. The heat of fusion of the intermediate phase is approximately one-fourth that of the normal orthorhombic form.[102] From this and the work of Wunderlich[117] there is little doubt that extended-chain material actually begins its existence as a chain-folded crystal with a rather large initial fold period that forms from the subcooled liquid as the intermediate phase, which then undergoes thickening to give lamellae of the average thickness commonly observed. Several factors may be involved in producing a large initial thickness in the intermediate phase at high pressures. It is seen from Eq. (4) that the term $2\sigma_e T_m^0/(\Delta h_f)(\Delta T)$ in l_g^* will, under comparable conditions of undercooling, give about four times the contribution in the intermediate phase than the orthorhombic phase, because of the lower Δh_f in the former. Another factor is that σ must be expected to be four times smaller for the intermediate phase because of its low heat of fusion, causing δl in Eq. (4) to make four times the usual contribution to l_g^* (see expressions $\delta l = kT/b\sigma$ and $\sigma = \alpha(\Delta h_f)(ab)^{1/2}$ given later in this chapter).

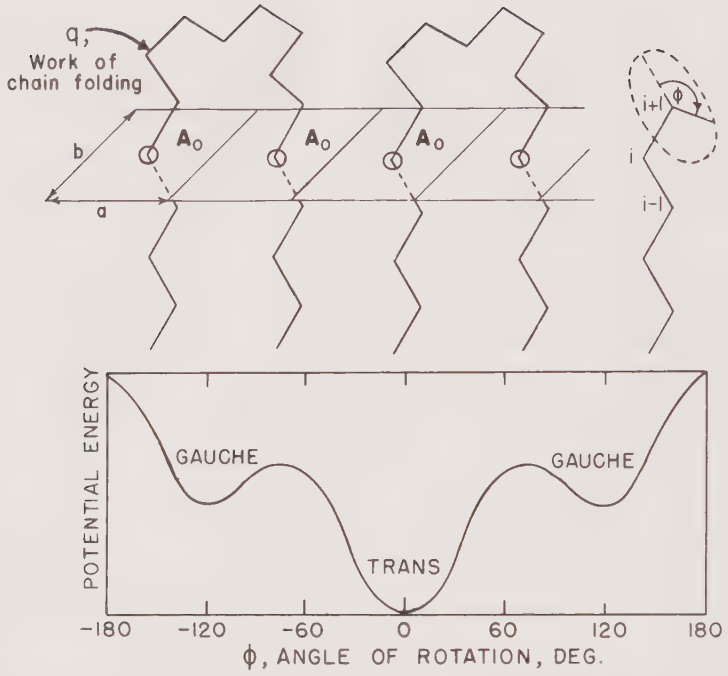

Fig. 20. Molecular basis of energetics of chain folding. Upper diagram: Fold with work of formation q formed by bending chain back on itself to reenter lattice, creating fold surface with area $2A_0$, where $ab = A_0$ is the cross-sectional area of chain. Lower diagram: Change in potential energy of a segment as it rotates through angle ϕ about the bond between the ith and the $(i + 1)$th chain backbone atom. The angle ϕ is measured from the plane determined by the $i - 1$, i, and $i + 1$ atoms as shown. The barriers between the trans and gauche positions, and the potential energy of the gauche positions, arise from the substituent groups on the $i + 1$ atom interacting with the ith atom. In polyethylene a set of trans states represents a straight chain, but the fold contains at least several gauche states that are the principal source of the work of chain folding q.

σ_{e0} to be roughly the same as the lateral surface free energy σ. In any case, one expects $q/2A_0$ to be considerably larger than σ_{e0}, and for certain applications σ_{e0} may be set equal to zero to a sufficient approximation.

The value of A_0 can be obtained from X-ray data and for polyethylene is close to 18.9×10^{-16} cm^2 near T_m^0. Then Eq. (9) with $\sigma_e = 93$ ergs/cm^2 and $\sigma_{e0} = 0$ leads to $q = 3.52 \times 10^{-13}$ erg/fold or 5.06 kcal/mole of folds. Had we assumed σ_{e0} was 15 ergs/cm^2, then q would have been 4.24 kcal/mole. We must now ask if a q value in

the vicinity of ~4–5 kcal/mole is a reasonable value in order to maintain the credibility of the chain-fold model.

Theoretical molecular potential energy calculations on the work of chain folding in polyethylene have been given by several authors.[119–121] Electron microscopy[1] and infrared spectroscopy[23] have revealed that the predominant fold plane in polyethylene solution-grown crystals is along (110) (see Figure 4). From geometric considerations the direction of the polymer chain can be reversed to fold back into the crystal in seven to ten $-CH_2-$ units by rotating five or six CH_2 units into gauche positions, as opposed to the trans positions that are characteristic of the straight part of the chain. Each gauche conformation increases the stored energy in the chain by about 0.8 kcal/mole.[122] This suggests that q is 4.0–4.8 kcal/mole. The atomic positions upon reentry into the crystal after these considerations do not coincide with normal lattice positions. Therefore a small additional energy must be included by either of two approaches: The bond angles and rotation angles of the units in the fold can be distorted slightly[120] or the atomic positions of the atoms in the lattice near the surface can be distorted to a certain extent.[121] The resulting minimum energy depends upon the model chosen and the functions used for the potential energy. Corradini *et al.*[120] obtain 4 kcal/mole of folds. This free energy compares reasonably well with the value of 4.24–5.06 kcal/mole found from the surface free energy determined thermodynamically by Eq. (3) and the use of Eq. (9). Crystals of polyethylene can also be grown in which some folding occurs along the (200) planes of the crystal (i.e., folds parallel to b axis of unit cell in Figure 4). Spherulites in melt-crystallized polyethylene exhibit this type of fold.[23] Analogous calculations for this case have been performed by the same authors and result in only slightly different energies. The calculation of fold energies from the properties of the polymer chain is a useful and challenging aspect of the field of polymer crystallization, and further activity and refinements in this area are to be anticipated.

The approximate agreement between the experimental value of the work of chain folding and that computed from intermolecular and intramolecular potential energy functions lends credence to the view that the basic chain-fold model is substantially correct on a molecular basis for polyethylene. In particular, the main contribution to the fold surface free energy is evidently the work required to bend the polymer chain back upon itself so that it can reenter the crystal in a manner consistent with the lattice structure. This is a quite different

origin of a surface free energy than is normally encountered in simple molecular, ionic, or metallic crystals. Values of q for various other polymers will be estimated subsequently.

The lateral surface free energy σ of a chain-folded crystal would be expected to be similar in origin and character to that found in a chain-type crystal such as an n-paraffin. The value of σ for simple molecules forming molecular crystals runs generally from 5 to 20 ergs/cm^2.[123] For n-octadecane σ is about 9.6 ergs/cm^2,[93] and for polyethylene it is in the range 10-15 ergs/cm^2 [93,124] (for details see the discussion given in Section 6). Accordingly, it is seen that in polymers we shall quite generally have to deal with situations where the fold surface free energy is perhaps five to ten times greater than the lateral or "normal" surface free energy.

2.4. The Driving Force for Crystallization in Strongly Subcooled Systems

One final point remains to be cleared up before proceeding to the theory of the rate of crystal growth and lamellar thickness. It is possible to highly subcool certain polymers and still observe crystal growth rates and the lamellar thickness. For instance, it is possible to measure crystal growth rates near 110°C for isotactic polystyrene,[7] for which $T_m^0 \cong 242$°C. This corresponds to an undercooling of 132°C, which is large by any accounting. In these extreme circumstances Eq. (2) must be modified to account for the fact that it overestimates Δf at high undercoolings. This error is caused by the fact that the customary derivation of Eq. (2) employs the assumption that the heat of fusion Δh does not vary with temperature. This is not a good assumption at high undercoolings because Δh decreases as the temperature is lowered, as shown schematically in Figure 21(a). At high undercoolings it is much better to use the formula

$$\Delta f = [\Delta h_f(\Delta T)/T_m^0]f \tag{10a}$$

where to one approximation the correction factor f is given by

$$f = 2T/(T_m^0 + T) \tag{10b}$$

which has been derived elsewhere.[81]

The factor f has little effect at low undercoolings, but decreases Δf considerably near the glass transition temperature T_g in the subcooled phase, which in most polymers occurs at about two-thirds of T_m^0. Suzuki and Kovacs[7] and Hoffman and Weeks[81] have

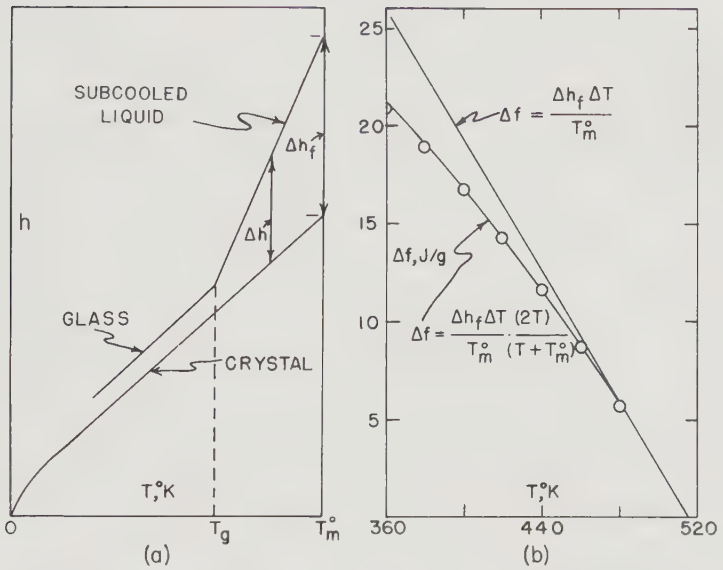

Fig. 21. Enthalpy and free energy of fusion in strongly subcooled glass-forming systems. (a) Schematic diagram showing drop in heat of fusion Δh with falling crystallization temperature as glass transition in subcooled state is approached. The symbol h is the enthalpy and Δh_f is the heat of fusion at T_m^0. (b) Open circles represent free energy of fusion Δf of polystyrene calculated from calorimetric data in Ref. 5. The departure from the linear relation $\Delta f = (\Delta h_f)(\Delta T)/T_m^0$ is a result of the falloff of Δh_f. The solid curved line shows how the factor f in Eq. (10b) accounts for the reduction in Δh_f.

discussed this topic in detail. Other forms for the factor f have been suggested, for example, by Sanchez and DiMarzio,[125] who have presented a form whose numerical effect is quite close to Eq. (10b). If one assumes the heat capacity of the polymer crystal is equal to that of the glass extrapolated to temperatures above T_g, it is possible to calculate Δf for polystyrene as a function of temperature from the calorimetric data of Karasz *et al.*[5] As shown in Figure 21(b), the variation of Δf with undercooling is approximated extremely well by Eq. (10).

3. Theory of Growth and Lamellar Thickness

3.1. Approach and Model

Various treatments of the problem of lamellar thickness and growth have been given in the literature.[15,16,28,66,67,126–130] The

particular treatments that yield both the growth rate and the lamellar thickness are all based on surface nucleation theory.[15,16,28,66,126 128] The one given here, which does not consider fluctuations of the fold period, is the simplest that allows prediction of the growth rate and lamellar thickness over a wide range of undercoolings and that leads to a successful comparison between theory and experiment; all earlier treatments lead to difficulties[110] at high undercoolings. Certain treatments with fluctuations[128,130] are considerably more complicated but are capable of predicting a slightly rough fold surface consonant with a defective density and reduced heat of fusion. Also, they justify *a priori* the fact that the fold period maintains itself at a value fluctuating about $l_g^* = (2\sigma_e/\Delta f) + \delta l$ during isothermal growth. Meanwhile, the elementary theory to be given here reproduces the main features of the growth process, including the prediction of both the growth rate and initial lamellar thickness at high undercoolings† and will be sufficient for introductory purposes. It is patterned after a paper by Lauritzen and Hoffman.[28]

The model used is shown in Figure 22. The polymer molecule is assumed to have a cross-sectional area ab. A surface nucleus of fixed thickness b and height l that is fixed at a specified undercooling grows along the g direction, where a is the width of the molecule. Overall growth is in the G direction. When v stems and $v_f = v - 1$ folds have been formed the free energy of formation (ignoring chain-end effects) is

$$\Delta\phi_v = 2bl\sigma + 2v_f ab\sigma_e - vabl\,\Delta f \tag{11a}$$

which for large v becomes

$$\Delta\phi_v = 2bl\sigma + vab(2\sigma_e - l\,\Delta f) \tag{11b}$$

where σ is the lateral surface free energy and σ_e the fold surface free energy [the meaning of σ and σ_e in Eq. (11) is exactly the same as in Eq. (1)].‡ The lateral surface free energy will be in the usual range for

† Some remarks suggesting reasons for assuming a kinetic rather than an equilibrium approach to the problem of the formation of thin, chain-folded crystals have already been given in previous sections. However, the most compelling reason for adopting such an approach is that the folds must surely go into a crystal on a sequential and continuous basis *as it is being formed.* Thus one suspects at the outset that the thickness of the crystal is established by the growth process itself.

‡ In adapting Eq. (1) to the more microscopic and molecular events implied by Eqs. (9) and (11), it has in effect been assumed that the macroscopic quantity σ_e, as defined in Eq. (1), can in fact describe the microscopic event of the formation of a single chain fold. This and the corresponding assumptions regarding σ will prove to be good approximations (see Sections 4 and 6).

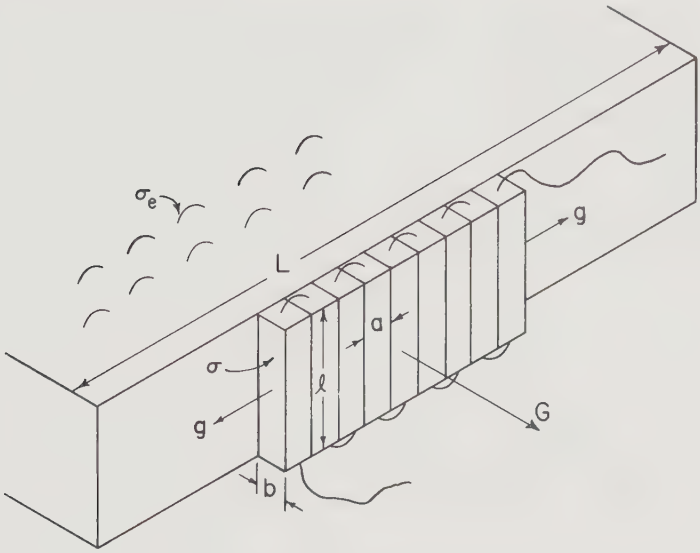

Fig. 22. Model for surface nucleation and growth of chain-folded crystal. A surface nucleus composed of v stems of length l, thickness b, and width a, forms on the substrate and spreads in the direction denoted g. The surface nucleus then completes a layer of thickness b by spreading to the crystal width L, causing the crystal to grow in the G direction. The lateral and fold-surface free energies σ and σ_e are also shown.

chain-type molecular crystals, and the fold surface free energy is given by Eq. (9). The length of the substrate under consideration is denoted by L.

We consider that the surface nucleus starts by a polymer segment or set of segments from the solution or undercooled melt attaching itself to the crystal surface, and then coming into crystallographic register with the substrate, forming the first stem at the cost $2bl\sigma$. The molecule then folds back on itself and starts to crystallize in a position adjacent to the first stem. *The adjacent position is by a considerable margin the most probable site for reentry after folding* since attachment on a nonadjacent position would incur a large extra term $2bl\sigma$ in addition to the term involving $2ab\sigma_e$ which occurs with both adjacent and nonadjacent reentry [cf. Eq. (11)]. By repeating this act, a surface nucleus begins to approach and then attain the region of stability as it spreads in the direction g. Many molecules can be involved in completing the surface strip to the substrate length L; a new molecule simply starts in the niche where the attached

one terminates and continues on the path of increasing v that gives the surface strip increased stability. The new molecule may leave a cilium or row vacancy embedded in the growth strip (Figures 4 and 7). The approximation used in this chapter ignores the effect of the chain ends and cilia, i.e., it assumes that the number of folds per molecule in the growth strip is fairly large ($\gtrsim 5$) so that the advent of new molecules in the growth strip does not represent a large perturbation. Interesting effects, such as the rejection of short polymer chains on a kinetic basis and variations in the growth rate, can be predicted by modifying the model to account for the effect of chain ends, but such considerations would create an undue diversion at this stage, and will be dealt with briefly in Section 3.6.

The surface nucleus goes through a maximum in its free energy of formation near or at $v = 1$, and then gradually approaches the region of stability as v increases. Thus we will be treating a case where

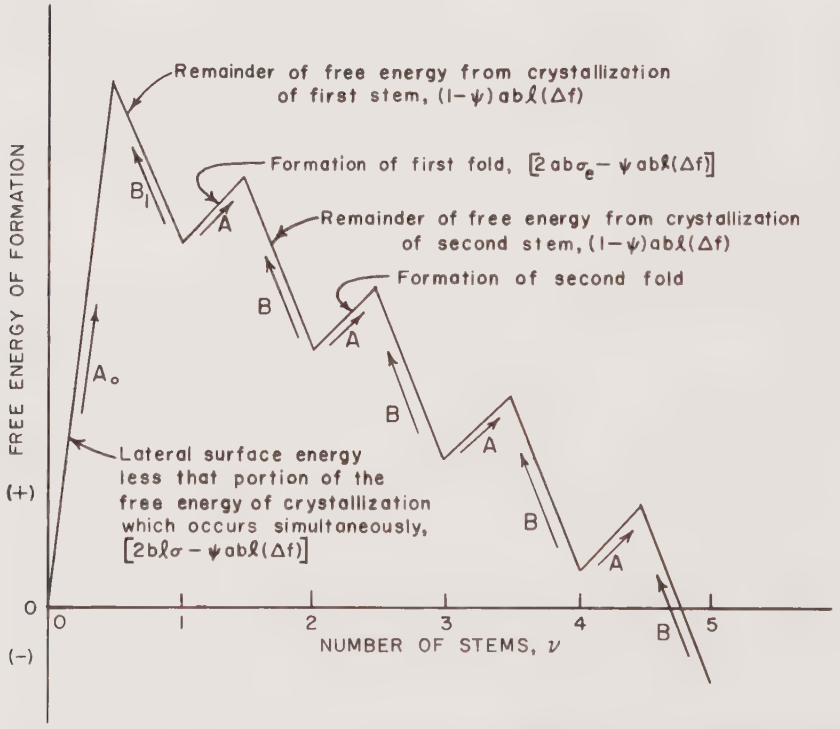

Fig. 23. Free energy of formation of a chain-folded surface nucleus. The diagram shows the relationship of the rate constants A_0, B_1, A, and B to the free energy of the processes involved in the formation and growth of the surface nucleus as it spreads in the g direction.

we have a set of connected rate processes such that the rates of forward and backward reactions between the states $v = 0$ and $v = 1$ are A_0 and B_1, respectively, and where all the subsequent forward and backward reactions are given by A and B as shown in Figure 23. We employ the notation $N_0, N_1, N_2, \ldots$ for the occupation numbers for $v = 0, 1, 2, \ldots$. This corresponds in general to a nucleation-controlled process where a large barrier resulting from creation of surfaces must first be surmounted to initiate the nucleus, with subsequent steps leading to the stable region.

3.2. Calculation of the Total Flux

The first step in the problem is to find the general steady-state expression for the flux S over the barrier to nucleation in terms of A_0, B_1, A, and B and the occupation numbers $N_0, N_1, \ldots$. The symbol S represents the net flow of polymer from sites in the liquid ($v = 0$) to the first step element (stem) of polymer in the nucleus ($v = 1$) of a new layer of polymer crystal. In terms of the rate constants and occupation numbers we have

$$S = N_0 A_0 - N_1 B_1 \tag{12}$$

Upon forming this first step element, two new surfaces are created at a cost in free energy of $2bl\sigma$, less the free energy of fusion associated with the volume abl of the element. The mechanism by which this element, composed of, say, 100 segments each of length l_u, attaches to the substrate is undoubtedly complex and involves many intermediate steps. In order to permit some characterization of these steps, we will apportion a fraction ψ of the free energy of fusion to the activation free energy of the forward reaction, and the remainder to the backward reaction.[28,128] (see Figure 23). (The symbol ϕ was used for ψ in the original reference.[28]) It will emerge subsequently that the value of ψ may be related to whether or not the polymer molecule is physically adsorbed on the surface prior to actual crystallographic attachment onto the substrate. The rate constants associated with the first step element can then be written as

$$A_0 = \beta \exp\{-(2bl\sigma/kT) + [\psi abl(\Delta f)/kT]\} \tag{13}$$

$$B_1 = \beta \exp[-(1 - \psi)abl(\Delta f)/kT] \tag{14}$$

where β is a factor that accounts for retardations to molecular motion resulting from the fact that polymer molecules or segments thereof

must be transported to the site of the crystallization act. The factor β contains the effects resulting from viscosity, surface transport, and the like. It is expressed in "events" per second, and is expected to be strongly dependent on temperature (especially at low temperatures) and will be discussed in more detail later. Note that ψ deals with the rates of the forward and backward reactions and not the equilibrium distribution. Thus the ratio A_0/B_1 is independent of ψ.

As the crystallizing molecule puts down step elements corresponding to $v = 2, 3, \ldots$, causing the surface nucleus to spread in the g direction, no new lateral surface is created, but each step does incur the cost in free energy of creating a fold, $2ab\sigma_e$, less the free energy of fusion $abl\,\Delta f$. Apportioning Δf in the same way as for the first step, one can write

$$A = \beta \exp\{-(2ab\sigma_e/kT) + [\psi abl(\Delta f)/kT]\} \tag{15}$$

$$B = \beta \exp[-(1 - \psi)abl(\Delta f)/kT] \tag{16}$$

In the steady-state approximation ($dN_v/dt = 0$) the flux through each state is the same as for the initial step and can be shown to be[28]

$$\begin{aligned} S = {} & \beta N_v \exp\{-(2ab\sigma_e/kT) + [\psi abl(\Delta f)/kT]\} \\ & - \beta N_{v+1} \exp[-(1 - \psi)abl(\Delta f)/kT] \end{aligned} \tag{17}$$

From the steady-state conditions and the dependence of each occupation number on the one preceding and the one following, it can be shown by a rigorous argument[28] that the flux can be expressed in terms of N_0 and the rate constants A, A_0, B, and B_1 as

$$S(l) = N_0 A_0 (A - B)/(A - B + B_1) \tag{18}$$

Noting that the portion of the free energy of fusion contributing to the backward reaction rate has been assumed to be the same for all steps, including the first (i.e., $B = B_1$), one finds that the net rate of formation of nuclei of length l is

$$\begin{aligned} S(l) = {} & \beta N_0 \exp\{[-2bl\sigma + \psi abl(\Delta f)]/kT\} \\ & \times \left(1 - \exp\{[-abl(\Delta f) + 2ab\sigma_e]/kT\}\right) \end{aligned} \tag{19}$$

The foregoing treatment has been arranged so that $B = B_1$, which allows the integration expressed in Eqs. (20) and (22) to follow to be carried out in closed form. In a more general model the value of ψ for the first step $v = 0 \rightarrow v = 1$ could be denoted ψ_0, and that for

all the subsequent steps $v = 1 \rightarrow v = 2, \ldots$, denoted ψ_1, where $\psi_0 \neq \psi_1$. Equations (20) and (22) for the case $\psi_0 \neq \psi_1$, corresponding to $B \neq B_1$, cannot be integrated in closed form, but numerical calculations show that both the flux and l_g^* depend almost entirely on the ψ_0 value of the first step, and but little on the value of ψ_1 assigned to the subsequent steps. The undercooling where the δl catastrophe occurs depends solely on ψ_0. (The δl catastrophe is discussed in detail in Section 3.3.) Accordingly, the case $\psi = \psi_0 = \psi_1$ where $B = B_1$ used in the treatment given here is closely illustrative of the more general case where $B \neq B_1$. For practical purposes the ψ value associated with the first step governs the behavior of the model.

It is worth noting that quantities similar in general effect to ψ appear either implicitly or explicitly in most theories of nucleation. For example, the general treatment of Turnbull and Fisher[131] contains an assumption apportioning the free energy between the forward and backward reactions similar in effect to $\psi = 1/2$ in the present treatment. The effect of ψ in other theories has gone mostly unnoticed because it did not relate to an experimentally observable quantity such as l_g^*.[28]

To find the total flux S_T, one sums Eq. (19) over all possible values of l. Assuming that possible values of l are increments of the monomer repeat length l_u, the summation can be replaced by the integral

$$S_T = (1/l_u) \int_{2\sigma_e/\Delta f}^{\infty} S(l)\, dl = N_0(\beta/l_u) P \exp(2ab\sigma_e \psi/kT) \times \exp[-4b\sigma\sigma_e/(\Delta f)kT] \qquad (20)$$

where the lower limit of integration corresponds to the minimum possible thickness of crystal, and where

$$P = \frac{kT}{2b\sigma - ab(\Delta f)\psi} - \frac{kT}{2b\sigma + (1 - \psi)ab(\Delta f)} \qquad (21)$$

The factor P is in cm, β is in "events" per second, and l_u is in cm; consequently S_T is in "events," i.e., "surface nuclei" per second, exclusive of units assigned to N_0. The principal variation of S_T with undercooling near T_m^0 is in the factor $\exp[-4b\sigma\sigma_e/(\Delta f)kT]$. It is therefore anticipated that the overall crystal growth rate G will be proportional to this factor at low undercoolings for growth processes that are proportional to the first power of the surface nucleation rate.

3.3. Initial Lamellar Thickness

The average value of l, which we denote $\langle l \rangle_{av}$ and identify with the initial lamellar thickness l_g^*, is calculated from the flux according to

$$l_g^* = \langle l \rangle_{av} = (1/l_u) \int_{2\sigma_e/\Delta f}^{\infty} lS(l)\, dl \Big/ (1/l_u) \int_{2\sigma_e/\Delta f}^{\infty} S(l)\, dl \tag{22}$$

and is found to be

$$l_g^* = \frac{2\sigma_e}{\Delta f} + \frac{kT}{2b\sigma} \cdot \frac{2 + (1 - 2\psi)a(\Delta f)/2\sigma}{[1 - a(\Delta f)\psi/2\sigma][1 + a(\Delta f)(1 - \psi)/2\sigma]} \tag{23}$$

The last term is the δl of Eq. (4), which is seen to be a function of ψ. An explicit value of δl was given by Lauritzen and Hoffman in their early treatment,[66] which was $kT/b\sigma$ for the case $\Delta f \to 0$; this same limit is obtained with Eq. (23). Observe that it is basically the total average flux that controls the crystal thickness.

It is of interest to investigate the behavior of S_T and l_g^* for various ψ. By setting $\psi = 1$, it is found that

$$\delta l = \frac{kT}{2b\sigma} \cdot \frac{(4\sigma/a) - \Delta f}{(2\sigma/a) - \Delta f} \tag{24}$$

a result obtained previously.[127] It is seen from the denominator of Eq. (24) and the fact that $\Delta f \cong (\Delta h_f)(\Delta T)/T_m^0$ that δl becomes infinite at the undercooling

$$\Delta T_c \cong 2\sigma T_m^0/(\Delta h_f)a \tag{25}$$

We refer to this as the "δl catastrophe." This effect is predicted for the case $\psi = 1$ at undercoolings corresponding to those encountered in some experiments. However, no sharp upswing in l_g^* is actually found in these experiments (see Section 4.3), so we investigate other ψ values. As an incidental point, we note that S_T rather abruptly approaches infinity for the case $\psi = 1$ at ΔT_c, as may be seen from an investigation of P [Eq. (21)].

By setting $\psi = 0$ in Eq. (24) it is found that[28]

$$\delta l = \frac{kT}{2b\sigma} \cdot \frac{(4\sigma/a) + \Delta f}{(2\sigma/a) + \Delta f} \tag{26}$$

In this case there is no δl catastrophe, and l_g^* falls continuously with decreasing temperature.†

The general effect of ψ on the initial lamellar thickness is shown in Figure 24, where l_g^* and δl are plotted for various values of ψ as a function of crystallization temperature for the values of T_m^0, σ, σ_e, Δh_f, and $a = b$ given in the legend. It is seen that the value of $T_c = T_m^0 - \Delta T_c$ corresponding to the δl catastrophe is lowered as ψ is lowered. The main contribution to l_g^* near the melting point is from the "classical" term $2\sigma_e/\Delta f$. As the undercooling is increased the contribution from $2\sigma_e/\Delta f$ decreases and that from δl increases in importance.

Some general observations are worthwhile at this point. Observe that we have called l_g^* the *initial* thickness of the chain-folded crystals. As mentioned earlier, in some systems the fold period slowly and spontaneously increases on isothermal storage. This is of course quite natural when the requisite molecular mobility exists in the chain-folded crystal, because a thick crystal is obviously more stable from a thermodynamic viewpoint than a thin one. Hence, the crystal will strive to increase its stability by decreasing the area of its high-energy surface, i.e., by reducing the number of chain folds. Such thickening is more rapid near the melting point. When crystals are grown at sufficiently low temperatures, they do not thicken appreciably, and the expressions given here for l_g^* may be applied.

The comments given above are useful in establishing the point that the initial lamellar thickness, and by implication, chain folding, is of strictly *kinetic* origin. According to the foregoing derivation, the thickness l_g^* is that which is consonant with the appropriate average rate of passage of the crystal into the stable region, i.e., l_g^* is controlled by kinetics. Nuclei with larger values of l than l_g^* can form, and are considered in the integration limits of Eq. (22), but they reach the stable region much more slowly than those with thickness l_g^*. Crystals whose thickness is exactly $2\sigma_e/\Delta f$ cannot reach the stable region at all [see Eq. (11)]. The crystal with thickness l_g^* is predicted to melt somewhat above its crystallization temperature because of δl, but well below T_m^0, as is observed. On the other hand, the most stable crystal is one with no folds at all, i.e., one where all the chains lie

† An upswing in δl at moderate undercoolings that is similar in character to that which obtains for the case $\psi = 1$ in the present treatment occurs in other treatments without fluctuations (see Refs. 110 and 127). An upswing in δl that has a somewhat different origin occurs in all the treatments involving fluctuations[126,128,130] of the fold period, again causing difficulties in applying the theories at moderate and high undercooling.

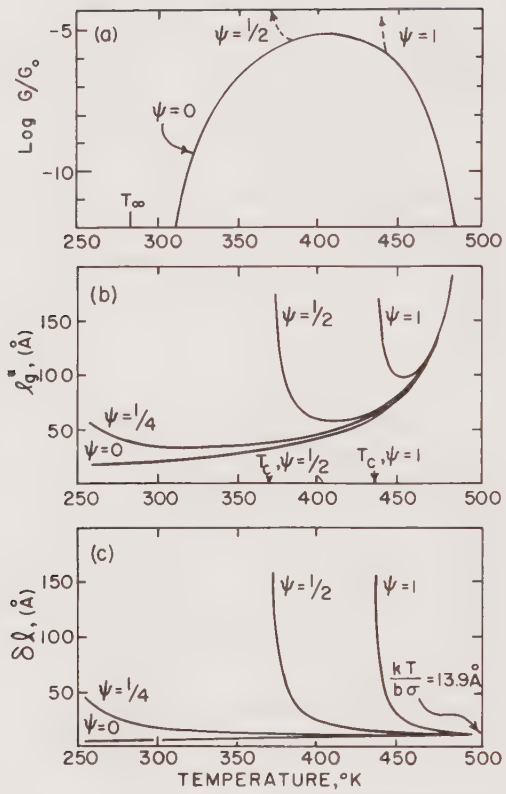

Fig. 24. Variation of growth rate, lamellar thickness, and δl with temperature for several values of ψ. The curves are calculated using $T_m^0 = 500°K$, $T_\infty = 280°K$, $\Delta h_f = 3 \times 10^9$ ergs/cm^3, $\sigma = 10$ ergs/cm^2, $\sigma_e = 100$ ergs/cm^2, $a = b = 5 \times 10^{-8}$ cm ($K_g = 2.39 \times 10^{5}°K^2$), $U^* = 1400$ cal/mole, and $G_0 = 10^{10}$ cm/sec. (a) Growth rate G. Dashed arrows indicate where S_T or G becomes invalid as T_c is approached. (b) Lamellar thickness l_g^*, showing onset of δl catastrophe as function of ψ. (c) The δl component of l_g^*.

side by side and where (assuming the molecular weights of the chains are identical) all the chain ends are in a plane. Such a crystal has the maximum stability and melts at T_m^0. The existence of chain-folded crystals is a striking manifestation of the dominance of kinetics in determining crystal shape. Though they differ in their details and degree of sophistication, all of the theories that give both the variation of the rate of growth and lamellar thickness with undercooling in terms

of surface nucleation theory share the basic explanation given above, namely that l_g^* is of kinetic origin. With some loss of rigor, the crystal of thickness l_g^* may be regarded as simply the fastest growing crystal in the system.

In the present case, the effect of kinetics is emphasized by the fact that one dimension of the original nucleus, namely l_g^*, is retained in the crystal as it grows to large size in the other two dimensions. Such a retention of a critical crystal nucleus dimension is not found elsewhere in nature, all other crystals growing at least to some extent in all three dimensions. Once a given polymer crystal has begun the folding process, it is essentially preempted from rapid growth in the direction perpendicular to the high-energy fold surface by the existence of the folds, and the fact that the chemical bonds in these are (with few exceptions) not easily broken.

The foregoing discussion refers to why a single crystal or lamella does not grow in such a way as to form a crystal that is large in all three dimensions. The discussion is not vitiated by the fact that one chain-folded lamella or crystal often grows in juxtaposition to another, as occurs, for example, in the vicinity of the screw dislocation in the crystal shown in Figure 9. (Screw dislocations are also found in melt-crystallized polymer.[132,133]) In general, growth based on such dislocations allows one chain-folded crystal layer to grow upon a substrate consisting of a similar crystal, leading to a spiral ramp. However, each growing edge of the crystal terminates at a corner, and a surface nucleation act is required to cause each face to grow. An act of a quite similar character is required for a molecule to go around a corner.[28] Accordingly, the outward growth of the crystal normal to the axis of the screw dislocation is controlled by the same laws of surface nucleation as apply to folded crystals without such dislocations. Screw dislocations have never been observed on the growing edge of the crystal, i.e., on the σ-type surface. Evidently the energy required to introduce such a dislocation in a crystal consisting of linear chains involving covalent bonds in the chain is prohibitive. As a consequence, growth on this face takes place by a surface nucleation mechanism.

Some comments on the probable reasons why strictly bundle-like or "fringed micelle" crystals do not appear in normal crystallization procedures have already been given. These may be summarized by saying that such structures, if taken as literally correct, lead to an end surface free energy that is, for topological and other reasons, even higher than σ_e for a folded surface.[15,16] In fact, Zachmann[134] has estimated the surface free energy in such a strained bundle end to be

as high as 280 ergs/cm^2. Bundlelike crystals are accordingly forbidden on kinetic grounds.[15,16] Insofar as cumulative strain[15,16] occurs at the bundle ends, such objects will not exist as crystals of large extent, for thermodynamic as well as kinetic reasons. Thus, chain folding is a pervasive phenomenon in highly crystallizable linear polymers.

It is not necessary to adduce any "special" structures in the normal or subcooled liquid in order to predict the rate of crystallization and the attendant lamellar thickness using the present approach. In particular, no *ad hoc* "prefolded" structures are required in the subcooled liquid in order to produce chain-folded crystals. The properties of the subcooled liquid enter the theory mainly in the driving force Δf, which is defined as the free energy *difference* between the subcooled liquid state and the crystalline state.

A brief comment[127] on the classical "saddle point" calculation of l^* and the nucleation rate is required. In this procedure, one estimates the dimensions of the critical surface nucleus at the hypothetical saddle point in a plot of $\Delta\phi$ in a system of l and va on Cartesian coordinates by minimizing $\Delta\phi_v$ of Eq. (11b) with respect to va and l, and finds that $(va)^* = 2\sigma/\Delta f$ and $l^* = 2\sigma_e/\Delta f$, which in turn leads to $\Delta\phi^*/kT = 4b\sigma\sigma_e/(\Delta f)kT$. Though frequently quoted in the literature, this procedure is not admissable since l of Eq. (11) for the secondary nucleus of folded chains must, for a given crystal, be regarded as fixed at a specified undercooling, and Eq. (11) has no saddle point under these conditions. Furthermore, the classical calculation suggests that δl is zero, which implies the formation of a crystal that melts at its own crystallization temperature, which is clearly wrong. In the revised treatment given here, each crystal in the ensemble is assumed to have a fixed thickness somewhere between $l = 2\sigma_e/\Delta f$ and $l = \infty$ at a specified undercooling, and the average value of l_g^* calculated according to Eq. (22), which leads to a positive value of δl.

As implied earlier, there is a distribution of crystal thicknesses about the mean value l_g^*. The mean square deviation is

$$\langle (l - l_g^*)^2 \rangle = \frac{(kT)^2}{[2b\sigma - \psi ab(\Delta f)]^2} + \frac{(kT)^2}{[2b\sigma + (1 - \psi)ab(\Delta f)]^2} \tag{27}$$

which approaches $\frac{1}{2}(kT/b\sigma)^2$ at very small undercoolings. This expression is similar in general effect to one derived previously for a slightly different case by the same method.[66] The value of $\langle (l - l_g^*)^2 \rangle$ is typically 25–100 Å^2, corresponding to a root mean square deviation of $\sim$5–10 Å, so that an ensemble of folded crystals formed at a specified undercooling will exhibit a slightly broadened melting point. In

systems where thickening of the crystals tends to occur during the crystallization or melting run a further broadening of the melting range will take place.[112]

The values of σ and σ_e that basically govern the lamellar thickness are not totally free parameters in the sense that they can be varied without limit to fit thickness data and growth rate data. The value of σ_e is limited in principle to a rather narrow range by reasonable values of the work of folding q, or, alternatively, by the values of σ_e obtained from plots of T_m versus $1/l$. Certainly a small dependence of σ and σ_e on temperature may be allowed. The value of σ will be substantially less than σ_e, and is bracketed by what is found for ordinary molecular crystals of the same general chemical nature by homogeneous nucleation or growth experiments. In general, these fall in the range of 5–25 ergs/cm^2, and in certain cases rather close estimates can be made for σ. The range of σ and σ_e is further limited by the fact that growth rate experiments under certain circumstances closely define the product $\sigma\sigma_e$. In a few cases homogeneous nucleation studies have been carried out in polymers[124,135] which give estimates of $\sigma^2\sigma_e$. The estimates of $\sigma^2\sigma_e$ must be used with due regard for the fact that σ_e and σ depend somewhat on temperature and that homogeneous nucleation experiments are of necessity carried out at temperatures far below T_m^0 (see Section 6).

3.4. Growth Rate

3.4.1. The Retardation Factor β

As will be noted in detail subsequently, the growth rate G associated with the model shown in Figure 22 will depend on some function of the product of the net surface nucleation rate $i = S_T/Na$ and the layer thickness b. In one limit (regime I, rapid substrate completion) G is given by biL, where $L = n_s a$, and n_s is the number of sites where surface nuclei can be initiated on the substrate, and in the other limit (regime II, slow substrate completion with a large number of acts of multiple nucleation) G is given by $b(ig)^{1/2}$. In both instances S_T is involved in calculating the growth rate, and S_T according to Eq. (20) contains the retardation factor β. It is thus necessary to comment on the nature of β, which governs the rate of transport of polymer molecules, or sections thereof, to the site of crystallization.

Polymers can often be undercooled more than 100°C at which temperatures they become extremely viscous so that the retardations represented by β are the controlling feature of the flux. Accordingly,

we need to establish the correct functional form for β in order to understand the growth rate experiments.

In the case of bulk polymeric systems that can undergo extensive undercooling, we use the jump rate appropriate to local motions, which is commonly expressed as[16]

$$\beta = (kT/h)J_1 \exp[-U^*/R(T - T_\infty)] \tag{28}$$

The factor $\exp[-U^*/R(T - T_\infty)]$ is usually thought of as representing the temperature dependence of the segmental jump rate in polymers. By far the largest part of the temperature dependence of β in polymers is a result of this factor. In bulk viscosity experiments the temperature T_∞ is a hypothetical temperature where all motion associated with viscous flow ceases, and is related to the glass transition temperature of the polymer, T_g. A brief explanation of the form of this factor is as follows. The fluidity of molten polymers is known to vary with temperature according to a factor of the form[16,136] $\exp[-U^*/R(T - T_\infty)]$ between T_g and $T_g + 100°K$. Though considerable departures from the "universal" values are known to occur, the quantity U^* is generally within 10–15% of 4100 cal/mole and T_∞ is usually within about 5–10°K of being 50°K below T_g. Neither U^* nor T_∞ is a strong function of the molecular weight, at moderate to high molecular weights where T_g does not vary significantly. According to current views, the variation of the fluidity with temperature is governed mostly by the temperature dependence of the jump rate, i.e., both are proportional to $\exp[-U^*/R(T - T_\infty)]$; the absolute value of the fluidity depends on additional factors, such as the molecular weight, which enters as $M^{-3.4}$. The jump rate does not depend strongly on the molecular weight.† Hence, we use a factor of the form $\exp[-U^*/R(T - T_\infty)]$ on a trial basis as the correct form for the principal temperature dependence of β, and expect it to apply, within broad limits, to the crystallization process in polymers of moderate to high molecular weight. The values of U^* and T_∞ that apply to the crystallization process need not, however, be exactly the same as those that apply to bulk fluidity. It will in fact emerge

† Note that it has not been implied that β is proportional to the absolute value of the fluidity. If this were done, β would vary as $M^{-3.4}$, where M is the molecular weight. As stated, $\exp[-U^*/R(T - T_\infty)]$ is not particularly dependent on molecular weight for polymers where the chain length is high enough so that T_g is essentially independent of molecular weight. The crystal growth rate of a polymer from its melt at a specified undercooling does not vary with molecular weight nearly so sharply as $M^{-3.4}$.

that the values of U^* and T_∞ applicable to the crystallization process probably refer to motions near and within a physically adsorbed layer of molecules that exists on the surface of the crystals.[28]

The factor J_1 is inserted into Eq. (28) to allow for any barriers not explicitly accounted for by $\exp[-U^*/R(T - T_\infty)]$ and is assumed to be of the usual form $\exp(-\Delta F^\ddagger/RT) = \exp[-(\Delta H^\ddagger/RT) + (\Delta S^\ddagger/R)]$. In general, we would expect J_1 to be 10^{-2} to perhaps 10^{-5}. Compared to $\exp[-U^*/R(T - T_\infty)]$, the temperature dependence of J_1 is small, so J_1 will generally act as a preexponential factor that simply reduces β.[28]

For dilute solutions $\exp[-U^*/R(T - T_\infty)]$ is inappropriate, and we write β as $c'(kT/h)\exp[-(\Delta H^*/RT) + (\Delta S^*/R)]$, where c' is a function of the polymer concentration. Here ΔH^* is the activation energy of diffusion in solution, which will usually be small, $\sim$1–3 kcal/mole.

The form of β is empirical in character, which is not surprising in view of the fact that no completely satisfactory molecular theory of fluidity applicable to polymers near the glass transition has yet been devised that gives an expression of the form that is known to fit experimentally, namely $\exp[-U^*/R(T - T_\infty)]$. We note, however, that Adam and Gibbs[137] have succeeded in obtaining an approximation to it. Most likely, a cooperative effect at least partly underlies this form of the temperature dependence. Nevertheless, we shall find the form of β to be quite satisfactory in understanding polymer growth rates at low temperatures. The known growth rate data in bulk polymers are not well accommodated by using the assumption of a constant activation energy whenever extensive and accurate data are available at low temperatures.

Having discussed β, we can now connect the net nucleation rate S_T to a growth rate G.

3.4.2. Growth Rate for the Case Where the Formation of a Surface Nucleus Is Followed by Rapid Completion of the Substrate (Regime I)

Assuming that each surface nucleation act, once accomplished, quickly completes the growth strip of length L, adding a layer of thickness b before a new nucleation act occurs, we have[28] $G = biL$ or

$$G\,(\text{cm/sec}) = bS_T n_s/N = bLS_T/aN \tag{29}$$

where N is Avogadro's number and n_s the number of sites or step elements corresponding to the length of the substrate, i.e., $n_s = L/a$. The number n_s will be perhaps 10^4–10^7. Taking $N_0 = N$, and inserting S_T from Eqs. (20) and (28) into Eq. (29), we have[28]

$$G = G_0 \exp[-U^*/R(T - T_\infty)] \exp[-4b\sigma\sigma_e/(\Delta f)kT] \qquad (30)$$

(regime I, bulk polymer)

for bulk polymers, where factors not strongly dependent on temperature are gathered into the preexponential factor

$$G_0 = b(kT/h)n_s J_1 \exp(2ab\sigma_e\psi/kT) \qquad (31)$$

(regime I, bulk polymer)

In writing Eq. (31) we have set $P/l_u = 1$, which is correct to within an order of magnitude under most conditions. The factor J_1 is perhaps 10^{-2}–10^{-4}, and the factor $\exp(2ab\sigma_e\psi/kT)$ varies from unity to 10^3 at the maximum. The factor $b(kT/h)$ is about 10^5. Accordingly, one would expect G_0 for regime I type crystallization to be within several orders of magnitude of $10^4 n_s$ cm/sec for bulk polymers. For dilute solutions $\exp[-U^*/R(T - T_\infty)]$ is replaced by $\exp(-\Delta H^*/kT)$ and G_0 becomes $c'b(kT/h)n_s \exp(2ab\sigma_e\psi/kT) \exp(\Delta S^*/R)$, where c' is a function of the concentration.

We remark here that Sanchez and DiMarzio[125] have treated theoretically the concentration dependence of the growth rate of folded crystals in the dilute range. Experimentally,[138] the dependence is somewhat surprising, the growth rate varying approximately as $c^{1/3}$, where c is the concentration. This is the reason that c' above is denoted as a function of the concentration rather than the concentration itself. This behavior was explained in terms of nucleation on the substrate by cilia from the previous layer.[125] We observe here that the "local" concentration resulting from surface adsorption of polymer molecules could vary less than the actual concentration c, and thus could also contribute to a growth rate that depended on less than the first power of the concentration.

3.4.3. Growth Rate for the Case Where Numerous Nuclei Form on the Substrate and Spread Slowly (Regime II)

In the event that surface nuclei form in large numbers on the substrate at a rate i and spread slowly at a velocity g, it has been pointed out by Sanchez and DiMarzio[139] that the polymer crystal

growth rate is proportional to the *square root* of the surface nucleation rate, i.e., $(ig)^{1/2}$. The basic difference between this type of growth and that where substrate completion on nucleation is rapid is shown in Figure 25. In our notation $i = S_T/Na$ in nuclei cm^{-1} sec^{-1}, and g is in cm/sec. Then we find

$$G \text{ (cm/sec)} = b(ig)^{1/2} = b(S_T g/aN)^{1/2} \tag{32}$$

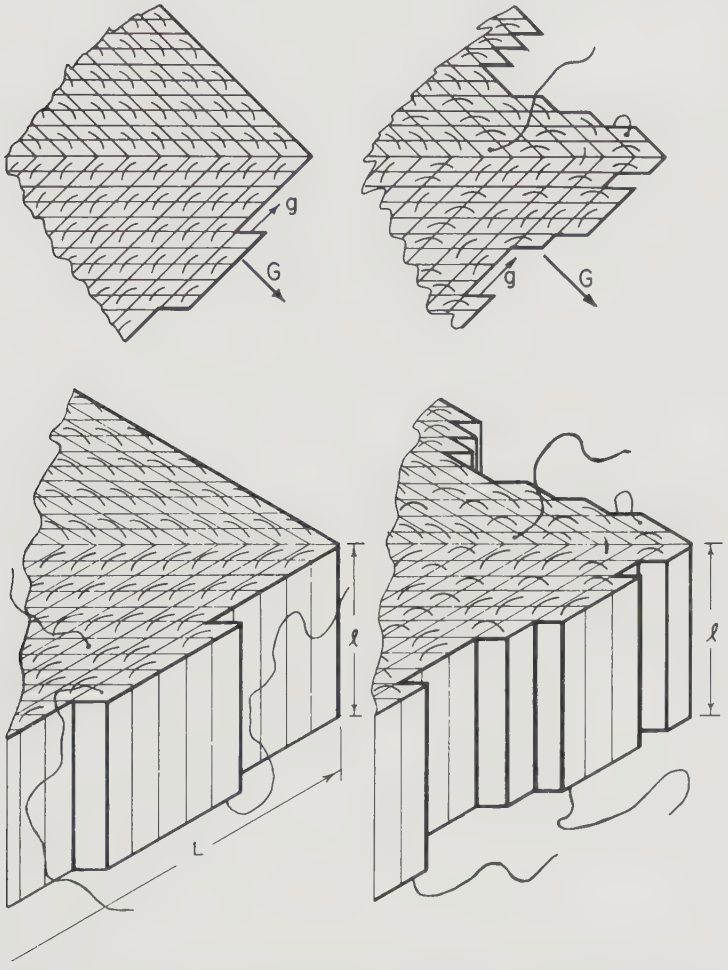

Fig. 25. Growth front morphology for regime I and regime II growth (schematic). Regime I: diagrams at left. Single nucleus forms on surface, rapidly completes new layer. Folds are all parallel to edge of crystal; $K_g = 4b\sigma\sigma_e T_m^0/(\Delta h_f)k$. Regime II: diagrams at right. Many new surface nuclei form before previous layer is complete, leading to reentrant or crenelated growth front. Some folds are now parallel to direction of overall growth; $K_g = 2b\sigma\sigma_e T_m^0/(\Delta h_f)k$.

where we have omitted a numerical factor multiplying $b(ig)^{1/2}$ that is within an order of magnitude of unity. In terms of the molecular width a and the rate constants (see Figure 23) the value of g in cm/sec is given by

$$g = a(A - B) \tag{33}$$

When A and B are evaluated for $l = (2\sigma_e/\Delta f) + \delta l$ we find

$$g = a\beta Q \exp[-2ab\sigma_e(1 - \psi)/kT] \tag{34}$$

where the factor Q is of the order of unity. Insertion of Eq. (20) and (28) for S_T and Eq. (34) for g into Eq. (32) for G leads to[28]

$$G = G_0 \exp[-U^*/R(T - T_\infty)] \exp[-2b\sigma\sigma_e/(\Delta f)kT] \tag{35}$$

(regime II, bulk polymer)

where

$$G_0 = b(kT/h)J_1 \exp[ab\sigma_e(2\psi - 1)/kT] \tag{36}$$

(regime II, bulk polymer)

where a factor $(PQ/l_u)^{1/2}$ has been set equal to unity.

Equation (35) for G for regime II differs from the corresponding expression for regime I, Eq. (30), by a factor of one-half in the nucleation exponent. By a procedure parallel to that used for regime I, it is estimated that G_0 for regime II (bulk) will be within several orders of magnitude of 10^2 cm/sec. As before $\exp[-U^*/R(T - T_\infty)]$ is replaced by $\exp(-\Delta H^*/RT)$ for dilute solutions, and G_0 becomes

$$c'b(kT/h) \exp(\Delta S^*/R) \exp[ab\sigma_e(2\psi - 1)/kT]$$

The ratio of the G_0 values for regimes I and II is†

$$G_0(\mathrm{I})/G_0(\mathrm{II}) = n_s \exp(ab\sigma_e/kT) \tag{37}$$

Thus it is certain from Eq. (37) that $G_0(\mathrm{I}) \gg G_0(\mathrm{II})$ for a given polymer. Regime II crystallization leads to a rough or crenellated growth front on a molecular scale, as depicted in Figure 25. Hillig[140] has considered somewhat similar situations in other types of crystals.

† A more exact derivation gives an extra factor $z^{1/2}$ in the right-hand-side of Eq. (37), where $z = l_g^*/l_u$ is the number of monomer units corresponding to the fold period l_g^* (see Ref. 160).

3.4.4. Criteria for Regimes I and II

A comparison of Eqs. (30) and (35) shows that the general expression

$$G = G_0 \exp[-U^*/R(T - T_\infty)] \exp[-K_g/T(\Delta T)f] \tag{38}$$

is consistent with both regimes I and II. When crystallization conforms with regime I

$$K_{g(\mathrm{I})} = 4b\sigma\sigma_e T_m^{\,0}/(\Delta h_f)k \tag{39}$$

and for regime II

$$K_{g(\mathrm{II})} = 2b\sigma\sigma_e T_m^{\,0}/(\Delta h_f)k \tag{40}$$

The factor f in Eq. (38) is the same as that in Eq. (10). As will be shown in some detail, Eq. (38) fits the growth rate data for polymers in bulk with high accuracy. It will be shown that the K_g values obtained from the analysis of data are consistent with the σ and σ_e values obtained by various independent methods. For dilute solutions $\exp[-U^*/R(T - T_\infty)]$ in Eq. (38) is replaced by $\exp(-\Delta H^*/RT)$.

It remains to be shown how an estimate is made of whether crystallization in a given polymer is in regime I or regime II.

Lauritzen[141] has shown that the parameter governing the distinction between regimes I and II is the dimensionless quantity

$$Z = iL^2/4g \tag{41}$$

If Z is 0.01 or less, strict adherence to regime I behavior is expected, and K_g is $4b\sigma\sigma_e T_m^{\,0}/(\Delta h_f)k$. If $Z = 0.1$, regime I behavior is approximated within about 10%. When $Z \geq 1$, regime II is approached, and K_g tends toward $2b\sigma\sigma_e T_m^{\,0}/(\Delta h_f)k$. The lamellar thickness is unaffected by whether crystallization occurs in regime I or regime II.

It is possible to estimate i/g within certain limits from the experimental value of K_g obtained by analyzing data on a polymer using Eq. (38). One finds that[28,141]

$$Z = iL^2/4g \approx 10^3(L/2a)^2 \exp[-X/T(\Delta T)] \tag{42}$$

$X = K_g$ for test of regime I, $Z \leq 0.01$

$X = 2K_g$ for test of regime II, $Z \geq 1$

Using the measured value of K_g, it is possible to estimate the range of L values consistent with regime I or regime II behavior. What

frequently happens is that such estimates give reasonable values of L for one regime and completely unrealistic values for the other, thus allowing a clear choice between them. The effective length L of a lamella in bulk is thought to be controlled by a number of factors, including impingements, noncrystallographic branching frequency, and accumulations of noncrystallizable impurities.[4]

Some comment is required on the conditions required to obtain lineal growth with the theories presented for regimes I and II. Lineal growth is defined as that where the growth rate dx/dt of some dimension x of a crystal is a constant at a fixed temperature. In regime I this condition is satisfied only if $n_s = L/a$ in Eq. (29) is a constant. It is well known that the growth rates of spherulites and axialites from the melt are usually lineal, which implies a constant n_s or L if they crystallize according to regime I kinetics. A constant n_s can be expected in a spherulite if the frequency of branching is constant as the object grows. (Recall that branching of the lamellae is required to allow a spherulite to become an essentially spherical body.) A constant branching frequency appears to be reasonable in terms of what is known from morphological studies, so lineal growth may be expected for spherulites whose growth follows regime I kinetics. Single crystals growing under regime I kinetics would appear to pose a problem if L in Eq. (29) is identified with the length of the edge of the crystal; in such a case dx/dt is proportional to L, and the growth would be nonlineal. Experimental data on single crystals generally support the concept of lineal growth. A closer examination suggests that L in such a case should be identified as a "persistence length" that is smaller than the crystal edge.[141,142] In such a case L will be a constant independent of the size of the crystal, which will give lineal growth.† Such a persistence length can exist well within regime I. Only crystals whose edges are less than the persistence length would show nonlineal growth. Nonlineal growth must be regarded as an extreme condition that will obtain only for extremely small crystals well within regime I. When the surface nuclei become extremely numerous, regime II is approached. It is seen from Eq. (32) and from Eq. (36) for G_0 that the growth rate for regime II does not contain a factor n_s, so the growth in regime II is always predicted to be lineal, as is observed experimentally.

† The persistence length effect should cause the edge of a crystal growing in a lineal manner in regime I to show crenelations or steps of different size whose average length corresponds to L, and under favorable circumstances these might be observable. Rough estimates for the case of polyethylene suggest that L is of the order of magnitude of 1 μm (see Ref. 160).

The behavior of Z is such that its temperature dependence is largely controlled by the variation of i. As a consequence, regime I behavior has a tendency to prevail at high temperatures, and regime II behavior at low temperatures, given anything approaching a slow variation of L with temperature. A number of polymers conform to regime I in the main nucleation-controlled region at high temperatures, e.g., poly(chlorotrifluoroethylene), while others, e.g., isotactic polystyrene, fall almost entirely into regime II.[28] As will be discussed subsequently, polyethylene fractions in bulk undergo a growth rate transition at about 127°C, above which regime I behavior obtains, and below which regime II behavior appears to occur. Usually, the question of whether growth is in regime I, regime II, or in between can be resolved, and examples will be given where this can be done.

3.5. Interpretation of ψ

Before proceeding to the analysis of growth rate and lamellar thickness data comment is required on the nature of ψ. This parameter is concerned with the path by which the first step element of the surface nucleus is attached to the surface.

If the polymer molecule goes down directly from the solution or subcooled melt onto the surface without an intervening state in such a manner that each segment simultaneously acquires its lateral surface and free energy of fusion, $\Delta\phi$ rises monotonically as ν goes from zero to unity. A comparison with Eq. (11) shows that this corresponds to $\psi = 1$ (see Figure 26). On the other hand, if the polymer molecule is physically adsorbed onto the surface prior to crystallographic attachment—a condition that we consider unavoidable at least as a transitory state in strongly undercooled systems—a term similar to $2b\sigma l$ will tend to be incurred first, and then crystallographic attachment leading to the free energy of fusion will take place after a localized migration (Figure 27). The adsorbed polymer molecule, whether it be from the melt or dilute solution, will resemble a two-dimensional random walk (or alternatively a considerably flattened three-dimensional one) with a number of contacts on the surface of the crystal.[29–33] Depending on the attraction energy ε of each segment to the surface, the fractional coverage θ will range from perhaps 10 to 50%, thus effectively blocking any deposition of a whole step element directly from the melt as for $\psi = 1$. Meanwhile the "loops" or sets of segments between the random contacts on the surface will in places become stretched out enough (in noncrystallographic planes) to in effect produce regions where a lateral surface free energy $4b\sigma l_u$ per monomer

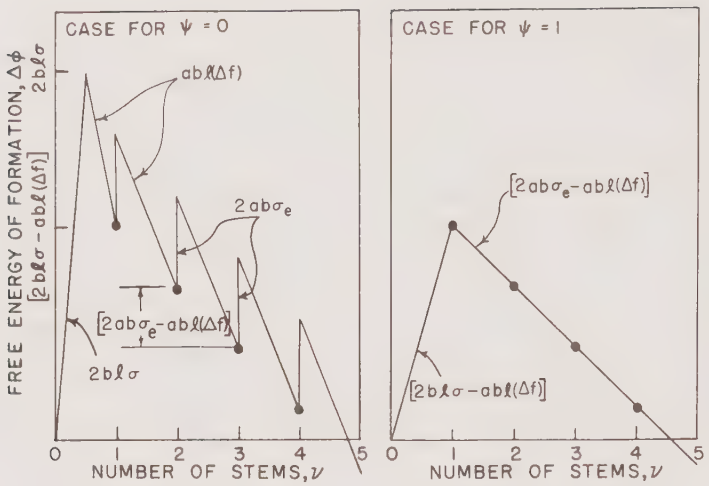

Fig. 26. Free energy of formation of surface nucleus for $\psi = 0$ and $\psi = 1$ (schematic). The case $\psi = 1$ corresponds to that where each polymer chain segment in the formation of the first stem simultaneously gains its free energy of fusion $abl_u \Delta f$ and incurs a cost of $2b\sigma l_u$. This corresponds to crystallographic attachment of the first stem directly from the subcooled state. The barriers between $\nu = 1$ and $\nu = 2$ and between all higher ν have been omitted. The case $\psi = 0$ corresponds to that where a chain is adsorbed in such a way as to first incur a cost $2b\sigma l$ without simultaneously regaining any free energy of fusion. The free energy of fusion is gained subsequently when the stem migrates and attaches crystallographically to the substrate. The cases $\psi = 1$ and $\psi = 0$ are extremes, and $1 > \psi > 0$ is expected in real systems.

unit is incurred without involving any corresponding free energy of fusion. (We refer to such segments as being in a state of "weak" physical adsorption.) It is polymer segments in this condition that will lead to ψ values below unity. Migrations and rotations then allow crystallographic attachment of these weakly adsorbed segments to take place.† It can be shown that one example where $\psi = 0$ corresponds

† The barrier between the steps $\nu = 0 \rightarrow \nu = 1$ is somewhat larger for the case $\psi = 0$ than for $\psi = 1$. It might therefore be argued that ψ must be unity for the first step since this represents the nucleation path with the lowest barrier. This argument is invalid since it ignores the fact that the presence of adsorbed molecules on the surface is essentially imposed on the system independent of the occurrence or absence of crystallization. The effect of these adsorbed molecules on the nucleation path must therefore be considered, and the result is that ψ values below unity must be anticipated. In simple terms, when the surface is initially partly covered with many segments in a state of weak adsorption the most probable initial nucleation path actually accessible to the system corresponds to a ψ value below unity.

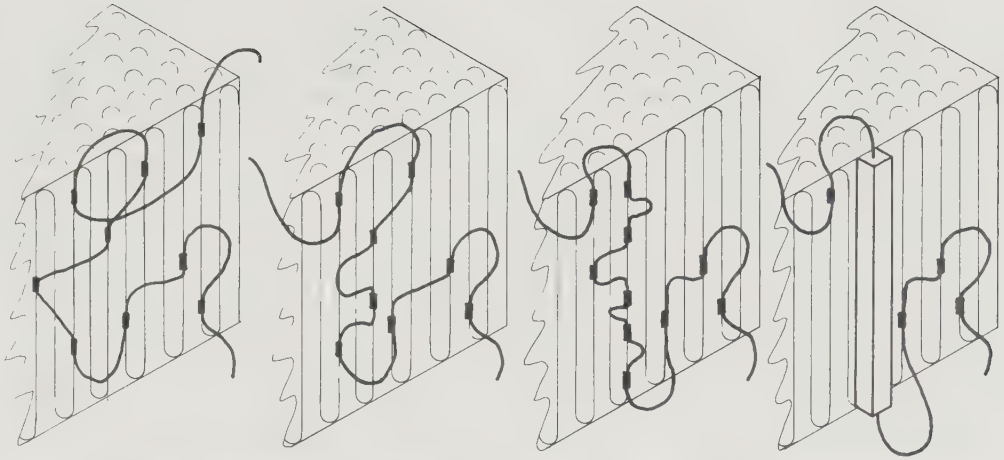

Fig. 27. Surface adsorption prior to crystallization. Physical adsorption and subsequent migration and rearrangement with time (left to right) prior to actual crystallographic attachment (extreme right) of first stem. "Stretched" segments between adsorption points indicate how lateral surface can be created without simultaneously gaining the free energy of crystallization, leading to values of ψ below unity. Although not shown, other polymer molecules will be adsorbed on the lateral surface, covering it sufficiently to prevent frequent acts of crystallographic attachment directly from the subcooled liquid or solution state. Molecules will also be adsorbed on the fold surface.

to the weak adsorption from the subcooled liquid of a set of segments between point contacts with a total length that is just half the fold period, followed by surface migration and crystallographic attachment of this set of units to the substrate, with simultaneous deposition of other units in the chain to complete the stem.[28]

Both the conditions $\psi = 1$ and $\psi = 0$ must be regarded as extremes, and the case $1 > \psi > 0$ is expected in real polymers.

The concept that mobile adsorbed atoms or molecules are involved in crystallization is not new. In crystallization directly from the gas phase onto a crystal of a simple substance the sequence diffusion to surface → surface attachment → surface migration → crystal attachment is sometimes involved. Such cases are well known, for instance, in crystallization of metals from the vapor. A theory for the crystallization of such mobile adsorbed atoms (adatoms) has been developed by Burton, Cabrera, and Frank[143] and is included in the comprehensive review of crystal growth mechanisms by Parker.[144]

3.6. Effect of Chain Ends

Although we do not give it here, a theory of the type proposed in this work for $G(T)$ and $l_g^*(T)$ can be generalized to include the effect of chain ends. In the approximation where chain ends are restricted to the zone of the fold surface[145] the results are as follows. Assuming a sharp fraction of a moderately low molecular weight, the theory predicts crystals with no folds at low undercoolings, once-folded chain crystals at slightly higher undercoolings, twice-folded crystals at a still higher undercooling, and so on. In brief, the l_g^* versus T curve no longer falls smoothly with lowering temperature according to $l_g^* = (C_1/\Delta T) + C_2$, but falls instead in definite steps where the lamellae have a thickness corresponding to the extended chain, then a once-folded chain, a twice-folded chain, and so on. The theory converges toward the one given here when the number of folds in the chain in the crystal exceeds three or four. Meanwhile the theory for the growth rate as a function of temperature shows corresponding changes of slope in a plot of G versus T at the temperatures where the breaks occur in the l_g^* versus T curve. The theory predicts no observable "quantization" of the l_g^* versus T and G versus T curves for moderate- and high-molecular-weight fractions.

The data of Arlie *et al.*[60] show the stepwise character of the l_g^* versus T data, and the extensive data of Kovacs and Gonthier[133] on sharp fractions of poly(oxyethylene) of low molecular weight

clearly exhibit both the breaks in the lamellar thickness curve and the corresponding disturbances in the growth rate curve.

Hoffman *et al.*† have shown that a large variation between high and low K_g values occurs as the molecular weight is increased in polyethylene fractions of low molecular weight crystallized from the melt. This variation was tentatively interpreted in terms of a cilium length associated with a surface nucleus forming on a substrate of fixed height l_g^* that could repeatedly vary between zero and l_g^* as the molecular weight (contour length) increased. This case differs from that where the chain ends are confined to the fold surface. It can be applied to molecular weights corresponding to two or more folds per molecule. The theory converges toward that outlined in this chapter when the number of folds per molecule exceeds about five.

The results noted above give further insight into the question of the chain length that is required to allow chain folding. The outcome is that the onset of folding is a function of the undercooling and the chain length that is used, with a high chain length and high undercooling both acting as effective agents for promoting the appearance of folded crystals. In addition, the data from the experiments quoted on poly(oxyethylene) and polyethylene fractions provide convincing examples of adjacent reentry type chain folding in melt-crystallized polymers. To our knowledge no one has seriously suggested that there is any important degree of nonadjacent or random ("switchboard") reentry in a once- or twice-folded chain crystal.

The theories that involve chain ends are capable of predicting fractionation of a polymer containing a distribution of chain lengths during crystallization on a kinetic basis. An elementary approach[16] suggests that the molecular length l_r below which a molecule will be rejected rather than crystallize varies as $1/(\Delta T)^2$.

4. Comparison of Theory and Experiment

4.1. Objectives

Although neither the treatment of crystal growth with chain folding allowing fluctuations of the fold period in the surface nucleus and growth strip, nor the treatment of homogeneous nucleation have been given, it is convenient at this point to carry out a considerable part of the comparison of theory and experiment. The theory without

† See Ref. 160 for a discussion of the case of polyethylene fractions.

fluctuations will prove to be adequate for most purposes. A discussion of the melting behavior associated with the theory has already been outlined in Section 2.

It will be shown first that the expression for the rate of growth developed for bulk polymers accurately fits the data for a number of polymers over a wide range of temperature. A similar result is shown for the expressions for the rate of crystallization from dilute solution, though the data are fewer and the temperature range rather limited. The foregoing provides values of U^* and T_∞ in the jump-rate term in the case of bulk polymers, and also yields values of the nucleation exponent K_g for both melt-crystallized and solution-crystallized polymers. Then it will be shown that the $\sigma\sigma_e$ value obtained from each K_g can be split into its two factors σ and σ_e by various techniques. These σ and σ_e values, when inserted into the expression for l_g^*, give an adequate description of the temperature dependence and magnitude of the initial thickness of the chain-folded crystals for two polymers where data are available to allow a comparison with experiment. It will also be noted in one case that the $\sigma\sigma_e$ values obtained from the rate of crystallization from dilute solution and from the melt are the same within experimental error. Furthermore, σ and σ_e agree closely with the values obtained by other means.

Next the prediction that the crystal thickness near the melting point is principally a function of the undercooling rather than the absolute temperature is considered. It is shown that the experimental data on single crystals in various solvents are consistent with the theoretical development. Finally, a generalized treatment is given that shows that the main variable in the nucleation constant K_g is actually the work of chain folding q. The value of q is estimated for a number of polymers, and shown to be consistent with simple considerations based on the flexibility of the linkages in the polymer chain.

4.2. Growth Rate versus Crystallization Temperature Curves

The first objective is to determine if Eq. (38),

$$G = G_0 \exp[-U^*/R(T - T_\infty)] \exp[-K_g/T(\Delta T)f]$$

which from a theoretical standpoint holds for both regime I and regime II crystallization from the melt, actually fits the data. Special emphasis is placed on obtaining estimates of U^*, T_∞, and K_g. This requires consistent data over a wide range of undercooling. The theoretical

curve for $G(T)$ at first rises rapidly as the temperature is lowered from T_m^0, goes through a maximum at an intermediate temperature, and then falls again at low temperatures (Figure 24). The rise is largely controlled by the factor $\exp[-K_g/T(\Delta T)f]$, and the fall at low temperatures is mostly controlled by the factor $\exp[-U^*/R(T - T_\infty)]$.

Accordingly, this part of the analysis is conducted with linear polymers where, with one exception, the growth rate data are extensive enough to exhibit the maximum in G. Also, the analysis is restricted to those polymers where reasonable estimates of T_g and T_m^0 are available.†

The procedure used is reminiscent of that given by Suzuki and Kovacs for isotactic polystyrene.[7] Fundamentally what is done once T_m^0 is fixed is to assume a set of values of T_∞ and U^* and then fit $\ln G + U^*/R(T - T_\infty)$ to a linear relation in $1/T(\Delta T)f$. (Recall that T_∞ is below the glass transition temperature T_g.) This analysis produces values of G_0 and K_g for each set of U^* and T_∞, and the precision of the fit may be expressed by a correlation coefficient. Values of U^* and T_∞ are then varied separately to maximize the correlation coefficient. Table 1 shows the results of some sample calculations. Any correlation coefficient above 0.99 represents an extremely good fit of the data. The correlation coefficient also reflects any scatter in the data. A comparison of the growth rate data with the straight line corresponding to the "best-fit" values in Table 1 are shown in Figure 28 for polystyrene, nylon 6, and TMPS as plots of $\log_{10} G + U^*/R(T - T_\infty)$ versus $1/T(\Delta T)f$.

Note that values of U^* in the vicinity of 1000–1600 cal/mole and T_∞ values that are about 30°K below T_g yield an excellent fit. This data analysis agrees with that of Suzuki and Kovacs[7] for polystyrene.

† The difficulties associated with determining an exact T_m^0 have been alluded to previously. Polyethylene has been investigated most thoroughly in this respect, and it is instructive to examine the results as a guide to other cases. The highest melting point observed for substantially chain-folded polyethylene crystallized from the melt at atmospheric pressure followed by long annealing is 138.5°C[146]; samples are readily made that melt in the range 136–137°C. A correlation between melting point and molecular length of the *n*-paraffins, when extrapolated to infinite chain length, leads to an estimated T_m^0 of 144.7 ± 0.5[147] and 145.5 ± 1.[148] The procedures involving T_m versus $1/l$ and T_m versus T_x (see Figures 17 and 18) lead to an estimated T_m^0 of 145.8 and 145.5°C, respectively. If one takes T_m^0 to be 145.5 ± 1°C, it is seen that T_m^0 is 6–8°C higher than the highest observed value for samples crystallized under "normal" conditions where chain folding occurs. (It is of interest to note that a melting point of 146.0°C has been reported based on dilatometer results with a very slow warming rate on fibrillar material.[149]) In the absence of such extensive data for T_m^0 on other polymers it will be helpful to refer to the aforementioned difference of 6–8°C in estimating T_m^0 from the highest melting point actually observed for the polymer crystallized under normal conditions.

TABLE 1

Illustration of Method of Determining Best Values of U^*, T_∞, and K_g in Eq. (38)†

T_m^0, °K	T_∞, °K (assumed)	U^*, cal/mole (assumed)	G_0, cm/sec	K_g, °K^2	Correlation coefficient
Isotactic polystyrene‡					
515.2	333.5 = $T_g - 30$	1560	2.7×10^{-2}	1.20×10^5§	0.998
515.2	333.5 = $T_g - 30$	4000	2.0×10^{10}	5.3×10^5	0.777
515.2	311.9 = $T_g - 51.6$	4120	1.5×10^5	3.00×10^5	0.905
527.2	0	21,000	6.9×10^3	0.21×10^5	0.012
Nylon 6[150]					
505.2	273 = $T_g - 30$	1430	6.5	1.74×10^5§	0.997
505.2	273 = $T_g - 30$	4000	2.7×10^8	4.1×10^5	0.894
505.2	251.4 = $T_g - 51.6$	4120	2.4×10^6	3.24×10^5	0.943
505.2	0	13,000	2.2×10^5	1.68×10^5	0.979
TMPS polymer M.W. = 56,000[151]					
427	219.2 = $T_g - 30$	990	2.16×10^{-1}	1.14×10^5§	0.995
427	219.2 = $T_g - 30$	4000	9.78×10^6	2.05×10^5	0.896
427	197.6 = $T_g - 51.6$	4120	1.84×10^5	1.75×10^5	0.945
427	0	13,000	2.12×10^6	1.39×10^5	0.990

† Analyzed using $f = 2T/(T_m^0 + T)$.

‡ Data of Suzuki and Kovacs.[7] Values of U^*, T_∞, G_0, and K_g for best fit are virtually identical to those given in Ref. 7.

§ "Best-fit" value.

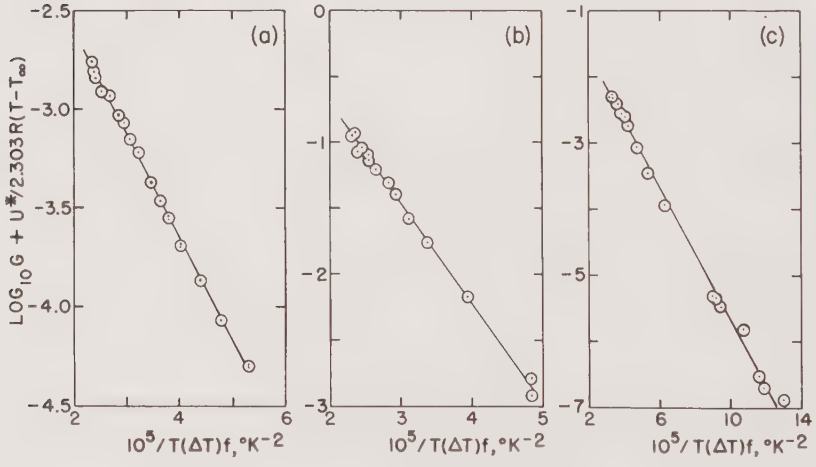

Fig. 28. Determination of K_g and G_0. Spherulitic growth rate G in cm/sec for three different polymers plotted according to Eq. (38). Values of T_m^0, T_∞, and U^* are the "best fit" values listed in Table 1. (a) Isotactic polystyrene, (b) Nylon 6, (c) TMPS (M.W. = 56,000).

Furthermore, the growth rate data of Nylon 6[150] and poly(tetramethyl-*p*-silphenylene siloxane),[151] which we denote TMPS, can be accounted for with about the same values for the jump-rate parameters U^* and T_∞. In the region of good fit K_g is not particularly sensitive to variations of U^*; if U^* is varied by ± 200 cal/mole, K_g shows a variation of only 0.02×10^5 for TMPS and 0.4×10^5 for polystyrene. In other treatments of growth rate data[152] the transport term $\exp[-U^*/R(T - T_\infty)]$ would be replaced by $\exp(-E_D^*/RT)$, where E_D^* is a constant activation energy that is independent of temperature. Such an expression yields a far inferior fit to the data for polystyrene, as was shown graphically by Suzuki and Kovacs,[7] and by the correlation coefficients for this case in Table 1 (see entry with $T_\infty = 0$). In the case of Nylon 6 the fit using $\exp[-U^*/R(T - T_\infty)]$ is also clearly superior to that using the best value of E_D^* in $\exp(-E_D^*/RT)$, and to a much lesser extent the same result is true for TMPS polymer. Figure 29(a–c) show the fit of the theoretical expression for $G(T)$, or more precisely $G(\Delta T)$, to the data for the polymers given in Table 1. It can be seen from these figures and the correlation coefficients in Table 1 that Eq. (38) fits the growth rate data extremely well.

The values of U^* and T_∞ obtained from growth rate data are rather different from those found from the temperature dependence of the bulk fluidity. From fluidity measurements $U^* \sim 4120$ cal/mole and $T_\infty \sim T_g - 51.6°\text{K}$,[136] while from growth rate measurements most of the data are accounted for by values in the vicinity of $U^* \cong 1500$ cal/mole and $T_\infty = T_g - 30°\text{K}$. (In the specific case of polystyrene U^* is 3830 cal/mole and T_∞ is $T_g - 60.9°\text{K}$, as determined from fluidity measurements.[7] It has been proposed that the U^* and T_∞ values in the case of crystallization relate to motions in a physically adsorbed yet mobile surface layer of molecules on the crystal.[28] It is reasonable to suppose that such a layer would tend to have a somewhat higher effective "glass transition" temperature than the bulk phase, which is consistent with the results. Also, a moderately low activation energy can reasonably be associated with the motion of weakly bound molecules in surface layers. It will be shown subsequently that l_g^* can only be predicted for polyethylene and polystyrene if $\psi < 1$. Recall from the theoretical development given in the previous section that the result $\psi < 1$ also implies that crystallization takes place with the intervention of an adsorbed surface layer.

As seen in Table 1, the variation of G_0 with various assumed values of U^* and T_∞ is extremely large. The latter two parameters, and hence G_0, are well defined by the data only when growth rates

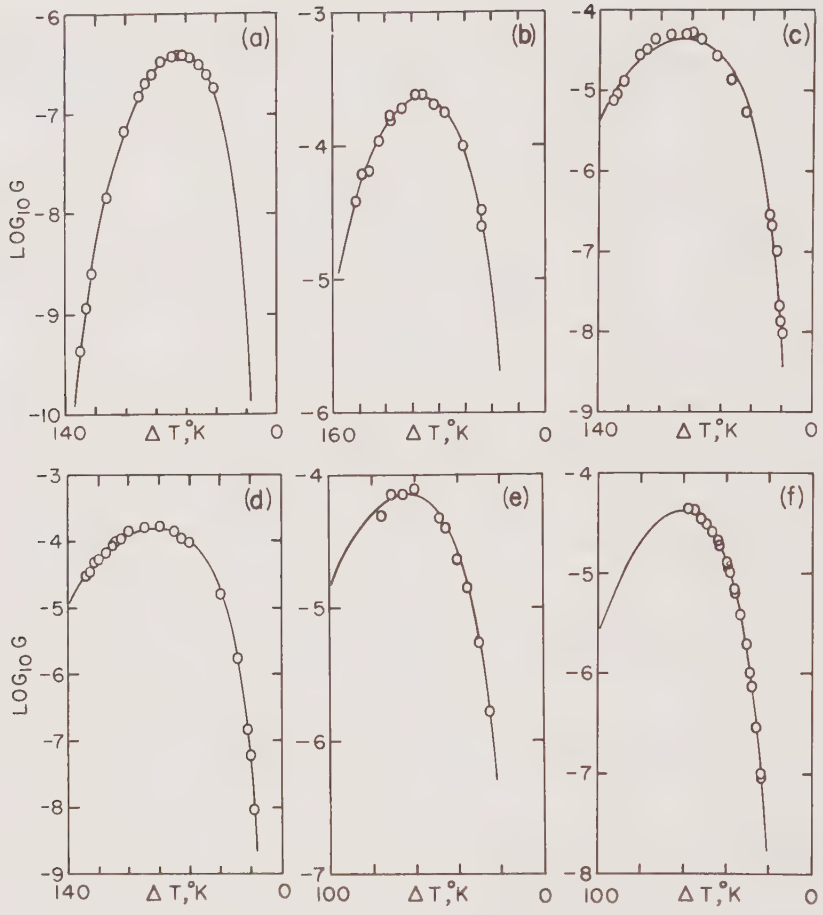

Fig. 29. Comparison of theory and experiment for $G(\Delta T)$. Spherulitic growth rate data in cm/sec (circles) as a function of undercooling are compared with the curves (solid lines) which result from the fitting procedure outlined in the text for Eq. (38). Values of T_m^0, T_∞, and U^* used in Eq. (38) are those indicated by "best fit" in Table I, and by entries in Table 2. (a) Isotactic poly(styrene), (b) Nylon 6, (c) TMPS (M.W. = 56,000), (d) TMPS (M.W. = 8700), (e) poly(oxypropylene), and (f) poly(chlorotrifluoroethylene).

are measured over a wide range of temperature, and most especially into the region where the jump-rate term becomes dominant. It is clear, then, that when only limited data are available and estimates of U^* and T_∞ must be used in the analysis of data, G_0 can easily be in error by several orders of magnitude. Despite this uncertainty, we find no justification in the present analysis for the assertion to be found in the literature[152] that G_0 is the same for various bulk polymers.

A value of G_0 that was constant for different polymers would not be expected on theoretical grounds, since in the present formulation G_0 can depend strongly on whether the crystallization occurs in regime I or regime II. According to Eq. (37), G_0 for regime I is apt to be, say, 10^4–10^8 times greater than that for regime II, and we would therefore not anticipate G_0 to be the same for various polymers. An example of this large variation will be given subsequently for polyethylene. Even within a given regime, factors such as $\Delta F^{\ddagger}$ in the transport factor J_1 can vary from one polymer to another, leading to a large variation of G_0. (For estimates of G_0 for various polymers see tables given later in this chapter.)

The type of analysis discussed above has been carried out for a number of other linear polymers where the data are quite extensive and where, with the exception of poly(chlorotrifluoroethylene), a maximum in the growth rate appears. The best fit of these data is given in Table 2. The nature of the agreement is depicted in Figures 29(d–f) for these polymers. For all the polymers in Tables 1 and 2, except poly(chlorotrifluoroethylene), the value of U^* which results in a best fit is within the limits 1300 ± 300 cal/mole. Poly(chlorotrifluoroethylene) is a definite exception. For this polymer no value of U^* much below 3000 cal/mole gives a good fit of the data for any reasonable assignment of T_∞.

Equation (38) is evidently suitable for fitting the growth rate data on a number of polymers with a value of U^* in the vicinity of 1500 cal/mole and a T_∞ that is close to $T_g - 30°K$. Of the six polymers subjected to the test, five obeyed Eq. (38) with a U^* of 1300 ± 300 cal/mole with acceptable accuracy, and all six gave a good fit with $T_\infty = T_g - 30°K$. Depending on the particular polymer, the value of K_g is either weakly or rather strongly sensitive to the choice of U^* and T_∞, but G_0 is always strongly dependent on these choices. A jump-rate term of the form $\exp(-E_D^*/RT)$ could be used,[152] but there are strong indications that it fails when extensive data at low temperatures are available for comparison of theory and experiment.

The fact that $U^* \cong 1500$ cal/mole and $T_\infty \cong T_g - 30°K$ fits much of the data on polymers where an extensive range of temperature is involved suggests their use to estimate K_g for polymers where for various reasons growth rate data can only be obtained in the main nucleation region near T_m^0, a region fortunately not very sensitive to a variation of these parameters. The values of K_g and G_0 obtained using $U^* = 1500$ cal/mole and $T_\infty = T_g - 30°K$ for a number of such polymers are summarized in Table 3.

TABLE 2
Values of U^*, T_∞, and K_g from Best Fit of Growth Rate Data†

Polymer	T_m^0, °K	T_∞, °K	U^*, cal/mole	G_0, cm/sec	K_g, °K^2	Correlation coefficient	Ref.
TMPS (M.W. = 8700)	423	208.7 = T_g − 30	1230	1.38	1.09×10^5	0.999	151
Poly(oxypropylene)	348.2	170 = T_g − 30	1320	2.96	0.785×10^5	0.997	116
Poly(chlorotrifluoroethylene)‡	497.2	295.2 = T_g − 30	4000	6.5×10^4	1.72×10^5	0.999	81
Poly(chlorotrifluoroethylene)‡	497.2	273.6 = T_g − 51.6	4120	1.1×10^4	1.63×10^5	0.999	81

† Analyzed using $f = 2T/(T_m^0 + T)$. Values of U^* and K_g are slightly higher (~5%) when $f = 1$ is used.
‡ Data do not go through a maximum in $G(T)$.

TABLE 3
K_g and G_0 for Polymers with Growth Rate Data in Narrow Temperature Range†

Polymer	T_m^0, °K	T_g, °K	K_g, °K^2	G_0, cm/sec	Correlation coefficient	Ref. T_m	Ref. T_g	Ref. G
trans-1,4-Poly(isoprene)‡	360.2	211	2.17×10^5	1.10×10^3	0.999	153	154	155
Poly(oxymethylene)	459.2	213	1.27×10^5	1.28×10^1	0.985	156	157	158
Poly(ethylene) (spherulites)§	417.8	231	1.15×10^5	2.24×10^3	0.994	147	159	160
Poly(ethylene) (axialites)#	417.8	231	2.16×10^5	4.40×10^9	0.984	147	159	160
Poly(oxyethylene)¶	348.4	206	0.81×10^5	1.15×10^5	0.994	133	161	133
Poly(butene-1) (form II)	401	219	0.79×10^5	2.49	0.981	162	161	162
Selenium	492.4	300	2.53×10^5	4.58	0.986	163	163	163

† Analyzed using $f = 2T/(T_m^0 + T)$. $U^* = 1500$ cal/mole, except for selenium, where $U^* = 2180$ cal/mole yields a better fit of the data. $T_\infty = T_g - 30$°K.
‡ High-melting form, data for M.W. = 165,000 and 400,000 combined.
§ Spherulite growth, M.W. = 30,600, growth temperatures below 127°C (regime II).
# Axialite growth, M.W. = 30,600, growth temperatures above 127°C (regime I).
¶ M.W. = 150,000, $T_m^0 = 6$°K + intercept of T_m versus 1/M.W. plot.

The lack of growth rate data over a wide range of temperature does not necessarily reflect a lack of patience on the part of an investigator. Even at moderate undercoolings the growth rate sometimes becomes so rapid that self-heating arising from the heat of crystallization prevents the attainment of isothermal conditions—even in very thin films—as is the case in polyethylene[112] and polypropylene.[164]† In the case of poly(chlorotrifluoroethylene) the rapid onset of what appears to be homogeneous nucleation at $\Delta T \cong 70°C$ suddenly induces a microcrystallinity in the sample preventing any growth rate data from being measured below 154°C.[81] The melting point of some polymers is high enough so that prolonged storage near the melting point results in thermal degradation and prevents accurate growth rate measurements.[7] Further, growth rates can be discontinuous when the polymer can crystallize in two different crystalline forms as in polypropylene[38] and *trans*-1,4-poly(isoprene)[165] (gutta percha). On the other hand, the lack of data over a wide range of temperature need not imply in all cases that they could not be obtained over a wider range.

The conclusions are as follows. The theoretical expression for $G(T)$ accurately fits the data. When experimental data are available over a sufficiently wide range of temperature, and no phase transitions occur, accurate values of G_0, U^*, T_∞, and K_g can be obtained if T_m^0 is known. The more extensive the data, especially at temperatures below the maximum in $G(T)$, the less likely it is that a constant activation energy in the jump-rate term (corresponding to $T_\infty = 0$) will fit the experimental results. Useful values of K_g can be obtained even on the basis of a limited range of growth rate data if these data are in the nucleation-controlled region near T_m^0, again with the proviso that T_m^0 is known, by carrying out the analysis with $U^* \cong 1500$ cal/mole and $T_\infty \cong T_g - 30°K$. This procedure increases the uncertainty in G_0. There is no indication that G_0 has even approximately the same value for different polymers, though those within a given regime are somewhat more alike.

† Problems connected with transport of heat are prominent in crystallization in systems other than polymers. A perusal of the growth rate scale for each of the polymers in Figure 29 shows that growth in these is everywhere so slow as to preclude any question of heat transport causing any serious temperature anomaly at the site of crystallization in thin films. Even in the case of polyethylene, isothermal crystallization can be achieved at and above about 124°C in thin films. No growth rate data that are affected by self-heating or other difficulties associated with transport of heat have been used in the analyses in this chapter.

We do not assume that because Eq. (38) can be used to fit the growth rate curves that this proves that the growth rate theory is correct. The results obtained so far simply mean that the theory given is consistent with the data. It remains to be shown that the value of $\sigma\sigma_e$ or q implicit in K_g makes physical sense. In the case of polymers where σ_e can be determined independently from T_m versus $1/l$ data, and where initial lamellar thickness data are available, a rather convincing analysis comprising a fit of both $G(T)$ and $l_g^*(T)$ can be made. The experience gained in such an analysis, which essentially amounts to splitting the value of $\sigma\sigma_e$ obtained from growth rate data into its components σ and σ_e, provides information on how to estimate σ empirically. This information can then be used to deal with other polymers.

The procedure for dealing with a polymer where K_g is known, and where σ_e is available independently, is best illustrated by an analysis of polyethylene, which is outlined below.

4.3. Polymers Where Data Allow Test of Expressions for Both Growth Rate and Lamellar Thickness

4.3.1. Polyethylene

The following discussion is patterned after Ref. 28. The value of K_g and hence $\sigma\sigma_e$ for polyethylene is available from several sources. Holland and Lindenmeyer[166] have measured the growth rate of single crystals from dilute xylene solution at various temperatures. These results are shown in Figure 30 as a plot of $\log_{10}G$ versus $1/T(\Delta T)$. The slope gives $K_g = 2.11 \times 10^5\ ^\circ\mathrm{K}^2$. The value of $\Delta H^*/RT$ has been taken as zero in the figure, but the value of K_g is relatively insensitive to the choice of ΔH^* in the range 0–3 kcal/mole. The dissolution temperature used is 387.2°K, which comes from the T_m versus $1/l$ data of Huseby and Bair (see Figure 17).[104] An analysis using Eq. (42) suggests that the growth rate data are just on the border of regime I type crystallization,[28,141] so that to an approximation $K_g = 4b\sigma\sigma_e T_d^0/(\Delta h_f)k$. Accordingly, one finds $\sigma\sigma_e = 1280\ \mathrm{erg}^2/\mathrm{cm}^4$ using the known T_d^0 and heat of fusion (Table 4).† The second source

† In a recent paper Cooper and Manley[167] report growth rates for polyethylene fractions of M.W. = 25,200 and 83,900 in xylene at concentrations of 0.001, 0.01, and 0.1% at temperatures from 86.9 to 90.3°C. As analyzed with $K_g = 4b\sigma\sigma_e T_d^0/(\Delta h_f)k$, which assumes regime I, the average $\sigma\sigma_e$ value is reported as $790\ \mathrm{erg}^2/\mathrm{cm}^4$. If these data are assumed to be midway between regimes I and II, then $\sigma\sigma_e$ may be estimated from $K_g = 3b\sigma\sigma_e T_d^0/(\Delta h_f)k$, and turns out to be approximately $1185\ \mathrm{erg}^2/\mathrm{cm}^4$. Most of the data of Holland and Lindenmeyer[166] were obtained between 88.5 and 93.5°C, where it would be more likely to conform to regime I behavior.

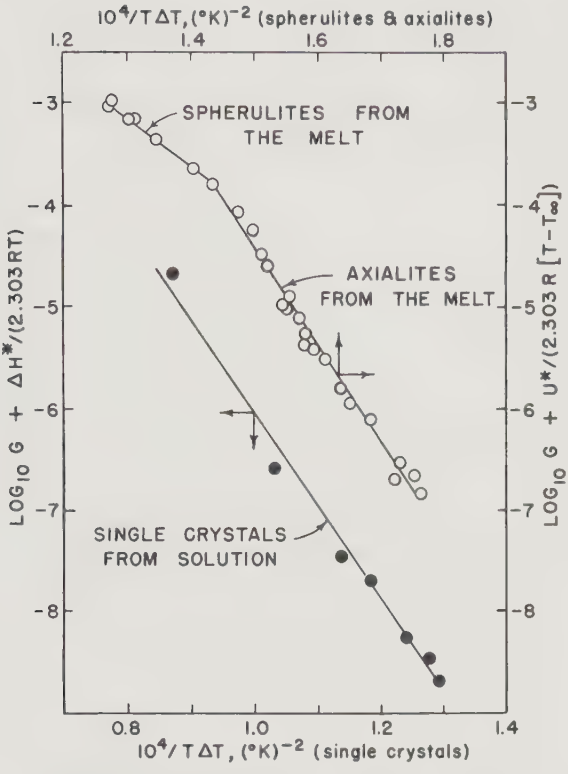

Fig. 30. Determination of K_g for polyethylene (melt-crystallized and dilute solution in xylene). Slope of lines gives K_g according to Eq. (38). Dilute solution data[166] analyzed using $T_d^0 = 387.2°K$ and $\Delta H^* = 0$. Melt-crystallized polymer (M.W. = 30,600) data[160] analyzed with $U^* = 1500$ cal/mole, $T_\infty = 201°K$, and $T_m^0 = 417.8°K$; G is in cm/sec. A change from regime I (axialites) at low undercoolings to regime II (spherulites) at high undercoolings is reflected by the change in slope (K_g) in the melt-crystallized data. Dilute solution data and axialites exhibit similar slopes. The $\sigma\sigma_e$ values calculated for single crystals, axialites, and spherulites are similar (see Table 4).

of K_g is to be found in the growth rate data of axialites[160] in bulk polyethylene, which form in relatively sharp fractions at temperatures above 127°C, and which lead to $K_g = 2.27 \times 10^5\,°K^2$ and thence to $\sigma\sigma_e = 1275\,\text{erg}^2/\text{cm}^4$, using $K_g = 4b\sigma\sigma_e T_m^0/(\Delta h_f)k$ since regime I is indicated by an analysis based on Eq. (42). The K_g given is the average for seven different samples ranging in molecular weight from 3×10^4 to 6.3×10^4. A typical plot of $\log_{10}G + U^*/R(T - T_\infty)$ against

TABLE 4
Polyethylene

Quantity	Value	Remarks
A. *Input data*		
Heat of fusion Δh_f	2.80×10^9 ergs/cm^3	Ref. 110
Dissolution temperature T_d^0 (xylene)	387.2 ± 1°K or 114 ± 1°C	Ref. 104
Molecular width a	4.55×10^{-8} cm	Valid at 100°C, Ref. 110
Layer thickness b	4.15×10^{-8} cm	Valid at 100°C, Ref. 110
Cross-sectional area of chain ab	18.9×10^{-16} cm^2	Valid at 100°C, Ref. 110
Fold surface free energy σ_e	93 ± 8 ergs/cm^2	From T_m versus $1/l$ data, Ref. 104
Work of chain folding q	5.06 kcal/mole	Calculated from $\sigma_e = q/2ab$
Work of chain folding q	4.24 kcal/mole	Calculated from $\sigma_e = (q/2ab) + \sigma_{e0}$ with $\sigma_{e0} = 15$ ergs/cm^2.
K_g (single crystals from xylene)	$(2.11 \pm 0.20) \times 10^5$ °K^2	From data in Ref. 166
K_g (axialites in bulk polymer)†	$(2.27 \pm 0.20) \times 10^5$ °K^2	From data in Ref. 160, using $T_m^0 = 146.5 \pm 1$°C†
K_g (spherulites in bulk polymer)‡	$(1.23 \pm 0.10) \times 10^5$ °K^2	From data in Ref. 160, using $T_m^0 = 146.5 \pm 1$°C‡
B. *Results*		
$\sigma\sigma_e$ (single crystals from xylene)	1280 ± 130 erg^2/cm^4	From $K_g = 4b\sigma\sigma_e T_d^0/\Delta h_f k$ (regime I)
$\sigma\sigma_e$ (axialites in bulk polymer)†	1275 ± 120 erg^2/cm^4	From $K_g = 4b\sigma\sigma_e T_m^0/\Delta h_f k$ (regime I)
$\sigma\sigma_e$ (spherulites in bulk polymer)‡	1380 ± 100 erg^2/cm^4	From $K_g = 2b\sigma\sigma_e T_m^0/\Delta h_f k$ (regime II)
σ	14.1 ± 1.7 ergs/cm^2§	From $\sigma\sigma_e/\sigma_e$
ψ	~0.7	From fit of l_g* versus T data, Ref. 168
y	0.014 °K^{-1}	From fit of l_g* versus T data, Ref. 168

† Average for seven fractions with M.W. between 3×10^4 and 6.3×10^4 calculated using $U^* = 1500$ cal/mole and $T_\infty = T_g - 30$°C $= 201$°K. The value of K_g for the axialites is 2.36×10^5 °K^2 if $U^* = 4120$ cal/mole and $T_\infty = T_g - 51.6$ is used.

‡ Average for five fractions with M.W. between 3×10^4 and 6.3×10^4, calculated using $U^* = 1500$ cal/mole and $T_\infty = T_g - 30 = 201$°K. The value of $T_m^0 = 146.5$°C for both spherulitic and axialitic samples of low M.W. was reduced by ~1.5°C in making the calculations.

§ Calculated using average $\sigma\sigma_e = 1310$ erg^2/cm^4 for single crystals, axialites, and spherulites. Value of σ is 13.7 ergs/cm^2 if $\sigma\sigma_e = 1275$ erg^2/cm^4 is used.

$1/T(\Delta T)f$ for the axialites in one of these specimens is also shown in Figure 30.

The growth rate data on the axialites in the melt-crystallized polyethylene fraction used in Figure 30 are depicted in Figure 31. These objects appear only above 127°C. As noted above, their growth conforms to regime I kinetics.

Spherulites form in bulk polyethylene fractions of molecular weight 3×10^4 to 6.3×10^4 below 127°C, and grow according to regime II kinetics[160] according to a test based on Eq. (42). The regime "transition" is readily seen in Figure 31. The transition is surprisingly abrupt, and accompanied by a marked change in morphology. There is no change in the subcell as this transition takes place. The value of K_g for the spherulites is close to one-half that found for single crystals or axialites.[160] When analyzed using $K_g = 2b\sigma\sigma_e T_m^0/\Delta h_f k$ the average value of $\sigma\sigma_e$ for five spherulitic specimens is found to be $1380 \pm 100\ \text{erg}^2/\text{cm}^4$, in fair agreement with the other determinations of $\sigma\sigma_e$.

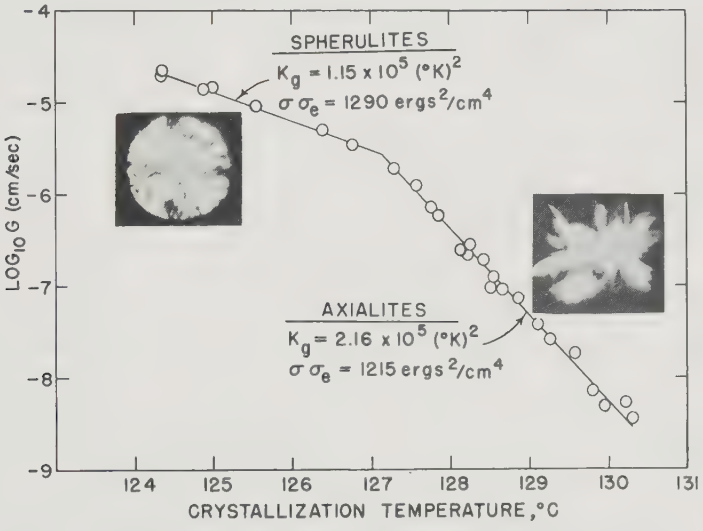

Fig. 31. Change in growth regime in melt-crystallized polyethylene. Growth rate[160] in melt-crystallized polyethylene is shown as a function of the crystallization temperature for fraction with molecular weight of 30,600. The pronounced change in slope is accompanied by a change in morphology, as shown by optical micrographs of the type from which the growth rate data were obtained. The values of $\sigma\sigma_e$ shown on the figure were calculated using $K_g = 4b\sigma\sigma_e T_m^0/(\Delta h_f)k$ (regime I) for axialites and $K_g = 2b\sigma\sigma_e T_m^0/(\Delta h_f)k$ (regime II) for spherulites (see also Figure 30).

It is of special interest to note that the value of G_0 for regime I axialites is much greater than that of the regime II spherulites, in accord with prediction [cf Eq. (37) and Table 3]. The ratio $G_0(\text{I})/G_0(\text{II})$ is $\sim 2 \times 10^6$.

The value $\sigma\sigma_e = 1280\,\text{erg}^2/\text{cm}^4$ is used in the analysis to follow, but no substantial differences in interpretation would result if it were carried out with a value within $200\,\text{erg}^2/\text{cm}^4$ of that quoted.

The similarity of the $\sigma\sigma_e$ values obtained for polyethylene crystallized from dilute solution, and axialites and spherulites in melt-crystallized material, points with considerable emphasis to the similarity that must exist in the chain-folded surface nucleus that controls the growth rate in the three cases. This was to have been anticipated from the fact that σ_e was previously shown in Section 2 by thermodynamic measurements to be similar in single-crystal and melt-crystallized polyethylene.

Consider now the value of the lateral surface free energy σ. Huseby and Bair[104] find $\sigma_e = 93 \pm 8\,\text{ergs/cm}^2$ from T_m versus $1/l$ plots for both dried single crystals and from single crystals in dilute solution. This gives $\sigma = \sigma\sigma_e(\text{kinetic data})/\sigma_e(\text{from } T_m \text{ versus } 1/l \text{ data}) = 1280/93 = 13.7\,\text{ergs/cm}^2$. This value of σ will be used in the calculations to follow.

Since it is rare that σ can be estimated in the manner described above, because an independent determination of σ_e is not usually available, one can proceed in such cases in the following manner. Using the empirical relationship[28]

$$\sigma/(\Delta h_f)(ab)^{1/2} = \alpha \tag{43}$$

which is patterned after the Thomas–Stavely relationship,[123] we estimate that $\alpha \cong 0.11$ from the value of $\sigma = 13.7\,\text{ergs/cm}^2$ for polyethylene. A similar calculation for poly(chlorotrifluoroethylene) to be mentioned shortly suggests $\alpha \cong 0.12 \pm 0.04$. This clearly implies that $\alpha \cong 0.1$ for the lateral surface free energy of a chain polymer crystal. There is an additional justification for a choice of α in this range in the case of polyethylene. Turnbull and Cormia[93] have measured homogeneous nucleation rates in *n*-octadecane and interpreted these data as $\sigma^3 \cong 890\,\text{erg}^3/\text{cm}^6$ or $\sigma = 9.6\,\text{ergs/cm}^2$. This leads to $\alpha \cong 0.12$ using Eq. (43) and the heat of fusion and lattice constants of *n*-octadecane. Accordingly, we use the approximation $\alpha \cong 0.1$ together with Eq. (43) to estimate σ when no other method of obtaining σ is available. For ordinary organic molecules the value of α is usually nearer to 0.3, as Thomas and Stavely have shown.[123]

The reason for the lower α in chain compounds is not understood in any detail, but may be related to the large configurational entropy associated with chain compounds, and the fact that the lateral surface is partly formed by chemical bonds already in existence in the molecule before the surface is itself created. Both σ and σ_e, being free energies, must be expected to depend somewhat on temperature.

Another rough estimate of α may be obtained for poly(chlorotrifluoroethylene), since it is one of the polymers with the rare status where T_m versus $1/l$ measurements have been carried out, so that σ_e can be estimated (Figure 19b). The value of σ_e is 40.3 ergs/cm^2, giving $q = 2.9 \times 10^{-13}$ erg/fold or 4.2 kcal/mole of folds. (If the data are analyzed assuming $T_m^0 = 224$°C, one obtains $\sigma_e = 57.3$ ergs/cm^2 and $q = 6.0$ kcal/mole.) The value of K_g is known accurately, but the value of $\sigma\sigma_e$ is subject to more uncertainty since the analysis using Z [Eq. (42)] shows that crystallization in this polymer lies roughly midway between regimes I and II; the kinetics are nearly regime I at high temperatures and close to regime II at low temperatures. The assumption that the appropriate K_g value is just midway between regimes I and II gives the estimate that $\sigma\sigma_e = 260\,\text{erg}^2/\text{cm}^4$. Combination of this with $\sigma_e = 40.3$ ergs/cm^2 then gives $\sigma = 6.4$ ergs/cm^2, which leads to $\alpha \cong 0.12 \pm 0.04$. This brackets the α value estimated for polyethylene and *n*-octadecane. The analysis of the growth rate of this polymer will be subsumed with a number of others, using a method that allows K_g to be converted directly to an estimate of q.

Returning now to the central problem, we wish to use the values $\sigma_e = 93$ ergs/cm^2 and $\sigma = 13.7$ ergs/cm^2, which are consistent with the observed $\sigma\sigma_e$ values from both bulk and dilute solution crystallization rates, to estimate the initial lamellar thickness as a function of temperature for polyethylene to compare with experiment. This is done using the data of numerous authors on the lamellar thickness of single crystals in xylene as collected and analyzed by Miller.[168] These data are shown in Figure 32. At the temperatures corresponding to growth in dilute solution, polyethylene crystals do not thicken at an appreciable rate, so that these data may be taken to represent the initial lamellar thickness l_g^*.

Use of the input data of Table 4 for σ, σ_e, a, b, and Δh_f in Eq. (23),

$$l_g^* = \frac{2\sigma_e}{\Delta f} + \frac{kT}{2b\sigma} \cdot \frac{2 + (1 - 2\psi)a(\Delta f)/2\sigma}{[1 - a(\Delta f)\psi/2\sigma][1 + a(\Delta f)(1 - \psi)/2\sigma]}$$

where from Eq. (10) $\Delta f = (\Delta h_f)(\Delta T) f / T_m^0$, allows l_g^* to be calculated for various values of ψ. The shapes of the curve so calculated cannot

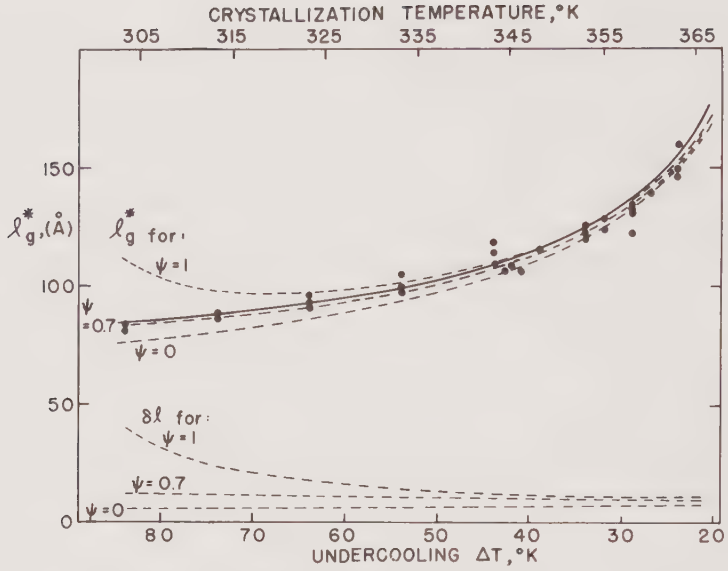

Fig. 32. Lamellar thickness of polyethylene single crystals from dilute xylene solution as a function of undercooling. (——) Best fit of data in literature according to Miller.[168] (●) Selected points from data in literature according to Miller.[168] (– – –) Theoretical curves for various ψ calculated from Eq. (23) using $T_d^0 = 114°C$, $\sigma_e = 93$ ergs/cm^2, $\sigma = 13.7$ ergs/cm^2, $\Delta h_f = 2.8 \times 10^9$ ergs/cm^3, $a = 4.15$ Å, and $b = 4.55$ Å. The δl component of l_g^* is also shown separately.

fit the data when ψ is unity (Figure 32). Values of ψ below about 0.8 and above roughly 0.2 give the best fit of the shape of $l_g^*(T)$. As noted earlier, the implication of a ψ value below unity is that the polymer molecules are physically adsorbed onto the substrate prior to the act of crystallographic attachment.[28] The fit of the theoretical l_g^* expression to the data is completed by recognizing that σ_e depends slightly on the undercooling at which a crystal is formed such that it must increase somewhat with lowering temperature. A convenient way to express this is

$$\sigma_e = \sigma_{e1}(1 + y\,\Delta T) \tag{44}$$

where y is a small, positive number and σ_{e1} the fold surface free energy as measured from a T_m versus $1/l$ plot, which closely approximates the equilibrium value of σ_e at T_m^0 or T_d^0. An examination shows that a positive value of y corresponds to a small and uniform upward shift of the entire $l_g^*(T)$ curve of $y\sigma_{e1}T_m^0/\Delta h_f$. For polyethylene, y is found to be $0.014°K^{-1}$.[110] This value of y is associated with the entropic

part of σ_e, and is probably partly caused by the fact that the fold surface is slightly rough (see Section 5).

The foregoing analysis is strongly supported by a strictly kinetic determination of σ and σ_e obtained by combining $\sigma\sigma_e$ from growth rate studies and $\sigma^2\sigma_e$ from homogeneous nucleation rates. The result is that $\sigma \cong 14.5$ ergs/cm^2 and $\sigma_e \cong 90$ ergs/cm^2 (see Section 6).

4.3.2. Isotactic Polystyrene

In the case of this polymer excellent $G(T)$ data are available on the bulk polymer as a result of the work of Boon,[6] Hay,[8] and Suzuki and Kovacs,[7] while Jones and co-workers[169] have measured the lamellar thickness over a wide range of undercoolings in dilute solution. The only apparent gap in the data situation is that no independent estimate of σ_e and T_m^0 (or T_d^0) is available from T_m versus $1/l$ data.† The analysis sketched below follows that given by Lauritzen and Hoffman.[28]

An analysis shows that the bulk crystallization falls clearly into regime II, so $K_g = 2b\sigma\sigma_e T_m^0/(\Delta h_f)k$. An estimate using Eq. (42) with the assumption of regime I gives $L \leq 1.7$ Å, which is completely unrealistic, while regime II gives $L \geq 440$ Å.[28] From the K_g value given by Suzuki and Kovacs (see also Table 1)[7] it is found that $\sigma\sigma_e = 266$ erg^2/cm^4.

We proceed by estimating σ, using Eq. (43), and then calculating σ_e from $\sigma\sigma_e$. When $\alpha = 0.1$ it is found that $\sigma = 7.65$ ergs/cm^2 and $\sigma_e = 34.8$ ergs/cm^2, which corresponds to $q = 7.0$ kcal/mole. Though the procedure basically depends on Eq. (43) and the value of α, the result can be judged as reasonable at this stage by the fact that q for polystyrene comes out to be somewhat larger than that for polyethylene, as would be expected from the steric hindrance of phenyl groups. Note also that the estimates of σ_e from melting point data include values near 35 ergs/cm^2 for samples crystallized at large undercoolings.[170b]

The procedure from this point on is the same as that used for polyethylene to calculate l_g^* from Eq. (23). It is found that $\psi = 0.382$ and $y = 0.0044°\text{K}^{-1}$ gives a good representation of the initial thickness data (see Figure 33). Again the value of ψ is less than unity, implying surface adsorption prior to crystallization.

† An estimate of T_m^0 for polystyrene has been made from T_m versus T_x data.[170a] Using the value of T_m^0 so obtained, Overbergh *et al.*[170b] have recently estimated σ_e from T_m and l data using Eq. (3) and report values near 35 ergs/cm^2 for samples crystallized at large undercoolings.

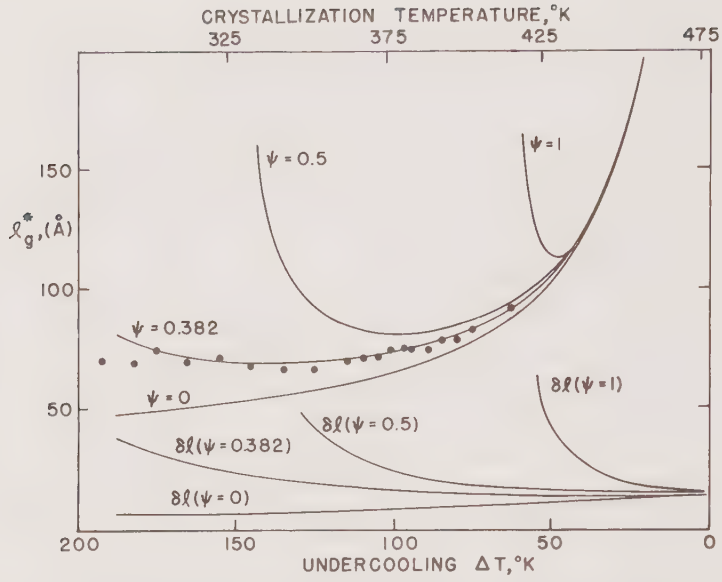

Fig. 33. Lamellar thickness of isotactic poly(styrene) crystals from dilute solution as a function of undercooling. (●) Lamellar thickness data of Jones *et al.*[169] (——) Theoretical curves according to Eq. (23) using $T_d^0 = 205°C$, $\Delta h_f = 9.11 \times 10^8$ ergs/cm^3, $\sigma_e = 34.8(1 + 0.0044\,\Delta T)$ ergs/cm^2, $\sigma = 7.64$ ergs/cm^2, $a = 12.8$ Å, and $b = 5.5$ Å for several values of ψ. The data are best represented when $\psi = 0.382$. The δl component of l_g^* is also shown separately.

4.3.3. Discussion

The basic thrust of the theory outlined in Section 3 is that the rate of formation of a chain-folded surface nucleus, i.e., the net flux, simultaneously governs the crystal growth rate and the initial thickness of the chain-folded crystal. The comparison of theory and experiment given above for polyethylene and polystyrene quantitatively supports the suggestion that the restriction of the crystals to a finite thickness l_g^* is fundamentally a result of kinetic considerations. The same surface free energies σ and σ_e whose product governs the temperature dependence of the growth rate according to Eq. (30) or (36) also control the principal features of the behavior of the initial thickness as given by Eq. (23). It is necessary to introduce a small temperature dependence in σ_e to obtain exact agreement between theory and experiment.

The theory emphasizes that the details of how the first step element and fold go on the substrate are of importance at high undercoolings, this feature being embodied in the parameter ψ. The values of ψ found for polystyrene and polyethylene are each well below unity, which means that physical adsorption of the molecules occurs prior

to actual crystallographic attachment of the first step element. A further suggestion that surface adsorption occurs prior to crystallographic attachment had previously been deduced from the fact that the jump-rate constants associated with the fluidity of the bulk polymer phase are not in general those that control the crystallization rate at low temperatures where the transport term is dominant.† It is also apparent that the jump-rate $\exp[-U^*/R(T - T_\infty)]$ describing the temperature dependence of the transport process refers to fairly short sections of a polymer chain rather than its contour length, but it is probably an oversimplification to describe U^* and T_∞ as strictly "segmental" properties in the case of crystallization.‡

Most previous theories of crystallization conformed to regime I kinetics, i.e., $K_g = 4b\sigma\sigma_e T_m{}^0/(\Delta h_f)k$. An analysis based on regime I was

† *Note added in proof*: In studies on the fracture of gold-decorated single crystals of poly(oxymethylene), poly(4-methylpentene-1), and "Penton," Geil and Breedon[191] have recently found clear evidence for the existence of a thin (less than ~20 Å) amorphous surface layer. The single crystals are first decorated with gold particles and then deformed and fractured. The position of the gold particles after fracture then reveals that a thin amorphous surface layer fractures at a different position than that of the underlying crystal and is mechanically removed from it. This work provides independent support for the views expressed here and in Ref. 28 that chain-folded crystals can have polymer molecules adsorbed on them. It also invites detailed consideration of the remarks in Section 1.3.2 concerning the possibility that the "amorphous" surface zone in single crystals that leads to a low density and heat of fusion may at least in part consist of an adsorbed layer of polymer molecules that resides on a rather regularly folded surface.

‡ The rate of crystallization of polyethylene axialities at a specified undercooling is essentially constant as the molecular weight is increased from 3×10^4 to 6.3×10^4, even though the $M^{-3.4}$ empirical law for the variation of bulk fluidity with molecular weight suggests that the bulk fluidity decreases by a factor of 12.5 at the same time. Meanwhile K_g does not vary significantly with molecular weight within this range. This implies that β and G_0 are approximately constant in the molecular weight range cited. Also, the data on TMPS for fractions of M.W. = 8700 and 56,000 where the bulk fluidity is estimated to fall by a factor of over 500 using $M^{-3.4}$, shows a decrease in G_0 by a factor of only 6.4 (suggesting that G_0 varies as $\sim M^{-1}$) and but little change in K_g. These results show, as was envisioned in the discussion of β and G_0 in Section 3, that these quantities (and hence the growth rate at a specified undercooling) are not proportional to the bulk fluidity, which varies as $M^{-3.4}$, but are instead only a weak function of the molecular weight in the range cited. These facts, together with the finding that the temperature dependence of G at low temperatures is accurately described by a transport term of the form $\exp[-U^*/R(T - T_\infty)]$, indicate that U^* and T_∞ refer to motions in the polymer chain that involve a length that is significantly smaller than its total contour length, though it is undoubtedly oversimplified to assume that these motions are strictly on a "segmental" scale. Nevertheless, it is valid to draw the conclusion that the transport term that dominates the growth process at low temperatures is not governed by the macroscopic viscosity (or fluidity), which involves the whole molecule, but rather by motions of parts of the long-chain molecule that have a characteristic jump rate proportional to $\exp[-U^*/R(T - T_\alpha)]$. At sufficiently high molecular weights these simple concepts may require revision.

successful with polyethylene, except for the spherulites, where regime II kinetics were required. The assumption of regime I kinetics for polystyrene would have led to $\sigma\sigma_e = 133\,\text{erg}^2/\text{cm}^4$ and a q value of 3.5 kcal/mole, which is unsatisfactory in that it is less than the value of q for polyethylene. The analysis using regime II kinetics, which was clearly indicated to be the correct choice by the value of Z, gave a q of 7.0 kcal/mole, which is more realistic relative to polyethylene. Also, it is in close accord with the q calculated from the σ_e value obtained from melting point depression experiments.[170b] This serves to emphasize the importance of correctly identifying the regime in which crystallization takes place.

Finally, we remark that it would be highly useful in checking nucleation theories of polymer crystal growth with chain folding if a method of measuring σ could be found that did not depend on a kinetic measurement. (Recall that the value of σ_e can be determined from the melting point depression of thin crystals.) One possibility would be to measure the equilibrium shape of a small, isolated crystal, which would have the dimensions $l/x = \sigma_e/\sigma$. This expression can be derived on the basis of finding the shape that has the minimum total surface free energy.[16] Then, if σ_e were known, σ could be estimated. However, this approach presents difficulties, for example, the attainment of the equilibrium shape.

4.4. The Fold Period as a Function of the Undercooling in Dilute Solutions: Verification of $l_g^* = (C_1/\Delta T) + C_2$

An important feature of the theory of polymer crystal growth from solution is that the initial thickness of the platelets near the melting point is predicted to depend primarily on the undercooling below the equilibrium dissolution temperature T_d^0 according to $l_g^* = (C_1/\Delta T) + C_2$, where $C_1 = 2\sigma_{e1} T_m^0/\Delta h_f$, and not the absolute temperature [see Eq. (5) as derived from Eq. (23) under the assumptions (a) δl is approximately constant, (b) Δf is given by Eq. (10) with $f \cong 1$, and (c) σ_e is given by Eq. (44)]. If this is so, then plots of the initial lamellar thickness against the temperature of crystallization for a given polymer in solvents with different T_d^0 values should be of the same shape, and be superposable by shifting the curves along the temperature coordinate for moderate to low undercoolings. This has been shown by many authors[106,107,171–174] and the data of Lieser and Fischer[173] for the thickness of polyethylene crystals grown isothermally from three different solvents are shown as a

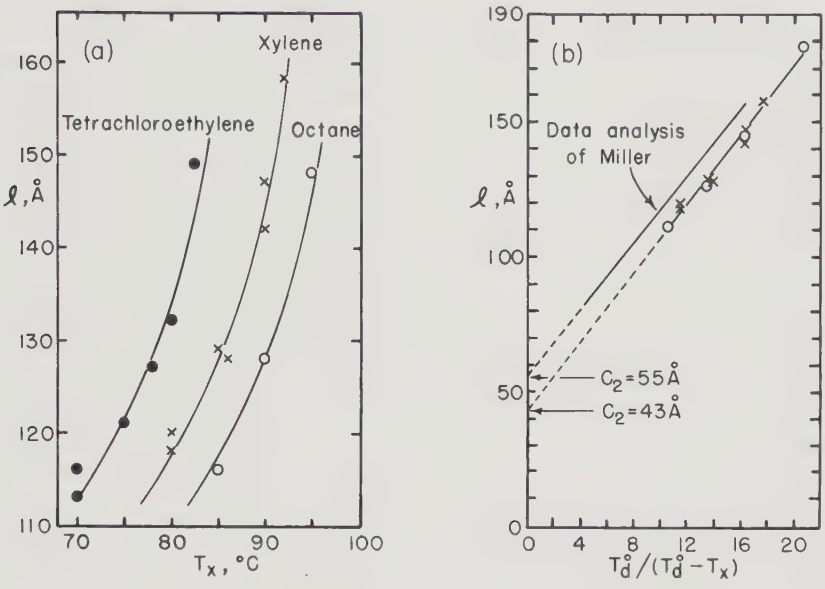

Fig. 34. Test of expression $l_g^* = (C_1/\Delta T) + C_2$. (a) Lamellar thickness versus crystallization temperature for polyethylene in various solvents. The dissolution temperature T_d^0 of the three solvents increases in the order tetrachlorethylene, xylene, and octane. This and the superposability of the curves imply that l depends on the undercooling rather than the absolute temperature at temperatures reasonably near to T_d^0. (Data courtesy of Dr. G. Lieser and Prof. E. W. Fischer.[173]) (b) Initial thickness l versus $T_d^0/\Delta T$ for polyethylene single crystals from xylene ($T_d^0 = 386.9°K$). (○) Data of Huseby and Bair.[104] (×) Data of Lieser and Fischer from Figure 32(a). Upper solid line represents "best" line from data analysis of Miller[168] (see Figure 32), which gives $C_2 = 55$ Å. Lower solid line gives linear regression fit of data of Huseby and Bair and of Lieser and Fischer, which yields $C_2 = 43$ Å. The latter data imply a value of y slightly lower than $0.014°K^{-1}$.

function of temperature in Figure 34(a). The curves are similar in shape and can be made to coincide within experimental error by shifting them horizontally along the temperature scale. The magnitude of the shift required corresponds to the difference in the dissolution temperatures of pressure-crystallized polyethylene ("extended-chain" crystals) in the three solvents.[173] The true value of T_d^0 is almost certainly somewhat above the observed dissolution temperature of "extended-chain" material, but it is also clear that the actual "extended-chain" dissolution temperature is substantially closer to the true T_d^0 for the various solvents than that of thin chain-folded crystals. Therefore the experiments cited above, when taken together, support the belief that the undercooling is the principal factor that governs the initial thickness of the crystals near the dissolution temperature.

Another convenient test of the theory is to plot l for unthickened crystals against $T_d^0/(T_d^0 - T)$, as is suggested by Eqs. (4), (23), and (44) with T_m^0 replaced by T_d^0. The prediction is that a plot of l against $T_d^0/(T_d^0 - T)$ will be linear and have a positive intercept of $C_2 = \delta l + 2y\sigma_{e1}T_d^0/\Delta h_f$ on the l coordinate.† The test is designed to be applied reasonably near T_d^0, where the value of $2\sigma_{e1}T_d^0/(\Delta h_f)(\Delta T)$ is fairly large. In the above expressions T represents the temperature of the solution and $l = l_g^*$ is the thickness of the platelet that comes out of solution at that temperature. These experiments are relatively easy to carry out for various solvents, and many exist in the literature. However, there is a paucity of T_d^0 determinations by the reliable T_d versus $1/l$ method which is capable of accurately establishing T_d^0 based on a thermodynamic expression. At the present time one of the few such determinations known to us is that of Huseby and Bair[104] for polyethylene in xylene and *n*-octadecane. A plot of l against $T_d^0/(T_d^0 - T)$ based on their determination of $T_d^0 = 386.9°K$ for xylene and their l versus T data, and that of Lieser and Fischer from Figure 34(a) for the same solvent, is shown in Figure 34(b). The data are well represented by a straight line with an intercept of $C_2 =$ 43 Å. Many more l versus T data for the same system[168] are available which show a rather similar result. For comparison, we have also shown in Figure 34(b) the l versus T data of many authors as analyzed by Miller,[168] which give $C_2 = 55$ Å. The results clearly show the reality of the C_2 term in the expression for l_g^*. Similar conclusions regarding the validity of the relation $l_g^* = (C_1/\Delta T) + C_2$, with C_2 being positive, have been drawn on the basis of careful studies on poly(oxymethylene) in five solvents by Korenaga, Hamada, and Nakajima.[174] These authors also give estimates of σ_e and T_d^0 in these solvents obtained from plots of T_d versus $1/l$.

Doubtless the reader has noticed that attempts to check theories are sometimes hampered by a lack of precise knowledge of T_d^0 in various solvents. The best method to obtain T_d^0 is based on Eq. (3), which suggests a T_d versus $1/l$ plot. [In one case[175] the value of $1/T_s^0$ in the expression $l^* = C/(T_s^0 - T_x)$ was obtained from the intercept in a plot of $1/T_x$ versus $1/T_x l$, thus arriving at a value of T_s^0, which was taken to be the equilibrium dissolution temperature. This procedure is erroneous, since l^* is actually of the form $[C_1/(T_d^0 - T_x)] + C_2$, with the result that T_s^0 is a fictive temperature that is higher than T_d^0.

† The term C_2 may contain an approximately constant thickness $2l_a$, where l_a is the thickness of the adsorbed layer of polymer molecules on one of the fold surfaces in the dried state. One might expect l_a to be roughly 10 Å. If such an estimate is used in the data analysis, the value of σ_e is slightly reduced and the value of y is lowered but there is no qualitative change in the overall conclusion.

Korenga *et al.* have also concluded that T_s^0 is not the equilibrium dissolution temperature.[174] Another way to resolve the question of T_m^0 and T_d^0 in polymers would be to measure the melting behavior of nearly defect-free extended-chain material. The preparation and defect characterization of such material stand as interesting and significant challenges to experimentalists.

One final point remains to be cleared up. A part of the approximately constant term $C_2 = 2(\sigma_{e1} y T_m^0/\Delta h_f) + \delta l$ is made up by the term involving y. It will be recalled that the term involving y arises from the assumed temperature dependence of σ_e written as $\sigma_e = \sigma_{e1}(1 + y\,\Delta T)$. The question then arises (from an analytical standpoint) as to why the constant C_2 in l_g^*, which constant clearly exists by any account, cannot be explained entirely by the temperature dependence of the surface free energy as $C_2 = 2\sigma_{e1} y T_m^0/\Delta h_f$ using an increased value of y so that δl is equal to zero. The answer is that, beginning with Eqs. (1) and (4), where σ_e is taken to be $\sigma_{e1}(1 + y\,\Delta T)$ in each, an expression for T_m identical to Eq. (6) with $\sigma_{e1}(1 + y\,\Delta T)$ replacing σ_e is found. This means that if δl is zero, the melting point is *still* exactly at the crystallization temperature even when $2\sigma_{e1} y T_m^0/\Delta h_f$ is greater than zero. The condition $\delta l > 0$ is thus required to obtain a melting point that is above the crystallization temperature, even when the fold surface free energy exhibits a dependence on temperature. Crystallization simply cannot occur when δl is zero, and theories for the formation of chain-folded crystals that imply that δl is zero require revision. A discussion of the temperature dependence of σ and σ_e is given in Sections 5 and 6.

4.5. Generalized Treatment to Obtain Work of Chain Folding from K_g

We now proceed to a more general analysis especially suited to include those polymers where only K_g is available from growth rate studies. This procedure is designed in such a way as to give an estimate of q directly from K_g so that a more general picture of the relationship between chain structure and q can be deduced.

By noting that to a good approximation $\sigma_e = q/2ab$ [see Eq. (9)], and taking $\sigma = \alpha(\Delta h_f)(ab)^{1/2}$ from Eq. (43), it is readily found by substitution in $K_{g(\mathrm{I})} = 4b\sigma\sigma_e T_m^0/(\Delta h_f)k$ and $K_{g(\mathrm{II})} = 2b\sigma\sigma_e T_m^0/(\Delta h_f)k$ that for regime I

$$K_{g(\mathrm{I})} = q(2\alpha T_m^0/k)[b/(ab)^{1/2}] \tag{45}$$

TABLE 5
Work of Chain Folding q from Experimental K_g Values Using Eqs. (45) and (46)

Polymer	T_m^0, °K	T_∞, °K	U^*, cal/mole	K_g, °K^2	"Molecular dimensions"			Work of chain folding, kcal/mole of folds		
					b, Å	ab, Å^2	Ref.	Regime I	Intermediate	Regime II
Polyethylene (spherulites)	417.8†	201	1500	1.15×10^5	4.15	18.9	176, 177	—	—	5.7
Polyethylene (axialites)	417.8†	201	1500	2.16×10^5	4.15	18.9	176, 177	5.4	—	—
Polyethylene (solution)	387.2‡	—	0	2.11×10^5	4.15	18.9	176, 177	5.3	—	—
Nylon 6	505.2§	273	1430	1.74×10^5	3.7	17.7	178	—	6 ± 2	—
trans-1,4-Poly(isoprene)	360.2#	181	1500	2.17×10^5	3.95	23.2	179	7.3	—	—
i-Polystyrene	515.2¶	333.5	1560	1.20×10^5	5.5	69.2	43, 180	—	—	7.0
Poly(chlorotrifluoroethylene)	497.2#	295.2	4000	1.72×10^5	5.6	36.4	16	—	5.6 ± 1.8	—
Poly(oxymethylene)	459.2¶	183	1500	1.27×10^5	3.86	17.15	181	3.0	—	—
Poly(oxyethylene)	348.4**	176	1500	0.81×10^5	4.65	21.7	182, 183	—	3.5**	—
Poly(oxypropylene)	348.2#	170	1320	0.78×10^5	5.2	24.3	161	—	3 ± 1	—
Poly(tetramethyl-*p*-silphenylene) siloxane M.W. = 56,000	427	219.2	990	1.14×10^5	6.41	41.2	151b	—	4.0 ± 1.3	—
Selenium	492.4††	270	2180	2.53×10^5	3.78	16.5	184	—	9 ± 3	—
	494.7¶	270	2200	2.74×10^5	3.78	16.5	184	—	9 ± 3	—

† T_m^0 adjusted for M.W. = 30,600.
‡ Dissolution temperature from T_d versus $1/l$ of Ref. 104.
§ Highest observed melting point by slow heating + 5°K.
# From intersection of T_m versus T_x plot with $T_m = T_x$.
¶ Highest observed melting point from melt-crystallized sample + 6°K.
** T_m^0 from intercept of T_m versus 1/M.W. + 6°K. Calculations show that POE crystallizes in regime I at high temperatures and in regime II at low temperatures. Estimate given corresponds to $K_g = 3b\sigma\sigma_e T_m^0/(\Delta h_f)k$ and $T_m^0 = 348.4$°K. If one uses $T_m^0 = 342.4$°K, $q = 1.8$ kcal/mole of folds.
†† From intercept of T_m versus $1/l$ of Ref. 163.

and for regime II

$$K_{g(II)} = q(\alpha T_m^0/k)[b/(ab)^{1/2}] \tag{46}$$

These expressions, which emphasize the dominant role of the work of chain folding q in determining K_g, differ from those of an earlier treatment[16] primarily in containing the factor $b/(ab)^{1/2}$.

The above expressions can be utilized to obtain estimates of q directly from the experimentally observed values of K_g, with the proviso that the regime of crystallization can be established. Observe that it is not necessary to know the heat of fusion. In most cases of interest it can be determined whether Eq. (45) or (46) is relevant. Then, assuming $\alpha \cong 0.1$, all that remains to be estimated is the ratio $b/(ab)^{1/2}$. This ratio depends on the orientation of the chain fold with respect to the unit cell. This is not known in many cases, but upper and lower bounds can be estimated. Usually $b/(ab)^{1/2}$ does not differ appreciably from unity for any reasonable assumption for the fold orientation. (Note that b and a are the thickness of the molecular layer being deposited and the width of a molecule, respectively, and not the unit cell dimensions; see Figures 20 and 22.)

Estimates of q obtained by the procedure outlined above together with the data used to obtain them are presented in Table 5 for a number of polymers.

These values of q when expressed as surface energies ($\sigma_e = q/2ab$) yield a kinetically determined value of σ_e which can then be compared with "equilibrium" values of σ_e obtained from T_m versus $1/l$ data or the equivalent. Such comparisons are summarized in Table 6 for a number of polymers. The relatively large error shown for the "kinetic" σ_e for some of the polymers is mainly a result of the uncertainty about the regime in which crystallization occurs. In the cases of polyethylene and poly(oxymethylene), where the regime assignment is quite certain, the agreement between the "kinetic" and "equilibrium" σ_e is good. The regime assignment in polystyrene is also quite certain and values for the equilibrium σ_e in good agreement with 35 ergs/cm^2 have been reported for samples crystallized at large undercoolings. In the other two cases where comparisons can be made, namely TMPS and poly(chlorotrifluoroethylene), the uncertainty limits of the kinetic σ_e are large but at least the equilibrium σ_e estimates are well inside them. In any event, there is no evidence of a serious disagreement between the two quite different methods of obtaining the fold surface free energy.

The data in Table 6 also serve to emphasize the fact that it is q rather than σ_e that correlates with the details of chain structure. The

TABLE 6
"Best Values" for Work of Chain Folding from Growth Rate Kinetics: Equilibrium and Kinetic σ_e Values

Polymer	Kinetic value of q [from Eqs. (45) and (46)],† kcal/mole of folds	Kinetic σ_e [from $\sigma_e = q/2ab$], ergs/cm^2	Equilibrium σ_e [from T_m versus $1/l$], ergs/cm^2
1. *Polymers with C–C chain backbone*:			
Polyethylene	5.5	101‡	93[104]
Nylon 6	6 ± 2	118 ± 40	—
trans-1,4-Poly(isoprene)	7.3	109	—
Polystyrene	7.0	35	35[170b]
Poly(chlorotrifluoroethylene)	5.6 ± 1.8	53 ± 17	40,§ 57#
Poly(tetrafluoroethylene)	7.5¶	—	94,[186] 61[185]
2. *Polymers with C–O–C linkages in chain backbone*:			
Poly(oxymethylene)	3.0	61	62**
Poly(oxyethylene)	2.3	37	—
Poly(oxypropylene)	3 ± 1	43 ± 14	—
3. *Other backbone linkages*:			
TMPS (M.W. = 56,000)	4 ± 1.3	34 ± 11	39††
Polymeric selenium	9 ± 3	190 ± 63	‡‡

† Calculated using $\alpha = 0.1$.
‡ This value would be 93 ergs/cm^2 and q would be 5.1 kcal/mole if the exact value of $\alpha = 0.11$ were used.
§ Reference 16; also see legend to Figure 19.
# From combination of T_m^0 from T_m versus T_x with $1/l$ data (see text).
¶ This value of q calculated from equilibrium σ_e given in Ref. 186.
** Reference 174, average for five solvents.
†† Reference 151e, data for M.W. = 331,000.
‡‡ Reference 163; surface bonds probably rearrange during heating and values of σ_e are unreliable.

value of q depends on a number of factors. Probably the most important is the inherent stiffness of the chain itself. Another factor is the length of the traverse of the fold as it leaves and reenters the crystal. A longer traverse, which is characteristic of molecules with a large cross-sectional area (ab), should allow more opportunities for a slight reduction in q resulting from smaller distortions from the potential minima in order to reenter the crystal in the required crystallographic position. The presence of large side-group substituents that hinder the formation of certain fold conformations of low energy would increase the value of q. Finally, many polymers consist of mixtures of "stiff" and "loose" linkages—poly(ethyleneterephthalate) being a good example—where the overall value of q could be close to the sum of

the loose linkages in the fold, or alternatively, the sum of a combination of the two types.

Although the estimation of q is in theory possible from potential energy calculations, it has only been carried out with the necessary detail in the case of polyethylene.[119 121] As noted previously, these calculations[120] yield $q \approx 4$ kcal/mole of folds, in fair agreement with experiment.

Centering our attention first on the case of polyethylene, and then extrapolating from this polymer to those that must have chains of lesser and greater stiffness, an approximate picture of q as a function of chain structure can be developed which appears to be a reasonable one. Polymers with linkages which have smaller differences in energy between gauche and trans conformations are found to yield folded chain crystals with smaller amounts of work stored in the chain fold. Although the *barriers* to rotation between flexed and unflexed positions in an ether linkage ($-CH_2-O-CH_2-$) and a hydrocarbon backbone linkage ($-CH_2-CH_2-CH_2-$) are about the same (2.8–2.9 kcal/mole),[187] the *difference* in energy between the possible potential energy minima defining the flexed positions in the fold is smaller for the ether linkage (300 cal/mole as opposed to 800 cal/mole).[122] As a consequence, then, one would expect polymers with ether linkages in the chain backbone to in general exhibit a lower q than polymers with a hydrocarbon backbone, provided neither had important contributions from bulky side groups. The three polymers containing ether linkages in Tables 5 and 6 yield q values of approximately 3 kcal/mole of folds, which is to be compared with about 5 kcal/mole of folds in the case of polyethylene and nylon.† In polystyrene the same backbone linkage exists as in polyethylene, but the bulky $-C_6H_5$ rings, when compared with an H atom, may safely be assumed to interfere in such a way as to require more work to form the "folded" configuration. This is reflected in the q value of 7 kcal/mole, as compared with the about 5 kcal/mole of folds for polyethylene. However, the presently available data for poly(butene-1) (form II) yields a value of q of 3 ± 1 kcal/mole, which is an apparent exception to this pattern.

At this juncture the correlation based on simplified considerations of chain structure is such that the values of q arising from the present nucleation theory of polymer crystal growth appear to be reasonable

† The inclusion of Nylon 6 in Table 6 under the heading of polymers with a –C–C– backbone is appropriate because of the five $-CH_2-$ sequences in the polymer between amide linkages.

with respect to their magnitude. Further information along this line must await independent measurements of σ_e and calculations of q from potential energy data for polymers other than polyethylene. Most polymers appear to have a work of chain folding between 3 and 8 kcal/mole of folds. The stiffest molecules are apparently those of polymeric selenium and poly(tetrafluoroethylene). Crystal[163] has suggested that the fold in the selenium molecule is so strained that it breaks on annealing, forming a nonfolded crystal.

The foregoing analysis shows that even within a given regime, K_g may not be regarded as a constant for all polymers. Once the regime of crystallization is established, the value of K_g depends on the work of chain folding q more than any other single factor, and this in turn is mainly a function of the details of the chain structure and the interior crystal lattice to which the fold must accommodate as it emerges from and then reenters the crystal. While the absolute value of q does not vary much more than a factor of two from 5 kcal/mole for the polymers studied, this leads to extremely large differences in growth rate at a specified undercooling.

In summary, the growth rate equations may be written to a sufficient approximation in an alternative form emphasizing the role of q as

$$G = G_0 \exp[-U^*/R(T - T_\infty)] \exp\{-q(\kappa\alpha T_m^{\,0}/k)[b/(ab)^{1/2}]/T(\Delta T)f\} \tag{47}$$

where κ is 2 for regime I, unity for regime II, and ~ 1.5 for intermediate cases. In the analysis given above we employed the approximations $\alpha = 0.1$ and $\sigma_{e0} = 0$. Once the regime of crystallization is fixed, the work of chain folding is the most important parameter affecting the temperature dependence of the growth rate at low undercoolings.

5. Theories with Fluctuations of Fold Period

We now address the problem of fluctuation of fold period. This has been treated by a number of authors,[126,128,130] but we emphasize here the treatment of Lauritzen and Passaglia[128] (LP) because it is the most general of the fluctuation theories, since it deals with all possible fold periods as the strip completion process in the g direction takes place.

Lauritzen, DiMarzio, and Passaglia[188] (LDP) have given a general and exact theory for the rate of growth and composition of a new strip of crystal growing from a multicomponent system. The same

authors applied the theory to a binary mixture of *n*-paraffins[189] and Lauritzen and Passaglia applied the theory to the kinetics of formation of chain-folded polymer crystals.[128] The details will not be presented here, but it is worthwhile to point out some of the essential differences between a theory that considers fluctuations and those that assume a constant fold period within a given crystal.

The LP theory considers the growth of a new layer of polymer crystal to be composed of a row of step elements or stems connected by chain folds just as has been outlined in earlier sections of this chapter. However, each step element may extend above or below the averaged substrate surface. The model is shown schematically in Figure 35. In the figure l_s is the average thickness of the previously completed layer, a concept introduced by Price,[130] which is now the substrate for nucleation. The symbols l_i and l_j represent the neighboring molecular stem lengths, not necessarily of the same length, and a is the thickness of the molecule on the substrate. The cross section of the molecule is assumed to be square, so the cross-sectional area is a^2. Only nearest-neighbor interactions are considered and the portions of the molecule that protrude above the surface are considered to be rigid rods. The authors realized the limitations of these assumptions, but pointed out the prohibitive mathematical complication of treating the model in any more detail.

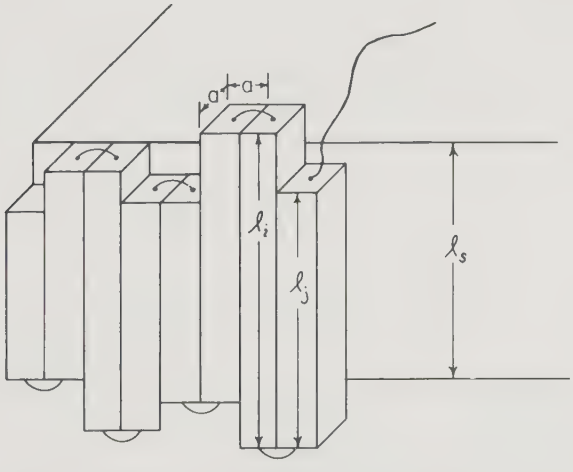

Fig. 35. Model for growth strip with fluctuations in fold period. The averaged thickness of the previously completed growth strip is denoted by l_s, the last step element is of length l_j, and the preceding one is of length l_i. For simplicity the molecule is assumed to be square in cross section.

In such a model additional lateral surface is exposed when $l_j > l_s$ and when $l_j > l_i$. For the first step element in the layer

$$\Delta\phi_1 = 2al_j\sigma + 2a\sigma U(l_j - l_s) - a^2 l_j \Delta f \tag{48}$$

where $U(x) = x$ for $x \geq 0$, and $U(x) = 0$ for $x \leq 0$; and for subsequent steps

$$\Delta\phi_v = 2a^2\sigma_e + 2a\sigma U(l_j - l_s) + 2a\sigma U(l_j - l_i) - a^2 l_j \Delta f \tag{49}$$

The rate constants for the forward and backward steps of the first element ${\alpha_0}^j$ and ${\beta_1}^j$ and the subsequent steps α_{ij} and β_{ij} are then expressed in terms of these free energies of formation. The symbol α_{ij} refers to the rate constant for adding a segment of length l_j to a layer whose terminal element is of length l_i, and β_{ij} is the rate of removal of a chain of length l_j from a layer whose terminal elements are l_i and l_j. The free energy (other than the chain-fold energy, $2a^2\sigma_e$) is then apportioned between the forward and backward steps by a parameter ψ and $1 - \psi$, and the kinetic equations solved for the case of steady-state growth. The reader is referred to the series of three papers[128,188,189] for any further assumptions involved and for details of the computer-assisted calculations.

The fold-surface free energy of such a "rough" surface is expected to be larger than that of a "regular" or "smooth" fold surface because of the additional exposed lateral surface. The entropy of mixing associated with the elements of different length also changes the fold-surface free energy, but with a sign opposite to the exposed lateral surface term. In the LP theory the "effective" fold-surface energy (which we refer to as "kinetic" surface free energy, $\sigma_{e(k)}$) is given by

$$\sigma_{e(k)} = \sigma_e - \frac{kT}{2a^2}\sum_j f_j \ln f_j + \frac{kT}{2a^2}\sum_{ij} f_{ij} \ln f_{ij}$$

$$+ \frac{\sigma}{2a}\sum_j f_j |l_j - l_s| + \frac{\sigma}{2a}\sum_{ij} f_{ij} |l_i - l_j| \tag{50}$$

where f_j is the fraction of elements of length l_j and f_{ij} is the fraction of ij pairs in the system.

Equation (50) may be expressed as

$$\sigma_{e(k)} = \sigma_e + \Delta\chi \tag{51}$$

where

$$\sigma_e = \sigma_{e0} + q/2a^2 \tag{52}$$

The quantity σ_e is the fold surface free energy of a completely smooth surface, q being the work of chain folding, and σ_{e0} a surface free energy roughly comparable to the lateral surface free energy σ. Even if σ_e is assumed to be independent of temperature, $\sigma_{e(k)}$ is dependent on temperature, as shown explicitly in Eq. (50) and implicitly by the variations in f_i and f_{ij} with undercooling. The calculated variation of $\sigma_{e(k)}$ with temperature (undercooling) with σ_e assumed constant is shown in Figure 36 for different values of the parameter ψ. The increase of $\sigma_{e(k)}$ at larger undercoolings, i.e., with increased driving force, is caused by the increase in exposed lateral surface as the fold surface becomes rougher. In brief, the fluctuations are greater the larger the driving force (undercooling).

The average thickness of the crystalline layer l_g^* and the flux S_T in the LP theory are analogous to the corresponding quantities in the theory without fluctuations, with $\sigma_{e(k)}$ replacing σ_e in each case.

The model gives an explanation of why the fold period maintains itself near l_g^* as the growth strip spreads across the surface. What

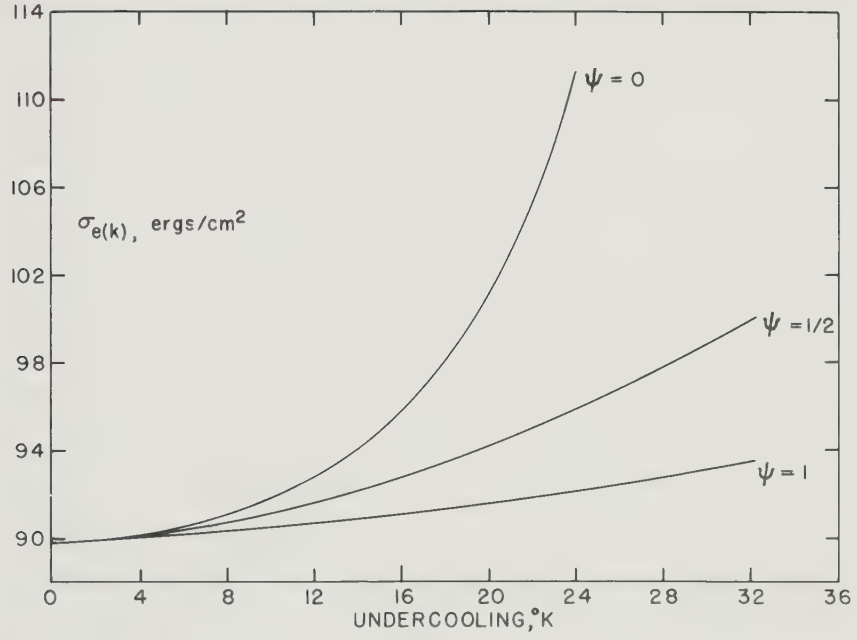

Fig. 36. Kinetically determined fold-surface free energy $\sigma_{e(k)}$ as a function of undercooling. The fold-surface energy predicted from a growth rate theory that allows fluctuations in fold period is shown as a function of undercooling for three different values of ψ. The rise in $\sigma_{e(k)}$ with increasing ΔT is mostly a result of the increased roughness of the fold surface. Curves calculated using LP theory for the case $\sigma = 10$ ergs/cm^2 and $\sigma_e = 90$ ergs/cm^2, adapted from Ref. 127.

fundamentally happens is that folds that protrude too far above the surface incur not only the fold energy q but also a large component of lateral surface free energy which adds to σ_e, and this discourages such excursions, on an energetic basis. Those step elements that fall short of the average substrate thickness have less free energy of fusion than the average, while still invoking work in the opposite sense to form the fold, so these tend to be less favored. For moderate values of undercooling, calculations have shown that the mean value of $l_g^* = 2\sigma_{e(k)}/\Delta f + \delta l$ is attained after less than 100 layers, even if the crystal is started at a thickness of $4\sigma_e/\Delta f$, i.e., the fold period of a homogeneous nucleus. The predicted fold-surface roughness is such as to be consistent with a crystal that has a density that is slightly less than that calculated from crystallographic data. The surface roughness is not zero at T_m^0, but has its minimum value there. The calculated roughness at T_m^0 for the parameters pertinent to polyethylene is in the vicinity of 10 Å (root mean square value).

It should be mentioned that a considerably smoother fold surface can be predicted by the fluctuation theory by inserting an attraction energy between adjacent folds into the model.[145] The roughness is still a minimum at T_m^0 and increases as before as the undercooling is increased. The equilibrium roughness decreases with decreasing temperature, as would be expected.[145]

The value of δl in the LP theory cannot be given in closed form, but it varies as σ^{-1} just as it does in Eq. (23) for the theory without fluctuations. For equivalent values of the input data such as σ and a, the LP theory gives a slightly larger value of δl at a specified small undercooling than Eq. (23).

Results of the type outlined above are in general a gratifying addition to the main theory we have discussed, which does not allow fluctuations. The theory given without fluctuations in Section 3 is in fact directly obtained from the LP theory if fluctuations of fold period are forbidden and the appropriate assignments of $\alpha_0{}^j = A_0$, $\beta_1{}^j = B_1$, $\alpha_{ij} = A$, and $\beta_{ij} = B$ in terms of ψ are carried out.

Despite these successes of the fluctuation theory, a difficulty attaches to all of them. This is that they all lead to a δl catastrophe at an undercooling of either $\Delta T_c = \sigma T_m{}^0/(\Delta h_f)a$ or $\Delta T_c = 2\sigma T_m{}^0(\Delta h_f)a$.[110] This effect is of a different origin than that which appears in the theory without fluctuations in Section 3 when $\psi > 0$.

In the theory without fluctuations, the flux and fold periods are governed by the first step element in the new layer. The so-called "δl catastrophe" mentioned earlier can be avoided by apportioning

the free energy of formation of this first strip between the forward and backward steps [ψ_0 and $(1 - \psi_0)$]. The apportionment of $\Delta\phi_v$ for subsequent steps has essentially no effect on the flux in the model without fluctuations in the growth strip. However, in the theory that considers fluctuations the flux is not independent of the steps which follow the first, and at sufficiently large undercoolings each successive layer becomes slightly thicker and the flux and fold periods rapidly approach infinite values when steady-state conditions are assumed. Certainly the δl catastrophe that appears in the fluctuation theory does not correspond to experiment at high undercoolings, where no such catastrophe is found. In their present state these theories must be regarded as approximations that are valid only at rather low undercoolings. Possibly some new restriction on the magnitude of the fluctuations of fold period will be required to offset the appearance of the prediction of an infinite l_g^* at high undercoolings. Meanwhile, at high undercoolings, the use of the steady-state approximation, which is indigenous to most nucleation theories, may fail. Further theoretical work clearly needs to be done, but it can be carried out with the knowledge that the closely corresponding theory without fluctuations in the fold period given here can simultaneously account for the overall growth rate, the average lamellar thickness, and the melting behavior in some detail.

6. Homogeneous Nucleation in Polymers

Homogeneous nucleation is caused by the occurrence, through spontaneous fluctuations, of embryos of sufficient size in a subcooled liquid to initiate crystallization. When polymers are sufficiently subcooled in the absence of heterogeneities, ordinary growth mechanisms that use these heterogeneities as initiators for crystal growth are averted and homogeneous nucleation can then be observed. The familiar small droplet technique is often quite effective as a means of getting a significant amount of material that contains no heterogeneities, which then allows the measurement of the rate of homogeneous nucleation. Homogeneous nucleation is generally characterized by an initiation process that is sporadic in time, and by a rate of change with temperature that is truly astronomical. The pioneering work on homogeneous nucleation in polymers was carried out by Cormia, Price, and Turnbull[135] (CPT) on polyethylene using the droplet technique. The reader is referred to their paper, and an ensuing paper by Gornick, Ross, and Frolen[124] for a discussion of the techniques and the method of data analysis.

From the standpoint of the present work, which emphasizes growth of chain-folded polymer crystals, the significance of homogeneous nucleation is that a proper consideration of it can provide important information concerning the surface free energies. This arises from the fact that for polymers, homogeneous nucleation experiments give the product $\sigma^2\sigma_e$, and do so at temperatures far below that where $\sigma\sigma_e$ is measured by growth rate studies. We will at the same time take the opportunity to point out how the measured preexponential factor I_0 in the expression for the rate of homogeneous nucleation is affected by the temperature dependence of σ and σ_e.

Consider a three-dimensional nucleus composed of v step elements corresponding to $v - 1$ folds. We may write its free energy of formation as[66]

$$\Delta\phi = 2v\boldsymbol{A}\sigma_e + C\boldsymbol{l}(v\boldsymbol{A})^{1/2}\sigma - v\boldsymbol{A}\boldsymbol{l}(\Delta f) \tag{53}$$

where $\boldsymbol{A}$ is the cross-sectional area of the chain in the nucleus, C is a numerical factor depending on the shape of the cross section of the segments in the crystal, and l is the length or "fold period" of the homogeneous nucleus. The quantity C is $2\pi^{1/2}$ for a cylindrical nucleus, 4 for a square parallelepiped, and 3.89 for the polyethylene subcell.

For this nucleus it is found (see Section 3.2 of Ref. 66) that the minimum barrier in the passage to the stable region has the free energy

$$\Delta\phi_h^* = 2C^2\sigma^2\sigma_e/(\Delta f)^2 \tag{54}$$

and the length

$$l_h^* = 4\sigma_e/\Delta f \tag{55}$$

Straightforward developments then lead to the homogeneous nucleation rate[15,110]

$$I = I_0 \exp[-U^*/R(T - T_\infty)] \exp[-2C^2\sigma^2\sigma_e/(\Delta f)^2 kT] \tag{56}$$

Here I_0 in nuclei cm^{-3} sec^{-1} is $n_0 kT/h = NkT/hM\bar{V}_l$, where n_0 is the number of polymer "segments" per cm^3, N is Avogadro's number, M is the molecular weight of a polymer "segment," and $\bar{V}_l$ is the specific volume of the subcooled liquid. The estimated value of the preexponential factor I_0 is within several orders of magnitude of 10^{34} for most polymers.† Except for the factor $\exp[-U^*/R(T - T_\infty)]$ and the

† Part of the uncertainty in I_0 is a result of the fact that the value of M in the expression for I_0 is not well defined. The lower bound is the molecular weight corresponding to a monomer unit of length l_u, and the reasonable upper bound is the molecular weight corresponding to the total contour length of the molecule in a homogeneous nucleus of critical size $l_h^* = 4\sigma_e/\Delta f$ and lateral dimensions (for a rectangular parallelepiped) $a^* = b^* = 4\sigma/\Delta f$. The estimate of I_0 given in the text is based on a molecular weight corresponding to two stems (with one fold) of length l_h^*.

use of the generalized geometric factor C, Eq. (56) differs in no essential manner from that employed earlier by CPT.[135]

The size of the chain-folded homogeneous nucleus is generally such that it can be formed out of only a portion of a single polymer molecule. Physically, the process may be pictured as beginning as a local fluctuation where a kink in the chain in the subcooled liquid allows one part of a molecule to bend back and come into contact with a nearby part of the same molecule.

Equation (56) can be converted to apply directly to the case of polyethylene by inserting the value of $C^2 = 15.1$ and by noting that at the high undercoolings that prevail in homogeneous nucleation experiments in this polymer ($\Delta T \cong 59°C$) it is important to use Eq. (10) for Δf. Then

$$I = I_0 \exp[-U^*/R(T - T_\infty)] \times \exp[-30.2\text{“}\sigma^2\sigma_e\text{”}(T_m^0)^2/(\Delta h_f)^2(\Delta T)^2 f^2 kT] \qquad (57)$$

where for the time being we regard “$\sigma^2\sigma_e$” to be independent of temperature. Equation (57) shows that a plot of $\ln I + U^*/R(T - T_\infty)$ against $1/T(\Delta T)^2 f^2$ will have a slope of $-30.2\text{“}\sigma^2\sigma_e\text{”}(T_m^0)^2/(\Delta h_f)^2 k$, from which “$\sigma^2\sigma_e$” can be determined. The intercept on the I coordinate will give I_0.

The homogeneous nucleation data from droplet experiments of Ross and Frolen[190] for a polyethylene fraction with a molecular weight of 5×10^4 are depicted in Figure 37(a). Notice that the homogeneous nucleation rate is only measurable in the vicinity of 87–89°C; at lower temperatures it is too rapid, and at higher temperatures it becomes far too slow to measure. Observe also that the homogeneous nucleation rate changes about two orders of magnitude in the 2°C range where it could be followed. Ross and Frolen obtained essentially similar results on other polyethylene fractions.[190]

A plot of $\log_{10} I + U^*/2.303R(T - T_\infty)$ against $1/T(\Delta T)^2 f^2$ for these data (not shown) leads to a value of “$\sigma^2\sigma_e$” of 17,400 erg^3/cm^6 and a value of $\log_{10} I_0$ of 46.5. The value of “$\sigma^2\sigma_e$” appears to be reasonable when σ is calculated from it in either of two ways: (1) $\sigma =$ “$\sigma^2\sigma_e$”(homogeneous nucleation)/$\sigma\sigma_e$(growth) = 17,400/1280 = 13.6 ergs/cm^2 and (2) “$\sigma^2\sigma_e$”(homogeneous nucleation)/σ_e(T_m versus $1/l$ plot) = 17,400/93 = σ^2 = 187, whence σ = 13.7 ergs/cm^2. However, the value of I_0 obtained from the plot differs from the theoretical value of 10^{34} by a factor of more than 10^{12}, and this points to the

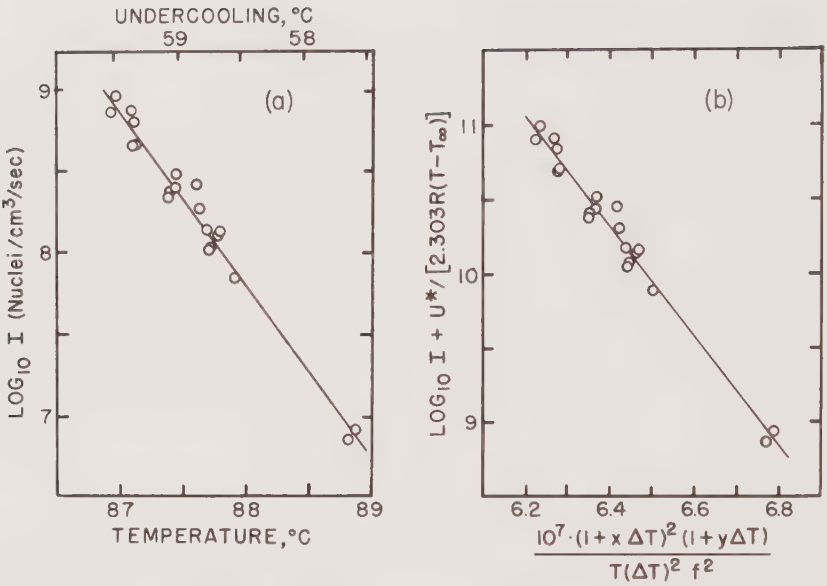

Fig. 37. Homogeneous nucleation rate in polyethylene. (a) Data of Ross and Frolen[190] obtained by the droplet experiment[135] on fraction of molecular weight 5×10^4. Note the one hundredfold increase in rate of homogeneous nucleation over a temperature range of only 2°C. (b) Determination of $\sigma^2\sigma_e$ and $\log_{10} I_0$ from homogeneous nucleation data using plot of $\log I + [U^*/2.303R(T - T_\infty)]$ versus $(1 + x\Delta T)^2(1 + y\Delta T)/T(\Delta T)^2 f^2$ for polyethylene data given in Figure 37(a). Analyzed using $U^* = 1500$ cal, $T_m^0 = 418.7°K$, $T_\infty = 201°K$, $x = -0.0069°K^{-1}$, and $y = 0.014°K^{-1}$. The intercept on the I coordinate gives $\log_{10} I_0 = 34$, and the slope gives $\sigma_1^2\sigma_{e1} = 17{,}460\ \text{erg}^3/\text{cm}^6$.

possibility that something is seriously amiss. Gornick, Ross, and Frolen[124] have also found preexponential factors in the vicinity of 10^{47} for homogeneous nucleation in polyethylene. Whatever the problem with the "experimental" value of the preexponential factor, it does not appear to be a question of the input data.†

A possible resolution to the problem that the experimental preexponential factor is far too large is found if it is recalled that σ and σ_e are free energies, and should be accordingly somewhat dependent on temperature. Already we have seen that $\sigma_e = \sigma_{e1}(1 + y\,\Delta T)$, with $\sigma_e = 93\ \text{ergs/cm}^2$ and $y = 0.014\ \text{deg}^{-1}$, gave the best fit of l_g^* from growth data.

† CPT[135] quote $\sigma^2\sigma_e$ (analogous to our "$\sigma^2\sigma_e$") as 15,500 erg^3/cm^6 based on an analysis of data where $T_m^0 = 141°C$, $C^2 = 4\pi$, and $f = 1$. A recalculation of their results on the same basis as is used in this chapter gives "$\sigma^2\sigma_e$" = 18,000 erg^3/cm^6. Ross and Frolen's result of "$\sigma^2\sigma_e$" = 19,000 erg^3/cm^6 (average "$\sigma^2\sigma_e$" for five samples ranging from M.W. = 23,000 to M.W. = 239,000) may be regarded as comparing favorably with theirs, especially in view of the different samples and experimental techniques that were used.

Now the lateral surface free energy σ will also be slightly dependent on temperature according to

$$\sigma = \sigma_1(1 + x\,\Delta T) \tag{58}$$

where on physical grounds to be outlined shortly we anticipate that x will be small and negative in sign. Inserting these slightly temperature-dependent quantities into the expression for I then leads to the situation where the appropriate plot is

$$\log_{10} I + [U^*/2.303R(T - T_\infty)] \quad \text{versus}$$
$$(1 + x\,\Delta T)^2(1 + y\,\Delta T)/T(\Delta T)^2 f^2 \tag{59}$$

and where the slope s is

$$s = -30.2\sigma_1{}^2\sigma_{e1}(T_m{}^0)^2/(\Delta h_f)^2 k \tag{60}$$

The value of "$\sigma^2\sigma_e$" obtained from the conventional plot of $\log_{10} I + [U^*/2.303R(T - T_\infty)]$ against $1/T(\Delta T)^2 f^2$ is related to $\sigma_1{}^2\sigma_{e1}$ by the relation[110]

$$\text{“}\sigma^2\sigma_e\text{”} = \sigma_1{}^2\sigma_{e1}\left[1 + (2x + y)\,\Delta T_h \frac{T_h - \Delta T_h}{2T_h - \Delta T_h} - (2xy + x^2 + x^2 y T_m{}^0)\frac{(\Delta T_h)^3}{2T_h - \Delta T_h}\right] \tag{61}$$

Here ΔT_h and T_h are the mean undercooling and the absolute temperature, respectively, where homogeneous nucleation takes place.

We are now in a position to ask if any reasonable value of x in Eq. (58) will give the theoretical value of $I_0 \sim 10^{34}$ nuclei $\text{cm}^{-3}\,\text{sec}^{-1}$. The value of y is already fixed at $0.014°\text{K}^{-1}$ by other experiments. Figure 37(b) shows a plot of the data exhibited in Figure 37(a) with $y = 0.014°\ \text{K}^{-1}$ and $x = -0.0069°\text{K}^{-1}$ as $\log_{10} I$ against $(1 + x\,\Delta T)^2 \times (1 + y\,\Delta T)/T(\Delta T)^2 f^2$ (the values of U^*, T_∞, $T_m{}^0$, and Δh_f are given in the legend). The value of $\sigma_1{}^2\sigma_{e1}$ is found to be 17,460 erg^3/cm^6, which is practically identical to the "$\sigma^2\sigma_e$" where σ and σ_e are taken to be independent of temperature, but the intercept $\log_{10} I_0$ now has the theoretical value of 34. This shows clearly that a slight dependence on temperature of the surface free energies, in this case hardly affecting the value of $\sigma^2\sigma_e$ because of the compensatory effects of the different signs of x and y, makes an enormous difference in what is obtained for the experimental value of the preexponential factor. Possibly the effect of the temperature dependence of surface free energies on the

experimental value of I_0 deserves the attention of workers interested in homogeneous nucleation in other types of systems.

The value $x = -0.0069°K^{-1}$ indicates that σ *increases* with increasing temperature, in contrast to the behavior of σ_e. While no claim can be made that the value of x is accurate, the negative sign that leads to the increase of σ is probably correct from a conceptual point of view, entirely apart from the fact that it eliminates a rather spectacular discrepancy in the experimental value of the pre-exponential factor I_0. Lauritzen[145] has developed a theory for the behavior of σ based on a model where the presence of the lateral polymer crystal surface reduces the number of allowed configurations of the polymer molecules in the subcooled liquid in juxtaposition with that surface. Part of the value of σ in this treatment is related to the entropy gradient in the surface zone, and this increases with an increase of temperature. It would thus appear that an increase of σ with an increase of temperature is physically reasonable.

The foregoing argument is not applicable to the fold surface free energy, where the main contribution to the work of chain folding arises from potential energy stored in the folds. The roughness of the fold surface, where present, leads to a decrease of σ_e with increasing temperature as discussed in Section 5.

Viewed in its most limited perspective, the value of σ could be regarded as a repository for any misconceptions in the theory, and any errors in the analysis. Since the estimates of "$\sigma^2\sigma_e$" and $\sigma_1{}^2\sigma_{e1}$ from homogeneous nucleation have been given for polyethylene, we may now examine the value of the lateral surface free energy σ as determined in various ways. Most of the estimates have been mentioned *passim* earlier in the text, and are summarized in Table 7. Based on this table, it seems fairly certain that σ lies between about 13.7 and 15.0 ergs/cm^2.† It is evident that there is some scatter, but nothing to suggest any major discrepancy in the various theoretical approaches that involve σ.

It should be recalled that the surface property that we have designated as σ is defined in Eq. (1), or, alternatively, in Eq. (11). This definition includes the meaning of σ in $\sigma\sigma_e$ in the nucleation constant K_g for growth, $\sigma^2\sigma_e$ for homogeneous nucleation, and σ in the expression

† Earlier estimates[110] of σ and σ_e obtained by combining $\sigma^2\sigma_e$(homogeneous nucleation) with $\sigma\sigma_e$ (growth) for polyethlylene led to difficulties. A value of "$\sigma^2\sigma_e$" of 18,500 erg^3/cm^6 was employed, together with a "$\sigma\sigma_e$" of 800 erg^2/cm^4. This gave $\sigma = 23$ ergs/cm^2 and $\sigma_e = 35$ ergs/cm^2, neither value being at all reasonable. The difficulty can be traced mainly to the fact that the regime I → regime II transition at 127°C

TABLE 7
Summary of Estimates of Lateral Surface Free Energy of Polyethylene by Various Methods

Method	σ, ergs/cm^2
1. $\sigma = (ab)^{1/2}(\Delta h_f)\alpha$, with $\alpha = 0.12$ from homogeneous nucleation data[82] on *n*-octadecane	14.6
2. Methods involving $\sigma_e = 93$ ergs/cm^2 from T_m versus $1/l$ data and $\sigma\sigma_e$ from growth data:	
$\sigma\sigma_e$(dilute solution)/σ_e(T_m vs. $1/l$) = 1280/93 = σ	13.7
$\sigma\sigma_e$(axialites)/σ_e(T_m vs. $1/l$) = 1275/93 = σ	13.7
$\sigma\sigma_e$(spherulites)/σ_e(T_m vs. $1/l$) = 1380/93 = σ	14.8
3. Methods involving $\sigma_e = 93$ ergs/cm^2 and $\sigma^2\sigma_e$ from homogeneous nucleation:	
"$\sigma^2\sigma_e$"(homogeneous nucleation)/σ_e(T_m vs. $1/l$) = 19,000†/93 = σ^2	14.3
$\sigma_1{}^2\sigma_{e1}$(homogeneous nucleation/σ_e(T_m vs. $1/l$) = 19,600‡/93 = σ^2	14.5
4. Methods involving homogeneous nucleation ($\sigma^2\sigma_e$) and growth data ($\sigma\sigma_e$) only§:	
"$\sigma^2\sigma_e$"(homogeneous nucleation)/$\sigma\sigma_e$(growth) = 19,000†/1310 = σ	14.5
$\sigma_1{}^2\sigma_{e1}$(homogeneous nucleation)/$\sigma\sigma_e$(growth) = 19,600‡/1310 = σ	15.0
	av = 14.4 ± 0.7

† Average "$\sigma^2\sigma_e$" for five fractions ranging from 23,000 to 249,000 in molecular weight according to Ref. 190.
‡ Average $\sigma_1{}^2\sigma_{e1}$ according to Ref. 190.
§ Note that combination of "$\sigma^2\sigma_e$" = 19,000 erg^3/cm^6 and $\sigma\sigma_e$ = 1310 ergs/cm^2 (average of three values noted in method 2) gives σ_e = 90.3 ergs/cm^2.

for δl, without any alteration or change of reference state. The lateral surface free energy σ is the work required to create 1 cm^2 of new lateral surface on the crystal from an equal amount of material from the interior of the crystal, that new surface being in contact with the surrounding liquid or solution. The lateral surface free energy σ_v for a crystal in a vacuum is an altogether different quantity, and must be expected to be considerably larger than σ.

We close on a point of general significance to nucleation theory and its application to real systems. At no juncture in our analysis did we encounter any clear evidence—or for that matter even a hint—that the macroscopic surface free energies σ and σ_e became invalid[144] when applied to microscopic systems. For example, one can relate the work of chain folding q calculated for an individual fold quite reasonably to the macroscopically measured fold surface free energy

was not then recognized, nor was the "regime" theory developed, and data covering *both* regimes were analyzed together using $K_g = 4b\sigma\sigma_e T_m{}^0/(\Delta h_f)k$, giving the incorrect value $\sigma\sigma_e \cong 800$ erg^2/cm^4. A recalculation using $\sigma^2\sigma_e = 18{,}500$ erg^3/cm^6 and $\sigma\sigma_e = 1310$ erg^2/cm^4 gives $\sigma = 14.1$ ergs/cm^2 and $\sigma_e = 92.8$ ergs/cm^2.

as determined by thermodynamic means, or, alternatively, to an estimate of q that depends on the $\sigma\sigma_e$ arising from surface nucleation theory. It is equally true that the same implication regarding σ derives from the approximate constancy of this quantity as estimated in various ways in Table 7. Note also that when σ_e for polyethylene is calculated from strictly kinetic measurements by combining $\sigma^2\sigma_e \cong 19{,}000\ \text{erg}^3/\text{cm}^6$ from homogeneous nucleation data (average for five samples) with $\sigma\sigma_e = 1310\ \text{erg}^2/\text{cm}^4$ from growth studies (average of three sources noted in Table 4) that σ_e comes to $\sim 90\ \text{ergs/cm}^2$. This is in good agreement with the "equilibrium" value obtained from a T_m versus $1/l$ plot, which is $93 \pm 8\ \text{ergs/cm}^2$ (Figure 17). Thus the free energy of formation of the folds in the "microscopic" rate-determining nuclei are essentially the same as those that exist in the macroscopic crystal as determined using thermodynamic means. Evidently the chain-folded surface nuclei and chain-folded homogeneous nuclei are large enough, at least in this polymer, to closely approximate systems that are macroscopic in the statistical mechanical sense.

Acknowledgments

The authors wish to thank Profs. A. Keller, E. W. Fischer, A. J. Kovacs, D. C. Bassett, and P. H. Geil and Drs. H. D. Keith and F. J. Padden, for a number of stimulating discussions and for furnishing data and other material used in preparation of this review. Thanks are also due Prof. J. H. Magill for supplying the original data points on TMPS polymer, and for helpful communications concerning these data. We also wish to acknowledge a considerable number of useful and critical discussions with Drs. R. K. Eby, E. A. DiMarzio, I. Sanchez, F. Khoury, E. Passaglia, and A. Peterlin. Finally, the authors wish to express their gratitude to Drs. G. S. Ross and L. Frolen for important contributions to the data analysis given in this chapter, which they carried out with care and patience, and for the use of their data on homogeneous nucleation in polyethylene fractions prior to publication.

Note Added in Proof

The reader may be interested in the following articles which have been published since completion of this chapter:

(1) J. B. Jones and P. H. Geil, Surface films on poly(oxymethylene) single crystals, *J. Res. Nat. Bur. Std.* (*U.S.*), **79A**, 609–611 (1975).

(2) J. D. Hoffman and G. T. Davis, On the origin of the amorphous component in polymer single crystals and the nature of the fold surface, *J. Res. Nat. Bur. Std. (U.S.)*, **79A**, 613–617 (1975).

References

1. P. H. Geil, *Polymer Single Crystals*, Interscience Publishers, New York (1963).
2. F. Khoury and E. Passaglia, This Treatise, Vol. 3, Chapter 6.
3. P. J. Flory, *Statistical Mechanics of Chain Molecules*, Interscience, New York (1969).
4. H. D. Keith and F. J. Padden, Jr., A phenomenological theory of spherulitic crystallization, *J. Appl. Phys.* **34**, 2409–2421 (1963).
5. F. E. Karasz, H. E. Bair, and J. M. O'Rielly, Thermal properties of atactic and isotactic polystyrene, *J. Phys. Chem.* **69**, 2657–2667 (1965).
6. J. Boon, The effect of extreme supercooling on the number of spherulitic centers in isotactic polystyrene, *J. Polymer Sci. C* **16**, 1739–1749 (1967).
7. T. Suzuki and A. J. Kovacs, Temperature dependence of spherulitic growth rate of isotactic polystyrene, *Polymer J.* **1**, 82–100 (1970).
8. J. N. Hay, Crystallization kinetics of high polymers: Isotactic polystyrene, *J. Polymer Sci. A* **3**, 433–447 (1965).
9. L. H. Bolz and R. K. Eby, Inclusion of perfluoromethyl groups in the crystals of copolymers of tetrafluoroethylene and hexafluoropropylene, *J. Res. Nat. Bur. Std. (U.S.)* **69A**, 481–486 (1965).
10. C. W. Bunn, The crystal structure of long-chain normal paraffin hydrocarbons. The "shape" of the CH_2 group, *Trans. Faraday Soc.* **35**, 482–491 (1939).
11. J. J. Point, Enroulement hélicoïdal dans les sphérolithes de polyéthylène. *Bull. Acad. Roy. Belg.* **41**, 982–990 (1955); J. J. Point and G. A. Homès, Fibre N du polyéthylène, *Compt. Rend.* **242**, 2557–2560 (1956).
12. R. Jaccodine, Observations of spiral growth steps in ethylene polymers, *Nature* **176**, 305–306 (1955).
13. H. D. Keith, F. J. Padden, Jr., and R. G. Vadimsky, Intercrystalline links: Critical evaluation, *J. Appl. Phys.* **42**, 4585–4592 (1971).
14. K. H. Storks, An electron diffraction examination of some linear high polymers, *J. Am. Chem. Soc.* **60**, 1753–1761 (1938).
15. J. D. Hoffman and J. I. Lauritzen, Jr., Crystallization of bulk polymers with chain folding: Theory of growth of lamellar spherulites, *J. Res. Nat. Bur. Std. (U.S.)* **65A**, 297–336 (1961).
16. J. D. Hoffman, Theoretical aspects of polymer crystallization with chain folds: Bulk polymers, *Soc. Plastics Eng. Trans.* **4**, 315–362 (1964).
17. A. Keller, A note on single crystals in polymers: Evidence for a folded chain configuration, *Phil. Mag.* **2**, 1171–1175 (1957).
18. E. W. Fischer, Stufen- und spiralförmiges Kristallwachstum bei Hochpolymeren, *Z. Naturforsch.* **12a**, 753–754 (1957).
19. P. H. Till, Jr., The growth of single crystals of linear polyethylene, *J. Polymer Sci.* **24**, 301–306 (1957).

20. W. D. Niegisch and P. R. Swan, Hollow pyramidal crystals of polyethylene and a mechanism of growth, *J. Appl. Phys.* **31**, 1906–1910 (1960).
21. P. H. Lindenmeyer, Crystallization in polymers, *J. Polymer Sci. C* **1**, 5–39 (1963).
22. D. C. Bassett, F. C. Frank, and A. Keller, Some new habit features in crystals of long chain compounds. Part IV. The fold surface geometry of monolayer polyethylene crystals and its relevance to fold packing and crystal growth, *Phil. Mag.* **8**, 1753–1787 (1963).
23. M. I. Bank and S. Krimm, Mixed crystal infrared study of chain folding in crystalline polyethylene, *J. Polymer Sci. A-2* **7**, 1785–1809 (1969).
24. G. M. Martin and E. Passaglia, Density of polyethylene crystals grown from solution, *J. Res. Nat. Bur. Std. (U.S.)* **70A**, 221–224 (1966).
25. A. Peterlin, The amount and location of amorphous component in polyethylene single crystals, *J. Macromol. Sci.-Phys.* **B3**, 19–31 (1969).
26. E. W. Fischer, H. Goddar, and G. F. Schmidt, A remark on the surface structure of polyethylene single crystals, *J. Polymer Sci. B* **5**, 619–624 (1969).
27. A. Keller, E. Martuscelli, D. J. Priest, and Y. Udagawa, Fold surface of polyethylene single crystals as assessed by selective degradation studies. III. Application of the improved techniques to single crystals, *J. Polymer Sci. A-2* **9**, 1807–1837 (1971).
28. J. I. Lauritzen, Jr. and J. D. Hoffman, Extension of theory of growth of chain-folded polymer crystals to large undercoolings, *J. Appl. Phys.* **44**, 4340–4352 (1973).
29. A. Silberberg, Adsorption of flexible macromolecules. III. Generalized treatment of the isolated macromolecule; the effect of self-exclusion, *J. Chem. Phys.* **46**, 1105–1114 (1967).
30. C. A. J. Hoeve, E. A. DiMarzio, and P. Peyser, Adsorption of polymer molecules at low surface coverage, *J. Chem. Phys.* **42**, 2558–2563 (1965).
31. E. A. DiMarzio and F. L. McCrackin, One-dimensional model of polymer adsorption, *J. Chem. Phys.* **43**, 539–547 (1965).
32. E. A. DiMarzio and R. J. Rubin, Adsorption of a chain polymer between two plates, *J. Chem. Phys.* **55**, 4318–4336 (1971).
33. R. R. Stromberg, D. J. Tutas, and E. Passaglia, Conformation of polystyrene adsorbed at the theta-temperature, *J. Phys. Chem.* **69**, 3955–3963 (1965).
34. W. H. Grant and R. R. Stromberg, Rates of adsorption and desorption of polystyrene, *ACS Polymer Preprints* **11** (September), 1397–1399 (1970).
35. P. H. Geil, Nylon single crystals, *J. Polymer Sci.* **44**, 449–458 (1960).
36. P. H. Geil, Jr., N. K. Symons, and R. G. Scott, Solution grown crystals of an acetal resin, *J. Appl. Phys.* **30**, 1516–1517 (1959).
37. B. G. Ranby, F. F. Morehead, and N. M. Walter, Morphology of *n*-alkanes, linear polyethylene, and isotactic polypropylene crystallized from solution, *J. Polymer Sci.* **44**, 349–367 (1960).
38. F. Khoury, The spherulitic crystallization of isotactic polypropylene from solution: On the evolution of monoclinic spherulites from dendritic chain-folded crystal precursors, *J. Res. Nat. Bur. Std. (U.S.)* **70A**, 29–61 (1966).
39. F. C. Frank, A. Keller, and A. O'Connor, Observations on single crystals of an isotactic polyolefin: Morphology and chain packing in poly-4-methyl-pentene-1, *Phil. Mag.* **4**, 200–214 (1959).

40. V. F. Holland, S. B. Mitchell, W. L. Hunter, and P. H. Lindenmeyer, Crystal structure and morphology of polyacrylonitrite in dilute solution, *J. Polymer Sci.* **62**, 145–151 (1962).
41. W. Kern, J. Davidovits, K. J. Rauterkus, and G. F. Schmidt, Röntgenographische Untersuchungen an linearen Oligurethanen, *Makromol. Chem.* **43**, 106–116 (1961).
42. R. St. J. Manley, Growth and morphology of single crystals of cellulose triacetate, *J. Polymer Sci. A* **1**, 1875–1892 (1963).
43. H. D. Keith, R. G. Vadimsky, and F. J. Padden, Jr., Crystallization of isotactic polystyrene from solution, *J. Polymer Sci. A-2* **8**, 1687–1696 (1970).
44. V. F. Holland and R. L. Miller, Isotactic polybutene-1 single crystals: Morphology, *J. Appl. Phys.* **35**, 3241–3248 (1964).
45. J. D. Barnes and F. A. Khoury, Formation of curved polymer crystals: Polychlorotrifluoroethylene, *J. Res. Nat. Bur. Std. (U.S.)*, **78A**, 363–373 (1974).
46. H. Bittiger and R. H. Marchessault, Formation of ribbonlike fibrils by crystallisation from dilute solution, *Bull. Am. Phys. Soc.* **15**, 305 (1970).
47. F. J. Padden, Jr., H. D. Keith, and G. Giannoni, Single crystals of poly-L-lysine, *Biopolymers* **7**, 793–804 (1969).
48. H. D. Keith, G. Giannoni, and F. J. Padden, Jr., Single crystals of poly-(L-glutamic acid), *Biopolymers* **7**, 775–792 (1969).
49. R. G. Crystal, The polymeric nature of selenium crystallization. I. Morphology and thermodynamic considerations, *J. Polymer Sci. A-2* **8**, 1755–1772 (1970).
50. Y. Yamashita, Single crystals of poly(ethylene terephthalate), *J. Polymer Sci. A* **3**, 81–92 (1965).
51. F. J. Baltá Calleja and A. Keller, On the relation between long spacings, molecular length, and orientation in long chain compounds with reference to the possibility of chain folding. Part II. Poly(ethylene oxide)s, *J. Polymer Sci. A***2**, 2171–2179 (1964).
52. F. J. Padden, Jr. and H. D. Keith, Crystalline morphology of synthetic polypeptides, *J. Appl. Phys.* **36**, 2987–2995 (1965).
53. S. H. Carr, A. G. Walton, and E. Baer, Epitaxial crystallization of poly(γ-benzyl L-glutamate) on alkali halide single crystals, *Biopolymers* **6**, 469–477 (1968).
54. G. Giannoni, F. J. Padden, Jr., and H. D. Keith, Crystallization of DNA from dilute solution, *Proc. Nat. Acad. Sci. (U.S.)* **62**, 964–971 (1969).
55. A. K. Kleinschmidt, D. Lang, D. Jackerts, and R. Zahn, Darstellung und Langenmessungen des Gesamten Desoxyribonucleinsaure-Inhaltes von T_2-Bakteriophagen, *Biochim. Biophys. Acta* **61**, 857–864 (1962).
56. A. C. T. North and A. Rich, X-ray diffraction studies of bacterial viruses, Nature **191**, 1242–1245 (1961).
57. A. Keller and Y. Udagawa, Crystallization of short aliphatic polymer chains. I. General chain-folding behavior, *J. Polymer Sci. A-2* **10**, 221–238 (1972).
58. L. D'Ilario, A. Keller, and E. Martuscelli, Crystallization of short aliphatic chains. II. Example of even fold surface with adjacent fold reentry and of a transition to chain extension, *J. Polymer Sci. A–2* **10**, 239–252 (1972).
59. H. Zahn, Röntgenstruktur von Linearen Oligomeren, IUPAC Symp. on Macromolecules, paper IB 8, Wiesbaden (1959).

60. J. P. Arlie, P. Spegt, and A. Skoulios, Etude de la cristallisation des polymères II. Structure lamellaire et repliement des chaînes du polyoxyéthylène, *Makromol. Chem.* **104**, 212–229 (1967).
61. W. D. Niegisch, Crystallography of poly-*p*-xylylene, *J. Appl. Phys.* **37**, 4041–4046 (1966).
62. A. J. Bur and D. E. Roberts, Rodlike and random-coil behavior of poly(*n*-butyl isocyanate) in dilute solution, *J. Chem. Phys.* **51**, 406–420 (1969).
63. G. K. Noren and J. K. Stille, Polyphenylenes, *Macromolecular Rev.* **5**, 385–430 (1971). (Also known as *J. Polymer Sci., Part D.*)
64. N. Yoda and M. Kurihara, New polymers of aromatic heterocycles by polyphosphoric acid solution methods, *Macromolecular Rev.* **5**, 109–193 (1971) (also known as *J. Polymer Sci*, Part D).
65. W. Traub and K. A. Piez, in *Advances in Protein Chemistry* (C. B. Anfinsen, Jr., J. T. Edsall, and F. M. Richards, eds.), Academic Press, New York (1971), p. 305.
66. J. I. Lauritzen, Jr. and J. D. Hoffman, Theory of formation of polymer crystals with folded chains in dilute solution, *J. Res. Nat. Bur. Std. (U.S.)* **64A**, 73–102 (1960).
67. F. P. Price, The growth habit of single polymer crystals, *J. Polymer Sci.* **42**, 49–56 (1960).
68. A. Keller and A. O'Connor, Study of single crystals and their associations in polymers, *Disc. Faraday Soc.* **25**, 114–121 (1958).
69. C. W. Bunn and T. C. Alcock, The texture of polythene, *Trans. Faraday Soc.* **41**, 317–325 (1945).
70. H. D. Keith and F. J. Padden, Jr., The optical behavior of spherulites in crystalline polymers. Part. I. Calculation of theoretical extinction patterns in spherulites with twisting crystalline orientation, *J. Polymer Sci.* **39**, 101–122 (1959).
71. H. D. Keith and F. J. Padden, Jr., The optical behavior of spherulites in crystalline polymers. Part II. The growth and structure of spherulites, *J. Polymer Sci.* **39**, 123–138 (1959).
72. F. P. Price, On extinction patterns of polymer spherulites, *J. Polymer Sci.* **39**, 139–150 (1959).
73. A. Keller, Investigations of banded spherulites, *J. Polymer Sci.* **39**, 151–173 (1959); A. Keller, Morphology of crystalline polymers, a review, in *Growth and Perfection of Crystals* (R. H. Doremus, B. W. Roberts, and D. Turnbull, eds.), pp. 499–532, Wiley, New York (1958).
74. H. D. Keith and F. J. Padden, Jr., Spherulitic crystallization from the melt. I. Fractionation and impurity segregation and their influence on crystalline morphology, *J. Appl. Phys.* **35**, 1270–1285 (1964).
75. H. D. Keith and F. J. Padden, Jr., Spherulitic crystallization from the melt. II. Influence of fractionation and impurity segregation on kinetics of crystallization, *J. Appl. Phys.* **35**, 1286–1296 (1964).
76. M. Herbst, Röntgenographische Untersuchung an Sphärolithen in Polyamid-Spritzgussmassen, *Z. Electrochemie* **54**, 318–320 (1950).
77. A. Keller, The spherulitic structure of crystalline polymers, Part II. The problem of molecular orientation in polymer spherulites, *J. Polymer Sci.* **17**, 351–364 (1955).
78. R. P. Palmer and A. J. Cobbold, The texture of melt crystallized polythene as revealed by selective oxidation, *Makromol. Chem.* **74**, 174–189 (1964).

79. A. Keller and S. Sawada, On the interior morphology of bulk polyethylene, *Makromol. Chem.* **74**, 190–221 (1964).
80. C. W. Hock, Selective oxidation with nitric acid reveals the microstructure of polypropylene, *J. Polymer Sci. B* **3**, 573–576 (1965).
81. J. D. Hoffman and J. J. Weeks, Rate of spherulitic crystallization with chain folds in polychlorotrifluoroethylene, *J. Chem. Phys.* **37**, 1723–1741 (1962).
82. E. Passaglia and H. K. Kevorkian, Specific heat of atactic and isotactic polypropylene and the entropy of the glass, *J. Appl. Phys.* **34**, 90–97 (1963).
83. F. Rybnikar, Mechanism of secondary crystallization in polymers, *J. Polymer Sci. A* **1**, 2031–2038 (1963); A. J. Kovacs, Cinétique de Cristallisation du Polyéthylène, *Ric. Sci.* **25A**, 668–685 (1955) (IUPAC Symp. on Macromolecular Chemistry, Milan, 1954).
84. W. L. Holt and A. T. McPherson, Change of volume of rubber on stretching: Effects of time, elongation, and temperature, *J. Res. Nat. Bur. Std. (U.S.)* **17**, 659–678 (1936).
85. E. Passaglia and G. M. Martin, Dependence of mechanical relaxation on morphology in isotactic polypropylene, *J. Res. Nat. Bur. Std. (U.S.)* **68A**, 519–527 (1964).
86. J. D. Hoffman, G. Williams, and E. Passaglia, Analysis of the α, β, and γ relaxations in polychlorotrifluoroethylene and polyethylene: Dielectric and mechanical properties, *J. Polymer Sci. C* **14**, 173–235 (1966).
87. E. Ergoz, J. G. Fatou, and L. Mandelkern, Molecular weight dependence of the crystallization kinetics of linear polyethylene. I. Experimental results, *Macromolecules* **5**, 147–157 (1972).
88. J. D. Hoffman and W. Elban, to be published.
89. R. K. Sharma and L. Mandelkern, The density of polyethylene crystallized in the bulk and from dilute solution, *Macromolecules* **2**, 266–271 (1969).
90. L. Mandelkern, A. L. Allou, Jr., and M. Gopalan, The enthalpy of fusion of linear polyethylene, *J. Phys. Chem.* **72**, 309–318 (1968).
91. D. Turnbull, Kinetics of heterogeneous nucleation, *J. Chem. Phys.* **18**, 198–203 (1950).
92. B. Vonnegut, Variation with temperature of the nucleation rate of supercooled liquid tin and water drops, *J. Colloid Sci.* **3**, 563–569 (1948).
93. D. Turnbull and R. L. Cormia, Kinetics of crystal nucleation in some normal alkane liquids, *J. Chem. phys.* **34**, 820–831 (1961).
94. A. J. Pennings, Hydrodynamically induced crystallization of polymers from solutions, in *Crystal Growth* (Proc. Int. Conf. on Crystal Growth, Boston, 1966; H. S. Peiser, ed.), Pergamon Press, New York (1967), pp. 389–393.
95. H. D. Keith, F. J. Padden, Jr., and R. G. Vadimsky, Further studies of intercrystalline links in polyethylene, *J. Appl. Phys.* **37**, 4027–4034 (1966).
96. A. Keller and M. S. Machin, Oriented crystallization in polymers, *J. Macromal. Sci. (Phys.)* **B1**, 41–91 (1967).
97. E. H. Andrews, Crystalline morphology in thin films of natural rubber. II. Crystallization under strain, *Proc. Roy. Soc. (London)* **A277**, 562–570 (1964).
98. E. H. Andrews, P. J. Owen, and A. Singh, Microkinetics of lamellar crystallization in a long chain polymer, *Rubber Chem. Tech.* **45**, 1315–1333 (1972); *Proc. Roy. Soc.* **A324**, 79–97 (1971).

99. P. H. Geil, F. R. Anderson, B. Wunderlich, and T. Arakawa, Morphology of polyethylene crystallized from the melt under pressure, *J. Polymer Sci. A* **2**, 3707–3720 (1964).
100. D. V. Rees and D. C. Bassett, Crystallization of polyethylene at elevated pressures, *J. Polymer Sci. A-2* **9**, 385–406 (1971).
101. P. D. Calvert and D. R. Uhlmann, Crystallization of polyethylene at high pressure: A kinetic view, *J. Polymer Sci. A-2* **10**, 1811–1836 (1972).
102. D. C. Bassett and B. Turner, New high-pressure phase in chain-extended crystallization of polythene, *Nature (Phys. Sci.)* **240**, 146–148 (1972).
103. B. Wunderlich, L. Melillo, C. M. Cormia, T. Davidson, and G. Snyder, Surface melting and crystallization of polyethylene, *J. Macromol. Sci.-Phys.* **B1**, 485–516 (1967).
104. T. W. Huseby and H. E. Bair, Dissolution of polyethylene single crystals in xylene and octadecane, *J. Appl. Phys.* **39**, 4969–4973 (1968).
105. H. E. Bair, T. W. Huseby, and R. Salovey, The equilibrium melting temperature and surface free energy of polyethylene single crystals, *ACS Polymer Preprints* **9**, 795–805 (1968).
106. A. Nakajima, F. Hamada, S. Hayashi, and T. Sumida, Effect of solvent on single crystal formation from dilute polyethylene solution. I. Surface free energy of single crystals estimated from kinetic theory, *Kolloid-Z. u. Z. Polymere* **222**, 10–16 (1968).
107. A. Nakajima, S. Hayashi, T. Korenaga, and T. Sumida, Effect of solvent on single crystal formation from dilute polyethylene solution. II. Surface free energy of single crystals estimated from dissolution temperatures, and density of those crystals, *Kolloid-Z. u. Z. Polymere* **222**, 124–130 (1968).
108. H. E. Bair and R. Salovey, The Effect of molecular weight on the structure and thermal properties of polyethylene, *J. Macromol. Sci.-Phys.* **B3**, 3–18 (1969).
109. R. G. Brown and R. K. Eby, Effect of crystallization conditions and heat treatment on polyethylene: Lamellar thickness, melting temperature and density, *J. Appl. Phys.* **35**, 1156–1161 (1964).
110. J. D. Hoffman, J. I. Lauritzen, Jr., E. Passaglia, G. S. Ross, L. J. Frolen, and J. J. Weeks, Kinetics of polymer crystallization from solution and the melt, *Kolloid-Z. u. Z. Polymere* **231**, 564–592 (1969).
111. J. D. Hoffman and J. J. Weeks, X-ray study of isothermal thickening of lamellae in bulk polyethylene at the crystallization temperature, *J. Chem. Phys.* **42**, 4301–4302 (1965).
112. J. J. Weeks, Melting temperature and change of lamellar thickness with time for bulk polyethylene, *J. Res. Nat. Bur. Std. (U.S.)* **67A**, 441–451 (1963).
113. A. Peterlin, Thickening of polymer single crystals during annealing, *J. Polymer Sci. B* **1**, 279–284 (1963); A. Peterlin, Molecular weight dependence of isothermal long period growth of polyethylene single crystals, *Polymer* **6**, 25–34 (1965).
114. L. A. Wood and N. Bekkedahl, Crystallization of unvulcanized rubber at different temperatures, *J. Res. Nat. Bur. Std. (U.S.)* **36**, 489–510 (1946); *J. Appl. Phys.* **17**, 362–375 (1946).
115. J. D. Hoffman and J. J. Weeks, Melting process and the equilibrium melting temperature of polychlorotrifluoroethylene, *J. Res. Nat. Bur. Std. (U.S.)* **66A**, 13–28 (1962).

116. J. H. Magill, Crystallization and morphology of *d, l-* and *l*-poly(propylene oxide), *Makromol. Chem.* **86**, 283–288 (1965).
117. B. Wunderlich and L. Melillo, Morphology and growth of extended chain crystals of polyethylene, *Makromol. Chem.* **118**, 250–264 (1968).
118. T. Arakawa and B. Wunderlich, Thermodynamic properties of extended chain polymethylene single crystals, *J. Polymer Sci. C* **16**, 653–658 (1967).
119. P. E. McMahon, R. L. McCullough, and A. A. Schlegel, Molecular mechanics of point defects in polyethylene, *J. Appl. Phys.* **38**, 4123–4139 (1967).
120. P. Corradini, V. Petraccone, and G. Allegra, Chain folding in polyethylene crystals. The cooperative effect of bond angle deformation and rotational strain, *Macromolecules* **4**, 770–771 (1971).
121. T. Oyama, K. Shiokawa, and T. Ishimaru, Chain conformations on the surface of polyethylene single crystals, in *The Solid State of Polymers* (P. H. Geil, E. Baer, and Y. Wada, eds.), Marcel Dekker, New York (1974), pp. 229–239.
122. S. W. Benson, F. R. Cruickshank, D. M. Golden, G. R. Haugen, H. E. O'Neal, A. S. Rodgers, R. Shaw, and R. Walsh, Additivity rules for the estimation of thermochemical properties, *Chem. Rev.* **69**, 279–324 (1969).
123. D. G. Thomas and L. A. K. Stavely, A study of the supercooling of drops of some molecular liquids, *J. Chem. Soc.* **1952**, 4569–4577 (1952).
124. F. Gornick, G. S. Ross, and L. J. Frolen, Crystal nucleation in polyethylene: The droplet experiment, *J. Polymer Sci. C* **18**, 79–91 (1967).
125. I. C. Sanchez and E. A. DiMarzio, Dilute-solution theory of polymer crystal growth. Some thermodynamic and predictive aspects for polyethylene, *Macromolecules* **4**, 677–687 (1971).
126. F. C. Frank and M. Tosi, On the theory of polymer crystallization, *Proc. Roy. Soc. (London)* **A263**, 323–339 (1961).
127. F. Gornick and J. D. Hoffman, Nucleation in polymers, *Ind. Eng. Chem.* **58**, 41–53 (1966).
128. J. I. Lauritzen, Jr. and E. Passaglia, Kinetics of crystallization in multicomponent systems: II. Chain folded polymer crystals, *J. Res. Nat. Bur. Std. (U.S.)* **71A**, 261–275 (1967).
129. J. I. Lauritzen, Jr. and J. D. Hoffman, Formation of polymer crystals with folded chains from dilute solution, *J. Chem. Phys.* **31**, 1680–1681 (1959).
130. F. P. Price, Markoff chain model for growth of polymer single crystals, *J. Chem. Phys.* **35**, 1884–1892 (1961).
131. D. Turnbull and J. C. Fisher, Rate of nucleation in condensed systems, *J. Chem. Phys.* **17**, 71–73 (1949).
132. P. H. Geil, Folded molecules in lamellas crystallized from molten polymers, *J. Appl. Phys.* **33**, 642–643 (1962).
133. A. J. Kovacs and A. Gonthier, Crystallization and fusion of self-seeded polymers. II. Growth rate, morphology and isothermal thickening of single crystals of low molecular weight poly(ethylene oxide) fractions, *Kolloid-Z. u. Z. Polymere* **250**, 530–551 (1972).
134. H. G. Zachman, Der Einfluss der Konfigurationsentropie auf des Kristallisations- und Schmelzverhalten von hochpolymeren Stoffen, *Kolloid-Z. u. Z. polymere* **216–217**, 180–191 (1967).
135. R. L. Cormia, F. P. Price, and D. Turnbull. Kinetics of crystal nucleation in polyethylene, *J. Chem. Phys.* **37**, 1333–1340 (1962).

136. J. D. Ferry, *Viscoelastic Properties of Polymers*, 2nd ed., John Wiley and Sons, New York (1970).
137. G. Adam and J. F. Gibbs, On the temperature dependence of cooperative relaxation properties in glass-forming liquids, *J. Chem. Phys.* **43**, 139–146 (1965).
138. D. J. Blundell and A. Keller, The concentration dependence of the linear growth rate of polyethylene crystals from solution, *J. Polymer Sci. B* **6**, 433–440 (1968).
139. I. C. Sanchez and E. A. DiMarzio, Dilute solution theory of polymer crystal growth: Fractionation effects, *J. Res. Nat. Bur. Std. (U.S.)* **76A**, 213–223 (1972).
140. W. B. Hillig, A derivation of classical two-dimensional nucleation kinetics and the associated crystal growth laws, *Acta Met.* **14**, 1868–1869 (1966).
141. J. I. Lauritzen, Jr., The effect of a finite substrate length upon the polymer crystal lamellar growth rate, *J. Appl. Phys.* **44**, 4353–4359 (1973).
142. I. C. Sanchez and E. A. DiMarzio, Dilute solution theory of polymer crystal growth: A kinetic theory of chain folding, *J. Chem. Phys.* **55**, 893–908 (1971).
143. W. K. Burton, N. Cabrera, and F. C. Frank, The growth of crystals and the equilibrium structure of their surfaces, *Trans. Roy. Soc.* **A243**, 299–358 (1951).
144. R. L. Parker, in *Solid State Physics* (H. Ehrenreich, F. Seitz, and D. Turnbull, eds.), Academic Press, New York (1970), Vol. 25, pp. 151–299.
145. J. I. Lauritzen, Jr., unpublished.
146. R. Chiang and P. J. Flory, Equilibrium between crystalline and amorphous phases in polyethylene, *J. Am. Chem. Soc.* **83**, 2857–2862 (1961).
147. M. G. Broadhurst, The melting temperatures of the *n*-paraffins and the convergence temperature for polyethylene, *J. Res. Nat. Bur. Std. (U.S.)* **70A**, 481–486 (1966).
148. P. J. Flory and A. Vrij, Melting points of linear-chain homologs. The normal paraffin hydrocarbons, *J. Am. Chem. Soc.* **85**, 3548–3553 (1963).
149. A. M. Rijke and L. Mandelkern, Melting behavior of linear polyethylene crystallized by solution stirring, *J. Polymer Sci. A-2* **8**, 225–242 (1970).
150. J. H. Magill, Crystallization kinetics of nylon 6, *Polymer* **3**, 655–664 (1962).
151a. J. H. Magill, Spherulitic crystillization studies of poly(tetramethyl-*p*-silphenylene)-siloxane (TMPS). Part III, *J. Polymer Sci. A-2* **7**, 1187–1195 (1969).
151b. J. H. Magill, Crystallization of TMPS polymers, Part II, *J. Polymer Sci. A-2* **5**, 89–99 (1967).
151c. J. H. Magill, Crystallization of TMPS polymers, *J. Appl. Phys.* **35**, 3249–3259 (1964).
151d. J. H. Magill, private communication.
151e. S. S. Pollack and J. H. Magill, Small-angle X-ray scattering from poly(tetramethyl-*p*-silphenylene)siloxane (TMPS) fractions, *J. Polymer Sci. A-2* **7**, 551–561 (1969).
152. L. Mandelkern, N. L. Jain, and H. Kim, Temperature dependence of the growth rate of spherulites, *J. Polymer Sci. A-2* **6**, 165–180 (1968).
153. E. G. Lovering and D. C. Wooden, Equilibrium melting points of the low-melting and high-melting crystalline forms of *trans*-1,4-polyisoprene, *J. Polymer Sci. A-2* **9**, 175–179 (1971).

154. M. L. Dannis, Thermal expansion measurements and transition temperatures, first and second order, *J. Appl. Polymer Sci.* **1**, 121–126 (1959).
155. E. G. Lovering, The relationship between molecular weight and spherulitic growth rates in *trans*-1,4-polyisoprene, *J. Polymer Sci. C***30**, 329–338 (1970).
156. D. R. Carter and E. Baer, Lamellar crystallization and melting of polyoxymethylene, *J. Appl. Phys.* **37**, 4060–4065 (1966).
157. W. H. Linton and H. H. Goodman, Physical properties of high molecular weight acetal resins, *J. Appl. Polymer Sci.* **1**, 179–184 (1959).
158. E. Baer and D. R. Carter, Rate of spherulitic crystallization with chain folds in polyoxymethylene, *J. Appl. Phys.* **35**, 1895–1897 (1964).
159. G. T. Davis and R. K. Eby, The glass transition of polyethylene: Volume relaxation, *J. Appl. Phys.* **44**, 4274–4281 (1973).
160. J. D. Hoffman, G. S. Ross, L. Frolen, and J. I. Lauritzen, Jr., On the growth rate of spherulites and axialites from the melt in poly(ethylene) fractions: Regime I and Regime II crystallization, *J. Res. Nat. Bur. Std. (U.S.)* **79A** (1975), in press.
161. J. Brandrup and E. H. Immergut (eds.), *Polymer Handbook*, Interscience Publishers, New York (1966).
162. J. Powers, J. D. Hoffman, J. J. Weeks, and F. A. Quinn, Jr., Crystallization kinetics and polymorphic transformations in polybutene-1, *J. Res. Nat. Bur. Std. (U.S.)* **69A**, 335–345 (1965).
163. R. G. Crystal, Polymeric nature of selenium crystallization. II. Crystallization kinetics and secondary crystallization *J. Polymer Sci. A-2* **8**, 2153–2161 (1970).
164. F. J. Padden, Jr. and H. D. Keith, Spherulitic crystallization in polypropylene, *J. Appl. Phys.* **30**, 1479–1484 (1959).
165. L. Mandelkern, F. A. Quinn, Jr., and D. E. Roberts, Thermodynamics of crystallization in high polymers: gutta percha, *J. Am. Chem. Soc.* **78**, 926–932 (1956).
166. V. F. Holland and P. H. Lindenmeyer, Morphology and crystal growth rate of polyethylene crystalline complexes, *J. Polymer Sci.* **57**, 589–608 (1962).
167. M. Cooper and R. St. John Manley, Growth kinetics of polyethylene crystals from dilute xylene solution, *J. Polymer Sci., Polymer Letters Ed.* **11**, 363–367 (1973).
168. R. L. Miller, Polymer crystal formation: On an analysis of the dilute solution lamellar thickness—crystallization temperature data for poly(ethylene), *Kolloid-Z. u. Z. Polymere* **225**, 62–69 (1968).
169. D. H. Jones, A. J. Latham, A. Keller, and M. Girolamo, Fold length of single crystals of polystyrene: A conflict with crystallization theories at high supercoolings, *J. Polymer Sci., Polymer Phys. Ed.* **11**, 1759–1767 (1973).
170a. N. Overbergh, H. Berghmans, and G. Smets, Influence of thermal history on the melting behavior of isotactic polystyrene, *J. Polymer Sci. C* **38**, 237–250 (1972).
170b. N. Overbergh, H. Berghmans, G. Groenickx, and H. Reynaers, Reorganization of semicrystalline isotactic polystyrene studied by electron microscopy and small-angle X-ray diffraction, Paper A-5 IUPAC Int. Sym. on Macromolecules, Aberdeen, Scotland, September 1973.

171. T. Kawai and A. Keller, On the effect of the crystallization temperature on the habit and fold length of polyethylene single crystals, *Phil. Mag.* **11**, 1165–1177 (1965).
172. N. Hirai, T. Tokumori, T. Katayama, S. Fujita, and Y. Yamashita, Thickness of high polymer single crystals precipitated from solution, *Rep. Res. Lab. for Surface Science, Okayama Univ.* **2**, 91–99 (1963).
173. G. Lieser and E. W. Fischer, private communication; G. Lieser, Master's Thesis, Univ. Mainz, Mainz, Germany, 1966.
174. T. Korenaga, F. Hamada, and A. Nakajima, Surface free energy of poly(oxymethylene) single crystals grown in various solvents, *Polymer J.* **3**, 21–27 (1972).
175. E. Ergoz and L. Mandelkern, Solvent influence on the dilute solution crystallization of polyethylene and polyoxymethylene, *J. Polymer Sci., Polymer Letters Ed.* **11**, 73–79 (1973).
176. P. R. Swan, Polyethylene unit cell variations with temperature, *J. Polymer Sci.* **56**, 403–407 (1962).
177. G. T. Davis, R. K. Eby, and J. P. Colson, Thermal expansion of polyethylene unit cell: Effect of lamella thickness, *J. Appl. Phys.* **41**, 4316–4326 (1970).
178. D. R. Holmes, C. W. Bunn, and D. J. Smith, Crystal structure of polycaproamide: nylon 6, *J. Polymer Sci.* **17**, 159–177 (1955).
179. D. Fisher, Crystal structures of gutta percha, *Proc. Phys. Soc.* **B66**, 7–16 (1953).
180. G. Natta, P. Corradini, and I. W. Bassi, Crystal structure of isotactic polystyrene, *Nouvo Cimento (Suppl. 1)* **15**, 68–82 (1960).
181. E. Sauter, Ein Modell der Hauptvalenzkette im Makromolekülgitter der Polyoxymethylene, *Z. Physik. Chem.* **21B**, 186–197 (1933).
182. G. Vidotto, D. Lévy, and A. J. Kovacs, Cristallisation et fusion des polymères autoensemencés. I. Polybutène-1, Polyéthylène et Polyoxyéthylène de haute masse moléculaire, *Kolloid-Z. u. Z. Polymere* **230**, 289–305 (1969).
183. H. Tadokoro, Y. Chatani, T. Yoshihara, S. Tahara, and S. Murahashi, Structural studies on polyethers $[-(CH_2)_m-O-]_nH$, molecular structure of polyethylene oxide, *Makromol. Chem.* **73**, 109–127 (1964).
184. A. J. Bradley, The crystal structures of the rhombohedral forms of selenium and tellurium, *Phil. Mag.* **48**, 477–496 (1924).
185. J. P. Colson and R. K. Eby, Melting temperatures of copolymers, *J. Appl. Phys.* **37**, 3511–3514 (1966); I. C. Sanchez and R. K. Eby, Crystallization of random copolymers, *J. Res. Nat. Bur. Std. (U.S.)* **77A**, 353–358 (1973).
186. D. C. Bassett and R. Davitt, private communication.
187. J. Hine, *Physical Organic Chemistry*, 2nd ed., McGraw-Hill, New York (1962), p. 35.
188. J. I. Lauritzen, Jr., E. A. DiMarzio, and E. Passaglia, Kinetics of growth of multicomponent chains, *J. Chem. Phys.* **45**, 4444–4454 (1966).
189. J. I. Lauritzen, Jr., E. Passaglia, and E. A. DiMarzio, Kinetics of crystallization in multi-component systems: I. Binary mixtures of *n*-paraffins, *J. Res. Nat. Bur. Std. (U.S.)* **71A**, 245–259 (1967).
190. G. S. Ross and L. J. Frolen, unpublished.
191. Private communication from Prof. P. H. Geil; see also J. E. Breedon, M.S. Thesis, Crack formation in polymer single crystals, Case–Western Reserve Univ., Cleveland, Ohio (1975).

8

*Organic Molecular Crystals: Anthracene**

R. G. Kepler
Sandia Laboratories
Albuquerque, New Mexico

1. Introduction

Interest in the electronic properties of organic solids has grown spectacularly in the last few years. The speculation that a superconducting transition was occurring near 60°K in a high-conductivity organic crystal[1] played a big role in focusing the attention of scientists on the field. More generally, however, it has been recognized that organic molecular crystals provide a medium for the study of excited molecular states and their interactions and that the knowledge gained from these studies will provide fundamental knowledge applicable to physical, chemical, and biological systems.

For example, it has long been known that photosynthetic tissues are organized into aggregates of light-harvesting pigments (highly conjugated organic molecules) closely associated with photochemical reaction centers. The light-harvesting pigments absorb light and transfer the energy to the reaction centers. The mechanism by which the energy is transferred is of considerable interest at the present time,[2] and the fundamental studies of energy transfer processes that are being carried out in organic crystals will clearly play a role in providing the answers. Similarly, the primary products of the photochemical reaction serve as starting points for electron transport that is coupled to phosphorylation. Studies of the interaction between electrons and molecules should help explain how this electron transport can occur without numerous extraneous side reactions.

* Work supported by U.S. Energy Research and Development Administration.

It is interesting to note that examination of the mechanisms of photosynthesis, in light of what has been learned about electrons and holes in molecular crystals, has led to a proposal that it may be possible to directly generate electricity from solar energy with a synthetic membrane system.[3] Kuhn and co-workers are carrying out closely related studies on the interaction of chromophores in monolayer assemblies.[4] They are able to study in considerable detail both the nature of the monolayer assemblies and the nature of the interactions.

Exciton and electron and hole concepts are expected to play an ever-increasing role in other areas of photobiology, photochemistry, and radiation chemistry. Recent studies of exciton motion in polymers[5] have not only led to basic understanding of some energy transfer processes in polymers, but they have shown that the energy transfer processes can serve as a sensitive probe of the microscopic mechanical properties of polymers.[6]

The theory of low-mobility transport is presently a very active area of solid-state physics.[7] Investigations of the mobility of electrons and holes and of diffusion of excitons in molecular crystals have shown that low-mobility transport processes are involved. It is anticipated that both theoretical and experimental studies of these processes will lead to significant advances in this important area of physics.

Important technological advances have already been made possible by fundamental studies of molecular crystals, and it is reasonable to anticipate more in the future. A polymeric photoconductor, the properties of which have been improved by utilizing concepts and knowledge derived from studies of molecular crystals, is presently in use commercially in photocopying applications,[8] and very recently it was proposed that it may be possible to construct a molecular rectifier, a single molecule that acts as a rectifier.[9]

For these reasons, as well as many others, the field of molecular crystals has been growing at a rapid pace. Anthracene crystals have become the model material, and this review will concentrate on the properties of this crystal. As early as 1908 it was observed that anthracene crystals both emitted fluorescent light and exhibited photoconductivity. Ever since then anthracene has served as the model compound for studies of the electronic properties of crystals of organic molecules. Anthracene is a member of a series of organic molecules in which the most weakly bound electrons are in orbitals delocalized over the entire molecule, and these electrons provide these molecules with a number of very interesting properties. The

simplest molecules in the series are benzene, naphthalene, anthracene, and tetracene, consisting of one, two, three, and four benzene rings, respectively. Benzene is a liquid at room temperature, naphthalene has a fairly high vapor pressure at room temperature, and tetracene—rather than melting—decomposes. Primarily because of these facts and because anthracene melts at 216°C, can be purified by zone-refining, and still has a fairly low vapor pressure at room temperature, it has to a large extent become the model compound in the series.

Some of the early work on anthracene began because it is such a good fluorescent material, exhibiting a fluorescence quantum efficiency of almost one. It has frequently been used as a standard against which other scintillator materials are compared and has itself been used extensively as a scintillator. In the 1940's it was suggested that the processes occurring in crystals like anthracene were related to biological processes, and a large amount of work has been justified on this basis.

Very many interesting processes have been observed in anthracene crystals. It has long been known that very efficient energy transfer processes were operative. If only one part in 10^6 tetracene molecules is present in an anthracene crystal, half of the fluorescent light comes from the tetracene molecules. The diffusion coefficients for two different types of excitons are now believed to be known, and mutual annihilation of these two types of excitons has been observed. Electrons and holes are both mobile, and it is relatively easy to prepare crystals in which the carrier lifetimes are in excess of 100 μsec. A number of rather unusual techniques for generating carriers have been devised, and these should ultimately provide very useful tools for further study of the electronic states of organic molecular crystals. In general, the transport process appears to be dominated by very small mean free path processes, perhaps hopping processes, and it appears that anthracene crystals will provide a convenient tool for in-depth studies of low-mobility transport processes.

In this chapter an attempt has been made to discuss briefly all the important areas of research into the physical properties of anthracene crystals. No attempt was made to be complete since there has been a tremendous amount of work reported, but it is hoped that the work that is discussed and those references that have been listed are adequate to lead the reader interested in further study to the appropriate literature. A list of review articles and books covering specific areas and containing extensive references is given at the end. In this

regard it should be pointed out that a series of guides to the literature on the physical properties of molecules and crystals like anthracene has been published. The latest in the series was published by Sheka *et al.*[10]

In Section 2 a brief description of the anthracene molecule is presented for the sake of readers unfamiliar with organic molecules. In Section 3 some of the more classical properties of the anthracene crystal, as well as preparation techniques, are discussed, and in subsequent sections optical absorption, energy transport, and electron and hole transport and generation are described. The final section consists of a very brief discussion of the status of the theory of excitons, electrons, and holes in molecular crystals.

2. The Molecule

The anthracene molecule is a planar molecule consisting of three hexagonal rings of carbon atoms with hydrogen atoms attached to the periphery. Each molecule contains 14 carbon atoms and 10 hydrogen atoms.

The shape of the molecule is determined by the 2*s* electrons and one of the 2*p* electrons of the carbon atoms. These electrons are in three hybrid orbitals which lie in a plane and which form an angle of 120° with respect to each other. It is these hybrid orbitals, called trigonal or sp^2 hybrids, which form the bonds between the carbon atoms and between the carbon and hydrogen atoms and which, therefore, determine the hexagonal ring shape of the molecule. A contour map of the electron density distribution in an anthracene molecule obtained from X-ray studies is shown in Figure 1.

The carbon 1*s* electrons are so tightly bound in the atoms that they play no role in the electronic structure of the molecule, but the one 2*p* electron per carbon atom, which has been left out of the discussion so far, gives the molecules and the crystals that they form their very interesting electronic properties. These electrons are in orbitals that are delocalized over the entire molecule. In the most frequently used description, the molecular orbitals are linear combinations of atomic *p* orbitals, and the coefficients for the linear combinations are obtained by assuming that there is no overlap between atomic orbitals, that the resonance integrals between neighboring atomic orbitals are all equal, and that the resonance integral between nonneighbors is zero. Orbitals obtained using these approximations are referred to as Hückel orbitals. In anthracene

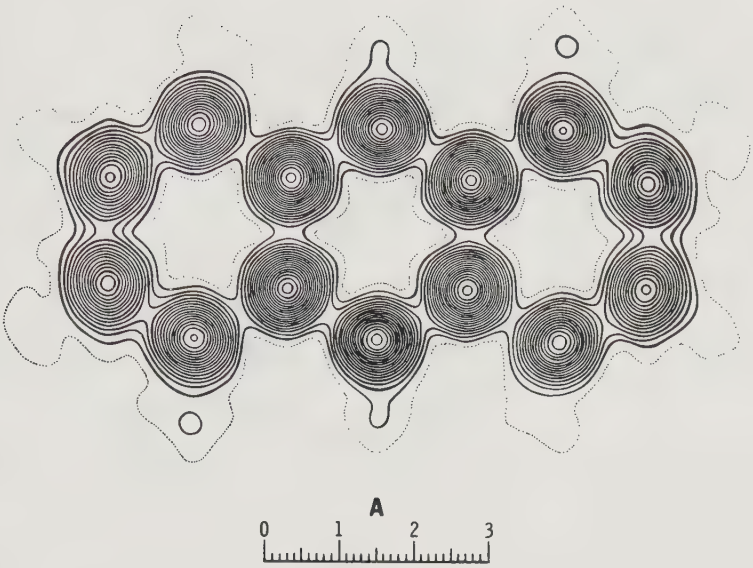

Fig. 1. Electron density map of the anthracene molecule. (From Robertson.[180])

there are 14 carbon atoms, and thus 14 independent molecular orbitals can be formed from linear combinations of the 14 atomic *p* orbitals. Two electrons, with their spins opposed, can be put in each orbital, so that in the ground state of the molecule the seven lowest-energy molecular orbitals are filled.

Excited states are formed by exciting an electron to a higher-energy molecular orbital, and both singlet and triplet excited states can be formed. The ground state is a singlet. The lowest-energy excited state is a triplet, and it lies 1.8 eV above the ground state. The first excited singlet state is 3.4 eV above the ground state. The oscillator strength of this transition is 0.1, and the dipole moment of the transition is parallel to the short axis of the molecule. There is a second, much stronger transition at 4.9 eV. The oscillator strength of this transition is parallel to the long axis of the molecule. In addition to the excited electronic states, excited vibrational states can be produced, the energy of which adds to the electronic energy, producing a series of absorption bands with spacing equal to the vibrational states in the anthracene absorption and fluorescence spectra; these vibrational states are at 1400 and 400 cm^{-1}. The 1400 cm^{-1} vibrational mode is associated with the symmetric breathing of the molecule.

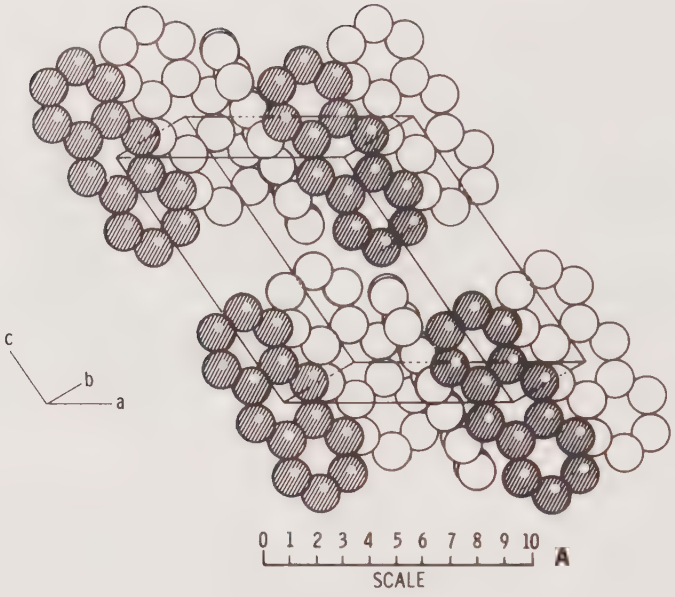

Fig. 2. Arrangement of the anthracene molecules in the unit cell. (From Robertson.[180])

3. The Crystal

In the anthracene crystal the molecules are held together by weak van der Waals forces and maintain their identity essentially completely. The molecular vibrations are still readily identifiable, and the vibrational frequencies are changed only slightly in the excited electronic states as well as the ground state. The unit cell is monoclinic with two molecules per unit cell, space group $P2_1/a$. The unit cell structure is shown in Figure 2.

It is possible to prepare crystals of very high purity*; impurity concentrations in the few parts per million range have been achieved. The purification procedure typically consists in chromatography to remove some impurities, which are not effectively removed by zone-refining, such as carbazole, followed by zone-refining. After zone-refining, the anthracene must be transferred to a crystal growing tube without exposure to the atmosphere, otherwise impurities are introduced which severely limit charge carrier lifetime. Large crystals can readily be grown from the melt by the Bridgman technique (see, e.g.,

* See Refs. 11 for review articles on purification and crystal growing techniques appropriate for organic solids.

Ref. 12). Anthracene melts at about 216°C. Crystals prepared by this technique have exhibited electron and hole lifetimes in excess of 1 msec and triplet exciton lifetimes of about 25 msec. It should be pointed out that if the crystal is exposed to room light while it is growing from the melt, the triplet exciton lifetime will generally be much shorter, of the order of 10 msec.

The above procedure is the technique that is generally used to prepare large single crystals. Very thin crystals, in the range of 0.1–10 μm, can readily be prepared by sublimation. For example, if anthracene is placed in the bottom of a beaker covered with filter paper and rapidly heated, many very thin crystals will quickly grow on the filter paper and around the top of the beaker. Crystals from a few square millimeters in area and about 0.1 μm thick to a few square centimeters but much thicker—more than 10 μm—can be prepared very quickly by this technique. This technique is readily adaptable to much more sophisticated apparatus, and a number of papers are available describing such apparatus (see, e.g., Ref. 12). The very thin crystals needed for optical absorption studies are usually prepared by this technique.

Thin crystals have also been prepared by melting anthracene between optically flat quartz plates and cooling slowly. Crystals can also be grown by slow cooling or evaporation of saturated solutions, but the crystals which result are relatively thin platelets which are too thin and too impure for the transport studies and too thick for optical studies.

The thin crystals grown by sublimation or from solution always grow so that the large flat surface of the crystal is the *ab* plane, and large single crystals readily cleave parallel to the *ab* plane. Crystals of anthracene are easily oriented because of strong double refraction exhibited by the crystal. If the *ab* plane of a crystal, the cleavage plane or the surface of a sublimation flake, is placed on a surface with a straight line on it, the line as viewed through the crystal will generally appear double. As the crystal is rotated, the two lines will come together at two positions 180° apart. At these two positions the *a* axis is parallel to the line, and the *b* axis is in the plane and perpendicular to the *a* axis. The *c* axis can be found by first finding one of the optical axes. According to Nakada,[13] this axis can be found by looking through the crystal at an angle of 29° $\pm$ 0.5° from the normal and in the direction of the *a* axis. The optical axis can readily be seen, as it is strongly colored by dispersion. The *c* axis lies in the plane defined by the *a* axis and the optical axis but is on the opposite side

of the normal to the *ab* plane from the optical axis and makes an angle of 34.7° to the normal. The relationship of the various axes is shown in Figure 3.

The above procedure cannot be used for very thin crystals and a polarizing microscope must be used. Detailed descriptions of orientation techniques have been given by Lipsett[12] and Nakada.[13]

The three principal indices of refraction at 5893 Å and one-half the angle between the optical axes as given by Nakada are $\alpha = 1.550 \pm 0.010$, $\beta = 1.775 \pm 0.010$, $\gamma = 2.04 \pm 0.08$, and $\Omega = 44.3° \pm 0.3°$.

Very accurate X-ray diffraction studies of anthracene crystals have provided some information about lattice vibrations, but in general very little work has been done on phonons in organic molecular crystals. Cruickshank[14] has shown that the amplitudes of translational motion parallel to the long molecular axis, parallel to the short molecular axis, and perpendicular to the molecular plane are 0.20, 0.16, and 0.16 Å, respectively. The rms amplitudes of angular vibrations about these axes are 3.8°, 2.2°, and 3.1°. The translational motion of the molecules corresponds to a Debye temperature of 85°K at room temperature.

Pawley[15] has investigated a model for the lattice dynamics of naphthalene and anthracene using intermolecular forces of "6-exp" interatomic type, that is, he assumed that the potential energy of atom pairs has the form

$$V(r) = (A/r^6) + B\exp(-\alpha r)$$

The dispersion curves calculated for anthracene in the [010] direction are shown in Figure 4. The solid dots in this figure are room-

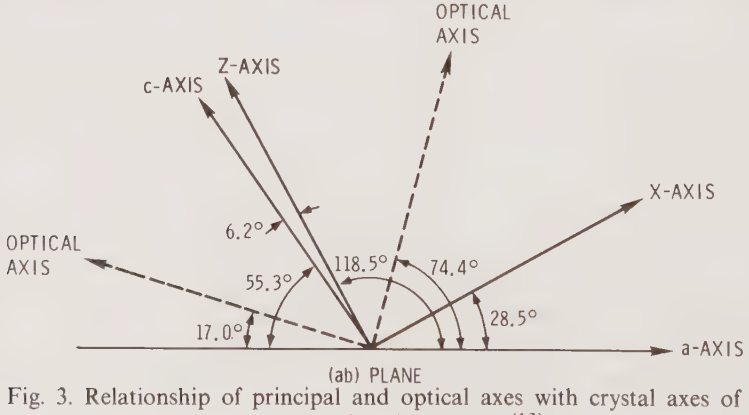

Fig. 3. Relationship of principal and optical axes with crystal axes of antracene as given by Nakada.[13]

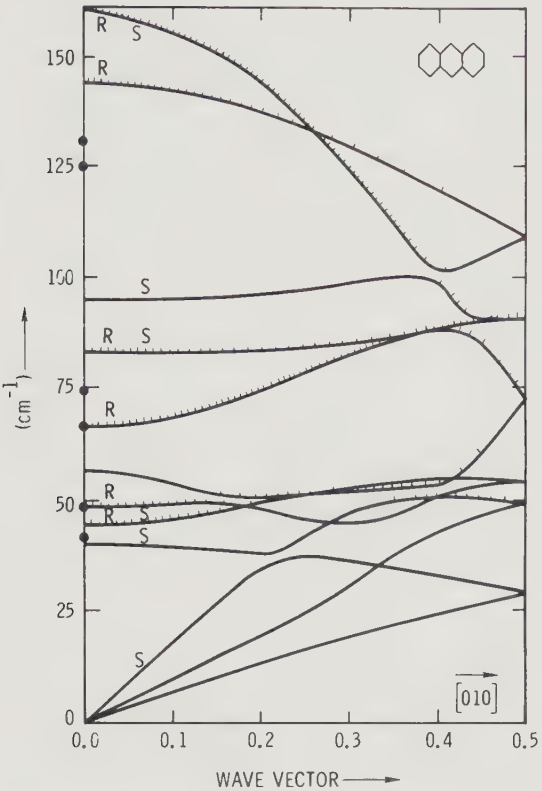

Fig. 4. Calculated dispersion curves for anthracene in the [010] direction. The solid dots at $k = 0$ are Raman measurements. (From Pawley.[15])

temperature Raman measurements. No attempt was made to fit the theoretical model to the experimental results, one reason being that the low-frequency internal mode of vibration of the molecules is about 200 cm^{-1}, and consequently it is expected that the upper branches of the dispersion curves would be in error owing to the neglect of the interaction with the distortion of the molecules. Ito *et al.*[16] have discussed the Raman spectra of anthracene.

4. Optical Absorption

A large percentage of the effort devoted to investigating the physics of anthracene crystals has been directed toward understanding the effect of the crystalline environment on the molecular electronic states. Since the molecules maintain their identity within the

crystal and the overlap of wave functions between molecules is almost negligible, these crystals allow investigations of the theory of crystal excited states in the limit of Frenkel or tightly bound excitons. In this limit the basis functions for the crystal states are assumed to be the localized eigenfunctions of free molecules rather than the delocalized Bloch electron and hole states that are more appropriate for excitons in the more familiar semiconductors. The theory in this limit was initially worked out by Frenkel[17] and Peierls[18] in the 1930's and subsequently extended to the case in which there are several molecules per unit cell and applied to organic molecular crystals by Davydov[19] in 1948. In crystals which have two molecules per unit cell, such as anthracene, Davydov showed that molecular absorption lines would be split into two lines, and the magnitude of this splitting is frequently referred to as the Davydov splitting. Detailed reviews of the state of exciton theory in organic molecular crystals have recently been written by Craig and Walmsley[20] and by Rice and Jortner.[21]

4.1. Singlet Excitons

The polarized absorption spectrum of anthracene obtained by Lyons and Morris[22] is shown in Figure 5. The solid line corresponds to the absorption spectrum obtained with the electric vector parallel to the *b* axis, the broken line to the absorption spectrum with the electric vector parallel to the *a* axis, and the dotted line to the spectrum of anthracene in solution in *n*-heptane. The lowest-energy transition at about 3.1 eV in the crystal is readily identified with the lowest-energy transition in the solution and is clearly separated from other transitions at higher energies. This transition is a ${}^1B_{2u} \leftarrow {}^1A_{1g}$ transition with its dipole moment parallel to the short axis of the molecule. In the crystal the oscillator strength of the transition with the electric vector parallel to the *a* crystal axis is 0.02, and that with the electric vector parallel to the *b* axis is 0.06.

A large percentage of the experimental and theoretical work devoted to understanding the optical absorption spectra of anthracene crystals has centered on measuring and calculating the Davydov splitting of the various vibrational states in this transition. In first order the crystalline environment splits each electronic transition into two lines, and this splitting is apportioned among the various vibronic states in accordance with their Frank–Condon factor. The splitting of the electronic state is caused by intermolecular interactions.

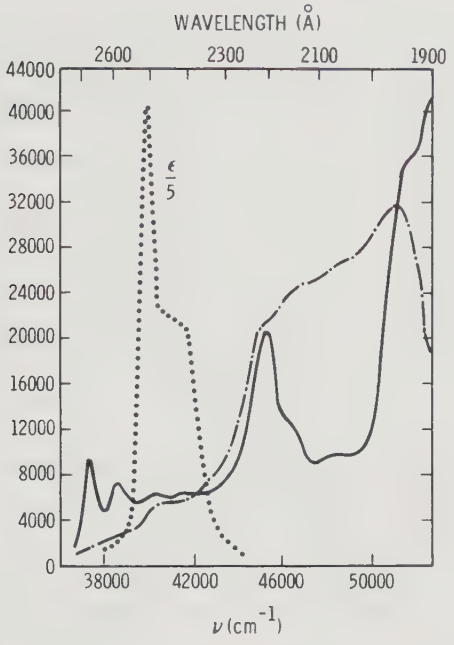

Fig. 5. Polarized absorption spectrum of anthracene. The solid line is for the light polarized parallel to the *b* axis, the broken line is for light polarized parallel to the *a* axis, and the dotted line is the absorption spectrum observed for anthracene molecules dissolved in *n*-heptane. (Lyons and Morris.[22])

Craig[23] was the first to attempt to calculate the magnitude of the Davydov splitting in anthracene. He approximated the interaction potential by a multipole expansion and retained only the dipole term. He also pointed out that in the situation where there is a strong transition above a relatively weak one, as is the case for the lowest-energy transition in anthracene, important contributions arise from interactions of the upper state of the weak transition in one molecule with the upper states of strong transitions in neighboring molecules. Craig and Hobbins[24] obtained reasonable agreement between theory and experiment, allowing them to make an assignment of the lowest crystal transition.

There have subsequently been many attempts to improve the agreement between theory and experiment and to investigate the crystal shape dependences that some theories predict. Various

authors have investigated the effects of retardation, the approximation of setting the crystal momentum equal to zero, and charge transfer exciton states. In general, it has been found that it is possible to fit the experimental results in several different ways theoretically, so that at the present time it is not possible to determine the importance of various effects that can be included.

The difficulty of obtaining agreement between theory and experiment has not all been the theoreticians' fault. The experimentalists have had their difficulty, too. The earliest experiments were carried out on extremely thin crystals (0.1 μm), and the thinnest crystals usually were mounted on silica or fluorite disks. Differential thermal expansion in this case causes distortion in the crystal, and it has been shown that uncertainty in the splitting from this cause may be as much as 40 cm^{-1} in the 0–0 transition (the transition for the lowest vibration state in the ground state to the lowest vibrational state in the excited electronic state).[24a] The use of incompletely polarized light also produced errors in the early measurements of both the Davydov splitting and the polarization ratio.

The most recent experimental measurements have been carried out using reflection spectra from relatively thick crystals.[25–30] Clark and Philpott[28] reported for the (0–0), (0–1), and (0–2) transitions (i.e., for transitions from the lowest vibrational state in the ground state to the lowest, first excited, and second excited vibrational states in the excited electron state) the values 190, 110, and 60 cm^{-1}, respectively, for the Davydov splittings. These results are for light incident on the (001) crystal face. They also investigated the absorption spectra for light incident on the $(20\bar{1})$ and $(\bar{1}10)$ faces and obtained qualitative agreement between theory and experiment. Detailed studies of the temperature dependence of the line shapes have been carried out for the (0–0) band and the experimental results compared with various theories of exciton–phonon interaction.[25]

Much less effort has been expended in attempts to understand the crystal spectra at higher energies. The free molecule exhibits an absorption maximum at 42,270 cm^{-1} with an oscillator strength of 1.6. In the crystal this absorption band is split into two Davydov components, one at 37,000 cm^{-1} with an oscillator strength of 0.047 and *b*-axis-polarized, and the other at 53,000 cm^{-1} with an oscillator strength of 0.37 and *a*-axis-polarized. The very large Davydov splitting, 16,000 cm^{-1}, results because the oscillator strength is large and the transition dipole moment is long-axis-polarized, allowing very strong interaction between neighboring

molecules in the two factor group states. Koch and Otto[30] have recently reported on a detailed study of this region of the spectrum.

The long-wavelength tail on the first or lowest-energy exciton absorption band has been investigated in considerable detail as a function of temperature.[31–35] It has been shown that the absorption coefficients obey Urbach's rule[36] in this region. This rule is an empirical relation derived from studies of exciton absorption bands in ionic crystals. Urbach showed that the absorption coefficient κ on the low-energy side of an exciton transition varied with the temperature as $\kappa = \kappa_0 \exp[\sigma(h\nu - h\nu_0)/kT]$, where σ is an arbitrary constant near one, ν is the frequency of the incident light, ν_0 is the frequency of the exciton transition, h is Planck's constant, k is the Boltzmann's constant, and T is the temperature. Sceats and Rice[37] have discussed the implications of the applicability of Urbach's rule to molecular crystals and argue that the Urbach-rule behavior can arise from the same class of weak exciton–phonon interactions that determine hot band absorption shapes. Very recently investigations of the nature of surface excitation on anthracene crystals have been reported.[38–40] Sugakov[39] has observed a sharp minimum in the reflection spectrum at the frequency of a surface level excitation, and Morris and Sceats[38] found evidence for a surface-roughness-induced molecular exciton. Brodin *et al.*[40] reported the observation of radiative surface excitons, but the same observations have been attributed by Morris and Sceats[25] to strain-induced phenomena.

4.2. Triplet Excitons

Optical transitions directly to the triplet state at 1.8 eV are forbidden in first order because of the spin selection rule. However, because of spin orbit coupling, the transition is sufficiently allowed that the absorption spectrum has been observed several different ways. At room temperature the absorption coefficient is so small that it is not possible to measure the spectrum directly, but Avakian *et al.*[41] utilized the fact that triplet excitons interact with one another to produce singlet excitons which in turn radiate a fluorescence photon. More will be said about this process later. By measuring the intensity of fluorescence as a function of the wavelength of the exciting light it is possible to obtain the absorption spectra. Figure 6 shows the results of such an experiment. The ordinate in this figure is proportional to the square of the absorption coefficient. From other experiments it was possible to show that the maximum absorption

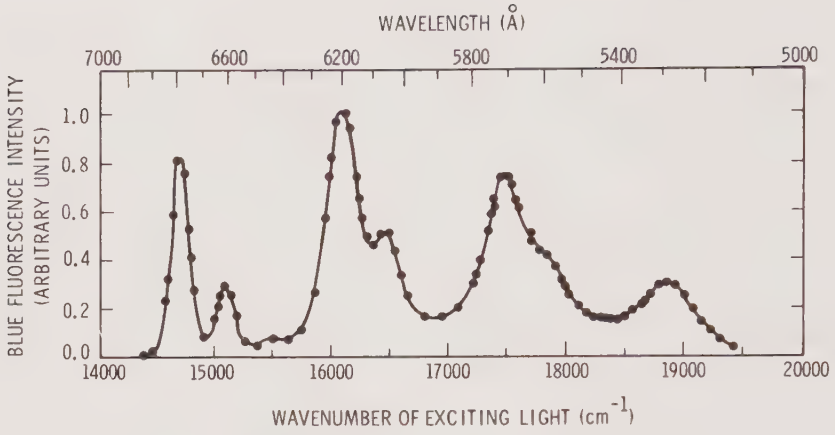

Fig. 6. Fluorescence excitation spectrum of anthracene crystals at room temperature in the vicinity of the triplet exciton absorption band. The ordinate is proportional to the square of the absorption coefficients. (From Avakian *et al.*[41])

coefficient was $(1/f)(3.4 \times 10^{-4}\ \text{cm}^{-1})$, where f is the fraction of triplet exciton annihilations that lead to delayed fluorescence. The fraction f is believed to be near one but has not been determined experimentally.

Smith[42] has shown that it is possible to measure the excitation spectra indirectly by measuring the phosphorescence excitation spectra. The phosphorescence was shown to result from the radiative decay of the triplet excitons. Sharp and Schneider[43] have shown that the triplet absorption spectrum is reproduced if the photoconductivity excitation spectrum is measured in the vicinity of the triplet exciton band. Presumably the triplet excitons diffuse to the surface and inject carriers into the crystal from surface states. Clarke and Hochstrasser[44] have shown that the absorption spectrum at 4.2°K is so sharp that it is possible to observe it directly in thick crystals. By observing the Zeeman splitting of the absorption in a magnetic field of 93,000 Oe they were able to make the absolute assignment of $^3B_{2u}$ for the spatial symmetry of the lowest triplet state of the anthracene molecules, and they observed a Davydov splitting of the 0–0 transition of 22 cm^{-1} at 4.2°K.

Jortner *et al.*[45] have calculated the magnitude of the intermolecular electron exchange integrals that contribute to the Davydov splitting. In the case of triplet states the Coulomb integrals, which provide the long-range interaction so important in the theory of singlet excitons, are negligible with respect to the intermolecular exchange

integrals because of spin selection rules. Only very short-range interactions, where wave functions overlap between molecules, are important. Jortner *et al.*[45] calculated that the total splitting for this state would be 35 cm^{-1}. Taking into account the various vibrational states, the splitting of the (0–0) transition attributable to this interaction was estimated to be 8 cm^{-1}. Choi *et al.*[46] considered the possible importance of charge transfer states in which an electron is transferred from one molecule to another and concluded that these states may contribute as much as 5 cm^{-1} to the Davydov splitting of the (0–0) transition.

5. Fluorescence

Anthracene crystals exhibit a very high fluorescence quantum efficiency and as a result have been used extensively as scintillators. The quantum efficiency for fluorescence is generally believed to be about 0.80 for thick crystals where fluorescence reabsorption is important and is about 0.94 for thin crystals where reabsorption is negligible.[47] The fluorescence lifetime of a uniformly excited thick crystal at room temperature is about 27 nsec. As the crystal thickness is decreased, however, the observed lifetime decreases to about 10 nsec.[48] The lifetime of 10 nsec is essentially obtained by the time the crystal thickness is 50 μm, showing that the decrease in lifetime is not a surface quenching phenomenon, but that lifetimes greater than 10 nsec result from reabsorption (see Figure 7). Similarly, as the temperature of a crystal is lowered the amount of fluorescence reabsorption decreases, as does the fluorescence lifetime.[48]

Early measurements of the anthracene fluorescence spectra were dominated by impurity effects but, measurements on very high-purity crystals have now provided very nearly the intrinsic fluorescence properties.[49] The relationship of the absorption and fluorescence spectra is shown schematically in Figure 8. In absorption, transitions occur from the ground vibrational state in the ground electronic state to various vibrational states in the excited electronic state. Fluorescence transitions at low temperatures occur only from the lower of the split levels, labeled A_u in Figure 8, giving a single *b*-polarized transition to the electronic ground state and both *a*- and *b*-polarized bands, with little or no splitting, in transitions to the vibrational sublevels. At higher temperatures the upper Davydov component in the excited electronic state becomes populated and the transitions indicated by dashed lines in Figure 8 become possible.

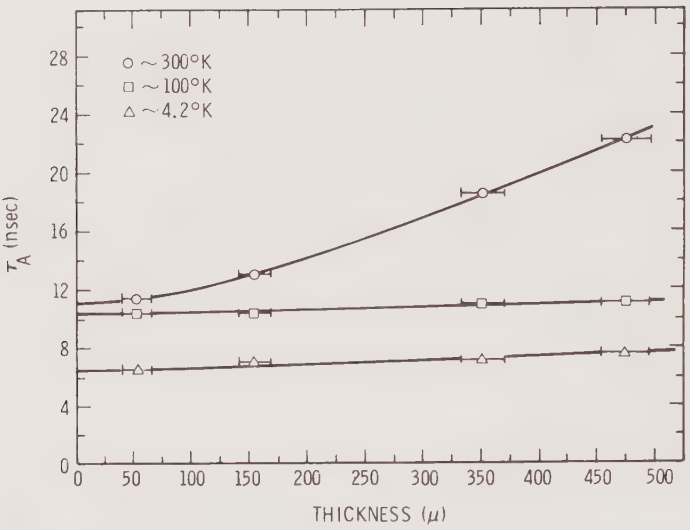

Fig. 7. Variation of fluorescence lifetime with crystal thickness in uniformly excited crystals. (From Powell.[48])

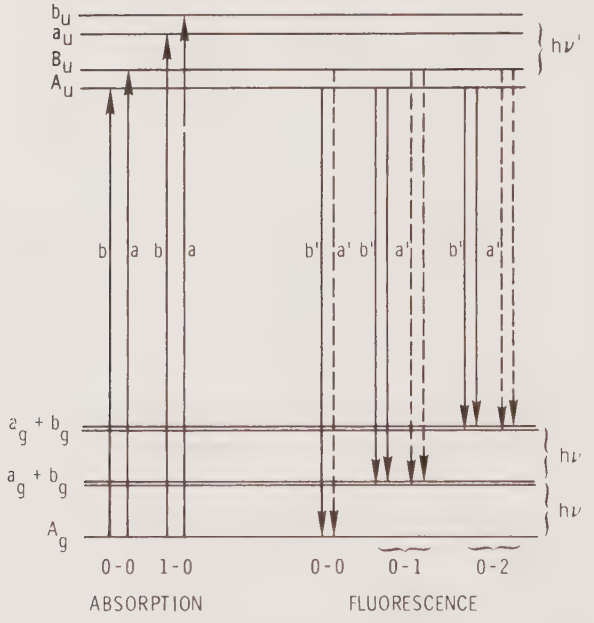

Fig. 8. Absorption and fluorescence transitions in anthracene crystals indicating polarization directions. (From Akon and Craig.[181])

Experimentally it has been found that, as expected theoretically, the polarization ratio for the 0–1, 0–2, and 0–3 transitions are equal to within experimental error and that the polarization ratios are about 5.

The low-temperature fluorescence spectrum of anthracene has been examined a number of times, but agreement on the assignment of bands is still not complete. The most recent investigations have been carried out by Lyons and Warren,[50] Glockner and Wolf,[51] and Limareva *et al.*[52] Lyons and Warren[53] have also investigated the effect of various impurity molecules on the fluorescence spectrum of anthracene, and Glockner and Wolf[54] have investigated the fluorescence spectra of the mixed crystal system anthracene–perdeuteroanthracene.

6. Energy Transport

There are three ways in which energy can be transferred over some distance in an anthracene crystal: fluorescence photon reabsorption, long-range resonance interaction, and exciton diffusion.

It is clear that fluorescence reabsorption plays a role, at least at temperatures above about 100°K, but very little work has been done regarding energy transfer by this process. It is known, for example, that reabsorption increases the fluorescence lifetime at higher temperatures for thick crystals.[55] Recent experimental results on fluorescence lifetime vs. crystal thickness obtained by Powell[48] are shown in Figure 7. Also, reabsorption has to be considered when fluorescence spectra are measured. If the fluorescent photons have to traverse a fairly large amount of the crystal, many of the higher energy photons will be absorbed, shifting the fluorescence spectra to lower energies. Beyond observations of this type, however, very little has been done, primarily because the process is of no fundamental interest.

The theory of long-range resonance interaction was initially treated by Förster[56] and Dexter.[57] When the emission spectrum of an excited molecule overlaps with the absorption spectrum of a nearby unexcited molecule it is possible for the excitation energy to be transferred from the excited molecule to the unexcited one. This process, which does not involve the emission and reabsorption of a photon, can take place over distances up to something on the order of 50 Å for strongly allowed transitions. Usually the dominant interaction is a dipole–dipole interaction and in this case the probability per unit time of energy transfer is given by $P = (1/\tau)(R_0/R)^6$, where τ

is the excited state lifetime and

$$R_0 = \left(\frac{3f\Phi}{4(2\pi n)^4 \bar{\nu}^4} \frac{e^2}{mc^2} \int g_E(\nu) g_u(\nu)\, d\nu \right)^{1/6}$$

Here $g_E(\nu)$ and $g_u(\nu)$ are the spectral distribution functions of the excited molecule emission and the unexcited molecule absorption spectra, respectively; $\bar{\nu}$ is the mean wave number in the region of spectral overlap; R is the distance between the excited and unexcited molecules; f is the oscillator strength of the transition in the unexcited molecules; and Φ is a molecular orientation factor. R_0 is the distance between the excited and the unexcited molecules at which the energy transfer probability is equal to the reciprocal of the lifetime of the excited molecule in the absence of energy transfer.

Energy transfer by long-range resonance interactions has been shown to take place between various types of impurity molecules imbedded in host lattices, and very good agreement between theory and experiment has been obtained.

6.1. Singlet Excitons

In general most of the energy transfer in anthracene crystals has been attributed to the motion of singlet excitons. It has long been known that a very efficient energy transfer process takes place in anthracene crystals. When only one part in 10^6 tetracene molecules is added to an anthracene crystal, about half of the fluorescence photons emitted by the crystal come from tetracene molecules. Photon reabsorption certainly cannot account for this result. Second, at a concentration of one part in 10^6 the average distance between tetracene molecules is over 1000 Å; therefore it appears that it is impossible to account for the very efficient energy transfer by long-range resonance interactions. For these reasons it has generally been concluded that exciton diffusion has to be involved to account for these results.

In order to discuss energy transfer from the host anthracene lattice to the tetracene impurity molecules, it is convenient to write the following rate equations:

$$\dot{n}_A(t) = G(t) - \beta_A n_A(t) - k n_A(t)$$

$$\dot{n}_T(t) = k n_A(t) - \beta_T n_T(t)$$

where n_A is the concentration of anthracene excitons, n_T is the concentration of excited tetracene molecules, β_A is the decay rate of the anthracene excitons in a pure crystal, β_T is the decay rate of excited

tetracene molecules in an anthracene crystal, and k is the energy transfer rate constant. Considering the exciton as a particle diffusing about in the crystal, there are two simple approximations that have been used for k, depending on the ratio of the exciton mean free path to the radius of interaction between the exciton and an impurity molecule. If the mean free path is large compared to the radius of interaction, then the energy transfer rate would be $k = \sigma v N_T$, where σ is the cross section for interaction between an exciton and an impurity molecule, v is the exciton wave packet velocity $(1/\hbar)\partial E(k)/\partial k$, where $E(k)$ is the energy of the exciton as a function of wave vector k, and N_T is the concentration of impurity molecules.[58] σv corresponds to a volume swept out per unit time by an exciton, and $\sigma v N_T$ therefore corresponds to the number of impurity molecules with which an exciton would interact per unit time. An equation of this type is valid only when the exciton mean free path is large compared to the radius of the interaction cross section.

When the exciton mean free path is shorter than the interaction radius it is not possible to think of it as sweeping out a certain volume per unit time because scattering events very frequently cause it to double back and cover volumes previously covered. It has been shown,[59] however, that if diffusing particles interact when they come within the distance R from an impurity and disappear from the diffusing population in the process, the rate at which they disappear is $4\pi DR[1 + R(\pi Dt)^{-1/2}]$ per impurity molecule, where D is the diffusion coefficient, and therefore $k = 4\pi DR[1 + R(\pi Dt)^{-1/2}]N_T$. The second term in this equation is important only at times shorter than the time it takes the diffusing species to diffuse a distance R and corresponds to the capture of some of those particles—excitons in the present problem—that started out very near an impurity.

There have been at least two attempts to take into account the fact that excitons diffuse and at the same time interact with impurities by long-range resonance interactions.[60,61] In the two above formulas for k, the simplifying assumption was made that the exciton did not interact with an impurity until it came within a distance R (setting $\sigma = \pi R^2$ in the kinetic gas formula) and that it interacted every time it came within that distance. In the theoretical treatment that takes into account long-range resonant interactions as well as diffusion it has always been assumed that the mean free path of the diffusing particles was small compared to the interaction distance.

In spite of the success of the delocalized exciton band picture in explaining the optical absorption spectra it has almost always been

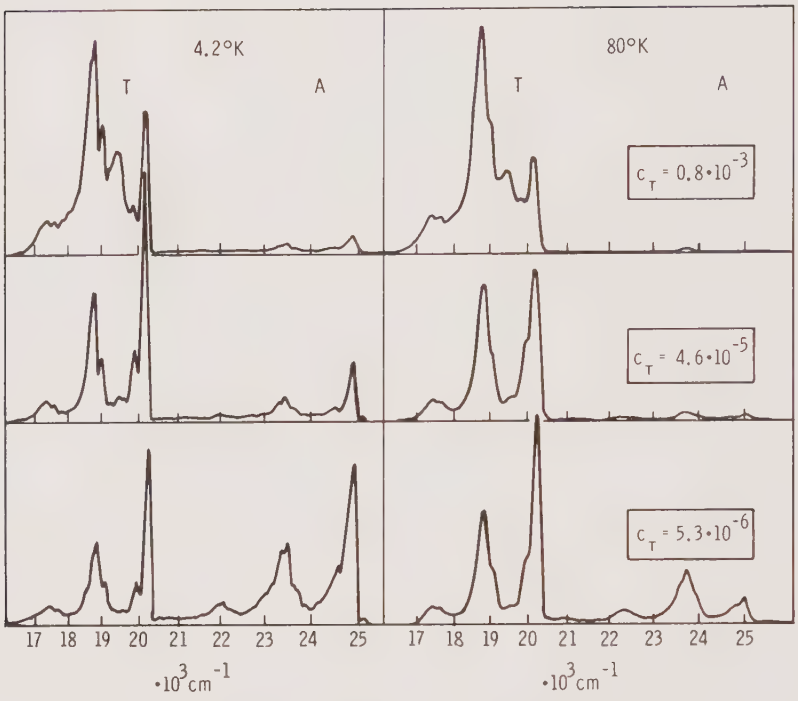

Fig. 9. Fluorescence spectra of anthracene–tetracene mixed crystals at 4.2 and 80°K and for the concentrations 0.8×10^{-3}, 4.6×10^{-5}, and 5.3×10^{-6} for the top, middle, and bottom spectra respectively. (From Benz and Wolf.[182])

assumed in discussions of exciton transport that the exciton is localized on a given molecule and moves by hops to neighboring molecules. For example, Trlifaj[62] has very extensively treated the case in which the exciton is self-trapped and moves about by hopping to nearby molecules through long-range resonance interactions. Using this model, he calculated a diffusion coefficient of 5×10^{-3} cm^2/sec.

There have been relatively extensive experimental investigations of energy transfer in doped anthracene crystals.* The energy transfer coefficient is measured by measuring the relative yield of fluorescence from the host and from the impurity molecule as a function of the impurity concentration or by measurement of decay time of the host and impurity molecule fluorescence as a function of impurity concentration. The fluorescence spectra observed for several different tetracene concentrations are shown in Figure 9. In the case

* See the review article by Wolf.[63]

of tetracene-doped anthracene it is found that k/N_T is about 6×10^{-10} cm^3/sec. Temperature dependence studies of k indicate that it is relatively independent of temperature except at very low temperatures, where experimental results disagree, and it appears that unidentified impurities play important roles.

In order to calculate a diffusion coefficient from these experimental data it is frequently assumed that the exciton mean free path is small or at most comparable to the exciton–tetracene interaction distance so that $k = 4\pi DRN_T$ can be used, and it is frequently further assumed that $R \sim 10$ Å, so that D turns out to be on the order of 5×10^{-4} cm^2/sec, about an order of magnitude smaller than predicted by Trlifaj's theory. Powell[64] has calculated D by using the experimental value of k and the combined theory of Yokota and Tanimoto and obtained the same value. He assumed that $R_0 = 30$ Å and that the exciton lifetime is 27 nsec.

The experiment most frequently cited as evidence for exciton diffusion is that carried out by Simpson.[65] On one side of a thin layer of pure anthracene he placed a layer of tetracene-doped anthracene to act as an exciton detector, and then he irradiated the other side of the thin layer of pure anthracene with 3650-Å light. In this experiment the luminescence emitted by the detector is derived partly from excitation by that fraction of the primary radiation not absorbed in the pure anthracene layer and partly from excitons originating in the pure anthracene but diffusing to the detector. A separate measurement of the transmission of the pure anthracene layer suffices to separate the two contributions and hence to determine the flux of excitons into the detector. From the experiment, Simpson determined a value of 460 Å for $(D\tau)^{1/2}$ for singlet excitons. Assuming that the exciton lifetime in these thin samples is 10 nsec, we find D to be about 2×10^{-3} cm^2/sec.

Studies of fluorescence quantum yield and photoconductivity as a function of wavelength have also been interpreted in terms of exciton diffusion and yielded diffusion coefficients of a similar order of magnitude. It has been shown that the fluorescence and photoconductivity quantum yields[66] are single-valued functions of the exciting light extinction coefficient, and if it is assumed that the excitons are quenched by the surface or yield carriers when they come in contact with the surface, an exciton diffusion length $(D\tau)^{1/2}$ of the order of 1000 Å is found. It has also been shown that the diffusion length derived from these experiments is shortened by impurities just as theory predicts.[67] Kurik and Piryatinskii[68] recently repeated both the

Simpson experiment and the photoconductivity vs. wavelength experiment. They obtained roughly the same results and concluded that the diffusion length decreased with decreasing temperature.

At very high exciton concentrations, Tolstoi and Abramov[69] have shown that the fluorescence quantum efficiency of anthracene crystals decreases and Bergman *et al.*[70] have shown that the exciton lifetimes decrease. These observations can be explained by assuming a bimolecular exciton interaction in which excitons are annihilated and the value reported for the interaction rate constant ranges from 4×10^{-8} to 2×10^{-9} cm^3/sec. If it is assumed that the excitons diffuse with a mean free path which is small compared to the distance R at which excitons interact, then the interaction rate constant is equal to $8\pi DR$, two times $4\pi DR$, because both excitons are diffusing. Therefore, $D \sim 10^{-3}$ cm^2/sec if R is of the order of a lattice constant and the lower value for the interaction rate constant is right. However, it appears likely that singlet excitons would interact rapidly at distances much greater than a lattice constant and that these experiments therefore imply that $D < 10^{-3}$ cm^3/sec.

In contrast to the general but relatively crude agreement among the various experimental results regarding exciton diffusion discussed so far, it was recently shown that exciton diffusion theory cannot be made to fit experimental results if the time evolution of energy transfer from the host lattice to impurity molecules is studied.[71] Experimentally it is found that energy transfer at short times is greater than can be accounted for by exciton diffusion, at least in the way exciton diffusion is presently treated. The effect is most pronounced for lightly doped samples, and an example of the type of experimental result obtained is shown in Figure 10. This figure shows the experimentally observed time dependence of the fluorescence from tetracene impurity molecules in an anthracene host crystal following excitation of the crystal by two-photon absorption of a single-mode, locked ruby laser light pulse. The dashed line indicates the expected time dependence assuming energy transfer by exciton diffusion. The solid line was calculated using the combined theory of energy transfer[60] treating D and R_0 as adjustable parameters. By simultaneously fitting experimental data from crystals containing several different impurity concentrations, the values of D and R_0 were found to be 10^{-5} cm^2/sec and 100 Å, respectively. Temperature dependence studies indicate that the need for a diffusion coefficient in order to fit the experimental data at high temperatures may result from fluorescence reabsorption. At low

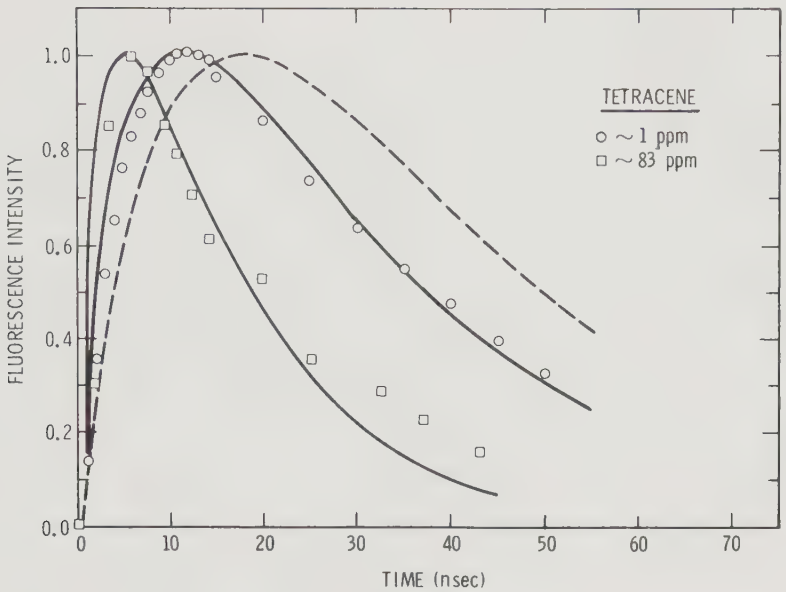

Fig. 10. Time dependence of the tetracene fluorescence intensity in anthracene doped with 1 ppm tetracene after excitation by two-photon absorption of a single-mode locked ruby laser pulse. The curves correspond to the best fit to the experimental data that could be achieved using the various theories. (From Powell and Kepler.[71d])

temperatures where fluorescence reabsorption is negligible, the data can be fit with Förster–Dexter theory assuming dipole–dipole interactions with no diffusion and $R_0 = 100$ Å. The difficulty with this approach is that 100 Å is much too large for R_0.

Soos and Powell[72] recently generalized the usual treatment of nearest-neighbor random walks with trapping on the first encounter to include both steps of arbitrary length and extended trapping regions. Using this model, they concluded that the exciton diffusion coefficient is of the order of 3×10^{-5} cm^2/sec, that the hopping time is $\sim 2 \times 10^{-11}$ sec, and that the radius of the extended trapping region is ~ 28 Å. Powell and Soos[73] have recently written a comprehensive review of the experimental investigations of singlet exciton diffusion.

The interactions of singlet excitons with metal electrodes,[74] with charge carriers,[75] and with each other[76] have been the subject of recent investigations.

6.2. Triplet Excitons

In contrast to the unsettled situation regarding singlet exciton diffusion, diffusion of triplet excitons is well-established. Prior to about 1962, however, it was generally believed that energy transport by triplet excitons could be neglected because, since the transition was spin forbidden, only an exchange integral was involved in the interaction of an excited state with its neighboring molecules. It was originally believed that the exchange integrals would be negligibly small. In 1962 and 1963 Robinson and co-workers,[77] however, showed that the interaction could be quite large, at least in benzene and naphthalene crystals, and that because of the long triplet state lifetime, energy could be transferred over much greater distances by triplet excitons than by singlet excitons.

Since the early observation that energy transport by triplet excitons was a very important process, a large number of experiments have been carried out investigating the properties of triplet excitons, particularly in anthracene. A very useful property of triplet excitons that has made the majority of the experiments possible is that two excitons can interact to produce a singlet exciton which, with a very high probability (about 0.80), radiatively decays emitting a fluorescence photon.[78] In anthracene each triplet exciton has an energy of 1.8 eV and a singlet exciton has an energy of 3.2 eV. It has been shown that the exciton concentration n in an anthracene crystal is given by the following equation at room temperature:

$$\partial n/\partial t = g - \beta n - \gamma n^2 + D\nabla^2 n \tag{1}$$

where g is the rate at which excitons are generated, β is the reciprocal of the exciton lifetime, and γ is the bimolecular annihilation rate constant. The intensity of fluorescence photons emitted is

$$\varphi = \tfrac{1}{2} f \gamma n^2$$

where f is the fraction of mutual annihilation events that result in a fluorescence photon. The factor 1/2 is included because two triplet excitons have to disappear to create one singlet exciton.

This behavior of triplet excitons has made possible many experiments designed to study the physical processes involved in exciton creation, migration, decay, and interaction with each other and traps. An important conclusion resulting from this work is that triplet excitons do not move as coherent wave packets, as might be

observed for excitons, but their diffusion can be described as independent energy transfer events between neighboring molecules.

Triplet excitons can be generated by direct absorption of photons, but the transition probability is very small, so that it is not possible to observe the absorption spectra directly. However, by observing the blue fluorescence light emitted by a crystal while exciting it with intense, variable-wavelength light in the exciton absorption band, the excitation spectrum shown in Figure 6 is obtained.[41] At the very low exciton concentrations that can be achieved in an experiment of this type, even with very intense xenon arc lamps and wide monochromator slit settings, the bimolecular annihilation term in Eq. (1) plays a negligible role, so that the exciton concentration is directly proportional to the incident light intensity and to the absorption coefficient. Therefore, the ordinate in Figure 6 is proportional to the square of the absorption coefficient since $\varphi = \frac{1}{2}\gamma f n^2$. This experiment does not provide an absolute value for the absorption coefficient, but by utilizing the intense light available from a ruby laser, it is possible to determine the absolute value within a factor f at 6943 Å and then use relative data such as those shown in Figure 6 to obtain absolute values at other wavelengths. The absolute value can be obtained because at very high exciton concentrations $\gamma n^2 \gg \beta n$, so that the dominant process for loss of excitons is bimolecular interactions. If the total number of fluorescence photons emitted by a crystal Φ is measured under these conditions, it is possible to determine the absorption coefficient within a factor $1/f$. Experiments with a ruby laser[78] have shown that at room temperature $\alpha = (1/f) \times 10^{-5}\ \text{cm}^{-1}$, so that at the peak of the absorption spectrum at 6200 Å, $\alpha = 3.4(1/f) \times 10^{-4}\ \text{cm}^{-1}$.

The lifetime of triplet excitons in very pure crystals is about 25 msec. The radiative lifetime, however, is about $60/f$ sec, so that only about one in 2000 free triplet excitons decays radiatively.[42] The phosphorescence spectrum has been measured, and at room temperature it has been shown that the 0–0 transition occurs at the same energy in both absorption and emission, and this observation has been interpreted to mean that the excitons are essentially free at room temperature.[42] At low temperatures trapping phenomena, mostly from unidentified impurities, are observed.

In addition to creation of triplet excitons by direct absorption of photons it is possible to create them indirectly by first creating singlet excitons, some of which decay by intersystem crossing into triplet excitons.[79] The rate constant for this process is about

1.5×10^7/sec,[80] and since the singlet exciton lifetime is 28 nsec, about 28% of the singlet excitons decay nonradiatively into triplet excitons.

One of the main reasons for the intensive studies that have been undertaken of triplet exciton behavior in anthracene is that it is a system in which rather detailed studies of the transport properties of an exciton can be carried out. It has been fairly well established that triplet exciton transport involves independent random jumps of excitation energy from one molecule to a neighboring molecule and that coherent motion such as that expected in an exciton band picture is not appropriate. It appears that a detailed understanding of triplet exciton motion may provide a new insight into the mechanism of low-mobility transport.

The absolute value of the exciton–exciton annihilation rate constant has been measured by a number of groups. Most of the experiments are based on the fact that at very high exciton concentrations such that $\beta n \ll \gamma n^2$, the concentration–time dependence after excitation has ceased is determined by the rate equation $dn/dt = -\gamma n^2$. The solution to this equation can be written as $1/n = 1/n_0 + \gamma t$, and since the rate of emission of fluorescence photons φ is $\frac{1}{2} f \gamma n^2$, then

$$\varphi^{-1/2} - \varphi_0^{-1/2} = (2\gamma/f)^{1/2} t$$

This experiment requires an absolute measurement of the number of photons emitted by the crystal.

In the first experimental determination of γ by Kepler *et al.*[78] a rather crude determination of the excited volume of the crystal was used and the value for γ/f was reported as 10^{-11} cm^3/sec. Hall *et al.*[81] used a Q-spoiled ruby laser and were thus able to excite a large crystal volume providing a more accurate determination of γ/f. They reported a value of 5.5×10^{-11} cm^3/sec with an uncertainty of 50%. Other reported values range from about 2 to 7×10^{-11} cm^3/sec. Avakian and Merrifield[82] estimated that the best value is 5×10^{-11} cm^3/sec with an error of at least 50%.

The annihilation rate constant does not appear to be much affected by crystal purity and temperatures between 25 and -100°C.[79] At lower temperatures, however, trapping effects become important, and there is evidence that the rate constant for interaction between a free and a trapped exciton is an order of magnitude larger than that for interaction between free excitons.[42]

Two models of exciton–exciton annihilation have been considered. If it is assumed that the excitons move coherently as in an exciton band with a mean free path large compared to the interaction distance R, then it is appropriate to set $\gamma = \sigma v$, where $\sigma = \pi R^2$ and v is the thermal velocity of the exciton wave packet. In the other extreme, where the exciton mean free path is small compared to the interaction distance, $\gamma = 8\pi DR$. Triplet excitons almost certainly have to be on nearest-neighbor molecules before they can interact, so that a reasonable upper limit for σ is of the order of 5×10^{-15} cm^2, and exciton band calculations and measurements of the Davydov splitting indicate that the exciton thermal velocity is probably in the range $(2–10) \times 10^4$ cm/sec. Therefore, an upper limit for γ is of the order of 5×10^{-10} cm^3/sec, which is an order of magnitude larger than the observed value and therefore consistent but not particularly informative.

Jortner *et al.*[45] have obtained a theoretical value of 1×10^{-11} cm^3/sec for γ by assuming that the excitation energy hops from one molecule to another. They concluded from their theoretical investigations that the annihilation rate constant is limited by the rate at which pairs of triplet excitons on nearest-neighbor molecules are formed and that the annihilation of a nearest-neighbor triplet pair involves an ion pair state. The hopping rate was estimated from the magnitude of the exchange integral and charge transfer interactions between nearest-neighbor molecules.

As the authors point out, the agreement between this theory and experiment is somewhat fortuitous because the uncertainties in the calculated electronic matrix elements and in the amount of overlap of the excited-molecule phosphorescence spectrum with the unexcited molecule absorption spectrum make the theoretical estimate uncertain to one order of magnitude.

Additional information regarding exciton–exciton annihilation is provided by studies of the effect of a magnetic field on the annihilation process. Johnson *et al.*[83] have found that at room temperature a magnetic field at very low fields in steady-state experiments causes the delayed fluorescence to increase up to a maximum increase of 5% for a field of about 350 Oe. As the field is increased to higher values, the delayed fluorescence decreases until at 3000 Oe the intensity has decreased to about 85% of the zero-field value. Very little further change in intensity takes place for fields up to 20,000 Oe. Typical experimental results are shown in Figure 11. Using pulsed magnetic fields, it was shown that the magnetic field was in fact affecting the

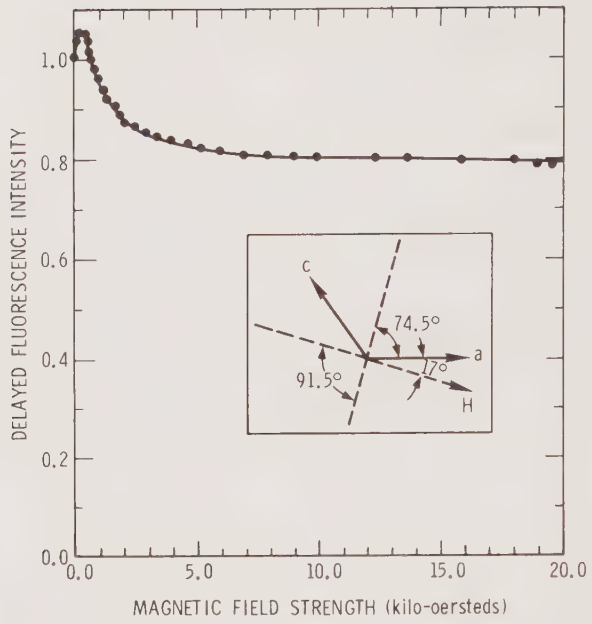

Fig. 11. Variation of delayed fluorescence intensity with magnetic field strength. The magnetic field was in the *ac* plane in the direction indicated in the inset. The dashed lines in the inset indicate the directions of greatest magnetic field effects. (From Johnson *et al.*[83])

annihilation rate constant γ and not the rate of generation of excitons nor the rate of their monomolecular decay. In these experiments it was shown that even though the risetime of the magnetic field pulse was fast compared to the exciton lifetime the delayed fluorescence intensity followed the magnetic field intensity essentially instantaneously. If the magnetic field had been affecting the generation or decay rate, the changes in delayed fluorescence intensity would have occurred with a time constant determined by the exciton lifetime. The magnitude of the magnetic field effect is orientation dependent. It has been shown that these effects can be explained by assuming that the rate of triplet pair annihilation is proportional to the fractional singlet character of the pair state. The fractional singlet character of the pair states is magnetic field dependent because of an interplay of the Zeeman interaction and the zero-field splitting of the triplet state.

Merrifield[84] has shown that an analysis of the field dependence of the annihilation rate leads to the conclusion that about one triplet–triplet encounter in 25 leads to annihilation rather than one

out of nine as had been commonly assumed. The factor 1/9 had come from the assumption that only singlet pair states could annihilate because of spin selection rules and that there were nine possible states for a triplet exciton pair, only one of which was a singlet.

The status of studies of magnetic field effects on triplet–triplet annihilation in organic crystals has been reviewed by Merrifield[85] and Avakian and Suna,[86] and studies of magnetic field effects on the annihilation rate constant of anthracene triplet states in solution have been reported recently.[87]

Considerably more has been learned about the details of exciton motion from studies of exciton diffusion. Avakian and Merrifield[88] were the first to directly measure the triplet exciton diffusion coefficient. They utilized the bimolecular nature of the exciton–exciton annihilation to measure the spatial distribution of excitons. The principle of their experiment was to generate triplet excitons in regions of a crystal sufficiently small such that during their lifetime a substantial fraction of the excitons would diffuse out of the illuminated region. Since the total delayed fluorescence intensity is $\frac{1}{2}\gamma \int n^2\, dv$, when the excitons diffuse out of the illuminated region the fluorescence intensity decreases even though the total number of excitons present in the crystal is unchanged. For example, if the total number of excitons in the crystal is N and they are distributed uniformly throughout the volume V of the crystal, the fluorescence intensity is $\frac{1}{2}\gamma(N/V)^2 V = \frac{1}{2}\gamma N^2/V$. Whereas, if the same number of excitons is concentrated in half the volume of the crystal the fluorescence intensity is $\frac{1}{2}\gamma(2N/V)^2 \frac{1}{2}V = \gamma N^2/V$, which is twice the previous intensity.

Avakian and Merrifield[85] achieved an appropriate spatial distribution by irradiating a crystal with light from a continuous helium–neon laser with a Ronchi ruling (a grating with alternating opaque and transparent strips of equal width) between the laser and the crystal. The dependence of the intensity of the delayed fluorescence on the ruling period was measured. Care was taken to be sure that the condition $\gamma n^2 \ll \beta n$ was fulfilled so that triplet–triplet annihilation only acted as a probe of the exciton density and did not significantly influence the exciton concentration. This first experiment was subsequently improved by the addition of time dependence measurements,[89] and the best experimental value for the diffusion length $l = (2D\tau)^{1/2}$ is believed to be 22 μm.

For a while it was believed that the exciton diffusion tensor was isotropic, but very careful measurements by Ern[90] have shown that it is anisotropic as predicted theoretically. He gives for the principal

components of the diffusion tensor the values 1.5×10^{-4}, 1.8×10^{-4}, and 1.2×10^{-5} cm^2/sec for D_{aa}, D_{bb}, and $D_{c^*c^*}$, where a and b are the crystal axes and c^* is perpendicular to a and b. The temperature dependence of the D_{aa} component has been studied by Ern *et al.*,[91] and they found that it increased from $(1.6 \pm 0.3) \times 10^{-4}$ cm^2/sec at 371°K to $(4.0 \pm 0.5) \times 10^{-4}$ cm^2/sec at 118°K.

Other groups have made measurements of the diffusion coefficient using different techniques,[92–94] and in general the results of these experiments agree with those obtained by Avakian and coworkers. Some of these experiments, however, involve interaction of the triplet excitons with a surface, and the nature of that interaction depends strongly on the condition of the surface. Kolb and Wolf[95] have used nuclear magnetic resonance to study exciton motion in anthracene. From their experiments they concluded that the hopping time is 5.5×10^{-12} sec and the diffusion coefficient 1.2×10^{-4} sec^{-1} at 300°K. At 77°K, they found that the hopping time had decreased to 4.1×10^{-12} sec and the diffusion coefficient increased to 1.7×10^{-4} cm^2/sec. Haarer and Wolf[96] have also reported the observation of triplet excitons in anthracene by electron spin resonance.

In general it has been concluded that the experimentally determined magnitude of the diffusion coefficient is evidence that triplet excitons are localized entities existing as an excited state of a given molecule and moving by random hops to nearest-neighbor molecules. Attempts to apply exciton band theory have led to estimates of the exciton mean free path which are unphysically small.[86] Jortner *et al.*[45] have obtained reasonable agreement between theory and experiment using the Förster–Dexter resonant interaction theory to calculate the hopping frequency. Francis and Harris[97] have reported experimental results on a molecular crystal which they interpret as evidence for coherent triplet exciton motion.

Triplet–triplet annihilation has recently been used to study radiation effects in anthracene,[98] and the interaction of triplet excitons with electrons and holes has been studied.[99] The interactions of free anthracene triplet excitons with excitons trapped by tetracene molecules[100] and dye-sensitized delayed fluorescence[101] have also been studied.

In 1969 it was found that one singlet exciton in tetracene crystals could produce two triplet excitons, and this process was called exciton fission.[102] It was originally thought that this process did not occur in anthracene because the activation energy would be too high, but recent experimental results show that it does.[103,104]

Klein *et al.*[104] have shown that the probability of exciton fission depends on the exciting light wavelength and propose that fission occurs from highly excited singlet states. Swenberg and Geacintov[105] have recently reviewed the work on exciton interactions in organic solids.

7. Electrons and Holes

The description of electron and hole transport in low-mobility materials is still an outstanding problem in solid-state physics, and anthracene is a good example of a low-mobility material. The electron and hole mobilities are of the order of 1 cm^2/V sec, and therefore it is questionable whether or not a band theory is applicable. In spite of an apparent complexity it turns out that anthracene crystals are really quite good materials to study, at least from an experimental point of view. It is easy to prepare very pure single crystals. Electron and hole lifetimes in excess of 100 μsec at room temperature are relatively easy to obtain, and crystals with carrier lifetimes in excess of 1 msec have been reported. A number of techniques are available to create electrons and holes in anthracene crystals, facilitating a wide variety of experiments, and an impressive number of experiments have been reported.

As in the case with triplet excitons, a wide variety of experimental observations indicate that the mean free path for motion by both electrons and holes is small, of the order of a lattice constant, and that the band of states in which they move is narrow in energy compared to kT. There is no satisfactory theoretical description of the experimental observations, and it seems that detailed considerations of the experimental observations available will provide new insight into the mechanism of low-mobility transport.

7.1. Electron and Hole Transport

In 1960 LeBlanc[106] and Kepler[107] independently reported that it was possible to study the drift mobility of both holes and electrons in anthracene using a crystal-counter-type technique. It was shown that if an anthracene crystal is placed in an electric field between parallel plate electrodes, one of which is semitransparent, and a pulse of light strongly absorbed by the crystal applied through the semitransparent electrode, both electrons and holes could be

observed to travel through the crystal, even for crystals several millimeters thick. Previous experiments on anthracene had been plagued by electrode and space charge effects, but the pulsed photoconductivity technique requires no electrical contact, and the number of carriers required for a measurement of the drift mobility is too small to introduce significant space charge fields. In this experiment the current observed in the external circuit is nev/d, where n is the number of carriers moving, e is the electronic charge, v is their drift velocity, and d is the distance between the electrodes. The drift velocity of the carriers is equal to $\mu E = \mu V/d$, where μ is the drift mobility, E is the electric field, and V is the voltage applied between the parallel plate electrodes.

This experimental technique made it possible to measure both the drift mobility and number of carriers generated. In the early experiments the carriers were generated essentially at the surface of the crystal near the illuminated electrode. Therefore, when the illuminated electrode was positive, only holes moved through the crystal, and when the illuminated electrode was negative, electrons moved through the crystal. The length of the current pulse τ corresponded to the time it took the carrier to move through the crystal and the carrier drift mobility μ was calculated from $\mu = d^2/V\tau$.

The drift mobilities of both holes and electrons were found to be about 1 cm^2/V sec and to be slightly anisotropic.[108] The experimentally observed anisotropy in the *ab* plane is shown in Figure 12. In the c' direction, perpendicular to the *ab* plane, the hole and electron drift mobilities are 0.8 and 0.4 cm^2/V sec, respectively. In general, as the temperature is lowered, the drift mobilities of both electrons and holes increase but there is disagreement regarding just how fast. The temperature dependence is generally represented as some inverse power of temperature T^{-n}, and values reported for n have ranged from 1 to more than 2. A notable exception is the electron drift mobility in the c' direction. In this direction the electron drift mobility is almost independent of temperature but decreases slightly as the temperature is lowered. The drift mobility temperature dependence experiments have, in general, been limited to temperatures above about 100°K by trapping effects.

Since a molecular crystal like anthracene is very compressible, it was anticipated that high pressures might markedly influence the drift mobility, and this has been shown to be true. Application of 3000 atm of hydrostatic pressure changes the crystal volume by about 3%[109] while it changes the drift mobility by about 50%.[108]

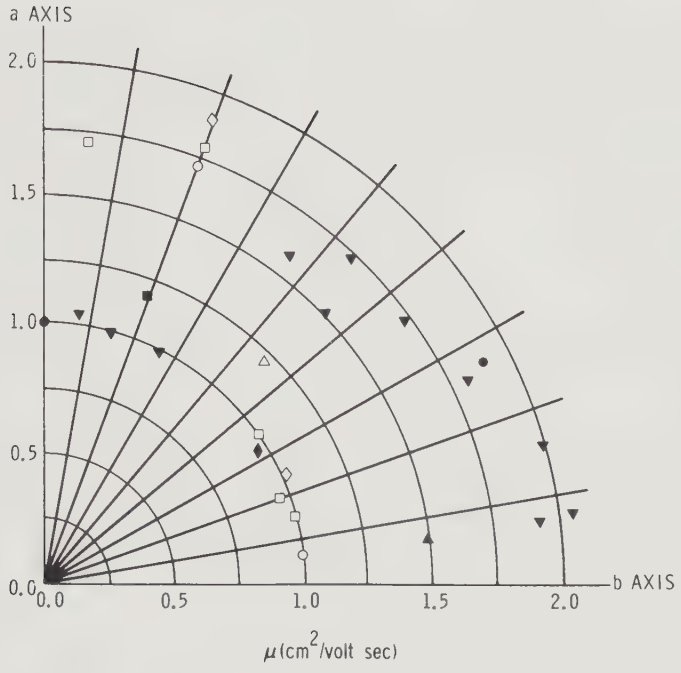

Fig. 12. One quadrant of polar plot of electron and hole mobility in the *ab* plane. The open symbols are for electrons and solid symbols are for holes. Different symbols indicate different origins of the small crystals used for measurements. (From Kepler.[108])

The observation of a drift mobility which increased with decreasing temperature prompted LeBlanc[110] to carry out a tight binding band calculation. He took linear combinations of the highest-energy, normally filled molecular orbitals, using the Hückel coefficients for the molecular orbital and a single Slater orbital to represent the carbon p orbital, to calculate the hole energy band, and similarly, he used the lowest-energy, normally unfilled molecular orbital to calculate the electron energy band. In order to calculate a mobility from the results of the energy band calculation, he assumed an isotropic, energy-independent mean free path or relaxation time. This calculation indicated that the bands were very narrow, on the order of kT wide, but they did appear to satisfy uncertainty principle requirements. It is generally recognized that the simple band approximation breaks down somewhere in the vicinity of 1–10 cm^2/V sec.

The mobility anisotropy predicted by this theory is in surprisingly good agreement with experiment. The ratio of the hole mobility parallel to the a axis to that parallel to the b axis is predicted

to be about 2 and experimentally was found to be 2. For electrons the same ratio was predicted to be about 0.8 and experimentally was found to be about 0.6. Similarly, the right order of magnitude was predicted for the pressure dependence.[111] The actual changes in the unit-cell distances and angles with pressure are not known so it was assumed that the unit-cell distances decreased 1%. Since the experimentally observed mobility anisotropy and pressure dependence seemed to support the theory, there have been numerous improvements added to the work of the initial paper.[111,112]

In these papers the electron–phonon interaction was introduced phenomenologically through the adjustable mean free path or mean free time, and no attempt was made to discuss the interaction quantitatively. Subsequently, there have been a number of papers on the electron–phonon interaction,[113–120] and in general the indications are that the electron–phonon interaction is stronger than is consistent with the simple tight binding band calculation, and some form of hopping motion seems to be called for.

At one time it was believed that a measurement of the Hall effect would be a good test of the validity of tight binding band theory. LeBlanc[121] and Friedman[122] pointed out that if the narrow band theory were right, an anomalous Hall effect would be observed. They found that the magnitude of the Hall current would indicate a mobility of the order 5–10 cm^2/V sec and that the sign of the current should be reversed from what would normally be expected. Numerous measurements of a Hall effect have been reported but the results disagree (see, e.g., Ref. 123). Recently, however, it has become clear that if an anomalous Hall effect were observed it would not necessarily be evidence for the validity of the band theory. A careful examination of small polaron transport theory shows that hopping transport can also exhibit an anomalous Hall effect.[124]

Similarly, it was initially believed that the experimental observation of an increasing mobility with decreasing temperature was strong evidence against hopping-type transport, but again, it appears that this is not necessarily true.[125]

In agreement with the theoretical calculations, it has been shown experimentally that holes move in bands less than kT wide and that the mean free paths for both electrons and holes are small compared to 100 Å. Hoesterey and Letson,[126] in a study of trap-modulated mobility in anthracene, showed that quantitative agreement between theory and experiment can be obtained if it is assumed that all the states in the hole band are within kT of the top. Tetracene molecules

were added in known quantities as an impurity in anthracene crystals, and the drift mobility of holes was studied as a function of both tetracene concentration and temperature. It was found that tetracene molecules act as a hole trap 0.43 eV deep, and holes go into and out of traps many times while traversing a crystal. With multiple trapping, the effective mobility μ^* is reduced from the microscopic mobility μ_0 according to $\mu^* = \mu_0 t_c/(t_c + t_r)$, where t_c is the trapping lifetime and t_r is the trap release time, i.e., the average time a carrier resides in a trap.

Shockley and Read[127] have shown that

$$t_c/t_r = (N_c/N_t)\exp(-E_t/kT)$$

where N_c is the effective density of states in the carrier band and N_t is the density of trapping sites.

The experimentally observed temperature and impurity concentration dependences are shown in Figure 13. It was found that the data could be fit quantitatively with a trap depth of 0.43 eV and with an effective density of states in the hole band equal to the density of anthracene molecules. The solid curves in Figure 13 were calculated

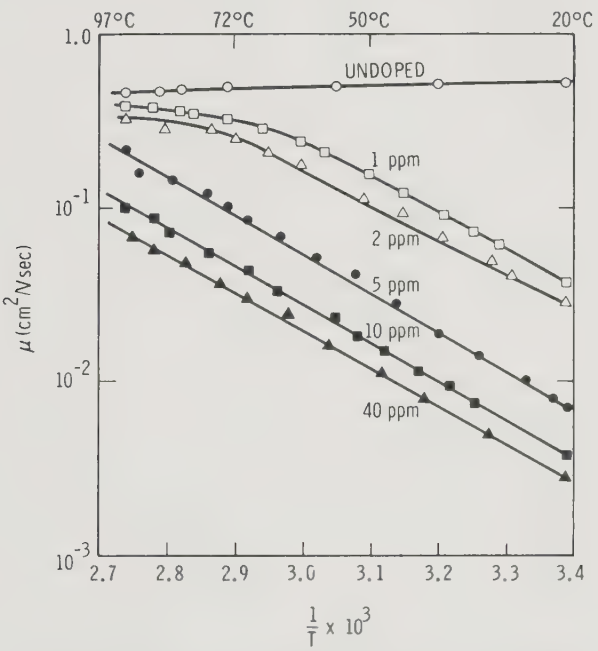

Fig. 13. The temperature dependence of the drift mobility of holes in pure and tetracene-doped anthracene crystals. (From Hoesterey and Letson.[126])

using this theory. Since the effective density of states in the hole band is approximately equal to the density of anthracene molecules, the width of the hole band must be of the order of or less than kT at room temperature.

It has also been shown experimentally in studies of electron–hole recombination and of carrier generation that both electrons and holes have very short mean free paths, small compared to 100 Å. The recombination coefficient studies will be discussed here, but discussion of the carrier generation experiments will be deferred to a later section. A number of laboratories have measured the electron–hole recombination coefficient[128] and found it to be about 1×10^{-6} cm^3/sec. This large value for the recombination coefficient requires that the mean free path of both electrons and holes be small compared to the dimensions of the Coulomb potential well, that is, small compared to the distance at which the potential of one carrier in the electric field produced by the other is equal to kT. This distance is about 120 Å in anthracene. Langevin (see Ref. 129) pointed out that under these conditions the relative drift velocity v_d of an electron and a hole when they are a distance r apart is $(\mu_h + \mu_e)(e/\varepsilon r^2)$, where μ_e and μ_h are the electron and hole drift mobilities, respectively, and ε is the dielectric constant. Therefore, the rate of influx of electrons into a sphere of arbitrary radius r drawn around a hole, and thus the recombination rate constant, is $4\pi r^2 v_d = (4\pi e/\varepsilon)(\mu_h + \mu_e)$. By substituting 1 cm^2/V sec for μ_e and μ_h and $\varepsilon = 3$, we find γ to be 1.2×10^{-6} cm^3/sec, in excellent agreement with the experimental values. For a given mobility the Langevin theory gives the upper limit for the recombination coefficient. If the mean free path were larger than 100 Å, the recombination coefficient would have to be smaller. Therefore, it is concluded that the carriers have mean free paths small compared to 100 Å.

An experimental observation which may ultimately be important in determining which theoretical model correctly describes electron and hole transport is that the drift mobility of carriers in anthracene is independent of applied fields up to fields of 1.6×10^5 V/cm.[130] At this field the drift velocities are comparable to estimates of the thermal velocity of the carriers, as calculated from the anthracene band structure.

In summary, it has been shown experimentally that electrons and holes in anthracene have drift mobilities of the order of 1 cm^2/V sec, and that the mobilities are weakly temperature dependent and independent of field up to 10^5 V/cm. Also, the carriers move in a band of

states which is less than kT wide with a mean free path which is small compared to 100 Å. It seems fairly certain that the tight binding band theory is inadequate to explain these observations and that some form of hopping motion needs to be incorporated into the theory.

7.2. Electron and Hole Generation

As might be expected, the carrier generation processes in these low-mobility, short-mean-free-path molecular crystals exhibit some differences from the well-understood high-mobility materials, and it appears that very careful studies of the carrier generation process will provide new insight into carrier transport processes in these low-mobility materials. Excitons play a large role in some of the processes, and discussions are in progress regarding the role of highly excited molecular states and geminate recombination, i.e., recombination of a newly created electron–hole pair before they have had a chance to separate from one another. Typically, the quantum efficiency for the various carrier generation mechanisms has been found to be extremely low, of the order of 10^{-4}.

In the early work on photoconductivity in anthracene the dominant carrier generation process involved creation of singlet excitons by photons, followed by interaction of some of the excitons with the crystal surface, where they produced free carriers. The photoconductivity excitation spectrum coincided with the absorption spectrum (the data of Steketee and de Jonge[131] are shown in Figure 14), and it has been shown that the experimental results can be interpreted in terms of an exciton diffusion coefficient of the order of 1×10^{-3} cm^2/sec. Assuming the illuminated crystal surface to be planar and letting the distance from the surface be x, the differential equation for the exciton density $n(x)$ in steady state is

$$0 = \varepsilon I_0 \exp(-\varepsilon_x) - n(x)/\tau + D\, d^2n/dx^2$$

where ε is the extinction coefficient, I_0 is the incident photon flux, τ is the fluorescence lifetime, and D is the exciton diffusion constant. With the boundary conditions $n(0) = n(\infty) = 0$ the exciton flux to the surface is $D(dn/dx)_{x=0} = I_0(1 + 1/\varepsilon l)^{-1}$, where $l = (D\tau)^{1/2}$. Since the number of carriers generated per unit time in a steady-state experiment is assumed to be proportional to the exciton flux to the surface, a plot of the reciprocal of the photocurrent vs. the reciprocal of the extinction coefficient should yield a straight line. A plot of this type is shown in Figure 15. The value for the exciton diffusion length can

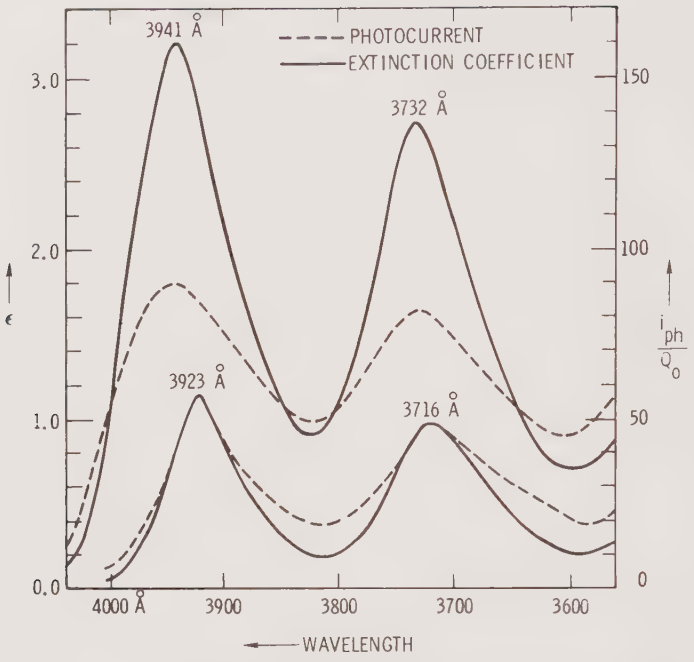

Fig. 14. Comparison of photocurrent excitation spectrum and the absorption spectrum of anthracene. The upper curves refer to light polarized parallel to the *b* axis and the lower curves to light polarized parallel to the *a* axis. (From Steketee and de Jonge.[131])

be obtained from the slope of the data in these graphs, and generally it is found that $(D\tau)^{1/2}$ is of the order of 500 Å, in agreement with Simpson's[65] measurement as discussed earlier. Eremenko and Medvedev[132] and Wright[133] have shown that similar considerations can account for the fluorescent quantum yield as a function of wavelength. Mulder and de Jonge[134] have observed some electrode effects on the measured diffusion length and Mulder[67] has shown that impurities in the crystal decrease the exciton diffusion length as expected.

Studies of carrier generation by X-rays in anthracene have provided strong evidence that geminate recombination plays a big role in carrier generation processes.[135] That is, it appears that many electron–hole pairs created by the radiation never contribute to the conductivity because they are unable to escape from each other's Coulomb field and immediately recombine. When X-rays interact with semiconductors, it is usually found that the average energy deposited per electron–hole pair created is of the order of three

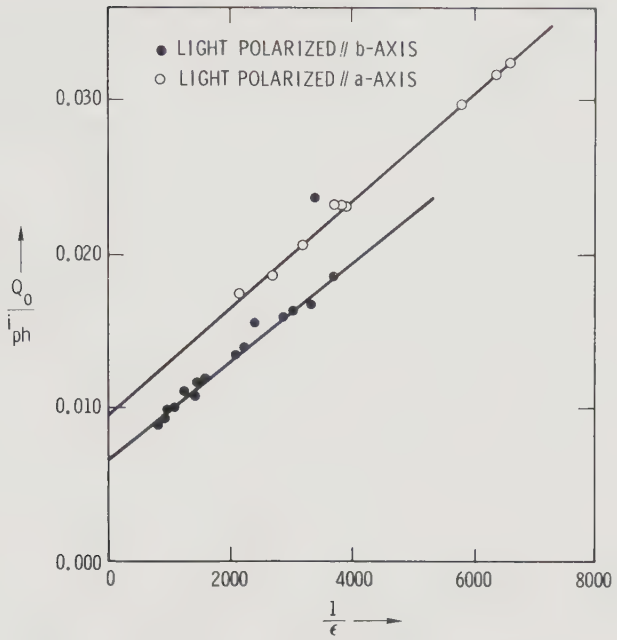

Fig. 15. The reciprocal of the photocurrent versus the reciprocal of the extinction coefficient of the incident light. (From Steketee and de Jonge.[131])

times the band gap, and in gases—even gases of fairly complex molecules—it is found that of the order of 30 eV is deposited for each ion pair created. In the case of anthracene crystals it was found that on the average 3000 eV was deposited for every electron–hole pair created, about 100 times as much as expected on the basis of the ion yield in gases and more than 200 times as much as that expected on the basis of experiments conducted on semiconductors. These results, however, have been shown to be consistent with the very large value of the recombination coefficient discussed in the last section.[135]

The large value of the recombination coefficient shows that the mean free paths for energy-losing collisions for electrons and holes are small compared to the dimensions of the Coulomb potential well, i.e., small compared to the distance r_0 at which the Coulomb potential energy of one carrier in the field of the other is equal to kT. Therefore, even when an electron is created with sufficient kinetic energy to escape from the Coulomb field of the hole left behind, there is a very high probability that it will lose the energy before it has had a chance to escape.

When it is appropriate to describe the motion of a charge carrier with the diffusion equation, that is, when the mean free path

is small compared to r_0, Onsager[136] has shown that the probability that a diffusing charge carrier will escape from a Coulomb potential well is $e^{-r_0/r}$, where r is the distance at which the carrier starts diffusing. He was investigating the creation of ion pairs by high-energy radiation in high-pressure gases. Onsager also showed that the number of charge carrier pairs created φ would depend on the applied field as $\varphi = A(T)[1 + (e^{3/2}\varepsilon k^2 T^2)E]$, where $A(T)$ depends on the initial distribution of diffusing carriers and is a function of temperature but does not depend on the electric field. Higher-order terms in E, the applied electric field, have been neglected.

Hummel and Allen[137,138] applied this theory in detail to some experimental studies of carrier generation by high-energy radiation in hexane and found excellent agreement between theory and experiment. In order to calculate the yield of carriers, it is necessary to know the energy spectrum of the electrons created by the radiation as well as the range–energy relation, and as a result there is considerable uncertainty in this quantity. However, if the yield of carriers is plotted as a function of the applied field, a straight line should result at relatively low fields, if geminate recombination is occurring, and, as Onsager pointed out, the slope of this line divided by the yield of carriers at zero electric field should be equal to $e^3/2\varepsilon k^2 T^2$, a quantity which contains no adjustable parameters. Therefore, the field dependence of the carrier yield provides an excellent test for this theory. It is interesting to note that in the studies of ion yields in dielectric liquids[139] the yield of ion pairs is very large in the high-mobility liquids, almost certainly indicating that the mean free path is becoming comparable to r_0, so that it is no longer valid to describe the carrier motion on the scale of a Coulomb potential well with a diffusion equation.

None of the experiments or theories discussed so far has given the size of the band gap in anthracene. The exciton surface interaction is an extrinsic process and only indicates that the band gap is probably greater than 3.2 eV, and the tight binding band theory only investigates the nature of the electron and hole bands but has nothing to say about how far apart they are. The X-ray generation experiment provides some insight into the carrier generation mechanism but not the width of the band gap.

Castro and Hornig[140] reported the first photoconductivity measurement of the band gap. In studies of quantum yields as a function of wavelength they observed a marked change in the carrier generation processes in the vicinity of 4 eV. At lower photon energies

they observed only the exciton surface interaction, but above 4 eV it appeared that electrons and holes were being generated directly by single photons. Their observations have subsequently been verified by other laboratories and further experiments.

The quantum yield for carrier generation by this process is very low, 10^{-4}. It was initially thought that in an organic molecular crystal like anthracene a direct band-to-band transition was a relatively improbable or forbidden process and that most of the adsorbed photons created excitons even when the energy was sufficiently high for a single photon to create a carrier. There have been discussions regarding whether the carriers are created by a weakly allowed band-to-band transition or by autoionization of excitons. The observation of germinate recombination has now added a new dimension to these discussions because it now provides a third possibility.

Batt *et al.*[141] and Geacintov and Pope (Ref. 142, see p. 293) have studied the electric field and temperature dependence of carrier generation in the wavelength range where carriers are created by the single-photon process. They found fairly good agreement between Onsager's theory and their experimental results, strongly indicating that the carriers are generated in a band-to-band transition and that the low quantum yield arises from geminate recombination. As was pointed out in the discussion of carrier generation by X-rays, the quantum efficiency will depend on the details of where the carriers started diffusing, but the electric field dependence, in terms of the slope of a graph of the number of carriers created as a function of electric field divided by the number of carriers created at zero electric field, should have a very specific value. The slope divided by the intercept should be $e^3/\varepsilon k^2 T^2$ and therefore should not only have a very specific value, but this value should vary as T^{-2}. The agreement between theory and experiment obtained by Batt *et al.*[141] is shown in Figure 16.

Experiments on anthracene crystals using photons of energy greater than about 3 eV are very difficult because these photons are absorbed very near the crystal surface and the excitons interact strongly with the surface. A number of second-order processes have been observed, however, and these processes can be used to study carrier generation processes now that variable-wavelength, high-intensity lasers are available.

Exciton–exciton annihilation is one second-order process and was first proposed in 1958.[143] The process was experimentally confirmed in 1965.[144] The existence of the process was questioned for a

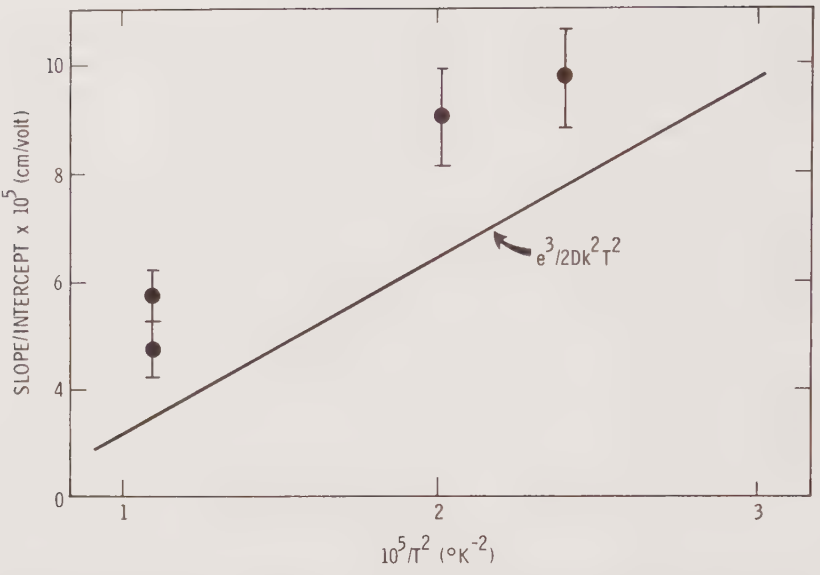

Fig. 16. Temperature variation of the electric field dependence of carrier generation by single-photon absorption. The points represent experimental results and the solid line is a theoretical prediction. (From Batt *et al.*[141])

time, but recent work[145] presents quite definite proof of its existence. It is, of course, not possible to vary the energy of excitation in this process and thus study the nature of carrier generation processes as a function of energy, but it has been shown that the yield of carriers per exciton–exciton annihilation is very low. Measurements of the exciton–exciton annihilation rate constant[146] have shown that it is about 10^{-8} cm^3/sec, while the rate of carrier generation by the same process is about 10^{-12} cm^3/sec. Therefore, the quantum efficiency for carrier generation by this process appears to be 10^{-4}, the same as that found for generation by the single-photon process.

Another process involving singlet excitons that has been well established is exciton photoionization.[147,148] In studies of carrier generation in anthracene crystals by light from a *Q*-spoiled ruby laser it was found that the number of carriers generated varied at the intensity of the light cubed. It is well known that excitons can be created in anthracene by two-photon absorption of ruby laser light,[149–152] and it was hypothesized that carriers were being generated by photons interacting with excitons created by two-photon absorption. In order to test this hypothesis an anthracene crystal was irradiated by two pulses of light from a laser separated in time of arrival at the crystal by from 0 to 40 nsec.[147] The two

pulses were obtained by sending the light from the laser through a partially reflecting mirror, and the difference in time of arrival was obtained by varying the length of the path one of the pulses took in getting to the crystal. The number of carriers created when the two pulses hit the crystal as well as the number created by each pulse separately were measured, and the experimental results are shown in Figure 17. The dashed curve indicates the results that would have been expected if no intermediate state were involved, that is, if the number of carriers created was just proportional to the integral over time of the intensity of the light cubed. The solid curve was calculated assuming that singlet excitons with a lifetime of 27 nsec were created by two-photon absorption and that carriers were created when these excitons were subsequently ionized by another photon. The cross section for exciton photoionization was found to be about 10^{-19} cm^2.

It has also been found that photons from a neodymium laser (1.18 eV) can photoionize excitons, but the cross section is about two orders of magnitude smaller than the cross section for ruby laser photons (1.8 eV).[153] In order to carry out this experiment excitons

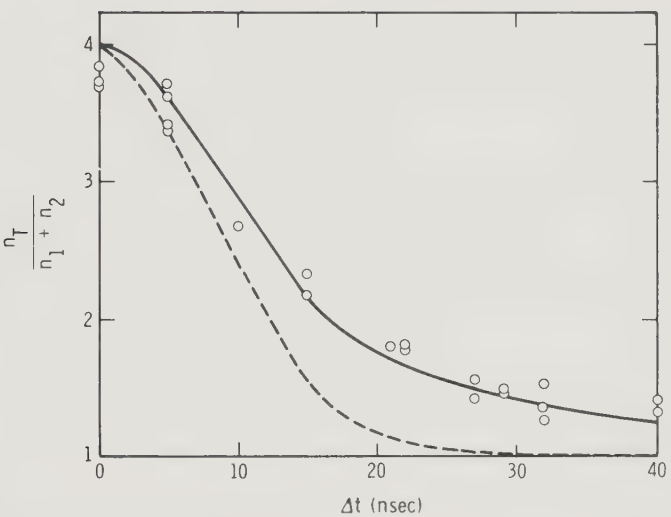

Fig. 17. Ratio of the number of carriers produced by two almost simultaneous light pulses incident on an anthracene crystal to the sum of the number produced by each pulse independently as a function of the differences in the times of arrival at the crystal of the two pulses. The solid line is the theoretical curve calculated for singlet exciton photoionization and the dashed line is the theoretical curve for three-photon absorption. (From Kepler.[147])

were created by 4250-Å light obtained by passing the light from a xenon flash tube (about a 2-μsec-long pulse) through a monochromator, and while the 4250-Å light was irradiating the crystal, a pulse of photons from a Q-spoiled neodymium laser was sent through the crystal. Since the 4250-Å light pulse created carriers by itself, it was necessary to measure both the number of carriers created by the 4250-Å light and the number of carriers created when both light pulses were incident on the crystals. It was assumed that the excess carriers created were created by exciton photoionization. It was possible to fire the neodymium laser at various times during the flash lamp pulse and measure the number of excess carriers created as a function of the 4250-Å intensity at the time the laser was fired. The number of excess carriers created was proportional to the intensity of the flash lamp light pulse as shown in Figure 18. The intensity of the 4250-Å light was about 5×10^{17} photons/cm^2 sec at peak intensity, and there were about 2×10^{16} photons/cm^2 in the laser pulse. From this experiment the cross section for photoionization of singlet excitons by neodymium laser photons was found to be about 2×10^{-21} cm^2.

Strome[154] was the first to show that carriers can also be generated by direct two-photon processes. He studied carrier generation

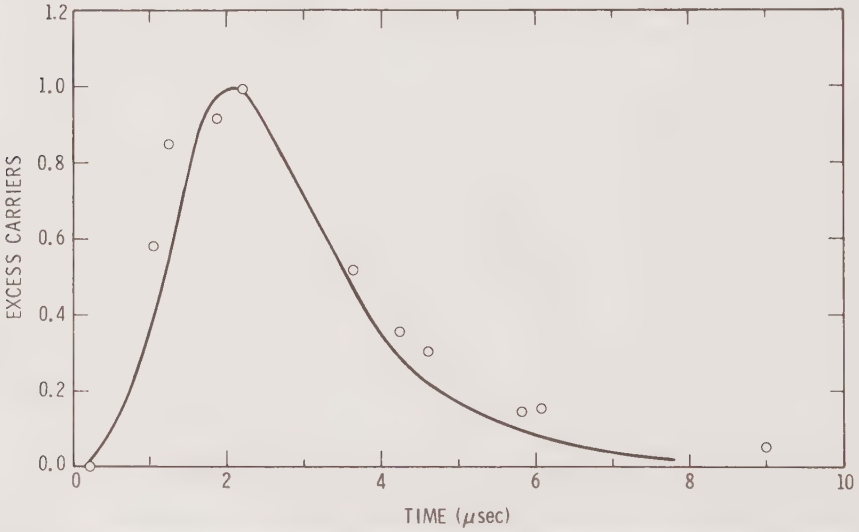

Fig. 18. The number of additional carriers created by applying a pulse of light from a neodydymium laser to an anthracene crystal during excitation of the crystal with a pulse of 4250-Å light versus time; the open circles are the number of excess carriers created by the laser pulse. The time at which the laser pulse fired is indicated by the time at which the dot is plotted.

in anthracene crystals with photons with energies of 2.07, 2.16, and 2.35 eV. At these energies, both the number of singlet excitons and the number of carriers created by the photon pulse were found to depend on the intensity squared. These data were interpreted as evidence for direct two-photon transitions.

Strome used a Q-spoiled ruby laser to generate anti-Stokes stimulated Raman lines in liquid nitrogen and liquid oxygen to obtain his light pulses. Dye lasers are now available, and studies of both two-photon absorption and carrier generation by two-photon absorption can be carried out in more detail.[151,152,155,156] Unfortunately, there is considerable disagreement among the experimental results from different groups in the two-photon energy region above 3.9 eV. A summary of the data available is shown in Figure 19.

The important question which needs to be answered is what is the nature of the highly excited electronic states. Are they exciton-like so that the carriers are created from the excitons by autoionization[157] or are they free-electron-like[158] and excitons are created by geminate recombination? In Ref. 156, the most recent study, it was concluded that there is very little, if any, structure in the two-photon absorption coefficient between two-photon energies of 3.9 and 5.0 eV, that two-photon-excited carrier generation begins at about 4.1 eV, and that the cross section for carrier generation increases approximately as $(E - E_G)^{1/2}$, where E is the two-photon energy and E_G is 4.1 eV. It was also found that even though the magnitude of the absorption coefficient does not change appreciably above 3.9 eV, there is a very significant decrease in the polarization ratio, the ratio of the two-photon absorption rate constant with the electric vector of the incident light parallel to the b axis to that with it parallel to the a axis. Fröhlich and Mahr[150] have concluded that there is a two-photon excited state at 3.58 eV, and it has been suggested[156] that the above polarization ratio data are an indication that in the energy range studied the two-photon excited states were gradually changing from predominantly molecular-like exciton states to a broad free-electron continuum. In the simplest case of allowed direct transitions between parabolic bands, the absorption coefficient for carrier generation can vary as $(E - E_G)^{1/2}$ as was observed for the wavelength dependence of the photoconductivity.

One reason that exciton autoionization[157] has been invoked by some is that theoretical investigations of band structure have indicated that the bands in anthracene are very narrow and experimental investigations have shown that the bands of states in which electron

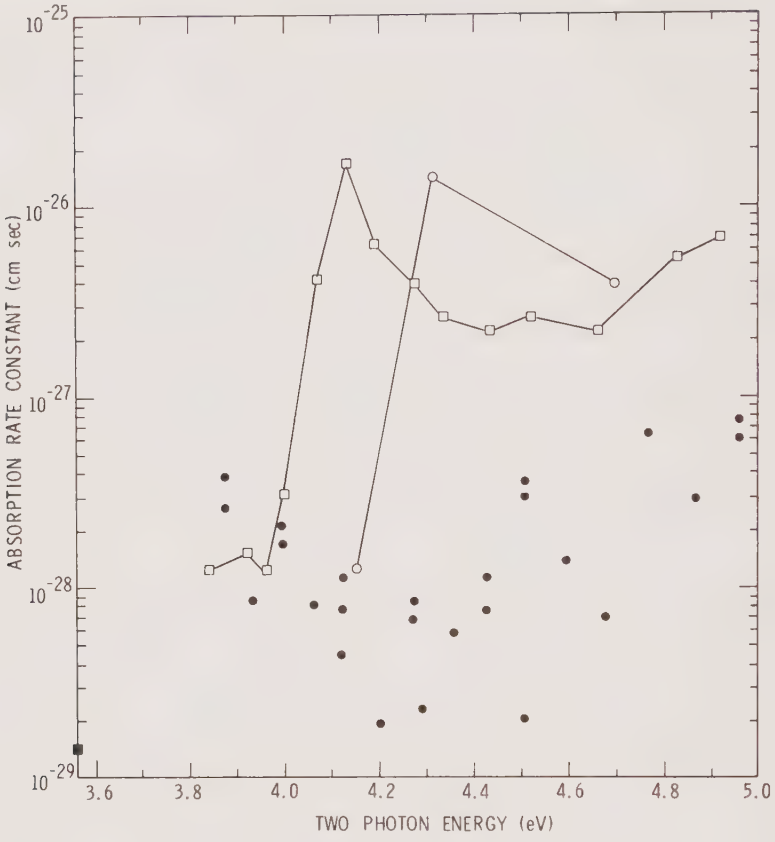

Fig. 19. The absolute magnitude of the two-photon absorption rate constant versus two-photon energy. The solid circles are from Ref. 156, the solid square at the two-photon energy 3.56 eV is from Ref. 81, the open circles are from Ref. 154, and the open squares are from Ref. 155. The data of Ref. 150 are not shown but they are in agreement with the solid circles where the data overlap (up to 4.25 eV) and it was found that there is a drop by a factor of ten in the absorption coefficient in going from 3.75 to 4.2 eV. (From Kepler[156])

and hole transport occurs are very narrow. Therefore, if a broad continuum begins at 4.1 eV, the lifetime of the electron in that state has to be very short so that significant transport occurs only in a narrow band of states, created perhaps by polaron effects.[159]

In summary, the photoconductivity experiments indicate that band-to-band transitions occur above about 4 eV, and experimental evidence that has been found for a narrow band is controversial. The quantum efficiency for carrier generation, however, is very low,

about 10^{-4}, for all experiments reported for which a quantum efficiency can be determined. There are reasons to believe that this small yield can be explained in terms of geminate recombination, i.e., recombination of an electron with the hole that was created along with the electron before the electron escapes from the Coulomb attraction of the hole, but autoionization of excitons[157] cannot be definitely ruled out. In general, the photoconductivity results appear to suggest that above about 4 eV there is something like a wide band of electron states to which transitions can occur.

Karl, in a recent review of organic semiconductors,[160] has summarized the data needed to calculate the band gap in anthracene as well as in crystals of other aromatic molecules. He concludes that the band gap calculated from ionization potentials, electron affinities, and lattice polarization is 3.7 eV. He and his co-workers[160,161] have carried out extensive investigations of the energy levels of traps for electrons and holes produced in anthracene by impurity molecules. Finally, how the electron and hole states in the crystal interact with various types of electrodes has been the subject of a number of recent investigations.[162–166]

8. Theory

In this section a brief summary of the status of the theory of excitons, electrons, and holes in molecular crystals will be presented. Extensive reviews of exciton theory have been prepared recently by Rice and Jortner,[21] Craig and Walmsley,[20] and Robinson,[167] and the reader is referred to these reviews for a more complete account of recent work on the theory of excitons in molecular crystals.

8.1. Excitons

As was pointed out at the beginning of this chapter, molecular crystals are made up of weakly interacting units, and therefore it is reasonable to assume for a first approximation that the manifold of states exhibited by a molecule is unperturbed by the crystal environment. If a particular molecule in a crystal is excited, however, that state of the crystal is degenerate with all other states in which one of the other molecules is excited. The removal of this degeneracy leads to a band of states in which a neutral packet of energy, an exciton, can move in the crystal, and the effect of this band of states on the optical

absorption by molecular crystals and on energy transport in crystals is the subject of exciton theory. The approximation in which the molecular states are used as the basis functions was first investigated by Frenkel[17] and Peierls,[18] and the excitons derived from this approximation are referred to as Frenkel or tight binding excitons. An alternate description of the exciton was developed by Wannier[168] in which the exciton states are derived from crystal electron and hole states. This treatment, which leads to a picture of the exciton as consisting of an electron and a hole bound together moving coherently throughout the crystal, has been used extensively for inorganic semiconductors.* There has been some discussion of the applicability of this approximation to molecular crystals,[21,170] and the exciton states derived have been referred to as charge transfer excitons. At the present time conclusive experimental evidence for such states does not exist[171] and they will not be discussed further.

Following Rice and Jortner,[21] an appropriate Hamiltonian for a crystal containing N unit cells and h molecules per unit cell is

$$H = \sum_{\mu=1}^{h} \sum_{k=1}^{N} H_{k\mu} + \sum_{k\mu<l\nu} V_{k\mu,l\nu} \tag{2}$$

where the double indices $k\mu$ and $l\nu$ label different molecules, $H_{k\mu}$ is the Hamiltonian for an isolated molecule, and $V_{k\mu,l\nu}$ is the intermolecular pair interaction. Using the ground-state wave functions of the individual molecules $\varphi^0_{k\mu}$, the ground state of the crystal is represented in the form

$$\Psi^0 = \mathscr{A} \prod_{k\mu=1}^{Nh} \varphi^0_{k\mu} \tag{3}$$

where $\mathscr{A}$ is the antisymmetrization operator permuting electrons between the molecules.

The wave function for the case in which only one molecule is excited can be written as

$$\phi^f_{m\alpha} = \mathscr{A}\varphi^f_{m\alpha} \prod'_{l\nu \neq m\alpha} \varphi^0_{l\nu} \tag{4}$$

where $\varphi^f_{m\alpha}$ is the f excited state of the molecule. If it is assumed that the exciton energy stays on a particular site in the unit cells, then we have the one-site exciton wave function

$$\Phi^f_\alpha = \left(\frac{h}{N}\right)^{1/2} \sum_{m=1}^{N} [\exp(i\mathbf{k} \cdot \mathbf{r}_{m\alpha})]\Phi^f_{m\alpha} \tag{5}$$

* The theory of both Wannier and Frenkel excitons is discussed at length by Knox.[169]

and when the full symmetry of the crystal is taken into account, the final exciton states are found to be

$$\psi_i{}^f = \frac{1}{\sqrt{h}} \sum_{\alpha=1}^{h} B_\alpha{}^i \Phi_\alpha{}^f \tag{6}$$

where the coefficients $B_\alpha{}^i$ are determined by the symmetry.

In the case in which there is one state per representation of the factor group[172] the energy of the fth molecular state above the ground state can be expressed in the form

$$E_f{}^i = E_f{}^0 + D_f + M_f{}^i(k) \tag{7}$$

where D_f leads to a uniform shift of all the bands and $M_f{}^i(k)$ produces a splitting between the bands. $E_f{}^0$ is in the excitation energy of the free molecule. The band shift and band splitting terms as given by Rice and Jortner[21] are

$$\begin{aligned} D_f = \sum_m \sum_\mu \{ &\langle \mathscr{A} \varphi_{n\nu}^f \varphi_{n\nu}^f | V_{n\nu,m\mu} | \mathscr{A} \varphi_{m\mu}^0 \varphi_{m\mu}^0 \rangle \\ &- \langle \mathscr{A} \varphi_{n\nu}^0 \varphi_{n\nu}^0 | V_{n\nu,m\mu} | \mathscr{A} \varphi_{m\mu}^0 \varphi_{m\mu}^0 \rangle \} \end{aligned} \tag{8}$$

$$\begin{aligned} M_f{}^i = \sum_{m \neq n} \sum_\nu &\{ (B_\nu{}^i)^* B_\mu{}^i \{ \exp[i\mathbf{k} \cdot (\mathbf{r}_{n\nu} - \mathbf{r}_{n\mu})] \} \\ &\times \langle \mathscr{A} \varphi_{n\nu}^f \varphi_{m\nu}^0 | V_{n\nu,m\mu} | \mathscr{A} \varphi_{n\nu}^0 \varphi_{m\mu}^f \rangle \} \end{aligned} \tag{9}$$

In anthracene there are two molecules per unit cell, and the appropriate linear combinations of the one-site excitons for the case where $\mathbf{k}$ is parallel to or perpendicular to the monoclinic axis are

$$\begin{aligned} \Psi_-{}^f(k) &= (1/\sqrt{2}) \{ \Phi_1{}^f(\mathbf{k}) - \Phi_2{}^f(k) \} \\ \Psi_+{}^f(k) &= (1/\sqrt{2}) \{ \Phi_1{}^f(k) + \Phi_2{}^f(k) \} \end{aligned} \tag{10}$$

The exciton band structure is determined by

$$\begin{aligned} M_f{}^{\pm}(k) = &\sum_{\substack{m1 \\ (m \neq n)}} (J_{n1,m1}^f + K_{n1,m1}) \exp[i\mathbf{k} \cdot (\mathbf{r}_{m1} - \mathbf{r}_{n1})] \\ &\pm \sum_{m\nu} (J_{n1,m\nu} + K_{n1,m\nu}^f) \exp[i\mathbf{k} \cdot (\mathbf{r}_{m2} - \mathbf{r}_{n1})] \end{aligned} \tag{11}$$

The term $J_{n1,m1}^f$ is the excitation transfer integral and is given by

$$J_{n1,m\mu}^f = \langle \varphi_{n1}^f \varphi_{m\mu}^0 | V_{n1,m\mu} | \varphi_{n1}^0 \varphi_{m\mu}^f \rangle \tag{12}$$

and the term $K^f_{n1,m\mu}$ is the electron exchange term, which is given by

$$K^f_{n1,m\mu} = \left\langle \left(\sum_P (-)^P P \right) \varphi^f_{n1} \varphi^0_{m\mu} | V_{n1,m\mu} | \varphi^0_{n1} \varphi^f_{m\mu} \right\rangle \tag{13}$$

The Davydov splitting, which is probably the main contact between theory and experiment, is given by the difference in energy between the two states M_f^+ and M_f^- at $k = 0$, and by far the largest amount of activity in exciton theory in molecular crystals has been devoted to attempts to calculate this splitting.

In the early work,[172] which was devoted essentially entirely to singlet exciton states, the electron exchange term was neglected and the excitation transfer integral calculated using a multipole expansion. A number of other approximations were made, such as truncating the multipole expansion at the dipole term. Silbey *et al.*,[173] in more recent work, directly evaluated the intermolecular interactions out to 50 Å and evaluated the longer range interactions using a dipole–dipole approximation. The most recent work in this area of the theory of excitons in molecular crystals has been published by Philpott.[174] In general, the conclusion is that there are so many approximations that might or might not be made and so many effects that might or might not be included that it is essentially impossible to arrive at definite conclusions about what is and what is not important. General agreement between theory and experiment can be obtained in many ways.

In the early work, triplet exciton theory was generally ignored because it was thought that triplet excited states would interact so weakly with their neighbors that no interesting phenomena would be observed. If there is no spin orbit coupling the excitation transfer integral, Eq. (12), is zero because of spin selection rules and the only interaction comes from the electron exchange term, Eq. (13). In 1962 Nieman and Robinson[77] found that in spite of the weak interaction, triplet excitation energy could be transported over large distances, and this observation renewed interest in the theory of triplet excitons.

Katz *et al.*[175] and Jortner *et al.*[45] have calculated the electron exchange integral for anthracene. The main problem with this calculation is that the results obtained depend critically on the form of the atomic wave function chosen because the main contribution to the integral comes from the value of the wave function far from the atoms. The calculated Davydov splitting was 43 cm^{-1} for anthracene.

Choi *et al.*[46] also considered the contribution of other states and concluded that configuration interaction with ion pair excited states was important, increasing the Davydov splitting to $59\,cm^{-1}$. The observed spectrum is spread over several vibrational subbands, indicating that the weak coupling limit[20] is appropriate. Therefore, the Davydov splitting which was calculated for the pure electronic level should be divided between the vibrational subbands in the ratio of the square of the Franck–Condon overlap factor. For the 0–0 band of the singlet–triplet system the overlap factor is about 0.25, so that the predicted splitting is $15\,cm^{-1}$. The experimentally observed values are $17 \pm 6\,cm^{-1}$ [176] and $22\,cm^{-1}$.[44]

At the present time most of the activity in exciton theory is centered on the nature of the exciton–phonon interaction. Experimental work on the diffusion of excitons has led to the conclusion that both singlet and triplet excitons hop from site to site rather than move coherently as a wave packet for several lattice spacings between scattering events.[73,91] Soos and Powell[72] have been able to explain recent experimental results by assuming that singlet excitons hop and by taking a detailed look at the random walk process, and a number of studies of exciton–phonon interactions and their relationship to line shapes have been reported.[37,177] A number of recent studies[178] have indicated that there is a strong similarity between exciton motion and the polaron theory originally developed by Holstein.[179]

Theoretical investigations of exciton–exciton interaction and exciton photoionization have been carried out. Reasonable agreement between theory and experiment was obtained.[21,158]

8.2. Electrons and Holes

In 1961 LeBlanc,[110] encouraged by the experimental observation that the mobility of electrons and holes increased as the temperature of the anthracene crystal was decreased, carried out a tight binding band calculation. One-electron wave functions ψ_k were constructed from linear combinations of one-electron molecular wave functions φ_n,

$$\psi_{\mathbf{k}}(\mathbf{r}) = \sum_{n=1}^{N} [\exp(i\mathbf{k} \cdot \mathbf{r}_n)]\varphi_n(\mathbf{r} - \mathbf{r}_n)$$

where $\mathbf{r}_n$ locates the geometrical center of molecule n and the sum extends over the N molecules in the crystal. Two separate bands are formed by the tight binding procedure, one in which electrons move

and one in which holes move. For the electron band the wave function φ_n describes the state where the excess electron is localized on molecule n and is therefore the one-electron wave function for the odd electron in the ground state of the isolated mononegative ion. For the hole band φ_n is the wavefunction of an electron in the highest filled orbital of the neutral molecule. LeBlanc approximated the crystalline field by

$$V(\mathbf{r}) = \sum_n V_n(\mathbf{r} - \mathbf{r}_n)$$

where V_n is the Hartree potential of an isolated neutral molecule.

The structure of the bands resulting from this calculation is given by[122]

$$E_{\pm}(\mathbf{k}) = 2E_b \cos(\mathbf{k}\cdot\mathbf{b}) \pm 2E_\alpha\left[\cos\left(\mathbf{k}\cdot\frac{\mathbf{a}+\mathbf{b}}{2}\right) + \cos\left(\mathbf{k}\cdot\frac{\mathbf{a}-\mathbf{b}}{2}\right)\right]$$
$$\pm 2E_\gamma\left\{\cos\left[\mathbf{k}\cdot\left(\frac{\mathbf{a}+\mathbf{b}}{2}+\mathbf{c}\right)\right] + \cos\left[\mathbf{k}\cdot\left(\frac{\mathbf{a}-\mathbf{b}}{2}+\mathbf{c}\right)\right]\right\}$$

where E_b, E_α, and E_γ are the intermolecular electron transfer integrals between the molecule at the origin of the unit cell and those at the relative vector positions $\mathbf{b}$, $(\mathbf{a}+\mathbf{b})/2$, and $[\mathbf{c}+(\mathbf{a}+\mathbf{b})/2]$, respectively, with $\mathbf{a}$, $\mathbf{b}$, and $\mathbf{c}$ being the unit cell axes. The intermolecular electron transfer integrals have the form

$$E = \int \varphi_{n+s} V_{n+s} \varphi_n \, d\tau$$

and the φ_n used were Hückel linear combinations of Slater type $2p_z$ atomic orbitals, using for the electron and hole bands, respectively, the Hückel coefficients for the lowest antibonding and highest bonding π orbitals.

In order to calculate the mobility tensor from the band structure, LeBlanc assumed that the relaxation time was isotropic and independent of energy. He also tried the assumption of a constant mean free path and obtained essentially the same results. For a constant free time τ_0 the components of the mobility tensor are

$$\mu_{ij} = e\tau_0 \langle v_i v_j \rangle / kT$$

where the v_i are the corresponding components of $\mathbf{v}(\mathbf{k})$ and

$$\mathbf{v}(\mathbf{k}) = (1/\hbar)\,\partial E(\mathbf{k})/\partial \mathbf{k}$$

Since the bands were found to be less than kT wide, it was assumed that the probabilities of occupation of all states in the band were equal.

The results of this calculation indicated that the electron and hole bands in anthracene were of the order of $0.5kT$ wide at room temperature and the calculated anisotropy of the mobility tensor for both electrons and holes, as pointed out earlier, was in remarkable agreement with experiment.

As a result of the success of this calculation a number of improvements have been incorporated in subsequent papers. Katz *et al.*[111] tried better representations of the carbon wave functions and concluded that the bands were considerably wider, and Silbey *et al.*[112] included the effect of molecular vibrations and used a different potential function for a neutral molecule. The conclusion of this latter paper was that the bands were about the same width LeBlanc had originally calculated, of the order of 10^{-2} eV.

In more recent work the applicability of band theory has been questioned and the nature of the electron–phonon interaction investigated.[113–119] Vilfan[120] has recently examined the possibility of applying small polaron theory[179] to carriers in anthracene and concluded that they are in a state between clearly bandlike states and the small polaron state.

The situation remains cloudy. The mobility of the electrons and holes in anthracene may be too low to be described by band theory and is too high to be described by small polaron theory. Transport in this transition region is not well understood. It appears that singlet and triplet excitons may well exist in the same regime.

References

1. L. B. Coleman, M. J. Cohen, D. J. Sandman, F. G. Yamagishi, A. F. Garito, and A. J. Heeger, Superconducting fluctuations and the Peierls instability in an organic solid, *Solid State Commun.* **12**, 1125 (1973).
2. R. K. Clayton, Physical mechanisms in photosynthesis: Past elucidations and current problems, *Proc. Nat. Acad. Sci. (USA)* **69**, 44 (1972).
3. M. Calvin, Solar energy by photosynthesis, *Science* **184**, 375 (1974).
4. H. Kuhn, Interaction of chromophores in monolayer assemblies, in *Organic Solid State Chemistry—2* (M. D. Cohen, ed.), Butterworths, London (1971), p. 421.
5. C. W. Frank and L. A. Harrah, Excimer formation in vinyl polymers. II. Rigid solutions of poly(2-vinylnaphthalene) and polystyrene, *J. Chem. Phys.* **61**, 1526 (1974).

6. C. W. Frank, Observation of relaxation processes near the glass transition by means of excimer fluorescence, *Macromolecules* **8**, 305 (1975).
7. D. Emin, The formation and motion of small polarons, in *Linear and Nonlinear Transport in Solids* (J. T. DeVreese, ed.), Plenum, New York (1976).
8. R. M. Schaffert, A new high-sensitivity organic photoconductor for electrophotography, *IBM J. Res. Dev.* **15**, 75 (1971); K. Morimoto and Y. Murakami, Organic photoconductive layers sensitized with triarylcarbonium salts, *Appl. Opt. Suppl.* **3**, 50 (1969).
9. A. Aviram and M. A. Ratner, Molecular rectifiers, *Chem. Phys. Lett.* **29**, 277 (1974).
10. E. F. Sheka, V. S. Makarova, and E. D. Simonovskaya, Spectroscopy of molecular crystals, *Mol. Cryst. Liq. Cryst.* **30**, 239 (1975).
11. G. J. Sloan, Definition and attainment of high purity of organic compounds, in *Physics and Chemistry of the Organic Solid State*, Vol. 1 (D. Fox, M. M. Labes, and A. Weissberger, eds.), Interscience, New York (1963), p. 180; G. F. Reynolds, Crystal growth, in *Physics and Chemistry of the Organic Solid State*, Vol. 1 (D. Fox, M. M. Labes, and A. Weissberger, eds.), Interscience, New York (1963), p. 224.
12. F. R. Lipsett, On the production of single crystals of naphthalene and anthracene, *Can. J. Phys.* **35**, 284 (1957).
13. I. Nakada, The optical properties of anthracene single crystals, *J. Phys. Soc. Japan* **17**, 113 (1962).
14. D. W. J. Cruickshank, On the lattice vibrations of benzene, naphthalene, and anthracene, *Rev. Mod. Phys.* **30**, 163 (1958); A detailed refinement of the crystal and molecular structure of anthracene, *Acta Cryst.* **9**, 915 (1956); A detailed refinement of the crystal and molecular structure of anthracene, *Acta Cryst.* **10**, 470 (1957).
15. G. S. Pawley, A model for the lattice dynamics of naphthalene and anthracene, *Phys. Stat. Sol.* **20**, 347 (1967).
16. M. Ito, M. Suzuki, and T. Yokayama, Phonons: spectra and density of states, in *International Symposium on Excitons, Magnons, and Photons in Molecular Crystals* (A. B. Zahlan, ed.), Cambridge University Press (1968), p. 1.
17. J. Frenkel, On the transformation of light into heat in solids—I, *Phys. Rev.* **37**, 17 (1931); On the transformation of light into heat in solids—II, *Phys. Rev.* **37**, 1276 (1931).
18. R. E. Peierls, Theory of the absorption spectra of solid bodies, *Ann. Physik* **13**, 905 (1932).
19. A. S. Davydov, Theory of adsorption spectra of molecular crystals, *Zh. Eksp. Teor. Fiz.* **18**, 210 (1948).
20. D. P. Craig and S. H. Walmsley, *Excitons in Molecular Crystals*, W. A. Benjamin, New York (1968); Visible and ultraviolet absorption by molecular crystals, in *Physics and Chemistry of the Organic Solid State*, Vol. I (D. Fox, M. M. Labes, and A. Weissberger, eds.), Interscience, New York (1965), p. 585.
21. S. A. Rice and J. Jortner, Comments on the theory of the exciton state of molecular crystals, in *Physics and Chemistry of the Organic Solid State*, Vol. III (D. Fox, M. M. Labes, and A. Weissberger, eds.), Interscience, New York (1967), p. 199.
22. L. E. Lyons and G. C. Morris, The intensity of ultraviolet light absorption by monocrystals. III. Absorption by anthracene at 295°K, 90°K, and 40°K of plane-polarized light of wavelengths 1600–2750 Å, *J. Chem. Soc. II* **1959**, 1551.

23. D. P. Craig, The polarized spectrum of anthracene, Part II. Weak transitions and second-order crystal field perturbations, *J. Chem. Soc. II* **1955**, 2302.
24. D. P. Craig and P. C. Hobbins, The polarized spectrum of anthracene. Part III. The system at 3800 Å, *J. Chem. Soc. III*, **1955**, 2309.
24a. J. Ferguson and W. D. Schneider, Absorption spectrum of crystalline anthracene. Measurements on the absorption edge, *J. Chem. Phys.* **28**, 761 (1958).
25. G. C. Morris and M. G. Sceats, Exciton dynamics in molecular crystals from line shape analysis. Spectral moments and correlation functions, *Chem. Phys.* **1**, 259 (1973); Exciton dynamics in molecular crystals from line shape analysis. Effects of crystal strain, *Chem. Phys.* **1**, 376 (1973).
26. G. C. Morris, S. A. Rice, M. G. Sceats, and A. E. Martin, Absorption band profile of the origin region of the *b* polarized 4000 Å anthracene crystal transition, *J. Chem. Phys.* **55**, 5610 (1971).
27. G. C. Morris, S. A. Rice, and A. E. Martin, Study of the reflection spectrum of crystalline anthracene: Evidence for the existence of defects, *J. Chem. Phys.* **52**, 5149 (1970).
28. L. B. Clark and M. R. Philpott, Anisotropy of the singlet transitions of crystalline anthracene, *J. Chem. Phys.* **53**, 3790 (1970).
29. M. S. Brodin, S. V. Marisova, and S. A. Shturkhetskaya, The form of dispersion, absorption, and reflection curves of an anthracene crystal and the character of exciton–phonon interaction, *Ukr. Phys. J.* **13**, 249 (1968).
30. E. E. Koch and A. Otto, Optical properties of anthracene single crystals in the excitonic region of the spectrum between 4 and 10.5 eV, *Chem. Phys.* **3**, 370 (1974).
31. I. Nakada, The optical absorption of anthracene crystal near 4000 Å, *J. Phys. Soc. Japan* **20**, 346 (1965).
32. A. Matsui, The polarized absorption edge and the Davydov splitting of anthracene, *J. Phys. Soc. Japan* **21**, 2212 (1966).
33. M. V. Kurik, N. N. Spendiarov, P. I. Savchinskii, and E. K. Frovola, Urbach Law in anthracene at low temperatures, *Sov. Phys.—Solid State* **12**, 1132 (1970).
34. E. K. Frolova and M. V. Kurik, Urbach Rule in 9.10 Dichloranthracene, *Phys. Stat. Sol.* **33**, K99 (1969).
35. M. V. Kurik, V. S. Manzhara, and L. I. Tsikora, Exciton–phonon interaction in naphthacene, *Sov. Phys.—Solid State* **13**, 591 (1971).
36. F. Urbach, The long-wavelength edge of photographic sensitivity and of the electronic absorption of solids, *Phys. Rev.* **92**, 1324 (1953).
37. M. G. Sceats and S. A. Rice, Applicability of Urbach's rule to molecular crystals, *Chem. Phys. Lett.* **25**, 9 (1974).
38. G. C. Morris and M. G. Sceats, Surface excitons in crystal anthracene, *Mol. Cryst. Liq. Cryst.* **25**, 339 (1974).
39. V. I. Sugakov, On surface states in anthracene, *Ukr. Fiz. Zh.* **15**, 2060 (1970).
40. M. S. Brodin, M. A. Dudinski, and S. V. Marisova, Spectral evidence of surface states in the anthracene crystal, *Opt. Spectrosc.* **31**, 401 (1971).
41. P. Avakian, E. Abramson, R. G. Kepler, and J. C. Caris, Indirect observation of singlet–triplet absorption in anthracene crystals, *J. Chem. Phys.* **39**, 1127 (1963).
42. G. C. Smith, Triplet exciton phosphorescence in crystalline anthracene, *Phys. Rev.* **166**, 839 (1968).

43. J. H. Sharp and W. G. Schneider, Photoconduction in anthracene induced by triplet excitons, *J. Chem. Phys.* **41**, 3657 (1964).
44. R. R. Clarke and R. M. Hochstrasser, Electronic Zeeman effect in anthracene. *J. Chem. Phys.* **46**, 4532 (1967).
45. J. Jortner, S. A. Rice, and J. L. Katz, Triplet excitons in crystals of aromatic molecules, *J. Chem. Phys.* **42**, 309 (1965).
46. S. Choi, J. Jortner, S. A. Rice, and R. Silbey, Charge-transfer exciton states in aromatic molecular crystals, *J. Chem. Phys.* **41**, 3294 (1964).
47. G. T. Wright, Ultraviolet properties of crystalline anthracene, *Chem. Rev.* **67**, 581 (1967).
48. R. C. Powell, Thermal and sample-size effects on the fluorescence lifetime and energy transfer in tetracene-doped anthracene, *Phys. Rev. B* **2**, 2090 (1970).
49. D. P. Craig and S. H. Walmsley, Fluorescence, in *Excitons in Molecular Crystals*, W. A. Benjamin, New York (1968), Chapter 8, p. 150.
50. L. E. Lyons and L. J. Warren, Anthracene fluorescence at low temperatures. I. Purified single crystals, *Aust. J. Chem.* **25**, 1411 (1972).
51. E. Glockner and H. C. Wolf, The fluorescence spectrum of anthracene crystals, *Z. Naturf. A* **24**, 943 (1969).
52. L. A. Limareva, A. S. Cherkasov, and V. I. Shirkov, Evidence of the radiating-centers inhomogeneity of crystalline anthracene in fluorometric phase spectra, *Opt. Spectrosc.* **25**, 132 (1968).
53. L. E. Lyons and L. J. Warren, Anthracene fluorescence at low temperatures. II. Doped single crystals, *Aust. J. Chem.* **25**, 1427 (1972).
54. E. Glockner and H. C. Wolf, Flashover spectra of the mixed crystal system anthracene–perdeuteroanthracene. Mixed exciton band, *Chem. Phys. Lett.* **27**, 161 (1974).
55. J. B. Birks, The fluorescence and scintillation decay times of crystalline anthracene, *Proc. Phys. Soc.* **79**, 494 (1962).
56. T. Förster, Intermolecular energy transference and fluorescence, *Ann. Physik* **2**, 55 (1948); Experimental and theoretical investigation of the intermolecular transition of electron excitation energy, *Z. Naturf.* **49**, 321 (1949).
57. D. L. Dexter, A theory of sensitized luminescence in solids, *J. Chem. Phys.* **21**, 836 (1953).
58. V. M. Agranovich and Yu. V. Konobeev, The diffusion of excitons in molecular crystals, *Sov. Phys.—Solid State* **5**, 999 (1962).
59. S. Chandrasekhar, Stochastic problems in physics and astronomy, *Rev. Mod. Phys.* **15**, 1 (1943).
60. M. Yokata and O. Tanimoto, Effects of diffusion on energy transfer by resonance, *J. Phys. Soc. Japan* **22**, 779 (1967).
61. Y. A. Kurskii and A. S. Selivanenko, On the theory of luminescence quenching in liquid solutions, *Opt. i Spektros.* **8**, 340, 643 (1960).
62. M. Trlifaj, The theory of diffusion of "localized" excitons in solids, *J. Phys.* **6**, 533 (1956); The diffusion of the excitation energy in molecular crystals, *J. Phys.* **8**, 510 (1958).
63. H. C. Wolf, Energy transfer in organic molecular crystals: A survey of experiments, in *Advances in Atomic and Molecular Physics* (D. R. Bates and I. Estermann, eds.), Academic Press (1967), p. 119.
64. R. C. Powell, private communication.

65. O. Simpson, Electronic properties of aromatic hydrocarbons. III. Diffusion of excitons, *Proc. Roy. Soc. A* **238**, 402 (1956).
66. V. V. Eremenko and V. S. Medvedev, Dependence of the photoconductivity and the intensity of luminescence of anthracene crystals on the excitation wavelength, *Fiz. Tverd. Tela* **2**, 1572 (1960) [English transl.: *Sov. Phys.—Solid State* **2**, 1426 (1960)]; B. J. Mulder and J. de Jonge, Exciton diffusion and the photoconductivity spectrum of anthracene, pyrene, and perylene, *Philips Res. Repts.* **21**, 188 (1966).
67. B. J. Mulder, Mean diffusion path of excitons in crystals of anthracene doped with tetracene, *Philips Res. Rpts.* **21**, 283 (1966).
68. M. V. Kurik and Yu. P. Piryatinskii, Diffusion length of singlet excitons in anthracene single crystals, *Sov. Phys.—Solid State* **13**, 2421 (1922).
69. N. A. Tolstoi and A. P. Abramov, Interactions of excitons in anthracene, *Sov. Phys.—Solid State* **9**, 255 (1967).
70. A. Bergman, M. Levine, and J. Jortner, Collision ionization of singlet excitons in molecular crystals, *Phys. Rev. Lett.* **18**, 593 (1967).
71. (a) R. C. Powell and R. G. Kepler, Energy transfer in doped organic cystals, *J. Mol. Cryst. Liq. Cryst.* **11**, 349 (1970); (b) Evidence for long range exciton–impurity interaction in tetracene doped anthracene crystals, *Phys. Rev. Lett.* **22**, 636 (1969); (c) Evidence for long-range exciton–impurity interaction in tetracene-doped anthracene crystals, *Phys. Rev. Lett.* **22**, 1232 (1969); (d) On the question of singlet exciton diffusion in anthracene, *J. Luminescence* **1**, 254 (1970); (e) R. C. Powell, Host-sensitized energy transfer in molecular crystals, *Phys. Rev. B* **2**, 1159; (f) Thermal and sample-size effects on the fluorescence lifetime and energy transfer in tetracene-doped anthracene, *Phys. Rev. B* **2**, 2090 (1970).
72. Z. G. Soos and R. C. Powell, Generalized random-walk model for singlet-exciton energy transfer, *Phys. Rev. B* **6**, 4035 (1972).
73. R. C. Powell and Z. G. Soos, Singlet exciton energy transfer in organic solids, *J. Luminescence* **11**, 1 (1975).
74. H. Callmann, G. Vaubel, and H. Baessler, Interaction of singlet excitons in organic materials with an absorbing surface, *Phys. Stat. Sol. B* **44**, 813 (1971); H. Killesreiter and H. Baessler, Exciton reaction at an anthracene/metal interface. Charge transfer, *Chem. Phys. Lett.* **11**, 411 (1971); G. Vaubel, H. Baessler, and D. Moebius, Reaction of singlet excitons at an anthracene/metal interface. Energy transfer, *Chem. Phys. Lett.* **10**, 334 (1971).
75. M. Pope, J. Burgos, and J. Wotherspoon, Singlet exciton–trapped carrier interaction in anthracene, *Chem. Phys. Lett.* **12**, 140 (1971); N. Wakayama and D. F. Williams, Singlet exciton–charge carrier interaction in anthracene, *Chem. Phys. Lett.* **9**, 45 (1971).
76. S. D. Babenko, V. A. Benderskii, V. I. Goldanskii, A. G. Lavrushko, and V. P. Tychinskii, Singlet exciton annihilation in anthracene crystals, *Phys. Stat. Sol. B* **45**, 91 (1971); V. A. Benderskii, V. Kh. Brikenshtein, and A. G. Lavrushko, Nonlinear quenching of fluorescence in anthracene crystals at low temperatures, *Fiz. Tverd. Tela* **15**, 270 (1973).
77. G. C. Nieman and G. W. Robinson, Rapid triplet excitation migration in organic crystals, *J. Chem. Phys.* **37**, 2150 (1962); H. Sternlicht, G. C. Nieman, and G. W. Robinson, Triplet–triplet annihilation and delayed fluorescence in molecular aggregates, *J. Chem. Phys.* **38**, 1326 (1963).

78. R. G. Kepler, J. C. Caris, P. Avakian, and E. Abramson, Triplet excitons and delayed fluorescence in anthracene crystals, *Phys. Rev. Lett.* **10**, 400 (1963).
79. S. Singh, W. J. Jones, W. Siebrand, B. P. Stoicheff, and W. G. Schneider, Laser generation of excitons and fluoresence in anthracene crystals, *J. Chem. Phys.* **42**, 330 (1965); S. Z. Weisz, A. B. Zahlan, M. Silver, and R. C. Jarnagin, Radiationless transition rate constant determination from delayed fluorescence, *Phys. Rev. Lett.* **12**, 71 (1964).
80. R. C. Hughes and Z. G. Soos, Yield of singlet and triplet excitons from x-ray and ruby laser excitation of anthracene single crystals, *J. Chem. Phys.* **63**, 1122 (1975).
81. J. L. Hall, D. A. Jennings, and R. N. McClintock, Study of anthracene fluorescence excited by the ruby giant-pulse laser, *Phys. Rev. Lett.* **11**, 364 (1963).
82. P. Avakian and R. E. Merrifield, Triplet excitons in anthracene crystals—A review, *Mol. Cryst.* **5**, 37 (1968).
83. R. C. Johnson, R. E. Merrifield, P. Avakian, and R. B. Flippen, Effects of magnetic fields on the mutual annihilation of the triplet excitons in molecular crystals, *Phys. Rev. Lett.* **19**, 285 (1967).
84. R. E. Merrifield, Theory of magnetic field effects on the mutual annihilation of triplet excitons, *J. Chem. Phys.* **48**, 4318 (1968).
85. R. E. Merrifield, Magnetic effects on triplet exciton interactions, *Pure Appl. Chem.* **27**, 481 (1971).
86. P. Avakian and A. Suna, Unusual magnetic field effects in organic solids, *Mater. Res. Bull.* **6**, 891 (1971).
87. P. Avakian, R. P. Groff, R. E. Kellogg, R. E. Merrifield, and A. Suna, Magnetic field dependence of the triplet–triplet fusion rate constant for anthracene in solution, in *Organic Scintillators and Liquid Scintillation Counting* (Proc. International Conference 1970, D. L. Horrocks, ed.), Academic Press, New York (1971), p. 499.
88. P. Avakian and R. E. Merrifield, Experimental determination of the diffusion length of triplet excitons in anthracene crystals, *Phys. Rev. Lett.* **13**, 541 (1964).
89. V. Ern, P. Avakian, and R. E. Merrifield, Diffusion of triplet excitons in anthracene—V, *Phys. Rev.* **148**, 862 (1966).
90. V. Ern, Anisotropy of triplet exciton diffusion in anthracene, *Phys. Rev. Lett.* **22**, 343 (1969).
91. V. Ern, A. Suna, Y. Tomkiewicz, P. Avakian, and R. P. Groff, Temperature dependence of triplet–exciton dynamics in anthracene crystals, *Phys. Rev. B* **5**, 3222 (1972).
92. R. G. Kepler and A. C. Switendick, Diffusion of triplet excitons in anthracene, *Phys. Rev. Lett.* **15**, 56 (1965).
93. D. F. Williams and J. Adolph, Diffusion length of triplet excitons in anthracene crystals, *J. Chem. Phys.* **46**, 4252 (1967); D. C. Hoesterey and G. W. Robinson, Diffusion coefficient of triplet excitons in anthracene, *J. Chem. Phys.* **54**, 1709 (1971); M. Drew and D. F. Williams, Diffusion coefficient of triplet excitons in anthracene, *J. Chem. Phys.* **54**, 1844 (1971).
94. B. Nickel and H. Maxdorf, New method for the determination of the diffusion coefficient of triplet excitons in the c' direction of crystalline anthracene, *Chem. Phys. Lett.* **9**, 555 (1971).

95. H. Kolb and H. C. Wolf, NMR studies of exciton motion in molecular crystals, *J. Magn. Resonance* **7**, 374 (1972).
96. D. Haarer and H. C. Wolf, ESR—investigations of triplet-excitons in anthracene and naphthalene single crystals, *Mol. Cryst.* **10**, 359 (1970).
97. A. H. Francis and C. B. Harris, Coherent triplet excitons and density of states functions in molecular crystals, *Chem. Phys. Lett.* **9**, 188 (1971); A. H. Francis and C. B. Harris, Relation between microwave spectroscopy, coherent triplet excitons, and density of state functions in molecular crystals, *Chem. Phys. Lett.* **9**, 181 (1971).
98. V. Ern and A. R. McGhie, Quenching of triplet excitons in anthracene crystals by internal β-irradiation, *Mol. Cryst. Liq. Cryst.* **15**, 277 (1971); E. Ya. Danil'chenko and E. L. Frankevich, Fluorescence of anthracene during slow-electron excitation, *Khim. Vys. Energ.* **7**, 113 (1973); D. W. Pearson and P. R. Moran, Fast neutron radiation damage in anthracene as a possible dosimeter, *Nucl. Sci. Abstr.* **25**, 5096 (1971).
99. H. Bouchriha, G. Delacote, P. Delannoy, and M. Schott, Interaction of triplet excitons with trapped and free holes in crystalline anthracene. Exciton quenching current enhancement and magnetic field effects, *J. Phys. (Paris)* **35**, 577 (1974); S. Z. Weisz, J. Levinson, and A. Cobas, Interaction of triplet excitons with trapped electrons in anthracene crystals, *Proceedings of the Third International Conference on Photoconductivity* (E. K. Pell, ed.), Pergamon, Oxford (1971), p. 297; V. Ern, H. Bouchriha, J. Fourney, and G. Delacote, Triplet exciton–trapped hole interaction in anthracene crystals, *Solid State Commun.* **9**, 1201 (1971); E. L. Frankevich, I. A. Sokolik, and L. V. Lukin, Triplet exciton–charge carrier interaction in anthracene, *Phys. Stat. Sol.* **B54**, 61 (1972); N. Wakayama and D. F. Williams, Carrier–exciton interactions in crystalline anthracene, *J. Chem. Phys.* **57**, 1770 (1972).
100. J. Füenfschilling and I. Zschokke-Gräenacher, Triplet triplet exciton annihilation in tetracene-doped anthracene crystals, *Helv. Phys. Acta* **43**, 768 (1970); M. Chabr, J. Füenfschilling, and I. Zschokke-Gräenacher, Magnetic field effects on exciton annihilation processes in tetracene doped anthracene crystals, *Chem. Phys. Lett.* **25**, 387 (1974); D. Goode, Y. Lupien, W. Siebrand, D. F. Williams, J. M. Thomas, and J. O. Williams, Triplet excitons as probes for structural imperfections in crystalline anthracene, *Chem. Phys. Lett.* **25**, 308 (1974).
101. R. P. Groff, R. E. Merrifield, A. Suna, and P. Avakian, Magnetic hyperfine modulation of dye-sensitized delayed fluorescence in an organic crystal, *Phys. Rev. Lett.* **29**, 429 (1972); B. Nickel, Intensity dependence of the sensitized delayed fluorescence of anthracene single crystals, *Mol. Cryst. Liquid Cryst.* **18**, 263 (1972); B. Nickel, Sensitized photoconduction and sensitized delayed fluorescence of anthracene single crystals, *Mol. Cryst. Liquid Cryst.* **18**, 227 (1972).
102. N. Geacintov, M. Pope, and F. Vogel, Effect of magnetic field on the fluorescence of tetracene crystals: Exciton fission, *Phys. Rev. Lett.* **22**, 593 (1969); R. E. Merrifield, P. Avakian, and R. P. Groff, Fission of singlet excitons into pairs of triplet excitons in tetracene crystals, *Chem. Phys. Lett.* **3**, 155 (1969); Errata, *Chem. Phys. Lett.* **3**, 728 (1969).
103. H. P. Schwob, Charge-transfer exciton fission in anthracene crystals, *Chem. Phys. Lett.* **13**, 581 (1972); H. P. Schwob and D. F. Williams, Charge transfer exciton fission in anthracene crystals, *J. Chem. Phys.* **58**, 1542 (1973); G. Klein,

R. Voltz, and M. Schott, Magnetic field effect on prompt fluorescence in anthracene. Evidence for singlet exciton fission, *Chem. Phys. Lett.* **16**, 340 (1972).
104. G. Klein, R. Voltz, and M. Schott, Singlet exciton fission in anthracene and tetracene at 77°K, *Chem. Phys. Lett.* **19**, 391 (1973).
105. C. E. Swenberg and N. E. Geacintov, Exciton interactions in organic solids, *Org. Mol. Photophys.* **18**, 489 (1973).
106. O. H. LeBlanc, Hole and electron drift mobilities in anthracene, *J. Chem. Phys.* **33**, 626 (1960).
107. R. G. Kepler, Charge carrier production and mobility in anthracene crystals, *Phys. Rev.* **119**, 1226 (1960).
108. R. G. Kepler, Charge carrier mobility and production in anthracene, in *Organic Semiconductors* (J. J. Brophy and J. W. Buttrey, eds.), Macmillan (1962), p. 1.
109. P. W. Bridgman, The compression of sixty-one solid substances to 25000 kg/cm^2, determined by a new rapid method, *Proc. Am. Acad. Arts Sci.* **76**, 9 (1945).
110. O. H. LeBlanc, Band structure and transport of holes and electrons in anthracene, *J. Chem. Phys.* **35**, 1275 (1961).
111. J. L. Katz, J. Jortner, S.-I. Choi, and S. A. Rice, On the excess electron and hole band structures and carrier mobility in naphthalene, anthracene, and several polyphenyls, *J. Chem. Phys.* **39**, 1683 (1963).
112. R. Silbey, J. Jortner, S. A. Rice, and M. T. Vala, Exchange effects on the electron and hole mobility in crystalline anthracene and naphthalene, *J. Chem. Phys.* **42**, 733 (1965); Erratum: Exchange effects on the electron and hole mobility in crystalline anthracene and naphthalene, *J. Chem. Phys.* **43**, 2925 (1965); R. M. Glaeser and R. S. Berry, Mobilities of electrons and holes in organic molecular solids. Comparison of band hopping models, *J. Chem. Phys.* **44**, 3797 (1966).
113. S. H. Glarum, Electron mobilities in organic semiconduconductors, *J. Phys. Chem. Solids* **24**, 1577 (1963).
114. W. Siebrand, Polaron band structure and carrier mobility in crystal of diatomic molecules and aromatic hydrocarbons, *J. Chem. Phys.* **41**, 3574 (1964).
115. L. Friedman, Electron–phonon interaction in organic molecular crystals, *Phys. Rev.* **140**, A1649 (1965).
116. P. Gosar and S.-I. Choi, Linear-reponse theory of the electron mobility in anthracene crystals, *Phys. Rev.* **150**, 529 (1966).
117. R. W. Munn and W. Seibrand, Theory of charge carrier transport in aromatic hydrocarbon crystals, *J. Chem. Phys.* **52**, 6391 (1970).
118. R. W. Munn and W. Siebrand, Theory of electron -phonon interactions in organic crystal, *Disc. Faraday Soc.* **51**, 17 (1971).
119. L. Friedman, Small polaron transport and narrow band semiconduction similarities and differences, in *Conduction in Low Mobility Materials* (N. Klein, M. Pollak, and D. S. Tannhauser, eds.), Taylor and Francis, London (1971).
120. I. Vilfan, Small polaron model of the electron motion in organic molecular crystals, *Phys. Stat. Sol. B* **59**, 351 (1973).
121. O. H. LeBlanc, Jr., Band theory and the Hall effect in organic crystals, *J. Chem. Phys.* **39**, 2395 (1963).
122. L. Friedman, Transport properties of organic semiconductors, *Phys. Rev. A* **133**, 1668 (1964).

123. G. C. Smith, Nonanomalous photo-Hall mobility in anthracene at room temperature, *Phys. Rev.* **185**, 1133 (1969).
124. R. W. Munn and W. Siebrand, Sign of the Hall effect for hopping transport in molecular crystals, *Phys. Rev. B* **2**, 3435 (1970); D. Emin, The Hall mobility of a small polaron in a square lattice, *Ann. Phys.* **64**, 336 (1971).
125. D. Emin, Correlated small-polaron hopping motion, *Phys. Rev. Lett.* **25**, 1751 (1970).
126. D. C. Hoesterey and G. M. Letson, The trappings of photocarriers in anthracene by anthraquinone, anthracene, and naphthalene, *J. Phys. Chem. Solids* **24**, 1609 (1963).
127. W. Shockley and W. T. Read, Jr., Statistics of recombinations of holes and electrons, *Phys. Rev.* **87**, 835 (1952).
128. W. Helfrich and W. G. Schneider, Recombination radiation in anthracene crystals, *Phys. Rev. Lett.* **14**, 229 (1965); M. Silver, Carrier recombination and generation in anthracene, *Bull. Am. Phys. Soc.* **11**, 269 (1966).
129. H. S. W. Massey and E. H. S. Burphop, Recombination, in *Electronic and Ionic Impact Phenomena*, Oxford University Press, New York (1952), Chapter X.
130. R. G. Kepler and D. C. Hoesterey, High field mobility in anthracene crystals, *Phys. Rev. B* **9**, 2743 (1974).
131. J. W. Steketee and J. de Jonge, Photoconductance and spectral absorption of anthracene, *Philips Res. Rpt.* **17**, 363 (1962).
132. V. V. Eremenko and V. S. Medvedev, Dependence of the photoconductivity and the intensity of luminescence of anthracene crystals on the excitation wavelength, *Sov. Phys.—Solid State* **2**, 1426 (1961).
133. W. H. Wright, Variations in the efficiency of fluorescence excitation in anthracene, *J. Chem. Phys.* **45**, 874 (1966).
134. B. J. Mulder and J. de Jonge, Exciton diffusion and the photoconductivity spectrum of anthracene, pyrene, and perylene, *Philips Res. Rpts.* **21**, 188 (1966).
135. R. G. Kepler and F. N. Coppage, Generation and recombination of holes and electrons in anthracene, *Phys. Rev.* **151**, 610 (1966).
136. L. Onsager, Initial recombination of ions, *Phys. Rev.* **54**, 554 (1938).
137. A. Hummel, A. O. Allen, and F. H. Watson, Jr., Ionization of liquids by radiation. II. Dependence of the zero-field ion yield on temperature and dielectric constant, *J. Chem. Phys.* **44**, 3431 (1966).
138. A. Hummel, A. O. Allen, and F. H. Watson, Jr., Ionization of liquids by radiation. I. Methods for determination of ion mobilities and ion yields at low voltage, *J. Chem. Phys.* **44**, 3426 (1966).
139. W. F. Schmidt and A. O. Allen, Free-ion yields in sundry irradiated liquids, *J. Chem. Phys.* **52**, 2345 (1970).
140. G. Castro and J. F. Hornig, Multiple-charge-carrier generation processes in anthracene, *J. Chem. Phys.* **42**, 1459 (1965).
141. R. H. Batt, C. L. Braun, and J. F. Hornig, Field and temperature dependent recombination in anthracene, *Appl. Opt. Suppl.* **3**, 20 (1969); Electric-field and temperature dependence of photoconductivity, *J. Chem. Phys.* **49**, 1967 (1968).
142. N. E. Geacintov and M. Pope, Intrinsic photoconductivity in organic crystals, in *Proceedings of the Third International Photoconductivity Conference* (E. M. Pell, ed.), Pergamon Press (1969), p. 289.

143. D. C. Northrup and O. Simpson, Electronic properties of aromatic hydrocarbons. IV. Photo-electric effects, *Proc. Roy. Soc. A* **244**, 377 (1958).
144. M. Silver, D. Olness, M. Swicord, and R. C. Jarnigan, Photogeneration of free carriers in organic crystals via exciton–exciton interactions, *Phys. Rev. Lett.* **10**, 12 (1963).
145. C. L. Braun, Singlet exciton–exciton interactions in anthracene, *Phys. Rev. Lett.* **21**, 215 (1968); M. Schott and J. Berrehar, Charge carrier generation by singlet–singlet exciton interaction in crystalline anthracene under weakly absorbed light illumination, *Phys. Stat. Sol. B* **59**, 175 (1973).
146. A. Bergman, M. Levine, and J. Jortner, Collision ionization of singlet excitons in molecular crystals, *Phys. Rev. Lett.* **18**, 593 (1967); N. Tolstoi and A. P. Abramov, Interaction of excitons in anthracene, *Sov. Phys.—Solid State* **9**, 255 (1967).
147. R. G. Kepler, Photoionization of excitons in anthracene, *Phys. Rev. Lett.* **18**, 951 (1967).
148. E. Courtens, A. Bergman, and J. Jortner, Photoionization of two-photon excited singlet excitons in anthracene—E, *Phys. Rev.* **156**, 948 (1967).
149. W. L. Peticolas, J. P. Goldsborough, and K. E. Rieckhoff, Double photon excitation in organic crystals, *Phys. Rev. Lett.* **10**, 43 (1963).
150. D. Fröhlich and H. Mahr, Two-photon spectroscopy in anthracene, *Phys. Rev. Lett.* **16**, 895 (1966).
151. I. Webman and J. Jortner, Energy dependence of two-photon-absorption cross sections in anthracene, *J. Chem. Phys.* **50**, 2706 (1969).
152. A. Bergman and J. Jortner, Two-photon spectroscopy utilizing dye lasers, *Chem. Phys. Lett.* **15**, 309 (1972).
153. R. G. Kepler, unpublished results.
154. F. C. Strome, Jr., Direct two-photon photocarrier generation in anthracene, *Phys. Rev. Lett.* **20**, 3 (1968).
155. A. Bergman and J. Jortner, Photoconductivity of crystalline anthracene induced by tunable dye lasers, *Phys. Rev. B* **9**, 4560 (1974).
156. R. G. Kepler, Two photon transitions to highly excited states in anthracene crystals, *Phys. Rev. B* **9**, 4468 (1974).
157. N. E. Geacintov and M. Pope, Generation of charge carriers in anthracene with polarized light, *J. Chem. Phys.* **47**, 1194 (1966); S. D. Druger, Photoionization and photogeneration of carriers in anthracene, *Chem. Phys. Lett.* **17**, 603 (1972).
158. J. P. Hernandez, Photo-ionization of crystalline anthracene, *Phys. Rev.* **169**, 746 (1968).
159. D. Emin, The formation and motion of small polarons, in *Linear and Nonlinear Electronic Transport in Solids* (J. T. DeVresse, ed.), Plenum, New York (1975).
160. N. Karl, Organic semiconductors, in *Festkörper Probleme XIV Advances in Solid State Physics* (H. J. Queisser, ed.), Pergamon Press (1974).
161. K. H. Probst and N. Karl, Energy levels of electron and hole traps in the band gap of doped anthracene crystals, *Phys. Stat. Sol. A* **27**, 499 (1975).
162. J. Singh and H. Baessler, Theory of exciton dissociation in molecular crystals at the interface of a metal, *Phys. Stat. Sol. B* **62**, 147 (1974); H. Baessler and H. Killesreiter, Hot carrier injection into crystals and its relevance to the field dependence of photocurrents, *Phys. Stat. Sol. B* **53**, 183 (1972); H. Killesreiter and H. Baessler, Field dependence of exciton-induced, contact-limited photocurrents in molecular crystals, *Phys. Stat Sol. B* **53**, 193 (1972); H. Baessler, H. Killesreiter,

and G. Vaubel, Exciton-induced photocurrents in molecular crystals, *Disc. Faraday Soc.* **51**, 48 (1971).

163. M. E. Michel-Beyerle, W. Harengel, R. Haberkorn, and J. Kinder, Role of image forces at organic crystal–electrode interfaces, *Mol. Cryst. Liquid Cryst.* **25**, 323 (1974).
164. R. R. Chance and A. Prock, Role of singlet and triplet excitons in extrinsic photocurrent production in the anthracene–gold system, *Phys. Stat. Sol. B* **57**, 597 (1973).
165. F. Vogel, N. E. Geacintov, and M. Pope, Photoinjection of holes into anthracene crystals using aqueous triiode (I_3^-) solutions. Magnetic field effects, *J. Chem. Soc., Faraday Trans. 2* **69** (Pt. 8), 1208 (1973).
166. J. M. Hale and W. Mehl, Quenching of excited states at the interface, molecular crystal/electrolyte, *Disc. Faraday Soc.* **51**, 54 (1971).
167. G. W. Robinson, Electronic and vibrational excitons in molecular crystals, *Ann. Rev. Phys. Chem.* **21**, 429 (1970).
168. G. Wannier, The structure of excitation levels in insulating crystals, *Phys. Rev.* **52**, 191 (1937).
169. R. S. Knox, *Theory of Excitons*, Academic Press, New York (1963).
170. M. Pope and J. Burgos, Charge-transfer exciton state and ionic energy levels in anthracene crystals, *Mol. Cryst.* **1**, 395 (1966).
171. D. Haarer and G. Castro, Exciton induced photoemission in anthracene, *Chem. Phys. Lett.* **12**, 277 (1971).
172. D. S. McClure, Electronic spectra of molecules and ions in crystals. Part I. Molecular crystals, in *Solid State Physics*, Vol. 8 (F. Seitz and D. Turnbull, eds.), Academic Press (1959), p. 1.
173. R. Silbey, J. Jortner, and S. A. Rice, On the singlet-exciton states of crystalline anthracene, *J. Chem. Phys.* **42**, 1515 (1965).
174. M. R. Philpott, Exciton transitions in crystalline anthracene for k perpendicular to the b axis, *J. Chem. Phys.* **59**, 4406 (1973).
175. J. L. Katz, J. Jortner, S. Choi, and S. A. Rice, Atom–molecule reaction of hydrogen studied by molecular beams, *J. Chem. Phys.* **39**, 1897 (1963); Triplet energy transfer and triplet–triplet interaction in aromatic crystals, *Phys. Rev. Lett.* **11**, 323 (1963); Triplet excitons in crystals of aromatic molecules, *J. Chem. Phys.* **42**, 309 (1965).
176. P. Avakian, V. Ern, R. E. Merrifield, and A. Suna, Spectroscopic approach to triplet exciton dynamics in anthracene, *Phys. Rev.* **165**, 974 (1968).
177. G. C. Morris and M. G. Sceats, Exciton dynamics in molecular crystals from line shape analysis. Time response function of singlet excitons in crystal anthracene, *Chem. Phys.* **3**, 332 (1974); Exciton dynamics in molecular crystals from line shape analysis. Spectral moment analysis of the origin region of the 4000 Å transition of crystal anthracene, *Chem. Phys.* **3**, 342 (1974).
178. V. M. Kenkee, Relations among theories of exciton transfer, *Phys. Rev. B* **11**, 1741 (1975); M. Grover and R. Silbey, Exciton migration in molecular crystals, *J. Chem. Phys.* **54**, 4843 (1971); H. Haken and G. Strobl, An exactly soluble model for coherent and incoherent exciton motion, *Z. Phys.* **262**, 135 (1973); H. Haken and P. Reineker, A coupled coherent and incoherent motion of excitons and its influence on the line shape of optical absorption, *Z. Phys.* **249**, 253 (1972); R. W. Munn, Direct calculation of exciton diffusion coefficient in molecular crystals, *J. Chem. Phys.* **58**, 3230 (1972).

179. T. Holstein, Studies of polaron motion, Part II. The small polaron, *Ann. Phys.* **8**, 343 (1959).
180. J. M. Robertson, *Rev. Mod. Phys.* **30**, 155 (1958).
181. C. D. Akon and D. P. Craig, *Trans. Faraday Soc.* **62**, 1673 (1966).
182. K. W. Benz and H. C. Wolf, *Z. Naturforsch.* **19a**, 177 (1964).

Recommended Reading

Review Articles

Single Excitons

D. S. McClure, Electronic spectra of molecules and ions in crystals. Part I. Molecular crystals, in *Solid State Physics*, Vol. 8 (F. Seitz and D. Turnbull, eds.), Academic Press (1959), p. 1.

H. C. Wolf, The electronic spectra of aromatic molecular crystals, in *Solid State Physics*, Vol. 9 (F. Seitz and D. Turnbull, eds.), Academic Press (1960), p. 1.

D. P. Craig and S. H. Walmsley, Excitons in molecular crystals, in *Physics and Chemistry of the Organic Solid State*, Vol. I (D. Fox, M. M. Labes, and A. Weissberger, eds.), Interscience, New York (1963), p. 586.

S. A. Rice and J. Jortner, Comments on the theory of the exciton states of molecular crystals, in *Physics and Chemistry of the Organic Solid State*, Vol. III (D. Fox, M. M. Labes, and A. Weissberger, eds.), Intersceicne, New York (1967), p. 199.

Triplet Excitons

P. Avakian and R. E. Merrifield, Triplet excitons in anthracene crystals—A review, *Mol. Cryst.* **5**, 37 (1968).

Electrical Properties

J. Kommandeur, Conductivity, in *Physics and Chemistry of the Organic Solid State*, Vol. II (D. Fox, M. M. Labes, and A. Weissberger, eds.), Interscience, New York (1965), p. 1.

O. H. LeBlanc, Conductivity, in *Physics and Chemistry of the Organic Solid State*, Vol. III (D. Fox, M. M. Labes, and A. Weissberger, eds.), Interscience, New York (1967), p. 133.

Books

D. P. Craig and S. H. Walmsley, *Excitons in Molecular Crystals*, W. A. Benjamin, New York (1968).

A. S. Davydov, *Theory of Molecular Excitions*, McGraw-Hill, New York (1962).

R. S. Knox, *Solid State Physics, Theory of Excitons*, Suppl. 5, Academic Press, New York (1963).

F. Gutman and L. E. Lyons, *Organic Semiconductors*, John Wiley and Sons (1967).

9

Organic Molecular Crystals: Charge-Transfer Complexes

Zoltán G. Soos
Department of Chemistry
Princeton University, Princeton, N.J.

and

Douglas J. Klein
Department of Physics
University of Texas, Austin, Texas

1. Introduction

1.1. Contrast of Solution and Solid-State Complexes

Solutions of electron donors (D) and acceptors (A) exhibit absorptions not associated with either individual molecule.[1] Mulliken[2] proposed that the new absorptions involve an electron transfer from D to A, as indicated by

$$\psi_{\text{complex}}(\text{DA}) \xrightarrow{h\nu_{\text{CT}}} \psi_{\text{complex}}(\text{D}^+\text{A}^-) \tag{1}$$

Here $h\nu_{\text{CT}}$ is the charge-transfer (CT) excitation energy, and the CT band is explicitly associated with the molecular complex formed between a D and an A molecule. The nature of such DA complexes has been the subject of extensive experimental and theoretical studies.[3–5] The energetics of dimer formation; the geometry of the complex; the systematics of varying D, A, and solvents; and the nature of CT absorption have been explored. The CT excitation is greatly enhanced,[3,4,6] as suggested by Mulliken,[2] via small ad-

mixtures of the excited singlet configuration $^1|D^+A^-\rangle$ into the ground state, $|DA\rangle$. However, the additional configuration-interaction stabilization due to this small admixture does not[6,7] usually dominate the binding energy or the geometry of the complex. As we will discuss in Section 2, the full quantum-mechanical treatment of a DA dimer thus requires explicit consideration of a variety of intermolecular forces.

There have also been extensive experimental studies of crystalline complexes of π-molecular donors and acceptors. It is now evident that aromatic donors and acceptors usually crystallize in molecular stacks.[9-11] All intermolecular separations are normal Van der Waals distances, except for a slight ($\lesssim 0.4$ Å) shortening of the interplanar separation. The π overlap of D and A molecules along the stacks then leads to a CT band in addition to the molecular (Frenkel) excitations expected in molecular crystals. In fact, the observation[12] of solid-state CT bands polarized perpendicular to the molecular plane, and thus parallel to the stack axis, was an early confirmation of Mulliken's proposed electron-transfer mechanism.[2-4]

In spite of the early recognition of CT bands in π-molecular solids, it has proved very difficult to apply the Mulliken theory to crystalline complexes. The reason is quite simple. Solid-state π-molecular complexes contain infinite molecular stacks,[9,10] for example, the type ...DADA... shown in Figure 1 for D = tetramethyl-*p*-phenylenediamine (TMPD) and tetracyanobenzene (TCNB).[13] Even the most highly idealized application of configuration interaction, with each donor restricted to D or D^+ and each acceptor to A or A^-, leads to an infinite secular determinant. The theoretical description of solid-state complexes thus lags far behind the analysis of DA dimers, however difficult and even controversial the dimer problem has been.[3,4,6] It must be clearly recognized at the outset that many results for dimers cannot be simply transferred to DA solids.

The thermodynamics of complex formation for dimers can readily be extended to DA crystals,[3,8,14] but it is then difficult to determine the various polarization, CT, and other processes relating the energy of the solid to that of isolated D and A molecules.* The importance of the stability of the dimer, which then controls the observed equilibrium in solution, is greatly diminished in the solid,

* For a comprehensive analysis and compilation of electric and optical properties see Ref. 14.

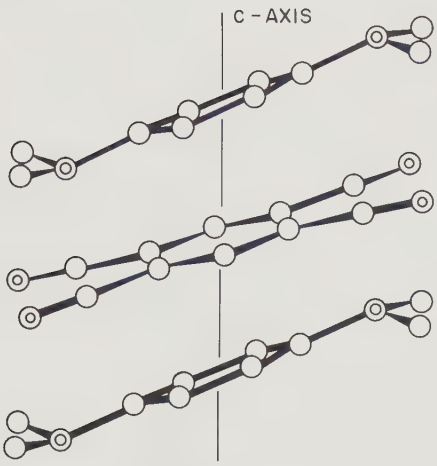

Fig. 1. The infinite donor-acceptor stack in TMPD-TCNB viewed along [1$\bar{1}$0]. (Reproduced with permission from Ohashi, Iwasaki, and Saito.[13])

which provides an inherently static problem. By contrast, the equilibrium geometry is readily available in the solids but must usually be inferred from rather incomplete data in solution. Thus the experimental focus also shifts on going from dimers in solution to DA solids. The fundamental CT excitation (1) is, in fact, the principal feature of interest in both dimers and solids.

1.2. Molecular-Exciton Approach

We will develop in Sections 2 and 3 a general analysis of charge transfer in π-molecular crystals. The underlying assumptions of molecular-exciton theory[15–18] are used throughout. The observation that the solid-state spectra of typical closed-shell molecular crystals, for example, benzene, naphthalene, and anthracene, are closely related to gas-phase spectra makes it natural to describe such molecular crystals in terms of weakly overlapping, unperturbed molecules. Molecular-exciton theory[15–18] then provides, often in great detail, a phenomenological approach for predicting the small crystal shifts and splittings relative to gas-phase transitions. In most cases, degenerate first-order perturbation theory suffices, since the

crystal interactions are small compared to the spacing of the molecular energy levels. Vibrational, triplet, and singlet excitons all reflect shifts and splittings induced by the lower symmetry of the crystalline environment.

The crystal-structures[9-11] of π-molecular CT crystals support the occurrence of weakly overlapping, essentially molecular D and A constituents. Their infrared and ultraviolet spectra also show absorptions characteristic of D and A molecules.[19,20] Even the strongest π donors and acceptors, which crystallize[9] in *ionic* lattices of D^+ and A^- radicals, show spectra characteristic of the molecular ion-radicals. These spectroscopic observations provide[9,19,20] the experimental basis for the sharp separation of π-molecular CT crystals into those with largely neutral and those with largely ionic ground states. The sharp separation has been understood theoretically[21,22] for weakly overlapping molecular crystals, with the Madelung (electrostatic) energy providing the stability of the ionic lattice.[22,23] Thus π-molecular CT solids contain largely unperturbed molecular constituents, and it is natural to use isolated-molecule wave functions in a phenomenological approach to solid-state complexes.[24]

Molecular-exciton theory[15-18] is especially useful when the crystal interactions are weak enough to permit focusing on a *single* molecular excitation, which becomes N-fold degenerate in a solid of N noninteracting molecules. In most cases, the *lowest* molecular triplet or singlet state provides the basis for the Frenkel excitons of typical closed-shell molecular solids. In sharp contrast, the restriction to the *lowest* electronic excitation in π-molecular CT crystals leads to a theory[25] in which only CT states are included. The occurrence of a lowest CT, rather than Frenkel, excitation results in a fundamentally different form of molecular-exciton theory.[24,25] The additional low-energy electron transfer in π-molecular CT solids is the decisive electronic feature of the solid-state complexes reviewed here. The two-state configuration-interaction picture of the idealized DA dimer[3,4] can then be extended to the infinite molecular stacks encountered in the solid state.

The most striking difference between CT and the usual molecular solids occurs in ion-radical solids based on the strongest π donors and acceptors. Crystals of these *open-shell* molecular ions, D^+ and/or A^-, are contrasted in Table 1 with crystals of nonoverlapping closed-shell molecules. The enormous spin degeneracy in either ionic CT or free-radical (FR) solids should especially be noted. The magnetic properties of ion-radical solids[23,24] provide important information

TABLE 1
Comparison of Ionic Charge-Transfer and Free-Radical Crystals with Molecular Solids in the Limit of Nonoverlapping Sites

Property	Ionic CT or FR crystal	Molecular crystal
Constituents	Ion-radicals D^+ or A^- open shell ($S = \frac{1}{2}$)	Neutral molecules closed shell
Crystal ground state	2^N spin degeneracy paramagnetic	Nondegenerate diamagnetic
Lowest excitation	CT ($\parallel$ to stack)	Frenkel (molecular)
Crystal binding	Madelung and intermolecular	Intermolecular

about the ground-state charge distribution and complement optical studies of CT absorptions. The molecular-exciton approach to solid-state complexes is applicable to any molecular solid with a low-lying CT excitations.[25] We nevertheless will focus primarily on the relatively rare *ionic* CT and FR solids, rather than on the more common *neutral* complexes of weak π donors and acceptors, because the ion-radical systems exhibit unusual magnetic, electric, and optical properties that have been central to solid-state studies.[24,26,27]

1.3. π-Molecular Ion-Radical Solids

The strong π acceptors tetracyanoquinodimethane (TCNQ) and chloranil are shown in Figure 2, together with the strong π donors *p*-phenylenediamine (PD), TMPD, and tetrathiofulvalene (TTF). While these molecules are by no means the only donors and acceptors that form ionic CT or FR crystals, they are certainly among the most versatile and thoroughly studied.[24] TMPD-TCNQ and TMPD-chloranil form mixed[9] stacks of ion-radicals, as shown by $\ldots D^+A^-D^+A^- \ldots$. The low-lying CT excitation is now a "back charge transfer"[21]

$$|\ldots D^+A^-D^+A^-\ldots\rangle \xrightarrow{h\nu_{CT}} |\ldots D^+ADA^-\ldots\rangle \qquad (2)$$

and involves returning the electron to the donor. TCNQ forms extensive series of FR salts,[28] with diamagnetic metallic or organic cations located between different $\ldots A^-A^-A^-A^-\ldots$ stacks providing electrical neutrality, as discussed in greater detail in Section 3.

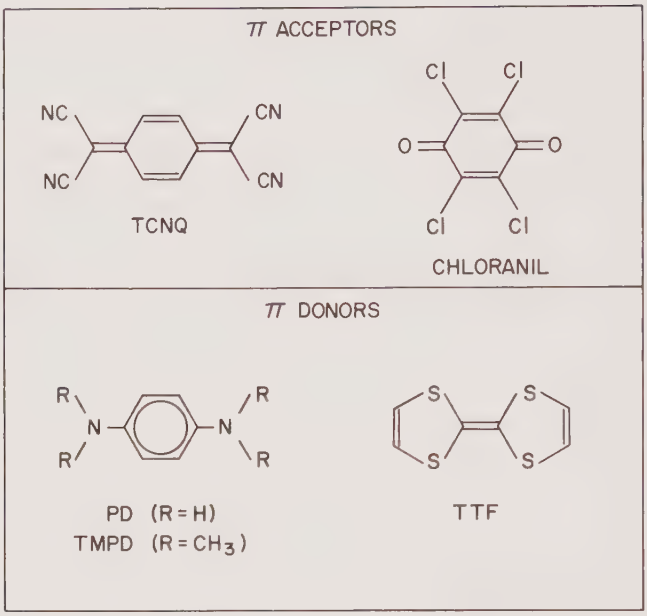

Fig. 2. Representative examples of strong π donors and strong π acceptors.

Chloranil also forms[29] FR salts with alkali metals and with organic or organometallic bases.[9] In these FR crystals, A^- acts as both the donor and the acceptor, as indicated by the CT excitation

$$|\ldots A^- A^- A^- A^- \ldots\rangle \xrightarrow{h\nu_{CT}} |\ldots A^- A A^{2-} A^- \ldots\rangle \qquad (3)$$

Ion-radical salts are therefore solid-state analogs of self-complexes.[30] TMPD and TTF form analogous self-complexes, for example with various halides, in which the cation radicals D^+ form stacks,[24] and the fundamental CT excitation is

$$|\ldots D^+ D^+ D^+ D^+ \ldots\rangle \xrightarrow{h\nu_{CT}} |\ldots D^+ D D^{2+} D^+ \ldots\rangle \qquad (4)$$

CT processes in self-complexes based on open-shell molecular ion-radicals do not involve an *orbital* excitation, since the highest occupied MO is half-filled and can accommodate another electron; $h\nu_{CT}$ is then related to the correlation energy for placing two electrons on the same molecular site.

As indicated in Section 3, there are many FR salts with complex stoichiometry, as shown by Cs_2TCNQ_3. Now formally neutral TCNQ sites also occur in the ion-radical stack.[9,31] When the sites

are crystallographically inequivalent, a mixed-valence organic system is achieved. Iida[32] has suggested that the additional, even lower-energy, CT bands in complex salts involve transfers between radical and neutral sites, as shown by

$$|\ldots AA^-A^-AA^-A^-AA^-A^-\ldots\rangle \xrightarrow{h\nu_{CT}} |\ldots AA^-AA^-A^-A^-AA^-A^-\ldots\rangle \qquad (5)$$

for a 2:3 salt like Cs_2TCNQ_3. Now there is no requirement that a TCNQ site become doubly charged, and the lower energy of (5) is readily understood. The complex salt $TMPD(TCNQ)_2$ contains segregated stacks[33] in which all TCNQ sites are equivalent; several other 1:2 salts have served to establish[9] the geometry of $TCNQ^{-1/2}$. It is evident that complex salts permit additional, potentially very facile[34,35] mechanisms for charge conduction along the FR stack.

Ion-radical crystals provide a small but versatile subclass of π-molecular solids with a lowest CT excitation. Their potentially very high conductivity, as shown by TTF-TCNQ[36,37] or NMP-TCNQ[38,39] (NMP = *N*-methylphenazine), makes them organic "metals," while other TCNQ systems span the entire spectrum from semiconductors to insulators.[24] The proceedings of two recent conferences[40] attest to the growing interest among both physicists and chemists in the unusual properties of organic conductors. The TTF-TCNQ family includes several conductors[41] in which S is replaced by Se and the TTF is methylated. The TTF halides are mixed-valence conductors. The observation[42] of superconductivity in polynitrile sulfide $(SN)_x$ may foreshadow even wider applications for low-dimensional organic conductors. Highly conducting organic solids are discussed[43] elsewhere in considerable detail. The far more numerous semiconducting CT crystals are emphasized here. Their varied physical properties provide a natural test for a phenomenological theory. Indeed, the occurrence of a lowest CT excitation will be combined with structural information to account qualitatively for unusual magnetic, optical, and electric properties.

1.4. Hubbard Models and CT Crystals

The Mulliken theory of CT in dimers and the related optical studies in solid-state complexes have been of primary interest to chemists. One of our major goals is to demonstrate that π-molecular CT solids have important common features with the widely used,

idealized Hubbard model[44] of solid-state physics. The physical origins of Hubbard models are illustrated by Van Vleck[45] for a hypothetical chain of H atoms which, like FR crystals, have one unpaired electron per site. The correlation $U > 0$ measures the energy for putting two spin-paired electrons on the same site, as might occur in a CT excitation. The Mulliken CT integral t defined in Section 2.1 allows electron transfer among adjacent sites while conserving the spin orientation. The resulting Hamiltonian for a one-dimensional lattice is

$$\mathscr{H}_{Hu} = t \sum_{n\sigma} (a^{+}_{n\sigma} a_{(n+1)\sigma} + a^{+}_{(n+1)\sigma} a_{n\sigma}) + U \sum_{n} a^{+}_{n\alpha} a^{+}_{n\beta} a_{n\beta} a_{n\alpha} \tag{6}$$

where the electron creation and annihilation operators $a^{+}_{n\sigma}$ and $a_{n\sigma}$ are defined for the odd electron at each site. The derivation of Hamiltonians related to (6) for CT crystals is given in Section 2. Their common feature is the one-site correlation U.

Hubbard Hamiltonians provide a simple, idealized model for studying both electron correlation effects, as represented by the U term in (6), and electron delocalization effects, as represented by the t term. The $t = 0$ and $U = 0$ limits correspond, respectively, to isolated sites and to a one-band metal. When t/U is small and there is one electron per site, $\mathscr{H}_{Hu}$ is a Mott insulator[46]; Hubbard models have consequently been applied to metal–insulator transitions in various transition-metal oxides.[47,48] The strong correlations for $U \gg t$ are further manifested by the effective Heisenberg spin Hamiltonian,[45,49] a limiting case of (6) discussed in Section 5.4:

$$\mathscr{H}_{H} = (4t^2/U) \sum_{n} (\mathbf{S}_n \cdot \mathbf{S}_{n+1} - \tfrac{1}{4}) \tag{7}$$

$\mathscr{H}_{H}$ describes the low-temperature magnetic properties of a free-radical chain with $\mathbf{S}_n = \frac{1}{2}$ at the nth site. The antiferromagnetic exchange $2J = 4t^2/U > 0$ provides a direct connection[23] between the magnetic and optical properties of CT and FR crystals, in which $h\nu_{CT} = \Delta E_{CT}$ is a measure of the energy for producing a doubly occupied site. The identification[23,50]

$$\Delta E_p \sim t^2/\Delta E_{CT} \tag{8}$$

relates the activation energy for paramagnetism, ΔE_p, to the CT excitation, ΔE_{CT}, and to the Mulliken integral, t, which also enters directly in electric conduction. The magnetic properties of CT crystals summarized in Section 4.4 illustrate the consequences of antiferromagnetic exchange.

These general considerations apply to any solid containing open-shell atomic or molecular sites. LeBlanc[34,51] noted that a large U could qualitatively explain the semiconductivity of most $TCNQ^-$ salts, which would be metallic on the basis of simple band theory ($U = 0$). The same conclusion holds for Wurster's blue perchlorate, TMPD-ClO_4, which contains a regular $TMPD^+$ stack above 186°K. Strebel and Soos[22] give a systematic analysis of π-molecular CT complexes in terms of modified Hubbard models. The restriction of π-electron overlap to the ion-radical or molecular stack produces a one-dimensional Hubbard model, with small t, while the occurrence of a low-lying CT excitation is associated with U. The theoretical development in Section 2 shows that π-molecular CT solids are, in fact, possibly the best available realizations of Hubbard models.

The long-standing theoretical interest in both the linear Heisenberg antiferromagnetic chain (7) and the linear Hubbard model (6) thus has direct bearing on π-molecular CT solids. The Mulliken problem for CT in solid-state complexes has, in effect, already been investigated as an idealized problem in electron correlations. Indeed, the same formal problem occurs in the analysis of π-electrons in polyenes[52] or in aromatic molecules.[53]

1.5. Relation to Other Work: Scope of the Review

The occurrence of a CT excitation below any Frenkel states is basic to our present formulation of a consistent phenomenological treatment of the electronic states of π-molecular CT complexes. The extension of the Mulliken treatment[2–4] for DA dimers is accomplished by a novel application[25] of molecular-exciton theory. Subsequent mathematical analysis is facilitated by solid-state results for Hubbard models. Thus crystalline π-molecular complexes lead to problems which overlap in part with experimental and theoretical studies in both chemistry and physics.[24] The one-dimensionality of the ion-radical stacks is a common structural feature with both inorganic conductors[27] based on stacked transition-metal complexes and inorganic insulators[54,55] based on exchange-coupled transition-metal ions. In addition to a structural focus, the fact that π-molecular CT crystals are organic solids, and even prototypes for polymers, naturally suggests a common approach to physical properties such as conductivity. Before outlining our development, we list previous reviews which overlap in part the present topic of charge-transfer molecular solids. These reviews also provide more comprehensive compilations of the voluminous original literature.

The books by Foster,[3] Mulliken and Person,[4] and Rose[5] focus primarily on DA dimers and review both the experimental and theoretical situations. Hanna and Lippert[6] provide a critical review of intermolecular and CT contributions in dimers. These problems are common to solid-state complexes, as we will discuss in Section 2.

Herbstein's[9] extensive compilation of π-molecular crystal structures (up to 1971) shows many of the ion-radical salts based on the molecules in Figure 2, with special emphasis on the overlap patterns of TCNQ and TMPD crystals. The crystal structure is a basic input in our phenomenological treatment, as we will discuss in Section 3. Prout and Kamenar[10] review the structures of other, primarily neutral complexes.

Briegleb's important book[8] still provides the most comprehensive optical and thermodynamic data on neutral π-molecular CT crystals. The extensive optical studies[32,56–63] of Matsunaga, Akamatu, Iida, Nagakura, and their colleagues have elucidated the CT transition and its polarization in both neutral and ionic stacked complexes. Offen[64] summarizes pressure effects on the optical spectra, while Prout and Wright's brief review[11] is an early attempt to relate structural and electronic features in solid-state complexes.

The conductivity of organic solids has been discussed by LeBlanc,[34] by Gutmann and Lyons,[14] and by Kommandeur.[65] The comprehensive (to 1967) conductivity data collected by Gutmann and Lyons[14] may be subject to reinterpretation, since they are largely based on compaction studies. The conductivity work by Siemons, Bierstedt, and Kepler[35] demonstrates the importance of single-crystal measurements in TCNQ salts.

The magnetic properties of insulating or semiconducting ion-radical salts have been reviewed by Nordio, Soos, and McConnell[23] and extended to ionic CT crystals by Soos.[66] Magnetic properties[67] are closely related to inorganic insulators with exchange-coupled ions and pose problems that at first are quite distinct from CT excitations or conductivity. Extensive reviews of exchange in one-dimensional inorganic spin systems are given by Richards and Hone[68] and by DeJongh and Miedema.[69] A principal focus is the unusual one-dimensional EPR line shape observed[70] in $N(CH_3)_4MnCl_3$ (TMMC), with a linear chain of $S = \frac{5}{2}$ Mn^{2+} ions, and subsequently in several linear chains of $S = \frac{1}{2}$ Cu^{2+} ions.

The vast inorganic literature of metal–metal interactions provides one-dimensional structures for halides for most of the first-row transition metals.[71] Hatfield and Whyman[72] survey the many possibilities afforded by Cu(II) systems. Kokoszka and Gordon,[73]

Kokoszka and Duerst,[54] Martin,[74] Sinn,[75] and Ginsberg[76] have all reviewed exchange interactions, primarily in small transition-metal clusters. The similarity of exchange-coupled inorganic and organic systems will certainly be exploited further,[67] even though the mechanisms for exchange are probably different. Thus exchange in inorganic magnetic chains is probably not dominated by CT interactions, and localized transitions (*d–d* bands) usually occur below CT excitations.

Shchegolev[26] has reviewed Soviet work on the highly conducting TCNQ salts, while Zeller[27] has focused on the partly oxidized Krogmann[77] salts, such as $K_2Pt(CN)_4Br_{0.3} \cdot xH_2O$, based on tetracyanoplatinate ions. There is little doubt that electron–phonon interactions will prove important not only for the good conductors, but also for charge carriers in either insulating or semiconducting organic solids. However, we do not consider the role of polarons[14,78,79] here. Indeed, we only mention current work[40,43,80] on highly conducting organic solids in passing. These often controversial models for conduction presuppose an understanding of the electronic states of π-molecular CT crystals and are consequently areas for potential extensions of our phenomenological model.

The underlying assumptions of the molecular-exciton theory have been extensively discussed.[15–18] Rice's and Jortner's[17] comprehensive analysis of theoretical difficulties with quantum-mechanical computations in even the simplest closed-shell molecular crystals emphasizes the need for a phenomenological approach and provides a background for the discussion of molecular parameters in Section 5. Mathematical properties of one-dimensional Hubbard models form another type of theoretical problem and are summarized elsewhere.*

We will present in Section 2 a phenomenological theory for the electronic states of a molecular crystal and show that the restriction to a lowest CT excitation permits a convenient fermion representation. The structural variety of ion-radical crystals based on strong π donors and acceptors will be shown in Section 3 to provide several different applications of the phenomenological theory. A qualitative analysis of optical, electric, and magnetic properties for semiconducting CT and FR solids follows in Section 4. In Section 5, we will consider the quantum-mechanical computation of various model parameters and the extensions of Hubbard models suggested by

* See Ref. 81. Section IV contains a compilation of one-dimensional Hubbard model results.

electrostatic and other interactions in actual π-molecular crystals. A general phenomenological approach to CT in solid-state complexes leads to far too many possible applications for a survey of finite length. Even the topics selected here span both theoretical and experimental work, as well as both optical and magnetic properties. We have consequently endeavored to make each section reasonably self-contained.

2. Development of Phenomenological Theory

2.1. The Ion-Radical Dimer

Instead of the more familiar[3–5] DA dimer, we discuss here a hypothetical ion-radical dimer, a complex whose ground state is primarily ionic, $|D^+A^-\rangle$. A CT excitation like (1) then produces a largely neutral $|DA\rangle$ pair. The occurrence of ion-radicals in both ionic CT and FR crystals reflects the Madelung stabilization of the ionic lattice.[22,23] Such stabilization simply shifts the relative energies of the ionic and neutral configurations, and we consider the situation shown in Figure 3, with $|D^+A^-\rangle$ the ground state. We follow Mulliken's[2] original definition that $|D^+A^-\rangle$ and $|DA\rangle$ are interacting, but strongly orthogonal wave functions. Such an approach is

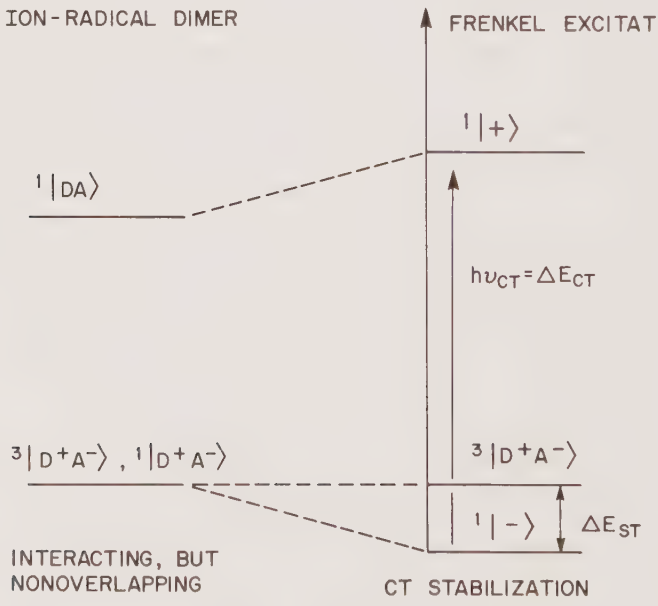

Fig. 3. Schematic energy-level diagram for an ion-radical dimer.

natural for solid-state problems, since it avoids the "nonorthogonality catastrophe"[82] for an infinite basis and is further indicated for a phenomenological theory in which explicit (*ab initio*, for example) computations are not attempted.

The highest occupied MO of D and the lowest unoccupied MO of A are both taken to be nondegenerate. Then the ion-radical dimer D^+A^- reduces to degenerate singlet and triplet configurations in the limit of zero differential overlap. The charge distributions of $^1|D^+A^-\rangle$ and $^3|D^+A^-\rangle$ are very nearly identical, and any multipole interactions are very nearly the same, as indicated in Figure 3. The Coulomb Hamiltonian $\mathscr{H}$ connects only states with the same spin multiplicity, since it is an excellent approximation to neglect spin–orbit interactions for aromatic molecules containing primarily such light atoms as C, H, or N. Configuration interaction then connects only $^1|D^+A^-\rangle$ and $|DA\rangle$, which is necessarily a singlet, if higher (Frenkel) states are neglected. Taking $E(D^+A^-)$ as the zero of energy, we obtain

$$\mathscr{H} = \begin{pmatrix} o & t \\ t & \Delta E \end{pmatrix} \tag{9}$$

where $\Delta E = E(DA) - E(D^+A^-) > 0$ and t is the Mulliken CT integral,

$$t = \langle D^+A^-|\mathscr{H}|DA\rangle \tag{10}$$

The Mulliken CT integral t is formally identified[22] with the Hubbard hopping integral in π-molecular CT complexes and plays a central role in correlating the physical properties of ion-radical crystals.[24] As indicated above, it represents the configuration interaction mixing of the singlet states $^1|D^+A^-\rangle$ and $|DA\rangle$ by the electrostatic Hamiltonian for the rigid dimer.

The solution of (9) leads to the eigenvalues

$$\lambda_\pm = \tfrac{1}{2}\Delta E \pm \tfrac{1}{2}[(\Delta E)^2 + 4t^2]^{1/2} \tag{11}$$

with λ_- corresponding to the ground state and λ_+ to the excited state. The corresponding eigenfunctions are

$$^1|\pm\rangle = a_\pm\,^1|D^+A^-\rangle + b_\pm|DA\rangle \tag{12}$$

where the expansion coefficients are

$$\begin{aligned} a_\pm &= (\lambda_\pm - \Delta E)/[t^2 + (\Delta E - \lambda_\pm)^2]^{1/2} \\ b_\pm &= t/[t^2 + (\Delta E - \lambda_\pm)^2]^{1/2} \end{aligned} \tag{13}$$

provided that $|^1D^+A^-\rangle$ and $|DA\rangle$ are normalized functions. The CT excitation in Figure 3 is given by

$$h\nu_{CT} = (\Delta E^2 + 4t^2)^{1/2} \tag{14}$$

while the stabilization of $^1|D^+A^-\rangle$ relative to $^3|D^+A^-\rangle$ provides a singlet–triplet splitting of

$$\Delta E_{ST} = -\lambda_- \approx t^2/\Delta E \tag{15}$$

for $t \ll \Delta E$. Thus the CT stabilization of $^1|D^+A^-\rangle$ relative to $|DA\rangle$ does not alter the usual results[3,5] for the CT transition, and in addition provides an important contribution[23] to the singlet–triplet splitting of the ion-radical dimer. The magnetic properties are, of course, strongly dependent on ΔE_{ST}.

An analogous treatment may be used for self-complex dimers, A^-A^- or D^+D^+, with the additional feature that both singlet excited states $|AA^{--}\rangle$ and $|A^{--}A\rangle$ or $|DD^{++}\rangle$ and $|D^{++}D\rangle$ now occur. If the dimer has a center of inversion, the allowed CT transition[30] is to the state $(1/\sqrt{2})(|AA^{--}\rangle - |A^{--}A\rangle)$ whose energy is not shifted by configuration interaction. The CT excitation then remains (14), but the stabilization of $^1|A^-A^-\rangle$, or of $^1|D^+D^+\rangle$, has increased to

$$\Delta E_{ST} = \tfrac{1}{2}(\Delta E^2 + 8t^2)^{1/2} - \tfrac{1}{2}\Delta E \approx 2t^2/\Delta E \tag{16}$$

Self-complexes without centers of inversion, or at crystallographically inequivalent sites, could show two CT transitions. Both $TCNQ^-$ anion radicals[83] and PD^+ or $TMPD^+$ cation radicals[84] form self-complex dimers in solution. A more complete theoretical analysis is of course possible for such dimers.

The CT stabilization of the singlet state, as indicated in (15) and (16), corresponds to the kinetic exchange in Anderson's theory[49] of superexchange between transition-metal ions. The direct, or Heisenberg, contribution to ΔE_{ST} is[49,85]

$$J_D = \langle D^+ \otimes A^- | \mathscr{H} P | D^+ \otimes A^- \rangle \tag{17}$$

where P permutes electrons between the two ion-radicals and $|D^+ \otimes A^-\rangle$ is a product function. Equation (17) reduces to $\langle D^+(1)A^-(2)|e^2/r_{12}|D^+(2)A^-(1)\rangle$ when only the two electrons in the half-filled MO are considered. Since π-electron overlap is small even along the stack, we assume that J_D is a small contribution to

ΔE_{ST}. As discussed in detail by Herring[85] and summarized below in Section 2.3, it is by no means straightforward to estimate the relative contributions to ΔE_{ST} even in the simplest case of two H atoms. The strong antiferromagnetic ($\Delta E_{ST} > 0$) exchange in ionic CT and FR solids suggests that (15) or (16), which are necessarily antiferromagnetic, is more important than J_D, which is generally ferromagnetic in sign.

2.2. Intermolecular Forces

The phenomenological treatment of the ion-radical dimer closely parallels the zeroth-order approach to the DA dimer. In particular, the connection between the isolated-molecule wave functions and the dimer states $|D^+A^-\rangle$ and $|DA\rangle$ has been studied in some detail by Murrell, Randic, and Williams[86] and, for π-molecular dimers, by Hanna and co-workers.[6,87] It is evident that a crystal of D and A molecules will present an even more difficult problem in intermolecular forces. The cataloging of various contributions to the ground-state energy and geometry of a rigid dimer, while not unique, nevertheless focuses attention on the different types of matrix elements of the electrostatic Hamiltonian. These considerations make it premature, in our opinion, to identify quantitatively various contributions to the stability of π-molecular CT crystals. As emphasized in Section 2.4, the general phenomenological theory is developed in terms of molecular wave functions that already contain many classical electrostatic contributions. The present subsection may be skipped by readers not interested in the details[88,89] of "exchange perturbation theories."

The wave function for an isolated, rigid DA complex has the general form

$$|DA\rangle = \sum_{rs} a_{rs}\mathscr{A}(|Dr\rangle \otimes |As\rangle) + \sum_{tu} b_{tu}\mathscr{A}(|D^+t\rangle \otimes |A^-u\rangle) \qquad (18)$$

Here $|Dr\rangle$, $|As\rangle$, $|D^+t\rangle$, $|A^-u\rangle$ are, respectively, the normalized molecular wave functions of the isolated donor, isolated acceptor, and their isolated ion-radicals. The coefficients a_{rs} and b_{tu} describe the configuration-interaction mixing for the dimer and $\mathscr{A}$ is the antisymmetrizer. The largest coefficient for a DA dimer is expected to be a_{00}, while the largest coefficient for an ion-radical dimer is b_{00}. It will clearly be necessary in practice to limit sharply the expansion (18) by selecting the physically most important terms.

The quantum theory of intermolecular forces[88,90–92] analyzes the contributions to (18) by comparing various types of matrix elements of the electrostatic Hamiltonian $\mathscr{H}$ of the dimer.

(1) Crystal field, or classical Coulomb, interactions represent the contribution of the *permanent* multipoles of the isolated molecular ground state, for example $|D^+0\rangle$ and $|A^-0\rangle$ in an ion-radical solid. If only these interactions were important, the neutral dimer $|DA\rangle$ would be accurately represented by the nonantisymmetrized product $|D0\rangle \otimes |A0\rangle$.

(2) Induction interactions represent the polarization, or distortion, of the charge distributions for $|D0\rangle$ and $|A0\rangle$ and are discussed in terms of *induced* multipoles. There is still no overlap of the molecular charge distributions. The ground states $|DA\rangle$ would then reduce to a product function of, for instance, the form $(\sum_r a_r|Dr\rangle)(\sum_s a_s|As\rangle)$. It is likely that induction is less important in the solid than in a dimer, since the solid generally contains D and A sites with considerable symmetry. There are often, for example, inversion centers at D^+ or A^- sites for ion-radical crystals based on TMPD, TTF, TCNQ, and chloranil.

(3) Resonance interactions involve off-diagonal Coulomb matrix elements which become important due to a degeneracy of the isolated molecular states. Such contributions arise primarily for identical molecules, one of which is excited, and are consequently important in theories[15–18] of molecular crystals.

(4) Dispersion, or Van der Waals, interactions also involve off-diagonal matrix elements and represent instantaneous electrostatic interactions between oscillating multipoles. If dispersion dominates, then a neutral $|DA\rangle$ state could be represented by a superposition of product functions $|Dr\rangle \otimes |As\rangle$, with all $b_{tu} = 0$ in (18), but $|DA\rangle$ would no longer separate into a simple product as was the case for induction interactions.

(5) Resonant charge-transfer interactions involve off-diagonal matrix elements like (10) that become important on account of a degeneracy of the isolated molecular states. Now specific electrons cannot be assigned to a given molecule and the charge distributions overlap. Such interactions arise when an extra (odd) electron occurs alternately with one molecule and then another, as can happen in complex FR salts.

(6) Exchange interactions also involve differential overlap and are most simply associated with the kinetic exchange contributions (15) or (16) or with the diagonal Heisenberg exchange (17). Both types

of exchange are second order in the intermolecular differential overlap.

CT stabilization is associated with the Mulliken CT integral t and may well be one of the smallest contributions to the interaction energy, but t leads directly to the additional absorption characteristic of CT solids or dimers. Furthermore, all these contributions arise from a *single* interaction, the quantum-mechanical electrostatic potential. (Additional coupling with the electron spins or the nuclear motions are usually small and are neglected.) Thus it is somewhat artificial to specify the relative importance of various intermolecular contributions, since there is no rigorous, unique theoretical decomposition. However, it is evident that once a finite basis is adopted in (18) then the matrix elements of $\mathscr{H}$ with respect to the approximate MOs can be classified as indicated above.

The crystal field, induction, dispersion, and exchange interactions are all comparable[87,93,94] in largely neutral dimers, such as tetracyanoethylene (TCNE) with benzene and *p*-xylene or benzene and I_2. Exchange contributions are also important. Thus the accurate representation of the dimer ground-state wavefunction and geometry remain quantum-mechanical problems of some complexity. The isolated molecular multipole moments and polarizabilities may be used to estimate crystal field or induction contributions even in the solid state. However, as already noted, the binding energy of the solid has not been of primary concern. Gutmann and Lyons[14] use, instead, such multipole and polarization arguments to estimate the stabilization of excited states, and in particular of charge carriers, in organic semiconductors.

As a final remark on the difficulty of applying quantum theory systematically to the weak, but complex, intermolecular forces[88–92] in molecular dimers or crystals, we note that there is even some difficulty in identifying the relative magnitudes of the neutral and ionic components of a dimer.[86] Thus care must be taken in speaking about the cofficients $a_\pm$ and $b_\pm$ in (13). The difficulty arises because both the neutral configurations $\{|Dr\rangle \otimes |As\rangle\}$ and the ionic configurations $\{|D^+t\rangle \otimes |A^-u\rangle\}$ are complete, and hence either would suffice for the expansion (18). Once again, the restriction to a finite (incomplete) set of neutral and ionic configurations restores linear independence. The use of neutral and ionic configurations is thus physically motivated and is dependent on the nearness to the isolated-molecule limit. An ionic configuration like $|D^+0\rangle|A^-0\rangle$ is certainly more sensible than the alternative of including many high-energy (continuum) neutral

configurations. No real difficulty arises for only a few configurations, and our discussion will necessarily be restricted to a few molecular states in any case.

2.3. Orthonormal Basis for Dimers

The neutral and ionic configurations in (9) need not be orthogonal in general, but may have an overlap matrix.

$$S = \begin{pmatrix} 1 & S' \\ S' & 1 \end{pmatrix} \tag{19}$$

with $S' = \langle D^+A^-|DA\rangle$. The triplet state $^3|D^+A^-\rangle$ is automatically orthogonal to $|DA\rangle$. The overlap was neglected in the introductory analysis of Section 2.1 and does not create difficulties. Indeed, we show that it is advantageous to *define* the phenomenological states $^1|D^+A^-\rangle$ and $|DA\rangle$ to be orthonormal. Such an approach is natural in our molecular-exciton treatment, which is in large part based on the realization that current *ab initio* quantum-theoretical computations are not nearly accurate enough to deal with the small energy shifts arising from the interactions of molecules containing around 100 electrons.

Since our overlap matrix (19) has only positive eigenvalues, the square root matrix is defined.[95] The new orthonormal dimer basis

$$\{S^{-1/2}|DA\rangle, \qquad S^{-1/2}\,{}^1|D^+A^-\rangle\} \tag{20}$$

could have been defined in the first place in Section 2.1. Contributions to intermolecular interactions which do not depend on a finite intersite differential overlap are not greatly changed on transforming to (20), at least when the molecules are weakly interacting. In fact, the usual estimates of the crystal field, induction, resonance, and dispersion interactions are predicated on vanishing S'. The charge transfer and exchange matrix element depend critically on S' and can be significantly changed on using an orthonormal basis.

The general result[85,96] is that an orthonormal basis tends to increase the kinetic exchange and to decrease the direct exchange J_D. To see this, we observe that orthogonalization will primarily require phase changes in the wave functions in the intermolecular region. Such oscillations in the orthogonal basis give large kinetic-energy derivatives and hence also large CT matrix elements t. Since J_D in (17) may be considered to be the classical self-energy of the exchange

charge distribution between A^- and D^+, orthogonalization leads to a small oscillatory exchange charge distribution with a vanishing net charge and hence to a reduced J_D. These qualitative conclusions have been verified by quantitative examples in very simple systems, and orthogonalization[96] can indeed make an order of magnitude difference in J_D. The importance of kinetic, or CT, exchange in Anderson's theory of superexchange[49] between transition-metal ions can be traced to his use of orthonormal (or Wannier) orbitals.

2.4. Site Representation for Molecular Crystals

It is evident that any molecular solid or metal may be described if all the localized site functions, including those for ionized sites, are known. The strength of the interactions between the sites does not matter, since the basis of localized states is complete. On the other hand, the general crystal Hamiltonian remains as insoluble in such a site representation as it was in the position representation. Molecular exciton theory[15–18] is a familiar site representation in which the weakness of the intermolecular forces between neutral, closed-shell molecules is invoked to allow a low-order perturbation expansion about isolated-molecule states. We will develop a similar restricted description for π-molecular CT crystals in Section 2.5. Since the generality of site representations for molecular solids has not been widely appreciated, we first discuss a general site representation, following Hubbard's analysis[97] of *d*-electrons in transition metals and Klein and Soos's treatment[25] of ionic CT and FR solids.

The basis functions for a molecular crystal are taken to be antisymmetrized products of the form

$$|1r_1, 2r_2, \ldots, Nr_N\rangle \equiv \mathscr{A}|1r_1\rangle \otimes |2r_2\rangle \ldots \otimes |Nr_N\rangle \tag{21}$$

where $|ir_i\rangle$ is a normalized wave function for the (r_i)th state of the ith molecule and $\mathscr{A}$ is the antisymmetrizer for all electrons in the crystal. The molecular states $|ir_i\rangle$ are taken to be *strongly orthogonalized*, with

$$\langle ir_i \otimes jr_j|P|ir_i \otimes jr_j\rangle = 0 \tag{22}$$

if the permutation P interchanges two or more electrons between sites i and j. Strong orthogonality is easily achieved, at least in principle, by constructing the molecular states $|ir_i\rangle$ from the Wannier functions of the solid.[17,25] Any crystal state can be constructed by superposition of functions of the form of (21), including states with different degrees of ionization.

We now define Hubbard's X operators[97] to induce transitions between the molecular states $|ir_i\rangle$. The matrix elements of the desired X operators are[25]

$$\langle 1r_1, 2r_2, \ldots, Nr_N|X_i^{rs}|1s_1, 2s_2, \ldots, Ns_N\rangle = \delta_{r_i r}\,\delta_{s_i s}\prod_{j\neq i}\delta_{r_j s_j} \tag{23}$$

X_i^{rs} changes state s of molecules i to state r, while leaving all other sites unchanged. The full electrostatic crystal Hamiltonian can be expanded in the basis (21) on which the shift operators X_i^{rs} are defined.

The general result is

$$\mathscr{H} = \sum_n h_n + \tfrac{1}{2}{\sum_{mn}}' V_{mn} \tag{24}$$

Here h_n contains all intrasite contributions and is given by

$$h_n = \sum_{rs} \varepsilon_n^{rs} X_n^{rs} \tag{25}$$

where ε_n^{rs} is, in the limit of isolated molecules, just the exact Hamiltonian matrix element between molecular states r and s. If we choose the molecular states to diagonalize ε_n^{rs}, then the ε_n^r are simply interpreted as molecular energies perturbed somewhat by an average crystalline environment.[25] The terms in V_{ij} represent interactions between sites i and j

$$V_{ij} = \sum_{rstu} v_{ij}^{rstu}(-1)^{n_{it}(n_{js}+n_{ju})} X_i^{rt} X_j^{su} \tag{26}$$

with $i \neq j$. The scalars ε_i^{rs} and v_{ij}^{rstu} are simply the one- and two-molecule matrix elements of $\mathscr{H}$ in the molecular configuration (21), while n_{it} in (26) gives the number of electrons in state t of the ith site. The coefficients ε_i^{rs} and v_{ij}^{rstu} may be chosen,[25] as summarized in Section 5.2, to account for crystal field and induction interactions and, in an average way, for other intermolecular interactions as well. Thus we define the canonical crystal-perturbed molecular states, $|nr_n\rangle$, for the nth site to be eigenfunctions of h_n in (25). It is perhaps worth emphasizing that, in a phenomenological treatment, the ε_n^{rs} appear as adjustable parameters and may therefore be defined, along with the associated eigenstates, in the most convenient fashion.

Explicit formulas for ε_n^{rs} and v_{mn}^{rstu} are summarized in Section 5.2. There is some freedom (or ambiguity) in their definition, even if we interpret them physically as crystal-perturbed molecular states. Such states, when close to the unambiguous limit of isolated molecules, may contain different types of intermolecular correlations. Since *all* intramolecular correlations are included, the $|nr_n\rangle$ will generally not

correspond to simple MO states. For completeness, we note that three- and four-site interactions also occur in (24), but that no more than four sites arise for pairwise Coulomb interactions. However, these terms involve only three- or four-center exchange integrals for different molecules and are expected[97] to be negligible in molecular solids, where intersite differential overlap is small. In any case, even (24) will have to be simplified further.

The commutation relations[25] of the X operators follow from their definition in (23):

$$[X_i^{rs}, X_i^{tu}] = \delta_{st} X_i^{ru} - \delta_{ur} X_i^{ts} \tag{27}$$

$$X_i^{rs} X_j^{tu} + (-1)^{(n_{ir}+n_{is})(n_{jt}+n_{ju})} X_j^{tu} X_i^{rs} = 0 \qquad (i \neq j) \tag{28}$$

Although there are techniques for dealing directly with such cumbersome commutation relations, it is almost always more convenient to transform to a second-quantized representation based on either fermion or boson operators. The general crystal Hamiltonian (24) for any molecular solid, whether containing closed- or open-shell sites, becomes quite different once we restrict the crystal states in (21). In the closed-shell systems encountered in molecular-exciton theory, Frenkel excitations lead[98,99] approximately to a boson description or, for a one-dimensional system with a single Frenkel excited state per site, to either[100] bosons or fermions. The restriction to the lowest CT excitation in the π-molecular solids discussed here also leads to a convenient fermion representation[25] of (24). The difference between the molecular-exciton theory of closed-shell systems and the theory of π-molecular CT crystals thus reflects the choice of the low-lying states retained in the general site representation (24). Since it has proved very difficult to extend molecular-exciton theory to include (higher-energy) ionized states[14,101] it will also be cumbersome in the present model to include (higher-energy) Frenkel states. In particular, such additional Frenkel states would lead to a complicated mixed representation.

2.5. Minimum Basis for CT Crystals

Several types of π-molecular crystals were identified in Section 1.3 as showing CT transitions below any Frenkel (molecular) state. The mixed stacks encountered in either neutral CT complexes (. . . DADA . . .) or ionic complexes (. . . $D^+A^-D^+A^-$ . . .) require at least the three states $|A\rangle$, $|A^-\alpha\rangle$, and $|A^-\beta\rangle$ for an A site, and three

states $|D\rangle$, $|D^+\alpha\rangle$, and $|D^+\beta\rangle$ for a D site. Then either the CT excitation (1) or (2) can be described by crystal states (21) in which only three molecular states per site are allowed. The self-complexes encountered in ion-radical stacks require, in addition, the molecular states $|A^{2-}\rangle$ for an A site and $|D^{2+}\rangle$ for a D site, as seen by inspection of the CT processes (3) and (4). These four states per site also suffice for complex FR stacks illustrated in (5) and are mathematically equivalent[25] to the one-electron orbital description used in Hubbard models.[45]

The minimum basis for CT crystals is therefore

$$|nr\rangle = |Ag\rangle, |A^-\alpha\rangle, |A^-\beta\rangle, \quad \text{or} \quad |A^{2-}\alpha\beta\rangle \tag{29}$$

for an acceptor at the crystal site n and

$$|nr\rangle = |D^{2+}g\rangle, |D^+\alpha\rangle, |D^+\beta\rangle, \quad \text{or} \quad |D\alpha\beta\rangle \tag{30}$$

for a donor at site n. The spin degeneracy of the ion-radicals A^- and D^+ is explicitly shown. Equations (29) and (30) represent the *ground states* for molecular species with different numbers of electrons and are conveniently taken to be the exact, orthogonal, crystal-perturbed site eigenfunctions of h_n in (25). The orbital nondegeneracy of the various states has been implicitly assumed. The restriction of the state index r to the four values g, α, β, and $\alpha\beta$ in (29) or (30) sharply limits the flexibility of the basis and excludes all Frenkel excitations. However, these four states per site, which may also be indexed by their charges, are the important ones for CT processes and become exact in the limit of unperturbed isolated-molecule states. In some applications, when electron correlations are large, the states $|A^{2-}\rangle$ and $|D^{2+}\rangle$ can be ignored to yield the simpler basis of the atomic limit.

The molecular states (29) and (30) are *exact* many-electron states and include, by definition, all electron correlations at a given molecular site, including core electrons. The basis (21) for a crystal of N molecules now contains 4^N states and, even in the most idealized application of the dimer discussed in Section 2.1, leads to a secular determinant of dimensions $4^N \times 4^N$. Some reduction is achieved by considering only states with the same number of electrons, but the number of allowed crystal states will nevertheless remain too large for direct computations. We therefore seek a second-quantized representation for the X operators connecting the states (29) and (30) of the minimum basis.

It is convenient to define the "vacuum" state $|ng\rangle$ to be $|A\rangle$ for an acceptor at site n and $|D^{2+}\rangle$ for a donor at n. Now the other states are formally obtained by adding electrons, although the appropriate X operators actually first annihilate a many-electron state and then create another many-electron state with a different number of electrons. The operator $a_{n\sigma}^{+}$ is defined[25] to create a z-component of spin, $\pm\frac{1}{2}\hbar$, by adding an electron at site n, as shown by

$$a_{n\sigma}^{+}|ng\rangle = |n\sigma\rangle \qquad \sigma = \alpha, \beta \tag{31}$$

and $|n\sigma\rangle$ is one of the ion-radical states in (29) or (30). The complete definitions in terms of shift operators are

$$\begin{aligned} a_{n\alpha}^{+} &\equiv X_n^{\alpha,g} + X_n^{\alpha\beta,\beta} \\ a_{n\beta}^{+} &\equiv X_n^{\beta,g} - X_n^{\alpha\beta,\alpha} \end{aligned} \tag{32}$$

where $\alpha\beta$ denotes either $|A^{2-}\rangle$ or $|D\rangle$, depending on whether n is an A or D site. The adjoint operator $a_{n\sigma}$ decreases the total number of electrons by one and changes the z-component of spin at site n by $\mp\frac{1}{2}\hbar$ for $\sigma = \alpha, \beta$. It follows from the commutation relations (27) and (28), after some tedious manipulation, that the site operators $a_{n\sigma}^{+}$ and $a_{n\sigma}$ satisfy fermion anticommutation relations,

$$\begin{aligned} [a_{n\sigma}^{+}, a_{n'\sigma'}^{+}]_{+} &= [a_{n\sigma}, a_{n'\sigma'}]_{+} = 0 \\ [a_{n\sigma}, a_{n'\sigma'}^{+}]_{+} &= \delta_{nn'}\,\delta_{\sigma\sigma'} \end{aligned} \tag{33}$$

These fermion operators connect the various states of the minimum basis (29) and (30) and automatically maintain antisymmetrization. Thus we have

$$|n\alpha\beta\rangle = a_{n\alpha}^{+}a_{n\beta}^{+}|ng\rangle = -a_{n\beta}^{+}a_{n\alpha}^{+}|ng\rangle \tag{34}$$

for the $|A^{2-}\rangle$ or $|D\rangle$ states.

The consequences of applying the operators $a_{n\sigma}^{+}$ or $a_{n\sigma}$ in the minimum basis are most simply seen by considering them to be one-electron operators for the highest occupied MO of D and the lowest unoccupied MO of A, depending on whether n is a D or an A site. This *formal* connection to one-electron creation and annihilation operators, which always satisfy the conventional fermion anticommutation relations (33), permits the borrowing of mathematical results[24,81] for Hubbard models in discussing π-molecular crystals.

2.6. Fermion Representation of $\mathscr{H}$

We expressed in (24) the full crystal electrostatic Hamiltonian in terms of one- and two-site contributions. The one-site operator h_n is given in (25) in terms of the shift operators, while the intermolecular contributions V_{mn} are given in (26). The restriction to the minimum basis (29) and (30) limits the state indices r and s to one of four choices for either D or A sites. The shift operators must, finally, be expressed in terms of the fermion operators $a^+_{n\sigma}$ and $a_{n\sigma}$. The inverse of (32) and of similar relations is thus needed to obtain a fermion representation for $\mathscr{H}$. We find,[25] for instance, that

$$\begin{aligned} X_n^{g,g} &= a_{n\alpha}a^+_{n\alpha}a_{n\beta}a^+_{n\beta} \\ X_n^{\sigma,g} &= a^+_{n\sigma}a_{n\bar{\sigma}}a^+_{n\bar{\sigma}} \\ X_n^{\alpha\beta,g} &= a^+_{n\alpha}a^+_{n\beta} \end{aligned} \tag{35}$$

Such relations may be verified by substituting (32) into the right-hand side of (35) and by using the fact that

$$X_n^{rs}X_n^{tu} = \delta_{st}X_n^{ru} \tag{36}$$

as follows from (27). The crystal Hamiltonian may therefore be systematically expanded in terms of the fermion operators of the minimum basis. The $v_{mn}^{gg,gg}$ contribution in (26) contains octic terms in a operators, as shown by taking $X_n^{g,g}X_m^{g,g}$ in (35). Thus $\mathscr{H}$ remains too cumbersome even after achieving a fermion representation. Instead of writing down the general expression, we examine the coefficients ε_n^{rs} and v_{nm}^{rstu} and seek approximations to the matrix elements that will result in no more than quartic terms in the operators $a^+_{n\sigma}$, $a_{n\sigma}$.

We note that the transformation to conventional fermion operators is done largely to render the expressions more familiar and simple, as is critical in phenomenological treatments. Actually, general methods of solution directly in terms of X operators are available.[102,103] The treatment in terms of X operators may in fact be advantageous for weakly interacting sites, while fermion methods are best in the opposite limit of weak correlations, as in self-consistent field problems.

The site Hamiltonian h_n does not contain products of X operators and is at most quartic in $a^+_{n\sigma}$, $a_{n\sigma}$. The phenomenological treatment of any site with four levels, two of which are degenerate, requires two splitting parameters. We take $\varepsilon_{ng} = 0$ as the zero of energy for $|\mathrm{A}\rangle$

or $|D^{2+}\rangle$ sites, respectively. Then ε_n is the energy of the spin-degenerate ion-radical states $|A^{-}\sigma\rangle$ or $|D^{+}\sigma\rangle$ and $\varepsilon_{n\alpha\beta}$ is the energy of the states $|A^{2-}\rangle$ or $|D\rangle$, with two electrons more than the vacuum state $|ng\rangle$. The ε_n and $\varepsilon_{\alpha\beta}$ may of course be quite different for D and A sites and are not restricted to be positive.

It is convenient to define the parameter U_n by

$$U_n \equiv \varepsilon_{n\alpha\beta} - 2\varepsilon_n \tag{37}$$

U_n represents the intrasite correlation for two spin-paired electrons above the vacuum state $|ng\rangle = |A\rangle$ or $|D^{2+}\rangle$. In Hubbard models with frozen cores, U_n is positive and only involves the repulsion between two electrons on site n

$$U_n^{(0)} \simeq e^2\langle r_{12}^{-1}\rangle \tag{38}$$

where r_{12} is the interelectronic separation. The dimensions of the typical molecules in Figure 2 indicate that $\langle r_{12}^{-1}\rangle \sim (5\text{ Å})^{-1}$, which leads to $U_n^{(0)} \sim 3$ eV. In the present analysis, the interactions with core electrons are also included, and U_n will not be equal to $U_n^{(0)}$. Furthermore, the crystal-perturbed site functions may contain an average polarization contribution, and such polarization has been argued[34,39,104] to reduce $U_n^{(0)}$ significantly. All such renormalizations are included in the phenomenological parameter U_n.

The site Hamiltonian h_n thus reduces to

$$h_n = \varepsilon_n(a_{n\alpha}^{+}a_{n\alpha} + a_{n\beta}^{+}a_{n\beta}) + U_n a_{n\alpha}^{+}a_{n\beta}^{+}a_{n\beta}a_{n\alpha} \tag{39}$$

The two parameters $U_n > 0$ and ε_n are related to the observed structures of specific π-molecular CT crystals. It is evident that crystal symmetry will usually reduce the number of adjustable parameters in (39), for example, by making both ε_n and U_n n-independent in any crystal with one site per unit cell.

2.7. Matrix Elements

The site representation developed in Section 2.4 is quite general, but needs further simplification to reduce the number of phenomenological parameters. The restriction to the minimum basis (29) and (30) in Section 2.5 is based on the experimental observation that π-molecular CT crystals are molecular solids with a lowest CT excitation. Although a fermion representation was achieved in Section 2.6, the resulting Hamiltonian is still complex, principally because the intermolecular coefficients v_{mn}^{rstu} in (26) are complicated

expressions for the $a_{n\sigma}^{+}$, $a_{n\sigma}$ operators. We have thus used the fact that CT crystals show a lowest excitation corresponding to an electron transfer, but have so far not invoked simplifications arising from the one-dimensional nature of π-molecular CT crystals or from the small π-electron overlap even along the stack, as indicated by only a modest shortening of the interplanar separations from the Van der Waals distance of 3.5–3.6 Å. It is then natural to assume, for example, that all intersite differential overlaps between molecules in different stacks vanish. We are fortunate that π-molecular CT crystals, in addition to the common *electronic* feature of a lowest CT band, have the common *structural* feature of stacks of planar molecules or molecular ions. The absence of magnetic ordering in organic ion-radical crystals is an immediate consequence of their one-dimensionality. The simplification of the intermolecular matrix elements of $\mathscr{H}$ can therefore be carried out in general for these crystals.

We consider first the intermolecular Coulomb interactions that provide the stability of ion-radical crystals. These long-range, three-dimensional interactions depend on the charge density at the various molecular sites. The charge operators are simply

$$\begin{aligned} \rho_n &= -\sum_{\sigma} a_{n\sigma}^{+} a_{n\sigma} \qquad (n = \text{A site}) \\ \rho_n &= 2 - \sum_{\sigma} a_{n\sigma}^{+} a_{n\sigma} \qquad (n = \text{D site}) \end{aligned} \tag{40}$$

and reflect the electron filling above the vacuum state $|\mathrm{A}\rangle$ or $|\mathrm{D}^{2+}\rangle$. The π-electron charge densities of the ion-radicals D^{+} or A^{-} are delocalized over the molecules. The point-charge approximation, as used in typical inorganic crystals,[105] must therefore be replaced by[106–108]

$$M(m, n) = \sum_{\mu \in m,\, \nu \in n} \rho_\mu \rho_\nu / |R_{\mu m} - R_{\nu n}| \tag{41}$$

The sum indicated has μ ranging over the charge density ρ_μ of the μth atom of the mth singly charged site and ν ranging over the charge densities ρ_ν of the nth site. Delocalization of π-electron charge densities reduces $|M(n, m)|$ by factors of two or more, but $M(m, n)$ can readily be evaluated.[106] The densities ρ_μ, ρ_ν may be taken from either approximate quantum-molecular computations[109]* or, via the McConnell

* There is a distinction between charge and spin densities in all but the simplest treatments. See Ref. 111 and, for spin densities, Metzger's[109] compilation.

relation, from solution hyperfine data.[110] Variations in different approximations are unimportant in $|M(n, m)|$, and the main point is that a delocalized distribution, however crudely known, should be used.

The crystal Coulomb interaction is then

$$V_C = \tfrac{1}{2}\sum_{mn}{}' |M(m, n)|\rho_n\rho_m \tag{42}$$

Two approximations should be noted in (42). First, the crystal perturbation of the site functions has been neglected, since (41) was computed from data on isolated ion-radicals. Induction forces (see Section 2.1) are neglected, with the relatively high symmetry of ion-radical sites in many crystals providing some justification for an inevitable assumption. Clearly, (41) cannot be evaluated unless the charge distribution is known. The second assumption in (42) is that the charge distribution in ion radicals simply scales with the MO of a singly charged radical. This is probably a good approximation for small deviations from unit charge, but not so good for a $TCNQ^{2-}$ site. Fortunately, the ground states of ion-radical solids are usually close to singly charged or uncharged, with only complex FR salts providing fractional charges like $\frac{1}{2}$ or $\frac{2}{3}$. The scaling approximation in (42) is therefore not expected to be seriously in error. An approximation similar to (41) is also used in largely neutral dimers[87] and converges more rapidly than a standard multipole expansion.

In the limit of nonoverlapping, singly charged sites with $\langle\rho_n\rangle = \pm 1$ in (42), the ground state expectation value of V_C is just the Madelung energy, $MN/2$. Metzger[106,107] has computed M for representative ionic CT and FR crystals. The very small Madelung energy[107] of NMP-TCNQ should be noted. In the more general[108] case of π overlap along the stack, the ground-state expectation value of V_C contains a scaled Madelung energy, as indicated by $\langle\rho_n\rangle\langle\rho_m\rangle$ in (42), as well as additional stabilization from $\langle\rho_n\rho_m\rangle - \langle\rho_n\rangle\langle\rho_m\rangle$. The latter may be important in the delicate balance between a neutral and an ionic lattice.[108] Improvements to the self-consistent, ground-state approximation to V_C are discussed in Section 5.3. Various contributions to the stability of TTF-TCNQ show a number of comparable terms.[111]

The Coulomb interactions (42) are thus simply approximated via $M(n, m)$ and contain only terms up to quartic in the $a^+_{n\sigma}, a_{n\sigma}$ operators, as may be verified by substituting (40) into (42). The treatment of

$M(m, n)$ illustrates how various coefficients in v_{mn}^{rstu} may be identified by looking for the largest multipole contribution. It also emphasizes that the great flexibility of ε_n^{rs} or v_{mn}^{rstu} in expressing various crystal perturbations does not preclude estimating various leading terms by considering either isolated sites or nonoverlapping charge distributions.

The π-electron overlap along the molecular or ion-radical stack leads to one-dimensional electron transport. The Mulliken CT integral (10) is regained in the solid, with all additional molecular states simply providing unit overlap in

$$t = \langle \ldots D^+A^-D^+A^- \ldots | \mathscr{H} | \ldots D^+ADA^- \ldots \rangle \tag{43}$$

Similar CT integrals occur for stacks of A^- or D^+ ion-radicals in simple FR salts. A variety of other CT processes involving electron transfers between sites with either fewer or more than two electrons also occur. They lead to additional modifications of the model and are discussed further in Section 5.3. Here we assume a single CT integral that is independent of the electron occupancy of the two adjacent sites. The transfer terms in v_{mn}^{rstu} then reduce to[25]

$$\mathscr{H}_t = \sum_{n\sigma} t_{n,n+1}(a_{n\sigma}^+ a_{(n+1)\sigma} + a_{(n+1)\sigma}^+ a_{n\sigma}) \tag{44}$$

where $t_{n,n+1}$ is the Mulliken CT integral for adjacent sites n and $n + 1$ in the molecular stack. Equation (44) preserves the restriction to transferring electrons with a fixed spin, which led in Section 2.1 to configuration stabilization of only the $^1|D^+A^-\rangle$ state of the ion-radical dimer. The first approximation for $\mathscr{H}_t$ thus leads to the usual Hubbard-model result in (6), again with the proviso that the site operators (44) connect many-electron states.

We have neglected many additional contributions[25] in v_{mn}^{rstu}: electron transfer between nonadjacent sites or between sites in different stacks; two-electron transfers; the direct exchange J_D in (17), which can be derived in the site representation and is small for the orthonormal crystal basis; induction and dispersion contributions that are contained in an average way in ε_n, U_n, and even in $M(m, n)$ if the molecular charge distributions are perturbed. As more information about π-molecular CT crystals becomes available, their inclusion, as summarized in Section 5, will become necessary. In the present state of refinement, the four crystal parameters afforded by the one-site term h_n, V_C and $\mathscr{H}_t$ are amply sufficient.

2.8. Charge-Transfer Hamiltonian

The leading terms of the crystal electrostatic Hamiltonian in the minimum basis (29) and (30) are

$$\mathscr{H}_{\mathrm{CT}} = \sum_{n\sigma} \varepsilon_n a^+_{n\sigma} a_{n\sigma} + \sum_n U_n a^+_{n\alpha} a^+_{n\beta} a_{n\beta} a_{n\alpha} + \tfrac{1}{2} \sum_{nn'}{}' |M(n, n')| \rho_n \rho_{n'} + \sum_{n\sigma} t_{n,n+1} (a^+_{n\sigma} a_{(n+1)\sigma} + a^+_{(n+1)\sigma} a_{n\sigma}) \tag{45}$$

$\mathscr{H}_{\mathrm{CT}}$ is the sum of the one-site Hamiltonian h_n in (39), the crystal Coulomb interaction V_C in (42), and the transfer term $\mathscr{H}_t$ in (44). The sums indicated in (45) are over all the sites in the crystal, with $\mathscr{H}_t$ restricted to transfers along the molecular stack. $\mathscr{H}_{\mathrm{CT}}$ is the molecular-exciton result for π-molecular CT crystals[25] and is the fundamental equation of the present model.

$\mathscr{H}_{\mathrm{CT}}$ contains at most quartic terms in the site creation and annihilation operators. Thus standard many-fermion techniques[112,113] can be applied to obtain approximate solutions for such modified Hubbard models.[81,22] Since $\mathscr{H}_{\mathrm{CT}}$ commutes with the number operator

$$N_e^{op} = \sum_{n\sigma} a^+_{n\sigma} a_{n\sigma} \tag{46}$$

for a given stack, the number of electrons is conserved not only for the entire crystal, but also within each stack. Solutions of $\mathscr{H}_{\mathrm{CT}}$ are therefore to be found in a particular subspace with N_e electrons above the vacuum states $|\mathrm{D}^{2+}\rangle$ and $|\mathrm{A}\rangle$. In most cases, the stoichiometry will dictate $N_e = \langle N_e^{op} \rangle$. For example, either neutral or ionic 1:1 CT crystals have $N_e = N$, the number of sites in the stack. *Simple* FR crystals based entirely on A^- or on D^+ stacks also have $N_e = N$ and are $\frac{1}{2}$-filled. *Complex* TCNQ salts, with formally neutral TCNQ sites, illustrate less than $\frac{1}{2}$-filled stacks with $N_e < N$, while complex TMPD salts would illustrate more than $\frac{1}{2}$-filled stacks with $N_e > N$. The second-quantized representation of $\mathscr{H}_{\mathrm{CT}}$ is natural for discussing molecular states with different numbers of electrons that occur for CT excitations.[24,25]

We emphasize that $\mathscr{H}_{\mathrm{CT}}$ is very likely the simplest realistic description for π-molecular CT crystals.[24] For example, single-ion (Frenkel) excitations in TCNQ salts usually begin around 1.5 eV, while the CT band is around 1.0 eV. Thus it is by no means guaranteed that such Frenkel excitations are always unimportant. It is certain, on the other hand, that including even a single Frenkel excitation per site

would considerably increase the mathematical complexity of the resulting site representation. Additional improvements in the intermolecular terms v_{mn}^{rstu} or in the crystal parameters ε_n, U_n, $t_{n,n+1}$, and $M(m, n)$ *within* the minimum basis can readily be envisioned, and such refinements will undoubtedly be required as experimental studies expand. The simplest molecular-exciton result for CT crystals, $\mathscr{H}_{CT}$, thus requires four states per site and is consequently somewhat more complicated than typical molecular-exciton theory, where two states (ground and excited) suffice.

Two-state models were in fact first proposed to deal with CT crystals. For example, each site in a ...DADA... stack can be taken as either charged or neutral in an effort to describe the charge distribution in the crystal.[100,114] However, the spin degeneracy associated with either D^+ or A^- sites is then inevitably lost. In the opposite limit of looking at the magnetic properties of ion-radical solids, the spin degeneracy of D^+ or A^- sites leads to a two-state model.[23] Now, however, the CT excitations and conductivity along the stack cannot be described. Two-level models are therefore quite useful for various aspects of π-molecular CT crystals, but cannot provide a general approach, and a four-state model like $\mathscr{H}_{CT}$ is required for these crystals. The conversion to a fermion representation allows us to express $\mathscr{H}_{CT}$ in a simple form that is mathematically equivalent to having only one orbital per site, as in the Hubbard model (6). The demonstration of this equivalence is an important result of the site representation.

3. Classification of π-Molecular CT Crystals

3.1. Structural Variations of Molecular Stacks

The vast majority of organic molecular solids are closed-shell systems with a lowest Frenkel (molecular) excitation. They may be analyzed in terms of molecular-exciton theory and will not be discussed here. We focus instead on molecular crystals with a lowest CT excitation, the vast majority of which have essentially neutral (...DADA...) ground states of closed-shell D and A sites. Only the strongest π donors and acceptors, such as those shown in Figure 2, form ion-radical crystals.

Mulliken and Person[4] review in some detail the various types of donor and acceptor MOs that participate in dimer formation. Such classification of dimers again emphasizes the relative primitiveness,

and the divergence of interests, in the description of solid-state complexes. The detailed character of the relevant MOs is suppressed in our phenomenological result (45) for $\mathscr{H}_{CT}$. It turns out π-molecular complexes involve the highest occupied D orbital and the lowest unoccupied A orbital, as indicated in the minimum basis (29) and (30). However, an infinite DA chain based on π–σ^* overlap would present no difficulties, and any molecular solid with a lowest CT excitation lends itself to a minimum basis site representation.

The central problem in solid-state complexes is to describe various collective properties. A DA dimer provides a two-level configuration interaction picture summarized in Section 2.1. The corresponding problem for a DA crystal is obviously more complicated. The charge distribution γ for a 1:1 CT complex is defined by the ground-state charge density, $\ldots D^{+\gamma}A^{-\gamma}D^{+\gamma}A^{-\gamma}\ldots$, along the molecular stack. Long-range Coulomb interactions must be included and provide the sharp experimental separation[9,23] between π-molecular CT crystals with largely neutral and largely ionic ground states. The magnetic properties of ion-radical crystals also require a collective description, since the antiferromagnetic exchange (7) along the molecular stack is by far the largest term in the spin Hamiltonian. These collective properties, as well as conduction along the stack and the crystal modification of the CT excitation (14), are to be described by $\mathscr{H}_{CT}$.

Detailed crystallographic information[9,10] is, as already emphasized, a basic input to our phenomenological theory of π-molecular CT crystals. We now use structural information to simplify $\mathscr{H}_{CT}$, without invoking additional approximations.

Figure 4 shows a partial classification[24] in which the first division is into complexes with neutral and ionic ground states. *Neutral* complexes are typically diamagnetic semiconductors or insulators that contain a lowest CT absorption polarized along the stack. Many such complexes based on weak donors and acceptors have been studied,[3,8–10] but will not be emphasized here. Kommandeur and co-workers[115,116] showed that the weak paramagnetism in small-gap semiconductors is associated with thermally produced charge carriers D^+ or A^-, since the same activation energy for conduction and for paramagnetism was observed in 1:2 pyrene–iodine and 2:3 perylene–iodine complexes.

The ion-radical complexes in Figure 4 are further divided into crystals containing mixed $(\ldots D^+A^-D^+A^-\ldots)$ stacks and FR crystals based on segregated ion-radical stacks. The former are

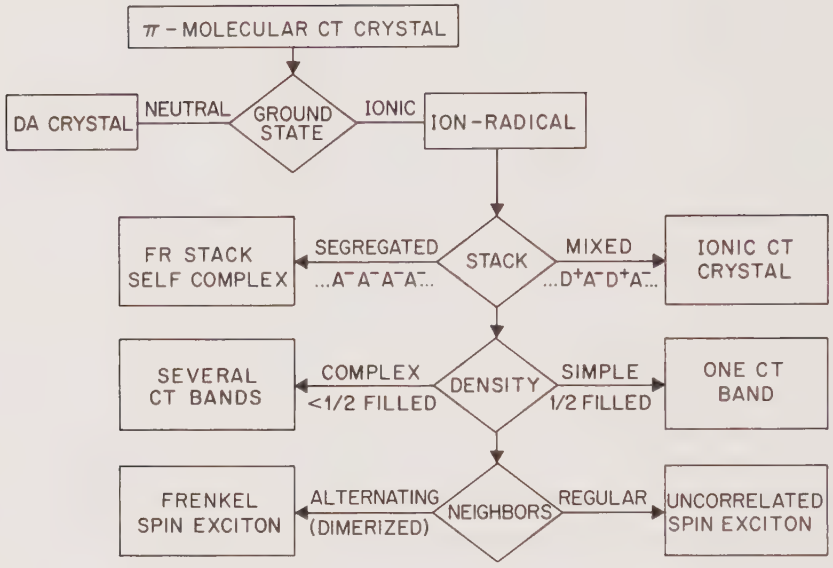

Fig. 4. Schematic classification of π-molecular CT crystals, with emphasis on the structural variations in ion-radical crystals.

illustrated in Section 3.3 and are typically paramagnetic semiconductors. The segregated stacking of either A^- or D^+ ion-radicals in self-complexes is best illustrated by the hundred or more TCNQ salts, but analogous series of FR salts based on D = PD, TMPD, or TTF and on A = chloranil or bromanil are also known.[9,24] FR crystals provide the few known examples of highly conducting, or "metallic," organic systems[26,40,43] that are currently at the focus of intensive solid-state studies, but the majority of FR systems are paramagnetic semiconductors.

The stoichiometry of ion-radical crystals provides another subdivision indicated in Figure 4. Ionic 1 : 1 complexes have one unpaired electron per site, as indicated by D^+ or A^- ion-radicals, and are simple, or $\frac{1}{2}$-filled, with $N_e = N$ electrons for N sites. Crystals with stoichiometries like DA_2, D_2A, or D_2A_3 are complex and have $N_e \neq N$ in (46). Partial fillings, not equal to $\frac{1}{2}$, for $\mathscr{H}_{CT}$ are often more difficult to treat accurately. TCNQ forms complex salts with many metals, and, when several stoichiometries are possible, the complex

salt is not only the better conductor,[34,35] but often shows additional low-energy CT absorptions.[32]

The final classification in Figure 4 is into regular and alternating stacks. In a regular stack, each ion-radical interacts equally strongly with its two neighbors in the stack; in an alternating stack, the interaction with one neighbor is much stronger, and ion-radical dimers (or higher *n*-mers) are produced.[23,117] Triplet spin excitons are characteristic of alternating stacks and were among the first features of ion-radical salts studied.[23,118–122] The regular versus alternating separation is primarily important for elucidating magnetic properties.[66,67]

The structural and stoichiometric possibilities in Figure 4 lead to rather different simplifications of $\mathscr{H}_{CT}$. The various physical properties of FR salts, which show the entire spectrum of simple/complex and regular/alternating, are thus qualitatively explained, as shown below, without detailed solutions to $\mathscr{H}_{CT}$. Other structural features, for example, the effects of crystallographically disordered cations[123,124] or of doping arising from slightly nonstoichiometric[125] complexes are also included[24] naturally into $\mathscr{H}_{CT}$. It is therefore possible to describe either neutral or ionic CT crystals and all the FR crystals by the same general site Hamiltonian (45).

3.2. Collective Physical Properties

There are thousands of neutral π-molecular CT crystals and several hundred with ion-radical ground states. It is unfortunate that only a handful of the many solids that have been studied have been subjected simultaneously to structural, optical, electric, and magnetic investigations. All provide information about CT in solid-state complexes and all are needed to estimate various crystal parameters in a theoretical analysis. The wider experimental range afforded by electric and magnetic studies in ionic complexes thus permits a far more detailed application of $\mathscr{H}_{CT}$ than is possible in neutral complexes. There are many additional results for a few highly conducting solid-state complexes such as NMP-TCNQ, TTF-TCNQ, and TTF halides, as summarized elsewhere.[40,43] The elementary physical properties discussed here represent, by contrast, the *minimum* requirement for correlating structural, optical, electrical, and magnetic properties.

The crystal structure is essential for reducing the parameters in $\mathscr{H}_{CT}$. The lack of structures, together with the occurrence of both

solvent-free and solvent-containing crystal modifications, has hampered static susceptibility studies in neutral FR systems.[24,126,127] Structures based on stacks of planar subunits of aromatics or of transition-metal complexes[71] often show several modifications. Rb-TCNQ,[128,129] NMP-TCNQ,[130,131]* and K-chloranil[132] are all examples and the two modifications may fall into different subclasses in Figure 4. Thus NMP-TCNQ(I) has segregated stacks,[130] while NMP-TCNQ(II) has mixed stacks.[131] Many ion-radical solids also undergo phase transitions,[23,29,133–135] as illustrated by the dimerization[136,137] of the $TMPD^+$ stack in Wurster's blue perchlorate below 186°K. Structural changes may alter the classification, but cannot be described by $\mathscr{H}_{CT}$ without additional terms for lattice vibrations and electron–phonon interactions. Herbstein's[9] compilation of π-molecular structures and the many recent TCNQ structures are therefore invaluable for a theoretical discussion of CT effects.[24]

The fundamental CT processes indicated in (1)–(5) have generally been investigated by diffuse reflectance spectroscopy in ion-radical crystals.[56–63,138] Their intensity is so large that transmission measurements require inconveniently thin, noncrystalline samples. The polarization of the CT band is, as expected, along the ion-radical stack. Only a few temperature-dependent studies have been reported: for TMPD-ClO_4,[63] for the neutral CT crystal NEP,[63] for Rb-TCNQ(I),[135] and for K-chloranil.[139] The intensity, but not position, of the CT absorption depends on temperature. Since $\mathscr{H}_{CT}$ does not describe the higher-energy Frenkel excitations, no discussion of these molecular transitions will be included beyond noting that they are beginning to be assigned.

The conductivity of organic semiconductors has been difficult to interpret, in part on account of the potentially large contribution of even trace impurities in very weakly conducting systems.[14,34,65] Ion-radical CT crystals are typically rather good conductors and include the most highly conducting organic materials. Thus impurity effects should be relatively less important. Studies on quinolinium (Q) $(TCNQ)_2$[140] and NMP-TCNQ[26,39] show that the activation energy for conduction along the stacks, ΔE_c, is reproducible even though the absolute conductivity varies from sample to sample. Both of these crystals have been discussed in terms of the disorder model,[123,124] which in one dimension yields an activation energy for

* A third NMP-TCNQ phase has been reported in Ref. 186 and is based on segregated stacks with two TCNQ per unit cell.

$T^{1/2}$ rather than T. The point here is that reasonably reproducible conductivity results are possible, although several rather different types of theoretical interpretations have been proposed. The single-crystal activation energy ΔE_c along the stack

$$\sigma \| \ = \sigma_0 \exp(-\Delta E_c/kT) \tag{47}$$

will be the characteristic electric property considered. Powder (compaction) data is often similar[14,35,141] but may show sufficient differences, especially when ΔE_c is small, to be distinctly less valuable than single-crystal data. Structural changes will of course change ΔE_c. It is perhaps worth pointing out that Magnus Green Salt,[142,143] a stacked inorganic solid of alternating square-planar $PtCl_4^{2-}$ and $Pt(NH_3)_4^{2+}$, has recently been shown to be an extrinsic (impurity) semiconductor,[144] and that its presumed CT band around 7kK has been reassigned.[145] The conductivities of organic solids are by no means free of artifacts.

The static susceptibility and EPR spectra of ion-radical CT crystals provide information that has not previously been successfully correlated with optical and electric data. Indeed, EPR and CT studies remained largely parallel and unrelated areas, even though it was recognized that CT stabilization was an important contribution to the antiferromagnetic exchange along the stack.[23,67] $\mathscr{H}_{CT}$ provides a relation between the magnetic properties associated with the ground-state spin-degeneracy in Table 1 and the optical and electric properties arising from CT excitations.[24] In many cases, the paramagnetic susceptibility or the EPR intensity satisfies

$$\chi T \sim \exp(-\Delta E_p/kT) \tag{48}$$

and defines an activation energy for paramagnetism, ΔE_p, of the order $t^2/\Delta E_{CT}$ in (8), or (15) for an ion-radical dimer and (16) for a self-complex dimer. ΔE_p, ΔE_c, and ΔE_{CT} thus provide characteristic energies associated, respectively, with magnetic, electric, and optical excitations. Section 4 summarizes very briefly the physical properties of π-molecular crystals with ionic ground states.

3.3. Mixed, Simple Stacks: Neutral or Ionic

1:1 complexes based on mixed stacking of D and A sites, as shown in Figure 1, are the solid-state analogs of DA dimers. The structure and CT bands of neutral complexes are well known.[8–11] Table 2 contains physical properties for several ionic 1:1 complexes.

TABLE 2
Physical Properties[a] of 1:1 Ionic CT Crystals with Mixed Simple Regular Stacks

Crystal structure	ΔE_{CT}	ΔE_c	ΔE_p
$\ldots D^+A^-D^+A^- \ldots$			
TMPD-TCNQ[146]	0.95[61]	0.36[151]	0.068[149] 0.075[150] 0.08[151]
TMPD-chloranil[147]	1.0[60]*b* 1.2[62] <1.2[138]	0.45[152]	0.13–0.15[152]
PD-chloranil[148]*c*	1.4[60]*b* 1.2[62]	0.43[153]*b*	0.13[148]

[a] All energies in electron volts.
[b] Powder data.
[c] Magnetically inequivalent stacks.

TMPD-TCNQ[146] and TMPD-chloranil[147] both crystallize in mixed stacks, as does the less completely characterized cosublimed[148] PD-chloranil (PDC). The small[149–151] ΔE_p in TMPD-TCNQ permits considerable variations in the paramagnetism in contrast to the larger[148,152] ΔE_p of PDC and TMPD-chloranil.* The CT bands of TMPD-TCNQ,[61] of TMPD-chloranil[60,62,138] and of PDC[60,62] are polarized parallel to the stack. Single-crystal conductivity data is available for TMPD-TCNQ[151] and for TMPD-chloranil,[152] but only compaction results[153] for PDC. There are many other potentially ionic complexes between TCNQ and aromatic amines,[151] as well as other chloranil, bromanil, or PD complexes,[9,154] and even mixed stacks of TCNQ and square-planar Pt or Pd complexes.[155] Additional structural information for ionic 1:1 complexes would be desirable.

The mixed stacks for the complexes in Table 2 are crystallographically equivalent. We focus attention on a single stack and treat the long-range Coulomb interactions self-consistently.[22] It is convenient to label the sites in the stack consecutively, with even integers assigned to A and odd integers to D sites. The intrasite Hamiltonian h_n in (39) now contains only two site energies, ε_A and ε_D, and two correlation terms U_D and U_A. If any multiple of N_e^{op} is added to $\mathscr{H}_{CT}$, all the energies for a given N_e are merely shifted. We neglect a shift of $-\frac{1}{2}(\varepsilon_A + \varepsilon_D)$ and represent the variation of the site energies

* The molionic interpretation is incorrect,[9,63] and TMPD-chloranil shows uncorrelated spin excitations.[219]

along the stack by

$$\varepsilon_n = (-1)^n \varepsilon \tag{49}$$

with $\varepsilon > 0$ indicating that the highest occupied MO on a D site (odd n) has lower energy than the lowest unoccupied A site (even n). The intrasite correlation

$$U = \langle \mathrm{D}(1,2)|h_n|\mathrm{D}(1,2)\rangle \tag{50}$$

is appropriate for a D site and, as indicated in (38), is a simple repulsion in the frozen-core approximation. Thus U may be estimated from quantum-molecular computations for either D or A^{2-} sites. No qualitatively new features occur on retaining both U_D and U_A, and (50) will be used for both D and A^{2-} sites.

Electron transfer along the stack is given by $\mathscr{H}_t$ in (44), and a single transfer integral t suffices in most 1:1 complexes, since each D or A site interacts equally strongly with two neighbors in the stack. The overall electric neutrality of the crystal requires equal ground-state charge densities on D and A sites, or $\langle \rho_D \rangle = -\langle \rho_A \rangle$ in (40). Thus the *ground-state* charge distribution is found from the Madelung approximation to the crystal Coulomb energy,

$$\langle V_C \rangle^{(0)} = -\tfrac{1}{2}|M|N\langle \rho_A \rangle^2 \tag{51}$$

for a stack containing $N/2$ sites of both D and A. $\langle V_C \rangle^{(0)}$ suppresses charge fluctuations and may therefore fail for excited state properties. It is the simplest self-consistent expression for describing a solid containing stacks of ionicity $\gamma = -\langle \rho_A \rangle$. The site representation of $\mathscr{H}_{CT}$ reduces, with the aid of (49) and the approximation (51), to the modified Hubbard model[22] for a mixed, simple, regular stack

$$\mathscr{H}_{MSR} = \sum_{n\sigma} \{(-1)^n \varepsilon a^+_{n\sigma} a_{n\sigma} + t(a^+_{n\sigma} a_{(n+1)\sigma} + a^+_{(n+1)\sigma} a_{n\sigma})\} + U \sum_n a^+_{n\alpha} a^+_{n\beta} a_{n\beta} a_{n\alpha} - \tfrac{1}{2}|M|N\langle \rho_A \rangle^2 \tag{52}$$

The solution of $\mathscr{H}_{MSR}$ and of other special cases[81] of $\mathscr{H}_{CT}$ illustrates consequences of the intrasite correlations retained in the U term.

It is instructive to examine the $t = 0$ limit of $\mathscr{H}_{MSR}$, which then reduces to a sharp neutral-ionic transition. The neutral lattice, with $\langle \rho_A \rangle = 0$, has ground-state energy $(-2\varepsilon + U)N/2$, as expected for $N/2$ doubly occupied neutral D sites. The ionic lattice has $\langle \rho_A \rangle = -1$ and energy $-\frac{1}{2}|M|N$ corresponding to singly occupied D^+ and A^- sites. A superionic lattice, with $\langle \rho_A \rangle = -2$ and energy $(-2M +$

$2\varepsilon + U)N/2$, would correspond to a $\ldots D^{2+}A^{2-}D^{2+}A^{2-}\ldots$ stack. The neutral-ionic transition for $t = 0$ thus simply requires

$$2\varepsilon - U \gtrless |M| \tag{53}$$

with $\gtrless$ corresponding to neutral and ionic, respectively. Relation (53) describes the balance between the monopole–monopole (for delocalized π electrons) stabilization of the ionic lattice relative to purely intrasite considerations. In zeroth order, we identify

$$2\varepsilon - U^{(0)} = I_D - A_A \tag{54}$$

where I_D is the ionization potential of D and A_A is the electron affinity of A. Here we have neglected not only exchange and CT forces for both the neutral and ionic lattice, but also the induction and dispersion interactions that are expected to stabilize the ionic lattice preferentially. The case $t = 0$ thus establishes the important result that, other things being equal, the lattice is completely neutral when $I_D - A_A$ is less than M and completely ionic when $I_D - A_A$ is greater than M. The self-consistent solution[22] of $\mathscr{H}_{MSR}$ shows that a sharp neutral-ionic boundary remains even for small finite t, with $\langle \rho_A \rangle$ changing discontinuously from almost zero to almost unity, as shown in Figure 5 for several values of t/ε as a function of U. A small gap against single-particle excitations persists even at the transition.[156]

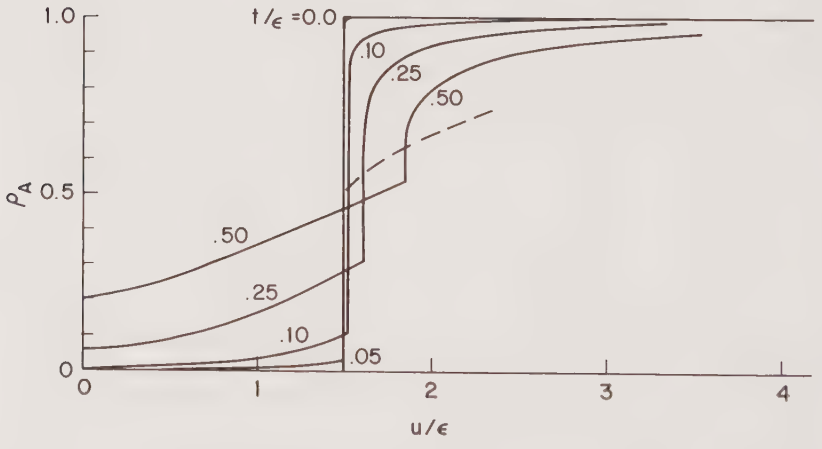

Fig. 5. The ground-state acceptor charge density $\langle \rho_A \rangle$ as a function of U/ε for $M = \frac{1}{2}\varepsilon$ and various t/ε values. The $t = 0$ result is exact. $\langle \rho_A \rangle$ increases discontinuously from its small U value to the dashed line defining the neutral → ionic transition. (Reproduced with permission from Strebel and Soos.[22])

Although CT complexes have been studied as a function of hydrostatic pressure[64,157,158] and are routinely examined as a function of temperature, it has not been possible to identify a truly borderline complex which can be cycled from neutral to ionic and back. There almost certainly are such CT crystals, but they are necessarily rare. After all, both M and $I_D - A_A$ are of the order of volts. Even if other intermolecular contributions are retained, the required crystals would need two energies of the order of volts that are so nearly balanced that changes in kT or in pressure can reverse the order.

The principal features of MSR stacks in Table 2 are readily understood. The CT excitation involves (2), and such excitations are also required for conduction. Spin excitations are at lower energy, since no doubly occupied sites are required.

3.4. Crystals of Dimers and Complex CT Crystals

The regular, mixed stacking of aromatic molecules or molecular ions is the most common structure encountered in π-molecular CT crystals. Prout and Kamenar[10] review the structures of $n - \sigma^*$ complexes, which often form crystals of DA dimers and two-dimensional sheets as well as molecular chains. Here the n donors are amines, nitrogens in heterocycles, or oxygen; the acceptor, usually a halogen, has an available σ^* level. All the complexes are apparently largely neutral, and their structural properties are complicated by twinning, disorder, and instability. We are not aware of physical studies that would warrant a detailed theoretical analysis at this time. The following remarks merely sketch how $\mathscr{H}_{CT}$ would appear for a molecular crystal of $n - \sigma^*$ dimers.

The D and A states of the minimum basis (29) and (30) are now the donor n orbital and the acceptor σ^* orbital, respectively. If only pairwise CT between a given D and A occurs, the crystal reduces to a collection of dimers. This is simulated by taking an *alternating* stack with two transfer integrals, a normal t for a dimer and a $t' \sim 0$ for interactions between dimers. Each DA dimer may be analyzed by the Mulliken method, illustrated in Section 2.1, whose second-quantized representation is

$$\mathscr{H}_{\text{dimer}} = \sum_{n=1}^{2} \sum_{\sigma} (-1)^n \varepsilon a_{n\sigma}^+ a_{n\sigma} + U \sum_{n=1}^{2} a_{n\alpha}^+ a_{n\beta}^+ a_{n\beta} a_{n\alpha} + \sum_{\sigma} t(a_{1\sigma}^+ a_{2\sigma} + a_{2\sigma}^+ a_{1\sigma}) + \langle V_C \rangle^{(0)} \tag{55}$$

This two-electron, six-state problem has ε, t and U defined as given above for the 1:1 stack, with $n = 1$ for D and $n = 2$ for A. The six two-electron states (55) are $|DA\rangle$, $^1|D^+A^-\rangle$, $^3|D^+A^-\rangle$, and $|D^{2+}A^{2-}\rangle$. The triplet does not configuration interact with $|DA\rangle$ and the high-energy state $|D^{2+}A^{2-}\rangle$ is neglected. It is typical that the second-quantized expression (55) for a dimer, with only a few states, is far more cumbersome than the direct position representation, whereas just the opposite is true for infinite systems.

Coulomb interactions couple the dimers to the rest of the crystal. The Madelung approximation (51) is again used and leads to a crystal shift of the ionic state $^1|D^+A^-\rangle$. Differential overlap between dimers is ignored. The ground state of a crystal of equivalent dimers then reduces to a product function of dimer states

$$^1\psi_{DA} = a|DA\rangle + b\,^1|D^+A^-\rangle \tag{56}$$

where the mixing coefficients a and b are identical for all dimers. The crystal-perturbed states $|DA\rangle$ and $^1|D^+A^-\rangle$ could, in principle, be different from isolated-dimer states on account of induction, resonance, and dispersion contributions. The assumption of zero-differential overlap between dimers nevertheless leads to a simple two-level Hamiltonian

$$\mathscr{H}_{\text{dimer}} = \begin{pmatrix} -2\varepsilon + U & t \\ t & -|M|b^2 \end{pmatrix} \tag{57}$$

The diagonal term $-|M|b^2$ represents the approximation (51) for the Madelung stabilization of the ionic form. We note that (57) is now a self-consistent problem, with the expansion coefficient b occurring in $\mathscr{H}_{\text{dimer}}$ also. When $2\varepsilon - U - |M| > 0$, the neutral crystal has lower energy even for complete electron transfer. In this case, we always have $B = E(DA) - E(D^+A^-)$ satisfying

$$B = 2\varepsilon - U - |M|b^2 > 0 \tag{58}$$

and the expansion coefficients for the λ_- ground state in (11) are given by (13). The value of b in (56) is therefore

$$b^2 = t^2\{t^2 + \tfrac{1}{4}[B + (B^2 + 4t^2)^{1/2}]\}^{-1} \tag{59}$$

Since $B > 0$ for any b according to (58), the limit $t \to 0$ leads to $b \to 0$, as in the isolated dimer. On the other hand, B decreases with increasing b and the crystal of dimers shows a greater degree of configuration interaction than the isolated dimer, with $b = 0$ in

$\mathscr{H}_{\text{dimer}}$. Finally, the most interesting case of $2\varepsilon - U - |M| \sim 0$ again leads to sharp neutral-ionic transitions for small t. Equation (59) provides a cubic self-consistency relation in b^2 for the case $B > 0$ and illustrates how the Coulomb stabilization in a crystal is important even in the limit of nonoverlapping DA dimers.

Complex CT crystals, for example with a 1:2 molecular stack of the type ...DAADAADAA..., provide another subclass whose physical properties have yet to be studied in detail. Some crystals are paramagnetic,[151] suggesting an ion-radical ground state. The assumption that all A sites are crystallographically equivalent leads to the choice

$$\varepsilon_n = -\varepsilon \cos \tfrac{2}{3}\pi n \tag{60}$$

for the site energies. The first D site has $n = 0$, the next two A sites have $n = 1, 2$ and have the same site energy, etc. Now two transfer integrals t between DA and AA overlaps are required in $\mathscr{H}_{\text{CT}}$, but otherwise there are no new features. 2:1 complexes of the type D_2A have $\varepsilon < 0$ in (60), and the labeling begins with an A site at $n = 0$.

The site energy ε_n in $\mathscr{H}_{\text{CT}}$ is therefore convenient for distinguishing between D and A sites in any solid-state complex. The zeroth-order approximation of using a single site energy for all D sites and another for all A sites is rigorously valid in many crystals with crystallography equivalent sites. The structure then determines the most important DA overlaps and thus the types of transfer integrals required in the site representation of (45) of $\mathscr{H}_{\text{CT}}$. The $n - \sigma^*$ crystals of dimers reduce to a slight modification of the isolated or solution dimer; the molecular stacks in π–π^* complexes lead to $\mathscr{H}_{\text{MSR}}$ for 1:1 CT crystals; complex CT crystals provide alternating stacks, with $\lessgtr \frac{1}{2}$ filling, in Figure 4; two- or three-dimensional CT crystals, presumably based on nonplanar donors and acceptors, require CT integrals leading to two- and three-dimensional networks.

Our main reason for including briefly these rather less common CT complexes is to emphasize that the crucial approximation leading to the site representation developed in Section 2 is the occurrence of a CT band below all Frenkel states. The topology of the crystalline D and A lattice is of secondary importance. This is somewhat obscured by the preponderance of one-dimensional stacks in the most extensively studied π-molecular complexes. We now consider the additional structural variations indicated in Figure 4 for the self-complexes of π-molecular ion radicals.

3.5. FR Crystals with Simple, Regular Stacks

A regular one-dimensional array of H atoms, or of any other free radical, is potentially a CT system, since no orbital excitation is required for an electron transfer. Neutral organic free radicals[126,127] are often rather bulky, as illustrated by DPPH (diphenyl picryl hydrazyl), PAC (picryl amino carbazyl), and BDPA (bisdiphenylene phenyl allyl). DPPH forms various solvent-free and solvent-containing structures[159] and is neither stacked nor a CT crystal.[160] NEP is a more compact neutral radical shown in Figure 6 whose CT band and paramagnetism point to a CT system,[30,63] although the crystal structure has not been published. The ion-radicals $TMPD^+$, TTF^+, $TCNQ^-$, and chloranil$^-$ based on the strong donors and acceptors in Figure 2 provide a variety of one-dimensional arrays of self-complexes with known structures.

The simplest ion-radical stack, the simple, regular case in Figure 4, occurs[136] in TMPD-ClO_4 above 186°K, in the recently reported[129] second form of Rb-TCNQ, in the α form[132] of K-chloranil, and possibly in NMP-TCNQ if the disorder[130] of the diamagnetic NMP^+ sites is neglected. However, the NMP-TCNQ(I) static susceptibility is inconsistent[161,162] with a simple salt and partial filling leads[24] to a complex $TCNQ^{-\gamma}$ stack. In TMPD-ClO_4 and Rb-TCNQ(II), there is a single type of ion in the stack. Single

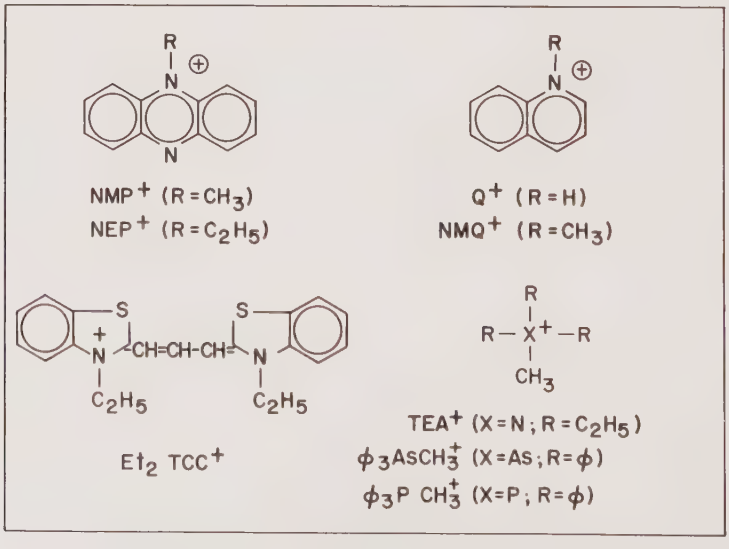

Fig. 6. Diamagnetic organic cations that occur as counterions in TCNQ salts.

TABLE 3
Physical Properties[a] of π-Molecular FR Crystals with Segregated Simple Regular Stacks

Crystal structure	ΔE_{CT}	ΔE_c	ΔE_p
$\cdots D^+D^+D^+D^+\cdots$			
TMPD-ClO_4[136]	1.47[63]	Weak semiconduction[164]	<0.01[167,168]
($T > 186°K$)	1.5[56b]		
TMPD I[166]	1.1[61]	–	0.009[167]
$\cdots A^-A^-A^-A^-\cdots$			
Rb-TCNQ (II)[129]	0.78[135b]	0.16–0.19[135]	–
($T > 230°K$)		0.16–0.22[163]	
K-chloranil[132]	1.5[58]	–	~0.05[29,165]
(α-form)	1.43[139]		($T < 150°K$)

[a] All energies in electron volts.
[b] Powder data.

values of U_n, of ε_n, and of $t_{n,n+1}$ are therefore required. Since both ClO_4^- and Rb^+ or K^+ are expected to occur as diamagnetic ions that help to isolate the FR stacks,[23] there is no doubt that the D^+ stack in TMPD-ClO_4 has one electron per site, as does the A^- stack in Rb-TCNQ(II) or K-chloranil. The site energy in $\mathscr{H}_{CT}$ then reduces exactly to

$$\left\langle \sum_{n\sigma} \varepsilon_n a^+_{n\sigma} a_{n\sigma} \right\rangle = \varepsilon \langle N_e^{op} \rangle = \varepsilon N \tag{61}$$

and is an additive constant that may be neglected without loss of generality. It is then also true that $\langle \rho_n \rangle = \pm 1$ not only in the ground state, but also in the 2^N spin states associated with the ground-state charge distribution of the FR stack. $\mathscr{H}_{CT}$ thus simplifies to

$$\mathscr{H}_{SSR} = \sum_{n\sigma} t(a^+_{n\sigma} a_{(n+1)\sigma} + a^+_{(n+1)\sigma} a_{n\sigma}) + U \sum_n a^+_{n\alpha} a^+_{n\beta} a_{n\beta} a_{n\alpha} \tag{62}$$

for a segregated, simple, regular stack. $\mathscr{H}_{SSR}$ is mathematically equivalent with the one-dimensional Hubbard model (6), although the complete identification holds best for the ground-state charge distribution in view of our treatment (51) of $\langle V_C \rangle^{(0)}$. The magnetic properties are, in favorable cases like $\mathscr{H}_{SSR}$, given by simple models, but electric or optical excitations which redistribute charge involve additional approximations for the long-range Coulomb interactions.

Table 3 contains activation parameters for SSR stacks. The Mott insulator expected for $\mathscr{H}_{SSR}$ when $t \ll U$ is consistent with the large activation energies[135,163] ΔE_c in Rb-TCNQ(II); TMPD-ClO_4 is also a fairly poor semiconductor,[164]* except possibly at the regular-

* For a refutation of the proposed disproportionation, see Refs. 9, 63, and 137.

to-dimer phase transition at 186°K; no ΔE_c value has been reported for K-chloranil, but it is likely to be a poor-to-medium semiconductor and undergoes phase changes,[29,165] accompanied by large hysteresis effects in χ_p, at low temperature. TMPD-I[166,167] and TMPD-Br[167] are probably similar to TMPD-ClO_4.

The highly conducting phase NMP-TCNQ(I) has recently been confirmed[169] to be a partially filled, or complex, system with $\gamma = 0.94 \pm 0.02$ in $NMP^{+\gamma}TCNQ^{-\gamma}$. The field dependence of the NMR second moment, which depends on purely static interactions, is different for NMP-TCNQ and its partly deuterated analog DMP-TCNQ, with a deuterated NMP methyl group in Figure 6. This provides a direct measure at 4.2°K of an unpaired electron density $(1 - \gamma) = 0.06$ on NMP or DMP. The unpaired moments are localized to a few NMP sites and provide another source of disorder, beyond that of the methyl orientation. As anticipated[24] from its physical properties, NMP-TCNQ is thus a complex salt, with $N\gamma$ electrons on N TCNQ sites, and it is listed in Section 3.7 under complex salts. Partial filling and localized NMP moments require reexamination[169,170] of this 1:1 salts that has eluded satisfactory analysis in terms of $\frac{1}{2}$-filled models. The construction of a theoretical model for NMP-TCNQ(I) illustrates[170] the increasingly detailed description possible for specific π-molecular solids for which a wide range of physical properties are available.

Various types of instabilities are associated with one-dimensional metals[171] and magnetic insulators.[172] The absence of π-molecular SSR stacks as $T \to 0$ is suggestive, but it should be emphasized that the driving force for dimerization in specific crystals must first be identified. For example, the measurement[173] of $\Delta H = T\Delta S$ for the TMPD-ClO_4 transition at 186°K immediately rules out[23] a purely spin-dependent interpretation, since the entropy of the spin systems is far too small to account for the observed ΔS. Phase transitions inevitably require a much fuller description of the lattice vibrations than is currently available for molecular crystals and pose difficult problems in any system. In some ways, the theorems about the instability of one-dimensional systems are misleading in that there is no guarantee that *all* relevant contributions are one-dimensional. Indeed, it is expected that the lattice dynamics are three-dimensional. The recent observation[174] of a dimerization in a TTF^+ ion-radical salt below 12°K thus provides the first case in which the degree of dimerization can be related to the parameters of the regular phase.

3.6. Segregated Simple Alternating Stacks

Simple FR salts with dimerized stacks of D^+ or A^- ion-radicals are relatively common, with the entries in Table 4 providing only some of the more extensively studied examples. The self-complexes now have two (or more) π overlaps along the stack, and the transfer Hamiltonian is

$$\mathscr{H}_{\text{alt}} = \sum_{n\sigma} \{t(a^+_{2n\sigma}a_{(2n+1)\sigma} + \text{h.c.}) + t'(a^+_{2n\sigma}a_{(2n-1)\sigma} + \text{h.c.})\} \quad (63)$$

where h.c. denotes the Hermitian conjugate. The limit $t' \longrightarrow 0$ of nonoverlapping dimers now corresponds to self-complex dimers A^-A^- or D^+D^+, rather than the DA dimers in Section 3.4. Thus ion-radicals at sites $2n$, $2n + 1$ interact strongly, while those at sites $2n$, $2n - 1$ have smaller transfer integrals t'. In general, we expect $t' < t$ to imply a larger interplanar separation, although the relative orientation of the molecules is also important. Some approximate computations[175] probe the geometry of $TCNQ^-$ stacking and favor having molecular planes either perpendicular to the stack axis or tilted about 30°, but the rich variety of observed π overlaps cataloged by Herbstein[9] have not been correlated with the magnitude of the CT integral.

TABLE 4
Physical Properties[a] of π-Molecular FR Crystals with Segregated Simple Alternating Stacks (Triplet Exciton Crystals)

Crystal structure	ΔE_{CT}	ΔE_c	ΔE_p
$\ldots(D^+D^+)(D^+D^+)\ldots$			
TMPD-ClO_4[137][c] ($T < 186$°K)	1.44[63]	Weak semiconduction[164]	0.031[121]
$(TMPD)_2Ni(mnt)_2$[177]	–	–	0.24[177]
$\ldots(A^-A^-)(A^-A^-)\ldots$			
Morpholinium-TCNQ[176]	1.2[57][b]	0.32[35]	0.36[118,179]
Rb-TCNQ(I)[128]	1.1[135]	0.44–0.53[163]	0.39[180]
($T \sim 110$°K structure)		($T < 370$°K)	
K-TCNQ[178]	0.96[59]	0.35[35]	~ 0.2[120]
		0.15–0.45[163]	
	1.1[57][b]	($T < 400$°K)	

[a] All energies in electron volts.
[b] Powder data.
[c] Magnetically inequivalent stacks.

In simple dimerized salts like[137] TMPD-ClO_4 below 186°K, Rb-TCNQ(I),[128] or morpholinium-TCNQ,[176] there is again no question about having diamagnetic counterions and ion-radical stacks. If, in addition, the ion-radical sites are crystallographically equivalent, then a single site energy suffices, and the argument in (61) for treating the site energy as an additive constant holds. It is a general feature of simple ($\frac{1}{2}$-filled) FR stacks that the site energy is exactly, or for inequivalent sites very nearly, an additive constant. By contrast, the mixed, simple stacking encountered in Section 3.3 for 1:1 CT crystals is characterized by very different energies for D and A sites.

The approximation (51) for using the self-consistent ground-state expectation value of the long-range Coulomb interaction then leads to

$$\mathscr{H}_{\mathrm{SSA}} = \mathscr{H}_{\mathrm{alt}} + U \sum_{n} a_{n\alpha}^{+} a_{n\beta}^{+} a_{n\beta} a_{n\alpha} \tag{64}$$

$\mathscr{H}_{\mathrm{SSA}}$ is the alternating form of $\mathscr{H}_{\mathrm{SSR}}$ and poses no additional theoretical difficulties, although there are fewer exact results.[81] The magnetic properties are again expected to be given more accurately, since charge fluctuations are neglected in $\langle V_C \rangle^{(0)}$. Any more complicated FR stack is readily described by introducing additional transfer integrals in (63). However, EPR is sensitive only to the distinction between regular and alternating cases.[67] The largest CT integral in an alternating stack defines the ion-radical dimer discussed in Section 2.1. The triplet $^3|A^-A^-\rangle$ or $^3|D^+D^+\rangle$ states at energy ΔE_{ST} in (16) are thermally accessible triplet spin excitons.[23]

Comparison of Tables 3 and 4 for SSR and SSA stacks shows that alternation is primarily reflected by an increased ΔE_p, which for SSA stacks is associated with ΔE_{ST} in (16). No important changes is ΔE_{CT} or ΔE_c are expected in a $\frac{1}{2}$-filled case of $\mathscr{H}_{\mathrm{CT}}$, since optical or charge-carrying excitations require high-energy, doubly occupied sites in both cases. The absence of extensive electron reorganization on forming an alternating stack is consistent with our molecular-exciton hypothesis of weakly overlapping, largely unperturbed molecular sites. The similarity of ΔE_{CT} and ΔE_c data in all three types of simple stacks, including the MSR case in Table 2, is quite remarkable in view of the different ion-radicals involved. The roughly similar ion-radical dimensions in Figure 2 support similar values of the correlation energy U for creating a doubly occupied site.

3.7. Complex, Regular FR Stacks: Fractional Charges

Complex TCNQ salts like $Q(TCNQ)_2$,[181] $TMPD(TCNQ)_2$,[33] and tetraphenylphosphonium (TPP) $(TCNQ)_2$[182] contain crystallographically equivalent, or nearly equivalent, TCNQ sites and help to establish[9] the dimensions of $TCNQ^{-0.5}$. A regular array[181] occurs in $Q(TCNQ)_2$, although the disordered Q^+ ions shown in Figure 6 lead to slightly different site energies. The $TCNQ^{-0.5}$ stack in $TMPD(TCNQ)_2$ is regular,[33] while $TPP(TCNQ)_2$ probably corresponds[182] more closely to stacks of $(TCNQ)_2^-$ dimers. CT in complex salts poses several difficulties. First, the question of the crystallographic equivalence of the ion-radicals often requires very accurate structures. Equivalent sites lead to fractional charges, while very inequivalent sites may be better represented as stacks with both A^- and A sites. The site energy ε_n in these self-complexes is entirely determined by the crystal field. Ditoluenechromium (DTC) $(TCNQ)_2$ contains[183] inequivalent TCNQ sites which probably cannot be assigned to be either fully neutral or ionic from the available data, but the spacing along the stack is apparently regular. Second, complex salts necessarily have several molecules per unit cell along the stack. There can then be a single t or several, perhaps quite different, CT integrals. Tetramers are especially common in 1:2 salts; they require four t integrals in general and three even when two of the molecular overlaps are crystallographically equivalent. Third, the enhanced mobility of the electrons makes the Madelung approximation (51) more tenuous. Complex salts are consequently less well understood than the three types of simple stacks already considered.

The crystals in Table 5 are definitely segregated and complex, but may not all be exactly regular. The operational definition suggested in Figure 4 for choosing between regular and alternating stacks is the observation of fine-structure EPR splittings. The small fine structure[184] of triethylammonium (TEA) $(TCNQ)_2$ thus places this tetrameric 1:2 salt, with almost equal spacings,[185] in the alternating class. Crystals with small variations in site energies or transfer integrals that do not result in triplet exciton behavior are naturally included among complex, regular stacks.

Regular stacking implies a single t in $\mathscr{H}_{CT}$, while equivalent sites lead to a single ε_n and to a single U_n in the FR stack. Thus the site energy is again an additive constant and $\mathscr{H}_{CT}$ reduces to

$$\mathscr{H}_{SCR} = \mathscr{H}_{SSR} + \tfrac{1}{2}\sum_{nn'}{}' |M(n, n')|\rho_n\rho_{n'} \tag{65}$$

TABLE 5

Physical Properties[a] of π-Molecular FR Crystals with Segregated Complex Regular Stacks

Crystal structure[d]	ΔE_{CT}	ΔE_c	ΔE_p
$\ldots A^{-1/2}A^{-1/2}A^{-1/2}A^{-1/2}\ldots$			
$Q(TCNQ)_2$[181][e]	<0.5[32][b]	0.023[140]	0.0[120]
	1.3[32][b]	(80–150°K)	(not activated)
$(Et_2TCC)(TCNQ)_2$[26]	–	0.16[26]	<0.001[193]
$DTC(TCNQ)_2$[183]	–	0.08[194]	–
$TMPD(TCNQ)_2$[182]	–	0.048[195]	0.004[195]
		($T < 100$°K)	($T < 100$°K)
$NMP^{+\gamma}TCNQ^{-\gamma}$[130][e]	0.53[57,196]	0.036[39]	0.0[26,39]
		($T < 150$°K)	(not activated)
$TTF^{+\gamma}TCNQ^{-\gamma}$[188][c]	0.35[196]	0.0031[36]	~0.015[197]
		($T < 10$°K)	~0.011[198]
			($T < 60$°K)

[a] All energies in electron volts.
[b] Powder data.
[c] Magnetically inequivalent stacks.
[d] Could be $\ldots A^{-1}AA^{-1}AA^{-1}A\ldots$ for highly inequivalent sites.
[e] Disordered cations.

for a segregated, complex, regular stack. $\mathscr{H}_{SCR}$ is $\frac{1}{4}$-filled for a 1:2 salt, $\frac{1}{3}$-filled for a 2:3 salt, etc. The solution of Hubbard models for electron filling other than $\frac{1}{2}$ is relatively less well understood.[81] An even greater difficulty centers on the treatment of the long-range Coulomb interactions in (65). A collection of A^- and A sites presents considerable orbital, as well as spin, degeneracy even in the limit of large U, with no doubly occupied A^{2-} site. The corresponding $\frac{1}{2}$-filled case is orbitally nondegenerate. Crystal equivalence may still be invoked to approximate the Coulomb interactions in (65) by their ground-state expectation value (51). However, now charge and spin excitations are expected to be of comparable energies, and the data in Table 5 generally support this view. It should be recalled that the idealized nature of Hubbard models in solid-state physics is associated with the potential inadequacy of applying the Madelung approximation to long-range Coulomb interactions. By contrast, the intrasite correlation U in $\mathscr{H}_{CT}$ arose from molecular considerations.

The partly filled $TCNQ^{-\gamma}$ stack for NMP-TCNQ(I) fits naturally with the systems in Table 5. The disorder[130] of the NMP^+ cations has been challenged by Kobayashi,[186] who reports an ordered segregated phase that may correspond to a *third* phase, NMP-TCNQ(III), for this 1:1 system. The NMR determination[169] of $\gamma = 0.94$ was verified[187] to be for NMP-TCNQ(I), as are the bulk

of the measurements on this organic conductor.[170] Localized NMP radicals provide an additional source of disorder in the cations.

TTF-TCNQ also forms[188] segregated, regular stacks, but now there are *two* ion-radical systems, one based on $TTF^{+\gamma}$, the other on $TCNQ^{-\gamma}$. The stacking is thus quite different from the mixed structure of TMPD-TCNQ, which also contains a strong donor that, like TTF,[43,189] forms an extensive series of ion-radical salts.[9] ESCA,[190] photoemission,[191] and X-ray[192] studies suggest that there is less than unit charge per site on either chain. Two complex FR stacks, $\ldots D^{+\gamma}D^{+\gamma}D^{+\gamma}D^{+\gamma}\ldots$ and $\ldots A^{-\gamma}A^{-\gamma}A^{-\gamma}A^{-\gamma}\ldots$, with $0.5 < \gamma < 1.0$, probably occur in TTF-TCNQ. NMP-TCNQ(I) and TTF-TCNQ are rare CT complexes in which chemical information about the stoichiometry does not suffice for the electron filling N_e of $\mathscr{H}_{CT}$. By contrast, the mixed 1:1 CT crystals, whether neutral or ionic, encountered in Section 3.3 are $\frac{1}{2}$-filled, and the degree of ionicity γ follows from the solution of $\mathscr{H}_{MSR}$ in (52). NMP-TCNQ(I) and TTF-TCNQ also differ from complex FR salts in that γ is not a simple fraction. Both the TTF and the TCNQ systems thus potentially represent arbitrary electron filling and therefore require whole classes of solutions to $\mathscr{H}_{CT}$, even if the previously noted difficulties with long-range Coulomb interactions in complex salts are overcome.

3.8. Complex, Segregated, Alternating FR Stacks

Complex ion-radical salts based on linear arrays of dimers, trimers, or tetramers provide all the complications of $\mathscr{H}_{SCR}$ and, in addition, have several CT integrals. The simplest electron-transfer term, with only two types of π overlaps and two CT integrals, is $\mathscr{H}_{alt}$ in (63). Many of the examples in Table 6 are based on tetramers and thus contain additional transfer integrals. Such systems as $(\phi_3AsCH_3)(TCNQ)_2$, $(\phi_3PCH_3)(TCNQ)_2$, and $Cs_2(TCNQ)_3$ were nevertheless among the first triplet spin–exciton systems studied,[23,118 122] since the pairwise correlations of the spins led to unmistakable and strongly temperature-dependent fine structure summarized in Section 4.4. $TEA(TCNQ)_2$ also belongs[184] in this class. This extensively studied[199] salt is, as pointed out by Farges,* the best conductor among the semiconducting salts. The ion-radical dimer introduced in Section 2.1 almost suffices for the EPR of alternating FR stacks. The only additional feature, that the triplet excitons

* See Ref. 200 for a summary of extensive work on $TEA(TCNQ)_2$ in terms of modified Hubbard models.

TABLE 6
Physical Properties[a] of π-Molecular FR Crystals with Segregated Complex Alternating Stacks (Triplet Exciton Crystals)

Crystal structure	ΔE_{CT}	ΔE_c	ΔE_p
$\ldots A^- A^- A A^- A^- A \ldots$			
$Cs_2\,TCNQ_3$[31][c]	0.5–0.7[32][b] 1.4[32][b]	0.30[35]	0.16[119]
	1.38[59]	0.32–0.35[163]	0.14[120]
$(Morpholinium)_2(TCNQ)_3$[200]	0.5–0.7[32][b] 1.4[32][b]	–	0.31[179]
$\ldots (A_2^- A_2^-)_n \ldots$			
$(\phi_3 XCH_3)(TCNQ)_2$[185][d]	<0.5[32][b]	0.30[35]	0.065[118]
X = P, As	1.3[32][b]	0.39[134]	
$TEA(TCNQ)_2$[185]	<0.5[32][b]	0.16[35]	0.041[120]
	1.3[32][b]	0.13[163]	0.034[118]
		0.12[200]	

[a] All energies in electron volts.
[b] Powder data.
[c] Magnetically inequivalent stacks.
[d] X = P undergoes a phase transition at 315°K, to a known structure[203]; mixed crystal studies[120,134,204] are available.

are mobile, is required primarily to average out any hyperfine structure. The alternating Heisenberg antiferromagnet

$$\mathcal{H}_{spin} = J \sum_n \{(1 + \delta)\mathbf{S}_{2n} \cdot \mathbf{S}_{2n+1} + (1 - \delta)\mathbf{S}_{2n} \cdot \mathbf{S}_{2n-1}\} \qquad (66)$$

for $\delta \approx 1$ (strong alternation) gives a surprisingly complete description of the magnetic properties.[23,67] The spin operators $\mathbf{S}_n$ are assigned to the nth spin. The EPR requires strongly correlated spins, but not a precise assignment of electrons to one or two sites.

$Cs_2(TCNQ)_3$ provides the best illustration of charge localization arising from inequivalent TCNQ sites.[9,31] The two noncentric sites in Figure 7 have bond lengths corresponding to $TCNQ^-$, while the centric site in the unit cell is close to TCNQ. The site energies are therefore of the form of (60), with $\varepsilon < 0$, and $n = 0, 3, 6, \ldots, 3n$ corresponding to the centric (large neutral) site. Soos and Klein[201] have applied the modified Hubbard model to such a $\frac{1}{3}$-filled stack, with the further approximations of a single transfer integral and ground-state Coulomb interactions. As expected, largely neutral and ionic sites emerge if the site energy difference, ε in (60), is comparable to or larger than the CT integral t. A spin Hamiltonian of the form of (66) then follows for the localized charges. The modified Hubbard model has also been applied[200] to the tetrameric stack in $TEA(TCNQ)_2$.

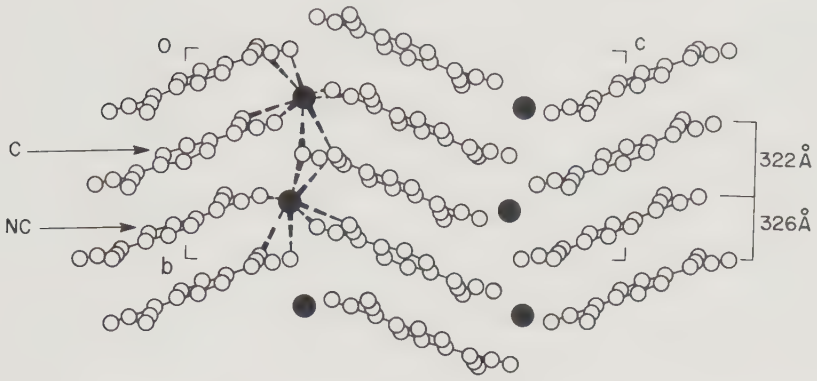

Fig. 7. The [100] projection of the $Cs_2(TCNQ)_3$ structure. The noncentric TCNQ sites are largely ionic, while the centric sites are largely neutral. The occurrence of magnetically inequivalent TCNQ stacks is clearly shown. (Reproduced with permission from Fritchie and Arthur.[31])

Complex FR salts, whether regular or alternating, provide too many parameters in $\mathscr{H}_{CT}$, require additional work on long-range (three-dimensional) interactions, and even then lead to mathematically less tractable Hubbard models. The orbital degeneracy afforded by formally neutral sites in the lattice should clearly enhance conduction, since carriers no longer require forming doubly occupied sites of energy $\sim U$. The greater conductivity of the complex stoichiometry of TCNQ systems that form both simple and complex salts was observed by Bierstedt, Siemons, and Kepler[35] and discussed further by LeBlanc.[34] Formally neutral sites should also permit additional low-energy CT bands, as indicated in (5), and Iida[32] has so assigned the powder reflectance spectra of many complex TCNQ salts. Thus the qualitatively different CT and electric properties of complex TCNQ salts are easily rationalized by $\mathscr{H}_{CT}$. Indeed, the realization that the collective properties of many types of π-molecular CT crystals point to a strongly correlated model[22,24] was a major incentive for developing a site representation.[25]

4. Electronic Properties of Ion-Radical Crystals

4.1. Excitations of the CT Hamiltonian

The general result (45) for $\mathscr{H}_{CT}$ was obtained for any π-molecular solid based on weakly perturbed sites in which a CT excitation occurs below any Frenkel state. The classification in Section 3 of various CT

and FR crystals is based on the crystal structure and on the stoichiometry. The former determines such parameters as the site energy ε_n or the types of transfer integrals $t_{n,n+1}$ along the stack. The latter specifies the number of electrons N_e in (46) in each stack. By identifying CT excitations with strong on-site correlations U, we found that different stacking patterns and stoichiometries lead to different optical, electric, and magnetic excitations in ion-radical crystals. Tables 2–6 summarize these qualitative features of the site representation.

The resulting Hubbard models for particular types of stacking are amenable to solutions, sometimes exact and sometimes rather approximate, as summarized in Section 5.5. In the limit $U \gg t$, the $\frac{1}{2}$-filled Hubbard model (6) reduces to the Heisenberg Hamiltonian (7) for a regular chain or to (66) for dimerized chains. These spin Hamiltonians have also been extensively analyzed,[67-69,81] and π-molecular crystals are simply a special case in which antiferromagnetic exchange along the stack is dominated by $t^2/\Delta E_{CT}$.

As pointed out in Section 5, the mathematical solution of various models and the quantum-mechanical evaluation of the model parameters are two quite separate problems. In the present phenomenological approach, the model parameters U, t, or ϵ are adjustable constants, and any renormalization due to improved treatments of the crystal or of either molecular or lattice vibrations is largely included.[25] Even so, it remains to be seen whether a Hamiltonian like $\mathscr{H}_{CT}$ can provide a satisfactory quantitative picture of the optical, electric, and magnetic properties of particular ion-radical crystals. The highly conducting TCNQ salts are naturally at the focus of such modeling,[40,170] since they have the most varied excitations. Neutral DA complexes[8] are, with rare exceptions noted in Section 3.1, diamagnetic solids with large activation energies for semiconduction. Open-shelled ion-radical crystals, on the other hand, show magnetic and electric excitations in addition to CT bands and are natural candidates for testing $\mathscr{H}_{CT}$. As summarized in Section 3, the vast majority of organic ion-radical solids are paramagnetic semiconductors.

We sketch here some of the physical properties of semiconducting ion-radical systems. Any satisfactory model for any ion-radical stack must certainly account for at least the optical, electric, and magnetic excitations listed in Tables 2–6. In addition, π-molecular crystals show many interesting effects peculiar to one or a few systems. Such considerations must be included in detailed analyses of particular

systems like $TEA(TCNQ)_2$,[200] or KCP,[40] or TTF-TCNQ,[43,80] or NMP-TCNQ(I).[170] No detailed modeling is attempted here. We consider instead some general features and limitations of $\mathscr{H}_{CT}$ as applied to semiconducting ion-radical solids.

It is evident that $\mathscr{H}_{CT}$ is restricted to the *ground-state* electronic configurations for D or A sites indicated in (29) and (30). The neglect of all Frenkel excitations clearly rules out any consideration of the single-molecule excitations starting around 1.5 eV for $TCNQ^-$ or $TMPD^+$. Such molecular excited states, whether in open- or closed-shell systems, present problems in molecular quantum mechanics. The highest-energy excitations of $\mathscr{H}_{CT}$ are thus the various CT processes (2)–(4) for creating a doubly occupied site. CT bands have a characteristic energy of 1 eV and are polarized along the molecular stack.

Electric conduction also depends on doubly occupied sites in simple salts, where $N_e = N$, and these consequently tend to be semiconductors with large energy gaps ΔE_c. Complex salts, as summarized in Tables 5 and 6, have lower ΔE_c. Electron transport in complex salts involves differences in site energies. Thus ΔE_c values range from 0.5 eV in simple salts to perhaps ~ 0.2 eV in complex salts and vanish in the good conductors.

The characteristic energy for magnetic excitations for $\mathscr{H}_{CT}$ is $J \sim t^2/U$ and is in the range of 0.0–0.3 eV. Now thermal population of excited states can easily be realized. The strong temperature dependence of the paramagnetism in fact provides a convenient method for obtaining information about exchange interactions.[23,67] These low-energy excitations of $\mathscr{H}_{CT}$ are collective crystal states and are very different from the magnetic properties of isolated ions.

Nuclear or molecular motions have been neglected in $\mathscr{H}_{CT}$. Thus we do not consider the many phase transitions of ion-radical systems.[23,29,40,133,203] On the other hand, the usual theoretical approach[205–210] for coupling to vibrations can readily be used in $\mathscr{H}_{CT}$ or any of the resulting modified Hubbard and Heisenberg exchange Hamiltonians. Any parameter like J or t or ϵ_n can be Taylor expanded about its equilibrium position. The linear term leads to displaced oscillators and can be treated by means of a canonical transformation.[205] Higher-order terms are neglected as a matter of convenience. Such terms are important, however, in radiationless transitions[211] in organic solids; their neglect for the lower-energy excitations of ion-radical crystals is consequently an approximation whose validity remains to be demonstrated.

4.2. Optical Properties: CT Bands

Figure 8 shows[61] the polarized absorption spectrum of single-crystal TMPD-TCNQ, whose structure[146] is based on a mixed $\ldots D^+A^-D^+A^- \ldots$ stack along the c axis. The molecular planes of $TMPD^+$ and $TCNQ^-$ are tilted somewhat relative to the stack axis. The bands II, III, IV, and V for light polarized perpendicular to the stack axis thus correspond to $\pi \rightarrow \pi^*$ molecular (Frenkel) excitations whose transition moments are in the molecular plane. Band I, on the other hand, is polarized along the stack and is consequently associated with the CT excitation (2). The CT excitation energy of 0.95 eV is obtained[61] from powder absorption in liquid paraffin mulls down to about 0.5 eV. The CT peak is very intense, rather broad ($\sim$0.5 eV), and in an inconvenient infrared region (0.5–1.0 eV) of the spectrum.

These general features are also found for the CT band of neutral DA complexes,[3,8,212] for the simple, regular $\ldots D^+D^+D^+ \ldots$ system TMPD-ClO_4,[63] and for simple TCNQ salts.[57] Until vibronic analysis of CT excitations is refined, it is evident that such broad peaks provide little additional information. The observed bandwidth is a very crude estimate for $4t$. Such estimates yield $t \sim 0.1$–0.3 eV, in agreement with equally crude computations or analysis for DA dimers.[4,50,213]

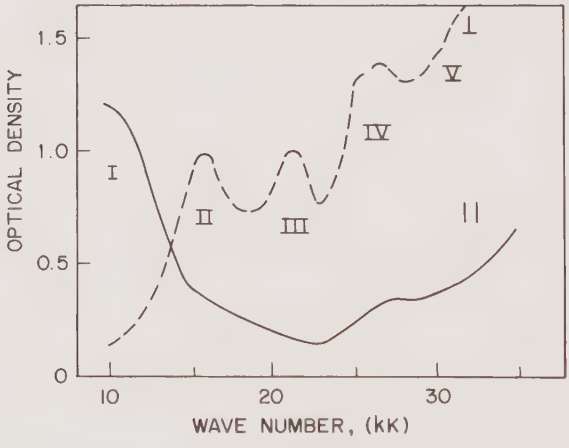

Fig. 8. Absorption spectra of a single crystal of TMPD-TCNQ for light polarized parallel and perpendicular to the stack axis c. (Reproduced with permission from Kuroda, Hiroma, and Akamatu.[61])

Additional CT absorptions characterize[32] complex TCNQ salts and are shown in Figure 9 for a whole series of complexes.[196] The low-energy peak A in $Cs_2(TCNQ)_3$, $TEA(TCNQ)_2$, or acridinium $(Ad)(TCNQ)_2$ is associated with intraband transitions such as (5) in which no doubly occupied A^{2-} site is created. No such absorption is possible in the simple salt K-TCNQ, whose polarized absorption spectrum consequently has a single, high-energy (~ 1 eV) CT band. Figure 9 suggests strongly that TTF-TCNQ is complex, with $\gamma < 1$ as discussed in Section 3.7. The TSeF complex[41] has Se instead of S in the TTF molecule (Figure 1) and also behaves like a

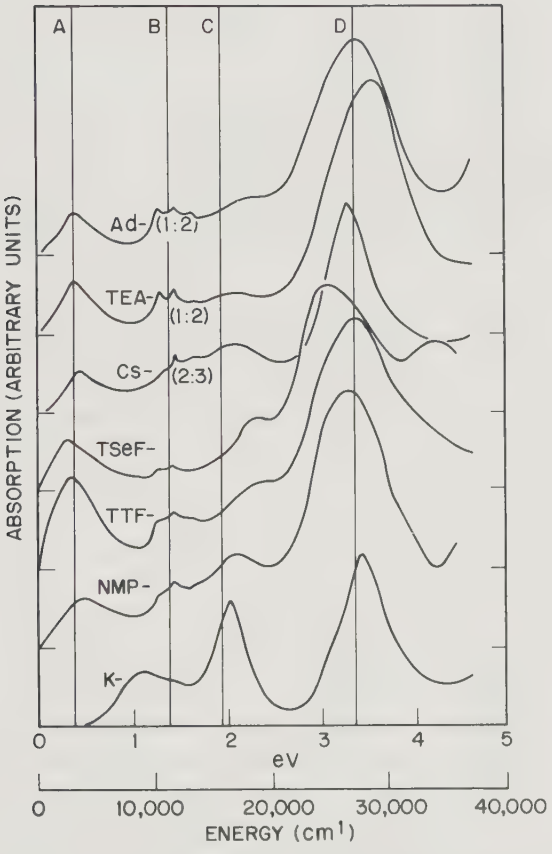

Fig. 9. Comparison of the absorption spectra for the simple salt K-TCNQ, the complex salts $TEA(TCNQ)_2$, $Cs_2(TCNQ)_3$, and $Ad(TCNQ)_2$, and the organic conductors NMP-TCNQ, TTF-TCNQ, and TSeF-TCNQ. (Reproduced with permission from Torrance, Scott, and Kaufman.[196])

complex salt. The polarization[214] of peak B in NMP-TCNQ is more in the molecular plane than along the stack axis and the CT excitation (3) in the almost $\frac{1}{2}$-filled system is more likely to be associated[170] with peak A, at 0.53 eV. No quantitative treatments of the absorption intensities or line shapes are currently available.

Polarized single-crystal reflectivity measurements have become important in two rather different contexts. First, the very intense CT bands in mixed ionic stacks require inconveniently thin crystals and suggest reflectance measurements.[56–63,138,199] Second, reflectivity studies on metals provide information about the complex dielectric constant $\epsilon(\omega)$ and have been applied to organic and inorganic conductors as well.[26,40] The interpretation of reflectance spectra needs considerable additional work. There is coupling[199] of charge excitations to intramolecular (e.g., CN) vibrations in the infrared region. Infrared studies[20] of molecular vibrations were among the first methods used to identify ion-radicals in π-molecular crystals. The assignment of the very rich infrared spectrum has not been possible, although the apparent breakdown of molecular selection rules in TCNQ salts is further evidence for electron motion along the stack.[215]

Both electronic absorptions in the visible and vibrational absorptions in the infrared involve molecular states whose analyses must proceed through highly nontrivial applications of molecular-exciton theory. The CT bands shown in Figures 8 and 9 reflect electron transfer along the chain and are the novel electronic excitation described by $\mathscr{H}_{CT}$.

4.3. Electric Conduction

Early work[34,35] on the single-crystal d.c. conductivity of several simple and complex TCNQ salts showed that conduction along the molecular stack was two to three orders of magnitude larger than perpendicular to the stack. The activation energy ΔE_c for semiconduction was, however, the same for parallel and perpendicular measurements. In simple salts, a CT excitation produces adjacent A^{2-} and A sites. These become carriers, formally electrons and holes, if they cease to be adjacent. Either a mobile A^{2-} state or a mobile A state can readily be envisioned in an ion-radical stack. The activation energies ΔE_c for simple salts in Tables 2, 3, and 4 are relatively large, on the order of 0.2–0.6 eV. For noninteracting electrons and holes, we expect $\Delta E_c = \frac{1}{2}\Delta E_{CT}$, since two carriers are produced in a

single CT excitation. Separating the adjacent A^{2-} and A sites requires energy of the order of e^2/R, however, while each of the separate carriers can be stabilized by lattice and/or electronic polarization. These two potentially large effects tend to cancel. Nevertheless, both will have to be included in any satisfactory computation for ΔE_c.

Complex TCNQ salts are summarized in Tables 5 and 6 and are generally more conductive,[26,35,163] as expected when charge motion along the stack does not require doubly occupied sites. When all the sites are equivalent, less than $\frac{1}{2}$-filled cases of $\mathscr{H}_{CT}$ have vanishing ΔE_c and are formally metallic. Highly conducting organic solids illustrate such partial filling,[43,169] with less than an electron per site in $TCNQ^{-\gamma}$ stacks. The temperature dependence[200] of the d.c. conductivity of $TEA(TCNQ)_2$ is shown in Figure 10 and again illustrates the essentially isotropic activation energy of $\Delta E_c \sim 0.12$ eV along three crystal axes. Deviations toward higher conduction at higher temperature are observed, especially along the chain axis. They are tentatively assigned[200] to a temperature dependence in the mobility. The high degree of anisotropy indicated by the conductivity along and perpendicular to the stack in Figure 10 is naturally associated with the anisotropy in the CT integral t along various

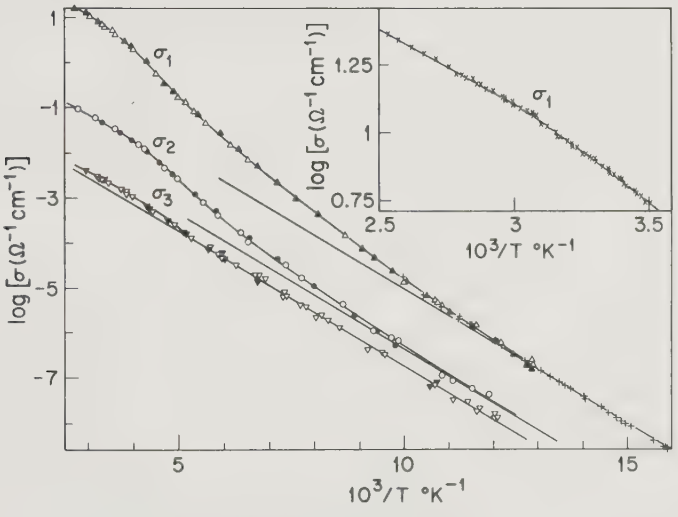

Fig. 10. Electric conduction along the three crystal axes for several different crystals of $TEA(TCNQ)_2$ as a function of temperature. The solid lines correspond to $\Delta E_c = 0.12$ eV in (47), with different σ_0 along each axis. (Reproduced with permission from J. P. Farges.[200])

axes. Such large anisotropy in t, on the other hand, can affect the mobility differently along different crystal axes.

Recent conductivity studies[135,163] on semiconducting TCNQ salts provide further evidence for the complicated nature of ΔE_c. Wider temperature ranges reveal that $\Delta E_c(T)$ depends on temperature. A series of relatively constant ΔE_c in smaller intervals may be evidence for several minor structural transitions or may be associated with different regimes for electron hopping. There is also always the possibility that impurities contribute to ΔE_c and that crystal perfection is the limiting effect for the small transverse currents. Hence any anisotropy is probably a lower bound, while observed ΔE_c values are more likely to be upper bounds.

The growing solid-state interest in highly conductive organic solids has led to alternatives to d.c. measurements.[26,40] Early thermopower or Hall-effect studies were hampered by experimental difficulties, but improvements in crystal quality and experimental procedures should permit increasingly more sophisticated measurements. Reproducible data and improved theoretical treatments should provide a more detailed picture of electric properties. Microwave conductivity[26,40,43] is another relatively new method that avoids some of the traditional difficulties with contacts. The rather complicated dielectric properties[26,40,43,200] of conducting ion-radical solids can also be studied using reflectivity. While electric conduction is likely to remain challenging both experimentally and theoretically, considerable progress can be anticipated for at least those subclasses of π-molecular systems which, like the good conductors, are intensively examined by a variety of techniques.

4.4. Magnetic Properties: Antiferromagnetic Exchange

The antiferromagnetic exchange $J \sim t^2/\Delta E_{CT}$ along the ion-radical stack is small on the scale of electronic energies, but enormous on the scale of magnetic interactions. One-dimensional antiferromagnetic exchange in ion-radical stacks leads to a number of different regimes,[67] depending on whether the stack is regular or alternating. As seen in (66), $\mathscr{H}_{spin}(\delta)$ has equally strong interactions between sites n and $n \pm 1$ in a regular ($\delta = 0$) stack and stronger interactions with one neighbor when $\delta > 0$. In the limit $\delta \to 1$, the chain becomes an array of noninteracting dimers. Then the thermal equilibrium number of dimers in the excited triplet state at energy $2J$ above the ground

state is

$$\rho(T) = \{1 + (\exp 2J/kT)/3\}^{-1} \tag{67}$$

A reasonable thermal population is possible for $2J \sim 0.1$ eV, a typical number. Equation (67) accounts qualitatively for the activated susceptibility (48) generally observed in alternating stacks. Static susceptibilities corresponding to regular ($\delta = 0$) stacks are realized in several inorganic chains.

The fact that the excited state of a dimer is a triplet ($S = 1$) state explains the fine-structure EPR splittings.[23,118] The spin Hamiltonian for a triplet state is

$$\mathcal{H}_T = \beta \mathbf{S} \cdot g \cdot \mathbf{B}_0 + \mathbf{S} \cdot D \cdot \mathbf{S} \tag{68}$$

where $\mathbf{B}_0$ is the applied static field and D is the dipole–dipole interaction of the two electrons. In high field $\mathbf{B} \gg D$, a splitting whose angular dependence goes as $D(3\cos^2\theta - 1)$ is observed in an axially symmetric system and establishes the triplet nature of the excitation. The temperature dependence[118] of the fine-structure splitting of the closely related salts $(\phi_3PCH_3)(TCNQ)_2$ and $(\phi_3AsCH_3)(TCNQ)_2$ is shown in Figure 11. At the lowest temperature, (67) leads to a few percent of triplets for $2J \simeq \Delta E_p = 0.065$ eV. The absence of hyperfine structure in the narrow EPR line is decisive evidence for rapid triplet motion.

The components D and E of the fine-structure tensor can be computed[23,216] from the known separation of the ion-radicals in the solid and the single-ion spin densities ρ_μ introduced in (41) for Madelung calculations. The success of such computations is summarized in Table 7. As crystal structures and molecular computations are further refined, fine-structure splittings will provide an increasingly sensitive method for testing the electron distribution in the crystal. For example, the recently reported[217] structure of a tetrameric $(TCNQ)_4^{-2}$ salt was postulated to contain A^- and A sites. However, the D and E values of 200 MHz and 30 MHz, respectively, point[218] to a dimer of $(TCNQ)_2^{-1}$ with $TCNQ^{-0.5}$ sites. Such values are indicated for 1 : 2 salts in Table 7 and are further supported by explicit computations[218] based on the crystal structure.

Exciton collisions become more frequent at higher temperature, since $\rho(T)$ in (67) increases. The effective exchange[66] between excitons goes as $\rho(T)J(1 - \delta)/4$ and, as shown in Figure 11, eventually averages out the fine-structure splittings. These many-spin problems have been reasonably well documented,[23] but will undoubtedly require further

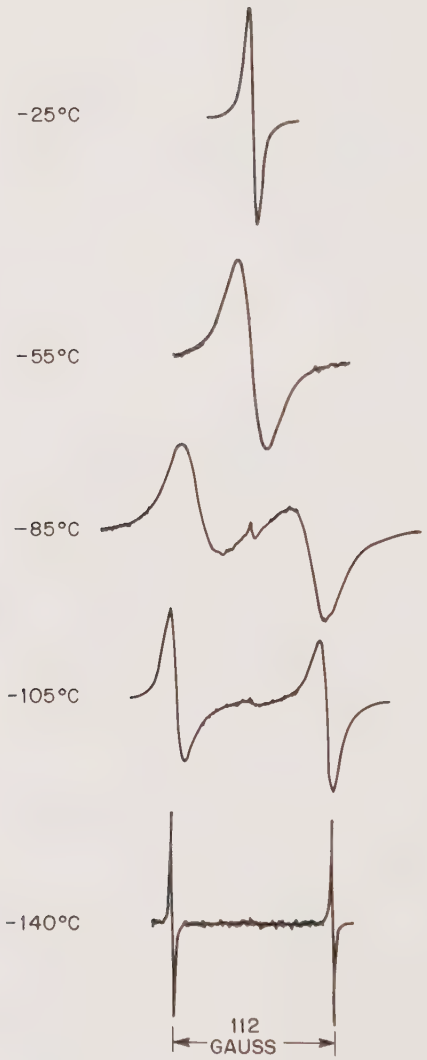

Fig. 11. Temperature dependence of Frenkel (triplet) spin–exciton EPR in a single crystal of $(\phi_3PCH_3)(TCNQ)_2$ or $(\phi_3AsCH_3)(TCNQ)_2$ showing the collapse of the fine-structure splitting. The orientation is fixed, but the spectrometer gain settings are different at each T. (Reproduced with permission from Chesnut and Phillips.[118])

TABLE 7

Fine-Structure Constants[a] for Selected Triplet Exciton Crystals[b]

Stoichiometry	Crystal	Experimental |D|	Experimental |E|	Theoretical |D|	Theoretical |E|	Ref. exp.	Ref. theo.
Simple	$\ldots(D^+D^+)_n\ldots$						
1:1	TMPD-ClO_4	~0	212	13	236	121	331
	$(TMPD)_2Ni(mnt)_2$	602	79.2	670	70	177	177[c]
	$\ldots(A^-A^-)_n\ldots$						
	Morpholinium	448	54	465	44	216	216[d]
	Rb(TCNQ)(I)	400	49	617	70	180	180
	Li(TCNQ)	461	69	–			-
Complex							
2:3	$Cs_2(TCNQ)_3$	281	45.3	–	–	119[c]	–
	$(Morpholinium)_2(TCNQ)_3$	282	45.3	262	34	179	180[e]
	$Rb_2(TCNQ)_3$	282	33.5	–	–	180	–
1:2	$(\phi_3PCH_3)(TCNQ)_2$ $(\phi_3AsCH_3)(TCNQ)_2$	190	30	186	22.5	118	180[e]

[a] In MHz.
[b] Additional 1:1 TCNQ salts with unknown structures are given in Ref. 180.
[c] Less than 10% variation for three different $TMPD^+$ spin densities at the observed separation.
[d] Huckel spin densities, assumed D_{2h} symmetry at 3.5 Å.
[e] For a scaled *n*-mer at 3.25 Å, as suggested in Refs. 23 and 119c.

work for a quantitative analysis. In *regular* ion-radical stacks, the treatment[67] of strong exchange is even more qualitative. The central idea[66] is that only a fraction of the spins contribute to the static susceptibility or the EPR absorption. The regime $kT < J$ is then characterized by a uniformly diluted spin system described by standard high-temperature results. The spin density cancels in the expression for the exchange-narrowed line width, whose angular dependence is given by the Van Vleck second moment for the delocalized π electrons. Figure 12 shows[219] such a fit for TMPD-chloranil, a mixed, simple, regular stack. The calculation is again based on spin densities for isolated ion-radicals.

Single-crystal EPR studies are a powerful probe of the ground-state charge distribution in ion-radical solids. In general, the single ion spin densities have sufficed, as in Madelung calculations, and such results strongly support the present picture of essentially unperturbed ion-radicals. Fine-structure computations further show that the unpaired electrons in the triplet state are on adjacent sites, as expected for strong on-site electron correlations. Another useful feature of strong exchange is the experimental realization of very few or many spin excitations by varying temperature. The detailed

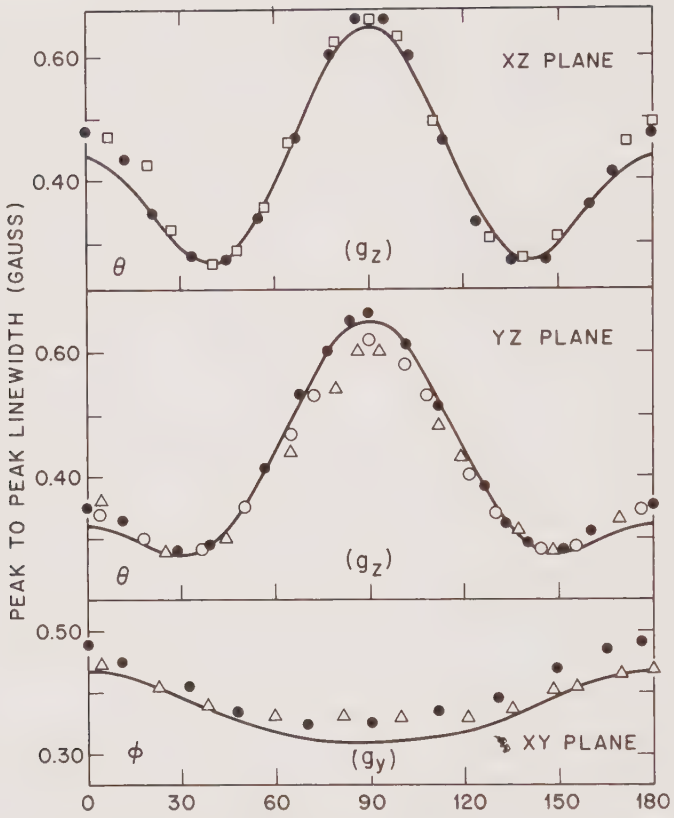

Fig. 12. Angular dependence of the 300°K EPR line width of TMPD-chloranil in the three principal axis planes of the g-tensor. The theoretical curve is based on the truncated Van Vleck second moment for a delocalized π electron at each ion-radical. (Reproduced with permission from Huang, Taylor, and Soos.[219])

application of magnetic resonance to organic ion-radicals thus promises to improve our understanding of ground state properties.

4.5. One-Dimensionality and Spin Dynamics

The anisotropy of the conductivity and the polarization of CT bands are ample evidence that the stacking of planar molecular ions produces highly anisotropic solids. The degree of anisotropy presents a more delicate question that eventually requires measurements of transverse properties. Such information about small exchange parameters between chains can be obtained from EPR data.[67,220] The occurrence of magnetically inequivalent stacks provides a very simple direct demonstration of one-dimensionality. The CSA stacks

in $Cs_2(TCNQ)_3$ shown in Figure 7 are magnetically inequivalent; two sets of fine-structure parameters are resolved[119] for a general orientation of $\mathbf{B}_0$. *All* interchain magnetic coupling must consequently be smaller than the resolved splitting. Since splittings of 1 G ($\sim 10^{-4}$ cm^{-1}) or less are readily resolved for the unusually sharp lines in these ion-radical solids, resolved splittings for magnetically inequivalent chains provide stringent upper bounds on interchain exchange. The low-temperature phase of the SSA system TMPD-ClO_4 contains[121] two magnetically inequivalent chains for each of two domains. The mosaic of twinned domains share a common axis and are resolved[121] for certain orientations of $\mathbf{H}_0$. Three magnetically inequivalent chains are found[148] in cosublimed PDC, with their g tensors related by rotations of $2\pi/3$ about the common chain axis. The angular variation of the three EPR lines in this MSR system is shown in Figure 13. The complex regular salt $(Et_2TCC)(TCNQ)_2$, where Et_2TCC = 3,3-diethyltiacarbocyaninium and is shown in Figure 6, also has inequivalent stacks[26,193] with resolved

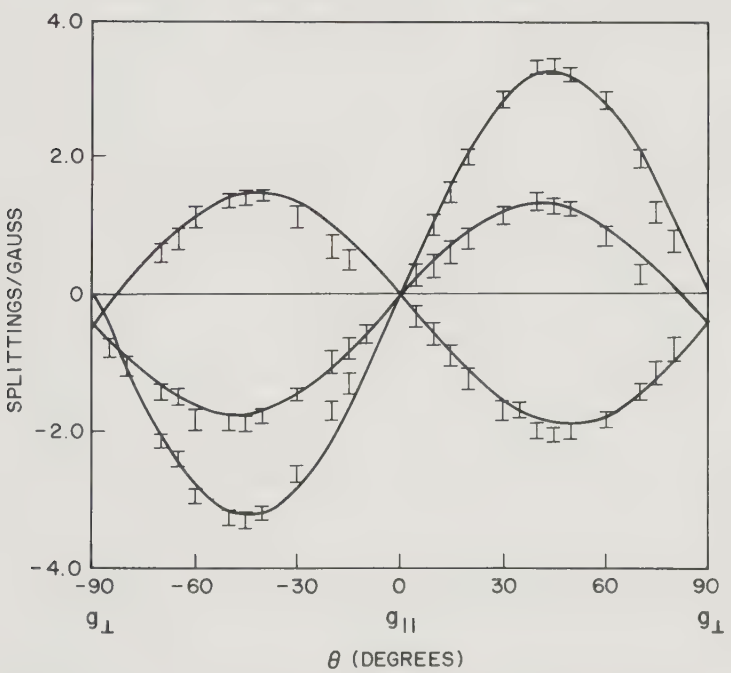

Fig. 13. Comparison of the angular dependence of the Q-band g-factor splittings in PDC at 263°K arising from magnetically inequivalent stacks with theory for three identical, noninteracting stacks. (Reproduced with permission from Hughes and Soos.[178])

uncorrelated spin excitations. These examples encompass the structural possibilities in Figure 4 for ion-radicals, with the exception of the SSR case. Thus magnetic inequivalence provides a powerful method for ruling out interchain exchange without invoking hypothetical arguments about the magnitude of the small π-electron overlaps.

There is now considerable evidence[40,68] from a variety of magnetic resonance and neutron diffraction studies, that the linear Heisenberg antiferromagnet (7) accounts for the *dynamics* of the spins, as well as for *static* magnetic properties. Current work has focused on the two-spin correlation functions

$$C_l(t) = [S(S+1)/3]\langle S^z_{i+l}(t)S^z_i(0)\rangle \tag{69}$$

where $S_i^z(t) = [\exp i\hbar\mathscr{H}_{\text{spin}}/t]S_i^z(0)[\exp -i\hbar\mathscr{H}_{\text{spin}}/t]$ and $\langle\ \rangle$ denotes a thermal average. The time evolution of the spins in (69) is then controlled by the dominant one-dimensional exchange. Purely magnetic interactions or weak interchain exchange constants are perturbations that can be observed[40,220] in single-crystal EPR or NMR studies. Several ideal systems based on insulating transition-metal chains have received careful study. The application of such NMR methods has been reported[221] for $(\phi_3\text{AsCH}_3)(\text{TCNQ})_2$ and supports the picture of one-dimensional random walks in this ion-radical solid. EPR studies have been more qualitative,[67] since the strong exchange $t^2/\Delta E_{\text{CT}}$ often precludes using the high-temperature approximation.

Spin correlations decay slowly, as $t^{-1/2}$, in a one-dimensional spin system. The long time contributions to $C_l(t)$ show up at $\omega = 0$ in the power spectrum and are consequently sampled by such low frequency probes as NMR or EPR. The former, in particular, is such a long time measurement that it may well show excitations in ion-radical solids to be higher dimensional.[222] For example, a transfer integral $t \sim 0.1$ eV corresponds to a frequency of over 10^8 MHz. For $U \sim 1$ eV, the exchange t^2/U is then about 0.01 eV, or over 10^7 MHz. The EPR timescale of 10^3–10^4 MHz is far longer, as is the NMR of 10–10^2 MHz. Even anisotropies of 10^3 in the motion of a triplet exciton or a charge along a chain are then likely to appear more than one-dimensional, especially in NMR.[222] The frequent occurrence[9] of TCNQ layers in ion-radical salts, with good π-electron overlap along a chain and layers of counterions, then may lead to two- or three-dimensional motion in spite of the high degree of anisotropy.

Magnetic measurements on either electrons or nuclei form a separate area of considerable interest. The study of spin dynamics in organic ion-radicals is a straightforward extension that should yield additional information about the degree of one-dimensionality, the nature of the model parameters of $\mathscr{H}_{CT}$, and the proposed picture of weakly perturbed molecular sites. Thus magnetic properties also complement higher-energy optical or conductivity studies.

5. Quantum Computations

5.1. Approximate Molecular Computations

We have emphasized the qualitative description of π-molecular CT crystals in the preceding development of a phenomenological theory based on molecular sites. A quantitative quantum-mechanical description of crystal properties is of course an ultimate goal. We now turn to the first steps that have already been taken toward such quantum calculations. More particularly, we discuss the methods that are applicable for such calculations and their relation to the CT Hamiltonian $\mathscr{H}_{CT}$ in (45).

There are many approximate computations[223,224] on single donor and acceptor molecules, including TCNQ, TMPD, TTF, and chloranil. Different methods for such quantum molecular calculations include CNDO/2,MS Xα, PPP-Cl, and *ab initio* SCF for an incomplete basis and amount to different parametrizations of the Schrödinger equation for the molecule. Most provide a fair degree of success in interpreting the energy levels, as observed for example in photoemission spectroscopy, of the single molecule or molecular ion. There are also many computations[4,6,7,87,93,94,224,225] on DA dimers at some fixed separation. Their reliability and success is more open to question,[6] however, and it has been difficult to assign the stability of a dimer. In particular, the use of SCF-related methods is suspect,[226] at least partly on account of neglecting important dispersion forces[6,7] in these complexes. Also, the energies associated with complex formation are typically small ($\lesssim 1$ eV) and thus harder to compute than single-molecule levels.

There are fewer computations[213,225] on crystals, except for straightforward Madelung sums.[106,107,111] Such CNDO/2 computations[213,225] for linear chains are subject to the same criticism concerning dispersion interactions as were dimer calculations. In addition, self-consistent methods have severe problems for weakly

interacting open-shell species, such as we are interested in here. These difficulties are best documented for the H_2 molecule at large internuclear separations, where the usual restricted Hartree–Fock theory artificially mixes in undesired contributions of different ionicities. The similar occurrence for more relevant linear chain systems such as the Hubbard model (6) is also well-known[22,44,201,227,228] and is illustrated in Figure 14, where restricted and unrestricted Hartree–Fock (RHF and UHF) ground-state solutions are compared to the exact[229] ground-state energy. The energy resulting from a simple second-order degenerate perturbation argument is also shown. In addition, even the UHF solution yields very poor results for the low-lying "spin-flip" electronic states. It is important to note that the various parameters arising in $\mathscr{H}_{CT}$ are quite small ($U \approx 1$ eV, $t \approx 0.2$ eV, $J \approx 0.04$ eV), so that quite accurate and careful calculations are necessary. Even for H_2 an accurate computation[85] of the exchange interaction J is a matter of great delicacy.

A general and useful method for the quantum calculation of crystal properties is to break the procedure up into two steps. The first step entails the restriction to a 4^N-dimensional space generated

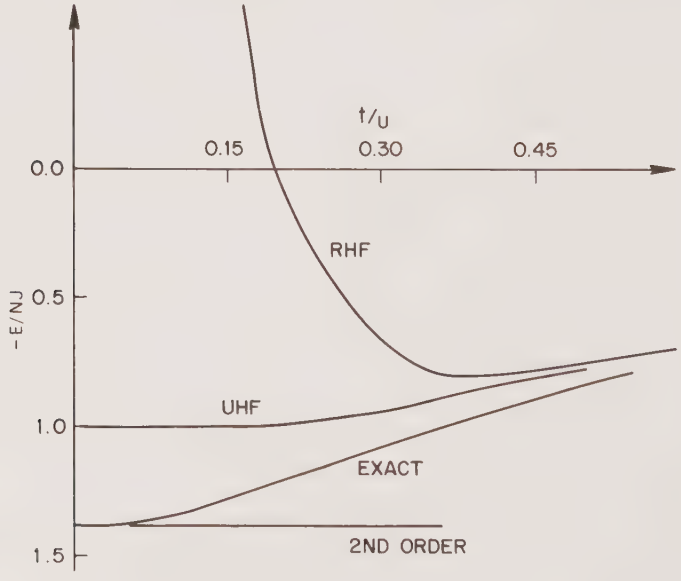

Fig. 14. Comparison of the restricted Hartree–Fock (RHF), the unrestricted Hartree–Fock (UHF), and the exact ground-state energy of the $\frac{1}{2}$-filled model. The second order result reduces to the Heisenberg chain (7) in the limit $t/U \to 0$.

by the four CT states per site, as already discussed in Section 2.5, and the computation of the various parameters which appear in the resulting $\mathscr{H}_{CT}$. Actually one may take into account interactions with other (e.g., Frenkel exciton or phonon) states by[230] applying a unitary transformation so that the more complete Hamiltonian becomes block-diagonalized with one block corresponding to a new $\mathscr{H}_{CT}$, now with "renormalized" parameters. In practice such unitary transformations are only approximated and the block-diagonalization is left incomplete, with temperature-dependent renormalized parameters. The second step is to solve the resulting many-spin or many-electron model Hamiltonian.

The general problem of site representations for $\mathscr{H}_{CT}$ is then simplified, as indicated schematically in Figure 15 and carried out explicitly in Section 3, for special cases by using the crystal structure and stoichiometry. Approximate methods for dealing with special cases of $\mathscr{H}_{CT}$, with extensions or refinements of its parameters, and with actual parameter computations are discussed below. In special cases of $U \gg t$ and simple stacks, a further unitary transformation leads to the "spin-flip" space in which only the orientation of the spins is important. As indicated in Figure 15, the magnetic properties of $\mathscr{H}_{CT}$ in such cases reduce to various one-dimensional Heisenberg chains. Now results for exchange-coupled spins can be used to provide accurate solutions for a restricted part of $\mathscr{H}_{CT}$.

5.2. Crystal-Perturbed States

In an explicit computational scheme, we typically first require a suitable set of orbitals from which complete wave functions are constructed. When isolated-molecule MOs for different molecules are brought close to one another, their overlap will in general increase from zero. Although such nonorthogonal orbitals have been commonly used in previous dimer work[7,87,93,94,224,225] their solid-state use can give rise to many problems, and expansions[86,231,232] in powers of the intermolecular overlap can be complicated. The general difficulties associated with the so-called "nonorthogonality catastrophe"[82] in explicitly exhibiting[85,232] the cancellation of nonphysical "unlinked" terms is easily avoided through the use of strongly orthogonal molecular states. Thus we orthogonalize the orbitals for different molecules to one another, as indicated in Section 2.3 for the dimer. The use of Löwdin's symmetric orthogonalization[95] procedure insures orthonormal orbitals bearing maximum

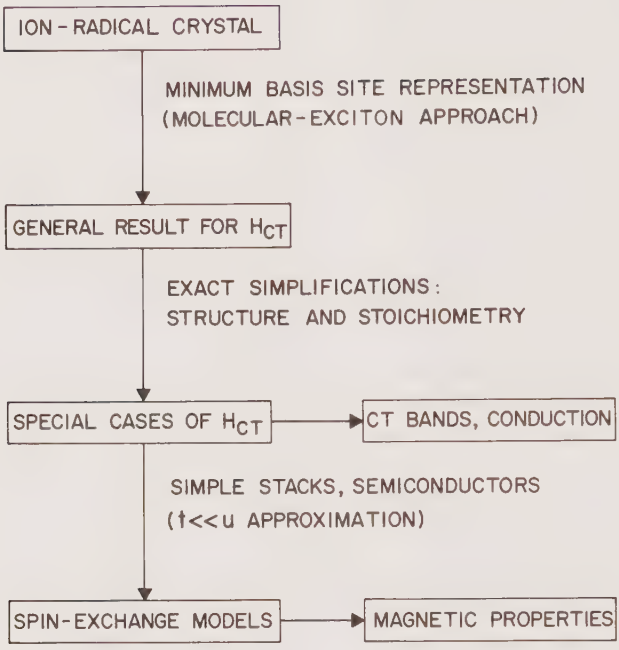

Fig. 15. Theoretical approach to the molecular-exciton analysis of π-molecular CT crystals in the minimum basis site representation.

similarity[233] to the original nonorthogonal orbitals. We presume the molecules to be weakly interacting and still speak of these orthonormal Wannier orbitals as isolated- or free-molecule orbitals, inasmuch as the usual descriptions of crystal field, induction, and dispersion interactions are not significantly modified.

The next general problem is to relate the crystal-perturbed states (29) and (30) to isolated-molecule functions. This can be done[25] by developing a free molecule site Hamiltonian h_n^{FM} similar to the crystal-perturbed site Hamiltonian referred to in (25). Such a choice has the added convenience that available gas-phase data on dimers might be incorporated, much as has been done[15 18] in the case of molecular-exciton theories of closed-shell molecular solids. With the μth Wannier spin-orbital for the ith molecule we associate fermion creation and annihilation operators $c_{i\mu}^{+}$ and $c_{i\mu}$. Then the Schrödinger

Hamiltonian is

$$\mathcal{H} = \tfrac{1}{2}\sum_{ij}{}' V_{ij} + \sum_{ij}\sum_{\mu\nu}\left\langle i\mu\left| -\frac{\hbar^2}{2m}\nabla^2 + \sum_k V_k(\mathbf{r})\right| j\nu\right\rangle c_{i\mu}^+ c_{i\nu}$$
$$+ \sum_{ijkl}\sum_{\mu\nu\pi\rho}\left\langle i\mu \wedge j\nu\left|\frac{e^2}{r_{12}}\right| k\pi \wedge l\rho\right\rangle c_{i\mu}^+ c_{j\nu}^+ c_{l\rho} c_{k\pi} \tag{70}$$

where the Roman indices $ijkl$ label molecules, while the Greek indices $\mu\nu\pi\rho$ label orbitals for each molecule. $V_k(\mathbf{r})$ is the interaction of an electron with the nuclei of molecule k, V_{ij} $(i \neq j)$ is the intermolecular nuclear repulsion, which is constant for a rigid lattice, and the symbol $\wedge$ indicates an antisymmetrized product.

The free-molecule site Hamiltonian

$$h_i^{\mathrm{FM}} \equiv \sum_{\mu\nu}\left\langle i\mu\left| -\frac{\hbar^2}{2m}\nabla_-^2 + V_i(\mathbf{r})\right| i\nu\right\rangle c_{i\mu}^+ c_{i\nu}$$
$$+ \tfrac{1}{2}\sum_{\mu\nu\pi\rho}\left\langle i\mu \otimes i\nu\left|\frac{e^2}{r_{12}}\right| i\pi \otimes i\rho\right\rangle c_{i\mu}^+ c_{i\nu}^+ c_{i\rho} c_{i\pi} \tag{71}$$

then consists simply of those terms of (70) that involve solely site i. The two-site interaction between free molecules is similarly obtained by selecting from (70) those terms involving exactly two sites. For the free-molecule interaction between sites i and j, we obtain

$$v_{ij}^{\mathrm{FM}} \equiv V_{ij} + \mathcal{U}_{i\leftarrow j}^{\mathrm{FM}} + \mathcal{U}_{i\rightarrow j}^{\mathrm{FM}} + \mathcal{U}_{i\leftrightarrow j}^{\mathrm{FM}} \tag{72}$$

where $\mathcal{U}_{i\leftarrow j}^{\mathrm{FM}}$ involves only orbitals on site i (and nuclei on site j), $\mathcal{U}_{i\rightarrow j}^{\mathrm{FM}}$ involves only orbitals on site j, and $\mathcal{U}_{i\leftrightarrow j}^{\mathrm{FM}}$ involves orbitals on both sites i and j. We find

$$\mathcal{U}_{i\leftarrow j}^{\mathrm{FM}} \equiv \sum_{\mu\nu}\langle i\mu|V_j(\mathbf{r})|i\nu\rangle c_{i\mu}^+ c_{i\nu}$$

$$\mathcal{U}_{i\leftrightarrow j}^{\mathrm{FM}} = \sum_{\mu\pi}\left[\left\langle i\mu\left| -\frac{\hbar^2}{2m}\nabla^2 + V_i(\mathbf{r}) + V_j(\mathbf{r})\right| j\pi\right\rangle c_{i\mu}^+ c_{j\pi} + \text{h.c.}\right]$$
$$+ \sum_{\mu\nu\pi\rho}\left\{\left[\left\langle i\mu \otimes i\nu\left|\frac{e^2}{r_{12}}\right| i\pi \wedge j\rho\right\rangle c_{i\mu}^+ c_{i\nu}^+ c_{j\rho} c_{i\pi} + \text{h.c.}\right]\right.$$
$$+ \left[\left\langle i\mu \otimes i\nu\left|\frac{e^2}{r_{12}}\right| j\pi \otimes j\rho\right\rangle c_{i\mu}^+ c_{i\nu}^+ c_{j\rho} c_{j\pi} + \text{h.c.}\right]$$
$$+ \left[\left\langle i\mu \wedge j\nu\left|\frac{e^2}{r_{12}}\right| i\pi \wedge j\rho\right\rangle c_{i\mu}^+ c_{j\nu}^+ c_{j\rho} c_{i\pi} + \text{h.c.}\right]$$
$$\left.+ \left[\left\langle i\mu \wedge j\nu\left|\frac{e^2}{r_{12}}\right| j\pi \otimes j\rho\right\rangle c_{i\mu}^+ c_{j\nu}^+ c_{j\rho} c_{j\pi} + \text{h.c.}\right]\right\} \tag{73}$$

$\mathscr{U}^{\mathrm{FM}}_{j\leftarrow i}$ involves interchanging i and j in $\mathscr{U}^{\mathrm{FM}}_{i\leftarrow j}$. Equation (72) leads to the usual multipole expansion, at least in the limit of zero differential overlap (ZDO) which holds quite accurately for van der Waals, or longer, intersite separations. In the ZDO limit, the only contribution to $\mathscr{U}^{\mathrm{FM}}_{i\leftrightarrow j}$ in (73) is

$$\lim_{\mathrm{ZDO}} \mathscr{U}^{\mathrm{FM}}_{i\leftrightarrow j} = \sum_{\mu\nu\pi\rho}\left[\left\langle i\mu \otimes jv\left|\frac{e^2}{r_{12}}\right|i\pi \otimes j\rho\right\rangle c^+_{i\mu}c^+_{jv}c_{j\rho}c_{i\pi} + \text{h.c.}\right] \tag{74}$$

and is used in (72). Matrix elements of v^{FM}_{ij} reduce at once to

$$\lim_{\mathrm{ZDO}} \langle \mathrm{ir} \wedge js|v^{\mathrm{FM}}_{ij}|it \wedge ju\rangle = \langle ir \otimes js| \lim_{\mathrm{ZDO}} v^{\mathrm{FM}}_{ij}|it \otimes ju\rangle$$

$$= \left\langle ir \otimes js\left|\left\{V_{ij} + \sum_{b\in j} V_i(\mathbf{r}_b) + \sum_{a\in i} V_j(\mathbf{r}_a) + \sum_{a\in i}\sum_{b\in j}\frac{e^2}{r_{ab}}\right\}\right|it \otimes ju\right\rangle \tag{75}$$

and involve only product functions $|ir \otimes js\rangle$ for the two sites. The ensuing multipole expansion[25] then includes both crystal field and permanent induced moments. Dispersion contributions are included in (75) only in an average way, just as the neglect of three- and four-site terms in $\mathscr{H}$ is partially accounted for[97] by retaining suitable averages in the one- and two-site terms. It should be emphasized that (75) leads to only a modest number of matrix elements in the minimum basis g, α, β, and $\alpha\beta$ defined in (29) and (30) and that it already represents a potentially far more accurate treatment of intersite Coulomb forces than the choice $\langle V_C\rangle^{(0)}$ in (51) for the ground-state value of the crystal Coulomb interactions.

Next we construct the crystal-perturbed site Hamiltonian, h_i, and the associated intersite interactions. The multipole perturbation of site i induced by all other sites is included directly in h_i through

$$h_i \equiv h^{\mathrm{FM}}_i + \sum_{\substack{j\\(j\neq i)}}\{\mathscr{U}^{\mathrm{FM}}_{i\leftarrow j} + \sum_{\mu\nu}\mathrm{Tr}[D_j c_{i\mu}\mathscr{U}^{\mathrm{FM}}_{i\leftrightarrow j}c^+_{iv}]c^+_{i\mu}c_{iv}\} \tag{76}$$

The trace over the states of the neighboring molecules j and D_j is a density matrix for the perturbing site j. In the minimum basis for a neutral DA crystal, D_j could be chosen as $|j\mathrm{D}\rangle\langle j\mathrm{D}|$ or $|j\mathrm{A}\rangle\langle j\mathrm{A}|$ for a donor or an acceptor at site j, respectively. A more accurate choice for D_j might include a small admixture of excited states or even of ionic states, possibly in a self-consistent manner dependent on the solution of $\mathscr{H}_{\mathrm{CT}}$, and even a temperature-dependent choice could be made. However, fairly simple choices for D_j are indicated in practice. It seems especially desirable to separate the development of $\mathscr{H}_{\mathrm{CT}}$ from

its final solution, since each step seems to tax current methods. The corresponding two-site interactions are

$$v_{ij} = V_{ij} + \mathscr{U}^{\mathrm{FM}}_{i\leftrightarrow j} - \sum_{\mu\nu} \mathrm{Tr}[D_j c_{i\mu} \mathscr{U}^{\mathrm{FM}}_{i\leftrightarrow j} c^{+}_{i\nu}] c^{+}_{i\mu} c_{i\nu} - \sum_{\pi\rho} \mathrm{Tr}[D_i c_{j\pi} \mathscr{U}^{\mathrm{FM}}_{i\leftrightarrow j} c^{+}_{j\rho}] c^{+}_{j\pi} c_{j\rho} \tag{77}$$

Summing h_i and v_{ij}, as indicated in (24) for the crystal Hamiltonian, demonstrates the important result that various choices for D_i merely change the partitioning of $\mathscr{H}$ into one- and two-site terms, without introducing any approximations.

It is straightforward to exhibit the matrix elements of (77) in the ZDO limit. After some manipulations we find

$$\lim_{\mathrm{ZDO}} \langle ir \wedge js | v_{ij} | it \wedge ju \rangle = \delta_{rt}\,\delta_{su} \left\{ V_{ij} - \mathrm{Tr}\left(D_i \otimes D_j \sum_{a\in i} \sum_{b\in j} \frac{e^2}{r_{ab}} \right) \right\} + \mathrm{Tr}\left\{ (|it\rangle\langle ir| - D_i) \otimes (|js\rangle\langle ju| - D_j) \times \sum_{a\in i} \sum_{b\in j} \frac{e^2}{r_{ab}} \right\} \tag{78}$$

The intersite interaction is now composed of two parts. The first contains internuclear repulsions and average electron–electron repulsions. Its primary monopole–monopole contribution need not be small if the sites have a net charge, but it is scalar and merely shifts all energy levels. The second, nonscalar part of (78) takes into account instantaneous charge fluctuations, as occur in dispersion interactions. We note that this dispersion term vanishes when the expectation value over v_{ij} is taken with sites i and j in states D_i and D_j. This demonstrates the inclusion of average intersite interactions in h_i, with a correspondingly weaker v_{ij}.

The free-molecular choice h_i^{FM} is natural for possible comparison with gas-phase data. The crystal perturbed choice (76) for h_i and (77) for v_{ij}, in which the maximum average crystal perturbation is included in h_i, is advantageous for the phenomenological theory developed in Section 2.

5.3. Improved Matrix Elements

The matrix elements of $\mathscr{H}_{\mathrm{CT}}$ were introduced in Section 2 as adjustable parameters, with additional approximations to reduce

their number. The resulting model was judged to be the simplest phenomenological model preserving the essential features of the CT problem. Here we investigate these approximations more thoroughly. We also seek more accurate expressions for the matrix elements in view of possible explicit computations of crystal parameters.

The Mulliken CT integral t defined in (43) connects sites with a pair of electrons above the dimer vacuum state $|D^{2+}A\rangle$. In general, different numbers of electrons may be involved and the CT integral depends on the occupancies of each of the sites. Thus the integrals

$$\begin{aligned} t' &\equiv \langle D^{+}A|\mathscr{H}|D^{2+}A^{-}\rangle \\ t'' &\equiv \langle DA|\mathscr{H}|D^{+}A^{-}\rangle \\ t''' &\equiv \langle D^{+}A^{-}|\mathscr{H}|D^{2+}A^{2-}\rangle \\ t^{\mathrm{iv}} &\equiv \langle DA^{-}|\mathscr{H}|D^{+}A^{2-}\rangle \end{aligned} \tag{79}$$

are in general all distinct. If we postulate a common "frozen" core for D, D^{+} and D^{2+} and for A, A^{-} and A^{2-}, as well as a single fixed orbital above these cores, then these integrals do in fact become identical. In a more accurate picture we believe that the core and "valence" orbitals will both contract as the number of electrons on the molecule is decreased. This leads us to expect

$$t' \leq t'' \leq t''' \leq t^{\mathrm{iv}} \tag{80}$$

The relative order in (80) should persist in even more accurate treatments not based on a core and valence electron picture at all. We note that correlations between the positions of pairs of electrons above a core can invalidate the simple valence-orbital picture, especially for extended molecules where these electrons can be partially localized in different portions of the molecule. Some authors[39] have suggested strong correlation of electrons in $TCNQ^{2-}$, with each electron largely localized on the pair of cyanide groups at opposite ends of the molecule. This useful picture is probably oversimplified, as is indicated by solution hyperfine data[110] and by calculations,[223–225] which both show some of the relevant MOs to be spread over the quinoidal double bonds also.

In some cases, a single average t can be used in place of the distinct values indicated in (79). For instance, in a paramagnetic $\frac{1}{2}$-filled case with t/U small, we expect the ground state usually to have one electron on any given site and the most important excited configurations to result from a CT yielding nearest-neighbor empty and

doubly occupied sites. Thus the CT integral connecting the more important configurations in the $\frac{1}{2}$-filled ground state will be t'' ($= t'''$ in self-complex FR stacks) or just (43). We then expect a single CT integral $t \simeq t''$ to give nearly the same result as if different CT integrals were used, at least for the low-lying magnetic states. More quantitatively, we could specify

$$t \equiv \langle (a^+_{i\alpha} a_{(i+1)\alpha} + a^+_{i\beta} a_{(i+1)\beta})(t' P_{0,i} P_{1,i+1} + t'' P_{1,i} P_{1,i+1} + t''' P_{0,i} P_{2,i+1} + t^{\mathrm{iv}} P_{1,i} P_{2,i+1}) \rangle \tag{81}$$

where $P_{p,j}$ is the projector onto configurations in which site j is occupied by p ($= 0, 1, 2$) valence electrons.

In some cases the different CT integrals of (79) may play an important role. For less than $\frac{1}{2}$-filled FR stacks, t' will govern the single occupancy motion while $t'' = t'''$ still governs the "magnetic" splittings; these two effects can be[234] approximately separated in theoretical treatments so that these different CT integrals, if known, could readily be taken into account. Even for the $\frac{1}{2}$-filled case, t' and t^{iv} are expected to play an important role in conduction processes; indeed, the ratio t'/t^{iv} should be a direct indication of whether hole or electron conduction is dominant.

The intersite Coulomb interaction and the attendant approximations deserve some further comment also. The Coulomb interaction between sites n and m was given in (42) for *ionic* molecules only, since the charge operators (40) vanish at a neutral site. Neutral sites nevertheless may contain partial charges, with vanishing sums, and an approximation like (42) leads to more rapid convergence[87] than a simple multipole expansion. Such partial charges in diamagnetic molecules must be computed rather than obtained from solution hyperfine data. The improvement to (42) is, still in the minimum basis,

$$V_C'(m, n) = \sum_{p,q=0}^{2} M_{pq}(m, n) P_{p,m} P_{q,n} \tag{82}$$

where $P_{p,m}$ are again the projectors onto a configuration with $p = 0$, 1, or 2 valence electrons and $M_{pq}(m, n)$ is the corresponding sum over the delocalized charge distributions for sites with p and q valence electrons. The previous choice for V_C in (42) is regained if only the $M_{11}(m, n)$ term is retained and, in addition, the average value of $P_{1,n}$ is simply taken to be the charge operator ρ_n in (40). The intermediate approximation of scaling the energy difference between

ionic and neutral sites leads to

$$M'(m, n) = \sum_{\mu \in n, \nu \in n} (\rho_\mu \rho_\nu - \rho_\mu' \rho_\nu') r_{\mu\nu}^{-1} \tag{83}$$

and is a straightforward improvement to (41) in which ρ_μ' and ρ_ν' refer to neutral sites. The assumption of identical geometries for both forms is inevitable, since only the actual structure will be available experimentally.

The Coulomb interactions were further simplified by introducing the Madelung approximation (51) in which we took

$$\langle \rho_i \rho_j \rangle = \langle \rho_i \rangle \langle \rho_j \rangle \tag{84}$$

for the ground-state expectation value of any two charges. Equation (84) neglects Coulomb exchange stabilization[108] for adjacent sites in the stack. A quite different objection to $\langle V_C \rangle^{(0)}$ or to (84) is that the interaction is effectively smeared over the whole crystal, as occurs in self-consistent treatments. Thus the Madelung approximation replaces the various intersite Coulomb interactions by an average value. Consequently, the stronger short-range Coulomb interactions are under represented, while the weaker long-range Coulomb interactions are over represented.

An ionic MSR stack illustrates some of the consequences of the Madelung approximation. The energy required to create a doubly occupied D site adjacent to an A site in a $\ldots D^+A^-D^+A^- \ldots$ crystal is just

$$U' = U_D + (\varepsilon_D - \varepsilon_A) + 2M - M(1, 2) \tag{85}$$

Here U_D is the intrasite correlation (37), $\varepsilon_D - \varepsilon_A$ is the change in site energy, and $2M - M(1, 2)$ is the change in the lattice electrostatic energy. Inspection of (51) shows that the decrease of ρ_A from unity by $2/N$ leads to a change of $2M$, as if the resulting neutral sites were infinitely far apart.[22] The electron–hole interaction $-M(1, 2)$ is similarly missed in CT excitations of a neutral MSR stack.[22] The inclusion of $M(1, 2)$ is essential for quantitative computations of ΔE_{CT}, and such a large term is missed in $\langle V_C \rangle^{(0)}$, which is basically a ground-state approximation. A simple, but partial remedy is to use the Madelung approximation to compute the ground-state charge

density and then estimate additional corrections for excited states. The polaron stabilization of the individual electron and hole excitations, which is neglected in $\mathscr{H}_{CT}$, must in fact be comparable to $M(1, 2)$, which is neglected in the Coulomb approximation, since we often find $\Delta E_c \sim \frac{1}{2}\Delta E_{CT}$ in Tables 2–4 for simple stacks.

Thus the phenomenological parameters appearing in $\mathscr{H}_{CT}$ may depend in part on the approximation in which the model is to be solved. Nevertheless, we see important advantages in separating the problem into two separate parts: first, the evaluation of the parameters and, second, the solution of the resulting model. The *ab initio* evaluation of the relevant matrix elements could be used in the refined definitions of the parameters for simpler models, for which solutions are already available. Should the reliability of the *ab initio* matrix elements be high enough and the initial comparisons using the simplified models be favorable, more extensive model calculations would be feasible. We conclude that the theoretical evaluation of at least some of the parameters occurring in $\mathscr{H}_{CT}$ is possible. Calculations of Coulomb interactions, intrasite correlations, and site energies are likely to be the most reliable, while CT and exchange integrals are more problematical.

5.4. Hubbard and Heisenberg Models

$\mathscr{H}_{CT}$ is defined on the same (or at least an isomorphic) space as the simple Hubbard model (6). All variations on $\mathscr{H}_{CT}$ retain the fundamental feature of four states per site, as in (6). Thus theoretical methods for solving $\mathscr{H}_{Hu}$ are anticipated to be applicable to $\mathscr{H}_{CT}$ as well. The properties of $\mathscr{H}_{Hu}$ and of related models have served as prototypes not only in the present context of CT in π-molecular crystals, but also for describing[52,53,235] the π electrons in conjugated hydrocarbons, for describing metal-insulator transitions[44,46–48] in transition-metal oxides,[47,48] and for other[236] purposes as well. There has consequently been considerable interest in the mathematical properties of (6).

Even for the simple Hubbard model, exact properties are very difficult to obtain, and one needs to apply approximations for any finite temperature results. Different schemes are relevant, depending on the values of the parameters t and U. The only exact results for (6) presently available are its symmetry properties,[229] ground-state energy,[229,237] a few low-lying excited-state energies,[238] zero-temperature susceptibilities,[237–239] and the zero-temperature

specific heat slope[240] of the $\frac{1}{2}$-filled case. Very few if any of these exact properties can be obtained for a more general $\mathscr{H}_{CT}$. Of course, for special extreme limits, such as $U \to 0$ or $t \to 0$, all properties of $\mathscr{H}_{Hu}$ can be obtained exactly.

The primary region of interest in the present application of $\mathscr{H}_{CT}$ to π-molecular CT crystals is for weakly interacting sites; i.e., when the Hubbard parameters satisfy $|t|/U < 1$. In this region near the separated site limit, many conventional SCF-type methods of solution mix in ionic states in a uniform manner independent of the local nature of the relevant interactions. Hence the resulting solutions and properties may be rather poor, as already mentioned in Section 5.1.

One of the most successful approaches for $|t|/U \ll 1$ is to apply a perturbation expansion based upon some sort of a separated site limit. Then the zeroth-order model is usually highly degenerate, and degenerate perturbation theory yields effective Hamiltonians defined on the zeroth-order eigenspaces. For the $\frac{1}{2}$-filled case, when $N_e = N$, we may reasonably take the entire t-term $\mathscr{H}_t$ in (44) to be the perturbation. Then one finds the effective Hamiltonian for the ground-state zeroth-order eigenspace to be[45,49,241,242] (through second order)

$$\mathscr{H}_{\text{spin}} = P^0 \mathscr{H}_t R^0 \mathscr{H}_t P^0 - \frac{1}{U} P^0 \mathscr{H}_t \mathscr{H}_t \mathscr{H}_t P^0 \tag{86}$$

where P^0 is the projector for this "spin-flip" space and R^0 is the associated zeroth-order resolvent. For a regular one-dimensional array, with a single t in (44), (86) leads directly to the regular Heisenberg chain (7), plus an additive constant. For alternating t parameters in (44), (86) leads to the alternating chain (66). Improved spin Hamiltonians can be obtained[241] by retaining higher-order terms in (t/U), which formally leads to more than nearest-neighbor interactions. Further simple generalizations are applicable[241] to $\frac{1}{2}$-filled cases of more general $\mathscr{H}_{CT}$ models. For the partially filled case a reasonable zeroth-order model and perturbation theory are more complicated, but physically useful choices are available[234] which still lead to Heisenberg spin models. Such Heisenberg spin models then are more readily soluble numerically, since they are defined on a smaller "spin-flip" space. A reasonably complete description of static magnetic properties is consequently possible.

5.5. Hubbard Model Computations

A variety of methods for solving the simple, and some slightly modified, Hubbard models have been carried out in the literature. Such static quantities as the paramagnetic susceptibility, χ_p, the specific heat, C_v, and the average density of doubly occupied sites, n_D, can be obtained as a function of temperature. Some of the more accurate (for small $|t|/U$) methods for thermodynamic properties are listed in Table 8. Since we estimate $U \sim 1\,\text{eV}$ and $t \sim 0.2\,\text{eV}$ in π-molecular CT crystals, the low-temperature results for Hubbard models are of primary interest at room temperature or below. Although many techniques[81] are applicable to more general cases of $\mathscr{H}_{\text{CT}}$, they have so far been applied primarily to the $\frac{1}{2}$-filled regular Hubbard model (6) or to the simple, segregated, regular (SSR) stack indicated in Table 8. The SCR case corresponds to less than $\frac{1}{2}$-filling and is of interest in connection with partly filled conductors like NMP-TCNQ(I) or TTF-TCNQ. More exotic models[43,255] have been proposed in such cases, but will not be considered here.

TABLE 8
Selected Finite Temperature Results for the Hubbard Model

Type of stack	Results[b]	Range of applicability	Method	Ref.
SSR	χ_p, C_v, n_D	$kT \gtrsim U$	Finite chain extrapolation	243
	χ_p, C_v	$kT \gtrsim U/4, U \geq 4t$	Perturbative high-temperature expansion	244
	χ_p, C_v, n_D	$kT \gtrsim 4t^2/U, U \geq 5t$	Numerical-perturbative extrapolation	245
	χ_p, C_v	$kT \gtrsim U$	Equation of motion	246
	χ_p, C_v	Larger t/U	Functional integral	247
SCR	χ_p, C_v	$kT \gtrsim U/3, U \geq 8t$	Perturbative high-temperature expansion	248
	χ_p, C_v	Larger kT(?)	High-order Green's function decoupling	249
	χ_p, C_v	$kT \gtrsim t, U \gtrsim 5tN/N_e$	Numerical-perturbative extrapolation	234
	χ_p, C_v	$U \to \infty$	Exact	250
SSA	$\chi_p{}^a$	$U \gtrsim 5t$	Self-consistent field	251
	$\chi_p, C_v{}^a$	$kT \gtrsim 2J(1+\delta)$	Finite chain extrapolation	252
	$\chi_p{}^a$	$t' \ll t$	Triplet-exciton expansion	253
	χ_p, C_v, n_D	$U = 0$	Exact	254

[a] These SSA results are for the alternating Heisenberg chain, (66), which is the second-order perturbation expansion of the Hubbard model.

[b] χ_p is the static magnetic susceptibility, C_v is the specific heat, and n_D is the average density of doubly occupied sites.

Dynamic properties require eigenkets in addition to the eigenvalues and have typically been less accurately treated, primarily via various SCF-type techniques. Beyond these mathematical difficulties one also finds physical difficulties in using the simple Hubbard models, since intersite Coulomb interactions, interactions with Frenkel excitations, and electron–phonon interactions are expected to play a more important role. The best understood dynamic properties are the spin correlation functions (69) that occur in the description of the magnetic properties of ion-radical solids.

For the optical and electrical properties, relatively few computations are available[227,256 258] for the linear Hubbard model. The dipole-moment and current operators, relevant for computing these properties, are[81] most simply approximated as

$$\begin{aligned} \boldsymbol{\mu} &= e\hat{z}M \sum_{i\sigma} (a_{i\sigma}^{+} a_{(i+1)\sigma} + a_{(i+1)\sigma}^{+} a_{i\sigma}) \\ \mathbf{j} &= ie\hat{z}V \sum_{i\sigma} (a_{i\sigma}^{+} a_{(i+1)\sigma} - a_{(i+1)\sigma}^{+} a_{i\sigma}) \end{aligned} \tag{87}$$

and

$$\begin{aligned} M &= \langle \mathrm{D}^{+}\mathrm{A}^{-}|z|\mathrm{DA}\rangle \\ V &= m_e^{-1}\langle \mathrm{D}^{+}\mathrm{A}^{-}|p_z|\mathrm{DA}\rangle \end{aligned} \tag{88}$$

where $\hat{z}$ and p_z are the unit vector and momentum along the stack axis and m_e is the mass of the electron. The computations so far on extended systems have assumed these simple forms with the elements treated as parameters, although more precise formulas could be obtained in the site representation via a treatment much like that for $\mathscr{H}_{\mathrm{CT}}$. Calculations[256,257] of optical absorptivities for the $\frac{1}{2}$-filled case show a CT absorption peak which is centered near U and which increases in breadth while shifting to lower frequencies as $|t|/U$ increases from 0, much as is expected. Calculations[257,258] of the electrical conductivity for the linear $\frac{1}{2}$-filled Hubbard model at small $|t|/U$ usually yield a small conductivity vanishing exponentially at low temperatures; indeed the zero-temperature conductivity is rigorously[229] zero, and the overall behavior is much as expected from the ideas[46,47] of Mott for transition-metal oxides. The partially filled Hubbard model can, however, show[227] very large conductivities even for $|t|/U \ll 1$, because of the ability of the electrons (or holes) to move about without creating additional (high-energy) doubly occupied sites; then interactions with the phonons are expected to become important, as indicated in some[207–209] rough estimates;

in fact, interesting sorts of Peierls gaps may[259] open up in the energy band spectrum, at least at low temperatures; most of these electron–phonon interactions indeed tend to decrease the conductivity yielding an activated form as in (47). Finally, there are several discussions[40,43,123,124] of the functional form of the temperature-dependent conductivity for disordered crystals, a fairly common structural feature of organic CT solids.

The site representation (45) for $\mathscr{H}_{CT}$ is based on strong intrasite (molecular) correlations in π-molecular CT solids. The classification of CT crystals in Section 3 and the qualitative features of their optical, electric, and magnetic properties in Section 4 show the usefulness of our phenomenological approach. On the other hand, no qualitative interpretation of CT bands, intensities, and line shapes or of charge carriers, polarization, and phonon interactions has yet been achieved, not even for the idealized Hubbard model. Thus $\mathscr{H}_{Hu}$ and even $\mathscr{H}_{CT}$ may prove to contain serious oversimplifications for single-particle excitations in real complexes. As emphasized in Section 2, however, a molecular-exciton approach leads naturally to a site representation, and $\mathscr{H}_{CT}$ is the *simplest* reasonable candidate for describing the magnetic, optical, and electric properties of the different types of ion-radical stacks.

6. Conclusion

We noted at the beginning that the infinite molecular stacks encountered in solid-state CT crystals have hindered the generalization of the Mulliken model of configuration interaction in a single DA complex. Since π-molecular CT and free-radical crystals contain nearly nonoverlapping molecular species, a molecular-exciton approach was adopted. The general site representation developed in Section 2 and applied to representative CT and FR structures in Sections 3 and 4 generalizes molecular-exciton theory to open-shell systems. The minimum-basis result for the CT Hamiltonian, $\mathscr{H}_{CT}$ in (45), is the natural extension of configuration interaction via CT states to an infinite crystal. Thus $\mathscr{H}_{CT}$ provides the general crystal analog for the Mulliken treatment of a DA dimer.

Just as DA dimers have eluded a complete quantum-mechanical analysis, the accurate computation of the crystal-perturbed states occurring in $\mathscr{H}_{CT}$ has yet to be achieved. The phenomenological nature of $\mathscr{H}_{CT}$ is characteristic of molecular-exciton theories. The collection in Section 3 of representative CT excitation energies and

activation energies for conduction and for paramagnetism indicates that the qualitative features of quite different crystal structures are contained in $\mathscr{H}_{CT}$ if strong intramolecular correlations and narrow bands are assumed. The experimental determination of the crystal parameters in $\mathscr{H}_{CT}$, for example by comparing related structures, will be greatly facilitated by additional physical studies of single crystals.

The reduction of $\mathscr{H}_{CT}$ to various one-dimensional Hubbard models facilitates comparison between theory and experiment, since the mathematical properties of such models have received considerable attention. These theoretical results can often be applied directly to $\mathscr{H}_{CT}$ and offer a variety of tests. The additional feature of long-range Coulomb interactions, various electronic polarization effects, and electron–phonon interactions are neglected in Hubbard models, but can in principle be partially included in $\mathscr{H}_{CT}$ by permitting a deformable lattice and by including additional electronic features discussed in Section 5. The reduction of $\mathscr{H}_{CT}$ to various spin systems in the limit of weak overlap and strong correlations ($t \ll U$) plays a central role in the magnetic properties of the semiconducting and insulating CT and FR crystals.

As has been emphasized throughout, $\mathscr{H}_{CT}$ is the simplest general Hamiltonian for the electronic states of molecular crystals in which a CT excitation occurs below any Frenkel excitation. The site representation of $\mathscr{H}_{CT}$ provides a typical phenomenological model: it is clearly related to both accurate molecular quantum mechanics and to observed optical, electric, and magnetic properties. Detailed comparisons must, however, await developments in the quantum theory of intermolecular forces, as well as in the experimental techniques for studying π-molecular CT crystals. Refinements and extensions may safely be anticipated in view of current interest in organic photoconductors, in highly conducting organic solids, and in low-dimensional magnetic systems.

Acknowledgments

We thank Drs. A. J. Silverstein, R. C. Hughes, W. A. Seitz, and Professor F. A. Matsen for many valuable discussions, criticisms, and assistance in the preparation of this manuscript. The financial support of the National Science Foundation and of the Alfred P. Sloan Foundation is gratefully acknowledged.

References

1. H. A. Benesi and J. H. Hildebrand, *J. Am. Chem. Soc.* **71**, 2703 (1949).
2. R. S. Mulliken, *J. Am. Chem. Soc.* **74**, 811 (1952); note added in proof, *ibid.*, **72**, 600 (1950); *J. Phys. Chem. Ithaca* **56**, 801 (1952); *J. Chim. Phys.* **61**, 20 (1964).
3. R. Foster, *Organic Charge Transfer Complexes*, Academic, New York (1969).
4. R. S. Mulliken and W. B. Person, *Molecular Complexes: A Lecture and Reprint Volume*, Wiley, New York (1969).
5. J. Rose, *Molecular Complexes*, Pergamon, Oxford (1967).
6. M. W. Hanna and J. L. Lippert, in *Molecular Complexes*, Vol. I, (R. Foster, ed.), pp. 1–48, Crane, Russak and Co., New York (1973).
7. M. J. S. Dewar and C. C. Thompson, Jr., *Tetrahedron Suppl.* **7**, 97 (1966).
8. G. Briegleb, *Electron-Donator-Acceptor-Komplexe*, Springer-Verlag, Berlin (1961).
9. F. H. Herbstein, in *Perspectives in Structural Chemistry*, Vol. IV, (J. D. Dunitz and J. A. Ibers, eds.), pp. 166–395, Wiley, New York (1971).
10. C. K. Prout and B. Kamenar, in *Molecular Complexes*, Vol. I, (R. Foster, ed.), pp. 151–208, Crane, Russak, and Co., New York (1973).
11. C. K. Prout and J. D. Wright, *Angew. Chem. Int. Ed. Engl.* **7**, 659 (1968).
12. K. Nakamoto, *J. Am. Chem. Soc.* **74**, 390, 392, 1739 (1952).
13. Y. Ohashi, H. Iwasaki, and Y. Saito, *Bull. Chem. Soc. Jpn.* **40**, 1789 (1967).
14. F. Gutmann and L. E. Lyons, *Organic Semiconductors*, Wiley, New York (1967).
15. D. P. Craig and S. H. Walmsley, *Excitons in Molecular Crystals*, Benjamin, New York (1968); R. S. Knox, *Theory of Excitons*, Academic, New York (1963).
16. G. W. Robinson, *Ann. Rev. Phys. Chem.* **21**, 429 (1970); R. M. Hochstrasser, **17**, 457 (1966); O. Schnepp, **14**, 35 (1963).
17. S. A. Rice and J. Jortner, in *Physics and Chemistry of the Organic Solid State*, Vol. III, (D. Fox, M. M. Labes, and A. Weissberger, eds.), pp. 199–497, Interscience, New York (1967).
18. A. S. Davydov, Theory of Molecular Excitons, Plenum, New York (1971).
19. R. Foster and T. J. Thompson, *Trans. Faraday Soc.* **59**, 296 (1963).
20. Y. Matsunaga, *J. Chem. Phys.* **41**, 1609 (1964); **42**, 1982 (1965).
21. H. M. McConnell, B. M. Hoffman, and R. M. Metzger, *Proc. Natl. Acad. Sci. USA* **53**, 46 (1965).
22. P. J. Strebel and Z. G. Soos, *J. Chem. Phys.* **53**, 4077 (1970).
23. P. L. Nordio, Z. G. Soos, and H. M. McConnell, *Ann. Rev. Phys. Chem.* **17**, 237 (1966).
24. Z. G. Soos, *Ann. Rev. Phys. Chem.* **25**, 121 (1974).
25. D. J. Klein and Z. G. Soos, *Mol. Phys.* **20**, 1013 (1971).
26. I. F. Shchegolev, *Phys. Status Solid: A* **12**, 4 (1972).
27. H. R. Zeller, *Adv. Sol. State Phys.* **13**, 31 (1973).
28. L. R. Melby, R. J. Harder, W. R. Hertler, W. Mahler, R. E. Benson, and W. E. Mochel, *J. Am. Chem. Soc.* **84**, 3374 (1962).
29. J. J. André, J. Clementz, R. Jesser, and G. Weill, *Comptes Rendu* **266**, 1057 (1968); J. J. André and G. Weill, **269**, 499 (1969).
30. K. Hausser and J. N. Murrell, *J. Chem. Phys.* **27**, 500 (1957).
31. C. J. Fritchie, Jr., and P. Arthur, Jr., *Acta Crystallogr.* **21**, 139 (1966).
32. Y. Iida, *Bull. Chem. Soc. Jpn.* **42**, 637 (1969).
33. A. W. Hanson, *Acta Crystallogr. B* **24**, 768 (1968).

34. O. H. LeBlanc, Jr., in *Physics and Chemistry of the Organic Solid State*, Vol. III, (D. Fox, M. M. Labes, and A. Weissberger, eds.), pp. 133–198, Interscience, New York (1967).
35. W. J. Siemons, P. E. Bierstedt, and R. G. Kepler, *J. Chem. Phys.* **39**, 3523 (1963).
36. J. P. Ferraris, D. O. Cowan, V. Walatka, Jr., and J. H. Perlstein, *J. Am. Chem. Soc.* **95**, 948 (1973); L. B. Coleman, M. J. Cohen, D. J. Sandman, F. G. Yamagishi, A. F. Garito, and A. J. Heeger, *Sol. State Commun.* **12**, 1125 (1973).
37. D. E. Schafer, F. Wudl, G. A. Thomas, J. P. Ferraris, and D. O. Cowan, *Sol. State Commun.* **14**, 347 (1974).
38. L. R. Melby, *Can. J. Chem.* **43**, 1448 (1965).
39. A. J. Epstein, S. Etemad, A. F. Garito, and A. J. Heeger, *Phys. Rev. B* **5**, 952 (1972); L. B. Coleman, J. A. Cohen, A. F. Garito, and A. J. Heeger, *Phys. Rev. B* **7**, 2122 (1973).
40. H. J. Keller, ed., *Low Dimensional Cooperative Phenomena*, Plenum, New York (1975), L. V. Interrante, ed., *Extended Interactions between Metal Ions in Transition Metal Complexes*, A. C. S. Symposium Series No. 5 (1974).
41. E. M. Engler and V. V. Patel, *J. Amer. Chem. Soc.* **96**, 7376 (1974); K. Bechgaard, D. O. Cowan, and A. N. Bloch, *Chem. Commun.*, 937 (1974).
42. R. L. Greene, G. B. Street, and L. J. Sater, *Phys. Rev. Lett.* **34**, 577 (1975).
43. F. Wudl, ed., *Highly Conducting Organic Materials*, Academic Press, New York (1977).
44. J. Hubbard, *Proc. R. Soc. London A* **276**, 238 (1963); *A* **277**, 237 (1964); 401 (1964).
45. J. H. Van Vleck, in *Quantum Theory of Atoms, Molecules, and the Solid State*, (P. O. Löwdin, ed.), pp. 475–484, Academic, New York (1966).
46. N. F. Mott, *Proc. R. Soc. London* **62**, 416 (1949); *Ad. Phys.* **13**, 325 (1964); *Rev. Mod. Phys.* **40**, 677 (1968).
47. D. Adler, in *Solid State Physics*, Vol. 21, (F. Seitz, D. Turnbull, and H. Ehrenreich, eds.), pp. 1–113, Academic, New York (1968).
48. C. Herring, in *Magnetism, IV: Exchange Interactions Among Itinerant Electrons* (G. T. Rado and H. Suhl, eds.), Academic Press, New York (1966).
49. P. W. Anderson, in *Solid State Physics*, Vol. 14, (F. Seitz and D. Turnbull, eds.), pp. 99-214, Academic, New York (1963).
50. Z. G. Soos and P. J. Strebel, *J. Am. Chem. Soc.* **93**, 3325 (1971).
51. O. H. LeBlanc, Jr., *J. Chem. Phys.* **42**, 4307 (1965).
52. A. A. Ovchinnikov, I. I. Ukranski, and G. V. Kventsel, *Usp. Fiz. Nauk* **108**, 81 (1972); English translation: *Sov. Phys. Uspekhi* **15**, 575 (1973).
53. J. Linderberg and Y. Öhrne, *Propagators in Quantum Chemistry*, Academic, New York (1973).
54. G. F. Kokoszka and R. W. Duerst, *Coord. Chem. Rev.* **5**, 209 (1970).
55. K. W. Plumlee, B. M. Hoffman, J. A. Ibers, and Z. G. Soos, *J. Chem. Phys.* **63**, 1926 (1975); J. A. McCleverty, *Progr. Inorg. Chem.* **10**, 49 (1968).
56. Y. Iida and Y. Matsunaga, *Bull. Chem. Soc. Jpn.* **41**, 2615 (1968).
57. Y. Iida, *Bull. Chem. Soc. Jpn.* **42**, 71 (1969).
58. Y. Iida, *Bull. Chem. Soc. Jpn.* **43**, 2772 (1970).
59. S. Hiroma, H. Kuroda, and H. Akamatu, *Bull. Chem. Soc. Jpn.* **44**, 9 (1971).
60. Y. Sato, M. Kinoshita, M. Sano, and H. Akamatu, *Bull. Chem. Soc. Jpn.* **43**, 2370 (1970).
61. H. Kuroda, S. Hiroma, and H. Akamatu, *Bull. Chem. Soc. Jpn.* **41**, 2855 (1968).

62. T. Amano, H. Kuroda, and H. Akamatu, *Bull. Chem. Soc. Jpn.* **41**, 83 (1968).
63. T. Sakata and S. Nagakura, *Bull. Chem. Soc. Jpn.* **42**, 1497 (1969).
64. H. W. Offen, in *Molecular Complexes*, Vol. I. (R. Foster, ed.), pp. 117–149, Crane, Russak, and Co., New York (1973).
65. J. Kommandeur, in *Physics and Chemistry of the Organic Solid State*, Vol. II, (D. Fox, M. M. Labes, and A. Weissberger, eds.), pp. 1–67, Interscience, New York (1965).
66. Z. G. Soos, *J. Chem. Phys.* **46**, 4284 (1967).
67. Z. G. Soos, in *Low-Dimensional Cooperative Phenomena*, (H. J. Keller, ed.), pp. 45–64, Plenum, New York (1975).
68. D. W. Hone and P. M. Richards, *Ann. Rev. Mat. Sci.* **4**, 337 (1974).
69. L. J. DeJongh and A. R. Miedema, *Adv. Phys.* **23**, 1 (1974).
70. R. E. Dietz, F. R. Merritt, R. Dingle, D. Hone, B. G. Silbernagel, and P. M. Richards, *Phys. Rev. Lett.* **26**, 1186 (1971).
71. R. Colton and J. H. Canterford, *Halides of the First Row Transition Metals*, Wiley-Interscience, London (1969).
72. W. E. Hatfield and R. Whyman, *Transition Met. Chem.* **5**, 47 (1969); N. Kato, H. B. Jonassen, and J. C. Fanning, *Chem. Rev.* **64**, 99 (1964).
73. G. F. Kokoszka and G. Gordon, *Transition Met. Chem.* **5**, 181 (1969).
74. R. L. Martin, in *New Pathways of Inorganic Chemistry*, (E. A. V. Ebsworth, A. G. Maddock, and A. G. Sharpe, eds.), Chapter 9, Cambridge University Press, Cambridge (1968).
75. E. Sinn, *Coord. Chem. Rev.* **5**, 313 (1970).
76. A. P. Ginsberg, *Inorg. Chim. Acta Rev.* **5**, 45 (1971).
77. K. Krogmann, *Angew. Chem. Int. Ed. Eng.* **8**, 35 (1969).
78. I. G. Austin and N. F. Mott, *Adv. Phys.* **18**, 41 (1969).
79. D. Emin, in *Electric and Structural Properties of Amorphous Semiconductors*, (P. G. LeCombre and J. Mort, eds.), pp. 261–329, Academic, New York (1973).
80. A. J. Heeger and A. F. Garito, in *Low-Dimensional Cooperative Phenomena*, (H. J. Keller, ed.), pp. 89–124, Plenum, New York (1975).
81. Z. G. Soos and D. J. Klein, in *Molecular Association*, (R. Foster, ed.), pp. 1–109, Academic Press, New York (1975).
82. D. C. Mattis, *The Theory of Magnetism*, pp. 45–55, Harper and Row, New York (1965).
83. R. H. Boyd and W. D. Phillips, *J. Chem. Phys.* **43**, 2927 (1965).
84. S. Nakayama and K. Suzuki, *Bull. Chem. Soc. Jpn.* **46**, 3694 (1973).
85. C. Herring, in *Magnetism*, Vol. II. B., (G. T. Rado and H. Suhl, eds.), pp. 1–185, Academic Press, New York (1963).
86. J. N. Murrell, M. Randic, and D. R. Williams, *Proc. R. Soc. London A* **284**, 566 (1965).
87. J. L. Lippert, M. W. Hanna, and P. J. Trotter, *J. Am. Chem. Soc.* **91**, 4035 (1968); M. W. Hanna and D. E. Williams, **90**, 5358 (1968); M. W. Hanna, **90**, 285 (1967).
88. P. R. Certain and L. W. Bruch, in *International Review of Science, Physical Chemistry, Series One, Volume 1, Theoretical Chemistry* (A. D. Buckingham and W. Byers Brown, eds.), pp. 113–165, Butterworth and Co., London (1972).
89. D. M. Chipman, J. D. Bowman, and J. O. Hirschfelder, *J. Chem. Phys.* **59**, 2830 (1973).
90. J. O. Hirschfelder, C. F. Curtis, and R. B. Bird, *Molecular Theory of Gases and Liquids*, Wiley, New York (1954).

91. H. Margenau and N. R. Kestner, *Theory of Intermolecular Forces*, Pergamon, New York (1969).
92. A. D. Buckingham and B. D. Utting, *Ann. Rev. Phys. Chem.* **21**, 287 (1970).
93. R. J. W. Le Fevre, D. V. Radford, and P. J. Stiles, *J. Chem. Soc.* **1968B**, 1297 (1968).
94. E. G. Cooke and J. C. Schug, *J. Chem. Phys.* **53**, 723 (1970).
95. P. O. Löwdin, *J. Chem. Phys.* **18**, 365 (1950).
96. I. Fischer-Hjalmers, *J. Chem. Phys.* **42**, 1962 (1965).
97. J. Hubbard, *Proc. R. Soc. London A* **285**, 542 (1965).
98. V. M. Agranovich, *Sov. Phys. JETP* **10**, 307 (1960); V. M. Agranovich and Y. M. Konobeev, *Sov. Phys. Solid State* **3**, 260 (1961).
99. R. Hoffman, *Radiat. Res.* **20**, 140 (1963).
100. J. I. Krugler, C. G. Montgomery, and H. M. McConnell, *J. Chem. Phys.* **41**, 2421 (1964).
101. D. M. Hanson, *CRC Crit. Rev. Solid State Sci.* **3**, 243 (1973).
102. M. Moshinsky, *Group Theory and the Many-Body Problem* Gordon and Breach, New York (1968); B. G. Wybourne, *Symmetry Principles and Atomic Spectroscopy*, Wiley, New York (1970).
103. J. Hubbard, *Proc. R. Soc.* **A 296**, 82 (1967); D. J. Klein, *J. Chem. Phys.* (in press).
104. J. Kommandeur and G. T. Pott, *Mol. Phys.* **11**, 93 (1966).
105. M. Tosi, in *Solid State Physics*, Vol. 16 (F. Seitz and D. Turnbull, eds.), pp. 1–120, Academic, New York (1964).
106. R. M. Metzger, *J. Chem. Phys.* **57**, 1870, 1876 (1972).
107. R. M. Metzger, *J. Chem. Phys.* **57**, 2218 (1972).
108. Z. G. Soos and A. J. Silverstein, *Mol. Phys.* **23**, 775 (1972).
109. A. D. McLachlan, *Mol. Phys.* **1**, 233 (1958); R. M. Metzger, Ph.D. Thesis, Cal. Inst. Tech. (1970) (unpublished), Tables I–VIII in Chapter II.
110. P. H. Rieger and G. K. Fraenkel, *J. Chem. Phys.* **37**, 2795 (1962); J. R. Bolton, A. Carrington, and J. Dos Santos-Veiga, *Mol. Phys.* **5**, 615 (1962); A. Carrington, *Quarterly Reviews* **17**, 67 (1963).
111. R. M. Metzger and A. N. Bloch, *J. Chem. Phys.* **63**, 5098 (1975); A. J. Epstein, N. O. Lipari, D. J. Sandman, and P. Nielsen, *Phys. Rev. B*, in press.
112. C. Kittel, *Quantum Theory of Solids*, Wiley, New York (1963).
113. P. W. Anderson, *Concepts in Solids*, Benjamin, New York (1963).
114. T. Sakata and S. Nagakura, *Bull. Chem. Soc. Jpn.* **43**, 1346 (1970).
115. J. Kommandeur and F. R. Hall, *J. Chem. Phys.* **34**, 129 (1961).
116. L. S. Singer and J. Kommandeur, *J. Chem. Phys.* **34**, 133 (1961).
117. H. M. McConnell and R. Lynden-Bell, *J. Chem. Phys.* **36**, 2393 (1962).
118. D. B. Chesnut and W. D. Phillips, *J. Chem. Phys.* **35**, 1002 (1961).
119. M. T. Jones and D. B. Chesnut, *J. Chem. Phys.* **38**, 1311 (1963); M. T. Jones, **40**, 1837 (1964); D. B. Chesnut and P. Arthur, Jr., **36**, 2969 (1962).
120. R. G. Kepler, *J. Chem. Phys.* **39**, 3528 (1963).
121. D. D. Thomas, H. Keller, and H. M. McConnell, *J. Chem. Phys.* **39**, 2321 (1963).
122. D. D. Thomas, A. W. Merkl, A. F. Hildebrandt, and H. M. McConnell, *J. Chem. Phys.* **40**, 2588 (1964).
123. A. N. Bloch, R. B. Weisman, and C. M. Varma, *Phys. Rev. Lett.* **28**, 753 (1972); J. H. Perlstein, M. J. Minot, and V. Walatka, Jr., *Mat. Res. Bull.* **7**, 309 (1972).
124. A. N. Bloch, in *Charge and Energy Transfer in Organic Semiconductors* (M. Masuda and M. Silver, eds.), p. 159, Plenum, New York (1974); A. N. Bloch, D. O. Cowan, and T. O. Poehler, p. 167 (1974).

125. M. J. Hove, B. M. Hoffman, and R. J. Loyd, *J. Phys. Chem.* **76**, 1849 (1972).
126. W. Duffy, Jr., J. F. Dubach, P. A. Pianetta, J. F. Deck, D. L. Strandburg, and A. R. Miedema, *J. Chem. Phys.* **56**, 2555 (1972); W. Duffy, Jr., and D. L. Strandburg, *J. Chem. Phys.* **46**, 456 (1967).
127. M. Mukai, N. Azuma, and K. Ishizu, *Bull. Chem. Soc. Jpn.* **43**, 3618 (1970).
128. A. Hoekstra, T. Spoelder, and A. Vos, *Acta Crystallogr. B* **28**, 14 (1970).
129. I. Shirotani and H. Kobayashi, *Bull. Chem. Soc. Jpn.* **46**, 2595 (1973).
130. C. J. Fritchie, Jr., *Acta Crystallogr.* **20**, 892 (1965).
131. L. B. Coleman, S. K. Khanna, A. F. Garito, A. J. Heeger, and B. Morosin, *Phys. Lett.* **42** *A*, 15 (1972); B. Morosin, *Acta Crystallog.*, in press.
132. M. Konno, H. Kobayashi, F. Marumo, and Y. Saito, *Bull. Chem. Soc. Jpn.* **46**, 1987 (1973).
133. J. G. Vegter, T. Hibma, and J. Kommandeur, *Chem. Phys. Lett.* **3**, 427 (1969).
134. Y. Iida, *J. Chem. Phys.* **59**, 1607 (1972); *Bull. Chem. Soc. Jpn.* **46**, 320 (1972); **43**, 3685 (1970); **44**, 3344 (1971).
135. N. Sakai, I. Shirotani, and S. Minomura, *Bull. Chem. Soc. Jpn.* **45**, 3321 (1972).
136. J. L. DeBoer and A. Vos, *Acta Crystallogr. B* **28**, 835 (1972).
137. J. L. DeBoer and A. Vos, *Acta Crystallogr. B* **28**, 839 (1972).
138. B. G. Anex and E. B. Hill, Jr., *J. Am. Chem. Soc.* **88**, 3648 (1966).
139. S. Hiroma and H. Kuroda, *Bull. Chem. Soc. Jpn.* **46**, 3645 (1973).
140. V. Walatka, Jr., and J. H. Perlstein, *Mol. Cryst. Liq. Cryst.* **15**, 269 (1971).
141. A. R. Blythe, M. R. Boon, and P. G. Wright, *Discuss. Faraday Soc.* **51**, 110 (1971).
142. R. E. Rundle, *J. Phys. Chem.* **61**, 45 (1957); J. R. Miller, *Adv. Inorg. Chem. Radiochem.* **4**, 133 (1962); *J. Chem. Soc.* 713 (1965).
143. P. S. Gomm, T. W. Thomas, and A. E. Underhill, *J. Chem. Soc.* (*A*) 2154 (1971); P. Day, A. F. Orchard, A. J. Thomson, and R. J. P. Williams, *J. Chem. Phys.* **43**, 3763 (1965).
144. L. V. Interrante, *J. Chem. Soc. Chem. Commun.* 302 (1972).
145. L. V. Interrante and R. P. Messmer, *Inorg. Chem.* **10**, 1174 (1971); L. V. Interrante and F. B. Bundy, *Inorg. Chem.* **10**, 1169 (1971).
146. A. W. Hanson, *Acta. Crystallogr.* **19**, 610 (1965).
147. J. L. DeBoer and A. Vos, *Acta Crystallogr. B* **24**, 720 (1967).
148. R. C. Hughes and Z. G. Soos, *J. Chem. Phys.* **48**, 1066 (1968).
149. M. Kinoshita and H. Akamatu, *Nature* **207**, 291 (1965).
150. B. M. Hoffman and R. C. Hughes, *J. Chem. Phys.* **52**, 4011 (1970); *Solid State Commun.* **7**, 895 (1969).
151. M. Ohmasa, M. Kinoshita, M. Sano, and H. Akamatu, *Bull. Chem. Soc. Jpn.* **41**, 1998 (1968).
152. G. T. Pott and J. Kommandeur, *Mol. Phys.* **13**, 373 (1967).
153. A. Ottenberg, C. Hoffman, and J. Osiecki, *J. Chem. Phys.* **38**, 1898 (1963).
154. K. Hatano, Y. Fujita, and T. Kwan, *Bull. Chem. Soc. Jpn.* **43**, 3022 (1970).
155. H. Masai, K. Sonogashira, and N. Hagihara, *J. Organometal Chem.* **34**, 397 (1972).
156. V. Y. Krivnov and A. A. Ovchinnikov, *Fiz. Tver. Tela* **15**, 172 (1973); English translation: *Sov. Phys. Solid State* **15**, 118 (1973).
157. W. H. Bentley and H. G. Drickamer, *J. Chem. Phys.* **42**, 1573 (1965).

158. R. C. Hughes, Ph.D. Thesis, Standford University, 1966 (unpublished); A. W. Merkl, R. C. Hughes, L. J. Berliner, and H. M. McConnell, *J. Chem. Phys.* **43**, 953 (1965); R. C. Hughes, A. W. Merkl, and H. M. McConnell, *J. Chem. Phys.* **44**, 1720 (1966).
159. D. E. Williams, *J. Am. Chem. Soc.* **89**, 4280 (1967).
160. K. Inokuchi, Y. Harada, and Y. Maruyama, *Bull. Chem. Soc. Jpn.* **35**, 1559 (1962).
161. D. J. Klein, W. A. Seitz, M. A. Butler, and Z. G. Soos, unpublished (1973).
162. D. Cabib and T. A. Kaplan, *Phys. Rev.* 7 *B*, 2199 (1973).
163. N. Sakai, I. Shirotani, and S. Minomura, *Bull. Chem. Soc. Jpn.* **45**, 3314 (1972).
164. G. T. Pott and J. Kommandeur, *J. Chem. Phys.* **47**, 395 (1967).
165. J. J. André and G. Weill, *Chem. Phys. Lett.* **9**, 27 (1971).
166. J. L. DeBoer, A. Vos, and K. Huml, *Acta Crystallogr. B* **24**, 542 (1968).
167. J. Tanaka, M. Inoue, M. Mizuno, and K. Horai, *Bull. Chem. Soc. Jpn.* **43**, 1998 (1970).
168. D. B. Chesnut, *J. Chem. Phys.* **40**, 405 (1964).
169. M. A. Butler. F. Wudl, and Z. G. Soos, *Phys. Rev. B* **12**, 4708 (1975).
170. Z. G. Soos, in *Highly Conducting Organic Materials*, (F. Wudl, ed.), Academic Press, New York (1976).
171. R. E. Peierls, *Quantum Theory of Solids*, p. 108, Oxford University Press (1955); M. Menyhard and J. Solyom, *J. Low Temp. Phys.* **12**, 529 (1973); J. Solyom, 547.
172. D. B. Chesnut, *J. Chem. Phys.* **45**, 4677 (1966); P. Pincus, *Solid State Commun.* **9**, 1971 (1971); G. Beni and P. Pincus, *J. Chem. Phys.* **57**, 3531 (1973).
173. H. Chihara, M. Nakamura, and S. Seki, *Bull. Chem. Soc. Jpn.* **38**, 1776 (1965).
174. J. W. Bray, H. R. Hart, Jr., L. V. Interrante, I. S. Jacobs, J. S. Kasper, G. D. Watkins, S. H. Wee, and J. C. Bonner, *Phys. Rev. Lett.* **35**, 744 (1975).
175. D. B. Chesnut and R. W. Mosely, *Theoret. Chim. Acta* (Berlin) **13**, 230 (1969).
176. T. Sundaresan and S. C. Wallwork, *Acta Crystallogr. B* **28**, 3507 (1972).
177. M. J. Hove, B. M. Hoffman, and J. A. Ibers, *J. Chem. Phys.* **56**, 3490 (1972).
178. G. R. Anderson and C. J. Fritchie, Jr., Paper 111, Second National Meeting, Society for Applied Spectroscopy, San Diego (1963).
179. J. C. Bailey and D. B. Chesnut, *J. Chem. Phys.* **51**, 5118 (1969).
180. T. Hibma, P. Dupuis, and J. Kommandeur, *Chem. Phys. Lett.* **15**, 17 (1972).
181. H. Kobayashi, F. Marumo, and Y. Saito, *Acta Crystallogr. B* **27**, 373 (1970).
182. P. Goldstein, K. Seff, and K. N. Trueblood, *Acta Crystallogr. B* **24**, 778 (1968).
183. R. P. Shibaeva, L. O. Atovmyan, and M. N. Orfanov, *J. Chem. Soc. Chem. Commun.* 1494 (1969).
184. S. Flandrois, J. Amiell, F. Carmona, and P. Delhaes, *Sol. State Commun.* **17**, 287 (1975).
185. H. Kobayashi, Y. Ohashi, F. Marumo, and Y. Saito, *Acta Crystallogr. B* **26**, 459 (1970); A. T. McPhail, G. M. Semeniuk, and D. B. Chesnut, *J. Chem. Soc. A*, 2174 (1971).
186. H. Kobayashi, *Bull. Chem. Soc. Jpn.* **48**, 1373 (1975).
187. B. Morosin, *Phys. Lett.* **53** *A*, 455 (1975).
188. T. Kistenmacher, T. E. Phillips, and D. O. Cowan, *Acta Crystallogr. B* **30**, 763 (1974).

189. F. Wudl and E. W. Southwick, *J. Chem. Soc. Chem. Commun.* 254 (1974); S. J. LaPlaca, P. W. R. Corfield, R. Thomas, and B. A. Scott, *Solid State Commun.* **17**, 635 (1975); R. B. Somoano, A. Gupta, V. Hadek, T. Datta, M. Jones, R. Deck, and A. M. Herman, *J. Chem. Phys.* **63**, 4970 (1975).
190. M. A. Butler, J. P. Ferraris, A. N. Bloch, and D. O. Cowan, *Chem. Phys. Lett.* **24**, 600 (1974).
191. W. D. Grobman, R. A. Pollak, D. E. Eastman, E. T. Mass, Jr., and B. A. Scott, *Phys. Rev. Lett.* **32**, 534 (1974); A. J. Epstein, N. O. Lipari, P. Nielsen, and D. J. Sandman, Comments in *Phys. Rev. Lett.* **34**, 914 (1975).
192. P. Coppens, *Phys. Rev. Lett.* **35**, (1975).
193. D. N. Fedutin, I. F. Shchegolev, V. B. Stryukov, E. B. Yagubskii, A. V. Zvarykina, L. O. Atovmyan, V. F. Kaminskii, and R. P. Shibaeva, *Phys. Status Solidi B* **48**, 87 (1971).
194. E. B. Yagubskii, M. L. Khidekel, I. F. Shchegolev, L. I. Buravov, B. G. Gribov, and K. M. Makova, *Izv. Akad. Nauk SSSR, Ser Khim.* 2124 (1968).
195. Somoano, V. Hadek, S. P. S. Yen, A. Rembaum, and R. Deck, *J. Chem. Phys.* **62**, 1061 (1975).
196. J. B. Torrance, B. A. Scott, and F. Kaufman, *Solid State Commun.* **17**, 1369 (1975).
197. J. C. Scott, A. F. Garito, and A. J. Heeger, *Phys. Rev. B* **10**, 3131 (1974).
198. Y. Tomkiewicz, B. A. Scott, L. J. Tao, and R. S. Title, *Phys. Rev. Lett.* **32**, 1363 (1974); Y. Tomkiewicz (private communication).
199. J. P. Farges and A. Brau, *Phys. Status Solidi B* **64**, 269 (1974); A. Brau, P. Bruesch, J. P. Farges, A. Hinz, and D. Kuse, *Phys. Stat. Sol.* (b) **62**, 615 (1974); A. Brau and J. P. Farges, *Phys. Stat. Sol.* (b) **61**, 257 (1974).
200. J. P. Farges, Thesis, University of Nice (1974) (unpublished).
201. Z. G. Soos and D. J. Klein, *J. Chem. Phys.* **55**, 3284 (1971).
202. T. Sundaresan and S. C. Wallwork, *Acta Crystallogr. B* **28**, 491 (172).
203. M. Konno and Y. Saito, *Acta Crystallogr. B* **29**, 2815 (1973).
204. Y. Suzuki and Y. Iida, *Bull. Chem. Soc. Jpn.* **46**, 2056 (1973).
205. J. M. Ziman, *Electrons and Phonons*, Chapter V, Clarendon, Oxford (1960).
206. Z. G. Soos and H. M. McConnell, *J. Chem. Phys.* **43**, 3780 (1965).
207. P. Pincus, *Solid State Commun.* **11**, 51 (1972); G. Beni, P. Pincus, and J. Kanamori, *Phys. Rev. B* **10**, 1896 (1974).
208. J. G. Vegter and J. Kommandeur, *Phys. Rev. B* **8**, 2887 (1973).
209. P. M. Chaikin, A. F. Garito, and A. J. Heeger, *J. Chem. Phys.* **58**, 2336 (1973); *Phys. Rev. B* **5**, 4966 (1972).
210. U. Bernstein and G. Beni, *Phys. Rev. B*, in press (1976).
211. R. W. Munn and W. Siebrand, *J. Chem. Phys.* **52**, 47 (1970); B. R. Henry and M. Kasha, *Ann. Rev. Phys. Chem.* **19**, 161 (1968).
212. H. Kuroda, T. Kunii, S. Hiroma, and H. Akamatu, *J. Mol. Spect.* **22**, 60, (1967).
213. A. J. Berlinsky, J. F. Carolan, and L. Weiler, *Solid State Commun.* **15**, 795 (1974).
214. J. B. Torrance, private communication.
215. G. R. Anderson and J. P. Devlin, *J. Phys. Chem.* **79**, 1100 (1975); G. R. Anderson and R. L. McNeely, Paper R5, Symposium on Molecular Structure and Spectroscopy, Ohio State University (1963); Z. Iqbal, C. W. Christoe, and D. K. Dawson, *J. Chem. Phys.* **63**, 4485 (1975).
216. M. A. Maréchal and H. M. McConnell, *J. Chem. Phys.* **43**, 497 (1965).
217. G. J. Ashwell, S. C. Wallwork, S. R. Baker, and P. I. C. Berthier, *Acta Crystallogr. B* **31**, 1174 (1975).

218. A. J. Silverstein and Z. G. Soos, *Chem. Phys. Letters*, in press.
219. T. Z. Huang, R. P. Taylor, and Z. G. Soos, *Phys. Rev. Lett.* **28**, 1054 (1972).
220. R. C. Hughes, B. Morosin, and P. M. Richards, *Phys. Rev. B* **11**, 1795 (1975); P. M. Richards in *Low-Dimensional Cooperative Phenomena*, (H. J. Keller, ed.), pp. 147–169, Plenum, New York (1975); T. Z. Huang and Z. G. Soos, *Phys. Rev. B* **9**, 4981 (1974); Z. G. Soos, T. Z. Huang, J. S. Valentine, and R. C. Hughes, *Phys. Rev. B* **8**, 993 (1973).
221. F. Devreux and M. Nechtschein, *Solid State Commun.* **16**, 275 (1975).
222. M. A. Butler, L. R. Walker, and Z. G. Soos, *J. Chem. Phys.*, in press.
223. G. Giacometti, P. L. Nordio, and M. V. Favan, *Theor. Chim. Acta* **1**, 404 (1963); D. A. Lowitz, *J. Chem. Phys.* **46**,4698 (1967); H. J. Monkhorst and J. Kommandeur, *J. Chem. Phys.* **47**, 391 (1967); H. T. Jonkman and J. Kommandeur, *Chem. Phys. Lett.* **15**, 496 (1972); P. S. Bagus, I. P. Batra, and E. Clementi, *Chem. Phys. Lett.* **23**, 305 (1973); A. Bieber and J. J. Andre, *Chem. Phys.* **5**, 166 (1974); H. T. Jonkman, G. A. Van der Welde, and W. C. Nieuwport, *Chem. Phys. Lett.* **25**, 62 (1974); F. Herman, A. R. Williams and K. H. Johnson, *J. Chem. Phys.* **61**, 3508 (1974); F. Herman and I. P. Batra, *Phys. Rev. Lett.* **33**, 94 (1974).
224. D. B. Chesnut and P. E. S. Wormer, *Theor. Chim. Acta* **20**, 250 (1971); M. Ratner, J. R. Sabin, and E. E. Ball, *Mol. Phys.* **26**, 1177 (1973); J. Ladik, A. Karpfen, G. Stollhoff, and F. Fulde, *Chem. Phys.* **7**, 267 (1975); A. Bieber and J. J. Andre, *Chem. Phys.* **7**, 137 (1975).
225. A. Karpfen, J. Ladik, G. Stollhoff, and P. Fulde, *Chem. Phys. Lett.* **31**, 291 (1975); *Chem. Phys.* **8**, 215 (1975).
226. P. E. S. Wormer and Ad Van der Avoird, *J. Chem. Phys.* **62**, 3326 (1975).
227. A. B. Harris and R. V. Lange, *Phys. Rev.* **157**, 295 (1967), D. M. Esterling, *Phys. Rev. B* **2**, 4686 (1970); D. R. Penn, *Phys. Lett. A* **26**, 509 (1968); W. Brinkman and T. M. Rice, *Phys. Rev. B* **2**, 1324 (1970).
228. J. H. Choi, R. P. Messmer, and W. R. Thorson, *J. Chem. Phys.* **57**, 238 (1972); E. H. Lieb, T. D. Schultz, and D. C. Mattis, *Ann. Phys.* **16**, 407 (1961).
229. E. H. Lieb and F. Y. Wu, *Phys. Rev. Lett.* **20**, 1445 (1968).
230. E. C. Kemble, *Fundamentals of Quantum Mechanics*, p. 395, Dover, New York (1937); H. Primas, *Helv. Phys. Acta* **34**, 331 (1961); D. J. Klein, *J. Chem. Phys.* **61**, 986 (1974).
231. F. A. Matsen and D. J. Klein, *J. Phys. Chem.* **75**, 1860 (1971).
232. T. Arai, *Phys. Rev.* **134**, A824 (1964); W. J. Mullin, *Phys. Rev.* **136**, 1126 (1964).
233. B. C. Carlson and J. M. Keller, *Phys. Rev.* **105**, 102 (1957).
234. D. J. Klein and W. A. Seitz, *Phys. Rev. B* **10**, 3217 (1974).
235. W. T. Borden, *Modern Molecular Orbital Theory*, Prentice-Hall, Inc., Englewood Cliffs, New Jersey (1975).
236. M. H. Cohen and J. C. Thompson, *Adv. Phys.* **17**, 857 (1968); H. O. Hooper and A. M. De Graaf, *Amorphous Magnetism*, Plenum, New York (1973); P. W. Anderson, *Phys. Rev. Lett.* **34**, 953 (1975).
237. H. Shiba, *Phys. Rev. B* **6**, 930 (1972).
238. A. A. Ovchinnikov, *Sov. Phys. JETP* **30**, 1100 (1970); F. Coll, *Phys. Rev. B* **9**, 2150 (1974).
239. M. Takahashi, *Prog. Theor. Phys.* **42**, 1098 (1969); **43**, 1619 (1970).
240. M. Takahashi, *Prog. Theor. Phys.* **52**, 103 (1974).

241. L. N. Buleavskii, *Sov. Phys. JETP* **24**, 154 (1967); D. J. Klein and W. A. Seitz, *Phys. Rev. B* **8**, 2236 (1973).
242. H. M. McConnell, *Molecular Biophysics*, (B. Pullman, ed.), p. 311, Academic Press, New York (1965); Y. Suezaki, *Phys. Lett.* **38** *A*, 293 (1972); P. Pincus, *Solid State Commun.* **11**, 51 (1972).
243. H. Shiba, *Prog. Theor. Phys.* **48**, 2171 (1972).
244. D. W. Hone and P. Pincus, *Phys. Rev. B* **7**, 4889 (1973).
245. W. A. Seitz and D. J. Klein, *Phys. Rev. B* **9**, 2159 (1974).
246. P. B. Visscher, *Phys. Rev. B* **10**, 932 (1974).
247. J. C. Kimball and J. R. Schreiffer, Proc. of the 7th Conf. on Mag. and Mag. Materials, Chicago, 1971, American Institute of Physics, New York (1975).
248. G. Beni, P. Pincus, and D. Hone, *Phys. Rev. B* **8**, 3389 (1973).
249. L. C. Bartel and H. S. Jarrett, *Phys. Rev. B* **10**, 942 (1974).
250. J. B. Sokoloff, *Phys. Rev. B* **2**, 779 (1970); G. Beni, T. Holstein, and P. Pincus, *Phys. Rev. B* **8**, 312 (1973); D. J. Klein, *Phys. Rev. B* **8**, 3452 (1973); J. Bernasconi, M. J. Rice, W. R. Schneider, and S. Strassler, *Phys. Rev. B* **12**, 1090 (1975).
251. Z. G. Soos, *J. Chem. Phys.* **43**, 1121 (1965); L. N. Buleavskii, *Sov. Phys. JETP* **17**, 684 (1963); D. B. Abraham, *J. Chem. Phys.* **51**, 3795 (1969).
252. W. Duffy and K. P. Barr, *Phys. Rev.* **165**, 647 (1968).
253. R. Lynden-Bell and H. M. McConnell, *J. Chem. Phys.* **37**, 794 (1962); A. B. Harris, *Phys. Rev. B* **8**, 2166 (1973).
254. P. A. Fedders and J. Kommandeur, *J. Chem. Phys.* **52**, 2014 (1970).
255. J. Bardeen, *Solid State Commun.* **13**, 357 (1973); P. Lee, T. M. Rice, and P. W. Anderson, *Phys. Rev. Lett.* **31**, 462 (1973); B. R. Patton and L. J. Sham, *Phys. Rev. Lett.* **31**, 462 (1973); **33**, 638 (1974); H. Fukuyama, T. M. Rice, and C. M. Varma, *Phys. Rev. Lett.* **33**, 305 (1974); D. Allender, J. W. Bray, and J. Bardeen, *Phys. Rev. B* **9**, 119 (1974); M. H. Cohen, J. A. Hertz, P. M. Horne, and V. K. S. Shante, *Int. J. Quantum Chem. S* **8**, 491 (1974).
256. K. Kubo, *J. Phys. Soc. Jpn.* **31**, 30 (1971).
257. I. Sadakata and E. Hanamura, *J. Phys. Soc. Jpn.* **34**, 882 (1973); Y. Suezaki, *J. Phys. Soc. Jpn.* **34**, 89 (1973).
258. R. A. Bari, D. Alder, and R. V. Lange, *Phys. Rev. B* **2**, 2898 (1970).
259. R. E. Peierls, *Quantum Theory of Solids*, p. 108, Oxford University Press (1955); H. Frohlich, *Proc. R. Soc. A* **223**, 296 (1954); C. G. Kuper, *Proc. R. Soc. A* **227**, 214 (1955).

Index

Addition polymers, 342-343
Alkali aluminosilicate glasses, 303
Alkali metal–graphite intercalation compounds, 107-110
β-Al_2O_3, 244-246
β-Alumina, 244-246
Amine intercalation compounds, 110-111
Amorphous films
  CuAg, 31-32, 35
  electrical properties, 30-32
  magnetic properties, 32-34
  structural analysis, 26-30
  transformation kinetics, 35-36
Amorphous phases, 19-36
  alloys, 24-26
  elemental, 20-24
Anthracene, 615-667
  carrier mean free path, 648-651
  crystals, 620-622
  electron and hole generation, 651-661
  electron and hole transport, 645-651, 665-667
  energy bands, 648-9, 654, 665-667
  energy transport in, 631-645
  fluorescence, 627, 629-631, 634-645
  impurity effects, 617, 632-637
  lattice dynamics, 622-623
  mobility of carriers, 645-648, 665-667
  molecules, 618-619
  optical absorption, 623-629
  photoconductivity, 635, 651-661
  singlet excitons, 624-627, 632-637, 656-658, 664
Anthracene *(cont'd)*
  theory of, 661-667
  traps, 648-650
  triplet excitons, 627-629, 638-645, 664
  two-photon processes, 658-659
Antiferromagnetism, 736-743
Atactic polymers, 345
Axialites, 519, 525

$BaO–SiO_2$ glasses, 307-310
Birefringence, 447
Block copolymers, 341, 414-416
Block structures, disorder in, 201-222
B_2O_3 glasses, 299, 301-302
Boron compounds, 95-106
  CeB_6, 104
  hexaborides, 96-106
  icosahedral grouping, 95-96
  LaB_6, 103-104
  octahedral groupings, 96-103
  SmB_6 104-106
Boron-rich phases, 95-106

CaF_2 structures (*see also* Fluorite structures), 223-238
Calcia-stabilized zirconia (CSZ), 242-244
Carbide interstitial phases, 253-284
CeB_6, 104
Ceramic-glass materials, 325-329
Chain ends, 564-565
Chain folding, 362-441, 497-604
  fluctuations of fold period, 592-597
  molecular description, 507-512

Chain folding *(cont'd)*
thermodynamics, 528-541
work of, 587-592
Chalcogenide intercalation compounds, 124-144
alkali metals, 127-131
alkaline earth, 127
layer chalcogenide compounds, 124-127
molecular, 134-144
organic, 134-144
posttransition elements, 131-133
rare earths, 127, 130-131
superconductivity, 130, 137-142
transition elements, 133-134
Charge-transfer complexes, 679-758
antiferromagnetism, 736-743
electrical properties, 712-713, 730-731, 734-736
Hubbard models, 685-687, 689, 691, 700-701, 706-708, 715, 721, 726, 728-731, 744, 753-758
intermolecular forces, 693-696
ion-radical dimer, 690-697
magnetic properties, 713, 731, 736-743
molecular-exciton approach, 681-683
π-molecular ion-radical solids, 683-685
optical properties, 712, 732-734
quantum computations, 743-757
structural features, 708-711, 713-729
theory of, 681-708
C_8K, 107-110
Clathrates, 90-95
electrical properties, 94
heat capacity, 94-95
Close packing, 256-8
Complexes, charge-transfer (*see also* Charge-transfer complexes), 679-758
Complex oxides, 167-248
Copolymers, 340-341
Crystallinity of polymers, 338-357, 497-604
chain folding, 362-441, 497-604
characterization of, 359-362
chemical regularity, 338-343, 500-502
crystal structures, 347-355
curved crystals, 423-435
degree of, 355-357, 524-525
degree lateral growth, 386-393
fold surfaces, 397-416
growth habits, 362-441
intercrystalline links, 504-505, 522
lamellae (*see also* Lamellae), 362-441, 528-597
lateral growth, 386-397, 416-423
molecular weight, 346
multilayered crystals, 381-385
Crystallinity of polymers *(cont'd)*
spherulites, 442-480
stereoregularity, 344-346, 501-502
twinning, 435-441
Crystallization of polymers, 335-605
driving force, 540-541
fold period, 541-565, 584-587
from melt, 441-480, 519-526
from solution, 357-441, 503-528
growth-rate data, 536-584
homogeneous nucleation, 597-604
kinetics (*see also* Kinetics of polymer crystallization), 497-604
morphology, 335-481
nucleation and growth, 541-565
pressure, 476-482
procedures, 358-359
single crystals, 506-519
spherulitic, kinetics, 458-460
spherulitic, theory of, 460-466
theory of, 541-565
thermodynamics, 587-592
under pressure, 476-480
Crystallographic shear (CS) structures, 173-222, 227-229
block structures, 201-222
composition, 178-179
disorder in block structures, 210-222
MoO_3 structures, 193-200
α-PbO_2, 179-182, 186
PdF_3 structures, 179-182
ReO_3 structures, 177-178, 193-197, 201
TiO_2, 179, 182-193
two-dimensional, 201-222
Curved polymer crystals, 423-435

Davydov splitting, 625-626, 628, 664-665
Defects
extended, 168-248
point, 167-168
Wadsley, 169, 181-182, 195, 199, 210
Degree of polymer crystallinity, 355-357, 524-525
Deposition of metals films, 11-19
Diselenides, 124-144
Disorder in block structures, 210-222
Disulfides, 124-144
DNA, 514

Electrical properties of amorphous films, 30-32
Electrodeposition, 16-17
Electrolytes, solid, 242-248
Electronic structure of glasses, 316-318

Energy transport in anthracene, 631-645
  singlet excitons, 632-637
  triplet excitons, 638-645
Ethylene–propylene copolymers, crystals, 417-419
Excitons
  annihilation, 636, 638-644, 655-656
  diffusion, 633-637, 643-644, 651-653
  photoionization, 656-658
  singlet, 624-627, 632-637, 656-658, 664
  theory of, 661-665
  triplet, 627-629, 638-645, 664
Extended defects, 167-248
  crystallographic shear structures, 173-223
  fluorite structures, 223-238
  NaCl structures, 238-241
  observation of, 170-173
  solid electrolytes, 242-248
Extended ordered metastable phases, 56-57

FeO phase, 240-241
Fibrils, 442-472, 519-528
Film preparation, 11-19
Fluorescence in anthracene, 627, 629-631, 634-645
Fluorite structures, 223-238
  pyrochlore phases, 234-236
  V_3O_8, 227-231
Fold period, 541-565, 584-587, 592-597
Fold surfaces, 397-416, 528-531, 537-540
Fringed micelle model, 504-506

Ga, amorphous films, 24
Ge, amorphous, 29-30, 304, 317-318
GeO_2 glasses, 302-303
Glass-ceramic materials, 325-329
Glasses, 293-330
  alkali aluminosilicate, 303
  atomic structure, 295-306
  B_2O_3 structures, 299, 301-302
  crystallite model, 296
  electronic structure, 316-318
  formation, 318-322
  GeO_2, 302-303
  glass-ceramic materials, 325-329
  irradiation effects, 305-306
  macrostructure, 322-324
  monoxides, structures, 303-305
  nucleation and growth, 311-318
  organic, 320-321
  oxides, structures, 298-303
  pentagonal-ring model, 297-298
  phosphate, 302
  pressure effects, 305-306
  random-network model, 296-297
Glasses *(cont'd)*
  semiconductors, 316-318
  SiO_2 structures, 299-302
  spinodal decomposition, 311-318
  submicrostructure, 306-316
  thermal history, 305-306
Glass transition, 294
Graphite intercalation compounds, 106-124
  alkali metal, 107-110
  amines, 110-111
  electrical properties, 115-120
  electronic structure, 115-120
  halogens, 111
  magnetic properties, 121-124
  metal halides, 111
  order–disorder transitions, 111-112
  reaction mechanisms, 112-115
  superconductivity, 108, 120
  transport properties, 115-120

Hardness, 276-279
Hexaborides, 96-106
Hubbard models, 685-687, 689, 691, 700-701, 706-708, 715, 721, 726, 728-731, 744, 753-758
Hydride interstitial phases, 253-284

Icosahedral groupings, 95-96
Inclusion compounds, 89-155
  boron compounds (*see also* Boron compounds), 95-106
  clathrates, 90-95
  intercalation compounds (*see also* Intercalation compounds), 106-148
  Tungsten bronzes, 148-155, 216-222
Intercalation compounds
  chalcogenide (*see also* Chalcogenide intercalation compounds), 124-144
  graphite (*see also* Graphite intercalation compounds), 106-124
  halide, 144-148
Intercrystalline links, 472-476
Intermediate alloy phases, 48-61
  crystal chemistry, 51-57
  crystal structure, 50-51
  extended ordered metastable phases, 56-57
  Hume-Rothery phases, 52-53
  inter-B-metal phases, 53-55
  inter-transition-metal phases, 55-56
  stoichiometric phases, 56
Interstitial carbides, 259-284
Interstitial compounds (*see* Interstitial phases)
Interstitial hydrides, 253-284
Interstitial nitrides, 253-284

Interstitial phases, 253-284
bonding, 283-284
carbides, 253-284
crystallography, 255-268
diffusion, 283
electrical resistivity, 280-281
hardness, 276-279
hydrides, 253-284
melting points, 272-273
nitrides, 253-284
ordered vacancy structures, 262-264
phase diagrams, 268-271
polymorphism, 266
superconductivity, 281-283
ternary phases, 267-268
thermal expansion, 279-280
thermodynamic properties, 273-276
Ionic conductivity, 152, 242-248
Ion-radical crystals (*see* Charge-transfer complexes)
Ion-radical dimer, 690-697
Isotactic polymers, 345

LaB_6, 103-104
Lamellae, 362-441, 528-597
fold surfaces, 397-416, 528-531, 537-540
growth, 362-441
growth, theory of, 541-565
lateral growth habits, 385-397, 404-423
polymer crystals, 362-441
surface energy, 589-590
surface free energy, 528-529, 531, 537-540
thickening, 531-536
thickness, 455-456, 528-531, 584-587
thickness, theory of, 541-565
twist, 352-353
Layered chalcogenides (*see also* Chalcogenide intercalation compounds), 124-144
Layered compounds (*see* Intercalation compounds)
Layered halide intercalation compounds, 144-148

Magnéli phases, 216, 227-228
Magnetic phases, 169
Màgnetic properties of amorphous films, 32-34
Melt crystallization, 441-480, 519-526
Melting of polymers, 531-537
Metal clathrates, 90-95
Metal films, deposition, 11-19
Metastable Hume-Rothery phases, 52-53
Metastable phases, 1-80
abnormal spherically close-packed, 46-48
alloys, 48-61
applications, 78-79
Metastable phases *(cont'd)*
elemental, 36-48
experimental methods for preparation of, 11-19
intermediate alloy, 48-61
pseudomorphic structures, 45-46
relation to high-pressure phases, 58-61
solid solutions (*see also* Metastable solid solutions), 61-75
structural considerations, 9-10
thermodynamics, 3-9
Metastable solid solutions, 61-75
characterization, 62-64
crystal chemistry, 64-75
formation, 62-64
solid solubility, 61-62
Mobility, carriers in anthracene, 645-648, 665-667
Molecular crystals, 615-667, 679-758
anthracene (*see also* Anthracene), 615-667
charge-transfer complexes (*see also* Charge-transfer complexes), 679-758
donors and acceptors, 679-758
Monoxides, 303-305
MoO_3 structures, 193-200

NaCl structures, extended defects in, 238-241
Nitride interstitial phases, 253-284
Nucleation and growth in glasses, 311-318
Nylon-6.6
chain structure, 340
crystal structure, 353-354, 405-413
Nylon-6.10, spherulites, 444, 519

Octahedral groupings, B compounds, 96-103
Optical absorption
anthracene, 623-629
singlet excitons, 624-7
triplet excitons, 627-629
Order–disorder transitions, 111-112
Organic glasses, 320-321
Oxides, complex, 167-248

α-PbO_2 structures, 179-183, 186
PdF_3 structures, 179-182
Phosphate glasses, 302
Photoionization of excitons, 656-658
Polyacrylonitrile crystals, 393-394
Polyamides (*see also* Nylon), crystals, 405-413
Poly(chlorotrifluoroethylene)
crystals, 395, 424-426, 431-435
growth-rate data, 579
melting, 535
morphology, 353

Polyethylene
chain folding, work of, 539, 591
chemical structure, 342
crystallized under pressure, 477, 479
crystals, 365-366, 370-376, 382, 384-391, 397-404, 435-437
crystal structure, 348
degree of crystallinity, 522-524
growth-rate data, 574-581
homogeneous nucleation, 599-604
lamellae, 521, 532-534
melting, 532-534
single crystals, 507-512
spherulites, 449, 451-453, 473-475, 519
Poly(ethylene terephthalate) single crystals, 517-518
Poly(L-glutamic acid), 514-516
Polymer morphology, 335-481, 497-604
chain folding, 362-441, 497-604
crystallinity, 338-357, 497-604
crystallization from solution, 357-441, 503-528
fibrils, 442-472, 519-528
fringed micelle model, 504-506
intercrystalline links, 504-505, 522
lamellae, 362-441, 528-597
melt crystallization, 441-480, 519-526
solution crystallization, 357-441, 503-528
spherulites, 336, 442-480, 519-526
tie molecules, 504-505, 522
theory, 541-565
Polymers, 335-667
addition, 342-343
atactic, 345
block copolymer, 341
copolymers, 340-341
crystallized from melt, 519-526, 441-480
crystallized from solution, 357-441, 503-528
isotactic, 345
melting behavior, 531-537
morphology (*see* Polymer morphology)
single crystals, 506-519
spherulitic (*see* Spherulites)
stereoregularity, 344-346
syndiotactic, 345
Poly(4-methylpentene-1)
crystals, 368-369, 425-429, 432-435
single crystals, 514-516
spherulites, 453-454, 469-470
Polyoxymethylene crystals, 367, 369, 377-383, 392-393, 425-426, 429-435
Polypeptides, 514
Polypropylene crystals, 438-439
Polystyrene
crystals, 396
spherulites, 464-465
Polystyrene, isotactic, growth-rate data, 581-582
Pressure crystallization of polymers, 476-482
Pseudomorphism, 45-46
Pyridine intercalation compounds, 134-144
Pyrochlore phases, 234-236

Quench-cooling, 1-80

Radius ratio, 253-254, 258-259
$RbAg_4I_5$, 246-247
ReO_3 structures, 177-178, 193-197, 201
Rubidium silver iodide, 246-247
Rutile (*see* TiO_2)

Semiconductors
glassy, 316-318
layered chalcogenide, 126-127
Shear, crystallographic (*see* Crystallographic shear)
Si, amorphous, 29-30, 304, 317-318
Silver beta-alumina, 246
Silver oxide clathrates, 90-95
Singlet excitons, 624-627, 632-637, 656-658, 664
SiO_2 glasses
$BaO-SiO_2$ system, 307-310
structure, 299-302
SmB_6, 104-106
Sodium beta-alumina, 244-245
Solid electrolytes, 242-248
β-Al_2O_3, 244-246
calcia-stabilized zirconia, 242-243
chalcogenides, 246-248
halides, 246-248
$RbAg_4I_5$, 246-248
Solid solubility, 61-62
Solid solutions, supersaturated, 61-75
Solution crystallization of polymers, 357-441
Solutions, solid, metastable (*see* Metastable solid solutions)
Spherulites, 336, 442-480, 519-526
intercrystalline links, 472-476
kinetics, 458-460
nucleation and growth of spherulites, 466-472
observation of, 446-457
tie molecules, 472-476
Spherulitic crystallization (*see* Spherulites)
Spinodal decomposition in glasses, 311-318
Splat cooling, 17

Sputtering, 13-16
Stereoregularity, 344-346
Superconductivity, 39, 93-94, 103, 108, 120, 130, 137-142, 149, 152-154, 281-283
Supersaturated solid solutions, 61-75
Syndiotactic polymers, 345

β-Ta, 40-44
TCNQ, 683-685, 687-689, 692, 694, 705, 707, 710, 712, 714, 720-739, 741-743
Tetracyanoquinodimethane (*see* TCNQ)
Thermodynamics of chain folding, 528-541
Thermodynamics of metastable phases, 3-9
Tie molecules, 472-476
TiO phase, 238-240
TiO_2 structures, 179, 182-193
Transformation kinetics of amorphous films, 35-36
Transition, glass, 294
Transition-metal oxides, 173-222, 148-155
Traps, 648-650
Triplet excitons, 627-629, 638-645, 664
β-Tungsten, 37-40
Tungsten bronzes, 148-155, 216-222
  bonding, 152
  crystal structures, 149-152
  disordered systems, 216-222
  ionic conductivity, 152
  magnetic phases, 216
  Nb_2O_5–WO_3 system, 216-222
  superconductivity, 149, 152-154

Vinyl polymers
  hydrocarbons, crystal structure, 348-352
  structure, 344-345
VO phase, 240
V_3O_8 structures, 227-231

β-W, 37-40
Wadsley defects, 169, 181-182, 195, 199, 210

Zirconia, calcia-stabilized, 242-244

255092

UNIVERSITY OF VICTORIA
Library
VICTORIA, B.C.

ISBN 0-306-35053-X